frontiers | Research Topics

Cohesive sedimentary systems: Dynamics and deposits

Edited by
Andrew James Manning, Claire Chassagne and Daniel R. Parsons

Published in
Frontiers in Earth Science

ISSN 1664-8714
ISBN 978-2-8325-4377-1
DOI 10.3389/978-2-8325-4377-1

About Frontiers

Frontiers is more than just an open access publisher of scholarly articles: it is a pioneering approach to the world of academia, radically improving the way scholarly research is managed. The grand vision of Frontiers is a world where all people have an equal opportunity to seek, share and generate knowledge. Frontiers provides immediate and permanent online open access to all its publications, but this alone is not enough to realize our grand goals.

Frontiers journal series

The Frontiers journal series is a multi-tier and interdisciplinary set of open-access, online journals, promising a paradigm shift from the current review, selection and dissemination processes in academic publishing. All Frontiers journals are driven by researchers for researchers; therefore, they constitute a service to the scholarly community. At the same time, the *Frontiers journal series* operates on a revolutionary invention, the tiered publishing system, initially addressing specific communities of scholars, and gradually climbing up to broader public understanding, thus serving the interests of the lay society, too.

Dedication to quality

Each Frontiers article is a landmark of the highest quality, thanks to genuinely collaborative interactions between authors and review editors, who include some of the world's best academicians. Research must be certified by peers before entering a stream of knowledge that may eventually reach the public - and shape society; therefore, Frontiers only applies the most rigorous and unbiased reviews. Frontiers revolutionizes research publishing by freely delivering the most outstanding research, evaluated with no bias from both the academic and social point of view. By applying the most advanced information technologies, Frontiers is catapulting scholarly publishing into a new generation.

What are Frontiers Research Topics?

Frontiers Research Topics are very popular trademarks of the *Frontiers journals series*: they are collections of at least ten articles, all centered on a particular subject. With their unique mix of varied contributions from Original Research to Review Articles, Frontiers Research Topics unify the most influential researchers, the latest key findings and historical advances in a hot research area.

Find out more on how to host your own Frontiers Research Topic or contribute to one as an author by contacting the Frontiers editorial office: frontiersin.org/about/contact

Cohesive sedimentary systems: Dynamics and deposits

Topic editors

Andrew James Manning — HR Wallingford, United Kingdom

Claire Chassagne — Delft University of Technology, Netherlands

Daniel R. Parsons — Loughborough University, United Kingdom

Citation

Manning, A. J., Chassagne, C., Parsons, D. R., eds. (2024). *Cohesive sedimentary systems: Dynamics and deposits*. Lausanne: Frontiers Media SA.

doi: 10.3389/978-2-8325-4377-1

Table of contents

frontiers in Earth Science

ORIGINAL RESEARCH
published: 19 July 2021
doi: 10.3389/feart.2021.658737

Contamination of Stream Sediment With Heavy Metals in the Awetu Watershed of Southwestern Ethiopia

Higemengist Astatkie[1], *Argaw Ambelu*[1]* *and Embialle Mengistie*[2]

[1]Department of Environmental Health Sciences and Technology, Institute of Health, Jimma University, Jimma, Ethiopia, [2]Department of Environmental Health, Hawassa University, Hawassa, Ethiopia

Surface sediment samples were collected from different streams of Awetu Watershed in southwestern Ethiopia. Sediment samples were analyzed for As, Cd, Cr, Pb, and Hg levels using inductively coupled plasma optical emission spectrometry. The heavy metal concentration ranged from 183.60 to 1,102.80 mg/kg for As (mean 623.32 ± 291.65 mg/kg), 4.40–303.20 mg/kg for Cd (151.09 ± 111.5 mg/kg), 149.20–807.20 mg/kg for Cr (375 ± 212.03 mg/kg), 485.60–3,748.80 mg/kg for Pb (2005.94 ± 954.99 mg/kg) and 3.6–5.6 mg/kg for Hg (4.64 ± 0.59 mg/kg). The mean heavy metal concentration in the streams followed the decreasing order of Pb > As > Cr > Cd > Hg. As, Cr and Pb are detected at high concentrations with values of 623.32, 375.00, and 2,005.94 mg/kg respectively. A low level of heavy concentration (3.6 mg/kg) was recorded for Hg. The contamination factor (CF) of all the studied heavy metals ranged from a low degree (CF < 1) to a very high degree (CF ≤ 6). Mainly, Dololo and Kito streams show a very high degree of contamination (CF ≤ 6) than Awetu and Boye streams. Specifically, As, Cd and Cr in the Dololo and Kito streams have significantly elevated concentrations than others. Geo-accumulation index (Igeo) shows low to moderate contamination level with As, Pb, and Hg; uncontaminated to heavily contaminated by Cr; and moderate to extreme contamination by Cd. Untreated solid waste, garages and farmlands were sources of contamination. Streams receiving wastewater effluents from teaching institutions had higher heavy metal concentrations. Dumping of electronic wastes and car washing discharges also identified as another source of pollution.

Keywords: Awetu watershed, contamination, Ethiopia, heavy metals, sediment

OPEN ACCESS

Edited by:
Daniel R. Parsons,
University of Hull, United Kingdom

Reviewed by:
Mike Rogerson,
University of Hull, United Kingdom
Venkatramanan Senapathi,
Ton Duc Thang University, Vietnam

***Correspondence:**
Argaw Ambelu
aambelu@yahoo.com

Specialty section:
This article was submitted to Sedimentology, Stratigraphy and Diagenesis, a section of the journal Frontiers in Earth Science

Received: *26 January 2021*
Accepted: *05 July 2021*
Published: *19 July 2021*

Citation:
Astatkie H, Ambelu A and Mengistie E (2021) Contamination of Stream Sediment With Heavy Metals in the Awetu Watershed of Southwestern Ethiopia. Front. Earth Sci. 9:658737. doi: 10.3389/feart.2021.658737

INTRODUCTION

Quality of water is affected by human-induced or natural activities in the upstream watershed (Sany et al., 2013). As a result of the natural flow of the water, most pollutants are drained into a one-point collection site, such as reservoirs that can serve as a sink for different pollutants (Nowrouzi and Pourkhabbaz, 2014a). Due to its potential and toxic environmental and public health effects and the ability to accumulate, heavy metal contamination of the aquatic ecosystems is becoming a potential global problem (Sharma et al., 2015).

Sediment contamination with heavy metals could be either from natural geogenic sources or sourced from anthropogenic activities (Giouri et al., 2010). The benthic environment of aquatic

ecosystems receives and absorbs heavy metals from natural weathering, erosion, industrial wastes, and atmospheric deposition (Jaishankar et al., 2014). Anthropogenic activities, such as industrial and agricultural discharges, inappropriate disposal of industrial wastes, dumping of domestic and municipal wastes, faulty drainage systems are some of the causes for heavy metal contamination of aquatic ecosystems (Hahladakis and Smaragdaki, 2013; Islam et al., 2015).

Several studies indicated that heavy metal concentration in stream sediments is relatively high due to significant anthropogenic metal loadings carried by tributary rivers (Li et al., 2011). As a result, surficial sediments may serve as a metal puddle that can release metals to the overlying water that could potentially adversely affect the riverine ecosystems (Evans et al., 2003; Reda and Ayu, 2016). It is well-known that the mobility and availability of heavy metals in aquatic environments are primarily affected by physicochemical parameters of water, such as pH, dissolved oxygen, and organic matter content (Sim et al., 2016).

Due to the absence of waste treatment facilities in cities and the discharge of wastes into the nearby water bodies, rivers located near cities are often suffering from heavy metal contamination (Giridharan et al., 2008). A study conducted by Mekonnen and his colleagues (2014) on the Akaki river that crosses Addis Ababa city showed severe contamination of the stream water with heavy metals sourced from industrial, residential, and agricultural wastes. The quality of the water gets worsened as heavy metals bioaccumulate in algal blooms in the downstream section of the water bodies where wastes are discharged from the upstream (Melaku et al., 2007).

Other studies of sediment and water pollution assessment in Ethiopia and in the region showed that the concentration of heavy metals rapidly increases when it entered Addis Ababa city (Akele et al., 2016; Aschale et al., 2016; Woldetsadik et al., 2017), Kombolcha city (north-central part of Ethiopia) (Zinabu et al., 2019), but significantly decreased downstream of the cities. This decrement of heavy metal in the downstream of the town might be due to heavy metals adsorbed into the sediment portion of the river (Khan et al., 2017). Bottom stream sediments are sensitive indicators for monitoring contaminants as they can act as a sink and a carrier for pollutants in the aquatic environment (Benson and Etesin, 2008; Asefa and Beranu, 2016). The presence and behavior of metals in the natural water is a function of the substrate sediment composition, the suspended sediment composition, and the water chemistry (Suresh et al., 2012). Heavy metals are potentially accumulated in sediments and aquatic organisms in the fresh water environment and subsequently transferred to man through the food chain. As a result the concentration of heavy metals in aquatic ecosystems are usually scrutinized by measuring their concentrations in sediments (Ekeanyanwu et al., 2010; El Bouraie et al., 2010).

Nowadays, various indices are developed to assess the level of sediment contamination and ecological risk. Geo-accumulation index (I_{geo}), enrichment factor (EF), contamination factor (CF), and pollution load index (PLI) methods have been commonly used for geochemical standardization approaches (Müller, 1979). The presence of heavy metals in stream sediments has created an alarming situation that requires immediate attention. Thus, sediment analysis plays a vital role in evaluating the aquatic environment (S. Li and Zhang, 2010). However, information on metal concentrations in stream sediments at a spatial scale along a course of streams in the urban and semi-urban environment is insignificant. Hence, this study addresses existing research gaps and provides valuable information regarding the spatial distributions of selected heavy metals in the urban rivers around the Awetu watershed catchment. This paper discusses the concentrations of heavy metals (As, Cd, Cr, Pb, and Hg) in the surface sediments of four streams around the Awetu watershed catchment, comparing with the Sediment Quality Guidelines (SQGs), and assess the heavy metal contamination using the I_{geo}, CF, and PLI methods.

METHODS AND MATERIALS

Study Area and Site Description

Awetu watershed encompasses Jimma City and the surrounding urban and semi-urban regions of southwestern Ethiopia. The streams under the Awetu watershed are receiving pollution from different sources, such as different laboratories of Jimma University, Jimma Medical Center, garages and carwashing points, untreated Jimma town municipal effluent, agricultural non-point source discharges, and animal feedlots. The watershed mainly contains four different streams, of which Awetu is the largest, which divides Jimma city into two while Dololo, Kito, and Boye are tributaries of Awetu stream. The major land-use activities in the Awetu watershed along with the site code and the coordinate points are listed in **Table 1**. Sampling sites were mapped using the ArcGIS 10.3 for Desktop (ESRI, Redlands, California, United States). Twenty surface integrated sediment samples were collected from each sampling point (**Figure 1**).

Sediment Samples Collection and Preparation

Submerged surface integrated sediment samples collected from 20 sampling stations in the urban and semi-urban streams of the Awetu watershed are used. As described by Decena et al., 2018, each sample constituted a 0–15 cm depth of sediment collected using a stainless steel bottom sampling dredge (grab sampler). Different grain size of the sediments were considered and homogenized to keep the uniformity of samples collected from each sampling stations (**Figure 2**). The grab sampler was washed with detergent and rinsed with distilled water before each use to reduce possible contamination. Sediment samples were placed in a new polyethylene zip-lock bag and placed in a cooler with ice, transported to the Environmental Health Laboratory of Jimma University within a few hours sampling, and kept at 4°C until analysis. During sample collection, a hand-held GPS was used to identify the sites (Garmin eTrex®). The sediment samples were air-dried and ground using a pestle and mortar after homogenized. Cobles, pebbles, and other coarse debris were manually removed. Finally, the grounded samples were sieved to pass through 63 μm mesh size to obtain fine-powdered

TABLE 1 | Sampling stations and their code, GPS coordinates, and major anthropogenic activities in the Awetu watershed streams.

Stream name	Site name	Site code	GPS coordinate	Major anthropogenic activities of the site
Awetu	Awetu 1	A1	36° 49′ 51.15″ E 7° 42′ 28.14″N	Agricultural activities and grazing
	Awetu 2	A2	36° 49′ 52.39″E 7 °42′ 4.03″N	Agricultural activities, grazing, washing clothes, and bathing
	Awetu 3	A3	36° 49′ 52.89″E 7° 41′ 43.38″N	Horticulture, recreational, residential and commercial, vehicle traffic, and agricultural runoff
	Awetu 4	A4	36° 49′ 57.27″E 7 °41′ 13.20″N	Washing, swimming, and fetching water for household consumption
	Awetu 5	A5	36° 50′ 5.95″E 7 °40′ 46.11″N	Vehicle traffic, washing, car washing, and seedling plantation
	Awetu 6	A6	36° 50′ 9.79″E 7 °40′ 15.47″N	High vehicle traffic, residential area, and small scale industries
Dololo	Dololo 1	D1	36° 50′ 50.67″E 7° 40′ 45.52″N	Public institutions, domestic activities, vehicle traffic, hospital, chemical and biological laboratories, and construction sites
	Dololo 2	D2	36° 50′ 41.99″E 7° 40′ 0.28″N	Car washing, small scale enterprises like garages, woodwork, and vehicle traffic
	Dololo 3	D3	36° 50′ 41.65″E 7° 39′ 44.82″N	Commercial area, high vehicle traffic, garages, gas/petro station, and seepage
	Dololo 4	D4	36° 51′ 4.81″E 7° 39′ 22.63″N	Car washing, gas/fuel station, garages, residential and commercial and seepage
	Dololo 5	D5	36° 51′ 43.74″E 7° 40′ 2.46″N	Commercial, recreational, vehicle traffic, bus park, gas/petrol station, cement stores, metal works and fabrications, and seepage
Kito	Kito 1	K1	36° 48′ 34.68″E 7° 40′ 23.97″N	Grazing, institutional wastes, waste stabilization pond, wood and metalwork enterprise, garage, car washing, agricultural activities, and bridge
	Kito 2	K2	36° 49′ 15.04″E 7° 40′ 19.80″N	Residential, commercial, garage, seepage, and agricultural activities
	Kito 3	K3	36° 49′ 32.86″E 7° 39′ 54.87″N	Residential, commercial, seepage, agricultural activities, and airport
	Kito 4	K4	36° 49′ 53.70″E 7° 39′ 31.91″N	Grazing, agricultural activities, and small scale enterprises like garages
	Kito 5	K5	36° 50′ 18.86″E 7° 39′ 1.56″N	Solid waste dump sites, horticulture, residential and vehicle traffic
Boye	Boye 1	B1	36° 50′ 46.97″E 7 °38′ 57.16″N	Car washing, vehicle traffic, residential and commercial area
	Boye 2	B2	36° 51′ 23.16″E 7° 39′ 19.66″N	Agriculture runoff, irrigation, and residential area
	Boye 3	B3	36° 51′ 44.99″E 7° 39′ 38.48″N	Irrigation, agricultural runoff, slaughterhouse, and residential area
	Boye 4	B4	36° 52′ 12.42″E 7° 39′ 42.30″N	Wetland, grazing, agricultural activities, fishing and recreational

particles and placed in a clean polyethylene zip-lock bag. The processed samples were refrigerated at −20°C until further analysis.

Analysis of Sediment Samples

A 0.25 g sediment sample was accurately weighed and placed in a dry and clean Teflon microwave digestion vessel and digested with 20 ml aqua regia (3 HNO_3:1 HCl v/v) until the solution turned colorless in an open thermostatically controlled hot plate. The digest samples were heated near to dryness and cooled to ambient temperature. The beaker walls were rinsed with 10 ml de-ionized water, and 5 ml HCl were added, mixed, and heated. After that, filtration of the sample into a 50 ml volumetric flask using Whatman No. 42 filter paper was made. Then the digest was allowed to cool and transferred into a 100 ml standard flask and filled to the mark with de-ionized water. The digested samples were subjected to metal analysis using inductively coupled plasma optical emission spectrometry (ICP-OES) (SPECTRO ARCOS Model: ARCOS FHS12, Germany). The calibration curves obtained from concentration and absorbance were used to determine the level of heavy metals of each sample. Data were statistically analyzed using the fitting of a straight line ($r > 0.999$). A blank reading was used to make a necessary correction during the calculation of concentrations.

Data Analyses

Different contamination indices were used to evaluate the findings with different standards. The contamination status of sediment was assessed based on the geo-accumulation index (I_{geo}), contamination factor (CF), and pollution load index (PLI) (Graça et al., 2002).

Contamination Factor

CF was used to determine the simple and effective tool in monitoring the level of heavy metal contamination at each site using the following formula (Graça et al., 2002).

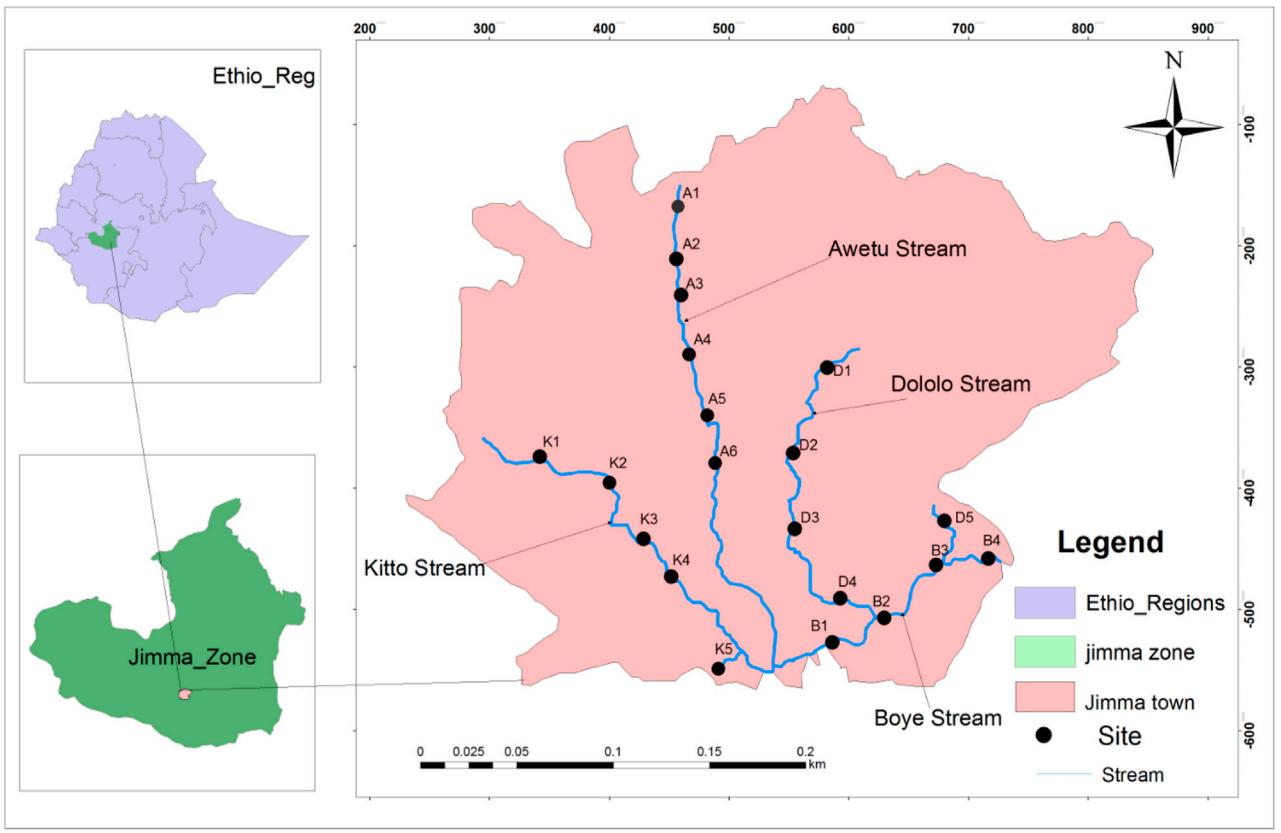

FIGURE 1 | Map showing the study area and location of sampling sites in the streams of Awetu watershed.

$$CF = \frac{C\ sample}{\text{C background}} \quad (1)$$

Where C_{sample} is the mean metal content in sample sediment, $C_{background}$ is the mean natural background value of the metal. The natural background sample was collected from A1, which is about 10 km from the main areas where maximum anthropogenic activities are performed. This area is assumed to be free from the known anthropogenic source of selected heavy metals. The ratio of the measured concentration to the natural abundance of a given metal had been proposed as the index CF being classified into four grades for monitoring the pollution of a single metal over a period of time (Ali et al., 2016): low degree (CF < 1), moderate degree (1 ≤ CF < 3), considerable degree (3 ≤ CF < 6), and very high degree (CF ≤ 6). Thus, the CF values can monitor the enrichment of a given metal in sediments over a while.

Pollution Load Index

PLI is used to evaluate sediment quality. PLI of the combined approaches of the five heavy metals were calculated according to (M. A. Islam et al., 2017). The PLI is defined as the nth root of the multiplications of the contamination factor of the target heavy metals (CF).

$$PLI = (CF1 \times CF2 \times CF3 \times \ldots \times CFn)1/n \quad (2)$$

Where CF_1 is the concentration of the first metal, CF_2 is the concentration of the second metal, CF_3 is the concentration of the third metal and CF_n is the concentration of metal nth, and n = the total number of studied heavy metals in the sample. PLI = 0 indicates excellence; PLI = 1 suggests the presence of only a baseline level of pollutants and PLI > 1 indicates progressive deterioration of the site and estuarine quality (Tomlinson et al., 1980). The PLI evaluated the overall toxicity status of the sample and its contribution to the contribution of the five metals.

Geo-Accumulation Index (I_{geo})

The degree of contamination from the heavy metals could be assessed by measuring the geo-accumulation index (I_{geo}). The index of geo-accumulation has been widely used for the assessment of sediment contamination (Islam et al., 2014). To characterize the level of heavy metal contamination in sediment samples, geo-accumulation index (I_{geo}) was calculated using the equation:

$$Igeo = Log2\left[\frac{Cn}{1.5\ Bn}\right] \quad (3)$$

Where; Cn is the content of measured metal "n" in the samples, Bn is the crustal shale background content of the metal "n", the constant of 1.5 is introduced to minimize the

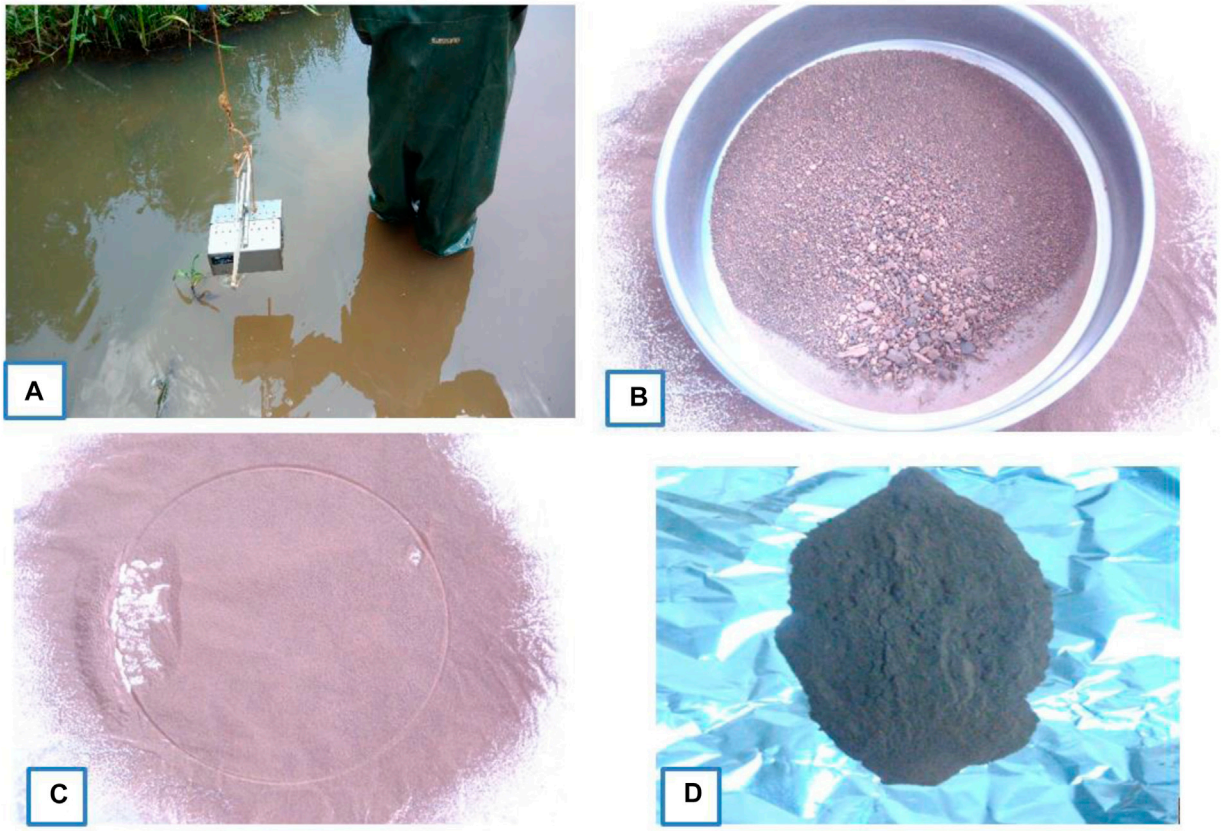

FIGURE 2 | Sample collection and preparation of sediment samples in Awetu watershed streams.

variation of background values due to lithogenic origins, and I_{geo} is a quantitative index of metal enrichment or contamination levels.

Geo-accumulation index (I_{geo}) values were interpreted as $I_{geo} \leq 0$ uncontaminated; $0 \leq I_{geo} \leq 1$—uncontaminated to moderately contaminated; $1 \leq I_{geo} \leq 2$—moderately contaminated; $2 < I_{geo} \leq 3$—moderately to heavily contaminated; $3 \leq I_{geo} \leq 4$— heavily contaminated; $4 \leq I_{geo} \leq 5$—heavily to extremely contaminated; and $5 < I_{geo}$—extremely contaminated (Müller, 1979).

Statistical Analyses

Heavy metal concentration data were log-transformed to reduce the variability and minimize outliers. R statistical package (R Core Team, 2019) was used to undertake a paired permutation test evaluating the presence of a statistically significant difference between the streams. To determine heavy metal concentrations variability among sediment samples between the urban and semi-urban sites, a one-way ANOVA was applied. Pearson's correlation was made to examine the correlation between heavy metals and selected physicochemical properties. A probability of 0.05 was considered as a level of significance.

Quality Control and Quality Assurance

The quality of the analytical results is assured by laboratory quality assurance and quality control methods. These were implemented by pre-cleaning of laboratory materials with 10% HNO_3, use of standard operating procedures, analysis of blanks, calibration with the standard, and recovery of known additions. Each heavy metal was analyzed in three replicates, and the results were presented as mean. The recovery percentages attained for the reference materials of sediment is between 97 and 120%, meeting the acceptable recovery of 80–120% recommended by the United States-EPA. In this study, the metal contents were measured according to dry weight to ensure consistency.

RESULTS AND DISCUSSION

Description of Anthropogenic Activities

Heavy metals concentration in stream sediment indicates the magnitude of pollution in water ecosystems and the capacity to accumulate contaminants (Nowrouzi and Pourkhabbaz, 2014b). Speciation and bio-availability of heavy metals in aquatic ecosystems are strongly dependent on pH, and values <4 increase the toxicity of heavy metals (Edokpayi et al., 2016). The average pH values determined varied between 5.82 and 7.60, reflecting the availability of carbonate hosts in the area (Moore et al., 2011). Mobility of metal is also affected by pH, adsorption/desorption processes, salinity, sulfur, and carbonates (Giouri et al., 2010). Bottom sediments with a higher concentration of

TABLE 2 | Heavy metal concentrations (mg/kg) of sediment samples in comparison with different world standards.

Heavy metals	Sampling stations																	Mean	StDev	[a]EC	[b]PEL	[c]WRSB
	A1	A2	A3	A4	A5	A6	D1	D2	D3	D4	D5	K1	K2	K3	K4	K5	B1	B2	B3	B4					
As	369.2	503.2	470	444	183.6	430.4	813.2	1026	1011.6	873.2	720.8	1102.8	1037.2	899.6	664	591.6	351.2	249.2	362.8	362.8	**623.32**	**284.26**	20	17	1
Cd	23.2	57.2	52.8	47.2	4.4	40.12	236.4	295.6	302	269.6	201.2	303.2	247.2	247.6	171.2	192	33.6	28	45.2	224	**151.09**	**108.67**	3	3.53	0.25
Cr	174	173.6	186.8	169.6	133.6	158.8	537.2	607.2	643.2	567.6	498.8	807.2	540.8	537.6	419.6	418.8	132.8	149.2	207.6	436	**375**	**206.66**	ND	90	55.5
Pb	952	1585.2	1472.4	1235.6	495.6	1382	2381.6	2940.8	3330.8	2908.4	2354.8	3748.8	3080.4	2767.6	2100.4	1811.6	900	880.8	1056	2744	**2005.94**	**930.81**	300	91.3	48
Hg	4.4	4.8	4.4	5.2	4.8	4.4	4.4	6	3.6	5.2	4.4	4	4.8	4.4	4	5.2	4	4.4	5.6	4.8	**4.64**	**0.57**	20	0.486	0.4

Background concentration of this study (A1). Bold values are the summary of the results as mean and StDv

[a]*European Commission*

[b]*Probable Effects Level (PEL) (Nadu et al., 2014) and Canadian Freshwater Sediment Guidelines (CFSG) (Shafie et al., 2015).*

[c]*World River Sediment Background Concentration (WRSB).*

organic matter also influence the solubility and mobility of the heavy metals in the aquatic ecosystems (Journal et al., 2010). The formation of potential mobile metal dissolved organic carbon complexes under oxidizing conditions prevents metals from co-precipitation with or adsorbing to oxides of metallic ions (Du Laing et al., 2009).

Heavy Metal Distribution

Heavy metal concentrations in sediments of the Awetu watershed catchment channelized streams with different world standards are summarised in **Table 2**. The present study exposed all the heavy metals in stream sediment were found above the permissible limit set by WHO (1993) and EU (1998) (Bhuyan et al., 2017). A significant difference in the concentration of As, Cr, Cd, and Pb between streams was identified ($p < 0.01$).

The heavy metal concentration ranged from 183.60 to 1,102.80 mg/kg for As (mean 623.32 ± 291.65 mg/kg), 4.40–303.20 mg/kg for Cd (151.09 ± 111.5 mg/kg), 149.20–807.20 mg/kg for Cr (375 ± 212.03 mg/kg), 485.60–3,748.80 mg/kg for Pb (2005.94 ± 954.99 mg/kg) and 3.6–5.6 mg/kg for Hg (4.64 ± 0.59 mg/kg). The mean heavy metal concentration in the streams followed the decreasing order of Pb > As > Cr > Cd > Hg. As, Cr and Pb are detected at high concentrations with values of 623.32, 375.00 and 2,005.94 mg/kg respectively and the minimum concentration found is Hg with a value of 3.6 mg/kg.

The heavy metals concentrations of sediment samples from individual streams showed high variability where the Dololo stream was the highest for all studied heavy metals except Hg. The concentration of heavy metals in all stream sediments are by far higher than the Sediment Quality Guidelines (SQG) values set by World Rivers Khan et al., 2005), EC and PEL (Nadu et al., 2014), USEPA water quality criteria (Hahladakis and Smaragdaki, 2013), Canadian Freshwater Sediment Guidelines (Gergen et al., 2015), and World River Sediment Background Concentration (WRSB) concentration and background concentration of this study.

The highest concentrations of As were observed in D2, D3, K1, and K2 sampling sites where it is the center of the city at which maximum anthropogenic activities are experienced. Some of the heavy metal sources of pollution are the burning of fossil fuels, the use of arsenical fungicides, herbicides and insecticides in agriculture, and wood preservatives in woodwork enterprises (Shankar et al., 2014). The highest value of As is perceived at lower pH (5.82). The study supports this; pH is the most critical factor controlling arsenic speciation under oxidizing conditions and $H_2AsO_4^-$ is dominant at a lower value (pH < 6.9) (Smedley and Kinniburgh, 2001). The interchange in oxidation and solubility of arsenic species affects the environmental behavior and subsequent transportation of arsenic species in the aquatic ecosystems (Chatterjee et al., 2017).

The highest values of Cd are found at K1, D2, and D3 sampling sites. The value at K1 could be attributed to the direct influence of effluents coming from institutional wastes, garage, car-washing, and agricultural activities where phosphate fertilizer has been in

TABLE 3 | Contamination categories based on a geo-accumulation index (I_{geo}), pollution load index (PLI), and contamination factor (CF).

I_{geo}			PLI			CF		
Class	**Value**	**Classification**	**Level**	**Value**	**Contamination**	**Level**	**Value**	**Level**
0	<0	Uncontaminated	1	CF < 1	Low degree	1	PLI = 0	Excellent
1	0–1	Uncontaminatedto moderately contaminated	2	CF = 1–3	Moderate degree	2	PLI = 1	Baseline
2	1–2	Moderately contaminated	3	CF = 3–6	Considerable degree	3	PLI >1	Progressive deterioration
3	2–3	Moderately and heavily contaminated	4	CF > 6	Very high degree			
4	3–4	Heavily contaminated						
5	4–5	Heavily to extremely contaminated						
6	>5	Extremely contaminated						

use. The values at D2 and D3 sites could be attributed to commercial waste, high vehicle traffic, garages, gas/petrol stations, and seepage from chemical laboratories and public institutions. The high level of Cd in the sediment compared to its levels in the water is to be expected for sediments that have been described as a sink or reservoir for pollutants in water (Topi et al., 2012). The concentration of Cd from all sites is significantly different from the background concentrations (23.2 mg/kg). It is also significantly differ World River Sediment background concentrations by EC (3 mg/kg), PEL and CFSG (3.53 mg/kg), and WRSB (0.25 mg/kg) (**Table 2**).

The highest values of Cr are found at the K1 sampling site, which could be attributed to the direct influence of effluents coming from institutional wastes like seepage of laboratory and electroplating (Song et al., 2000; Baig et al., 2013). The high level of Cr (VI) in sediment is expected more than water, mainly in the mobile environment but has low mobility under moderately oxidizing and reducing conditions and nearly neutral pH (Decena et al., 2018) and discharged into the nearby natural waters bodies without treatment (**Figure 3**). Such contaminated environmental resources could be hazardous to humans, wildlife, and highly toxic to aquatic life (Olafisoye et al., 2013).

As explained on **Figure 4**, the highest values of Pb was recorded in Dololo (D1-D5), and Kito (K1-K3) streams with areas near intensive anthropogenic activities like garages, gasoline stations, chemical laboratories, and construction industries (Wuana and Okieimen, 2011). The other factors contributing to higher Pb concentrations might be due to the waste generated from public and private institutions released

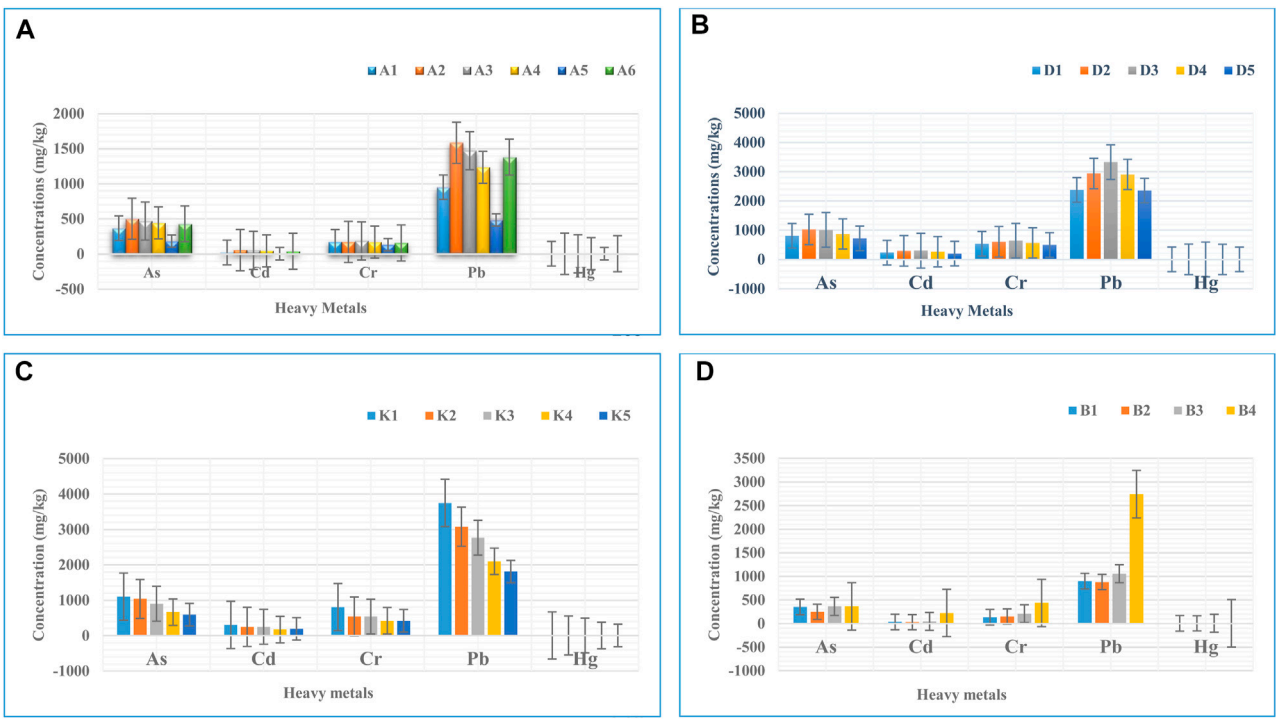

FIGURE 3 | Mean metals contents in mg/kg (mean ± standard deviations) in sediments samples collected from stations in Awetu **(A)**, Dololo **(B)**, Kitto **(C)** and Boye **(D)** streams in Awetu watershed.

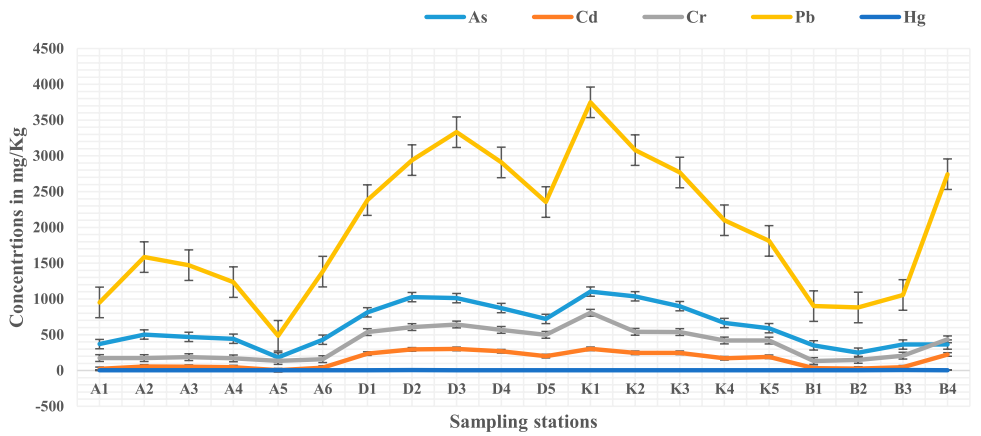

FIGURE 4 | Mean metal contents in mg/kg (mean ± standard deviations) in sediments samples of the study area.

to the adjacent water bodies without treatment and old water pipelines (Adela et al., 2012). These values exceed the background concentrations of this study (952 mg/kg), EC (300 mg/kg), PEL and CFSG (91.3 mg/kg) and WRSB (48 mg/kg) guideline values (Nadu et al., 2014). Exposure to elevated concentration of Pb through drinking water or food may damage the kidney, increase blood pressure, and anemia (Basim and Khoshnood, 2016). Pb is a threat to public health even at very low concentrations because it usually bioaccumulates in the body. Specifically, it is essentially

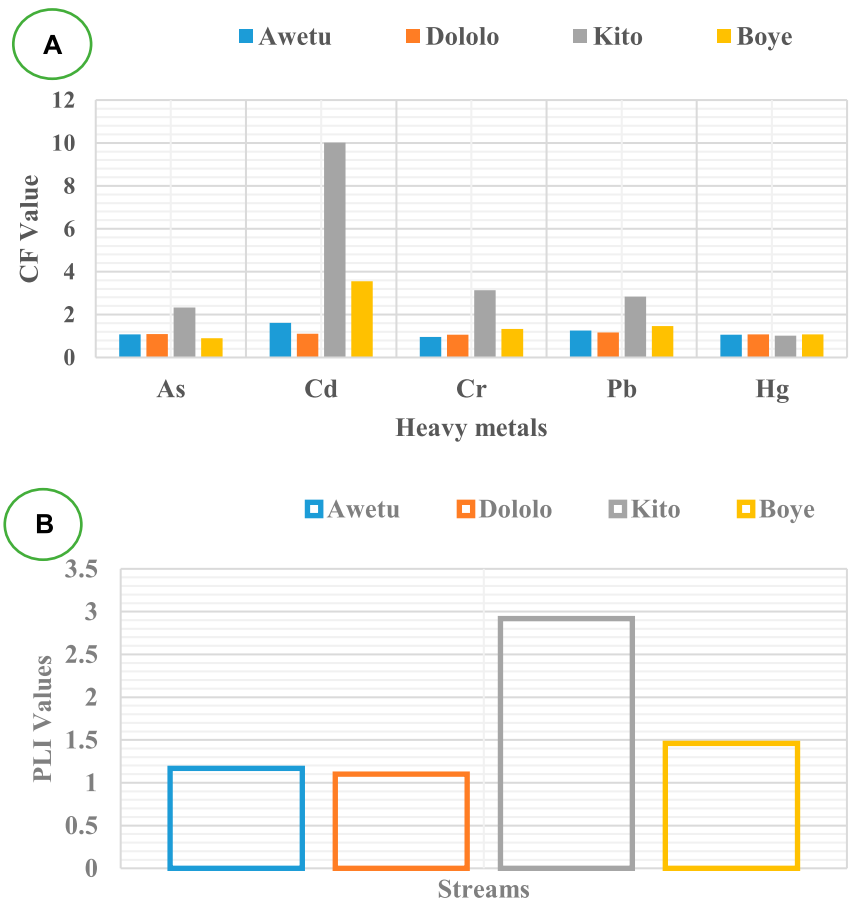

FIGURE 5 | The results of CF **(A)** and PLI **(B)** in sampling stations of the study area.

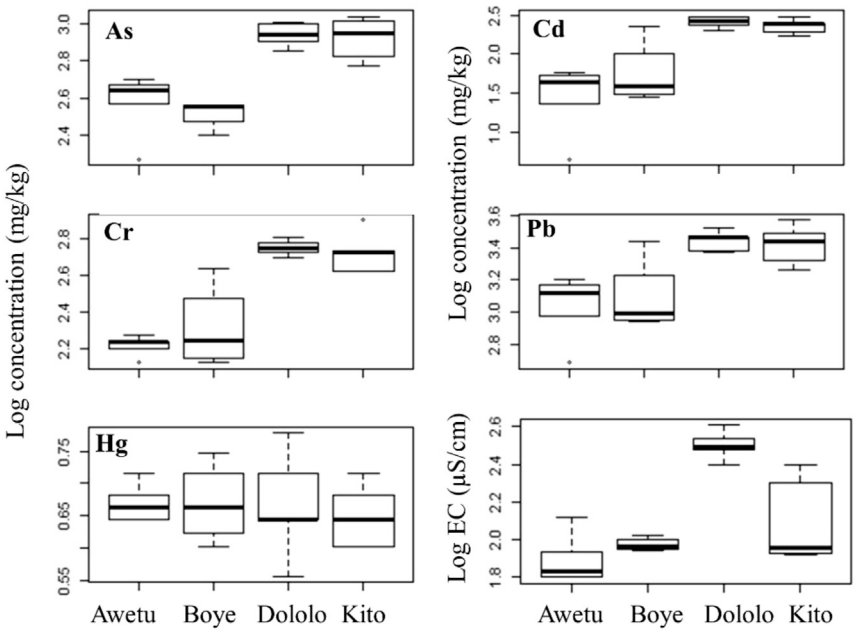

FIGURE 6 | Box and whisker plot of heavy metals concentrations and level of electrical conductivity (EC) along with the different streams in Awetu watershed.

harmful to children under six and causes mental and physical retardation (Kathuria, 2017).

The highest values of Hg is recorded D2 (6 mg/kg) followed by B3 (5.6 mg/kg) and D4 (5.2 mg/kg). This might be due to the anthropogenic emission sources of mercury, mostly from solid wastes (municipal and medical) incineration (Wang et al., 2004). As shown in **Table 2**, these values exceeded the background concentrations of this study (4.4 mg/kg), PEL (0.486 mg/kg) and WRSB (0.4 mg/kg).

The concentration of heavy metals alone does not provide sufficient information on the mobility and potential toxicity of contaminants or their potentially harmful effects on the environment, because different chemicals can inactivate and promote synergistic effects. Igeo, CF, and PLI determine the potentially harmful effect of heavy metals in the environment (**Table 3**). These indices provide a basis for assessing the effects of sediment-associated contaminants in sediment compared to the values concerning each index (Moore et al., 2011).

Contamination Level of the Tributaries Against the Different Indices

Based on the I_{geo} values, As and Pb made moderate pollution (0), Cr moderately to heavily polluted, Cd extreme pollution, Hg unpolluted to moderately polluted in the Dololo stream (**Table 4**).

The CF and PLI values are indicated in **Figure 5**. These values for heavy metals in sediments are essential to monitoring the enrichment of a given metal over time (Ali et al., 2016). The results indicate that the CF of As in all streams except Boye (0.9) shows a moderate degree of pollution ($1 \leq CF < 3$) while Awetu, Dololo, and kito streams with the values of 1.08, 1.09, and 2.33 respectively showing a moderate degree of pollution ($1 \leq CF < 3$). The CF of Cd in Awetu and Dololo streams are 1.62 and 1.1, respectively, which shows the sediment is in the status of a moderate degree of pollution ($1 \leq CF < 3$). CF of Cd in the Boye riverine wetland is 3.56, which shows a considerable degree ($3 \leq CF < 6$), and Kito stream is 10.01, which shows a very high degree of pollution ($CF \leq 6$). The CF of Cr in Awetu stream is 0.95, which indicates the sediment is in a low degree of pollution ($CF < 1$) while the CF of kito stream is 3.13, which indicates the sediment is in a considerable degree of pollution ($3 \leq CF < 6$). Dololo and Boye streams with the CF values of 1.06 and 1.33 respectively, show a moderate degree ($1 \leq CF < 3$). The CF values of Pb in Awetu, Dololo, Kito, and Boye streams are 1.25, 1.17, 2.84, and 1.47 respectively, which shows these streams are in a moderate degree of pollution ($1 \leq CF < 3$) by Pb. The CF values of Hg in Awetu, Dololo, Kito, and Boye streams are 1.06, 1.07, 1.02, and 1.07 respectively, indicating streams are in a moderate degree of pollution ($1 \leq CF < 3$).

The PLI values calculated for each stream revealed the decreasing order of contamination: Kito > Boye > Awetu > Dololo. All the studied streams were found to be polluted (PLI > 1), suggesting inputs from anthropogenic sources. PLI was found to increase in sediments downstream along with Boye and

TABLE 4 | I_{geo} values for heavy metals in surface sediments of Awetu watershed streams.

Streams	As	Cd	Cr	Pb	Hg
Awetu	−0.47 (0)	0.11 (1)	−0.64 (0)	−0.27 (0)	−0.49 (0)
Dololo	1.61 (1)	7.5 (6)	2.19 (3)	1.95 (2)	0.72 (1)
Kito	0.63 (1)	2.74 (3)	1.09 (2)	0.92 (1)	−0.56 (0)
Boye	−0.74 (0)	1.25 (2)	−0.17 (0)	−0.03 (0)	−0.49 (0)

TABLE 5 | Correlation between heavy metals, DO, EC, pH, and Turbidity in sediment (n = 20).

	DO	EC	pH	Turbidity	As	Cd	Cr	Pb	Hg
DO	1								
EC	−0.227	1							
pH	0.224	0.087	1						
Turbidity	0.444*	0.046	−0.227	1					
As	−0.040	0.467*	−0.054	0.574**	1				
Cd	−0.218	0.484*	−0.170	0.441	0.901**	1			
Cr	−0.166	0.448*	−0.268	0.513*	0.916**	0.978**	1		
Pb	−0.094	0.411	−0.172	0.555*	0.912**	0.963**	0.958**	1	
Hg	−0.241	−0.121	−0.121	−0.151	−0.209	−0.220	−0.186	−0.235	1

*, ** *Correlation is significant at 0.05 and 0.01 level respectively.*

TABLE 6 | Correlation between heavy metals in sediment (n = 20).

	As	Cd	Cr	Pb	Hg
As	1				
Cd	0.901[a]	1			
Cr	0.916[a]	0.978[a]	1		
Pb	0.912[a]	0.963[a]	0.958[a]	1	
Hg	−0.065	−0.018	−0.084	−0.103	1

[a]*Correlation is significant at the 0.01 level.*

Awetu channelized streams. The I_{geo} of As shows practically unpolluted in Awetu and Boye, which shows a very low value (<0), unpolluted to moderately polluted in Kito (0–1), and moderately polluted in Dololo (1–2).

The I_{geo} values calculated for each stream of the studied metals is also indicated in **table 4**. Accordingly, the concentration level of As indicates unpolluted to moderately polluted status in Awetu and Boye (0–1) and moderately polluted in Dololo and kitto streams (1–2). Cd indicates unpolluted to moderately polluted status in Awetu (0–1), moderately polluted in Boye (1–2), moderately to heavily polluted in Kito (2–3), and extremely polluted in Dololo streams (>5). Cr shows practically unpolluted in Awetu and Boye (<0), moderately polluted in Kito (1–2), and moderately to heavily polluted in Dololo streams (3–4). Pb shows practically unpolluted in Awetu and Boye (<0), unpolluted to moderately polluted in Kito (1–2), and moderately polluted in Dololo (1–2) streams. Hg shows practically unpolluted in Awetu, Kito, and Boye streams (<0) and unpolluted to moderately polluted in the Dololo stream (0–1). The anthropogenic pressures largely contribute to the observed heavy metal concentrations rather than the mineralogical composition of the crust along the watershed. The higher values of I_{geo} were observed in samples from the Dololo stream as compared to other streams, which might be due to the kind and magnitude of anthropogenic pressures on the areas and differences in industrial and household waste management. However, both factors are likely to be the most significant cause of the observed differences. When compared with results from other developing nations, the concentrations measured in this study are much higher than rural and urban streams (Bai et al., 2011).

The box and whisker plot (**Figure 6**) indicates that relatively higher heavy metal concentrations were identified in the Dololo and Kito streams, except for Hg. Pairwise permutation test using R statistical package (R Core Team, 2019) showed no significant concentration difference between Awetu and Boye, and Dololo and Kito streams for As, Cd, and Cr concentrations between. These streams are known to receive wastewater discharges from Jimma University compasses. For example, the Dololo stream receives untreated wastewater discharge from the main campus and the Jimma Medical Center. Similarly, Kito stream receives the wastewater effluent from the waste stabilization pond of Jimma Institute of Technology. These campuses have different laboratories which could be a source of these contaminants. The highest level of electrical conductivity at Dololo, followed by Kito streams, could be a clear indication that the sources of contamination could be from those campuses. Though the further investigation of tracing which exact laboratory source from these campuses is crucial, this might be the possible reason why these two differently located streams showed a similar pattern of heavy metal contamination.

The interrelationship among metals in sediment of the aquatic environment provided important information on sources and pathways of variables (heavy metals). The result of bivariate correlations between parameters is shown in **Table 5**, **6**. The elemental pairs, As and Cd (r = 0.901, $p < 0.01$); As and Cr (r = 0.916, $p < 0.01$); As and Pb (0.912, $p < 0.01$); Cd and Cr (0.978, $p < 0.01$); Cd and Pb (0.963, $p < 0.01$); Cr and Pb (r = 0.958, $p < 0.01$) showed significant positive correlation. This result might indicate that similar pollution sources of two or more heavy metals. The elemental association may signify that each paired elements have a common sink in the stream sediments discharged from municipal wastes and agricultural inputs (Bhuyan et al., 2017). Metal and physicochemical associations show pairs EC/As (r = 0.467, $p < 0.05$), EC/Cd (r = 0.484, $p < 0.05$) and EC/Cr (0.448, $p < 0.05$) are correlated with each other, whereas the rest are not significantly correlated. The positive correlations of heavy metals concentration of the sediment with EC might be attributed to anthropogenic impacts (Alghobar and Suresha, 2017). Turbidity has correlated with As (r = 0.574, $p < 0.01$), Cr (r = 0.513, $p < 0.05$) and Pb (r = 555, $p < 0.05$). DO and pH are negatively correlated with all studied heavy metals in the stream sediment, which significantly affects heavy metals (Sekabira et al., 2010). The concentrations of heavy metals were significantly correlated

TABLE 7 | Heavy metal concentrations in sediment samples from ou study and from other studies from river sediment.

Study area	Mean concentrations of heavy metals in the sediment (mg/Kg dw)					Source of contamination identified	References
	As	Cd	Cr	Pb	Hg		
Awetu watershed, Ethiopia	623.3	151.1	375.0	2005.9	4.6	Untreated municipal wastewater discharge and solidewaste damping sites	The present study
Tisza River and its tributaries, Serbia	[a]	[a]	11.37	19.13	[a]	Industrial activities, municipal sewage discharges, and agricultural inputs	Manojlovic (2009)
Yangtze River intertidal zone, China	[a]	0.261	78.9	27.3	[a]	Not mentioned	Zhang et al. (2009)
Yilong Lake wetland, China	15.46	0.76	86.73	53.19	[a]	Industrial discharges, coal and lead mining areas, and domestic effluents	Bai et al. (2011)
The northern part of Lake Babrukas, Lithuania	24.59	31.79	76.97	7.25	10.25	Municipal wastewater discharge	Raulinaitis (2012)
Butrinti Lagoon, Albania	[a]	0.125	56.5	31.2	0.16	Pedo-geological processes and human activity	Topi et al. (2012)
Upper Tigris River, Turkey	5.90	3.02	135.81	380.4	[a]	Copper mine plant	Varol and Şen, (2012)
Jinjiang river, China	9.6	1.6	32.2	95.1	0.08	Residential, industrial, and agricultural pollutant loads	Chen et al. (2013)
Turag, Buriganga and Shitalakha rivers, Bangladesh	35	17	695	356	[a]	From residents and household waste and sewage treatment facility	M. S. Islam et al. (2014)
Korotoa River of Bogra district urban area, Bangladesh	25	1.2	109	58	[a]	Domestic raw sewage, household waste, and industrial wastes	S. Islam et al., (2015)
Karnaphuli River, Bangladesh	81.1	2.01	20.3	43.7	[a]	Industrial effluent and domestic sewage discharge	Ali et al. (2016)
Lake Edku, Egypt	[a]	[a]	113.1	44.6	[a]	Run-off from agricultural fields	Waheshi (2017)
Jiaozhou Bay rivers, China	7.7	0.159	69.3	20.2	[a]	Industrial and domestic waste discharge	Xu et al. (2017)
Zhelin Bay, China	[a]	0.063	23.07	35.7	[a]	Not mentioned	Gu (2018)
Mustafakemalpaş, Turkey	154	8.78	516	65.6	[a]	Mining and industrial activities	Omwene et al. (2018)
Miyun District, China	15.1	0.18	31.5	33.01	[a]	Not mentioned	Pan et al. (2018)

[a]*No data.*

with pH (negatively), turbidity (positively) except for Hg (negatively).

The absence of a significant correlation between the heavy metals and pH might be due to variation in sediment composition that implies, minerals are the only factors controlling the fixation of heavy metals (Ali et al., 2016). Other studies also showed that there is a significant variation in the concentrations of heavy metals based on the type of waste discharge at different sites (Nagajyoti et al., 2010). Heavy metals originate by their natural occurrence in soil and their concentrations depend on the rock type and environmental conditions, activating the weathering processes. Our findings showed elevated heavy metal concentration than many other published studies (**Table 7**). This indicates how much the aquatic environment and probably the biota is at risk of elevated heavy metal contamination.

Besides the teaching institutions' wastewater discharge, run-off and waste discharges from different sources, such as car washing facilities, hotels, garages are directly entering the stream system. This could be the main reason for the extremely exceeded Pb concentration than the other studies done in China, Turkey, and Bangladesh. Similarly, Liao et al. (2017) found that the concentrations of heavy metals were upto 120 fold than the background concentration, which was mainly sourced from mining activities. However, for our case, multiple sources of aquatic pollution might have contributed to these very high concentrations of heavy metals.

CONCLUSION

An investigation was made on sediments of streams from Awatu watershed that showed heavy metal contamination (As. Cd, Cr, Pb, and Hg) at various degrees in southwestern Ethiopia. The concentration of the metals in sediments decreased in the order of Pb > As > Cr > Cr > Hg. The concentrations of heavy metals in the streams of Awetu watershed sediments were remarkably high and varied among sampling points. The data analyses by I_{geo}, CF, and PLI values showed contamination of the sediments by all the studied heavy metals which exceeded the limits of average world concentration. Correlation analysis shows that heavy metals have common anthropogenic pollution sources that resulted in rapid urbanization and inappropriate waste discharge. As a result, the higher concentration level of heavy metals in sediment poses a risk of water pollution during sediment disturbance or changes in sediment chemistry, which eventually intermix and transferred easily with the water in the hydraulic movement. The results suggested that special attention must be given to the issue of heavy metal pollution since a considerable portion of elements in sediments is likely to release back into the water column. Therefore, public institution and commencial centers shold properly manage their waste discharge. Besides, authorities of in low income countries should inforce waste generating institutions to have waste treatment facilities before releasing to the environment. Studying seasonal influence of heavy meatal concentration in sedimets is recommended.

DATA AVAILABILITY STATEMENT

The raw data supporting the conclusions of this article will be made available by the authors, without undue reservation.

AUTHOR CONTRIBUTIONS

HA Conceived the idea, draft the methodology, collect and analyze samples, statistical analysis of the data AA Review the methodology made statistical analysis, reviewed and edited the manuscript EM Review the methodology, reviewed and edited the manuscript.

ACKNOWLEDGMENTS

We are grateful for Jimma University for supporting data collection and laboratory work.

REFERENCES

Adela, Y., Ambelu, A., and Tessema, D. A. (2012). Occupational lead Exposure Among Automotive Garage Workers - a Case Study for Jimma Town, Ethiopia. *J. Occup. Med. Toxicol.* 7, 15–19. doi:10.1186/1745-6673-7-15

Akele, M. L., Kelderman, P., Koning, C. W., and Irvine, K. (2016). Trace Metal Distributions in the Sediments of the Little Akaki River, Addis Ababa, Ethiopia. *Environ. Monit. Assess.* 188 (7), 389. doi:10.1007/s10661-016-5387-z

Alghobar, M. A., and Suresha, S. (2017). Evaluation of Metal Accumulation in Soil and Tomatoes Irrigated with Sewage Water from Mysore City, Karnataka, India. *J. Saudi Soc. Agric. Sci.* 16 (1), 49–59. doi:10.1016/j.jssas.2015.02.002

Ali, M. M., Ali, M. L., Islam, M. S., and Rahman, M. Z. (2016). Preliminary Assessment of Heavy Metals in Water and Sediment of Karnaphuli River, Bangladesh. *Environ. Nanotechnology, Monit. Manag.* 5, 27–35. doi:10.1016/j.enmm.2016.01.002

Aschale, M., Sileshi, Y., Kelly-Quinn, M., and Hailu, D. (2016). Evaluation of Potentially Toxic Element Pollution in the Benthic Sediments of the Water Bodies of the City of Addis Ababa, Ethiopia. *J. Environ. Chem. Eng.* 4 (4), 4173–4183. doi:10.1016/j.jece.2016.08.033

Asefa, W., and Beranu, T. (2016). Levels of Some Trace Metals in Fishes Tissues, Water and Sediment at Tendaho Water Reservoir, Afar Region, Ethiopia. *J. Aquac. Res. Dev.* 07 (01), 1–6. doi:10.4172/2155-9546.1000387

Bai, J., Cui, B., Chen, B., Zhang, K., Deng, W., Gao, H., et al. (2011). Spatial Distribution and Ecological Risk Assessment of Heavy Metals in Surface Sediments from a Typical Plateau lake Wetland, China. *Ecol. Model.* 222 (2), 301–306. doi:10.1016/j.ecolmodel.2009.12.002

Baig, J. A., Kazi, T. G., Elci, L., Afridi, H. I., Khan, M. I., and Naseer, H. M. (2013). Ultratrace Determination of Cr (VI) and Pb (II) by Microsample Injection System Flame Atomic Spectroscopy in Drinking Water and Treated and Untreated Industrial Effluents. *J. Anal. Methods Chem.* 2013, 629495. doi:10.1155/2013/629495

Basim, Y., and Khoshnood, Z. (2016). Target hazard Quotient Evaluation of Cadmium and lead in Fish from Caspian Sea. *Toxicol. Ind. Health* 32 (2), 215–220. doi:10.1177/0748233713498451

Benson, N. U., and Etesin, U. M. (2008). Metal Contamination of Surface Water, Sediment and Tympanotonus Fuscatus Var. Radula of Iko River and Environmental Impact Due to Utapete Gas Flare Station, Nigeria. *Environmentalist* 28 (3), 195–202. doi:10.1007/s10669-007-9127-3

Bhuyan, M. S., Bakar, M. A., Akhtar, A., Hossain, M. B., Ali, M. M., and Islam, M. S. (2017). Heavy Metal Contamination in Surface Water and Sediment of the Meghna River, Bangladesh. *Environ. Nanotechnology, Monit. Manag.* 8, 273–279. doi:10.1016/j.enmm.2017.10.003

Chatterjee, S., Moogoui, R., and Gupta, D. K. (2017). *Arsenic Contamination in the Environment*. Cham: Springer International Publishing. doi:10.1007/978-3-319-54356-7

Chen, H., Teng, Y., Wang, J., Song, L., and Zuo, R. (2013). Source Apportionment of Trace Element Pollution in Surface Sediments Using Positive Matrix Factorization Combined Support Vector Machines: Application to the Jinjiang River, China. *Biol. Trace Elem. Res.* 151, 462–470. doi:10.1007/s12011-012-9576-5

Decena, S. C., Arguilles, M., and Robel, L. (2018). Assessing Heavy Metal Contamination in Surface Sediments in an Urban River in the Philippines. *Pol. J. Environ. Stud.* 27 (5), 1983–1995. doi:10.15244/pjoes/75204

Du Laing, G., Rinklebe, J., Vandecasteele, B., Meers, E., and Tack, F. M. G. (2009). Trace Metal Behaviour in Estuarine and Riverine Floodplain Soils and Sediments: A Review. *Sci. Total Environ.* 407 (13), 3972–3985. doi:10.1016/j.scitotenv.2008.07.025

Edokpayi, J., Odiyo, J., Popoola, O., and Msagati, T. (2016). Assessment of Trace Metals Contamination of Surface Water and Sediment: A Case Study of Mvudi River, South Africa. *Sustainability* 8 (2), 135. doi:10.3390/su8020135

Ekeanyanwu, C. R., Ogbuinyi, C. A., and Etienajirhevwe, O. F. (2010). Trace Metals Distribution in Fish Tissues, Bottom Sediments and Water from Okumeshi River in Delta State, Nigeria. *Ethiopian J. Environ. Stud. Manag.* 3 (3), 12–17. doi:10.4314/ejesm.v3i3.63959

Evans, G., Howarth, R. J., and Nombela, M. A. (2003). Metals in the sediments of Ensenada de San Simón (inner Ría de Vigo), Galicia, NW Spain. *Appl. Geochem.* 18 (7), 12–17. doi:10.1016/S0883-2927(02)00203-2

Gergen, I., Harmanescu, M., Basim, Y., Khoshnood, Z., Journal, I., Environmental, O. F., et al. (2015). No Title. *J. Hazard. Mater.* 16 (1), 1–5. doi:10.1007/978-94-007-0253-0

Giouri, A., Christophoridis, C., Melfos, V., and Vavelidis, M. (2010). ASSESSMENT OF HEAVY METALS CONCENTRATIONS IN SEDIMENTS OF BOGDANAS RIVER AT THE ASSIROS-LAGADAS AREA. 100, 63–70.

Giridharan, L., Venugopal, T., and Jayaprakash, M. (2008). Evaluation of the Seasonal Variation on the Geochemical Parameters and Quality Assessment of the Groundwater in the Proximity of River Cooum, Chennai, India. *Environ. Monit. Assess.* 143, 161–178. doi:10.1007/s10661-007-9965-y

Graça, M. A., Pardal, M. Â., and Marques, J. C. (2002). *Aquatic Ecology of the Mondego River basin Global Importance of Local Experience*. coimbra: Imprensa da Universidade de Coimbra, 576. doi:10.14195/978-989-26-0336-0

Gu, Y.-G. (2018). Heavy Metal Fractionation and Ecological Risk Implications in the Intertidal Surface Sediments of Zhelin Bay, South China. *Mar. Pollut. Bull.* 129 (2), 905–912. doi:10.1016/j.marpolbul.2017.10.047

Hahladakis, J., Smaragdaki, E., Vasilaki, G., and Gidarakos, E. (2013). Use of Sediment Quality Guidelines and Pollution Indicators for the Assessment of Heavy Metal and PAH Contamination in Greek Surficial Sea and lake Sediments. *Environ. Monit. Assess.* 185, 2843–2853. doi:10.1007/s10661-012-2754-2

Islam, M. A., Romić, M. A., and Romić, M. (2017). Trace Metals Accumulation in Soil Irrigated with Polluted Water and Assessment of Human Health Risk from Vegetable Consumption in Bangladesh. *Environ. Geochem. Health* 40, 59–85. doi:10.1007/s10653-017-9907-8

Islam, M. S., Ahmed, M. K., Raknuzzaman, M., Habibullah -Al- Mamun, M., and Islam, M. K. (2015). Heavy Metal Pollution in Surface Water and Sediment: A Preliminary Assessment of an Urban River in a Developing Country. *Ecol. Indicators* 48, 282–291. doi:10.1016/j.ecolind.2014.08.016

Islam, M. S., Han, S., Ahmed, M. K., and Masunaga, S. (2014). Assessment of Trace Metal Contamination in Water and Sediment of Some Rivers in Bangladesh. *J. Wat. ↑ Envir. Tech.* 12 (2), 109–121. doi:10.2965/jwet.2014.109

Jaishankar, M., Tseten, T., Anbalagan, N., Mathew, B. B., and Beeregowda, K. N. (2014). Toxicity, Mechanism and Health Effects of Some Heavy Metals. *Interdiscip. Toxicol.* 7 (2), 60–72. doi:10.2478/intox-2014-0009

Kathuria, P. (2017). "Video Capturing and Streaming over Ad-Hoc Networks," in 2017 International Conference on Big Data Analytics and Computational Intelligence (ICBDAC), Chirala, Andhra Pradesh, India, 23-25 March 2017 (IEEE), 1–6. doi:10.1109/icbdaci.2017.8070867

Khan, M. Z. H., Hasan, M. R., Khan, M., Aktar, S., and Fatema, K. (2017). Distribution of Heavy Metals in Surface Sediments of the bay of Bengal Coast. *J. Toxicol.* 2017, 1–7. doi:10.1155/2017/9235764

Khan, R., Israili, S. H., Ahmad, H., and Mohan, A. (2005). Heavy Metal Pollution Assessment in Surface Water Bodies and its Suitability for Irrigation Around the Neyevli lignite Mines and Associated Industrial Complex, Tamil Nadu, India. *Mine Water Environ.* 24 (3), 155–161. doi:10.1007/s10230-005-0087-x

Li, S., and Zhang, Q. (2010). Risk Assessment and Seasonal Variations of Dissolved Trace Elements and Heavy Metals in the Upper Han River, China. *J. Hazard. Mater.* 181 (1–3), 1051–1058. doi:10.1016/j.jhazmat.2010.05.120

Li, Y., Li, C.-k., Tao, J.-j., and Wang, L.-d. (2011). Study on Spatial Distribution of Soil Heavy Metals in Huizhou City Based on BP--ANN Modeling and GIS. *Proced. Environ. Sci.* 10, 1953–1960. doi:10.1016/j.proenv.2011.09.306

Liao, J., Chen, J., Ru, X., Chen, J., Wu, H., and Wei, C. (2017). Heavy Metals in River Surface Sediments Affected with Multiple Pollution Sources, South China: Distribution, Enrichment and Source Apportionment. *J. Geochemical Exploration* 176, 9–19. doi:10.1016/j.gexplo.2016.08.013

Manojlovic, D. D., Sakan, S. M., Dordević, D. S., and Predrag, P. S. (2009). Assessment of Heavy Metal Pollutants Accumulation in the Tisza River Sediments. *J. Environ. Manage.* 90, 3382–3390. doi:10.1016/j.jenvman.2009.05.013

Melaku, S., Wondimu, T., Dams, R., and Moens, L. (2007). Pollution Status of Tinishu Akaki River and its Tributaries (ethiopia) Evaluated Using Physico-Chemical Parameters, Major Ions, and Nutrients. *Bull. Chem. Soc. Eth.* 21 (1), 13–22. doi:10.4314/bcse.v21i1.61364

Moore, F., Esmaeili, K., and Keshavarzi, B. (2011). Assessment of Heavy Metals Contamination in Stream Water and Sediments Affected by the Sungun Porphyry Copper Deposit, East Azerbaijan Province, Northwest Iran. *Water Qual. Expo. Health* 3, 37–49. doi:10.1007/s12403-011-0042-y

Müller, V. G. (1979). Schwermetalle in den Sedimenten des Rheins-Veränderungen seit 1971. *Umschau* 79, 778–783. doi:10.1055/s-2007-1023171

Nadu, T., Khan, R., Israili, S. H., Ahmad, H., and Mohan, A. (2014). Heavy Metal Pollution Assessment in Surface Water Bodies and its Suitability for Irrigation Around the Neyevli Lignite Mines and Associated Industrial. *Mine Water Environ.* 24, 155–161. doi:10.1007/s10230-005-0087-x

Nagajyoti, P. C., Lee, K. D., and Sreekanth, T. V. M. (2010). Heavy Metals, Occurrence and Toxicity for Plants: A Review. *Environ. Chem. Lett.* 8 (3), 199–216. doi:10.1007/s10311-010-0297-8

Nowrouzi, M., and Pourkhabbaz, A. (2014a). Application of Geoaccumulation index and Enrichment Factor for Assessing Metal Contamination in the Sediments of Hara Biosphere Reserve, Iran. *Chem. Speciation Bioavailability* 26 (2), 99–105. doi:10.3184/095422914X13951584546986

Nowrouzi, M., and Pourkhabbaz, A. (2014b). Application of Geoaccumulation index and Enrichment Factor for Assessing Metal Contamination in the Sediments of Hara Biosphere Reserve, Iran. *Chem. Speciation Bioavailability* 26 (2), 99–105. doi:10.3184/095422914X13951584546986

Olafisoye, O. B., Adefioye, T., and Osibote, O. A. (2013). Heavy Metals Contamination of Water. *Soil , Plants around Electron. Waste Dumpsite* 22 (5), 1431–1439.

Omwene, P. I., Öncel, M. S., Çelen, M., and Kobya, M. (2018). Heavy Metal Pollution and Spatial Distribution in Surface Sediments of Mustafakemalpaşa Stream Located in the World's Largest Borate basin (Turkey). *Chemosphere* 208, 782–792. doi:10.1016/j.chemosphere.2018.06.031

Pan, L., Fang, G., Wang, Y., Wang, L., Su, B., Li, D., et al. (2018). Potentially Toxic Element Pollution Levels and Risk Assessment of Soils and Sediments in the Upstream River, Miyun Reservoir, China. *Ijerph* 15 (11), 2364. doi:10.3390/ijerph15112364

Reda, A. H., and Ayu, A. A. (2016). Accumulation and Distribution of Some Selected Heavy Metals in Both Water and Some Vital Tissues of Two Fish Species from Lake Chamo Ethiopia. *Int. J. Fish. Aquat. Stud.* 4, 6–12.

Sany, S. B. T., Salleh, A., Sulaiman, A. H., Sasekumar, A., Rezayi, M., and Tehrani, G. M. (2013). Heavy Metal Contamination in Water and Sediment of the Port Klang Coastal Area, Selangor, Malaysia. *Environ. Earth Sci.* 69 (6), 2013–2025. doi:10.1007/s12665-012-2038-8

Sekabira, K., Origa, H. O., Basamba, T. A., Mutumba, G., and Kakudidi, E. (2010). Assessment of Heavy Metal Pollution in the Urban Stream Sediments and its Tributaries. *Int. J. Environ. Sci. Technol.* 7 (3), 435–446. doi:10.1007/bf03326153

Shafie, N. A., Aris, A. Z., and Haris, H. (2015). Geoaccumulation and Distribution of Heavy Metals in the Urban River Sediment. *Int. J. Sediment Res.* 29 (3), 368–377. doi:10.1016/S1001-6279(14)60051-2

Shankar, S., Shanker, U., and Shikha (2014). Arsenic Contamination of Groundwater: A Review of Sources, Prevalence, Health Risks, and Strategies for Mitigation. *Scientific World J.* 2014, 1–18. doi:10.1155/2014/304524

Sharma, H., Blessy, B. M., and Neetu, R. (2015). The Characteristics, Toxicity and Effects of Cadmium. *Int. J. Nanotechnology Nanoscience* 3, 1–9.

Sim, S. F., Ling, T. Y., Nyanti, L., Gerunsin, N., Wong, Y. E., and Kho, L. P. (2016). Assessment of Heavy Metals in Water, Sediment, and Fishes of a Large Tropical Hydroelectric Dam in Sarawak, Malaysia. *J. Chem.* 2016, 1–10. doi:10.1155/2016/8923183

Smedley, P. L., and Kinniburgh, D. G. (2001). "Source and Behaviour of Arsenic in Natural Waters Importance of Arsenic in Drinking Water," in *United Nations Synthesis Report on Arsenic in Drinking Water* (Geneva, Switzerland: World Health Organization), 1–60. doi:10.1055/s-0030-1270755

Song, Z., Williams, C. J., and Edyvean, R. G. J. (2000). Sedimentation of Tannery Wastewater. *Water Res.* 34 (7), 2171–2176. doi:10.1016/S0043-1354(99)00358-9

Suresh, G., Sutharsan, P., Ramasamy, V., and Venkatachalapathy, R. (2012). Assessment of Spatial Distribution and Potential Ecological Risk of the Heavy Metals in Relation to Granulometric Contents of Veeranam lake Sediments, India. *Ecotoxicology Environ. Saf.* 84, 117–124. doi:10.1016/j.ecoenv.2012.06.027

Tomlinson, D. L., Wilson, J. G., Harris, C. R., and Jeffrey, D. W. (1980). Problems in the Assessment of Heavy-Metal Levels in Estuaries and the Formation of a Pollution index. *Helgolander Meeresunters* 33 (1–4), 566–575. doi:10.1007/BF02414780

Topi, T., Bani, A., Malltezi, J., and Sulce, S. (2012). Heavy Metals in Soil, Sediments, Mussels, and Water from Butrinti Lagoon (Albania). *Fresenius Environ. Bull.* 21 (10 A), 3042–3051.

Varol, M., and Şen, B. (2012). Assessment of Nutrient and Heavy Metal Contamination in Surface Water and Sediments of the Upper Tigris River, Turkey. *Catena* 92, 1–10. doi:10.1016/j.catena.2011.11.011

Waheshi, Y. A. A. (2017). Distribution and Assessment of Heavy Metal Levels Using Geoaccumulation Index and Pollution Load Index in Lake Edku Sediments, Egypt. *Ijema* 5 (1), 1. doi:10.11648/j.ijema.20170501.11

Wang, Q., Kim, D., Dionysiou, D. D., Sorial, G. A., and Timberlake, D. (2004). Sources and Remediation for Mercury Contamination in Aquatic Systems-A Literature Review. *Environ. Pollut.* 131 (2), 323–336. doi:10.1016/j.envpol.2004.01.010

Woldetsadik, D., Drechsel, P., Keraita, B., Itanna, F., and Gebrekidan, H. (2017). Heavy Metal Accumulation and Health Risk Assessment in Wastewater-Irrigated Urban Vegetable Farming Sites of Addis Ababa, Ethiopia. *FoodContamination* 4 (1), 9. doi:10.1186/s40550-017-0053-y

Wuana, R. A., and Okieimen, F. E. (2011). Heavy Metals in Contaminated Soils: A Review of Sources, Chemistry, Risks and Best Available Strategies for Remediation. *ISRN Ecol.* 2011, 1–20. doi:10.5402/2011/402647

Xu, F., Liu, Z., Cao, Y., Qiu, L., Feng, J., Xu, F., et al. (2017). Assessment of Heavy Metal Contamination in Urban River Sediments in the Jiaozhou Bay Catchment, Qingdao, China. *Catena* 150, 9–16. doi:10.1016/j.catena.2016.11.004

Zhang, W., Feng, H., Chang, J., Qu, J., Xie, H., and Yu, L. (2009). Heavy Metal Contamination in Surface Sediments of Yangtze River Intertidal Zone: An Assessment from Different Indexes. *Environ. Pollut.* 157 (5), 1533–1543. doi:10.1016/j.envpol.2009.01.007

Zinabu, E., Kelderman, P., van der Kwast, J., and Irvine, K. (2019). Monitoring River Water and Sediments within a Changing Ethiopian Catchment to Support Sustainable Development. *Environ. Monit. Assess.* 191 (7), 455. doi:10.1007/s10661-019-7545-6

Conflict of Interest: The authors declare that the research was conducted in the absence of any commercial or financial relationships that could be construed as a potential conflict of interest.

frontiers in Earth Science

ORIGINAL RESEARCH
published: 03 November 2021
doi: 10.3389/feart.2021.747567

Current- and Wave-Generated Bedforms on Mixed Sand–Clay Intertidal Flats: A New Bedform Phase Diagram and Implications for Bed Roughness and Preservation Potential

Jaco H. Baas[1]†, Jonathan Malarkey[1,2]†, Ian D. Lichtman[3]†, Laurent O. Amoudry[3], Peter D. Thorne[3], Julie A. Hope[2,4], Jeffrey Peakall[5], David M. Paterson[6], Sarah J. Bass[7], Richard D. Cooke[3], Andrew J. Manning[2,7,8], Daniel R. Parsons[2] and Leiping Ye[2,9]*

[1]School of Ocean Sciences, Bangor University, Bangor, United Kingdom, [2]Energy and Environment Institute, University of Hull, Hull, United Kingdom, [3]Joseph Proudman Building, National Oceanography Centre, Liverpool, United Kingdom, [4]Sediment Ecology, Research Group, University of St. Andrews, St. Andrews, United Kingdom, [5]School of Earth and Environment, University of Leeds, Leeds, United Kingdom, [6]Scottish Oceans Institute, School of Biology, University of St. Andrews, St. Andrews, United Kingdom, [7]School of Biological and Marine Sciences, University of Plymouth, Plymouth, United Kingdom, [8]HR Wallingford, Wallingford, United Kingdom, [9]School of Marine Sciences, Sun Yat-sen University, Zhuhai, China

OPEN ACCESS

Edited by:
Amanda Owen, University of Glasgow, United Kingdom

Reviewed by:
Roberto Tinterri, University of Parma, Italy
Kurt Eric Sundell, Idaho State University, United States

***Correspondence:**
Jaco H. Baas
j.baas@bangor.ac.uk

†*These authors have contributed equally to this work and share first authorship*

Specialty section:
This article was submitted to Sedimentology, Stratigraphy and Diagenesis, a section of the journal Frontiers in Earth Science

Received: *26 July 2021*
Accepted: *14 October 2021*
Published: *03 November 2021*

Citation:
Baas JH, Malarkey J, Lichtman ID, Amoudry LO, Thorne PD, Hope JA, Peakall J, Paterson DM, Bass SJ, Cooke RD, Manning AJ, Parsons DR and Ye L (2021) Current- and Wave-Generated Bedforms on Mixed Sand–Clay Intertidal Flats: A New Bedform Phase Diagram and Implications for Bed Roughness and Preservation Potential. Front. Earth Sci. 9:747567. doi: 10.3389/feart.2021.747567

The effect of bedforms on frictional roughness felt by the overlying flow is crucial to the regional modelling of estuaries and coastal seas. Bedforms are also a key marker of palaeoenvironments. Experiments have shown that even modest biotic and abiotic cohesion in sand inhibits bedform formation, modifies bedform size, and slows bedform development, but this has rarely been tested in nature. The present study used a comprehensive dataset recorded over a complete spring–neap cycle on an intertidal flat to investigate bedform dynamics controlled by a wide range of wave and current conditions, including the effects of wave–current angle and bed cohesion. A detailed picture of different bedform types and their relationship to the flow, be they equilibrium, non-equilibrium, or relict, was produced, and captured in a phase diagram that integrates wave-dominated, current-dominated, and combined wave–current bedforms. This bedform phase diagram incorporates a substantially wider range of flow conditions than previous phase diagrams, including bedforms related to near-orthogonal wave–current angles, such as ladderback ripples. Comparison with laboratory-derived bedform phase diagrams indicates that washed-out ripples, lunate interference ripples and upper-stage plane beds replace the subaqueous dune field; such bedform distributions may be a key characteristic of intertidal flats. The field data also provide a means of predicting the dimensions of these bedforms, which can be transferred to other areas and grain sizes. We show that an equation for the prediction of equilibrium bedform size is sufficient to predict the roughness, even though the bedforms are highly variable in character and only in equilibrium with the flow for approximately half the time. Whilst the effect of cohesive clay is limited under more active spring conditions, clay does play a role in reducing the bedform dimensions under more quiescent neap conditions. We also investigated which combinations of waves, currents, and bed clay contents in the

intertidal zone have the highest potential for bedform preservation in the geological record. This shows that combined wave–current bedforms have the lowest preservation potential and equilibrium current ripples have the highest preservation potential, even in the presence of moderate and storm waves. Hence, the absence of wave ripples and combined-flow bedforms and their primary stratification in sedimentary successions cannot be taken as evidence that waves were absent at the time of deposition.

Keywords: mixed sand–clay, tidal currents, waves, intertidal flat, bedform size predictor, bedform phase diagrams, bed roughness, preservation potential

INTRODUCTION

Bedforms are amongst the most common and important sedimentary structures in modern and ancient marine depositional environments. They characterise the roughness of the modern seabed, cause flow modification and energy dissipation, and enhance sediment suspension (e.g., Allen, 1984; Soulsby and Whitehouse, 2005; Soulsby et al., 2012). Currents, waves, and combined flows generate different types of bedform, which are used routinely as a proxy for reconstructing depositional environments and near-bed hydrodynamic processes in the sedimentary record (e.g., Allen 1984; Clifton and Dingler, 1984; Van den Berg and Van Gelder, 1993; Baas et al., 2016; Parsons et al., 2016; Collinson and Mountney, 2019). The development of accurate models for tidal and wave energy dissipation, sediment transport, flooding, and acoustic reflectivity of the seabed relies on correct predictions of bedform dimensions, shape, and plan morphology, and the parameterization of bed roughness (e.g., Soulsby et al., 2012; Aldridge et al., 2015). Existing bedform predictors, encompassing bedform stability diagrams and empirical equations based on laboratory flume and field studies, focus on specific bedform types, such as wave ripples, current ripples, and dunes (Allen, 1984; Van Rijn, 1984; Southard and Boguchwal, 1990; Van den Berg and Van Gelder, 1993; Soulsby, 1997; Kleinhans, 2005; Soulsby and Whitehouse, 2005; Camenen, 2009; Pedocchi and García, 2009a, 2009b; Nelson et al., 2013). In contrast to stability diagrams for current- and wave-generated bedforms, stability diagrams for combined-flow bedforms of the basic form shown in **Figure 1** (e.g., Arnott and Southard, 1990; Dumas et al., 2005; Kleinhans, 2005; Perillo et al., 2014) cover such a small fraction of the parameter space that their application is challenging. This is because laboratory flume investigations typically do not allow for the evaluation of more than two or three variables, and field studies of more complex combined-flow bedform dynamics are poorly integrated into these stability diagrams (Amos et al., 1988, 1999; Gallagher et al., 1998; Li and Amos, 1998; Gallagher, 2003; Hay and Mudge, 2005; Smyth and Li, 2005; Larsen et al., 2015; Wengrove et al., 2018, 2019; Wu and Parsons, 2019; Cuadrado, 2020). For example, despite being the most comprehensive flume study available in the literature, the experimental dataset of Perillo et al. (2014) is limited to co-linear waves and currents, a single sand size, and three closely spaced wave periods. In geological outcrops, the comparison of observed combined-flow bedforms with existing predictors for these bedforms is often cursory (e.g., Myrow and Southard, 1991; Myrow et al., 2002; Harazim and McIlroy, 2015; Wang et al., 2015; Taral and Chakraborty, 2017; Bádenas et al., 2018; Isla et al., 2018), possibly because the existing stability diagrams for combined-flow bedforms use different bedform terminologies and do not include all the bedform types recognised in nature (e.g., ladderback ripples; Klein, 1970).

A better understanding of the hydrodynamic conditions required to form current-dominated, wave-dominated, and combined-flow bedforms requires field measurements that integrate methods to record hydrodynamics, sediment dynamics, biogenic effects, and bedform development. To cover a parameter space that flume experiments cannot mimic, such measurements should include time-series of all variables that are known to affect the shape, size, and plan morphology of bedforms, i.e., sediment size, physical and biological cohesion, flow depth, bed shear stress, angle between wave and current, suspended sediment concentration, bedform migration rate, and adaptation time of bedforms in waning and waxing flow.

From a geological perspective, the shape and size of bedforms, and their primary stratification patterns, are essential for interpreting the relative importance of waves and currents in the depositional environment. Up to now, this has focussed mainly on hydrodynamic conditions that result in the formation of hummocky cross-stratification (e.g., Duke, 1985; Dumas and Arnott, 2006; Tinterri, 2011), but published research in laboratories and modern environments suggest that a wider range of bedform types exists in combined flows, such as ladderback ripples and different kinds of ripple-sized and dune-sized, symmetric and asymmetric, and two-dimensional and three-dimensional bedforms (Klein, 1970; Arnott and Southard, 1990; Dumas et al., 2005; Perillo et al., 2014). Process interpretations from geological outcrops and cores require that combined-flow bedforms are preserved after their formation. Given that mixed wave–current forcing is highly variable temporally, especially in tidal environments, we hypothesise that preservation potential varies with bedform type, because some types are more common than others and because the preservation potential depends on the hydrodynamic and sediment dynamic conditions after the formation of each bedform type. Conditions expected to promote preservation are rapidly waning flows, rapid deposition of sediment on top of the bedforms, and bed stabilisation by cohesive clay and biological polymers.

The present paper uses field data from a mixed sand–mud intertidal flat in the Dee estuary (NW England, United Kingdom) collected with state–of–the–art instrumentation (**Figure 2**) and incorporates an unprecedented combination of the above controls on bedform dynamics, including variations in bed cohesion, current, wave, and combined-flow bed shear stresses, water depth, and wave–current angle. This dataset has allowed us to link equilibrium bedform size, shape, and plan morphology to flow dynamics, but also distinguish between equilibrium, relict, and non-equilibrium bedforms, based on evolutionary trends in bed morphology. The specific aims of this study were to:

1) Classify equilibrium bedform type as a function of wave, current, and combined-flow forcing, and bed material properties using a bedform phase diagram;
2) Establish the relative importance of non-equilibrium, relict, and equilibrium bedforms in a full spring–neap tidal cycle with and without wave forcing;
3) Determine the residence time and preservation potential of various wave-dominated, current-dominated, and combined-flow bedforms;
4) Make recommendation for sediment transport rate predictions and preservation potential of intertidal bedforms in modern environments and the geological record.

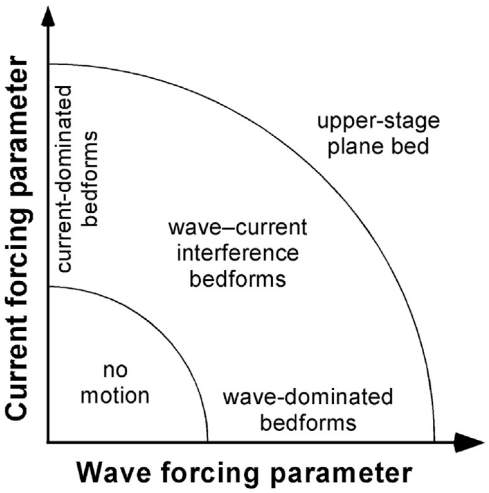

FIGURE 1 | Basic form of phase diagrams for combined-flow bedforms used in literature and in the present study. The wave and current forcing parameters can be wave velocity amplitude and depth-averaged current velocity or dimensional or non-dimensional wave and current bed shear stresses. Here, bed shear stress is preferred, because it describes near-bed bedform dynamics better than velocity. It should be noted that specific bedform types and phase boundaries may vary with sediment size and wave–current angle.

MATERIALS AND METHODS

The hydrodynamic and sediment dynamic data used in this study were acquired on a mixed sand–mud intertidal flat in the Dee Estuary near Hilbre Island, United Kingdom (**Figure 2**). The Dee Estuary is connected to Liverpool Bay, and it is funnel-shaped and macrotidal, with a mean spring tidal range of 7–8 m at Hilbre Island. Hilbre Island separates Hilbre Channel from intertidal flats west of the town of West Kirby (**Figure 2**). These tidal flats are flood-dominated and rich in fine-grained sediment (Moore et al., 2009), especially towards the landward limit of the estuary (Halcrow, 2013). Waves are mainly generated locally within Liverpool Bay; north-westerly waves have the strongest influence on the sedimentary processes in the Dee Estuary (Brown and Wolf, 2009; Villaret et al., 2011). The intertidal flats to the north-west of Little Eye (**Figure 2**) are ideal for studying bedform dynamics in mixed sand–mud, owing to the large variation in sand–mud ratio, ranging from pure sand to sandy mud, and the variable hydrodynamic forcing by currents and waves (Way, 2013; Lichtman et al., 2018; Baas et al., 2019). Three sites were studied over a spring–neap tidal cycle from neap to neap between May 21st and June 3rd, 2013, to record a time-series of bedform evolution controlled by tides, waves, and sediment dynamics. These sites were located in or near a shallow intertidal gully within 140 m of each other, differing in bed elevation by 0.19 m.

Sediment samples taken at regular intervals during the field deployment revealed a seabed dominated by medium sand with a median size of 0.227 mm. The cohesive clay fraction in this sediment ranged from 0.6 to 5.4 volume %, and the fraction of cohesive extracellular polymeric substances (EPS) was between 0.02 and 0.30 weight %, with the lowest bed clay and EPS fractions between May 21st and 29th and gradually increasing bed clay and EPS contents between May 29th and June 3rd (Lichtman et al., 2018: their **Figure 4**).

A suite of instruments on the SEDbed frame of the National Oceanography Centre was deployed at each site. The present study used water velocity data collected with an Acoustic Doppler Velocimeter (ADV; located at 0.53 m height in **Figure 2**; **Supplementary Table S1**) and measuring at 0.37 m above the sediment surface. These data were acquired at a frequency of 8 Hz, and tidal currents were extracted by applying a 5-min running mean. The ADV time-series were used to compute the equivalent linear current-only, wave-only and non-linear combined-flow bed shear stresses associated with skin friction, using the two-layer logarithmic model of Malarkey and Davies (2012) and the PUV method of Gordon and Lohrmann (2001), as elaborated by Lichtman et al. (2018). In flows where both currents and waves are present, the combined bed shear stress is affected by the angle between the wave and current directions. For a vector addition of the wave-only and current-only stresses, the maximum linear combined bed shear stress during the wave cycle, τ_{max}, is:

Eq. 1, maximum linear combined bed shear stress:

$$\tau_{max} = \left(\tau_c^2 + \tau_w^2 + 2\tau_c\tau_w \cos\varphi\right)^{0.5} \quad (1)$$

where τ_c is the current-only shear stress, τ_w is the wave-only shear stress, and φ is the angle between the wave and the current ($0 \leq \varphi \leq 90^{\circ}$). In the present paper, only these linear skin-friction stresses are considered and referred to as simply the wave, current and combined stresses. For combined flows, the threshold for

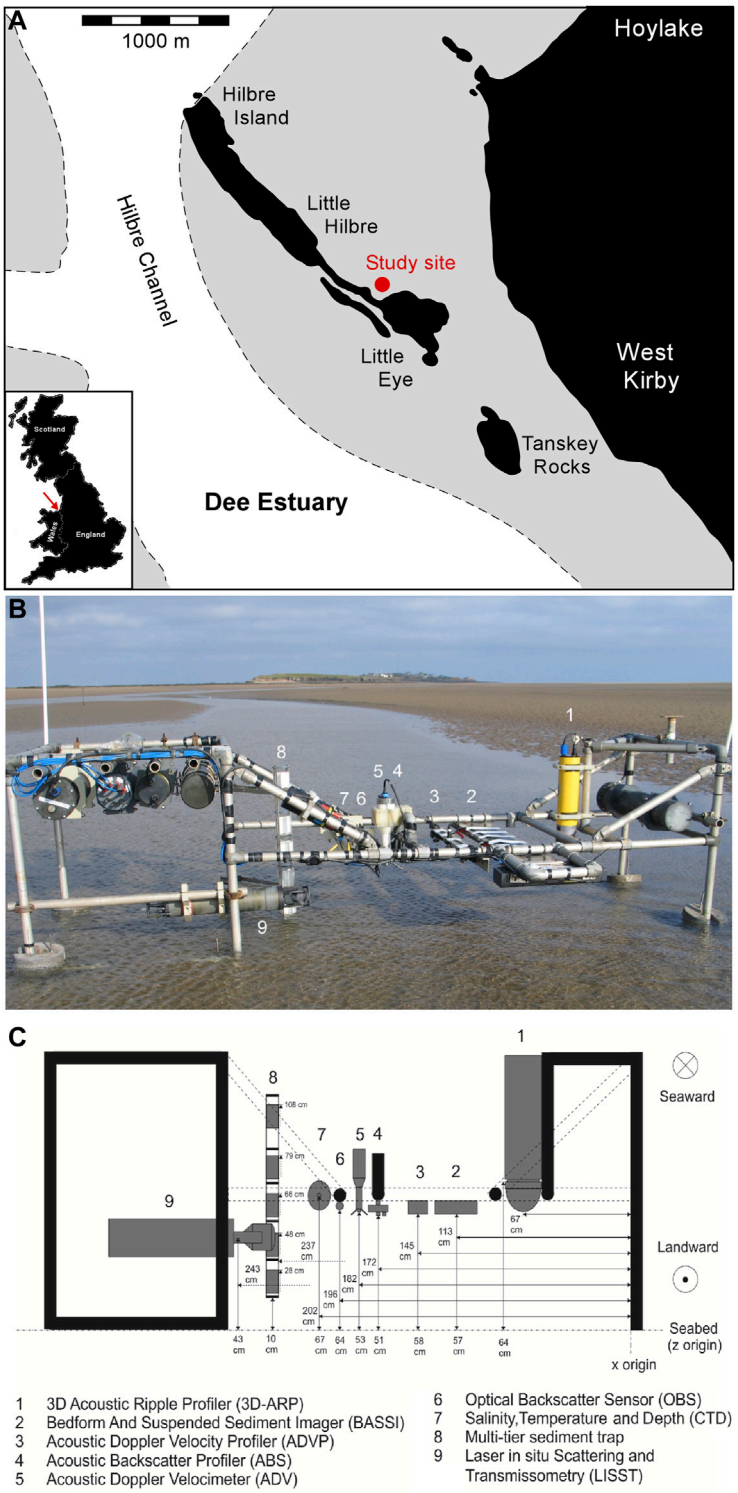

FIGURE 2 | Schematic map of the Dee Estuary around Hilbre Island **(A)**, with the main tidal channel in white and the study area located on the grey-coloured intertidal flat to the north-west of Little Eye. The four islands are defined by the area above the mean highwater mark and by any area of bedrock exposed at low water immediately below this mark. SEDbed instrument frame. looking seaward towards Little Hilbre and Hilbre Island **(B)**, and diagram of instruments on frame **(C)**. Vertical and horizontal distances in centimetres are above the sediment bed and relative to the edge of the frame, respectively.

cohesionless sediment movement corresponds to $\tau_{max} = \tau_0$, where τ_0 is the critical shear stress for movement, with $\tau_0 = 0.18$ Nm^{-2} for 0.227 mm sand (**Appendix Equation A1**). In the two wave–current directional extremes of co-linear ($\varphi = 0^{\circ}$) and orthogonal ($\varphi = 90^{\circ}$), τ_0 can thus be expressed as:

Eq. 2, critical shear stresses for sediment movement for co-linear and orthogonal waves and currents:

$$\tau_{max} = \tau_0 = \begin{cases} \tau_c + \tau_w, & \varphi = 0^{\circ}, \\ \left(\tau_c^2 + \tau_w^2\right)^{0.5}, & \varphi = 90^{\circ} \end{cases} \quad (2)$$

or for a particular current shear stress, $\tau_c = \tau_0 - \tau_w$, for $\varphi = 0^{\circ}$, and $\tau_c = (\tau_0^2 - \tau_w^2)^{0.5}$, for $\varphi = 90^{\circ}$. Thus, τ_0 requires a larger current shear stress for orthogonal than for co-linear waves and currents. All other intermediate angles ($0 < \varphi < 90^{\circ}$) lie between these two directional extremes.

The ADV also measured water pressure at 0.53 m above the seabed, which, in combination with pressure data from a Conductivity, Temperature, and Depth (CTD) system (**Figure 2**; **Supplementary Table S1**) and after correction for air pressure, were converted to water depth, following the procedure described in Lichtman et al. (2018). A 3D Acoustic Ripple Profiler (3D–ARP; **Figure 2**; **Supplementary Table S1**) provided seabed topography data. The 3D–ARP is a dual-axis, mechanically rotated, pencil beam scanning sonar operating at 1.1 MHz (Thorne and Hanes, 2002; Marine Electronics, 2009; Krämer and Winter 2016; Thorne et al., 2018). It measured a 12 m^2 area of the bed every 30 min, from which a central region of c. 1.4 m^2 was selected for analysis over the entire field deployment (**Supplementary Video S1**). The initial step in the analysis of the 3D–ARP data was to remove the large-scale bed morphology from the scans using a linear fit. The 3D–ARP scans were then corrected for the bedform orientation. Lichtman et al. (2018) found that the bedform migration was closely associated with the maximum stress in the wave cycle. Thus, the default bedform orientation was aligned with the maximum stress direction. This was a reasonable assumption for the vast majority of the bedforms in the 3D–ARP scans. However, there were exceptions. If the bedforms were relict, i.e. the maximum shear stress was below τ_0, the last above-threshold orientation was used. These orientations were determined by eye in cases where two types of bedform with different orientations were superimposed on one another. The orientations were not necessarily orthogonal to one another or aligned with the wave or current stresses, because the 3D–ARP scanning process takes longer to complete than some rapid changes in bedform orientation. Once the orientation had been decided, the bedform dimensions were determined along three fixed transects, and subsequently averaged together. The dimensions were calculated by the zero-crossing method (Van der Mark et al., 2008; Krämer and Winter 2016) once outliers greater than four standard deviations from the mean were removed. The zero-crossing method was used to locate the position of the crests and troughs, but these were also checked by eye for consistency and to ensure that the dominant dimensions were being faithfully represented. The asymmetry of the bedforms was quantified by the longer crest to trough distance divided by the total bedform length along each transect. The method applied herein to determine bedform heights, lengths and asymmetries was distinct from that of Lichtman et al. (2018), because it allowed for the measurement of separate heights and lengths for the wave-induced and current-induced parts of combined-flow bedforms.

The bedforms on the seabed were also visualised using a Bedform And Suspended Sediment Imager (BASSI; **Figure 2**; **Supplementary Table S1**). The BASSI produces an acoustic curtain over a 2D vertical slice of the near-bed water column, with centimetric resolution over intrawave and turbulence timescales (Moate et al., 2016; Thorne et al., 2018). The BASSI can thus be used to trace trains of moving bedforms and suspended sediment above these bedforms at higher temporal resolution than the 3D–ARP. In the present study, the BASSI was set to record vertical cells of 3.3 mm length. The rate of recording was 12.5 Hz, the burst length was 10 min, and the burst interval was 30 min. The analysis of the BASSI data focussed on the bedforms, to obtain an independent check of the bedform dimensions obtained with the 3D–ARP as well as a record of high-frequency changes in bed morphology.

During the field deployment, the tidal flats experienced a wide range of current, wave and combined flow conditions (**Figures 3A,B**). Maximum current stresses were largest during the spring tide, 0.7 Nm^{-2}, and up to one order of magnitude smaller during the neap tides. From May 21st to 24th, when neap tide progressed towards spring tide, waves had a strong influence on the hydrodynamics and the bedform evolution, caused by wind ranging from a moderate breeze to gale force (Beaufort scale 4–8: 5.8–17.6 ms^{-1}). Moderate waves were present at around noon on May 27th (spring tide) and after midnight on May 30th (spring tide progressing towards neap tide). On the other days, waves had little to no influence on the hydrodynamic forcing of the bedforms on the seabed. Wave period ranged from 2 to 10 s and wave height was up to 0.5 m (Lichtman et al., 2018).

LINKING BEDFORMS TO HYDRODYNAMIC DATA: OBSERVATIONS AND PROCESS INTERPRETATIONS

General

Figures 3–10, **Table 1**, **Supplementary Table S2**, and **Supplementary Video S1** provide a detailed summary of all the field data collected on the tidal flat during the spring–neap cycle between May 21st and June 3rd, 2013. **Figure 3** presents time-series of water depth (**Figure 3A**), wave and current stresses (**Figure 3B**), bedform types (**Figure 3C**), bedform length (**Figure 3D**), bedform height (**Figure 3E**), and asymmetry index (**Figure 3F**). The relative importance of currents, waves, and combined flow for the generation of these bedforms is shown in **Figures 3G,H** shows the percentage equilibrium, relict, and transitional bedform states. The wave–current angles for ladderback ripples, tile-shaped interference ripples, lunate interference ripples, and upper-stage plane beds are plotted in **Figure 3I**. **Figures 4–8** show characteristic 3D–ARP and BASSI data for selected tidal inundations, and **Figure 9** displays the main geometric properties of the equilibrium, relict, and transitional

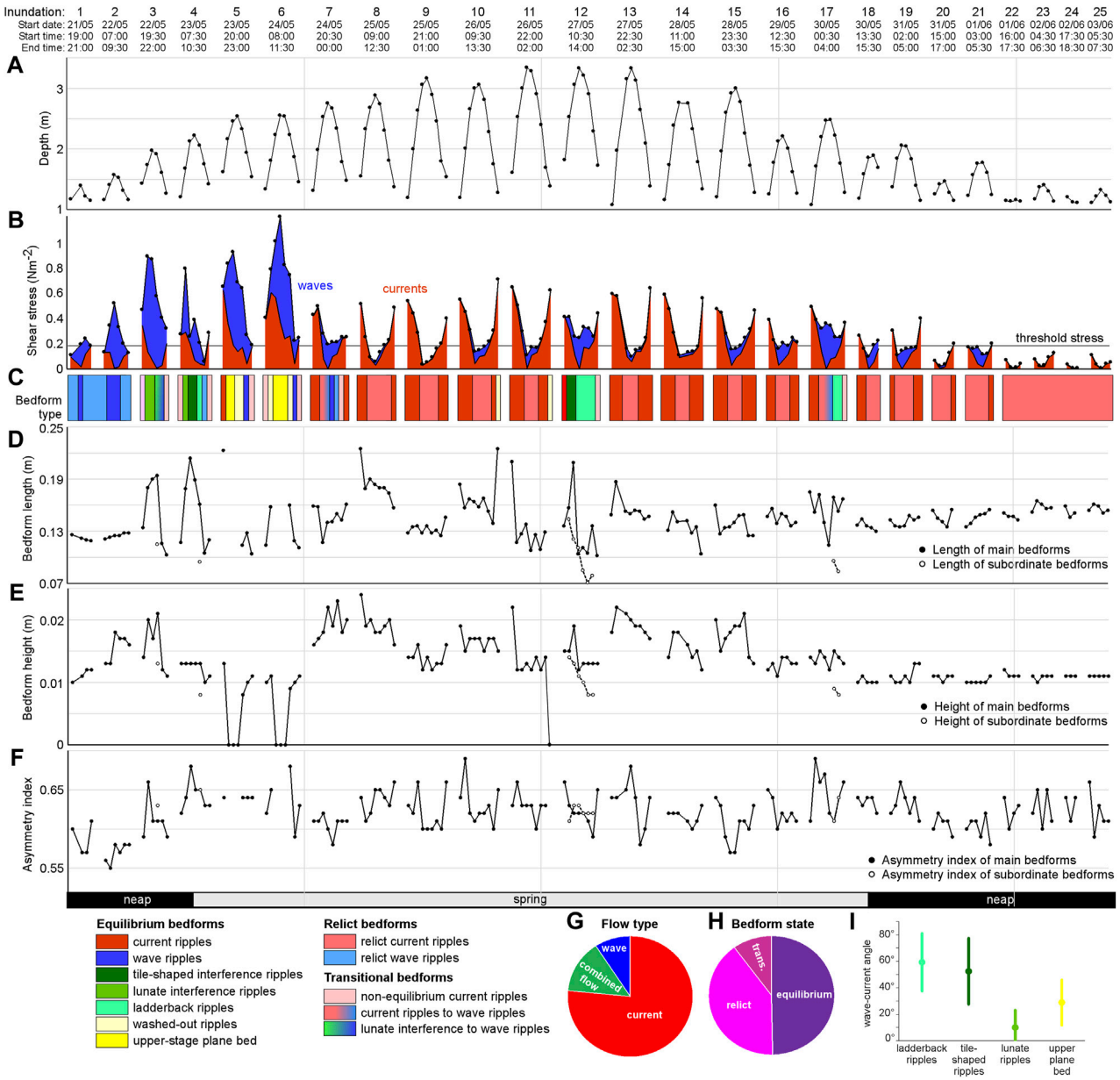

FIGURE 3 | Summary of observations during the spring–neap cycle. The dates and times for each tidal inundation shown at the top are for time-series of: **(A)** water depth; **(B)** maximum combined stress showing wave and current stress contributions; **(C)** bedform types; **(D)** bedform length; **(E)** bedform height; and **(F)** asymmetry index. The graphs at the bottom right denote: **(G)** distribution of flow types; **(H)** distribution of equilibrium, relict, and transitional bedform states, given in shades of purple; and **(I)** mean and standard deviation of wave–current angles for three types of combined-flow ripples and upper-stage plane bed. Colour legend for bedform types in **(C,I)** is shown on bottom left. **(B,C,G,I)** Wave stress and wave ripples are given in shades of blue, current stress and current ripples in shades of red, and combined-flow bedforms in shades of green. The transitional bedforms include non-equilibrium current ripples, which in turn comprise incipient and straight-crested current ripples sensu Baas (1994). Clay and EPS content gradually increased from 2 to 5% and 0.05 to 0.08%, respectively, from inundation 16 onwards (Lichtman et al., 2018).

bedform types present, as well as the characteristic hydrodynamic conditions at which these bedforms formed. The phase diagram in **Figure 10A** shows how the various bedform types are related to the wave and current stresses, and **Figure 10B** shows the equivalent for the wave velocity amplitude, U_0, and depth-averaged current velocity, $\bar{u}$, as used by Perillo et al. (2014). Whilst both the stresses and velocities are dimensional, the stresses in **Figure 10A** can more readily be made non-dimensional, e.g., by using Shields parameters (Kleinhans, 2005), since the median size of the sand particles on the bed was constant in the study area.

Tidal Inundations 1 and 2

In tidal inundations 1 (May 21st, pm) and 2 (May 22nd, am), the current stresses were below τ_0 at all times, whereas the wave stresses exceeded τ_0 around high slack water (**Figures 3A,B**). In

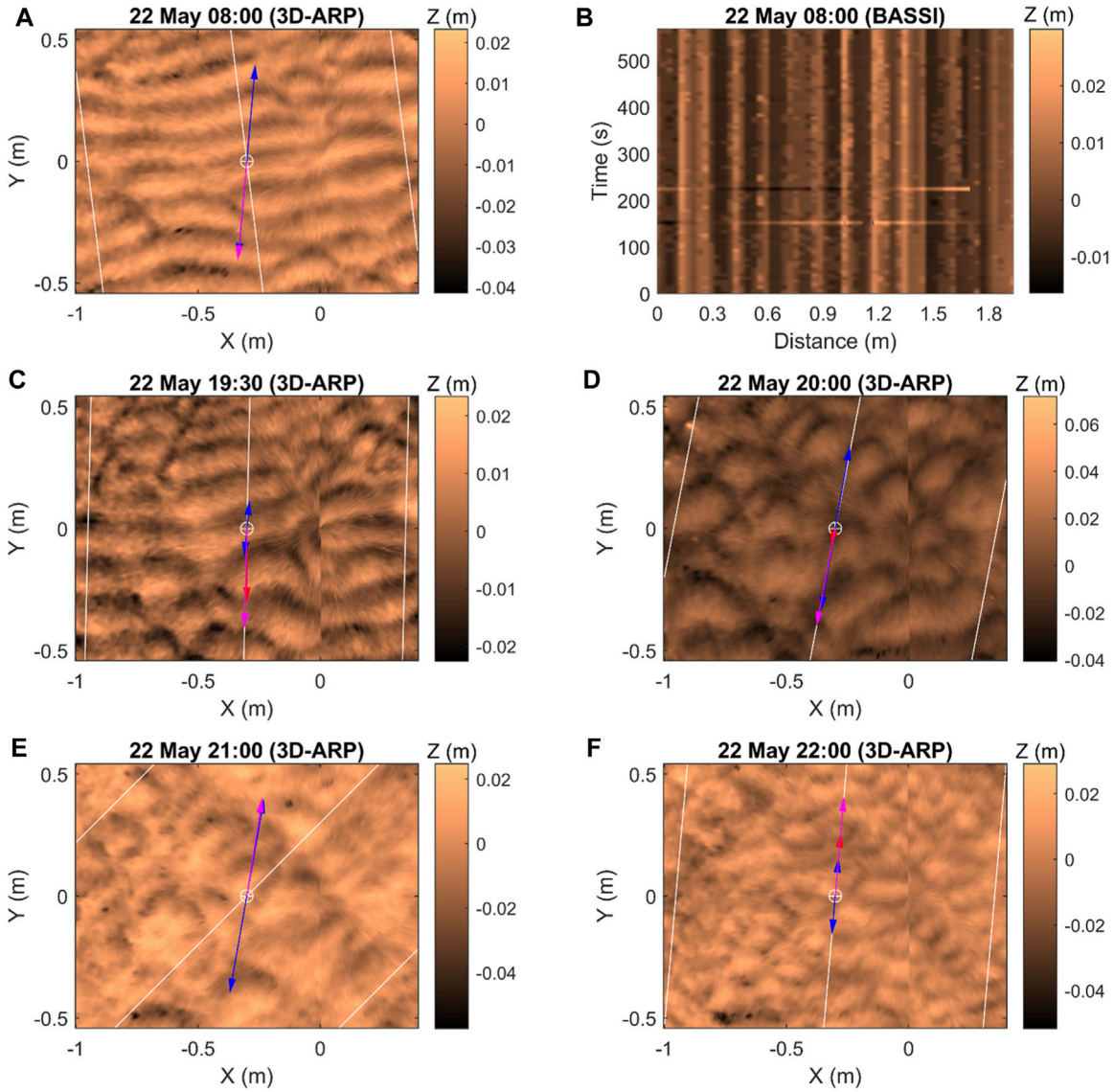

FIGURE 4 | Equilibrium wave ripples recorded by the **(A)** 3D ARP and **(B)** BASSI at high slack water in tidal inundation 2 (May 22nd, am). **(C–F)** Bedforms generated during tidal inundation 3: **(C)** Wave ripples evolving into lunate interference ripples during flood; **(D)** Lunate interference ripples during flood; **(E)** Lunate interference ripples evolving into wave ripples at high slack water; **(F)** Small incipient current ripples during ebb. Red, blue and magenta arrows indicate current, wave, and combined flow directions, respectively. The length of the arrows is a qualitative measure of the relative shear stress magnitude. White lines indicate cross-sections along which ripple heights and lengths were measured. The discontinuities in **C,D,F** relate to morphological changes that took place during the 30-min radial scanning time.

both inundations, the currents and waves were co-linear. The 3D–ARP shows small, straight-crested, near-symmetric ripples with bifurcation patterns that are typical of *wave ripples* (**Figures 4A**, **9C**, **10**; **Table 1**; Allen, 1984; Perron et al., 2018). Since the wave stress was close to zero at the start of inundation 1, these wave ripples are interpreted as relict bedforms generated by waves in an earlier inundation. During flood and ebb, when current stresses reached 0.09–0.18 Nm^{-2}, the wave ripples migrated slowly in the downstream direction (slightly inclined vertical lines in BASSI data in **Figure 4B**), possibly because these weak currents helped the combined stresses to exceed τ_0 (**Figure 3B**). Relatively high, equilibrium wave ripples were present around high slack water on May 22nd, when the wave stress reached 0.5 Nm^{-2} (**Figures 3B,C,E**), which signifies the precursor of the storm that started to affect the field site later that day. The length of the wave ripples in tidal inundations 1 and 2 was 124 mm (**Figures 3C,D**), whereas the height of these bedforms increased from 10 to 16 mm, reaching a temporary maximum of 18 mm during the period of large wave stresses in tidal inundation 2 (**Figures 3B,C,E**).

Tidal Inundation 3

Tidal inundation 3 (May 22nd, pm) experienced a peak current stress of 0.34 Nm^{-2} during flood and a peak wave stress of

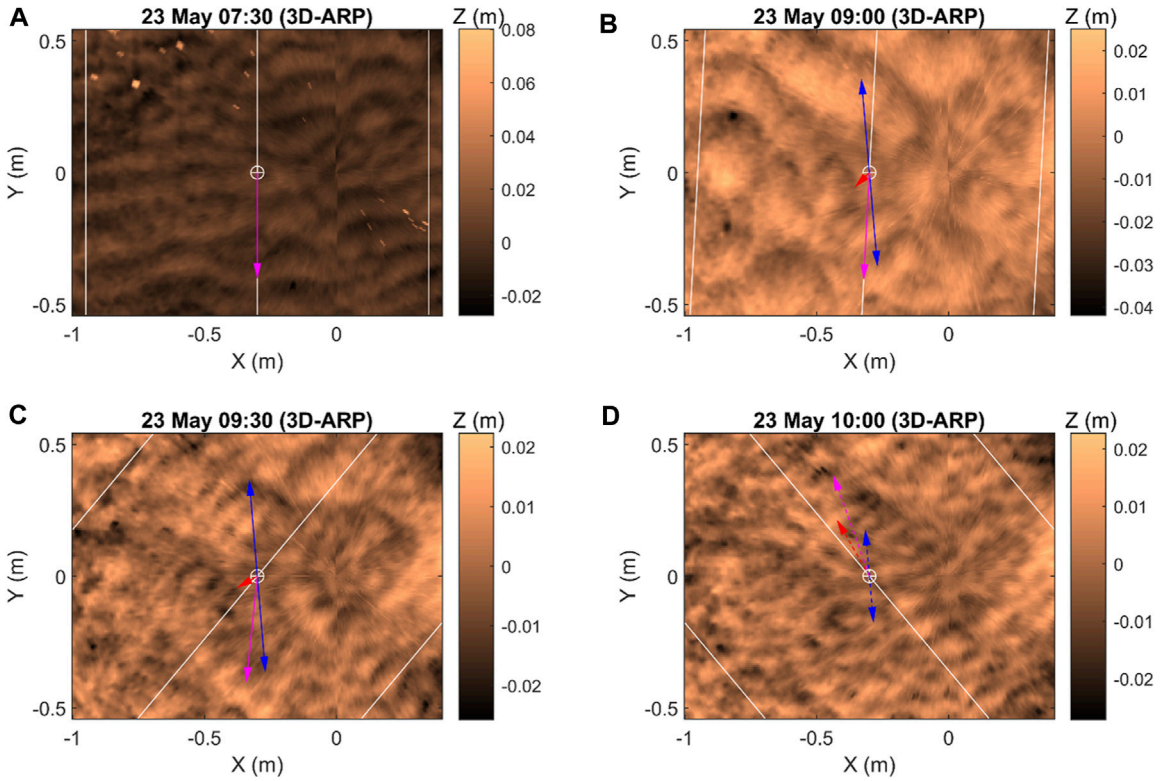

FIGURE 5 | Bedforms generated during tidal inundation 4. **(A)** Straight-crested current ripples during flood; **(B)** Relict tile-shaped interference ripples at the end of flood; **(C)** Ladderback ripples during high slack water; **(D)** Relict wave ripples with straight but discontinuous crestlines near the end of high slack water. See **Figure 4** for explanation of line colours. Dashed arrows in **(D)** denote stresses below threshold of motion.

0.8 Nm^{-2} immediately before high slack water (**Figures 3A,B**), and the currents and waves remained co-linear. Strong combined currents and waves during the flood (τ_{max} < 0.88 Nm^{-2}; **Figure 3B**) caused the two-dimensional wave ripples of inundation 2 to evolve into larger, more asymmetric bedforms with a moon-shaped plan morphology, classified as *lunate interference ripples* (**Figures 3A–F**, **4C,D**, **9F**, **10**; **Table 1**). **Figure 4C** shows that this process included an initial period in which both bedform types were present on the sediment bed. The lunate interference ripples were particularly high and long for c. 1 h around high slack water (**Figures 3C–E**, **4D**), Thereafter, when the current stress was small and the wave stress decreased, the lunate interference ripples changed back gradually to smaller wave ripples (**Figures 3B–E**, **4E**). During the ebb, these transitional bedforms formed the nucleus for the formation of *incipient current ripples* (Baas, 1994; **Table 1**), which were about half the size of the lunate interference ripples (**Figures 3A,C–E**, **4F**). The current stress was larger than the wave stress at the end of inundation 3 (**Figure 3B**), which supports the presence of these non-equilibrium current ripples.

Tidal Inundation 4

Tidal inundation 4 (May 23rd, am) reveals complex and rapidly changing hydrodynamics, which caused rapidly changing bed morphology. The wave stress was 0–0.50 Nm^{-2} during the flood, it decreased around high slack water, and waves were absent during the ebb (**Figures 3A,B**). The tidal currents rotated clockwise from south-southeast to north-west and the wave direction varied between east and south-east. The 3D–ARP recordings start with small, asymmetric, two-dimensional bedforms formed by the flood current (**Figures 3A–F**, **5A**). These bedforms resemble *straight-crested current ripples* (**Figures 9A**, **10**; **Table 1**), which probably evolved around low slack water from the incipient current ripples in inundation 3. The bed then changed to lunate interference ripples, similar to those in inundation 3 under large co-linear wave and current stresses. Thereafter, the wave stresses fluctuated between 0.06 Nm^{-2} and 0.34 Nm^{-2} (**Figure 3B**), the tidal current waned, and the wave–current angle increased to 65°. This resulted in the formation of tile-shaped bedforms that were clearly asymmetric in cross-section on the 3D–ARP and BASSI profiles, with two crest-line orientations that corresponded to the current and wave directions (**Figures 5B**, **9E**; **Table 1**). These *tile-shaped interference ripples* became relict towards the end of the flood (**Figures 3A–C**), but waves continued to reshape the bed during high slack water by forming small wave ripples in the troughs of the tile-shaped interference ripples, classified as *ladderback ripples* (**Figures 5C**, **9D**, **10**; **Table 1**; Klein, 1970). Near the end of high slack water, the ladderback ripples had evolved into wave ripples. Local remnants of the tile-shaped interference ripples caused the wave ripples to have straight but discontinuous crestlines

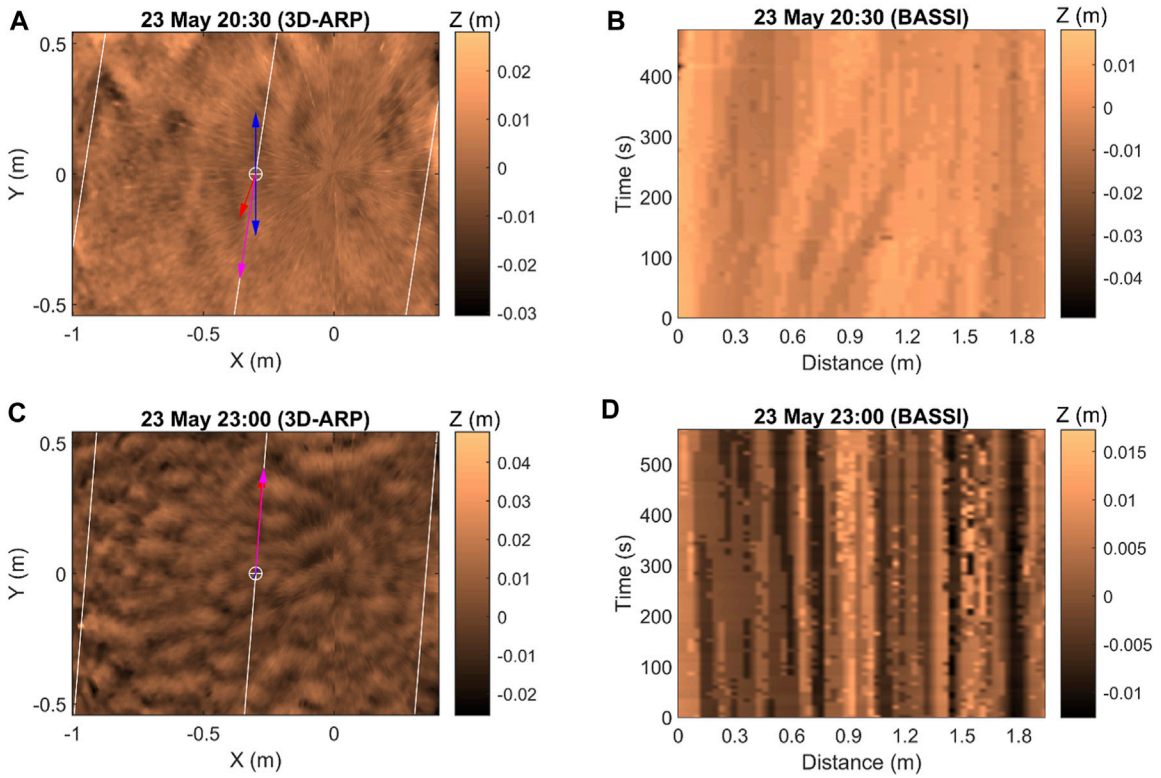

FIGURE 6 | Bedforms generated during tidal inundation 5. Upper-stage plane bed recorded by the **(A)** 3D–ARP and **(B)** BASSI during flood. The 3D–ARP image shows wave-parallel longitudinal ribbons. Slowly migrating wave ripples in the process of transforming into straight-crested current ripples, recorded by the **(C)** 3D–ARP and **(D)** BASSI during ebb. See **Figure 4** for explanation of line colours.

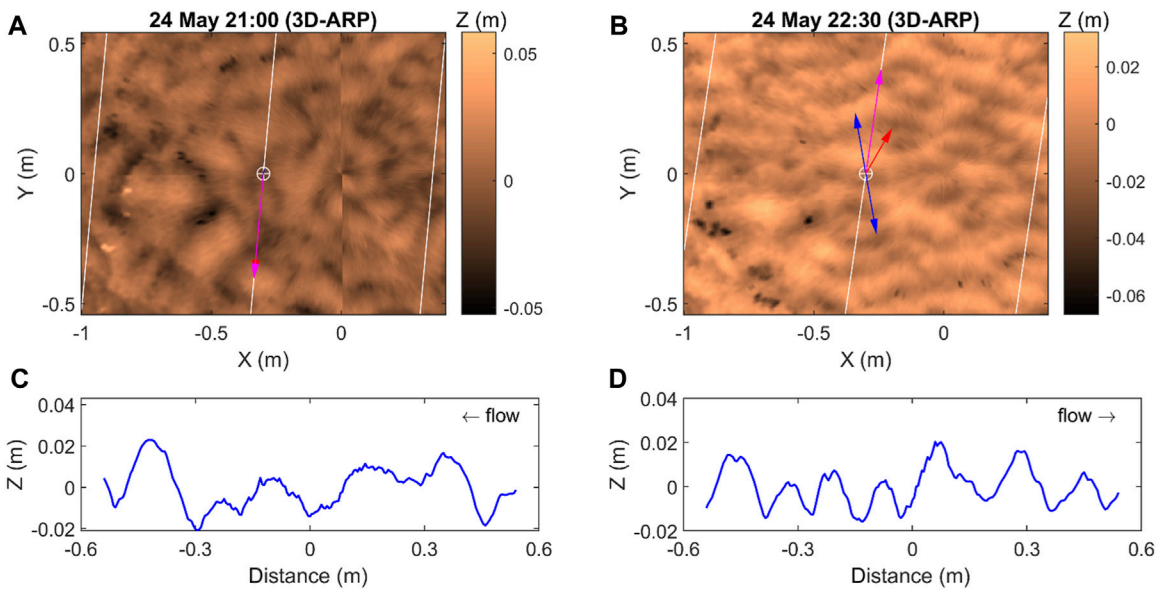

FIGURE 7 | Plan and cross-sectional views (central transect) of bedforms generated during tidal inundation 7. **(A,C)** Equilibrium linguoid current ripples during flood; **(B,D)** Equilibrium wave ripples during high slack water. See **Figure 4** for explanation of line colours.

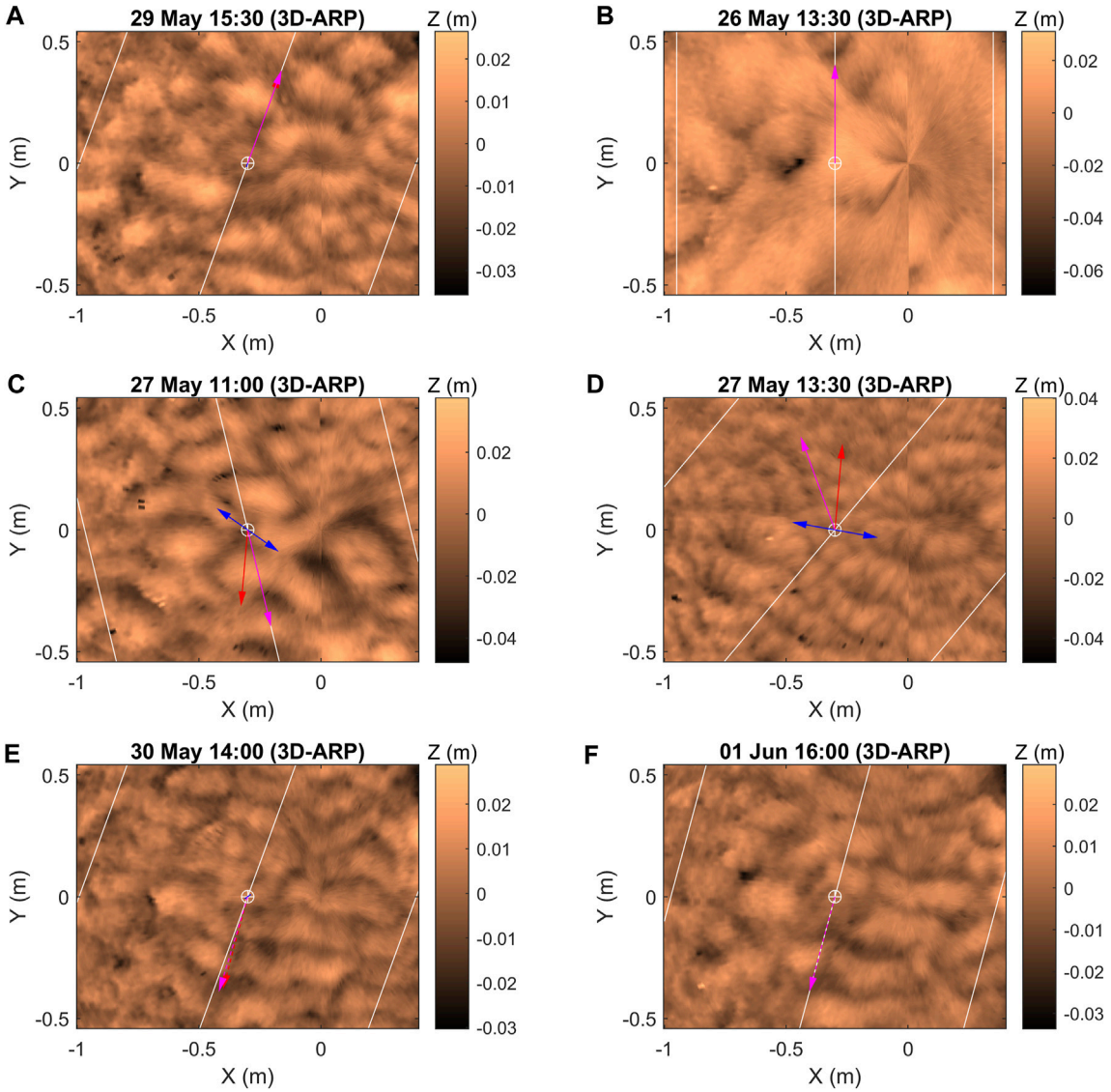

FIGURE 8 | (A) Equilibrium linguoid current ripples formed during ebb in tidal inundation 16; **(B)** Washed-out ripples formed during ebb in inundation 10; **(C)** Tile-shaped interference ripples formed during ebb in inundation 12; **(D)** Ladderback ripples formed during ebb in inundation 12. **(E–F)** Current ripples in plan form during the neap tide: **(E)** Migrating equilibrium linguoid current ripples formed during ebb in tidal inundation 18; **(F)** Stationary, relict linguoid current ripples at high slack water in tidal inundation 22. See **Figure 4** for explanation of line colours.

(**Figure 5D**) and possibly also an uncharacteristically large asymmetry (**Figures 3C,F**). The ebb current, in the absence of waves, was strong enough to form small, quickly migrating, incipient to locally straight-crested current ripples (**Figures 3A–E**).

Tidal Inundations 5 and 6

A storm passed the field site during tidal inundations 5 (May 23rd, pm) and 6 (May 24th, am). The current stresses were generally close to or well above τ_0, with a peak stress of c. 0.6 Nm^{-2} during flood, more than twice the peak stress in inundation 4 (**Figure 3B**). The wave stresses were also larger than in inundation 4, particularly around high slack water (**Figures 3A,B**). *Upper-stage plane beds* (**Figures 6A,B**, **10**; **Table 1**) prevailed during most of the flood tide when the combined stress was in the sheet flow regime (**Figures 3A–C**). The 3D–ARP recorded ribbon-like features (McLean, 1981), oriented parallel to the wave direction (**Figure 6A**), on these plane beds. In inundation 5, the upper-stage plane bed was preceded during the flood tide by a bed covered in asymmetric, *equilibrium linguoid current ripples* (cf., Baas, 1994; **Figures 9B**, **10**; **Table 1**), formed when strong currents acted in the same direction as weak waves in relatively shallow water. In inundation 6, however, the plane beds were preceded by *washed-out*, lunate interference *ripples* (**Table 1**) during somewhat weaker combined flow. The 3D–ARP recorded

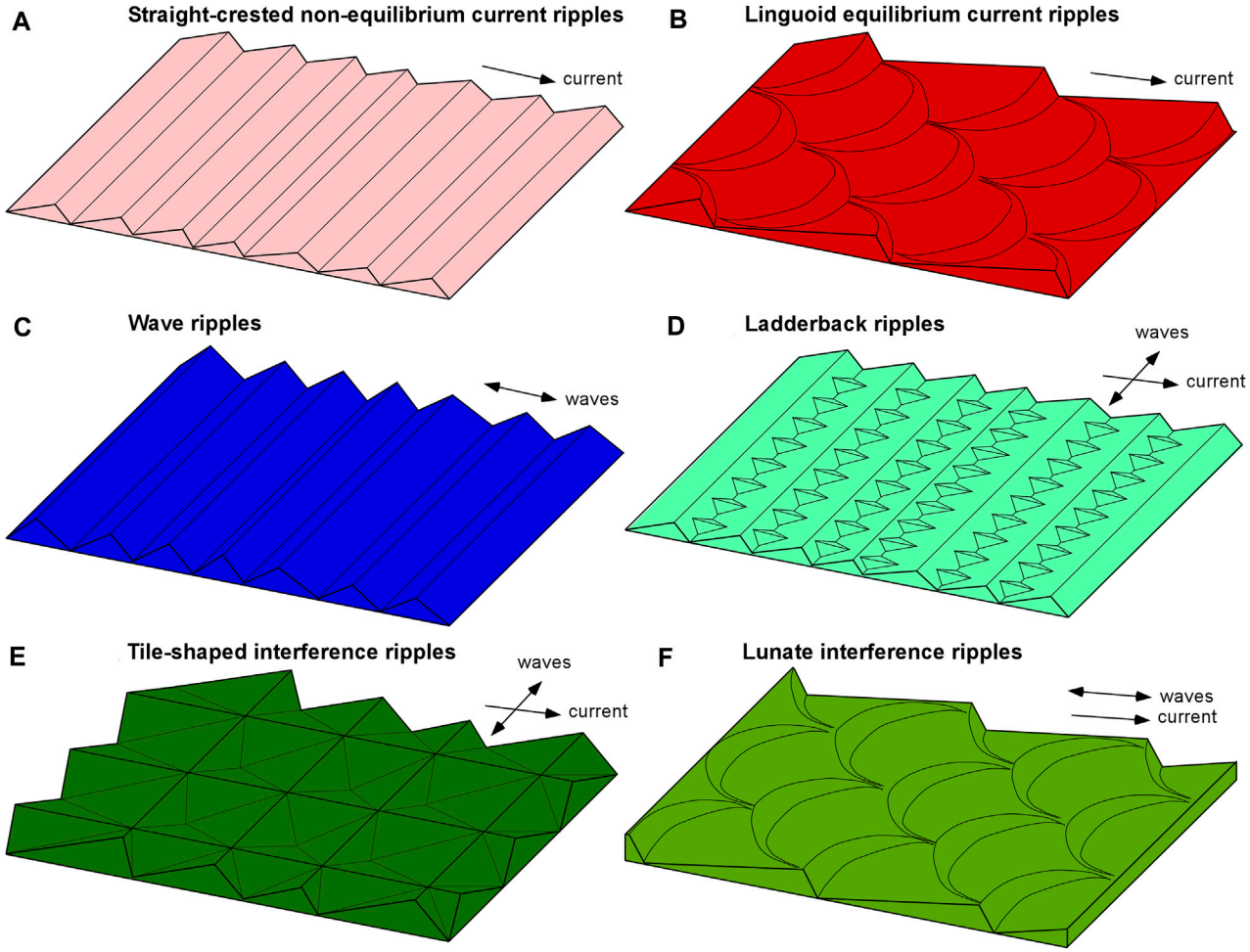

FIGURE 9 | Schematic drawings of **(A)** straight-crested non-equilibrium current ripples, **(B)** linguoid equilibrium current ripples, **(C)** wave ripples, **(D)** ladderback ripples, **(E)** tile-shaped interference ripples, **(F)** lunate interference ripples. Not to scale.

smaller straight-crested to slightly three-dimensional current ripples, when the hydrodynamics were current-dominated, half an hour before the bed was covered with the washed-out ripples (**Figures 3B,C**). After the flood in both inundations, when the current stresses were small, but the wave stresses caused $\tau_{max} >> \tau_0$, washed-out ripples (**Table 1**) and then more pronounced ripples with straight but discontinuous crestlines appeared on the flat bed. Based on the dominance of wave action and the large wave–current angle, these bedforms are interpreted as wave ripples in which the weak tidal current disrupted the two-dimensional plan morphology. The wave-free ebb current (**Figures 3A,B**) may have been just powerful enough to move the wave ripples in a downstream direction (**Figure 6C**), given their low migration rate (**Figure 6D**), and initiate a change to current ripples at the end of the inundation.

Tidal Inundation 7

At the start of tidal inundation 7 (May 24th, pm), the storm had peaked and the tide was midway between neap and spring. The current stresses dominated the combined stresses during the flood and ebb, reaching $0.48\,Nm^{-2}$ and $0.25\,Nm^{-2}$, respectively, and the wave stresses pushed the combined stresses above τ_0 around high slack water (**Figures 3A,B**). Current ripples and wave ripples dominated this inundation. Downstream-migrating equilibrium linguoid current ripples (Baas, 1994) formed during the flood (**Figures 3A–C**, **7A,C**). At high slack water, moderate waves slowly modified these current ripples into wave ripples by slightly decreasing the asymmetry and forming more continuous crestlines. Upon the decrease in wave stress during ebb, these wave ripples became relict and then changed gradually to more asymmetric equilibrium linguoid current ripples (**Figures 3A–C,F**, **7B,D**).

Tidal Inundations 8 to 16

Except for tidal inundation 12 (May 27th, am), the wave stresses were small or absent in tidal inundation 8 (May 25th, am) to inundation 16 (May 29th, pm) (**Figure 3B**). Current-generated bedforms therefore dominated these inundations. Equilibrium linguoid current ripples formed during the flood and ebb tides (**Figures 3A–C**, **8A**). These bedforms were stationary and thus

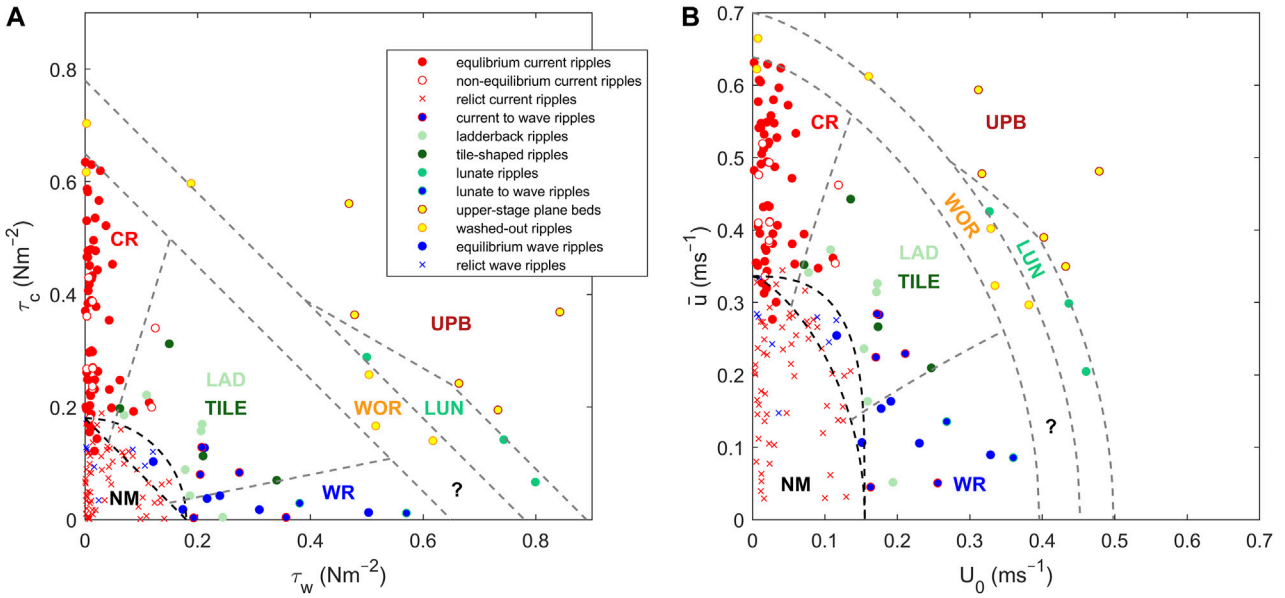

FIGURE 10 | (A) Wave stress, τ_w, against current stress, τ_c, for all bedform types. **(B)** Equivalent phase diagram for the wave velocity amplitude, U_0, against depth-averaged current velocity, $\bar{u}$, based on approximate parameterisations that are specific to this dataset applied to **(A)** ($\tau_w = 2.313U_0^{1.37}$ and $\tau_c = 1.593\bar{u}^2$); symbols are the same as in **(A)**. Black dashed curves indicate maximum combined stresses for critical limit of sediment motion (based on orthogonal and co-linear wave–current end members). Grey dashed curves separate the stability regimes of different bedform types. NM = no motion; CR = current ripples; WR = wave ripples; LAD = ladderback ripples; TILE = tile-shaped interference ripples; WOR = washed-out ripples; LUN = lunate interference ripples; UPB = upper-stage plane bed. The question mark denotes a field in which washed-out ripples may not form, since lunate interference ripples were found to change into wave ripples without going through a washed-out phase in inundation 3 (**Figure 3A**).

relict during high slack water, even when the bed was exposed to weak waves in inundations 10, 11, 15, and 16. The BASSI data show that the migration rate of these ripples increased, as the current stresses increased (cf., Lichtman et al., 2018). Spring tidal current stresses peaked at 0.6–0.7 Nm^{-2} in the final recording of the ebb in inundations 10 and 11 (**Figures 3A,B**), resulting in the formation of washed-out ripples (**Figures 3C, 8B**). On either side of these peak spring inundations, the ebb current formed merely linguoid current ripples.

Spring tide inundation 12 was different in that it captured large maximum current stresses in combination with moderate wave stresses during high slack water that caused the combined stresses to be above τ_0 throughout the inundation (**Figures 3A,B**). These conditions led to a dominance of two types of combined-flow bedforms, both of which formed at large wave–current angles of between 40° and 85°. Tile-shaped interference ripples were recorded during the last hour of the flood tide (**Figures 3A–C, 8C**). These bedforms replaced equilibrium linguoid current ripples that formed earlier, when the current stress was at its peak and waves were absent. The second type of combined-flow bedforms were ladderback ripples (**Figure 8D**). These bedforms formed during high slack water and the ebb, mostly when the wave stresses were larger than the current stresses, and they were roughly 50% lower and shorter than the tile-shaped interference ripples (**Figures 3A–E**). The height and length of the subordinate bedforms in the trough of the ladderback ripples gradually decreased in time in parallel with a gradual change from wave-dominated to current-dominated flow. The final recording during the ebb, when the flow depth had reduced to 1.72 m and waves were absent, revealed asymmetric, non-equilibrium current ripples that were partly straight-crested and in the process of replacing the ladderback ripples (**Figures 3A–C**).

Tidal Inundation 17

The wave stress had a significant influence on the bedform dynamics during tidal inundation 17 (May 30th, am). Wave stress dominated the combined stress around high slack water, whereas the current stress was dominant during the flood and ebb (**Figures 3A,B**). Consequently, the 3D–ARP data show a bed occupied by equilibrium linguoid current ripples during most of the flood. The waves gradually changed these current ripples into wave ripples over high slack water and then into ladderback ripples at the start of the ebb. The final recording shows bedforms in which the wave-generated "steps" of the ladderback patterns had almost disappeared and the current-generated crests had become more pronounced; these bedforms thus started to resemble non-equilibrium straight-crested current ripples. All the bedforms in inundation 17 migrated in the direction of the flood and ebb current, helped by the waves when the current stress was small. The current ripples were more asymmetric than the wave ripples and the ladderback ripples (**Figures 3C,F**).

Tidal Inundations 18 to 25

Tidal inundations 18 (May 30th, pm) to 21 (June 1st, am) experienced small wave stresses and peak current stresses that

TABLE 1 | Main properties and characteristic flow conditions for all equilibrium, relict, and transitional bedform types.

Bedform type	Geometry	Flow conditions	# Cases
Equilibrium bedforms			
Current ripples	Larger than equilibrium wave ripples; 3D in plan view, typically linguoid to irregular; asymmetric in vertical cross-section	Tide-dominated conditions, weak to no wave action; most common in ebb and flood currents; present as relict bedforms at high slack water and during weakest neap tides	52
Wave ripples	Smaller than equilibrium current ripples; 2D in plan view, straight to sinuous crests with bifurcations; symmetric in vertical cross-section	Wave-dominated conditions, weak to no current; formed at high slack water; may be relict	7
Lunate interference ripples	Moon-shaped 3D ripples; asymmetric in vertical cross-section; usually larger than equilibrium current ripples	Strong combined flow, with waves usually stronger than currents; wave direction parallel to current direction	3
Tile-shaped interference ripples	Square, tile-shaped in plan view; asymmetric in vertical cross-section; usually larger than equilibrium current ripples	Combined flow, variable in strength, but weaker than for lunate interference ripples; large angle between wave and current direction, reflected in two crestline orientations	4
Ladderback ripples	Current ripples with small wave ripples in trough; crestlines at right angles to each other	Usually formed by waves that modify the trough of larger current ripples in weak combined flow; tend to migrate intact in the current direction	7
Washed-out ripples	Low-height, washed-out lunate interference ripples and 3D current ripples	Formed by strong waves or currents, but weaker than for upper-stage plane bed	6
Upper-stage plane bed	Flat bed, possibly with longitudinal ribbons or scours subparallel to wave direction	Very strong waves, currents, or combined flow; sheet flow conditions	5
Relict bedforms			
Current ripples	As equilibrium linguoid current ripples	Present below τ_0 for tides (and waves); formed by earlier stronger currents; most common around high slack water and during neap tides, with preservation around low slack water during weakest neap tides	60
Wave ripples	As equilibrium wave ripples	Present below τ_0 for waves (and tides); preserved after a period of wave action, usually during weak neap tides or high slack water	8
Transitional bedforms			
Non-equilibrium current ripples	Smaller than equilibrium current ripples; incipient or 2D in plan view; partial preservation of antecedent bedforms may cause variation in plan form; asymmetric in vertical cross-section	Present during weak tides above τ_0; mainly forming during flood and ebb currents in relatively shallow water when waves are absent; mostly preceded by wave or interference ripples in ebb currents	10
Current ripples changing to wave ripples	Combination of 3D and 2D ripples; may resemble the tile-shaped interference ripples	Moderate waves, weak to no currents; waves change 3D current ripples, formed during flood, into 2D wave ripples; characteristic of high slack water	5
Lunate interference ripples changing to wave ripples	Combination of 3D moon-shaped bedforms and 2D straight-crested bedforms	Combined flow with current direction parallel to wave direction changes into wave-dominated regime; Waves gradually re-establish straight crestlines	2

progressively decreased, in line with the change from spring to neap tide, but were above τ_0 (**Figures 3A,B**). This current dominance resulted in the formation of asymmetric equilibrium current ripples (**Figures 3C**, **8E**) that were stationary, and therefore classified as relict, when the current stress was below c. 0.18 Nm^{-2}. These current ripples migrated during part of the flood in inundation 18, but this swapped to migration during the ebb in inundations 20 and 21. In the intermediate inundation 19, the current ripples migrated during both the flood and ebb tides (**Figure 3A**). The bed morphologies can be followed across the low slack water between the tidal inundations, as the current ripples migrated over a short distance without radically changing their plan morphology. When waves were present, the wave stress was largest during high slack water, but this did not significantly modify the current ripples.

During the neap tide inundations 22–25, the linguoid current ripples that were actively migrating earlier became stationary and therefore relict (**Figure 8F**). Waves were entirely absent, and all flood and ebb current stresses were below 0.12 Nm^{-2} and thus too weak to move the current ripples (**Figures 3A,B**), even at shallow depths around low slack water.

LINKING BEDFORMS TO HYDRODYNAMIC DATA: SYNTHESIS

Bedform Phase Diagram for Combined-Flow Bedforms

As expected, equilibrium current ripples (**Figure 9B**) formed when the combined stress was above τ_0 = 0.18 Nm^{-2} for 0.227 mm sand and current-dominated (**Figure 10A**). The equilibrium current ripples formed at stresses below c. 0.65 Nm^{-2}. Likewise, equilibrium wave ripples (**Figure 9C**) formed at wave-dominant combined stresses between 0.18 Nm^{-2} and 0.65 Nm^{-2}. The grey dashed lines near to the axes in **Figure 10A** delimit the stability regimes of equilibrium wave ripples and equilibrium current ripples, based, on the following equations:

Eq. 3, regime boundaries for equilibrium wave ripples:

$$\tau_c < 0.2\,\tau_w, \quad 0.18 < (\tau_c + \tau_w) < 0.65 \tag{3}$$

Eq. 4, regime boundaries for equilibrium current ripples:

$$\tau_c > 3.3\,\tau_w, \quad 0.18 < (\tau_c + \tau_w) < 0.65 \tag{4}$$

Using **Eq. 2** to calculate τ_0 for single and combined currents and waves, the black dashed quarter circle in **Figure 10A**, based on $\varphi = 90^{\circ}$, accurately delimits a no-motion regime with stationary, and therefore relict current ripples and wave ripples. The black dashed straight line, based on $\varphi = 0^{\circ}$, is shown for comparison. Non-equilibrium, incipient and straight-crested current ripples (**Figure 9A**) plot mostly within the current ripple stability regime, but these bedforms are characterised by combined stresses between 0.18 Nm^{-2} and 0.44 Nm^{-2} (**Figure 10A**). Such small current stresses explain the transitional state of these bedforms, as non-equilibrium current ripples need more time to reach linguoid equilibrium morphology as the current stress is reduced (Baas, 1994, 1999; Oost and Baas, 1994) and therefore are more likely to be recorded at small than at large current stresses. For a similar reason, bedforms that were transitional from current ripples to wave ripples plot at small, combined stresses, where the wave stresses dominate (**Figure 10A**).

With few exceptions, the combined-flow bedforms plot well outside the stability regimes for current ripples, wave ripples, and no motion in **Figure 10**. Lunate interference ripples (**Figure 9F**) have combined wave–current stresses between 0.8 Nm^{-2} and 0.9 Nm^{-2}, when the wave direction was almost parallel to the current direction (**Figure 3I**) and the wave stresses were larger than the current stresses (**Figure 10A**). The lunate interference ripples may correspond to the lunate megaripples and the oriented hummocks in the combined-flow phase diagram of Kleinhans (2005). The ladderback ripples (**Figure 9D**) and tile-shaped interference ripples (**Figure 9E**) were stable at smaller combined stresses than the lunate interference ripples. The ladderback ripples formed at combined stresses of 0.26 ± 0.04 Nm^{-2}. The tile-shaped interference ripples formed at a slightly larger combined stress of 0.33 ± 0.08 Nm^{-2}, but there is a substantial overlap in the combined stresses for these two bedform types. The angles between the wave and current directions for the ladderback and tile-shaped interference ripples were mostly above 45° (**Figure 3I**). The ladderback and tile-shaped interference ripples may correspond to the mixed wave–current ripples and the three-dimensional asymmetrical ripples in the combined-flow phase diagrams of Kleinhans (2005) and Perillo et al. (2014), respectively. These phase diagrams also include symmetric and asymmetric dunes between ripples and upper-stage plane beds for a similar grain size, but these large bedforms were not present at the study site. This may be because the flow conditions changed too quickly for dunes to develop, causing wave ripples and current ripples to change directly to and from washed-out ripples and upper-stage plane bed.

Washed-out ripples formed mainly at large shear stresses in current-dominant and wave-dominated flow, averaging 0.69 Nm^{-2} (**Figure 10A**). In contrast, upper-stage plane beds mostly required strong combined stresses between 0.81 Nm^{-2} and 1.20 Nm^{-2}. The formation of upper-stage plane beds appears independent of the wave–current angle, because it covers a wide range of angles from 0° to 70° (**Figure 3I**) whereas the lunate interference ripples are confined to angles less than 25°. Combined stresses of 0.78 Nm^{-2} and 0.89 Nm^{-2} can be used to separate the stability regime of the lunate interference ripples from that of washed-out ripples and upper-stage plane bed under strong wave-dominated conditions (**Figure 10**). Lunate interference ripples do not appear to form under current-dominated conditions, approximated by a gradual tapering of the phase boundary between lunate interference ripples and upper-stage plane bed in **Figure 10A**, according to the following equation:

Eq. 5, regime boundaries for lunate interference ripples:

$$\tau_c < -0.593\,\tau_w + 0.621, \quad 0.39 < \tau_w < 0.66 \tag{5}$$

Comparing the field-based bedform phase diagrams in **Figure 10** with laboratory-based phase diagrams (e.g., Arnott and Southard, 1990; Yokokawa et al., 1995; Dumas et al., 2005; Kleinhans, 2005; Tinterri, 2011; Perillo et al., 2014) is complicated by the large number of physical variables that bedform dynamics are controlled by under natural wave–current conditions. Phase diagrams of the principal form presented in **Figure 1** do not incorporate the effects of, for example, grain diameter, water depth, wave–current angle, wave period, bed clay content, and tide-induced shear-stress variations. Although Dumas et al. (2005) and Perillo et al. (2014) proposed phase diagrams for different wave periods and grain diameters, no diagram covers a full range of controlling parameters yet. Another difference is that the field data were collected in an intertidal environment, where the hydrodynamic forcing changed on the scale of tens of minutes, whereas the laboratory-based phase diagrams used constant wave and current forcing, thus essentially simulating subtidal conditions in which bedforms are more likely to be in equilibrium with the hydrodynamic forcing and water depth plays a smaller role than in intertidal environments. For example, storm waves were found to have only a small effect on bedform dynamics during shallow water at the field site.

Despite these complications, some of the bedforms found at the field site can be matched to those recognised in experimental flumes. The linguoid current ripples and wave ripples in **Figure 10** correspond to the 3D current ripples and 2D/3D symmetric ripples of Perillo et al. (2014), respectively. These bedforms also appear in the phase diagrams of Arnott and Southard (1990), Yokokawa et al. (1995), and Dumas et al. (2005), but a comparison of forcing parameters is hampered by the small current velocities simulated in these experiments. The stability regime of the tile-shaped interference ripples overlaps with the 3D quasi-asymmetrical and asymmetrical ripples of Perillo et al. (2014), although the plan morphology of the tile-shaped interference ripples in this study is more regular. This difference might be explained by the fact that the tile-shaped interference ripples were formed at large wave–current angles and Perillo et al. (2014)'s 3D quasi-asymmetric and asymmetric ripples were associated with co-linear waves and currents. Subaqueous dunes were not found at

the field site. Instead, the stability fields of 3D symmetric and asymmetric dunes and current dunes of Perillo et al. (2014) are occupied by washed-out ripples, lunate interference ripples, and upper-stage plane beds in **Figure 10**. This may be a key characteristic of intertidal environments, where water depths are generally shallow and rapidly changing, thus hindering the development of dunes, which need greater water depths and more time to form than ripple-sized bedforms. Dunes were seen on intertidal flats adjacent to the field site, but these dunes were poorly defined, with large form indices—the ratio between length and height. The 3D-ARP data did not show any hummocks, which have been considered to form in combined flow (Duke, 1985; Arnott and Southard, 1990; Dumas et al., 2005; Dumas and Arnott, 2006; Tinterri, 2011). The washed-out ripples at the field site are probably nearest to small-scale hummocks (Tinterri, 2011), because these share a similar size and large form index, but their shape is closer to flattened current ripples and lunate interferences ripples. The lack of conventional hummocks at the field site agrees with the facts that: 1) hummocks have not been described in estuarine sedimentary sequences (Tinterri, 2011, his Table 2); 2) hummocky cross-stratification serves "as a useful indicator of deposition in unrestricted, open-water conditions" (Dumas et al., 2005) instead of semi-enclosed esturaries, and; 3) hummocks form by wave-dominated combined flows with wave periods of 8–10 s (Dumas et al., 2005), whereas the measured wave periods at the field site were c. 6–8 s for the lunate interference ripples, washed-out ripples, and upper-stage plane beds and c. 3–6 s for the wave ripples. Hence, a dominance of ladderback ripples and tile-shaped and lunate interference ripples over hummocks and dunes might be diagnostic in sedimentary successions of estuarine mixed sand–mud tidal flats.

Temporal Distribution of Bedforms

The time-series in **Figures 3A–F** reveal that equilibrium current ripples dominated the flood and ebb during spring tides; these bedforms were relict for a short period around high slack water. Some of the highest-energy ebb currents during the spring tide, at current stresses of 0.6 Nm^{-2} – 0.7 Nm^{-2} (inundations 10 and 11), were able to form washed-out ripples from these equilibrium current ripples. The flood currents during spring tide did not form washed-out ripples within the measurement period, even though the shear stress was occasionally as large as in the ebb currents (e.g., tidal inundation 11). The relict current ripples became progressively less frequent in the runup to spring tide and more frequent during the transition from spring to neap tide. Around neap tide, the current ripples stopped moving altogether and near-identical bed morphologies could be traced across areal exposure in tidal inundations 22–25 (**Figures 8E,F**).

Water surface waves modified or replaced the current-generated bedforms during nine tidal inundations. The wave stresses were largest just before and at high slack water, suggesting that during ebb and most of the flood, when water depths were up to 3 m lower than during high slack water, waves largely dissipated before reaching the study site. This resulted in 23% of the bedforms showing wave-dominance or combined-flow properties (**Figure 3G**). The storm waves between May 22nd and 24th (inundations 3–6) had the largest influence on the bed morphology. The relict wave ripples at the start of inundation 2 evolved into equilibrium wave ripples when the waves were strong enough to move sediment around high slack water. Combined flow was dominant at the peak of storm intensity, resulting in the development of tile-shaped interference ripples and ladderback ripples at relatively weak current stresses, and lunate interference ripples, washed-out ripples and upper-stage plane beds at relatively large current stresses. The bedform evolution closely followed temporal changes in wave stress, best exemplified in inundations 4 and 6. In inundation 4, non-equilibrium current ripples existed when waves were absent. These current ripples then rapidly evolved into lunate interference ripples as the wave stress quickly increased, followed by tile-shaped interference ripples, ladderback ripples and wave ripples during decreasing current and wave stresses, and ending with non-equilibrium current ripples in the wave-free ebb current. Inundation 6 also started and ended with non-equilibrium current ripples. In between these, washed-out ripples followed by upper-stage plane beds formed around peak wave stress. Eventually, wave ripples and then current ripples formed during decreasing wave stress and small current stresses. The wave stress during tidal inundation 7 was just large enough to form wave ripples from relict current ripples during high slack water. These wave ripples became relict and then evolved into current ripples during the ebb. In inundation 17, ladderback ripples formed as an intermediate stage between the wave ripples and the current ripples. Finally, relatively weak waves affected the bed during the spring tide of inundation 12, forming a temporal sequence of tile-shaped interference ripples to ladderback ripples over high slack water and the ensuing ebb tide.

In summary, the field data show that strong waves lead to the formation of predominately lunate interference ripples, washed-out ripples and upper-stage plane beds, whereas weaker waves generate merely tile-shaped interference and ladderback ripples. Spring tides promote the development of upper-stage plane beds. In this dynamic environment, only 50% of the bedforms were found to be in equilibrium with the flow conditions (**Figure 3H**).

Comparison of Bedform Dimensions and Geometric Properties

Figures 3D,E show that the bedforms found in the study area are remarkably similar in height and length, even though the sediment bed was exposed to substantial variations in current stresses during the neap–spring cycle and to several periods of large wave and combined stresses. Except for the upper-stage plane beds, bedform height and length ranged from 11 to 17 mm (average: 14 ± 2 mm) and from 122 to 192 mm (average: 149 ± 23 mm), respectively. However, within this small range of bedform dimensions, which will be covered in more detail in the following sections, distinct differences in the asymmetry index and form index were distinguished, when grouped based on bedform type (**Figure 11**).

Although fully symmetric ripples, i.e., with an asymmetry index of 0.5, did not form, the wave ripples were more symmetric than the current ripples and the interference ripples, with the lunate interference ripples, tile-shaped interference ripples, and

washed-out ripples showing the highest asymmetry (**Figure 11**). Based on their phase space positions in **Figure 10**, a set of wave-dominated bedforms can be grouped together, including the transitional current–to–wave, lunate interference, transitional lunate–to–wave, and wave ripples. The ladderback and tile-shaped interference ripples are wave-influenced, but these bedforms are grouped with the remaining current-dominated ripples, because the near orthogonal waves and currents resulted in two distinct sets of bedforms where those associated with the waves were subordinate. Except for the transitional current–to–wave and lunate interference ripples, the asymmetry index for the wave-dominated bedforms was below 0.61, the significance of which will be explained in the next section, and this provides a way of distinguishing wave- and current-dominated bedforms. The wave ripples had the lowest form index of all the bedform types encountered at the study site, and indeed a form index of below 10 distinguishes all but the lunate interference ripples in the wave-dominated set. The tile-shaped interference ripples had relatively high asymmetry and form indices whereas the ladderback ripples had indices much more in keeping with current ripples. Although being considerably smaller, the subordinate bedforms in the trough of the ladderback ripples had similar form and asymmetry indices to the main bedforms. As expected, the washed-out ripples had the highest form and asymmetry indices (Baas and De Koning, 1995; **Figure 11**). The size and shape of the transitional lunate–to–wave and current–to–wave ripples were in between their end members. For the transitional current–to–wave ripples, the form index already represented that of the wave ripples, but the asymmetry was still closer to that of the current ripples (**Figure 11**).

Predicting the Size of Bedforms Affected by Waves

The bedforms that were affected by waves in the field area include equilibrium and relict wave ripples, ladderback ripples, tile-shaped and lunate interference ripples, and transitional current–to–wave and lunate–to–wave ripples. The widely used wave bedform size predictor of Wiberg and Harris (1994) is chosen to verify if it is sufficiently accurate to generalise the relationships between wave-generated and combined-flow bedform size, and flow and sediment parameters found in this study. The non-iterative version of Wiberg and Harris' (1994) predictor (Malarkey and Davies, 2003; **Appendix Equation A2**) depends only on the ratio of the wave orbital diameter, d_0, (= TU_0/π, where T is the wave period and U_0 is the wave velocity amplitude; Lichtman et al., 2018) and the median grain diameter, D_{50}. The predictor distinguishes between orbital ripples ($d_0/D_{50} < 1754$), where the bedform dimensions depend on the orbital diameter, anorbital ripples ($d_0/D_{50} > 5{,}587$), where the bedform dimensions depend on the grain diameter, and suborbital ripples ($1754 < d_0/D_{50} < 5{,}587$) where the bedform dimensions depend on both the orbital and grain diameters. Soulsby and Whitehouse (2005) produced a similar wave ripple predictor, whereas some researchers have done away with the intermediate suborbital range (e.g., Traykovski, 2007). The presence of a small current is accounted for with an enhanced orbital diameter, d_{wc}, following the approach of Lacy et al. (2007):

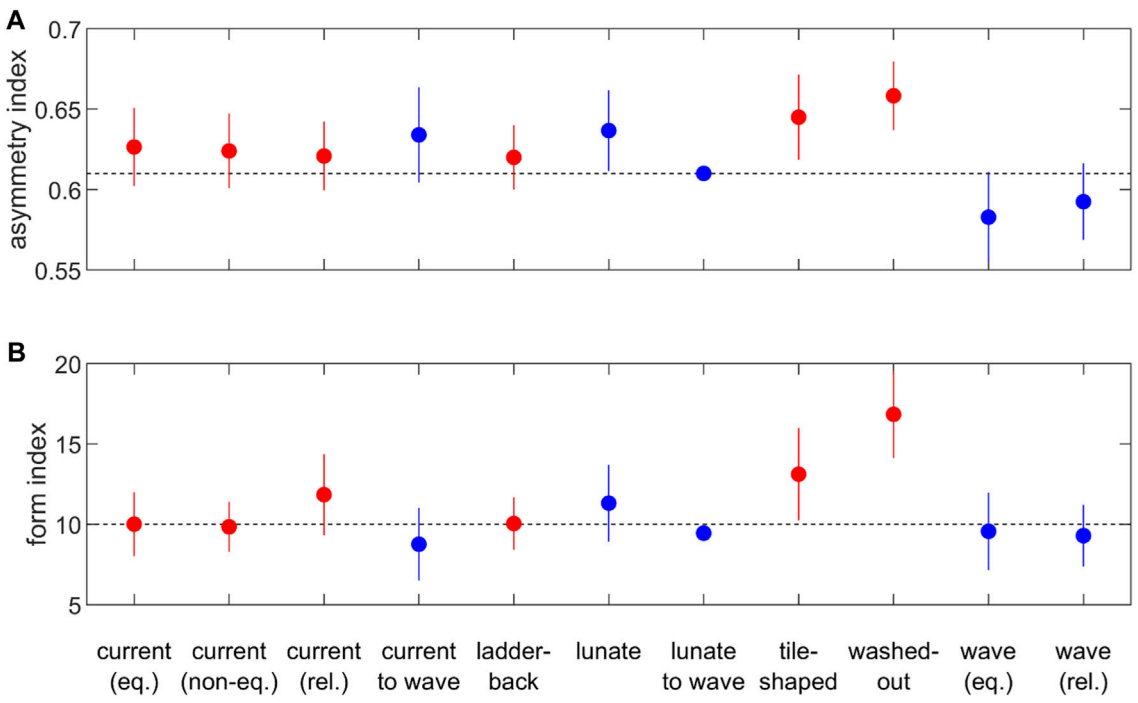

FIGURE 11 | (A) Mean asymmetries and **(B)** form indices, including standard deviation of the mean, for all bedform types observed in the field campaign and separated into wave-dominated (blue) and current-dominated (red).

Eq. 6, Enhanced orbital diameter:

$$d_{wc} = \sqrt{d_0^2 + 0.25\,(Tu_\delta)^2 + d_0 T u_\delta \cos\varphi} \qquad (6)$$

where $u_\delta = 0.65\bar{u}$ is the current velocity at c. 20 mm above the bed in terms of $\bar{u}$, the depth-averaged current velocity. In the absence of a current, $\bar{u} = 0$, the enhanced orbital diameter returns to its wave-only value, $d_{wc} = d_0$. As in the wave-only case, **Eq. 6** determines the distance a particle is advected in half a wave cycle. This definition is only meaningful if the magnitude of the freestream velocity has two minima in the wave cycle, corresponding to $(u_\delta/U_0)\cos\varphi < 1$. Therefore, **Eq. 6** was applied only when this condition was met. The comparison for the measured bedform heights and lengths is shown in **Figures 12A,B**.

The subordinate bedforms in the ladderback and tile-shaped interference ripples are of interest here, since the crest of these bedforms tend to be oriented perpendicular to the wave propagation direction. It is therefore anticipated that these subordinate bedforms are dependent on the wave-only orbital diameter d_0, rather than d_{wc}. The subordinate dimensions of the ladderback and tile-shaped interference ripples tend to be lower than the dimensions of the wave ripples. Their lengths are in the orbital range, but their heights are lower than expected for orbital ripples (**Figures 12A,B**). This may be because the subordinate bedforms are topographically constrained by their

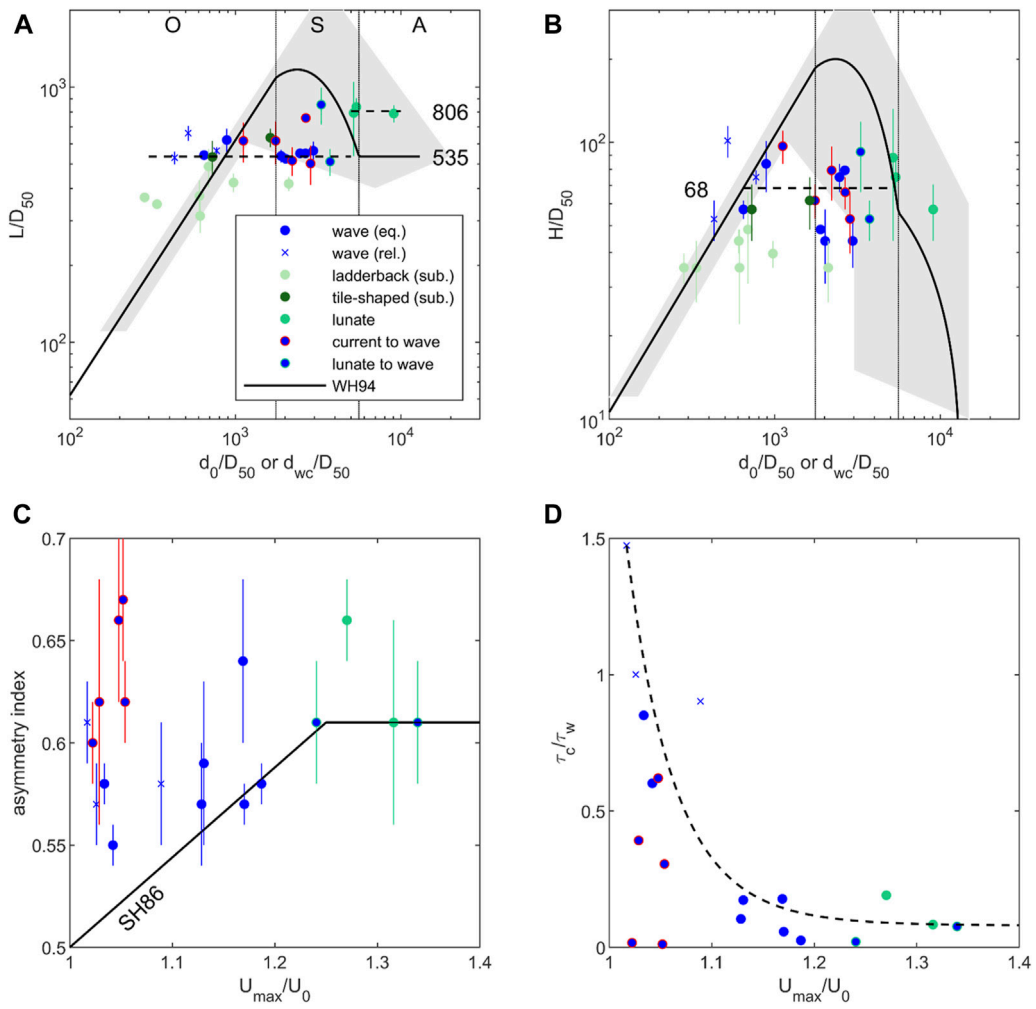

FIGURE 12 | (A) Length and **(B)** height for equilibrium wave ripples and relict, above-threshold (based on $\varphi = 0°$ in **Eq. 2**) wave ripples, lunate interference ripples and transitional current–to–wave and lunate–to–wave ripples, using d_{wc} (**Eq. 6**), and for the subordinate bedforms in ladderback and tile-shaped interference ripples, using d_0 (**Appendix Equation A2**), compared to the Wiberg and Harris (1994) predictor (WH94). **(C)** Asymmetry index and Sato and Horikawa's (1986) asymmetry prediction (SH86) against freestream wave velocity asymmetry from Stokes second order theory, U_{max}/U_0. **(D)** Relative current shear stress against wave asymmetry. Symbols in **(B,C,D)** are the same as in **(A)**, with vertical lines denoting error bars (one standard deviation); grey shading reflects the spread of the original data; O = orbital, S = suborbital, A = anorbital, and dashed lines in **(A)** correspond to $535D_{50}$ and $806D_{50}$ and in **(B)** correspond to $68D_{50}$. **(C,D)** do not show the lunate interference ripples with the largest d_{wc}/D_{50} values from **(A,B)** with an asymmetry index of 0.64 and relative current shear stress of 0.58, because of an unrealistically large wave asymmetry. The dashed line in **(D)** is an inverse trend line.

superimposition on the main bedforms in the ladderback and tile-shaped interference ripples.

Figure 12A shows that the relict wave ripples fall to the left of the grey shading associated with the original experimental scatter of Wiberg and Harris' (1994) predictor, because the orbital diameters of the waves were too weak to influence the bedforms. Moreover, most equilibrium wave ripples and transitional current–to–wave ripples fall within the original laboratory and field data scatter and have lengths that are close to Wiberg and Harris' (1994) anorbital value of $535D_{50}$. Most of these ripple types can be considered as suborbital, but their dimensions correspond to anorbital ripples. This agrees with a laboratory study by Lacy et al. (2007), who found that wave-dominated ripples in combined wave–current flow fall in a similar suborbital region of the Wiberg and Harris (1994) plot. Anorbital ripples are analogous to current ripples in that their size depends only on the grain diameter. This may explain why there were only modest changes in the ripple dimensions during the field campaign when evolving from wave-dominated to current-dominated conditions. Indeed, since several wave ripples developed from current ripples at the beginning of the flood and weak currents commonly accompanied the wave ripples (**Figures 3A–C**), we infer that these currents may have forced the wave ripples towards becoming anorbital.

Because of their formation under wave-dominated conditions (**Figure 10**), it is reasonable to test the lunate interference ripples against the Wiberg and Harris (1994) predictor. These bedforms tend towards the anorbital range, but their length is larger than the predicted value for anorbital bedforms. Various researchers have found that the dimensions of anorbital ripples can have wave-period dependence (Mogridge et al., 1994; O'Donoghue et al., 2006), which is reflected in the scatter in the original Wiberg and Harris (1994) data in **Figure 12A**. This wave-period dependence may thus also apply to the lunate interference ripples.

For practical purposes, the length of the equilibrium and relict wave ripples and the transitional current–to–wave ripples can be considered constant, hence independent of the orbital diameter, at Wiberg and Harris' (1994) anorbital value of $535D_{50}$. However, the length of the lunate interference ripples, which is distinct from the wave ripples, is better described by $806D_{50}$. Hence, $L = 535D_{50}$, for $d_{wc}/D_{50} < 5{,}320$ and $L = 806D_{50}$, for $d_{wc}/D_{50} \geq 5{,}320$ (**Figure 12A**). Assuming that the bedform height can also be represented by a constant value, the mean of all the heights, other than for the lunate interference ripples, gives $H = 68D_{50}$ (**Figure 12B**). Since the lunate interference ripples represent wave-dominated bedforms with the highest combined stress before upper-stage plane beds develop and are well described by Wiberg and Harris' (1994) predicted heights for anorbital ripples, a better predictor in this case would be $H = 68D_{50}$ for $d_{wc}/D_{50} < 5{,}320$ and $H = H_{WH}$, for $d_{wc}/D_{50} \geq 5{,}320$, where H_{WH} is the height from the Wiberg and Harris (1994) predictor. This yields a representative form index of c. 7.7 for the wave ripples and transitional current–to–wave ripples and 12.5 for the lunate interference ripples. These predicted form indices are close to those shown in **Figure 11B**.

Since it is anticipated that wave ripples are more symmetric than current ripples and perhaps combined-flow bedforms, it is worth comparing the asymmetry indices of the wave ripples, lunate interference ripples and transitional current–to–wave ripples with the asymmetry indices found in literature. Sato and Horikawa (1986) determined that the asymmetry of wave ripples formed in the laboratory has an upper limit of 0.61, based on the steepest part of the upstream slope reaching the angle of repose. The ripple asymmetry increased up to this limit with increasing wave asymmetry (skewness), as determined by U_{max}/U_0, where U_{max} is the maximum near-bed velocity in the wave cycle, U_{max}/U_0 is calculated by Stokes 2nd order ($U_{max}/U_0 = 1+3kH/8\sinh^3 kh$, where H and k are the surface wave height and number and h is the water depth, Soulsby, 1997), and $U_{max}/U_0 = 1$ corresponds to a symmetric wave. Sato and Horikawa's (1986) prediction is shown in **Figure 12C** together with all the bedforms shown in **Figures 12A,B**. The accompanying **Figure 12D** shows τ_c/τ_w versus U_{max}/U_0. **Figure 12C** reveals that the asymmetry is generally in the correct range for the wave ripples and the transitional lunate–to–wave ripples, even though Sato and Horikawa's (1986) expression tends to underpredict the ripple asymmetry as a function of wave asymmetry. **Figure 12D** shows that there is an inverse relationship between the relative current stress and the wave asymmetry, and **Figure 12C** shows that the weaker the wave asymmetry is the more substantial the ripple asymmetry underprediction, thus strongly suggesting that the presence of the current causes additional ripple asymmetry. This is valid in particular for the transitional current–to–wave ripples, which have ripple asymmetries that are completely independent of wave asymmetry and generally greater than 0.61. The lunate interference ripples, although fitting the general predicted trend in wave asymmetry (**Figures 12C,D**), show a slightly larger asymmetry (**Figure 11A**), possibly because their larger form index (**Figure 11B**) means they are not constrained by Sato and Horikawa's (1986) angle-of-repose limit.

Predicting the Size of Current-Dominated Bedforms

Most of the bedforms in the field area were either wholly or partially influenced by currents. These include the equilibrium, non-equilibrium, and relict current ripples; the dominant bedforms in the ladderback ripples and tile-shaped interference ripples; washed-out ripples; and upper-stage plane beds. These bedforms can be used to test the accuracy of the Soulsby and Whitehouse (2005) equilibrium current ripple predictor (**Appendix Equation A3**) and possibly extend its use to combined wave–current flows under natural conditions. **Appendix Equation A3** has a grain size dependence but also predicts a linear decrease in ripple height with increasing stress for washed-out ripples, with the height becoming zero for sheet flows on upper-stage plane beds. Because waves and currents were both present at the field site, it is the maximum shear stress, τ_{max}, rather than the current stress, that controls the ripple height. Also, we optimised the Soulsby and Whitehouse (2005) descriptor for this dataset by forcing $H_{max} = 67D_{50}$ and $L = 655D_{50}$, based on the mean height and length of the equilibrium current ripples, and $\tau_{wo} = 0.65\ \mathrm{Nm}^{-2}$ and $\tau_{sf} = 0.78\ \mathrm{Nm}^{-2}$, based on the lower and upper boundaries of washed-out ripples in

Figure 10A (according to **Appendix Equation A3**, $H_{max} = 84D_{50}$ and $L = 674D_{50}$, $\tau_{wo} = 0.76\ Nm^{-2}$ and $\tau_{sf} = 1.08\ Nm^{-2}$).

The heights and lengths of all the current-dominated ripples are plotted against τ_{max} in **Figures 13A,B**, respectively. These figures also show the predicted values according to Soulsby and Whitehouse (2005). The range in the dimensions of the current ripples appears to increase, as the maximum stress increases, with the largest mean heights and lengths at $\tau_{max} > 0.5\ Nm^{-2}$. This increase in current ripple size agrees with the presence of relatively large ripples at high shear stresses in laboratory experiments with 0.238 mm sand, interpreted as bedforms transitional to subaqueous dunes (Baas, 1999).

The dominant bedforms in the ladderback and tile-shaped interference ripples are also well described by the Soulsby and Whitehouse (2005) predictor. However, the non-equilibrium current ripples have lower heights and lengths, and some relict current ripples have lower heights (c. 10 mm instead of 15 mm), but not lower lengths, than predicted. The non-equilibrium current ripples were clearly not fully developed, and therefore plot below the equilibrium heights and lengths predicted by Soulsby and Whitehouse (2005) in **Figures 13A,B**. Moreover, these non-equilibrium ripples were most common during ebb, near the end or directly after periods of declining wave stress. The low-amplitude relict current ripples were present during neap tides with increased bed clay and EPS content (inundations 16–24). The greater reduction in height than in length of these relict ripples is consistent with increased bed clay and EPS content in the experiments of Baas et al. (2013) and Malarkey et al. (2015), respectively. The gradual reduction in ripple height during inundations 15, 16, and 17 is inferred to relate to the increase in bed clay and EPS content measured by Lichtman et al. (2018, their **Figure 4**) by drawing cohesive clay into the bed through hyporheic processes (Dallmann et al., 2020; Wu et al., 2021).

DISCUSSION AND IMPLICATIONS: ROUGHNESS PREDICTION

Determining turbulence and hence sediment transport rates is crucially dependent on the bed roughness. When bedforms are present, the main contribution to the roughness is through the form drag associated with their dimensions, as defined by the quantity H^2/L (for example, $k_s" = 20H^2/L$ in the Chézy coefficient definition of Van Rijn (2006; 2011), where $k_s"$ is the form roughness height of Nikuradse). In certain field settings, waves and currents each have their own roughness, e.g., combined strong waves and weak orthogonal currents over two-dimensional bedforms (Guerrero et al., 2021). However, it is reasonable to assume that there is a common wave–current roughness based on the main bedform heights and lengths in the study area, because of the varied wave–current angle, varied relative strengths of the waves and the currents, and the general three-dimensionality of the bedforms. The H^2/L values, based on the measured bedform heights and lengths for all the different types of bedform, are shown in **Figure 13C** together with the H^2/L values determined from the equilibrium current ripple and wave ripple predictors described in the previous sections. **Figure 13C** shows that the uncertainty in roughness is almost always larger than the variation over a tidal inundation, such that there is a limit to how well the roughness can be defined. However, **Figure 13C** also reveals that, with the exception of the 10-mm high relict current ripples in inundations 16–24, where the black dashed line is the roughness calculated with $H = 10$ mm, the predicted roughness agrees reasonably well with the measured roughness. This includes the non-equilibrium current ripples, despite the fact that these bedforms had smaller heights and lengths than their equilibrium and relict counterparts.

However, this independence of bed roughness on current ripple development stage may be particular to the study site. In other field studies, the need to adjust bedforms towards equilibrium may therefore require a more involved hysteresis-type calculation. Another aspect of the roughness predictions at the study site is that the wave ripple predictor makes only a modest difference to the roughness calculations. The current ripple predictor alone could therefore be considered sufficient to do the roughness calculations for most of the bedforms encountered at the study site. However, there are notable exceptions. The low roughness of the current ripples affected by high bed clay and EPS content in tidal inundations 16–24 indicates that cohesive forces can significantly reduce the bed roughness, and can start to do this at bed clay contents of 2%, corresponding to inundation 16 at the study site (Lichtman et al., 2018). This lower boundary of 2% clay corresponds reasonably well with the 3% clay proposed by Baas et al. (2019) as the lower boundary for the onset of bed stabilisation by cohesive forces. Moreover, the most substantial reductions to the bed roughness relate to the low-relief washed-out ripples and the upper-stage plane beds (**Figure 13C**). These bedform types were relatively rare at the study site, but their effect could be greater in areas that are exposed to larger waves and longer periods of wave forcing during ebb–flood tidal cycles.

DISCUSSION AND IMPLICATIONS: PRESERVATION POTENTIAL OF INTERTIDAL BEDFORMS

Conditions for Preservation of Bedforms

The large variety of sedimentary bedforms in the study area underlines the complex interactions between hydrodynamics and sediment dynamics on intertidal flats (e.g., Deloffre et al., 2007; Gao, 2009). However, this large variety does not necessarily mean that each bedform type has a preservation potential in sedimentary successions of intertidal flats that matches its frequency of occurrence on modern intertidal flats. The present study shows that bedform type is often related in a predictable way to tidal phase and bed shear stress, the presence or absence of waves, and large (near orthogonal) or small (near co-linear) wave–current angles (**Table 1**). Since previous studies have shown at which conditions intertidal sediment is most likely to be preserved (e.g., Deloffre et al., 2007; Gao, 2009), it should also be possible to predict which

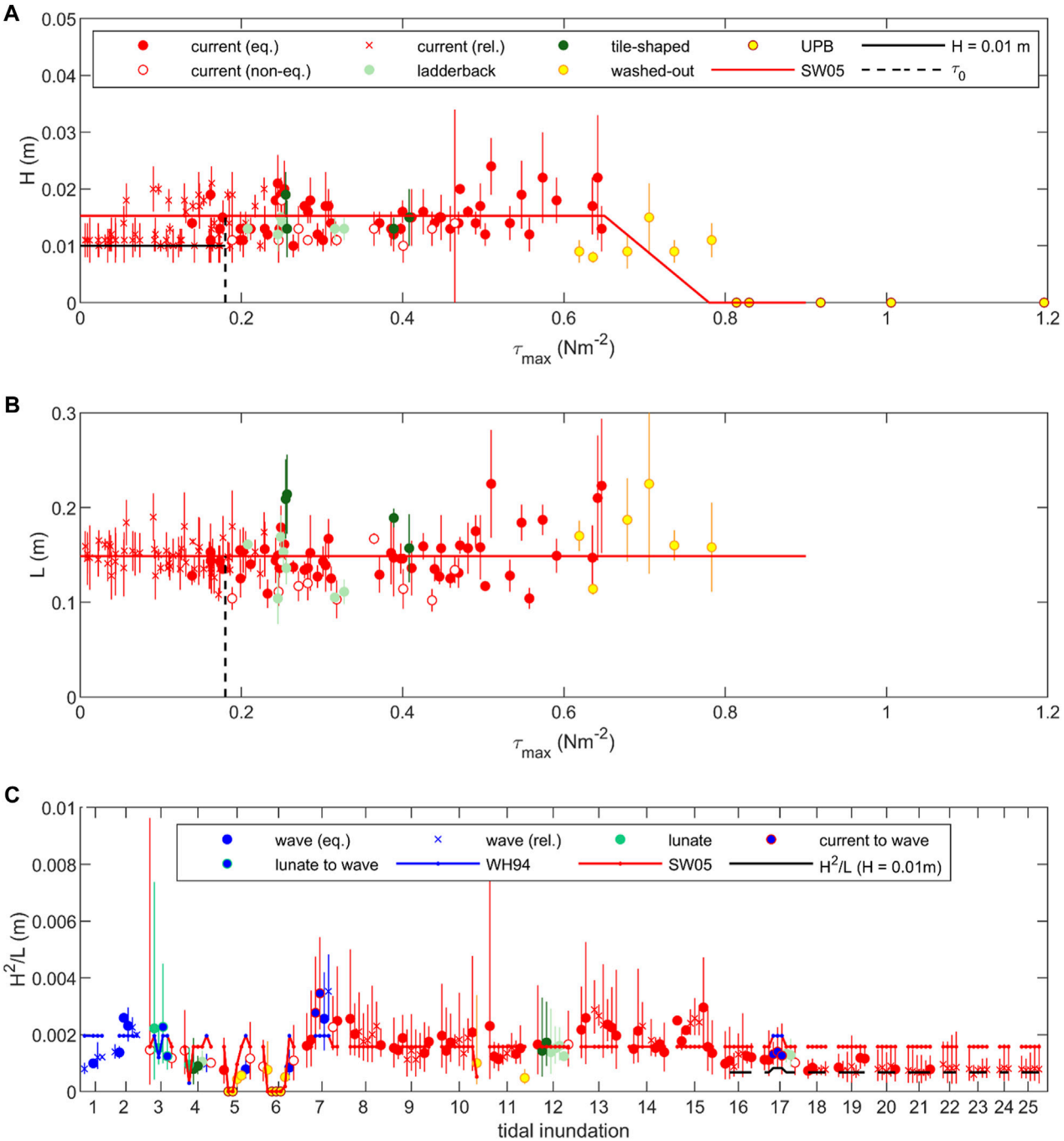

FIGURE 13 | (A) Ripple height and **(B)** length against the maximum shear stress for all current-dominated bedforms, i.e., equilibrium, non-equilibrium, and relict current ripples, ladderback and tile-shaped interference ripples, washed-out ripples and upper-stage plane beds, compared to Soulsby and Whitehouse's (2005) equilibrium current ripple predictor (SW05). **(C)** Bed roughness over the measurement campaign for all bedforms, including wave-dominated ripples, compared to bed roughness calculations based on the SW05 predictor and the modified Wiberg and Harris (1994) predictor (WH94) (cf., **Figures 12A,B**).

intertidal bedform types have the highest preservation potential in the sedimentary record.

Using a combination of numerical modelling and field validation, Gao (2009) found that supratidal, high intertidal, and subtidal environments have a higher preservation potential than low intertidal environments, such as the study area. This reflects the notion that salt marshes and tidal channels usually have more space to accommodate net sediment accumulation than intertidal flats. Intertidal flat sediment can be preserved when the rate of bed aggradation is higher than the rate of bed erosion, but such aggradation rates are often too low to preserve entire bedforms, as exemplified by a comparative study

of three estuaries by Deloffre et al. (2007). Even in the highly dynamic Seine estuary, NW France, the aggradation rates did not exceed 6 mm per semi-diurnal tidal cycle (Deloffre et al., 2007). Specific conditions are therefore required to preserve diagnostic sets of cross-stratification or entire bedform profiles in vertical cross-section. These include: 1) rapid aggradation after a sudden large influx of sediment by decelerating current-dominated or combined flow; 2) deposition of a protective layer of cohesive, 'sticky' clay during high slack water; 3) formation of a biofilm, i.e. a protective surface layer of extracellular polymeric substances (EPS) produced by benthic micro-organisms, during low slack water (Hope et al., 2020); and 4) a prolonged period of small stress and absence of strong bed erosion after these events, most likely around neap tide after the largest spring tides (Deloffre et al., 2007), and in the absence of strong waves over periods of at least weeks to months. Examples of large influxes of sediment are river floods, strong flood tides combined with strong onshore wind, and upstream breaching of, for example, the cut bank of a meandering tidal channel (e.g., Van den Berg et al., 2002). The formation of a protective layer of cohesive clay is most effective during long high slack water periods, i.e. at spring tide, in the estuarine turbidity maximum and in estuaries with strong ebb–flood asymmetry (Deloffre et al., 2007; Friedrichs, 2011; Kirwan and Guntenspergen, 2012; Lichtman et al., 2018). Protection from erosion by biofilm growth is most common during spring and summer, when storm events are less frequent along most coastlines, and during neap tides, when the period of bed strengthening by drying owing to atmospheric exposure is longest (Amos et al., 1988; Lichtman et al., 2018).

Preservation of Bedforms in the Absence of Waves

Although the sediment bed in the Dee estuary was not exposed to significant periods of deposition or erosion during the field study, the above-mentioned conditions for bedform preservation can be used to predict the preservation potential of the various types of bedform in the sedimentary record (**Figure 3**). In the absence of wave stresses, the tidal stresses almost exclusively formed current ripples. Upper-stage plane beds and washed-out ripples were found only for maximum ebb stresses during spring tides, although their generation during flood tides at depths below the minimum measurement depth of the instruments on the SEDbed frame cannot be ruled out. The upper-stage plane beds and the washed-out ripples have a low preservation potential, because these bedforms transform rapidly into current ripples, as the flow decelerates to slack water. Their preservation is probably limited to periods of rapid bed aggradation, thus forming sequences of plane-parallel lamination or climbing washed-out ripples. Migrating equilibrium current ripples were most common during flood and ebb in between neap and spring, whereas relict equilibrium current ripples were characteristic of high, and possibly also low, slack water periods and neap tides in the study area. In the absence of waves, these equilibrium ripples have a high preservation potential, not only because of their abundance, but also because these bedforms are stationary under the small current stresses around neap and become covered by increasing amounts of cohesive clay and EPS in the transition from spring to neap (Lichtman et al., 2018). The preservation potential of current ripples is expected to be even higher under weaker hydrodynamic forcing than at the study site, e.g. towards salt marshes or in estuaries with a lower tidal range, where the stresses are weaker and bed strengthening by cohesive clay and EPS is enhanced. However, such conditions are more likely to lead to the preservation of non-equilibrium than equilibrium current ripples, because the bedform development rate decreases exponentially with decreasing current stress (Baas, 1993, 1999). Even though upper-stage plane beds and washed-out ripples will be more common under stronger hydrodynamic forcing than at the study site, e.g. towards tidal channels, where tidal stresses are larger and cohesive clay and EPS are less abundant, the sediment bed is still subjected to rapid current ripple development when entering the current ripple stability regime during flow deceleration. An exception is fast runoff on steep local slopes during late ebb by sheet flow, which is prone to preserving upper stage plane beds (e.g., Collinson and Mountney, 2019). Hence, equilibrium current ripples are expected to remain the dominant bedform type in sedimentary successions of such dynamic intertidal environments, provided that $\tau_w << \tau_c$.

Effect of Weak and Moderate Waves on Preservation

Weak waves ($\tau_w < \tau_0$) had little effect on the bedforms in the study area, even for large combined stresses. Moderate waves ($\tau_w > \tau_0$), such as in inundations 2, 7, 12, and 17, were able to modify the currents and thus change the bedform type. During neap tides, equilibrium wave ripples formed around high slack water and these bedforms became relict during the flood and ebb. This suggests that wave ripples can replace current ripples and persist as relict bedforms on the bed during neap tides, when currents are not strong enough to move bed sediment, as exemplified by tidal inundation 1. However, moderate waves are unlikely to be accompanied by a large influx of sediment during neap when $\tau_c < \tau_0$. Hence, the high aggradation rates required to preserve wave ripples in this way are inferred to be rare. This leaves the potential to preserve wave ripples by the bed strengthening effect of clay and EPS, as discussed above. The clay would be preserved as a drape over the wave ripples in the sedimentary record.

During spring tides and the transitions between spring and neap, moderate waves modified the flow field to form tile-shaped interference ripples, wave ripples, and ladderback ripples at the study site. The ladderback ripples evolved rapidly from wave ripples or tile-shaped interference ripples around high slack water and then into current ripples in late ebb (e.g., tidal inundations 12 and 17). Because of these rapid changes in bed morphology, we anticipate the tile-shaped interference ripples, wave ripples, and ladderback ripples to be preserved only in exceptional circumstances, also because the formation of the tile-shaped interference ripples and ladderback ripples requires large wave–current angles, and the moderate waves prevent the tide from reaching zero stress at high slack water (e.g., tidal inundation 12 in **Figures 3A,B**) needed for bed strengthening by clay deposition. This leaves rapid sediment

delivery and bed aggradation—here, during a period of up to 3 h (tidal inundation 12; **Figure 3C**)—combined with rapid waning of the waves, as the only scenario at which the tile-shaped interference ripples and ladderback ripples might be preserved. This rapid aggradation without clay deposition would be reflected in the sedimentary record as co-sets of climbing bedforms, but the lack of descriptions of such co-sets in the geological literature might be indicative of their scarcity. Instead of exhibiting a clay drape, the tops of these rare co-sets may be reworked into current ripples and cross-lamination, since $\tau_w < \tau_0$ in the late ebb, presumably because the moderate waves are dissipated before reaching the study site. In fact, these non-equilibrium and equilibrium current ripples have a higher preservation potential than the tile-shaped interference ripples, wave ripples, and ladderback ripples, because they may be stabilised by EPS and clay around low slack water (Lichtman et al., 2018; Hope et al., 2020). In contrast, the equilibrium current ripples formed in the early flood (**Figures 3A–C**) have a low preservation potential, because these bedforms are rapidly replaced by wave ripples or tile-shaped interference ripples during late flood.

Although it is reasonable to assume that the preservation potential of wave ripples and combined-flow ripples increases as moderate waves recur more often, it is more difficult to predict their preservation potential under conditions of weaker and stronger current stresses than at the study site. Smaller current stresses during neap may lead to an increased preservation potential of wave ripples (cf., inundation 2; **Figures 3A–C**). Larger current stresses during neap may cause tile-shaped interference ripples and ladderback ripples to become more common, with their preservation potential requiring the same specific conditions as those mentioned above. Smaller current stresses during spring may induce a shift in preservation from tile-shaped interference ripples and ladderback ripples to wave ripples (cf., inundation 7; **Figures 3A–C**), whereas larger current stresses during spring may cause a change to washed-out ripples, upper-stage plane beds, and possibly lunate interference ripples. However, it should be mentioned that the present dataset lacks a clear picture of stable bedform types at moderate wave stresses and large current stresses (**Figure 10A**).

Effect of Storm Waves on Preservation

During the transition from neap to spring in tidal inundations 3–6, storm waves ($\tau_w >> \tau_0$), with wave stresses up to 0.84 N m^{-2}, formed upper-stage plane beds, washed-out ripples, lunate interference ripples, tile-shaped interference ripples, and ladderback ripples under the rapidly changing contributions of waves and currents to the combined stresses. For reasons similar to those discussed for moderate waves above, we anticipate these bedforms to be preserved only in exceptional circumstances, limiting the preservation to sets of plane-parallel lamination and co-sets of climbing current ripples without clay drapes, but possibly with the tops reworked into non-climbing current ripples during the late ebb. Again, these current ripples have a higher preservation potential than the storm-wave induced bedforms, because the current ripples may be stabilised by EPS and clay around low slack water (Hope et al., 2020), if the storm wanes rapidly. The relatively high preservation potential of these late-ebb current ripples is remarkable because it may conceal evidence of waves, including storm waves, in the sedimentary record.

No recordings of storm waves during neap, spring, and the transition from spring to neap are available from the study site. Predicting bedform types and their preservation potential is therefore more challenging. Storm waves affecting the bed during neap are hypothesised to induce a dominance of wave ripples and wave-induced upper-stage plane beds around high slack water. The upper-stage plane beds are unlikely to be preserved because they change into wave ripples as water levels drop during the ebb, and rapid bed aggradation and clay drape formation are unlikely to take place during large wave stresses combined with small current stresses. The wave ripples may be larger than those formed by moderate waves during neap, discussed earlier, but their preservation potential is similar. Storm waves occurring during spring ($\tau_{max} >> \tau_0$) are expected to promote the formation of bedforms typical of large combined stresses, i.e., upper-stage plane beds, washed-out ripples and lunate interference ripples (**Figure 10A**). Upper-stage plane beds and washed-out ripples may also dominate shallow-water flood and ebb tides, when the wave stresses are small and the current stresses are in or just below the sheet flow regime. The preservation potential of these bedforms is probably similar to that of the bedforms formed by storm waves during the transition from neap to spring and by tidal currents in the absence of waves during spring at the field site, as discussed earlier. However, the highly dynamic conditions induced by storm waves during spring tides may cause bed scouring that removes bedforms preserved in earlier tidal inundations. Finally, it seems reasonable to assume that bedforms forming in the transition from spring to neap are similar to those forming in the transition from neap to spring. However, their preservation potential may be somewhat higher because current stresses progressively decrease from spring to neap, thus the potential for bed reworking also decreases.

Summary: Bedform Preservation

Figure 14 summarises the preservation potential of bedforms on intertidal flats using a relative scale, as quantification of the preservation potential is not possible yet. The schematic drawings of sedimentary deposits in **Figure 14** are based on the most likely scenarios at which each bedform type can be preserved. Current ripples generated under wave-free conditions have the highest preservation potential, as individual ripple trains or climbing ripple co-sets covered by clay drapes and further stabilised by EPS. Wave ripples formed by moderate or strong oscillatory flow combined with relatively weak currents, for example during neap, have a moderate preservation potential, as individual wave ripple trains stabilised by clay and EPS, but not as climbing ripple co-sets. These deposits comprised of current ripples or wave ripples resemble flaser and lenticular bedding (Reineck and Singh, 1980). In contrast, combined-flow ripples, upper-stage plane beds, and washed-out ripples have a low to very low preservation potential, limited to conditions of rapid aggradation. These bedforms are unlikely to form part of flaser and lenticular

bedform type	wave stress	preservation potential	no waves	mod. waves	storm waves
equilibrium current ripples	no waves moderate waves storm waves	high low–moderate (ebb), very low (flood) low–moderate (ebb), very low (flood)		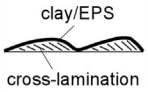	
non-equilibrium current ripples	no waves moderate waves storm waves	high low–moderate (ebb), very low (flood) low–moderate (ebb), very low (flood)	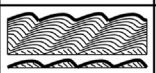		
upper-stage plane bed	no waves moderate waves storm waves	low ? low (spring>neap), very low (neap & neap>spring)		?	
washed-out ripples	no waves moderate waves storm waves	low ? low (spring>neap), very low (neap & neap>spring)		?	
equilibrium wave ripples	moderate waves storm waves	moderate (neap) moderate (neap)			
tile-shaped interference ripples	moderate waves storm waves	very low low (spring>neap), very low (neap>spring)			
ladderback ripples	moderate waves storm waves	very low low (spring>neap), very low (neap>spring)		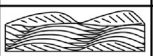	
lunate interference ripples	storm waves	low (spring>neap), very low (neap>spring)			

FIGURE 14 | Summary of preservation potential of bedforms on intertidal flats without wave influence and with moderate and storm waves. No data are available for upper-stage plane beds and washed-out ripples under moderate waves.

bedding, but the plane-parallel laminated sets and climbing-ripple co-sets they generate may be covered by current ripples and their cross-lamination that form during ebb and around low slack water. So even under storm conditions, current ripples are more likely to be preserved than upper-stage plane beds, wave ripples and combined-flow ripples. **Figure 14** is primarily based on the synthesis of the data collected in the Dee Estuary, so further work is needed to test the concepts presented. This should include combined hydrodynamic and sediment dynamic data acquisition on microtidal, mesotidal, and other macrotidal sand and mixed sand–mud flats in different wave climates, as well as targeted studies of bedforms and primary current lamination in sedimentary successions of intertidal flats.

CONCLUSION

Our comprehensive 2-week times-series of bedform dynamics on a mixed sand–mud flat in the Dee Estuary, United Kingdom, allowed us to propose a new bedform phase diagram in which the stability regimes of different types of bedform are delineated using the relative contributions of the current stress and wave stress to the maximum combined stress. As expected, non-equilibrium and equilibrium current ripples form in current-dominated flows without significant wave influence, and wave ripples form in wave-dominated flows without significant current influence. Relict current ripples and wave ripples are stable bedform phases below the critical combined flow shear stress of 0.18 Nm^{-2}, and ladderback ripples and tile-shaped interference ripples form when the maximum combined stress is between 0.18 and c. 0.65 Nm^{-2}, and both the wave and current stress make a significant contribution to the maximum combined stress. For maximum combined stresses above 0.65 Nm^{-2}, the bedform type changes from washed-out ripples (0.65–0.78 Nm^{-2}) via lunate interference ripples (0.78–0.89 Nm^{-2}) to upper-stage plane bed (>0.89 Nm^{-2}). The lunate interference ripples were only observed in flows where the wave stress has the largest contribution to the maximum combined stress. The subaqueous dune field in

laboratory-derived bedform phase diagrams was found to be occupied by washed-out ripples, lunate interference ripples and upper stage plane beds; this absence of dunes may be a key characteristic of intertidal flats.

The dataset also reveals that current ripples are the dominant bedform type on tidal flats, with actively migrating equilibrium current ripples dominating spring tides, stationary relict current ripples dominating neap tides, and non-equilibrium and equilibrium current ripples dominating early flood and late ebb tides, even under conditions of moderate or strong wave forcing. Wave ripples and combined-flow ripples form around high slack water when surface water waves are present. These bedforms change to washed-out ripples and upper-plane stage beds under storm waves. Around half of the bedforms were in equilibrium with the flow conditions, the remainder being either relict or in a transitional state between two bedform types. This confirms that the lack of a one–to–one relationship between flow forcing and bedform size might be a source of error in sediment transport rate predictions. However, most of the bedforms at the study site can be described by a single roughness value of H^2/L = 1.6 mm, even the non-equilibrium current ripples, thus potentially simplifying sediment transport rate predictions. Exceptions are washed-out ripples and upper-stage plane beds, as controlled by the maximum combined stress, and current ripples in sand with at least 2% clay, which all have a significantly lower roughness.

Based on an assessment of the frequency of the various bedform types, their probability of being modified in flood–ebb and neap–spring tidal cycles as a function of bed aggradation rate and bed strengthening by clay drapes and biofilms, and extrapolation to tidal flats with weaker and stronger wave and current forcing, current ripples are inferred to have the highest preservation potential. Wave ripples have moderate preservation potential, and combined flow bedforms, such as ladderback and tile-shaped interference ripples, have the lowest preservation potential in sedimentary successions of intertidal flats. Since current ripples were the stable bedform phase near the end of the ebb in almost all the tidal inundations, even in the presence of moderate waves and storm waves, the waves and combined flows may rarely leave a permanent imprint on the sediment bed in intertidal environments. Therefore, the absence of wave ripples and combined-flow bedforms and their primary stratification in sedimentary successions cannot be taken as evidence that waves were absent at the time of deposition.

DATA AVAILABILITY STATEMENT

The original contributions presented in the study are included in the article/**Supplementary Materials**, further inquiries can be directed to the corresponding author.

AUTHOR CONTRIBUTIONS

All authors listed have made a substantial, direct, and intellectual contribution to the work and approved it for publication.

FUNDING

This work was supported by the United Kingdom's Natural Environment Research Council (NERC) under Grant NE/I027223/1 (COHBED). JM, Julie Hope, and Daniel Parsons were partially funded by a Horizon 2020 European Research Council Consolidator Award (GEOSTICK, Grant 725955). The GEOSTICK project also kindly contributed the article processing fees. Andrew Manning's contribution toward this research was partly supported by the National Science Foundation grants OCE-1924532 and OCE-1736668, TKI-MUSA project 11204950-000-ZKS-0002, and the HR Wallingford company research project FineScale (Grant Nos. ACK3013_62). DP received funding from the MASTS pooling initiative (The Marine Alliance for Science and Technology for Scotland) and their support is gratefully acknowledged. MASTS is funded by the Scottish Funding Council (Grant reference HR09011) and contributing institutions.

ACKNOWLEDGMENTS

The authors are grateful to Roberto Tinterri and Kurt Eric Sundell, who made valuable suggestions for improvement of an earlier version of this paper. We are grateful to the NOC Ocean Technology and Engineering group and the field technicians of the School of Ocean Sciences of Bangor University for instrument set up and deployment.

SUPPLEMENTARY MATERIAL

The Supplementary Material for this article can be found online at: https://www.frontiersin.org/articles/10.3389/feart.2021.747567/full#supplementary-material

REFERENCES

Aldridge, J. N., Parker, E. R., Bricheno, L. M., Green, S. L., and Van der Molen, J. (2015). Assessment of the Physical Disturbance of the Northern European Continental Shelf Seabed by Waves and Currents. *Continental Shelf Res.* 108, 121–140. doi:10.1016/j.csr.2015.03.004

Allen, J. R. L. (1984). *Sedimentary Structures: Their Character and Physical Basis*. Amsterdam: Elsevier.

Amos, C. L., Bowen, A. J., Huntley, D. A., Judge, J. T., and Li, M. Z. (1999). Ripple Migration and Sand Transport under Quasi-Orthogonal Combined Flows on the Scotian Shelf. *J. Coastal Res.* 15, 1–14.

Amos, C. L., Van Wagoner, N. A., and Daborn, G. R. (1988). The Influence of Subaerial Exposure on the Bulk Properties of fine-grained Intertidal Sediment from Minas Basin, Bay of Fundy. *Estuarine, Coastal Shelf Sci.* 27, 1–13. doi:10.1016/0272-7714(88)90028-5

Arnott, R. W., and Southard, J. B. (1990). Exploratory Flow-Duct Experiments on Combined-Flow Bed Configurations, and Some Implications for Interpreting Storm-Event Stratification. *J. Sediment. Petrol.* 60, 211–219. doi:10.1306/212f9156-2b24-11d7-8648000102c1865d

Baas, J. H. (1994). A Flume Study on the Development and Equilibrium Morphology of Current Ripples in Very fine Sand. *Sedimentology* 41, 185–209. doi:10.1111/j.1365-3091.1994.tb01400.x

Baas, J. H. (1999). An Empirical Model for the Development and Equilibrium Morphology of Current Ripples in fine Sand. *Sedimentology* 46, 123–138. doi:10.1046/j.1365-3091.1999.00206.x

Baas, J. H., Baker, M. L., Malarkey, J., Bass, S. J., Manning, A. J., Hope, J. A., et al. (2019). Integrating Field and Laboratory Approaches for Ripple Development in Mixed sand-clay-EPS. *Sedimentology* 66, 2749–2768. doi:10.1111/sed.12611

Baas, J. H., Best, J. L., and Peakall, J. (2016). Predicting Bedforms and Primary Current Stratification in Cohesive Mixtures of Mud and Sand. *J. Geol. Soc.* 173, 12–45. doi:10.1144/jgs2015-024

Baas, J. H., Davies, A. G., and Malarkey, J. (2013). Bedform Development in Mixed Sand-Mud: The Contrasting Role of Cohesive Forces in Flow and Bed. *Geomorphology* 182, 19–32. doi:10.1016/j.geomorph.2012.10.025

Baas, J. H., and De Koning, H. (1995). Washed-out Ripples; Their Equilibrium Dimensions, Migration Rate, and Relation to Suspended-Sediment Concentration in Very fine Sand. *J. Sediment. Res.* A65, 431–435. doi:10.1306/d42680e5-2b26-11d7-8648000102c1865d

Baas, J. H. (1993). Dimensional Analysis of Current Ripples in Recent and Ancient Depositional Environments. *Geologica Ultraiectina* 106, 199.

Bádenas, B., Aurell, M., and Gasca, J. M. (2018). Facies Model of a Mixed Clastic-Carbonate, Wave-dominated Open-coast Tidal Flat (Tithonian-Berriasian, north-east Spain). *Sedimentology* 65, 1631–1666. doi:10.1111/sed.12441

Brown, J. M., and Wolf, J. (2009). Coupled Wave and Surge Modelling for the Eastern Irish Sea and Implications for Model Wind-Stress. *Continental Shelf Res.* 29, 1329–1342. doi:10.1016/j.csr.2009.03.004

Camenen, B. (2009). Estimation of the Wave-Related Ripple Characteristics and Induced Bed Shear Stress. *Estuarine, Coastal Shelf Sci.* 84, 553–564. doi:10.1016/j.ecss.2009.07.022

Clifton, H. E., and Dingler, J. R. (1984). Wave-formed Structures and Paleoenvironmental Reconstruction. *Mar. Geology.* 60, 165–198. doi:10.1016/0025-3227(84)90149-x

Collinson, J., and Mountney, N. (2019). *Sedimentary Structures*. 4th Edition. Edinburgh: Dunedin Academic Press, 320.

Cuadrado, D. G. (2020). Geobiological Model of Ripple Genesis and Preservation in a Heterolithic Sedimentary Sequence for a Supratidal Area. *Sedimentology* 67, 2747–2763. doi:10.1111/sed.12718

Dallmann, J., Phillips, C. B., Teitelbaum, Y., Sund, N., Schumer, R., Arnon, S., et al. (2020). Impacts of Suspended Clay Particle Deposition on Sand-Bed Morphodynamics. *Water Resour. Res.* 56, e2019WR027010. doi:10.1029/2019WR027010

Deloffre, J., Verney, R., Lafite, R., Lesueur, P., Lesourd, S., and Cundy, A. B. (2007). Sedimentation on Intertidal Mudflats in the Lower Part of Macrotidal Estuaries: Sedimentation Rhythms and Their Preservation. *Mar. Geology.* 241, 19–32. doi:10.1016/j.margeo.2007.02.011

Duke, W. L. (1985). Hummocky Cross-Stratification, Tropical Hurricanes, and Intense winter Storms. *Sedimentology* 32, 167–194. doi:10.1111/j.1365-3091.1985.tb00502.x

Dumas, S., and Arnott, R. W. C. (2006). Origin of Hummocky and Swaley Cross-Stratification- the Controlling Influence of Unidirectional Current Strength and Aggradation Rate. *Geol* 34, 1073–1076. doi:10.1130/g22930a.1

Dumas, S., Arnott, R. W. C., and Southard, J. B. (2005). Experiments on Oscillatory-Flow and Combined-Flow Bed Forms: Implications for Interpreting Parts of the Shallow-marine Sedimentary Record. *J. Sediment. Res.* 75, 500–513. doi:10.2110/jsr.2005.039

Friedrichs, C. T. (2011). "Tidal Flat Morphodynamics," in *Treatise on Estuarine and Coastal Science*. Editors E. Wolanski and D. McLusky (Waltham: Academic Press), 137–170. doi:10.1016/b978-0-12-374711-2.00307-7

Gallagher, E. L. (2003). A Note on Megaripples in the Surf Zone: Evidence for Their Relation to Steady Flow Dunes. *Mar. Geology.* 193, 171–176. doi:10.1016/s0025-3227(02)00662-x

Gallagher, E. L., Elgar, S., and Thornton, E. B. (1998). Megaripple Migration in a Natural Surf Zone. *Nature* 394, 165–168. doi:10.1038/28139

Gao, S. (2009). Modeling the Preservation Potential of Tidal Flat Sedimentary Records, Jiangsu Coast, Eastern Chinaflat Sedimentary Records, Jiangsu Coast, Eastern China. *Continental Shelf Res.* 29, 1927–1936. doi:10.1016/j.csr.2008.12.010

Gordon, L., and Lohrmann, A. (2001). "Near-shore Doppler Current Meter Wave Spectra," in Ocean Wave Measurement and Analysis: Proceedings of ASCE Waves 2001 conference (Reston, VA: ASCE).

Guerrero, Q., Williams, M. E., Guillén, J., Lichtman, I. D., Thorne, P. D., and Amoudry, L. O. (2021). Small-scale Bedforms and Associated Sediment Transport in a Macro-Tidal Lower Shoreface. *Continental Shelf Res.* 225, 104483. doi:10.1016/j.csr.2021.104483

Halcrow (2013). *North West Estuaries Processes Reports: Dee Estuary*. Merseyside: Sefton Council.

Harazim, D., and McIlroy, D. (2015). Mud-rich Density-Driven Flows along an Early Ordovician Storm-Dominated Shoreline: Implications for Shallow-marine Facies Models. *J. Sediment. Res.* 85, 509–528. doi:10.2110/jsr.2015.38

Hay, A. E., and Mudge, T. (2005). Principal Bed States during SandyDuck97: Occurrence, Spectral Anisotropy, and the Bed State Storm Cycle. *J. Geophys. Res.* 110, C03013. doi:10.1029/2004JC002451

Hope, J. A., Malarkey, J., Baas, J. H., Peakall, J., Parsons, D. R., Manning, A. J., et al. (2020). Interactions between Sediment Microbial Ecology and Physical Dynamics Drive Heterogeneity in Contextually Similar Depositional Systems. *Limnol Oceanogr* 65, 2403–2419. doi:10.1002/lno.11461

Isla, M. F., Schwarz, E., and Veiga, G. D. (2018). Bedset Characterization within a Wave-Dominated Shallow-marine Succession: an Evolutionary Model Related to Sediment Imbalances. *Sediment. Geology.* 374, 36–52. doi:10.1016/j.sedgeo.2018.07.003

Kirwan, M. L., and Guntenspergen, G. R. (2012). Feedbacks between Inundation, Root Production, and Shoot Growth in a Rapidly Submerging Brackish Marsh. *J. Ecol.* 100, 764–770. doi:10.1111/j.1365-2745.2012.01957.x

Klein, G. D. V. (1970). Depositional and Dispersal Mechanics of Intertidal Sand Bars. *J. Sediment. Petrol.* 40, 1095–1127.

Kleinhans, M. G. (2005). Phase Diagrams of Bed States in Steady, Unsteady, Oscillatory and Mixed Flows. *SANDPIT Rep.*, 16.

Krämer, K., and Winter, C. (2016). Predicted Ripple Dimensions in Relation to the Precision of *In Situ* Measurements in the Southern North Sea. *Ocean Sci.* 12, 1221–1235. doi:10.5194/os-12-1221-2016

Lacy, J. R., Rubin, D. M., Ikeda, H., Mokudai, K., and Hanes, D. M. (2007). Bed Forms Created by Simulated Waves and Currents in a Large Flume. *J. Geophys. Res.* 112, C10018. doi:10.1029/2006JC003942

Larsen, S. M., Greenwood, B., and Aagaard, T. (2015). Observations of Megaripples in the Surf Zone. *Mar. Geology.* 364, 1–11. doi:10.1016/j.margeo.2015.03.003

Li, M. Z., and Amos, C. L. (1998). Predicting Ripple Geometry and Bed Roughness under Combined Waves and Currents in a continental Shelf Environment. *Continental Shelf Res.* 18, 941–970. doi:10.1016/s0278-4343(98)00034-x

Lichtman, I. D., Baas, J. H., Amoudry, L. O., Thorne, P. D., Malarkey, J., Hope, J. A., et al. (2018). Bedform Migration in a Mixed Sand and Cohesive clay Intertidal Environment and Implications for Bed Material Transport Predictions. *Geomorphology* 315, 17–32. doi:10.1016/j.geomorph.2018.04.016

Malarkey, J., Baas, J. H., Hope, J. A., Aspden, R. J., Parsons, D. R., Peakall, J., et al. (2015). The Pervasive Role of Biological Cohesion in Bedform Development. *Nat. Commun.* 6, 6257. doi:10.1038/ncomms7257

Malarkey, J., and Davies, A. G. (2003). A Non-iterative Procedure for the Wiberg and Harris (1994) Oscillatory Sand Ripple Predictor. *J. Coastal Res.* 19, 738–739.

Malarkey, J., and Davies, A. G. (2012). A Simple Procedure for Calculating the Mean and Maximum Bed Stress under Wave and Current Conditions for Rough Turbulent Flow Based on Method. *Comput. Geosciences* 43, 101–107. doi:10.1016/j.cageo.2012.02.020

Marine Electronics (2009). *User Manual for the 3D Sand Ripple Profiling Logging Sonar, Issue 1.1*. Vale, Channel Islands, U.K.: Marine Electronics Ltd.

McLean, S. R. (1981). The Role of Non-uniform Roughness in the Formation of Sand Ribbons. *Mar. Geology.* 42, 49–74. doi:10.1016/0025-3227(81)90158-4

Moate, B. D., Thorne, P. D., and Cooke, R. D. (2016). Field Deployment and Evaluation of a Prototype Autonomous Two Dimensional Acoustic Backscatter Instrument: The Bedform and Suspended Sediment Imager (BASSI). *Continental Shelf Res.* 112, 78–91. doi:10.1016/j.csr.2015.10.017

Mogridge, G. R., Davies, M. H., and Willis, D. H. (1994). Geometry Prediction for Wave-Generated Bedforms. *Coastal Eng.* 22, 255–286. doi:10.1016/0378-3839(94)90039-6

Moore, R. D., Wolf, J., Souza, A. J., and Flint, S. S. (2009). Morphological Evolution of the Dee Estuary, Eastern Irish Sea, UK: A Tidal Asymmetry Approach. *Geomorphology* 103, 588–596. doi:10.1016/j.geomorph.2008.08.003

Myrow, P. M., Fischer, W., and Goodge, J. W. (2002). Wave-modified Turbidites: Combined-Flow Shoreline and Shelf Deposits, Cambrian, Antarctica. *J. Sediment. Res.* 72, 641–656. doi:10.1306/022102720641

Myrow, P. M., and Southard, J. B. (1991). Combined-flow Model for Vertical Stratification Sequences in Shallow marine Storm-Deposited Beds. *J. Sediment. Res.* 61, 202–210. doi:10.1306/d42676d1-2b26-11d7-8648000102c1865d

Nelson, T. R., Voulgaris, G., and Traykovski, P. (2013). Predicting Wave-Induced Ripple Equilibrium Geometry. *J. Geophys. Res.* 97 (C8), 17245–12761. doi:10.1002/jgrc.20241

O'Donoghue, T., Doucette, J. S., van der Werf, J. J., and Ribberink, J. S. (2006). The Dimensions of Sand Ripples in Full-Scale Oscillatory Flows. *Coastal Eng.* 53, 997–1012. doi:10.1016/j.coastaleng.2006.06.008

Oost, A. P., and Baas, J. H. (1994). The Development of Small Scale Bedforms in Tidal Environments: an Empirical Model for Unsteady Flow and its Applications. *Sedimentology* 41, 883–903. doi:10.1111/j.1365-3091.1994.tb01430.x

Parsons, D. R., Schindler, R. J., Hope, J. A., Malarkey, J., Baas, J. H., Peakall, J., et al. (2016). The Role of Biophysical Cohesion on Subaqueous Bed Form Size. *Geophys. Res. Lett.* 43, 1566–1573. doi:10.1002/2016gl067667

Pedocchi, F., and García, M. H. (2009a). Ripple Morphology under Oscillatory Flow: 1. Prediction. *J. Geophys. Res.* 114, C12014. doi:10.1029/2009JC005354

Pedocchi, F., and García, M. H. (2009b). Ripple Morphology under Oscillatory Flow: 2. Experiments. *J. Geophys. Res.* 114, C12015. doi:10.1029/2009JC005356

Perillo, M. M., Best, J. L., and Garcia, M. H. (2014). A New Phase Diagram for Combined-Flow Bedforms. *J. Sediment. Res.* 84, 301–313. doi:10.2110/jsr.2014.25

Perron, J. T., Myrow, P. M., Huppert, K. L., Koss, A. R., and Wickert, A. D. (2018). Ancient Record of Changing Flows from Wave Ripple Defects. *Geology* 46, 875–878. doi:10.1130/g45463.1

Reineck, H. E., and Singh, I. B. (1980). *Depositional Sedimentary Environments: With Reference to Terrigenous Clastics*. Berlin: Springer, 551.

Sato, S., and Horikawa, K. (1986). "Laboratory Study on Sand Transport over Ripples Due to Asymmetric Oscillatory Flows," in Proceedings of 20th International Conference on Coastal Engineering (New York: ASCE), 1481–1495. doi:10.9753/icce.v20.109

Smyth, C. E., and Li, M. Z. (2005). Wave-current Bedform Scales, Orientation, and Migration on Sable Island Bank. *J. Geophys. Res.* 110, C02023. doi:10.1029/2004JC002569

Soulsby, R. (1997). *Dynamics of Marine Sands: A Manual for Practical Applications*. London: Thomas Telford.

Soulsby, R. L., Whitehouse, R. J. S., and Marten, K. V. (2012). Prediction of Time-Evolving Sand Ripples in Shelf Seas. *Continental Shelf Res.* 38, 47–62. doi:10.1016/j.csr.2012.02.016

Soulsby, R. L., and Whitehouse, R. J. S. (2005). Prediction of Ripple Properties in Shelf Seas; Mark 2 Predictor for Time Evolution. *Rep. TR 154, Release 2.0, HR Wallingford*, 99.

Southard, J. B., and Boguchwal, L. A. (1990). Bed Configuration in Steady Unidirectional Water Flows; Part 2, Synthesis of Flume Data. *J. Sediment. Res.* 60, 658–679. doi:10.1306/212f9241-2b24-11d7-8648000102c1865d

Taral, S., and Chakraborty, T. (2017). Deltaic Coastline of the Siwalik (Neogene) Foreland basin: Evidences from the Gish River Section, Darjeeling Himalaya. *Geol. J.* 53, 203–229. doi:10.1002/gj.2886

Thorne, P. D., and Hanes, D. M. (2002). A Review of Acoustic Measurement of Small-Scale Sediment Processes. *Continental Shelf Res.* 22, 603–632. doi:10.1016/s0278-4343(01)00101-7

Thorne, P. D., Hurther, D., Cooke, R. D., Caceres, I., Barraud, P. A., and Sánchez-Arcilla, A. (2018). Developments in Acoustics for Studying Wave-Driven Boundary Layer Flow and Sediment Dynamics over Rippled Sand-Beds. *Continental Shelf Res.* 166, 119–137. doi:10.1016/j.csr.2018.07.008

Tinterri, R. (2011). Combined Flow Sedimentary Structures and the Genetic Link between Sigmoidal and Hummocky-Cross Stratification. *Geologica Acta* 10, 43–85.

Traykovski, P. (2007). Observations of Wave Orbital Scale Ripples and a Nonequilibrium Time-dependent Model. *J. Geophys. Res.* 112, C06026. doi:10.1029/2006JC003811

Van den Berg, J. H., and Van Gelder, A. (1993). "A New Bedform Stability Diagram, with Emphasis on the Transition of Ripples to Plane Bed in Flows over fine Sand and silt," in *Alluvial Sedimentation. International Association of Sedimentologists Special Publication 17*. Editors M. Marzo and C. Puigdefábregas (Oxford, UK: Blackwell Publishing Ltd.), 11–21.

Van den Berg, J. H., Van Gelder, A., and Mastbergen, D. R. (2002). The Importance of Breaching as a Mechanism of Subaqueous Slope Failure in fine Sandfine Sand. *Sedimentology* 49, 81–95. doi:10.1111/j.1525-139x.2006.00168.x-i1

Van der Mark, C. F., Blom, A., and Hulscher, S. J. M. H. (2008). Quantification of Variability in Bedform Geometry. *J. Geophys. Res.* 113, F03020. doi:10.1029/2007JF000940

Van Rijn, L. C. (2006). *Bed Form Tracking, Manual Sediment Transport Measurements in Rivers Estuaries and Coastal Seas, Sub-section 5.5.2.* Delft, Netherlands: Delft Hydraulics Laboratory.

Van Rijn, L. C. (2011). *Principles of Fluid Flow and Surface Waves in Rivers, Estuaries, Seas and Oceans*. Amsterdam: Aqua Publications, 900.

Van Rijn, L. C. (1984). Sediment Transport, Part III: Bed Forms and Alluvial Roughness. *J. Hydraul. Eng.* 110, 1733–1754. doi:10.1061/(asce)0733-9429(1984)110:12(1733)

Villaret, C., Huybrechts, N., Davies, A. G., and Way, O. (2011). "Effect of Bed Roughness Prediction on Morphodynamic Modelling: Application to the Dee Estuary (UK) and to the Gironde Estuary (France)," in Proceedings of 34th IAHR World Congress, 26 June-1 July 2011, Brisbane, Australia. International Association for Hydro-Environment Engineering and Research (IAHR), 1149–1156.

Wang, J., Jiang, Z., and Zhang, Y. (2015). Subsurface Lacustrine Storm-Seiche Depositional Model in the Eocene Lijin Sag of the Bohai Bay Basin, East China. *Sediment. Geology.* 328, 55–72. doi:10.1016/j.sedgeo.2015.07.014

Way, O. (2013). "The Migration of Large Scale Bed Forms in the Dee Estuary," (Wales, U. K.: Bangor University), 398. PhD Thesis.

Wengrove, M. E., Foster, D. L., Lippmann, T. C., de Schipper, M. A., and Calantoni, J. (2018). Observations of Time-Dependent Bedform Transformation in Combined Wave-Current Flowsflows. *J. Geophys. Res. Oceans* 123, 7581–7598. doi:10.1029/2018jc014357

Wengrove, M. E., Foster, D. L., Lippmann, T. C., de Schipper, M. A., and Calantoni, J. (2019). Observations of Bedform Migration and Bedload Sediment Transport in Combined Wave-Current Flows. *J. Geophys. Res. Oceans* 124, 4572–4590. doi:10.1029/2018jc014555

Wiberg, P. L., and Harris, C. K. (1994). Ripple Geometry in Wave-Dominated Environments. *J. Geophys. Res.* 99 (C1), 775–789. doi:10.1029/93jc02726

Wu, X., Fernández, R., Baas, J., Malarkey, J., and Parsons, D. (2021). Discontinuity in Equilibrium Wave-Current Ripple Size and Shape Caused by a Winnowing Threshold in Cohesive Sand-clay Beds. *EarthArxiv*. doi:10.31223/X5HC98

Wu, X., and Parsons, D. R. (2019). Field Investigation of Bedform Morphodynamics under Combined Flow. *Geomorphology* 339, 19–30. doi:10.1016/j.geomorph.2019.04.028

Yokokawa, M., Masuda, F., and Endo, N. (1995). Sand Particle Movement on Migrating Combined-Flow Ripples. *J. Sediment. Res.* A65, 40–44.

Conflict of Interest: The authors declare that the research was conducted in the absence of any commercial or financial relationships that could be construed as a potential conflict of interest.

APPENDIX A: THRESHOLD OF MOTION AND RIPPLE PREDICTORS

According to Soulsby (1997), the threshold Shields parameter is:

Eq. A1, Shields parameter for threshold of motion:

$$\theta_0 = \frac{0.3}{1 + 1.2D_*} + 0.055\left(1 - e^{-0.02D_*}\right) \tag{A1}$$

where $\theta_0 = \tau_0/(\rho_s - \rho)gD_{50}$, ρ is the density of sea water, ρ_s is the density of sediment, g is the acceleration due to gravity (= 9.81 ms^{-2}), $D_* = D_{50}\,[(\rho_s - \rho)g/\rho\nu^2]^{1/3}$ and ν is the kinematic viscosity. For the non-iterative Wiberg and Harris (1994) ripple predictor (Malarkey and Davies, 2003), the equilibrium length and height are:

Eq. A2, equilibrium bedform length and height according to Wiberg and Harris (1994):

$$\frac{L}{D_{50}} = \begin{cases} 0.62\Delta, & \Delta \le 1754, \\ 535\exp\left[f\left(\Delta\right)\right], & 1754 < \Delta \le 5587, \\ 535, & \Delta > 5587, \end{cases} \qquad \frac{H}{D_{50}} = \Delta\exp\{[B_3 - B_1\ln\left(\Delta D_{50}/L\right)] - B_2\} \tag{A2}$$

where $\Delta = d_0/D_{50}$, $f\left(\Delta\right) = -\ln\left(0.62x\right)[Q - (B_3 - B_3\ln x)^{1/2}]$, $x = \Delta/535$, $Q = \ln\left(0.01\right) + B_3$, $B_1 = 1/0.095$, $B_2 = 0.721B_1$, and $B_3 = B_2^{\,2} - 2.28B_1$. For the Soulsby and Whitehouse (2005) equilibrium current ripple predictor the equilibrium height and length are:

Eq. A3, equilibrium bedform height and length according to Soulsby and Whitehouse (2005):

$$\frac{H_{\max}}{D_{50}} = 202D_*^{-0.554}, \qquad \frac{L}{D_{50}} = 500 + 1881D_*^{-1.5} \tag{A3}$$

where H is controlled by θ_c, the Shields parameter associated with the current stress [$= \tau_c/(\rho_s - \rho)gD_{50}$], $H = H_{\max}$ for $\theta_c \le \theta_{wo}$, $H = H_{\max}\,(\theta_{sf} - \theta_c)/(\theta_{sf} - \theta_{wo})$ for $\theta_{wo} < \theta_c \le \theta_{sf}$, $H = 0$ for $\theta_c > \theta_{sf}$ and θ_{wo} and θ_{sf} are the wash-out and sheet-flow Shields parameters, given by $\theta_{wo} = 1.66D_*^{-1.3}$ or 0.916 and $\theta_{sf} = 2.26D_*^{-1.3}$ or 1.25, for $D_* > 1.58$ or $D_* \le 1.58$, respectively [$\theta_{wo} = \tau_{wo}/(\rho_s - \rho)gD_{50}$ and $\theta_{sf} = \tau_{sf}/(\rho_s - \rho)gD_{50}$].

frontiers in Earth Science

ORIGINAL RESEARCH
published: 14 December 2021
doi: 10.3389/feart.2021.762176

Shallow Compaction Modeling and Upscaling: A One-Dimensional Analytical Solution and Upscaling

Jingchen Zhang[1,2]*, *Jingsheng Ma*[2], *Gary D. Couples*[2] and *Nicholas Izuchukwu Osuji*[1]

[1]China University of Petroleum, Beijing, China, [2]Institute of Petroleum Engineering, Heriot-Watt University, Edinburgh, United Kingdom

Natural depositional processes frequently give rise to the heterogeneous multilayer system, which is often overlooked but essential for the simulation of a geological process. The sediments undergo the large-strain process in shallow depth and the small-strain process in deep depth. With the transform matrix and Laplace transformation, a new method of solving multilayer small-strain (Terzaghi) and large-strain (Gibson) consolidations is proposed. The results from this work match the numerical results and other analytical solutions well. According to the method of transform matrix which can consider the integral properties of multilayer consolidation, a relevant upscaling method is developed. This method is more effective than the normally used weighted average method. Correspondingly, the upscaling results indicate that the upscaled properties of a multilayer system vary in the consolidation process.

Keywords: Terzaghi, Gibson, multilayer consolidation, analytical solution, upscaling

OPEN ACCESS

Edited by:
Andrew James Manning,
HR Wallingford, United Kingdom

Reviewed by:
Zhixiong Shen,
Coastal Carolina University,
United States
Hooman Fatoorehhi,
University of Tehran, Iran

***Correspondence:**
Jingchen Zhang
jingchen120@126.com

Specialty section:
This article was submitted to Sedimentology, Stratigraphy and Diagenesis, a section of the journal Frontiers in Earth Science

Received: *21 August 2021*
Accepted: *18 November 2021*
Published: *14 December 2021*

Citation:
Zhang J, Ma J, Couples GD and Osuji NI (2021) Shallow Compaction Modeling and Upscaling: A One-Dimensional Analytical Solution and Upscaling. Front. Earth Sci. 9:762176. doi: 10.3389/feart.2021.762176

INTRODUCTION

Sediment compaction involves the process of reduction in pore volume of the sediment accompanied by an increase in density (Bjørlykke et al., 2009). The physical characteristics of the sediment change after deposition due to stress from overburden (gravitational), biological, or chemical reactions. To explain the major processes for the sediment compaction and help visualize the relationship of porosity loss with depth, various models were developed over the years to better capture the compaction process.

Athy's (1930a, 1930b) compaction model illustrates that the decrease in porosity with depth is as a result of expulsion of the interstitial fluid within the pores. Hence, porosity reduction and density increase are directly proportional to the increase of overburden and tectonic stresses. Hedberg (1936) classified the process of sediment compaction into four stages: 1) mechanical rearrangement and dewatering of sediments as porosity reduces from 90 to 75%; 2) loss of adsorbed water as porosity reduces from 75 to 35%; 3) mechanical deformation as the sediment resists further compaction, leading to grain recrystallization with porosity from 35 to 10% to even below 10%; and 4) chemical readjustment stage. Athy's, Hedberg's, and Terzaghi's data were adopted for Weller's model (1959) which states that clay particles occupy the void spaces as the non-clay particles deform and share mutual contact. In addition, Power's (1967) compaction model is based on changes in clay mineralogy with burial depth and explains clay transformation and changes in the adsorbed water content at different depths.

Teodorovich and Chernov (1968) in their model explained that compaction occurs in three stages: 1) fast expulsion of a large volume of fluid takes place with initial porosity loss, from 66 to 40% for clays and sandstones, and from 56 to 40% for siltstones; 2) porosity falls sharply to approximately

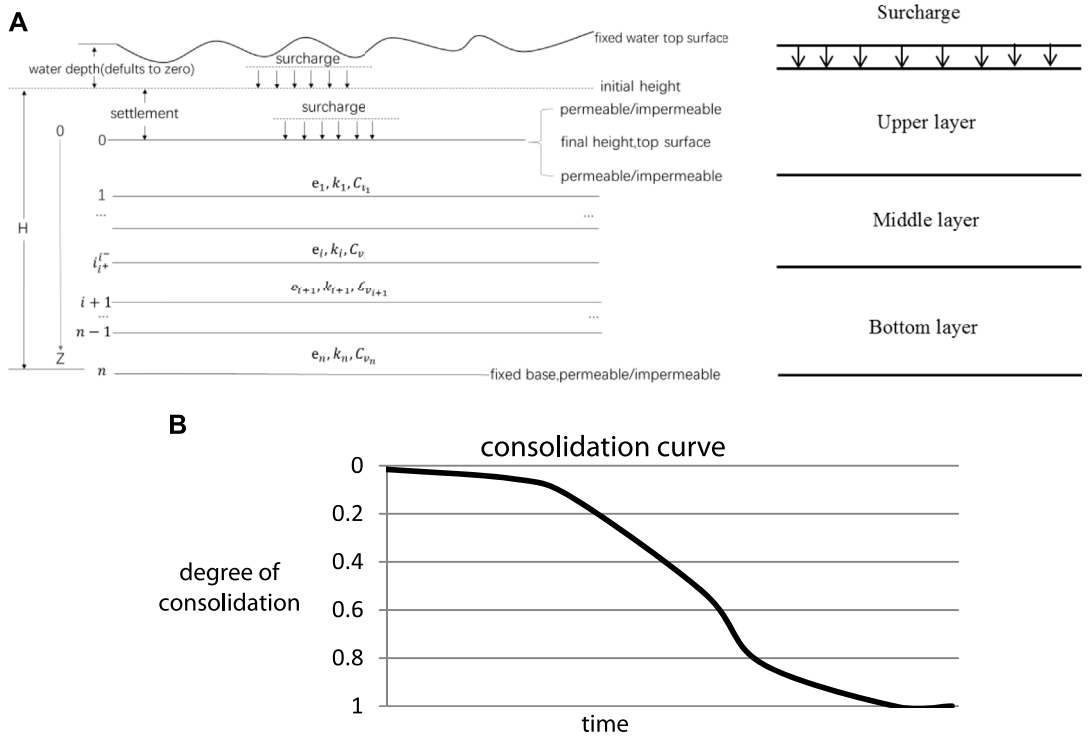

FIGURE 1 | (A) Consolidation model sketch map **(left)**, simplified sketch map of three layers with different properties **(right)**. **(B)** Consolidation curve.

20%; and 3) porosity plunges to about 7–8% for shale and sandstones, at 1,400–6,000 m burial depth. Burst's (1969) compaction model resembles the previous models of clay transformation and dehydration, and states that the amount of water in movement should constitute 10–15% of the compacted bulk volume. However, this model has not been substantiated by experimental investigation. Interestingly, Beall's model (1970) is based on his study on core data from offshore Louisiana and from high-pressure experiments on marine muds. Beall's model involves the expulsion of fluid during initial stages of sediment burial with a pore throat angle at approximately six around a depth of 1,006 m. Here, the porosity decreases at a slower rate during the third stage of compaction where the angle is > 1 Å. In Overton and Zanier's (1970) model, the compaction of sediments in four stages resembles Beall's model. This model states that in the Gulf Coast, sands and shales are difficult to distinguish on self-potential electric log at depths less than 3,000 ft due to similarities of water in them. Consequently, Overton and Zanier's model focused on the different water types in four stages at different depths.

Natural deposition processes frequently give rise to layered soil deposits with alternating or random layers, which are characterized by varying properties such as permeability, compressibility, and thickness. The deposited sediments undergo a large-strain process at shallow depth and a small-strain process in deeper locations. The existence of these processes has been recognized in geology/geotechnical engineering to influence compaction. Small-strain mechanical compaction typically involves minimal deformation of compacted grains due to vertical load and captures the behavior of sediments buried deeply in a basin, whereas large-strain compaction involves large deformation of compacted grains due to its interaction with varying loads at shallow depths. These heterogeneous fine-grained sediments at shallow burial (<1000 m) below the seafloor experience not only large strain but also variable degrees of overpressure in their pore space as a result of disequilibrium dissipation of pore fluid (Mondol et al., 2007). Consequently, the shallow overpressure poses a significant risk to the economics and safety of hydration production and may impact hydrocarbon generation deep in a basin and hydrocarbon migration to traps during basin evolution. In fine-grained sediments, deformations related to mechanical processes are dominant in the very first kilometers of depth (Hedberg, 1936; Maltman, 1994). At greater depths and temperatures, chemically modified consolidation becomes an important porosity-reducing process (Schmid and Mcdonald, 1979; Bjørlykke et al., 1989; Bjørlykke, 1998; Bjørlykke, 1999).

A sketch map for a one-dimensional consolidation model is shown in **Figure 1** (left). The surcharge, which is an additional load in the form of a concentrated force or distributed load that acts on a ground surface or inside the soil body, is applied on the top of the sediment with an infinite horizontal width and is surmounted by a certain depth of water on the top of the sediment. The sediment undergoes consolidation processes, in which water flows out from the top and/or bottom boundaries as the sediment height decreases. The top (T) and bottom (B) boundaries may be permeable (P) or impermeable (I) and, hence, can be marked as PTIB (permeable top and

impermeable bottom) and PTPB (permeable top and permeable bottom). **Figure 1B** shows a typical consolidation curve, depicting the consolidation degree versus the time. The consolidation degree is the ratio of the settlement at time t to the final settlement. Hence, the consolidation curve captures the sediment's consolidation characteristics.

Some geotechnical engineering studies such as basin modeling require the research object to be discretized into blocks, with sizes in kilometers laterally and hundreds of meters vertically. Each block is then assumed to behave according to a single (homogeneous) compaction and flow relationship, even though the material is typically heterogeneous to variable degrees. The basin modeling ignores the heterogeneity of the sediment, large-strain deformation, and fluid flow conditions that occur at smaller length- and/or time-scales than those at basin scales. This can lead to incorrect predication of shallow compaction and overpressure, and subsequently basin evolution (refer to general software in the basin simulation field, such as PetroMod). Therefore, the effects of intra-block heterogeneity must be taken into account by upscaling, which then substitutes the heterogeneous property region consisting of fine grid cells with an equivalent homogeneous region of a single coarse-grid cell having an effective property value (Jingchen 2015).

Theories have been developed by researchers to describe the large-strain and small-strain consolidation processes. However, the widely adopted theories are the Terzaghi theory (Terzaghi, 1943) for small-strain and the Gibson theory (Gibson et al., 1967) for large-strain consolidations. The Terzaghi consolidation theory is widely adopted for small-strain consolidation due to its convenience and its improved methods which are still widely adopted in geotechnical engineering and other fields (Terzaghi, 1943; ArminKauerauf, 2009). As for the large-strain consolidation, the Gibson consolidation theory is more effective (Gibson et al., 1967; Gibson et al., 1981; Gibson et al., 1982), and the equation solutions are primarily based on numerical solution. However, some analytical solutions have been provided under certain conditions (Xie and Leo, 2004; Morris and Dux, 2010).

As for the multilayer system, analytical solutions such as state space (Ai et al., 2008a), three-dimensional transfer matrix solution (Ai et al., 2008b), and differential quadrature method (Chen et al., 2005) have been developed, and numerical finite difference is also widely adopted. In addition, a great deal of research has been done on multilayer consolidation, considering small-strain and large-strain processes (Schiffman and Stein, 1970; Lee et al., 1992; Xie et al., 1999; Xie et al., 2002; Chen, 2004; Chen et al., 2005; Abbasi et al., 2007; Cai et al., 2007; Ai et al., 2008b; Geng, 2008; Ai et al., 2011). However, there are two main drawbacks associated with the previous research studies. The first is that the solutions are under restricted (some parameters such as permeability, compressibility, and height are the same for different layers), and second, none of those researches focused on upscaling and supplying integral property for the multilayer consolidation system. Our work therefore focuses on overcoming these drawbacks.

As earlier mentioned, the effects of intra-block heterogeneity must be taken into account by upscaling. Since the weighted average method commonly adopted in geological engineering for multilayer systems is presently not supported by theoretical derivation, we then implemented the transform matrix and Laplace transformation to solve the multilayer small-strain (Terzaghi) and large-strain (Gibson) consolidations. According to the method of transform matrix which considers the properties of multilayer consolidation, an upscaling method is developed. Results obtained accurately match the numerical and other analytical solutions. Hence, this method is more effective than the common weighted average method. The upscaling results indicate that the properties of multilayer systems change during the consolidation processes.

ANALYTICAL SOLUTION AND UPSCALING FOR MULTILAYER TERZAGHI CONSOLIDATION

Governing Equations of Solution and Upscaling for Multilayer Terzaghi Consolidation

The Terzaghi theory for one-dimensional consolidation states that all quantifiable changes in the stress of a soil (compression, deformation, and shear resistance) are a direct result of changes in effective stress. The effective stress σ' is related to total stress σ and the pore pressure p by the following relationship:

$$\sigma = \sigma' + p \tag{1}$$

The overpressure dissipation is described by the following equation:

$$C_{\mathrm{v}}\frac{\partial^2 u}{\partial z^2} = \frac{\partial u}{\partial t}, \tag{2}$$

$$C_{\mathrm{v}} = \frac{kE_s}{\gamma_w}, \tag{3}$$

where C_{v} is the coefficient of consolidation, E_s is the modulus of compressibility, k is the hydraulic conductivity, γ_w is the unit weight of water, and u is the excess pore pressure.

In addition, Terzaghi's consolidation theory (Terzaghi, 1929; Terzaghi, 1943) was put forward under the following assumptions:

(1) The soil is homogeneous.
(2) The soil is fully saturated.
(3) The solid particles and water are incompressible.
(4) Soil compression and flow are one-dimensional.
(5) Strains in the soil are relatively small.
(6) Darcy's law is valid for all hydraulic gradients.
(7) The coefficient of permeability and the coefficient of volume compressibility remain constant throughout the process.
(8) There is a unique relationship, independent of time, between the void ratio and the effective stress.

It is therefore necessary to point out that according to the principle of effective stress, total stress increment is produced by the load applied on the multilayer systems. Resultantly, the effective stress increases with excess pore pressure decrease as time goes on.

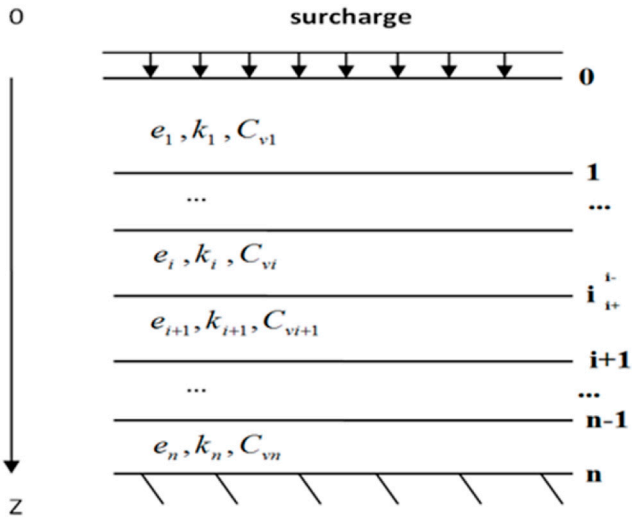

FIGURE 2 | Schematics of multilayer Terzaghi consolidation (positive axis from 0 to z).

$$\sigma' = \sigma - P \tag{4}$$

According to **Eq. 4**, the following equation with the variable of effective stress increment can be obtained, which will benefit our solution.

$$C_v \frac{\partial^2 \sigma'}{\partial z^2} = \frac{\partial \sigma'}{\partial t} \tag{5}$$

The common weighted average method generates a C_v for the whole multilayer system according to

$$C_v = \frac{\sum_{i=1}^{n} h_i \times C_{v_i}}{\sum_{i=1}^{n} h_i}. \tag{6}$$

The Laplace transform is a widely used integral transform with many applications in physics and engineering. Hence, Stehfest numerical inversion of Laplace transforms is adopted (Stehfest, 1960) for our study, and we utilize the transformation matrix to connect parts within the multilayer system. According to the integral multilayer transformation matrix and transformation matrix between different layers, the distribution of effective stress increments and excess pore pressure can be obtained. Moreover, results are verified with an implicit finite difference numerical solution. **Figure 2** shows a schematic plot of the multilayer Terzaghi consolidation.

Consequently, the Laplace transform of **Eq. 5** can be expanded to

$$C_v \frac{\partial^2 \tilde{\sigma}'(z,s)}{\partial z^2} = s\tilde{\sigma}'(z,s) - \sigma'(z,0), \tag{7}$$

where $\tilde{\sigma}'(z,s)$ is the Laplace transform of $\sigma'(z,t)$.

At the beginning of consolidation, according to the effective stress principle, pore pressure is equal to overburden stress, which is zero initial effective stress; thus **Eq. 7** can be obtained.

$$C_v \frac{\partial^2 \tilde{\sigma}'(z,s)}{\partial z^2} = s\tilde{\sigma}'(z,s). \tag{7a}$$

Then, the general solution of the ordinary differential equation for **Eq. 7** is as follows:

$$\tilde{\sigma}'(z,s) = c_1 \exp(\beta z) + c_2 \exp(-\beta z), \tag{8}$$

where c_1 and c_2 are constants, $\beta = \sqrt{\frac{s}{c_v}}$.

Combining **Eq 9** 错误!未找到引用源。 and its partial derivative about z, the following expression can be derived:

$$\begin{bmatrix} \tilde{\sigma}'(z,s) \\ \frac{\partial \tilde{\sigma}'(z,s)}{\partial z} \end{bmatrix} = \begin{bmatrix} \exp(\beta z) & \exp(-\beta z) \\ \beta \exp(\beta z) & -\beta \exp(-\beta z) \end{bmatrix} \begin{bmatrix} c_1 \\ c_2 \end{bmatrix}. \tag{9}$$

When **z** = 0:

$$\begin{bmatrix} \tilde{\sigma}'(0,s) \\ \frac{\partial \tilde{\sigma}'(0,s)}{\partial z} \end{bmatrix} = \begin{bmatrix} 1 & 1 \\ \beta & -\beta \end{bmatrix} \begin{bmatrix} c_1 \\ c_2 \end{bmatrix}. \tag{9a}$$

Combining **Eq 10** and **Eq 11** yields **Eq. 12**:

$$\begin{bmatrix} \tilde{\sigma}'(0,s) \\ \frac{\partial \tilde{\sigma}'(0,s)}{\partial z} \end{bmatrix} = \begin{bmatrix} \frac{1}{2}[\exp(-\beta z) + \exp(\beta z)] & \frac{1}{2\beta}[\exp(-\beta z) - \exp(\beta z)] \\ \frac{\beta}{2}[\exp(-\beta z) - \exp(\beta z)] & \frac{1}{2}[\exp(-\beta z) + \exp(\beta z)] \end{bmatrix} \times \begin{bmatrix} \tilde{\sigma}'(z,s) \\ \frac{\partial \tilde{\sigma}'(z,s)}{\partial z} \end{bmatrix}. \tag{10}$$

And when z_i is not zero:

$$\begin{bmatrix} \tilde{\sigma}'(z_i,s) \\ \frac{\partial \tilde{\sigma}'(z_i,s)}{\partial z} \end{bmatrix} = \begin{bmatrix} 1 & 1 \\ \beta & -\beta \end{bmatrix} \begin{bmatrix} \exp(\beta z_i) & 0 \\ 0 & \exp(-\beta z_i) \end{bmatrix} \times \begin{bmatrix} \frac{\beta}{2\beta \exp(\beta z)} & \frac{1}{2\beta \exp(\beta z)} \\ \frac{\beta}{2\beta \exp(-\beta z)} & \frac{-1}{2\beta \exp(-\beta z)} \end{bmatrix} \begin{bmatrix} \tilde{\sigma}'(z,s) \\ \frac{\partial \tilde{\sigma}'(z,s)}{\partial z} \end{bmatrix}. \tag{11}$$

Then the relationship between the top surface stress and the bottom stress can be derived. When considering the equation of continuous stress, and flow conservation, between two layers, the relationship between different layers can be derived.

$$k_i \frac{\partial \tilde{\sigma}'(z_i^-,s)}{\partial z} = k_{i+1} \frac{\partial \tilde{\sigma}'(z_i^+,s)}{\partial z}, \tag{12}$$

$$\tilde{\sigma}'(z_i^-,s) = \tilde{\sigma}'(z_i^+,s). \tag{13}$$

Combining **Eq 12** and **Eq 13** yields **Eq. 16**:

$$\begin{bmatrix} \widetilde{\sigma'}(z_i^-, s) \\ \dfrac{\partial \widetilde{\sigma'}(z_i^-, s)}{\partial z} \end{bmatrix} = \begin{bmatrix} 1 & \\ & \dfrac{k_{i+1}}{k_i} \end{bmatrix} \begin{bmatrix} \widetilde{\sigma'}(z_i^+, s) \\ \dfrac{\partial \widetilde{\sigma'}(z_i^+, s)}{\partial z} \end{bmatrix}. \tag{14}$$

Stress distribution in the same layer and in the interface can be derived, respectively, by using **Eq. 11** and **Eq. 14**. With the equation of each layer combined together, a transform matrix T can be obtained to express the relationship between $z = 0$ and $z = z_n$.

$$\begin{bmatrix} \widetilde{\sigma'}(0, s) \\ \dfrac{\widetilde{\partial \sigma'}(0, s)}{\partial z} \end{bmatrix} = T \begin{bmatrix} \widetilde{\sigma'}(z_n, s) \\ \dfrac{\widetilde{\partial \sigma'}(z_n, s)}{\partial z} \end{bmatrix} \tag{15}$$

Here, this article only considers the situation of the pervious top surface and impervious bottom PTIB for illustration.

The following boundary conditions are implemented:

$$\mathrm{z} = 0, \mathrm{u}(\mathrm{z}, \mathrm{t}) = 0;\ \mathrm{z} = \mathrm{z_n},\ \frac{\partial \mathrm{u}(z, t)}{\partial z} = 0. \tag{16}$$

The corresponding Laplace transformation:

$$z = 0, \widetilde{\sigma'}(0, s) = \frac{\sigma}{s}; z = z_n, \frac{\widetilde{\partial \sigma'}(z_n, s)}{\partial z} = 0 \tag{17}$$

Hence

$$\widetilde{\sigma'}(z_n, s) = \frac{\sigma}{T_{11} S}, \tag{18}$$

where σ is the pressure on the surface and T_{11} is the value of the first column and the first row of T.

With $\widetilde{\sigma'}(z_n, s)$, the stress at each upper point $\widetilde{\sigma'}(z, s)$ can be obtained by the transformation matrix. Moreover, the real stress distribution can be derived by the inverse of Laplace transformation.

As for an n-layer consolidation system, the multilayer consolidation transform matrix is

$$T_1 = \begin{bmatrix} \frac{1}{2}\left[\exp(-\beta_1 h_1) + \exp(\beta_1 h_1)\right] & \frac{k_2}{k_1}\frac{1}{2\beta_1}\left[\exp(-\beta_1 h_1) - \exp(\beta_1 h_1)\right] \\ \frac{\beta_1}{2}\left[\exp(-\beta_1 h_1) - \exp(\beta_1 h_1)\right] & \frac{k_2}{k_1}\frac{1}{2}\left[\exp(-\beta_1 h_1) + \exp(\beta_1 h_1)\right] \end{bmatrix}$$

$$T_i = \begin{bmatrix} \frac{1}{2}\left[\exp(-\beta_i h_i) + \exp(\beta_i h_i)\right] & \frac{k_{i+1}}{k_i}\frac{1}{2\beta_i}\left[\exp(-\beta_i h_i) - \exp(\beta_i h_i)\right] \\ \frac{\beta_i}{2}\left[\exp(-\beta_i h_i) - \exp(\beta_i h_i)\right] & \frac{k_{i+1}}{k_i}\frac{1}{2}\left[\exp(-\beta_i h_i) + \exp(\beta_i h_i)\right] \end{bmatrix}$$

$$T_n = \begin{bmatrix} \frac{1}{2}\left[\exp(-\beta_n h_n) + \exp(\beta_n h_n)\right] & \frac{1}{2\beta_n}\left[\exp(-\beta_n h_n) - \exp(\beta_n h_n)\right] \\ \frac{\beta_n}{2}\left[\exp(-\beta_n h_n) - \exp(\beta_n h_n)\right] & \frac{1}{2}\left[\exp(-\beta_n h_n) + \exp(\beta_n h_n)\right] \end{bmatrix}$$

$$\begin{bmatrix} \widetilde{\sigma'}(0, s) \\ \dfrac{\widetilde{\partial \sigma'}(0, s)}{\partial z} \end{bmatrix} = T_1 \cdot \cdot T_i \cdot \cdot T_n \cdot \begin{bmatrix} \widetilde{\sigma'}(z_n, s) \\ \dfrac{\widetilde{\partial \sigma'}(z_n, s)}{\partial z} \end{bmatrix}, \quad i = 2, 3 \ldots\ldots n-1 \tag{19}$$

The common weighted average method will lead to the following weighted average method transform matrix:

$$\begin{bmatrix} \widetilde{\sigma'}(0, s) \\ \dfrac{\widetilde{\partial \sigma'}(0, s)}{\partial z} \end{bmatrix} = \begin{bmatrix} \frac{1}{2}\left[\exp(-\beta z_n) + \exp(\beta z_n)\right] & \frac{1}{2\beta}\left[\exp(-\beta z_n) - \exp(\beta z_n)\right] \\ \frac{\beta}{2}\left[\exp(-\beta z_n) - \exp(\beta z_n)\right] & \frac{1}{2}\left[\exp(-\beta z_n) + \exp(\beta z_n)\right] \end{bmatrix} \times \begin{bmatrix} \widetilde{\sigma'}(z_n, s) \\ \dfrac{\widetilde{\partial \sigma'}(z_n, s)}{\partial z} \end{bmatrix}. \tag{20}$$

When $t \to \infty, s \to 0, \beta \to 0$, by applying the following Taylor expansion we obtain

$$e^x = \sum_{n=0}^{\infty} \frac{x^n}{n!}. \tag{21}$$

As for a multilayer transform matrix, **Eq. 18** will develop into

$$\begin{bmatrix} \widetilde{\sigma'}(0, s) \\ \dfrac{\widetilde{\partial \sigma'}(0, s)}{\partial z} \end{bmatrix} = \begin{bmatrix} 1 & -\left(h_n + \sum_{i=1}^{n-1} \dfrac{k_n}{k_i} h_i\right) \\ 0 & \dfrac{k_n}{k_1} \end{bmatrix} \begin{bmatrix} \widetilde{\sigma'}(z_n, s) \\ \dfrac{\widetilde{\partial \sigma'}(z_n, s)}{\partial z} \end{bmatrix}. \tag{22}$$

Then, the weighted average method transform matrix given in **Eq. 20** will develop into

$$\begin{bmatrix} \widetilde{\sigma'}(0, s) \\ \dfrac{\widetilde{\partial \sigma'}(0, s)}{\partial z} \end{bmatrix} = \begin{bmatrix} 1 & -z \\ 0 & 1 \end{bmatrix} \begin{bmatrix} \widetilde{\sigma'}(z, s) \\ \dfrac{\widetilde{\partial \sigma'}(z, s)}{\partial z} \end{bmatrix}. \tag{23}$$

It can therefore be concluded that when conductivities in different layers are nearly the same, the weighted average method can be adopted for the whole multilayer system, which is the situation of homogenous.

Verification

This analytical solution is verified against the results of Lee et al. (1992), as shown in **Figure 3**. The parameters used in Lee's model are shown in **Table 1**, and the model sketch map follows the illustration in **Figure 1** (right), showing a simplified sketch map of four layers with a PTIB and without overlaying water.

To compare different upscaling methods, an implicit finite-difference numerical model is developed. This study utilizes a numerical model as a benchmark model and is verifiable with both laboratory tests and a basin model (Jingchen Zhang., 2015). Analytical results are also compared with implicit finite difference numerical solution for verification. The parameters of the three different layers are shown in **Table 2**. Comparison of the results is then shown in **Figure 4**. Hence, a conclusion can be reached that this method can be applied to multilayer Terzaghi consolidation compaction. It should be noted that the values of m_{vl} and surcharge ensure the small

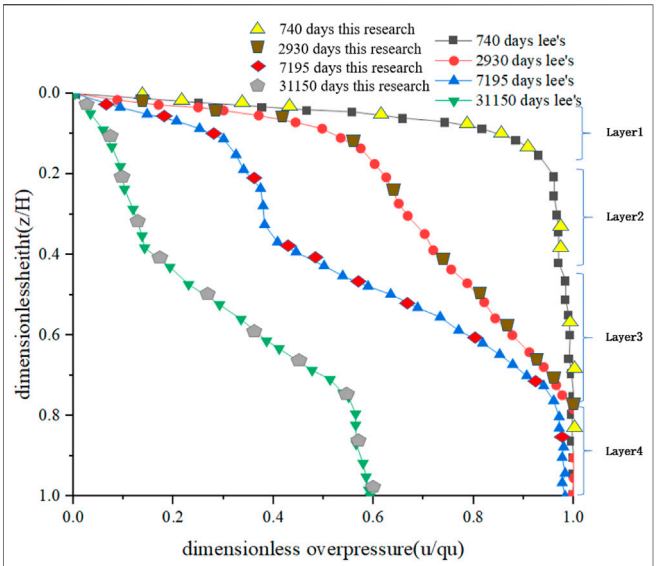

FIGURE 3 | Verification with Lee—excess pore water pressure isochrones and PTIB (q_u is the surcharge on the surface and H is the height of the multilayer system).

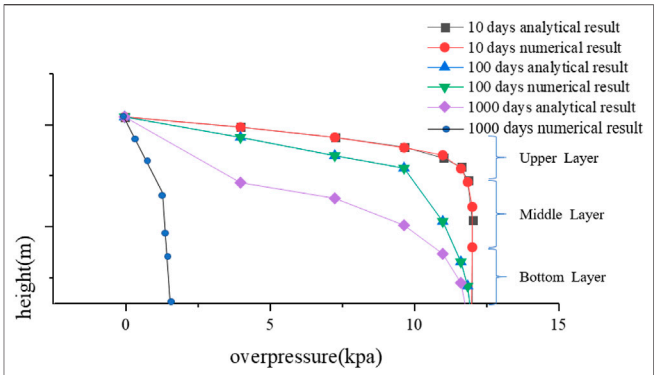

FIGURE 4 | Comparison of overpressure evolution of three layers with different properties between analytical and numerical results for 10, 100, 1,000 days.

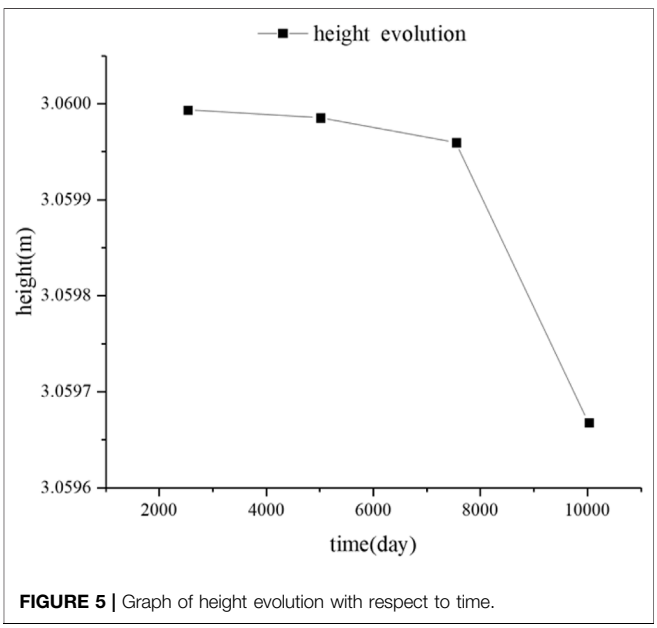

FIGURE 5 | Graph of height evolution with respect to time.

TABLE 1 | Parameters of Lee's model ($m_{vl} = 1/E_s$).

Layer number	C_v (m^2/d)	k (m/d)	Height (m)	m_{vl} (Pa^{-1})
1	0.0038	2.4049×10^{-6}	3.048	6.41×10^{-5}
2	0.0178	0.7132×10^{-5}	6.096	4.07×10^{-5}
3	0.0051	1.0150×10^{-6}	9.144	2.034×10^{-4}
4	0.0064	2.5451×10^{-6}	12.192	4.07×10^{-5}

TABLE 2 | Model parameters ($m_{vl} = 1/E_s$).

Layer	C_v (m^2/s)	k (m/s)	Height (m)	m_{vl}(kPa^{-1})
Upper	3.125×10^{-8}	1.038×10^{-12}	1.02	3.3948×10^{-6}
Middle	2.662×10^{-8}	6.8403×10^{-12}	1.02	2.6221×10^{-5}

strain, and correspondingly nearly no settlement can be seen in **Figure 4**. Resultantly, the small changes in height are shown in **Figure 5**.

Comparisons of Different Upscaling Methods

Here, T represents the properties of the multilayer system; then a new consolidation coefficient C_v is needed to represent the whole multilayer system. With the new C_v, a new transform matrix for the multilayer consolidation T' can be obtained. The new C_v should be the one that makes the minimum of **Eq. 24**, to numerically match T and T'.

$$\sqrt{(T'(1,1)-T(1,1))^2+(T'(1,2)-T(1,2))^2+(T'(2,1)-T(2,1))^2+(T'(2,2)-T(2,2))^2} \tag{24}$$

Under the condition of PTIB, it can be found that $\frac{\partial\widetilde{\sigma'}(z_n,s)}{\partial z}=0$, so $\tilde{\sigma}(0,s)=T(1,1)\times\widetilde{\sigma'}(z_n,s)'$. This provides a thought of using a homogeneous layer $T(1,1)$ to represent multilayer nonhomogeneous consolidation. A new β is required to fit the value of $T(1,1)$. The example of the afore-mentioned three layers with different properties is adopted for this illustration. The new C_v can be derived from

$$\frac{1}{2}\left[e^{-\beta z}+e^{\beta z}\right]=T(1,1). \tag{25}$$

C_v changes with time according to **Eq. 25**, as shown in **Figure 6**.

In light of the long-time consolidation, C_v is set to be 1.4×10^{-8} (m^2/s). A homogeneous layer with the new upscaling C_v can then be compared with the three-layer system. Specifically, the transform matrix for a three-layer system is

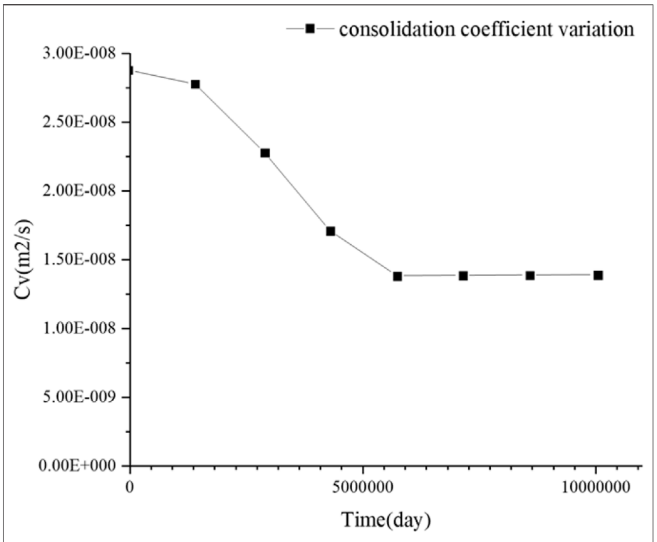

FIGURE 6 | Plot of consolidation coefficient c_v versus time.

$$T_1 = \begin{bmatrix} \frac{1}{2}\left[e^{-\beta_1 h_1} + e^{\beta_1 h_1}\right] & \frac{k_2}{k_1}\frac{1}{2\beta_1}\left[e^{-\beta_1 h_1} - e^{\beta_1 h_1}\right] \\ \frac{\beta_1}{2}\left[e^{-\beta_1 h_1} - e^{\beta_1 h_1}\right] & \frac{k_2}{k_1}\frac{1}{2}\left[e^{-\beta_1 h_1} + e^{\beta_1 h_1}\right] \end{bmatrix}$$

$$T_2 = \begin{bmatrix} \frac{1}{2}\left[e^{-\beta_2 h_2} + e^{\beta_2 h_2}\right] & \frac{k_3}{k_2}\frac{1}{2\beta_2}\left[e^{-\beta_2 h_2} - e^{\beta_2 h_2}\right] \\ \frac{\beta_2}{2}\left[e^{-\beta_2 h_2} - e^{\beta_2 h_2}\right] & \frac{k_3}{k_2}\frac{1}{2}\left[e^{-\beta_2 h_2} + e^{\beta_2 h_2}\right] \end{bmatrix}. \quad (26)$$

$$T_3 = \begin{bmatrix} \frac{1}{2}\left[e^{-\beta_3 h_3} + e^{\beta_3 h_3}\right] & \frac{1}{2\beta_3}\left[e^{-\beta_3 h_3} - e^{\beta_3 h_3}\right] \\ \frac{\beta_3}{2}\left[e^{-\beta_3 h_3} - e^{\beta_3 h_3}\right] & \frac{1}{2}\left[e^{-\beta_3 h_3} + e^{\beta_3 h_3}\right] \end{bmatrix}$$

$$\begin{bmatrix} \tilde{\sigma}'(0,s) \\ \frac{\partial\tilde{\sigma}'(0,s)}{\partial z} \end{bmatrix} = T_1 T_2 T_3 . \begin{bmatrix} \tilde{\sigma}'(z_3,s) \\ \frac{\partial\tilde{\sigma}'(z_3,s)}{\partial z} \end{bmatrix}.$$

Meanwhile, the common weighted average method will lead to another C_v. Here, $C_v = 3.0093 \times 10^{-8}$ (m^2/s) in the weighted average method is used. With this C_v, a new β and a weighted average transform matrix can be derived. Comparisons between the three methods are shown in **Figure 7**.

$$R = \frac{\sum_{i=1}^{n}\left|u_i' - u_i\right|/u_i}{n} \quad (27)$$

According to **Eq. 27**, the relative error between the weighted average method or the new upscaling method and the three-layer numerical results can be obtained, as shown in **Figure 8**.

When it comes to 20,000 days, there is nearly no overpressure; hence, the multilayer system's characteristics are studied within 20,000 days. As can be seen from **Figure 9**, in the first 100 days,

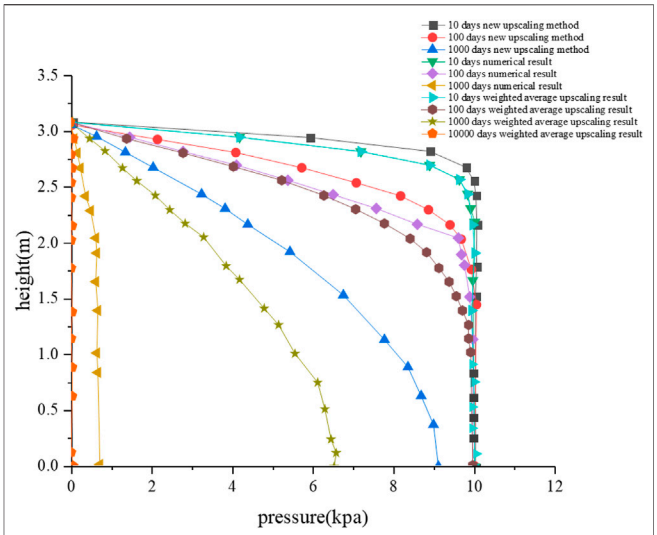

FIGURE 7 | Overpressure evolution comparison between the two upscaling methods (weighted average and the new method) and numerical results for 10, 100, 1,000, and 10,000 days.

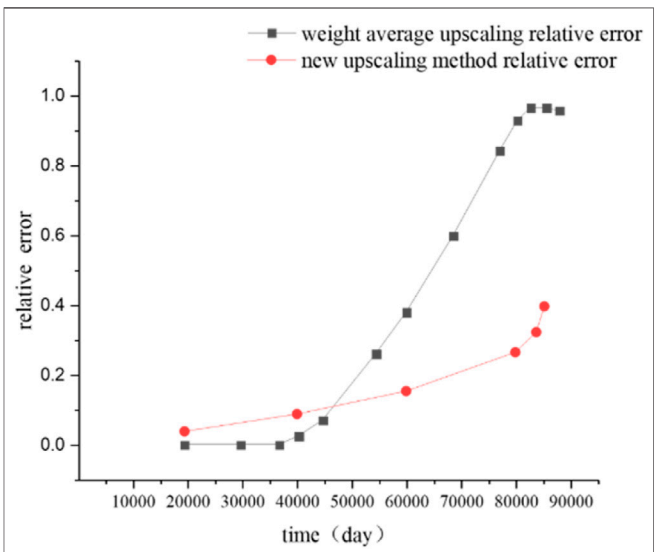

FIGURE 8 | Plot of relative error change with time for weighted average upscaling and the new upscaling method.

the weighted average method is more efficient than the upscaling method. As fluid flows out through the top surface, the whole system is determined by the properties of the first layer before pressure reduction reaches the second layer. Overpressure distributions of one homogeneous layer (same properties with the upper layer) and three nonhomogeneous layers' consolidation are the same. This can explain why the results of changing C_v and the weighted average method compact faster than the real situation. The possible explanation is that bigger C_v of the upper layer is applied to the whole layers with small C_v characteristics. The multilayer consolidation will show the integral properties more accurately after the stimulation reaches the bottom.

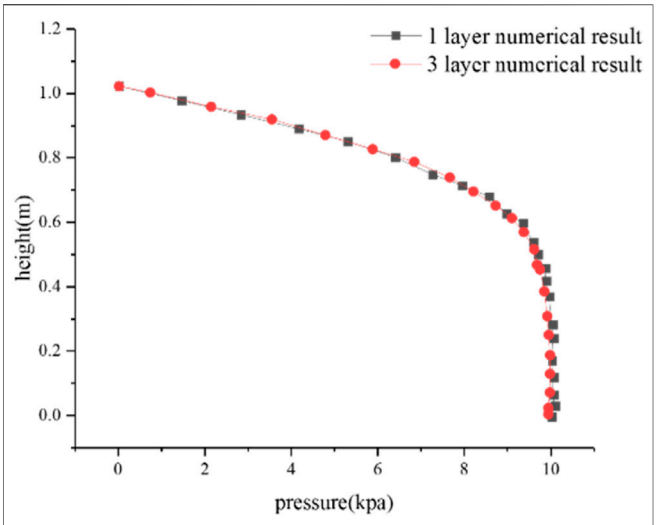

FIGURE 9 | Result of one homogeneous layer and three layers' consolidation before the stimulation reaches the second layer, overpressure distribution at 10 days.

ANALYTICAL SOLUTION AND UPSCALING FOR MULTILAYER GIBSON CONSOLIDATION

Governing Equations of Solution and Upscaling for Multilayer Gibson Consolidation

Gibson et al. (1967) developed a large-strain consolidation theory with more general basic assumptions than the small-strain theory in (3), (5), and (7) of Terzaghi's assumptions. The limitation of small strains was not imposed, and the soil compressibility and permeability are allowed to vary with the void ratio during consolidation. These assumptions are closer to the actual scenario. Furthermore, Darcy's law is assumed to be valid, but it is recasted in a form in which it is the relative velocity of the soil skeleton and the pore fluid. The fluid velocity is related to the excess pore pressure gradient.

$$-\frac{1}{1+e_0}\frac{\partial e}{\partial t}+\left(\frac{\gamma_s}{\gamma_w}-1\right)\frac{d}{de}\left[\frac{k}{1+e}\right]\frac{\partial e}{\partial z}+\frac{\partial}{\partial z}\left[-\frac{k(1+e_0)}{\gamma_w(1+e)}\frac{d\sigma'}{de}\frac{\partial e}{\partial z}\right]=0, \tag{28}$$

where e is the void ratio; e_0 is the initial void ratio; k is the conductivity; γ_w and γ_s are the unit weight of water and soil, respectively;z is the solid coordinate; and σ' is the effective stress.

To apply the transfer matrix method to large-strain consolidation, the simplification of Xie et al. is adopted to simplify Gibson's equation (Xie and Leo, 2004). The influence and theoretical analysis of this simplification can be found in his research.

The coefficient of volume compressibility of the soil skeleton for a large strain is defined as

$$-\frac{1}{1+e}\frac{de}{d\sigma'}=m_{vl}. \tag{29}$$

Then Gibson's equation can be changed to

$$\frac{1}{\gamma_w}\frac{\partial}{\partial z}\left[\frac{k(1+e_0)}{(1+e)}\frac{\partial u}{\partial z}\right]=m_{vl}\frac{1+e}{1+e_0}\left(\frac{\partial u}{\partial t}-\frac{\partial q_u}{\partial t}\right), \tag{30}$$

where q_u is the surcharge and m_{vl} is constant during consolidation.

The relationship between conductivity k and void ratio is

$$\frac{k}{k_o}=\left(\frac{1+e}{1+e_0}\right)^2, \tag{31}$$

where k_o is the initial conductivity at time $t = 0$, k is often found empirically to be a logarithmic function of the void ratio, and e_0 is the initial void ratio.

A load q_u is applied suddenly at $t = 0$ on the top surface of the model and remains constant thereafter. According to the effective stress principle and Xie's assumption (Xie, K. & Leo, C., 2004), the relationship between the void ratio and the excess pore water pressure can be deduced as follows.

$$\frac{1+e}{1+e_0}=\exp\left(-m_{vl}(q_u-u)\right) \tag{32}$$

With **Eq. 29**, **Eq. 30** and **Eq. 32** can now be changed to the following one, which determines excess pore evolution in Lagrangian coordinates:

$$c_{vo}\left[\frac{\partial^2 u}{\partial z^2}+m_{vl}\left(\frac{\partial u}{\partial z}\right)^2\right]=\frac{\partial u}{\partial t}, \tag{33}$$

where c_{vo} is the initial coefficient of consolidation at time t = 0 given by

$$c_{vo}=\frac{k_o}{m_{vl}r_w}. \tag{34}$$

The solution to the large consolidation theory is facilitated by the following transformation.

$$\omega=\omega(z,t)=\exp(m_{vl}u) \tag{35}$$

In consideration of the permeable top impermeable base (PTIB) boundary condition, with **Eq. 35** and **Eq. 33**, the equation of the Terzaghi form will be obtained as follows:

$$\begin{aligned} &c_v\frac{\partial^2\omega}{\partial z^2}=\frac{\partial\omega}{\partial t}\\ &\omega(0,t)=1\\ &\frac{\partial\omega}{\partial z}(H,t)=0\\ &\omega(H,0)=\exp(m_{vl}q_u). \end{aligned} \tag{36}$$

Then the transfer matrix can be adopted for the solution and upscaling of multilayer Gibson consolidation. To use the transfer matrix method, ω should be continuous; hence, different layers

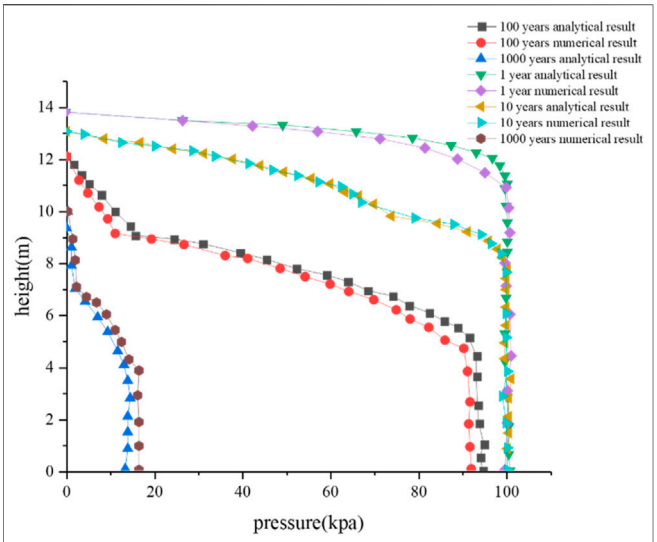

FIGURE 10 | Overpressure evolution comparison of numerical and analytical results for the three layers with different properties for 1, 10, 100, and 1,000 years.

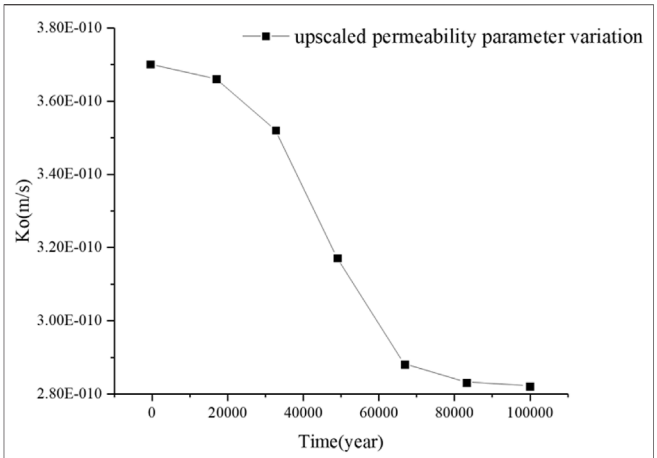

FIGURE 11 | lot of upscaled permeability k_o changes with respect to time.

share the same m_{vl}. Then according to **Eq. 34**, what upscaled is actually k_o, i.e., conductivity upscaling.

Verification

Analytical solution is compared with the developed implicit finite difference numerical code for verification. The model sketch map follows **Figure 1** 错误!未找到引用源。 (right), PTIB, and no overlying water. A three-layer model is adopted for comparison, with the surcharge 1 × 105 Pa, γ_s = 26.950 kN/m^3, and γ_w = 10.045 kN/m^3. For each layer, $m_{vl} = 4 \times 10^{-6}$ Pa^{-1} and thickness = 5 m. The k_o of the surface, middle, and bottom layers are 1.00×10^{-9} m/s, 1.16×10^{-10} m/s, and 1.04×10^{-9} m/s. The e_0 of the surface, middle, and bottom layers are 3, 4, and 5. **Figure 10** shows the comparison results, which are consistent and proves the effectiveness of this method in solving large-strain multilayer consolidation.

Comparisons of Different Upscaling Methods

To evaluate this upscaling method, comparison with the weighted average method is carried out here, utilizing the same three-layer model in Verification. When it comes to 1,000 years, there are nearly no excess pore pressures according to the weighted average method; hence, we focus within 1,000 years.

Upscaling k_{vo} changes with time as shown in **Figure 11**. In consideration of the long geology process, the k_o value is set to be 2.8356×10^{-10} (m/s), and C_v is 7.2337×10^{-9} (m^2/s). While for the weighted average method, k_o is 7.1867×10^{-10} (m/s) and C_v is 1.8333×10^{-9} (m^2/s). The comparisons of the two upscaling methods and numerical solution are shown in **Figure 12**.

The whole model only shows properties of the first layer before the pressure reduction reaches the second layer. Also, the weighted average k_o is closer to the first layer's k_o than the upscaled k_o. Hence, within the first 10 years, the results obtained through the weighted average method are closer to the numerical results than those obtained through the upscaling method. However, as a whole, the upscaling method is more effective than the weighted average method.

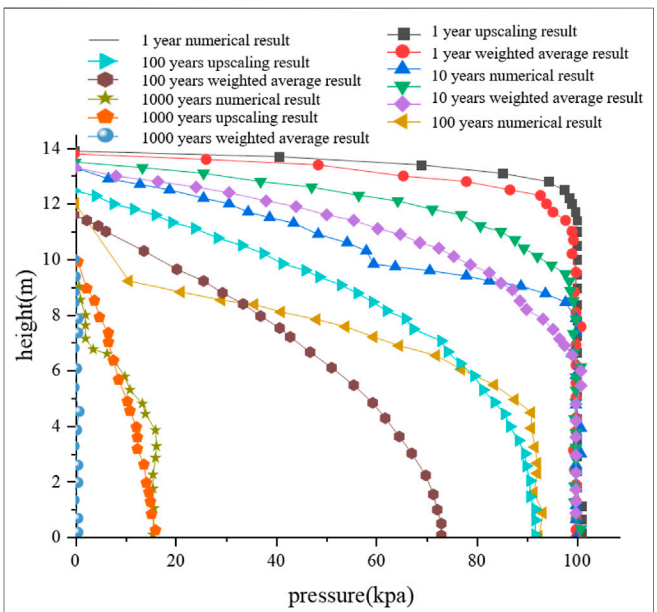

FIGURE 12 | Overpressure evolution comparison between the two upscaling methods (weighted average and the new method) and numerical results for 1, 10, 100, and 1,000 years.

The multilayer system only shows properties of the place affected by the stimulation, and the integral properties will change with the increase in the affected region. This can partly explain the result of a changing upscaled k_o. Consequently, this upscaling method is more accurate than the common weighted average method as a whole for multilayer large-strain consolidation.

CONCLUSION

This work studies the modeling and upscaling of a shallow compaction using a one-dimensional analytical solution approach. The basic law of one-dimensional basin sedimentary simulation is revealed considering the effects of intra-block heterogeneity for both small-strain (deep compaction in the basin) and large-strain (shallow compaction in the basin) consolidations. And the following conclusions are made:

1. Multilayer small-strain (Terzaghi) and large-strain (Gibson) consolidations are solved with the transform matrix and Laplace transformation. The transfer matrix can upscale the heterogeneous multilayer system into one homogenous layer; therefore, it is more convenient and effective in both physical significance and the numerical form than the common weighted average method.
2. The upscaling properties of the whole multilayer system are dynamic, and the multilayer systems only show integral properties of the place affected by the stimulation. The integral properties vary with the increase in the affected region for both small-strain and large-strain consolidations.

DATA AVAILABILITY STATEMENT

The original contributions presented in the study are included in the article/Supplementary Material. Further inquiries can be directed to the corresponding author.

AUTHOR CONTRIBUTIONS

JZ is the key contributor. JM plays a guiding role. GDC: research supervision and obtaining fund.

ACKNOWLEDGMENTS

The research content reported here is part of the first author's PhD research at Heriot-Watt University, Edinburgh, United Kingdom, under CAPROCKS consortium of United Kingdom universities, Newcastle University, Cardiff University, Heriot-Watt University, and University of Leeds. This study was funded by the following companies: Anadarko, BG, BHP Billiton, BP, Chevron, ConocoPhillips, ENI, ExxonMobil, Petrobras, Shell, StatoilHydro, Total, and Unocal.

REFERENCES

Abbasi, N., Rahimi, H., Javadi, A. A., and Fakher, A. (2007). Finite Difference Approach for Consolidation with Variable Compressibility and Permeability. *Comput. Geotechnics* 34, 41–52. doi:10.1016/j.compgeo.2006.09.003

Ai, Z. Y., Cheng, Y. C., and Zeng, W. Z. (2011). Analytical Layer-Element Solution to Axisymmetric Consolidation of Multilayered Soils. *Comput. Geotechnics* 38, 227–232. doi:10.1016/j.compgeo.2010.11.011

Ai, Z. Y., Cheng, Z. Y., and Han, J. (2008a). State Space Solution to Three-Dimensional Consolidation of Multi-Layered Soils. *Int. J. Eng. Sci.* 46, 486–498. doi:10.1016/j.ijengsci.2007.12.003

Ai, Z. Y., Wu, C., and Han, J. (2008b). Transfer Matrix Solutions for Three-Dimensional Consolidation of a Multi-Layered Soil with Compressible Constituents. *Int. J. Eng. Sci.* 46, 1111–1119. doi:10.1016/j.ijengsci.2008.04.005

ArminKauerauf, I. T. H. (2009). *Fundamentals of Basin and Petroleum Systems Modeling*.

Athy, L. F. (1930b). Compaction and Oil Migration. *AAPG Bull.* 14, 25–35. doi:10.1306/3d93289f-16b1-11d7-8645000102c1865d

Athy, L. F. (1930a). Density, Porosity, and Compaction of Sedimentary Rocks. *AAPG Bull.* 14 (1), 1–24. doi:10.1306/3d93289e-16b1-11d7-8645000102c1865d

Beall, A. O., Jr, and Fisher, A. G. (1969). "Sedimentology". Editors (Washington, D.C: US. Govt. Printing Office), 1, 672. doi:10.2973/dsdp.proc.1.124.1969*Initial Reports of the Deep-Sea Drilling Project*

Bjørlykke, K. (1998). Clay Mineral Diagenesis in Sedimentary Basins - a Key to the Prediction of Rock Properties. Examples from the North Sea Basin. *Clay Minerals* 33, 15–34.

Bjørlykke, K., Jahren, J., Mondol, N. H., Marcussen, O., Croize, D., Christer, P., et al. (2009). "Sediment Compaction and Rock Properties," in *AAPG International Conference and Exhibition*.

Bjørlykke, K. (1999). *Muds and Mudstones: Physical and Fluid Flow Properties*. London, United Kingdom: The Geological Society (London) Special Publications, 73–78.Principal Aspects of Compaction and Fluid Flow in Mudstones

Bjørlykke, K., Ramm, M., and Saigal, G. C. (1989). Sandstone Diagenesis and Porosity Modification during Basin Evolution. *Geologische Rundschau* 78, 243–268.

Burst, J. F. (1969). Diagenesis of Gulf Coast Clayey Sediments and its Possible Relation to Petroleum Migration. *AAPG Bull.* 53, 73–93. doi:10.1306/5d25c595-16c1-11d7-8645000102c1865d

Cai, Y.-Q., Geng, X.-Y., and Xu, C.-J. (2007). Solution of One-Dimensional Finite-Strain Consolidation of Soil with Variable Compressibility under Cyclic Loadings. *Comput. Geotechnics* 34, 31–40. doi:10.1016/j.compgeo.2006.08.008

Chen, G. J. (2004). Consolidation of Multilayered Half Space with Anisotropic Permeability and Compressible Constituents. *Int. J. Sol. Structures* 41, 4567–4586. doi:10.1016/j.ijsolstr.2004.03.019

Chen, R. P., Zhou, W. H., Wang, H. Z., and Chen, Y. M. (2005). One-Dimensional Nonlinear Consolidation of Multi-Layered Soil by Differential Quadrature Method. *Comput. Geotechnics* 32, 358–369. doi:10.1016/j.compgeo.2005.05.003

Geng, X. (2008). *Proceedings of the 2008 International Conference on Advanced Computer Theory and Engineering*. IEEE Computer Society, 773–777. doi:10.1109/icacte.2008.219Multi-Dimensional Consolidation Theory for Cyclic Loadings

Gibson, R. E., England, G. L., and Hussey, M. J. L. (1967). The Theory of One-Dimensional Consolidation of Saturated Clays. *Géotechnique* 17, 261–273. doi:10.1680/geot.1967.17.3.261

Gibson, R. E., Schiffman, R. L., and Cargill, K. W. (1982). The Theory of One-Dimensional Consolidation of Saturated Clays: Reply. *Can. Geotech. J.* 19, 116. doi:10.1139/t82-013

Gibson, R. E., Schiffman, R. L., and Cargill, K. W. (1981). The Theory of One-Dimensional Consolidation of Saturated Clays. Ii. Finite Nonlinear Consolidation of Thick Homogeneous Layers. *Can. Geotech. J.* 18, 280–293. doi:10.1139/t81-030

Hedberg, H. D. (1936). Gravitational Compaction of Clays and Shales. *Am. J. Sci.* s5-31, 241–287. doi:10.2475/ajs.s5-31.184.241

Jingchen, Zhang. (2015). *Modelling and Upscaling of Shallow Compaction in Basins*. PHD thesis: Heriot-watt university.

Lee, P. K. K., Xie, K. H., and Cheung, Y. K. (1992). A Study on One-Dimensional Consolidation of Layered Systems. *Int. J. Numer. Anal. Methods Geomech.* 16, 815–831. doi:10.1002/nag.1610161104

Maltman, A. (1994). *The Geological Deformation of Sediments*. London: Chapman & Hall, 1–35. doi:10.1007/978-94-011-0731-0_1Introduction and Overview

Mondol, N. H., Bjørlykke, K., Jahren, J., and Høeg, K. (2007). Experimental Mechanical Compaction of clay mineral Aggregates-Changes in Physical Properties of Mudstones during Burial. *Mar. Pet. Geology.* 24 (5), 289–311. doi:10.1016/j.marpetgeo.2007.03.006

Morris, P. H., and Dux, P. F. (2010). Analytical Solutions for Bleeding of Concrete Due to Consolidation. *Cement Concrete Res.* 40, 1531–1540. doi:10.1016/j.cemconres.2010.06.007

Overton, H. L., and Zanier, A. M. (1970). *Hydratable Shales and the Salinity High enigma*, 2989. Houston, TX, Pap: Fall Meeting of the Society of Petroleum Engineers of AIMESociety of Petroleum Engineers, 9.

Powers, M. C. (1967). Fluid-release Mechanism in Compacting marine Mud-Rocks and Their Importance in Oil Exploration. *AAPG Bull.* 51, 1240–1245. doi:10.1306/5d25c137-16c1-11d7-8645000102c1865d

Schiffman, R. L., and Stein, J. R. (1970). One-Dimensional Consolidation of Layered Systems. *J. Soil Mech. Found. Div.* 96 (4), 1499–1504. doi:10.1061/jsfeaq.0001453

Schmidt, V., and Mcdonald, D. A. (1979). "The Role of Secondary Porosity in the Course of Sandstone Diagenesis,". Editors P. A. SchoUe and P. R. Schluger (Tulsa, Oklahoma: SEPM Spec. Pub), 26, 175–207. doi:10.2110/pec.79.26.0175*The Role of Secondary Porosity in the Course of Sandstone Diagenesis.* Aspects Of Diagenesis

Stehfest, H. (1960). Numerical Inverse of Laplace Transform. *Commun. ACM* 3 (3), 171–173.

Teodorovich, G. I., and Chernov, A. A. (1968). Character of Changes with Depth in Productive Deposits of Apsheron Oil-Gas-Bearing Region. *Soviet Geol.* 4, 83–93.

Terzaghi, K. V. (1929). *Settlement Analysis - the Backbone of Foundation Research*. Tokyo): Word Engineering Congress, 8.

Terzaghi, K. V. (1943). *Theoretical Soil Mechanics*. New York: John Wiley & Sons.

Weller, E. A. (1959). Compaction of Sediments. *AAPG Bull.* 43, 273–310. doi:10.1306/0bda5c9f-16bd-11d7-8645000102c1865d

Xie, K.-H., Xie, X.-Y., and Gao, X. (1999). Theory of One Dimensional Consolidation of Two-Layered Soil with Partially Drained Boundaries. *Comput. Geotechnics* 24, 265–278. doi:10.1016/s0266-352x(99)00012-9

Xie, K.-H., Xie, X.-Y., and Jiang, W. (2002). A Study on One-Dimensional Nonlinear Consolidation of Double-Layered Soil. *Comput. Geotechnics* 29, 151–168. doi:10.1016/s0266-352x(01)00017-9

Xie, K. H., and Leo, C. J. (2004). Analytical Solutions of One-Dimensional Large Strain Consolidation of Saturated and Homogeneous Clays. *Comput. Geotechnics* 31, 301–314. doi:10.1016/j.compgeo.2004.02.006

Conflict of Interest: The authors declare that the research was conducted in the absence of any commercial or financial relationships that could be construed as a potential conflict of interest.

frontiers in Earth Science

CORRECTION
published: 31 March 2022
doi: 10.3389/feart.2022.878024

Corrigendum: Shallow Compaction Modeling and Upscaling: A One-Dimensional Analytical Solution and Upscaling

Jingchen Zhang[1,2]*, *Jingsheng Ma*[2], *Gary D. Couples*[2] and *Nicholas Izuchukwu Osuji*[1]

[1]China University of Petroleum, Beijing, China, [2]Institute of Petroleum Engineering, Heriot-Watt University, Edinburgh, United Kingdom

Keywords: Terzaghi, Gibson, multilayer consolidation, analytical solution, upscaling

A Corrigendum on

Shallow Compaction Modeling and Upscaling: A One-Dimensional Analytical Solution and Upscaling

by Zhang, J., Ma, J., and Osuji, N. I. (2021). Front. Earth Sci. 9:762176. doi: 10.3389/feart.2021.762176

In the original article, we neglected to include the following **Acknowledgements**: "The research content reported here is part of the first author's PhD research at Heriot-Watt University, Edinburgh, United Kingdom, under CAPROCKS consortium of United Kingdom universities, Newcastle University, Cardiff University, Heriot-Watt University, and University of Leeds. This study was funded by the following companies: Anadarko, BG, BHP Billiton, BP, Chevron, ConocoPhillips, ENI, ExxonMobil, Petrobras, Shell, StatoilHydro, Total, and Unocal."

In the published article, there was an error in **Affiliation**. "Affiliation 1 should appear as Affiliation 2, and the first author is affiliated to amended Affiliation 1 only."

Gary D. Couples, affiliated to amended Affiliation 2, was not included as an author in the published article. The corrected **Author Contributions** statement is as follows: "GDC: research supervision and obtaining fund."

The authors apologize for this error and state that this does not change the scientific conclusions of the article in any way. The original article has been updated.

OPEN ACCESS

Approved by:
Frontiers Editorial Office, Frontiers Media SA, Switzerland

***Correspondence:**
Jingchen Zhang
jingchen120@126.com

Specialty section:
This article was submitted to Sedimentology, Stratigraphy and Diagenesis, a section of the journal Frontiers in Earth Science

Received: *17 February 2022*
Accepted: *28 February 2022*
Published: *31 March 2022*

Citation:
Zhang J, Ma J, Couples GD and Osuji NI (2022) Corrigendum: Shallow Compaction Modeling and Upscaling: A One-Dimensional Analytical Solution and Upscaling. Front. Earth Sci. 10:878024. doi: 10.3389/feart.2022.878024

frontiers in Earth Science

ORIGINAL RESEARCH
published: 24 February 2022
doi: 10.3389/feart.2022.786108

Effect of Composition on the Compressibility and Shear Strength of Dredged Cohesive Sediment

Maria Barciela-Rial[1,2]*, *Philip J. Vardon*[1], *Thijs Van Kessel*[3], *Jasper Griffioen*[4,5] and *Johan C. Winterwerp*[1]

[1]Faculty of Civil Engineering and Geosciences, Delft University of Technology, Delft, Netherlands, [2]Sustainable River Management, Built Environment Academy, HAN University of Applied Sciences, Arnhem, Netherlands, [3]Deltares, Delft, Netherlands, [4]Faculty of Geosciences, Copernicus Institute of Sustainable Development, Utrecht University, Utrecht, Netherlands, [5]TNO Geological Survey of the Netherlands, Utrecht, Netherlands

OPEN ACCESS

Edited by:
Andrew James Manning,
HR Wallingford, United Kingdom

Reviewed by:
Chiara Deangeli,
Politecnico di Torino, Italy
Lucas Merckelbach,
Helmholtz Centre for Materials and Coastal Research (HZG), Germany

***Correspondence:**
Maria Barciela-Rial
m.barcielarial@tudelft.nl

Specialty section:
This article was submitted to Sedimentology, Stratigraphy and Diagenesis, a section of the journal Frontiers in Earth Science

Received: 29 September 2021
Accepted: 14 January 2022
Published: 24 February 2022

Citation:
Barciela-Rial M, Vardon PJ, Van Kessel T, Griffioen J and Winterwerp JC (2022) Effect of Composition on the Compressibility and Shear Strength of Dredged Cohesive Sediment. Front. Earth Sci. 10:786108. doi: 10.3389/feart.2022.786108

Progressively, more dredged sediments are being reused for engineering projects. For example, the Marker Wadden is a new wetland constructed in lake Markermeer, the Netherlands, with dredged cohesive sediments originating from the bed of the lake. Such dredged sediments are often dominated by cohesive sediment particles with varying amounts of sand and organic matter. In addition, during and after the construction process, the material consolidates and is often compressed from a very loose state into a significantly denser condition. To assess the mechanical behavior of this material, the compressibility of the Markermeer dredged sediment samples with various sand and organic matter contents was analyzed with incremental loading oedometer tests, whereas the undrained shear strength was studied using the fall cone test. The behavior was theoretically analyzed assuming a fractal structure of the sediment and applying power law constitutive equations for effective stress, hydraulic conductivity, and undrained shear strength. These constitutive equations, usually used at low initial sediment densities, worked well at the relatively high initial densities studied and proved to be a useful tool to identify the transition fines content TFC. The constitutive equations were put in context with indicators traditionally used in soil mechanics. Samples, each with an identical composition of the fines fraction (particles< 63 μm), but with a sand content varying from 9 to 40%, showed the same compressibility and undrained shear strength behavior when considering the sand a filler material. For a natural sand content of 70%, the behavior was dominated by sand. The organic matter oxidation was observed to drastically decrease the compressibility and the shear strength, and even to decrease the amount of sand needed to exhibit sand-dominated behavior, showing the importance of the reactivity or state of organic matter on the TFC.

Keywords: dredged sediment, organic matter, compressibility, cohesive, shear strength, fractal structure, composition

INTRODUCTION

Large amounts of sand are used in infrastructure projects and industries. Sandy sediments are becoming scarce (Vörösmarty et al., 2003), while billions of cubic meters of fine cohesive sediments are dredged worldwide to maintain navigation channels. It is likely that significantly more of these fines will be used in infrastructure development (Barciela-Rial et al., 2021). An example is the Marker Wadden pilot, a new wetland constructed in lake Markermeer, the Netherlands, using dredged cohesive sediment from the bed of the lake itself. However, dredged sediments are more complex to use because they consist of a heterogeneous mixture of water, fines, sand, and organic matter. Furthermore, the composition of the dredged sediment varies largely within the same natural system, which presents a challenge when using these sediments in building projects. This large variation of sediment composition occurs also at lake Markermeer, as shown by Barciela–Rial et al. (2020).

A key aspect in building with dredged sediment projects is to understand how the heterogeneity in sediment composition will affect the consolidation and strength behavior and how, based on a limited number of laboratory tests, the behavior of a wide range of compositions can be characterized. The sand content can largely vary locally at the dredging site, and sand segregation can occur during dredging, transportation, and deposition. The effect of the sand content on the mechanical properties of clayey sediments has been substantially studied over the last decades. For example, Cabalar and Mustafa (2015) showed a decrease in the liquid limit and undrained shear strength with an increasing percentage of sand in a clay matrix. Al-Shayea (2001) found a large decrease in permeability with decreasing sand content from 100 to 60% sand, below which the reduction was less significant. Other authors (e.g., Thevanayagam, 1998; Monkul and Ozden, 2007; Peters and Iv, 2010; Jacobs, 2011) studied the effect of the sand content on the behavior of clay–sand mixtures and determined a transitional fines content (TFC) threshold. This threshold characterizes the amount of fines at which a sand-dominated sediment changes from a granular behavior to a cohesive fines-dominated behavior. Simpson and Evans (2016) found that the TFC depended on the mechanical property studied, that is, they found a threshold of 20% fines for consistency, while 40–60% fines for conductivity. At lower fines content, hydraulic conductivity increases because pores become more interconnected, creating pore water flow paths. Miftah et al. (2020) found a transitional fines content of 10% for shear strength, that is, additional fines increased the shear strength until reaching the TFC of 10% fines, after which shear strength decreased. The effect of organic matter (OM) has also been studied. For example, Santagata et al. (2008) related an increase of 8–10% in OM with a three- to fivefold increase in permeability of a normally consolidated soil, and Zentar et al. (2009) found an increase in the consistency limits with increasing OM content. In a study linked to the work presented here, Barciela–Rial et al. (2020) found a correlation between the lability (reactivity) of the OM and the drying behavior of the sediment: labile OM decreased the unsaturated hydraulic conductivity and increased the water retention capacity at low matric suctions. They found that the effect on water retention was even larger for coarse-textured than for fine-textured samples. Moreover, in building projects using dredged sediments containing OM, the OM may oxidize over time during the dredging and filling processes and specially during drying as the material is more in contact with the atmosphere and which can further change properties (e.g., Oliveira et al., 2017). The TFC seems to be both soil- and process-dependent, which makes the comparison of findings challenging.

The initial densities of the dredged sediment are at the interface between those traditionally studied in fluid and soil mechanics, which have not been studied widely. The indicators used in these two disciplines are different, and there is a knowledge gap between the fields. The sediments investigated in this work have a density between those typically used by the two disciplines, offering an opportunity to compare the relationships and coefficients traditionally used in fluid and soil mechanics. Traditionally, the mechanical behavior of dense soils at large stresses is modeled with exponential relations. From the perspective of low-density virgin soils, derived from soil particles settling in water, Merckelbach and Kranenburg (2004a) presented a model that assumes scale invariance or fractal structure of the sediment. From this model, constitutive equations for effective stress and permeability are derived. These equations can be used in a large strain model such as the Gibson model (Gibson et al., 1967). The Merckelbach and Kranenburg model yields power relationships between the volumetric concentration of solids (defined as the ratio between the volume of solids and the total volume) and hydraulic conductivity and effective stress in normally consolidated sediments. Winterwerp and van Kesteren (2004) promoted the use of such power law relationships for these soft dredged sediments, instead of exponential relationships traditionally used with denser soils (e.g., Wichman, 1999; Bartholomeeusen et al., 2002; Van Kessel and de Boer, 2009). Various studies have shown that the density can be modeled with a fractal coefficient based on the constitutive relations found by Merckelbach and Kranenburg (Chassagne, 2019). Barciela–Rial (2019) showed that the Merckelbach and Kranenburg model works well with soft dredged sediments.

In this study, the consistency (Atterberg limits), undrained shear strength, and compressibility of natural as well as sieved, and treated (dried–rewet and oxidized) Markermeer dredged sediment samples with varying sand and organic matter contents are analyzed. The differences in undrained shear strength upon fall cone tests and compressibility upon incremental loading (IL) oedometer testing and the TFC are quantified using the Merckelbach and Kranenburg constitutive equations. The results put these equations in context with indicators traditionally used in soil mechanics and provide insights useful for building with dredged sediment projects, in particular regarding varying sand contents and the effect of oxidation of organic matter.

METHODS

In this section, the sampling sites and the sample collection and preparation method are presented, including the composition of the different samples. The tests performed for determining the sample composition as well as the compressibility and shear strength are described.

Sediment Collection and Preparation

Different sediment samples were collected with a Van Veen grab at two locations in lake Markermeer: the southwest (SW) and the

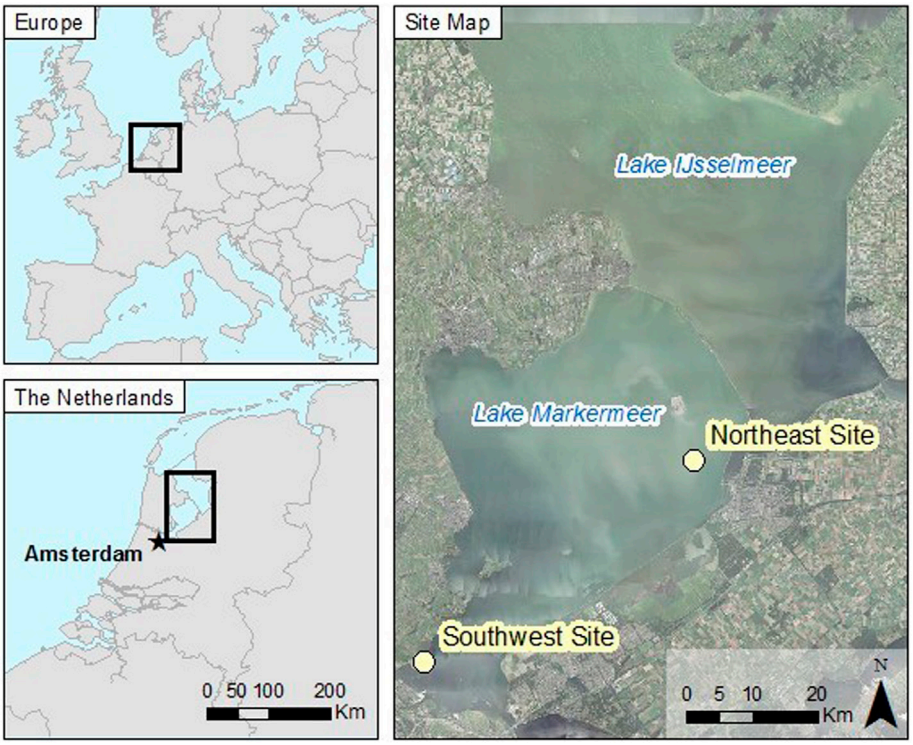

FIGURE 1 | Location of lake Markermeer **(left)** and sampling sites **(right)**. Source image: Publieke Dienstverlening Op de Kaart (PDOK) 2016.

northeast (NE) sites (see **Figure 1**). The upper layer of the lake bed consists of a thin (circa 0.1 m) layer of soft sediment, of which only the few upper millimeters are oxic (Van Duin, 1992). The sediment composition of this soft sediment layer is detailed in **Table 1**, labeled as sample NE2B-70%. Underneath this soft sediment layer, a thick layer of Holocene deposits (clay/silt mixtures, peat, or sand) is present (Rijkswaterstaat, 1995). The material from this layer tested in this study is referred to as clayey silt and was sampled at the southwest sampling site (**Table 1**). Markermeer sediment mineralogy is dominated by illite and smectite at all sampling sites, while kaolinite (<11%) and chlorite (<6%) are present in small amounts (see Barciela–Rial, 2019). After sampling, all samples were transported to the laboratory and stored in dark conditions at 4°C.

For the incremental loading (IL) oedometer test and the fall cone test, sample NE2B-70% (NE site) was used as the "mother" sample (where the suffix indicates the percentage sand content). From this material, subsamples were prepared in the laboratory with 0, 10, 20, and 40% sand content with respect to the total dry mass ($M_{sand}/M_{dry;total}$): samples NE2B-0%, NE2B-10%, NE2B-20, and NE2B-40%, respectively. These subsamples were obtained by separating the fines and sand fractions by sieving and recombining afterward. The value of the % sand contents in mass is almost identical to their correspondent % sand in volume because of the similar particle densities measured for the sand and fine fractions. The water content with respect to the fine fraction was kept constant for all subsamples. For the fall cone test, a sample from the deeper clayey silt material SW1B was also tested.

Additionally, a subsample from the 40% sand sample from the NE (sample NE2B-40%), tested with IL and fall cone tests, and sample SW1B, tested with the fall cone test, were oxidized to mimic the behavior of the Markermeer sediment after being in contact with atmospheric conditions for a long time. As natural oxidation is slow, the oxidation process was accelerated in the laboratory. This was done by treatment with hydrogen peroxide (H_2O_2), following an adapted procedure from the British Standards (British Standards Institute, 1990a) including two drying–rewetting cycles. First, the samples were dried in an oven at a constant temperature of 50°C until there was no further mass loss. Then, subsamples of 100 g were rewet by adding demineralized water and oxidized according to the standard. After centrifuging to remove the oxidant, the material was dried again at 50°C and rewet with filtered Markermeer water. pH was measured before and after oxidation by immersing a pH electrode in the samples, which showed that the treatment did not change the pH of the sediment. The labels of the treated samples are identified with the identifier T: samples SW1BT and NE2B-40%-T. The origin and composition of all the samples for the IL and fall cone tests are described in **Table 1**.

Sample Characterization

Atterberg limits and undrained shear strength were determined according to ISO (2016) and ISO/TS (2004b), respectively. For the liquid limit (LL), 80 g/30° tip angle fall cone tests were performed. The plastic limit (PL) was determined using the

TABLE 1 | Sediment properties of all samples studied.

Site	Depth	Type	ID	Sand	Silt	Clay	D_{50}	TOM	TOC	ρ_s	LL	PL	PI
	[m]			[%mass]	[μm]	[%]	[%]	[kg/m^3]	[%]	[%]	[%]	[%]	[%]
Southwest	0.1–0.5	Bulk clayey silt	SW1B	8	63	29	10	8.6	3.3	2,530	104	46	58
		Bulk treated	SW1T	8[a]	63[a]	29[a]	10[a]	6.7	2.0	2,620	60	31	29
Northeast	0.0–0.1	Bulk silty sand[b]	NE2B-70%	69	21	10	87	2.1	0.7	2,640	41	25	16
		Laboratory prepared	NE2B-0%	0	68	32	17	5.1	2.2	2,540	89	34	55
		Laboratory prepared	NE2B-10%	10	61	29	13	4.8	1.9	2,550	80	30	50
		Laboratory prepared	NE2B-20%	20	54	26	25	3.8	1.5	2,570	69	27	42
		Laboratory prepared	NE2B-40%	40	41	19	51	3.4	1.2	2,600	52	23	29
		Treated	NE2B-40%-T	40[a]	41[a]	19[a]	51[a]	2.1	0.5	2,700	33	23	10

[a]*Not measured. Assumed to not vary with the oxidation treatment.*
[b]*Mother sample from the sampling site NE.*

rolling thread test. The total organic matter (TOM) content was obtained by loss on ignition (LOI), according to the European Standard (EN, 2012), and the amount of total organic carbon (TOC) and its reactivity were determined using the Rock Eval machine (Behar et al., 2001). The particle density was measured using a gas pycnometer (ISO/TS, 2004c), and the particle size was determined using a hydrometer and by dry sieving according to the British Standards Institute (1990b). Sample characteristics are presented in **Table 1**. In this table, sand particles are defined as those with size >63 μm, silt as the particles between 2 and 63 μm, and clay particles as those smaller than 2 μm.

Undrained Shear Strength

The undrained shear strength c_u was obtained with the fall cone test following the ISO/TS (2004b) standard for each sample prepared with a range of different water contents.

Incremental Loading Oedometer Test

IL tests were undertaken according to ISO/TS (2004a) to determine the compression and consolidation properties. With an IL test, a cylindrical soil sample is enclosed in a stiff steel ring in between two porous stones and incrementally loaded through the upper porous stone. The typical test interpretation is based on the Terzaghi consolidation theory (Terzaghi, 1923), which assumes small deformations. For a comparison with the more general large strain consolidation theory (Gibson et al., 1967), check the supplementary materials. As the initial water contents of the thick dredged sediment samples studied were higher than soil samples traditionally studied with this device, the loading protocol was adapted according to the initial water content of the sample to ensure small deformations to enable typical test interpretation to be undertaken. For most of the samples, the initial load was 0.6 kPa (**Table 3**). The IL experiments were performed in a climate-controlled room with a constant temperature of 10°C. The bulk and dry densities of the test specimens were determined by weighing before the test and after drying for 24 h in an oven at 105°C.

The samples tested had 0, 10, 20, 40, and 70% sand, and the tests are thus referred to as I-NE2B-0, I-NE2B-10, I-NE2B-20, I-NE2B-40, and III-NE2B-70%, where the first identifier (I, II, or III) indicates differences in the initial ratio of the water content and LL. Two additional IL tests were performed to investigate the different compression behaviors of the treated (oxidized) samples with 40% sand content with different initial water contents: test II-NE2B-40%-T and test III-NE2B-40%-T. Test II-NE2B-40%-T was started at a water content of 1.6 times the LL, and test III-NE2B-40%-T at 1.2 LL. This corresponds with a water content of the fines fraction of 0.9 and 0.7 [$M_w/M_{s,fines}$], where $M_{s,fines}$ is the dry mass of the fraction <63 μm (**Table 2**). The 1.6 LL water content test was selected because it was the maximum water content of the sample below which no self-weight consolidation occurred (Barciela–Rial, 2019). The reduction in the water content until 1.6 LL (sample II-NE2B-40%-T) or below (sample III-NE2B-40%-T) was done by atmospheric drying.

For the second additional test (III-NE2B-40%-T) and for the 70% sand content test (III-NE2B-70%), a different loading program with higher initial stresses was applied. This was necessary because of the higher stiffness of these samples. The three different loading plans (for the different initial fines water contents I, II, and III) are described in **Table 3**.

INTERPRETATION MODEL

The power law constitutive equations for clays presented by Merckelbach and Kranenburg (2004a) are based on the volumetric concentration of sediment ϕ_s. When only fines (i.e., particles <63 μm) are present, $\phi_s = \phi_s^f$, where ϕ_s^f is the volumetric concentration of fines. However, if the sediment also contains some passive sand (i.e., there is not a sand skeleton), ϕ_s can be adapted to ϕ_{mod} (Merckelbach and Kranenburg, 2004a). This is because sand particles in this situation merely act as space-filling material, and the behavior of the sediment is dominated by the fine fraction. ϕ_{mod} can then be calculated according to **Eq. 1**:

$$\phi_{\mathrm{mod}} = \left(\frac{\phi_s^f}{1-\phi_s^{sa}}\right), \tag{1}$$

where ϕ_s^{sa} is the volumetric concentration of sand. When sand is present, ϕ_{mod} should be used instead of ϕ_s in the equations presented in this section.

In the constitutive equations from Merckelbach and Kranenburg, the relation theory between the vertical effective stress and the volumetric concentration is given as follows

TABLE 2 | Initial and final water contents of the IL tests, including water content of the fine fraction and ratios between initial and final water contents and the liquid limit.

Sample ID	Fines content	Initial				Final			
	[–]	*w* [–] [M_w/M_s]	*w*/LL [–]	*w* fines [–] [$M_w/M_{s,fines}$]	ϕ_{mod} [–]	*w* [–] [M_w/M_s]	*w*/LL [–]	*w* fines [–] [$M_w/M_{s,fines}$]	ϕ_{mod} [–]
I- NE2B-0%	1.0	1.38	1.55	1.38	0.23	0.62	0.70	0.62	0.39
I-NE2B-10%	0.9	1.23	1.54	1.36	0.23	0.58	0.73	0.65	0.38
I- NE2B-20%	0.8	1.05	1.53	1.31	0.24	0.52	0.75	0.65	0.38
I-NE2B-40%	0.6	0.80	1.53	1.33	0.24	0.38	0.74	0.64	0.38
III- NE2B-70%	0.3	0.42	1.02	1.39	0.22	0.28	0.68	0.93	0.29
II- NE2B-40%-T	0.6	0.53	1.62	0.89	0.31	0.30	0.90	0.50	0.44
III- NE2B-40%-T	0.6	0.40	1.20	0.66	0.39	0.23	0.71	0.39	0.50

TABLE 3 | IL tests loading plan (kPa).

	Series I	Series II	Series III
Loading step 1	0.6	0.6	3.1
Loading step 2	1.3	1.3	6.3
Loading step 3	4.3	4.3	12.6
Loading step 4	10.2	10.2	25.1
Loading step 5	25.0	25.0	50.3
Loading step 6	—	57.9	100.5
Loading step 7	—	119.1	—
Loading step 8	—	241.3	—

$$\sigma_{\text{eff}} = K_\sigma \phi_{\text{mod}}^{\frac{2}{3-n_f}}, \tag{2}$$

where the coefficient K_σ is material-specific and n_f [−] is the fractal dimension, representing the fractal structure of the sediment flocs.

The undrained strength c_u can be approximated by the yield strength τ_y (e.g., Winterwerp and van Kesteren, 2004). Therefore, c_u takes the mathematical form of the effective stress model of Merckelbach and Kranenburg. The empirical intrinsic parameter K_y [Pa], representing the effect of the sediment particles on the strength of the sediment, can then be obtained as follows (Winterwerp and van Kesteren, 2004):

$$c_u \approx \tau_y = K_y \phi_{\text{mod}}^{\frac{2}{3-n_f}}. \tag{3}$$

On the other hand, for denser soils, often exponential laws and traditional soil mechanics indicators are used. The compression index C_c is often used as an indicator to quantify the compressibility behavior using the IL oedometer test. This C_c coefficient is defined in the ISO/TS 17892 (2004a) as follows:

$$C_c = -\frac{\mathrm{d}e}{\mathrm{d}\log(\sigma_t)} \approx -\frac{\Delta e}{\Delta \log(\sigma_t)}, \tag{4}$$

where Δe is the change in void ratio along a linear section of the compression curve and $\Delta \log \sigma_t$ is the change in logarithm of applied stress along that linear section of the compression curve (ISO/TS 17892-5, 2004a), which at the end of each loading steps equals to the effective stress. Next to this traditional compression index, the modified compression index $C_{c,\text{mod}}$ can be calculated by using the modified void ratio e_{mod} in **Eq. 4**. This modified void ratio is defined as follows:

$$e_{\text{mod}} = \frac{1 - \phi_{\text{mod}}}{\phi_{\text{mod}}}. \tag{5}$$

To allow a comparison between the power law relation (**Eq. 4**) and the commonly calculated compression index, **Eq. 4** can be written using volumetric concentration definitions as follows:

$$C_c = \frac{3 - n_f}{2} \frac{\ln(10)}{\phi_s}, \tag{6}$$

where instead of ϕ_s, ϕ_{mod} can be used to modify for the sand content for fine contents above the TFC, thus obtaining $C_{c,\text{mod}}$. In this article, the power-law plots between c_u and σ_{eff} against ϕ_{mod} were used to identify the TFC. This criterion is based on the following three assumptions:

1. Further to Winterwerp and van Kestern (2004), the transition between cohesive and non-cohesive behaviors occurs at a plasticity index of 7%, which yields a critical clay content in the activity plot.
2. Further to Kranenburg (1994), the mechanical properties of cohesive sediment follow power law relations.
3. Further to Merckelbach and Kranenburg (2004a), these power law relations are unaffected by the presence of some sand, as long as no sand skeleton is formed, that is, below the critical sand content.

Thus, the power law relations for samples at different sand content are expected to collapse or overlap on one single curve after correcting for this sand content, as long as this is below its critical value.

RESULTS

Undrained Shear Strength

Figure 2 shows the undrained shear strength (c_u) results. Herein, c_u is plotted against the non-corrected ϕ_s (i.e., $\phi_s^f + \phi_s^{sa}$) and ϕ_{mod}. They follow a linear relationship on the log–log scale (i.e., power law). For each sample, a

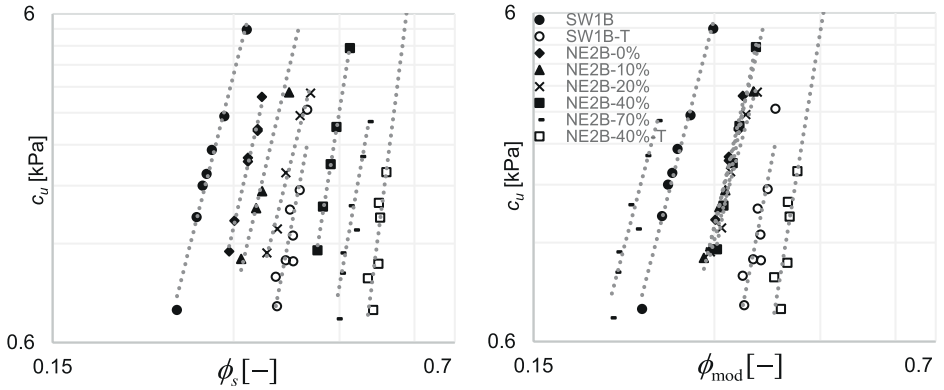

FIGURE 2 | Undrained shear strength as a function ϕ_s (left) and ϕ_{mod} (right).

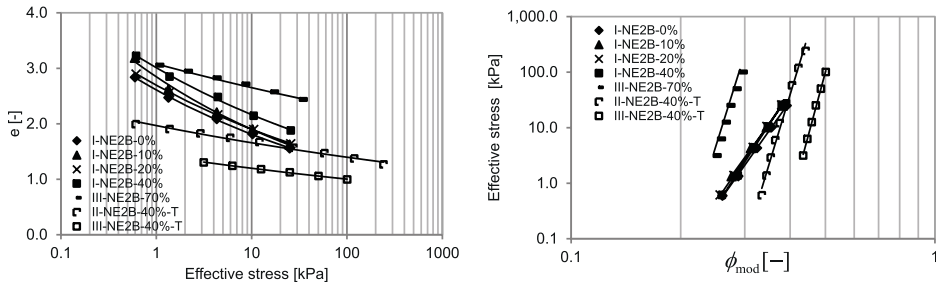

FIGURE 3 | Left: log effective stress–void ratio (e) graph. Right: Effective stress as a function of ϕ_{mod} for the IL tests.

decrease in undrained shear strength with a larger water content (lower ϕ_s or ϕ_{mod}) is observed. Plotting against ϕ_s does not allow to identifying the TFC nor determining patterns of similar behavior. However, plotting against ϕ_{mod} shows that the samples containing 0, 10, 20, and 40% sand overlap because they have the same OM composition (same mother sample). Thus, the TFC has not yet been reached at 40% sand. This is not the case for the sample with 70% sand content, implying that a TFC somewhere between 40 and 70% sand content. Therefore, the mechanical behavior of sample NE2B-70% is governed by a granular skeleton. Other authors found TFCs at similar sand content. For example, Thevanayagam (1998) found that the clay matrix governed the undrained shear strength behavior below 70% (mass) sand content, while Kumar and Wood (1999) found a TFC between 30 and 40% (mass) fines contents.

Sample SW1B exhibits lower initial ϕ_{mod} than the samples originating from the other sampling sites because of its larger amount of OM and subsequent larger ability to bind water (different sampling sites). This sample is therefore located at the left in **Figure 2**. On the other hand, treated samples SW1B-T and NEB-40%-T moved to the right because of their loss in ability to bind water given the lower lability (reactivity) of the remaining OM, reflected in a lower PI. It is remarkable that the slopes of the curves remain almost identical, suggesting a similar internal structure of the clay matrix.

Incremental Loading Oedometer Test

Figure 3 shows the traditional log(effective stress)—void ratio (e) space and shows the effective stress against the corrected volumetric concentration ϕ_{mod} obtained from the IL tests. All the non-treated samples with sand contents up to 40% (i.e., tests I-NE2B-0%, I-NE2B-10%, I-NE2B-20%, and I-NE2B-40%) show virtually the same power law relation with overlapping lines in the log–log plot (right panel). This indicates that the TFC occurs for sand contents above 40% but below 70%. This agrees with the findings for the undrained shear strength.

The treated samples (tests II-NE2B-40%-T, III-NE2B-40%-T) also follow a power law relationship. The σ_{eff}–ϕ_{mod} correlations from these treated samples have a steeper slope, implying a larger increase in effective stress for an increase in ϕ_{mod} with respect to the non-treated samples (i.e., larger n_f, see **Eq. 2** and the Supplementary Material). This indicates that the floc structure became denser as a result of the treatment, and primary particles may touch each other. This is in accordance with the findings of Barciela–Rial (2019), who found the same change of behavior after oxidation treatment for samples tested upon the constant rate of strain (CRS) consolidation tests for other Markermeer sediment samples.

The σ_{eff}–ϕ_{mod} correlation of sample of test III-NE2B-70% does not overlap with the other non-treated samples. This is because the fines content is below the TFC, and therefore, a granular skeleton is present. Remarkably, it still follows a power law, while,

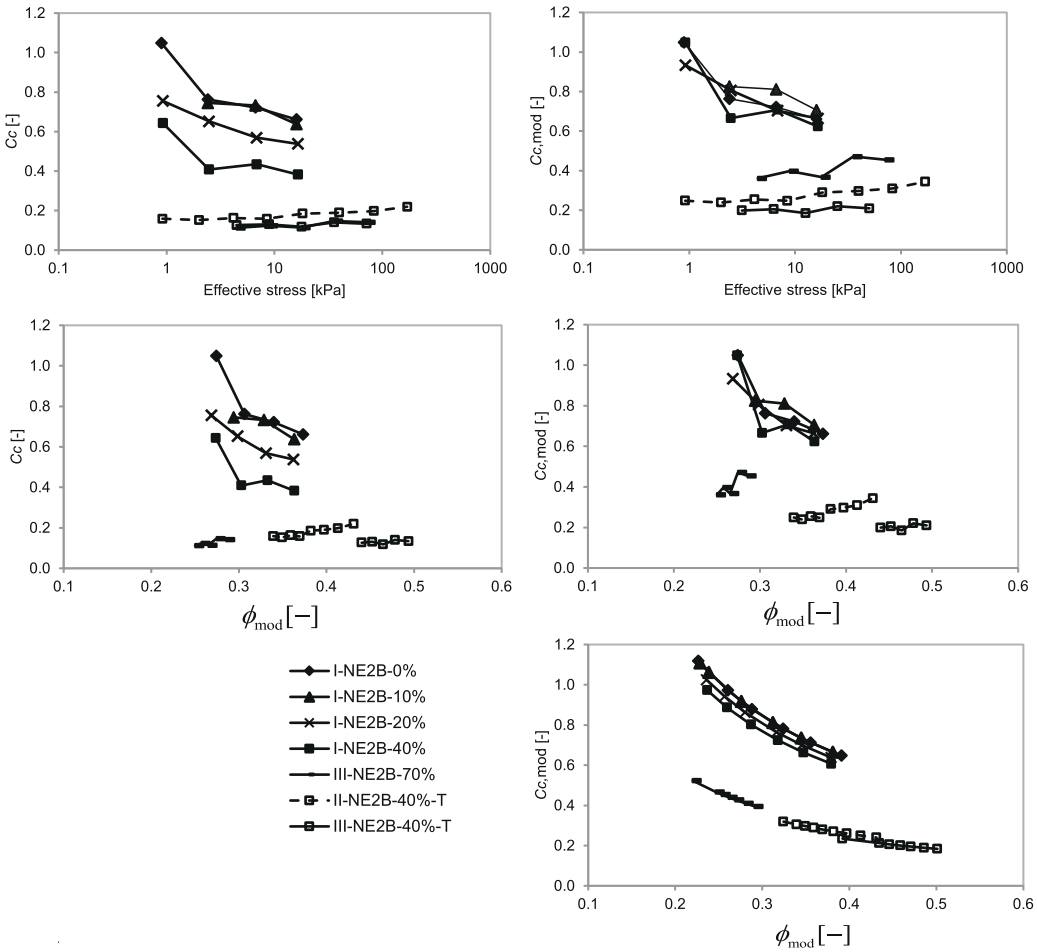

FIGURE 4 | (A,C) Compressibility coefficient C_c without correcting for the presence of sand. **(B,D)** C_c,mod calculated with the corrected void ratio. **(E)** $C_{c,mod}$ calculated following fractal theory using material parameters with proposed **Eq. 6** as function of ϕ_{mod}.

for instance, Schultze and Moussa (1961) presented exponential relationships for sand compressibility.

The compression index C_c calculated according to the geotechnical standard (i.e., applying **Eq. 4** with e, instead of e_{mod}) is presented in **Figure 4A,C** as a function of the effective stress and corrected solid content ϕ_{mod}. Overall, C_c decreases with both increases in effective stress and solid contents but becomes nearly constant during the last phases of the tests. C_c appeared to be invariant with sand contents up to 10%. Possibly the sand particles are too diluted in the fines matrix to affect the compression, although an experimental error may have affected the results as well. For sand contents of 20% or more, C_c decreases with sand content. This is caused by the incompressibility of sand particles as has frequently been reported in the literature (e.g., Monkul and Ozden, 2007; Watabe et al., 2011; Simpson and Evans, 2016). However, when correcting C_c for the amount of sand ($C_{c,mod}$ calculated by using e_{mod} in **Eq. 4**; **Figure 4B,D**), the $C_{c,mod}$ for samples with 0–40% sand overlap, indicating that the TFC has not yet been reached with sand contents up to 40% (see **Figure 4**).

Regarding the effect of the oxidation treatment, the treated samples have smaller C_c values because of a lower ability to bind water (Barciela-Rial et al., 2020); thus, less pore water is expelled upon loading. The C_c–effective stress plot also shows that when using the void ratio e, instead of the corrected void ratio e_{mod} to calculate C_c (**Figure 4A**), the compressibility behavior of the treated sample with 40% sand (III-NE2B-40%-T) and the natural sample with 70% sand (III-NE2B-70%) is the same for loading scheme III (starting at higher initial stress). For the test with the treated sample at higher initial water contents (II-NE2B-40%T), the compressibility values were slightly larger.

The treated sample III-NE2B-40%-T and the sandy sample III-NE2B-70% exhibit a different tendency; the compression index increases with the effective stress. This is likely to be because both samples behave as silty sand. The increase in compressibility with effective stress for sandy sediment has been shown by multiple authors. For instance, Mesri and Vardhanabhuti (2009) showed an increase in C_c with effective stress for dense quartz sands with a maximum C_c value below 0.01 for stresses of 100 kPa. It is therefore concluded that the oxidation

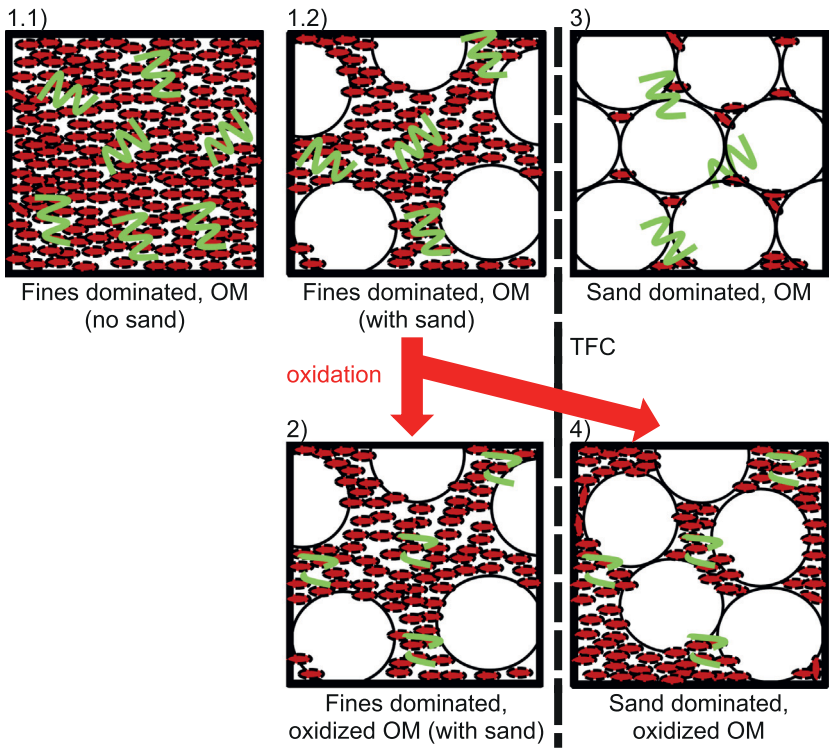

FIGURE 5 | Schematic of mechanical behavior of the studied sediment as a function of its composition. Legend: curly lines represent OM, dashed curly lines represent oxidized OM, small oval particles represent fines, and big round particles represent sand.

treatment for the material with 40% sand content changed the TFC.

Figure 4E shows $C_{c,\mathrm{mod}}$ as obtained from **Eq. 6** with the fitting parameters determined from results presented in **Figure 3**. For sand contents of 40% or smaller, the $C_{c,\mathrm{mod}}$ curves overlap. The values obtained also agree with the ones calculated with e_{mod} and **Eq. 4**, that is, **Figure 4D**. This implies that **Eq. 6** may be used to determine $C_{c,\mathrm{mod}}$ as a function of ϕ_{mod}, directly with the material parameters determined from standard settling experiments (e.g., Merckelbach and Kranenburg, 2004b).

DISCUSSION

Conceptual Model

Figure 5 presents a schematic of the mechanical behavior of the cohesive sediment with organic material. Herein, a possible collapse of flocs upon loading is not addressed. In this schematic, the different behavior found for Markermeer samples are classified into four (sub)categories: (1.1) fines dominated with OM (no sand), (1.2) fines dominated with OM and some sand (passive sand particles), 2) fines dominated with oxidized OM and some sand (passive sand particles), 3) sand dominated with OM and some fines (passive fines), and 4) sand dominated with oxidized OM and some fines (passive fines). The transition from case 1.2 to case 3 and that from case 2 to case 4 determine the TFC.

For sand contents of 40% and lower, the behavior of the Markermeer sediment is dominated by the fines. However, for the sediment sample with 70% sand, the sand particles form a skeleton which dominates its behavior. The same sand-dominated behavior is observed for the treated samples. This means that the material parameters have changed. However, the constitutive model still appears to be applicable for these samples as the $\sigma_{\mathrm{eff}}-\phi_{\mathrm{mod}}$ curves still follow the power law (e.g., **Figure 3**). The fact that oxidation of the OM changed the behavior of a sample with 40% sand from fines-dominated to sand-dominated suggests that the physical particle interactions are affected by the presence of OM and by the type of the organic matter present (fresh organic matter or oxidized organic matter). Thus, the type of OM is also relevant, as discussed by Barciela–Rial et al. (2020) who showed that the mechanical behavior upon drying of the Markermeer sediment is correlated stronger with the reactivity of OM than with the total organic matter content.

The activity plot (Skempton, 1953) reflects the relation between the plasticity index (PI) as a function of the clay content, yielding the sediment's activity (the slope of the curve) and the critical clay content above which the sediment depicts cohesive behavior. Active sediments undergo considerable changes of volume when wetted (swelling) or dried (shrinkage), for example, Mitchell and Soga (2005). **Figure 6** presents the activity plot for the samples used for the IL-tests with an activity A = 1.8 and critical clay content of 6%. The removal of the OM (treated sample) shifts the activity plot to

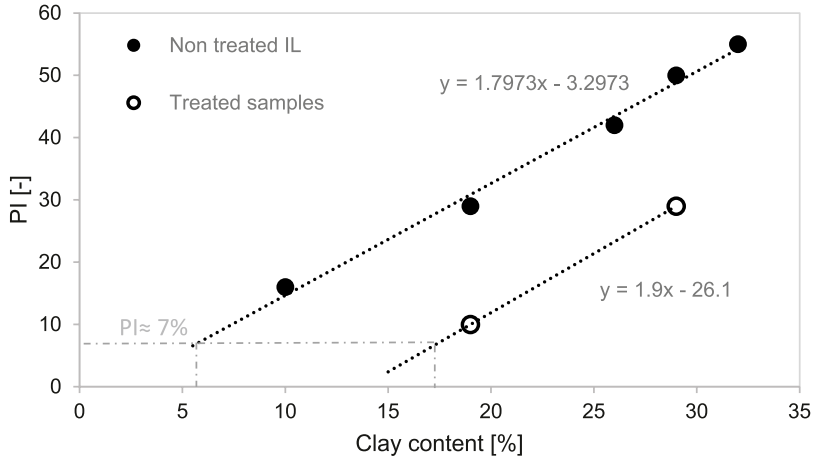

FIGURE 6 | Activity plot for the natural samples tested upon IL and for the treated samples. The natural samples presented here have the same composition of the OM because they originate from the same mother sample.

the right, at the same slope (activity). However, the critical clay content increases substantially to 17%, which is in agreement with the aforementioned analyses on the impact of treatment on the mechanical behavior of the sediment.

Power Law Constitutive Equations

The sediment studied in the present work has much larger initial water content than usually studied in classical soil mechanics yet lower than those at which the Merckelbach and Kranenburg model has traditionally been applied. The results showed that at these relative low water contents, the constitutive equations of Merckelbach and Kranenburg work well. The mechanical response to external stresses can be described with these equations. This is in line with the findings of, for example, Chassagne (2019); Barciela–Rial (2019), who showed that the fractal theory could reproduce the evolution in time of consolidation for natural sediment mixtures also at large initial concentrations of sediment. A higher fractal dimension applies than traditionally available in the literature (between 1.8 and 2.2 for flocs, e.g., Merckelbach, 2000), which makes sense as a higher fractal dimension is an indication of a more compacted clay. However, the fact that the samples obey power law relationships does not prove that they are fractal, and further research would be needed to quantify this, which is out of the scope of this study.

When building with the dredged sediment, the initial water content and sand content may vary considerably, and which will also affect the consolidation behavior. The practical question is how to cover various sand or water contents with as few tests as possible. The present study shows that trends in behavior can be identified from σ_{eff}–ϕ_{mod} and c_u–ϕ_{mod} relations. At sand contents below the TFC, the effect of sand can be accounted for through a correction of the sediment volumetric concentration, and all σ_{eff}–ϕ_{mod} and c_u–ϕ_{mod} curves collapse (overlap). However, the behavior of the treated samples NE2B-40%-T and SW1B-T did not overlap with the natural samples and exhibited a steeper increase with the volumetric fraction. This is consistent with the increase in the critical clay content after treatment, as discussed before.

CONCLUSION

Progressively, more and more soft sediments are being used as construction materials. However, most studies refer either to fluid-like or very stiff sediment water mixtures, that is, sediment suspensions with a low initial concentration of solids or highly consolidated soil samples. This article shows how the Merckelbach and Kranenburg constitutive equations can be used for soft soils with an intermediate initial density, which is relevant for the dredged sediment that forms a bed while initially being in suspension. Based on their constitutive equations, a useful tool to identify the TFC is developed, correcting for relatively small sand contents in sediments with a fines-dominated behavior. A new formulation of C_c is presented as an inverse function of the volumetric concentration of solids. The results obtained from this equation are satisfactory when compared with the results obtained with standard procedures of the geotechnical norm.

Quantitatively small changes in the amount of organic matter, for example, oxidation, had a big impact on the compressibility and undrained shear strength of the material. The results suggest a large decrease in the ability of the Markermeer sediment to bind water, after long-term exposure to atmospheric conditions. The undrained shear strength after oxidation at the same solid content (density) decreases for the samples from both sampling sites. For the material with 8% sand (SW1B), a more pronounced change in behavior was observed upon oxidation, given the larger initial amount of OM present. Furthermore, the differences in behavior of the Markermeer sediment caused by the natural variability or segregation of sand were studied. This behavior is dominated by the fine fraction, except when the threshold of transitional fines content TFC was passed somewhere between 40 and 70% sand content. In the same way, treatment by oxidation reduced the amount of fines at which the transitional behavior to sand-dominated behavior occurred. The results show that the type of organic matter (oxidized or labile) may impact the TFC by changing the critical clay content. This is an important

observation as OM reactivity is generally ignored in the literature and technical standards.

DATA AVAILABILITY STATEMENT

The raw data supporting the conclusion of this article will be made available by the authors, without undue reservation.

AUTHOR CONTRIBUTIONS

MB-R designed and performed the experiments, analyzed the data, and wrote the manuscript; PV helped with the design of the experiments, data interpretation, and writing of the manuscript; TV assisted with data interpretation; JG assisted with the design of the geochemical analysis and experimental data interpretation; and JW assisted with the mathematical model, experimental data interpretation, and the writing of the manuscript.

FUNDING

This study was supported with funding from the Netherlands Organization for Scientific Research (NWO, project no. 850.13.031) and from Boskalis, Van Oord, Deltares, RHDHV, and Natuurmonumenten. Open access fee was paid by TU Delft.

ACKNOWLEDGMENTS

The authors would like to thank Arno Mulder for his help with the performance of the IL oedometer tests.

SUPPLEMENTARY MATERIAL

The Supplementary Material for this article can be found online at: https://www.frontiersin.org/articles/10.3389/feart.2022.786108/full#supplementary-material

REFERENCES

Al-Shayea, N. A. (2001). The Combined Effect of clay and Moisture Content on the Behavior of Remolded Unsaturated Soils. *Eng. Geology.* 62 (4), 319–342. doi:10.1016/S0013-7952(01)00032-1

Barciela-Rial, M., van Paassen, L. A., Griffioen, J., van Kessel, T., and Winterwerp, J. C. (2020). The Effect of Solid-phase Composition on the Drying Behavior of Markermeer Sediment. *Vadose Zone J.* 19 (1), e20028. doi:10.1002/vzj2.20028

Barciela-Rial, M., van der Star, W., Meshkati Shahmirzadi, E., Haarman, F., Besseling, E., Sittoni, L., et al. (2021). "Desalination of dredged sediments for circular reuse: two Eems-Dollard cases," in International SedNet conference, Lille, France, 28 June – 2 July 2021.

Barciela-Rial, M. (2019). *Consolidation and Drying of Slurries: A Building with Nature Study for the Marker Wadden*. Doctoral dissertation. Delft (Netherlands): Delft University of Technology.

Bartholomeeusen, G., Sills, G. C., Znidarčić, D., Van Kesteren, W., and Merckelbach, L. M. (2002). Sidere: Numerical Prediction of Large-Strain Consolidation. *Géotechnique* 52 (9), 639–648. doi:10.1680/geot.52.9.639.38842

Behar, F., Beaumont, V., and De B. Penteado, H. L. (2001). Rock-eval 6 Technology: Performances and Developments. *Oil Gas Sci. Techn. - Rev. IFP* 56 (2), 111–134. doi:10.2516/ogst:2001013

British Standards Institute (1990b). *Methods of Test for Soils for Civil Engineering Purposes. Classification tests*. BS1377-2:1990.

British Standards Institute (1990a). *Methods of Test for Soils for Civil Engineering Purposes. General Requirements and Sample Preparation*. BS1377-1:1990.

Cabalar, A. F., and Mustafa, W. S. (2015). Fall Cone Tests on Clay-Sand Mixtures. *Eng. Geology.* 192, 154–165. doi:10.1016/j.enggeo.2015.04.009

Chassagne, C. (2019). "Understanding the Natural Consolidation of Slurries Using Colloid Science," in Proceedings of the European Conference on Soil Mechanics and Geotechnical Engineering, Reykjavik, Iceland, 1–6 September 2019.

EN (2012). *Sludge, Treated Biowaste, Soil and Waste -determination of Loss on Ignition*. Geneva, Switzerland: International Organization for Standardization. EN 15935:2012.

Gibson, R. E., England, G. L., and Hussey, M. J. L. (1967). The Theory of One-Dimensional Consolidation of Saturated Clays. *Géotechnique* 17 (3), 261–273. doi:10.1680/geot.1967.17.3.261

ISO (2016). *Geotechnical Investigation and Testing - Laboratory Testing of Soil - Part 12: Determination of Atterberg Limits*. ISO 17892-12:2016.

ISO/TS (2004c). *Geotechnical Investigation and Testing - Laboratory Testing of Soil - Part 3: Determination of Particle Density - Pycnometer*. ISO/TS 17892-3:2004.

ISO/TS (2004a). *Geotechnical Investigation and Testing - Laboratory Testing of Soil - Part 5: Incremental Loading Oedometer Test*. ISO/TS 17892-5:2004.

ISO/TS (2004b). *Geotechnical Investigation and Testing - Laboratory Testing of Soil - Part 6: Fall Cone Test*. ISO/TS 17892-6:2004.

Jacobs, W. (2011). *Sand-mud Erosion from a Soil Mechanical Perspective*. Doctoral dissertation. Delft (Netherlands): Delft University of Technology.

Kranenburg, C. (1994). The Fractal Structure of Cohesive Sediment Aggregates. *Estuarine, Coastal Shelf Sci.* 39 (6), 451–460. doi:10.1016/S0272-7714(06)80002-8

Kumar, G. V., and Wood, D. M. (1999). Fall Cone and Compression Tests on Clay-Gravel Mixtures. *Géotechnique* 49 (6), 727–739. doi:10.1680/geot.1999.49.6.727

Merckelbach, L. M. (2000). *Consolidation and Strength Evolution of Soft Mud Layers*. Doctoral dissertation. Delft (Netherlands): Delft University of Technology.

Merckelbach, L. M., and Kranenburg, C. (2004b). Determining Effective Stress and Permeability Equations for Soft Mud from Simple Laboratory Experiments. *Géotechnique* 54 (9), 581–591. doi:10.1680/geot.2004.54.9.581

Merckelbach, L. M., and Kranenburg, C. (2004a). Equations for Effective Stress and Permeability of Soft Mud-Sand Mixtures. *Géotechnique* 54 (4), 235–243. doi:10.1680/geot.2004.54.4.235

Mesri, G., and Vardhanabhuti, B. (2009). Compression of Granular Materials. *Can. Geotech. J.* 46 (4), 369–392. doi:10.1139/T08-123

Miftah, A., Garoushi, A. H. B., and Bilsel, H. (2020). Effects of Fine Content on Undrained Shear Response of Sand-Clay Mixture. *Int. J. Geosynth. Ground Eng.* 6 (2), 10. doi:10.1007/s40891-020-0193-7

Mitchell, J. K., and Soga, K. (2005). *Fundamentals of Soil Behavior*. 3rd Edition. Hoboken: John Wiley & Sons.

Monkul, M. M., and Ozden, G. (2007). Compressional Behavior of Clayey Sand and Transition Fines Content. *Eng. Geology.* 89 (3-4), 195–205. doi:10.1016/j.enggeo.2006.10.001

Oliveira, B. R. F., Smit, M. P. J., van Paassen, L. A., Grotenhuis, T. C., and Rijnaarts, H. H. M. (2017). Functional Properties of Soils Formed from Biochemical Ripening of Dredged Sediments-Subsidence Mitigation in Delta Areas. *J. Soils Sediments* 17 (1), 286–298. doi:10.1007/s11368-016-1570-7

Peters, J. F., and Berney, E. S. (2010). Percolation Threshold of Sand-clay Binary Mixtures. *J. Geotech. Geoenviron. Eng.* 136 (2), 310–318. doi:10.1061/(ASCE)GT.1943-5606.0000211

Rijkswaterstaat (1995). *Geologische en bodemkundige atlas van het markermeer*. Lelystad: Rijkswaterstaat, Directie IJsselmeergebied. Tech. rep.

Santagata, M., Bobet, A., Johnston, C. T., and Hwang, J. (2008). One-dimensional Compression Behavior of a Soil with High Organic Matter Content. *J. Geotech. Geoenviron. Eng.* 134 (1), 1–13. doi:10.1061/(asce)1090-0241(2008)134:1(1)

Schultze, E., and Moussa, A. (1961). "Factors Affecting the Compressibility of Sand," in 5th International Conference of Soil Mechanics and Foundation Engineering, 1, 335340.

Simpson, D. C., and Evans, T. M. (2016). Behavioral Thresholds in Mixtures of Sand and Kaolinite clay. *J. Geotechnical Geoenvironmental Eng.* 142 (2), 1–10. doi:10.1061/(ASCE)GT.1943-5606.0001391

Skempton, A. W. (1953). *The Colloidal "Activity" of Clays, 3rd International Conference of Soil Mechanics and Foundation Engineering*, Vol. 1. Zurich: Organizing Committee, ICOSOMEF, 57–61. [1953-1954].

Terzaghi, K. (1923). "Die Berechnung der Durchlassigkeitzifer des Tones aus dem Verlauf der hydrodynamischen Spannungserscheinungen," in *Mathematish-naturwissenschaftliche, Klasse. Part IIa (In German)* (Vienna: Akademie der Wissenschaften), 132, 125–138.

Thevanayagam, S. (1998). Effect of Fines and Confining Stress on Undrained Shear Strength of Silty Sands. *J. Geotechnical Geoenvironmental Eng.* 124 (6), 479–491. doi:10.1061/(asce)1090-0241(1998)124:6(479)

Van Duin, E. H. S. (1992). *Sediment Transport, Light and Algal Growth in the Markermeer*. Doctoral dissertation. Wageningen: Agricultural University.

Van Kessel, T., and de Boer, G. (2009). *Calibration Suspended Sediment Model Markermeer, Deltares Report 4612*. Delft, The Netherlands.

Vörösmarty, C. J., Meybeck, M., Fekete, B., Sharma, K., Green, P., and Syvitski, J. P. M. (2003). Anthropogenic Sediment Retention: Major Global Impact from Registered River Impoundments. *Glob. Planet. Change* 39 (1–2), 169–190. doi:10.1016/S0921-8181(03)00023-7

Watabe, Y., Yamada, K., and Saitoh, K. (2011). Hydraulic Conductivity and Compressibility of Mixtures of Nagoya Clay with Sand or Bentonite. *Géotechnique* 61 (3), 211–219. doi:10.1680/geot.8.p.087

Wichman, B. (1999). *Consolidation Behavior of Gassy Mud: Theory and Experimental Validation*. Doctoral dissertation. Delft (Netherlands): Delft University of Technology.

Winterwerp, J. C., and van Kesteren, W. G. (2004). *Introduction to the Physics of Cohesive Sediment Dynamics in the Marine Environment*, Vol. 56. Amsterdam: Elsevier Science. Developments in Sedimentology.

Zentar, R., Abriak, N.-E., and Dubois, V. (2009). Fall Cone Test to Characterize Shear Strength of Organic Sediments. *J. Geotech. Geoenviron. Eng.* 135 (1), 153–157. doi:10.1061/(asce)1090-0241(2009)135:1(153)

Conflict of Interest: The authors declare that the research was conducted in the absence of any commercial or financial relationships that could be construed as a potential conflict of interest.

frontiers in Earth Science

ORIGINAL RESEARCH
published: 03 March 2022
doi: 10.3389/feart.2022.806721

Estimating P- and S-Wave Velocities in Fluid Mud Using Seismic Interferometry

Xu Ma[1,2]*, *Alex Kirichek*[3], *Karel Heller*[1] and *Deyan Draganov*[1]

[1]Section of Applied Geophysics and Petrophysics, Department of Geoscience and Engineering, Faculty of Civil Engineering and Geosciences, Delft University of Technology, Delft, Netherlands, [2]State Key Laboratory of Earthquake Dynamics, Institute of Geology, China Earthquake Administration, Beijing, China, [3]Section of Rivers, Ports, Waterways and Dredging Engineering, Department of Hydraulic Engineering, Faculty of Civil Engineering and Geosciences, Delft University of Technology, Delft, Netherlands

Fluid mud plays an important role in navigability in ports and waterways. Characterizing and monitoring the seismic properties of the fluid mud can help understand its geotechnical behavior. Estimation of the wave velocities in fluid mud with high accuracy and repeatability enables investigating the behavior of parameters like the yield stress in a nonintrusive and reliable way. We perform ultrasonic reflection measurements in a laboratory to investigate the wave propagation in a water/fluid-mud layered system. The component of wave propagation in the water layer inevitably brings kinematic dependence on the characteristics of that layer, making the estimation of exact velocities in the fluid mud more challenging. In order to extract the wave velocities only in the fluid-mud layer, we use a reflection geometry imitating field measurement to record the ultrasonic data from sources and receivers in the water layer. We then use seismic interferometry to retrieve ghost reflections from virtual sources and receivers placed directly at the water-mud interface. Using velocity analysis applied to the ghost reflections, we successfully obtain the P-wave and S-wave velocities only inside the fluid-mud layer, and investigate the velocity change during the self-weight consolidation of the fluid mud. Our results indicate that the S-wave velocities of the fluid mud increase with consolidation time, and show that reflection measurements and ghost reflections can be used to monitor the geotechnical behavior of fluid mud.

Keywords: ultrasonic measurement, fluid mud, p- and s-wave velocities, seismic interferometry, yield stress

OPEN ACCESS

Edited by:
Andrew James Manning,
HR Wallingford, United Kingdom

Reviewed by:
Claudia Finger,
Fraunhofer IEG—Fraunhofer Research Institution for Energy Infrastructures and Geothermal Systems, Germany
Katrin Löer,
University of Aberdeen, United Kingdom

***Correspondence:**
Xu Ma
xuma@vt.edu

Specialty section:
This article was submitted to Sedimentology, Stratigraphy and Diagenesis, a section of the journal Frontiers in Earth Science

Received: *01 November 2021*
Accepted: *07 February 2022*
Published: *03 March 2022*

Citation:
Ma X, Kirichek A, Heller K and Draganov D (2022) Estimating P- and S-Wave Velocities in Fluid Mud Using Seismic Interferometry. Front. Earth Sci. 10:806721. doi: 10.3389/feart.2022.806721

INTRODUCTION

The geotechnical behavior of fluid mud significantly affects the navigability in ports and waterways. Better understanding of the geotechnical behavior of the fluid mud can thus help to estimate accurately the nautical depth and thus safe navigating through fluid mud, as well as decrease the dredging costs (McAnally et al., 2007; McAnally et al., 2016; Kirichek et al., 2018). The strength of the fluid mud is low but could increase over time due to the consolidation effect to form a layer with high rigidity (Abril et al., 2000). Port authorities usually have their own methods to determine the navigability of the fluid mud. For example, the Port of Rotterdam uses the levels of 1.2 kg/L while the Port of Emden uses the yield stress of 100 Pa as criteria for estimating the water/mud interface (Kirichek et al., 2018). These levels are chosen based on the combination of seismic data and yield

stress/density vertical profiles, which are measured in a water/mud column by mud profilers (Kirichek et al., 2020; Kirichek and Rutgers 2020). Because of the individual differences in mud composition, an accurate parameter that can be adopted by different ports is needed. It is challenging to accurately measure the *in-situ* geotechnical behaviors of the fluid mud, because the common techniques of measurement, including yield strength and density measurement, will inevitably disturb the fluid mud during the intrusive sampling process (Kirichek et al., 2020). That is, why, a laboratory protocol was developed to determine the fluidic yield stresses (Shakeel et al., 2020). On the basis of this protocol, a link was found between the S-wave velocities and the fluidic yield stress (Ma et al., 2021). The non-intrusive measurements such as x-ray and ultrasonic measurements are favorable because other measurements will alter the characteristic of the fluid mud and the result will be inaccurate (Kirichek et al., 2018; Carneiro et al., 2020).

The ultrasonic measurements for fluid mud include transmission measurements and reflection measurements. The transmission measurements are straightforward and simple to use in a laboratory. In recent years, most commonly used seismic survey techniques for marine sediment, such as sonar and velocimeter, employ longitudinal (P-) waves (Gratiot et al., 2000; Schrottke et al., 2006). In a marine seismic survey, the sources and receivers need to be located in the water column. In practice, they are often close to the water surface, meaning that the sources, such as airgun arrays, and the receivers, usually towed by a vessel as streamers, send and receive only P-waves, respectively. Therefore, the utilization of S-waves is limited in the marine environment and extracting the S-wave information is challenging and time-consuming (Drijkoningen et al., 2012). At the same time, P-waves are related to the bulk properties of the materials and the geotechanical properties of marine sediments cannot be inferred only from P-waves. S-waves can be used to precisely characterize the fluid mud as the propagation velocity and amplitude of the S-waves strongly depend on the geotechanical properties of the marine sediments (Meissner et al., 1991). Developing an accurate and reliable way of using S-waves for the seismic survey in a marine environment without the complications of deploying receivers at the water bottom to characterize the marine sediments can greatly facilitate the investigation of the geotechnical behavior of the marine sediments. Leurer (2004), Ballard et al. (2014), Ballard and Lee (2016) performed transmission measurement in a laboratory to measure the velocities of the seismic waves. Leurer (2004) used high frequencies and found that the S-wave velocities ranged from 450 to 975 m/s. The S-wave velocity is calculated using travel distance and traveltime along the travelpath, which usually is a straight line (Ma et al., 2021). However, there are limitations using the transmission measurements in the field because there are no open side positions to plant the transducers as used in containers in the laboratory-measurement setup. In contrast, reflection measurements in marine exploration allow deploying the transducers or hydrophones in the water column. Using such measurements, layer-specific propagation velocities of the fluid mud can be estimated to monitor the variation of the shear strength of the fluid mud. Given that correlations are found between the S-wave velocity and the yield strength, the S-wave velocity can be used as a proxy to estimate the yield strength of the fluid mud; therefore, ultrasonic measurements have a great potential in helping estimate the yield strength of the fluid mud (Ma et al., 2021).

The goal of this study is to measure the layer-specific propagation velocities and investigate the temporal variation of these velocities with the consolidation of the fluid mud using seismic reflection measurement and retrieval of layer-specific reflections. To obtain the latter, we apply seismic interferometry (SI) to the recorded reflection data to eliminate the travelpaths inside the water layer and retrieve reflections only inside the fluid-mud layer. SI is a technique to retrieve new seismic recordings between receivers from cross-correlation of existing recordings at the receivers (e.g., Shapiro and Campillo 2004; Wapenaar and Fokkema 2006; Draganov et al., 2009; Draganov et al. 2010; Draganov et al. 2012; Draganov et al. 2013). In this study, we first briefly introduce the reflection measurements. We, then, show the process of retrieving seismic traces based on ghost-reflection retrieval, followed by the velocity-calculation process. We show the temporal variation of the propagation velocity inside the fluid-mud layer and the correlation between the S-wave velocities and yield strengths. Additionally, we compare the S-wave velocities from the reflection measurement to those of a transmission measurement that was performed in a previous study (Ma et al., 2021).

MATERIALS AND METHODS

We have developed a seismic reflection system to measure the layer-specific propagation velocities. Below, we give a short description of the main measurement steps. The sample and the system are described in detail in Ma et al. (2021). The mud sample was retrieved from the Calandkanaal (Port of Rotterdam). The sampling location is shown in **Figure 1A**. Before the reflection measurement, a two-layer system is formed due to the density difference between water and fluid mud (**Figures 1C,D**). We first stir the fluid mud using a mechanical mixer to ensure that the fluid mud is in a homogeneous form with a uniform density (**Figure 1B**). We deposit the fluid mud in the fluid-mud tank and gently add water above it without eroding the fluid-mud layer in the tank. The fluid mud in the tank settles and consolidates during the self-weight consolidation process. At the start of the measurements, the water layer is about 82 mm thick, the mud layer below it is about 100 mm thick.

The Reflection Measurement System

The reflection measurement system includes a signal control part, a fluid-mud tank, and ultrasound transducers (**Figure 1D**). We use a transparent glass tank that allows to visually see the settlement of the fluid-mud layer (**Figure 1C**). The multiple positions of the receiver transducer along the horizontal direction are evenly distributed so that a common-source gather (CSG) can be constructed by placing one after the other the measurements (traces) at each consecutive horizontal position of the receiver. The horizontal distance between the

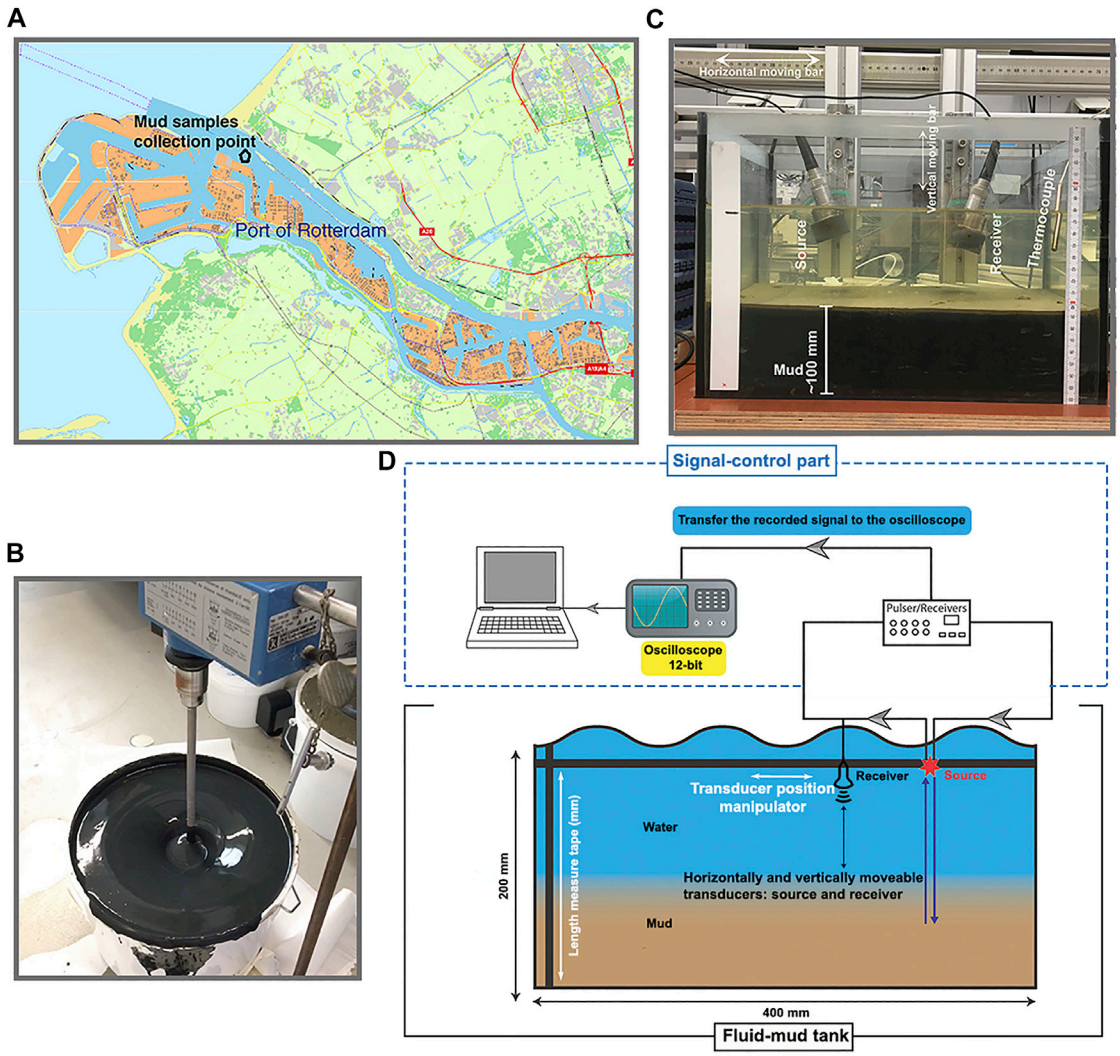

FIGURE 1 | (A) Mud-samples collection location in the Calandkanaal (Port of Rotterdam). **(B)** Mud-stirring process using a mechanical mixer. **(C)** A glass tank with fluid mud, transducers, and a thermocouple. **(D)** A cartoon showing the reflection measurement system.

receiver positions is 5 mm. The distance between the first and last receiver positions, which correspond to the shortest and longest source-receiver offsets, respectively, is 95 mm, meaning that a CSG includes 20 traces at different offsets. The parameters of the acquisition geometry and the different kinds of expected arrivals for this two-layer system are shown in **Figure 2**. For our analysis, we use the P-wave reflection of the mud top and the primary reflections of the mud bottom (explained in the following section).

Time-Lapse Measurement and Data Acquisition

We place the source transducer at two positions, labeled S1 and S2 in **Figure 2**, the signals of which are recorded by the same receiver array. The sources are distanced 50 mm and 100 from the leftmost receiver. The excitation frequency of the sources is 100 kHz. By applying SI to the recordings from the two sources at a specific receiver position to retrieve a ghost source and a ghost receiver that are effectively placed on the top of the mud, i.e., the water/mud interface (**Figure 3**). Cross-correlating the reflection from the mud top with the reflection from the mud bottom effectively eliminates the common travelpath from S1 to the receiver and S2 to the receiver in the water layer (dashed lines in **Figure 3**). Because the specific receiver position depends on the thickness and velocity of the mud layer, and thus changes with time, we record CSGs.

We monitor the changes in the propagation velocities in the two-layer system during a 2-week period. During several days in this period, we conduct measurements to obtain a CSG from each source. In the first week, we perform reflection measurements every day from Monday to Friday. In the second week, we only conduct a reflection measurement on Friday. As shown in **Figure 4**, there are two kinds of primary

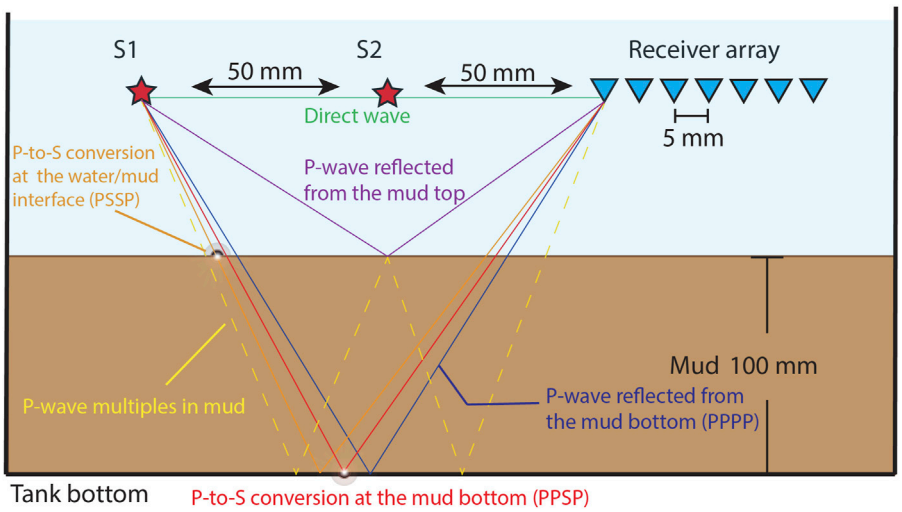

FIGURE 2 | Illustration of the acquisition geometry and different kinds of arrivals expected to be recorded in a reflection measurement. The receiver array illustrates only the first seven receiver; the proportions are exaggerated; the paths through the water/mud interface are shown as straight lines for illustration purposes.

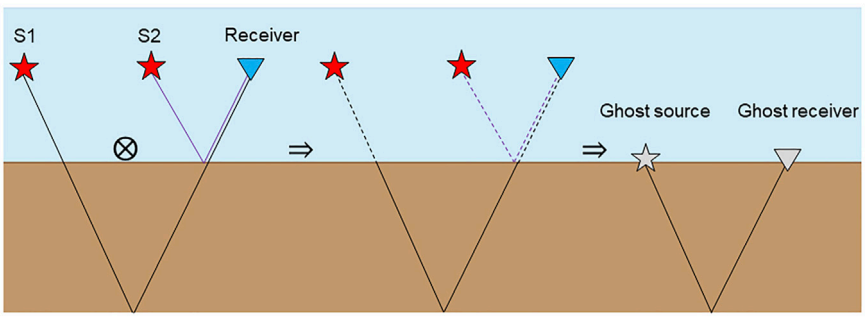

FIGURE 3 | Sketch of the retrieving a ghost reflections using seismic interferometry by correlating two traces that effectively eliminates the common travelpaths in the water layer (dashed lines).

reflections that we emphasize in this study. One kind is the arrival that is, reflected by the mud top (**Figure 4A**). The other kind are the arrivals that are reflected by the mud bottom (**Figures 4B–D**). The latter represents three reflections with different travelpaths according to their possible partial conversions. During the propagation of the P-wave originating from the source transducer, part of the energy propagates as a P-wave along the complete downward and upward travelpaths (**Figure 4B**). A part of the energy converts to an S-wave when the P-wave is reflected by the mud bottom (**Figure 4C**). Yet another part of the energy converts to an S-wave when the P-wave hits the water/mud interface and continues to propagate as such downward to the mud bottom and up to the water/mud interface (**Figure 4D**). In order to compute the propagation velocities of the P- and S-wave inside the fluid mud, we need to obtain the travel distances and traveltimes along the travelpaths within the fluid mud. However, the travelpaths of the primary reflections contain also the travelpaths inside the water, as shown in **Figures 4B–D**. **Figure 4B** illustrates the travelpaths of the reflected P-wave which does not undergo any conversion (PP). In this way, the wave has the same incidence and reflection angle at the mud bottom and thus the downward and upward travelpaths are symmetrical. **Figures 2**, **4C** shows the travelpaths of the reflected P-wave that converts to an S-wave after reflecting at the mud bottom (PPSP). Due to conversion, the incidence and reflection angle are different and thus the downward and upward travelpaths are asymmetrical. As shown in **Figures 2**, **4D**, the P-wave also converts to an S-wave when hitting the water/mud interface and the S-wave converts again to a P-wave only at the water/mud interface along the upward travelpath (PSSP). Because of this, the downward and upward travelpaths are symmetrical. Note that the primary reflection PSPP has an identical arrival time as the PPSP primary for a laterally homogeneous medium, the PPSP arrival essentially is the superposition of

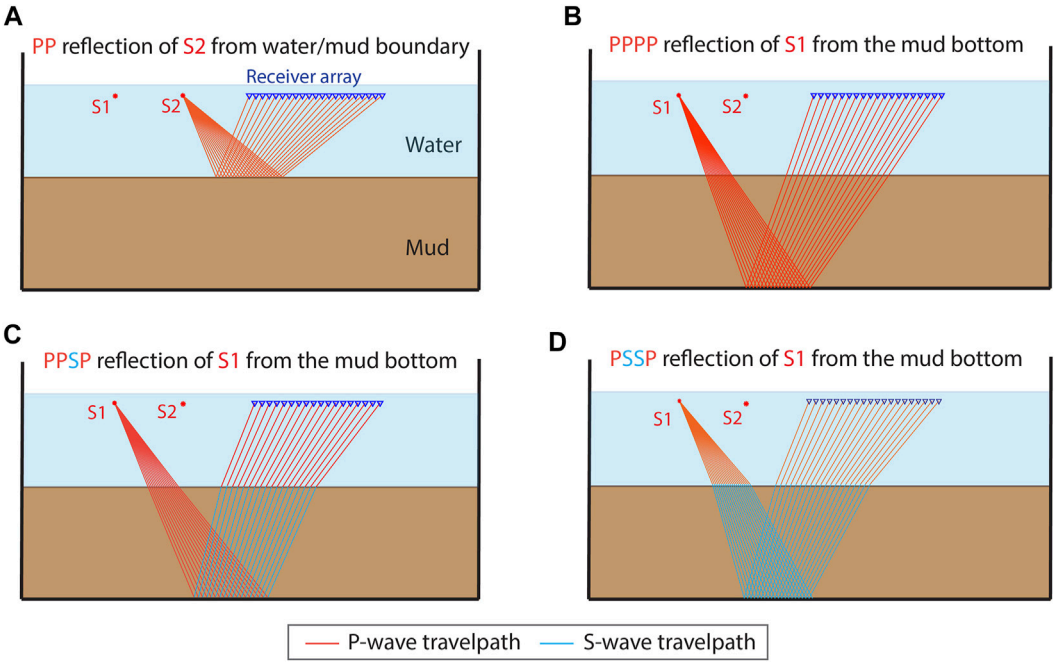

FIGURE 4 | Travelpaths of the primary reflections in the ultrasonic reflection measurement: **(A)** the P-wave reflection (PP) from the water/mud interface from source S2; **(B)** the P-wave reflection (PPPP) from the bottom of the mud layer from source S1; **(C)** the reflection from the bottom of the mud layer partly converted to an S-wave (PPSP) from source S1; **(D)** the reflection from the bottom of the mud layer completely converted to an S-wave (PSSP) from source S1. The primary reflection in **(A)** is used to correlate with the primary reflections in **(B–D)**.

both PPSP and PSPP. In **Figures 2**, **4C**, we only illustrate the PPSP travelpaths. From here on, we only use the label PPSP but we understand the superposition of PPSP and PSPP.

We apply the SI method for retrieval of ghost reflections. For this, we correlate trace-by-trace the PP reflection arrivals in the CSG from source S2 (**Figure 4A**) with each of the three primary reflection arrivals, i.e., PPPP, PPSP, and PSSP, in the CSG from source S1 (**Figures 4B–D**). The results are three correlation gathers containing correlated traces. The final step of SI is the summation of the traces inside each of the three correlation gathers. In this way, we retrieve three ghost reflections that appear to have propagated only inside the fluid-mud layer by effectively removing the travelpaths inside the water layer. These three ghost reflections represent a PP, PS, and SS reflection arrivals. Next, we pick the two-way traveltimes of the ghost reflection inside the fluid mud and calculate the travel distances along the travelpaths. Calculation of the travel distances is possible as the distance between the source and receiver of the three ghost reflections is always the same and equal to the distance between the sources S1 and S2, while we monitor the thickness of the fluid-mud layer using a ruler along the vertical wall of the tank. We then estimate the P- and S-wave velocities in the fluid-mud layer by dividing the travel distance by the picked two-way traveltimes While the calculations for the PP and SS ghost reflections are straightforward, to calculate the velocities from the PS ghost reflection, we form a system of three equations with three unkowns x, y, and v_s:

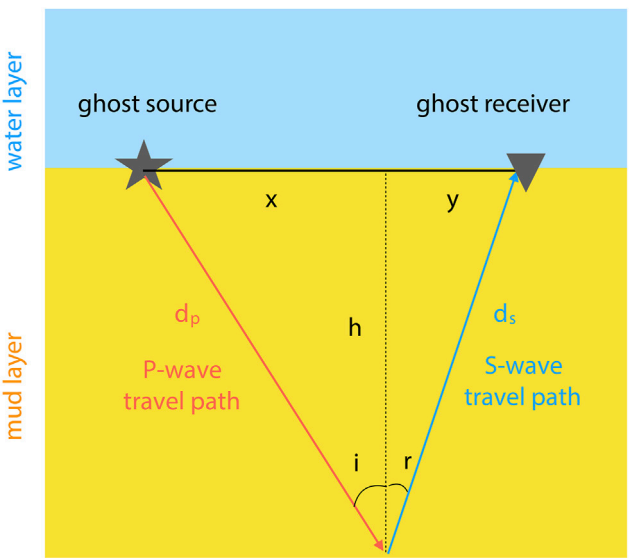

FIGURE 5 | Geometry and parameters (see text for their explanation) for S-wave velocity calculation based on Snell's law.

$$x + y = 50 \tag{1}$$

$$\frac{sin(i)}{sin(r)} = \frac{x/d_p}{y/d_s} = \frac{v_p}{v_s} \tag{2}$$

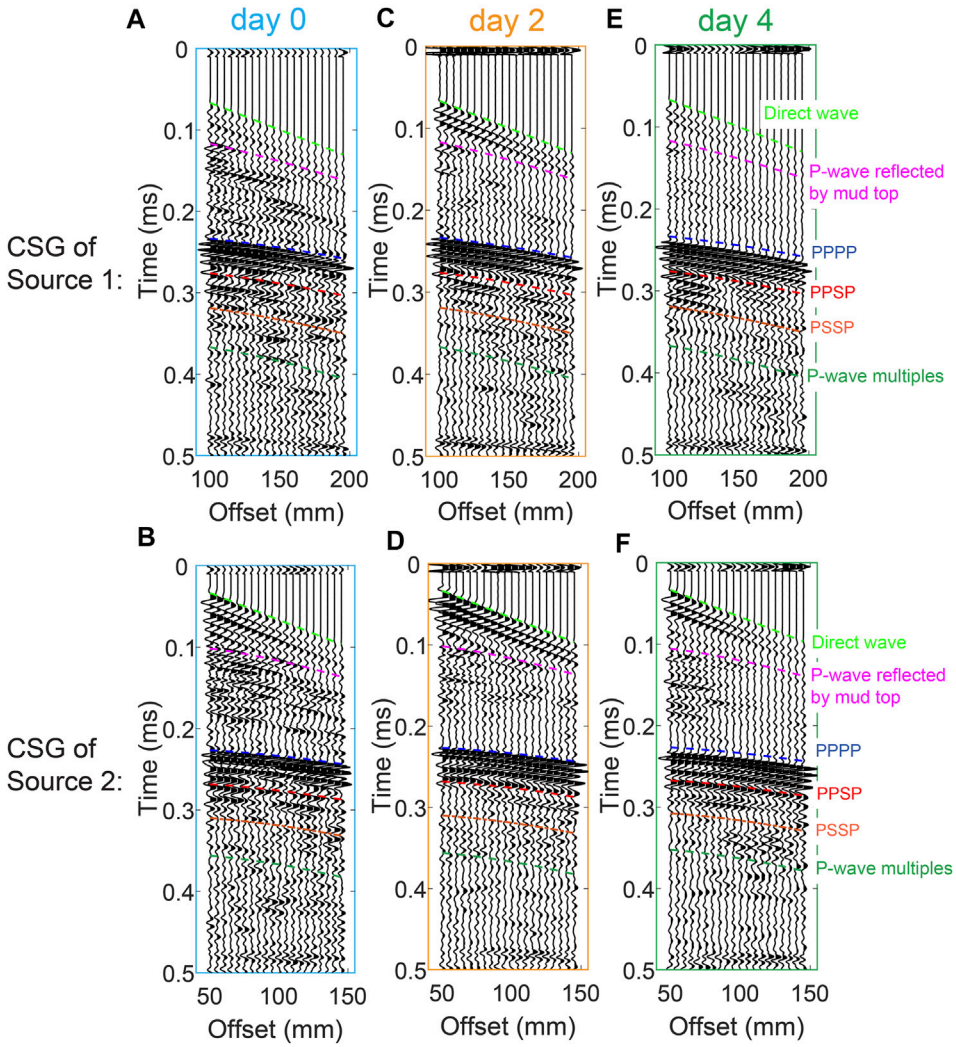

FIGURE 6 | Common-source gathers (CSGs) for sources S1 **(A, C, E)** and S2 **(B, D, F)** for day **(A, B)** 0, **(C, D)** 2, **(E, F)** 4. The CSGs for days 1, 3, 11 are shown in **Supplementary Appendix S1**. The color coding indicates different arrivals.

$$\frac{d_p}{v_p} + \frac{d_s}{v_s} = t_{two-way\ travel} \tag{3}$$

Equation 1 states that the distance between the ghost source and the ghost receiver is 50 mm, which is the sum of the horizontal projection x of the P-wave travelpath and y of the S-wave travelpath of the PS travelpath inside the fluid-mud layer (**Figure 5**). **Eq. 2** is established based on the Snell's law, where d_p is the P-wave travelpath, d_s is the S-wave travelpath, and v_P and v_s are the velocities of the P- and S-wave inside the fluid-mud layer. **Eq. 3** shows that the two-way traveltime is the sum of the traveltimes of P-wave and S-wave inside the layer. Additionally, h represents the thickness of the mud layer (**Figure 5**). As shown in **Figure 5**, $d_p = \sqrt{x^2 + h^2}$ and $d_s = \sqrt{y^2 + h^2}$. We consider v_P known as we calculate it using the PP ghost reflection.

RESULTS AND DISCUSSION

We record CSG from S1 and S2 on each of the days from Monday to Friday during the first week and on Friday during second week. **Figure 6** shows the CSGs for days 0, 2, 4. The arrivals from S1 appear to be characterized by lower amplitudes than those from S2 which is expected because the receiver array is 50 mm closer to S2 compared to S1. The recording order in time of the different arrivals depends on the propagation velocities of the seismic waves in the water and fluid-mud layers and the travel distances along the travelpaths. The different arrival types we identify are color-coded in **Figure 6**. As we explained above, we aim to utilize the PP, PPPP, PPSP, and PSSP reflection arrivals to monitor for velocity changes during the 2-week self-weight consolidation. Although with the consolidation the two-way traveltime of the reflection arrivals PPP, PPSP, and PSSP gradually decreases, it is

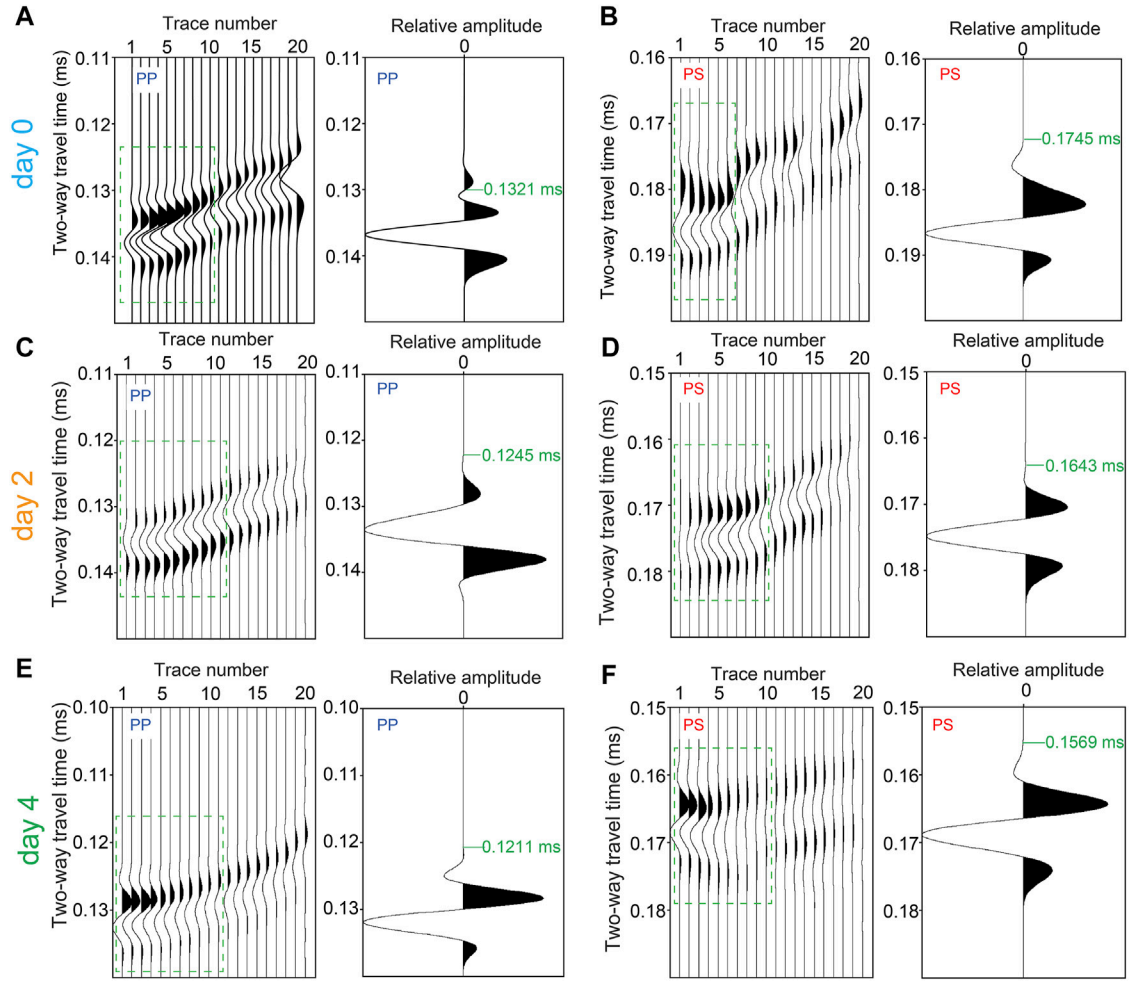

FIGURE 7 | Correlation gathers (left columns) and retrieved ghost reflections (right columns) from inside the fluid-mud layer for **(A, B)** day 0, **(C, D)** day 2, and **(E, F)** day 4. The results in the right columns are obtained by summing the traces inside stationary-phase region (the green rectangles) in the corresponding left columns. **(A, C, E)** Retrieval of PP ghost reflections. **(B, D, F)** Retrieval of PS ghost reflections. The green numbers in the right columns indicate the picked arrival times of the retrieved ghost reflections.

still uncertain whether the P- and/or S-wave velocities can increase because the thickness of the fluid-mud layer decrease due to the settling. The decrease of the two-way traveltime could result from decrease of the travel distance or from increase of the P- and/or S-wave velocities. Note that simultaneously with the decrease of the thickness of the fluid-mud layer, the thickness of the water layer increases. It is thus necessary to accurately calculate the velocities inside the fluid-mud layer using the travelpaths and two-way traveltimes of reflection arrivals from only inside the fluid mud. As we explain above, we achieve this using SI for retrieval of ghost reflections.

Figures 6B,D,F show the interpreted direct waves and reflection arrivals from S2. The direct waves (light green color) interfere with the PP reflections (magenta color) from the fluid-mud top. In the SI process for retrieval of ghost reflections, we need to correlate the PP reflection from S2 with the primary reflections from the fluid-mud bottom from S1—PPPP, PPSP, and PSSP. In order to suppress the influence of the direct waves on the PP reflections, we use a frequency-wave number filter (Ma et al., 2021). After the correlation, we obtain correlation gathers (left columns in **Figures 7A,B**), which we have to sum along the receiver positions to obtain the final retrieved ghost reflections. As shown in Ma et al. (2021), more accurate retrieval is obtained when summing only the traces inside the so-called stationary-phase region (Snieder, 2004). In the summation process, such traces contribute constructively to the final result, while traces outside the stationary-phase region should interfere destructively with each other if sufficiently long receiver array is available. AS our array is limited in length, we taper the traces outside the stationary-phase region. The results of the summations (right columns in **Figures 7A,B**) represent retrieved ghost reflections with travelpaths only inside the fluid-mud layer. In **Figure 7**, we show the retrieved ghost reflections PP and PS. The ghost reflections SS are not included in this study because the energy of the PSSP reflections is relatively lower when the settling time is not long enough, making the retrieval of SS for the earlier days difficult. Longer

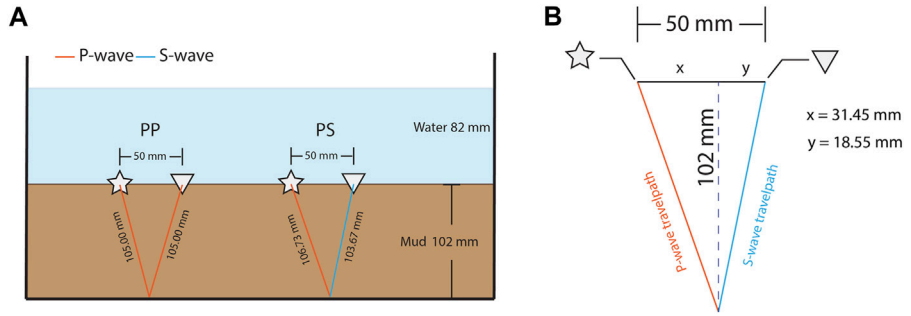

FIGURE 8 | (A) The travelpath distances for ghost reflections PP and PS; **(B)** Illustration of the calculation for the unsymmetrical travelpath of PS.

TABLE 1 | Parameters for calculating the P- and S-wave velocities inside the fluid-mud layer for the six different days of measurements.

Fluid-mud thickness (mm)	Two-way travel time for PP (s)	Travel path length for PP (mm)		PP velocity (m/s)	Two-way travel time for PS (s)	Travel path length for PS (mm)		PS velocities (m/s) using individual measurements		PS velocities (m/s) using the mean P-wave velocity	
	Left leg P-wave; right leg P-wave	Left leg P-wave	Right leg P-wave	P-wave	Left leg P-wave; right leg S-wave	Left leg P-wave	Right leg S-wave	Left leg P-wave	Right leg S-wave	Left leg P-wave	Right leg S-wave
102.0	0.1321	105.02	105.02	1590	0.1745	106.74	103.67	1590	966	1588	967
99.0	0.1283	102.10	102.10	1592	0.1695	103.88	100.72	1592	967	1588	968
96.0	0.1245	99.20	99.20	1593	0.1643	101.03	97.77	1593	969	1588	971
95.0	0.1243	98.23	98.23	1581	0.1619	100.00	96.84	1581	981	1588	979
92.5	0.1211	95.82	95.82	1582	0.1569	97.60	94.41	1582	988	1588	989
86.0	0.1125	89.56	89.56	1592	0.1463	91.51	88.01	1592	991	1588	993

settling time causes a larger difference between the densities of the water and the fluid mud meaning that a greater portion of the P-wave energy turns into S-wave energy when stricking the water/mud interface. Only the measurement after 1 week can ensure an accurate pick and reliable retrieval for the ghost reflection SS, the result of which was presented in Ma et al. (2021). So, in this study, we calculate S-wave velocities from the retrieved ghost reflections PS. We then use the retrieved ghost reflections to pick the first break to determine the two-way traveltime of these arrivals (green numbers in the right columns in **Figure 7**). We do the same also for days 1, 3, and 11 (see figures in **Supplementary Appendix SA**).

Using the picked two-way traveltimes, we can estimate the P- and S-wave velocities using the travelpath distances. **Figure 8** shows the PP and PS travelpath distances for day 0. The travelpath of PP is symmetrical so that the travel distances for the left leg and the right leg are equal. In contrast, the travelpath of PS is asymmetrical, and thus the travel distances of the left leg for the P-wave and the right leg for the S-wave need to be calculated by solving the system of **Eqs 1–3** using the two-way traveltime pick and the known P-wave velocity from the ghost reflection PP. Here, we calculate the velocities using the parameters from **Table 1** for day 0. The P-wave velocity is estimated to be 1,590 m/s. The S-wave velocity is thus estimated to be 966 m/s.

Using the same process, we analyze the seismic traces of the measurement from day 0 to day 11 and monitor the time-lapse evolution of the P- and S-wave velocities (**Table 1**). For comparison, **Table 1** also includes the S-wave velocities estimated using the mean P-wave velocity from the reflection measurement. The S-wave velocities estimated using the mean P-wave velocity and the individual P-wave velocities are very close to each other. As shown in **Table 2**, the P-wave velocities suggest that, although we observe fluctuations, there is no obvious pattern for P-wave velocity change in relation to the consolidation. On the other hand, the S-wave velocities appear to be clearly increasing with the consolidation process, despite the apparent close velocities for day 0 and day 1.

Additionally, we synchronously measure the yield stress of the fluid mud using a rheometer with Couette geometry and Vane geometry. We compare the progress of the fluidic yield stress with consolidation and examine the correlation with the S-wave velocities. As shown in **Figure 9**, the S-wave velocities (green dots; calculated using the P-wave velocities estimated from the PP ghost reflection for each day) appear to be positively correlated with the fluidic yield stress with the progress of the consolidation for both the reflection measurement in this study and the transmission measurements (blue dots) from Ma et al. (2021). The overall change of the S-wave velocities with the evolution of the fluidic yield stress indicates a nonlinear process. From day 0 to day 2, although the fluidic yield stress shows a pronounced increase, the S-wave velocities show a limited increase, especially for the measurement with Vane geometry. This could be ascribed to the initial homogeneous status of the fluid mud. We start the measurements after homogenizing the fluid mud. The conversion from the homogeneous to inhomogeneous condition could certainly strengthen the fluidic yield stress of the fluid mud. However, during the conversion from homogeneous to

TABLE 2 | Time-lapse velocities from transmission and the ghost-reflection measurements.

Settling day	Velocities from transmission measurements (m/s)		Velocities from ghost-reflection measurements (m/s)	
	P-wave	S-wave	P-wave	S-wave
0	1570	959	1590	966
1	1570	957	1592	967
2	1570	959	1593	969
3	1570	970	1581	981
4	1570	995	1582	988
11	1570	998	1592	991

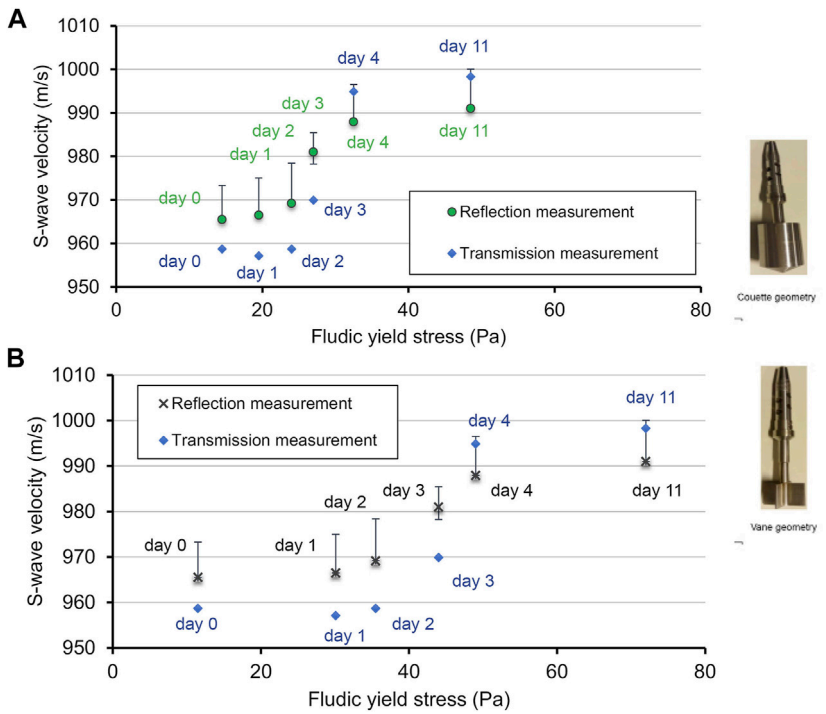

FIGURE 9 | Evolution of the S-wave velocity (green dots) with the fluidic yield stress, where the latter is measured by **(A)** the Couette geometry and **(B)** the Vane geometry. The protocol to determine the fluidic yield stresses was developed by Shakeel et al. (2020). The black bars indicate the uncertainty interval. The uncertainty is estimated by taking the larger difference per day between the S-wave velocity estimated using the P-wave velocities from the corresponding daily ghost-reflection measurement and either the S-wave velocity estimated using the average of the P-wave velocities from the daily ghost-reflection measurements or the S-wave velocity estimated using the P-wave velocity from the transmission measurement. The transmission-measurement result is from Ma et al. (2021).

inhomogeneous mud, the effect of the consolidation probably cannot contribute to the immediate increase of the S-wave velocities. From day 2 to day 3, the S-wave velocities notably increase with a mild rise of the fluidic yield stress. This implies that the S-wave velocities are more sensitive to the increase of the yield stress when the consolidation has started with a duration more than 24 h. From day 2 to the last day—day 11, the correlation between the S-wave velocities and the fluidic yield stress shows a good apparently linear relationship. The measurements from day 2 to day 11, which are within the linear increase duration, show that the average increase rate of the fluidic yield stress is 1.84 m/(s*Pa) with the Couette geometry and is 1.03 m/(s*Pa) with the Vane geometry.

We also compare the estimated S-wave velocities from our ghost-reflection measurements with the S-wave velocities from seismic transmission measurements that were also conducted synchronously (Ma et al., 2021). The comparison in **Table 2** shows that, the S-wave velocities from both the ghost-reflection and the transmission measurement are close but nevertheless they exhibit small differences. One reason for this could be that the directional difference of the seismic transmission measurement and the reflection measurement causes a discrepancy. In the transmission measurements, the source and the receiver transducers are mounted at the same height on opposite sides of the measurement tank, and thus the travelpath from the source transducer to the receiver transducer is along the horizontal direction. The seismic transmission measurement essentially sample the S-wave velocities horizontally along the middle part of the fluid-mud layer because the transducers were

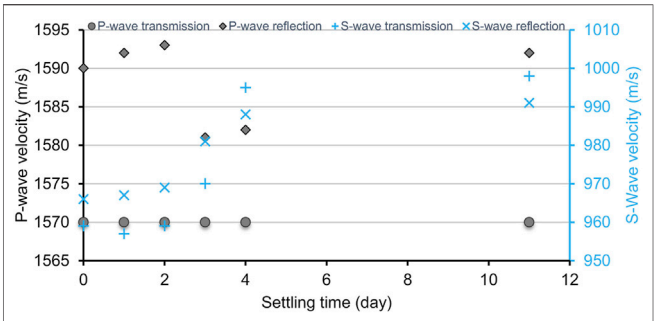

FIGURE 10 | Comparison of P- and S-wave velocities from the transmission measurement in Ma et al. (2021) and the reflection measurement.

mounted there. In contrast, the waves in the reflection measurements travel the complete height of the fluid-mud layer twice along paths as in **Figure 8**. Thus, the two measurement geometries might be facing the effect of anisotropy between the horizontal and vertical directions. This means that the S-wave velocities estimated from the ghost reflections might reflect possible changes in consolidation with depth.

Another reason for differences in the S-wave velocities from the transmission and ghost-reflection measurements is that we estimate the S-wave velocities from the ghost reflections using the estimated P-wave velocities from the PP ghost reflections. Comparing the P-wave velocities estimated from the transmission and ghost-reflection measurements in **Table 2**; **Figure 10**, we see that they are also slightly different. An error in estimating the P-wave velocity might be coming from insufficient sampling of the stationary-phase region. Another error might be due to the differences in the directionality in the measurement geometries of the transmission and reflection measurements, just like for the S-waves. Still, the maximal error in the estimated P-wave velocities is 0.29%, which can ensure a reliable estimation of the S-wave velocities. To visualize this, we compare the estimated S-wave velocities using the estimated P-wave velocities from the PP ghost reflections for each of the 6 days of the measurements to the S-wave velocities estimated using the average P-wave velocity obtained by averaging the six individual PP ghost-reflection velocities. We show these results in the rightmost column in **Table 1**. As we can see, the differences are very small, i.e., less than 0.9%. We visualize the comparison also in **Figure 9** by the black uncertainty intervals. We calculate the intervals for each measurement day: using the P-wave velocity averaged from the six individual PP ghost-reflection velocities and using the P-wave velocity from the transmission measurements; taking the maximum difference between the S-wave velocity for each measurement day and the S-wave velocity obtained using the average or transmission P-wave velocity; the maximum difference is assigned as the uncertainty interval. We can see that the uncertainly interval is again less than 0.9%.

The results from our laboratory experiments show that using ghost reflections has a good potential for monitoring the seismic-velocity characteristics, and consequently also the fluidic yield stress, of fluid mud. Our experiment used fluid-mud layer with thickness of about 100 mm and source signals with center frequency of 100 kHz. We expect that this could upscaled to the field situation of a port or waterway with a thickness of the fluid-mud layer of about 2 m by using a source signal with a center frequency of 5 kHz as this would keep the same proportions relative to the dominant wavelengths in the fluid mud. The length of the acquisition geometry, which in our experiment had a maximum source-receiver offset of about 200 mm could be upscaled in the same way, i.e., relative to the thickness of the fluid-mud layer. An extra factor to take here into account is the thickness of the water layer. The length of an acquisition setup in a port or waterway should be such that the expected incidence angles at the water/fluid-mud interface are sufficiently away from vertical to allow P-to-S-wave conversions at the interface. I.e., the deeper the interface, the longer the maximum source-receiver offset. This would also entice assuming local lateral homogeneity in the water at the scale of the maximum source-receiver offset; inside the fluid-mud layer, the assumption for local lateral homogeneity would still be at the scale of the distance between the two source only.

CONCLUSION

We investigated longitudinal (P-) and transverse (S-) wave velocities in fluid mud for time-lapse monitoring of the geotechnical behavior of fluid mud in a water/fluid-mud system. For this, we used ultrasonic laboratory data from measurements in reflection geometry. We estimated P- and S-wave velocities directly from inside the fluid mud by removing the influence of the water layer by application of seismic interferometry for retrieval of ghost reflections. The latter allowed us to retrieve a P-wave reflection and a P-to-S-wave converted reflection from the bottom of the fluid mud as if from measurements with a source and receiver directly placed at the top of the fluid mud. We compared the estimated P- and S-wave velocities to values estimated from direct transmission measurements made horizontally along the middle height of the fluid-mud layer. The comparison showed that the transmission velocity of P-wave was more stable than the reflection velocity, which appeared to be fluctuated. The reflection S-wave velocity and the transmission S-wave velocity were close to each other. The S-wave velocities we estimated in the fluid-mud layer from the ghost reflections increase with the self-weight consolidation of the fluid mud, while the P-wave velocities did not show a trend. Concurrently, the yield stress of the fluid mud also increased with the consolidation. We found that the S-wave velocities are positively correlated with the fluidic yield stress of the fluid mud. This relationship implies that the time-lapse change in S-wave velocities might be used to indicate the progress of consolidation, which would provide a basis for a new non-intrusive ultrasound measurement tool in ports and waterways for monitoring the condition of the fluid mud.

DATA AVAILABILITY STATEMENT

The original contributions presented in the study are included in the article/**Supplementary Material**, further inquiries can be directed to the corresponding author.

AUTHOR CONTRIBUTIONS

XM: Conceptualization, Formal analysis, Investigation, Methodology, Validation, Visualization, Writing—original draft, Writing—review and editing. AK: Funding acquisition, Resources, Validation, Writing—review and editing, Supervision, Project administration. KH: Formal analysis, Investigation, Methodology, Validation. DD: Funding acquisition, Formal Analysis, Methodology, Resources, Writing—review and editing, Supervision, Project administration.

FUNDING

This research is supported by the Division for Earth and Life Sciences (ALW) with financial aid from the Netherlands Organization for Scientific Research (NWO) with grant no. ALWTW.2016.029.

ACKNOWLEDGMENTS

The project is carried out within the framework of the MUDNET academic network https://www.tudelft.nl/mudnet/. The authors thank Ahmad Shakeel for helping the rheological experiments and data analysis.

SUPPLEMENTARY MATERIAL

The Supplementary Material for this article can be found online at: https://www.frontiersin.org/articles/10.3389/feart.2022.806721/full#supplementary-material

REFERENCES

Abril, G., Riou, S. A., Etcheber, H., Frankignoulle, H., De Wit, R., and Middelburg, J. J. (2000). Transient, Tidal Time-Scale, Nitrogen Transformations in an Estuarine Turbidity Maximum—Fluid Mud System (The Gironde, South-West France). *Estuar. Coast. Shelf Sci.* 50 (5), 703–715.

Ballard, M. S., and Lee, K. M. (2016). Examining the Effects of Microstructure on Geoacoustic Parameters in fine-grained Sediments. *The J. Acoust. Soc. America* 140 (3), 1548–1557. doi:10.1121/1.4962289

Ballard, M. S., Lee, K. M., and Muir, T. G. (2014). Laboratory P- and S-Wave Measurements of a Reconstituted Muddy Sediment with Comparison to Card-House Theory. *J. Acoust. Soc. America* 136 (6), 2941–2946. doi:10.1121/1.4900558

Carneiro, J. C., Gallo, M. N., and Vinzón, S. B. (2020). Detection of Fluid Mud Layers Using Tuning Fork, Dual-Frequency Echo Sounder, and Chirp Sub-Bottom Measurements. *Ocean Dyn.* 1–18.

Draganov, D., Campman, X., Thorbecke, J., Verdel, A., and Wapenaar, K. (2009). Reflection Images From Ambient Seismic Noise. *Geophys.* 74, A63–A67. doi:10.1190/1.3193529

Draganov, D., Ghose, R., Heller, K., and Ruigrok, E. (2013). Monitoring Changes in Velocity and Q Using Non-physical Arrivals in Seismic Interferometry. *Geophys. J. Int.* 192, 699–709. doi:10.1093/gji/ggs037

Draganov, D., Ghose, R., Ruigrok, E., Thorbecke, J., and Wapenaar, K. (2010). Seismic Interferometry, Intrinsic Losses andQ-Estimation. *Geophys. Prospecting* 58 (3), 361–373. doi:10.1111/j.1365-2478.2009.00828.x

Draganov, D., Heller, K., and Ghose, R. (2012). Monitoring CO2 Storage Using Ghost Reflections Retrieved from Seismic Interferometry. *Int. J. Greenhouse Gas Control.* 11, S35–S46. doi:10.1016/j.ijggc.2012.07.026

Drijkoningen, G., Allouche, N., Thorbecke, J., and Bada, G. (2012). Nongeometrically Converted Shear Waves in marine Streamer Data. *Geophysics* 77 (6), P45–P56. doi:10.1190/geo2012-0037.1

Gratiot, N., Mory, M., and Auchere, D. (2000). An Acoustic Doppler Velocimeter (ADV) for the Characterisation of Turbulence in Concentrated Fluid Mud. *Continental Shelf Res.* 20 (12-13), 1551–1567. Sep 10. doi:10.1016/s0278-4343(00)00037-6

Jackson, D., and Richardson, M. (2007). *High-Frequency Seafloor Acoustics*. Springer Science & Business Media.

Kirichek, A., Chassagne, C., Winterwerp, H., and Vellinga, T. (2018). How Navigable Are Fluid Mud Layers. *Terra Aqua: Int. J. Public Works, Ports Waterways Dev.* 151.

Kirichek, A., and Rutgers, R. (2020). Monitoring of Settling and Consolidation of Mud after Water Injection Dredging in the Calandkanaal. *Terra et Aqua* 160, 16–26.

Kirichek, A., Shakeel, A., and Chassagne, C. (2020). Using *In Situ* Density and Strength Measurements for Sediment Maintenance in Ports and Waterways. *J. Soils Sediments* 20 (6), 2546–2552. doi:10.1007/s11368-020-02581-8

Leurer, K. C. (2004). Compressional- and Shear-Wave Velocities and Attenuation in Deep-Sea Sediment during Laboratory Compaction. *J. Acoust. Soc. America* 116 (4), 2023–2030. doi:10.1121/1.1782932

Ma, X., Kirichek, A., Shakeel, A., Heller, K., and Draganov, D. (2021). Laboratory Seismic Measurements for Layer-specific Description of Fluid Mud and for Linking Seismic Velocities to Rheological Properties. *J. Acoust. Soc. America* 149 (6), 3862–3877. Jun 3. doi:10.1121/10.0005039

McAnally, W. H., Friedrichs, C., Hamilton, D., Hayter, E., Shrestha, P., and Rodriguez, H. (2007). Management of Fluid Mud in Estuaries, Bays, and Lakes. I: Present State of Understanding on Character and Behavior. *J. Hydraul. Eng.* 133 (1), 9–22.

McAnally, W. H., Kirby, R., Hodge, S. H., Welp, T. L., Greiser, N., Shrestha, P., et al. (2016). Nautical Depth for US Navigable Waterways: A Review. *J. Waterw. Port Coast. Ocean Eng.* 142 (2), 04015014.

Meissner, R., Rabbel, W., and Theilen, F. (1991). "The Relevance of Shear Waves for Structural Subsurface Investigations," in *Shear Waves in Marine Sediments* (Dordrecht: Springer), 41–49.

Schrottke, K., Becker, M., Bartholomä, A., Flemming, B. W., and Hebbeln, D. (2006). Fluid Mud Dynamics in the Weser Estuary Turbidity Zone Tracked by High-Resolution Side-Scan Sonar and Parametric Sub-bottom Profiler. *Geo-mar Lett.* 26 (3), 185–198. Sep 1. doi:10.1007/s00367-006-0027-1

Shakeel, A., Kirichek, A., and Chassagne, C. (2020). Rheological Analysis of Mud from Port of Hamburg, Germany. *J. Soils Sediments* 20 (6), 2553–2562. doi:10.1007/s11368-019-02448-7

Shapiro, N. M., and Campillo, M. (2004). Emergence of Broadband Rayleigh Waves from Correlations of the Ambient Seismic Noise. *Geophys. Res. Lett.* 31 (7). doi:10.1029/2004gl019491

Snieder, R. (2004). Extracting the Green's Function from the Correlation of Coda Waves: a Derivation Based on Stationary Phase. *Phys. Rev. E Stat. Nonlin Soft Matter Phys.* 69 (4), 046610. doi:10.1103/PhysRevE.69.046610

Wapenaar, K., and Fokkema, J. (2006). Green's Function Representations for Seismic Interferometry. *Geophysics* 71 (4), SI33–SI46. doi:10.1190/1.2213955

Conflict of Interest: The authors declare that the research was conducted in the absence of any commercial or financial relationships that could be construed as a potential conflict of interest.

Publisher's Note: All claims expressed in this article are solely those of the authors and do not necessarily represent those of their affiliated organizations, or those of the publisher, the editors and the reviewers. Any product that may be evaluated in this article, or claim that may be made by its manufacturer, is not guaranteed or endorsed by the publisher.

frontiers in Earth Science

ORIGINAL RESEARCH
published: 14 March 2022
doi: 10.3389/feart.2022.805130

Controls on Sediment Bed Erodibility in a Muddy, Partially-Mixed Tidal Estuary

Cristin L. Wright, Carl T. Friedrichs and Grace M. Massey*

Virginia Institute of Marine Science, William & Mary, Gloucester Point, VA, United States

The objectives of this study are to better understand controls on bed erodibility in muddy estuaries, including the roles of both sediment properties and recent hydrodynamic history. An extensive data set of erodibility measurements, sediment properties, and hydrodynamic information was utilized to create statistical models to predict the erodibility of the sediment bed. This data set includes >160 eroded mass versus applied stress profiles collected over 15 years along the York River estuary, a system characterized by "depth-limited erosion," such that the critical stress for erosion increases rapidly with depth into the bed. For this study, erodibility was quantified in two ways: the mass of sediment eroded at 0.2 Pa (a stress commonly produced by tides in the York), and the normalized shape of the eroded mass profile for stresses between 0 and 0.56 Pa. In models with eroded mass as the response variable, the explanatory variables with the strongest influence were (in descending order) tidal range squared averaged over the previous 8 days (a proxy for recent bottom stress), salinity or past river discharge, sediment organic content, recent water level anomalies, percent sand, percent clay, and bed layering. Results support the roles of 1) recent deposition and bed disturbance increasing erodibility and 2) cohesion/consolidation and erosion/winnowing of fines decreasing erodibility. The most important variable influencing the shape of the eroded mass profile was eroded mass at 0.2 Pa, such that more (vs. less) erodible cases exhibited straighter (vs. more strongly curved) profiles. Overall, hydrodynamic variables were the best predictors of eroded mass at 0.2 Pa, which, in turn, was the best predictor of profile shape. This suggests that calculations of past bed stress and the position of the salt intrusion can serve as useful empirical proxies for muddy bed consolidation state and resulting erodibility of the uppermost seabed in estuarine numerical models. Observed water content averaged over the top 1 cm was a poor predictor of erodibility, likely because typical tidal stresses suspend less than 1 mm of bed sediment. Future field sampling would benefit from higher resolution observations of water content within the bed's top few millimeters.

Keywords: bed erodibility, muddy sediment, bed properties, bed disturbance, estuarine hydrodynamics, multiple linear regression

OPEN ACCESS

Edited by:
Andrew James Manning,
HR Wallingford, United Kingdom

Reviewed by:
Henry Bokuniewicz,
The State University of New York (SUNY), United States
Kyungsik Choi,
Seoul National University, South Korea
Lawrence Sanford,
University of Maryland Center for Environmental Science (UMCES), United States

****Correspondence:***
Carl T. Friedrichs
Carl.Friedrichs@vims.edu

Specialty section:
This article was submitted to Marine Geoscience, a section of the journal Frontiers in Earth Science

Received: *29 October 2021*
Accepted: *04 February 2022*
Published: *14 March 2022*

Citation:
Wright CL, Friedrichs CT and Massey GM (2022) Controls on Sediment Bed Erodibility in a Muddy, Partially-Mixed Tidal Estuary. Front. Earth Sci. 10:805130. doi: 10.3389/feart.2022.805130

INTRODUCTION

High sediment bed erodibility can lead to a number of ecological and societal complications within an estuarine or coastal system. Ecological implications relating to high bed erodibility include bed disturbance influencing benthic community structure (Schaffner et al., 2001) and increased suspended sediment concentrations decreasing photosynthesis (Cloern, 1987; Kruk et al., 2015). Additionally, sorption of harmful contaminants and excess nutrients to fine-particles can cause re-introductions of these pollutants during sediment erosion, which can lead to harmful bioaccumulation (Yujun et al., 2008) or increased nutrient loadings within a system (Moriarty et al., 2021). Aside from ecological complications, societal ramifications of high sediment bed erodibility relate to infilling of shipping channels (Brouwer et al., 2018) and potential burial or exposure of dangerous unexploded ordinance (Cooper and Cooke, 2018).

Sediment bed erodibility describes how susceptible sediment is to being entrained into suspension in response to the bed stress (τ_b) caused by the movement of the water immediately above the bed. The more sediment mass a given stress erodes in a given amount of time, the greater the bed erodibility. A widely applied equation for predicting the rate of fine sediment mass eroded into suspension as a function of bed stress is the Ariathurai-Partheniades equation (e.g., Mehta, 2014):

$$E = M(z)(\tau_b - \tau_c(z)) \quad (1)$$

where E is the sediment mass erosion rate, z is depth into the bed, τ_c is the critical stress for erosion of the sediment, and M is the empirical erosion rate parameter which linearly relates the excess shear stress (τ_b–τ_c) to the observed erosion rate, E. Assuming that **Eq. 1** holds, then observations of E as a function of τ_b can be used to determine best-fit values for τ_c and M, which then quantifies the sediment's erodibility.

When applying **Eq. 1** to many natural estuarine environments, it is helpful to recognize the endmember case of "depth-limited" erodibility that is characterized by values of τ_c that increase rapidly with depth into the bed (Sanford and Maa, 2001; Rinehimer et al., 2008). In that case, if a continuous, constant bed stress (τ_b) is applied that is greater than the surface value of τ_c, the total amount of sediment eventually eroded in a given "long" period of time depends only on (and is limited by) the depth into the bed at which $\tau_c = \tau_b$. The value of M does not matter. The "long" period of time needed for this adjustment to $\tau_c \approx \tau_b$ in muddy tidal estuaries with moderate sediment concentrations (10–100 s of mg/L) is commonly as little as 15 min, which is effectively instantaneous relative to the timescale of a tidal cycle (Sanford and Maa, 2001). This means that in such systems, one can quantify and, ultimately, predict the erodibility of the sediment bed simply by quantifying and modeling the τ_c profile, without needing to model the behavior of M.

The magnitude of erodibility can be influenced by physical, geochemical, and biological sediment properties and processes (Grabowski et al., 2011). Sediment bulk density (or conversely, sediment water content) is often found to be a prominent physical property influencing erodibility of mud (e.g., Jepsen et al., 1997; Roberts et al., 1998; Mehta, 2014). Grain size and minerology can also affect sediment erodibility. For sand, a decrease in grain size increases erodibility. But for muds, a further decrease in grain size below medium silt (~20 microns) tends to decrease erodibility (Roberts et al., 1998; Grabowski et al., 2011; Mehta, 2014). However, erodibility trends for mixed grain sediment can be more complex (Barry et al., 2006; Jacobs et al., 2011; Wu et al., 2018). With regards to mud composition, muds rich in more cohesive clays, such as smectite, are generally less erodible than those rich in less cohesive clays, such as kaolinite (Mehta, 2014). Higher organic content of seabed mud is commonly associated with biofilms that stabilize the bed and decrease erodibility, especially on intertidal flats (e.g., Andersen, 2001; Lucas et al., 2003; Zhu et al., 2019). Alternatively, a positive relationship between organic content and erodibility may indicate the presence of freshly deposited flocs rather than older, more consolidated muds (Dickhudt et al., 2009; Kraatz, 2013). The relationship between sediment erodibility and bioturbation has been reported to both increase and decrease sediment stability, depending on species and grain size present (Li et al., 2017; Cozzoli et al., 2019) and the burrowing and feeding style of the organisms (Luckenbach, 1986; Grabowski et al., 2011). For example, compaction of loose muddy flocs into denser, resilient pellets by suspension-feeding polychaetes increases the settling velocity of mud aggregates while decreasing their cohesion, which could increase or decrease their ease of resuspension (Haven and Morales-Alamo, 1968; Kraatz, 2013).

Although sediment properties and biological influences are locally important in determining erodibility, it is hydrodynamic forces that ultimately create bottom stresses and circulation patterns that determine the patterns of recent erosion and deposition that then influence subsequent erodibility (Sanford, 2008; Brouwer et al., 2018). Increasing or decreasing tidal range over the past several days has been shown to influence bed erodibility (Kraatz, 2013; Huang et al., 2020), presumably due to its correlation with recent tidal bed stress and associated bed disturbance. Patterns of erodibility within a partially-mixed estuary can also be related to location within the estuary and position along the salinity gradient (Dickhudt et al., 2009; Burchard et al., 2018). In stratified estuaries, higher (or lower) river discharge changes the salinity distribution and locations of sediment transport convergence, pushing easily suspended pools of mud down (or up) the system. Analogous along-channel migrations of highly erodible deposits are seen in well-mixed estuaries in response to temporally-varying competitions between tidal asymmetry and river discharge (Friedrichs et al., 1998; Brouwer et al., 2018).

In this study, we build upon previous findings regarding controls on estuarine sediment bed erodibility by empirically analyzing an extensive set of erodibility data collected over the last 15 years in the York River estuary, VA, United States. Our goal is to investigate the relative importance of various sediment properties and environmental forcings in predicting bed erodibility in a representative muddy, moderately turbid,

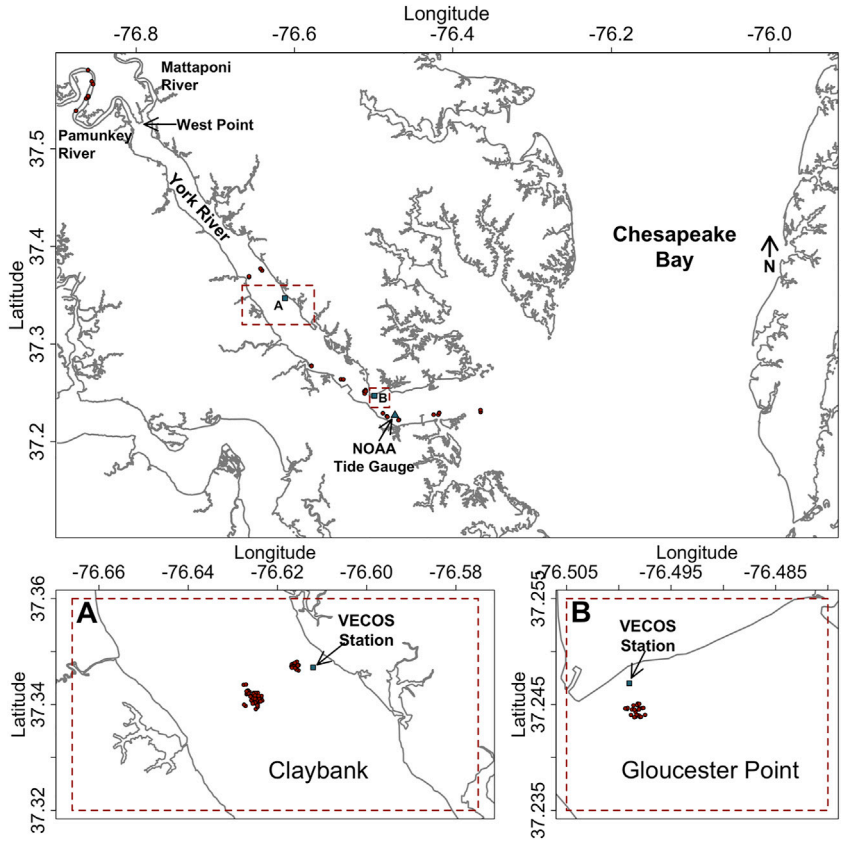

FIGURE 1 | Map of the field setting. Red circles are coring locations. **(A)** and **(B)** indicate Claybank and Gloucester Point coring areas.

partially-mixed, tidal estuary. In the following section, the estuarine setting of the study is reviewed, followed by a presentation of data collection and analysis methods, including the multiple linear regression approach used to rank the relative importance of the explanatory variables. Next, results are presented for linear models that predict 1) the total mass erosion at a characteristic bed stress (0.2 Pa) reached during most tidal cycles and 2) the normalized shape of the eroded mass profile as a function of applied bed stress from 0 to 0.56 Pa. Finally, the last two sections provide a discussion and summary of the study's most important findings, their implications, and directions for future work.

ESTUARINE SETTING

The York River estuary (**Figure 1**) is an opportune location for examining years of available observations of erodibility to statistically investigate the relative importance of multiple factors that may influence estuarine bed erodibility. Numerous individual studies involving erodibility measurements have focused on this estuary (Friedrichs et al., 2008; Cartwright et al., 2009; Dickhudt et al., 2009; Fall, 2012; Kraatz, 2013; Bilici et al., 2019; Massey et al., 2019), taking advantage of its relatively wide range of environmental conditions, as well as its convenient proximity to the Virginia Institute of Marine Science. Along with this, a variety of research has been conducted in the York aligning with the motivations highlighted in the introduction, such as benthic organism communities and sediment interactions (Schaffner et al., 2001; Hinchey, 2002; Gillett and Schaffner, 2009) and sediment effects on water clarity and light limitation of primary production (Moore et al., 1997; Sin et al., 1999; Reay, 2009; Fall, 2020).

The York River, which is a tidally-dominated, partially-mixed estuary, is one of the major tidal tributaries of the Chesapeake Bay and is formed at its head by two additional tidal tributaries, the Pamunkey and the somewhat smaller Mattaponi (**Figure 1**). Although its tidal range (0.7 m at the York's mouth, increasing to 1 m in the upper Pamunkey) defines the system as microtidal, the tidal current along the estuary can reach 1 m/s at spring tide (Schaffner et al., 2001; Friedrichs, 2009). The impact of wind waves is generally limited to quite shallow water (<~2-m depth), given that the mean wave period is only 1.9 s, and significant wave heights exceed 0.3 m only 1% of the time (Vandever, 2007). Nonetheless, winds are still important to mean currents in deeper water, with the typical pattern of estuarine circulation enhanced or reduced by down- or up-estuary winds, respectively (Scully et al., 2005). The main channel that reaches from the mouth to West Point ranges in depth from 6 to 20 m, deepening towards the mouth, and salinity stratification increases seaward in

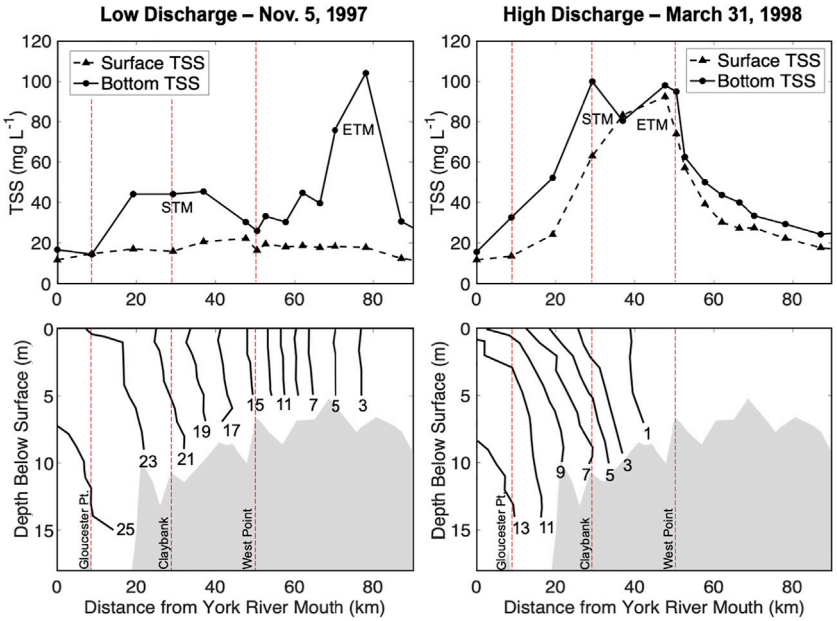

FIGURE 2 | Total suspended solids (TSS) collected 1-m below the surface and 1-m above the bottom (top panels) and salinity contours (bottom panels) along the York River estuary during low river discharge (left panels) and high river discharge (right panels) Adapted by permission from Springer Nature, Estuaries (Lin and Kuo, 2001), copyright 2001.

response to the depth increase. There is also a 5-m deep secondary channel that runs from Gloucester Point to Claybank that is separated from the main channel by a shallow channel-parallel shoal (Schaffner et al., 2001; Friedrichs, 2009). The salt intrusion limit for the York River—Pamunkey River system lies between 40 and 90 km upstream of the York River mouth and moves up and downriver with fluctuations in river discharge.

The areas of highest erodibility along the York tend to mirror the region of the estuary containing its main estuarine turbidity maximum (ETM) and secondary turbidity maximum (STM) (Dickhudt et al., 2009). Thus, understanding large-scale controls on bed erodibility in the York requires understanding the dynamics of the STM and ETM. The main ETM in the York (**Figure 2**) follows the migration of the salt intrusion limit and is formed largely by a decrease in the strength of near-bed estuarine circulation with distance upstream, which traps easy to resuspend sediment in the upper estuary (Lin and Kuo, 2001; Friedrichs, 2009). In addition to the ETM, a seasonal secondary turbidity maximum (STM) is often observed in the York River, with the downstream extent falling in the Claybank region, 30 km from the mouth (**Figure 2**) (Lin and Kuo, 2001). The STM tends to be more intense during times of high river discharge and low salinity (Lin and Kuo, 2001; Dickhudt et al., 2009). The STM is formed by similar mechanisms as the ETM, but is located downstream of the salt intrusion limit, at a transition zone between the shallower, more well-mixed water column upriver, and the deeper, more stratified water column downriver (Lin and Kuo, 2001). The STM and ETM in the York are more intense at spring tide than neap tide, but their along-channel locations do not notably change at spring versus neap (Lin and Kuo, 2001).

Grain-size distributions of the sediment bed of the York are largely dependent on location and water depth. The upper and mid-river locations have high percentages of mud (>80% mud) in the tidal channels with sediments coarsening (<40% mud) on the narrow shoals and along the shoal between the primary and secondary channels (40–80% mud) (Nichols et al., 1991). In the lower river, the main channel remains muddy (>80% mud), but with broad, sandy shoals with coarser sediment (<40% mud) (Nichols et al., 1991).

DATA AND METHODS

Field Data Collection and Laboratory Analysis

Erodibility data, along with a suite of sediment and water column parameters, were collected from cores over 160 times in the York River—Pamunkey River system (**Figure 1**) between 2005 and 2019. A GOMEX box core (surface area 625 cm^2) was collected at each location, and then multiple 10-cm diameter sub-cores were collected by hand from the box core. These sub-cores were used for analysis of erodibility and for determining disaggregated sediment grain size, resilient pellet content, organic content, and water content. For this project, parameter values from only the top centimeter were used. Disaggregated fractions of sand (>63 μm), silt (63 to 4 μm), and clay (<4 μm) by mass were determined by sonification followed by a combination of wet

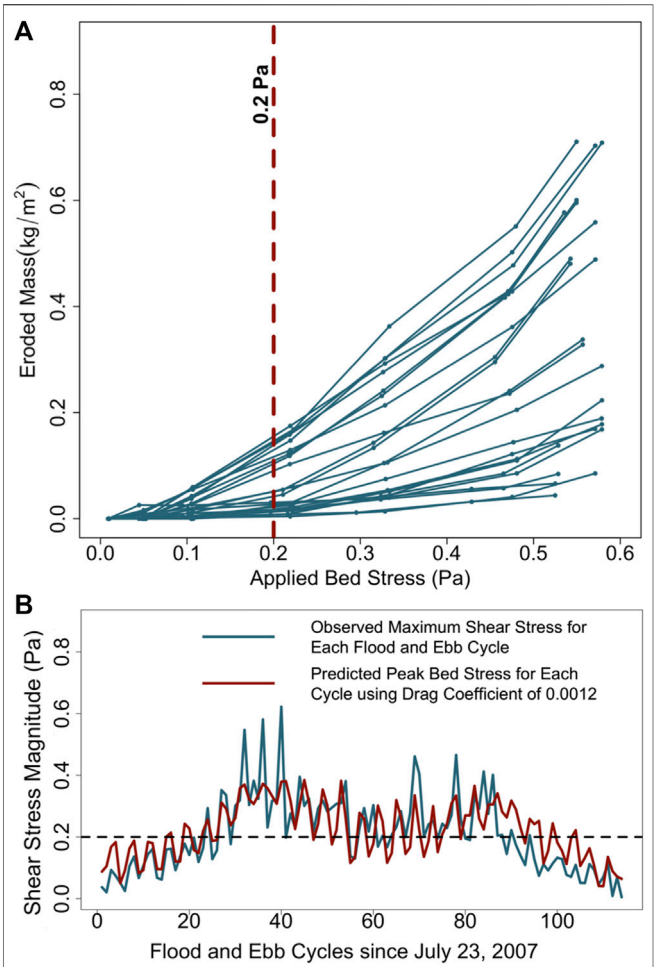

FIGURE 3 | (A) Examples of interpolation at 0.2 Pa of erosion curves from the Gust microcosm experiments. **(B)** Bottom shear stress observed in the Claybank region of the York River (Fall, 2012) along with bed stress estimated from $\tau_b = C_D U^2$, where U is cross-sectionally averaged tidal velocity amplitude (see Section *Quantifying the Erodibility Profile*).

sieving and pipette analysis. Starting in 2010, resilient fecal pellet abundance was determined by wet sieving untreated sediment following the methods of Kraatz (2013). This involved first using a 63-μm sieve to isolate sand plus resilient sand-sized mud pellets and then subtracting out the previously calculated disaggregated sand component. More details regarding steps in the field data collection and laboratory analysis are provided in Wright (2021).

Sediment erodibility at each location was evaluated using a Gust microcosm (e.g., Dickhudt et al., 2009). During erodibility analysis, a sediment core is topped with a specially designed cap that is equipped with a rotating disk. The disk spins at varying speeds to create known stresses on the sediment bed while site water is pumped through the core. The water pumped out of the core is analyzed for turbidity and then filtered for suspended solids, and the calibrated turbidity time series is used to determine the mass of sediment eroded at each applied stress (**Figure 3A**). After a 30-min initial interval at 0.01 Pa, the stress is increased stepwise from 0.02 to 0.56 Pa, each lasting 20 min. These stresses are within the range of natural shear stresses observed in the York River in response to typical tidal and fluvial processes (**Figure 3B**).

Water content of each sediment sample by mass was determined by calculating the difference in mass from wet weight and dry weight after being thoroughly dried in an oven at 103–105°C. Due to most samples having high contents of mud, the percent water of the mud portion [100 × water mass/(water + dry mud mass)] was used instead of percent water of the total sample, similar to analysis performed by Dickhudt et al. (2011). The logic behind this approach is that at high mud content (when interlocking sand grains are not supporting the weight of the sediment), the most relevant role of water is to indicate the compaction of the mud matrix, not the compaction of the sand. The samples used for percent water were then muffled at 550°C to determine percent organic based on loss on ignition.

In the majority of cases, a 11.5 cm by 2.5 cm rectangular sub-core was also collected for X-radiography, and the resulting X-ray images were manually sorted into two categories. One category included samples that had a clearly mottled fabric (**Figure 4A**), and the other category included those that were laminated (**Figure 4B**) or that had a distinct low-density deposit layer at the surface (**Figure 4C**). Because 1) there were individually far fewer cases that were either laminated or that had a detectable surface layer relative to those that displayed mottling up to the surface, and 2) the hypothesized meaning of lamination or layering was similar (i.e., recent net deposition without time for extensive bioturbation), the laminated and surface layer categories were combined into one "layered" category. "Layered" vs. "Not layered" (i.e., mottled) was then included as an explanatory variable in model runs.

It is important to note that on each sampling cruise, a Gust erodibility sub-core was typically collected from each of two consecutive box cores, and the two sub-cores were then each analyzed by the Gust microcosm. The two box cores were usually collected on the order of a few to 10 s of meters apart, as dictated by the boat's movement around its anchor point, typically close to slack tide. Two sediment property sub-cores were taken (one from each box core), and sediment from corresponding depths from both cores were combined for an average for the location. Because of this, many of the Gust experiment data have independent erodibility measurements but identical grain size, percent organic, percent water, and pellet content for a single sampling station. Limitations of sampling approaches in this study with regards to the interpretation of statistical analyses are further addressed in the discussion section.

Quantifying the Erodibility Profile

In the depth-limited erodibility extreme, which has been found to apply very well to the muddy bed of the York River estuary (Rinehimer et al., 2008; Cartwright et al., 2009; Dickhudt et al., 2011; Fall, 2012), the sediment's critical stress profile (τ_c) alone is sufficient to fully quantify its erodibility. As surficial sediment is removed during active bed erosion in estuaries like the York, the magnitude of τ_c at the newly exposed, underlying bed surface typically approaches the value of the bed stress (τ_b) imposed by the overlying flow within ~15 min (Sanford and Maa, 2001). This

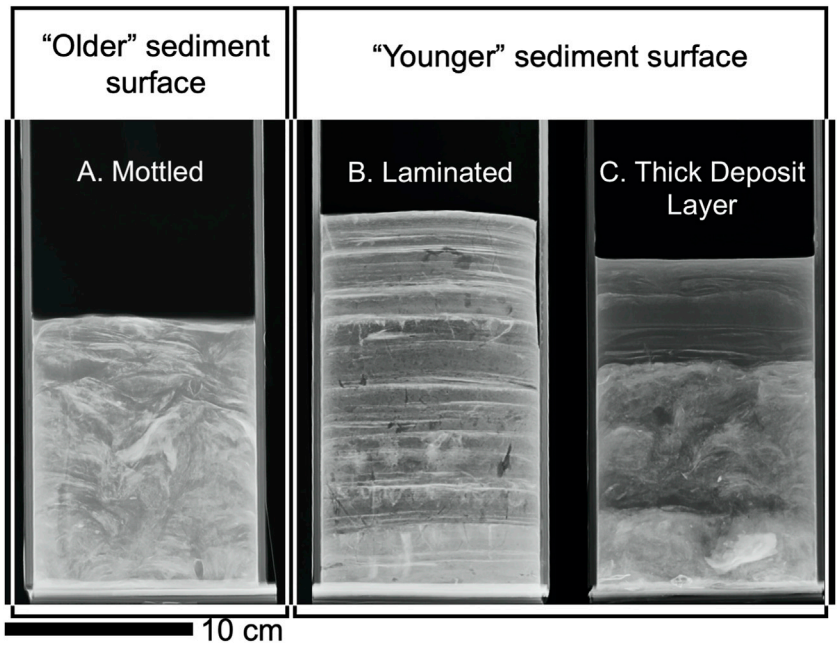

FIGURE 4 | X-ray images representing **(A)** mottled, **(B)** laminated, and **(C)** thick deposit layer fabrics. These "negative" images are darker where wet sediment density is lower. The laminated and deposit layer classes were combined and likely represent younger near-surface sediments, whereas the mottled class likely represents older near-surface sediments.

means that at the end of each of the 20–30 min periods of constant stress utilized by the Gust microcosm on cores from the York as τ_b was increased incrementally from 0.01 to 0.56 Pa, one could assume that $\tau_c \approx \tau_b$. The corresponding mass of sediment eroded at each of these levels of $\tau_c \approx \tau_b$ was known from integrating the flow rate through microcosm times the recorded time-series of suspended sediment concentration. Thus, the vertical profile of τ_c as a function of eroded mass was successfully quantified.

The next step was to condense the information provided by the τ_c profile at each site (i.e., seven eroded masses at seven corresponding values of τ_b) into just two values, one representing the overall magnitude of erodibility, and the other representing the shape of the τ_c profile. Each of these values was used as a response variable in subsequent statistical models. The first response variable was chosen to be the mass of sediment that had been eroded at a single representative bed stress common to all of the Gust microcosm experiments (and also characteristic to typical tidal flows in the York). The second response variable was obtained by using the dominant component of a principal component analysis to describe the erosion profile shape.

As noted above, the first erodibility response variable was the mass of sediment that had been eroded at a specific applied bed stress. In this study, the cumulative eroded mass at 0.2 Pa was interpolated and used as the characteristic eroded mass value for each Gust erosion experiment (**Figure 3A**). Based on observations of τ_b from acoustic Doppler velocimeters (ADVs), previous investigators have identified τ_b = 0.2 Pa as a representative tidal stress for the York River estuary (Friedrichs et al., 2008; Fall, 2012; Kraatz, 2013). For example, Fall (2012) found that during the summer of 2007 (**Figure 3B**), τ_b during that time often reached ~0.2 Pa during peak flood and ebb flows, with a few maximum stresses reaching ~0.5–0.6 Pa. Similar magnitudes for τ_b can be found for each tide based on the analytical solution for the amplitude of cross-sectionally averaged tidal velocity (U) in a long, straight channel with weak friction (Friedrichs, 2010):

$$U = (R_T/2)(g/\langle h \rangle)^{0.5} \quad (2)$$

where R_T is the observed range between each low and high tide, g = 9.8 m/s^2, $\langle h \rangle$ is spatially- averaged water depth, and $\tau_b = C_D U^2$. For the York, $\langle h \rangle \approx 6$ m (Nichols et al., 1991; Friedrichs, 2009), and $C_D \approx$ 0.0012 based on the ADV measurements of Fall (2012) (**Figure 3B**).

In channelized tidal estuaries such as the York-Pamunkey system, the amplitude of tidal shear stress associated with a given tidal range is often relatively uniform for long distances along the main tidal channels. For example, observations by Cartwright et al. (2009) found a similar range of τ_b at both Gloucester Point and Claybank during several months of ADV deployments, and 3-D modeling by Fall et al. (2014) calculated relatively similar τ_b in channels along the York in both downstream and upstream locations. Thus, tidal range squared at a given time is expected to be approximately proportional to the amplitude of τ_b within channels along much of the system. Morphodynamics favors relatively uniform peak tidal velocity and τ_b along channelized tidal estuaries in general, and this pattern has been noted along additional systems such as the Delaware, Gironde, Hudson, James, Thames, and many others (Friedrichs, 1995; Lanzoni and Seminara, 2002; Olabarrita et al., 2018).

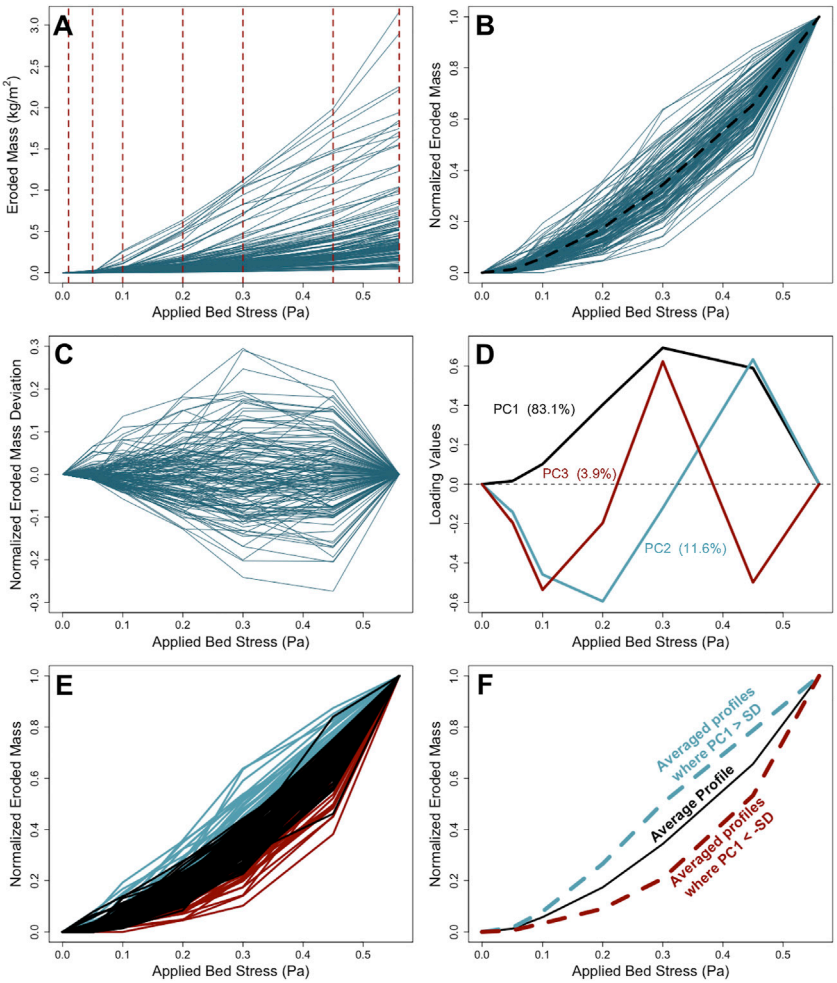

FIGURE 5 | Erosion profile shape normalization process. **(A)** Interpolated Gust output data with interpolation points highlighted by dashed red lines. Each profile in **(A)** was divided by its eroded mass value at 0.56 Pa, resulting in normalized erosion shapes bounded between 0 and 1 in panel **(B)**. The average profile in **(B)** (dashed black line) was subtracted from all normalized profiles to center the data around zero in **(C)**. **(D)** Loading values for PC1, PC2, and PC3 determined from **(C)** for the All Sites data subset. **(E)** All Sites profile shapes with PC1 scores within ± 1 standard deviation (SD) of zero (black), PC1 > 1 SD (blue), and PC1 < -1 SD (red). **(F)** Average profile shapes for all normalized profiles in **(E)**, for those with PC1 > 1 SD, and for those with PC1 < -1 SD.

Erodibility was also quantified by the shape of the eroded mass profile. Profiles for each Gust experiment were compiled (**Figure 5**) and analyzed using principal component analysis (PCA) to determine the shape of the most common deviation for the mean profile. Eroded masses for τ_b = 0.01, 0.05, 0.1, 0.2, 0.3, 0.45, and 0.56 Pa were interpolated for each profile produced by the Gust experiments (**Figure 5A**). When profiles did not reach τ_b = 0.56 Pa, but the final experimental stress point exceeded 0.50 Pa, the last data point was linearly extrapolated. All Gust erosion profiles were divided by the mass eroded at τ_b = 0.56 Pa, resulting in a normalized erosion profile shape constrained between 0 and 1 (**Figure 5B**). The normalized values were then averaged across all the profiles, and the average normalized profile was subtracted from the individual normalized profiles to center the data around a global mean of zero (**Figure 5C**). Finally, the deviations from the average normalized profile were used as input to the PCA. Similar PCA methods for describing profile shapes have been used for the topography of tidal flats and are described in Bearman et al. (2010). Note that for this analysis, some Gust experiments did not have applied τ_b exceeding 0.45 Pa. These profiles were removed (see Wright et al., 2021 for a list of the removed profiles), which created a slightly smaller data subset for this response variable relative to the set for eroded mass at τ_b = 0.2 Pa. **Figures 5D–F** display the output of the PCA analysis, which is described in the results section.

Additional Environmental Data Compilation

Observed and predicted tidal ranges were downloaded from the National Oceanic and Atmospheric Administration (NOAA, 2021) for the tide gauge located at the Yorktown Coast Guard pier (see **Figure 1**) to provide a variable proportional to the amplitude of the tidal current. Tidal ranges are defined as the absolute difference between each high tide and its preceding low

TABLE 1 | List of data subset names and sample sizes for the Eroded Mass Model Set and the Erosion Shape Model Set.

Subset name	*n* for eroded Mass model set	*n* for erosion shape model set
All Sites	165	146
Estuarine Sites	158	139
Claybank & Gloucester Point	136	119
Claybank & Gloucester Point w/X-rays	104	85
Claybank	110	93
Claybank w/X-rays	82	63

TABLE 2 | Data and variance statistics for variables prior to log transformation or standardization, but after low-pass averaging recent tidal range squared, water level anomaly, and river discharge.

Variable name	Units	Mean	Standard Dev.	Min	Max
Eroded Mass @ 0.2 Pa	kg/m^2	0.089	0.105	0.004	0.559
Tide Range Squared	m^2	0.497	0.115	0.273	0.751
Salinity	PSU	16.0	4.4	0.1	23.6
% Organic by Dry Mass	%	5.8	3.2	0.5	11.7
Water Level Anomaly	m	0.050	0.020	0.020	0.130
River Discharge	m^3/s	50.0	27.0	5.9	108.4
% Sand by Dry Mass	%	18.8	21.0	0.8	94.5
% Clay of Dry Mud Mass	%	58.3	10.2	29.2	90.0
Distance Upriver	km	27.0	11.6	2.1	71.7
% Water of Mud by Mass	%	75.5	4.5	62.3	92.2

tide and vice versa; so, each day includes an average of 3.9 tidal ranges. The observed tidal ranges were then squared to transform that variable into one proportional to the amplitude of the tidal bed stress. Time series of tidal range squared prior to each box core collection were used to produce running averages of progressively increasing length, preceding the timing of each associated erodibility measurement. The preceding running average length that produced the highest correlation between past tidal range squared and eroded mass at 0.2 Pa was then used for calculating the tidal range squared explanatory variable. In addition to observed tidal ranges, the absolute difference between NOAA predicted and observed tidal ranges was recorded, which here is termed the water level anomaly. This variable was used to determine if meteorological events that drive relatively rapid changes in set-up or set-down of water level along the estuary influence sediment erodibility. The water level anomaly was likewise put through a series of preceding running averages of increasing length, and the case with the best correlation with eroded mass at 0.2 Pa was retained as the water level anomaly explanatory variable.

River discharge and salinity were also compiled for use as explanatory variables. Changing discharge and salinity are expected to serve as proxies for the movement of temporary, highly erodibility mud deposits which migrate, up- and down-river in concert with the ETM and STM. Daily river discharge data were downloaded from the United States Geological Survey (USGS, 2021) and summed for the two main tributaries of the York River: the Pamunkey and Mattaponi. An approach similar the treatment to tidal range and water level anomaly was used to create an optimal running average of river discharge prior to sampling of eroded mass. Salinity data for erodibility samples collected at Claybank and Gloucester Point were downloaded from the Virginia Estuarine and Coastal Observing System (VECOS, 2021) stations (see **Figure 1**) that are also located near Claybank and Gloucester Point. Because short-term salinity variation was high due to tidal advection, the previous 25 h before sampling (the approximate length of two M_2 tidal constituent cycles) was averaged for each set of VECOS salinity readings and used for data analysis. For sample sites not located in close proximity to the VECOS buoys (only 26 out of ≥160 erodibility measurements), depth-averaged salinity collected at the coring site at the time of sampling was used as a best available estimate of the recent characteristic salinity.

Data Subsets

Different data subsets with increasingly more common attributes (and smaller sample size) were created and were explored with multiple statistical methods (**Table 1**). The entire data set included 167 erodibility profiles collected at various locations (see **Figure 1**) along the York River system (which here includes the lower Pamunkey). The means, standard deviations, and ranges for the entire data set are provided in **Table 2**. Two of the 167 data points were found to be extreme outliers in all models over the course of model exploration and were removed from further model-fitting. [A complete listing of all data points and their individual properties are provided in Wright et al. (2021)]. The first data subset analyzed statistically included all the remaining observations (n = 165). Most samples were located below the ETM except those in the Pamunkey River. The next data subset removed the Pamunkey River samples and only contained the fully "estuarine" sites (i.e., sites located seaward of the transition to fresh water) (n = 158), the logic being that distinct physical processes (such as density-driven estuarine circulation) occur in brackish conditions.

The two sampling locations that were the most consistently visited over the 15-year sampling period were Claybank and Gloucester Point. Thus, these two locations were combined within one subset (n = 136). Previous studies (Dickhudt et al., 2009, 2011; Fall, 2012) focused on these two areas because of their contrasting degrees of physical bed disturbance and deposition frequency as revealed in X-rays. Due to a large percentage of samples being within the Claybank region alone, these samples were also analyzed separately (n = 110). The logic behind the focus on Claybank and Gloucester Point and then on Claybank alone is the larger number of quasi-replicates available to strengthen detection of meaningful statistical trends relative to

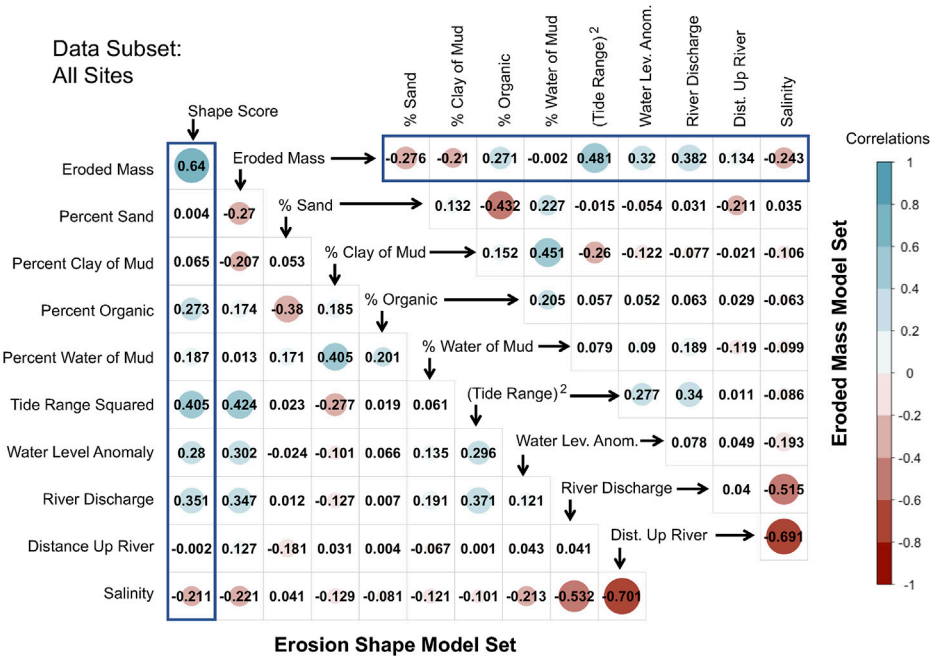

FIGURE 6 | Pearson correlation plot results for the All Sites data subset. Upper and lower diagonal plots show correlation values for the Eroded Mass and Erosion Shape model sets, respectively. Correlations with the response variables are boxed in blue.

other inherent environmental "noise." Most, but not all, of the Claybank and Gloucester Point samples include X-ray classifications. Because near surface layering could be an important driver of erodibility, both the Claybank and Gloucester Point subset and the Claybank subset were divided further, with each subset containing only samples that included an X-ray classification (n = 104 and n = 82, respectively).

Many samples from 2010 to 2019 also included data for fecal pellet abundance. Kraatz (2013) hypothesized that pellet abundance could alter erodibility, and therefore various fecal pellet subsets were initially included in the analysis. However, none of the statistical models considered produced a linear dependence of erodibility on fecal abundance in a manner that was consistent with the simultaneous linear effects of other variables. Thus, fecal pellets were dropped from further modelfitting. Possible non-linear associations between fecal pellets and erodibility are revisited in Section *Variables That Could Also Have High Impact but Were Not Included*.

Statistical Approaches

Data set familiarization techniques included histograms and scatter plot matrices. Histograms of eroded mass at 0.2 Pa appeared log normal, and eroded mass at 0.2 Pa was log-transformed for subsequent analysis. River discharge was also log-transformed because it is common practice in the hydrological literature (e.g., Iddrisu et al., 2017). All variables were then linearly standardized by subtracting their means and dividing by their standard deviations. To allow standardization, "mottled" and "layered" X-rays were first assigned values of 0 and 1, respectively, before being standardized. Scatter plot matrices were then used to examine the size and sign of correlations between the explanatory and response variables and to assess co-linearity between the explanatory variables themselves (**Figure 6**). Any two explanatory parameters with high correlation values were monitored if included in the same model, and variance inflation factor (vif) values were evaluated for each model as a test for severe collinearity. If strong collinearity existed (common threshold of vif values >5) (James et al., 2013), each explanatory variable was tested separately in similar models and only one of the pair was retained.

Two different model sets (**Table 3**) were used to evaluate the two erodibility response variables identified for this study: 1) eroded mass at τ_b = 0.2 Pa and 2) the shape of the erosion vs. τ_b profile as determined by its principal shape component. The goal of the first grouping of explanatory variables (the "Eroded Mass Model Set") was to determine the relative importance of various sediment properties and hydrodynamic conditions in determining erodibility at a representative, commonly occurring bed stress within the York River. The goal of the second variable grouping (the "Erosion Shape Model Set") was to determine which sediment and hydrodynamic factors may be important in determining the overall shape of the τ_c versus eroded mass profile. Explanatory variables that were considered for this second model set were identical to those in the previous model set, but also include eroded mass at 0.2 Pa.

Multiple linear regressions were run for each data subset within each model set (see **Table 3** for model framework). The general equation for multiple linear regression is:

$$y = \beta_0 + \beta_1 X_1 + \beta_2 X_2 + \cdots + \beta_q X_q + \varepsilon \quad (3)$$

TABLE 3 | Model set and data subset framework for multiple linear regression analysis.

Model set Name	Model set goal	Response variable	Explanatory variables	Data subsets applied
Eroded Mass Model Set	Evaluate eroded mass at a common bottom shear stress	Eroded Mass @ 0.2 Pa	• Percent Sand • Percent Clay of Mud • Percent Organic • Tidal Range Squared • Water Level Anomaly • River Discharge OR Salinity • X-Ray Layering (where applicable)	• All Sites • Estuarine Sites • Claybank & Gloucester Point • Claybank & Gloucester Point with X-rays • Claybank • Claybank with X-rays
Erosion Shape Model Set	Evaluate how sediment may erode at higher and lower shear stresses	Shape Score	• Eroded Mass @ 0.2 Pa • Percent Sand • Percent Clay of Mud • Percent Organic • Tidal Range Squared • Water Level Anomaly • River Discharge OR Salinity • X-Ray Layering (where applicable)	• All Sites • Estuarine Sites • Claybank & Gloucester Point • Claybank & Gloucester Point with X-rays • Claybank • Claybank with X-rays

where y is the predicted response variable, β_0 is the model intercept, X_1 though X_q represent individual explanatory variables, and β_1 through β_q represent the corresponding best-fit regression coefficients. Lastly, ϵ is the model residual, i.e., the component of y not reproduced by the other terms on the right-hand-side. Due to the data being standardized prior to model formulation, the absolute value of the β coefficients can be ranked to show which explanatory variables resulted in the largest change in the response variable. For instance, for a β coefficient of 0.3, for every increase of one standard deviation of the explanatory variable, the response variable will increase by 0.3 standard deviations.

All possible combinations of the explanatory variables for each data subset were used in assessing **Eq. 3**, and the relative likelihood of any given model being the best among the available choices for that data subset was assessed using the Corrected Akaike Information Criterion (AICc). A lower AICc value indicates that a model is more likely to be best, and a model's ΔAICc value is defined as its own AICc minus that of the model with the lowest AICc value in its model subset. In this study, all models with a ΔAICc value ≤2.0 units are considered comparable models with useful information regarding trends (Burnham and Anderson, 2004). Because ΔAICc values are relative within a given model subset, they cannot be used to compare the explanation of variance of response variables across model subsets. To remedy this, adjusted R^2 values were included to describe how much of the data variation was explained by the combination of parameters in each model across sub-model categories.

RESULTS

Time-Lags for Tidal Range, Water Level Anomaly, and Discharge

Application of running means indicated that the average of the past 33 tidal range squared observations (8.5 days—i.e., centered around conditions 4.3 days prior) had the highest correlation with eroded mass at τ_b = 0.2 Pa. The best correlation between the water level anomaly and eroded mass was found to be over the past 27 cycles (7.0 days). For river discharge, the running average with the highest correlation with eroded mass at 0.2 Pa was over the previous 170 days (i.e., centered around conditions 2.8 months prior).

Principal Component Analysis for Gust Erosion Shape Profiles

PCA for Gust profiles was completed to reduce the shape profile containing seven eroded mass values and seven stress values, to one shape score that could be used as a response variable in multiple linear regression. Principal component one (PC1) (i.e., the shape score) explained approximately 83% of the variation of shape within all data subsets (**Figure 5D**). Positive and negative values of PC1 made the normalized eroded mass profile less and more concave, respectively, than the average profile shape (**Figures 5E,F**). Negative shape scores corresponded to a geometrically increasing shape profile, such that each increase in stress resulted in a proportionately greater increase in eroded mass. In contrast, positive shape scores tended to indicate a more linear profile or, when most positive, a proportionally smaller increase in eroded mass with each increase in stress. PC1 was the only component whose scores were used as a response variable in the models reported here because PC1 explained ~83% of the variability in erosion profile shape in all data subsets. PC2 described only ~11–13% of variation in the erosion profile shapes, and PC3 accounted for just ~3–4% (**Figure 5D**).

Initial Assessment of Data *via* Correlations

Initial assessment of relationships among variables was facilitated by correlation plot results (**Figure 6**) applied to each of the six

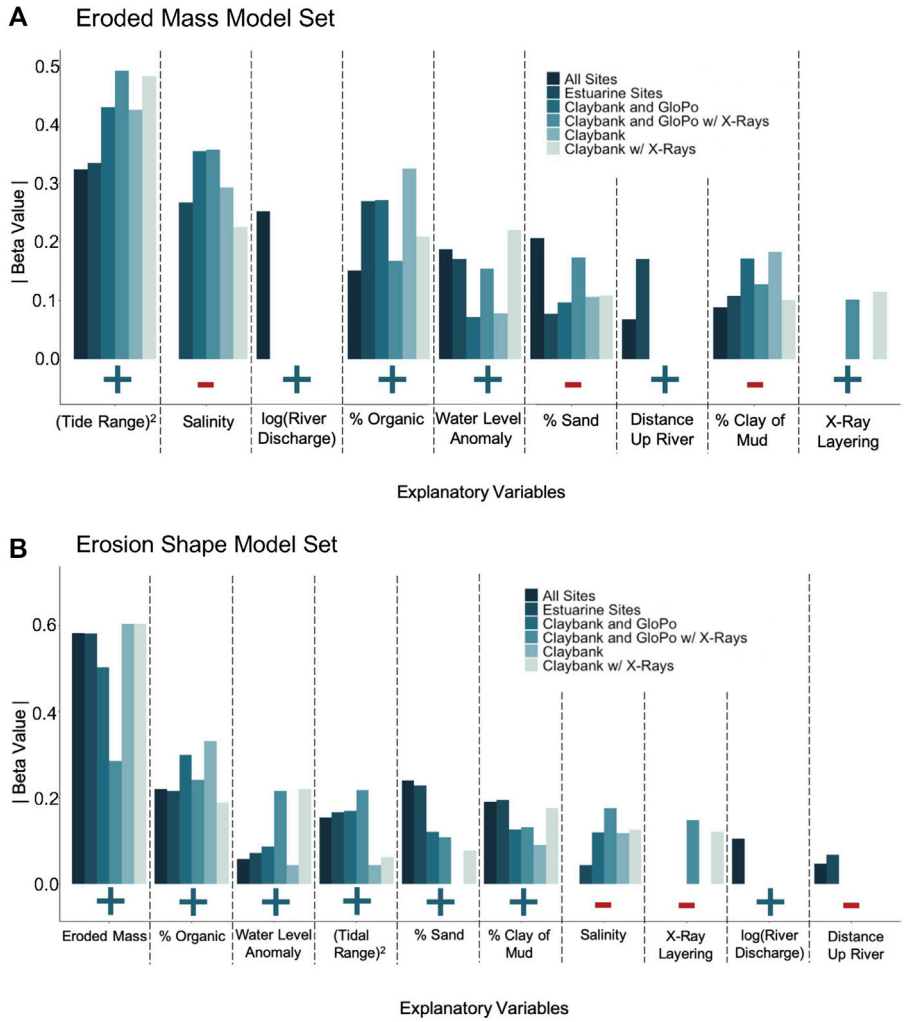

FIGURE 7 | Bar graphs showing average absolute β values for each explanatory variable for each data subset (corresponding colors) that were included in candidate models. Signs below bar graphs indicate whether the β value was positive (blue "+" = direct relationship) or negative (red "−" = inverse relationship). Absent lines indicate parameters that were not considered in the model or parameters that were not present in any of the candidate models.

data subsets listed in **Table 1** and **Table 3**. (The X-ray layering parameter is not part of the All Sites data set in **Figure 6** because X-rays were not collected at every site.) A complete set of correlation plot results for all six data subsets are included in Wright et al. (2021).

Despite its dominant role in the erodibility literature (e.g., Mehta, 2014), percent water of mud was consistently found to be poorly or nonsensically correlated with erodibility, and percent water was ultimately dropped from all multiple regression models for all six data subsets. For example, for the All Sites data subset, percent water of mud had the poorest correlation with eroded mass at 0.2 Pa of any variable, with $r = -0.002$ in the Eroded Mass Model Set (**Figure 6**). Across the other five data sets, the average magnitude of the correlation between percent water of mud and eroded mass was likewise quite poor, with a mean $|r|$ of 0.111 (Wright et al., 2021). Furthermore, when included in multiple regressions with the other variables, the few models for eroded mass with $\Delta AICc < 2.0$ that retained water content produced a negative β value for percent water (Wright, 2021). This is physically nonsensical given that there is a rich and long-established literature (see Mehta, 2014 and references within) demonstrating that erodibility for fine sediment should be negatively correlated with sediment bulk density (and thus positively correlated with percent water). Possible explanations for the unexpected result for the role of percent water are discussed in Section *Limitations Associated With Sampling Approach and Resolution of Bed Properties*.

Collinearity among explanatory variables was also assessed using correlation plot results. Among the All Sites explanatory variables that were further considered, salinity had the highest correlations with other variables: namely, with distance upriver (at $r = -0.701$) and with river discharge (at $r = -0.532$) within the Erosion Shape Model Set (**Figure 6**). This is not unexpected, since salinity along the

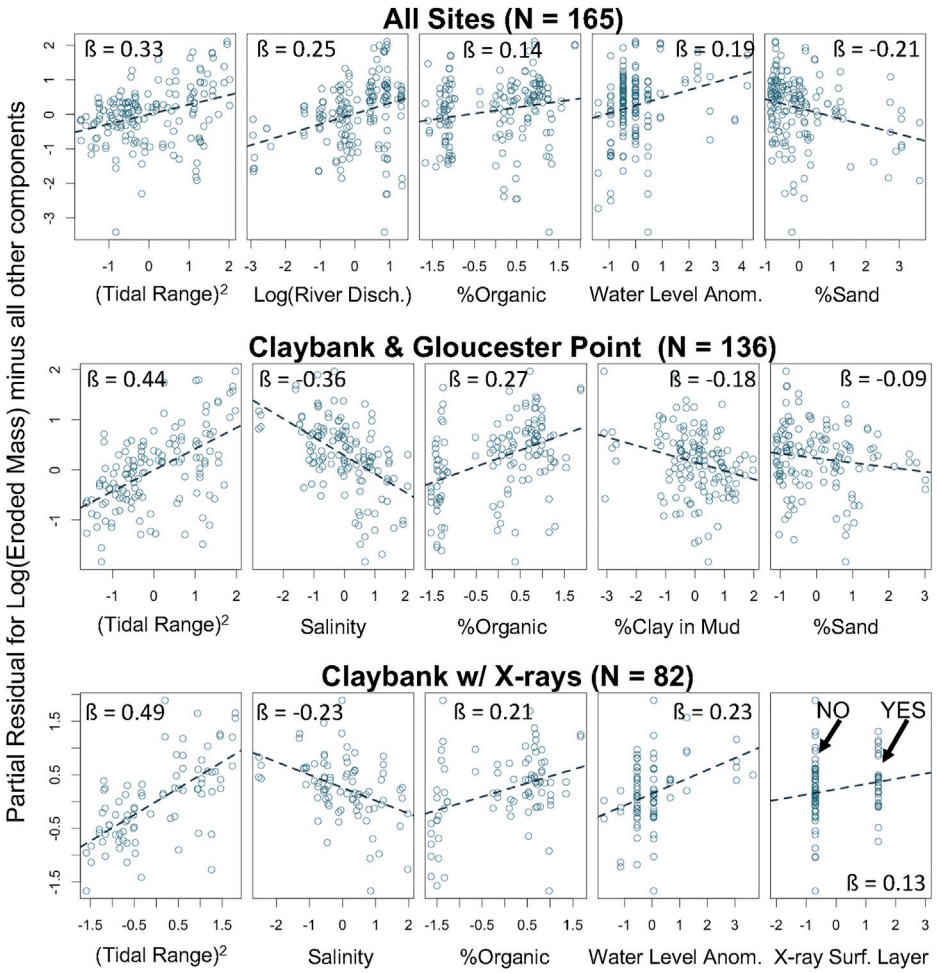

FIGURE 8 | Partial residual plots from the Eroded Mass Model Set for three representative, 5-component models from three data subsets. Each plot has standardized units for X_q and for $\beta_q X_q + \varepsilon$ on the *x*- and *y*-axis, respectively. Trend lines each have a slope equal to the parameter's β value.

York River estuary is predicted well by a nonlinear model based only on position along the estuary and past river discharge (Parrish et al., 2019). Thus, for the All Sites linear models, salinity was dropped from further consideration. However, for the other data subsets, salinity turned out to be a better predictor of the response variables than river flow, so salinity was utilized in its place. Across all data subsets, which include 452 explanatory variable correlations, only three other cases (not involving river discharge or salinity) had correlation values over 0.6. However, in the individual candidate and global models for those data subsets, vif factors were all below 5.0, so the associated variables were retained.

Linear Model Sets for Eroded Mass at 0.2 Pa

There were 33 candidate models identified (i.e., models with ΔAICc ≤2.0) within the six data subsets for the Eroded Mass Model Set. Overall, tidal range squared and salinity/river discharge were the most consistent explanatory variables throughout the entire model set, with these variables being retained in 100% of the models in which they were considered. **Figure 7A** shows average $|\beta|$ values for each individual data subset, with each subset corresponding to a given bar color. [All individual β and adjusted R^2 values for all 33 models are provided in Wright et al. (2021)]. The variables with the highest average $|\beta|$ values across all of the Eroded Mass Model subsets included past tidal range squared (0.424), salinity (−0.294) / river discharge (0.252), and percent organic (0.226). Variables that were less important, but still had consistent trends in average β were past water level anomaly (0.171), percent sand (−0.143), distance upriver (0.136), percent clay of mud (−0.135), and presence of X-ray layering (0.108).

Model performance tended to increase as data subsets became more spatially focused and otherwise specific. Partial residual plots are shown in **Figure 8** for representative 5-component models from the All Sites, Claybank & Gloucester Point, and Claybank with X-rays

subsets. The slope of the line in each panel is the β value for the corresponding explanatory variable within the model. The β value for the most important explanatory variable (tidal range squared) (**Figure 8**) increased as the data sets became more localized, and the overall performance of the models with ΔAICc scores of 0 also tended to improve (Appendix **Figure A1**). As presented in detail in Wright et al. (2021), the multiple All Sites subset models had an average adjusted R^2 of 0.392, which increased to an average of 0.464 in the Estuarine Sites subset. Furthermore, both Claybank & Gloucester Point subsets (with and without X-rays) had an average of 0.585, and both Claybank subsets resulted in an average adjusted R^2 of 0.609.

Linear Model Sets for Shape of the Erosion Profile

The model set for profile shape score consisted of 39 candidate models throughout the six different data subsets. Throughout all data subsets, eroded mass at 0.2 Pa was by far the most prominent explanatory variable for all candidate models, being included in 100% of candidate cases and exhibiting an absolute value for β twice as large as any other variable (**Figure 7B**, **Figure 9**). In every model, the relationship between eroded mass and profile shape was positive, such that greater erodibility favored a straighter (or less concave-up) profile (see **Figure 5F**). Following eroded mass at $|\beta| = 0.519$ (averaged across all data sets), the next highest $|\beta|$ values were for organic proportion at 0.249, water level anomaly at 0.182, tidal range squared at 0.171, and percent sand at 0.166. Six other variables had moderately low average $|\beta|$ values, ranging between 0.136 and 0.058.

Given the strong positive relationship between profile shape score and eroded mass at 0.2 Pa, one might initially expect the remaining explanatory variables to show relationships with shape score such that the sign of their β values matched the signs relating them to eroded mass in the previous section. This was indeed the case for percent organic, water level anomaly, tidal range squared, river discharge, and salinity. However, the signs for the β values relating percent sand, percent clay of mud, X-ray layering, and distance upriver to profile shape score were all opposite to signs of the β values relating them to eroded mass.

As was the case for eroded mass at 0.2 Pa, the models for profile shape score also tended to increase in performance as data subsets became more spatially focused, although not as dramatically (**Figure 9** and **Figure A2**). Partial residual plots are shown in **Figure 9** for representative 6-component models from the All Sites, Claybank & Gloucester Point, and Claybank with X-rays subsets. The All Sites subset had an averaged adjusted R^2 of 0.537, which slightly decreased in the Estuarine Sites subset to 0.517 (see Wright et al., 2021). However, adjusted R^2 averages increased again in the Claybank & Gloucester Point subsets and the Claybank subsets to 0.581 and 0.703, respectively.

Validation Test of the Stability of the Best Models

Using the top-performing (ΔAICc = 0) model from each model subset (Blue circles and blue dashed lines in Appendix **Figure A1** and **Figure A2**), a validation exercise was performed to test the general stability the model fits. Each data subset was split into two halves, with one half used to calibrate new best-fit β values. The new β values were then used to predict the response variable for the validation half (red squares and red dashed lines in Appendix **Figure A1** and **Figure A2**). To help ensure that each half encompassed a similar range of variable values, the calibration half consisted of the first and fourth quarters of each subset in time, and the validation set consisted of the second and third quarters. This was done because the lower- and upper-most estuary had mainly been sampled during the first and second halves of the 15-year time record, respectively.

The adjusted R^2 values for the validation data fits were generally similar to the adjusted R^2 values for the best model sets (**Figure A1** and **Figure A2**), which demonstrates that the model fits were reasonably stable. In several cases, adjusted R^2 was larger for the validation set than the corresponding full data set, indicating that some of the validation data subsets were less noisy than their corresponding full data sets. The regression lines for the validation sets (red dashed lines), however, were almost always somewhat farther from the 1:1 line relative to the full data sets (blue dashed lines), as would be expected.

DISCUSSION

Recent Bed Disturbance and/or Deposition Increase Erodibility

Two of the explanatory variables with the strongest positive effects on eroded mass at 0.2 Pa across all data subsets highlight the influence of recent physical bed disturbance on bed erodibility. Past tidal range squared, the most influential variable of all, represents the role of recent tidal bed stress in repeatedly suspending and depositing mud, such that the newly disturbed sediment is unconsolidated and easier to subsequently entrain into the water column again. Past water level anomaly, or the absolute difference between observed and predicted tidal range, is interpreted here to represent the role of recent winds causing set-up or set-down of water level, which is also associated with winddriven currents that further physically disturb the seabed, enhancing erodibility.

Several explanatory variables also emphasize that recent deposition increases erodibility as measured by eroded mass at 0.2 Pa. When considering observations from a location that is seaward of the ETM, such as data from Claybank, a decrease in salinity indicates the continued progression of the pool of easily suspended sediment down the estuary and net deposition of mud. Thus, erodibility increases at Claybank as salinity decreases. An increase in percent organic matter in the upper 1 cm of the bed also suggests recent deposition of "fresher," easier to resuspend muddy flocs. So, erodibility increases with percent organics. Likewise, the presence of layering at the surface as seen by X-radiographs indicates recent deposition, and layering was found to be positively correlated with erodibility. The past water level anomaly may also be associated with recent deposition events in the channels where most of the erodibility measurements were collected. Episodic wind waves associated with the water level anomaly might winnow mud from the shoals, which then might

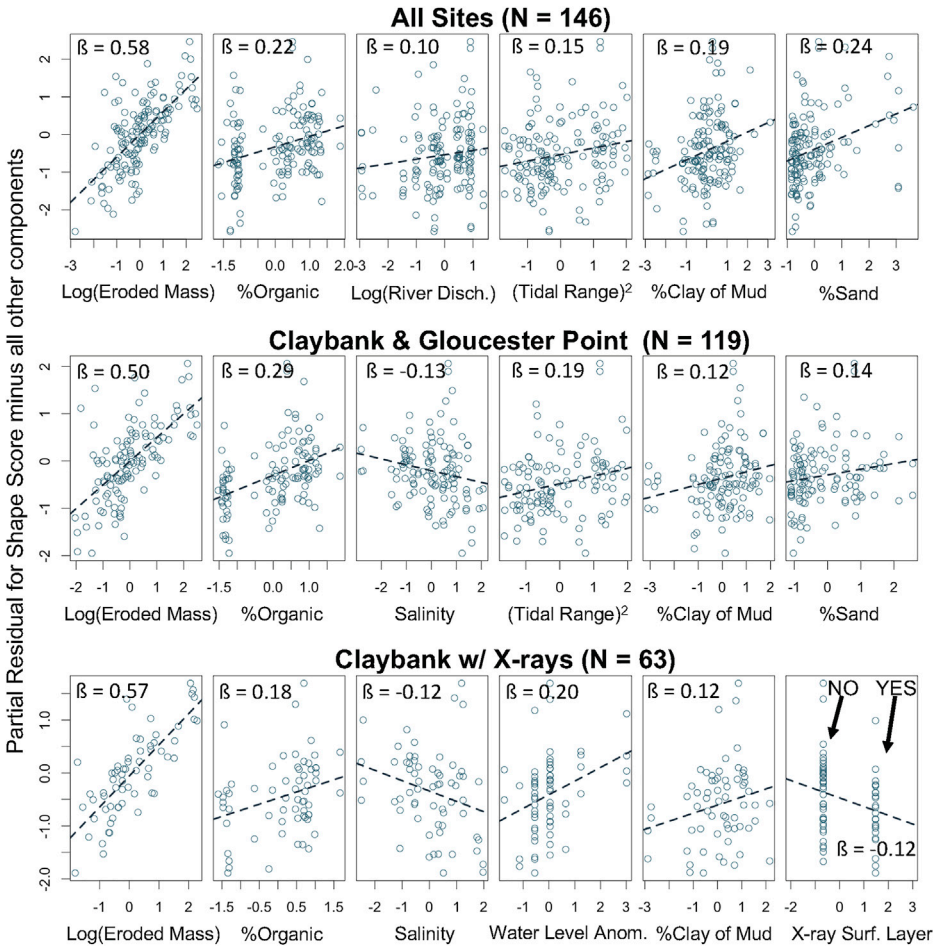

FIGURE 9 | As in Figure 8, but from the Erosion Shape Model Set for representative 6-component models.

produce temporary deposition and higher erodibility in the neighboring channels.

Greater Consolidation Time, Erosion, and/or Winnowing of Fines Decrease Erodibility

Multiple explanatory variables highlight the role of time since deposition (i.e., consolidation time), the effect of erosion exposing older sediment, and/or the past winnowing of fines decreasing eroded mass at 0.2 Pa. At a given site below the ETM, an increase in salinity indicates the likely net movement of mud upstream and away from the site, exposing older sediment and decreasing erodibility. As "fresher" mud migrates away, one would expect lower percent organics and higher percent sand, trends which are each seen to be associated with reduced erodibility in all models in which they appear. Likewise, the negative association between mottled X-radiographs and eroded mass at 0.2 Pa indicates that older sediment (i.e., that which has had time to be fully bioturbated) is less erodible. A lower fraction of silts (as indicated by a higher clay fraction of mud and/or higher sand fraction overall) is associated with lower erodibility in the York. As previously recognized by many investigators, fine sediments tend to become harder to erode as their clay-sized grain content increases because of an increase in grain-to-grain cohesion as grains become smaller (e.g., Postma, 1967; Dade et al., 1992; Roberts et al., 1998; Mehta, 2014). In contrast, mixtures containing sand-sized sediments eventually become harder to erode as their sand content increases, because suspension of non-cohesive sediment is more difficult as grain size increases.

An important finding in this study with regards to consolidation of the uppermost seabed is that the strong increase in erodibility due to recent physical disturbance (as parameterized by tidal range squared and water level anomaly) only lasts several days. For both tidal range squared and water level anomaly, the average of the previous ~7 to 8 days of observations—i.e., a time period centered around conditions ~4 days prior—had the highest correlation with eroded mass at 0.2 Pa. This timescale of a few days is consistent with consolidation times scales reported for high water content muds in laboratory studies (Mehta, 2014 and references within), with those found to work well in modeling studies (Rinehimer et al., 2008; Sanford, 2008; Sherwood et al., 2018), and is also close to the time scale for the transition from spring to neap tides (as likewise noted by

Mehta, 2014). Similar results have also been seen in the field by others. Based on a weekly time-series of five cores from the York River estuary, Kraatz (2013) previously found that eroded mass at 0.2 Pa was best correlated to the tidal range averaged over the previous 5 days, and Huang et al. (2020) found that it took approximately 7 days for sediment layers to consolidate after being deposited by tides in the Pearl River Estuary.

Hydrodynamics Can Serve as a Proxy for Effects of Bed Properties on Erodibility

Throughout the Eroded Mass Model Set, the hydrodynamic explanatory variables had a statistically stronger relationship to eroded mass at 0.2 Pa than did the sediment property variables, according to average $|\beta|$ values. However, hydrodynamic variables influence erodibility indirectly. Physically, erodibility is associated more directly with the properties of the bed, as seen in laboratory consolidation and erosion experiments focusing on specific sediment grain sizes and bulk densities (Roberts et al., 1998; Mehta, 2014). Nonetheless, for the Eroded Mass Model Set, the parameter with the highest average $|\beta|$ value was past tidal range squared (0.424; **Figure 7A**). Past tidal range squared was present in all candidate models, and it had the highest $|\beta|$ within all 33 cases. The mechanistically similar parameter of past water level anomaly was also present in every subset of models. These two hydrodynamic parameters, which are interpreted as proxies for physical bed disturbance and reduced consolidation, predicted erodibility more successfully than most directly measured sediment properties. The second most important variable of all, salinity at an average $|\beta|$ of 0.294, is also a hydrodynamic variable, as is river discharge at third most important (average $|\beta| = 0.226$).

The overall importance of hydrodynamic variables may have ramifications for enhanced performance of bed erodibility routines within computationally-intensive, multiparameter numerical models, such as 3D hydrodynamic codes that include biogeochemistry. It is easier to accurately model hydrodynamic environmental variables than to reproduce centimeter or millimeter-scale sediment bed properties. By applying these empirical relationships between hydrodynamics and erodibility in the York or by developing similar relationships for other estuaries, modelers may be able to produce a more accurate representation of sediment bed critical stresses and associated eroded mass in given areas of an estuary by only having to include the effects of external variables such as recent velocities (or bed stresses), salinity, and/or river discharge. These parameters are likely more straightforward to model than having to precisely reproduce sediment properties throughout the estuary, especially when they are spatially heterogeneous. If it is possible to represent bed grain size and organic matter well in the estuarine numerical model, a multiple regression to predict erodibility could also use these variables to further improve erodibility results.

Profile Shape Becomes More Linear as Erodibility and Physical Disturbance Increases

The Erosion Shape Model Set included an additional sediment property, namely eroded mass at 0.2 Pa, as an explanatory variable, which ended up having the largest influence on shape score by far. Eroded mass at 0.2 Pa had the highest average $|\beta|$ in all the candidate models across all Erosion Shape Model subsets, with an average of 0.519 which was more than twice as large as $|\beta|$ for the next most important erosion shape variable (**Figure 7B**). Higher eroded mass at 0.2 Pa tended to make the shape score more positive, which indicated a more linear eroded mass profile (blue PC1 > SD lines in **Figures 5E,F**). Conversely, beds with low erodibility tended to have a more strongly curved, concave-upward relationship between applied stress and total eroded mass (red PC1 < -SD lines in **Figures 5E,F**). Although they did not comment on this shape trend, Dickhudt et al. (2009) also observed more strongly curved profiles at low stress and an increase in profile linearity at higher erodibility. Dickhudt et al. (2009) fit a curve of the form $\tau_c \sim m^b$ plus an offset to groupings of their York River erodibility profiles, where m is cumulative eroded mass. Values of b closer to 1 indicate a more strongly linear fit, whereas smaller b indicates a more concave fit. For their "low," "transitional," and "high" erodibility groups, Dickhudt et al. (2009) found b = 0.51, 0.65, and 0.75, respectively. An analogous fit to the lower erodibility (red), intermediate (black), and higher erodibility (blue) curves from the present study (**Figure 5F**) yields b = 0.29, 0.60, and 0.89, which is a consistent trend.

The low erodibility, concave-upward shape may represent a near-steady-state erodibility profile present in the absence of significant recent bed disturbance, such as immediately following neap tide. This shape is similar to the concave equilibrium eroded mass vs. applied stress profile assumed by modelers of muddy bed erodibility in the absence of disturbance (Rinehimer et al., 2008; Sanford, 2008; Sherwood et al., 2018). The transition towards a more linear erodibility profile in the presence of more frequent recent disturbance (and higher overall erodibility), such as immediately following spring tide, reflects a relatively larger increase in incremental eroded mass in the range of ~0.2 to 0.4 Pa than at higher or lower applied stress (**Figure 5F**). This makes sense, since the frequency at which the τ_b = 0.2 to 0.4 Pa is reached in the York notably increases during spring tides (see **Figure 3B**). Stresses larger than 0.4 Pa are not reached very often, even on spring tides, and stresses less than 0.2 Pa are reached on nearly every tide, so spring-neap variability in bed disturbance does not change erodibility as dramatically at either of these τ_b end members.

Similar to the magnitude of erodibility, the erosion shape profile can potentially be predicted by numerical models in some cases based solely on hydrodynamic forcings. As discussed in Section *Hydrodynamics Can Serve as a Proxy for Effects of Bed Properties on Erodibility*, eroded mass for very muddy beds can be predicted relatively well based on recent hydrodynamic conditions. In turn, eroded mass is the most influential predictor of erosion shape, with $|\beta|$ values twice that of any other explanatory variable. Thus, modelers can constrain both the magnitude and profile shape of the critical stress in very muddy sediments by focusing largely on the hydrodynamic history of a study area. In this respect, the findings of this study are highly consistent with the conceptual approach of Sanford (2008), who included a mud-only case for which changes in erodibility in time

were predicted based only on a time history of tidally varying applied bed stress.

Limitations Associated With Sampling Approach and Resolution of Bed Properties

This study was largely an opportunistic analysis of an extensive sediment erodibility data set that was not collected for a single purpose. The samples were collected over 15 years at differing temporal and spatial scales for various projects. Due to clustered sampling in time and space associated with the past measurements, many standard statistical assumptions were not well adhered to. Thus, formal statistical significance levels such as *p*-values were not reported here for any of the multiple linear regressions. Over 75% of the samples used in this study were taken during the spring and summer months (March through August). Therefore, it is hard to definitively state that explanatory variables with seasonal changes like discharge, salinity, and water level anomaly follow the same predictive models all year round. For example, the average wind speed and freshwater discharge along the York are greater in winter than in summer by a factor of ~1.3 and ~3.2, respectively. Additionally, the data set was heavily skewed by the Claybank location, with over 65% of samples being in that subset. Given these sampling design limitations, the goal here was not to rigorously focus on the absolute level of the statistical significance of the results. Rather, the focus was on trends in the responses and the relative importance of one explanatory variable versus another.

In addition, the field methodology for subsampling sediment cores for water content analysis most likely did not sufficiently resolve the very surface of the sediment core. Based on a mean water content of 75.5% (**Table 2**), the upper 1 mm of the seabed contained, on average, 0.29 kg/m^2 of dry sediment. The average dry sediment mass eroded at 0.2 Pa was only 0.089 kg/m^2 (**Table 2**), and >90% of cases eroded less than 0.29 kg/m^2 (Wright et al., 2021). Thus, the Gust experiments, on average, eroded only ~0.3 mm into the bed at 0.2 Pa, and >90% of Gust experiments eroded less than 1 mm at 0.2 Pa. Unfortunately, subsamples from box cores did not attempt to resolve the uppermost 1 mm, and instead the top 1 cm from sub-cores was homogenized. Quite possibly, the water content of the full 1 cm of the upper seabed was not sensibly correlated to the water content of the uppermost 0.3 to 1 mm. The same methodology was used in the Dickhudt et al. (2009, 2011) studies, and it may be a contributing factor to why they also found no meaningful relationships between the variation of water content of mud in the York River estuary and sediment erodibility. In contrast, sensible and meaningful correlations with eroded mass at 0.2 Pa were found for the clay content of mud, sand content, and organic content of the top 1 cm. A logical explanation is that vertical gradients in clay, sand, and organic content over the top 1 cm are not nearly as strong as the vertical gradients in water content.

There may be additional factors relevant to moderately turbid, muddy tidal estuaries like the York that could make the correlation between water content over the top 1 cm and erodibility noisier than that observed in well-controlled lab experiments. As also noted by Dickhudt et al. (2009), the water content of mud over the top 1 cm in the York varies much less than other potential controls on erodibility. The standard deviation of water content divided by its mean was only 0.06 (**Table 2**). This means that even modest errors in quantifying water content could overwhelm the signal in the variance. In contrast, standard deviations divided by the mean for the bed properties with the most observed influence on erodibility, namely organic content and sand content, were 0.55 and 1.1, respectively, meaning that their signals were more likely to exceed their noise. Another complication when averaging over the top 1 cm may be that water content at this scale is positively correlated to percent clay of mud (**Figure 6**), possibly because high clay content reduces mud permeability (Zhang et al., 2015). Clay content of mud, in turn, was found to reduce erodibility. So, given the relatively small variation in water content in York River mud when averaged over the top cm of the bed, variations in clay content may at least partly counteract the influence of the mud's water content.

Variables That Could Also Have High Impact but Were Not Included

There are variables that were not included in this analysis that could also influence sediment erodibility and produce some of the unexplained variance remaining in the models. These include local mean water depth, position across the channel, and bedform types. Mean water depth and across-channel position were considered but were not found to notably account for variance in erodibility in this study's data set within the context of general linear models. This may be because so much of the data in this study were repeatedly collected at a few specific sites with relatively little sample-to-sample variation in depth or lateral location. Bedform types were not used because of a lack of observations corresponding with each sample, although mud furrows have been shown to potentially play a role in physical disturbance of the bed in the York River estuary (Dellapenna et al., 1998, 2003). In general, additional explanatory variables were not available because this data set dates back to 2005. The variables used in the final model formulations are either those that were collected according to lab protocol and have stayed consistent from 2005 to 2019 or ones that were accessible from online sources for each of the sediment cores. For example, the smaller number of pellet abundance samples (58 samples) versus most other bed properties (165 samples) stems in part from it not becoming a standard variable until later in the sampling record.

Within estuaries characterized by a main channel bordered by distinct shoals, such as the York River, lateral changes in sediment properties and hydrodynamic properties may especially influence sediment bed erodibility. The northeast and the southwest shoals of the York River tend to differ in terms of grain-size distribution and the mechanisms of sediment reworking (Hinchey, 2002; Dellapenna et al., 2003; Kniskern and Kuehl, 2003). For example, the northeast shoal of the river is sandier than the southwest shoal. Ideally, the inclusion of grain-size distribution and distance upriver might be able to adequately account for these observed differences. However, Huzzey (1988) reported lateral density gradients at Claybank, with homogenous lateral

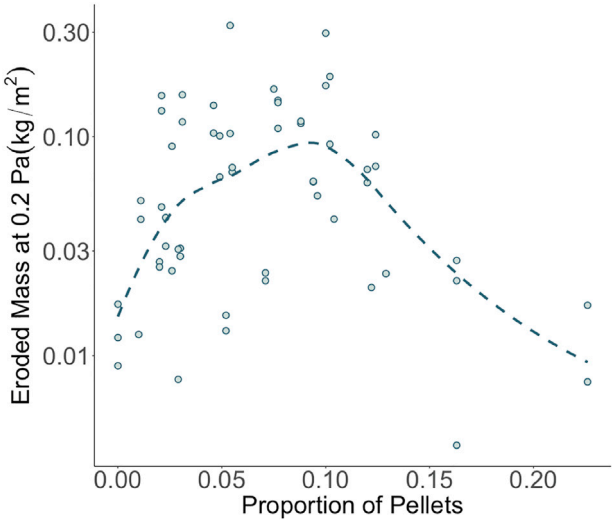

FIGURE 10 | Eroded mass at 0.2 Pa versus the proportion of total sediment mass composed of resilient pellets for the top centimeter of all cores sampled for pellets. A superimposed smoother highlights the possibility of a non-linear relationship between eroded mass and pellet proportion.

densities only present during maximum tidal currents. Huzzey (1988) also states that the cross-estuarine gradients could drive significant lateral water circulation in the area, which may likely be strong enough to preferentially erode sediment and deposit in different areas of a channel cross-section, especially in such a soft-bottomed area such as Claybank. The influence of lateral circulation and resulting changes in lateral transport convergence and erodibility have been suggested for the neighboring James River Estuary (Huijts et al., 2006). In the current study, only longitudinal estuary circulation was considered in the form of river discharge and salinity affecting the presence of the estuarine turbidity maxima.

Future Directions

Only linear relationships were reported here, but non-linear relationships were also considered during early stages of the analysis. Generalized additive models (GAMs) were initially included, but they tended to show exaggerated, oscillatory, and unrealistically non-linear relationships with many of the explanatory variables due to overfitting. When this tendency was compensated for by increased smoothing in the GAM settings, the results then provided insights very similar to multiple linear regression, suggesting that the added complexity of GAMs was not warranted. Nonetheless, at least one potential explanatory variable, namely resilient fecal pellets, seemed to have a systematically non-linear relationship with erodibility (**Figure 10**). In the pellet subset, there was an initial increase in eroded mass with pellet abundance at a low proportion of pellets, but then eroded mass began to decrease again at a higher proportion of pellets. Perhaps the initial increase in pellet abundance is acting as a proxy for decreasing clay content of mud, which would increase erodibility. Eventually, continued increases in pellet abundance may be a proxy for behavior similar to coarser non-cohesive sediment, such as sand, which would decrease erodibility once more. It could be beneficial to better explore these non-linear relationships in further investigations of this or other similar datasets.

The current study would have likely explained a greater amount of variance within the dataset had it included more accurate measurements for water content in the upper few mm of the seabed. The upper few mm of very soft muddy sediments, like those found in the York River estuary, can be difficult to sample. Perhaps higher resolution methodologies for measuring water content, such as resistivity profiling (Wheatcroft and Borgeld, 2000), fiber optical backscatter profiling (Hooshmand et al., 2015), or freeze coring followed by thin slicing (Harrison et al., 2016) could be used in conjunction with future sediment sampling to better determine the true fine-scale influence of this parameter on sediment erodibility.

Finally, future statistical studies of controls on bed erodibility in muddy estuaries would also benefit from improved field sampling in terms of experimental design. Choices for future erodibility coring sites should utilize aspects of random sampling in time and space to reduce potential autocorrelation of samples and better ensure that the true range of variability in explanatory and response variables is well represented. Nonetheless, the large sample size and temporal duration of the present data set still makes it a uniquely valuable resource for better understanding controls on estuarine sediment bed erodibility, as long as its inherent limitations are recognized.

CONCLUSION

Multiple linear regressions were applied to an extensive, 15-year data set from the York River estuary to determine and better understand which sediment and hydrodynamic properties are most important in controlling estuarine bed erodibility in terms of 1) the magnitude of eroded mass at a characteristic bed stress (0.2 Pa), also termed "eroded mass" and 2) the normalized shape of the eroded mass profile between 0 and 0.56 Pa, also termed "erosion shape." Major conclusions from the study include:

- The explanatory variables in the Eroded Mass Model Set (past tide range squared, salinity, percent organic, past water level anomaly, past river discharge, percent sand, percent clay of mud, and distance upriver) supported the roles of 1) recent deposition and bed disturbance increasing erodibility and 2) cohesion/consolidation and erosion/winnowing of fines decreasing erodibility. Trends regarding the effects of explanatory variables were highly consistent across multiple models.
- The Eroded Mass Model Set resulted in larger magnitude regression coefficients for hydrodynamic properties than for sediment properties, indicating that hydrodynamics can serve as a proxy for the effect of consolidation state on erodibility. Past increases in tidal range squared and water level anomaly are related to previous disturbance of the surface sediment layers and likely create a less stable, more erodible sediment surface. Seaward of the turbidity maximum, lower salinity/higher discharge are related to new deposition, which also drives higher erodibility. The best-fit ~7 to 8 days lag for the

effects of tidal range squared and water level anomaly identifies a characteristic time-scale for mud consolidation that is close to the period between spring and neap tide.

- The response of the Erosion Shape Model Set was dominated by the effect of eroded mass on the shape of the eroded mass profile, such that a strongly concave profile shape under low erodibility conditions became substantially more linear as erodibility increased. The low erodibility, strongly curved shape may represent a near-steady-state erodibility profile present in the absence of significant recent bed disturbance, such as immediately after neap tide. The transition towards a more linear erodibility profile in the presence of more frequent recent disturbance, such as immediately following spring tide, reflects a relatively larger increase in incremental eroded mass in the mid-to-upper-mid range of periodically observed bed stresses.
- The results of this study suggest that numerical modelers may be able to use their simulations of hydrodynamic variables in very muddy estuarine systems as a proxy for consolidation state to help predict the magnitude and shape of the eroded mass versus critical stress profile, rather than relying solely on predicted sediment bed properties. Some muddy sediment properties, like bulk density and clay content of mud can be difficult to model, especially where they are spatially and temporally heterogeneous. Parameters like past river discharge, salinity, and recent velocities (or bed stresses) are often much more accessible.
- Although many of the variables were adequately described with linear relationships, some may be better represented with non-linear modeling. Also, future sampling would benefit from higher resolution measurements of water content within the upper few millimeters of the seabed. Finally, improved distribution of spatial and temporal sampling would likely enhance understanding and prediction of erodibility across the entire estuarine system.

DATA AVAILABILITY STATEMENT

The datasets presented in this study can be found in online repositories. The names of the repository/repositories and accession number(s) can be found below: William & Mary ScholarWorks https://doi.org/10.25773/nm2b-hy57.

AUTHOR CONTRIBUTIONS

All authors played an essential role in designing this project. In addition, CW completed formal analysis and wrote the original draft manuscript as part of her master's thesis; CF provided critical feedback in reviewing and editing the manuscript; and GM played a key role in overseeing field data collection and laboratory analysis.

FUNDING

This work was funded by the Virginia Institute of Marine Science, SERDP Projects MR-2409, MR18-1233, and MR-1265, and NSF Awards OCE-0536572, OCE-1061781, and OCE-1459708.

ACKNOWLEDGMENTS

The authors would like to thank all past members of the Coastal Hydrodynamics and Sediment Dynamics lab that had a hand in collecting and/or processing these data, with special thanks to P. Dickhudt, K. Fall, and L. Kraatz. C. Harris, L. Schaffner, and N. Stark provided helpful comments on an early version of this manuscript, and three Frontiers reviewers provided especially insightful suggestions for improvement. This is contribution 4068 of the Virginia Institute of Marine Science, William & Mary.

REFERENCES

Andersen, T. J. (2001). Seasonal Variation in Erodibility of Two Temperate, Microtidal Mudflats. *Estuarine, Coastal Shelf Sci.* 53, 1–12. doi:10.1006/ecss.2001.0790

Barry, K. M., Thieke, R. J., and Mehta, A. J. (2006). Quasi-hydrodynamic Lubrication Effect of Clay Particles on Sand Grain Erosion. *Estuarine, Coastal Shelf Sci.* 67, 161–169. doi:10.1016/j.ecss.2005.11.009

Bearman, J. A., Friedrichs, C. T., Jaffe, B. E., and Foxgrover, A. C. (2010). Spatial Trends in Tidal Flat Shape and Associated Environmental Parameters in South San Francisco Bay. *J. Coastal Res.* 262, 342–349. doi:10.2112/08-1094.1

Bilici, C., Stark, N., Friedrichs, C. T., and Massey, G. M. (2019). Coupled Sedimentological and Geotechnical Data Analysis of Surficial Sediment Layer Characteristics in a Tidal Estuary. *Geo-Mar. Lett.* 39, 175–189. doi:10.1007/s00367-019-00565-3

Brouwer, R. L., Schramkowski, G. P., Dijkstra, Y. M., and Schuttelaars, H. M. (2018). Time Evolution of Estuarine Turbidity Maxima in Well-Mixed, Tidally Dominated Estuaries: The Role of Availability- and Erosion-Limited Conditions. *J. Phys. Oceanogr* 48, 1629–1650. doi:10.1175/JPO-D-17-0183.1

Burchard, H., Schuttelaars, H. M., and Ralston, D. K. (2018). Sediment Trapping in Estuaries. *Annu. Rev. Mar. Sci.* 10, 371–395. doi:10.1146/annurev-marine-010816-060535

Burnham, K., and Anderson, D. (2004). *Model Selection and Multi-Model Inference. Second*. New York: Springer-Verlag.

Cartwright, G. M., Friedrichs, C. T., Dickhudt, P. J., Gass, T., and Farmer, F. H. (2009). Using the Acoustic Doppler Velocimeter (ADV) in the MUDBED Real-Time Observing System. *OCEANS 2009*. New York: Institute of Electrical and Electronics Engineers, 642–655. doi:10.23919/OCEANS.2009.5422146

Cloern, J. E. (1987). Turbidity as a Control on Phytoplankton Biomass and Productivity in Estuaries. *Continental Shelf Res.* 7, 1367–1381. doi:10.1016/0278-4343(87)90042-2

Cooper, N., and Cooke, S. (2018). "Risky Business: Dealing with Unexploded Ordnance (UXO) in the marine Environment," in *Coasts, Marine Structures and Breakwaters 2017*. Editor K. Burgess (London: Institution of Civil Engineers), 157–167. doi:10.1680/cmsb.63174.0157

Cozzoli, F., Gjoni, V., Del Pasqua, M., Hu, Z., Ysebaert, T., Herman, P. M. J., et al. (2019). A Process Based Model of Cohesive Sediment Resuspension under Bioturbators' Influence. *Sci. Total Environ.* 670, 18–30. doi:10.1016/j.scitotenv.2019.03.085

Dade, W. B., Nowell, A. R. M., and Jumars, P. A. (1992). Predicting Erosion Resistance of Muds. *Mar. Geology.* 105, 285–297. doi:10.1016/0025-3227(92)90194-M

Dellapenna, T. M., Kuehl, S. A., and Schaffner, L. C. (2003). Ephemeral Deposition, Seabed Mixing and fine-scale Strata Formation in the York River Estuary, Chesapeake Bay. *Estuarine, Coastal Shelf Sci.* 58, 621–643. doi:10.1016/S0272-7714(03)00174-4

Dellapenna, T. M., Kuehl, S. A., and Schaffner, L. C. (1998). Sea-bed Mixing and Particle Residence Times in Biologically and Physically Dominated Estuarine Systems: a Comparison of Lower Chesapeake Bay and the York River Subestuary. *Estuarine, Coastal Shelf Sci.* 46, 777–795. doi:10.1006/ecss.1997.0316

Dickhudt, P. J., Friedrichs, C. T., and Sanford, L. P. (2011). Mud Matrix Solids Fraction and Bed Erodibility in the York River Estuary, USA, and Other Muddy Environments. *Continental Shelf Res.* 31, S3–S13. doi:10.1016/j.csr.2010.02.008

Dickhudt, P. J., Friedrichs, C. T., Schaffner, L. C., and Sanford, L. P. (2009). Spatial and Temporal Variation in Cohesive Sediment Erodibility in the York River Estuary, Eastern USA: A Biologically Influenced Equilibrium Modified by Seasonal Deposition. *Mar. Geology.* 267, 128–140. doi:10.1016/j.margeo.2009.09.009

Fall, K. A. (2012). Relationships Among Fine Sediment Settling and Suspension, Bed Erodibility, and Particle Type in the York River Estuary, Virginia. Master's Thesis. William & Mary. doi:10.25773/v5-hfz9-5r79

Fall, K. A., Harris, C. K., Friedrichs, C. T., Rinehimer, J. P., and Sherwood, C. R. (2014). Model Behavior and Sensitivity in an Application of the Cohesive Bed Component of the Community Sediment Transport Modeling System for the York River Estuary, VA. *J. Mar. Sci. Eng.* 2, 413–436. doi:10.3390/jmse2020413

Fall, K. A. (2020). Influence of Suspended Particle Size and Composition on Particle Image Processing, Estuarine Floc Fractal Properties, and Resulting Estuarine Light Attenuation. Dissertation. William & Mary. doi:10.25773/v5-nn75-t992

Friedrichs, C., Cartwright, G., and Dickhudt, P. (2008). Quantifying Benthic Exchange of fine Sediment via Continuous, Noninvasive Measurements of Settling Velocity and Bed Erodibility. *Oceanog.* 21, 168–172. doi:10.5670/oceanog.2008.14

Friedrichs, C. T. (1995). Stability Shear Stress and Equilibrium Cross-Sectional Geometry of Sheltered Tidal Channels. *J. Coast. Res.* 11, 1062–1074. https://www.jstor.org/stable/4298411.

Friedrichs, C. T., Armbrust, B. A., and de Swart, H. E. (1998). Hydrodynamics and Equilibrium Sediment Dynamics of Shallow, Funnel-Shaped Tidal Estuaries. *Physics of Estuaries and Coastal Seas*. Editors J. Dronkers and M. Scheffers (Rotterdam: A.A. Balkema), 315–328.

Friedrichs, C. T. (2009). York River Physical Oceanography and Sediment Transport. *J. Coastal Res.* SI 57, 17–22. doi:10.2112/1551-5036-57.sp1.17

Friedrichs, C. T. (2010). Barotropic Tides in Channelized Estuaries. *Contemporary Issues in Estuarine Physics*. Editors A. Valle-Levinson (Cambridge: Cambridge University Press), 27–61. doi:10.1017/CBO9780511676567.004

Gillett, D. J., and Schaffner, L. C. (2009). Benthos of the York River. *J. Coastal Res.* 10057, 80–98. doi:10.2112/1551-5036-57.sp1.80

Grabowski, R. C., Droppo, I. G., and Wharton, G. (2011). Erodibility of Cohesive Sediment: The Importance of Sediment Properties. *Earth-Science Rev.* 105, 101–120. doi:10.1016/j.earscirev.2011.01.008

Gust, G., and Müller, V. (1997). Interfacial Hydrodynamics and Entrainment Functions of Currently Used Erosion Devices. *Cohesive Sediments*. Editors N. Burt, R. Parker, and J. Watts (New York: Wiley), 149–174.

Harrison, B. K., Myrbo, A., Flood, B. E., and Bailey, J. V. (2016). Identification of Subannual Patterns in Microbial Community Signatures from Individual Sedimentary Laminae Using a Freeze-Coring Approach. *Limnol. Oceanogr* 61, 735–747. doi:10.1002/lno.10250

Haven, D. S., and Morales-Alamo, R. (1968). Occurrence and Transport of Faecal Pellets in Suspension in a Tidal Estuary. *Sediment. Geology.* 2, 141–151. doi:10.1016/0037-0738(68)90033-X

Hinchey, E. K. (2002). Organism-Sediment Interactions: The Role of Seabed Dynamics in Structuring the Mesohaline York River Macrobenthic Community. Dissertation. William & Mary. doi:10.25773/v5-qt91bm43

Hooshmand, A., Horner-Devine, A. R., and Lamb, M. P. (2015). Structure of Turbulence and Sediment Stratification in Wave-supported Mud Layers. *J. Geophys. Res. Oceans* 120, 2430–2448. doi:10.1002/2014JC010231

Huang, W., Zhang, H., Zhu, L., Chen, L., Zhang, G., Gong, W., et al. (2020). *In-situ* Study of the Spatiotemporal Variability of Sediment Erodibility in a Microtidal Estuary. *Estuarine, Coastal Shelf Sci.* 232, 106530. doi:10.1016/j.ecss.2019.106530

Huijts, K. M. H., Schuttelaars, H. M., De Swart, H. E., and Valle-Levinson, A. (2006). Lateral Entrapment of Sediment in Tidal Estuaries: An Idealized Model Study. *J. Geophys. Res.* 111, C12. doi:10.1029/2006JC003615

Huzzey, L. M. (1988). The Lateral Density Distribution in a Partially Mixed Estuary. *Estuarine, Coastal Shelf Sci.* 26, 351–358. doi:10.1016/0272-7714(88)90017-0

Iddrisu, W. A., Nokoe, K. S., Luguterah, A., and Antwi, E. O. (2017). Generalized Additive Mixed Modelling of River Discharge in the Black Volta River. *Ojs* 07, 621–632. doi:10.4236/ojs.2017.74043

Jacobs, W., Le Hir, P., Van Kesteren, W., and Cann, P. (2011). Erosion Threshold of Sand-Mud Mixtures. *Continental Shelf Res.* 31, S14–S25. doi:10.1016/j.csr.2010.05.012

James, G., Witten, D., Hastie, T., and Tibshirani, R. (2013). *An Introduction to Statistical Learning*. New York: Springer.

Jepsen, R., Roberts, J., and Lick, W. (1997). Effects of Bulk Density on Sediment Erosion Rates. *Water Air Soil Pollut.* 99, 21–31. doi:10.1007/bf02406841

Kim, S. C., Friedrichs, C. T., Maa, J. Y., and Wright, L. D. (2000). Estimating Bottom Stress in Tidal Boundary Layer from Acoustic Doppler Velocimeter Data. *J. Hydraul. Eng.* 126, 6. doi:10.1061/(asce)0733-9429(2000)126:6(399)

Kniskern, T. A., and Kuehl, S. A. (2003). Spatial and Temporal Variability of Seabed Disturbance in the York River Subestuary. *Estuarine, Coastal Shelf Sci.* 58, 37–55. doi:10.1016/S0272-7714(03)00052-0

Kraatz, L. M. (2013). Acoustic and Sedimentological Investigations of Seabed Conditions and Related Biogeological Parameters in a Tidally Energetic, Fine-grained Environment. Dissertation. William & Mary, Virginia: York River Estuary. doi:10.25773/v5-cq0w-8d39

Kruk, C., Martínez, A., Nogueira, L., Alonso, C., and Calliari, D. (2015). Morphological Traits Variability Reflects Light Limitation of Phytoplankton Production in a Highly Productive Subtropical Estuary (Río de la Plata, South America). *Mar. Biol.* 162, 331–341. doi:10.1007/s00227-014-2568-6

Lanzoni, S., and Seminara, G. (2002). Long-term Evolution and Morphodynamic Equilibrium of Tidal Channels. *J. Geophys. Res. Oceans* 107, C1. doi:10.1029/2000JC000468

Li, B., Cozzoli, F., Soissons, L. M., Bouma, T. J., and Chen, L. (2017). Effects of Bioturbation on the Erodibility of Cohesive versus Non-cohesive Sediments along a Current-Velocity Gradient: A Case Study on Cockles. *J. Exp. Mar. Biol. Ecol.* 496, 84–90. doi:10.1016/j.jembe.2017.08.002

Lin, J., and Kuo, A. Y. (2001). Secondary Turbidity Maximum in a Partially Mixed Microtidal Estuary. *Estuaries*, 24, 707–720. doi:10.2307/1352879

Lucas, C. H., Widdows, J., and Wall, L. (2003). Relating Spatial and Temporal Variability in Sediment Chlorophylla and Carbohydrate Distribution with Erodibility of a Tidal Flat. *Estuaries* 26, 885–893. doi:10.1007/BF02803347

Luckenbach, M. W. (1986). Sediment Stability Around Animal Tubes: The Roles of Hydrodynamic Processes and Biotic Activity. *Limnol. Oceanogr.* 31, 779–787. doi:10.4319/lo.1986.31.4.0779

Massey, G. M., Wright, C. L., Friedrichs, C. T., Stark, N., and Kiptoo, D. (2019). York River Estuary Data in Support of: Improved Penetrometer Performance in Stratified Sediment for Cost-Effective Characterization, Monitoring and Management of Submerged Munitions Sites. Report. *Va. Inst. Mar. Sci.* William & Mary. doi:10.25773/2rze-fg21

Mehta, A. (2014). *An Introduction to Hydraulics of Fine Sediment Transport*. New Jersey: World Scientific.

Moore, K. A., Wetzel, R. L., and Orth, R. J. (1997). Seasonal Pulses of Turbidity and Their Relations to Eelgrass (Zostera marina L.) Survival in an Estuary. *J. Exp. Mar. Biol. Ecol.* 215, 115–134. doi:10.1016/s0022-0981(96)02774-8

Moriarty, J. M., Friedrichs, M. A., and Harris, C. K. (2021). Seabed Resuspension in the Chesapeake Bay Implications for Biogeochemical Cycling and Hypoxia. *Estuaries Coasts* 44, 103–122. doi:10.1007/s12237-020-00763-8

National Oceanic and Atmospheric Administration (2021). Tides and Currents for Yorktown USCG VA. Access: https://tidesandcurrents.noaa.gov/waterlevels.html?id=8637689.

Nichols, M. M., Kim, S. C., and Brouwer, C. M. (1991). Sediment Characterization of Coastal Lagoons and Bays, Virginian Province. Report. *Va. Inst. Mar. Sci.* William & Mary. doi:10.21220/V5BQ60

Olabarrieta, M., Geyer, W. R., Coco, G., Friedrichs, C. T., and Cao, Z. (2018). Effects of Density-Driven Flows on the Long-Term Morphodynamic Evolution of Funnel-Shaped Estuaries. *J. Geophys. Res. Earth Surf.* 123, 2901–2924. doi:10.1029/2017JF004527

Parrish, D., Reay, W., Shields, E., and Friedrichs, C. (2019). "Investigation of an Historic Low Salinity Event in the York River Estuary, Chesapeake Bay," in *25th*

Biennial Conference of the Coastal and Estuarine Research Federation, 3–7. https://cerf.confex.com/cerf/2019/meetingapp.cgi/Paper/6256.

Postma, H. (1967). Sediment Transport and Sedimentation in the Estuarine environment. *Estuaries*. Editor G. H. Lauff (Washington, DC: American Association for the Advancement of Science), 158–179.

Reay, W. G. (2009). Water Quality within the York River Estuary. *J. Coastal Res.* SI 57, 23–39. doi:10.2112/1551-5036-57.sp1.23

Rinehimer, J. P., Harris, C. K., Sherwood, C. R., and Sanford, L. P. (2008). Estimating Cohesive Sediment Erosion and Consolidation in a Muddy, Tidally-Dominated Environment: Model Behavior and Sensitivity. *Estuarine and Coastal Modeling (2007)*. Editor M. L. Spaulding (Reston, VA: American Society of Civil Engineers), 819–838. doi:10.1061/40990(324)44

Roberts, J., Jepsen, R., Gotthard, D., and Lick, W. (1998). Effects of Particle Size and Bulk Density on Erosion of Quartz Particles. *J. Hydraul. Eng.* 124, 12. doi:10.1061/(asce)0733-9429(1998)124:12(1261)

Sanford, L. P., and Maa, J. P. Y. (2001). A Unified Erosion Formulation for fine Sediments. *Mar. Geol.* 179. doi:10.1016/s0025-3227(01)00201-8

Sanford, L. P. (2008). Modeling a Dynamically Varying Mixed Sediment Bed with Erosion, Deposition, Bioturbation, Consolidation, and Armoring. *Comput. Geosciences* 34, 1263–1283. doi:10.1016/j.cageo.2008.02.011

Schaffner, L. C., Hinchey, E. K., Dellapenna, T. M., Friedrichs, C. T., Neubauer, M. E., Smith, M. E., et al. (2001). "Physical Energy Regimes, Sea-Bed Dynamics and Organism-Sediment Interactions along an Estuarine Gradient," in *Organism–sediment Interactions*. Editors J. Y. Aller, S. A. Woodin, and R. C. Aller (Columbia, SC: University of South Carolina Press), 161–182.

Scully, M. E., Friedrichs, C., and Brubaker, J. (2005). Control of Estuarine Stratification and Mixing by Wind-Induced Straining of the Estuarine Density Field. *Estuaries* 28, 321–326. doi:10.1007/BF02693915

Sherwood, C. R., Aretxabaleta, A. L., Harris, C. K., Rinehimer, J. P., Verney, R., and Ferré, B. (2018). Cohesive and Mixed Sediment in the Regional Ocean Modeling System (ROMS v3.6) Implemented in the Coupled Ocean-Atmosphere-Wave-Sediment Transport Modeling System (COAWST R1234). *Geosci. Model. Dev.* 11, 1849–1871. doi:10.5194/gmd-11-1849-2018

Sin, Y., Wetzel, R. L., and Anderson, I. C. (1999). Spatial and Temporal Characteristics of Nutrient and Phytoplankton Dynamics in the York River Estuary, Virginia: Analyses of Long-Term Data. *Estuaries* 22, 260275. doi:10.2307/1352982

United States Geological Survey (2021). Current Water Data for Virginia. Access. https://waterdata.usgs.gov/va/nwis/rt.

Vandever, J. P. (2007). Acoustic Measurement and Modeling of Waves in Estuarine and Coastal Environments. Master's Thesis. William & Mary. doi:10.25773/v5-32s9-ya69

Virginia Estuarine and Coastal Observing System (2021). *Chesapeake Bay National Estuarine Research Reserve*. Virginia. Access http://vecos.vims.edu.

Wheatcroft, R. A., and Borgeld, J. C. (2000). Oceanic Flood Deposits on the Northern California Shelf: Large-Scale Distribution and Small-Scale Physical Properties. *Continental Shelf Res.* 20, 2163–2190. doi:10.1016/S0278-4343(00)00066-2

Wright, C. L. (2021). Controls on Estuarine Sediment Bed Erodibility: Insights from the York River Estuary. Master's Thesis. William & Mary. doi:10.25773/dmv9-fj68

Wright, C. L., Massey, G. M., Dickhudt, P. J., and Friedrichs, C. T. (2021). Controls on Sediment Bed Erodibility in a Muddy, Partially-Mixed Tidal Estuary, York River, Supporting Data. *Va. Inst. Mar. Sci.* William & Mary. doi:10.25773/nm2b-hy57

Wu, W., Perera, C., Smith, J., and Sanchez, A. (2018). Critical Shear Stress for Erosion of Sand and Mud Mixtures. *J. Hydraulic Res.* 56, 96–110. doi:10.1080/00221686.2017.1300195

Yujun, Y. I., Zhaoyin, W., Zhang, K., Guoan, Y. U., and Xuehua, D. (2008). Sediment Pollution and its Effect on Fish through Food Chain in the Yangtze River. *Int. J. Sediment. Res.* 23, 338–347. doi:10.1016/S0278-4343(00)00066-2

Zhang, M., Zhu, X., Yu, G., Yan, J., Wang, X., Chen, M., et al. (2015). Permeability of Muddy clay and Settlement Simulation. *Ocean Eng.* 104, 521–529. doi:10.1016/j.oceaneng.2015.05.031

Zhu, Q., Van Prooijen, B. C., Maan, D. C., Wang, Z. B., Yao, P., Daggers, T., et al. (2019). The Heterogeneity of Mudflat Erodibility. *Geomorphology* 345, 106834. doi:10.1016/j.geomorph.2019.106834

Conflict of Interest: The authors declare that the research was conducted in the absence of any commercial or financial relationships that could be construed as a potential conflict of interest.

Publisher's Note: All claims expressed in this article are solely those of the authors and do not necessarily represent those of their affiliated organizations, or those of the publisher, the editors and the reviewers. Any product that may be evaluated in this article, or claim that may be made by its manufacturer, is not guaranteed or endorsed by the publisher.

APPENDIX

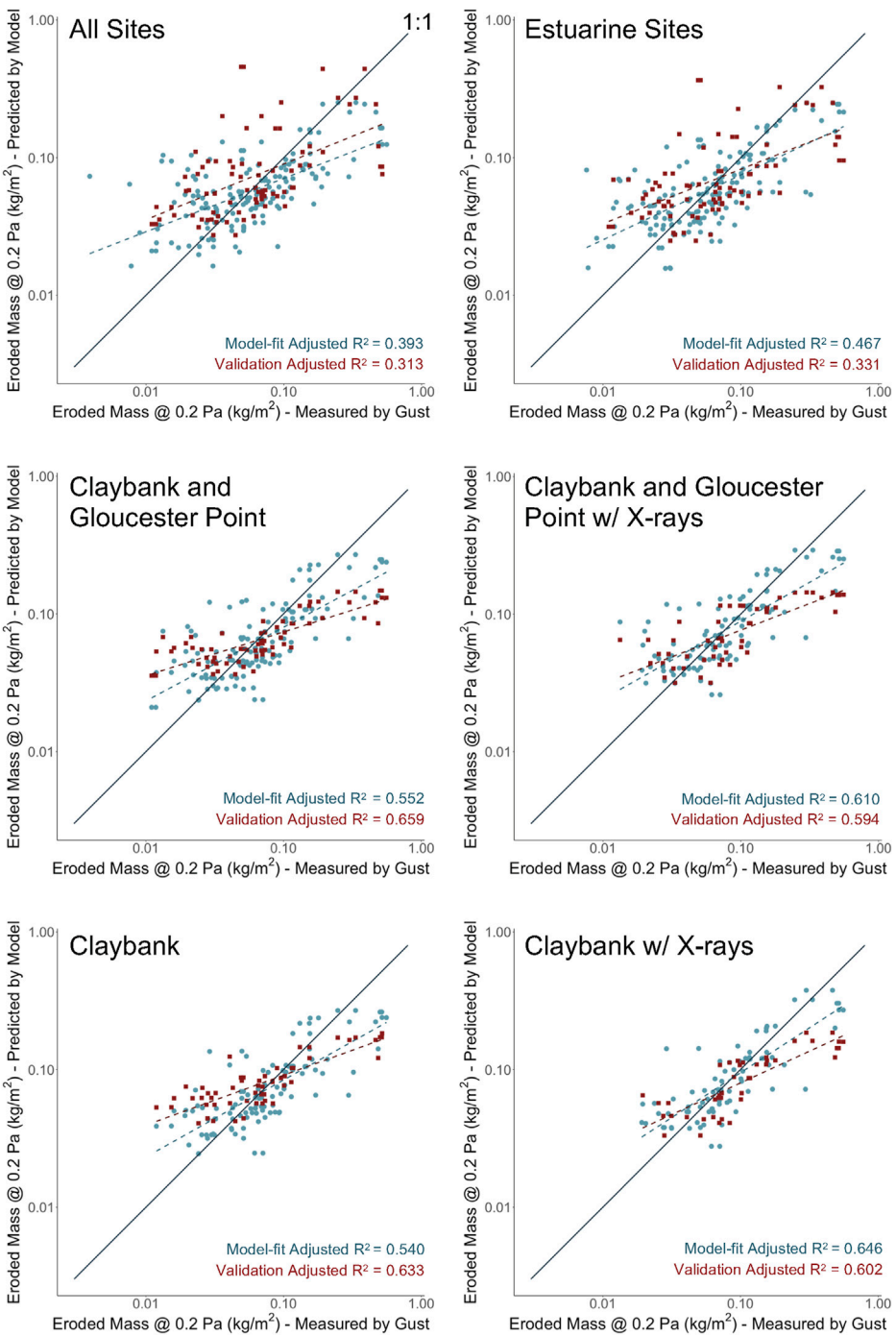

FIGURE A1 | Blue circles and blue dashed line show performance for models with ΔAICc = 0 from each data subset in the Eroded Mass Model Set relative to a black 1:1 line. Red squares and red dashed line show validation model performance when half of the data were chosen to reset the models' coefficients, and the same reset coefficients predicted erodibility using the other half of the data.

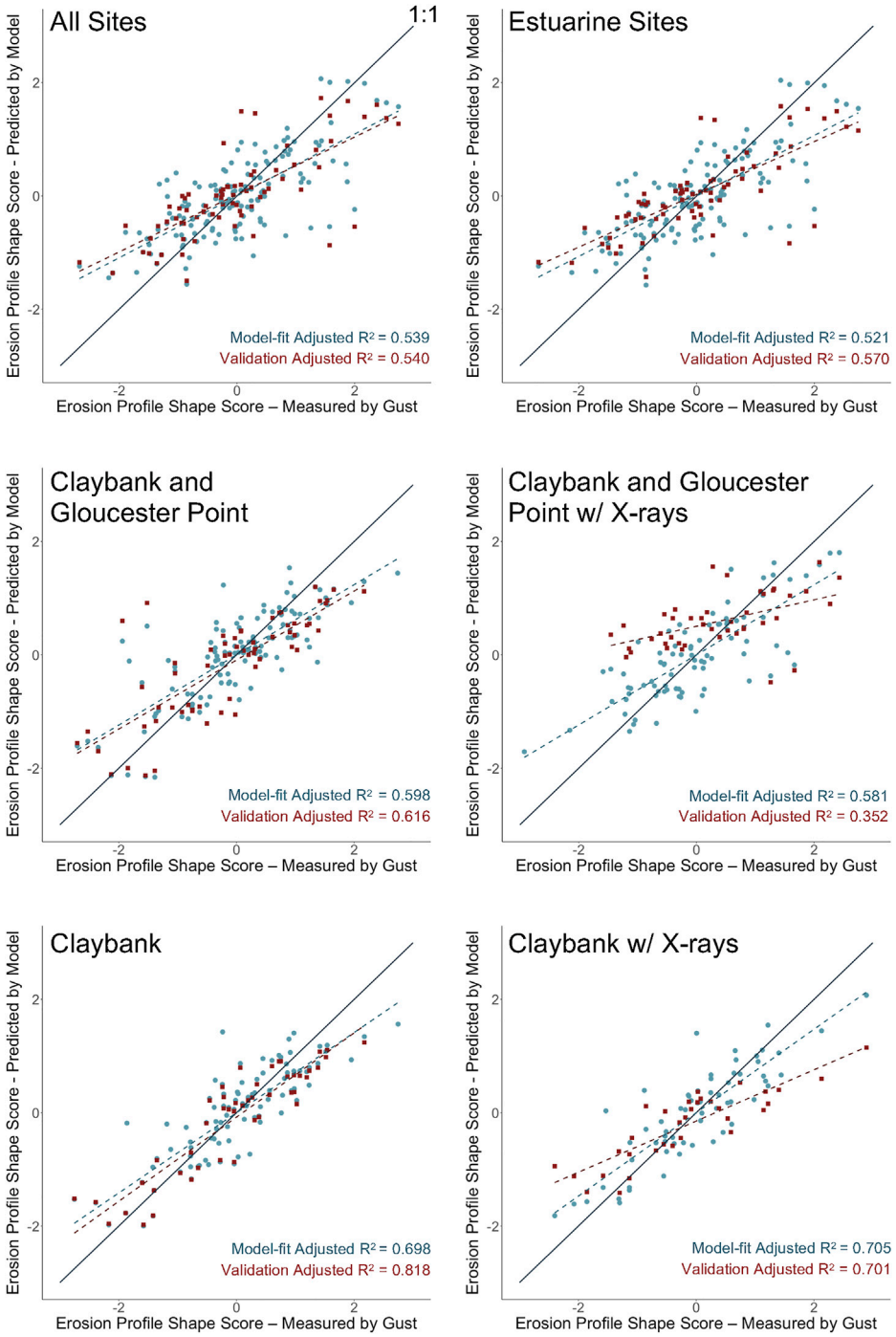

FIGURE A2 | As in Figure A1, but for the Erosion Shape Model Set.

frontiers | Frontiers in Earth Science

METHODS
published: 08 April 2022
doi: 10.3389/feart.2022.820866

Grain-Size Analysis of Ancient Deep-Marine Sediments Using Laser Diffraction

Hannah L. Brooks[1,2]*, *Elisabeth Steel*[2] *and Mikaela Moore*[2]

[1]EMR—Geological Institute, RWTH Aachen University, Aachen, Germany, [2]Department of Geological Sciences and Geological Engineering, Queen's University, Kingston, ON, Canada

Grain-size analysis of siliciclastic sedimentary rocks provides critical information for interpreting flow dynamics and depositional environments in sedimentary systems and for analysing reservoir quality of sandstone. Methods such as sieving and thin-section analysis are time consuming and unsuited for large sample numbers. Laser diffraction particle analysis is quick and reliable for analysing 100s of samples, assuming successful disaggregation. Here, we evaluate this method utilizing samples from three siliciclastic formations in Northern Italy: the Miocene Castagnola and Marnoso-Arenacea Formations, and the Cretaceous to Palaeocene Gottero Formation, which vary in degree of lithification. We focus on: 1) methods of whole-rock disaggregation; 2) methods of subsampling sediment for laser diffraction analysis; and 3) comparison of thin-section analysis with laser-diffraction particle size analysis. Using an ultrasonic bath and a SELFRAG (high voltage selective fragmentation) as disaggregation tools, this study evaluates separation of whole, undamaged grains subsequently measured by laser diffraction analysis. We show that it is possible to disaggregate ancient, well cemented rocks using an ultrasonic bath. When disaggregating samples with the SELFRAG method, grain-size measurements become less accurate and less precise with increasing sample lithification and increased presence of cement. This is likely a combination of incomplete grain disaggregation in the SELFRAG and heterogeneity within samples. Following disaggregation, we compare sub-sampling methods using a stirrer plate versus a pipette. Both produce accurate analyses, but the stirrer method is the most reliable and replicable. A comparative small subsample method, run as one whole sample with no need for subdivision into aliquots, is found to be reliable and replicable but is more susceptible to heterogeneity within field samples. When comparing laser diffraction results to grain-size volume methods estimated from thin-section analysis, thin-section sand grains are overestimated, and clay/silt grains are inaccurate. These results provide a framework for understanding potential biases introduced through various sample preparation and measurement methods.

Keywords: grain-size analyses, hybrid event bed, turbidites, method, laser-diffraction grain-sizing

OPEN ACCESS

Edited by:
Daniel R. Parsons,
University of Hull, United Kingdom

Reviewed by:
Roberto Adrián Scasso,
University of Buenos Aires, Argentina
Roberto Tinterri,
University of Parma, Italy

***Correspondence:**
Hannah L. Brooks
hannah.brooks@emr.rwth-aachen.de

Specialty section:
This article was submitted to Sedimentology, Stratigraphy and Diagenesis, a section of the journal Frontiers in Earth Science

Received: *23 November 2021*
Accepted: *22 March 2022*
Published: *08 April 2022*

Citation:
Brooks HL, Steel E and Moore M (2022) Grain-Size Analysis of Ancient Deep-Marine Sediments Using Laser Diffraction. Front. Earth Sci. 10:820866. doi: 10.3389/feart.2022.820866

INTRODUCTION

Grain-size analysis is ubiquitously employed by sedimentologists, geomorphologists, geographers and civil engineers working with outcrop and core datasets in clastic sedimentary systems. In detailed studies, where a description using a hand-lens is insufficient, further methods are required to build a more quantitative description of grain-size and sorting. Older methods for grain-size analysis are based on sedimentation rates for fine-grained (clay to silt) fractions and sieving for coarse-grained (silt and larger) fractions (Buller and McManus, 1972; Gee and Bauder, 1986). These methods have some drawbacks, such as they are time-consuming, very dependent on laboratory technique and operator error (Syvitski, 1991) and a large amount of material is needed (at least 10 g). These classic techniques are therefore not suitable for rapid, accurate analysis of many samples. Techniques such as thin-section analysis and laser particle-size analysis have become the norm when analysing cemented rock (Krumbein, 1935; Chayes, 1950; Greenman, 1951; Rosenfeld, et al., 1953; Friedman, 1958; Smith, 1966; Sahu, 1968; Harrell and Eriksson, 1979; Kong, et al., 2005) and unconsolidated sediment/soil (Konert and Vandenberghe, 1994; Blott, et al., 2004; Di Stefano, et al., 2010; Zihua, et al., 2009), respectively.

The time-consuming nature of thin-section point counting has been somewhat abated by newer image analysis techniques (Mazzullo and Kennedy, 1985; Francus, 1999; Persson, 1998; Van den Berg, et al., 2002; Van Den Berg, et al., 2003; Seelos and Sirocko, 2005; Fernlund, et al., 2007; Resentini, et al., 2018), but these methods can have their own technical issues, and beyond that, the time and money necessary to make thin-sections significantly limits the number of samples that can be processed. Within the last couple of decades, laser diffraction analysis has become more common, but is primarily utilized for unconsolidated sediment and soil (Konert and Vandenberghe, 1994; Sperazza, et al., 2004; Cheetham, et al., 2008; Di Stefano, et al., 2010) or in relatively young, Holocene/Pliocene-Pleistocene sedimentary rocks that are poorly lithified (Barrett and Anderson, 2000; Ito, 2008; Zihua, et al., 2009; Bralower, et al., 2010). In deepwater clastic systems, laser diffraction analysis has been effective at characterizing subtle changes in grain-size distributions in unconsolidated sediment (Stevenson et al., 2014), but the method has been under-utilized in ancient clastic systems because of challenges in disaggregating well-lithified samples (Loope, et al., 2012; Maithel, et al., 2019).

Recent studies have shown that disaggregation of lithified rocks and grain-size measurement of the sand-sized fraction through laser diffraction can be a useful tool in ancient sand-rich sedimentary systems (Maithel, et al., 2019), but the clay fraction can be altered or damaged by disaggregation methods, which commonly include crushing or chemical disaggregation. Crushing of aggregate grains (Barrett and Anderson, 2000; Jiang and Liu, 2011; Maithel, et al., 2019) can add uncertainties by fracturing or damaging grains and should therefore be avoided where possible. Chemical disaggregation has often been applied to well-lithified samples (Suczek, 1983; Triplehorn, et al., 2002; Maithel, et al., 2019). This is a useful method, but it may dissolve or abrade some minerals and can be time consuming, taking hours or days. Sodium hexametaphosphate (Na_6 $[(PO_3)_6]$/NaHMP) is a relatively gentle chemical method of disaggregation which is used to deflocculate clays within a sample (Sridharan, et al., 1991; Andreola, et al., 2004; Andreola, 2006) and therefore is useful as a complimentary method after other disaggregation techniques are used on the larger grains (Zihua, et al., 2009).

High-voltage selective fragmentation (SELFRAG) can be an effective tool in rock disaggregation (van der Wielen, et al., 2013). This method is most commonly used for mineral analysis in the mining industry (Andres, 2010; Wang, et al., 2011; Wang, et al., 2012; Zuo, et al., 2015), but in this study the SELFRAG method is used for siliciclastic sedimentary rocks in order to establish whether it is a reliable method for disaggregation prior to laser diffraction grain-size analysis.

Aims/Objectives

The aim of this study is to create a replicable and relatively quick method for disaggregating ancient clastic sediments and preparing them for laser diffraction grain-size analysis. This will therefore allow quicker and more accurate processing of multiple samples from the ancient rock record. Objectives are: i) to produce a reliable and repeatable workflow for disaggregating ancient mudstone and sandstone utilizing an ultrasonic bath and/or a SELFRAG machine; ii) Evaluate the reliability and potential biases associated with various subsampling methods for laser diffraction grain-size analysis; and iii) to compare the results to thin-section analysis of the same samples.

METHODS

Sampling

The samples used in this study were collected from deepwater turbidites and hybrid event beds/linked debrites (Haughton, et al., 2003; Hodgson, 2009; Sumner, et al., 2009; Talling, 2013) from three basins located in north-west and central Italy with ages spanning from the Cretaceous to Miocene (**Figure 1A**). In total, 338 samples were collected and processed for grain-size analysis. Results from nine field samples are presented in this paper as examples for method development.

Castagnola Formation

The Castagnola Formation is a deep-marine unit of the Aquitanian-Burdigalian sedimentary fill of the eastern part of the Tertiary Piedmont Basin of north-west Italy (Andreoni, et al., 1981; Cavanna, et al., 1989; Di Giulio and Galbiati, 1993). The sandstone composition of the Castagnola Formation varies throughout the sections from Arkosic to Mixed to Litharenite (**Figure 7** of Patacci et al., 2020). The sandstone composition of the studied interval (Beds 208, 209 and 210 *sensu* Southern et al., 2015) is arkosic with calcite cementation (on average Q60, F30, L10) and is interpreted to be sourced from continental basement units with limited Permian cover (Patacci, et al., 2020). Samples were taken vertically through these three beds from four logged locations (VI, V, IV and II; Southern et al., 2015; **Figure 1B**) in a

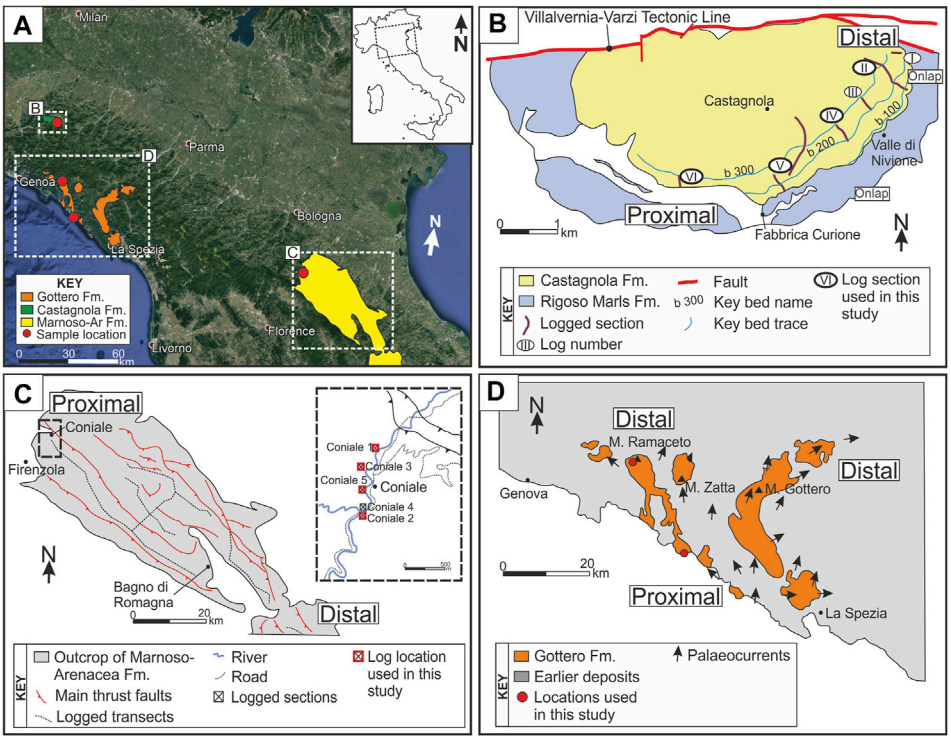

FIGURE 1 | (A) Locations of three basins in Northern Italy, the Castagnola Formation, the Marnoso-Arenacea Formation and the Gottero Formation, inset map of Italy in the top right corner. **(B)** Outline of the Castagnola Formation outcrops (deepwater sandstone and mudstone succession) stratigraphically above the Rigoso Marls Formation, South of the Villalvernia—Varzi tectonic line (modified from Patacci et al., 2020). **(C)** Outline of outcrops of the Marnoso-Arenacea Formation in the Northern subbasin of the Marnoso-Arenacea foredeep, with the location of the main thrust faults through the section and logged tracts from Amy and Talling (2006). Inset map of key proximal locations in the village of Coniale (modified from Amy and Talling, 2006). **(D)** Location of Gottero Formation outcrops with proximal locations on the coast and distal location at Mount Ramaceto, modified from Fonnesu et al., 2018.

dip to oblique section to overall palaeoflow. Bed thicknesses range from 1.5—5 m and samples were selected vertically through beds at 20 cm intervals. This formation is poorly lithified. Sandstone was easily sampled with a hammer and chisel and mudstone-rich samples were broken by hand.

In this methodological analysis, we present results from the following samples (naming convention is log—bed—sample; **Figure 1B** and Southern et al., 2015 for log locations and bed details):

- IV B210 S5 is from the sand-rich lower division (H1) of a hybrid event bed.
- II B209 S9 is from a dewatered/soft-sediment deformed, clast-rich lower division (H1b) of a hybrid event bed.
- V B209 S22 is from an argillaceous upper division (H5) of a hybrid event bed.
- VI 208 S2 is from sand-rich lower division (H1) of a hybrid event bed.

Marnoso- Arenacea Formation

The Miocene Marnoso-Arenacea Formation was deposited in a deepwater basin plain environment of a foreland basin (Lucchi and Valmori, 1980; Argnani and Lucchi, 2001; Amy and Talling, 2006; Muzzi Magalhaes and and Tinterri, 2010) and is now exposed in the Apennine fold-and-thrust belt within Central Italy. The samples were collected from a section that is Serravillian in age, directly above the marker Contessa megabed (Lucchi and Valmori, 1980; Amy and Talling, 2006). The sandstone is a calcite cemented quartz arenite with subordinate feldspar, biotite and lithic grains (Amy, et al., 2016), with an estimated 54% Quartz, 28% Feldspar and 18% lithic fragments (Valloni and Zuffa, 1984).

Samples were collected at 20 cm stratigraphic intervals through four beds (Bed 0, 0.4, one and two *sensu* Amy and Talling, 2006) from four logged locations (Coniale 1, 2, 4 and 5; locations 1, 81, 27 and 82 from **Figure 9** of Amy and Talling, 2006) in a oriented perpendicular to the overall palaeoflow (**Figure 1C**). Bed thicknesses range from 0.3 to 1.8 m. This formation has "moderate" lithification. Sandstone samples was easily sampled with a hammer and chisel, while finer, mudstone-rich sections were more cemented and difficult to sample, with one sample uncollectable with the tools at hand.

Analysed samples come from two sections in the Coniale area—Coniale 1 (C1), which corresponds to log one of Amy and Talling (2006) and Coniale 2 (C2), which corresponds to log 80 of Amy and Talling (2006). Naming convention is Log—Bed—Sample:

- C1 B2 S1 is in the lower sand-rich division of a turbidite bed (Ta/b).
- C1 B2 S4 is in the mud-rich division of a turbidite bed (Te).
- C2 B0.4 S7 is from the argillaceous upper division (H5) of a hybrid event bed.
- C2 B1 S5B is from the argillaceous upper division (H5) of a hybrid event bed.

Gottero Formation

The Gottero deepwater turbidite system is Maastrichtian to early Palaeocene in age (Passerini and Pirini, 1964; Marroni, 1990; Marroni, et al., 2004) and was deposited onto oceanic crust in a trench basin (Abbate and Sagri, 1970; Nilsen and Abbate, 1984). The Gottero sandstone is a feldspathic wackestone, with an estimated 51% Quartz, 39% Feldspar and 10% lithic fragments (Valloni and Zuffa, 1984). Grains contain fragments of metamorphic, volcanic and sedimentary rocks (Malesani, 1966; Pandolfi, 1997) derived from the Sardo-Corso massif, where large igneous crystalline masses were exposed (Parea, 1965; Valloni and Zuffa, 1981; van de Kamp and Leake, 1995). Samples are cemented with quartz and calcite (van de Kamp and Leake, 1995). Samples were collected through three beds in a proximal area (**Figure 1D**) and two beds in a distal area (**Figure 1D**) at 50 cm intervals or at major lithological changes. Beds in the proximal area are 0.3–1.6 m thick and beds in the distal area are 1.5–2.2 m thick. This formation is well lithified with sandstone samples very difficult to take with a hammer and chisel. Wider spacing in sampling was necessary due to the difficulty in removing samples and time constraints in the field.

From the distal area, Mount Ramaceto:

- GOT A B13 S3- Location 'A' is in the vicinity of Log F (Fonnesu et al., 2018), B13 is Bed 13 of (Fonnesu et al., 2016; Fonnesu et al., 2018), sample 3 is from a mud clast-rich section of the lower sand-rich division of a hybrid event bed (H1).

Nomenclature for Samples

The samples collected in the field were subsampled in various ways and using several methods. For clarity, we describe sample terminology for field samples, large and small subsamples, and aliquots below.

Field Samples

These are samples taken directly from the beds in the field at 20 cm intervals in the Castagnola and Marnoso-Arenacea Formations and at 50 cm intervals in the Gottero Formation. Due to the debritic nature of the deposits, some heterogeneity within field samples was unavoidable. Field samples weighed between 50 and 1,000 g.

Large or Small Subsamples

Subsamples are taken directly from field samples. A small (0.5–5 g) or large (5–10 g) piece is gently hammered from the field sample and then disaggregated for grain size analysis. Effort is made so that the piece chosen looks representative of the whole sample. Small subsamples (designated 'S' in **Supplementary Table S1**) can be directly introduced into a laser particle size analyser (LPSA) in one batch without the need for further subdivision (see obscuration limitations below for explanation on sample size). Large subsamples (designated 'L' in **Supplementary Table S1**) are over the obscuration limit and must be further split into aliquots before processing with the LPSA.

Aliquots

An aliquot is a subdivision of the larger subsamples that is sufficiently small to be introduced directly into the LPSA. These are sampled using the pipette or stirrer method (outlined below) for wet samples disaggregated with the ultrasonic bath method, or the riffle splitter for dry samples disaggregated with the SELFRAG method. Aliquots are placed directly into the laser diffraction grain-size analyser for measurement.

Equipment and Techniques Used

Samples were taken from the formations described above and disaggregated. The full method for disaggregation can be seen in **Figure 2**. Equipment used can be seen in **Figure 3**.

Mechanical Disaggregation

Two mechanical disaggregation methods were used in this study: an ultrasonic bath and a SELFRAG machine (**Figure 2**).

Ultrasonic Bath

Ultrasonic baths (**Figures 2**, **3**) use ultrasonic vibrations to break aggregate sediment apart along grain boundaries. Ultrasonic sound waves radiate through the water bath causing alternating higher and lower pressures (**Figure 3C**). During the low-pressure stage, microscopic bubbles form and grow, increasing cracks along grain boundaries until they eventually break apart. This has been used as a rapid and efficient sediment disaggregation method for many decades (Edwards and Bremner, 1967; Walker and Hutka, 1973; Rendigs and Commeau, 1987). There is very low risk of quartz grains being abraded and minor risk for feldspar and mica grains (Hayton, et al., 2001) and, overall, this is considered a gentle method of disaggregation with low risk of breaking sediments beyond grain-boundaries. This method is therefore used as the primary tool for disaggregation and only when unsuccessful should the SELFRAG be used. The steps for disaggregation in the ultrasonic bath method can be seen in the dark blue boxes in **Figure 2**. Samples took from 10 min to 1 h to be disaggregated in total. Despite this method being relatively mild, there is still the possibility that grains are broken down beyond natural grain boundaries and therefore made artificially 'finer' if it is overused (discussed further in "Sensitivity Test"below).

SELFRAG

A SELFRAG is a high-voltage-pulse fragmentation machine (**Figures 2, 3B**). This instrument can generate 90–200 kV with the number of pulses set by the user and is used on samples up to ~1 kg. The sample is placed in a vessel and energy is discharged by electrodes with water used as a conductor. User-controlled

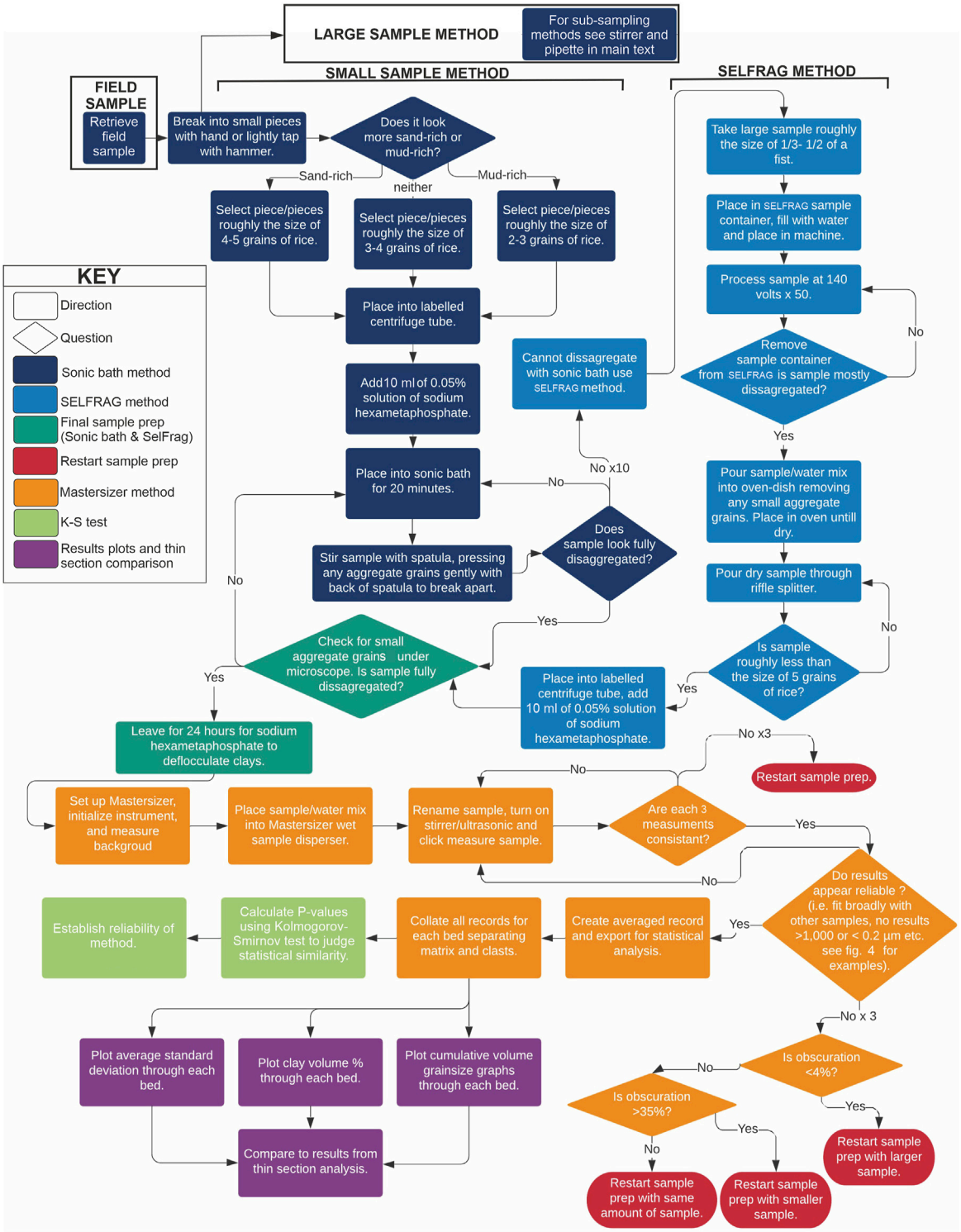

FIGURE 2 | Flow chart depicting entire workflow of study, including sample disaggregation methods, grain-size analysis and data processing. Each method is further explained in the text.

settings are: number of pulses; discharge voltage (90–200 kV), i.e., energy per pulse; electrode gap (10–40 mm); and frequency of discharge (1–5 Hz). It works most efficiently on coarser grain-sizes (van der Wielen, et al., 2013) and was therefore used on sand-rich samples in this study. This method of disaggregation has traditionally been used on ore minerals (Wang, et al., 2011;

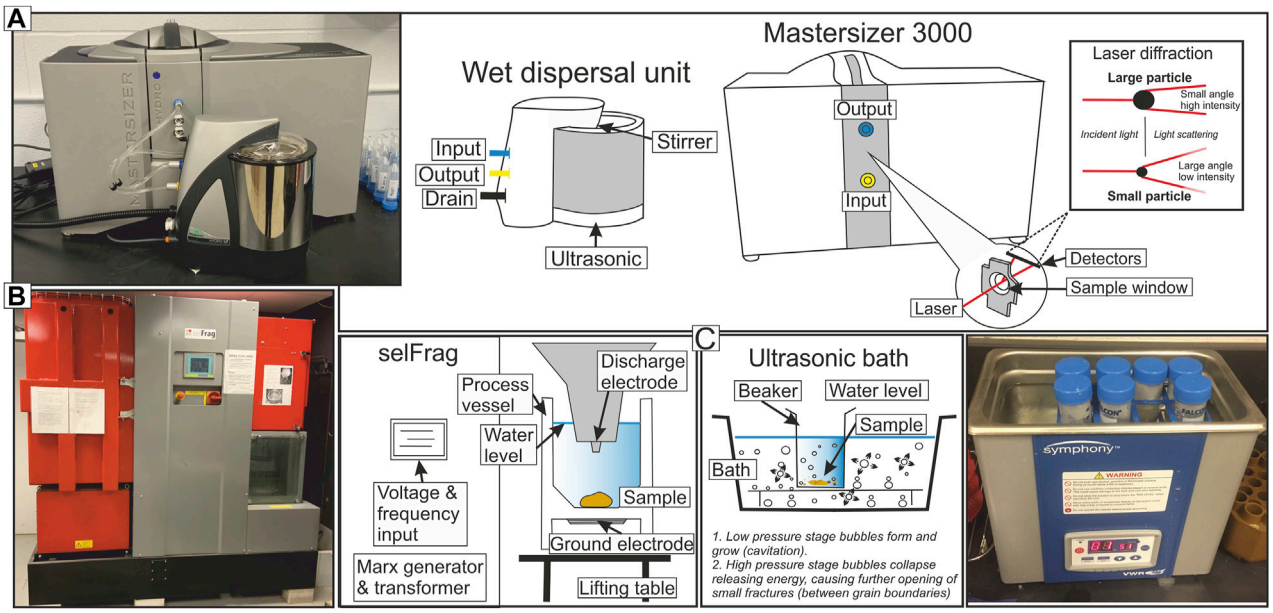

FIGURE 3 | Key equipment used in this study **(A)** Mastersizer 3000 laser diffraction unit with wet dispersal system. **(B)** SELFRAG selective fragmentation machine and **(C)** ultrasonic bath. For use of equipment see methods flow chart in **Figure 2**.

van der Wielen, et al., 2013) and for fossil preparation (Saini-Eidukat and Weiblen, 1996). In this study we started with a lower number of pulses (e.g., 20–50) and discharge voltage (100–140 kV) and repeated as necessary to disaggregate.

Chemical Disaggregation

Sodium Hexametaphospate

Sodium hexametaphosphate (NaHMP) was added to samples after disaggregation in the ultrasonic bath or in the SELFRAG (**Figure 2**). This chemical is commonly used as a dispersant, not only in grain-size separation (Maithel, et al., 2019; Sperazza, et al., 2004) but in pigmenting and dyeing operations, in oil well drilling muds, and as a water softener (van Olphen, 1977; Andreola, 2006). The NaHMP solution separates clay particles, preventing them from bonding together to form 'flocs' through forming soluble undissociated complexes with many cations which prevents the flocculation effects (Wintermyer and Kinter, 1955). In this study we use a solution of 0.5% NaHMP in water, within the range of 0.025–0.06 g per 100 cc (Chilingar, 1952), with roughly 20 ml added to each sample. Samples are left in the NaHMP solution for 24 h before analysis.

Laser Diffraction Analysis

In this study, grain-size analysis was conducted using the Malvern Panalytical Mastersizer 3000 particle size analyser (**Figures 2,3**). Laser-diffraction size analysis is based on the principle that particles of a given size diffract light through a given angle, with the angle increasing as particle size decreases. The Mastersizer 3000 uses two different light sources to analyse the entire granulometric range light sources to analyse the entire granulometric range. In particular, there is a red laser with Ne-He source producing a radiation with 632.8 nm of wavelength and a blue laser emitted by a LED source with a characteristic wavelength of 470 nm. These light sources pass through a sample cell containing an upward moving suspension and the diffracted light is focused onto detectors (**Figure 3A**). The grain-size distribution is calculated from the light intensity reaching the array of detectors. The Mastersizer 3000 uses the full Mie theory to calculate grain-size, which completely solves the equations for interaction of light with matter. Mie theory requires the knowledge of the: Refractive Index (RI) of the grains—this value relates to the speed of light within the material, which in turn allows the degree of refraction (light bending) to be predicted when light passes from one medium to another—and the Absorption Index (AI)—a number that describes the amount of absorption that takes place as the light enters the particle. For this study the value of quartz was used with a RI of 1.54 and AI of 0.01. The size distribution is measured while the suspension is continuously pumped around, which ensures random orientation of most particles relative to the laser beam so that the equivalent spherical cross-sectional diameter is measured. The Mastersizer 3000 measures particles in the range of 10 nm–3,500 µm. This study used a wet-dispersion unit, which circulates the mixture of water and sample through the glass cell. Mie theory also assumes that the particle is spherical, therefore the grain-size results correspond to the equivalent diameter of the sphere of a grain. This means that the same grain-size will be given if two particles have the same volume but vary significantly in sphericity and roundness, allowing for more accurate comparison of grain size within and between samples. This also does not compare directly to sieving because sieving compares the b-axis of grains. The Mastersizer 3000 was set to measure each aliquot three times whilst it circulates through the glass cell, which is standard procedure to ensure that repeated

measurements of the same aliquot are consistent. If these three measurements are consistent with each other, their average is used for analysis. Reasons for inconsistency could be flocculation of clays or dissolution of material during measurement. Dissolution is not relevant here because the sediment is stable, and to prevent clay flocculation during measurement an internal ultrasonic instrument was turned on during measurements. Deionized water was used for sample processing. Although the Mastersizer 3000 is used in this study, our results are broadly applicable to other brands of LPSA instruments.

RESULTS AND METHOD DEVELOPMENT

The ideal grain-size analysis method is one that provides the ability to analyse several hundred samples within a reasonable timeframe, while remaining as accurate as possible. In order to establish the ideal sample preparation and measuring procedure, several different methods of sample preparation are compared. The steps investigated here focus on 1) disaggregation of lithified samples, and 2) subsampling of disaggregated sediment for laser particle size analysis. Disaggregation methods include an ultrasonic bath or high voltage electrical discharges (SELFRAG). Presumably, large samples (~5–10 g when dry) would provide the most representative grain size distributions that span the full range of grain sizes within a given field sample, however, large subsamples typically exceed the obscuration limit (the level at which the lasers can no longer shine clearly through the sample and water mixture) of laser particle-size analysers. Division into aliquots is therefore necessary prior to running samples through the LPSA. Aliquot methods compared below include subdividing lithified samples prior to disaggregation or subdividing wet samples after disaggregation using either a) the stirrer method, or b) the pipette method, described below. A sub-sampling method for dry samples using the SELFRAG method is discussed later.

In order to compare results between various methods, and whether differences between methods is comparable to the natural variability within the samples themselves, we use the two-sample Kolmogorov-Smirnov test (KS test; Chakravarti et al., 1967) to test whether samples are statistically likely to come from the same distribution. In the KS test, the null hypothesis is that both samples come from a population with the same distribution. A high p-value therefore suggests that two distributions could be generated from the same population and a low p-value suggests the distributions are significantly different from each other. The typical significance threshold for p-values is taken as 0.05, however as illustrated by **Supplementary Table S2** the p-values for all samples compared to other samples are quite high (rarely <0.1). This is likely because we are comparing samples with extremely similar distributions to one another, so statistically they are all similar. However, we can qualitatively take the p-values as an indication of how similar the distributions are to one another, with the understanding that small changes in p-value are not particularly meaningful but samples with very low p-values (e.g., $p < 0.3$) are likely less similar than those with very high p-values (e.g., $p > 0.9$).

Obscuration Limits

The suggested obscuration limits for the Mastersizer 3000 are roughly between 8 and 24% (**Figure 4**). The obscuration of the sample depends on the number of grains in the sample. Finer-grained samples therefore provide a higher obscuration for a given sample weight. During the measurements of this study, results were reliable with lower (3–8%) obscuration, especially with mud dominated samples, as well as with a much higher obscuration (up to 45%). Blott et al. (2004) also found that reproduceable results can be obtained with lower than recommended obscuration values. An obvious change within the grain size distribution was observed if obscuration values were too high (**Figure 4**), with results showing an additional smaller peak in grain sizes <0.1 μm, which is considered unreasonably small for these samples because it is not recorded in any reliable measurements. For samples with fewer grains or finer grain-sizes, increasing the measurement time for each sample may help to improve measurement accuracy, however for this study the standard measurement time of 10 s was kept throughout for consistency.

Sensitivity Test

In order to understand the efficacy of the ultrasonic bath in disaggregating sediments, a time trial was undertaken by measuring the grain size of the same sample after increasing intervals of time in the ultrasonic bath (**Figure 5**). This was also important to assess whether the ultrasonic bath was significantly breaking down grains beyond grain boundaries if left in the ultrasonic bath for a longer time period than necessary for disaggregation.

This trial was undertaken with two field samples (**Figure 5**): II B 209 S9 (**Figures 5A–C**), a sand-rich sample from the Castagnola Formation; and V B209 S22 (**Figure 5D**), a more silt-rich sample from the Castagnola Formation. Both samples were calcite cemented. For each of these field samples, a large subsample was put into a beaker with 50 ml of NaHMP solution and placed into the ultrasonic bath. Every 10 min, an aliquot was taken from the beaker and placed into the LPSA for analysis, allowing for comparison of how the grain-size distribution changed with increasing time in the ultrasonic bath. The grain-size curves initially get slightly finer through time, which we interpret as a record of larger grains disaggregating with more time in the ultrasonic bath. Eventually, around 70 min for V B209 S9 and 40 min for II B209 S9, the curves maintain similarity despite additional time in the ultrasonic bath, indicating that the samples are fully disaggregated and the distribution is remaining stable with any additional time in the ultrasonic bath. Moreover, after 20 min for V B209 S9 and 10 min for II B209 S9, the minimum grain size is stable, indicating that clay particles aren't further broken down by further time in the ultrasonic bath and therefore no micro-fragmentation is occurring.

For Field sample II B209 S9, an additional timing test was conducted by taking 4 small subsamples (B—D in

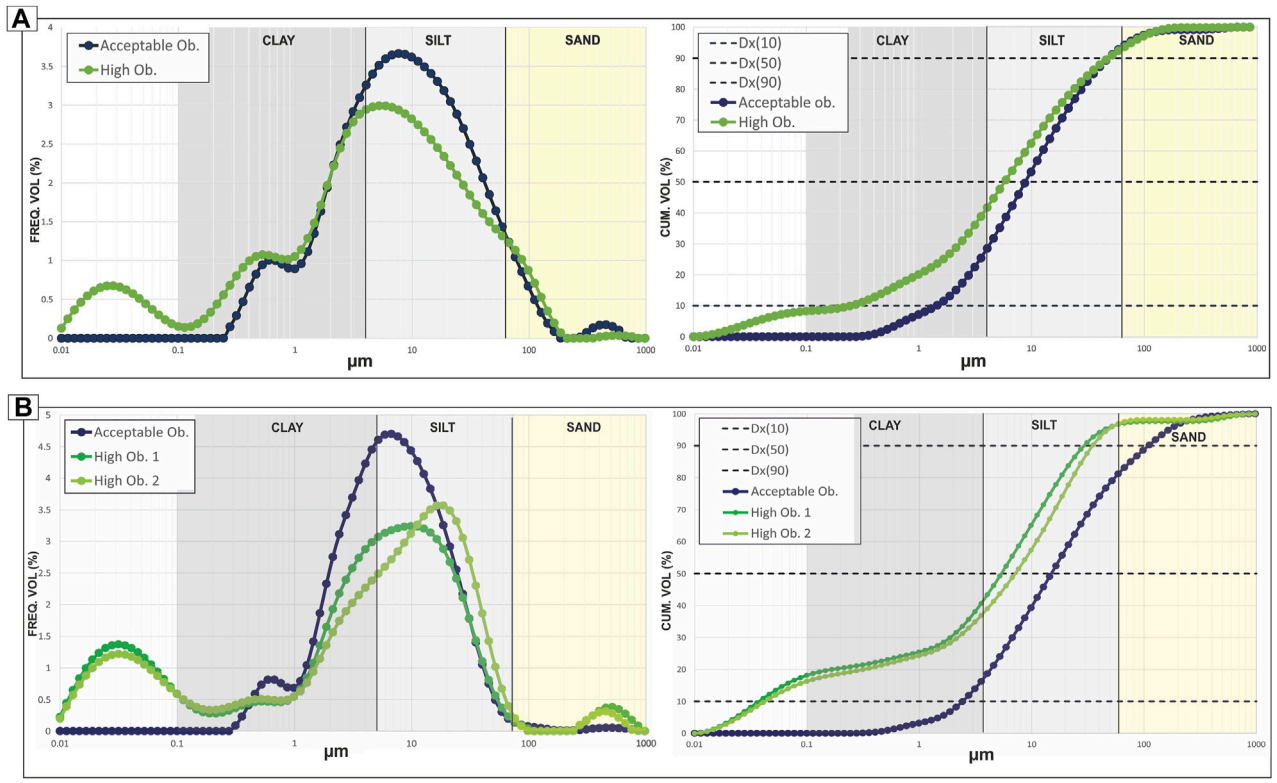

FIGURE 4 | Volume frequency and cumulative frequency graphs showing two versions of the same subsample: the green with too much material added to the Mastersizer, resulting in obscuration that is above reliable measurement, and the blue showing a sample that is within obscuration limits. Data are from the Marnoso-Arenacea Formation. **(A)** Location Coniale 1, Bed 2 (Amy and Talling, 2006), Sample 4, interpreted as a turbidite. The acceptable obscuration in blue is 20.61%, the high obscuration in green is 26.46%. **(B)** Location Coniale 2, Bed 0.4 (Amy and Talling, 2006), Sample 7, interpreted as a hybrid event bed. The acceptable obscuration in blue is 19.74%, the high obscuration examples are 44.21 and 44.66%. For details **Supplementary Table S1**.

Supplementary Table S1) and each small subsample was given 20, 30, 40, and 50 min in the ultrasonic bath, respectively, and placed directly into the LPSA for analysis. This removed any potential bias tied to repeated aliquot sampling but increased potential uncertainty about whether changes in grain size were due to natural sample variability or degree of disaggregation. Overall, very little difference can be seen between the results of these subsamples (**Supplementary Table S1**; **Figure 5B**), showing that after 20 min in the ultrasonic bath the sample is well disaggregated. When the data is examined in detail (**Supplementary Table S1**) some evidence of further disaggregation can be noted; The d_{50} decreases through time from 83 to 65 μm. This change in average appears to be mostly due to a decrease in the larger grains (d_{90}) change from 271 to 255 μm) and to a lesser extent by a slight increase in fines (d_{10}) changes from 5.38–4.8 μm, and increase in clay % from 7.03–8.01%). Despite this overall increase in clay and silt the minimum grain size is stable after 20 min for all samples, indicating that micro-fragmentation and breakdown along grain boundaries is not occurring.

Both sets of tests (A–C and B–D) indicate that the ultrasonic bath effectively disaggregates lithified siliciclastic rocks. Furthermore, there is no apparent concern in "over-sonicating" samples and damaging grains and the length of time needed to fully disaggregate samples will vary based on sample size, lithology, degree of cementation and modal composition. However, care should be taken with biogenic sediments because they may be at greater risk of 'over-sonication'.

Aliquot Methods for Large Subsamples

Large subsamples weighing ~ 5–10 g were used in order to get a representative grain size distribution for measurement. These large subsamples were placed into 50 ml centrifuge tubes with 20 ml of NaHMP solution, disaggregated with the ultrasonic bath method (**Figure 2**), and left for 24 h. These subsamples were too large to be processed in one pass with the Mastersizer 3000 because they would increase the obscuration beyond measurable levels (see above). Two aliquot sampling methods were therefore tested for wet dispersions and the average of all measured aliquots for a given large subsample were compared to one another in order to establish the reliability of each method.

The two aliquot sampling methods used were the stirrer method and the pipette method, outlined below.

Aliquot Sampling Method

The challenge of extracting representative aliquots from samples is not trivial, and a consistent methodology does not exist within the sedimentology community. Two common aliquot sampling

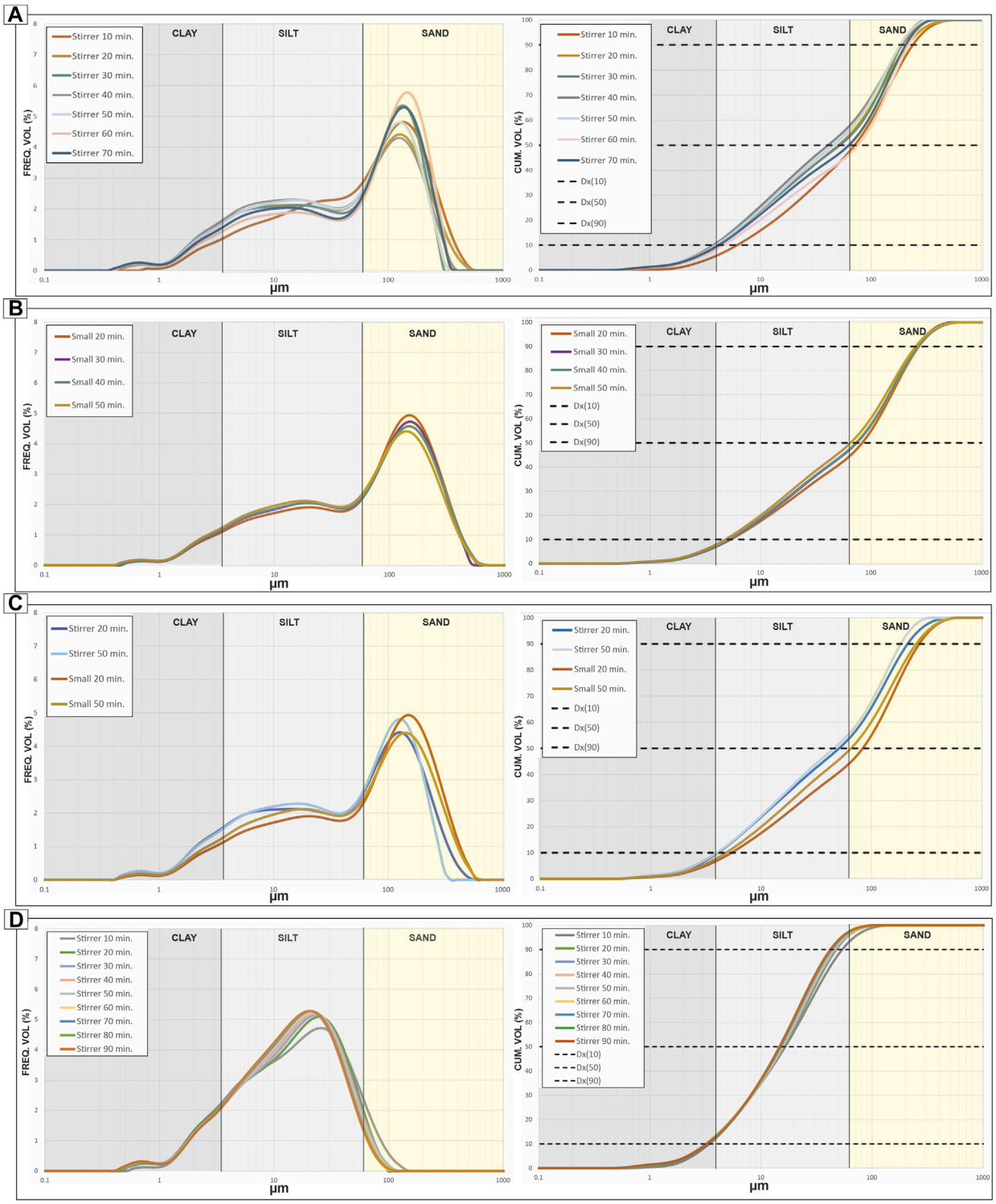

FIGURE 5 | Volume frequency and cumulative frequency graphs showing timing tests for sub-samples and aliquots processed using the ultrasonic bath method. **Supplementary Table S1** for full data results. **(A)** Field sample II B 209 S9, Large Subsample A- aliquots extracted using the stirrer method every 10 min to establish how the result changes with more time disaggregating in the ultrasonic bath. **(B)** Field sample II B209 S9, Subsample B,C,D,E - Small subsamples, sample tested every 10 min from 20 min to establish how result changes with more time in the ultrasonic bath disaggregating. **(C)** Comparison of results from **(A,B)** to demonstrate similarities and differences. **(D)** Field sample V B209 S22, Large Subample - aliquots extracted using the stirrer method, testing one sample every 10 min to establish how the result changes with more time disaggregating in the ultrasonic bath.

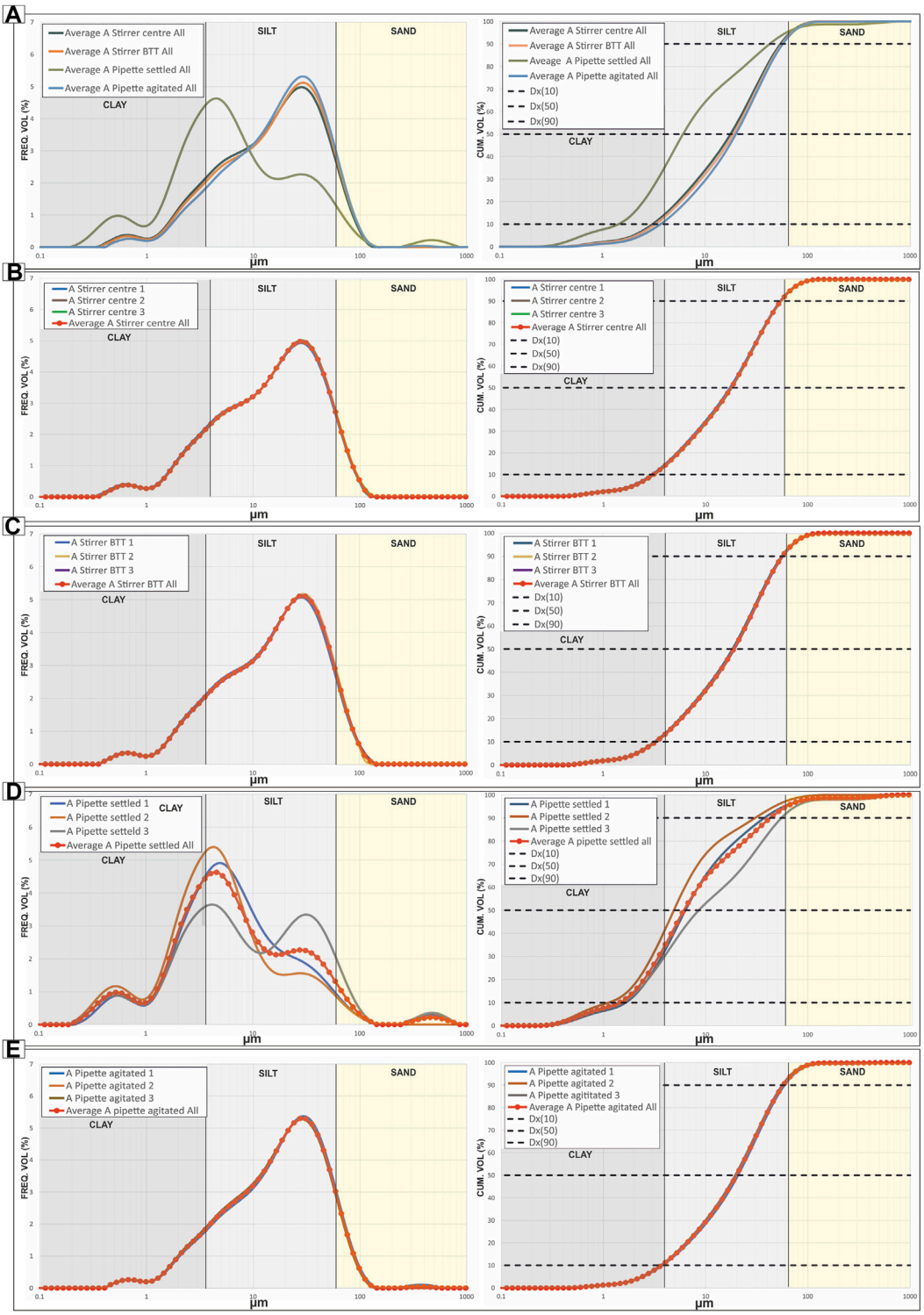

FIGURE 6 | Volume frequency and cumulative frequency of aliquots for mud-rich field sample V B209 S22 using various trial methods. See text for full details. **(A)** Average results for all trial methods for comparison. **(B)** Individual results and average for the 'Stirrer centre' method. **(C)** individual results and average for "Stirrer base to top" method. **(D)** Individual results and average for 'Pipette settled' method. **(E)** Individual results and average for 'Pipette agitated method'. For full data **Supplementary Table S1**, for corresponding *p*-values **Supplementary Table S2**.

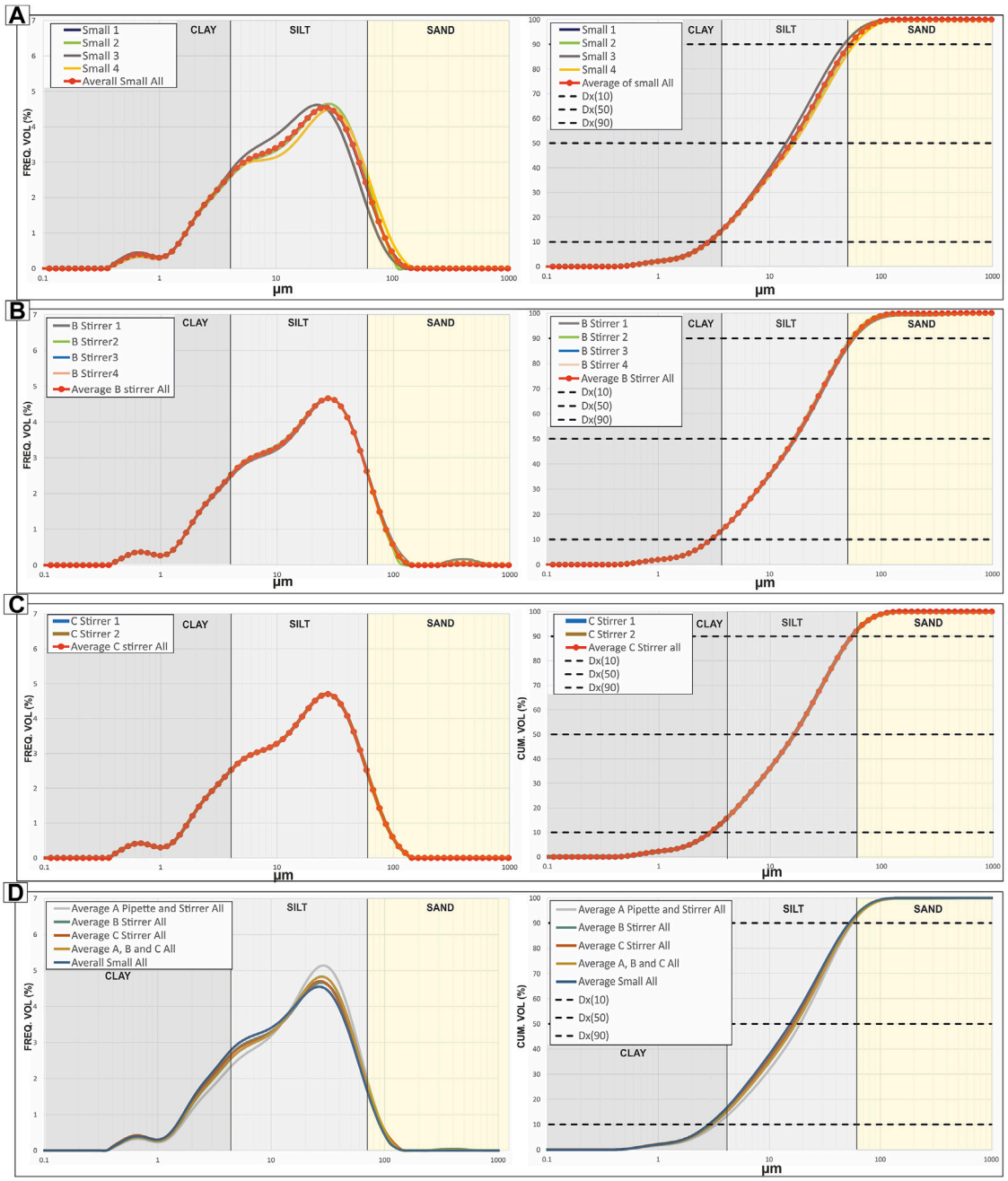

FIGURE 7 | Volume frequency and cumulative frequency of aliquots for mud-rich field sample V B209 S22. These are further tests using the stirrer method and small samples to compare to subsample A results in **Figure 6**. **(A)** Small sub-samples D, E, F, G and average small sample result. **(B)** Sub-sample B, Stirrer aliquots 1-4 and average of aliquots. **(C)** Sub-sample C, Stirrer aliquots 1 and 2, and average of both aliquots **(D)** Averages of subsamples A, B and C, compared to an average of all of these sub-samples and an average of the small samples. For detailed results **Supplementary Table S1**, for *p*-values **Supplementary Table S2**.

methods are evaluated here: the pipette method, in which a pipette is used to agitate and then extract material from a centrifuge tube, and the stirrer method, in which the samples are placed in a beaker and a magnetic stirrer creates a suspension from which aliquots are extracted. These methods are explained in more detail below. In order to validate both the pipette and stirrer methods, two different forms of each method were evaluated using field sample V B209 S22 from the Castagnola Formation (**Figure 6**). This sample was collected from an argillaceous section at the top of a hybrid event bed (H5 of Haughton et al., 2009). Results are documented in **Supplementary Table S1**; **Figures 6**, **7**. Three large subsamples (A, B, and C) were used for method comparison (**Figure 7**).

Trial 1: Stirrer "Centre"
Subsample A was placed in a beaker with a NaHMP solution and mixed with a magnetic stir plate. The rotation of the stirrer was increased until all grains appeared to be in suspension. A 7 ml pipette with a 3 mm opening was used to extract an aliquot, approximately halfway up the sediment/water mixture and halfway between the centre and the outer edge of the beaker. Three aliquots were measured for comparison.

Results (**Supplementary Table S1**; **Figure 6B**): All recorded parameters for aliquots A Stirrer Centre 1, two and 3 are very similar. Calculated *p* values between the three aliquots (**Supplementary Table S2**) give values of 0.9999–1.0000 (at 4 decimal places), showing this method to be highly replicable.

Trial 2: Stirrer "Base to Top"
Stirring plates were set up as above, with the remaining subsample A prepared in a beaker and the rotation of the stirrer increased until all grains appeared to be in suspension. A 7 ml pipette with a 3 mm opening was then used to extract an aliquot by placing it halfway between the centre and outer edge of the beaker and sampling while moving it upwards from the base to the top of the beaker.

Results (**Supplementary Table S1**; **Figure 6C**): All recorded parameters for aliquots "A stirrer base to top" 1, 2 ,and 3 are very similar. Calculated *p* values (**Supplementary Table S2**) give values of 0.9999–1.0000. This shows this method to be highly replicable. When comparing between the "centre" and 'base to top' methods, *p* values are between 0.9956 and 1.0000, with a *p* value between the averages of each method of 1.0000. Therefore, little difference can be noted between these two methods for aliquot sampling, and both are replicable and representative of the subsample. This also suggests that potential grain-size stratification within the suspension was not significant.

Trial 3: Pipette "Settled"
Grains were left to fully settle to the base of the of the beaker, without any stirring. A 7 ml pipette with a 3 mm opening was inserted into the base of the mixture and whilst collecting the sample slowly moved upwards until the pipette was out of the sediment/water mixture.

Results (**Supplementary Table S1**; **Figure 6D**): Results from this method ('A Pipette settled' 1, 2 and 3, **Supplementary Table S1**; **Figure 6D**) were highly variable. The d_{50} results were considerably lower when compared to both stirrer methods, with the clay content up to 28% higher than in the stirrer method. *p* values for comparisons between samples (**Supplementary Table S2**) are 0.2713–0.4938. This is still above the 0.05 range suggesting that these results are not statistically significantly different, but is less so than the other trialled methods. Therefore, this method is considered less reliable and replicable.

Trial 4: Pipette "Agitated"
For this trial, the remainder of subsample A was placed into a 50 ml centrifuge tube. A 7 ml pipette with a 3 mm opening was inserted into the mixture and pumped vigorously and continuously until all sediment was in suspension. An aliquot was then quickly taken by moving the pipette from the base of the centrifuge tube upwards through the mixture while sampling.

Results (**Supplementary Table S1**; **Figure 6E**): All parameters from aliquots 'A pipette agitated' 1, two and 3 are very similar. Calculated *p* values (**Supplementary Table S2**) between aliquots are 0.7695–1.0000. So, although this method is not as replicable as either stirrer method, it is still sufficiently replicable. When compared to the pipette settled method, *p*-values are 0.0219–0.1317 ranging below the 0.05 limit of statistical significance, again indicating that the Pipette settled method is less reliable.

Outcomes From Aliquot Trial Methods

Overall, the "centre" method for the stirrer and the 'agitated' method for the pipette are the most replicable methods for the stirrer and pipette, respectively (**Figure 6A**). These are therefore the methods used when "pipette" and "stirrer" methods are referred to hereafter. Because the stirrer method was the most replicable, additional subsamples (B & C) were used to re-test this method for comparison and to further interrogate its reliability.

Additional Stirrer Samples

Subsamples B and C (**Supplementary Table S1**) were taken from field sample V B209 S22 for further testing using the stirrer (centre) method (Table 1; **Figures 7B–D)**.

Comparisons of aliquot results between subsamples A, B, and C show very little difference in d_{50} or any other measured parameters (**Supplementary Table S1**). An anomaly is seen in the Average Standard Deviation (ASD) of B stirrer 1, which may be due to an anomalously large grain incorporated into this first pipette aliquot, but it does not seem to have significantly altered the d_{90} (57.5 μm compared to average 54.9 μm values) or clay and silt percentages (92.00 compared to 93.12%). This is further distinguished by the *p*-values in B Stirrer one compared to all other B aliquots, which range from 0.3722–0.4938, whereas comparisons between B aliquots 2, 3 and 4 provide *p*-values of 1.000 (**Supplementary Table S2**). This indicates that averages of multiple aliquots are important to avoid any small anomalous results likely due to picking up one or two large grains.

p-values comparing "A stirrer (centre)" average and "C stirrer (centre)" average are 0.9999 (**Supplementary Table S2**). When A Stirrer and C Stirrer are compared to the B Stirrer average values the *p*-value is from 0.4938 to 0.6307 (**Supplementary Table S2**), due to the issue with the 1st aliquot in B. Overall, this stirrer method is still judged to be reliable, but care should be taken and multiple aliquots should be used and averaged to reduce risk of anomalous grains skewing results.

Small Subsample Comparison

Small Subsample Method

When evaluating aliquot sampling methods, it is important to understand natural variability within samples in order to ensure that changes are due to sampling methods and not real variability between subsamples. As discussed above, large subsamples (roughly 5–10 g) were used initially to get a representative sample that might account for slight heterogeneity within samples. Next, we investigate measurement differences between disaggregating smaller

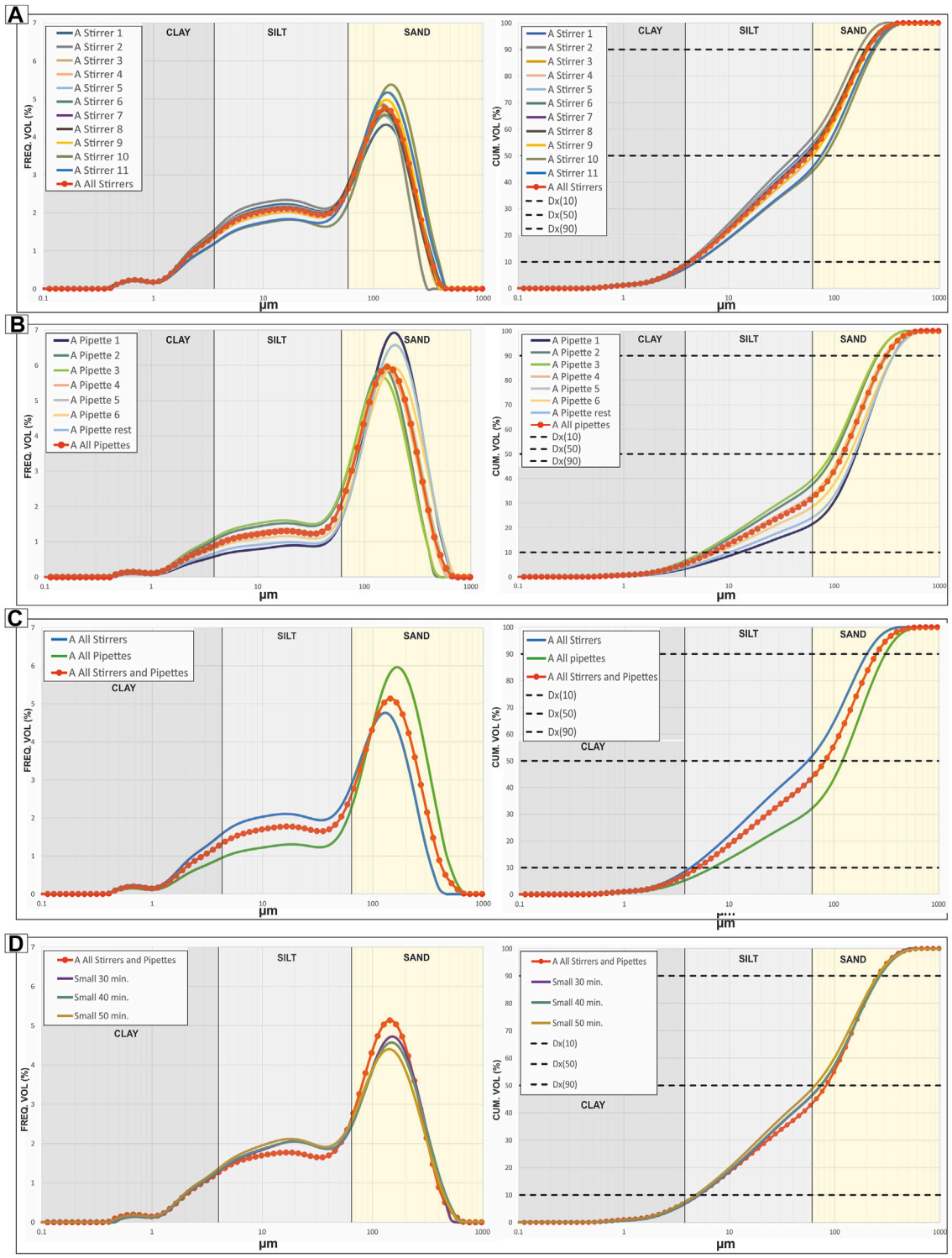

FIGURE 8 | Volume frequency and cumulative frequency graphs showing aliquots for sand-rich field sample II B209 S 9, Sub-sample A, showing aliquots from the establish Pipette and Stirrer methods. **(A)** Stirrer aliquots 1–11 and average of all stirrer aliquots. **(B)** Pipette aliquots 1–7 and average of all pipette aliquots. **(C)** Comparison of stirrer and pipette averages and averages for all sub-sample A aliquots. **(D)** Average of all subsample A stirrers and pipettes compared to 3 small samples (taken from the time test in **Figure 5**). For detailed results **Supplementary Table S1**, for *p*-values **Supplementary Table S2**.

subsamples (0.2–2 g) that could be run in one batch and do not require aliquot subsampling, therefore speeding up the measurement process and potentially reducing bias introduced during the extraction of aliquots. Small subsamples ranging from 0.2 to 2.0 g were taken from field samples, with sandier samples on the large end of that range and muddier samples on the small end because mud and silt have a greater effect on obscuration and therefore require less material for measurement (**Figure 2**). These samples were placed in a small centrifuge tube (15 ml) along with 10 ml of NaHMP solution. The centrifuge tubes were placed in the ultrasonic bath until the samples were fully disaggregated (**Figure 2**). Disaggregation was determined by eye and by inspection under a microscope. The samples were then left for 24 h to ensure clays were deflocculated. Results for this method were compared to the average of subsamples for the "large subsample" methods above in order to compare natural variability between samples in the absence of any potential biases introduced through aliquot subsampling.

Small Subsample Results

Four small subsamples were taken from the same field sample used in previous trials, V B209 S22, designated D, E, F and G (Table 1; **Figures 7A,D**). These four small subsamples showed little variation from each other in d_{50} (varying from 16.2 to 17.1 μm) or the clay percentage which varied from 15.48 to 16.48% (**Supplementary Table S1**). KS test comparisons between the small samples provided *p*-values ranging from 0.9956 to 1.000 (**Supplementary Table S2**).

The small samples have very similar d_{50} values to the stirrer results from subsamples A, B and C. KS test comparisons between small subsamples (D–G) and stirrer samples A and C provide *p*-values greater than 0.9956. When compared to stirrer sample B, the *p*-values range from 0.2713 to 0.6307, again due to the issues with the first aliquot from the B sample. Overall, this indicates that the small subsample method is as reliable as the large subsample method, provided that the field samples are relatively homogenous. It also does not risk the inaccuracies incurred in the aliquot sampling for the stirrer method (i.e. B Stirrer 1).

Applicability to Sand-Rich Samples

Having validated the best methods for aliquot subsampling and compared these to the small sub-sample method, we now explore the utility of each method with a more sand-rich sample, which may be more susceptible to aliquot biases due to the difficulty in suspending coarser grains. Small and large subsamples were taken from the field sample II B209 S9 (**Figure 8**; **Supplementary Table S1**), which is from a dewatered, clast-rich lower division (H1b) of a hybrid event bed (Southern et al., 2015).

Three small samples were analysed to provide context for the natural variability within the field sample and to provide a baseline for comparing potential biases introduced with the stirrer and pipette aliquot methods. The small subsamples are overall consistent with one another (**Supplementary Table S1**; **Figure 8D**), with *p*-values ranging from 0.8887 to 0.9998 (**Supplementary Table S2**) and allow for comparison between pipette and stirrer aliquot methods extracted from a large sub-sample.

From a large subsample (subsample A), 11 aliquots were extracted using the stirrer method (**Figure 8A**) and seven aliquots using the pipette method (**Figure 8B**). Overall, the stirrer method slightly underestimates the grain size and the pipette method slightly overestimates the grain size (**Figure 8C**) when compared to the small samples, which we take here as a representative 'true' distribution of the field sample. A general increase in d_{50} can be noted from the stirrer method aliquots 1–11, ranging from 42.7 to 75.6 μm, however these values are still much lower than the average d_{50} value of 121 μm from the pipette method aliquots (**Supplementary Table S1**). The increasing trend in d_{50} values with continued aliquot sampling is likely due to the tendency for this method to preferentially select finer grains that are more easily-suspended, meaning that continued sampling results in distributions becoming progressively coarser. However, this trend is subtle compared to the differences between the pipette and stirrer methods and the averages of all stirrer and pipette aliquots highlight the tendency for the stirrer method to preferentially select clay and silt while the pipette method preferentially selects sand-sized particles.

The stirrer method is slightly more replicable than the pipette method (**Figures 8A–C**), however both methods appear to be internally consistent; Grain-size distributions of aliquots sampled from sand-rich samples with the same method—either pipette or stirrer—come with their own biases. Pipette method aliquots are slightly coarser than the average of the whole sample and stirrer method aliquots are slightly finer (**Figure 8C**). Each method is potentially sufficient depending on whether the focus of the analysis is on fine- or coarse-grained constituents and results from different methods should be compared with caution.

p-values (**Supplementary Table S2**; **Supplementary Material S1**) are generally lower for the sand-rich sample (II B209 S9), particularly when compared to the average of all samples. However, many of the stirrer aliquots had high *p*-values ($p > 0.6$), particularly those that were sampled in close succession (**Supplementary Table S2**). The pipette aliquot comparisons show lower *p*-values, with most aliquot comparisons showing $p < 0.2$ and many with $p < 0.05$ (**Supplementary Table S2**).

A Note on Sample Heterogeneity

To further validate the comparisons between the stirrer, pipette and small subsample methods, analysis was undertaken using a mud-rich sample from the more lithified Marnoso-Arenacea Formation. Field sample C2 B0.4 S7 was taken from the upper mud-rich H5 division (Haughton et al., 2009) of a hybrid event bed. Importantly, this interval is also affected by bioturbation, with sand-filled burrows infilled during emplacement of the bed above. Burrows themselves were not sampled but some contamination was possible. From this field sample, two large subsamples were taken (A and B) and were analysed using both the stirrer and pipette aliquot methods, and 5 small subsamples were taken (C—G) in order to provide a baseline for natural variability within the field sample.

Small subsamples (placed directly into the LPSA with no aliquot subsampling) show significant variability between one another (**Figure 9**; **Supplementary Table S1**). With the exception of small samples E and F, which are very similar to each other, the

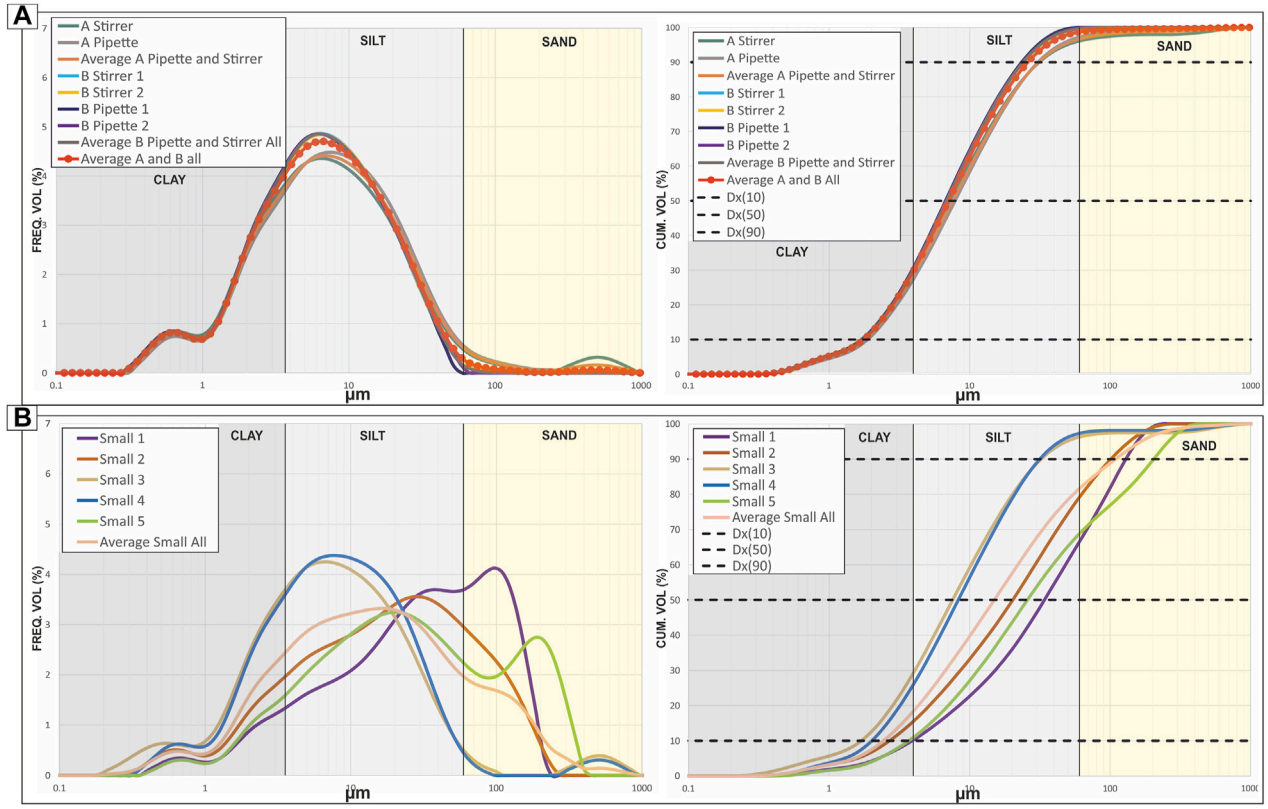

FIGURE 9 | Volume frequency and cumulative frequency graphs for field sample C2 B0.4 S7. **(A)** Results from subsample A, pipette and stirrer, with average, and sub-sample B stirrer 1 and 2 as well as pipette 1 and 2, with average. An average for both sub-sample A and B combined is also shown. **(B)** Results for small sub-samples A, B, C, D, E, F, corresponding names small sample 1-5 and an average of all combined. For detailed results **Supplementary Table S1**, for *p*-values **Supplementary Table S2**.

small subsamples have very different distributions from one another. The mud content in these samples ranges from 67.7 to 97.5% and the d_{50} values range from 8.3 to 34.1 µm. This natural variability within a single field sample highlights the extent to which small-scale heterogeneity can drastically affect grain-size results. Analysing several small subsamples can provide context for how much variability there may be within a single field sample, which in this case can be attributed to the fact that this sample comes from a debritic bed that is bioturbated. Debrites are inherently heterogeneous and bioturbation can add an additional level of variability within field samples. One way to account for sample heterogeneity is to disaggregate larger samples, which may span a wider range of grain sizes and may capture a broader picture of the outcrop itself.

Two large subsamples were disaggregated and analysed using the stirrer and pipette aliquot methods. Subsample A was processed as two aliquots: A stirrer and A pipette (**Supplementary Table S1**), all parameters measured were very similar except for the ASD which is significantly higher for the stirrer aliquot. Visual comparison of the stirrer and pipette aliquots from subsample A show very consistent results between the two methods (**Figure 9**) and the KS test provides a *p*-value of 0.6307 for these distributions. Four aliquots were extracted from subsample B: two stirrer aliquots and two pipettes. The parameters measured for this sub-sample are also very similar between aliquots. Accordingly, the P-vales are between 0.8888 and 1.000. Both subsample A and B are similar to the small samples E and F described above, and both aliquot sampling methods are consistent within each sample, again suggesting that either method can provide dependable results in mud-rich samples.

Comparison of Ultrasonic Bath to SELFRAG Disaggregation

Although the ultrasonic bath is a very useful method for disaggregating most samples, some well lithified samples with quartz cement (such as some from the Gottero Formation) were difficult or sometimes impossible to disaggregate through this method. A SELFRAG machine was utilized to disaggregate these more lithified samples. In order to establish how replicable the SELFRAG disaggregation method is, a sample from each of the 3 formations (Gottero, Marnoso-Arenacea and Castagnola), which vary in lithology and lithification, were compared to corresponding small subsamples disaggregated in the ultrasonic bath.

Method

In order to compare to the samples disaggregated using the ultrasonic bath method, three samples were disaggregated using the SELFRAG method (**Figure 2**). A significantly

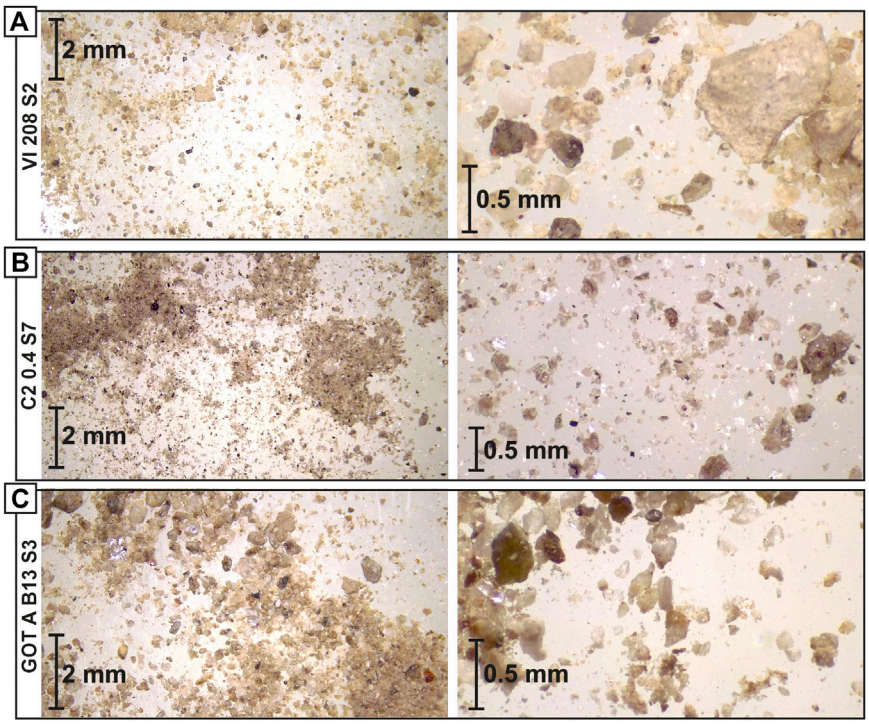

FIGURE 10 | Photos taken under magnification of three samples disaggregated in SELFRAG, results shown in **Figure 11**. **(A)** Sample from Marnoso-Arenacea Formation **(B)** sample from Gottero Formation and **(C)** sample from Castagnola Formation. For data **Supplementary Table S1**.

larger subsample was selected (roughly 25–100 g) and placed into the SELFRAG vessel and filled with water. The voltage (140 v) and number of discharges (50) was selected for the SELFRAG and the machine was activated. This was repeated until samples were sufficiently disaggregated, determined by feeling with a hand, and the sediment-water mixture was placed into the oven to dry. Dry samples were poured through a riffle splitter until they were deemed of sufficient size to be within obscuration limits for the Mastersizer 3000. This aliquot was then placed into a small centrifuge tube (15 ml) along with 10 ml of NaHMP and left for 24 h to deflocculate clays. Samples were checked under the microscope for disaggregation. These aliquots were then placed into the ultrasonic bath for a few minutes before measurement in the LPSA.

Results Castagnola Formation- VI 208 S2

Results from the three formations vary significantly. The poorly lithified formation (Castagnola Formation; **Figures 10A**, **11A**), shows variable consistency between SELFRAG samples, with *p* values varying from 0.1317 to 1.0000. When compared to an average of small samples, SELFRAG samples S1-3 results are relatively similar in d_{10}, d_{50} and d_{90} values (**Supplementary Table S1**; **Figure 11A**). *p*-values between the small sample and SELFRAG samples range from 0.4938 to 0.6307 (**Supplementary Table S2**). These results suggest there is some inconsistency in the SELFRAG preparation method, but overall, they compare well to an average of small samples from the SELFRAG method (**Figure 11A**).

Results Marnoso-Arenacea Formation- C2 B0.4 S7

The formation with an intermediate lithification (Marnoso-Arenacea Formation, **Figures 10A**, **11B**), shows consistency between SELFRAG samples, with *p*-values between 0.8888 and 0.9999 (**Supplementary Table S2**).

When compared to an average of small sample, SELFRAG samples S1-3 shows more significant variation. The d_{10} and d_{50} values are relatively similar, particularly between the average small subsample and Selfrag S3 sample, but the d_{90} values are significantly lower for the small sample as is the ASD (**Figure 11B**; **Supplementary Table S1**). Therefore, either the SELFRAG samples are not sufficiently disaggregated during processing, or the small subsample is not capturing the largest grain sizes in the field sample. *p*-values between the small sample and SELFRAG samples are 0.0878–0.3722.

Results Gottero Formation- GOT a B13 S3

The most lithified formation (Gottero Formation, **Figures 10C**, **11C**), shows variability between SELFRAG samples 1–3, with *p* values varying from 0.0130 to 0.4938 (**Supplementary Table S2**). When comparing these SELFRAG samples to an average of small subsamples, d_{50}, d_{90} and d_{10} values for the SELFRAG samples are all significantly higher than for the small subsamples. Again, the higher d_{90} value indicates that the SELFRAG samples are not sufficiently disaggregated during processing, or the small sample is not capturing the largest grain sizes in the field sample. The lower percentages of silt and clay volume for the SELFRAG samples, may be an indication that the SELFRAG is not sufficiently separating the finer portion from these well lithified samples. *p*-values between the small sample and SELFRAG samples show 0.0878–0.7695.

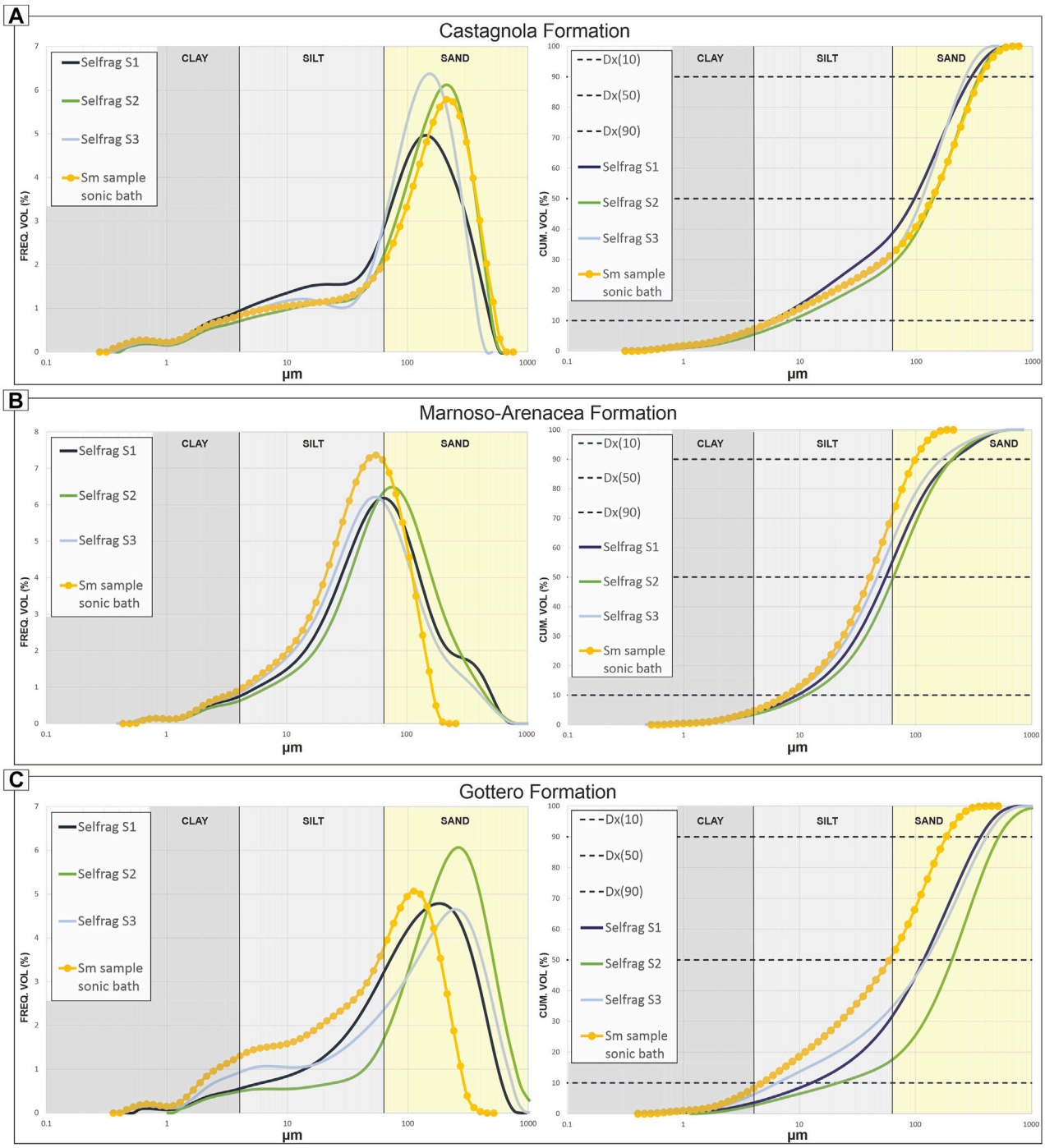

FIGURE 11 | Volume frequency and cumulative frequency graphs for field sample showing comparison of samples disaggregated in SELFRAG and split with a riffle splitter (see text for details) and small subsample (yellow). **(A)** Example from the Castagnola formation, VI 208 S2 from the lower H1 division of a hybrid event bed. **(B)** Example from the Marnoso-Arenacea Formation, Location Coniale 2, Bed 0.4 (Amy and Talling, 2006), Sample 7, interpreted as part of the upper debritic portion of a hybrid event bed. **(C)** Example from the Gottero formation, GOT A B13 S3 from the matrix of a debritic portion, H3, of a hybrid event bed. For detailed results **Supplementary Table S1**, for *p*-values **Supplementary Table S2**.

Recommendations

Overall, there is a general trend that the poorly lithified formation is efficiently disaggregated using the SELFRAG method, but the formation of intermediate lithification and the more lithified formation show more variability in statistical similarities. For the latter two formations, this trend is particularly noticeable in the d_{90} values, which are significantly higher for the SELFRAG

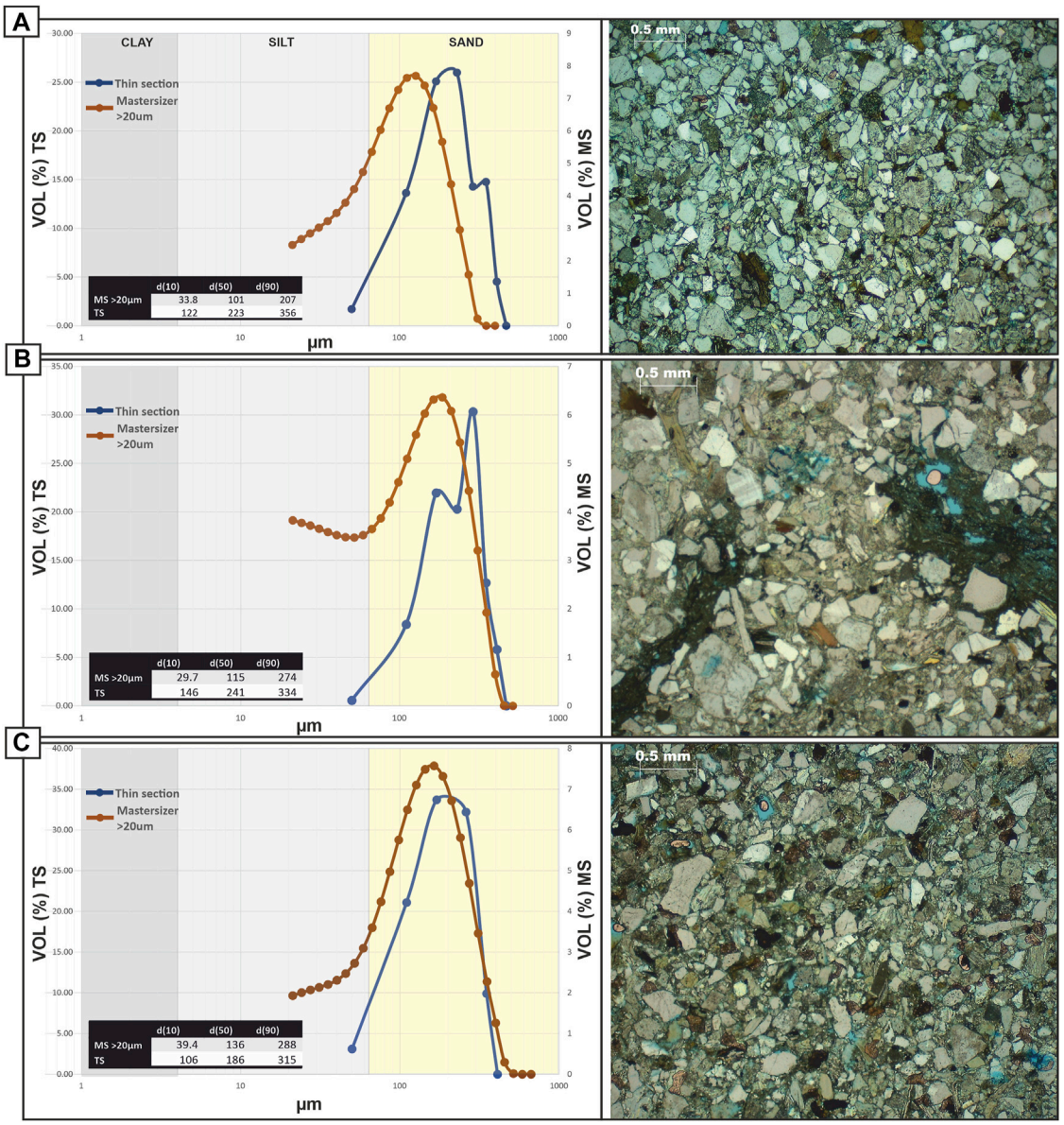

FIGURE 12 | Volume frequency graphs from Mastersizer data compared to volume frequency graphs plotted from thin section measurement. The grain-size at the 10th, 50th and 90th percentile for the Mastersizer curve (MS) and from thin-section (TS) are shown in the inset graph. Data less than 20 µm were removed from the Mastersizer for more accurate comparison with thin section. Representative photos are shown for each thin section. **(A)** Example from the Marnoso-Arenacea Formation, location Coniale 1 (**Figure 1B**), bed 2, sample 1, collected from a sand-rich turbidite (Amy and Talling, 2006). **(B)** Example from the Marnoso-Arenacea Formation, location Coniale 2 (**Figure 1**), bed 1, sample 5B, collected from a clast within a hybrid event bed (Amy and Talling, 2006). **(C)** Example from the Castagnola Formation from log IV, bed 210 (**Figure 1B**), sample 5, collected from the sand-rich base of a hybrid event bed (Southern et al., 2015).

samples. This indicates that either the SELFRAG is not sufficiently disaggregating the most lithified samples or that the small samples from the most lithified formation are not accurately including the full range of grain sizes in the sample, particular the coarse grain-sizes. Further samples are needed to establish this. As this method could be highly beneficial for use with samples too cemented to be disaggregated in the sonic bath, this method is still recommended for use when necessary but must be used with caution and some trial for reproducibility.

Comparison to Thin Section Grain-Size Analysis

Method

Three samples are used to compare thin-section analysis with laser particle-size analysis: two from the Marnoso-Arenacea Formation and another from the Castagnola Formation (**Figure 12**). Three to five images were analysed for each thin section by measuring the long and short axes of individual grains. A grid was displayed over each image and each grain at the intersection of the vertical and

horizontal lines was measured in order to assure grains were randomly selected. This measurement was undertaken manually by one single user for consistency of method.

Grains from thin section are not a direct comparison to those from laser diffraction analysis because Mie theory gives results as volume equivalent spheres. Therefore, we can assume that a volume calculated from long and short axis measurement from the thin section will only show an approximation for any individual grain compared to the laser diffraction analysis. Due to the random cut of thin sections through grains, it is unlikely that the true long axis or short axis is captured. Long- and short-axes for 152–376 grains were measured for each thin section. To estimate the volume of each grain, the long axis was used as length, the short axis as the height and short axis again as the depth. The volumes were used to calculate a volume percentage of the whole for each grain in order to compare more directly with LPSA results. Grains were grouped into bins of 60 μm starting from 20 μm which was selected as the smallest reliable measurable value in thin-section. Results were then plotted at the midpoint for each distribution. There is some error involved in the comparison of volume distribution graphs between thin-section and LPSA results due to the large size of these bins.

Additionally, there is some human error involved in the manual measurement of grain-size in thin section. No grains under 20 μm were measured and grains under 100 μm are likely significantly underrepresented due to difficulty recognising and measuring these smaller grains. In order aid comparisons, LPSA results have been recalculated omitting grains <20 μm, therefore simulating measurements where finer grains are unmeasured. These LPSA curves are then compared to the thin section results (**Figure 12**). Unlike the LPSA samples, where calcite cement may have dissolved in the preparation process or be disaggregated, cement is still present in the thin sections. This cement is identified using cross-polarised light and therefore omitted from any measurement.

Results of Comparison

Thin Section 1- Marnoso-Arenacea Formation (Bed 2, Turbidite).

This section is the from the Marnoso-Arenacea Formation, location Coniale 1 (**Figure 1B**), bed 2, sample 1, collected from a sand-rich turbidite (Amy and Talling, 2006). Grain size curves and d_{10}, d_{50} and d_{90} values are shown in **Figure 12A**.

Description

Grain size curves are broadly similar for the coarser values, although a distinct finer tail can be shown in the LPSA data, which is not seen in the thin section data (**Figure 12A**). The thin section curve is shifted coarser by 60 μm for the silt to very fine sand component and 10 μm for the fine to coarse sand component, with the peak shifting 100 μm coarser for the thin section data (from very fine to fine sand). The d_{10}, d_{50} and d_{90} values are all significantly higher for the thin section compared to the LPSA (**Figure 12A**). The d_{10} value varies from coarse silt in the LPSA results to very fine sand in thin section. The d_{50} value varies from very fine sand in the LPSA results to fine sand in the thin section. The d_{90} value varied from fine sand in the LPSA results to medium sand in the thin section.

Thin Section 2- Marnoso-Arencea Formation, Clast (Bed 1, Hybrid Event Bed).

This section is the from the Marnoso-Arenacea Formation, location Coniale 2 (**Figure 1B**), bed 1, sample 5B, collected from a rip-up clast within a hybrid event bed (Amy and Talling, 2006). Grain size curves and d_{10}, d_{50} and d_{90} values are shown in **Figure 12B**.

Description

The grain size curves are broadly similar shapes for the coarser grain-size fraction (>100 μm) but differ significantly for the finer fraction (<100 μm). The data from the LPSA and the thin section indicate that this sample has a larger portion of clay and silt grains compared to the previous sample (**Figure 12A**). The finer tail and significant silt portion shown in the LPSA curve are not seen in the thin section curve. The grain sizes greater than 300 μm are a similar volume distribution for both the LPSA and thin section curves. A double peak is seen in the thin section curve that is not apparent in the LPSA curve. The tallest peak is around 100 μm coarser for the thin-section curve (from fine to medium sand). The d_{10}, d_{50} and d_{90} values are all significantly higher for the thin section compared to the LPSA, with the d_{10} value varying from medium silt in the LPSA to fine sand in thin section and the d_{50} value varying from very fine sand in the LPSA to fine sand in the thin section. The d_{90} is medium sand for both the LPSA and the thin section curves.

Thin Section 3- Castagnola Formation (Bed 210, Hybrid Event Bed).

This sample is from the Castagnola Formation from log IV, bed 210 (**Figure 1B**), sample 5, collected from the sand-rich base of a hybrid event bed (Southern et al., 2015). Graph of data and d_{10}, d_{50} and d_{90} values are shown in **Figure 12C**.

Description

The LPSA and thin-section curves are broadly similar shapes for the coarser portion, with the thin section missing the finer tail present in the LPSA curve (**Figure 12C**). Both curves have peaks at fine sand grain sizes. Like the previous examples, the d_{10}, d_{50} and d_{90} values are all higher in the thin section analysis, although they are most similar out of all three examples. The d_{10} value varies from coarse silt in the LPSA to very fine sand in thin section. The d_{50} value is fine sand for both the LPSA and thin section curve. The d_{90} is medium sand for both the LPSA and the thin section curve.

Interpretation

Overall, there are significant differences between the LPSA and thin section grain-size distributions. Most importantly, the thin section curves are missing the finer tail present in the LPSA data and correspondingly all graphs show significantly coarser d_{10}, d_{50} and d_{90} values. Major differences between LPSA and thin section results could arise from difficulty in measuring small grains in thin section, volume approximation methods, spherical grain assumptions made by the LPSA, and error introduced by sample preparation prior to LPSA analysis. The higher d_{10}

values likely result from the difficulty in accurate measurement of silt-sized grains and the smaller sample size of grains measured in thin section. This is most notable in thin **section 2** (**Figure 12B**), which is the most clay/silt-rich (according to the LPSA data and images). This in turn affects the d_{50} and d_{90} values, with distribution weighted more towards the coarser grains in the thin section. Additionally, the method used to create a volume approximation could be influencing the result. Using the long axis and the short axis twice is a best estimate and may not result in realistic volumes for each grain. The double peak apparent in the thin **section 2** curve (**Figure 12B**) is likely a result of the lower number of grains counted (262) compared to thousands in the LPSA as well as the grouping of samples into 60 μm bins. The angularity of the grains is likely not a large factor, as all three samples appear to be of similar angularity (sub-angular to sub-rounded, **Figure 12**). There is a possibly that the finer-grained LPSA values, both the increased fine-grained component and the decreased maximum grain size, could result from sample breakdown beyond grain boundaries in the preparation process for the LPSA, but due to the replicability of samples in the LPSA this is unlikely.

Despite all effort being made to take field samples within proximity of each other, some natural variation between samples is possible, particularly from thin-**section 2** (**Figure 12B**) which is from a clast within a hybrid event bed. Due to the large sample size needed to make a thin section, samples can be estimated as only being within the same 20 cm section of each bed. It is therefore possible that, like for the large and small subsamples described above, some differences between thin section and LPSA curves represent real variation between samples.

The comparison between thin section and LPSA results suggest that care should be taken when comparing grain-size analysis methods to one another. While trends within a given method may be meaningful, specific values of d_{10}, d_{50}, or d_{90} may vary significantly between methods. Thin sections in this study underestimate the silt-sized fraction and were unable to measure clay fraction, which results in a coarse-grained shift in cumulative grain size values (e.g., d_{50}).

DISCUSSION AND RECOMMENDATIONS

Aliquot Methods

Overall, aliquots measured using the stirrer method were more replicable than the pipette method. This is likely due to the mechanisation of the stirrer being more consistent than manual pumping with the pipette when dispersing grains into suspension. However, individual aliquots can show inaccuracies due to a few anomalously large grains. One way to avoid this potential error is to take a large subsample and continue to extract aliquots until the entire sample has been measured. This is the most accurate representation of grain size available because using all of a large subsample allows for more individual grains to be measured. By averaging multiple subsamples there is also less risk of an anomalous aliquot or measurement error interfering with the dataset. However, using a very large number of aliquots (>6) will significantly increase processing time.

Large Subsamples or Small Subsamples?

Although larger subsamples give more representative data, smaller subsamples negate any aliquot sampling error and are accurate when compared to an average of large subsamples in most cases. Overall, small subsamples are significantly less time consuming and were sufficiently accurate for the samples in this study. However, it is advised that multiple small samples are measured for a given field sample to account for any potential heterogeneity.

Speed and Accuracy Ultrasonic Bath Method

Overall, samples were highly replicable and therefore the ultrasonic bath method is reliable. The speed at which samples could be processed was a few minutes for the sample preparation, 20 min to 1 h in the ultrasonic bath, 24 h for clay deflocculation, 3 min to run through the Mastersizer 3000 and 1 min for cleaning in between samples. As 10s of samples could be placed in the ultrasonic bath together and left to deflocculate overnight, it was possible to get through approximately 30 samples per day.

Speed and Accuracy SELFRAG Method

Disaggregating samples using the SELFRAG method was much more time consuming than the ultrasonic bath. Approximately 5 samples could be processed in the SELFRAG per day and left to dry overnight. These were then subsampled in the riffle splitter the following day and left in a 0.5% NaHMP solution over a second night before being measured in the LPSA (**Figure 2**). The results suggest that the SELFRAG method was not fully disaggregating clasts in the most lithified formations, and because the least lithified formations can be more easily disaggregated in the ultrasonic bath method, it is not recommended to use the SELFRAG method without further testing. The SELFRAG method could potentially be used in conjunction with the ultrasonic bath method, however further testing is required.

Comparison With Thin Section

There are many issues with the direct comparison between laser diffraction methods and thin section for grain-size analysis. Most thin section studies use the long axes measured in a 2D thin section, which does not represent the true longest axes of the original grains and will therefore likely underestimate the size of larger sand grains in most cases (Smith, 1966; Sahu, 1968; Johnson, 1994), but will also not accurately capture clay and silt grains. In this study, we attempted to offset this issue through calculating an artificial volume. Other methods for converting 2D to 3D grain-size distributions have been developed (e.g., Heilbronner and Barrett, 2014), but these are not straightforward. In general, results show an overestimation of grain size using thin section analysis, which could be due to using the short axis as both the height and depth, potentially overestimating the *z*-axis.

Recent work by Maithel et al. (2019) comparing laser diffraction and thin section analysis for sandstones found a good comparison between their results, with the laser

diffraction being slightly coarser overall, which was expected because they used the long-axis method in thin section. The difference between the medians for thin-section and laser-diffraction data sets (based on average grain sizes for each sample) was 33.7 μm. They hypothesised the difference could be due to numerous variables such as natural sample variation and sources of error or potentially due to measurement of quartz overgrowths in disaggregated samples. The more consistent relationship between laser diffraction and thin-section methods by Maithel et al. (2019) compared to this study is likely to due to the removal of fines in their sample preparation stage. Silt particles are underrepresented in thin section measurements and clay was not measured at all. Despite this, Maithel et al. (2019) did also find issues relating to disaggregation quality and correspondence with thin section samples, like those demonstrated by the SELFRAG samples in this study. Overall Maithel et al. (2019) conclude that consistency between their laser diffraction and thin section results confirms the robustness of both methods for textural analysis, which may be the case when using only sand-sized grains, but which this study demonstrates is not the case when including silt and clay.

Issues With Clays

In comparison with thin-section analysis, the LPSA was more accurate in documenting the presence of silt and was able to measure clay particles. Although this is likely missing in the thin section analysis due to the limitations of the method, some studies (Buurman, et al., 1997; Buurman, et al., 2001) have shown that laser diffraction methods can inaccurately measure the size of clay and fine silt fractions of a sample. Work carried out using soil profiles (Bah, et al., 2009), suggested that the relationship between clay determined by settling method (e.g., sieve-hydrometer method) and clay determined by laser diffraction analysis may depend on the physical properties of the clay. This can be due to the heterogeneity of sediment particle density and the deviation of particle shapes from sphericity (Bah, et al., 2009). Therefore, in the LPSA, an irregular shaped soil particle reflects a cross-sectional area greater than that of a sphere having the same volume. Thus, particles are assigned to larger size fractions of the particle size distribution and the clay fraction is underestimated. Non-spherical particles in settling methods have longer settling times than their equivalent spheres, which results in an overestimation of the clay fraction. This is likely only a minor consideration when mixed sand, silt, clay samples are used, but should be taken into consideration when exact clay volumes are more pertinent to the study.

What Are the Limits of This Method Overall?

Overall, this study found that the laser diffraction grain size analysis with the Malvern Mastersizer 3000 is generally replicable and reliable for mixed sand-silt-clay samples of varying distributions. The small subsample method is the most time efficient sub-sampling method for analysing datasets with hundreds of field samples, but care needs to be taken to re-run samples that appear anomalous. Despite the accuracy and speed of the small subsample method, there are still some drawbacks. Natural samples will almost always vary spatially, which will add error to the dataset. Despite this drawback, sieving and thin section analysis will also have issues with subsampling and therefore this is a source of error that cannot be completely negated. There is a certain amount of specialist equipment required for laser diffraction grain-size analysis, but this method may be more cost effective when compared to thin section preparation in the long run or labour in processing sieved samples. Users can be trained in the methods described in this study (**Figure 2**) within a day. Ultrasonic baths are cheap and easily accessible. The SELFRAG on the other hand is a large, expensive, and specialised piece of equipment, which requires more training and has been shown in this study to give variable results. It is therefore not recommended unless access is already available.

CONCLUSION

This study demonstrated that it is possible to produce a reliable and repeatable workflow for disaggregating ancient mudstone and sandstone utilizing an ultrasonic bath for variably cemented samples. This study also demonstrates these techniques are possible on moderately-cemented rocks up to Cretaceous age, opening the opportunity for laser-diffraction grain size analysis on ancient sedimentary rocks. The most efficient samples to run were "small" (0.2–2 g) subsamples, which were found to be sufficiently accurate when compared to an average of "large" (5—10 g) subsamples. Multiple small samples can be run relatively quickly to rule out anomalous results. Alternatively, large subsamples, which are presumably more representative of the entire field sample, can be measured using aliquots obtained with either the pipette or stirrer method. In argillaceous samples, the "agitated" pipette method and "centre" stirrer method were found to be replicable, and the stirrer provided more consistent results in general. In sand-rich samples, the pipette method is slightly skewed towards coarser grain sizes and the stirrer method is slightly skewed towards finer grain sizes, however each method was internally precise.

The SELFRAG method for disaggregation was possible, but due to the large amount of sample needed for this method, drying and splitting the dry sample with a riffle-splitter was time consuming. This method is therefore only suitable with a small number of field samples. Moreover, there were potentially some remaining aggregate grains for the samples from moderately lithified and most lithified formations. Therefore, this method may need to be further developed or combined with the ultrasonic bath method to be fully reliable. However, the SELFRAG does have the potential to allow disaggregation of older and more well-cemented sedimentary rocks.

When compared to thin section analysis, laser diffraction results showed significant differences, including LPSA results being finer due to a more accurate measurement of the silt portion and inclusion of the clay portion of samples. Grain-size of the sand portion was over-estimated in the thin-section analysis, potentially due to the overestimation of the unmeasured *z*-axis of grains.

Despite some issues, the ultrasonic bath method of disaggregation and measurement using the Mastersizer 3000 has made it possible to measure accurate grain size distributions for hundreds of samples in a reasonable amount

of time. Therefore, by following the workflow outlined in this study and using the processing techniques most suitable for the dataset, it is possible to greatly expand the amount of quantitative grain-size datasets for ancient siliciclastic sedimentary rocks.

DATA AVAILABILITY STATEMENT

The original contributions presented in the study are included in the article/**Supplementary Material**, further inquiries can be directed to the corresponding author.

AUTHOR CONTRIBUTIONS

HB and ES conceived and designed the study, underwent fieldwork and collected samples. HB, ES and MM ran the experiments in the laboratory. HB wrote the first draft of the manuscript, ES reviewed and redrafted manuscript. All authors contributed to manuscript revision, read and approved the submitted version.

FUNDING

This work was carried out with funding from the Queen's University postdoctoral fund. Supportive funding was used from the Natural Sciences and Engineering Research Council of Canada (NSERC), RGPIN-2019-04760 and Research Initiation Grant awarded to ES from Queen's University.

ACKNOWLEDGMENTS

The Authors would like to thank Marco Patacci for introducing us to the Castagnola and Gottero field areas where samples were collected, and Esther Sumner for providing data on the Marnoso-Arenacea field area. We would also like to thank Michele Malavolta, Yvonne Spychala and Sarah Cobain for assistance in the field, Gillian Ivey and Valentin Zuchuat for assistance in the Lab, Steve Beyer at Queens University for cutting thin sections and assistance with the SELFRAG and Pam Frail at Acadia University for preparation of thin section. A big thank you to Bob Dalrymple for providing the funds for the Mastersizer 3000. Thank you to Peir Pufahl for assistance and use of lab equipment. Finally, thank you to Megan Baker, Chris Stevenson, Assoc. Prof. Roberto Tinterri and RS for their insightful and helpful reviews. We acknowledge the support of the Natural Sciences and Engineering Research Council of Canada (NSERC), RGPIN-2019-04760.

SUPPLEMENTARY MATERIAL

The Supplementary Material for this article can be found online at: https://www.frontiersin.org/articles/10.3389/feart.2022.820866/full#supplementary-material

REFERENCES

Abbate, E., and Sagri, M. (1970). The Eugeosynclinal Sequences. *Sediment. Geology.* 4, 251–340. doi:10.1016/0037-0738(70)90018-7

Amy, L. A., and Talling, P. J. (2006). Anatomy of Turbidites and Linked Debrites Based on Long Distance (120 X 30 Km) Bed Correlation, Marnoso Arenacea Formation, Northern Apennines, Italy. *Sedimentology* 53 (1), 161–212. doi:10.1111/j.1365-3091.2005.00756.x

Amy, L. A., Talling, P. J., Sumner, E. J., and Malgesini, G. (2016). Current-aligned Dewatering Sheets and 'enhanced' Primary Current Lineation in Turbidite Sandstones of the Marnoso-Arenacea Formation. *Sedimentology* 63 (5), 1260–1279. doi:10.1111/sed.12260

Andreola, F., Castellini, E., Manfredini, T., and Romagnoli, M. (2004). The Role of Sodium Hexametaphosphate in the Dissolution Process of Kaolinite and Kaolin. *J. Eur. Ceram. Soc.* 24 (7), 2113–2124. doi:10.1016/s0955-2219(03)00366-2

Andreola, F. (2006). Effect of Sodium Hexametaphosphate and Ageing on the Rheological Behaviour of Kaolin Dispersions. *Appl. Clay Sci.* 31 (1-2), 56–64. doi:10.1016/j.clay.2005.08.004

Andreoni, G., Galbiati, B., Maccabruni, A., and Vercesi, P. (1981). Stratigrafia e paleogeografia deidepositi oligocenici sup. – miocenici inf. nell'estremita' orientale del bacino ligure-piemontese. *Riv. Ital. Paleontol. Stratigr.* 87, 245–282.

Andres, U. (2010). Development and Prospects of mineral Liberation by Electrical Pulses. *Int. J. Mineral Process.* 97 (1-4), 31–38. doi:10.1016/j.minpro.2010.07.004

Argnani, A., and Lucchi, F. R. (2001). *The Apennines and Adjacent Mediterranean Basins*. Dordrecht: Springer.

Bah, A. R., Kravchuk, O., and Kirchhof, G. (2009). Fitting Performance of Particle-Size Distribution Models on Data Derived by Conventional and Laser Diffraction Techniques. *Soil Sci. Soc. Am. J.* 73 (4), 1101–1107. doi:10.2136/sssaj2007.0433

Barrett, P., and Anderson, J. (2000). Grain Size Analysis of Samples from CRP-2/2A. *Terra Antarctica* 7 (3), 373–378.

Blott, S. J., Croft, D. J., Pye, K., Saye, S. E., and Wilson, H. E. (2004). "Particle Size Analysis by Laser Diffraction," Geol. Soc. Lond. Spec. Publications in *Forensic Geoscience: Principles, Techniques and Applications*. Editors K. Pye and D. J. Croft (London: The Geological Society of London), 232, 63–73. doi:10.1144/gsl.sp.2004.232.01.08

Bralower, T., Eccles, L., Kutz, J., Yancey, T., Schueth, J., Arthur, M., et al. (2010). Grain Size of Cretaceous-Paleogene Boundary Sediments from Chicxulub to the Open Ocean: Implications for Interpretation of the Mass Extinction Event. *Geology* 38 (3), 199–202. doi:10.1130/g30513.1

Buller, A. T., and McManus, J. (1972). Modes of Turbidite Deposition Deduced from Grain-Size Analyses. *Geol. Magazine* 109(6), 491–500.

Buurman, P., Pape, T., and Muggler, C. C. (1997). Laser Grain-Size Determination in Soil Genetic Studies 1. Practical Problems. *Soil Sci.* 162 (3), 211–218. doi:10.1097/00010694-199703000-00007

Buurman, P., Pape, T., Reijneveld, J. A., De Jong, F., and Van Gelder, E. (2001). Laser-diffraction and Pipette-Method Grain Sizing of Dutch Sediments: Correlations for fine Fractions of marine, Fluvial, and Loess Samples. *Neth. J. Geosciences* 80 (2), 49–57. doi:10.1017/s0016774600022319

Cavanna, F., Di Giulio, A., Galbiati, B., Mosna, S., Perotti, C. R., and Pieri, M. (1989). Carta geologica dell'estremità orientale del Bacino Terziario Ligure Piemontese. Atti Ticinesi Sc. Terra, 32.

Chakravarti, I. M., Laha, R. G., and Roy, J. (1967). *Handbook of Methods of Applied Statistics, Volume I* John Wiley and Sons, Hoboken, pp. 392-394

Chayes, F. (1950). On the Bias of Grain-Size Measurements Made in Thin Section. *J. Geology.* 58 (2), 156–160. doi:10.1086/625716

Cheetham, M. D., Keene, A. F., Bush, R. T., Sullivan, L. A., and Erskine, W. D. (2008). A Comparison of Grain-Size Analysis Methods for Sand-Dominated

Fluvial Sediments. *Sedimentology* 55, 1905–1913. doi:10.1111/j.1365-3091.2008.00972.x

Chilingar, G. V. (1952). Study of the Dispersing Agents. *J. Sediment. Res.* 22 (4), 229–233. doi:10.2110/jsr.22.229

Di Giulio, A., and Galbiati, B. (1993). *Escursione nell'estremitaorientale del Bacino Terziario Piemontese. Interazione tettonica-eustatismo nella sedimentazione di un bacino tardo-post orogenico*. 3 Convegno del Gruppo Informale di Sedimentologia del CNR. Dip. di Scienza della Terra, Università di Pavia, Salica Term, 1–28.

Di Stefano, C., Ferro, V., and Mirabile, S. (2010). Comparison between Grain-Size Analyses Using Laser Diffraction and Sedimentation Methods. *Biosyst. Eng.* 106, 205–215. doi:10.1016/j.biosystemseng.2010.03.013

Edwards, A. P., and Bremner, J. M. (1967). Dispersion of Soil Particles by Sonic Vibration1. *J. Soil Sci.* 18, 47–63. doi:10.1111/j.1365-2389.1967.tb01487.x

Fernlund, J., Zimmerman, R., and Kragic, D. (2007). Influence of Volume/mass on Grain-Size Curves and Conversion of Image-Analysis Size to Sieve Size. *Eng. Geology.* 90 (3-4), 124–137. doi:10.1016/j.enggeo.2006.12.007

Fonnesu, M., Felletti, F., Haughton, P. D., Patacci, M., and McCaffrey, W. D. (2018). Hybrid event bed character and distribution linked to turbidite system sub-environments: The North Apennine Gottero Sandstone (North-West Italy). *Sedimentology* 65(1), 151–190.

Fonnesu, M., Patacci, M., Haughton, P. D., Felletti, F., and McCaffrey, W. D. (2016). Hybrid Event Beds Generated by Local Substrate Delamination on a Confined-Basin Floor. *J. Sediment. Res.* 86(8), 929–943.

Francus, P. (1999). Using Image Analysis to Estimate Quantitatively Some Microstructural Parameters of Detrital Sediments. *Geologica Belgica* 2, 173–180.

Friedman, G. M. (1958). Determination of Sieve-Size Distribution from Thin-Section Data for Sedimentary Petrological Studies. *J. Geology.* 66 (4), 394–416. doi:10.1086/626525

Gee, G. W., and Bauder, J. W. (1986). "Particle-size Analysis," in *Methods of Soil Analysis: Part 1 Physical and Mineralogical Method*. Editor A. Klute (Madison, Wisconsin, USA: the American Society of Agronomy, Inc. Soil Science Society of America, Inc.).

Greenman, N. N. (1951). The Mechanical Analysis of Sediments from Thin-Section Data. *J. Geology.* 59 (5), 447–462. doi:10.1086/625889

Harrell, J., and Eriksson, K. (1979). Empirical Conversion Equations for Thin-Section and Sieve Derived Size Distribution Parameters. *J. Sediment. Petrology* 49, 273–280. doi:10.1306/212f7711-2b24-11d7-8648000102c1865d

Heilbronner, R., and Barrett, S. (2014). Spatial Distributions. *Image Analysis in Earth Sciences* eds. Heilbronner, R. and Barrett, S. Springer, Berlin, Heidelberg, 351–368. doi:10.1007/978-3-642-10343-8_18

Haughton, P. D. W., Barker, S. P., and McCaffrey, W. D. (2003). 'Linked' Debrites in Sand-Rich Turbidite Systems - Origin and Significance. *Sedimentology* 50 (3), 459–482. doi:10.1046/j.1365-3091.2003.00560.x

Haughton, P., Davis, C., McCaffrey, W., and Barker, S. (2009). Hybrid Sediment Gravity Flow Deposits-Classification, Origin And Significance. *Marine Petrol. Geol.* 26(10), 1900–1918.

Hayton, S., Nelson, C. S., Ricketts, B. D., Cooke, S., and Wedd, M. W. (2001). Effect of Mica on Particle-Size Analyses Using the Laser Diffraction Technique. *J. Sediment. Res.* 71 (3), 507–509. doi:10.1306/2dc4095b-0e47-11d7-8643000102c1865d

Hodgson, D. M. (2009). Distribution and Origin of Hybrid Beds in Sand-Rich Submarine Fans of the Tanqua Depocentre, Karoo Basin, South Africa. *Mar. Pet. Geology.* 26 (10), 1940–1956. doi:10.1016/j.marpetgeo.2009.02.011

Ito, M. (2008). Downfan Transformation from Turbidity Currents to Debris Flows at a Channel-To-Lobe Transitional Zone: the Lower Pleistocene Otadai Formation, Boso Peninsula, Japan. *J. Sediment. Res.* 78 (10), 668–682. doi:10.2110/jsr.2008.076

Jiang, Z., and Liu, L. a. (2011). A Pretreatment Method for Grain Size Analysis of Red Mudstones. *Sediment. Geology.* 241, 13–21. doi:10.1016/j.sedgeo.2011.09.008

Johnson, M. R. (1994). Thin Section Grain Size Analysis Revisited. *Sedimentology* 41, 985–999. doi:10.1111/j.1365-3091.1994.tb01436.x

Konert, M., and Vandenberghe, J. (1994). Comparison of Laser Grain Size Analysis with Pipette and Sieve. *Sedimentology* 44, 523–535. doi:10.1046/j.1365-3091.1997.d01-38.x

Kong, M., Bhattacharya, R. N., James, C., and Basu, A. (2005). A Statistical Approach to Estimate the 3D Size Distribution of Spheres from 2D Size Distributions. *Geol. Soc. America Bull.* 117, 244–249. doi:10.1130/b25000.1

Krumbein, W. C. (1935). Thin-section Mechanical Analysis of Indurated Sediments. *J. Geology.* 43 (5), 482–496. doi:10.1086/624330

Loope, D. B., Elder, J. F., and Sweeney, M. R. M. (2012). Downslope Coarsening in Aeolian Grainflows of the Navajo Sandstone. *Sediment. Geology.* 265-266, 156–162. doi:10.1016/j.sedgeo.2012.04.005

Lucchi, F. R., and Valmori, E. (1980). Basin-wide Turbidites in a Miocene, Over-supplied Deep-Sea plain: a Geometrical Analysis. *Sedimentology* 27 (3), 241–270. doi:10.1111/j.1365-3091.1980.tb01177.x

Maithel, S. A., Brand, L. R., and Whitmore, J. H. (2019). A Methodology for Disaggregation and Textural Analysis of Quartz-Cemented Sandstones. *J. Sediment. Res.* 89 (7), 599–609. doi:10.2110/jsr.2019.35

Malesani, P. (1966). Ricerche Sulle Arenarie, XV; L'Arenaria Superiore. *Rendiconti della Società Italiana di Mineralogia e Petrologia* 22, 113–175.

Marroni, M. a. P. N. (1990). The Age of the Ophiolite Sedimentary Cover from the Mt. Gottero Unit (Internal Ligurid Units, Northern Apennines): New Data from Calcareous Nannofossils. *Ofioliti* 15, 251–267.

Marroni, M., Meneghini, F., and Pandolfi, L. (2004). From Accretion to Exhumation in a Fossil Accretionary Wedge: a Case History from Gottero Unit (Northern Apennines, Italy). *Geodinamica Acta* 17, 41–53. doi:10.3166/ga.17.41-53

Mazzullo, J., and Kennedy, S. K. (1985). Automated Measurement of the Nominal Sectional Diameters of Individual Sedimentary Particles. *J. Sediment. Res.* 55 (4), 593–595. doi:10.2110/55.4.593

Muzzi Magalhaes, P., and Tinterri, R. (2010). Stratigraphy and Depositional Setting of Slurry and Contained (Reflected) Beds in the Marnoso-Arenacea Formation (Langhian-Serravallian) Northern Apennines, Italy. *Sedimentology* 57 (7), 1685–1720. doi:10.1111/j.1365-3091.2010.01160.x

Nilsen, T., and Abbate, E. (1984). Turbidite Facies and Facies Associations of Cretaceous and Paleocene Gottero sandstone, Northern Italy. *AAPG Bull.* 68 (4), 512–513. doi:10.1306/ad461061-16f7-11d7-8645000102c1865d

Pandolfi, L. (1997). Stratigrafia ed Evoluzione Strutturale delle Succession Torbiditiche Cretacee della Liguria Orientale (Appennino Settentrionale). PhD thesis, Università di Pisa, 175 pp.

Parea, G. C. (1965). Evoluzione Della Parte Settentrionale Della Geosinclinale Appenninica dall'Albiano all'Eocene Superiore. *Atti e Memorie della Accademia Nazionale di Scienze, Lettere, e Arti, Modena* 6 (7), 97.

Passerini, P., and Pirini, C. (1964). Microfaune paleoceniche nella formazione dell'Arenaria del M. Ramaceto e degli Argilloscisti di Cichero. *Societa Geologica Italiana Bolletin* 83, 211–218.

Patacci, M., Marini, M., Felletti, F., Di Giulio, A., Setti, M., and McCaffrey, W. (2020). Rigin of Mud in Turbidites and Hybrid Event Beds: Insight from Ponded Mudstone Caps of the Castagnola Turbidite System (north-west Italy). *Sedimentology* 67. doi:10.1111/sed.12713

Persson, A.-L. (1998). Image Analysis of Shape and Size of fine Aggregates. *Eng. Geology.* 50, 177–186. doi:10.1016/s0013-7952(98)00009-x

Rendigs, R. R., and Commeau, J. A. (1987). Effects of Disaggregation on a fine-grained marine Mud by Two Ultrasonic Devices. *J. Sediment. Res.* 57 (4), 786–787. doi:10.1306/212f8c51-2b24-11d7-8648000102c1865d

Resentini, A., AndÒ, S., and Garzanti, E. (2018). Quantifying Roundness of Detrital Minerals by Image Analysis: Sediment Transport, Shape Effects, and Provenance Implications. *J. Sediment. Res.* 88 (2), 276–289. doi:10.2110/jsr.2018.12

Rosenfeld, M. A., Jacobsen, L., and Ferm, J. C. (1953). A Comparison of Sieve and Thin-Section Technique for Size Analysis. *J. Geology.* 61 (2), 114–132. doi:10.1086/626060

Sahu, B. (1968). The Determination of the Grain-Size Distribution of a Spherical Granular Material Embedded in Matrix. *Sedimentology* 10, 293–309. doi:10.1111/j.1365-3091.1968.tb01107.x

Saini-Eidukat, B., and Weiblen, P. W. (1996). A New Method of Fossil Preparation, Using High-Voltage Electric Pulses. *Curator* 39, 139–144. doi:10.1111/j.2151-6952.1996.tb01085.x

Seelos, K., and Sirocko, F. (2005). RADIUS - Rapid Particle Analysis of Digital Images by Ultra-high-resolution Scanning of Thin Sections. *Sedimentology* 52 (3), 669–681. doi:10.1111/j.1365-3091.2005.00715.x

Smith, R. E. (1966). Grain Size Measurement in Thin Section and in Grain Mount. *J. Sediment. Res.* 36, 841–843. doi:10.1306/74d715aa-2b21-11d7-8648000102c1865d

Southern, S. J., Patacci, M., Felletti, F., and McCaffrey, W. D. (2015). Influence of Flow Containment and Substrate Entrainment upon sandy Hybrid Event Beds Containing a Co-genetic Mud-Clast-Rich Division. *Sediment. Geology.* 321, 105–122. doi:10.1016/j.sedgeo.2015.03.006

Sperazza, M., Moore, J. N., and Hendrix, M. S. (2004). High-Resolution Particle Size Analysis of Naturally Occurring Very Fine-Grained Sediment through Laser Diffractometry. *J. Sediment. Res.* 74 (5), 736–743. doi:10.1306/031104740736

Sridharan, A., Jose, B., and Abraham, B. (1991). Determination of clay Size Fraction of marine Clays. Geotechnical Testing Journal. *Geotechnical Test. J.* 14 (1), 103–107.

Stevenson, C. J., Talling, P. J., Masson, D. G., Sumner, E. J., Frenz, M., and Wynn, R. B. (2014). The Spatial and Temporal Distribution of Grain-Size Breaks in Turbidites. *Sedimentology* 61, 1120–1156. doi:10.1111/sed.12091

Suczek, C. A. (1983). Disaggregation of Quartzites. *J. Sediment. Res.* 53 (2), 672–673. doi:10.1306/212f8279-2b24-11d7-8648000102c1865d

Sumner, E. J., Talling, P. J., and Amy, L. A. (2009). Deposits of Flows Transitional between Turbidity Current and Debris Flow. *Geology* 37 (11), 991–994. doi:10.1130/g30059a.1

Syvitski, J. M. P. (1991).*Principles, Methods, and Application of Particle Size Analysis*. Cambridge, UK: Cambridge University Press.

Talling, P. J. (2013). Hybrid Submarine Flows Comprising Turbidity Current and Cohesive Debris Flow: Deposits, Theoretical and Experimental Analyses, and Generalized Models. *Geosphere* 9 (3), 460–488. doi:10.1130/ges00793.1

Triplehorn, D. M., Bohor, B. F., and Betterton, W. J. (2002). Chemical Disaggregation of Kaolinitic Claystones (Tonsteins and Flint Clays). *Clays and Clay Minerals* 50 (6), 766–770. doi:10.1346/000986002762090164

Valloni, R., and Zuffa, G. G. (1981). *Detrital Modes of Arenaceous Formations of the Northern Apennines*. Bologna, Italy: Second European Meeting of the International Association of Sedimentologists, Abstracts, 198–201.

Valloni, R., and Zuffa, G. G. (1984). Provenance Changes for Arenaceous Formations of the Northern Apennines, Italy. *Geol. Soc. Am. Bull.* 95(9), 1035–1039.

van de Kamp, P. C., and Leake, B. E. (1995). Petrology and Geochemistry of Siliciclastic Rocks of Mixed Feldspathic and Ophiolitic Provenance in the Northern Apennines, Italy. *Chem. Geology.* 122, 1–20. doi:10.1016/0009-2541(94)00162-2

Van Den Berg, E. H., Bense, V. F., and Schlager, W. (2003). Assessing Textural Variation in Laminated Sands Using Digital Image Analysis of Thin Sections. *J. Sediment. Res.* 73 (1), 133–143. doi:10.1306/061502730133

Van den Berg, E. H., Meesters, A. G. C. A., Kenter, J. A. M., and Schlager, W. (2002). Automated Separation of Touching Grains in Digital Images of Thin Sections. *Comput. Geosciences* 28 (2), 179–190. doi:10.1016/s0098-3004(01)00038-3

van der Wielen, K. P., Pascoe, R., Weh, A., Wall, F., and Rollinson, G. (2013). The Influence of Equipment Settings and Rock Properties on High Voltage Breakage. *Minerals Eng.* 46-47, 100–111. doi:10.1016/j.mineng.2013.02.008

van Olphen, H. (1977). *An Introduction to clay Colloid Chemistry, for clay Technologists, Geologists, and Soil Scientists*. 2 ed. New York: Wiley.

Walker, P. H., and Hutka, J. (1973). Grain Fragmentation in Preparing Samples for Particle-Size Analysis. *Soil Sci. Soc. America J.* 37 (2), 278–280. doi:10.2136/sssaj1973.03615995003700020032x

Wang, E., Shi, F., and Manlapig, E. (2012). Mineral Liberation by High Voltage Pulses and Conventional Comminution with Same Specific Energy Levels. *Minerals Eng.* 27-28, 28–36. doi:10.1016/j.mineng.2011.12.005

Wang, E., Shi, F., and Manlapig, E. (2011). Pre-weakening of mineral Ores by High Voltage Pulses. *Minerals Eng.* 24 (5), 455–462. doi:10.1016/j.mineng.2010.12.011

Wintermyer, A. B., and Kinter, E. B. (1955). Dispersing Agents for Partical-Size Analysis of Soils. *Highw. Res. Board Bull.* 95, 1–14.

Zihua, T., Guijin, M., and Dongmei, C. (2009). Palaeoenvironment of Mid- to Late Holocene Loess deposit of the Southern Margin of the Tarim Basin, NW China. *Environ. Geol.* 58, 1703–1711. doi:10.1007/s00254-008-1670-9

Zuo, W., Shi, F., van der Wielen, K. P., and Weh, A. (2015). Ore Particle Breakage Behaviour in a Pilot Scale High Voltage Pulse Machine. *Minerals Eng.* 84, 64–73. doi:10.1016/j.mineng.2015.09.025

Conflict of Interest: The authors declare that the research was conducted in the absence of any commercial or financial relationships that could be construed as a potential conflict of interest.

frontiers | Frontiers in Earth Science

ORIGINAL RESEARCH
published: 25 April 2022
doi: 10.3389/feart.2022.820326

ADCP Observations of Currents and Suspended Sediment in the Macrotidal Gulf of Martaban, Myanmar

Courtney K. Harris[1]*, *Jacob T. Wacht*[2], *Matthew J. Fair*[1] and *Jessica M. Côté*[3]

[1]Virginia Institute of Marine Science, William & Mary, Gloucester Point, VA, United States, [2]William and Mary, Williamsburg, VA, United States, [3]Blue Coast Engineering, Seattle, WA, United States

The Ayeyarwady and Thanlwin Rivers, which drain Myanmar, together form one of the largest point sources of freshwater and sediment to the global ocean. Combined, these rivers annually deliver an estimated 485 Mt of sediment to the northern Andaman Sea. This sediment contributes to a perennially muddy zone within the macro-tidal Gulf of Martaban, but little is known about the processes that dominate dispersal and trapping of sediment there, as very few water column observations are available. A research cruise in December 2017 provided a rare opportunity to obtain Acoustic Doppler Current Profiler (ADCP) data along transects from the Gulf of Martaban and adjacent continental shelf. Two transects were obtained from the outer portion of the Gulf of Martaban in water depths that ranged from about 20–35 m. These showed very fast currents, especially during flood tide conditions, exceeding 1.5 m/s. The backscatter record from the ADCP indicated asymmetries in distribution of suspended sediment during the ebb versus flood phase of the tide. During ebb tidal conditions, the backscatter record indicated that sediment was transported in either a surface advected layer, or fairly well-mixed throughout the water column. In contrast, during flood tidal conditions, sediment was confined to the bottom boundary layer, even though the velocities were faster during flood than the ebb conditions. The vertical structure of the currents during flood tide conditions indicated the presence of sediment–induced stratification because currents within the near-bed turbid layers were relatively slow, but speeds increased markedly above these layers. This albeit limited dataset provides an exciting glimpse into the dynamics of sediment transport within the muddy, macrotidal Gulf of Martaban, and implies the importance of tidal straining and bottom nepheloid layer formation there.

Keywords: Gulf of Martaban, tidal currents, suspended sediment, macrotidal estuary, ADCP

OPEN ACCESS

Edited by:
Daniel R. Parsons,
University of Hull, United Kingdom

Reviewed by:
Kyungsik Choi,
Seoul National University, South Korea
Anabela Oliveira,
Instituto Hidrográfico, Portugal

***Correspondence:**
Courtney K. Harris
ckharris@vims.edu

Specialty section:
This article was submitted to Marine Geoscience, a section of the journal Frontiers in Earth Science

Received: *22 November 2021*
Accepted: *15 March 2022*
Published: *25 April 2022*

Citation:
Harris CK, Wacht JT, Fair MJ and Côté JM (2022) ADCP Observations of Currents and Suspended Sediment in the Macrotidal Gulf of Martaban, Myanmar. Front. Earth Sci. 10:820326. doi: 10.3389/feart.2022.820326

1 INTRODUCTION

Riverine discharge accounts for the majority of sediment input to the ocean, with the largest ~25 rivers accounting for 40% of this sediment (see Milliman and Meade, 1983; Meade, 1996; McKee et al., 2004). Once delivered to oceanic environments, a number of transport processes operate on, and transform sediment and associated nutrients such as organic carbon, before their eventual deposition and burial (McKee et al., 2004). Large Asian rivers draining the Tibetan Plateau are especially significant and account for 25% of global sediment delivery to marginal seas (Kuehl et al., 2020). The third–largest contributor from the Tibetan Planteau is

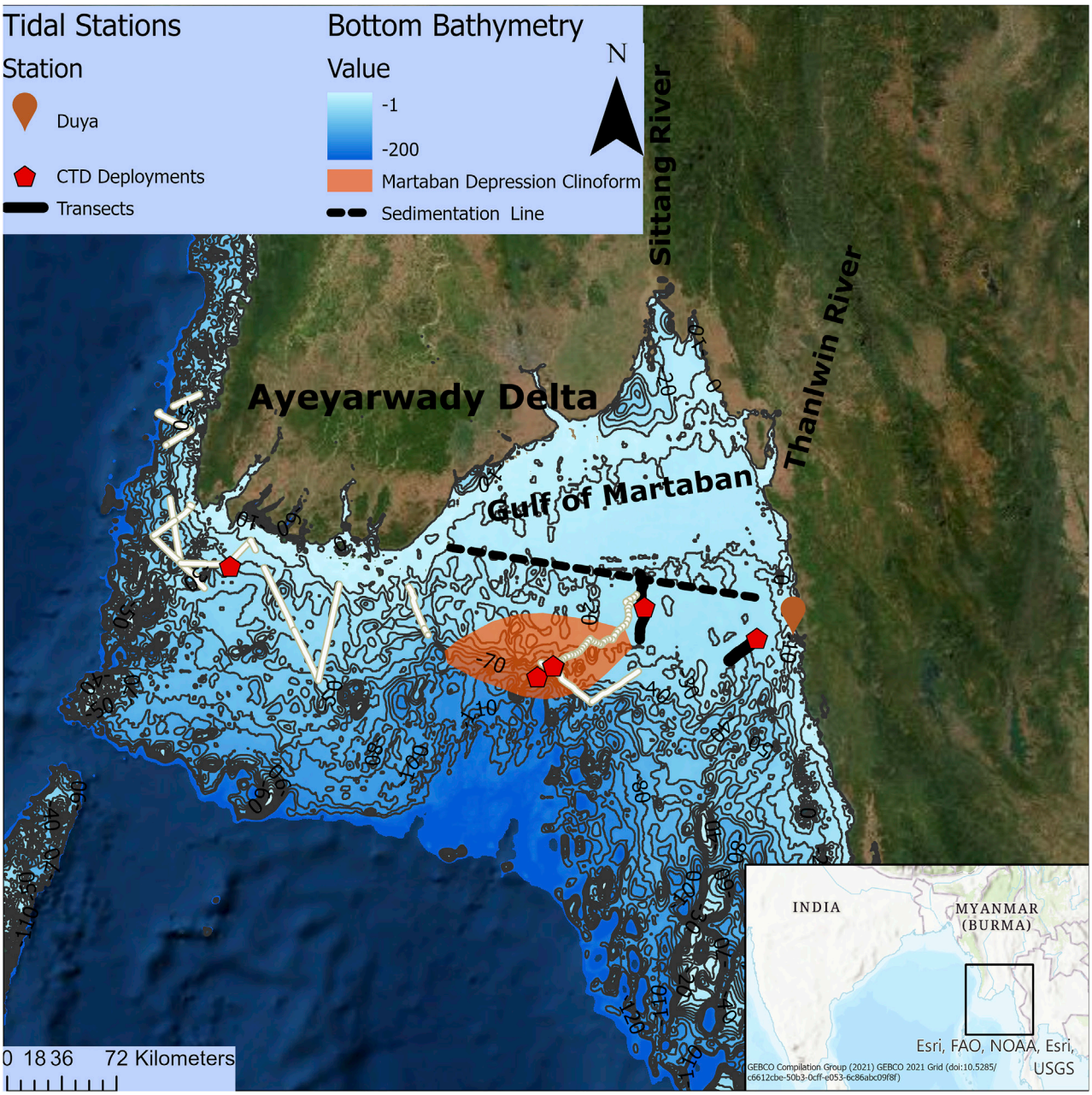

FIGURE 1 | Map of study area in the northern Andaman Sea (see inset for location within Indian Ocean). Black and white lines show locations of all ADCP transects. This manuscript focused on the eastern-most ADCP Transects #5 and #21, shown as black lines. Red markers show locations of CTD-Tu samples. Orange marker shows location of Duya, Myanmar. The dotted black line demarcates areas identified as the mud blanket to the north; and a zone of accumulation to the south (Flynn et al., in press). The orange area in the zone of accumulation represents the location of the Martaban Depresssion Clinoform (Kuehl et al., 2019; Liu et al., 2020).

the combined Ayeyarwady and Thanlwin Rivers (Kuehl et al., 2020). Its combined freshwater discharge is estimated at 528 km^3/year, and sediment discharge at approximately 485 MT per year (Baronas et al., 2020). Additionally, these rivers annually output 5.7–8.8 MT of organic carbon to the coastal ocean, globally ranking second behind the Amazon River (Bird et al., 2008). The Ayeryarwady and Thanlwin Rivers are also relatively unaltered by damming, and as such have been identified as the last non-Arctic long rivers in Asia that remain free flowing (Grill et al., 2019).

Located between the Bay of Bengal and Andaman Sea, the coastal ocean offshore of the Ayeyarwady delta includes a deltaic ramp directly south of the delta; and a shallow but expansive embayment to the east, called the Gulf of Martaban (**Figure 1**). The funnel–shaped Gulf of Martaban is macrotidal, with semi-diurnal tides and a strong spring/neap cycle. Tidal energy

increases toward the eastern side of the Gulf of Martaban, where tidal ranges can exceed 7 m, and tidal current speeds reach 3 m/s (Ramaswamy et al., 2004; Rao et al., 2005). The combination of the influx of riverine muds with strong tidal energy is likely the reason that the Gulf of Martaban exhibits one of the largest perennially muddy coastal areas in the world, covering 45,000 km^2 during spring tides (Ramaswamy et al., 2004). Additionally, the Gulf of Martaban has been identified as one of the most productive areas within the Bay of Bengal; the nutrients delivered by rivers here seem to play a critical role in supporting vital fisheries (Hossain et al., 2020).

The Gulf of Martaban receives sediment and freshwater from the Ayeyarwady River, the Thanlwin River, and the smaller Sittang River; their combined sediment discharge accounts for about 600 MT of sediment potentially input to the Gulf each year (Kuehl et al., 2020). The smallest of these, the Sittang River discharges an estimated 50 MT of sediment annually (Milliman and Farnsworth, 2013). Previous studies have indicated that flows and sediment transport in tidal flats within the Sittang estuary tend to be dominated by the flood tide, but that the morphology may be heavily influenced by ebbing flows during high discharges in the rainy season (Choi et al., 2020). Similarly, *in situ* observations of three distributaries that drain the Ayeyarwady Delta showed these to be exporters of sediment during the rainy season, while during low flow conditions the distributaries may retain sediment delivered from offshore (Glover et al., 2021). While these studies showed that sediment delivery to the Gulf of Martaban responds to spatial, seasonal, and interannual variability; studies have yet to directly link the fluvial sediment sources to the depositional record offshore.

Previous studies have mapped seabed sediment texture within the Gulf (Rao et al., 2005) which has been characterized as a "mud blanket" (Hanebuth et al., 2015). Recently, however, analysis of sediment cores and CHIRP seismic data have provided insight into the depositional environment in this area. The seabed within the shallow Gulf of Martaban contains a thick mixed layer (0.25–1.2 m thick) which is evidence of intense resuspension, but exhibits relatively low accumulation rates (Kuehl et al., 2019). It has been characterized as a "fluid mud reactor" (i.e., Aller, 1998), because the frequent resuspension and apparent trapping within the Gulf likely impact geochemical cycling of organic matter there (Kuehl et al., 2019; Flynn et al., in press). Accumulation rates generally increase offshore in the Gulf of Martaban, and Flynn et al. (in press) note a general transition from the mud blanket to a zone of accumulation at about the mouth of the Gulf (**Figure 1**).

Offshore of the Gulf of Martaban a clinoform depocenter has developed spanning water depths from ~40–130 m (Kuehl et al., 2019; Liu et al., 2020). Termed the Martaban Depression Clinoform (**Figure 1**), this depocenter has been active over the Holocene (Liu et al., 2020); and currently accumulates approximately 6–8 cm/year (Flynn et al., in press; Kuehl et al., 2020). This feature appears to trap a significant fraction of the Ayeryarwady/Thanlwin River discharge of sediment and organic matter (Kuehl et al., 2019; Flynn et al., in press). However, the transport mechanisms that carry material from fluvial sources to the clinoform; and the residence time of material within the mud blanket/fluid mud reactor of the Gulf of Martaban are poorly constrained and limited by our lack of observations from the site.

The oceanographic and coastal dynamics in this region are influenced by tides and seasonal monsoons (Rodolfo, 1969; Ramaswamy and Rao, 2014). From the months May to September the region experiences Southwest (SW) monsoon conditions, dominated by strong winds from the southwest. During the months December through February, the area experiences Northeast (NE) monsoons with moderately strong winds typically from the NE (Ramaswamy and Rao, 2014).

Seasonal fluctuations in circulation have been argued to produce a bi-directional transport pathway; wherein fine-grained sediment would be imported into the Gulf of Martaban during the energetic SW monsoon, but exported westward during NE monsoon conditions (Anthony et al., 2019; Kuehl et al., 2019; Liu et al., 2020; Glover et al., 2021). Generally, historical data from this location and satellite observations have been used to characterize surface currents (Rodolfo, 1975; Rao et al., 2005), but the directions of the near-bed flows that dictate sediment movement and fate remain unclear. Additionally, CTD-Tu (Currents/Temperature/Depth/Turbidity) casts obtained in December 2017 indicated the presence of fluid mud in the bottom meters of the water column within the Gulf of Martaban (Kuehl et al., 2019). The presence of these fluid mud layers implies that the surface currents that have been characterized may be very different from near-bed currents that control sediment movement. Little is known about the near-bed processes and circulation that are responsible for maintaining the turbidity within the Gulf of Martaban, or for delivering material to offshore depocenters.

Direct observations of suspended concentrations for the Gulf of Martaban are limited to an april/May 2002 study that used filtered water samples to characterize sediment concentrations as being in the 100s of mg/L, and composed of terrigenous silty clays (Ramaswamy et al., 2004). Satellite data have been used to infer spatial patterns and have shown that turbidity in the Gulf of Martaban is especially responsive to the spring/neap cycle, with the extent of the turbid zone being largest during spring tides (Ramaswamy et al., 2004). Compilations of satellite images have also indicated a seasonal signal to the surface turbidity, with the turbid zone covering the largest expanse during the NE monsoon season of December–February (Matamin et al., 2015). Analysis of satellite data has indicated that seasonal suspended sediment concentrations are highest in December, when monthly averaged surface concentrations were estimated to exceed 200 mg/L throughout the Gulf of Martaban (Anthony et al., 2019).

In summary, the Gulf of Martaban has a global significance in terms of sediment and organic carbon transfer from land to ocean, and in basin-scale fisheries productivity. In spite of this, very little has been observed regarding estuarine hydrodynamics or suspended sediment transport within the Gulf. At present we lack data to constrain the sediment transport mechanisms that carry material from fluvial sources, through their residence in the muddy Gulf of Martaban, to their ultimate deposition in the clinoform depocenter. Observations of currents and turbidity at depth are needed to test numerical and conceptual models of hydrodynamics and sediment transport, and constrain sediment

transport pathways there. This manuscript presents data from two ADCP (Acoustic Doppler Current Profiler) transects that were obtained during December 2017 from the outer Gulf of Martaban.

2 MATERIALS AND METHODS

Within this paper, we provide a unique glimpse at hydrodynamics and sediment dynamics for the Gulf of Martaban, based primarily on water column observations taken during a research cruise.

2.1 Cruise Data

During December 2017 a research cruise was conducted on the vessel the Sea Princess over the Ayeyarwady subaqueous delta and within the Gulf of Martaban (Kuehl et al., 2019; Liu et al., 2020). Though the primary focus of the cruise was to obtain sediment bed samples and map the seafloor, it afforded a rare opportunity to obtain water column data.

2.1.1 ADCP Data

During the cruise, which surveyed over 1500-km in the northern Andaman Sea and Bay of Bengal, an ADCP was mounted from the boat, facing vertically downward to record current velocities and acoustic backscatter within the water column. Though it was not calibrated, the backscatter intensity of the ADCP acts as a proxy for the relative magnitudes and vertical distribution of suspended sediment concentrations (e.g., Holdaway et al., 1999). During this cruise, over fifteen ADCP transects were recorded covering a large geographic portion of the coastal Ayeyarwady delta and Gulf of Martaban (**Figure 1**). The TRDI (Teledyne RD Instruments) 600 kHz ADCP was configured in mode 12 and recorded measurements from 255 vertical bins each with a thickness of 33 cm for a maximum coverage of 84 m water depth. Bottom tracking that assumed the presence of a static seafloor was used to adjust current velocities to account for the boat's speed relative to the sea floor. Of these ADCP transects, six were chosen for initial analysis. Data from transects located south and west of the Ayeyarwady Delta showed a general westward direction to currents, consistent with seasonal patterns of circulation that have been published (Rodolfo, 1975; Ramaswamy and Rao, 2014). However, because the sampling period was short relative to the expected variability of non-tidal currents, this paper is limited to analyzing the ADCP data from within the tidally dominated area.

This paper focuses on two transects taken in the outer Gulf of Martaban. Transects #5 and #21 (see **Figure 1**) provided insight into the tidal control on sediment dispersal in the outer Gulf of Martaban. These two transects covered water depths that ranged from about 20–35 m. Transect #5 was located along the eastern side of the outer Gulf, while Transect #21 was located in the central area of the outer Gulf (**Figure 1**). In discussing the ADCP data, locations will be referenced with respect to distance along the transects.

Suspended sediment concentrations cannot be directly inferred from the backscatter data, because they were not calibrated. Sediment cores taken prior to both transects showed variations in grain size, indicating that sand fraction varied from ~3 to ~30% within the area sampled by these transects (data from Kuehl et al., 2019), while suspended material was previously characterized as silty clay (Ramaswamy et al., 2004). Seabed organic content in this area was fairly uniform at about 0.6–0.7% (Flynn et al., in press). Water column samples were not obtained with which to characterize suspended grain sizes or concentrations, but the ADCP backscatter remains useful for characterizing the vertical distribution of, and relative concentrations of suspended material.

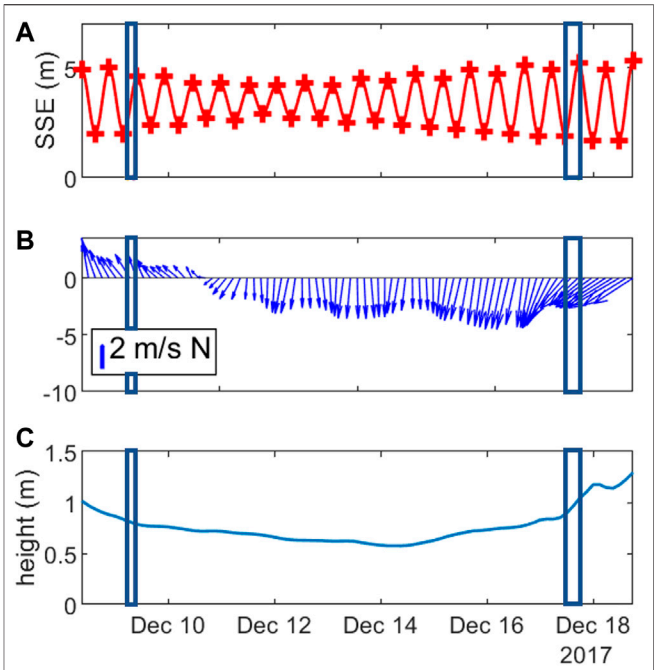

FIGURE 2 | Timeseries of oceanographic and meteorological conditions during the December 2017 research cruise. Transects #5 and #21 were obtained during the times marked. **(A)** Times of high and low tidal elevation for Duya, Myanmar (Egbert and Erofeeva, 2002). **(B)** Wind vectors and **(C)** Wave heights from GFS (Environmental Modeling Center, 2003). Wind vectors show direction toward which the modeled wind blew.

For each transect, a principal axis for the current velocity was identified using a Principal Component Analysis (PCA). The principal axes for both transects were generally oriented in a northeast/southwest direction, and the majority of the variability in the currents was along the major axes. This manuscript reports velocities components that are rotated to be along and perpendicular to the major axis of the currents, which we term the local "along Gulf" direction.

2.1.2 CTD-Tu Data

While on the cruise, several CTD-Tu (Conductivity, Temperature, Depth, and Turbidity) profiles were taken when the ship was anchored. Specifically, the CTD-Tu (RBR XRX-620) package was manually deployed, sampling at 6 Hz during descent through the water column at a rate of ~20 cm s−1. An OBS was mounted on the CTD and its voltage readings indicate relative turbidity, but were not calibrated to provide suspended sediment concentration. These were analyzed previously and shown to provide evidence that fluid muds

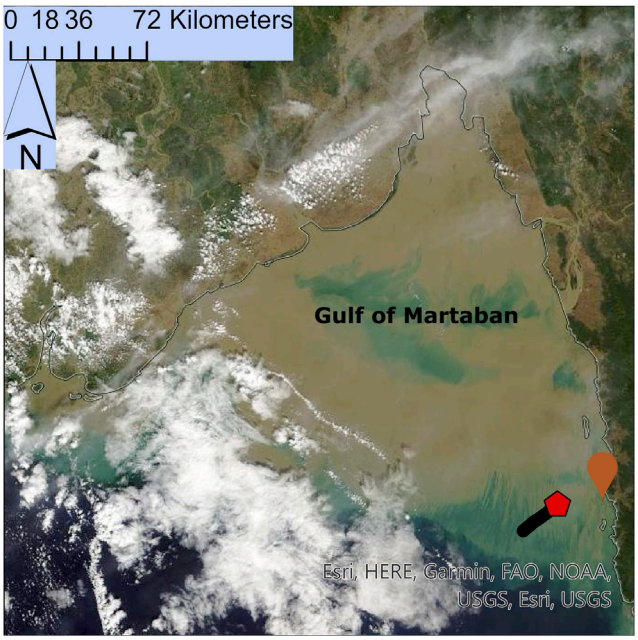

FIGURE 3 | Satellite image taken within a day of ADCP Transect #5. Location of transect (black line) and CTD-Tu (red circle) shown. Duya, Myanmar shown as orange marker. Image from NASA Worldview.

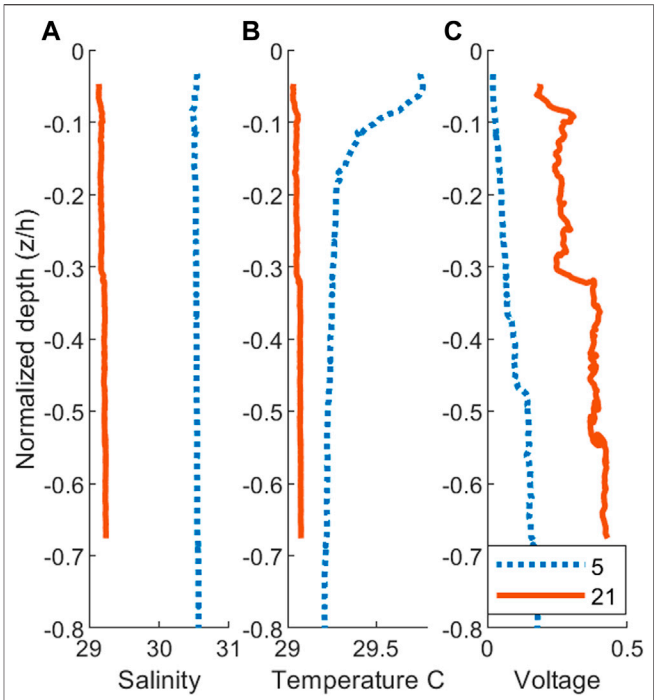

FIGURE 4 | Vertical profiles of **(A)** Salinity, **(B)** Temperature, and **(C)** Voltage from CTD-Tu. Vertical axes represent the normalized depth (z/total water depth). CTD-Tu profiles taken directly before Transect #5 (red lines) and during Transect #21 (blue dashed lines).

exist within the Gulf of Martaban, having vertical thicknesses of a few meters (Kuehl et al., 2019). Two of these CTD-Tu profiles, obtained nearly concurrently with ADCP Transects #5 and #21, are used within this manuscript to characterize water column structure to as a complement to the ADCP data.

2.2 Ancillary Data

Observations of oceanographic and meteorological data are largely unavailable for the Gulf of Martaban. Therefore, data from global numerical models provided useful information for placing the ADCP data in the context of the oceanographic and meteorological conditions present during the cruise. Data from a global tidal model (Egbert and Erofeeva, 2002) for the location of Duva, Myanmar (see **Figure 1**) allowed us to characterize the tidal conditions at the time of ADCP deployment (**Figure 2A**). Because local measurements of winds and waves were not available for the Gulf of Martaban, we used a global numerical model, the Global Forecast System (GFS (Environmental Modeling Center, 2003)) to classify the meteorological conditions during the cruise (**Figures 2B–C**). Additionally, satellite imagery from NASA Worldview Application (2021) allowed us to put the ADCP transect observations into the larger spatial context.

3 RESULTS

This section provides the observed current velocities and ADCP backscatter for two transects from the outer Gulf of Martaban recorded in December 2017. Both of these ADCP transects were initiated near the end of ebb tide; continuing through low tide and the transition into flood tide conditions (**Figure 2A**). Output from the global GFS model indicated that conditions during the cruise were rather calm, with wave heights estimated to be ~1 m (**Figure 2C**). Wind speeds were estimated at < 5 m/s, and the GFS model indicated that winds turned from being from the northwest early in the cruise, and then were primarily from the northeast (**Figure 2B**).

3.1 Eastern Gulf of Martaban: Transect #5

Transect #5 was recorded on 9 December 2017 beginning at 05:34 UTC and finishing at 08:40 UTC. The transect covered about 22 km on the eastern side of the Gulf of Martaban, with the boat traveling westward toward the middle of the Gulf of Martaban (**Figure 3**). Water depths along the transect spanned from about 25 to 35 m, with the shallowest region sampled earliest in the transect. Based on water level at the closest tidal station to the transect (Duya), tidal conditions during the 3-h transit spanned from the end of ebb tide, through slack, to flood tide (**Figure 2A**). Sediment cores were taken immediately prior to, and following the ADCP transect. These data indicate that there was little change in organic content (~0.6%); though seabed texture changed from muddy near the start of the transect, to mixed sediments (sand, silt, and clay) at the deeper end of the transect (Kuehl et al., 2019; Flynn et al., in press). The satellite imagery from the day prior to the ADCP deployment shows the sampling location to be within the fringe of the extent of the turbid waters of the Gulf of Martaban (**Figure 3**).

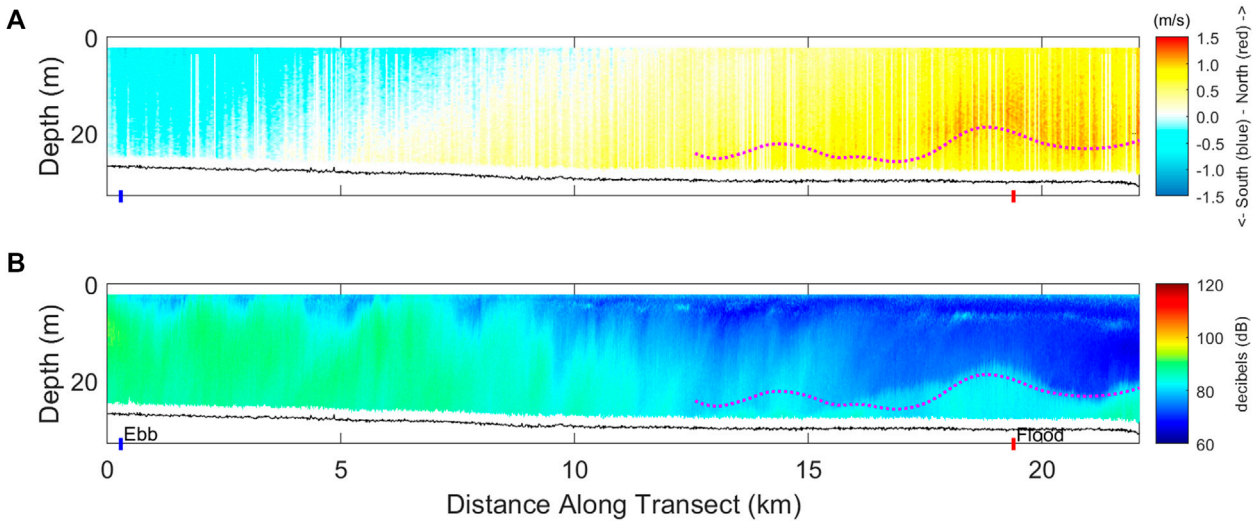

FIGURE 5 | Data observed along Transect #5. The distance traveled along the transect is shown on the horizontal axis, and water depth along the vertical axes. Depth in the water column was estimated after accounting for the approximate submerged depth of the ADCP sensor. The black line represents approximate location of the seafloor. **(A)**: water speed (m/s) in direction of primary axis, which was 9.4° clockwise from North. Blue colors indicate southward flow; red indicates northward flow. **(B)**: backscatter intensity (a measure of the return energy in decibels [dB]). The data was filtered using the Winriver II software and then a triangular smoothing filter was applied. The white vertical bars in **(A)** represent data that was removed because either the GPS or bottom tracking was deemed unreliable. The blue and red tick marks on the *x*-axis represent the position along the transect of ebb and flood, respectively, shown in **Figure 8**. The dotted lines during flood tide (~12–25 km) represent the approximate thickness of the near-bed turbid layer, as described in **Section 4.1**.

Additionally, a CTD-Tu was obtained immediately before Transect #5. This showed that the water column was well-mixed, with a thin (~few meters) surface layer that had slightly depressed salinity and increased temperature (**Figures 4A,B**). The voltage for the OBS (Optical Backscatter Sensor) provides a measure of the vertical structure of water column turbidity. It showed relatively low backscatter (~0.3 V) and indicated that the suspended sediment was well mixed at this time (**Figure 4C**). For comparison, OBS readings reached 4 V at other locations and times during this cruise (Kuehl et al., 2019).

The Principal Component Analysis (PCA) performed on the velocity data from Transect #5 showed that the principal axis of the velocities was directed 9.4° clockwise from North, aligned generally in "along Gulf" and "across Gulf" directions. The currents were strongly oscillatory, with components along the principal axis containing most (93%) of the variability in the currents. The component of the currents perpendicular to the principal axis had much smaller magnitudes (0.1 m/s), compared to velocity components that exceeded 1 m/s along the principal axis.

Considering the ADCP data in terms of the spatial variations along the 22-km transect, conditions observed over the shallower portion of the transect (0–7 km on **Figure 5A**) had a well–mixed water column with moderate current velocities. The backscatter in this portion of the transect indicated that suspended sediment was mixed throughout the water column, except for surface layers that had small backscatter (0–7 km on **Figure 5B**). This was consistent with the CTD-Tu record that showed little evidence of stratification or isolated layers of turbidity. When the boat traveled into deeper water away from the coast (17–23 km on **Figure 5**), current velocities accelerated, and the backscatter indicated that a near-bed turbid layer developed.

The changes observed along the transect correspond to tidal forcing. Considering the temporal changes in the current speed and direction (**Figure 5A**), the ADCP data show the transition from ebb to flood conditions. Initially, during the first ~5 km of the transect, which coincided with the end of ebb tide, there were moderate speeds of about 0.5 m/s that flowed southward (**Figure 5A**). Next, the speeds slowed to zero during slack water at low tide from ~5–10 km along the transect. Then, as the tide turned to flood, the current direction shifted northward and speeds exceeded 1 m/s from ~17 km to the end of the transect (**Figure 5A**).

Similarly, the backscatter intensity showed a strong relationship to the tides, indicating tidal forcing of suspended sediment. Initially, during ebb (from 0 to 5 km along the transect) there was usually a high return at all depths suggesting suspended sediment was well mixed throughout the water column (**Figure 5B**). At some times, there was evidence of clear surface plumes in the upper 3–5 m of the water, for example at 1, 3 and 5 km along the transect (**Figure 5B**). As the water speeds slowed during slack water at low tide, the upper water column cleared (at about 6–12 km in **Figure 5B**). As tidal currents turned to flood tide and accelerated, a two-layer system developed (20 km to the end of the transect, **Figure 5B**). There was evidence of suspended sediment in the bottom-most 5 m of the water column, above which the backscatter intensity showed a sharp decrease indicating the presence of a near-bed turbid layer overlain by clearer water. The current velocity also showed speeds were slow within the turbid layer but reached very fast speeds (~1.5 m/s) directly above the turbid layer (**Figure 5**).

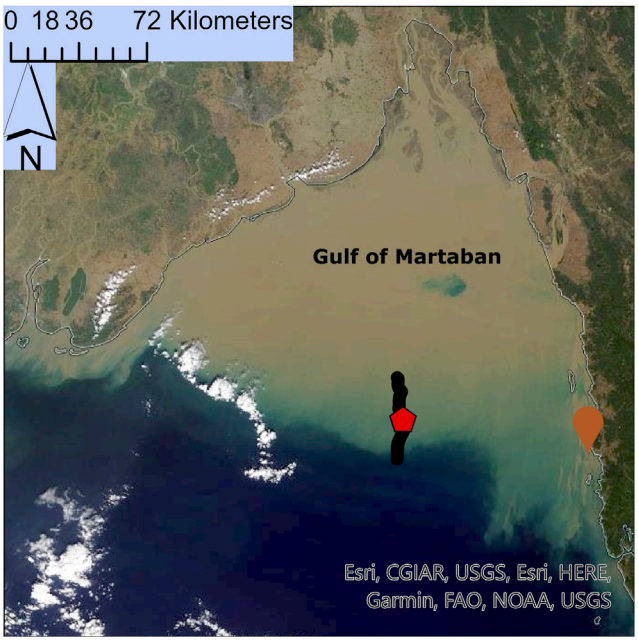

FIGURE 6 | Satellite image taken on the same day that Transect #21 was sampled. Location of transect (black line) and CTD-tu (red mark) shown. Duya, Myanmar shown as orange mark. Image from NASA Worldview.

3.2 Central Gulf of Martaban: Transect #21

Transect #21 was collected in two sections in the outer portion of the central Gulf of Martaban, with a gap of about 10-min between the two collection periods. Sampling began on December 17, at 11:39 UTC, and concluded on 17:26 UTC (**Figure 6**). The data from these two sections covered about 39 km, and were obtained over about 6 h. It sampled water depths that ranged from 20–30 m with the boat traveling southward. Additionally, a CTD-Tu was obtained during the gap in the ADCP collection. Similar to Transect #5, during the time when Transect #21 was sampled, the tides went from ebbing, through low tide at slack water, and then reached flood tide (**Figure 2**). A sediment core taken adjacent to Transect #21 showed that the seabed was about 20% sand and 80% mud; with an organic content of about 0.6% (Kuehl et al., 2019; Flynn et al., in press).

Principal Components Analysis (PCA) of the velocity data from Transect #21 showed that the principal axis of the velocities was directed 20.5° clockwise from North; roughly aligned with "along Gulf" and "across Gulf" directions. The currents at this location were strongly oscillatory, with components along the principal axis containing most (92%) of the variability in the currents. The velocity components perpendicular to the principal axis were an order of magnitude smaller (0.12 m/s) than the velocity components along the principal axis, which reached magnitudes of 1.5 m/s.

Three distinct portions of Transect #21 are evident. At the most shoreward portion of the transect (0–7 km), velocities were high (~1 m/s) and southward, and the backscatter indicated the presence of a surface turbid plume (**Figure 7**). In the next region (~7–17 km), current velocities slowed, and the turbid water was found at increasing water depths (**Figure 7**). The CTD-Tu taken in the middle of Transect 21 was located around 20 km (**Figure 4**). It showed a fairly well-mixed water column with relatively low voltage by the OBS (~0.5 V), indicating low sediment concentrations compared to other locations that were sampled during the cruise (i.e. Kuehl et al., 2019). In the more seaward portion of the transect (~25–39 km), the backscatter indicated the presence of a near-bed turbid layer, while turbidity in the upper water column was reduced (**Figure 7B**). At this point in the transect (~25–39 km), the northward directed current velocities reached high speeds (~1.5 m/s; **Figure 7A**).

The temporal changes in the current speed and direction along Transect #21 correspond to tidal forcing and show the transition from ebb to flood conditions (**Figure 7A**). The first ~10 km of the transect coincided with the timing of the ebb tide. The highest observed currents during the ebb were about 1 m/s, flowing offshore (**Figure 7A**). Next, the speeds fell to zero during slack water at low tide from ~12–17 km along the transect. Then, as the tide turned to flood, the current direction shifted northward, and speeds exceeded 1.2 m/s from ~25 km to the end of the transect (**Figure 7A**).

The backscatter record indicated that the vertical distribution of suspended sediment also responded to tidal forcing. At the beginning of the transect (0–8 km), the current was ebbing, and there were two distinct backscatter layers (**Figure 7B**). At this time, the surface waters showed much more backscatter than the lower water column, indicating that the ebb tide was exporting muddy water in the surface layer from the Gulf of Martaban. During slack tide, from 8–18 km along the transect, sediment appeared to settle as the turbid layer shifted from surface waters toward the mid-water column (**Figure 7B**). Then, flood tide commenced, and current speeds increased (20–35 km along the transect), and a near-bed turbid layer appeared in the bottom few meters of the water column (**Figure 7B**). This suspended layer experienced northward flux in the relatively thin near-bed bottom layer. Sediment concentrations during the flood tide appeared to be smaller than during the ebb tide, based on comparing the backscatter intensity during these times (**Figure 7B**).

In summary, over the conditions observed for Transect #21, fast currents (>1 m/s) occurred during both ebb and flood tidal conditions. The backscatter indicated more sediment was suspended during the ebb tide than the flood tide, even though observed currents were faster during flood. This was expected since the ebb transports water from the more turbid estuarine waters, carrying it seaward (see **Figure 6**). During the strong flows observed during the flood tidal phase, a two-layer flow developed with a turbid near-bed layer.

4 DISCUSSION

Here, the ADCP data from both transects are synthesized to look for common features during ebb and flood tide conditions, and qualitatively assessed to evaluate net sediment fluxes over the ebb–to–flood tide.

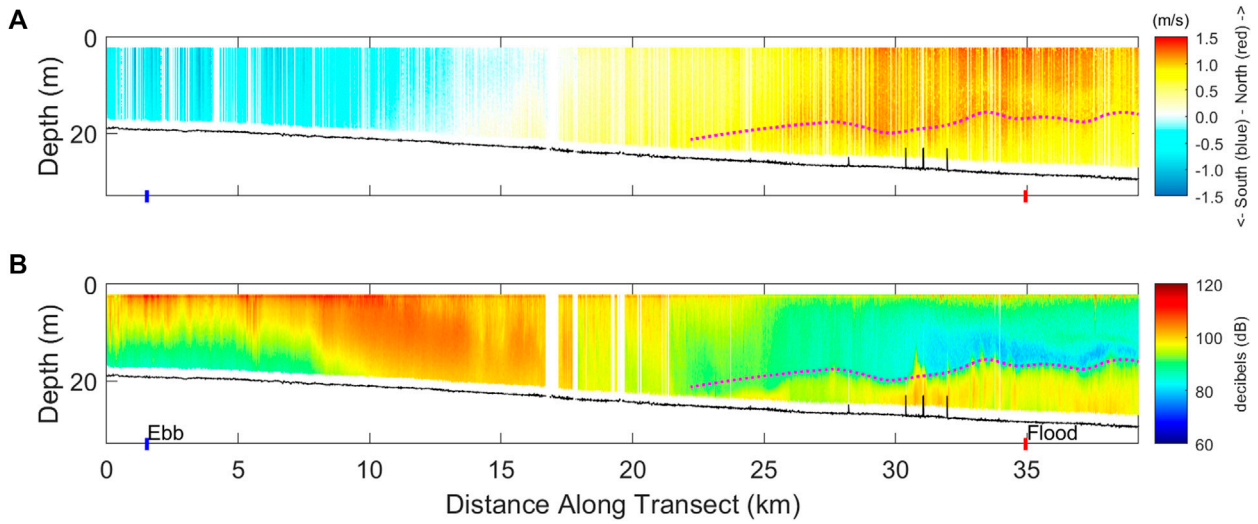

FIGURE 7 | Data observed along Transect #21. The distance traveled along the transect is shown on the horizontal axis, and water depth along the vertical axes. Depth in the water column was estimated after accounting for the approximate submerged depth of the ADCP sensor. The black line represents approximate location of the seafloor. **(A)**: water speed in direction of primary axis is displayed in the colorbar in m/s, which was 20.5 ° clockwise from North. Blue colors indicate flow out of the Gulf, red indicates flow into the Gulf **(B)**: backscatter intensity (a measure of the return energy in decibels [dB]) in the colorbar. High values of backscatter intensity indicate the presence of suspended sediment. The data was filtered using the Winriver II software and then a triangular smoothing filter was applied. The white vertical bars in **(A)** represent data that was removed because either the GPS or bottom tracking was deemed unreliable. The blue and red tick marks on the *x*-axis represent the position along the transect of ebb and flood, respectively, shown in **Figure 8**. The dashed lines during flood tide (~23–40 km) represent the approximate thickness of the near-bed turbid layer, as described in **Section 4.1**.

4.1 Vertical Structure of Ebb vs Flood

Comparing conditions observed at these two transects (e.g., **Figure 4**), the eastern Gulf of Martaban (Transect #5) had higher salinity than the transect from the central Gulf of Martaban (Transect #21). Satellite imagery indicated that the surficial suspended sediment concentrations would be higher in the central region compared to the eastern Gulf of Martaban (**Figure 3**, **Figure 6**), and the ADCP backscatter was consistent with this: showing higher backscatter for Transect #21 than #5 (**Figure 5B**, **Figure 7B**). Additionally, the ADCP transects show that the eastern region had lower current velocities than the central region, at least for the time sampled (**Figure 5A**, **Figure 7A**). Current speeds along both transects reached magnitudes of about 1.5 m/s during flood tide, and for both transects the fastest currents occurred in the mid-water column during flood (**Figure 5A**, **Figure 7A**).

To better visualize the vertical structure of the currents and suspended sediment, profiles for each were taken from Transects #5 and #21 that were representative of ebb and flood conditions (**Figure 8**). These profiles present data that was smoothed by time-averaging the samples for 1-min along the transect, and by applying a 1-m running average in the vertical. For both transects, the profiles for flood tide had faster current velocities than the ebb tide (**Figures 8A,C**). Additionally, the vertical structure for the flood tides showed more shear at both locations than the ebb tide; and the flood tide had a mid-water column peak in speed, whereas the ebb tides showed current speeds to increase toward the surface water (**Figures 8A,C**).

Though currents were faster for these profiles during flood conditions than ebb, the acoustic backscatter were higher during ebb than flood (**Figure 8**). This indicates that concentrations were higher during ebb than flood. The acoustic backscatter from both transects showed that the vertical distribution of suspended sediment differed during ebb tide compared to flood (**Figures 8B,C**). During ebb tide, suspended sediment was fairly well–mixed at Transect #5 (**Figure 8B**), while a surface turbid layer was seen in the central Gulf of Martaban (Transect #21; **Figure 8D**). During flood conditions, however, the acoustic backscatter from both transects indicated the presence of near-bed turbid layers, with high backscatter evident in the bottom 40% of the water column (**Figures 8B,D**).

The backscatter records from both transects were analyzed to look for a sharp vertical gradient in suspended sediment concentrations, i.e., a lutocline. The thickness of the near-bed turbid layer for the flood portions of the transects were identified and are shown as dotted lines in **Figure 5B**, **Figure 7B**. The lutocline was identified as the deepest point for which a threshold backscatter reading was observed. High-frequency variability in the layer thickness was removed by application of a Robust Loess smoothing function. Thus identified, these near-bed layers ranged from about 2–11 m in thickness (dotted lines in **Figure 5B**, **Figure 7B**). Interestingly, the velocity structure of the flood–tidal currents showed a similar behavior to the thickness of the near-bed turbid layer. Velocities within the turbid layer tended to be lower than the velocities immediately above the turbid layer, and the thickness of these turbid layers aligned with the approximate height of the mid-water column peak in speeds (**Figure 5A**, **Figure 7A**).

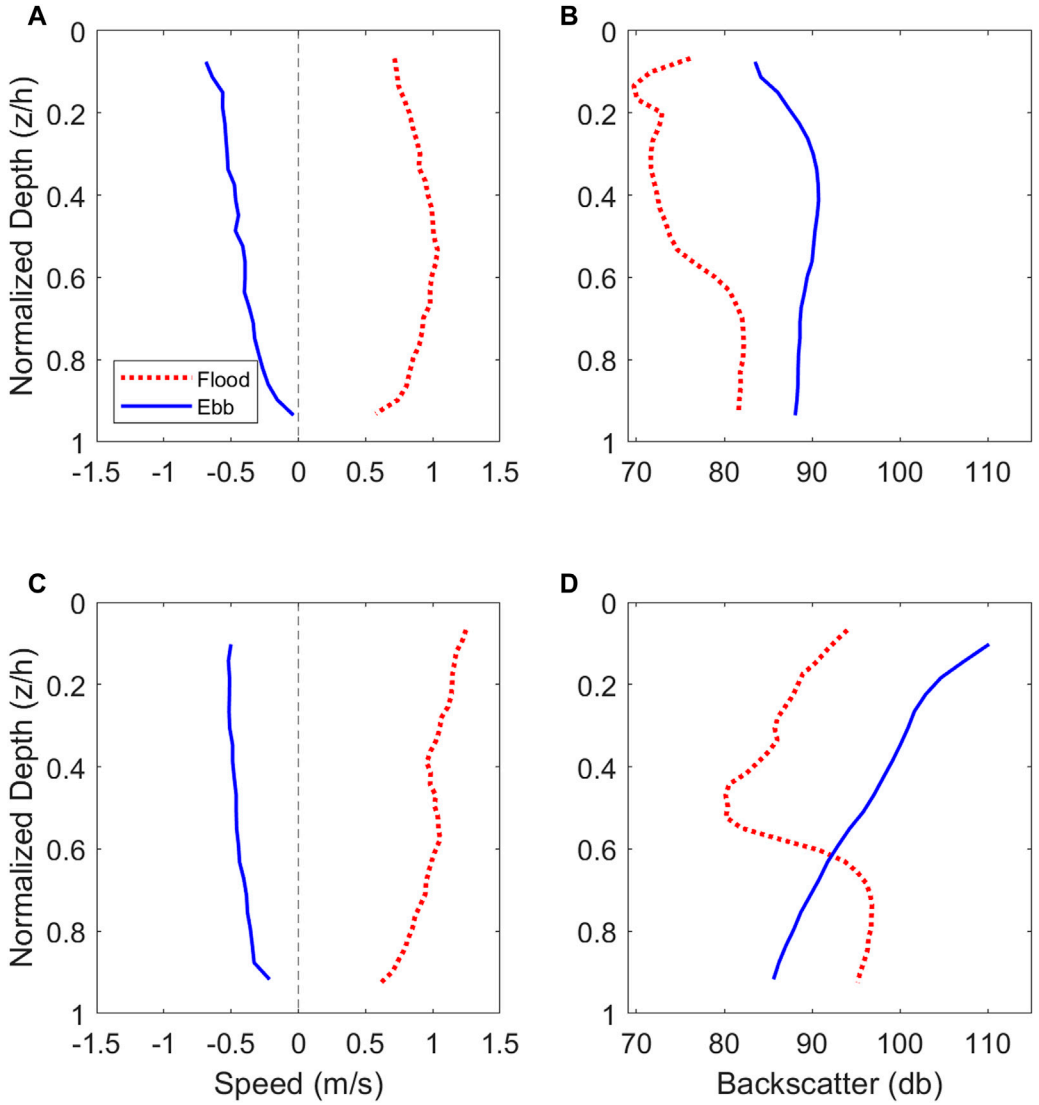

FIGURE 8 | Vertical profiles of velocity and backscatter from Transects #5 and #21 taken during Ebb and Flood conditions. The profiles averaged the measurements for 1-min; and over1-m depth intervals. Panels **(A)** and **(C)** display the velocity components and speed. Panels **(B)** and **(D)** show the backscatter return.

This provides evidence that sediment–induced stratification (Smith and McLean, 1977; Glenn and Grant, 1987) dampened vertical mixing and influenced the vertical structure of the observed currents during flood tide conditions. The reduced velocities within the turbid bottom layer could be attributed to enhanced drag and reduced turbulent mixing due to the increased density gradient in the bottom layers (e.g., Trowbridge and Kineke 1994; Friedrichs et al., 2000).

4.2 Tidal Modulation of Sediment Flux

Because the ADCP backscatter was not calibrated for suspended sediment, and because the transects did not cover a full ebb–to–flood tidal cycle, it is impossible to quantitatively assess sediment fluxes. However, the backscatter and current velocity data indicate that seaward sediment flux was an important component of the net flux for the conditions sampled. The ADCP backscatter was higher during ebb conditions than flood for both transects (**Figures 8B,D**). During flood conditions at both transects, near-bed turbid layers appeared, but they had lower backscatter values than those seen for ebb conditions (**Figures 8B,D**). Additionally, current velocities were depressed in the bottom boundary layer where these turbid layers formed (**Figures 8A,C**). Furthermore the transects were begun during the waning portion of ebb conditions, when velocities were decreasing and therefore likely underestimated the capacity of the ebb tides to transport sediment. Taken together, these indicate that the flood tides would not be very effective at transporting sediment, so that

the ebb tides may contribute a significant part of the net sediment flux.

The ADCP data, made in water depths of ~30 m, contrast somewhat with the observations that have been made in the shallower, tidal-river portions of the sedimentary system. For example, water column observations obtained over a 3-day period on a tidal flat of the Sittang River, saw sediment fluxes were dominated by landward pulses during flood tidal bores (Choi et al., 2020). Geomorphology indicated that over longer-term timescales (seasonal to century), however, ebbing conditions during high discharges (i.e., during the southeast monsoon, or tropical cyclones) were important to maintaining the structures of the Sittang River channels and meander bends (Choi et al., 2020). Water column observations from three distributary channels that spanned the Ayeyarwady Delta similarly showed a seasonal variation in ebb vs flood-tide dominance of sediment flux (Glover et al., 2021). During the rainy season, the three distributary channels showed export of fluvial sediment to the shelf. During the low flow season, however, the eastern-most distributary (the Yangon River estuary) appeared to have sediment fluxes dominated by the flood tide indicating that sediment from the Gulf of Martaban was transported landward in this channel during these conditions (Glover et al., 2021).

These ADCP transects were located in the transition zone between what has been characterized as a "fluid mud reactor" (i.e., Aller 1998) within the shallow Gulf of Martaban and the clinoform depocenter (Kuehl et al., 2019; Liu et al., 2020). Transect #21, in particular, was located at the landward edge of the clinoform (**Figure 1**). The residence time of sediment within the Gulf, and resultant geochemical cycling of organic matter associated with the sediment, depend on the specific transport mechanisms that deliver material from the muddy Gulf of Martaban to the depocenter. Mechanisms that have been suggested for delivering sediment from the turbid Gulf of Martaban to the clinoform include bottom nepheloid layers, seasonal variations in wind-driven currents, storm-driven transport, and tidally modulated fluxes (Ramaswamy et al., 2004; Liu et al., 2020).

Though limited in scope, the data from this study indicate that tidal pumping creates export of sediment during ebb tides that deliver sediment from the Gulf of Martaban to the depocenter. It also implies that tidal straining, whereby stratification effects impact the vertical distribution of momentum and suspended sediment concentration may play a role. Classically, tidal straining has been attributed to variations in density due to salinity (i.e., Simpson et al., 1990), and many estuaries exhibit the straining effect during ebb tides when freshwater is carried over more salty water (e.g., Scully and Friedrichs 2007). In the Gulf of Martaban data, however, the suppression of turbulence appears to occur during flood conditions, when the clearer water from the deep–sea is carried over the muddy water from the Gulf of Martaban. Similar behavior has been observed in the Huanghe Estuary, and attributed to longitudinal variations in suspended sediment availability (Wang and Wang 2010).

The apparent importance of ebb tidal sediment flux for these locations within the Gulf of Martaban provide an interesting contrast to other estuaries that have been classified as flood dominant. To better quantify the sediment residence times within the Gulf of Martaban, and delivery mechanisms from riverine sources to the clinoform depocenter, however, obviously requires consideration of larger spatical scales and longer timescales. Numerical models that couple hydrodynamics and suspended sediment that can reproduce the vertical structure of these ebb and flood conditions may provide insight into the transport mechanisms that carry sediment from the turbid zone to depocenters. Multi-scale numerical models would be needed to place in context the relative contributions of seasonal, tidal, and spatial variations in sediment delivery that have been observed in the tidal rivers of the system (e.g., Choi et al., 2020; Glover et al., 2021), with the larger scale development of the Gulf mud blanket and Martaban Depression clinoform. Additionally, a three-dimensional numerical model could put these limited observations into the larger context of the Gulf of Martaban by accounting for exchanges with the Ayeryarwady delta region, the impact of baroclinic forcings, spring/neap variability, and seasonal variations in winds and wave energy.

5 CONCLUSION

Though limited, this dataset provides rare observations of currents and acoustic backscatter for the outer portion of the central and eastern Gulf of Martaban, one of the world's largest perennially turbid coastal areas. The observations, made in ~20–35 m water depths, indicated that the currents are strongly oscillatory. The primary axes of the currents were directed in generally northeast/southwest direction at both transects. Over the times sampled, surface currents oscillated between 1 m/s seaward (during ebb) to >1.5 m/s landward (during flood), and velocity components were much larger in the along-Gulf directions compared to the across-Gulf directions. Both transects were sampled as ebb tide conditions gave way to slack, and then flood conditions. For the situations that were sampled, the flood velocities exceeded the current speeds observed during ebb conditions. The ADCP backscatter also indicated that the vertical distribution of suspended sediment varied spatially and with the tidal conditions. Acoustic backscatter and satellite imagery indicated larger suspended sediment concentrations in the central Gulf of Martaban than in the eastern Gulf of Martaban. For both transects, the backscatter signal was larger during ebb conditions than flood, even though current velocities were faster during flood. During ebb tidal conditions, suspended sediment appeared vertically well–mixed in the eastern Gulf transect; or formed a surface plume in the central Gulf transect. During slack tide, both transects recorded that the suspended sediment seemed to settle toward the bottom. For both transects as slack gave way to flood tide, fast currents coincided with the appearance of a near-bed turbid area that ranged from 2–11 m in thickness. During flood tide at both transects, the velocity profiles showed mid-water column maximums in current speeds. The upper limit of the thickness of the near-bed turbid layer was similar to the height of the maximums in velocity. This could indicate a feedback

mechanism between the near-bed turbidity and velocity shear, such as suspended–sediment induced stratification that would be expected for conditions of near-bed fluid muds or bottom nepheloid layers. Though it bears more consideration, the data indicate that tidal straining during flood conditions limited the flood-tidal sediment inputs into the Gulf of Martaban, while export of sediment during ebb conditions is an important component of the net sediment balance for the outer Gulf of Martaban. This data indicates that ebb-tidal delivery may be an important mechanism for delivering material from the Gulf of Martaban mud blanket to the Martaban Depression clinoform.

DATA AVAILABILITY STATEMENT

This article uses data from two online repositories. The ADCP datasets can be found in Harris and Wacht (2021). *"Acoustic Doppler Current Profiler (ADCP) data 2017: Ayeyarwady Delta, Myanmar"*. William & Mary. https://doi.org/10.25773/e55p-dd70. The CTD-Tu data was archived in Kuehl and Harris (2020) *"Fate of Ayeyarwady and Thanlwin River sediment: relative importance of oceanographic and tectonic controls - Associated dataset"*. William & Mary. https://doi.org/10.25773/g7zk-sg96.

AUTHOR CONTRIBUTIONS

CH, JW: conceptualization writing-original draft preparation. CH, JW, and JC: ADCP methodology. MF and JW: ancilliary data. CH: supervision and funding acquisition. All: writing-review and editing. All authors have read and agreed to the published version of the manuscript.

FUNDING

This research was supported by the National Science Foundation, USA grant OCE-1737221.

ACKNOWLEDGMENTS

This paper is Contribution No. 4080 of the Virginia Institute of Marine Science, William and Mary. The authors thank Steve Kuehl (VIMS) who acted as chief scientist on the research cruise and commented on earlier presentations of this work; and Danielle Tarpley (VIMS, ACOE) who oversaw the ADCP deployment. Additionally, Paul Liu (NC State University) aided with ADCP deployment, cruise logistics, and project design. We appreciate conversations with Todd Averett and Jeff Nelson (both William and Mary) and Andrea Ogston (U. Washington) that improved the work. The authors express their deepest appreciation to the students and faculty at University of Yangon and Mawlamyine University who supported and participated in the research cruise. We also thank the Captain and crew of the Yangon-based Sea Princess, as this study would not have been possible without their efforts. Finally, we appreciate the helpful and insightful comments of two reviewers, which we feel helped improve the manuscript.

REFERENCES

Aller, R. C. (1998). Mobile Deltaic and Continental Shelf Muds as Suboxic, Fluidized Bed Reactors. *Mar. Chem.* 61 (3-4), 143–155. doi:10.1016/s0304-4203(98)00024-3

Anthony, E. J., Besset, M., Dussouillez, P., Goichot, M., and Loisel, H. (2019). Overview of the Monsoon-Influenced Ayeyarwady River Delta, and Delta Shoreline Mobility in Response to Changing Fluvial Sediment Supply. *Mar. Geology* 417, 106038. doi:10.1016/j.margeo.2019.106038

Baronas, J. J., Stevenson, E. I., Hackney, C. R., Darby, S. E., Bickle, M. J., Hilton, R. G., et al. (2020). Integrating Suspended Sediment Flux in Large Alluvial River Channels: Application of a Synoptic Rouse-Based Model to the Irrawaddy and Salween Rivers. *J. Geophys. Res. Earth Surf.* 125 (9), e2020JF005554. doi:10.1029/2020JF005554

Bird, M. I., Robinson, R. A. J., Win Oo, N., Maung Aye, M., Lu, X. X., Higgitt, D. L., et al. (2008). A Preliminary Estimate of Organic Carbon Transport by the Ayeyarwady (Irrawaddy) and Thanlwin (Salween) Rivers of Myanmar. *Quat. Int.* 186 (1), 113–122. doi:10.1016/j.quaint.2007.08.003

Choi, K., Kim, D., and Jo, J. (2020). Morphodynamic Evolution of the Macrotidal Sittaung River Estuary, Myanmar: Tidal versus Seasonal Controls. *Mar. Geology* 430, 106367. doi:10.1016/j.margeo.2020.106367

Egbert, G. D., and Erofeeva, S. Y. (2002). Efficient Inverse Modeling of Barotropic Ocean Tides. *J. Atmos. Oceanic Technol.* 19 (2), 183–204. doi:10.1175/1520-0426(2002)019<0183:eimobo>2.0.co;2

Environmental Modeling Center (2003). *The GFS Atmospheric Model.* College Park, MD: National Centers for Environmental Prediction Office. Note 442, 14.

Flynn, E. R., Kuehl, S. A., Harris, C. K., and Fair, M. J. (in press). Sediment and Terrestrial Organic Carbon Budgets for the Offshore Ayeyarwady Delta, Myanmar: Establishing a Baseline for Future Change. *Mar. Geology*. 106782. doi:10.1016/j.margeo.2022.106782

Friedrichs, C. T., Wright, L. D., Hepworth, D. A., and Kim, S. C. (2000). Bottom-Boundary-Layer Processes Associated with Fine Sediment Accumulation in Coastal Seas and Bays. *Continental Shelf Res.* 20 (7), 807–841. doi:10.1016/s0278-4343(00)00003-0

Glenn, S. M., and Grant, W. D. (1987). A Suspended Sediment Stratification Correction for Combined Wave and Current Flows. *J. Geophys. Res. Oceans* 92 (C8), 8244–8264.

Glover, H. E., Ogston, A. S., Fricke, A. T., Nittrouer, C. A., Aung, C., Naing, T., et al. (2021). Connecting Sediment Retention to Distributary – Channel Hydrodynamics and Sediment Dynamics in a Tide-dominated delta: The Ayeyarwady Delta, Myanmar. *J. Geophys. Res. Earth Surf.* 126 (3), e2020JF005882. doi:10.1029/2020jf005882

Grill, G., Lehner, B., Thieme, M., Geenen, B., Tickner, D., Antonelli, F., et al. (2019). Mapping the World's Free-Flowing Rivers. *Nature* 569 (7755), 215–221. doi:10.1038/s41586-019-1111-9

Hanebuth, T. J. J., Lantzsch, H., and Nizou, J. (2015). Mud Depocenters on Continental Shelves-Appearance, Initiation Times, and Growth Dynamics. *Geo-Mar Lett.* 35 (6), 487–503. doi:10.1007/s00367-015-0422-6

Holdaway, G. P., Thorne, P. D., Flatt, D., Jones, S. E., and Prandle, D. (1999). Comparison Between ADCP and Transmissometer Measurements of Suspended Sediment Concentration. *Continental Shelf Res.* 19 (3), 421–441. doi:10.1016/s0278-4343(98)00097-1

Hossain, M. S., Sarker, S., Sharifuzzaman, S. M., and Chowdhury, S. R. (2020). Primary Productivity Connects Hilsa Fishery in the Bay of Bengal. *Sci. Rep.* 10 (1), 5659–5716. doi:10.1038/s41598-020-62616-5

Kuehl, S. A., Williams, J., Liu, J. P., Harris, C., Aung, D. W., Tarpley, D., et al. (2019). Sediment Dispersal and Accumulation Off the Ayeyarwady Delta–Tectonic and

Oceanographic Controls. *Mar. Geology* 417, 106000. doi:10.1016/j.margeo.2019.106000

Kuehl, S. A., Yang, S., Yu, F., Copard, Y., Liu, J., Nittrouer, C. A., et al. (2020). Asia's Mega Rivers: Common Source. Diverse Fates. *Eos Trans. Am. Geophys. Union* 101. doi:10.1029/2020EO143936

Liu, J. P., Kuehl, S. A., Pierce, A. C., Williams, J., Blair, N. E., Harris, C., et al. (2020). Fate of Ayeyarwady and Thanlwin Rivers Sediments in the Andaman Sea and Bay of Bengal. *Mar. Geology* 423, 106137. doi:10.1016/j.margeo.2020.106137

Matamin, A. R., Ahmad, F., Mamat, M., Abdullah, K., and Harun, S. (2015). Remote Sensing of Suspended Sediment Over Gulf of Martaban. *Ekologia* 34 (No. 1), 54–64. doi:10.1515/eko-2015-0006

McKee, B. A., Aller, R. C., Allison, M. A., Bianchi, T. S., and Kineke, G. C. (2004). Transport and Transformation of Dissolved and Particulate Materials on Continental Margins Influenced by Major Rivers: Benthic Boundary Layer and Seabed Processes. *Continental Shelf Res.* 24 (7-8), 899–926. doi:10.1016/j.csr.2004.02.009

Meade, R. H. (1996). "River-Sediment Inputs to Major Deltas," in *Sea-Level Rise and Coastal Subsidence* (Dordrecht: Springer), 63–85. doi:10.1007/978-94-015-8719-8_4

Milliman, J. D., and Farnsworth, K. L. (2013). *River Discharge to the Coastal Ocean: A Global Synthesis*. Cambridge, United Kingdom: Cambridge University Press.

Milliman, J. D., and Meade, R. H. (1983). World-Wide Delivery of River Sediment to the Oceans. *J. Geology* 91 (1), 1–21. doi:10.1086/628741

NASA Worldview Application (2021). Part of the NASA Earth Observing System Data and Information System (EOSDIS). Available at: https://worldview.earthdata.nasa.gov.

Ramaswamy, V., and Rao, P. S. (2014). Chapter 17 the Myanmar Continental Shelf. *Geol. Soc. Lond. Mem.* 41 (1), 231–240. doi:10.1144/M41.17

Ramaswamy, V., Rao, P. S., Rao, K. H., Thwin, S., Rao, N. S., and Raiker, V. (2004). Tidal Influence on Suspended Sediment Distribution and Dispersal in the Northern Andaman Sea and Gulf of Martaban. *Mar. Geology* 208 (1), 33–42. doi:10.1016/j.margeo.2004.04.019

Rao, P. S., Ramaswamy, V., and Thwin, S. (2005). Sediment Texture, Distribution and Transport on the Ayeyarwady Continental Shelf, Andaman Sea. *Mar. Geology* 216 (4), 239–247. doi:10.1016/j.margeo.2005.02.016

Rodolfo, K. S. (1969). Sediments of the Andaman Basin, Northeastern Indian Ocean. *Mar. Geology* 7 (5), 371–402. doi:10.1016/0025-3227(69)90014-0

Rodolfo, K. S. (1975). "The Irrawaddy Delta: Tertiary Setting and Modern Offshore Sedimentation," in *Deltas: Models for Exploration* (United States: Houston Geological Society), 329–348.

Scully, M. E., and Friedrichs, C. T. (2007). Sediment Pumping by Tidal Asymmetry in a Partially Mixed Estuary. *J. Geophys. Res. Oceans* 112 (C7), C07028. doi:10.1029/2006jc003784

Simpson, J. H., Brown, J., Matthews, J., and Allen, G. (1990). Tidal Straining, Density Currents, and Stirring in the Control of Estuarine Stratification. *Estuaries* 13 (2), 125–132. doi:10.2307/1351581

Smith, J. D., and McLean, S. R. (1977). Spatially Averaged Flow Over a Wavy Surface. *J. Geophys. Res.* 82 (12), 1735–1746.

Trowbridge, J. H., and Kineke, G. C. (1994). Structure and Dynamics of Fluid Muds on the Amazon Continental Shelf. *J. Geophys. Res.* 99 (C1), 865–874. doi:10.1029/93jc02860

Wang, X. H., and Wang, H. (2010). Tidal Straining Effect on the Suspended Sediment Transport in the Huanghe (Yellow River) Estuary, China. *Ocean Dyn.* 60 (5), 1273–1283. doi:10.1007/s10236-010-0298-y

Conflict of Interest: JC was employed by Blue Coast Engineering.

The remaining authors declare that the research was conducted in the absence of any commercial or financial relationships that could be construed as a potential conflict of interest.

Publisher's Note: All claims expressed in this article are solely those of the authors and do not necessarily represent those of their affiliated organizations, or those of the publisher, the editors, and the reviewers. Any product that may be evaluated in this article, or claim that may be made by its manufacturer, is not guaranteed or endorsed by the publisher.

frontiers | Frontiers in Earth Science

REVIEW
published: 19 May 2022
doi: 10.3389/feart.2022.868701

Dispersion of Benthic Plumes in Deep-Sea Mining: What Lessons Can Be Learned From Dredging?

Rudy Helmons[1,2]*, *Lynyrd de Wit*[3], *Henko de Stigter*[4] and *Jeremy Spearman*[5]

[1]Technische Universiteit Delft, Offshore and Dredging Engineering, Delft, Netherlands, [2]Norwegian University of Science and Technology, Mineral Production and HSE, Trondheim, Norway, [3]Stichting Deltares, Ecosystems and Sediment Dynamics, Delft, Netherlands, [4]Royal Netherlands Institute for Sea Research, Texel, Netherlands, [5]HR Wallingford, Dredging and Coasts & Oceans, Wallingford, United Kingdom

Over the past decade, deep-sea mining (DSM) has received renewed interest due to scarcity of raw materials. Deep-sea mining has been spurred by the need for critical resources to support growing populations, urbanization, high-tech applications and the development of a green energy economy. Nevertheless, an improved understanding of how mining activities will affect the deep-sea environment is required to obtain more accurate assessment of the potential environmental impact. In that regard, the sediment plumes that are generated by the mining activity have received the highest concern, as these plumes might travel for several kilometers distance from the mining activity. Various plume sources are identified, of which the most profound are those generated by the excavation and collection process of the seafloor mining tool and the discharge flow to be released from the surface operation vessel after initial dewatering of the ore. In this review, we explore the physical processes that govern plume dispersion phenomena (focusing in the main on benthic plumes), discuss the state of the art in plume dispersion analysis and highlight what lessons can be learned from shallow water applications, such as dredging, to better predict and reduce the spread and impact of deep-sea mining plumes.

Keywords: sediment transport, negatively-buoyant plumes, flocculation, aggregation, sediment spill

OPEN ACCESS

Edited by:
Daniel R. Parsons,
University of Hull, United Kingdom

Reviewed by:
Anabela Oliveira,
Instituto Hidrográfico, Portugal
Vera Van Lancker,
Royal Belgian Institute of Natural Sciences, Belgium

***Correspondence:**
Rudy Helmons
r.l.j.helmons@tudelft.nl

Specialty section:
This article was submitted to Marine Geoscience, a section of the journal Frontiers in Earth Science

Received: *03 February 2022*
Accepted: *25 April 2022*
Published: *19 May 2022*

Citation:
Helmons R, de Wit L, de Stigter H and Spearman J (2022) Dispersion of Benthic Plumes in Deep-Sea Mining: What Lessons Can Be Learned From Dredging? Front. Earth Sci. 10:868701. doi: 10.3389/feart.2022.868701

1 INTRODUCTION

The demand for critical raw materials, such as cobalt and rare earth elements is growing worldwide. This growth in demand is driven by the increasing world population and its increasing welfare, urbanization and development of technology (Hein et al., 2020). One of the main drivers nowadays is the electrification of the energy supply, e.g., cars, batteries, PV cells and wind-turbines. There is an increased global attention to the potential of deep-sea mineral deposits as an unexploited resource for various (critical) raw materials, and they is considered as a potential alternative to terrestrial deposits, hence they are of high economic interest (Wedding et al., 2015).

In general, three types of deposits, each with their own characteristics, are considered, i.e., polymetallic nodules, seafloor massive sulfides and cobalt-rich crusts. Polymetallic nodules are found on the surface of abyssal plains of the oceans, typically at water depths of 4–6 km. Polymetallic nodules are rich in metals and rare earth elements. The most extensive known nodule deposits are found in the Clarion Clipperton Fracture Zone (CCFZ) in the Pacific Ocean and the Indian Ocean Nodule Field (Hein et al., 2020). Seafloor massive sulphide (SMS) deposits are areas of hard substratum with high base metal and sulphide content that form through hydrothermal

circulation and are commonly found at hydrothermal vents. Such vents are typically found at tectonic plate boundaries and undersea volcanoes, e.g., Mid-Atlantic Ridge, Indian Ocean and Bismarck Sea (Boschen et al., 2013). Cobalt-rich crusts (CRC) are rock-like metalliferous mineral layers that form on the flanks of seamounts. Depending upon the concentration of metal compounds in the sea water, crusts with different thicknesses have formed in different ocean regions, ranging from 2 to 26 cm thickness. Most crusts have been found in the Prime Crust Zone (north-west Pacific), north-east of the Pacific Island states and Indian Ocean (Hein and Petersen, 2013).

While being of economic interest, these deposits are also essential habitats for benthic communities (Kaiser et al., 2017). Concerns exist on the recovery rate of the area affected by the mining activity (Gollner et al., 2017).

The structure of this paper is as follows. First, we provide an overview of a typical mining system and discuss the main comparisons and differences for the three main marine mineral deposit types. In the next chapter, we introduce the turbidity plume theory and apply it to plume sources originating from a seafloor mining tool, based on publicly available equipment properties. We will discuss relevant sediment properties and we will elaborate on to what extent particle aggregation might be of influence on the behavior of turbidity plumes. Next will be an analysis of how specific conditions at marine mineral deposits might be of influence on the generated turbidity plumes. Finally, we will take a closer look about what knowledge is currently lacking for deep-sea mining, but where we might benefit from experiences in shallow waters, e.g., in the field of dredging. This will be done mainly through analysis of near-bed turbidity discharges occurring from trailing suction hopper dredges. In addition, we will indicate what experiences from dredging might bring to the new field of deep-sea mining, aiming at improved prediction of plume dispersion and what might be done to minimize environmental impact caused by the equipment.

1.1 Mining Process

For each of the deposits, the lay-out of the entire mining system will be comparable. The ore is to be excavated and collected by one or more seafloor mining tools. For nodules, this pick-up process can be either hydraulic, mechanical or a combination of both. Typically, such collectors not only collect nodules, but also sediments and an excess of water. In the collector, nodules are to be separated from the entrained water. The excess of water and sediments will then be discharged as a plume behind the collector, which is often referred to as a collector plume.

In the case of SMS and CRC, the hard substrate needs to be excavated by rock cutting machines. So far, little is known about what particle size distribution is to be expected, especially to what extent fines (also referred to as fine sediment, here defined as having a grain size diameter <63 μm) will be generated, which will depend on rock properties, water depth and the excavation tool (Alvarez Grima et al., 2015; Helmons et al., 2016). As a result, little is known about the amount of fines that will be generated and spilled (not collected) by the seafloor mining tool. The spilled fines might result in a turbidity flow. To date there has been no deep-sea mining of SMS although the Solwara project, which concerned the mining of SMS in Papua New Guinea in 1,450–1,700 m water depth, progressed as far as a full Environmental Impact Assessment (Nautilus Minerals, 2008) and production of a full-scale mining plant. The project collapsed in 2019 when the developer, Nautilus, went into administration. There has been no full-scale mining of cobalt-rich crust to date although in July 2020 Japan Oil, Gas & Metals National Corporation (JOGMEC, 2020), successfully undertook test mining of cobalt-rich crust from the Takuyo No. 5 Seamount approximately 400 km east of Tokyo (JOGMEC, 2020).

The seafloor mining tool will feed the ore to a vertical transport system to transport the ore to surface. Once the stream of ore, water and remaining sediments arrives at the production support vessel, the ore needs to be dewatered and the excess water and sediment will be returned back to the deep sea, creating a discharge plume of fine particulate material (Oebius et al., 2001). Scenarios considered for the return water plume foresee that it will be released 1) in the water column below the thermocline, or 2) near the seabed (Washburn et al., 2019).

In the exploitation phase of nodule mining, a typical seafloor mining tool would have a width of 10–20 m and would move forward at a speed of approximately 0.3–0.5 m/s (Global Sea Mineral Resources NV, 2018). Estimations of seabed disturbance (or erosion depth) are in the region of 7 cm (Lang et al., 2019), but others state a range of potentially 5–15 cm (Global Sea Mineral Resources NV, 2018), or 10–15 cm (Nauru Ocean Resources Inc, 2021). Little information is publicly available regarding the estimated amount of excess water discharged by the collector system, these vary in the range of 125—375 L/s per meter width of a collector (Lang et al., 2019). Based on the estimated erosion depth and the discharge flow rate, a volumetric sediment concentration of approximately 1–3% is expected, which is equivalent to 25–80 g/L (initial bed porosities have been reported to be in the range of 0.8–0.9 (Jones, et al., 2021)). In the mining concepts published so far, independent of the choice of the collection method, the excess water and sediment will be discharged behind the mining vehicle, creating a plume of fine particulate material.

In the case of the near-bed generated plumes, i.e., nodule collector, SMS/CRC excavator or return water, sediment redeposition and bottom blanketing within the vicinity of the mining site could potentially bury benthic organisms, clog the respiratory surfaces of filter feeders and pollute the food supply for most benthic organisms. Both processes would affect the deep-sea ecosystem structure and functioning to a certain, although presently unknown, extent (Ramirez-Llodra, et al., 2011; Jones, et al., 2017). Currently, it is not yet known how large the affected area will turn out to be, and thus it is uncertain how severe the resulting environmental impact will be. From a technical point of view, it is of utmost importance to 1) be able to accurately predict where these plumes will travel and what deposition layer will be generated and 2) minimize the area affected by said near-bed plumes. Experience gained in turbidity management and analysis by the dredging industry can be of help to achieve aforementioned objectives.

2 TURBIDITY PLUME THEORY

The mixture of water, sediment and fine-grained nodule debris that is discharged behind the mining vehicle can be characterized as a negatively buoyant jet or plume. Due to its higher density, the plume will sink quickly to the seabed, from where it will propagate as a turbidity current. The following analysis is valid for any type of mining plume, but here special emphasis will be put on the sediment plume generated by a nodule collector (as this is the source of a turbidity plume that is best described in literature in terms of flow rate, concentration and the sediment properties). A similar approach can be used for other plume sources as well.

The source term exiting from the mining vehicle is characterized by its volume, momentum and buoyancy flux, in the frame of reference of the moving vehicle, defined as:

$$Q_{j0} = Au_{j0}$$
$$M_{j0} = \rho_{j0} Q_{j0} u_{j0}$$
$$g'_{j0} = g\frac{\rho_{j0} - \rho_{cf}}{\rho_{j0}}$$
$$B_{j0} = Q_{j0} g_{j0}'$$

With the volume flux exiting from the discharge Q_{j0}, cross-sectional area A, initial discharge velocity u_{j0}, initial momentum flux M_{j0}, discharge density ρ_{j0}, ambient density ρ_{cf}, reduced gravity g'_{j0}, gravity g, and initial buoyancy flux B_{j0}. It is worth mentioning, that in the case of an operational mining vehicle, the source is moving, discharging at an approximate neutral velocity. This is envisaged by adjusting the discharge opening to accommodate a similar discharge velocity of the mixture opposing the forward velocity of the mining tool, aiming for a minimum net momentum. The conditions of the flow exiting from the vehicle diffusers can be described with Reynolds Re, densimetric Froude Fr , Richardson Ri numbers, and the ratio of net vehicle-discharge velocity relative to the current velocity ratio (square root of the momentum ratio) γ, respectively given by

$$Re = \frac{\rho_{j0} u_{j0} H}{\mu}$$
$$Fr = \frac{u_{j0}}{\sqrt{g_0' H}}$$
$$Ri = \frac{g_0' H}{u_{j0}^2}$$
$$\gamma = \sqrt{\frac{\rho_{j0}\left(u_{j0} - u_v\right)^2}{\rho_{cf} u_{cf}^2}}$$

With height of the discharge opening H, vehicle velocity u_v and dynamic viscosity μ.

For Re > 10^4, the outflowing mixture will be turbulent. As long as the jet starts fully turbulent, mixing of the jet is not strongly affected by the jet Reynolds number (Jirka, 2007) but it is primarily governed by Ri (equal to $1/Fr^2$) and γ. For Fr < 1 the outflow is subcritical, for Fr > 1 the outflow is supercritical.

TABLE 1 | Range of dimensionless numbers for the discharge conditions. Values are based on design specifications,–indicates lower bound, + indicates upper bound for concentration c (0.01–0.03) (mol/L), vehicle velocity v (0.25–0.5) [m/s] and discharged volume Q (0.125–0.375) [m^3/s per meter width]. Values are taken from (Lang et al., 2019).

	Re	Fr	Ri	$\frac{l_s}{H}$	$\frac{l_m}{H}$
c–, v–, Q-	13255	0.96	1.08	11885	1.14
c–, v+, Q-	6627	1.36	0.54	37733	3.85
c–, v–, Q+	39765	0.56	3.24	8241	0.50
c– v+, Q+	19883	0.79	1.62	26162	1.69
c+, v–, Q–	27230	1.11	0.81	12099	0.66
c+, v+, Q-	13615	1.57	0.41	38413	2.22
c+, v–, Q+	81690	0.64	2.40	8389	0.29
c+, v+, Q+	40845	0.91	1.22	26634	0.97

For Ri < 1, the flow is dominated by momentum, for Ri > 1 the flow is dominated by buoyancy. Based on the numbers provided by (Lang et al., 2019), the range of the dimensionless numbers is provided in **Table 1**. The current velocities close to the seabed in the abyssal plains are generally rather low, with typical mean current velocities in the range of 5–15 cm/s (Gillard et al., 2019). During the mining operation, it must be assumed that the current can come from any direction, cross or parallel.

It remains to be seen how the mining systems will perform operationally. However, based on the analysis of the Froude and Richardson number, some regime changes, e.g., sub- or supercritical flow being discharged from the mining collector. In the case where the outflow is subcritical (Fr < 1), the mixture will automatically redistribute to arrive at $Fr = 1$ with a discharge at higher concentration and velocity in the lower half of its height compared to the upper part of the discharge. In severe cases, water from the environment can even flow into the discharge. As a result, the assumed neutral exit velocity does not hold and thus the outflow maintains more energy than anticipated. To minimize the chance of heterogeneous outflow, various options are available, e.g., guided vanes and/or vortex generators.

2.1 Length Scales

Initially the horizontal momentum is important, but eventually (negative) buoyancy will force the flow towards the seabed. After impinging on the bed, it will continue as a turbidity current. Various regimes can be distinguished for a (negatively) buoyant jet in crossflow (Fischer et al., 1979). An x-z reference frame is used, i.e., x is in horizontal direction and z is in vertical direction.Within a distance of $z < l_m$ from the source a buoyant jet acts as a jet and when $z > l_m$ a buoyant jet acts as a plume. A length scale z_M is defined for the influence of the initial momentum compared to the ambient current. Length scale z_B is defined for the influence of the initial buoyancy, when $z < z_B$ initial buoyancy is dominant over the ambient current. These length scales are given by

$$l_m = \frac{\left(Q_{j0} u_{j0}\right)^{3/4}}{\sqrt{B_{j0}}}$$
$$z_M = \frac{\sqrt{Q_{j0} u_{j0}}}{u_{cf}}$$

$$z_B = \frac{B_{j0}}{u_{cf}^3}$$

See **Figure 1** for a sketch of the different flow regimes in relation to the different length scales. As the discharged flow is sediment laden, an additional length scale can be defined, based on the jet momentum flux and the particle settling velocity

$$l_s = \frac{M_{j0}^{2/3}}{w_s}$$

This length scale plays an important role in the analysis of the sedimentation spatial variation. The horizontal distance when particle fallout first occurs can be linearly correlated to l_s. A larger value suggests that the particles mainly follow the plume trajectory, while low values of l_s result in settling velocity dominating the flow response.

According to experiments performed by (Lee et al., 2013), the particle concentration contours may be divided into three regions. For $x < 0.5l_s$, the sediment jets behave like a pure jet with concentric contours. For $0.5l_s < x < l_s$, the sediment cloud starts to depart from the water jet and for $x > l_s$, the particle jet is separated significantly from the water jet. They also found a longitudinal deposition rate F_s based on l_s. According to their experiments, sediment starts to fall out of the jet at approximately $x/l_s \approx 0.2 - 0.3$, the peak deposition rate at approximately $x = 0.93\, l_s$ and at $x = 2.4l_s$ over 90% of the sediment input has settled. It has to be noted, that these experiments have been conducted for various narrow particle size distributions consisting of sand or glass spheres.

Laboratory experiments for horizontal sediment-laden plumes have been conducted by (Bleninger, 2000) and (Neves et al., 2002) who conducted experiments where the sediment deposition was found to be log-normal distributed. These experiments were coupled with dimensional analysis to determine the deposition rate of small particles based on a momentum-settling length scale.

(Cuthbertson et al., 2008) and (Liu and Lam, 2013) demonstrated experimentally and numerically that for initial sediment concentrations below 0.1% of volume, no significant changes to the properties of the jet flow are noticeable. For jets with higher initial sediment concentrations, the settling of particles is observed to drag the jet with a downward bending trajectory.

It is worth noting that hardly any publications so far have taken into consideration that in the case of a mining vehicle for the collection of polymetallic nodules, the vehicle will be moving. The research conducted in laboratory seems to be entirely based on stationary jets.

The work of (Decrop and De Wachter, 2019) is only one of the very few public articles that address the effect of the moving vehicle on the discharged sediment plume. This work is based on a Computational Fluid Dynamics (CFD) model based on Reynolds Averaged Navier Stokes (RANS) turbulence modelling. In this work, various vehicle scenarios are considered, mainly for different vehicle velocities and discharge conditions. It also considers the effect of the wake of the vehicle in the initial mixing phase. So far, no validation through experiments has been provided.

Recently, (Ouillon et al., 2021) presented research on gravity currents originating from moving sources. In their research, they conducted experiments in a towing tank where a model collector discharges a dense dyed fluid in its wake. These experiments have been used to validate CFD results based on Direct Numerical Simulations (DNS). It is identified that the ratio of the speed of the source (mining vehicle) to buoyancy velocity can be used to define sub- and supercritical gravity current formation. In the case of supercritical flow (where the mining vehicle is able to stay in front of its own generated turbidity current), a wedge-shaped gravity current occurs behind the collector. In this supercritical regime, the turbidity current goes through a second transition in which the head of the turbidity current moves approximately normal to the vehicle's direction, and the time evolution of the front in lateral direction tends to be comparable to a constant volume lock-release gravity current. Their research provides valuable insights on the near-field behavior of the mining vehicle plumes. For obvious reasons, their experiments have not considered the presence of actual sediments in the discharged flow. The effects of sediments will be discussed in the next section.

2.2 Deep-Sea Sediments

Where coastal and shelf sediments usually are predominantly composed of lithogenic clay, silt and sand produced by weathering and erosion of the adjacent land mass (except on subtropical and tropical carbonate shelves), deep-sea sediments encountered at sites of potential DSM are usually a mixture of clay and silt transported from distant land masses by ocean currents or wind, or produced by weathering of oceanic rock, and silt to sand-sized skeletal remains of mostly pelagic organisms composed of carbonate (mostly coccolithophores and planktonic foraminifera) or silica (mostly diatoms and radiolarians). Volcanic debris and authigenic minerals precipitated from seawater or local pore water contribute a relatively minor fraction, with areas rich in polymetallic sulphide or oxide precipitates as a notable exception. On the crests of mid-ocean ridges and seamounts, enhanced bottom currents associated with internal waves often winnow out the finest sediment fractions, producing a relatively coarse-grained

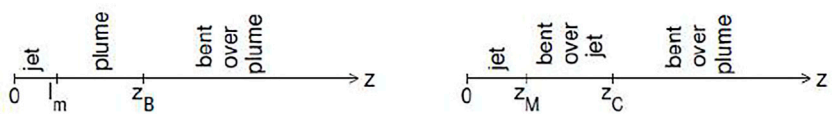

FIGURE 1 | Length scales and flow regimes of a buoyant jet in cross flow in case $z_B > z_M$ (**left**) **or in case** $z_M > z_B$ (**right**) with $z_C = z_M (\frac{z_M}{z_B})^{1/3}$, (de Wit, 2015).

TABLE 2 | Fraction distribution of sediments. GSR and NTNU data from (Lang et al., 2019), IOM data from (Zawadzki et al., 2020). Averaged data is provided by Global Sea Resources, based on the Belgium license area in the CCFZ, NTNU data is data of specific box-cores of the GSR data average. IOM data is based on data of the Inter Ocean Metal license area in the CCFZ.

Fraction	Diameter range (μm)	GSR data average (%)	NTNU data BC062 (%)	NTNU data BC064 (%)	IOM data average (%)	Gillard et al. (2019)
Clay	< 2	12.0	11.3	14.5	23.24	25.3
Silt	2—63	76.2	85.7	82.5	70.36	52.11
Sand	63—2000	11.8	3	3	6.13	22.5

TABLE 3 | Percentages of mineral groups in deep-sea sediment. IOM data from (Zawadzki et al., 2020), GSR data from (Global Sea Mineral Resources NV, 2018), Sites A-C (Bisschof et al., 1979). Note that for IOM 1, 2, 3, clay mineral % is given relative to total sediment. For Site A, B, C and GSR clay mineral % is relative to sum of clay minerals only.

	IOM 1	IOM 2	IOM 3	Site A	Site B	Site C	GSR	IOM
Smectite (%)	12.71	17.33	16.49	52	38	40	36.41	16.3
Illite (%)	13.82	12.05	14.25	31	42	50	48.34	13.2
Kaolinite (%)	0.65	0.43	0.54	17	20	10	10.33	1
Chlorite (%)	1.7	1.85	2.35				4.92	1.5
Amorphic (%)	50.47	47.09	44.42					

residue. Corals, sponges and other benthic megafauna which at these sites find favourable conditions for nutrition, often produce a significant amount of coarse-grained bioclastic sediment. In contrast, sediment of the abyssal plains is mostly very fine grained, reflecting the sluggish bottom current regime. Characteristic particle size distributions in nodule-rich areas are presented by (Lang et al., 2019; Zawadzki et al., 2020), see **Table 2**. The local clay composition varies to a larger extent. However, in all publicly reported cases, smectite and illite are the most abundant, see **Table 3**.

Since large parts of the abyssal seafloor are located well below the carbonate compensation depth (CCD), biogenic carbonate settling out from the euphotic zone is mostly not preserved. The deep-sea clay is therefore typically poor in carbonate, and predominantly composed of a mixture of clay minerals and siliceous remains of plankton like diatoms and radiolarians. Only below biologically productive surface waters such as the equatorial upwelling zones, where the supply of biogenic carbonate exceeds the dissolution below the CCD, is carbonate preserved in the sediment.

The supply of fresh organic matter to the seabed, which may play an important role in the aggregation of suspended sediment (Fettweis and Baeye, 2015), varies greatly depending on the overall productivity regime of the surface water and the water depth. In general, organic matter flux to the seabed decreases with increasing water depth due to progressive degradation and remineralisation of organic matter as it sinks to greater depths. Seamounts reaching to shallow depths below biologically productive surface waters receive an orders of magnitude higher flux of fresh organic matter than abyssal plains. As is clearly reflected by abundance and biomass of benthic life depending on the vertical flux of organic matter. The upper few centimeters of the sediment in the CCFZ have a carbon content of less than 0.5% of the mass of the sediment. Below 30 cm, this declines to 0.1% of the mass of the sediment (Volz et al., 2018).

2.3 Sediment Flocculation and Cohesive Sediment

The discharge flow of the nodule collection vehicle is expected to consist of sediment, water and nodule debris. It might be assumed that the nodule debris exiting from the discharge has a significantly larger settling velocity than that of the sediment, and that this nodule debris will settle close by. The exact composition of the discharged flow will strongly depend on the nodule collection method and separation method that is used to separate the nodules from the excess of water entering the collector. Under influence of turbulence, differences in settling velocity and Brownian motion, mud particles can cluster together to form flocs with typical sizes of 0.05—1 mm (Gillard et al., 2019). The density of the flocs is less than the density of the individual particles, but the settling velocity is larger. Flocculation is especially relevant when the mud concentration is large. In shallow water, Strong flocculation effects have been found for mud fractions in the overflow dredge plume of a TSHD, with floc diameters of 40–800 micron and floc settling velocities of 0.1–6 mm/s (Smith and Friedrichs, 2011). Similar floc settling velocities have been found for CCFZ sediment by (Gillard et al., 2019).

As shown in **Table 3**, the clay fraction of CCFZ sediment mainly consists of smectite (montmorillonite) and illite. Smectite particles are relatively small and have a large specific surface area (SSA, which is defined as the ratio of the surface area of a material to either its volume or mass (Baker et al., 2017). The SSA affects the magnitude of the interparticle forces, where larger SSA leads to larger interparticle forces (Atkinson, 2017). The SSA of smectite is further enhanced by its ability to absorb water into

TABLE 4 | Typical values of thickness, planar diameter, specific surface area and cation exchange capacity for common clay minerals (Yong et al., 2012).

Edge view	Typical thickness (nm)	Planar diameter (nm)	Specific surface area (m^2/kg)	Cation exchange capacity (mEq/100 g)
Montmorillonite	2	10–1,000	700–800	80–100
Illite	20	100–2000	80–120	10–40
Chlorite	30	100–2000	70–90	10–40
Kaolinite	100	10–1,000	10–15	3–15

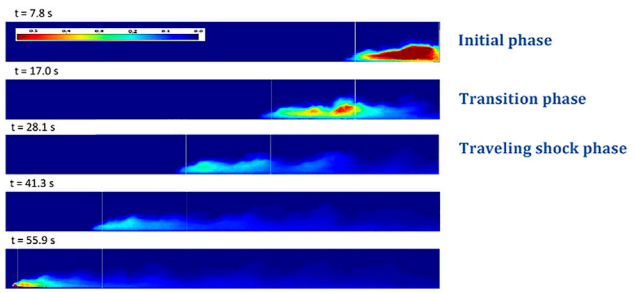

FIGURE 2 | Results of low concentration suspended sediment lock-exchange experiment, depicting the different phases of a particle-driven current, (Helmons et al., 2019)

its crystal lattice structure (Yong et al., 2012), see **Table 4**. The cation exchange capacity (CEC) provides the potential chemical activity of a clay mineral, which in turn is directly related to the magnitude of the cohesive forces. For higher CEC, the clay will behave more plastic and higher cohesive and adhesive shear strengths may be expected as well (Kooistra et al., 1998; Baker et al., 2017).

2.4 Particle-Driven Gravity Currents

After the impinging on the seabed, the remaining plume will continue as a particle-driven gravity current. While the current spreads, particles fall out and the effective driving strength of the current, compared to a homogeneous current, decays (Ungarish, 2009). Alternatively, sediment may be entrained if the current is passing sufficiently rapid over an erodible bed, which will increase the particle concentration and thus the driving buoyancy force.

The behavior of the resulting particle-driven current can be divided into three phases, i.e., the initial or starting phase, the transition phase and a traveling shock phase, see **Figure 2**. During the initial or starting phase, the initial volume of the current collapses, which typically happens in the impingement region. In the transition phase, the height of the nose increases and the particle concentration is declining faster in the tail than at the head. In the last phase, the traveling shock phase, a bore is

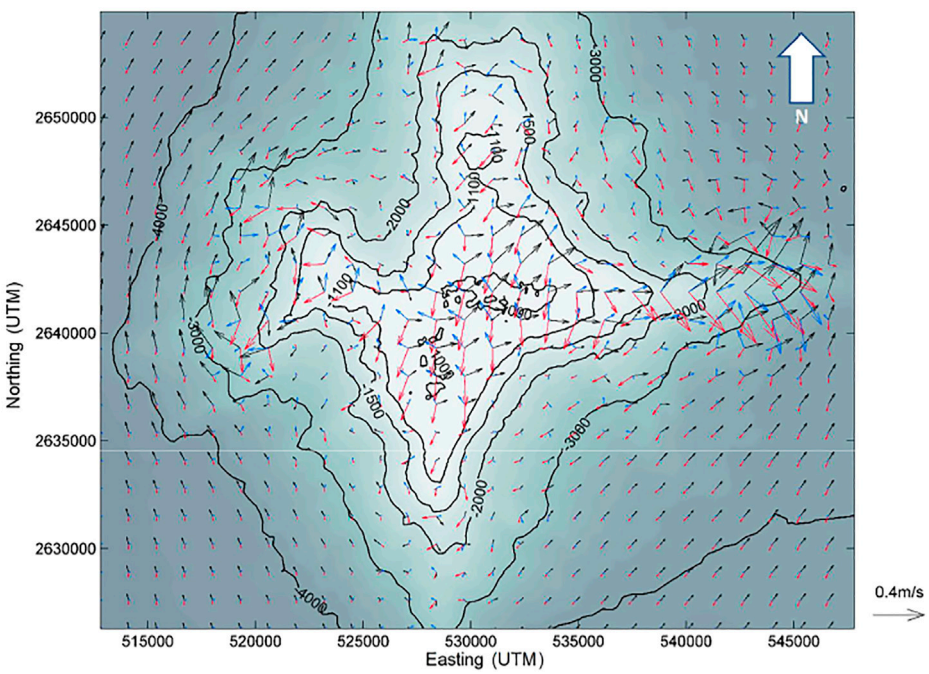

FIGURE 3 | Snapshots of currents 10 m above the bed in the vicinity of the Tropic Seamount, during a spring tide at HW (black), HW+4 h (ref) and HW+8 h (blue) (Spearman et al., 2020).

developed within the current, which rapidly changes the height and velocity of the current (Bonneaze et al., 1993).

(Gladstone et al., 1998) conducted non-cohesive lock exchange experiments (where fluids of higher density, in this case due to suspensions of particles, are released into fluids of lower density) with bi-disperse particle size distributions. They found that the mixing of different sizes of particles has a strong non-linear effect on both the motion of the current and the sedimentation patterns. Adding small amounts of coarse particles to a current composed of small particles has little effect on the dynamics of the current. In the opposite case, adding a fraction of fine particles to a dominantly coarse material has a significant effect as the flow will travel further and will be able to maintain its velocity for a longer duration. This non-linearity arises from the presence of modest amounts of fines which cause the current to maintain an excess density difference for a longer time. The decay of velocity is dominated by particle settling, which is reduced by the presence of fines. In conclusion, the transport of bi-disperse and poly-disperse mixtures depends strongly on the amount of fines present.

(Marr et al., 2001) conducted experiments of cohesive sand-rich sub-aqueous gravity flows in a flume which also carried bentonite or kaolinite. They found that between 0.7 and 5% by mass bentonite was sufficient to produce coherent flows, compared with 7% for kaolinite.

In their definition, coherent flows are flows that resist breaking apart and becoming completely turbulent under the dynamic stress associated with the head of the propagating gravity flow. That this phenomenon occurs for lower concentrations of bentonite is caused by the mixtures' higher yield strength. (Baas et al., 2016) found similar results in channel flow experiments of low concentration kaolinite and bentonite mixtures.

(Baker et al., 2017) conducted lock exchange experiments for various concentrations and clay types, i.e., silica flour, kaolinite and bentonite, all in ambient seawater. Based on these experimental results, there is no significant difference in flow response for low concentrations of sediment. For volumetric concentrations of 10% for bentonite, 15% for kaolinite and up to 44% for silica flour, the resulting flow exhibits strong turbulent mixing. The only significant differences for comparable initial densities would be the result of the effective settling velocity of the sediment used. In the case of volumetric concentrations >15% for kaolinite and >10% for bentonite, the flow behavior is affected by gelling of the mixture.

3 DEEP-SEA MINING

3.1 Deep-Sea Conditions

In dredging operations in coastal waters, the dispersion of the sediment plume in vertical direction is often confined within a few metres to tens of metres between the sea surface and the seabed. In deeper waters of the shelf, strong vertical density gradients associated with a seasonal or permanent thermocline and present below the upper few tens of metres of mixed surface water, may also limit the vertical dispersion of plumes. Spreading of the plume in coastal and shelf waters thus occurs mostly in horizontal direction by relatively strong wind- or tide-driven currents, whilst turbulence makes the plume expand vertically within the boundaries set by sea surface, seabed and density stratification. Plumes generated by DSM, in contrast, are much less vertically confined.

Although density stratification is normally also present in waters below the thermocline, it is less strongly present than in shallower waters. Especially in their initial phase after release, sediment plumes have substantial excess density relative to the water of the receiving environment, which will make the plume sink vertically if released in open water or roll downslope as a turbidity current if released above a sloping seabed. Thus, DSM plumes may spread out over a considerable vertical distance before mixing with ambient water slows down their descent. In addition to the negative buoyancy of the plume itself, vertical dispersion may be further enhanced by vertical water motions induced by internal waves. These are oscillations within a water mass produced when stratified water flows over abrupt seabed topography, such as typically the case at the shelf break, or on mid-ocean ridges or isolated seamounts. Internal waves may induce large vertical water mass motions of more than 100 m in the ocean interior, and especially where they break they produce strong turbulence and water mass mixing (van Haren and Gostiaux, 2012; van Haren et al., 2017) although they may also lead to hydrodynamic conditions which hinder the wider dispersion of sediment plumes, such as tidally rotating currents (Spearman et al., 2020). Internal waves are thus an important factor to be taken into account when considering plume dispersion for DSM in topographically complex terrain, such as mining of SMS and polymetallic crusts (both deposit types are typically found at or near seamounts). But even in abyssal plain settings, away from major topographic features, significant turbulence and mixing has been observed, generated by internal waves produced over abyssal hills (van Haren, 2018).

3.2 Return Flow of Sediments, Waste and Other Effluents

In all types of DSM, ore slurry pumped up from the seabed through the riser system needs to be dewatered to allow safe storage on board of the mining vessel. Subsequent transfer of the ore to a bulk carrier for transport to land will require a second dewatering step, if the ship-to-ship ore transfer is done in a slurrified state. The dewatering on board of the mining vessel may also involve further separation of valuable ore from unwanted sediment entrained in the flow. The excess water produced in the dewatering process, loaded with sediment and also the fine-grained ore fraction that cannot be retrieved by sieving and centrifugation, will have to be returned back to sea, creating a discharge plume of fine particulate material (Oebius et al., 2001). In the case of nodule mining, the amount of fine-grained material discharged from the mining vessel may be substantial. The total discharge of water and solids has been estimated previously at 50,000 m^3 per day, with a solids concentration on the order of 10 kg/m^3 (Oebius et al., 2001). More recent estimates give an order of magnitude higher numbers for total discharge and solids

concentration (Lang et al., 2019). According to the latter, fine-grained sediment entrained with the nodules will make up the bulk of the solid material discharged. Nodule fines, produced by abrasion and fragmentation of nodules during pickup, vertical transport and dewatering, and too small to be retrieved during on-board processing, would constitute only a few percent of the solid mass. In the case of SMS and crust mining, any sediment overburden will likely be removed prior to ore excavation, and the excavated material pumped up as a slurry to the mining vessel will thus consist predominantly of valuable ore. The solids discharged with dewatering fluid will likewise consist mostly of fine-grained ore material. Estimates of total dewatering discharge for SMS mining are between 22,000 and 38,000 m^3 per day (Nautilus Minerals, 2008; Okamoto et al., 2019). The only available estimate of solids concentration is from the Nautilus Solwara EIA which was estimated as around 6 kg/m^3 (Nautilus Minerals, 2008).

Discharge of dewatering water and solids directly at the surface is expected to have multiple and potentially harmful impacts on surface ocean pelagic life, such as shading out of photosynthesizing plankton, phytoplankton blooms due to input of mineral nutrients, clogging of feeding apparatus of pelagic suspension feeders, reduced buoyancy of plankton, reduced visibility interfering with predators hunting on sight, toxic effects of trace metals released from ore particles. To avoid these impacts, ISA draft regulations for exploitation of polymetallic nodules (Lenoble, 2000) prescribe that water and solids should be discharged below 1,000 m water depth, well below the biologically productive sunlit surface ocean layer, and below the steep density gradient of the permanent thermocline which will impede return of the discharged material to the surface. (Munoz-Royo et al., 2021) have studied such a mid-water plume in dynamic discharge experiments at approx. 60 m water depth with mixtures based on CCFZ sediment. They identified that its vertical and horizontal extent is notably influenced by 1) the amount of discharged sediment and 2) background turbulent diffusivity. Another key finding in their work is that flocculation of sediment does not play a notable role due to initially high turbulent shear rates near the discharge opening and low concentration downstream due to rapid turbulent entrainment.

However, (Drazen, et al., 2020) have pointed out that there is a wide variety of pelagic life also below 1,000 m depth, which will be impacted likewise by discharge plumes. The authors argue that the pelagic ecosystems should be an integral part of environmental impact assessment and environmental monitoring plans. To mitigate impacts on pelagic life, they suggest delivering the discharge to the seafloor where a sediment plume will already exist from seafloor activities. This would result in additional pressure on benthic organisms but would relieve pressures on the mid-water ecosystem.

Releasing the dewatering discharge at short distance above the seabed brings about the risk that erosive turbidity currents are generated at the point where the plume impinges on the seabed, due to initial momentum of the discharge and the relatively high excess density relative to the ambient deep-sea water (van Grunsven et al., 2018). In the path of the turbidity current, the seabed may be stripped of the surface sediment layer including benthic life and organic material serving as primary food resource for the benthos, whereas the resuspended sediment will be dispersed and settle out downslope, aggravating the impact of the plume generated by the mining vehicle. Adjustment of the discharge height above the seabed and the direction of the discharge jet and a diffuser may help to prevent or reduce the formation of erosive turbidity currents.

3.3 Plume Generation When Mining Seafloor Massive Sulphides and Cobalt-Rich Crusts

Sea-floor massive sulphides (SMS) are deposits of metal-bearing minerals that form on and below the seabed as a consequence of the interaction of seawater with magma below the seabed. During this process, cold seawater penetrates through cracks in the sea floor and is heated to high temperatures causing metals to be leached out from the surrounding rock. The resulting chemical reactions that take place in this process result in seawater enriched in dissolved metals and sulphur. Due to the lower density of this evolved seawater, it rises rapidly to the sea floor, where most of it is expelled into the overlying water column as focused flow at chimney vent sites. The dissolved metals precipitate when the fluid mixes with cold seawater. Much of the metal is transported in the hydrothermal plume and is deposited as fallout of particulate debris. The remainder of the metal precipitates as metal sulphides and sulphates, producing black and white smoker chimneys (Baker and Beaudoin, 2013).

Fe–Mn crusts occur on hard-rock substrates throughout the ocean basins. They form at the seabed on the flanks and summits of seamounts, ridges, and plateaus where the rocks are largely depleted of sediment (Hein and Koschinsky, 2014). The most metal-rich crusts occur at depths of about 800–2500 m (Hein and Petersen, 2013). The thickest crusts on individual seamounts commonly occur on outer-rim summit terraces and broad saddles on the summit of guyots (flat-topped seamounts).

3.3.1 Estimating the Loss of Crust/SMS Particles Into the Water Column

Crust and SMS plumes are in principle similar to those arising from dredging of weak rock (crusts; (Yamazaki et al., 1995) and moderately strong rock (SMS; (Spagnoli et al., 2014) by cutter suction dredger (CSD) in shallow waters (Spearman et al., 2020). The near-field processes which contribute to losses from CSD are complex and difficult to model numerically. However, a reasonable estimate of the resulting loss of fines can be established by using standard dredging industry approaches, e.g., (den Burger, 2003; Becker, et al., 2015), based on field and laboratory measurements, to estimating cutter suction losses. (van Wijk et al., 2019) showed that polymetallic nodules can fragment upon impact with (in) the mining equipment, potentially complicating preliminary subsea separation processes. It should be pointed out that for mining, particles lost to the surroundings represent a loss of resource and there is an incentive for the developer to reduce these losses further, as much as is practically possible, through design of the mining plant.

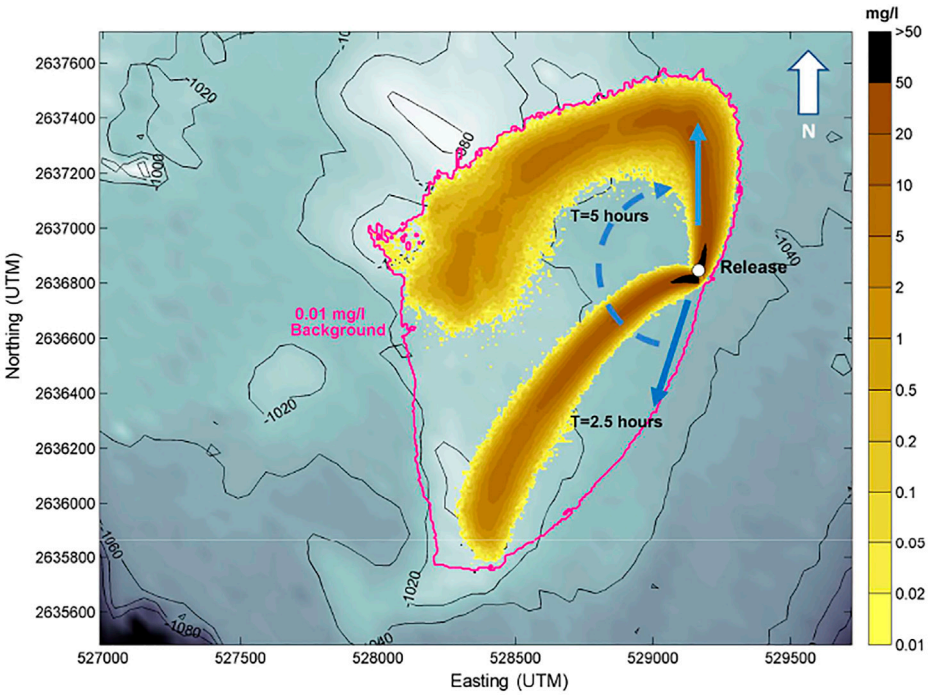

FIGURE 4 | Snapshots of predicted increases in suspended sediment concentration (averaged over bottom 10 m of water column) resulting from 5-h simulation of mining on the Tropic Seamount with representative rates of release. Snapshots shown at +2.5 h and +5 h. Envelope of increases greater than 0.01 mg/L (equivalent to background) over whole of simulation are indicated by magenta line (Spearman et al., 2020).

3.3.2 Effect of Topography on Hydrodynamics

Cobalt-rich crusts occur on the summits and sides of seamounts (and other similar topographical features) which exhibit specific dominating hydrodynamic features, including Taylor caps, an isolated region of flow situated above the seamount, and internal tides, where surface tides move stratified water up and down sloping topography, producing a wave in the ocean interior (Lavelle and Mohn, 2010). SMS fields also commonly occur on ridge features with steep slopes and display great variation in bathymetry, which can result in similar hydrodynamic features. The nature of the resulting hydrodynamics will always be site-specific but the typical features are here discussed using the results of the Marine E-tech project (Spearman et al., 2020) which investigated the hydrodynamics (as well as the topography, geology, geochemistry, ecology and potential mining plume dispersion) in the vicinity of the Tropic Seamount around 300 nautical miles SSW of the Canary Islands. The seamount has a star-shaped platform with a width of approximately 40 km at the base and about 15 km at the crest. Its summit rises 3,000 m from the abyssal floor to a depth of ~1,000 m where it forms a flat plateau partially covered by mobile sediment deposits of silty sand, with the remainder being covered by pavement crusts see **Figure 3**.

The currents just above the surface of the Tropic Seamount were observed to be dominated by internal tide-generated currents that rotate in an anti-cyclonic direction about the seamount's centre. Validated hydrodynamic modelling (using the TELEMAC modelling suite, *opentelemac.org*) identified that current speeds (driven by internal tides) varied up to 0.3 m/s, with the highest values on the east and west "spurs" of the seamount, and that a weak Taylor cap exists around the seamount, close to the seabed. The tidal variation was observed to be semi-diurnal but transfer of energy via sub-harmonic resonance from the semi-diurnal internal tidal harmonic can also result (as here) in significant diurnal components of current flow, even though there is minimal external diurnal influence (Gerkema et al., 2006; van Haren et al., 2010).

The rotating currents found at the seamount were identified in the Marine E-tech project as one of the key processes limiting the dispersion of fine sediment from a (potential) mining source. **Figure 4** shows the results of a 5-h simulation of continual release of fine sediment, (Spearman et al., 2020). The figure shows snapshots of the plume (here at 2½ and 5 h) and the envelope of predicted increases in suspended sediment concentration above 0.01 mg/L (which represents the background sediment concentration). During the simulation, the current starts in a SSW direction and rotates clockwise, finishing in a north direction by the end of the simulation. The figure shows that the excursion of the plume towards the west and south (the principal direction of the currents during the simulation) is limited to around 1.4 km due to the combination of rotating tidal currents. This result indicates the importance of reproducing tidal processes in deep-sea mining studies, at least where they interact with bathymetry

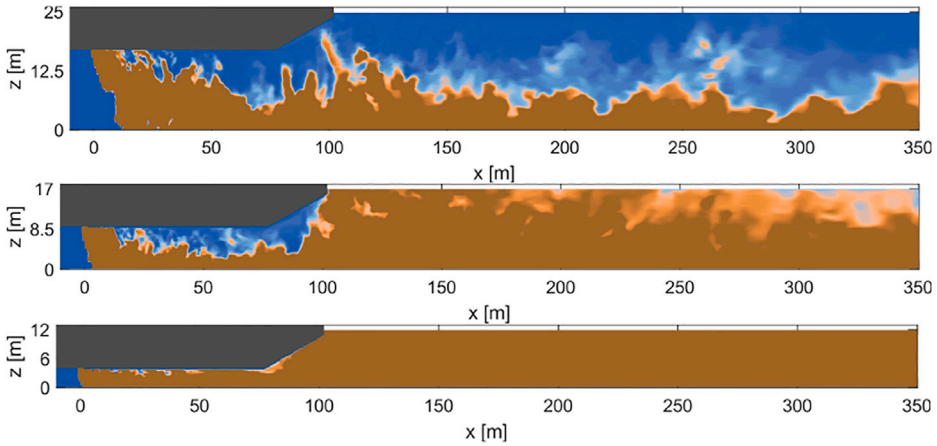

FIGURE 5 | Illustration of the influence of the depth/under keel clearance on TSHD overflow dredge plume mixing (de Wit et al., 2014a, b) for three different depths with all else similar (Ri = 1.2 and γ = 1.3). The propellers of the TSHD are included in the simulation and by entrainment pull some of the plume upward.

and density gradients to induce currents much larger than those normally associated with the deep ocean.

3.3.3 Effect of Substrate Type

While little research has been undertaken on the flocculation of debris particles likely to result from SMS mining, detailed video-imaging tests (LabSFloc-2 high resolution video-technology, (Manning and Dyer, 2007) of cobalt-rich crust debris in *in situ* seawater strongly indicates that crust particles flocculate more readily than normal sediment particles (including the clay/silt ooze found in the CCFZ—see Section 1.2). The Marine E-tech project (Spearman et al., 2020) found that, due to flocculation processes, 57% of particles less than 63 microns settled at a rate of around 10 mm/s with only 3.5% of particles settling at less than 0.1 mm/s. Like the rotational effect of internal tides, this strong flocculation effect causes a significant reduction in the dispersion of the benthic plume caused by mining.

4 SHALLOW WATER APPLICATIONS (DREDGING)

So far, we have discussed the most relevant aspects of deep-sea mining turbidity flows. In this section we will discuss how turbidity flows occur in shallow water applications like dredging (and wet mining). While dredging sediment plumes can be generated and dispersed to surrounding areas, just like when executing DSM. The dredging industry is well established and dredging projects take place all over the world. The environmental impact of dredging, often with dredge plumes as important component, has been the source of research for many decades, e.g. (Pagliai et al., 1985; Nichols et al., 1990; Bray, 2008; Erftemeijer et al., 2012; Laboyrie and Kolman, 2018). Knowledge gained from dredge plumes is used in this section to learn lessons for DSM plume modelling. Specific focus is made here on Trailing Suction Hopper Dredger (TSHD) overflow plumes as a TSHD is an often-used type of dredge equipment and TSHD overflow plumes bear similarities with DSM plumes because both are generated by moving equipment.

4.1 Overflow Plume (Near Field)

A TSHD is a high production dredging plant, which is often used for both maintenance dredging (e.g., recurrent dredging to maintain or improve existing waterways) and capital dredging (e.g., dredging in a new location and in material that has not been dredged before, such as land reclamation, deepening and widening channels). The overflow plume is generally the most important source of turbidity while dredging with a TSHD (Bray, 2008; Laboyrie and Kolman, 2018). A TSHD overflow dredge plume is generated while loading a TSHD and letting the excess process water overboard. Typically, overflow is done via a vertical pipe in the hopper which ends at the keel of the vessel, see **Figure 5** for an impression. During loading and overflowing a TSHD is moving. For TSHD overflow dredge plumes both initial buoyancy and initial momentum are important. The sediment release is downward, perpendicular to the crossflow which is formed by the combination of sailing speed and ambient current velocity. The outflow velocity is often in the same order of magnitude as the crossflow velocity. This is illustrated by the typical velocity ratios and Richardson numbers of $\gamma = 0.3 - 4$ and $Ri = 0.01 - 22$ (de Wit et al., 2014a, b; Decrop, 2015). Near-field TSHD overflow plumes can behave dynamically driven by negative buoyancy, while more diluted ones behave passively driven by ambient currents (Winterwerp, 2002). Far away from the dredger all overflow plumes are diluted so much that they end up as passively driven. Especially at the end of loading a TSHD the overflow discharge density can be high, growing to more than 400 kg/m^3 sediment concentration (van Rhee, 2002; Spearman et al., 2011; Spearman, 2014).

When dredging in deeper waters the distance from the release point at the keel of a TSHD and seabed is large, and the plume will descend under influence of its excess density and initial downward momentum. But when dredging in shallower water the seabed is rather close and the propellers driving a TSHD can

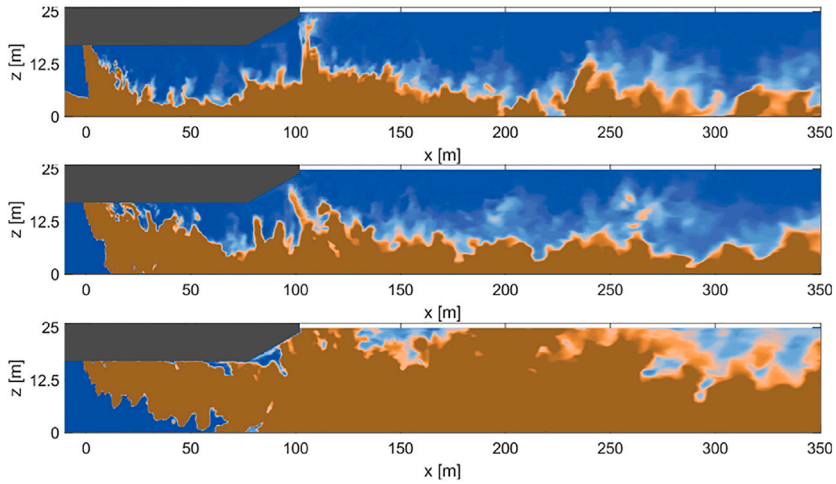

FIGURE 6 | Illustration of the influence of the crossflow velocity on TSHD overflow dredge plume mixing (de Wit et al., 2014a, b) for three different u_{cf} (0.5 m/s, 1.5 m/s and 3 m/s respectively, $\gamma = 0.6$ $\gamma = 1.3$ $\gamma = 3.8$) with all else similar (Ri = 1.2). The propellers of the TSHD are included in the simulation and by entrainment pull some of the plume upward.

impact the plume behavior seriously by entraining the sediment plume upwards to the water surface (de Wit et al., 2014a, b). In addition, when a TSHD is sailing fast with respect to the ambient current direction the upward movement of the plume to the water surface is helped by the upward flow at the aft of the TSHD hull. An example of the influence of the distance from release point and seabed on TSHD overflow plume mixing is shown in **Figure 5** and an example of the influence of the crossflow magnitude is given in **Figure 6**.

This clearly illustrates how the equipment generating a plume and interaction between plume and immediate surroundings can significantly impact the resulting plume behavior. Also, for DSM this should be considered when assessing plume dispersion. Although mixing up a sediment plume all the way to the water surface, like for TSHD plumes, is not possible for DSM plumes, also for DSM plumes some additional mixing up by either the equipment movement, its wake, or by the local details how the plume is released can impact the travel distance and concentrations significantly. Details of the initial release density, release momentum, release direction (horizontal, vertical or at a certain angle), influence of crossflow by the combination of ambient currents and potential moving speed of the release structures, distance from the seabed, and the presence of the collector vehicle, should all be assessed and taken into account when significant influence on plume mixing and travel distance is expected. When local influences close to the equipment are important, different plume models are required for far-field plume dispersion and for near-field details of the release. Both the far-field and near-field will have their own appropriate level of detail and length/timescales involved, and it may not be feasible to combine both fields into one model. The near-field considers the zone of typically a few hundred meters where the plume behaves dynamically and local influences from equipment are important. This zone is likely to be smaller for DSM applications, as the mining vehicle and current speeds are lower than in dredging applications.

4.2 Overflow Plume (Far Field)

Far field considers the zone beyond the near field where the plume behaves passively being influenced by ambient currents, bathymetry, settling, deposition and resuspension. Depending on the zone of influence the far field for a TSHD plume can extend for tens of kilometers round a dredging project site. For DSM of nodules, it is not known what the exact far-field plume area will be. In laboratory experiments in a water column simulator, flocculation characteristics were observed (Gillard et al., 2019). These characteristics were then implemented in a plume dispersion model which estimated a far-field plume extent in the range of 4–9 km distance from the source Our results in **Section 2** indicate a similar range in the more favorable discharge scenarios as do validated models of DSM of crusts on seamounts (Spearman et al., 2020).

For dredge plumes in estuary mouths variations of velocity direction and magnitude in the vertical must be taken into account for correct plume dispersion simulations. When DSM process water is planned to be released higher in the water column it is very important to have the vertical stratification and velocity distribution included in the plume modelling. It is possible that higher in the water column the ambient currents have completely different magnitudes and directions than near the seabed and a plume can stay hanging on a gradient in ambient density for instance induced by temperature or salinity gradients.

4.3 Lessons Learned From Dredging for Deep-Sea Mining

A resemblance between DSM plumes from a collector and TSHD dredge plumes is that they are generated by a moving device. Especially when simulating deposition layers and potential for

smothering it is important to consider the details of operations like the work sequence, moving device locations in time, pauses in production. Because when simulations would be simplified with stationary sediment sources especially the amount of deposition and potential smothering near the release location can be overestimated while at the same time plume concentrations and deposition at locations further away could be underestimated.

Near-bed dredge plumes can stay near the bed for a long time because of turbulence damping at the steep density gradient at the top of the suspended sediment layer and when the density difference is large enough start behaving as a density current (Kirichek et al., 2021). DSM plumes are released near the seabed and ambient currents are weak so they can form a density current as well. Such density current will flow down bathymetry slopes which can be significant in the deep sea and a numerical tool used for DSM plumes should be able to deal with density currents when the release concentrations are high enough for a density current. Such numerical tool should have sufficient near-bed resolution and also include numerical measures to prevent artificially mixing up such near-bed density layer by for instance appropriate turbulence damping functions (Violeau, et al., 2002) otherwise the density current would numerically be destroyed which leads to underestimation of travel distances, deposition amounts, near-bed concentrations and overestimation of sediment concentrations further away from the bed.

Sediment spill fractions will be different for different types of equipment and will be dependent on sediment composition and equipment handling and production rate. For a proper DSM plume assessment, the spill characteristics, spill magnitude and sediment composition should be determined by taking into account the details of the spill generating processes of the specific equipment being used. This has to be done for all process steps which can generate spill including potential release of tailings and process water. Examples from dredging industry can serve as an example for such methodology (Becker et al., 2015; Laboyrie and Kolman, 2018) and a modelling framework for dredge plume assessment can be found in (Lisi et al., 2019).

DSM can also learn much from the experience of, and measurement protocols which are routinely applied to, dredge plume measurements (VBKO, 2003; CEDA, 2015a, b; Laboyrie and Kolman, 2018). Proper choice in measurement devices, calibration, measurement location, moment in time (interval and duration) are paramount to obtain the right insights into plume behavior. Stationary monitoring locations can be used or moving ones, or a combination of both. It is advisable to conduct proper baseline monitoring to know the natural sediment dynamics in the system at hand. In this way the increases in suspended sediment concentration (SSC) arising from plumes can be put into the context of natural background variation in SSC. This has been highlighted as an important issue for DSM (Spearman et al., 2020). For improving DSM plume modelling and spill term assessment it is important to make a connection between the measured plumes and the spill generating operations.

For dredging projects often turbidity (or SSC) limits, i.e., agreed thresholds in measured turbidity/SSC which establish the points at which more detailed measurements should be taken or when dredging activities should cease, are used to manage the environmental aspects of the dredging project. These limits should be based on the local situation and ecosystem at hand or otherwise there is the risk of having not enough protection of the environmental system or having too strict limits which unnecessarily make a project (much) more expensive. In practice turbidity/SSC limits are sometimes simply copied from another project without assessing whether they make sense for this different situation. For the new DSM industry there is an opportunity to do things better in this perspective and some ideas for determining appropriate environmental limits can be found in (CEDA, 2020)).

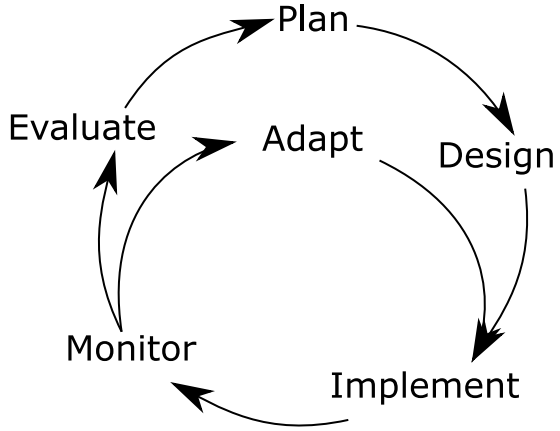

FIGURE 7 | Adaptive management cycle, adapted from (CEDA, 2015a, b) copyright CEDA.

4.4 The Adaptive Management Concept for Managing the Environmental Effects of Plumes

For some years, albeit not ubiquitously, the dredging industry has utilized a concept referred to as "adaptive management" to overcome the difficulties associated with production targets in an environment with (strict) environmental limits (CEDA, 2015a, b; Laboyrie and Kolman, 2018).

In (CEDA, 2015a, b) adaptive management is defined as decision framework that facilitates flexible decision-making that can be refined in response to future uncertainties, as outcomes from current and future management actions become better understood. **Figure 7** illustrates the adaptive management cycle. Adaptive management typically involves developing and implementing a management plan that defines the project goals, reviewing progress towards those goals periodically, and, in response to the outcomes of (environmental) monitoring, implementing corrective actions (and refining the plan), as needed, in future. Adaptive management is a formal process, with specifically agreed upon steps to deal with uncertainties. Adaptive management in

dredging projects prescribes a process wherein management actions can be changed in response to monitored system response, so as to maximise efficiency while maintaining or achieving a good ecological state. Adaptive management is suitable for those dredging projects where the outcome is less certain or accompanied by a low confidence in the prediction of effects. This applies to DSM as well and therefore adaptive management is a very useful decision framework for DSM.

5 SUMMARY AND CONCLUSIONS

Within this paper, we have addressed one of the environmental pressures that cause most concern for deep-sea mining, i.e., sediment plume dispersion. Before deep-sea mining can take place, it is of paramount importance that environmental pressures are investigated and measures are enacted to make sure that impacts are not too large. There is vast experience within the field of dredging engineering on how to manage and mitigate suspended sediment plumes. Although some of the characteristics of the processes might differ, there are many similarities in equipment and processes among dredging and deep-sea mining. Experience and best practices from the field of dredging engineering might be used to reduce, mitigate and manage suspended sediment plumes that would be generated by mining equipment. Our main findings are:

1. Based on the dimensional analysis presented in **Section 2**, the least plume dispersion for nodule DSM would be expected for slower mining vehicles. In that sense, for a comparable nodule production rate, it would be best to design the mining vehicle to be as wide as possible. That would then enable the collector to move forward more slowly, resulting in more favorable source conditions of the turbidity plume.
2. The suspended sediment plume is a direct result of the equipment-seabed interaction. Optimization of the mining equipment and processes are paramount to reduce the quantity of entrained water and/or sediment, and thus the source term of the sediment plume. Equal sediment fluxes are likely to disperse less when discharged at higher initial concentrations due to aggregation of particles.
3. In applications with production targets in an environment with (strict) environmental limits, adaptive management on environmental impact can be of assistance.
4. Various researchers have shown that the deep-sea sediment can aggregate, resulting in a net higher settling velocity. There are indications that flocculation processes in turbidity plumes can play a role in reducing its dispersion. However, at this stage, to what extent aggregation will occur in a dynamic flow is not well understood. It might well be that aggregation might be more profound for higher initial concentrations of a source term, as an additional effect to conclusion 2.

AUTHOR CONTRIBUTIONS

RH developed DSM context and near-field sediment plume characterization, both in dredging and DSM application. HdS carried out overview and contributions of relevant deep-sea sediment, especially at SMS and nodule deposits. LdW developed guidelines and shallow water near-bed plume interactions (dredging). JS provided dredging expertise, flocculation/particle aggregation and SMS/crusts modeling/experiments. RH coordinated and helped to draft the manuscript. All authors read and approved the final manuscript.

ACKNOWLEDGMENTS

RH and HS acknowledge funding from Blue Harvesting, EIT RM project 18138.

REFERENCES

Alvarez Grima, M., Miedema, S. A., Van de Ketterij, R. G., Yenigül, N. B., and Van Rhee, C. (2015). Effect of High Hyperbaric Pressure on Rock Cutting Process. *Eng. Geol.* 196, 24–36. doi:10.1016/j.enggeo.2015.06.016

Atkinson, J. (2017). *The Mechanics of Soils and Foundations*. London: Taylor & Francis.

Baas, J. H., Best, J. L., and Peakall, J. (2016). Comparing the Transitional Behaviour of Kaolinite and Bentonite Suspension Flows. *Earth Surf. Process. Landforms* 41, 1911–1921. doi:10.1002/esp.3959

Baker, E., and Beaudoin, Y. (2013). *Deep Sea Minerals: Sea-Floor Massive Sulphides, a Physical, Biological, Environmental and Technical Review*. Suva, Fiji: Secretariat of the Pacific Community and GRID-Arendal.

Baker, M. L., Baas, J. H., Malarkey, J., Jacinto, R. S., Craig, M. J., Kane, I. A., et al. (2017). The Effect of Clay Type on the Properties of Cohesive Sediment Gravity Flows and Their Deposits. *J. Sediment. Res.* 87, 1176–1195. doi:10.2110/jsr.2017.63

Becker, J., van Eekelen, E., van Wiechen, J., de Lange, W., Damsma, T., Smolders, T., et al. (2015). Estimating Source Terms for Far Field Dredge Plume Modelling. *J. Environ. Manag.* 149, 282–293. doi:10.1016/j.jenvman.2014.10.022

Bisschof, J., Heath, G., and Leinen, M. (1979). "Geochemistry of Deep-Sea Sediments from the Pacific Manganese Nodule Province DOMES Sites A, B and C," in *Marine Geology and Oceanography of the Pacific Manganese Nodule Province, Marine Science*. Editors J. Bisschof and D. Piper (Boston: Springer), 397–436.

Bleninger, T. (2000). *Sedimentation in Particle-Laden Jets*. Karlsruhe: University of Karlsruhe. PhD Dissertation.

Bonneaze, R., Huppert, H., and Lister, J. (1993). Particle-driven Gravity Currents. *J. fluid Mech.* 250, 339–369.

Boschen, R. E., Rowden, A. A., Clark, M. R., and Gardner, J. P. A. (2013). Mining of Deep-Sea Seafloor Massive Sulfides: A Review of the Deposits, Their Benthic Communities, Impacts from Mining, Regulatory Frameworks and Management Strategies. *Ocean Coast. Manag.* 84, 54–67. doi:10.1016/j.ocecoaman.2013.07.005

Bray, R. (2008). *Environmental Aspects of Dredging*. London: Taylor & Francis /Balkema.

CEDA (2020). *Assessing and Evaluating Environmental Turbidity Limits for Dredging*. Information paper. Retrieved from http://www.dredging.org/media/ceda/org/documents/resources/cedaonline/2020-05-AETL.pdf (Accessed March 7, 2022).

CEDA (2015a). *Environmental Monitoring Procedures*. Information paper. Retrieved from http://www.dredging.org/media/ceda/org/documents/resources/cedaonline/

2015-02-ceda_informationpaper-environmental_monitoring_procedures.pdf. (Accessed March 7, 2022).

CEDA (2015b). *Integratin Adaptive Environmental Management into Dredging Ports*. Position paper. CEDA. Retrieved from http://www.dredging.org/media/ceda/org/documents/resources/cedaonline/2015-01-ceda_positionpaper-integrating_adaptive_environmental_management_into_dredging_projects.pdf (Accessed March 7, 2022).

Cuthbertson, A. J. S., Apsley, D. D., Davies, P. A., Lipari, G., and Stansby, P. K. (2008). Deposition from Particle-Laden, Plane, Turbulent, Buoyant Jets. *J. Hydraul. Eng.* 134, 1110–1122. doi:10.1061/(asce)0733-9429(2008)134:8(1110)

de Wit, L. (2015). *3D CFD Modelling of Overflow Dredging Plumes*. Delft: Delft University of Technology. PhD. Dissertation.

de Wit, L., Talmon, A. M., and van Rhee, C. (2014a). 3D CFD Simulations of Trailing Suction Hopper Dredger Plume Mixing: A Parameter Study of Near-Field Conditions Influencing the Suspended Sediment Source Flux. *Mar. Pollut. Bull.* 88, 47–61. doi:10.1016/j.marpolbul.2014.08.043

de Wit, L., Talmon, A. M., and van Rhee, C. (2014b). 3D CFD Simulations of Trailing Suction Hopper Dredger Plume Mixing: Comparison with Field Measurements. *Mar. Pollut. Bull.* 88, 34–46. doi:10.1016/j.marpolbul.2014.08.042

Decrop, B., and De Wachter, T. (2019). "Detailed CFD Simulations for Near-Field Dispersion of Deep Sea Mining Plumes," WODCON XXII in 22nd World Dredging Conference, Shanghai, China, 116–127.

Decrop, B. (2015). *Numerical and Experimental Modelling of Near Field Overflow Dredging Plumes*. Ghent: Ghent University /KU Leuven. PhD Dissertation.

den Burger, M. (2003). *Mixture Forming Processes in Dredge Cutter Heads*. Delft: Delft University of Technology. PhD Dissertation.

Drazen, J. C., Smith, C. R., Gjerde, K. M., Haddock, S. H. D., Carter, G. S., Choy, C. A., et al. (2020). Opinion: Midwater Ecosystems Must Be Considered when Evaluating Environmental Risks of Deep-Sea Mining. *Proc. Natl. Acad. Sci. U.S.A.* 117, 17455–17460. doi:10.1073/pnas.2011914117

Erftemeijer, P., Riegl, B., Hoeksema, B. W., and Todd, P. A. (2012). Environmental Impacts of Dredging and Other Sediment Disturbances on Corals: A Review. *Mar. Pollut. Bull.* 64, 1737–1765. doi:10.1016/j.marpolbul.2012.05.008

Fettweis, M., and Baeye, M. (2015). Seasonal Variation in Concentration, Size, and Settling Velocity of Muddy Marine Flocs in the Benthic Boundary Layer. *J. Geophys. Res. Oceans* 120, 5648–5667. doi:10.1002/2014jc010644

Fischer, H., List, E., Koh, R., Imberger, J., and Brooks, N. (1979). *Mixing in Inland and Coastal Waters*. London: Academic Press.

Gerkema, T., Staquet, C., and Bouret-Aubertot, P. (2006). Decay of Semi-diurnal Internal-Tide Beams Due to Subharmonic Resonance. *Geophys. Res. Lett.* 33, L08604. doi:10.1029/2005gl025105

Gillard, B., Purkiani, K., Chatzievangelou, D., Vink, A., Iversen, M., and Thomsen, L. (2019). Physical and Hydrodynamic Properties of Deep Sea Mining-Generated, Abyssal Sediment Plumes in the Clarion Clipperton Fracture Zone (Eastern-central Pacific). *Elem. Sci. Anthropocene* 7. doi:10.1525/elementa.343

Gladstone, C., Phillips, J., and Sparks, P. (1998). Experiments on Bidisperse, Constant-volume Gravity Currents: Propagation and Sediment Deposition. *Sedimentology* 45, 833–843. doi:10.1046/j.1365-3091.1998.00189.x

Global Sea Mineral Resources NV (2018). *Environmental Impact Statement: Small-Scale Testing of Nodule Collector Components on the Seafloor of the Clarion-Clipperton Fracture Zone and its Environmental Impact*. Retrieved from https://www.isa.org.jm/files/files/documents/GSR-EIS-compact.zip (Accessed March 7, 2022).

Gollner, S., Kaiser, S., Menzel, L., Jones, D. O. B., Brown, A., Mestre, N. C., et al. (2017). Resilience of Benthic Deep-Sea Fauna to Mining Activities. *Mar. Environ. Res.* 129, 76–101. doi:10.1016/j.marenvres.2017.04.010

Hein, J., and Koschinsky, A. (2014). "Deep Ocean Ferromanganese Crusts and Nodules," in *Treatise in Geochemistry*. Editors H. Holland and K. Turekian. second edition (Elsevier), Vol. 13. chapter 11. doi:10.1016/b978-0-08-095975-7.01111-6

Hein, J., and Petersen, S. (2013). *The Geology of Cobalt-Rich Ferromanganese Crusts*. Noumea: SPC.

Hein, J. R., Koschinsky, A., and Kuhn, T. (2020). Deep-ocean Polymetallic Nodules as a Resource for Critical Materials. *Nat. Rev. Earth Environ.* 1 (3), 158–169. doi:10.1038/s43017-020-0027-0

Helmons, R., Elerian, M., Bedon Vasquez, A., and de Stigter, H. (2019). "Sediment Discharges from Mining Vehicles, Experiments to Fin the Optimal Release Conditions," in 49th Underwater Maining Conference, Sanya, China.

Helmons, R. L. J., Miedema, S. A., Alvarez Grima, M., and Van Rhee, C. (2016). Modeling Fluid Pressure Effects when Cutting Saturated Rock. *Eng. Geol.* 211, 50–60. doi:10.1016/j.enggeo.2016.06.019

Jirka, G. H. (2007). Buoyant Surface Discharges into Water Bodies. II: Jet Integral Model. *J. Hydraul. Eng.* 133, 1021–1036. doi:10.1061/(asce)0733-9429(2007)133:9(1021)

JOGMEC. (2020). JOGMEC Conducts Worlds First Successful Excavation of Cobalt-Rich Seabed in the Deep Ocean. Retrieved from http://www.jogmec.go.jp/english/news/release/content/300368332.pdf (Accessed March 7, 2022).

Jones, D. O. B., Kaiser, S., Sweetman, A. K., Smith, C. R., Menot, L., Vink, A., et al. (2017). Biological Responses to Disturbance from Simulated Deep-Sea Polymetallic Nodule Mining. *PLoS One* 12, e0171750. doi:10.1371/journal.pone.0171750

Jones, D. O. B., Simon-Lledó, E., Amon, D. J., Bett, B. J., Caulle, C., Clément, L., et al. (2021). Environment, Ecology, and Potential Effectiveness of an Area Protected from Deep-Sea Mining (Clarion Clipperton Zone, Abyssal Pacific). *Prog. Oceanogr.* 197, 102653. doi:10.1016/j.pocean.2021.102653

Kaiser, S., Smith, C. R., and Arbizu, P. M. (2017). Editorial: Biodiversity of the Clarion Clipperton Fracture Zone. *Mar. Biodiv.* 47, 259–264. doi:10.1007/s12526-017-0733-0

Kirichek, A., Cronin, K., de Wit, L., and van Kessel, T. (2021). "Advances in Maintenance of Ports and Waterways: Water Injection Dredging," in *Sediment Transport - Recent Advances*.

Kooistra, A., Verhoef, P., Broere, W., Ngan-Tillard, D., and Tol, A. (1998). "Appraisal of Stickiness of Natural Clays from Laboratory Tests," in *Publications of the Applied Earth Sciences, Section Engineered Geology*.

Laboyrie, V., and Kolman, R. (2018). *Dredging for Sustainable Infrastructure*. Revision no. 673. Voorburg: CEDA /IADC.

Lang, A., Dasselaar, S., Aasly, K., and Larsen, E. (2019). Blue Nodules Deliverable Report D3.4: Report Describing the Process Flow Overview.

Lavelle, J. W., and Mohn, C. (2010). Motion, Commotion, and Biophysical Connections at Deep Ocean Seamounts. *Oceanog.* 23, 90–103. doi:10.5670/oceanog.2010.64

Lee, W. Y., Li, A. C. Y., and Lee, J. H. W. (2013). Structure of a Horizontal Sediment-Laden Momentum Jet. *J. Hydraul. Eng.* 139, 124–140. doi:10.1061/(asce)hy.1943-7900.0000662

Lenoble, J. (2000). *Overview of the Authority's Regulations and Recommendations to Ensure the Effective Protection of the Marine Environment from Harmful Effects that May Arise from Activities in the Area*. Kingston, Jamaica: International Seabed Authority.

Lisi, I., Feola, A., Bruschi, A., Pedroncini, A., Pasquali, D., and Di Risio, M. (2019). Mathematical Modeling Framework of Physical Effects Induced by Sediments Handling Operations in Marine and Coastal Areas. *J. Mar. Sci. Eng.* 7 (5), 149.

Liu, P., and Lam, K. M. (2013). Two-phase Velocity Measurement in a Particle-Laden Jet. *J. Hydro-Environ. Res.* 7, 18–29. doi:10.1016/j.jher.2012.08.001

Manning, A. J., and Dyer, K. R. (2007). Mass Settling Flux of Fine Sediments in Northern European Estuaries: Measurements and Predictions. *Mar. Geol.* 245, 107–122. doi:10.1016/j.margeo.2007.07.005

Marr, J. G., Harff, P. A., Shanmugam, G., and Parker, G. (2001). Experiments on Subaqueous Sandy Gravity Flows: The Role of Clay and Water Content in Flow Dynamics and Depositional Structures. *Bull. Geol. Soc. Am.* 113, 1377–1386. doi:10.1130/0016-7606(2001)113<1377:eossgf>2.0.co;2

Munoz-Royo, C., Peacock, T., Alford, M., Smith, J., Le Boyer, A., Kulkarni, C., et al. (2021). Extent of Impact of Deep-Sea Nodule Mining Midwater Plumes Is Influenced by Sediment Loading, Turbulence and Thresholds. *Commun. Earth Environ.* 2 (1), 1–16. doi:10.1038/s43247-021-00213-8

Nauru Ocean Resources Inc (2021). *Collector Test Study: Environmenta Impact Statement*. Nauru Ocean Resources Inc.

Nautilus Minerals (2008). *Environmental Impact Statement, Nautilus Mineral Niugini Limited, Solwara 1 Projects, Volume B, Appendix 12, Modelling the Dispersion of Returned Water Discharge Plume from the Solwara 1 Seabed Mining Project*. Manus Basin, Papua New Guinea: Nautilus Minerals.

Neves, M., Neves, A., and Bleninger, T. (2002). "Prediction on Particle Deposition in Effluent Disposal System," in Proceeding 2nd International Conference On Marine Waste Water Discharges.

Nichols, M., Diaz, R. J., and Schaffner, L. C. (1990). Effects of Hopper Dredging and Sediment Dispersion, Chesapeake Bay. *Environ. Geol. Water Sci.* 15, 31–43. doi:10.1007/bf01704879

Oebius, H. U., Becker, H. J., Rolinski, S., and Jankowski, J. A. (2001). Parametrization and Evaluation of Marine Environmental Impacts Produced by Deep-Sea Manganese Nodule Mining. *Deep Sea Res. Part II Top. Stud. Oceanogr.* 48, 3453–3467. doi:10.1016/s0967-0645(01)00052-2

Okamoto, N., Shiokawa, S., Kawano, S., Yamaji, N., Sakurai, H., and Kurihara, M. (2019). "World's First Lifting Test for Seafloor Massive Sulphides in the Okinawa Trough in the EEZ of Japan," in The 29th International Ocean and Polar Engineering Conference (Honolulu, Hawaii, USA: ISOPE), ISOPE-1-19-655.

Ouillon, R., Kakoutas, C., Meiburg, E., and Peacock, T. (2021). Gravity Currents from Moving Sources. *J. Fluid Mech.* 924, A43. doi:10.1017/jfm.2021.654

Pagliai, A., Varriale, A., Crema, R., Galletti, M., and Zunarelli, R. (1985). Environmental Impact of Extensive Dredging in a Coastal Marine Area. *Mar. Pollut. Bull.* 16, 483–488. doi:10.1016/0025-326x(85)90381-9

Ramirez-Llodra, E., Tyler, P. A., Baker, M. C., Bergstad, O. A., Clark, M. R., Escobar, E., et al. (2011). Man and the Last Great Wilderness: Human Impact on the Deep Sea. *PLoS One* 6, e22588. doi:10.1371/journal.pone.0022588

Smith, S. J., and Friedrichs, C. T. (2011). Size and Settling Velocities of Cohesive Flocs and Suspended Sediment Aggregates in a Trailing Suction Hopper Dredge Plume. *Cont. Shelf Res.* 31, S50–S63. doi:10.1016/j.csr.2010.04.002

Spagnoli, G., Freudenthal, T., Strasser, M., and Weixler, L. (2014). "Development and Possible Applications of Mebo200 for Geotechnical Investigations for the Underwater Mining," in Offshore Technology Conferene, Houston, Texas, USA, OTC-25081.

Spearman, J., De Heer, A., Aarninkhof, S., and Van Koningsveld, M. (2011). Validation of the TASS System for Predicting the Environmental Effects of Trailing Suction Hopper Dredging. *Terra Aqua* 125, 14.

Spearman, J. (2014). Prediction of the Overflow of Sediment from Trailing Dredgers. *Marit. Eng.* 167, 82–96. doi:10.1680/maen.13.00019

Spearman, J., Taylor, J., Crossouard, N., Cooper, A., Turnbull, M., Manning, A., et al. (2020). Measurement and Modelling of Deep Sea Sediment Plumes and Implications for Deep Sea Mining. *Sci. Rep.* 10, 5075. doi:10.1038/s41598-020-61837-y

Ungarish, M. (2009). *An Introduction to Gravity Currents and Intrusions*. New York, NY: CRC Press.

van Grunsven, F., Keetels, G., and van Rhee, C. (2018). "The Initial Spreading of Turbidity Plumes - Dedicated Laboratory Experiments for Model Validation," in 48th Underwater Mining Conference (UMC) 2018, Bergen, Norway.

van Haren, H. (2018). Abyssal Plain Hills and Internal Wave Turbulence. *Biogeosciences* 15, 4387–4403. doi:10.5194/bg-15-4387-2018

van Haren, H., and Gostiaux, L. (2012). Energy Release through Internal Wave Breaking. *oceanog* 25, 124–131. doi:10.5670/oceanog.2012.47

van Haren, H., Hanz, U., de Stigter, H., Mienis, F., and Duineveld, G. (2017). Internal Wave Turbulence at a Biologically Rich Mid-Atlantic Seamount. *PLoS ONE* 12, e0189720. doi:10.1371/journal.pone.0189720

van Haren, H., Maas, L. R. M., and Gerkema, T. (2010). Patchiness in Internal Tidal Beams. *J. Mar. Res.* 68, 237–257. doi:10.1357/002224010793721451

van Rhee, C. (2002). *On the Sedimentation Process in a Trailing Suction Hopper Dredger*. Delft: Delft University of Technology. PhD Dissertation.

van Wijk, J. M., Haalboom, S., de Hoog, E., de Stigter, H., and Smit, M. G. (2019). Impact Fragmentation of Polymetallic Nodules under Deep Ocean Pressure Conditions. *Miner. Eng.* 134, 250–260. doi:10.1016/j.mineng.2019.02.015

VBKO (2003). *Protocol for the Field Measurement of Sediment Release from Dredgers*. The Hague: VBKO TASS project.Issue I.

Violeau, D., Bourban, S., Cheviet, C., Markofsky, M., Petersen, O., Roberts, W., et al. (2002). "Numerical Simulation of Cohesive Sediment Transport : Intercomparison of Several Numerical Models," in *Fine Sediment Dynamics in the Marine Environment*. Editors J. Winterwerp and C. Kranenburg (Elsevier), 75–89. doi:10.1016/s1568-2692(02)80009-2

Volz, J. B., Mogollón, J. M., Geibert, W., Arbizu, P. M., Koschinsky, A., and Kasten, S. (2018). Natural Spatial Variability of Depositional Conditions, Biogeochemical Processes and Element Fluxes in Sediments of the Eastern Clarion-Clipperton Zone, Pacific Ocean. *Deep Sea Res. Part I Oceanogr. Res. Pap.* 140, 159–172. doi:10.1016/j.dsr.2018.08.006

Washburn, T. W., Turner, P. J., Durden, J. M., Jones, D. O. B., Weaver, P., and Van Dover, C. L. (2019). Ecological Risk Assessment for Deep-Sea Mining. *Ocean Coast. Manag.* 176, 24–39. doi:10.1016/j.ocecoaman.2019.04.014

Wedding, L. M., Reiter, S. M., Smith, C. R., Gjerde, K. M., Kittinger, J. N., Friedlander, A. M., et al. (2015). Managing Mining of the Deep Seabed. *Science* 349, 144–145. doi:10.1126/science.aac6647

Winterwerp, J. C. (2002). Near-field Behavior of Dredging Spill in Shallow Water. *J. Waterw. Port. Coast. Ocean. Eng.* 128, 96–98. doi:10.1061/(asce)0733-950x(2002)128:2(96)

Yamazaki, T., Cung, J., and Tsurusaki, K. (1995). Geotechnical Parameters and Distribution Characteristics of the Cobalt-Rich Manganese Crust for the Mining Design. *Int. J. Offshore Polar Eng.* 5 (01), 75–79.

Yong, R., Nakano, M., and Pusch, R. (2012). "Nature of Soils," in *Environmental Soil Properties and Behavior*, 133–161.

Zawadzki, D., Maciąg, Ł., Abramowski, T., and McCartney, K. (2020). Fractionation Trends and Variability of Rare Earth Elements and Selected Critical Metals in Pelagic Sediment from Abyssal Basin of NE Pacific (Clarion-Clipperton Fracture Zone). *Minerals* 10, 320. doi:10.3390/min10040320

Conflict of Interest: Author JS was employed by the company HR Wallingford, Dredging and Coasts & Oceans.

The remaining authors declare that the research was conducted in the absence of any commercial or financial relationships that could be construed as a potential conflict of interest.

Publisher's Note: All claims expressed in this article are solely those of the authors and do not necessarily represent those of their affiliated organizations, or those of the publisher, the editors and the reviewers. Any product that may be evaluated in this article, or claim that may be made by its manufacturer, is not guaranteed or endorsed by the publisher.

frontiers | Frontiers in Earth Science

ORIGINAL RESEARCH
published: 15 July 2022
doi: 10.3389/feart.2022.886006

Impact of the Salt Concentration and Biophysical Cohesion on the Settling Behavior of Bentonites

Ellen Krahl[1], Bernhard Vowinckel[1], Leiping Ye[2], Tian-Jian Hsu[3] and Andrew J. Manning[3,4,5]*

[1]Leichtweiß-Institute for Hydraulic Engineering and Water Resources, Braunschweig, Germany, [2]School of Marine Sciences, Sun Yat-sen University, Zhuhai, China, [3]Center for Applied Coastal Research, Department of Civil and Environmental Engineering, University of Delaware, Newark, NJ, United States, [4]HR Wallingford Ltd, Coasts and Oceans Group, Wallingford, United Kingdom, [5]School of Biological and Marine Sciences, University of Plymouth, Plymouth, United Kingdom

The flocculation behavior of clay minerals in aquatic environments is an important process in estuarine and riverine dynamics, where strong gradients in salinity can locally occur. Various contradicting observations have been reported in the literature on the impact of salt concentration on the settling process of cohesive sediments. To address this issue in a systematic manner, we investigate the settling behavior of clay minerals as a function of the salt concentration of the ambient water. Specifically, we focus on montmorillonite as a prototype clay mineral with a high cation exchange capacity (CEC). To this end, we study suspensions of Wyoming bentonite (Volclay SPV) as a very important constituent for many constructional and industrial purposes. We perform an experimental campaign to study the settling behavior of moderately turbid montmorillonite concentrations in monovalent salt solutions with different salinities (sodium chloride) to represent different environments ranging from deionized to ocean water, respectively. The subsequent settling process was monitored by taking pictures by a camera in regular time intervals over a total observation time up to 48 h. In addition, a modified hydrometer analysis is conducted to determine the grain size distribution (in terms of an equivalent diameter) of the flocculated clay suspension in salt water. Despite the rather high cation exchange capacity of the investigated clay (CEC=88.1), our results show that the settling speed drastically increases within a range of 0.6–1.0 PSU and stays approximately constant for higher salinities. This critical salt concentration is defined here as the critical coagulation concentration (CCC) and lies well below the salinity of natural open water bodies. The hydrometer analysis revealed that 60% of the agglomerates exceed the equivalent grain size of 20 µm. Finally, the findings of this study are supplemented with experiments studying the effect of Extracellular Polymeric Substances (EPS) on the flocculation behavior of bentonite in salt water. Our results demonstrate that salinity is the original trigger for flocculation, whereas EPS allows for even larger floc size but it does not play a significant role for the settling processes of bentonite in estuarine environments.

Keywords: bentonite, suspension, settling, flocculation, critical coagulation concentration, extracellular polymeric substances

OPEN ACCESS

Edited by:
Eduardo Siegle,
University of São Paulo, Brazil

Reviewed by:
Yasuhisa Adachi,
University of Tsukuba, Japan
Zhongfan Zhu,
Beijing Normal University, China

****Correspondence:***
Bernhard Vowinckel
b.vowinckel@tu-braunschweig.de

Specialty section:
This article was submitted to Marine Geoscience, a section of the journal Frontiers in Earth Science

Received: *28 February 2022*
Accepted: *24 June 2022*
Published: *15 July 2022*

Citation:
Krahl E, Vowinckel B, Ye L, Hsu T-J and Manning AJ (2022) Impact of the Salt Concentration and Biophysical Cohesion on the Settling Behavior of Bentonites. Front. Earth Sci. 10:886006. doi: 10.3389/feart.2022.886006

1 INTRODUCTION

The fate and transport of cohesive sediments is an important constituent of sediment transport in natural open water bodies (Winterwerp and van Kesteren, 2004). Due to their small grain size and their cohesiveness, fine-grained sediments can act as vehicles for the transport of nutrients but also contaminants (Ahmerkamp et al., 2022). Cohesive sediments are grains that have a diameter size of smaller than 63 μm and can be further sub-divided into silt (2–63 μm) and clay (< 2 μm). Silt are larger silica grains that are similar in shape to sand grains (Te Slaa et al., 2015), whereas clay particles are platelets with ionic charges that create forces comparable with, or exceeding, the gravitational force, and these cause the clay particles to interact electrostatically. Such particles can be described by theories from colloidal science (Lagaly et al., 2013), i.e., the mutual forces experienced by two or more clay particles in close proximity are the result of the relative strengths of the repulsive and attractive forces (e.g., van Olphen, 1977; Manning, 2001). If clay minerals are dispersed to their primary clay platelets smaller than 1 μm, suspended particles of this size can form ideal sols, where the weight of the particles is balanced by Brownian motion and particles do not settle out over time (Partheniades, 2009; Berg, 2010). There has been evidence that such a state can be obtained in the laboratory if clay particles are dispersed in de-ionized water and flocculation is triggered at a critical salt concentration (e.g., Seiphoori et al., 2021; Mietta et al., 2009; Mehta, 2014; Sutherland et al., 2015; Adachi et al., 2020; Ghazali et al., 2020). However, this critical salt concentration to trigger coagulation, often times referred to as the Critical Coagulation Concentration (CCC, van Olphen, 1977), has not been reported for natural aquatic environments in such a consistent manner (e.g., Gibbs et al., 1989; Droppo and Ongley, 1994; Thill et al., 2001; Kumar et al., 2010; Mikeš and Manning, 2010).

In freshwater suspensions, which contain very few positive ions or possess low electrolyte concentration, the repulsive forces between negatively charged particles dominate, and the particles repel each other. The attractive forces dominate in saline waters due to the abundance of sodium ions that form a cloud of positive ions (cations in a high electrolyte concentration) around the negatively charged clay particles. Consequently, the sediment particles do not behave as individual particles but tend to stick together and form flocs (e.g., Krone, 1962). Krone (1963) found that flocculation quickly reaches equilibrium at a salinity of about 5–10 ppt, which is much less than that for sea water (approx. 35 ppt). Numerous field studies have observed large natural macroflocs (>100 μm) present in very low salinity conditions, including estuarial turbidity maximum zones (e.g., Eisma, 1986; Eisma et al., 1990; Fennessy et al., 1994; Manning and Dyer, 2002; Manning and Bass, 2006; Manning et al., 2006). Part of the difficulty to properly determine threshold conditions for the onset of flocculation may be the fact that open water bodies are complex mixtures with many constituents (e.g., Gibbs, 1983; Mikeš and Manning, 2010). For example, it has been shown that adhesive biofilms and Extracellular Polymeric Substances (EPS) are ubiquitous in environmental flows and have a dramatic impact on the stability and morphodynamics of sheared sediment beds (Malarkey et al., 2015; Schindler et al., 2015; Parsons et al., 2016) as well as the flocculation of clay minerals (Ye et al., 2020; Ye et al., 2021). These forces can act as an adhesive coating of the clay minerals that prevents them from being torn apart under shear.

Typical sediment values of suspended particulate matter concentrations (SPMC) in riverine, estuarine and marine environments range from 2–500 mg/l. Determining the governing mechanism for the onset of flocculation is, therefore, crucial. Applying the Stokes law to estimate the settling velocity of single fine-grained particles, we would expect settling rates so small that the particles will not make contact with the sediment bed in riverine transport. For this reason, this part of the sediment load of a river has been called wash load. In a recent contribution by Lamb et al. (2020), it has been questioned that this is indeed true for clays transported in natural aquatic environment. Lamb et al. (2020), however, investigated datasets from eight low-land rivers and argued that nearly all fine-grained sediments in natural open water bodies are in a flocculated state even in freshwater environments, so that flocs settle over time and make contact with the sediment bed as they are resuspended. The question remained, however, whether flocculation is triggered by either (very low) salinity or EPS or a combination of both. This is an important aspect as it may help to manage and mitigate sediment transport processes. It can also be useful in the modeling of cohesive sediments by means of continuum models (Jarvis et al., 2005; Verney et al., 2011; Kuprenas et al., 2018; Hsu et al., 2021) and newly emerging techniques of particle-resolved simulations (Vowinckel et al., 2019a,b; Vowinckel, 2021; Zhao et al., 2021, Zhu et al., 2022).

Consequently, this question is the focus of the present study. We present results for different experimental campaigns analyzing the impact of salt concentration and EPS in setups for differential settling and shear, respectively. The first setup is built on the work of Rommelfanger et al. (2022), who investigated the impact of salt concentration for kaolinite clay. For the present study, we follow this example and use pure mineral as sediment which allows us to isolate the effect of salinity, since the picture becomes more complicated for natural sediment (Zhu et al., 2018) or even sediment sampled in estuaries (Gibbs et al., 1989; Mikeš and Manning, 2010). In these naturally occurring environments, the effects of EPS and mineral mixtures may also play a role. We therefore deliberately focus on bentonite with a large cation exchange capacity (CEC). A higher CEC creates a larger surface charge as the governing colloidal parameter to control flocculation so that conclusions can be drawn for all clay minerals compositions with a similar or smaller CEC. The setup of differential settling allowed for a very controlled variation of the salt concentration in the semi-dilute regime ranging from 4 to 8 ppt mass concentration (Zhu et al., 2018; Adachi et al., 2020; Ghazali et al., 2020) and, hence, the determination of the CCC for sediment concentrations similar to the turbidity reported for the Gironde estuary in France (Gibbs et al., 1989; Mikeš and Manning, 2010). Second, we compare these findings with a jar test from the LabSFLOC-2 experimental stand of Ye et al. (2020;

2021) to investigate the impact of EPS on the flocculation of bentonite in salt water under shear.

This manuscript is structured as follows. First, we explain in detail our materials and methods in **Section 2** before we present detailed results for flocculation of bentonite during differential settling and under fluid shear, respectively, in **Section 3**. Finally, we provide a discussion of the implications of our study in **Section 4**.

2 MATERIALS AND METHODS

Since the idea of the present study is to focus on clays with a high cation exchange capacity (CEC) to provide an extreme case for the determination of the CCC, we investigated montmorillonite dominated bentonites in a monovalent salt solution of sodium chloride. This choice provides a reference, whether or not the CCC may be an important parameter in naturally occurring environments. We note that we focus on pH-neutral ambient fluids, which is in close agreement with the salinity of riverine waters (e.g., Gundersen and Steinnes, 2003) and any deviation from pH=7 lowers the CCC even further (Goldberg and Glaubig, 1987).

Three different setups are considered in the present study. First, an experimental stand was designed along the lines of Rommelfanger et al. (2022) to conduct experiments of differential settling of clays. This allows to determine the settling time and thereby the CCC for the onset of flocculation. Second, a standard hydrograph analysis was conducted to analyze the grain size distribution of the sediment. Third, a selection of floc size and settling measurements are included to analyze flocs generated by a jar test facility. For this batch, the novel LabSFLOC-2 video floc camera system was used to observe the resultant floc populations. Here, the relative level of flocculation produced by a bentonite clay in salt water was compared with the flocculation response from the addition of pure xanthan gum, a proxy for EPS found in natural sediment (e.g., Tolhurst et al., 2002; Parsons et al., 2016). EPS-coatings are ubiquitous in natural muddy sediments and can act as an adhesive to enhance flocculation (Black et al., 2002; Fang et al., 2016).

2.1 Fluid and Clay Properties

The fluid used in this study was de-ionized (DI) water with a conductivity of 0.5–1.0 µS/cm. In addition, sodium chloride (supplier Carl Roth, article number 9265) as a monovalent salt was used to prepare saltwater solutions with different salinities. Here, salinity is given in practical salt units (PSU) as it is equivalent to ppt used as a measure to quantify the clay concentration. The molar mass of the salt is 58.44 g/mol and it has a density of 2.17 g/cm^3. Note that the pH-value was not modified in this way, but remained neutral at pH=7.

For the present study, we focus on Wyoming bentonite as a montmorillonite rich clay with a rather high CEC. To this end, we use Volclay SPV as a popular clay mineral for geo-engineering (e.g., Studds et al., 1998). The batch of Volclay SPV used in this study has been well characterized by the German Federal Institute for Geosciences and Natural Resources (BGR) (Dohrmann, 2020). **Table 1** shows the mineralogical composition. The large fraction of Na_2O reflects the fact that most of the exchangeable cations are Na^+. The total CEC was determined via the X-ray diffraction method as 88.1 cmol$_c$/kg (Dohrmann, 2020) as a sum of different exchangeable ions in terms of their mass fraction. These constituents comprise sodium (64.4 cmolc/kg), potassium (1.6 cmol$_c$/kg), magnesium (4.1 cmol$_c$/kg) and calcium (18.0 cmol$_c$/kg). As expected from the mineralogical composition, sodium provides the majority of 73% exchangeable ions.

The grain size distribution was determined using X-ray granulometry (Micromeritics SediGraph 5100). As desired, the majority of the grains (>87%) has a diameter smaller than 2 µm and only 5% of the grains are larger than 20 µm (Dohrmann, 2020). For our analysis, we will use clay suspensions with a concentration of 4, 6, and 8 ppt, respectively (ppt in parts per thousand as the mass fraction) which corresponds to the semi-dilute regime (Zhu et al., 2018; Adachi et al., 2020; Ghazali et al., 2020). After the preparation of the suspensions, the samples were stored in a dark environment for a minimum of 7 days to establish an equilibrium between the exchangeable ions and the ions in the salt water solution.

2.2 Experimental Setup to Determine the CCC

To guarantee reproducibility, we follow the example of Rommelfanger et al. (2022) and design a test stand that provides controlled conditions for differential settling. Suspensions were prepared in newly purchased bottles that are otherwise known as cell culture flasks of size 10 cm × 3.8 cm × 2.4 cm (supplier Carl Roth, article number CE48.1). The fluid volume inside the bottles is 50 ml and the vertical extent as the distance available for settling is 5.5 cm. The mass of the clay was determined with a scale of up to 0.001 g accuracy (Sartorius Handy Type: H160-**V20). Preliminary tests showed that clay concentrations within the range of 4–8 ppt yield good results. Using lower concentrations does not provide sufficient contrast for the optical analysis, whereas larger concentrations do not allow for the investigation of the settling of the suspension within the volume provided by the bottles. The salt concentration ranges between 0 PSU and 35 PSU. The latter value corresponds to the salinity of seawater. Small salt concentrations were achieved by preparing a dilution series. The clay was not rinsed by removing the supernatant as it was shown by Rommelfanger et al. (2022) that this technique does not have an effect on the settling behavior of clay suspensions.

Upon the initialization of the different experimental runs, the suspensions were homogenized by shaking the bottles with a platform shaker for a duration of 10 s at a frequency of 6.7 Hz and a stroke of 2 cm, which yields a maximal velocity and acceleration of 26.7 cm/s and 0.0225 cm/s^2, respectively. Afterwards, the bottles were placed in rack with fixed, marked position. This process took approximately another 10 s before the recordings of the experiment actually started. The rack was illuminated by a light panel (Walimex pro Soft LED 200 Flat Bi Color, article number 21243) with a light intensity of 10% at a light temperature of 4400 K. The panel was placed at 7.5 cm distance from the rack. This distance ensures that the bottles do not experience any

TABLE 1 | Mineralogical composition of the bentonite used in this study. The mass fractions were determined by X-ray fluorescence analysis (Dohrmann, 2020) following the procedure by Dohrmann et al. (2009).

XRF	SiO_2	Al_2O_3	Fe_2O_3	CaO	MgO	K_2O	Na_2O	MnO	TiO_2	P_2O_5	LOI	Sum
wt%	59.2	19.2	3.7	1.3	2.3	0.5	2.3	0	0.2	0.1	10.7	99.5

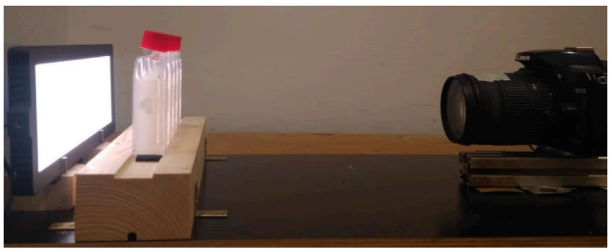

FIGURE 1 | Experimental setup to determine the CCC. The distances between the light panel and the bottles, and the bottles and the camera are 7.5 and 28.5 cm, respectively.

significant heat flux from the light panel. As a result, the temperature within the test stand was kept constant at 19.8°–20°C throughout the entire experimental campaign. The settling of the suspended clay was monitored by a single-lens reflex camera (Canon EOS 1000D, aperture F14, shutter speed 1/8). Pictures were taken in backlight at a distance of 28.5 cm and an interval of 5 min for observation periods up to 48 h. The experimental stand is shown in **Figure 1**.

The camera produced digital pictures with a resolution of 72 dpi in JPEG-format that are converted to gray scale images using Matlab R2020b, so that the pictures can be analyzed as a 2D-matrix of gray scale pixels. Hence, the raw data provides values within the range of 0 (black) to white (256) for pixels with a grid size that represent squares of 0.096 mm edge length.

2.3 Experimental Setup to Determine the Equivalent Diameter of the Flocculated Clay

The hydrometer analysis is used to determine the settling velocity of flocculated and non-flocculated clay suspensions. The hydrometer analysis according to DIN 18123 is generally used to determine the grain size distribution of soil samples (Brüggemann, 1982). This type of analysis is especially useful to determine the grain size distribution for very fine sediments. The change in density of the suspension is measured as the buoyancy of the hydrometer submerged into the suspension. As a result, the grain size distribution can be determined by the differential settling behavior of the individual grain size fractions and particles with grain sizes in the range of 2 and 20 µm can be represented by this analysis.

The standard protocol after Brüggemann (1982) was derived to determine the grain size of the primary particles. Here, we apply the same methodology to analyze the primary particles of our clay samples and conduct an additional, modified set of experiments, where we determine the size distribution of the flocculated clay. According to the standard protocol of the hydrometer analysis, 25 ml dispersant (sodium pyrophosphate) was mixed with 100 ml DI-water and the mixture sat for 15 h. Afterwards, an additional 200 ml of DI-water was added and the fluid was stirred for 30 min. Subsequently, the dispersion was poured into a larger cylinder and filled with more DI-water up to 990 ml. The larger cylinder was sealed, shaken and filled with more DI-water to contain precisely 1,000 ml before the time recording started. Hydrometer measurements were taken after 30 s, 1 min, 2, 5, 15, 45 min, 2, 6, and 24 h alongside with the fluid temperature (where the first reading was after 15 min). An example of this procedure is shown in **Figures 2A,C** for pure DI-water and DI-water with dispersant and clay, respectively. The buoyancy effect on the draught of the hydrometer due to the clay suspension is clearly visible.

To determine the grain size distribution, we follow the protocol of Brüggemann (1982) and use Stokes' law to compute the settling velocity, v, of individual grains/flocs:

$$v = \frac{(R + C_T) \cdot a + b}{t} = \frac{h_{pi}}{t} \tag{1}$$

where C_T is an empirical correction due to temperature changes

$$C_T = 6.67 \cdot 10^{-7} \cdot T^4 - 1 \cdot 10^{-4} \cdot T^3 + 9.58 \cdot 10^{-3} \cdot T^2 - 0.105 \cdot T - 1.03872 \tag{2}$$

and R is the correction due to the reading of the hydrometer

$$R = \left(\rho' - 1\right) \cdot 10^3 + C_m. \tag{3}$$

Here, ρ' is the density of the suspension at time t and a, b and C_m are constants that have to be calibrated for the hydrometer at use to yield the comprehensive hydrometer correction as the total submersed depth h_{pi}. To this end, the calibration procedure was to plot R as a function of h_{pi} for predefined densities ρ' to determine a, b and C_m. The settling velocity is directly connected to a characteristic diameter via Stokes' law

$$d = \sqrt{\frac{18.85 \eta v}{\rho_s - \rho}}. \tag{4}$$

where ρ_s and ρ are the densities of the grain material and the clear fluid, respectively, η is the dynamic viscosity of the clear fluid as a function of temperature

$$\eta = \frac{0.00178}{1 + 0.0337 \cdot T + 0.0022 \cdot T^2}. \tag{5}$$

Using these considerations, we can determine the grain size distribution as follows

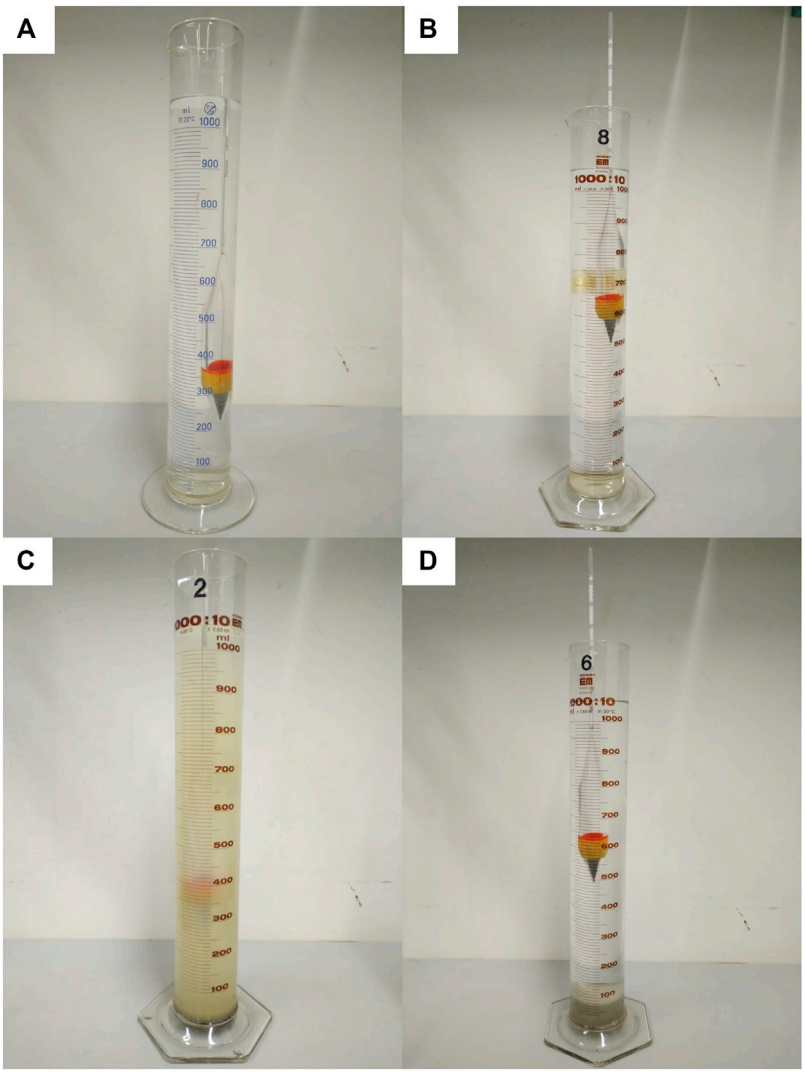

FIGURE 2 | Examples of the immersion depth of the hydrometer in **(A)** DI-water, **(B)** salt water 35 PSU, **(C)** DI water with clay suspension, and **(D)** salt water 35 PSU with clay suspension. The images with suspensions were taken after 24 h observation time. Note in **(D)** how the clay is already deposited at the bottom of the cylinder.

$$P = \frac{100}{m_d} \cdot \frac{\rho_s}{\rho_s - 1} \cdot (R + C_T) \tag{6}$$

where m_d is the dry mass of the sediment. **Eq. 6** is a measure to quantify the sieving size smaller than a certain mass percentage. Every measurement was performed three times in an independent experimental sequence to guarantee reproducibility. For the standard procedure, we choose $a = -0.415$ [−], $b = 20.555$ [−], and $C_m = 1$ [−] as calibration parameters in **Eqs 1**, **3**.

As mentioned above, a second set of hydrometer experiments was carried out with a modified procedure to analyze the grain size distribution of the flocculated clay. In contrast to the standard protocol, saltwater was used with a salinity of 35 PSU and no dispersant was added. This allowed the clay suspension to aggregate, so that the analysis reveals the characteristic floc diameter. Another difference to the standard procedure is that we stopped the recording after 900 s, because all clay had settled out at that time. An example of the modified procedure is given in **Figures 2B,D**, where the effect of salt water and flocculation becomes apparent in the respective panels. The modifications required a re-calibration of the hydrometer, which yielded the following calibration parameters $a = -0.4166$ [−], $b = 20.194$ [−], and $C_m = -22.5$ [−].

2.4 Experimental Setup to Determine the Effect of EPS

We analyze the effect of EPS on flocculation of bentonite by means of jar tests and the LabsFLOC-2 experimental setup previously conducted by Ye et al. (2020). Here, we provide a

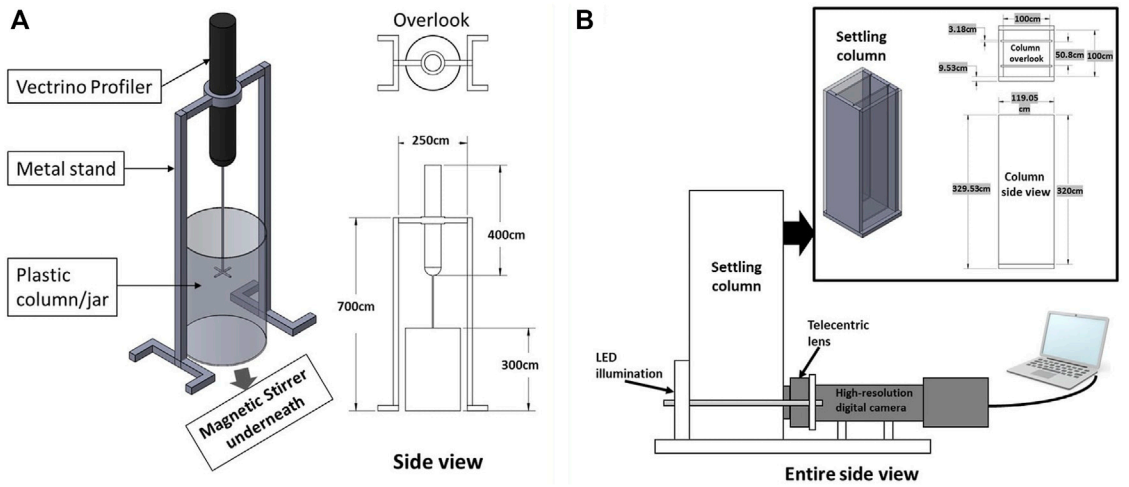

FIGURE 3 | Schematic of the laboratory setup to test the influence of EPS on flocculation. Panel **(A)** shows the self-designed Vectrino stand and panel **(B)** shows the LabSFLOC-2 system.

brief summary to keep the manuscript self-contained. Full details of the experimental procedure for reproducibility can be found in Ye et al. (2020).

2.4.1 Jar Tests and LabSFLOC-2 Experimental Setup

Laboratory jar test experiments were undertaken at the Center for Applied Coastal Research, University of Delaware utilizing a magnetic stirring system, with a self-designed turbulence monitoring frame attached (cf. **Figure 3A**). The resultant floc populations were measured with a LabSFLOC-2 (the 2nd version of Laboratory Spectral Flocculation Characteristics instrument, Gratiot and Manning, 2004; Manning and Dyer, 2007) aside of the jar test apparatus (**Figure 3B**). Each experimental run adopted a uniform stirring speed of 490 rpm (equivalent to a turbulence shear rate parameter $G = 140\,s^{-1}$, as predetermined by three-component flow velocities measured by a Vectrino Profiler (Nortek), see Ye et al., 2020). As discussed in Ye et al. (2020), this was a relatively high shear rate parameter similar to the highly turbulent conditions experienced under breaking waves. To prepare each sample, 1 L of artificial seawater was used for each run and the salinity was set nominally to 35 PSU using laboratory grade sodium chloride. Wyoming sodium Bentonite clay (85.2 ±2.3% Montmorillonite) and xanthan gum as a proxy for EPS were each added to the artificial seawater solution using a mini pipette. This artificial EPS, xanthan gum, has been widely used in many flume experiments or jar tests in mimicking natural cohesive particles in sediment transport studies (such as Tolhurst et al., 2002; Schindler et al., 2015; Parsons et al., 2016; Ye et al., 2021). In fact, many field studies measuring transparent exopolymer particle (TEP) concentration in the coastal/estuarine zone show EPS concentration as Xanthan gum equivalent concentration (e.g., Passow, 2012; Malpezzi et al., 2013). The Xanthan gum equivalent concentration is based on colorimetric determination.

Each experimental jar test run had a nominal 2 h duration before they were collected for analysis using the LabSFLOC-2 system (Manning et al., 2007). As demonstrated by Ye et al. (2020), for the given turbulence level, the flocculation process reaches equilibrium within the 2-h experimental run time. The total floc population characteristics were observed using the LabSFLOCS-2 system which comprised a high-resolution (one pixel ~5 microns) video camera that observes and records individual flocs whilst settling in a dedicated settling column. The analyzed digital floc data provided by LabSFLOCS-2 includes complete population mass-balances: floc numbers, floc size, floc effective density (floc bulk density minus the fluid density), settling velocity, and porosity.

2.4.2 Data Processing–LabSFLOC-2 Camera Floc Data

The LabSFLOC-2 system produces visible floc images that are analyzed to obtain other essential quantitative floc properties including floc size, floc shape and floc settling velocity (Manning et al., 2010). Through additional theories, other floc quantities can be derived, such as floc density, porosity and floc mass. The recorded videos of floc settling videos can be analyzed with Matlab software routines based on the HR Wallingford Ltd. DigiFloc software (Benson and Manning, 2013) and a Java Script to semi-automatically process the digital recording image stack to obtain floc size and settling velocity spectra (Manning et al., 2010; Uncles and Mitchell, 2017). Using the measured floc diameter D, settling velocity W_s, and floc shape, a modified Stokes Law (Stokes, 1851) is used to estimate individual floc effective density ρ_e (Manning and Schoellhamer, 2013) as:

$$\rho_e = \rho_f - \rho = \frac{18 W_s \eta}{g D^2}, \tag{7}$$

in which ρ_f is the floc bulk density, ρ is the saltwater density, η is the dynamic viscosity, and g is gravitational acceleration. To

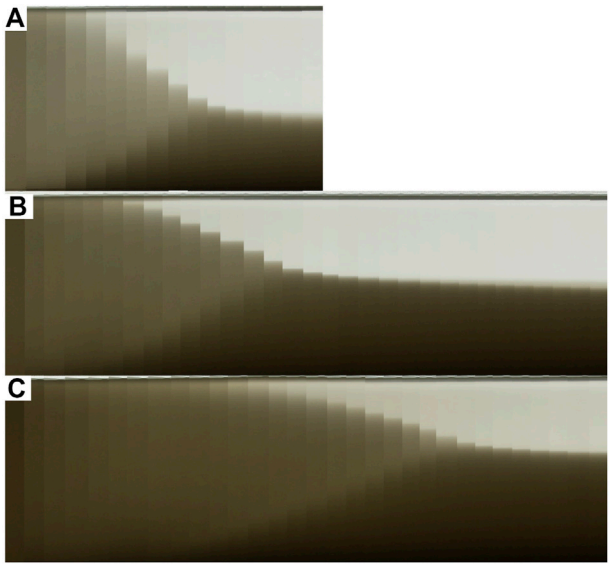

FIGURE 4 | Example of the settling process over time for **(A)** 4 ppt and 0.98 PSU for a total observation period of 7.5 h, **(B)** 6ppt and 0.75 PSU for a total observation period of 15.5 h and **(C)** 8 ppt and 0.62 PSU.

account for the floc shape effect, the diameters associated with the major and minor axes are identified and the sphere-equivalent diameter is used to calculate the floc diameter $D = \sqrt{(D_{major} \cdot D_{minor})}$. Using specially derived algorithms, Fennessy et al. (1997), Manning (2004) and Manning et al. (2007) accurately calculated other physical characteristics for each individual floc, including porosity and fractal dimension (Kranenburg, 1994; Winterwerp, 1998). To compute porosity ϕ, we consider the difference of solid and fluid density, i.e., $(\rho_s - \rho)$, to obtain $\phi = 1 - \rho_e/(\rho_s - \rho_f)$. For the pure bentonite, we assume $(\rho_s - \rho) = 1256$ [kg/m^3]. For the EPS + bentonite sample, we assume $(\rho_s - \rho) = 200$ [kg/m^3] for the xanthan gum and compute the weighted mean of the of the 1:1 mixture, which yields $(\rho_s - \rho) = 728$ [kg/m^3].

3 RESULTS

3.1 Settling Behavior

To illustrate the general settling behavior of the clay suspension, we show exemplary runs as a collage of snapshot photographs taken at a regular interval of 30 min over time in **Figure 4**. Looking at the three different figures that represent the different clay concentrations, 4 ppt, 6 ppt, and 8 ppt, respectively, we can identify three different characteristic regions. First, a light grey area that dominates the water column at the initial period of the experiments. During this time, sediment particles move around due to the differential settling dictated by their weight and frequently come into contact. This is the so-called flocculation and hindered settling stage (Winterwerp, 2002), which will be the main focus within the study. Second, a dark grey area that builds on the bottom of the bottle and grows in thickness over time. This region represents sediment that has settled out and has made contact with the bottom wall via force chains among the sediment grains (Mehta and McAnally, 2008; Adachi et al., 2020; Ghazali et al., 2020). Third, a light region, where the fluid is mostly cleared up and only small amounts of sediment are still in suspension. This region also grows in thickness over time.

At some instant in time, the first light grey region vanishes so that the bottle volume contains only clear fluid and sediment deposit. This instant is called the point of contraction, where the settling stops and the sediment column enters the process of self-weight consolidation. Consequently, the settling behavior observed in our experiments is in very good agreement with the overall phenomenology of settling suspensions (Winterwerp and van Kesteren, 2004; Mehta and McAnally, 2008), and we conclude that the present data set is very well suited for the present analysis. As a main difference among the different experimental runs with different clay concentrations, the flocculation and hindered settling process was completed after 7.5 h for 4 ppt (**Figure 4A**), whereas particles stay in suspension for longer in higher clay concentrations and the settling process takes a longer time to reach the point of contraction (here, we show an observation time of 15.5 h). However, we will show that the settling with different clay loadings yields similar scaling behavior.

3.2 Critical Coagulation Concentration

To determine the CCC, we conducted a systematic campaign of settling experiments as depicted in **Figure 4** for the three clay concentrations 4 ppt, 6 ppt, and 8 ppt. For those three batches, the salinity was varied in small increments in the range from 0 PSU (pure DI-water) to 35 PSU (sea water salinity). For salinities lower than the CCC, we expect no or slow aggregation, so that the settling process should take much longer than the settling for aggregated clays submerged in fluids with a salinity that exceeds the CCC. To this end, we determine an observation level in the bottles, where we record the gray level of the photograph as a surrogate for the clay concentration of the suspension (red horizontal line in **Figure 5A**), i.e., the lower the gray value of the pixel the higher the clay concentration. Hence, we refer to this quantity as light intensity. For the settling analysis, the recorded light intensity is averaged over the entire observation level and normalized by a reference value that was taken from a bottle filled with DI-water only. These results for normalized light intensities are plotted against time for various clay concentrations and salinities in **Figures 5B–D**.

Despite the qualitative differences observed in **Figure 4**, the settling behavior shown in **Figures 5B–D** is remarkably similar among the different clay concentrations. As expected, for large salt concentrations, rapid aggregation occurs that speeds up the settling process so that the fluid in the observation level clears up much more rapidly than for lower salt concentrations. For lower salt concentrations, the increase in light intensity takes a much longer time and transitions from a stepwise to a more gradual increase. The present results are in contrast with the recent findings of Rommelfanger et al. (2022), who investigated the CCC of Kaolin clay with a similar experimental protocol. In this

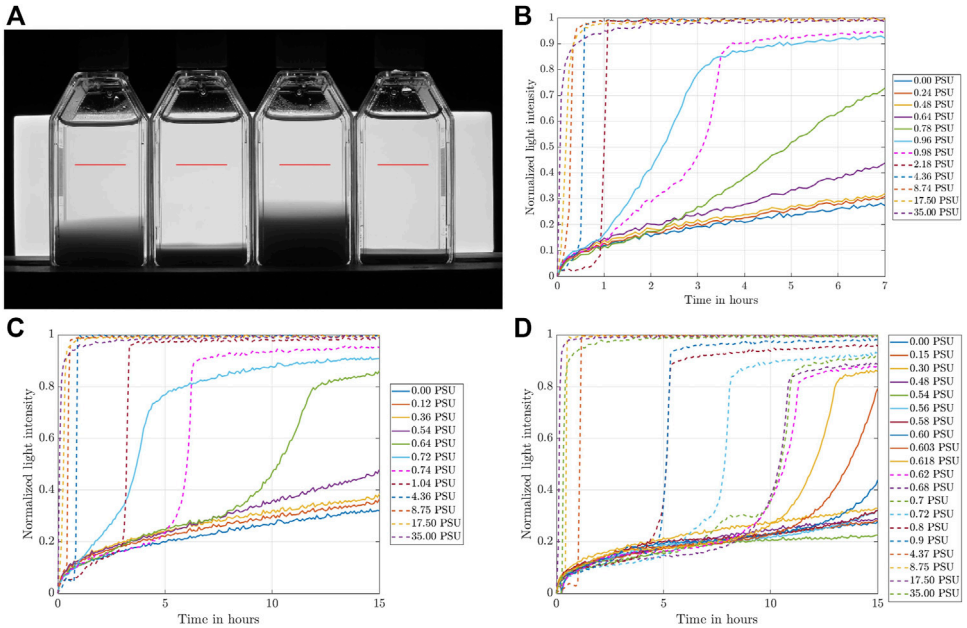

FIGURE 5 | (A) Characteristic picture taken by the camera and observation level to measure the light intensity over time (marked in red), and normalized light intensity over time for various salt concentrations recorded at the observation level for **(B)** 4 ppt, **(C)** 6 ppt, and **(D)** 8 ppt.

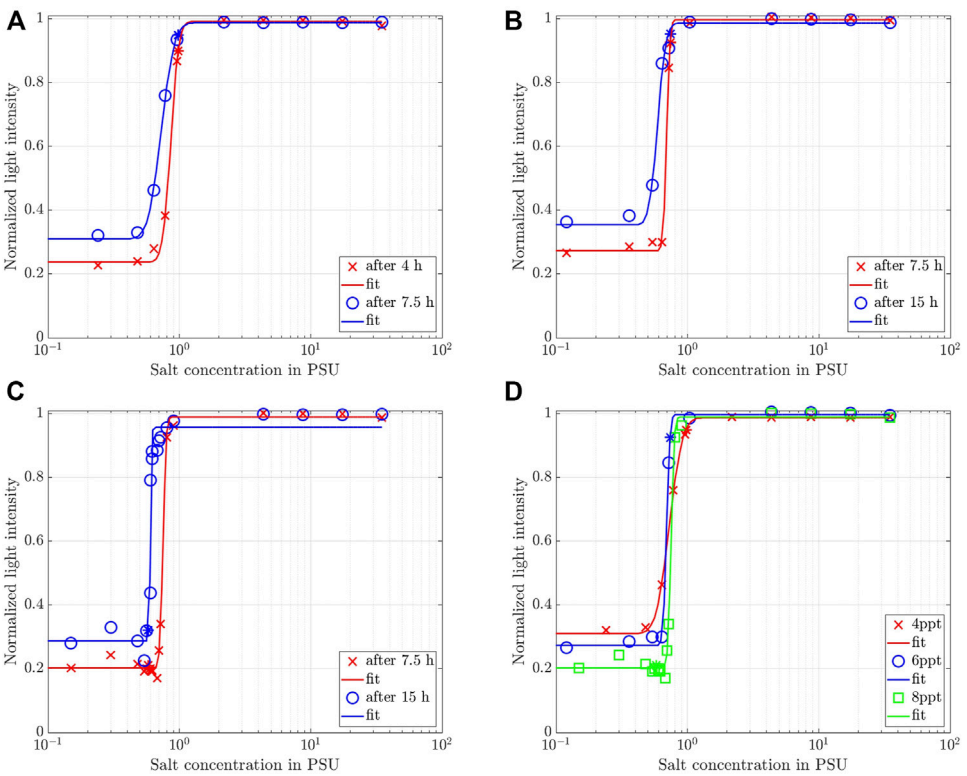

FIGURE 6 | Normalized light intensity for 4 ppt recorded at the observation level marked in **Figure 5A** at two different observation times as a function of salinity for **(A)** 4 ppt, **(B)** 6 ppt, **(D)** 8 ppt. Solid lines represent a best fit of **Eq. 7**. **(D)** Synoptic comparison among the three different clay concentrations at t = 7.5 h.

TABLE 2 | Summary of the parameter fits using **Eq. 7** for the data in **Figure 6**.

Observation Time	Clay Concentration (ppt)	*A*	*B*	s_{CCC}	95% Confidence Bounds		ϵ
					lower	Upper	
4.0 h	4	0.377	14.31	0.859	0.844	0.874	0.614
7.5 h	4	0.339	8.97	0.728	0.716	0.740	0.649
	6	0.362	34.68	0.694	0.686	0.702	0.635
	8	0.394	36.51	0.751	0.745	0.757	0.596
15.5 h	6	0.316	13.93	0.591	0.573	0.610	0.670
	8	0.336	79.56	0.602	0.598	0.607	0.623

study, the settling process of 4–40 ppt Kaolin clay over a vertical distance of 4.5 cm was completed within 10 min, which is substantially shorter than the settling process observed with 4–8 ppt Montmorillonite in the present study. This suggests that the different clay properties, namely different CECs of 3 $cmol_c/kg$ and 88.1 $cmol_c/kg$ for kaolinite and montmorillonite, respectively, yield settling speeds that differ by orders of magnitude. Montmorillonite as used in the present study can, therefore, be seen as an extreme case in terms of its CEC and, hence, its ability to flocculate.

It is now interesting to compare the observed light intensity recorded for different salinities at different observation times to provide a quantitative comparison among the settling behavior with different salinities (Rommelfanger et al., 2022). This was done at $t = 4$ h and $t = 7.5$ h for 4 ppt as well as at $t = 7.5$ h and at $t = 15$ h for 6 and 8 ppt to investigate the impact of salt concentration on the settling behavior of the clay at different characteristic times. The results of this analysis are shown in **Figure 6**. We can clearly identify a range of salt concentration, where we see a rapid increase in light intensity at the given observation times. For later observation times, the light intensities at low salt concentrations increases gradually, whereas the maximum was reached for all observation times and all clay concentrations at higher salt concentrations as the settling process was already finished at the observation level for these times. To provide a comparison among the three clay concentrations, we plot the data taken at $t = 7.5$ h in **Figure 6D**. All three batches show a similar behavior, except for the slower settling process with higher clay concentrations as indicated by the lower light intensity levels for low salt concentrations.

A similar behavior was reported for kaolin clay by Rommelfanger et al. (2022). Hence, we follow their reasoning and fit an error function of the form

$$I_{norm}(s) = A\,\mathrm{erf}\left[B\,log\left(\frac{s}{s_{CCC}}\right)\right] + \epsilon \tag{7a}$$

where $I_{norm}(s)$ is the normalized light intensity as a function of salinity s, and A, B, s_{ccc} and ϵ are fit parameters. In this regard, s_{ccc} marks the inflection point, i.e., the maximum rate of change, of the error function, which we define here as an estimate for the CCC. The results of this fit are shown as solid lines in **Figure 6**. Fitting **Equation 7** worked remarkably well. The resulting fitting parameter together with the 95% confidence interval for s_{CCC} are given in **Table 2** for all observation times and clay concentrations. While results for A and ϵ are very similar among the different runs, the value of B increases with the progressing observation time as the bottle clears up only gradually with lower salt concentrations. Consequently, the results for s_{CCC} also increases over time but are very much comparable among the different clay concentrations at the same observation time (cf. results for 7.5 and 15.5 h). For an early observation time of 4 h, $s_{CCC} = 0.859$ was recorded, whereas the value decreased to an average value of 0.724 PSU and 0.597 PSU at 7.5 and 15.5 h, respectively. This transient evolution of the s_{CCC} was not addressed by the criterion for the onset of flocculation of Rommelfanger et al. (2022), because the settling process was too rapid to account for such an effect.

3.3 Characteristic Settling Time

Another way to analyze the data compiled in **Figures 5B–D** in more detail is to cut horizontally to determine the time it takes for the supernatant to clear to a normalized light intensity of 0.4, which we denote as $t_{0.4}$. As can be seen from these data, this condition is not reached for every run that is shown. Especially the suspensions with a lower salt concentration took a much longer time to reach a normalized light intensity of 0.4. Hence, these experimental runs were extended up to 48 h observation time to guarantee that every sample shown in **Figure 5** had cleared up to the desired threshold value. We plot $t_{0.4}$ as a function of the salt concentration in **Figure 7**. Note the double-logarithmic plot-style to reflect the wide range of $t_{0.4}$ encountered in our analysis.

Looking at the data for the three clay concentrations in **Figure 7A**, it becomes immediately obvious that two data ranges exist for all three clay concentrations that demarcate low from high salinities and, hence, the ability of the sediment to flocculate. For low salt concentrations, $t_{0.4}$ decreases only gradually with the increase of salinity. These data are plotted as circles in **Figures 7B–D** and range until ~0.6 PSU. For larger salt concentrations (indicated as crosses in **Figures 7B–D**), sediment settles out much more rapidly and $t_{0.4}$ decreases exponentially as salinity increase. This observation suggests that $t_{0.4}$ obeys a power law of the form

$$t_{0.4}(s) = as^b \tag{8}$$

where, again, s denotes the salinity of the fluid, and a and b are fitting parameters. Note that the fit was performed to the

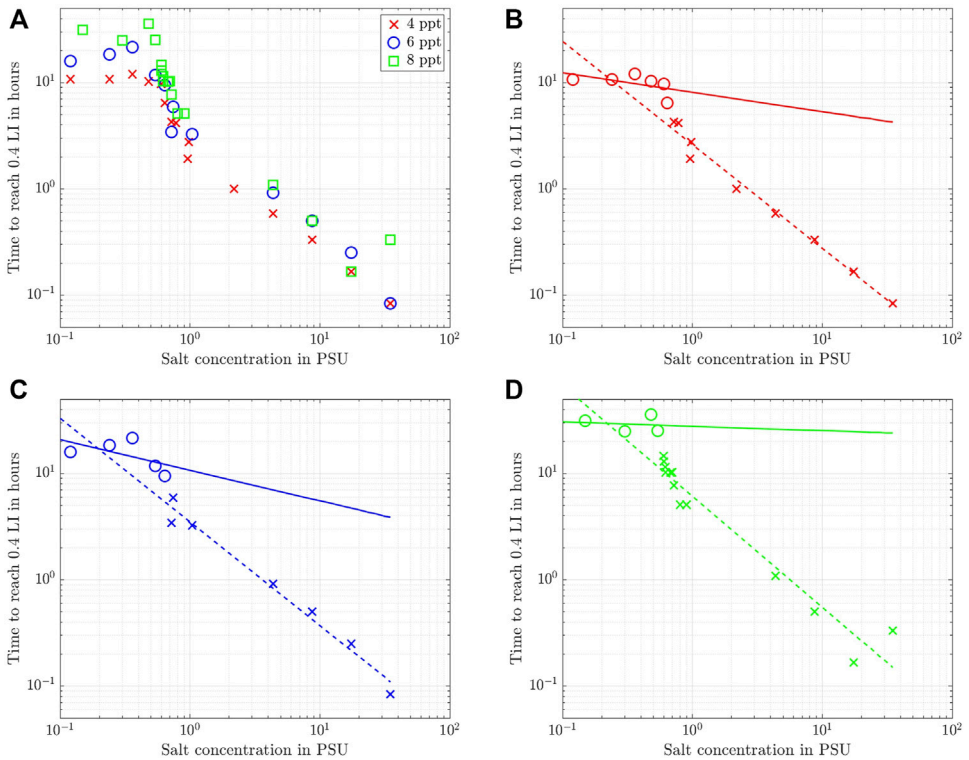

FIGURE 7 | Time required for the normalized light intensity to clear up to 0.4. **(A)** For all three batches for comparison, **(B)** 4 ppt, **(C)** 6 ppt, and **(D)** 8 ppt. The solid and dashed lines represent power law fits to the circles and crosses, respectively.

TABLE 3 | Results for the fit of **Equation 8** to the data shown in **Figure 7**.

Clay Concentration	*A*	*b*	Data Range [PSU]
4 ppt	8.58	−0.14	[0, 0.64]
	2.58	−0.97	[0.72, 35]
6 ppt	10.72	−0.29	[0, 0.64]
	3.49	−0.97	[0.72, 35]
8 ppt	27.76	−0.04	[0, 0.54]
	6.06	−1.04	[0.6, 35]

logarithmic data of $t_{0.4}$ to avoid over-emphasizing the large values of $t_{0.4}$ at low salinities.

The results of the fit are shown in **Figures 7B–D** as solid and dashed lines for the low and high salinity data ranges, respectively. To this end, the data was truncated into two different sets (circles and crosses) by visual inspection of the graphs. Due to this heuristic choice to distinguish between high and low salinity, a bit of scatter exists for the data with low salt concentrations, but the overall agreement of these fits with the experimental data is very good, especially for the high salt concentrations. Note, however, that the good fit with a power law at higher salt concentrations does not imply $t_{0.4} \to 0$ as $s \to \infty$, because the maximum salinity of 35 PSU used in the present study reflects the maximum solubility of sodium chloride in water. The results of the fit in terms of the values determined for a and b are summarized in **Table 3**. While a comparison among the different clay concentrations yields very similar results, the two regimes are clearly visible in the different values of a and b for low and high salinities. Especially the parameter b that reflects the slope of the solid and dashed lines in **Figures 7B–D** increases significantly to a value around unity for all three clay concentrations at high salinities (dashed lines). This result expands the interpretation of **Figure 6**, where an abrupt change in settling behavior was detected for a salinity in the range 0.6–0.85 PSU, which we denoted as the CCC.

The analysis of $t_{0.4}$, on the other hand, shows that a salinity of about 0.6 PSU can be taken as the onset of flocculation, where a non-linear process is triggered that allows the clay particles to aggregate more easily with increasing salt concentration. This value also coincides with the CCC determined in **Section 3.2** for an observation time of 15.5 h. Hence, we conclude that 0.6 PSU serves as a threshold for the onset of flocculation that has an impact on the characteristic settling time, but becomes negligible with increasing salt concentration. On the other hand, depending on the quantity one may be interested in, local gradients in salt concentrations may continue to affect the settling process even for salinities typically encountered in estuaries, but the sensitivity decreases exponentially for salinities that exceed the CCC.

Overall, we conclude for the Wyoming bentonite with a CEC of 88.1 cmol_c/kg used in this study that a change in the settling dynamics sets in for salinities in the range 0.5 PSU to 1 PSU. This value range is about 25 times larger than the one determined for kaolin clay with a CEC of 3 cmol_c/kg by

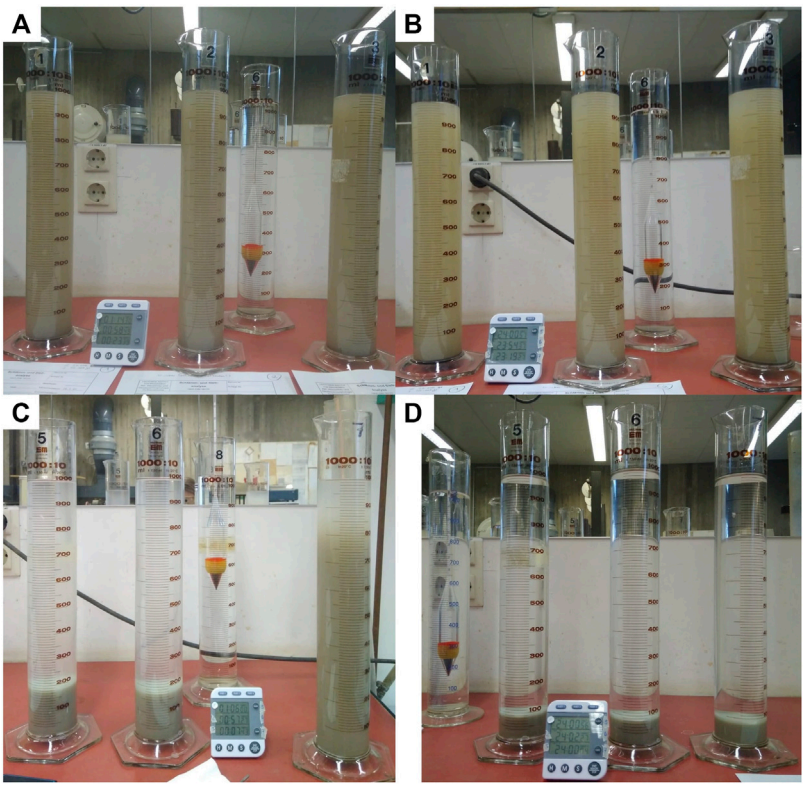

FIGURE 8 | Experimental setup for the hydrometer analysis to determine the grain size distributions with three identical probes per run to guarantee reproducibility. **(A)** montmorillonite clay in DI-water after 1 h 15 min, **(B)** same as **(A)** but after 24 h, **(C)** montmorillonite clay in salt water (35 PSU) after 1 h (cylinder 5 and 6) and 7 min (cylinder 7), and **(D)** same as **(C)** but after 24 h.

Rommelfanger et al. (2022), who reported a critical salinity of 0.04 PSU for suspensions as dense as 40 ppt. Since the CEC of the clay used in the present study is 30 times higher and the suspensions are much more dilute than the material used by Rommelfanger et al. (2022), the present study confirms the linear dependency of the CCC on the CEC that was postulated by Rommelfanger et al. (2022). We furthermore note, that even though the s_{ccc} is much higher for the Wyoming bentonite, water with a salinity of 0.5–1 PSU is still far below the salinities typically encountered in estuaries. In fact, the s_{ccc} barely exceeds the threshold value of a salinity of 0.5 PSU that is typically used to distinguish fresh water from brackish water (Cañedo-Argüelles et al., 2013). The CCC can be expected to even further reduce in slightly acidic conditions (Kaufhold et al., 2018). Evidence for a similarly low CCC was reported by Krone (1963), Gibbs (1983), Gibbs et al. (1989) and Le Floch et al. (2002), but these authors could not determine the threshold value with the precision given here. Since the clay material used in our study represents an extreme case in terms of CEC, we can conclude that local salt gradients are likely to only have negligible influence on the hydrodynamics of flocculated fine-grained sediments and we suspect that this may also be the case in estuarine environments such as the Gironde estuary (Gibbs et al., 1989; Mikeš and Manning, 2010) or the Ems estuary (van Leussen, 1999), because the salinities in these environments are well above the threshold for the onset of flocculation determined here.

3.4 Hydrometer Analysis to Determine the Equivalent Floc Size

For the analysis of the settling velocity outlined in **Section 2.3**, we choose a grain density of 2.753 g/cm^3. This value was determined so as to obtain a sieving curve, where grain sizes larger than 20 µm describe the entire sediment sample, i.e., the cumulative sum of all grain size fractions come out to be 100%. This value is also in good agreement with previous analyses of the Volclay SPV (Kaufhold, 2021).

Figures 8A,B show characteristic photos of the standard hydrometer analysis for the suspension settling process at the initial stage and the end of the experiment. Every run was conducted in three parallel batches to ensure reproducibility. Readings of the hydrometer were taken after 30 s, 1 min, 2, 5, 15, 45 min, 2, 6, and 24 h. For the initial readings, no or only little difference in the submersion depth of the hydrometer was detected (**Figure 8A**). This is the consequence of having only a small fraction of grains larger than 20 µm in the sample. After a total of 24 h of observation time, a good part of the particles still remains in suspension (**Figure 8B**), which reflects the high proportion of grain sizes smaller than 2 µm. Owing to the

added dispersant, these types of grains did not flocculate so that their weight is entirely supported by Brownian motion to form a stable sol that will not settle out (Partheniades, 2009). Indeed, we tested this for more than a week of observation time, but it is not shown here as it does not add to the analysis of the grain size distribution.

Using the standard hydrometer analysis, a bulk settling velocity of 0.0105 cm/s was determined following the methodology described in **Section 2.3**. Furthermore, we can determine the grain size distribution from this analysis to compare it to the granulometry analysis provided by the BGR (Dohrmann, 2020). Based on the chosen time intervals for the reading, the standard hydrometer analysis yields 85% grains smaller than 2 μm, 4% of the grains within the range 2–6.3 μm, 4% of the grains within the range 6.3–20, and 7% larger than 20 μm. These values are in very good agreement with the grain size distribution determined via X-ray ganulometry by the BGR (cf. **Section 2.1**).

As expected, the modified hydrometer analysis revealed a very different behavior. Omitting the addition of the dispersant, but instead using DI water to create a solution with sodium chloride (salinity 35 PSU) promoted flocculation, so that rapid settling of the suspension can be observed. In fact, the experiment was ended after 15 min observation time, because by this point most of the sediment had already settled on the bottom of the cylinder. This becomes visible in **Figure 8C** that shows the modified hydrometer procedure after 7 min 43 s (most right cylinder) and about 1 h (middle and left cylinder). After 24 h, the fluid was completely clear and sediment on the bottom of the cylinder had consolidated (**Figure 8D**). Even at the early observation time (~7 min), the suspension had already cleared the top third of the right cylinder. Recall that this modified procedure, therefore, does not yield the actual grain size diameter as a result, but a diameter that is equivalent to a solid sphere that would settle with the same velocity than the flocculated clay.

With the same framework of the hydrometer analysis outlined in **Section 2.3**, we determine an equivalent settling velocity of 0.345 cm/s, which is 30 times more than the settling velocity determined for the standard procedure. Consequently, the flocs of this experiment all have an equivalent diameter larger than 6.3 μm. A proportion of 35% has an equivalent grain size in the range 6.3–20 μm and 65% exceed an equivalent grain size diameter of 20 μm. The drastic increase in equivalent grain size once more illustrates the strong effect of flocculation on the settling process. Since we found in **Section 3.2** and **Section 3.3** that this effect sets in at ~0.6 PSU and rapidly reaches a well-developed stage with increasing salinity, we conclude that the grain size distribution for the flocculated sediment represents the characteristic sediment composition for most aquatic environments.

3.5 LabSFLOC-2 Results

The results reported so far demonstrate that a very low salinity is sufficient to serve as the critical constituent to trigger flocculation in pH-neutral conditions. To investigate how biogenic cohesion can add to the flocculation behavior of bentonite, we analyze additional data from previously conducted experiments of bentonite in salt water with and without EPS (Ye et al., 2020, 2021). The two batches one with pure bentonites and with EPS + bentonite in saltwater of 35 PSU have been evaluated in terms of their floc size D, effective density ρ_e and settling velocity. The floc size and the settling velocity were determined by visual inspection, whereas the effective density was inferred using **Equation 7**. The data of the settling velocity as a function of floc size are shown in **Figures 9A,B**. We also plot solid lines for the settling velocity computed via **Equation 7** assuming effective density ρ_e =1,600, 160 and 16 kg/m^3 (in magenta, green and orange, respectively) as an orientation.

To understand the diverse properties of the generated flocs, the floc population is often classified into different floc size classes (Eisma, 1986; Dyer et al., 1996). Particularly, the floc diameter has often been used by numerical models of cohesive sediment transport to distinguish between micro- and macrofloc (e.g. Lee et al., 2011). Here, we follow this approach and define those two size classes by choosing a critical floc size of 160 μm (**Table 4**).

Looking at the entire floc population of the pure bentonite sample (**Figure 9A** and **Table 4**), the 1705 individual flocs demonstrated sizes ranging from 20 to 600 μm with a mean floc size of the entire population of 184.8 μm. Settling velocities spanned 0.1–16 mm/s with a mean of 2.00 mm/s. Of note, we observe about 30 very large size flocs up to 400–600 μm (1.7% of the entire floc population). A total of 460 flocs (or 27%) are of very low effective density (less than 50 kg/m^3).

Making the distinction of micro- and macroflocs for the pure bentonite, we find a total of 680 microflocs ($D < 160\ \mu$ m) in the sample with a mean floc size of 105 ± 199 μ m, a settling velocity of 1.1 ± 1.4 mm/s, a density 185 ± 199 kg/m^3 and a porosity of 85 ± 16 %. On the other hand, if we consider the macrofloc ($D > 160\ \mu$ m) sub-fraction, we obtain a mean size of D_{Macro} of 238 ± 71 μ m and a mean settling velocity $W_{s,macro}$ of 2.6 ± 2.2 mm/s. The Bentonite macroflocs had a mean porosity and effective density of 93 ± 6 % and 87 ± 80 kg/m^3, respectively. Here, we represent the measurement deviations as their standard deviations. In addition, we find that the macroflocs represented 77% of the total Bentonite floc mass. **Figure 9C** illustrates an example of a large, low-density Bentonite macrofloc.

For the batch of bentonite flocs with EPS, we perform the same statistical analysis. We detected a total of 1732 flocs and find that among the total floc populations the flocs are larger in size ranging between 34 and 993 μm. As expected, the EPS acts as an adhesive and created a total of 94 flocs larger than 400 μm, which is 5.4% of the entire floc population and triples the number (1.7%) of the pure bentonite sample. Specifically, there are 10 flocs that substantially exceeded the maximum floc size observed for pure bentonite, i.e., ($D > 600\ \mu$ m). On the other hand, the flocs settled at speeds ranging between 0.16 and 9.7 mm/s, with a mean of 2.26 mm/s which is only slightly faster than that of pure bentonite (**Table 4**). Adding EPS to bentonite also increases the density of flocs as we find that only 18% (or 318 flocs) show an effective density lower than 50 kg/m^3.

More insights of EPS bentonite flocs can be found in the analysis of the two floc size classes (**Table 4**). The microflocs of bentonite with EPS are of almost the same size (109 ± 32 μ m) as the pure bentonite flocs, but with a much smaller standard deviation (i.e., more uniform in size). Consequently, the microflocs of bentonite with EPS settle

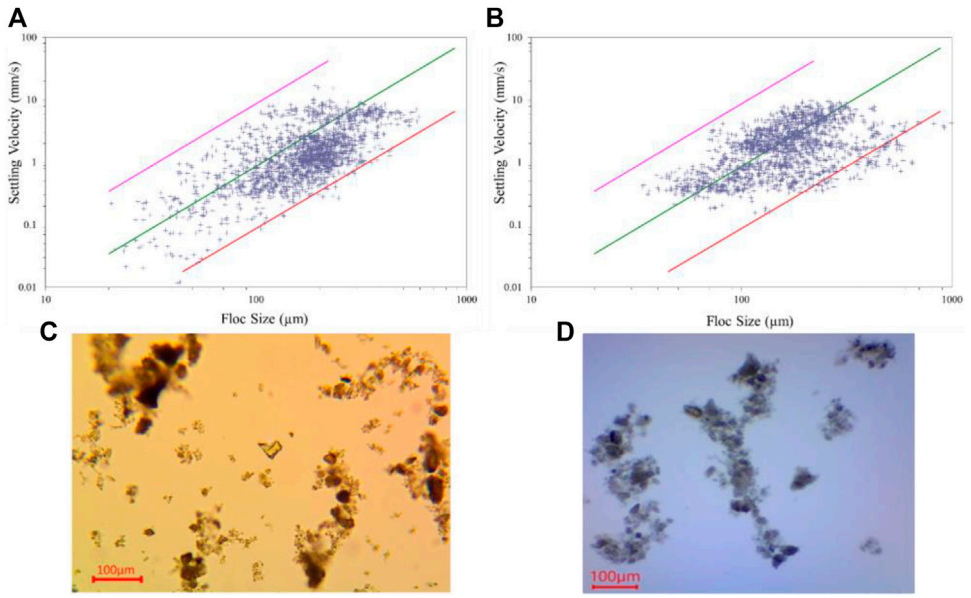

FIGURE 9 | Settling velocity as a function of floc size measured in the LabSFLOC-2 experimental setup. **(A)** pure bentonite and **(B)** bentonite with EPS. The solid lines provide settling velocities for different effective densities according to **Eq. 7** (magenta ρ_e = 1600 kg/m^3, green ρ_e = 160 kg/m^{3}and red ρ_e = 16 kg/m^3). The bottom panelsshow examples of microscopy images of **(C)** bentonite and **(D)** bentonite with EPS.

TABLE 4 | Summary of microflocs ($D < 160\,\mu$ m) and macrofloc ($D > 160\,\mu$ m) fraction key properties of pure bentonite and EPS-bentonite samples.

	Pure bentonite			EPS+Bentonite		
	Microfloc	**Macrofloc**	**Total**	**Microfloc**	**Macrofloc**	**Total**
Floc numbers	681	1,023	1705	855	877	1732
Size (μm)	105.6	237.5	184.8	109.2	253.7	192.3
Effective density (kg/m^3)	185.8	87.5	126.7	231.3	113.8	171.9
Settling velocity (mm/s)	1.08	2.61	2.00	1.81	2.83	2.29
Fractal dimension (nf)	2.30	2.30	2.30	2.45	2.34	2.39
Porosity [vol%]	85.2	93.0	89.9	68.2	84.4	76.4

faster (1.5 ± 1.3 mm/s), are much denser (232 ± 158 kg/m^3) and the porosity is lower (68 ± 13 %). Also note that the standard deviation of the effective density has decreased substantially for the microflocs, which means that EPS tends to homogenize floc properties. For the macroflocs, we found similar results. Compared to the pure bentonite, the macroflocs of bentonite with EPS show an increased floc size (253 ± 106 μ m), larger settling velocities (3.06 mm/s), effective density (114 ± 93 kg/m^3) and smaller porosity (84 ± 7 %). Interestingly, we obtain a larger spread in floc size and a smaller variability in effective densities for macroflocs with EPS, presumably because the additional adhesion of the EPS allows for larger flocs to remain more stable than pure bentonite floc. An example of a bentonite floc with EPS is shown in microscope image of **Figure 9D**. Compared to **Figure 9C** (image of pure bentonite flocs), the two macroflocs are larger in size and seem to be more complex in shape, which is in line with previous experimental evidence (Spencer et al., 2021).

The findings of this analysis confirm the results obtained from the differential settling analysis of **Section 3.2** that particles flocculate in salt water under shear and form aggregates that are much larger than the individual primary clay platelets. Adding EPS to bentonite in salt water enhances the ability to flocculate by allowing the clay minerals to form larger aggregates that are more stable and having a slightly faster settling based on the mean value. However, the overall effect of EPS on bentonite floc settling velocity is not significant.

4 DISCUSSION AND CONCLUSION

In the present study, we conducted three experimental campaigns to clarify the importance of different mechanisms for flocculation of bentonite clay minerals as a prototype clay with a high cation exchange capacity. First, experiments based on differential settling of moderately turbid suspensions in the semi-dilute regime with varying salinity revealed that there exists a critical salt concentration at about 0.6 ppt, where flocculation is triggered. This salt concentration is barely above the threshold for the salinity of fresh water and exceeds most of the salinities reported for natural

surface waters. It can therefore be concluded that nearly all natural occurring aquatic environments exceed this critical threshold concentration of salinity for the onset of flocculation. Evidence of similarly low values have been reported by Krone (1963) and Gibbs (1983) for sediments sampled in various estuarine environments, but the precise threshold value was not determined in such a systematic manner. For example, Gibbs (1983) reported a salinity of 0.5–1 ppt for various clay compositions by varying salinity in the range 0.5–17.5 ppt in only four increments, whereas we varied salinity from 0 to 35ppt in up to 20 increments that are systematically refined in the range of threshold conditions. Nevertheless, the results of our study seemingly contradict a number of field studies that reported varying floc sizes as a function of salt concentration in estuaries, i.e. the higher the salt concentration the larger the flocs (e.g., Thill et al., 2001; Huang, 2017), but it is very hard to identify single parameters as a key trigger for flocculation in these complex environments (Mikeš and Manning, 2010). It is well known that estuaries show a systematic decrease of local shear rates along with an increase in salinity as one moves from riverine to coastal conditions. In particular, the shear rate is known to play a governing role in the control of floc sizes (Verney et al., 2011).

The results of the present study, however, give clear indication that fine-grained suspended sediments are in the flocculated state even in freshwater environments, which has important consequences on their hydrodynamic properties such as their settling velocities. Indeed, this is confirmed by the second experiment conducted in the present study, the modified hydrometer analysis, where it was revealed that the floc size increases to aggregates larger than 20 μm in a salient ambient fluid with 35 PSU. Consequently, such particles in suspension can no longer be described as individual clay platelets (smaller than 2 μm) but the primary particle becomes an assembly of several hundred coagulated platelets (Partheniades, 2008). In addition, it was shown by Rommelfanger et al. (2022) that the CEC can be used as an indicator for the capacity of the suspended clay mineral to bind cations before flocculation sets in. We can, therefore expect that the threshold salinity for the onset of flocculation decreases further for clay minerals with an even lower cation exchange capacity (e.g., kaolinite).

We subsequently conducted a third analysis based on the LabSFLOC-2 experimental setup to clarify the role of EPS on bentonite flocs in salt water at salinity 35 PSU. Since the bentonite is already flocculated at this salinity, this allows to investigate, whether there is an additional flocculation effect due to the adhesive nature of the EPS coating of the clay minerals. Our data show that, while there is a change in the specific density and size distribution between microflocs and macroflocs, the overall floc size was approximately the same for the two batches of pure bentonite and bentonite with EPS. Nevertheless, we see effects in terms of enhanced settling velocities and larger effective densities for flocs of bentonite with EPS and the adhesive EPS coating allows for larger maximum floc sizes.

Our results confirm the findings of Lamb et al. (2020) that all fine-grained sediments in open water are likely to be flocculated and challenge the existence of wash-load, where all sediments are transported in suspension and never make contact with the sediment bed (Partheniades, 1977). The salinity of natural open waters is already sufficient to trigger flocculation. Depending on the microbiological activity in open-water bodies, EPS coatings on flocculated clay minerals can enhance the effect even further, but this was not found to be a prerequisite for flocculation to take place. We derive these findings from pure bentonite but we hypothesize that these observations will also hold for mixtures of mineral compositions (Zhu et al., 2018). This conclusion is in contrast to the study by Guo and He (2011), who claimed that biochemical factors are more important in riverine environments due to the more favorable hydrodynamic (shear) and biochemical conditions (particulate and dissolved organic carbon). Nevertheless, since biofilms are ubiquitous even in salt water conditions (Malarkey et al., 2015), the effect of biofilms is likely to be less important and the salt concentration can be regarded as the governing trigger for the onset of flocculation.

Future work of these types of experiments should focus on sediment compositions sampled from natural environments (Mikeš and Manning, 2010) and the effect of naturally grown EPS instead of xanthan gum (Ye et al., 2020) as well as the impact of varying shear rates as another important control mechanism for the maximum floc size in estuarine environments (Guo et al., 2021).

DATA AVAILABILITY STATEMENT

The raw data supporting the conclusion of this article will be made available by the authors, without undue reservation.

AUTHOR CONTRIBUTIONS

EK and BV performed the experiments and conducted the analysis of the differential settling setup. LY, T-JH, and AM conducted the LabSFLOCS-2 experiments. BV conceived the idea of the research project and helped with the data analysis of the LabSFLOCS-2 experiments. All authors read and approved the manuscript.

FUNDING

BV gratefully acknowledges the financial support by the German Research Foundation (DFG) grant VO2413/2-1. LY, T-JH, and AM contribution towards this research was supported by the National Science Foundation (OCE-1924532) and a grant from the Gulf of Mexico Research Initiative to support CSOMIO (Consortium for Simulation of Oil-Microbial Interactions in the Ocean) (Grant No. SA18-10). AM contribution toward this research was also partly assisted by the TKI-MUSA project 11204950-000-ZKS-0002, HR Wallingford company research FineScale project (Grant no. ACK3013_62), and NSF grant OCE-1736668.

ACKNOWLEDGMENTS

The authors thank Reiner Dohrmann from the German Federal Institute of Geosciences and Natural Resources (BGR) for the mineralogic analysis of the bentonite clay.

REFERENCES

Adachi, Y., Kawashima, Y. T., and Ghazali, M. E. B. (2020). Rheology and Sedimentation of Aqueous Suspension of Na-Montmorillonite in the Very Dilute Domain. *KONA Powder Part. J.* 37, 145–165. doi:10.14356/kona.2020019

Ahmerkamp, S., Liu, B., Kindler, K., Maerz, J., Stocker, R., Kuypers, M. M. M., et al. (2022). Settling of Highly Porous and Impermeable Particles in Linear Stratification: Implications for Marine Aggregates. *J. Fluid Mech.* 931, A9. doi:10.1017/jfm.2021.913

Benson, T., and Manning, A., 2013. Digifloc: the Development of Semi-automatic Software to Determine the Size and Settling Velocity of Flocs. HR Wallingford Report DDY0427-Rt001.

Berg, J. C. (2010). *An Introduction to Interfaces & Colloids: The Bridge to Nanoscience*. Singapore: World Scientific.

Black, K. S., Tolhurst, T. J., Paterson, D. M., and Hagerthey, S. E. (2002). Working with Natural Cohesive Sediments. *J. Hydraul. Eng.* 128 (1), 2–8. doi:10.1061/(asce)0733-9429(2002)128:1(2)

Brüggemann, K. (1982). *Die Bodenprüfverfahren bei Straßenbauten*. Düsseldorfin, German: Werner Verlag.

Cañedo-Argüelles, M., Kefford, B. J., Piscart, C., Prat, N., Schäfer, R. B., Schulz, C. J., et al. (2013). Salinisation of Rivers: an Urgent Ecological Issue. *Environ. Pollut.* 173, 157–167. doi:10.1016/j.envpol.2012.10.011

Dohrmann, R., Rüping, K. B., Kleber, M., Ufer, K., and Jahn, R. (2009). Variation of Preferred Orientation in Oriented Clay Mounts as a Result of Sample Preparation and Composition. *Clays Clay Min.* 57 (6), 686–694. doi:10.1346/ccmn.2009.0570602

Dohrmann, R. (2020). *Private Communication*. Hannover.

Droppo, I. G., and Ongley, E. D. (1994). Flocculation of Suspended Sediment in Rivers of Southeastern Canada. *Water Res.* 28 (8), 1799–1809. doi:10.1016/0043-1354(94)90253-4

Dyer, K., Cornelisse, J., Dearnaley, M., Fennessy, M., Jones, S., Kappenberg, J., et al. (1996). A Comparison of *In Situ* Techniques for Estuarine Floc Settling Velocity Measurements. *Neth. J. Sea Res.* 36 (1-2), 15–29. doi:10.1016/s0077-7579(96)90026-5

Eisma, D., Schuhmacher, T., Boekel, H., Van Heerwaarden, J., Franken, H., Lann, M., et al. (1990). A Camera and Image Analysis System for *In Situ* Observation of Flocs in Natural Waters. *J. Hydraulic Res.* 27, 43–56. doi:10.1080/00221686.2016.1212938

Eisma, D. (1986). Flocculation and De-flocculation of Suspended Matter in Estuaries. *Neth. J. sea Res.* 20 (2-3), 183–199. doi:10.1016/0077-7579(86)90041-4

Fang, H., Fazeli, M., Cheng, W., and Dey, S. (2016). Transport of Biofilm-Coated Sediment Particles. *J. Hyraul. Res.* 54 (6), 631–645.

Fennessy, M. J., Dyer, K. R., and Huntley, D. A. (1994). Size and Settling Velocity Distributions of Flocs in the Tamar Estuary during a Tidal Cycle. *Neth. J. Aquat. Ecol.* 28, 275–282. doi:10.1007/bf02334195

Fennessy, M. J., Dyer, K. R., Huntley, D. A., and Bale, A. J. (1997). "Estimation of Settling Flux Spectra in Estuaries Using INSSEV," in Cohesive Sediments – Proceedings of INTERCOH Conference, Wallingford, England. Editors N. Burt, R. Parker, and J. Watts (Chichester: John Wiley & Sons), 87–104.

Ghazali, M. E. B., Argo, Y., Kyotoh, H., and Adachi, Y. (2020). Effect of the Concentration of NaCl and Cylinder Height on the Sedimentation of Flocculated Suspension of Na-Montmorillonite in the Semi-dilute Regime. *Paddy Water Environ.* 18 (2), 309–316. doi:10.1007/s10333-019-00783-6

Gibbs, R. J., Tshudy, D. M., Konwar, L., and Martin, J. M. (1989). Coagulation and Transport of Sediments in the Gironde Estuary. *Sedimentology* 36 (6), 987–999. doi:10.1111/j.1365-3091.1989.tb01536.x

Gibbs, R. J. (1983). Coagulation Rates of Clay Minerals and Natural Sediments. *J. Sediment. Res.* 53 (4), 1193–1203.

Goldberg, S., and Glaubig, R. A. (1987). Effect of Saturating Cation, pH, and Aluminum and Iron Oxide on the Flocculation of Kaolinite and Montmorillonite. *Clays Clay Miner.* 35 (3), 220–227. doi:10.1346/ccmn.1987.0350308

Gratiot, N., and Manning, A. (2004). An Experimental Investigation of Floc Characteristics in a Diffusive Turbulent Flow. *J. Coast Res.*, 105–113.

Gundersen, P., and Steinnes, E. (2003). Influence of pH and TOC Concentration on Cu, Zn, Cd, and Al Speciation in Rivers. *Water Res.* 37 (2), 307–318. doi:10.1016/s0043-1354(02)00284-1

Guo, C., Manning, A. J., Bass, S., Guo, L., and He, Q. (2021). A Quantitative Lab Examination of Floc Fractal Property Considering Influences of Turbulence, Salinity and Sediment Concentration. *J. Hydrol.* 601, 126574. doi:10.1016/j.jhydrol.2021.126574

Guo, L., and He, Q. (2011). Freshwater Flocculation of Suspended Sediments in the Yangtze River, China. *Ocean Dyn.* 61 (2), 371–386. doi:10.1007/s10236-011-0391-x

Hsu, T.-J., Penaloza-Giraldo, J., Yue, L., Manning, A. J., Meiburg, E., and Vowinckel, B. (2021). "Toward Modeling Flocculation in Turbulence-Resolving Simulations for Cohesive Sediment Transport," in AGU Fall Meeting, 2021.

Huang, I. B. (2017). *Cohesive Sediment Flocculation in a Partially-Stratified Estuary*. PhD thesis. Stanford: Stanford University.

Jarvis, P., Jefferson, B., Gregory, J. O. H. N., and Parsons, S. A. (2005). A Review of Floc Strength and Breakage. *Water Res.* 39 (14), 3121–3137. doi:10.1016/j.watres.2005.05.022

Kaufhold, S., Kaufhold, A., and Dohrmann, R. (2018). Comparison of the Critical Coagulation Concentrations of Allophane and Smectites. *Colloids Interfaces* 2 (1), 12. doi:10.3390/colloids2010012

Kaufhold (2021). *Bentonites – Characterization, Geology, Mineralogy, Analysis, Mining, Processes and Uses*. Stuttgart: Schweizerbart.

Kranenburg, C. (1994). The Fractal Structure of Cohesive Sediment Aggregates. *Estuar. Coast. Shelf Sci.* 39, 451–460. doi:10.1006/ecss.1994.1075

Krone, R. B. (1962). *Flume Studies of the Transport of Sediment in Estuarial Shoaling Process: Final Report*. Berkeley: Hydraulic Engineering Laboratory and Sanitary Engineering Research Laboratory, University of California.

Krone, R. B. (1963). *A Study of Rheological Properties of Estuarial Sediments*. Report No. 63–68. Berkeley: Hydraulic Engineering Laboratory and Sanitary Engineering Research Laboratory, University of California.

Kumar, R. G., Strom, K. B., and Keyvani, A. (2010). Floc Properties and Settling Velocity of San Jacinto Estuary Mud under Variable Shear and Salinity Conditions. *Cont. Shelf Res.* 30 (20), 2067–2081. doi:10.1016/j.csr.2010.10.006

Kuprenas, R., Tran, D., and Strom, K. (2018). A Shear-limited Flocculation Model for Dynamically Predicting Average Floc Size. *J. Geophys. Res. Oceans* 123 (9), 6736–6752. doi:10.1029/2018jc014154

Lagaly, G., Schulz, O., and Zimehl, R. (2013). *Dispersionen und Emulsionen: eine Einführung in die Kolloidik feinverteilter Stoffe einschließlich der Tonminerale*. Berlin: Springer-Verlag.

Lamb, M. P., de Leeuw, J., Fischer, W. W., Moodie, A. J., Venditti, J. G., Nittrouer, J. A., et al. (2020). Mud in Rivers Transported as Flocculated and Suspended Bed Material. *Nat. Geosci.* 13 (8), 566–570. doi:10.1038/s41561-020-0602-5

Le Floch, S., Guyomarch, J., Merlin, F.-X., Stoffyn-Egli, P., Dixon, J., Lee, K., et al. (2002). The Influence of Salinity on Oil Mineral Aggregate Formation. *Spill Sci. Technol. Bull.* 8 (1), 65–71. doi:10.1016/s1353-2561(02)00124-x

Lee, B. J., Toorman, E., Molz, F. J., and Wang, J. (2011). A Two-Class Population Balance Equation Yielding Bimodal Flocculation of Marine or Estuarine Sediments. *Water Res.* 45 (5), 2131–2145. doi:10.1016/j.watres.2010.12.028

Malarkey, J., Baas, J. H., Hope, J. A., Aspden, R. J., Parsons, D. R., Peakall, J., et al. (2015). The Pervasive Role of Biological Cohesion in Bedform Development. *Nat. Commun.* 6 (1), 6257. doi:10.1038/ncomms7257

Malpezzi, M. A., Sanford, L. P., and Crump, B. C. (2013). Abundance and Distribution of Transparent Exopolymer Particles in the Estuarine Turbidity Maximum of Chesapeake Bay. *Mar. Ecol. Prog. Ser.* 486, 23–35. doi:10.3354/meps10362

Manning, A. J., and Bass, S. J. (2006). Variability in Cohesive Sediment Settling Fluxes: Observations under Different Estuarine Tidal Conditions. *Mar. Geol.* 235, 177–192. doi:10.1016/j.margeo.2006.10.013

Manning, A. J., and Dyer, K. R. (2002). "A Comparison of Floc Properties Observed during Neap and Spring Tidal Conditions," in *Fine Sediment Dynamics in the Marine Environment – Proceedings in Marine Science 5*. Editors J. C. Winterwerp and C. Kranenburg (Amsterdam: Elsevier), 233–250.

Manning, A., and Dyer, K. (2007). Mass Settling Flux of Fine Sediments in Northern European Estuaries: Measurements and Predictions. *Mar. Geol.* 245 (1e4), 107–122. doi:10.1016/j.margeo.2007.07.005

Manning, A. J., and Schoellhamer, D. H. (2013). Factors Controlling Floc Settling Velocity along a Longitudinal Estuarine Transect. *Mar. Geol.* 345, 266–280. doi:10.1016/j.margeo.2013.06.018

Manning, A. J., Bass, S. J., and Dyer, K. R. (2006). Floc Properties in the Turbidity Maximum of a Mesotidal Estuary during Neap and Spring Tidal Conditions. *Mar. Geol.* 235, 193–211. doi:10.1016/j.margeo.2006.10.014

Manning, A. J., Baugh, J. V., Spearman, J. R., and Whitehouse, R. J. (2010). Flocculation Settling Characteristics of Mud: Sand Mixtures. *Ocean. Dyn.* 60 (2), 237–253. doi:10.1007/s10236-009-0251-0

Manning, A. J. (2001). *A Study of the Effects of Turbulence on the Properties of Flocculated Mud*. Ph.D. Thesis. Institute of Marine Studies, University of Plymouth.

Manning, A. J. (2004). "The Observed Effects of Turbulence on Estuarine Flocculation," in *Sediment Transport in European Estuaries*. Editors P. Ciavola and M. B. Collins, 41, 90–104. Journal of Coastal Research.

Manning, A. J., Friend, P. L., Prowse, N., and Amos, C. L. (2007). Preliminary Findings from a Study of Medway Estuary (UK) Natural Mud Floc Properties Using a Laboratory Mini-flume and the LabSFLOC system. *Cont. Shelf Res.* 27 (8), 1080–1095. doi:10.1016/j.csr.2006.04.011

Mehta, A. J., and McAnally, W. H. (2008). "Fine Grained Sediment Transport," in *Sedimentation Engineering: Processes, Measurements, Modeling, and Practice*. Editor M. Garcia (Reston, Va: ASCE), 253–306.

Mehta, A. J. (2014). *An Introduction to Hydraulics of Fine Sediment Transport. Advanced Series on Ocean Engineering*, 38. Hackensack, NJ: World Scientific Publishing Co.

Mietta, F., Chassagne, C., Manning, A. J., and Winterwerp, J. C. (2009). Influence of Shear Rate, Organic Matter Content, pH and Salinity on Mud Flocculation. *Ocean. Dyn.* 59 (5), 751–763. doi:10.1007/s10236-009-0231-4

Mikeš, D., and Manning, A. J. (2010). Assessment of Flocculation Kinetics of Cohesive Sediments from the Seine and Gironde Estuaries, France, through Laboratory and Field Studies. *J. Waterw. Port. Coast. Ocean. Eng.* 136 (6), 306–318. doi:10.1061/(asce)ww.1943-5460.0000053

Parsons, D. R., Schindler, R. J., Hope, J. A., Malarkey, J., Baas, J. H., Peakall, J., et al. (2016). The Role of Biophysical Cohesion on Subaqueous Bed Form Size. *Geophys. Res. Lett.* 43 (4), 1566–1573. doi:10.1002/2016gl067667

Partheniades, E. (1977). Unified View of Wash Load and Bed Material Load. *J. Hydr. Div.* 103 (9), 1037–1057. doi:10.1061/jyceaj.0004825

Partheniades, E. (2009). *Cohesive Sediments in Open Channels: Erosion, Transport and Deposition*. Oxford: Butterworth-Heinemann.

Passow, U. (2012). The Abiotic Formation of TEP under Different Ocean Acidification Scenarios. *Mar. Chem.* 128, 72–80. doi:10.1016/j.marchem.2011.10.004

R. J. Uncles and S. B. Mitchell (Editors) (2017). *Estuarine and Coastal Hydrography and Sediment Transport* (Cambridge: Cambridge University Press).

Rommelfanger, N., Vowinckel, B., Wang, Z., Dohrmann, R., Meiburg, E., and Luzzatto-Fegiz, P. (2022). *A Simple Criterion and Experiments for Onset of Flocculation in Kaolin Clay Suspensions*. arXiv preprint arXiv:2203.15545. https://arxiv.org/abs/2203.15545.

Schindler, R. J., Parsons, D. R., Ye, L., Hope, J. A., Baas, J. H., Peakall, J., et al. (2015). Sticky Stuff: Redefining Bedform Prediction in Modern and Ancient Environments. *Geology* 43, 399–402. doi:10.1130/G36262.1

Seiphoori, A., Gunn, A., Kosgodagan Acharige, S., Arratia, P. E., and Jerolmack, D. J. (2021). Tuning Sedimentation through Surface Charge and Particle Shape. *Geophys. Res. Lett.* 48 (7). e2020GL091251. doi:10.1029/2020gl091251

Spencer, K. L., Wheatland, J. A., Bushby, A. J., Carr, S. J., Droppo, I. G., Manning, A. J., et al. (2021). A Structure–Function Based Approach to Floc Hierarchy and Evidence for the Non-fractal Nature of Natural Sediment Flocs. *Sci. Rep.* 11 (1), 14012. doi:10.1038/s41598-021-93302-9

Stokes, G. G. (1851). On the Effect of the Internal Friction of Fluids on the Motion of Pendulums. *Trans. Camb. Philosophical Soc.* IX, 8.

Studds, P. G., Stewart, D. I., and Cousens, T. W. (1998). The Effects of Salt Solutions on the Properties of Bentonite-Sand Mixtures. *Clay Miner.* 33 (4), 651–660. doi:10.1180/claymin.1998.033.4.12

Sutherland, B. R., Barrett, K. J., and Gingras, M. K. (2015). Clay Settling in Fresh and Salt Water. *Environ. Fluid Mech. (Dordr).* 15 (1), 147–160. doi:10.1007/s10652-014-9365-0

Te Slaa, S., van Maren, D. S., He, Q., and Winterwerp, J. C. (2015). Hindered Settling of Silt. *J. Hydraul. Eng.* 141 (9), 04015020. doi:10.1061/(asce)hy.1943-7900.0001038

Thill, A., Moustier, S., Garnier, J. M., Estournel, C., Naudin, J. J., Bottero, J. Y., et al. (2001). Evolution of Particle Size and Concentration in the Rhône River Mixing Zone:. *Cont. Shelf Res.* 21 (18-19), 2127–2140. doi:10.1016/s0278-4343(01)00047-4

Tolhurst, T. J., Gust, G., and Paterson, D. M. (2002). "The Influence of an Extracellular Polymeric Substance (EPS) on Cohesive Sediment Stability," in *Proceedings in Marine Science* (Elsevier), 5, 409–425.

van Leussen, W. (1999). The Variability of Settling Velocities of Suspended Fine-Grained Sediment in the Ems Estuary. *J. sea Res.* 41 (1-2), 109–118. doi:10.1016/s1385-1101(98)00046-x

van Olphen, H. (1977). *An Introduction to Clay Colloid Chemistry*. 2nd edn.. New York, NY: John Wiley & Sons.

Verney, R., Lafite, R., Brun-Cottan, J. C., and Le Hir, P. (2011). Behaviour of a Floc Population during a Tidal Cycle: Laboratory Experiments and Numerical Modelling. *Cont. Shelf Res.* 31 (10), S64–S83. doi:10.1016/j.csr.2010.02.005

Vowinckel, B., Biegert, E., Luzzatto-Fegiz, P., and Meiburg, E. (2019a). Consolidation of Freshly Deposited Cohesive and Noncohesive Sediment: Particle-Resolved Simulations. *Phys. Rev. Fluids* 4 (7), 074305. doi:10.1103/physrevfluids.4.074305

Vowinckel, B., Withers, J., Luzzatto-Fegiz, P., and Meiburg, E. (2019b). Settling of Cohesive Sediment: Particle-Resolved Simulations. *J. Fluid Mech.* 858, 5–44. doi:10.1017/jfm.2018.757

Vowinckel, B. (2021). Incorporating Grain-Scale Processes in Macroscopic Sediment Transport Models. *Acta Mech.* 232 (6), 2023–2050. doi:10.1007/s00707-021-02951-4

Winterwerp, J. C., and van Kesteren, W. G. (2004). *Introduction to the Physics of Cohesive Sediment Dynamics in the Marine Environment*. Amsterdam: Elsevier.

Winterwerp, J. C. (1998). A Simple Model for Turbulence Induced Flocculation of Cohesive Sediment. *J. Hydraulic Res.* 36, 309–326. doi:10.1080/00221689809498621

Winterwerp, J. C. (2002). On the Flocculation and Settling Velocity of Estuarine Mud. *Cont. shelf Res.* 22 (9), 1339–1360. doi:10.1016/s0278-4343(02)00010-9

Ye, L., Manning, A. J., and Hsu, T. J. (2020). Oil-mineral Flocculation and Settling Velocity in Saline Water. *Water Res.* 173, 115569. doi:10.1016/j.watres.2020.115569

Ye, L., Manning, A. J., Holyoke, J., Penaloza-Giraldo, J. A., and Hsu, T. J. (2021). The Role of Biophysical Stickiness on Oil-Mineral Flocculation and Settling in Seawater. *Front. Mar. Sci.* 8. doi:10.3389/fmars.2021.628827

Zhao, K., Pomes, F., Vowinckel, B., Hsu, T. J., Bai, B., Meiburg, E., et al. (2021). Flocculation of Suspended Cohesive Particles in Homogeneous Isotropic Turbulence. *J. Fluid Mech.* 921, A17. doi:10.1017/jfm.2021.487

Zhu, Z., Xiong, X., Liang, C., and Zhao, M. (2018). On the Flocculation and Settling Characteristics of Low-And High-Concentration Sediment Suspensions: Effects of Particle Concentration and Salinity Conditions. *Environ. Sci. Pollut. Res.* 25 (14), 14226–14243. doi:10.1007/s11356-018-1668-0

Zhu, R., He, Z., Zhao, K., Vowinckel, B., and Meiburg, E. (2022). Grain-resolving Simulations of Submerged Cohesive Granular Collapse. *J. Fluid Mech.* 942, A49. doi:10.1017/jfm.2022.404

Conflict of Interest: AM was employed by the HR Wallingford Ltd.

The remaining authors declare that the research was conducted in the absence of any commercial or financial relationships that could be construed as a potential conflict of interest.

Publisher's Note: All claims expressed in this article are solely those of the authors and do not necessarily represent those of their affiliated organizations, or those of the publisher, the editors and the reviewers. Any product that may be evaluated in this article, or claim that may be made by its manufacturer, is not guaranteed or endorsed by the publisher.

frontiers | Frontiers in Earth Science

ORIGINAL RESEARCH
published: 19 July 2022
doi: 10.3389/feart.2022.815652

Floc Size Distributions of Cohesive Sediment in Homogeneous Isotropic Turbulence

Minglan Yu [1], Xiao Yu [1], S. Balachandar [2] and Andrew J. Manning [1,3,4]*

[1]Department of Civil and Coastal Engineering, Engineering School of Sustainable Infrastructure & Environment, University of Florida, Gainesville, FL, United States, [2]Department of Aerospace & Mechanical Engineering, University of Florida, Gainesville, FL, United States, [3]HR Wallingford, Coasts and Oceans Group, Wallingford, United Kingdom, [4]University of Plymouth, Plymouth, United Kingdom

Floc size distribution is one of the key parameters to characterize flocculating cohesive sediment. An Eulerian–Lagrangian framework has been implemented to study the flocculation dynamics of cohesive sediments in homogeneous isotropic turbulent flows. Fine cohesive sediment particles are modeled as the dispersed phase by the discrete element method, which tracks the motion of individual particles. An adhesive contact model with rolling friction is applied to simulate the particle–particle interactions. By varying the physicochemical properties (i.e., stickiness and stiffness) of the primary particles, the dependence of the mathematical form of the floc size distribution on sediment properties is investigated. At the equilibrium state, the aggregation and breakup processes reach a dynamic equilibrium, in which construction by aggregation is balanced with destruction by breakup, and construction by breakup is balanced with destruction by aggregation. When the primary particles are less sticky, floc size distribution fits better with the lognormal distribution. When the primary particles are very sticky, both the aggregation of smaller flocs and breakup from larger flocs play an equally important role in the construction of the intermediate-sized flocs, and the equilibrium floc size distribution can be better fitted by the Weibull distribution. When the Weibull distribution develops, a shape parameter around 2.5 has been observed, suggesting a statistically self-similar floc size distribution at the equilibrium state.

Keywords: cohesive sediment, floc size distribution, two phase approach, discrete element method (DEM), dynamic equilibrium

OPEN ACCESS

Edited by:
Katrien Van Landeghem,
Bangor University, United Kingdom

Reviewed by:
Guoxiang Wu,
Ocean University of China, China
Chris Unsworth,
Bangor University, United Kingdom

****Correspondence:***
Xiao Yu
xiao.yu@essie.ufl.edu

Specialty section:
This article was submitted to Marine Geoscience, a section of the journal Frontiers in Earth Science

Received: *15 November 2021*
Accepted: *21 June 2022*
Published: *19 July 2022*

Citation:
Yu M, Yu X, Balachandar S and Manning AJ (2022) Floc Size Distributions of Cohesive Sediment in Homogeneous Isotropic Turbulence. Front. Earth Sci. 10:815652. doi: 10.3389/feart.2022.815652

1 INTRODUCTION

The transport of fine-grained cohesive sediment in nearshore and estuarine environments plays a critical role in ecosystem dynamics, water quality, bed morphology, and engineering applications, for example, the rapid siltation in navigation channels and harbors (Hayter and Mehta, 1986; Winterwerp et al., 2000), cohesive sediment transport in salt marsh (Graham and Manning, 2007), depositional rates of contaminated muddy sediments (Ye et al., 2020), and long-term morphology of deltas (Edmonds and Slingerland, 2010). Cohesive sediment can bind together through both physical (van Olphen, 1964; Winterwerp and van Kesteren, 2004) and biological (Tolhurst et al., 2002) cohesion to form large aggregates, namely, flocs. A floc size distribution develops in sediment suspension (Sheremet et al., 2017). Due to the variability in floc's structure and

effective density, flocs of different size settle at different velocities (Manning, 2004; Mehta et al., 2014). The larger, low-density macroflocs (van Leussen, 1994) tend to settle faster than smaller microflocs (Eisma, 1986; Manning, 2001), but they are more fragile and more prone to break up by turbulent shear. Macroflocs often dominate the depositional mass flux (Mehta and Lott, 1987; Manning et al., 2006). The floc size distribution is therefore of crucial importance in understanding the spatiotemporal transport patterns of cohesive sediment (e.g., Geyer et al. (2000); Baugh and Manning (2007); Prandle et al. (2005)).

Turbulence plays an important role in the flocculation process of cohesive sediment in natural environments (Dyer, 1989; van Leussen, 1997; Winterwerp, 1998; McAnally and Mehta, 2001; Manning, 2004). On the one hand, turbulence enhances the aggregation through the collision frequency, which scales with the turbulent dissipation rate (Sundaram and Collins, 1997). On the other hand, large flocs break in turbulent flows by turbulent eddies *via* turbulent shear or hydrodynamic drag (Saha et al., 2016). Several phases exist during the flocculation. Initially, the aggregation dominates with the rapid growth of the floc size. As flocs continue to grow, large flocs with porous structures form. Large flocs are vulnerable to fragmentation by fluid shear (Tambo and Watanabe, 1984). Breakup starts to play an increasingly important role in late stages of flocculation. When the two competing mechanisms, namely, the aggregation and breakup processes, balance, an equilibrium floc size distribution develops (Manning and Dyer, 1999; Soulsby et al., 2013; Mehta et al., 2014).

Due to the large variability in the floc size, cohesive sediment is often characterized by the floc size distribution. The mathematical properties of floc size distributions have drawn a lot of attention from the cohesive sediment transport research community, and the interest in unifying the properties of floc size distribution has remained strong. Various statistics for floc size distribution have been proposed to serve as indices of the quality of sediment flocs, as well as sludge in waste treatment. However, theoretical studies, field observations, and laboratory experiments yield different statistics. It is important to investigate the physical mechanisms that lead to different floc size distributions, and the potential implication of different mathematical forms of the floc size distribution.

By applying a dimensional analysis, Hunt (1982) showed the steady state floc size distribution follows a power law. Pushkin and Aref (2002) later developed a more rigorous self-similarity theory of stationary coagulation and showed the floc size distribution follows a power law in the coagulating system. In these studies, the system is forced with particle injection at small sizes, and breakup is not considered. The breakup of large flocs can lead to a skewed floc size distribution with a peak (Hunt, 1982). Spicer and Pratsinis (1996) conducted laboratory experiments to study the evolution of floc size distribution induced by shear and showed the steady state floc size distribution normalized by the average floc size to be self-preserving, which is independent of the shear rate.

Floc size distribution is skewed and hence does not tend to follow the normal distribution. The lognormal distribution and Weibull distribution are commonly used to model skewed distributions; however, the physical origin of the distribution is not well understood. Brown and Wohletz (1995) derived the Weibull distribution with respect to the fragmentation process, in which a power law was used to describe the breakup of a single particle into smaller particles. The Weibull distribution has been widely used as particle size distribution for coarse grains (Fang et al., 1993; Kondolf and Adhikari, 2000). Previous studies of fiber pulp suspension in a flat channel (Huber et al., 2006) and activated sludge flocs (Li and Ganczarczyk, 1991) showed that Weibull distribution is the best descriptor for the floc size distribution. On the other hand, Kiss et al. (1999) developed a model for particle growth that predicts the lognormal particle distribution. They assumed the rate of change of the particle mass is proportional to the surface area, and the particle residence time in the active zone of particle interactions is lognormally distributed. Floc growth is due to collisions with other flocs, and the collision frequency is proportional to the surface area of the floc. A lognormal distribution of velocity fluctuations (Mouri et al., 2009) or dissipation rate (Yeung et al., 2006) that drive inter-particle collisions could also lead to the lognormal floc size distribution. Byun and Son (2020) applied a stochastic approach to model the size distribution of suspended flocs, in which the breakup process is modeled by a lognormal distribution. They showed the lognormal distribution is the best descriptor for the floc size distribution. Hosoda et al. (2011) showed that a stochastic process of halving followed by addition can yield a stationary lognormal distribution. For cohesive sediment flocs, this suggests the breakup of a large floc into two small flocs of equal size followed by the aggregation with another floc could lead to a lognormal floc size distribution. Overall, it is difficult to distinguish the lognormal and Weibull distribution in floc size distribution curves and hence the physical origin of the size distribution, which requires priori knowledge on both the particle–particle and particle–fluid interactions during flocculation.

In the mathematical approach, the aggregation and breakup processes are parameterized. The accuracy of the predictive cohesive sediment transport model strongly depends on the aggregation and breakup models. The two-phase Eulerian-Lagrangian model can resolve both the particle–particle and particle–fluid interactions and can provide the particle-level information on the aggregation and breakup processes. In Eulerian-Lagrangian two-phase models, the carrier fluid is modeled as the continuous phase and the particles are modeled as the dispersed phase (Balachandar and Eaton, 2010). In total, two approaches, namely, the particle-resolving approach (PR) and the point-particle approach (PP), have been developed and implemented to study cohesive sediment dynamics. In both approaches, the discrete element method (DEM) models the particle–particle interactions. Particles are modeled as soft spheres, allowing a small overlap when two particles collide. When one particle collides with another particle or floc, they may stick together. In DEM, the motion of an individual particle is tracked, along with the aggregation and breakup of flocs. Collisions among particles are modeled by the contact mechanics theory, such as Hookean or Hertzian contact models (Johnson, 1985). In the particle-resolving approach

(Vowinckel et al., 2019), flows around individual particles are fully resolved. Due to the large computational cost, the particle resolving approach is often limited to systems with a few thousands of particles, which may not generate satisfactory statistics for flocculation dynamics. On the other hand, in the point-particle approach (Marshall, 2009; Zhou et al., 2010), hydrodynamic forces, such as drag force, lift force, and inertial force, on the particle are modeled. The point-particle approach can be implemented to millions of particles easily. However, the accuracy of the point-particle approach strongly depends on the hydrodynamic force models (Akiki et al., 2017). To investigate the flocculation processes in homogeneous isotropic turbulence, the point-particle approach is implemented to get better statistics of particle dynamics.

In this study, we investigate the floc size distribution in homogeneous isotropic turbulence using a two-phase Eulerian-Lagrangian model, in which the particle–particle interactions are modeled by the discrete element method. Due to the limit of computational resources, we focused on flocculation processes in high-energy estuaries or near-field river plumes with high turbulent shear rate, in which turbulence dictates the aggregation, breakup, and restructuring processes of flocs. We investigated how the primary particle properties affect the aggregation and breakup processes and hence the floc size distribution by varying the stickiness, stiffness, and size of the primary particle while keeping the turbulent shear rate the same. We focus on the physical origin of the floc size distribution and assess the performance of the lognormal distribution and the Weibull distribution at the equilibrium stage. This study is organized as follows. Methods are described in **Section 2**, including the adhesive contact model and the one-way coupling of the fluid and particle phases. Model validation and model setup are also presented in **Section 2**. Model results are presented in **section 3** followed by the discussion in **Section 4** and concluding remarks in **Section 5**.

2 MODEL DESCRIPTION

2.1 Direct Numerical Simulation of Homogeneous Isotropic Turbulence

Turbulence is characterized by a wide range of length scales. Interactions between turbulent eddies of different length scales with flocs play a critical role in flocculation dynamics. The primary particles are smaller than the Kolmogorov length scale (Kolmogorov, 1941a,b) in this study. Although the flow around the particle is not resolved, all turbulent scales including the Kolmogorov scale and larger, are fully resolved. Thus, the present approach is the particle-unresolved direct numerical simulations (DNS).The homogeneous isotropic turbulence is implemented in this study, which is an idealized version of the realistic turbulence and a reasonable approximation of the turbulent flow away from bottom boundary. To generate homogeneous isotropic turbulence, the linear forcing model (Lundgren, 2003; Rosales and Meneveau, 2005) was implemented. Instead of applying forces only to low-wavenumber modes, a force proportional to velocity is introduced in the momentum equation in the form of $\alpha\mathbf{u}$. Because the volumetric sediment concentration is dilute ($\ll 1\%$) and the dominant effect is that of the turbulent carrier flow on the particle dynamics, the one-way coupling approach is adopted, and the governing equations of the fluid phase are as follows:

$$\nabla \cdot \mathbf{u} = 0 \tag{1}$$

and

$$\frac{\partial \mathbf{u}}{\partial t} + \mathbf{u} \cdot \nabla \mathbf{u} = -\frac{1}{\rho}\nabla p + \nu \nabla^2 \mathbf{u} + \alpha \mathbf{u}, \tag{2}$$

in which $\mathbf{u}$ is the fluid velocity, p is the pressure, ρ is the density of the fluid, ν is the kinematic viscosity of the fluid, and α is the linear forcing coefficient. The direct numerical simulations were conducted with the open source code Nek5000 (Fischer et al., 2008; Zwick and Balachandar, 2020), which uses a high-order spectral element method.

2.2 Discrete Element Method for Cohesive Sediment

To resolve particle–particle interactions, the sediment phase is modeled by using the discrete element method (DEM), in which motions of individual particles are tracked.

$$\frac{d\mathbf{x}_i}{dt} = \mathbf{v}_i, \tag{3}$$

$$m_i \frac{d\mathbf{v}_i}{dt} = \sum \mathbf{F}_i, \tag{4}$$

$$I_i \frac{d\boldsymbol{\omega}_i}{dt} = \sum \mathbf{T}_i. \tag{5}$$

$\mathbf{x}$ is the position vector, $\mathbf{v}$ is the particle velocity vector, $\mathbf{F}$ is the force vector, and m is the mass of the particle. The subscript "i" is the particle label. The force on particle "i" is the sum of the collision force ($\mathbf{F}_c$) between particle i and all other particles j, the hydrodynamic force ($\mathbf{F}_f$), and the gravitational force ($\mathbf{F}_g$) as $\mathbf{F}_i = \sum_j \mathbf{F}_{c,ij} + \mathbf{F}_{f,i} + \mathbf{F}_{g,i}$. I is the moment of inertia, ω is the angular velocity of the particle, and $\mathbf{T}$ is the torque on the particle. In this study, we coupled the CFD code nek5000 with the molecular dynamic code LAMMPS (Plimpton, 1995). The granular package in LAMMPS provides a variety of options for the normal, tangential, rolling, and twisting forces resulting from the contact between two particles, and hence is used to model the complex interactions among cohesive sediment particles. For soft clay particles, the Johnson–Kendall–Roberts (JKR) model is adopted.

$$\mathbf{F}_{ne,jkr} = \left(\frac{4Ea^3}{3R} - 2\pi a^2\sqrt{\frac{4\gamma E}{\pi a}}\right)\mathbf{n}, \tag{6}$$

where a is the radius of the contact zone and is related to the overlap δ according to

$$\delta = \frac{a^2}{R} - 2\sqrt{\frac{\pi\gamma a}{E}}, \tag{7}$$

where E is the Young's Modulus, R is the radius of the particle, and γ is the surface energy density. The overlap between particle

"i" and particle "j" is given as $\delta = R_i + R_j - |\mathbf{x}_i - \mathbf{x}_j|$. The JKR model allows for a tensile force beyond contact ($\delta < 0$), up to a maximum of $3\pi\gamma R$. When two particles are not in contact initially, they will not experience this force until they come into contact ($\delta > 0$), then as they move apart, they experience a tensile force up to $3\pi\gamma R$ till they lose contact. This force can be used to define the yield strength of the floc. In addition, a viscoelastic damping force model is used.

$$\mathbf{F}_{n,d} = -\eta_D \mathbf{V}_n, \tag{8}$$

where η_D is the viscoelastic damping coefficient, and $\mathbf{V}_n$ is the relative velocity along the direction of the vector $\mathbf{n}$, which is the unit vector along the line connecting the centers of the two particles. The total normal force is the sum of the adhesive JKR and viscoelastic damping terms.

$$\mathbf{F}_n = \mathbf{F}_{ne,kjr} + \mathbf{F}_{n,d}. \tag{9}$$

The Mindlin no-slip model (Mindlin, 1949) is used to compute the tangential force ($\mathbf{F}_t$), as follows:

$$\mathbf{F}_t = -\min\left(\mu_t F_{n0}, |-k_t a\boldsymbol{\xi} + \mathbf{F}_{t,d}|\right)\mathbf{t}, \tag{10}$$

where μ_t is the friction coefficient, k_t is the elastic constant for tangential contact, and $\boldsymbol{\xi}$ is the tangential displacement accumulated during the entire duration of the contact. The vector $\mathbf{t}$ is the unit vector in the relative tangential velocity direction. $\mathbf{F}_{t,d}$ is the damping term for the tangential force, which follows the same general form as the normal damping force (**Eq. 9**) but uses the relative velocity along the direction of the tangential vector $\mathbf{t}$. The normal force value F_{n0} used to compute the critical force is given as follows:

$$F_{n0} = |\mathbf{F}_n + 2\mathbf{F}_{pulloff}| = |\mathbf{F}_{ne,jkr} + 6\pi\gamma R|. \tag{11}$$

The floc restructuring, in which particles change their relative positions while remaining connected, could also play an important role in the flocculation dynamics. Compaction of flocs by turbulent shear may occur with preferential floc structures. To account for floc restructuring, a rolling friction model of a pseduo-force formulation (Luding, 2008) was implemented. The rolling friction model allows the adjustment of rolling displacement of the contacting pair. The rolling pseudo-force is computed analogously to the tangential force, as follows:

$$\mathbf{F}_{roll,0} = k_{roll}\boldsymbol{\xi}_{roll} - \gamma_{roll}\mathbf{v}_{roll}, \tag{12}$$

where k_{roll} is the elastic constant for rolling, γ_{roll} is the damping constant for rolling, $\boldsymbol{\xi}_{roll}$ is the rolling displacement, and $\mathbf{v}_{roll}$ is the relative rolling velocity (Wang et al., 2015). A Coulomb friction criterion truncates the rolling pseudo-force if it exceeds a critical value of

$$\mathbf{F}_{roll} = \min\left(\mu_{roll}F_{n0}, |\mathbf{F}_{roll,0}|\right)\mathbf{k}, \tag{13}$$

where $\mathbf{k}$ is the direction of the pseudo-force. The rolling pseudo-force does not contribute to the total force on either particle, but it acts only to induce an equal and opposite torque on each particle.

$$\mathbf{T}_{roll,i} = \frac{R_i R_j}{R_i + R_j}\mathbf{n} \times \mathbf{F}_{roll}, \tag{14}$$

$$\mathbf{T}_{roll,j} = -\mathbf{T}_{roll,i}. \tag{15}$$

2.3 Hydrodynamic Force

The total hydrodynamic force on particle "i" is given as follows:

$$\mathbf{F}_{hd,i} = \mathbf{F}_{d,i} + \mathbf{F}_{p,i}, \tag{16}$$

where $\mathbf{F}_d$ and $\mathbf{F}_p$ are the quasi-steady force and stress-divergence force, respectively. The added-mass force is neglected in this study assuming the small particle Stokes number. The drag force $\mathbf{F}_d$ on particle "i" is given as follows:

$$\mathbf{F}_{d,i} = \frac{1}{2}\rho C_D A|\mathbf{u} - \mathbf{v}_i|(\mathbf{u} - \mathbf{v}_i). \tag{17}$$

where ρ is the fluid density and $A = \pi D_p^2/4$ is the projected area of the spherical particle with D_p as the diameter of the spherical particle. For very dilute flow with sediment concentration $\phi \ll 0.1\%$, the standard drag coefficient C_D for an individual particle is used, which is given as follows:

$$C_D = \begin{cases} \dfrac{24}{Re_p}\left(1 + 0.15Re_p^{0.687}\right), & \text{if} \quad Re_p < 1000 \\ 0.44, & \text{otherwise,} \end{cases} \tag{18}$$

where $Re_p = |\mathbf{u} - \mathbf{v}|D_p/\nu$ is the particle Reynolds number. The stress-divergence force experienced by the particle is calculated as follows:

$$\mathbf{F}_{p,i} = (-\nabla p + \nabla \cdot \tau)V_{p,i}, \tag{19}$$

where the pressure gradient and stress divergence are interpolated to the particle center. In the current formulation, only the hydrostatic pressure is used to calculate the force F_p for simplicity. The buoyancy force due to the hydrostatic pressure is $\mathbf{F}_{p,i} = -\rho_f \mathbf{g} V_{p,i}$, where $\mathbf{g}$ is the gravitational acceleration vector and $V_p = \pi D_p^3/6$ is the volume of the particle.

2.4 Model Setup and Model Validation

The aforementioned governing equations are solved in non-dimensional forms. With the characteristic velocity scale U and length scale L, the non-dimensionalized variables are defined as follows:

$$\mathbf{x}^* = \frac{\mathbf{x}}{L}, \quad \mathbf{u}^* = \frac{\mathbf{u}}{U}, \quad p^* = \frac{p}{\rho U^2}, \quad \mathbf{F}^* = \frac{\mathbf{F}}{\rho U^2 L^2}. \tag{20}$$

In homogeneous isotropic turbulence, the Reynolds number based on the Taylor microscale (λ) and the root mean square of turbulent velocity fluctuations (u_{rms}) is commonly used, which is defined as $Re_\lambda = \lambda u_{rms}/\nu$. The Taylor microscale is computed by $\lambda = \sqrt{15\nu/\epsilon}u_{rms}$, where ϵ is the viscous dissipation rate and computed from the simulation results. We varied the properties of primary particles, including the particle diameter ($D_p^* = D_p/L$), Young's modulus ($E* = E/\rho U^2$), viscoelastic damping coefficient ($\eta_D^* = \eta_D/\rho U L^2$), and the surface energy density ($\gamma* = \gamma/\rho U^2 L$). Properties of primary particle used in

this study are summarized in **Table 1**. Coefficients in the tangential force and rolling friction models were kept the same for all simulations. The Young's modulus of soft clay particle is on the order of 1 MPa, which can significantly restrict the critical time step for DEM simulations. In practice, the Young's modulus used in the model is often several orders of magnitude smaller than the actual value to accelerate the computation. Tsuji et al. (1993) showed that stiffness can be reduced by orders of magnitude without altering the collisional behaviors of particles. In this study, the Young's modulus and the surface energy density are scaled down properly to make sure the relative importance of the elastic force and adhesive force is kept the same and the same floc structures can be reproduced. For simplicity, the superscript "*" in the non-dimensionalized variables are omitted in the analysis.

The computational domain is a periodic box of size $8 \times 8 \times 8$, and 16 elements of uniform size were used in each direction. A polynomial order $P_N = 8$ was used within each element, which yields a total resolution of around 2.1 million grid points. The third order Adams–Bashforth method was used for time integration. A fixed time step was chosen in all simulations, which ensures the maximum Courant–Friedrichs–Lewy (CFL) number to remain around 0.2. The "3/2" rule was used for de-aliasing. The PNPN-2 algorithm was applied (Maday et al., 1990; Fischer, 1997), in which pressure is solved on a coarser grid with polynomial order 6.

The DNS Model has been validated with previous DNS study by Rosales and Meneveau (2005) using the time-averaged energy spectrum. Due to the small Reynolds number used in both studies, there is no clear "−5/3" slope. The red solid curve represents the averaged non-dimensional energy spectra over cases with different Reynolds numbers. Our model results agree with the previous DNS study reasonably well (**Figure 1**). The forcing coefficient ($\alpha = 0.033$) and the viscosity ($\nu = 5 \times 10^{-3}$) are kept the same for all cases. This gives the Reynolds number of 200 based on unit characteristic velocity and length scales, and Taylor Reynolds number (Re_λ) of 32. For homogeneous isotropic turbulent flow, there are no intrinsic characteristic scales for the mean flow. The Taylor Reynolds number is commonly used in homogeneous isotropic turbulence because it uses the fundamental length scale and velocity scale of turbulence to define the Reynolds number. To relate the idealized simulation conducted in this study with field condition, the Taylor Reynolds number can be used to obtain the turbulent shear rate when characteristic scales in dimensional form are given. The average Kolmogorov length scale is $\eta = 0.049$ and the average turbulent kinetic energy is $k_t = 0.12$.

To make results relevant to geophysical or engineering applications, simulation results can be interpreted in the dimensional forms with given characteristic length scale and velocity scale. Due to the limitation of computational resources, the present study focuses on energetic environment with high turbulent shear only. For a characteristic length scale of $L = 10^{-3}$ m, the characteristic velocity scale is $U = 0.2$ m/s, based on the Reynolds number, and the particle diameter is $D_p = 12.8\,\mu$m for cases P_2. The particles can be interpreted as the smallest clay-based aggregates, namely, flocculi. Flocculi seldom break down to the lowest-level primary particles even at the high

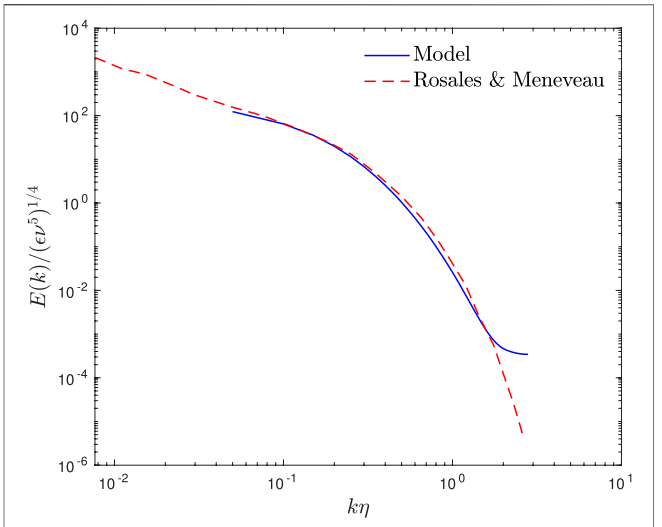

FIGURE 1 | Model validation with DNS simulation results from Rosales and Meneveau (2005).

turbulent shear and hence are the building blocks of large flocs. The turbulent shear rate based on the characteristic scales is 350 s^{-1} for all cases. The shear rate is higher than the values in most laboratory experiments and field observations; however, the model captures how turbulence affects flocculation dynamics. The Young's modulus for soft clay is in the range of 0.5 to 5MPa, and the Poisson ratio of clay is 0.3. The Young's modulus used in the simulation is between 6.4 and 16 kPa, which is reduced by two order of magnitude to accelerate the computation. In the JKR theory, the pull-off force to separate two particles is $3\pi\gamma_{JKR}D_p/2$, which can be used to define the yield strength of the floc. The softness of particles does not affect the yield-strength of flocs directly and hence the aggregation of particles. Detailed measurement on the surface energy density γ is still lacking. In this study, the surface energy density used in the JKR model is in the range of 2×10^{-4} to 1×10^{-3} J/m^2. The stickiness of the particle can be characterized by the adhesive number, which is defined as the ratio of the yield strength of flocs represented by the surface energy density γ to the turbulent kinetic energy $Ad = \gamma/\rho k_t D$. Because the turbulent intensity remains the same in all cases, the average floc size increases with the adhesive number as expected when the primary particle is kept the same (**Table 1**). In addition, the averaged floc size is almost three times greater than the Kolmogorov length scale for the cases with the largest adhesive number. However, for cases with relatively small adhesive number (case P_2S_2 and P_2S_3), the floc size is limited by the Kolmogorov length scale, and the average floc size is comparable to the Kolmogorov length scale.

3 MODEL RESULTS

3.1 Flow Visualization

The flow velocity field from case P_1S_1 is shown in **Figure 2A**. The horizontal $x - y$ plane is located at $z_0 = 0$. Only particles whose

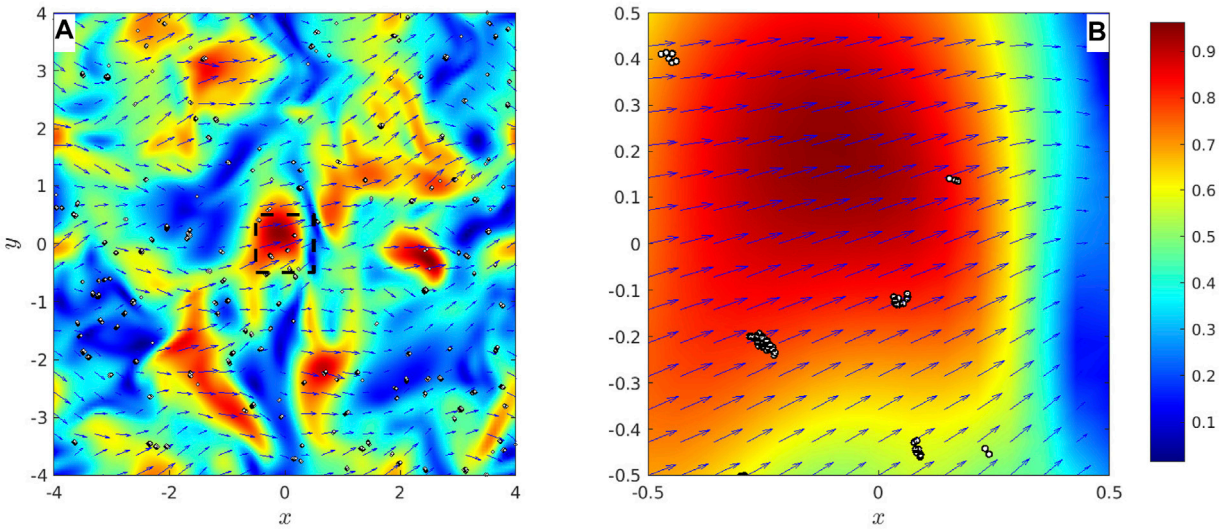

FIGURE 2 | Model results. **(A)** Horizontal (*x*–*y*) plane of the flow field with particles from case P_1S_1 with relatively larger primary particles. The streamwise velocity component is used as background color. **(B)** Zoom in view of the velocity field and particles [black box in panel **(A)**].

centers are located between $z_0 - D_p/2$ and $z_0 + D_p/2$ are projected to the $x - y$ plane. The zoom in view is shown in **Figure 2B** to show the detailed structures of the flocs. Clusters of primary particles can be observed as flocs form. The Stokes numbers $St = sD_p u^*_{rms}/18\nu$ are 0.2 and 0.13 for P_1 and P_2 cases with the specific gravity of $s = 2.65$, therefore we did not observe strong local preferential accumulation of particles.

3.2 Time Evolution of the Floc Size Distribution

All simulations are initialized with mono-dispersed spherical particles, which are uniformly distributed in the simulation domain. Initially, the particle velocity is set to zero. Due to collisions driven by turbulence, flocs start to form gradually and the floc size distribution evolves into an equilibrium distribution. In total, two contrasting cases, P_2S_1 (softer and more sticky primary particles) and P_2S_2 (more stiff and less sticky primary particles), are selected to investigate the dynamics. **Figure 3** shows the time-evolution of the floc population (N_{n_f}) from case P_2S_1, where the primary particles of size $D_p = 0.0128$ are the stickiest (the adhesive number Ad is the greatest), and n_f represents the number of primary particles consisting the floc. At the beginning stage ($t = 2$), a power law relation can be observed. With the formation of larger flocs ($t = 1000$–3000), the power–law relation can still be observed for small flocs, but the slope starts to decrease. The slope is significantly different from the beginning stage. At the early stage, small flocs form mainly due to aggregation, and the power–law relation can well capture the size distribution for those small flocs (Hunt, 1982). At the intermediate stage ($t = 4000$–6000), we observe the accumulation of intermediate-sized flocs with n_f between 20 and 90, which forms a staircase in the floc size distribution (for instance at $t = 5000$). At the late stage ($t \geq 7000$), the population of floc (N_{n_f}) with n_f between 20 and 90 starts to decrease and a peak appears around $n_f = 95$. N_{n_f} only changes slightly for relatively large flocs at $t \geq 10{,}000$, suggesting the equilibrium floc size distribution is reached. The floc size distribution shows an asymmetric shape with respect to the peak of N_{n_f} at $n_f = 95$ on the log-log plot.**Figure 4** shows the time-evolution of floc size distribution from a contrasting case P_2S_2 with less sticky and more stiff particles. Similarly, at the early stage ($t \leq 2000$), the power–law relation between N_{n_f} and n_f can be observed. However, there is no formation of the staircase-shaped structure at the intermediate stage, and the peak around $n_f = 16$ shows up at a much earlier time and is evident for $t \geq 3000$. In addition, the population (N_{n_f}) of large flocs of size $n_f \geq 16$ does not change with time much. However, the depletions of small flocs of size $n_f \leq 5$ due to aggregation can still be observed at the late stage. The floc size distribution shows a more symmetric shape with respect to the peak at $n_f = 16$ on the log-log plot compared to the case P_2S_1.

To further investigate the aggregation process of flocs, the time-evolution of the floc population for given floc sizes are shown in **Figures 5**, **6**. For case P_2S_1, small flocs of size n_f between 2 and 5 show a similar pattern (**Figure 5A**). The population N_{n_f} first increases and reaches a peak, then it drops and approaches to an asymptotic value at the late stage when the equilibrium is reached. For relatively large flocs (**Figure 5B**), the time of the first appearance of the floc of size n_f increases with floc size n_f, since the flocs are built gradually when the floc grows. For intermediate flocs of size $10 < n_f < 40$, we observed a similar pattern to small flocs, N_{n_f} increases, peaks, and then decreases and approaches to the asymptotic value. However, for large flocs of size $n_f \geq 50$, N_{n_f} increases to the peak value and then approaches to the asymptotic value. Continuous aggregation and breakup keep

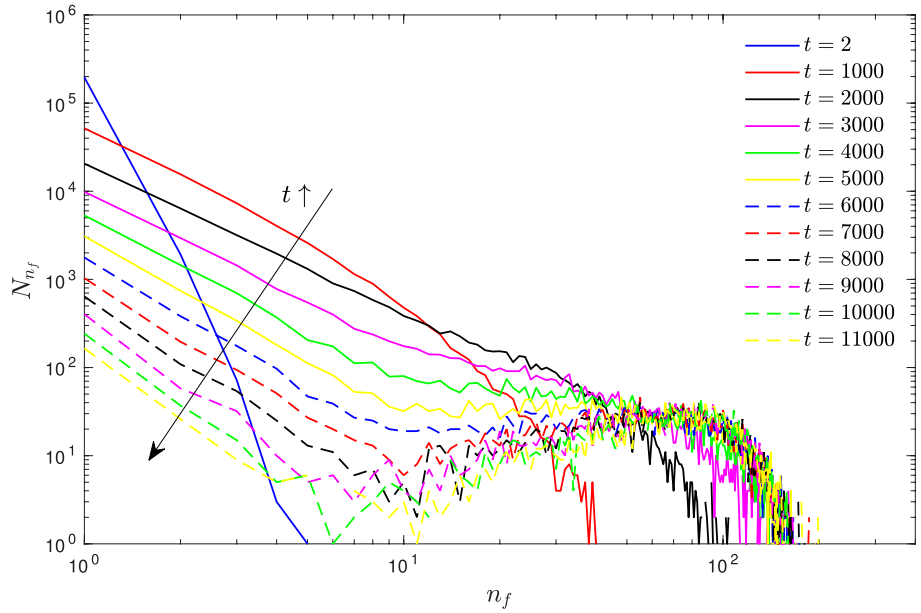

FIGURE 3 | Time evolution of the floc population N_{n_f} as function of floc of size n_f from case P_2S_1 with the most sticky primary particles.

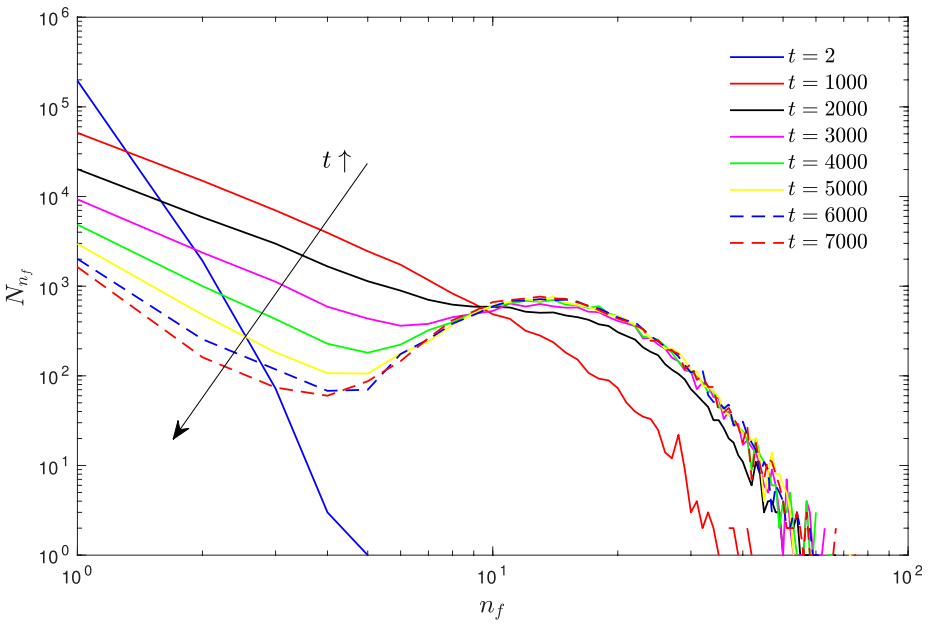

FIGURE 4 | Time evolution of the floc population N_{n_f} as function of floc of size n_f from case P_2S_2 with less sticky and more stiff primary particles.

occurring at the equilibrium stage. The oscillations in N_{n_f} at the late stage are due to the intermittent nature of turbulence.

The time evolution of floc population N_{n_f} from case P_2S_2 is shown in **Figure 6**. Similar patterns for small flocs of size $n_f \leq 5$ can be observed. However, large flocs of size $n_f \geq 10$ show a different pattern that N_{n_f} first increases and then approaches the asymptotic constant at the equilibrium stage. This is consistent with the time evolution of the floc size distribution that the peak appears in the early case P_2S_2 and the population of large flocs does not change much with time at the late stage (**Figure 4**). The time of the first appearance of large floc of $n_f \geq 10$ also increases with floc size, again suggesting the flocs grow gradually. Again, we observe oscillations of N_{n_f} at the equilibrium stage due to the intermittent nature of turbulence. The oscillation is much stronger for larger flocs because large flocs are more fragile and more susceptible to breakup by turbulent shear.

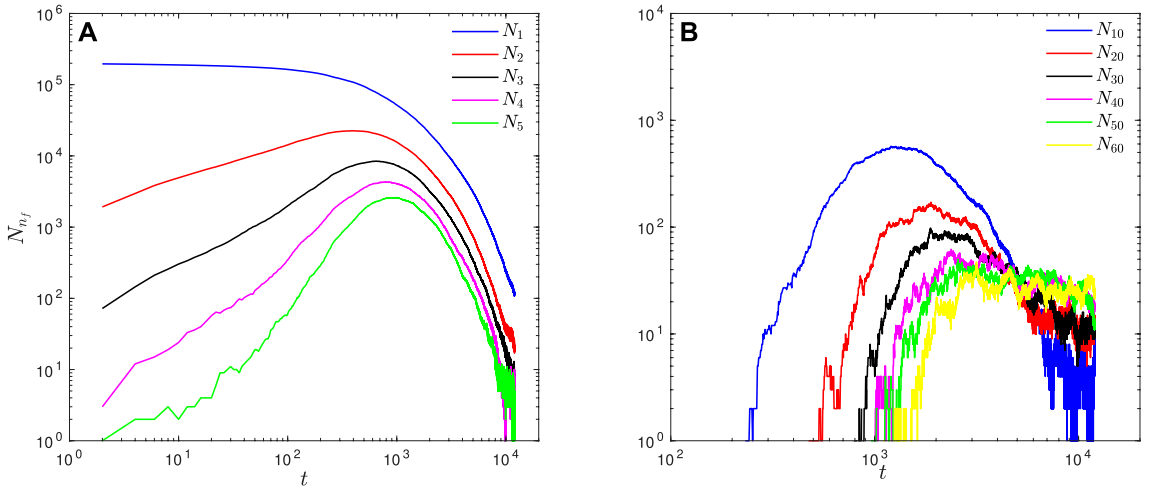

FIGURE 5 | Time evolution of floc population N_{n_f} for given floc size n_f from case P_2S_1. **(A)** Small flocs of size n_f = 1 to 5. **(B)** Large flocs of size n_f = 10, 20, 30, 40, 50, and 60 and 60.

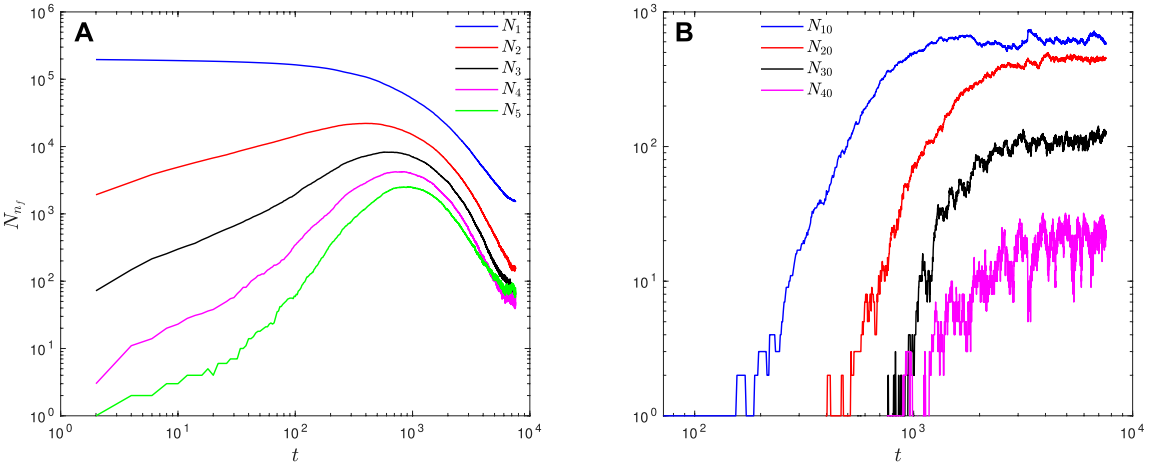

FIGURE 6 | Time evolution of floc population N_{n_f} for given floc size n_f from case P_2S_2. **(A)** Small flocs of size n_f = 1 to 5. **(B)** Large flocs of size n_f = 10, 20, 30, and 40.

3.3 Flocculation Dynamics: Breakup and Aggregation

To better understand how physicochemical properties of the primary particle (i.e, stickiness) affect the equilibrium floc size distribution, we examine the flocculation dynamics using the population balance equation as follows:

$$\frac{\partial n(v,\mathbf{x},t)}{\partial t} - \frac{\partial n(v,\mathbf{x},t)\left[u_i(\mathbf{x},t) - \delta_{i3}W_s\right]}{\partial x_i} - \frac{\partial}{\partial x_i}\left(\kappa\frac{\partial n(v,\mathbf{x},t)}{\partial x_i}\right) = \underbrace{\frac{1}{2}\int_0^v n(v-v',\mathbf{x},t)n(v',\mathbf{x},t)Q(v-v',\mathbf{x},v')dv'}_{\text{I: Construction by aggregation}} + \underbrace{\int_v^\infty \beta(v,v')\Gamma(v')n(v',\mathbf{x},t)dv'}_{\text{II: Construction by breakup}} - \underbrace{\int_0^\infty n(v,\mathbf{x},t)n(v',\mathbf{x},t)Q(v,v')dv'}_{\text{III: Destruction by aggregation}} - \underbrace{\Gamma(v)n(v,\mathbf{x},t)}_{\text{IV: Destruction by breakup}}, \quad (21)$$

where n (v, $\mathbf{x}$, t) is the number density of flocs with volume (or size) v at time t and location $\mathbf{x}$, W_s is the floc settling velocity, u_i is the fluid velocity component in the i-th direction, and κ is the sum of the molecular and turbulent diffusivity. On the right hand side of the equation, Q is the aggregation kernel and Γ is the breakup kernel. β is the fragmentation distribution, which describes the created number of daughter flocs of volume v after the breakage of a mother floc of volume v'. The aggregation kernel (Q) is a function of the collision frequency and collision efficiency. The collision frequency is a function of the turbulent shear rate and increases with the turbulent shear rate. The collision efficiency is defined as the rate of successful collisions resulting in the aggregation of flocs to the total number of collisions, which is a function of the properties of sediment particles.

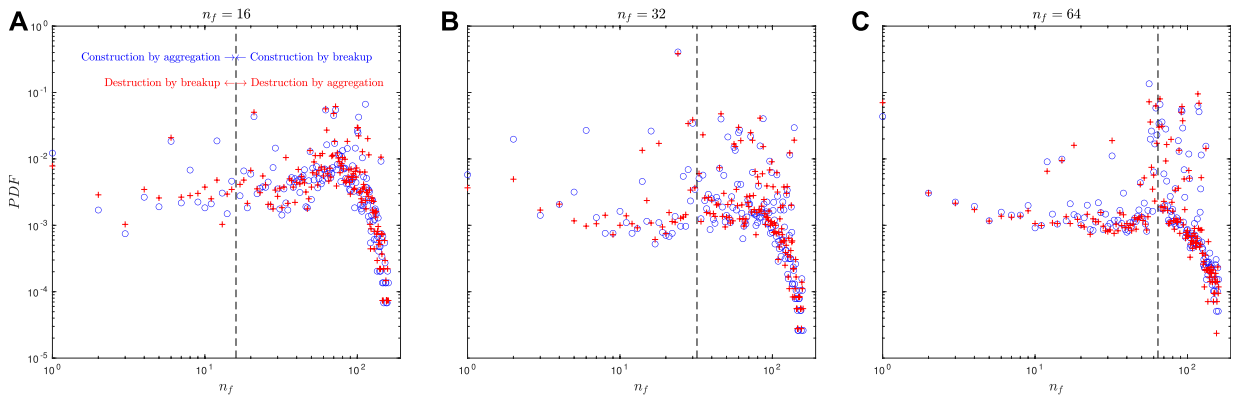

FIGURE 7 | Case P_2S_1 with the largest stickiness. **(A)** Probability density function (PDF) that a floc of size n_f becomes a floc of size $n_f = 16$ in a non-dimensional time period of 2 (blue circles) and the PDF that a floc of size $n_f = 16$ evolves into a floc of size n_f over the same period (red pluses). **(B,C)** Same as frame-(A) for $n_f = 32$ and 64.

The first term (term I) on the right hand side represents the formation of a floc of volume v by the aggregation of two smaller flocs of volume $v - v'$ and v'. The second term (term II) on the right hand side represents the formation of a floc of volume v from the breakup of a larger floc of volume v'. In both term I and term II, a new floc of volume v is generated, and hence they are the construction terms. The third term (term III) represents the aggregation of a floc of volume v with another floc of volume v' to form a larger floc of volume $v + v'$. The last term (term IV) represents the breakup of a floc of volume v. In both term III and term IV, a floc of volume v is consumed, and hence they are the destruction terms.

In **Eq. 21**, both aggregation and breakup processes in the population balance equation require parameterization, including the aggregation kernel, the breakup kernel, and the fragmentation distribution (Jeldres et al., 2015). By modeling the sediment phase as the dispersed phase using the Lagrangian framework, we can track the time-evolution of individual flocs of different size n_f (or volume $v = n_f V_p$, with V_p as the volume of the primary particle) to understand the aggregate and breakup processes at the particle scale. By comparing simulation results at two consecutive time instances, aggregation and breakup of flocs can be obtained in the time-driven Lagrangian model. Considering all the flocs of size $n_f = 16$, we investigate the state of each one of them at a time interval $\Delta t = 2$ before. Most of the flocs of size $n_f = 16$ have remained the same over this small time interval. Some flocs would have been of a smaller size (i.e., $n_f < 16$) at the previous time ($t - \Delta t$) and have grown to flocs of $n_f = 16$ due to aggregation, while some of the flocs would have been larger at the previous time and have reduced in size to $n_f = 16$ due to breakup. We refer to the previous time floc size at $t - \Delta t$ as the "prior-size". **Figure 7A** shows the probability density function (PDF) of the prior-size of flocs whose current size is $n_f = 16$. Most of the flocs of prior-size $n_f = 16$ that have remained the same without aggregation or breakup and are not included in the analysis. In **Figure 7A**, the blue circle symbols represent the source of $n_f = 16$ flocs. The circles to the left of the dash line correspond to the PDF of smaller flocs aggregating and becoming $n_f = 16$ floc, while circles to the right of the dash line correspond to the PDF of larger flocs breaking up and generating a daughter floc of size n_f=16. These are terms I and II on the right hand side of **(21)**.

In a similar manner, the red plus symbols represent the sink of $n_f = 16$ flocs, i.e., they measure the PDF of what a floc of size $n_f = 16$ floc becomes after a small time interval of $\Delta t = 2$. The pluses to the left of the dash line correspond to the PDF of smaller flocs that form from the breakup of $n_f = 16$ flocs, while pluses to the right of the dash line correspond to the PDF of larger flocs that are formed by the aggregation of a floc of size $n_f = 16$ with another floc (or other flocs). These are terms III and IV on the right hand side of **(Eq. 21)**. The collapse of the two curves (circle sources and plus sinks) suggests a dynamic equilibrium with the balance between the aggregation and breakup processes. The PDF is almost uniform for small flocs. A peak is evident at $n_f \approx 80$. A power–law distribution of the PDF can be observed for the large flocs with $n_f > 80$. For small flocs, we observe a drastic drop from the peak to $n_f \approx 30$, and the distribution is quite uniform for $n_f \leq 30$.

We carried out the same analysis for flocs of size $n_f = 32$ (**Figure 7B**), the power–law distribution is evident for large flocs of $n_f > 80$. A uniform distribution can be observed between $n_f = 32$ and 80. For smaller flocs of $n_f < 32$, the distribution shows a minimum around $n_f \approx 9$ and peaks around $n_f = 32$ and $n_f = 1$ (primary particles). For floc of size $n_f = 64$ (**Figure 7C**), the power–law distribution is still evident for large flocs of $n_f > 80$. In addition, a significant change of the slope for large flocs of size greater than $n_f = 150$ can be identified. For small flocs of $n_f < 64$, the distribution shows a uniform distribution between 20 and 60 and two peaks near $n_f = 64$ and $n_f = 1$ (primary particles). For case P_2S_2 with less sticky and more stiff primary particles, the terms are plotted for flocs of size $n_f = 8$, 16, and 24 (**Figure 8**). The PDFs for flocs of different size are quite similar. It shows a power–law relation for large flocs of $n_f \geq 16$. For smaller flocs of $n_f < 16$, the distribution exhibits a minimum at $n_f = 5$ and two peaks at $n_f = 16$ and $n_f = 1$ (primary particle). Compared to the case P_2S_1 with the stickies primary particles, the presence of the uniform distribution for intermediate-sized flocs (n_f between 30 and 50 in case P_2S_1) is not evident in case P_2S_2.

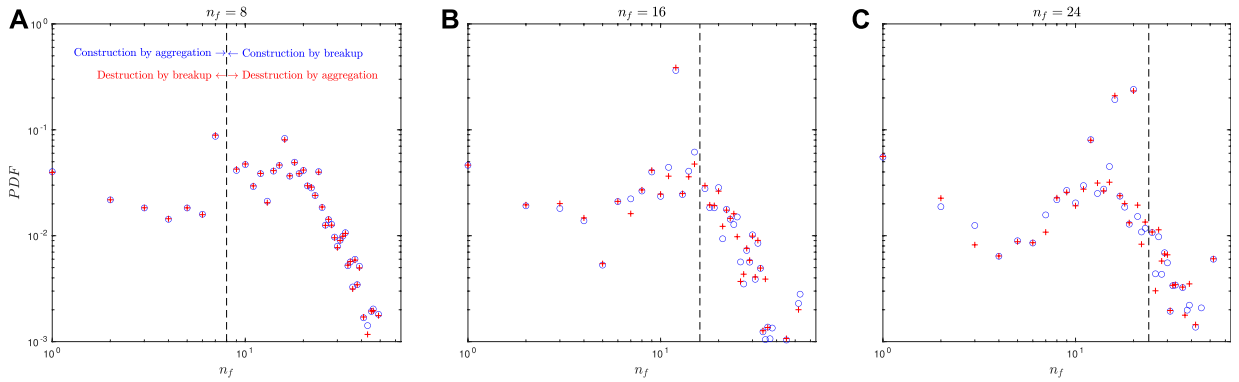

FIGURE 8 | Case P_2S_2 with smaller stickiness and larger stiffness. **(A)** Probability density function (PDF) that a floc of size n_f becomes a floc of size $n_f = 8$ in a non-dimensional time period of 2 (blue circles) and the PDF that a floc of size $n_f = 8$ evolves into a floc of size n_f over the same period (red pluses). **(B,C)** Same as frame-(A) for $n_f = 16$ and 24.

In both cases, at the equilibrium stage when the breakup and aggregation processes balance with each other, simulation results show that the construction by aggregation is primarily balanced by the destruction by breakup and the construction by breakup is primarily balanced by the destruction by aggregation. At the microscopic level, each aggregation or breakup pathway is reversible and hence in a dynamic equilibrium. With given aggregation and breakup kernels, equilibrium solutions of the floc size distribution exist (Vigil, 2009), and the mathematical form of the equilibrium floc size distribution could be derived.

3.4 Equilibrium Floc Size Distribution

An equilibrium floc size distribution develops when the aggregation process balances with the breakup process. The floc size distribution is modeled as a function of n_f, instead of the floc size D_f, because the number density (n) in **Equation (21)** is expressed as a function of the floc volume v. In this study, flocs are consisted of slightly overlapping identical spheres, and the volume of a floc consisted of n_f primary particles can be approximated by n_f as $v \approx n_f \pi D_p^3/6$. To calculate the floc volume using the actual floc size D_f requires *a priori* knowledge of the floc internal structure, which is difficult to obtain. Because of the asymmetry around the peak, we tested the floc size distribution against two widely used asymmetric distributions, namely, the lognormal distribution and the Weibull distribution. The lognormal probability distribution function is expressed as follows:

$$f\left(n_f;\mu,\sigma^2\right) = \frac{1}{n_f\sigma\sqrt{2\pi}}\exp\left(-\frac{\left(\ln n_f - \mu\right)^2}{2\sigma^2}\right), \qquad (22)$$

where $\ln n_f$ follows the normal distribution, μ is the mean, and σ^2 is the variance.

The Weibull distribution is a special form of Gamma distribution with two parameters, namely, the scaling parameter λ and the shape parameter k.

$$f\left(n_f;\lambda,k\right) = \frac{k}{\lambda}\left(\frac{n_f}{\lambda}\right)^{k-1}\exp\left(-\left(n_f/\lambda\right)^k\right) \qquad n_f \geq 0. \qquad (23)$$

The Weibull distribution interpolates between the exponential distribution and Rayleigh distribution. The shape parameter k affects the shape of the distribution rather than simply shifting or stretching it. **Figure 9** shows the curve fitting for case P_2S_1 (panel a), P_2S_2 (panel b), and P_2S_3 (panel c). For case P_2S_1 with the stickiest primary particles, model results fit better with the Weibull distribution, while results from case P_2S_2 with less sticky but more stiff primary particles fit better with the lognormal distribution. For case P_2S_3, neither lognormal nor Weibull distribution can fit the data for the entire range of the floc size n_f. To assess the performance of different distributions, the Anderson–Darling (AD) test (Anderson and Darling, 1952) was conducted, which is based on the empirical cumulative distribution obtained from the sample. The AD test is commonly used to test if a sample of data comes from a population with a specific distribution. We used the significant level of $\alpha = 0.01$, which is commonly used in statistical hypothesis test (Fisher, 1992). The results are summarized in **Table 2**, where E_s is the sum of squared residual errors. The accepted hypothesis for each case is shown with "*" in **Table 2**, which means the optimal descriptor for the floc size distribution. For the case with less sticky primary particles (case P_2S_2), the lognormal distribution fits better and for the cases with very sticky primary particles (case P_1S_2 and P_2S_1), the Weibull distribution fits better. The AD test rejects both lognormal and Weibull distribution hypothesis for most cases, suggesting neither lognormal nor Weibull distribution can accurately predict the floc size distribution. For instance, the lognormal distribution fits better for small flocs and also captures the peak more accurately in case P_2S_3 (**Figure 9C**), while the Weibull distribution fits better for large flocs ($n_f > 35$). The adjusted coefficient of determination (R^2_{adj}) was then used to evaluate the goodness of the fit (Ezekiel, 1930). However, the R^2_{adj} for both distributions are quite close, and hence it is difficult to distinguish the two distributions. Based on curve fitting results, the shape parameter k is around 2.5 for all cases, suggesting a similarity in the floc size distribution.

Floc size distribution from P_2S_1 fits better with the Weibull distribution. To further investigate the floc size distribution from case P_2S_1, we plotted model results under log-log scale

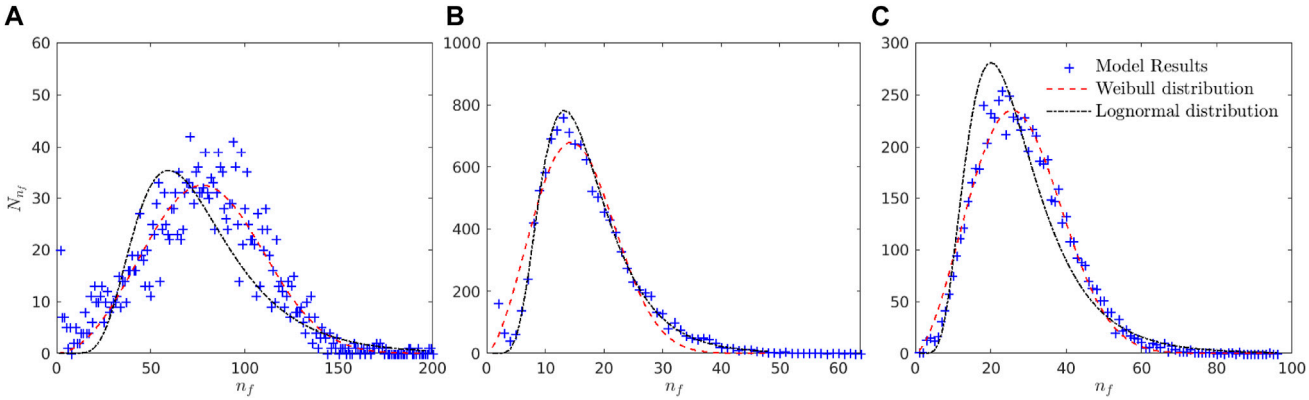

FIGURE 9 | Floc size distribution represented by N_{n_f}. **(A)** Case P_2S_1, **(B)** case P_2S_2, and **(C)** case P_2S_3.

TABLE 1 | Summary of parameters for all simulations, all parameters are normalized. $\bar{D}_f$ is the average floc size at the equilibrium state and *Ad* represents the adhesive number.

Case	N_{total}	ϕ	D_p	E	η_D	γ	$\bar{D}_f$	*Ad*
P_1S_1	50,000	4.09, ×, 10^{-4}	0.02	400.0	40.0	0.01	0.1044	4.09
P_1S_2	50,000	4.09, ×, 10^{-4}	0.02	400.0	40.0	0.025	0.1474	10.23
P_2S_1	200,000	4.29, ×, 10^{-4}	0.0128	160.0	20.0	0.008	0.0773	5.12
P_2S_2	200,000	4.29, ×, 10^{-4}	0.0128	400.0	40.0	0.005	0.0578	3.20
P_2S_3	200,000	4.29, ×, 10^{-4}	0.0128	200.0	20.0	0.005	0.0645	3.20
P_2S_4	200,000	4.29, ×, 10^{-4}	0.0128	160.0	20.0	0.006	0.0701	3.83

TABLE 2 | Anderson–Darling test results and the adjusted coefficient of determination R^2_{adj}.

Case	Range of n_f	Number of flocs *N*	Distribution	μ, λ	σ, k	E_s	R^2_{adj}
P_1S_1	[6,80]	6683	Lognormal	3.295	0.4438	7.45×10^{-4}	0.9228
			Weibull	33.40	2.537	8.20×10^{-4}	0.9150
P_1S_2	[6,180]	6035	Lognormal	4.259	0.5350	1.29×10^{-3}	0.5792
			Weibull*	89.92	2.4160	8.23×10^{-4}	0.7311
P_2S_1	[6,180]	4967	Lognormal	4.2884	0.4527	1.29×10^{-3}	0.6512
			Weibull*	87.87	2.8550	3.73×10^{-4}	0.8988
P_2S_2	[6,65]	11,389	Lognormal*	2.765	0.4158	1.49×10^{-4}	0.9943
			Weibull	19.56	2.442	2.14×10^{-3}	0.9182
P_2S_3	[6,80]	6924	Lognormal	3.267	0.4393	4.88×10^{-4}	0.9573
			Weibull	32.39	2.567	3.88×10^{-4}	0.9660
P_2S_4	[6,100]	5340	Lognormal	3.520	0.4622	4.33×10^{-4}	0.9445
			Weibull	42.14	2.464	4.62×10^{-4}	0.9408

(**Figure 10A**) and semi-log scale (**Figure 10B**). We averaged N_{n_f} from t = 11,000 to 12,000, when the equilibrium is achieved for large flocs. For flocs with size n_f between 30 and 75, a power–law relation can be identified when the aggregation and breakup processes balance. For large flocs with n_f greater than 110, we observe an exponential decay of N_{n_f} with n_f. For case P_2S_2 with lognormal distribution, we did not observe the power–law relation, and hence the results are not shown.

4 DISCUSSION

Different mathematical formulas of floc size distribution arise in the aggregation or breakage processes (Huber et al., 2006). Lognormal distribution has been observed in particle growth or coagulation processes (Smoluchowski, 1918; Friedlander and Wang, 1966), in which aggregation process dominates the dynamics. On the other hand, Weibull distribution has been commonly observed in the fragmentation process of large

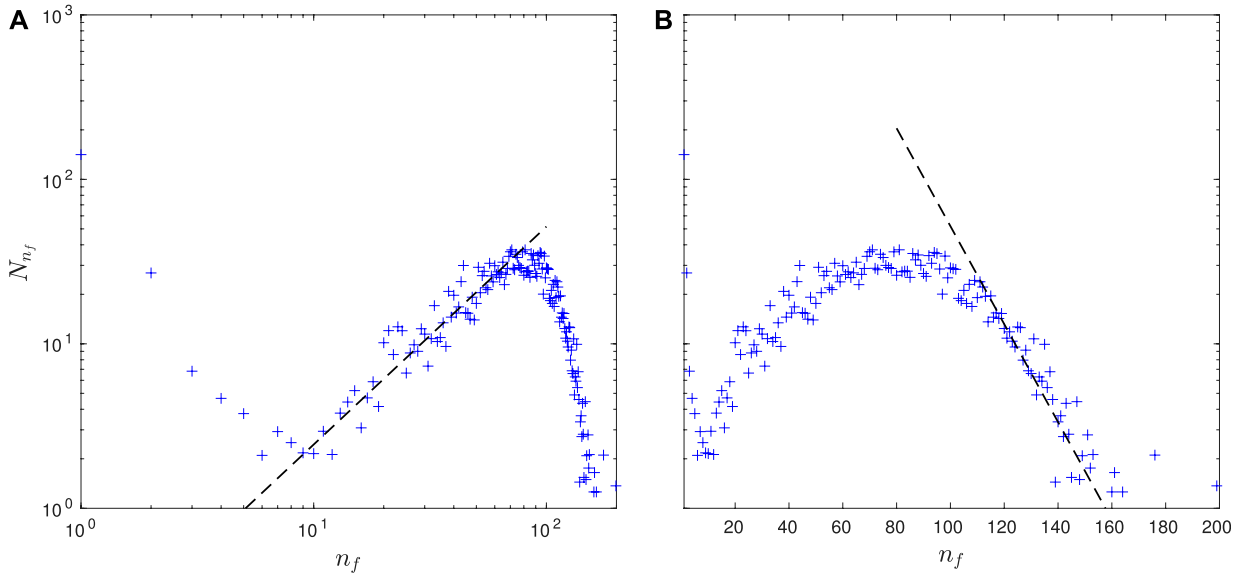

FIGURE 10 | Floc size distribution from case P_2S_1 **(A)** power-law fit and **(B)** exponential fit.

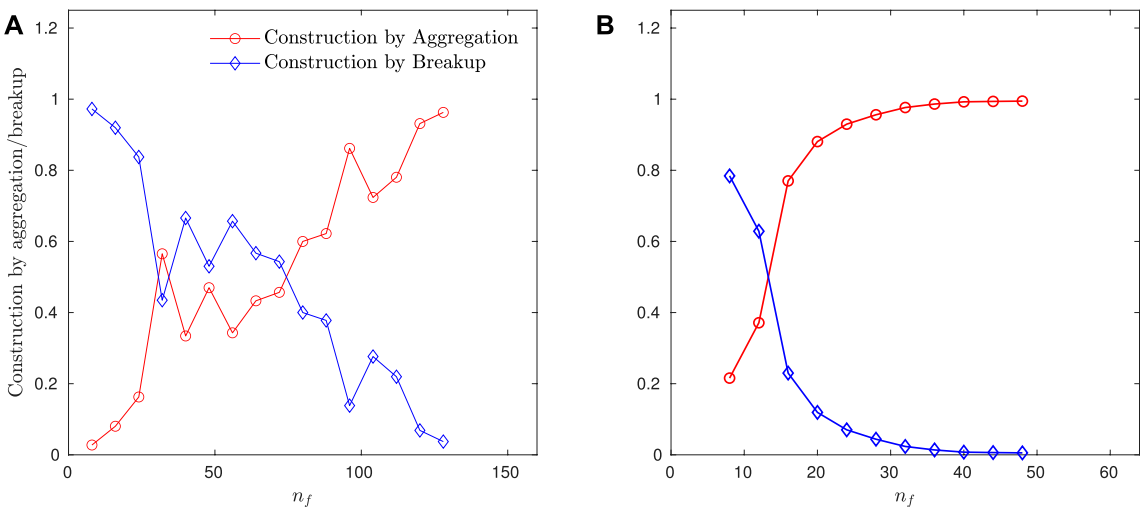

FIGURE 11 | Relative importance of the two construction mechanisms for flocs of size *n*. **(A)** Case P_2S_1 and **(B)** P_2S_2.

particles (Brown and Wohletz, 1995). In the flocculation process, both the aggregation and fragmentation processes play an important role. At the equilibrium state, a floc can be constructed either by aggregation of smaller flocs or breakup from larger flocs. To further understand under which circumstances a lognormal or Weibull distribution performs better, we analyzed the dominant floc construction mechanisms at the equilibrium stage. **Figure 11** shows the relative importance of construction by aggregation and construction by the breakup for flocs of size n_f from the two contrasting cases P_2S_1 and P_2S_2. In case P_2S_1 (**Figure 11A**), the majority of small flocs are constructed by breakup of larger flocs, while large flocs ($n_f > 75$) are mainly constructed by aggregation as expected. The aggregation and breakup processes play equally important roles for flocs in the range of $30<n_f<75$. The primary particles first aggregate into microflocs, the microflocs are quite resilient to turbulent shear and serve as the building blocks for larger flocs. For case P_2S_2 (**Figure 11B**), we observe a monotonic increase in relative importance for aggregation and a decrease for breakup process with respect to n_f. In general, a large portion of flocs ($n_f < 75$) in case P_2S_1 are generated mainly from breakup of larger flocs. However, in case P_2S_2, breakup only controls the formation of a small portion of flocs with $n_f < 15$, and the aggregation process dominates the formation of flocs for a

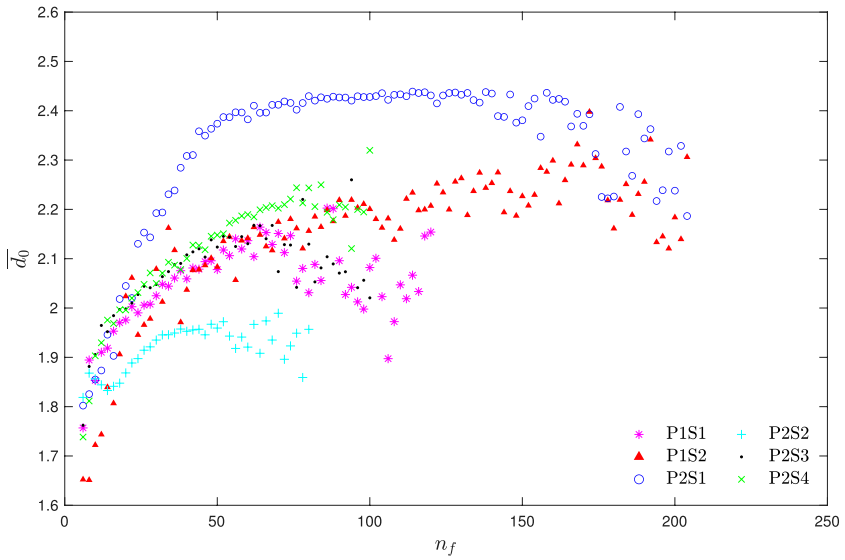

FIGURE 12 | Averaged fractal dimension ($\overline{d_0}$) as function of floc size n_f for different cases.

wide range of flocs. The lognormal distribution (case P_2S_2) develops when the large flocs grow gradually from primary particles without the intermediate stage (the formation of "microflocs"). This behavior has not been observed in laboratory experiments before, and future laboratory studies are required to test whether this is an artifact of the numerical model or an actual physical process.

Mathematical approach of floc modeling that has gained much interest by modelers is the fractal representation of flocs (Kranenburg, 1994; Merckelbach, 2000; Graham and Manning, 2007). Fractal theory is dependent on the successive aggregations of self-similar flocs, thereby producing a structure that is independent of the scale (or scale invariant). This is similar to the order-of-aggregation theory (Krone, 1963). Following the fractal theory, simple power laws can be used to describe floc properties such as floc density and settling velocity, as well as the aggregation and breakup processes (Winterwerp, 1998). Although some studies suggest that individually some natural muddy flocs (particularly those with high organic contents) may not be fully fractal in structure (Zhang et al., 2018; Spencer et al., 2021), the wider examination of *in situ* floc populations shows that a fractal representation of flocs still has many merits (Dyer and Manning, 1999; Winterwerp et al., 2006). The fractal dimension d_0 used to characterize the floc structure is defined as

$$n_f = \left(\frac{D_f}{D_p}\right)^{d_0}, \tag{24}$$

where n_f is the total number of the primary particles consisting the floc, D_f is the floc size and D_p is the primary particle diameter. The major axis length (longest axis) is used as floc size D_f, which is obtained by the principal component analysis (PCA). In general, the fractal dimension (d_0) is 1 for chain-like flocs and 2 for flat plane-like flocs. Flocs with fractal dimension close to 3 have compact structure and spherical shape.

Flocs with the same number of primary particles (n_f) can exhibit different structures, and the averaged fractal dimension ($\overline{d_0}$) for flocs with the same n_f is shown in **Figure 12**. For case P_2S_1, the fractal dimension first increases and reaches a constant value around 2.4 for flocs of size n_f between 50 and 120, suggesting compact and similar floc structures. Fractal dimension $\overline{d_0}$ decreases for large flocs of n_f > 120. The increase in $\overline{d_0}$ for small flocs is due to the limited configurations of floc structure by finite n_f. For instance, the most compact structure for a dimer (aggregate consisted of exact two spheres) is a rod with a fractal dimension of 1, and the most compact structure for a trimer (aggregate consisted of exact three spheres) is an equilateral triangle of fractal dimension of 1.7. The "microflocs" in the range of $30<n_f<75$ (**Figure 11A**) have relatively small fractal dimensions. The primary particles in case P_2S_1 are the stickiest and the turbulent shear stress is less efficient to break these 'microflocs' at the scale. The decrease of $\overline{d_0}$ for large flocs suggests that they are more porous. Similar trends can be observed for cases P_1S_2, in which Weibull distribution better describes the flocs size distribution.

In contrast, in case P_2S_2 with the least sticky primary particles, the fractal dimension increases to the peak value around 1.95 and then drops for large flocs. The decrease in the fractal dimension for large flocs has also been observed by Khelifa and Hill (2006) and Maggi (2007). Our numerical results suggest the scale-dependence of floc structure as the fractal dimension is not constant for the entire range of the floc size. A variable fractal dimension should be considered to characterize the flocs.

In general, for the cases with the same primary particle diameter, primary particles with small adhesive numbers (or surface energy density) lead to flocs with smaller fractal

dimensions, and primary particles with large adhesive numbers generate more compact flocs with fractal dimension as large as 2.4 in case P_2S_1. Floc compaction by the breakage-regrowth and restructuring mechanisms are more pronounced in the case with the stickiest primary particle. By comparing case P_2S_2 and P_2S_3, the stiffness of the particle also affects the floc structures. Primary particles with larger Young's modulus (case P_2S_2) lead to flocs with smaller fractal dimension.

5 CONCLUSION

A two-phase Eulerian–Lagrangian framework was implemented to investigate the equilibrium floc size distribution of cohesive sediment in homogeneous isotropic turbulence. The primary particles are modeled as identical sticky soft spheres, and particle–particle interactions are modeled by the discrete element method. The adhesive contact JKR model was implemented to model cohesive sediment particles, which is a tensile force model with hysteretic effect. In the adhesive contact model, the pull-off force to break two particles apart scales with both the particle size and the surface energy density (i.e., the physicochemical properties of the primary particle).

A series of numerical simulations were conducted by varying the size and properties of the primary particles. At the equilibrium state, the construction by breakup is balanced with the destruction by aggregation, and the construction by aggregation is balanced with the destruction by breakup. The equilibrium floc size distribution depends on primary particle properties, including the stiffness and the surface energy density. For cases with more sticky primary particles, the floc size distribution can be better described by the Weibull distribution with a shape parameter around 2.5. In addition, at the intermediate stage, a staircase structure develops in the floc size distribution. The primary particles first form the 'microflocs', which serve as the building blocks for large flocs. For the case with less sticky primary particles, the lognormal distribution performs better. Flocs grow gradually from primary particles without the intermediate stage of 'microflocs'.

By analyzing the construction mechanisms of flocs of different size, when the Weibull distribution develops, construction by breakup and construction by aggregation are of equal importance for the intermediate-sized flocs. The fractal dimension of large flocs then decreases with floc size, suggesting large "macroflocs" are more porous and fragile. For less sticky particles, the lognormal distribution develops, and the aggregation dominates the floc construction for a wide range of flocs. The fractal dimension of flocs first increases with floc size, reaches the peak value, and then decreases with the floc size. However, given the similarity between the lognormal and Weibull distributions and hence the difficulties in distinguishing between them in confidence, it is recommended to choose the floc size distribution and make interpretations in practice with caution.

Due to the limited computational resources, the current simulation focuses on the high-energy environments with large turbulent shear rate (350 s^{-1} in this study). Simulations with more particles (several millions to billions of particles) are therefore required for more realistic cohesive sediment transport studies in low-to moderate-energy environments. In addition, current model framework oversimplifies the hydrodynamic interactions among particles without the influence from neighboring particles. For cohesive sediment, the particle Reynolds number based on Stokes settling velocity is small, and hence the sheltering and blockage effects from neighboring particles could play an important role. The sheltering effects from neighboring particles lead to reduced hydrodynamic drag, and hence could affect the breakup processes. A more sophisticated efficient model that can accurately predict hydrodynamic interactions among a large amount of particles is required and will be the future work.

DATA AVAILABILITY STATEMENT

The datasets presented in this study can be found in online repositories. The names of the repository/repositories and accession number(s) can be found at: https://figshare.com/articles/dataset/FlocSizeDistribution/16619734.

AUTHOR CONTRIBUTIONS

MY: methodology; formal analysis; and writing—original draft, review, and editing. XY: supervision; conceptualization; methodology; formal analysis; writing—original draft, review, and editing. SB: conceptualization; methodology, and writing—review and editing. AM: writing–review and editing.

FUNDING

This work is funded by the United States Army Engineering Research and Development Center under the Cooperative Ecosystem Studies Unit (CESU) grant W912HZ-21-2-0035. AM's contribution toward this research was also partly supported by the United States National Science Foundation under grants OCE-1736668 and OCE-1924532, TKI-MUSA project 11204950-000-ZKS-0002, and HR Wallingford company research FineScale project (ACK3013-62).

ACKNOWLEDGMENTS

All simulations were carried out on the HiperGator super computer at the University of Florida. Computer resources, technical expertise, and assistance provided by the HiperGator are gratefully acknowledged. The CFD model nek5000 is developed primarily by the Argonne National Laboratory at https://nek5000.mcs.anl.gov/, and the DEM model LAMMPS is developed by Sandia National Laboratories at https://lammps.sandia.gov/.

REFERENCES

Akiki, G., Moore, W. C., and Balachandar, S. (2017). Pairwise-interaction Extended Point-Particle Model for Particle-Laden Flows. *J. Comput. Phys.* 351, 329–357. doi:10.1016/j.jcp.2017.07.056

Anderson, T. W., and Darling, D. A. (1952). Asymptotic Theory of Certain "Goodness of Fit" Criteria Based on Stochastic Processes. *Ann. Math. Stat.* 23, 193–212. doi:10.1214/aoms/1177729437

Balachandar, S., and Eaton, J. K. (2010). Turbulent Dispersed Multiphase Flow. *Annu. Rev. Fluid Mech.* 42, 111–133. doi:10.1146/annurev.fluid.010908.165243

Baugh, J. V., and Manning, A. J. (2007). An Assessment of a New Settling Velocity Parameterisation for Cohesive Sediment Transport Modeling. *Cont. Shelf Res.* 27 (13), 1835–1855. doi:10.1016/j.csr.2007.03.003

Brown, W. K., and Wohletz, K. H. (1995). Derivation of the Weibull Distribution Based on Physical Principles and its Connection to the Rosin-Rammler and Lognormal Distributions. *J. Appl. Phys.* 78 (4), 2758–2763. doi:10.1063/1.360073

Byun, J., and Son, M. (2020). On the Relationship between Turbulent Motion and Bimodal Size Distribution of Suspended Flocs. *Estuar. Coast. Shelf Sci.* 245, 106938. doi:10.1016/j.ecss.2020.106938

Dyer, K. R., and Manning, A. J. (1999). Observation of the Size, Settling Velocity and Effective Density of Flocs, and Their Fractal Dimensions. *J. Sea Res.* 41 (1-2), 87–95. doi:10.1016/s1385-1101(98)00036-7

Dyer, K. R. (1989). Sediment Processes in Estuaries: Future Research Requirements. *J. Geophys. Res.* 94 (C10), 14327–14339. doi:10.1029/jc094ic10p14327

Edmonds, D. A., and Slingerland, R. L. (2010). Significant Effect of Sediment Cohesion on Delta Morphology. *Nat. Geosci.* 3, 105–109. doi:10.1038/ngeo730

Eisma, D. (1986). Flocculation and De-flocculation of Suspended Matter in Estuaries. *Neth. J. Sea Res.* 20 (2-3), 183–199. doi:10.1016/0077-7579(86)90041-4

Ezekiel, M. (1930). *Methods of Correlation Analysis*. Oxford, England: Wiley.

Fang, Z., Patterson, B. R., and Turner, M. E., Jr (1993). Modeling Particle Size Distributions by the Weibull Distribution Function. *Mater. Charact.* 31 (3), 177–182. doi:10.1016/1044-5803(93)90058-4

Fischer, P. F. (1997). An Overlapping Schwarz Method for Spectral Element Solution of the Incompressible Navier-Stokes Equations. *J. Comput. Phys.* 133 (1), 84–101. doi:10.1006/jcph.1997.5651

Fischer, P. F., Lottes, J. W., and Kerkemeier, S. G. (2008). Nek5000. Available at: http://nek5000.mcs.anl.gov.

Fisher, R. A. (1992). "Statistical Methods for Research Workers," in *Breakthroughs in Statistics* (New York, NY: Springer), 66–70. doi:10.1007/978-1-4612-4380-9_6

Friedlander, S. K., and Wang, C. S. (1966). The Self-Preserving Particle Size Distribution for Coagulation by Brownian Motion. *J. Colloid interface Sci.* 22 (2), 126–132. doi:10.1016/0021-9797(66)90073-7

Geyer, W. R., Hill, P., Milligan, T., and Traykovski, P. (2000). The Structure of the Eel River Plume during Floods. *Cont. Shelf Res.* 20 (16), 2067–2093. doi:10.1016/s0278-4343(00)00063-7

Graham, G. W., and Manning, A. J. (2007). Floc Size and Settling Velocity within a Spartina Anglica Canopy. *Cont. Shelf Res.* 27 (8), 1060–1079. doi:10.1016/j.csr.2005.11.017

Hayter, E. J., and Mehta, A. J. (1986). Modelling Cohesive Sediment Transport in Estuarial Waters. *Appl. Math. Model.* 10 (4), 294–303. doi:10.1016/0307-904x(86)90061-2

Hill, P. S. (1996). Sectional and Discrete Representations of Floc Breakage in Agitated Suspensions. *Deep Sea Res. Part I Oceanogr. Res. Pap.* 43 (5), 679–702. doi:10.1016/0967-0637(96)00030-1

Hosoda, K., Matsuura, T., Suzuki, H., and Yomo, T. (2011). Origin of Lognormal-like Distributions with a Common Width in a Growth and Division Process. *Phys. Rev. E Stat. Nonlin Soft Matter Phys.* 83, 031118. doi:10.1103/PhysRevE.83.031118

Huber, P., Roux, E., Mauret, J. C., and Carre, B. (2006). Characterising the Floc Size Distribution of Flowing Pulp Suspensions: from Fibre Flocculation to Sheet Formation. *Appita Technol. Innov. Manuf. Environ.* 59, 37. doi:10.3316/informit.586267214881170

Hunt, J. R. (1982). Self-similar Particle-Size Distributions during Coagulation: Theory and Experimental Verification. *J. Fluid Mech.* 122, 169–185. doi:10.1017/s0022112082002158

Jeldres, R. I., Concha, F., and Toledo, P. G. (2015). Population Balance Modelling of Particle Flocculation with Attention to Aggregate Restructuring and Permeability. *Adv. colloid interface Sci.* 224, 62–71. doi:10.1016/j.cis.2015.07.009

Johnson, K. L. (1985). *Contact Mechanics*. Cambridge University Press.

Khelifa, Ali, and Hill, Paul S. (2006). Models for Effective Density and Settling Velocity of Flocs. *J. Hydraulic Res.* 44 (3), 390–401. doi:10.1080/00221686.2006.9521690

Kiss, L. B., Söderlund, J., Niklasson, G. A., and Granqvist, C. G. (1999). New Approach to the Origin of Lognormal Size Distributions of Nanoparticles. *Nanotechnology* 10 (1), 25–28. doi:10.1088/0957-4484/10/1/006

Kolmogorov, A. N. (1941b). Dissipation of Energy in Locally Iscotropic Turbulence. *Proc. USSR Acad. Sci.* 32, 16.

Kolmogorov, A. N. (1941a). The Local Structure of Turbulence in Incompressible Viscous Fluid for Very Large Reynolds Numbers. *Proc. USSR Acad. Sci.* 30, 301.

Kondolf, G. M., and Adhikari, A. (2000). Weibull vs. Lognormal Distributions for Fluvial Gravels. *J. Sediment. Res.* 70 (3), 456–460. doi:10.1306/2dc4091e-0e47-11d7-8643000102c1865d

Kranenburg, C. (1994). The Fractal Structure of Cohesive Sediment Aggregates. *Estuar. Coast. Shelf Sci.* 39 (5), 451–460. doi:10.1006/ecss.1994.1075

Krone, R. B. (1963). *A Study of Rheological Properties of Estuarial Sediments*. Report No. 63-68. Berkeley: Hydraulic Engineering Laboratory and Sanitary Engineering Research Laboratory, University of California.

Li, D., and Ganczarczyk, J. (1991). Size Distribution of Activated Sludge Flocs. *Res. J. water Pollut. control Fed.* 63 (5), 806–814

Luding, S. (2008). Cohesive, Frictional Powders: Contact Models for Tension. *Granul. matter* 10 (4), 235–246. doi:10.1007/s10035-008-0099-x

Lundgren, T. S. (2003). *Linearly Forces Isotropic Turbulence*. Minnesota Univ Minneapolis. Ph.D. thesis.

Maday, Y., Patera, A. T., and Rnquist, E. M. (1990). An Operator-Integration-Factor Splitting Method for Time-dependent Problems: Application to Incompressible Fluid Flow. *J. Sci. Comput.* 5, 263–292. doi:10.1007/bf01063118

Maggi, F. (2007). Variable Fractal Dimension: A Major Control for Floc Structure and Flocculation Kinematics of Suspended Cohesive Sediment. *J. Geophys. Res. Oceans* 112 (C7), 3951. doi:10.1029/2006jc003951

Manning, A. J. (2001). *A Study of the Effects of Turbulence on the Properties of Flocculated Mud*. Ph.D. Thesis. Institute of Marine Studies, University of Plymouth.

Manning, A. J., Bass, S. J., and Dyer, K. R. (2006). Floc Properties in the Turbidity Maximum of a Mesotidal Estuary during Neap and Spring Tidal Conditions. *Mar. Geol.* 235 (1-2), 193–211. doi:10.1016/j.margeo.2006.10.014

Manning, A. J., and Dyer, K. R. (1999). A Laboratory Examination of Floc Characteristics with Regard to Turbulent Shearing. *Mar. Geol.* 160 (1-2), 147–170. doi:10.1016/s0025-3227(99)00013-4

Manning, A. J., and Schoellhamer, D. H. (2013). Factors Controlling Floc Settling Velocity along a Longitudinal Estuarine Transect. *Mar. Geol.* 345, 266–280. doi:10.1016/j.margeo.2013.06.018

Manning, A. J. (2004). The Observed Effects of Turbulence on Estuarine Flocculation. *J. Coast. Res.* 41, 90–104

Marshall, J. S. (2009). Discrete-element Modeling of Particulate Aerosol Flows. *J. Comput. Phys.* 228 (5), 1541–1561. doi:10.1016/j.jcp.2008.10.035

McAnally, W. H., and Mehta, A. J. (2001). Collisional Aggregation of Fine Estuarine Sediments. *Coast. Estuar. Fine Sediment Process. - Proc. Mar. Sci.* 3, 19

Mehta, A. J., and Lott, J. W. (1987). Sorting of Fine Sediment during Deposition. *Proc. Conf. Adv. Underst. Coast. Sediment Process.* 1, 348

Mehta, A. J., Manning, A. J., and Khare, Y. P. (2014). A Note on the Krone Deposition Equation and Significance of Floc Aggregation. *Mar. Geol.* 354, 34–39. doi:10.1016/j.margeo.2014.04.002

Merckelbach, L. (2000). *Consolidation and Strength Evolution of Soft Mud Layers*.

Mindlin, R. D. (1949). Compliance of Elastic Bodies in Contact. *J. Appl. Mech. ASME* 16 (3), 259–268. doi:10.1115/1.4009973

Mouri, H., Hori, A., and Takaoka, M. (2009). Large-scale Lognormal Fluctuations in Turbulence Velocity Fields. *Phys. fluids* 21, 7936. doi:10.1063/1.3147936

Plimpton, S. (1995). Fast Parallel Algorithms for Short-Range Molecular Dynamics. *J. Comput. Phys.* 117 (1), 1–19. doi:10.1006/jcph.1995.1039

Prandle, D., Lane, A., and Manning, A. J. (2005). Estuaries Are Not So Unique. *Geophys. Res. Lett.* 32 (23), 24797. doi:10.1029/2005gl024797

Pushkin, D. O., and Aref, H. (2002). Self-similarity Theory of Stationary Coagulation. *Phys. fluids* 14, 694–703. doi:10.1063/1.1430440

Rosales, C., and Meneveau, C. (2005). Linear Forcing in Numerical Simulations of Isotropic Turbulence: Physical Space Implementations and Convergence Properties. *Phys. fluids* 17 (9), 095106. doi:10.1063/1.2047568

Saha, D., Babler, M. U., Holzner, M., Soos, M., Lüthi, B., Liberzon, A., et al. (2016). Breakup of Finite-Size Colloidal Aggregates in Turbulent Flow Investigated by Three-Dimensional (3d) Particle Tracking Velocimetry. *Langmuir* 32 (1), 55–65. doi:10.1021/acs.langmuir.5b03804

Sheremet, A., Sahin, C., and Manning, A. J. (2017). Flocculation: A General Aggregation-Fragmentation Framework. *Int. Conf. Coast. Eng.* 35, 27. doi:10.9753/icce.v35.sediment.27

Smoluchowski, M. v. (1918). Versuch einer mathematischen Theorie der Koagulationskinetik kolloider Lösungen. *Z. für Phys. Chem.* 92U (1), 129–168. doi:10.1515/zpch-1918-9209

Soulsby, R. L., Manning, A. J., Spearman, J., and Whitehouse, R. J. S. (2013). Settling Velocity and Mass Settling Flux of Flocculated Estuarine Sediments. *Mar. Geol.* 339, 1–12. doi:10.1016/j.margeo.2013.04.006

Spencer, K. L., Wheatland, J. A. T., Bushby, A. J., Carr, S. J., Droppo, I. G., and Manning, A. J. (2021). A Structure-Function Based Approach to Floc Hierarchy and Evidence for the Non-fractal Nature of Natural Sediment Flocs. *Sci. Rep.* 11, 14012. doi:10.1038/s41598-021-93302-9

Spicer, P. T., and Pratsinis, S. E. (1996). Coagulation and Fragmentation: Universal Steady-State Particle-Size Distribution. *AIChE J.* 42 (6), 1612–1620. doi:10.1002/aic.690420612

Sun, R., Xiao, H., and Sun, H. (2018). Investigating the Settling Dynamics of Cohesive Silt Particles with Particle-Resolving Simulations. *Adv. Water Resour.* 111, 406–422. doi:10.1016/j.advwatres.2017.11.012

Sundaram, S., and Collins, L. R. (1997). Collision Statistics in an Isotropic Particle-Laden Turbulent Suspension. Part 1. Direct Numerical Simulations. *J. Fluid Mech.* 335, 75–109. doi:10.1017/s0022112096004454

Tambo, N., and Watanabe, Y. (1984). Physical Aspect of Flocculation Process-III. *Water Res.* 18 (4), 695–707. doi:10.1016/0043-1354(84)90165-9

Tolhurst, T. J., Gust, G., and Paterson, D. M. (2002). The Influence of an Extracellular Polymeric Substance (EPS) on Cohesive Sediment Stability. *Proc. Mar. Sci.* 5, 409–425. doi:10.1016/s1568-2692(02)80030-4

Tsuji, Y., Kawaguchi, T., and Tanaka, T. (1993). Discrete Particle Simulation of Two-Dimensional Fluidized Bed. *Powder Technol.* 77 (1), 79–87. doi:10.1016/0032-5910(93)85010-7

van Leussen, W. (1994). *Estuarine Macroflocs and Their Role in Fine-Grained Sediment Transport*. Ph.D. Thesis. The Netherlands: University of Utrecht.

van Leussen, W. (1997). "The Kolmogorov Microscale as a Limiting Value for the Floc Sizes of Suspended Fine-Grained Sediments in Estuaries," in *Cohesive Sediments* (New York: Wiley), 45–62

van Olphen, H. (1964). An Introduction to Clay Colloid Chemistry. *Soil Sci.* 97 (4), 290.

Vigil, R. D. (2009). On Equilibrium Solutions of Aggregation-Fragmentation Problems. *J. colloid interface Sci.* 336 (2), 642–647. doi:10.1016/j.jcis.2009.04.061

Vowinckel, B., Withers, J., Luzzatto-Fegiz, P., and Meiburg, E. (2019). Settling of Cohesive Sediment: Particle-Resolved Simulations. *J. Fluid Mech.* 858, 5–44. doi:10.1017/jfm.2018.757

Wang, Y., Alonso-Marroquin, F., and Guo, W. W. (2015). Rolling and Sliding in 3-D Discrete Element Models. *Particuology* 23, 49–55. doi:10.1016/j.partic.2015.01.006

Wen, C. Y. (1966). Mechanics of Fluidization. *Chem. Eng. Prog. Symp. Ser.* 62, 100

Winterwerp, J. C. (1998). A Simple Model for Turbulence Induced Flocculation of Cohesive Sediment. *J. Hydraulic Res.* 36 (3), 309–326. doi:10.1080/00221689809498621

Winterwerp, J. C., Manning, A. J., Martens, C., de Mulder, T., and Vanlede, J. (2006). A Heuristic Formula for Turbulence-Induced Flocculation of Cohesive Sediment. *Estuar. Coast. Shelf Sci.* 68 (1-2), 195–207. doi:10.1016/j.ecss.2006.02.003

Winterwerp, J. C., Uittenbogaard, R. E., and De Kok, J. M. (2000). Rapid Siltation from Saturated Mud Suspensions. *Proc. Mar. Sci.* 3, 125–146. doi:10.1016/s1568-2692(00)80117-5

Winterwerp, J. C., and van Kesteren, W. G. M. (2004). Introduction to the Physics of Cohesive Sediment in the Marine Environment, Amsterdam, Netherlands: Elsevier.

Ye, L., Manning, A. J., and Hsu, T.-J. (2020). Oil-mineral Flocculation and Settling Velocity in Saline Water. *Water Res.* 173, 115569. doi:10.1016/j.watres.2020.115569

Yeung, P. K., Pope, S. B., Lamorgese, A. G., and Donzis, D. A. (2006). Acceleration and Dissipation Statistics of Numerically Simulated Isotropic Turbulence. *Phys. Fluids* 18, 065103. doi:10.1063/1.2204053

Zhang, N., Thompson, C. E. L., Townend, I. H., Rankin, K. E., Paterson, D. M., and Manning, A. J. (2018). Nondestructive 3D Imaging and Quantification of Hydrated Biofilm-Sediment Aggregates Using X-Ray Microcomputed Tomography. *Environ. Sci. Technol.* 52 (22), 13306–13313. doi:10.1021/acs.est.8b03997

Zhou, Z. Y., Kuang, S. B., Chu, K. W., and Yu, A. B. (2010). Discrete Particle Simulation of Particle-Fluid Flow: Model Formulations and Their Applicability. *J. Fluid Mech.* 661, 482–510. doi:10.1017/s002211201000306x

Zwick, D., and Balachandar, S. (2020). A Scalable Euler-Lagrange Approach for Multiphase Flow Simulation on Spectral Elements. *Int. J. High Perform. Comput. Appl.* 34 (3), 316–339. doi:10.1177/1094342019867756

Conflict of Interest: Author AM was employed by the company HR Wallingford.

The remaining authors declare that the research was conducted in the absence of any commercial or financial relationships that could be construed as a potential conflict of interest.

Publisher's Note: All claims expressed in this article are solely those of the authors and do not necessarily represent those of their affiliated organizations, or those of the publisher, the editors, and the reviewers. Any product that may be evaluated in this article, or claim that may be made by its manufacturer, is not guaranteed or endorsed by the publisher.

frontiers | Frontiers in Earth Science

ORIGINAL RESEARCH
published: 09 August 2022
doi: 10.3389/feart.2022.916056

Spatial and Temporal Variability of Bed Exchange Characteristics of Fine Sediments From the Weser Estuary

J. Patzke[1]*, *E. Nehlsen*[1], *P. Fröhle*[1] and *R. F. Hesse*[2]

[1]Institute for River and Coastal Engineering (IWB), Hamburg University of Technology, Hamburg, Germany, [2]Federal Waterways and Engineering Institute (BAW), Hamburg, Germany

Sedimentation of fine-grained sediments in estuaries is a natural physical phenomenon influenced by biogeochemical processes. In the estuarine turbidity maximum (ETM), enhanced net deposition of sediments is observed even in areas with higher hydrodynamic exposure, such as the navigational channel. Maintenance dredging is a common method to maintain the navigational channel, which requires large financial effort and has potential negative impacts on the environment. Research at the Institute for River and Coastal Engineering addresses the challenge of understanding the processes leading to net sedimentation and accumulation in estuarine navigational channels in reach of the ETM. In this contribution, investigations of bed exchange properties of estuarine cohesive sediments conducted in field and laboratory studies are presented. The results provide rarely available and estuary-specific parameters characterizing sediment transport, mainly related to erosion processes. By performing field campaigns within the ETM of the Weser estuary, cores of freshly deposited sediments have been sampled from two sites (Blexer Bogen and Nordenham) along the center of the navigational channel. Sediment characteristics (grain size distribution, water content, loss on ignition, density profiles) have been derived, and the erodibility of the deposits is investigated both quasi *in situ* and in the laboratory using an erosion microcosm system. Erodibility experiments are run in a closed system so sediment concentration above the lutocline increases during the experiment. This is a unique feature of this study, and it is expected to produce more natural characteristics of net erosion. By proving the reproducibility of the natural structure of the deposited sediments (stratification and density profiles) in the laboratory, systematic studies for analyzing the sensitivity of determined parameters (shear stresses and erosion rates) to varying environmental conditions (settling conditions and density) could be performed. Temporal development of suspended sediment concentration and erosion rates is the main result of the erodibility experiments, from which we derive bandwidths for erosion parameters, like floc erosion rate, critical shear for floc erosion, and critical shear for mass erosion.

Keywords: cohesive sediment, erodibility characteristics, field and laboratory experiments, microcosm, Weser estuary

OPEN ACCESS

Edited by:
Andrew James Manning,
HR Wallingford, United Kingdom

Reviewed by:
Ruei-Feng Shiu,
National Taiwan Ocean University, Taiwan
Anabela Oliveira,
Instituto Hidrográfico, Portugal
Fangfang Zhu,
The University of Nottingham Ningbo (China), China

***Correspondence:**
J. Patzke
Justus.Patzke@tuhh.de

Specialty section:
This article was submitted to Marine Geoscience, a section of the journal Frontiers in Earth Science

Received: *08 April 2022*
Accepted: *01 June 2022*
Published: *09 August 2022*

Citation:
Patzke J, Nehlsen E, Fröhle P and Hesse RF (2022) Spatial and Temporal Variability of Bed Exchange Characteristics of Fine Sediments From the Weser Estuary. Front. Earth Sci. 10:916056. doi: 10.3389/feart.2022.916056

1 INTRODUCTION

Fine sediment transport plays a significant role in the marine environment, making a detailed understanding and capable modeling approaches of transport processes crucial for the strategic maintenance of estuaries. While the transport of non-cohesive sediment is understood reasonably well, the depiction and prediction of cohesive sediment transport are still a challenge because of their complex composition of inorganic minerals and organic material (Grabowski et al., 2011). Particle mixtures are referred to as cohesive sediments when they exhibit intrinsic cohesion (Winterwerp et al., 2021), which is the case when a mixture of fine sediments (fine sand, silt, and clay) exceeds a critical threshold for clay minerals, often reported to be 10% (van Rijn, 1993; Grabowski et al., 2011). Because almost all processes defining the properties of cohesive sediments vary with time and location, derived parameters for process description are sediment- and estuary-specific. When cohesion is dominant, particles are interconnected, forming flocs and aggregates, resulting in transport dynamics that are significantly different from non-cohesive sediment transport. Affected by tidal asymmetry, stratification, and estuarine circulation, suspended cohesive sediments tend to retain and accumulate in estuaries, resulting in a zone of relatively high concentration of suspended sediments, the estuarine turbidity maximum (ETM). The ETM accounts for the main sediment deposition in many systems, while the location and extent of the ETM are predominantly affected by river discharge and the tidal cycle (Grabemann, 1992). Anthropogenic impacts, e.g., the deepening of waterways to enhance navigability, have the potential to cause intensified sedimentation and deposition because tidal asymmetry may increase. Even in the deeper navigational channel, where high flow velocities may support sediment transport and erosion, partly intensive net sedimentation and accumulation can be observed with a resulting formation of temporary deposits of high concentrated mud suspensions (HCMS). Depending on the conditions, HCMS can occur either in a stationary or mobile state, the extent of which varies greatly in space and time. Maintenance dredging is a common method of preserving the essential water depths for navigability but requires high financial effort and has potential negative impacts on the environment. Against this background, research at the Institute for River and Coastal Engineering (IWB) of the Hamburg University of Technology (TUHH) is carried out to improve the understanding of bed exchange processes in the ETM exemplary for the Weser estuary.

In this study, natural sediments gathered from the navigational channel of the Weser estuary within the ETM are investigated. Determining the characteristics of erodibility is one major aspect of experiments undertaken. Sediments are investigated in two different states. First, mostly undisturbed samples containing natural sediments are characterized in field trips. Second, sediment characteristics are investigated by generating representative samples consisting of nature-like density profiles, salinity, and composition. Being the second-largest German estuary, the Weser discharges into the North Sea, like the other two major German estuaries of Elbe and Ems. All of the mentioned estuaries are facing similar challenges in fine sediment transport. The Weser is divided into different sections: The Upper Weser originates in Hann. Münden, where the headwaters of the Werra and Fulda rivers converge. The Middle Weser runs between Minden and Bremen, and the Lower and Outer Weser mark the tide-influenced area. While multiple definitions exist, here the Weser estuary and its kilometry is defined from the head at the tidal weir in Bremen-Hemelingen (def. as Weser-km 0), which marks the artificial tidal limit (Lange et al., 2008). Having a tidal range roughly between 3 m (Outer Weser) to 4 m (Bremen) and, as of today, a bottom at −11 m NHN in the navigational channel up to Blexen (Weser-km 65) and −16 m NHN further seawards, the Weser estuary is classified as mesotidal and hypersynchronical (Grabemann, 1992; Kösters et al., 2018; Hesse 2020). In general, deposited sediments reduce in size along the Weser from its origin to its mouth. In the Upper Weser, rubble sediment, in the Middle Weser, gravel, and in the Lower and Outer Weser, medium and fine sand are dominating most parts. Due to tidal dynamics and freshwater discharge, bed forms like dunes and ripples appear in the Lower Weser until Nordenham (NH, Weser-km 55). In the mixing zone of freshwater and seawater, density gradients lead to gravitational circulation and contribute to a resulting residual import of fine sediments. An ETM is formed, causing high sedimentation rates of up to 5 cm/d (internal analysis of echo sounder data), depending on several influencing factors, e.g., freshwater discharge, temperature, salinity, and sediment availability. In the ETM, suspended sediment concentrations (SSCs) of 300–600 mg/L in the water column and up to 2000 mg/L near the bottom are observed regularly (Lange et al., 2008). Multiple processes of deepening of the navigational channel from the past has affected the tidal symmetry, e.g., causing increased flood current velocities. Because of the resulting net sediment import, large sedimentation and deposition rates are noted. The resulting accumulation of sediments intensifies the challenge of keeping the main channel navigable. With frequent measurement campaigns conducted by the Federal Waterways and Shipping Administration (WSV), changes in bathymetry are surveyed using multibeam echo sounders (MBES). On the basis of the MBES results, maintenance dredging volumes are commissioned. In the range of km 55 of the Weser near NH to km 65 near Blexen, which is the major hotspot of dredging activity and the focus area of this research work (see **Figure 1**), 0.5–2 million cubic meters are dredged on a yearly base (Eberle, 2014). Because dredging activities require investments of 8–18 Mio. €/year and each displacement of dredged material has a potential ecological impact in the Lower and Outer Weser, it becomes clear that optimized maintenance resulting from an improved understanding of estuarine processes is of true value for the environment, citizens, authorities, and other stakeholders.

In the following paragraph, a hypothesis is formulated as to how the accumulation of cohesive sediments in the navigation channel of the Weser occurs. Echo sounder data indicate that sedimentation and deposition within the ETM dominate in phases of low flow velocities. Depositing flocs and particles form a layered structure above the (dense) bed of the

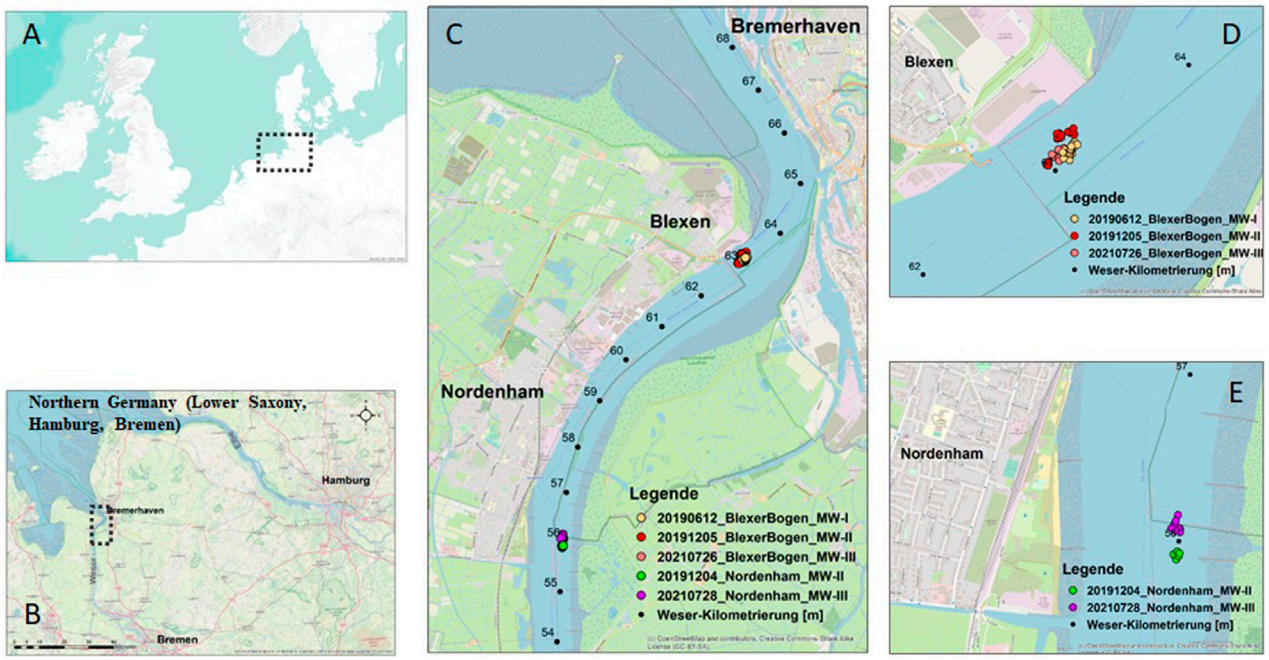

FIGURE 1 | Location of German estuaries in Europe **(A)**, Weser and Elbe estuaries located in northern Germany **(B)**, sampling sites in the estuarine turbidity zone of the Weser estuary **(C)**, and a close view at Blexer Bogen **(D)** and Nordenham **(E)**; maps by ©OpenStreetMap.

waterbody of several decimeters up to meters in height (Papenmeier et al., 2013; Becker et al., 2018). This structure forms a fresh layer of mobile benthic suspension with initial densities in the range of ρ = 1,050 kg/m³, being well below the gelling point. Depending on the conditions during the formation of a mud layer and its state of consolidation, a sediment is composed of different percentages of sand, silt, and clay. If a mud layer is formed naturally due to sedimentation in phases of low velocities, differential settling likely leads to the segregation of particles (Torfs et al., 1996). As a result, one will find higher percentages of silt and clay in the upper part and higher sand contents in the lower part of the upmost sediment layer above the bed. The upper part of a freshly deposited layer may be eroded during the adjacent flood or ebb phase, while the lower part is affected by reduced shear stresses and will thus be able to increase its density over one to several tides. The lower part of that layer, now forming stationary fluid mud, is, on the one hand, more resilient to erosion and, on the other hand, protected against erosion by the concentrated benthic suspension (CBS) above. The CBS might be regenerated with every tide. In the stationary fluid mud layer, concentrations exceed structural density (also called the gelling point/concentration), meaning that particles and flocs form a coherent structure (van Rijn, 2016). At structural density, effective stresses start to emerge when expelled water reduces excess pore pressure. This indicates the beginning of the consolidation process. The transition between settling and consolidation is, for example, characterized by its vertical velocities. Settling velocities w_s are well above the rate of consolidation w_c (approx. by an order of magnitude), although both parameters characterize the process of vertical reduction of the suspension layer. In this way, during each phase of slack water, deposits accumulate near the bottom, forming a consolidated and stratified bed over time. Well-mixed, homogeneous sediment beds are rare in nature (van Rijn, 2020), but when it comes to dredging activities, homogeneous and stationary fluid mud layers might be formed without being affected by differential settling beforehand. Hence, dredging removes sediments, but the remaining sediments might be homogenized, forming a layer of stationary mud. This results in a resistive layer supporting the consolidation of fresh sediments. The mentioned type of bed formation is even expected to occur in the center of a tidal channel with relatively high flow velocities. With and without dredging influences, stratified and non-stratified suspensions have been observed in the Weser estuary throughout the field campaigns.

According to the current state-of-the-art, processes of fine sediment transport are replicated more or less accurately using morphodynamical-numerical modeling techniques. Morphodynamical-numerical models enable a process-based simulation of dynamics on a large spatial and temporal scale, allowing for impact studies of anthropogenic intervention and helping to understand the effect of several mechanisms consistently. Nevertheless, the underlying processes of those models are increasingly physically based, but major processes like the bed exchange processes are still based on empirical relationships. The parameters required for these approaches have to be derived by sensitivity studies in the laboratory and/or by intensive on-site measurement campaigns. In this context, erosion of cohesive sediments is a major mechanism that still needs empirical estimation of parameters to represent their

erodibility properly. Investigation on the erosion behavior of sand-only deposits, on the one hand, and mud-only deposits, on the other hand, has been conducted for several decades. While the relationship between given flow conditions and the movement of sand particles can be described reasonably well with references from Shields (1936), it remains difficult to predict the behavior of mud-only, and especially sand–mud, mixtures because of interparticle forces, leading to transport properties depending on several further factors besides gravity (e.g., sand to clay ratio, concentration/density, consolidation and its history, organic matter content and type, temperature, salinity, sodium adsorption ratio, and pH). Those factors underlie a huge variability on different spatial and time scales, especially in estuaries (Winterwerp and van Kesteren, 2004). So far, no generally valid relation to describe bed exchange processes could be established using only physically based formulations (van Rijn, 2020).

However, several authors have provided empirical relationships to describe the erosion behavior of muddy sediments (Partheniades, 1965; Parchure und Mehta, 1985; Kranenburg und Winterwerp, 1997; Krishnappan, 2000; Whitehouse et al., 2000; Sanford und Maa, 2001; Schweim, 2005; Mengual et al., 2017; Krishnappan et al., 2020; Chen et al., 2021), mostly by relating applied shear stress to resulting erosion rates, but only a few models have made their way into engineering and modeling practice (Partheniades, 1965; Parchure und Mehta, 1985; Sanford und Maa, 2001). Models can be distinct by depth-dependent or depth-independent erosion resistance (summary in William et al., 2000). Erosion is observed to occur in different modes depending on the range of applied shear stress (Winterwerp and van Kesteren, 2004; Kombiadou und Krestenitis, 2013; van Rijn, 2020; Chen et al., 2021). At low shear stresses, single particles and flocs are eroded from locations of weak erosion resistance when sudden peaks (turbulence) in applied shear stress occur. This mode is called floc erosion. The erosion rate for floc erosion is observed to be approx. 10^{-8}–10^{-4} kg/(m^2 s) (Schweim, 2005). When medium shear is applied, an intermediate stage of erosion, sometimes referred to as surface erosion, might occur, in which several layers of particles and flocs are mobilized (a failure of local networks). The transition between floc and surface erosion is smooth; hence, we do not make a distinction at this point in time. At higher shear, mass or bulk erosion dominates, eroding lumps or chunks of bed material. The erosion rate for mass erosion is observed to be approx. 10^{-3}–10^{-1} kg/(m^2/s) (van Rijn, 2020). Although it was proposed for homogeneous consolidated beds (constant in time and within the sediment), the "Partheniades law" (Partheniades, 1965) is used very commonly in modeling practice. The Partheniades law relates the applied shear to the erosion rate, which is the eroded mass per unit surface and unit time. In fact, erosion resistance depends on various factors, including sediment composition, porosity, and degree of consolidation (Kombiadou und Krestenitis, 2013). This means, in turn, that sediment deposits regularly are thought to have heterogeneous properties with depth and time. However, it is possible to argue that the composition of sediment deposits can be homogeneous over a limited depth to apply Partheniades law and use individual fitting parameters for depth (e.g., fresh fluid mud deposits). In the past, the Partheniades law was extended to become valid for depth-dependent erosion resistance:

$$E = E_{0,mud}\left(\frac{\tau_b}{\tau_{cr}(z)} - 1\right)^n, \; if \; \tau_b \geq \tau_{cr}, \tag{1}$$

where E [kg/(m^{2}s)] is the erosion rate, $E_{0,mud}$ [kg/(m^{2}s)] is an empirical erosion constant, τ_b[N/m^2] is the applied shear , n is an empirical parameter, and $\tau_{cr}(z)$ [N/m^2] is the depth-dependent critical shear for erosion. The simplicity of this model is most likely a major reason why the Partheniades law is used very commonly in modeling practice. Sanford and Maa (1985) proposed a relationship for more soft mud deposits, taking the state of consolidation and the depth-dependent density $\rho(z)$ [kg/m^3] at the sediment–water boundary into account:

$$E = \beta * \rho(z) * (\tau_b - \tau_{cr}(z)) \, if \; \tau_b \geq \tau_{cr}, \tag{2}$$

where E [kg/(m^{2}s)] is the erosion rate, τ_{cr} [N/m^2] is the depth-dependent critical shear for erosion, τ_b [N/m^2] is the applied shear, and β [m^{2}s/kg] is the empirical fitting parameter. The difference of critical to applied shear is referred to as effective stress.

Parchure and Mehta (1985) proposed a relationship for soft mud deposits, assuming a constant floc erosion rate ε_f and depth-dependent erosion resistance τ_{cr}:

$$\varepsilon = \varepsilon_f e^{\alpha(\tau_b - \tau_{cr}(z))^{nm}}, \; if \; \tau_b \geq \tau_{cr}, \tag{3}$$

where ε [kg/(m^{2}s)] is the erosion rate, ε_f [kg/(m^{2}s)] is the floc erosion rate, τ_b [N/m^2] is the applied shear, α [m/N^{0,5}] is an empirical parameter, and $\tau_{cr}(z)$ [N/m^2] is the depth-dependent critical shear for erosion. The floc erosion rate ε_f appears to vary greatly for individual sediment deposits, with a range of 10^{-4} to 10^{-8} [kg/(m^{2}s)], while α appears to range between 1 and 30 (Schweim, 2005). When focusing on bed exchange, sediment deposition has to be taken into account:

$$D = C_S * w_S, \tag{4}$$

where D [kg/(m^{2}s)] is the deposition flux, C_S [kg/m^2] is the sediment concentration near the bed, and w_s [m/s] represents the mean settling velocity of sediment particles.

The research at IWB addresses the challenge of understanding the process leading to net sedimentation and accumulation in estuarine navigational channels by investigating rarely available information on the vertical transport and bed exchange properties of estuarine sediments in field and laboratory studies. The sediment samples are taken from the navigational channel of the Weser estuary. We provide estuary-specific transport parameterizations and adjusted bed exchange formulations to advance the representation of sediment transport processes in large-scale 3D morpho- and hydrodynamic-numerical models. This contribution focuses on results from investigating natural cohesive sediments with measurements conducted in the field and in laboratory experiments, mainly

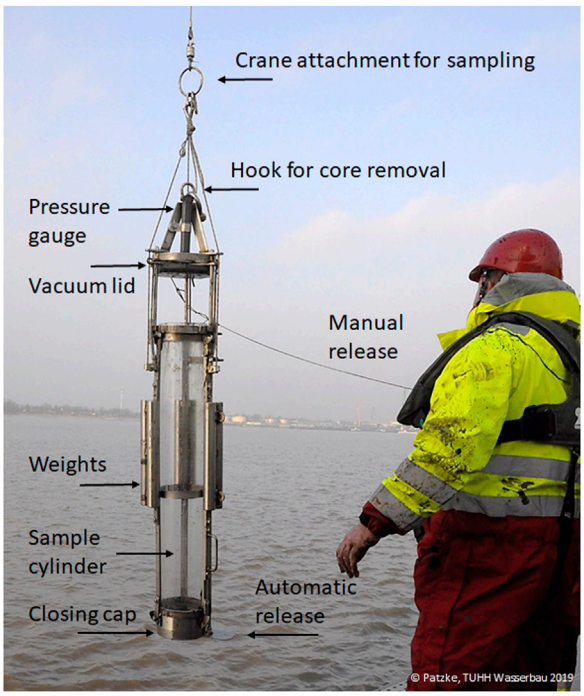

FIGURE 2 | Sediment corer developed at the Institute for River and Coastal Engineering.

related to erosion processes. Erosion rates and critical shear for floc and mass erosion are derived for sediments from two locations. The influence of consolidation history and density is further investigated in sensitivity studies.

2 MATERIALS AND METHODS

2.1 Field Campaigns

To examine the assumptions made in **Section 1**, natural sediments from the Weser estuary are collected during slack water within the ETM of the Weser at Weser-km 56 (NH) and Weser-km 63 (Blexer Bogen, BB). Field campaigns have been realized with regard to meeting the following requirements of sediment samples:

i) Undisturbed (almost)
ii) From the navigational channel within the ETM zone
iii) Collected during slack water ($v \leq 0.4$ m/s) with upstream river discharge conditions of approx. $Q \sim 150\ m^3/s$ (late spring and autumn discharge, when sedimentation rates peak)
iv) Being ideally composed of a water layer, a soft mud layer of fresh deposits, and a consolidating/consolidated layer.

To meet these requirements, a sediment corer for collecting undisturbed sediment samples (of soft mobile mud as well as consolidated mud) from the center of the navigational channel has been developed at the Institute for River and Coastal Engineering (Patzke et al., 2019), see also **Figure 2**. The samples are collected in Plexiglas cylinders of 20-cm diameter and 1.2-m height. At the top, the corer is equipped with a pressure gauge to determine the sampling depth. The timespan for the sampling of a single cylinder (preparing, coring, releasing) using the corer is under 10 min.

Three campaigns, MW-I (06/2019), MW-II (12/2019), and MW-III (07/2021), have been conducted on the Weser, where a set of six sediment cores could be obtained during the estimated slack water period of 1 h. Each core receives a sample code in the format "site abbreviation-campaignnumber/corenumber-subsamplenumber." Campaign numbers start at 0. For example, code "BB-01-03" describes the third subsample from the first core taken in BB during MW-I. Specific cores are subsampled, representing layers of about 5–10 cm. By measuring the density of homogenized subsamples, profiles of the near-bottom layers are generated. Information on size segregation in the top and bottom layers is provided by additionally using the subsamples to determine grain size distribution. The remaining sediment cores are used to observe settling behavior and to provide sediment material for further laboratory studies. In MW-III, two cores of each sampling site could be used to perform quasi *in situ* erosion experiments, providing information on the erodibility of naturally stratified and composed sediments.

2.2 Sample Preparation and Sediment Characterization

2.2.1 Sample Preparation for Laboratory Experiments

To perform experiments in the laboratory, natural sediments collected during the field campaigns are used to prepare representative samples. A sample is defined as a representative if it comprises both natural material including solids and organic phase as well, having nature-like density profiles close to the sediment–water interface where erosion processes are investigated. In practice, the best results could be achieved by first predefining an initial density/concentration that was observed in the field. Second, a fraction of natural sediments was taken from a core to generate a suspension of the predefined density. In case fluid mud with a homogeneous density profile was extracted from the river bed, the whole core was used to generate a representative suspension. Then, the suspension is homogenized at time t_0 exhibiting the initial density ρ_0. Those generated suspensions are called remolded samples. The density evolution within those suspensions is recorded to describe and parameterize consolidation processes and to relate the erosion process to the state of consolidation. When erodibility experiments are conducted, the experiment starts at specific time intervals between t_0 and t_{start}. In that way, the consolidation history is taken into account. The influence of density on erodibility is specifically investigated by varying the initial density ρ_0.

2.2.2 Sediment Characterization

The natural sediments are characterized by performing standard soil mechanical laboratory tests. Grain size distribution is obtained by performing a combined sieve and sedimentation

TABLE 1 | Sediment properties: percentage breakdown of grain sizes (clay (f_C), silt (f_{Si}), sand (f_S), d_{50}, d_{90}), water content (W), loss on ignition (LOI), and bulk density (ρ_b) of sediment samples taken during field campaigns (MW-I, MW-II, MW-III) on the Weser estuary.

Location	Sample	Date	f_C	f_{Si}	f_S	λ_{CS}	λ_{SiC}	λ_{SiCS}	d_{50}	d_{90}	LOI	W	ρ_b
[−]	[−]	[dd.mm.jj]	[%]	[%]	[%]	[−]	[−]	[−]	[mm]	[mm]	[%]	[%]	[kg/m³]
Nordenham	NH-11	05.12.19	22	62	16	1.44	0.36	5.4	0.022	0.069	13	395	1,217
Nordenham	NH-13	05.12.19	27	62	11	2.51	0.44	8.2	0.015	0.059	13	504	1,173
Nordenham	NH-21	29.01.21	24	57	19	1.26	0.42	4.3	0.023	0.080	9	307	1,325
Nordenham	NH-22	29.01.21	21	65	14	1.50	0.32	6.1	0.018	0.070	12	175	1,305
Nordenham	NH-35	28.07.21	22	74	4	5.42	0.30	23.7	0.012	0.049	13	492	1,126
Blex. Bogen	BB-01	12.06.19	20	58	22	0.9	0.34	3.6	0.031	0.079	11	257	[-]
Blex. Bogen	BB-11	04.12.19	19	60	21	0.93	0.32	3.8	0.030	0.077	11	257	[-]
Blex. Bogen	BB-21	29.01.21	18	44	38	0.47	0.41	1.6	0.040	0.120	7	110	1,435
Blex. Bogen	BB-22	29.01.21	16	54	30	0.53	0.30	2.3	0.035	0.120	8	106	1,465
Blex. Bogen	BB-36	26.07.21	18	58	23	0.78	0.31	3.3	0.037	0.092	10	210	1,276

analysis following the standardized procedure of DIN EN ISO 17892-4. Water content (WC) is derived following DIN EN ISO 17892-1, in which the samples have to be oven-dried at 105°C for 24 h and weighed before and after drying. To estimate the organic content, loss on ignition (LOI) tests are performed following DIN 18128.

Sediment characterization is performed as a sample average of five samples from NH and five samples from BB as well. At campaign MW-I, only site BB is approached and sample BB-01 is chosen for sediment characterization. At campaigns MW-II and MW-III, both sites are approached. Two cores from NH, NH-11 and NH-13, and one core from BB, BB-11, have been separated into subsamples during MW-II. At campaign MW-III, one sample from NH, NH-35, and one sample from BB, BB-36, are chosen for sediment characterization. In addition, the cores of NH-11, NH-13, NH-35, BB-01, BB-11, and BB-36 are divided into subsamples to derive depth-dependent sediment parameters. In total, information for 80 samples and subsamples is derived. A summary of the results is shown in **Section 3.1** in **Table 1** and **Figure 7**.

2.3 Density

Besides mean values for density and sedimentary composition (**Table 1**), density profiles are generated by applying two types of measurements. Density is measured using a suspension balance, and measurements are taken using the Anton Paar DMA 35 densimeter. Comparative measurements have proven the comparability of the measurement results with the two methods.

A. In the case of natural samples, density profiles are generated by subdividing the sample into layers of approximately 5 cm and measuring the mean density of each subsample using the suspension balance or the densimeter (depending on the sand content). In this way, a density profile is generated. After density measurements, the subsamples are still feasible for further investigation in soil mechanical tests (see Section 2.2).
B. In the case of remolded samples, a set of small pipes is used to extract tiny subsamples of approx. 5 ml at predefined depths using a syringe. The density of those subsamples is measured using the densimeter. To avoid the lower layers from being affected by the measurements, the procedure is undertaken from the top to the bottom of the sample. By restoring and remolding the sample after measuring a density profile, it becomes possible to investigate the temporal evolution of densities in the column. Besides the densities, the lutocline evolution is also recorded over time.

An internal analysis of dredging and echo-sounding data showed that the river discharge of 150 m³/s results in sedimentation foci predominantly in NH, but this also affects the BB area. Hence, differences in the density profiles from BB and NH may be explained by the position of the ETM being located rather nearer NH. The density of a sediment is seen as key information influencing erosion behavior.

2.4 Erosion

This study presents and discusses results from erodibility experiments performed quasi *in situ* and in the laboratory. Sediment cores taken from the Weser estuary are either preserved in natural stratification or being remolded to provide controlled initial conditions. Three types of erosion experiments have been performed.

- First, cores with sediments in natural stratification have been investigated almost fully undisturbed during the field trips.
- Second, remolded samples have been prepared with similar density profiles and sediment composition to investigate the representability of erodibility in laboratory experiments.
- Third, erosion behavior of remolded samples has been investigated with initial densities below (~1,060 kg/m³) and above (~1,125 kg/m³) structural density and a consolidation history between 1 h and 24 h.

To investigate the influence of initial density and consolidation time on the erodibility of remolded mud–sand mixtures, a set of 47 experiments has been carried out for this study in addition to the experiments performed quasi *in situ*. In the following section, the experimental setup is described, discussing the facility, the experimental methodology, and the processing of data.

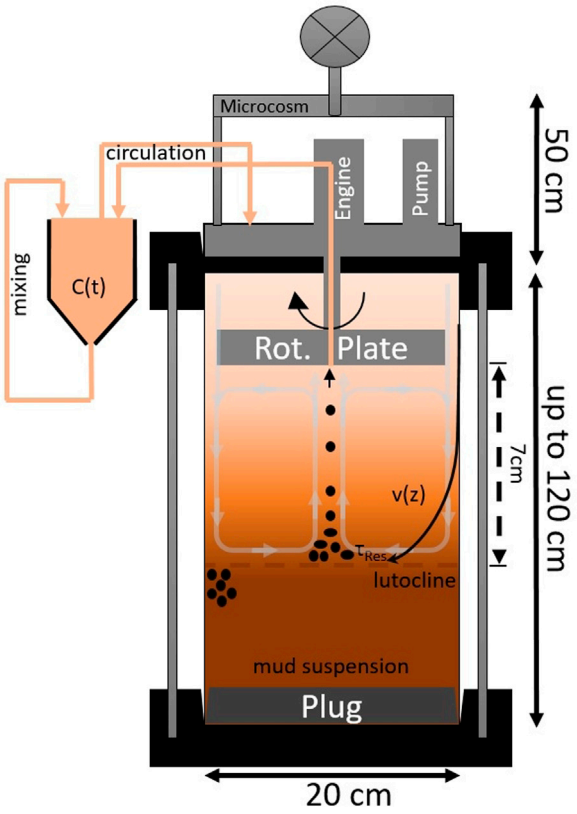

FIGURE 3 | Sketch of the adapted Gems; sediments are eroded using a rotating plate to apply defined shear stresses at a specific depth; erodibility is derived from suspended sediment concentration concentration measurements.

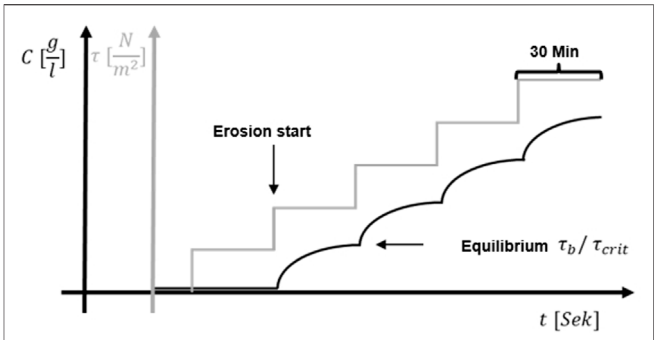

FIGURE 4 | Methodology of load steps and suspended sediment concentration during an erosion experiment.

2.4.1 Erosion Apparatus and Experimental Procedure

Erosion experiments in the laboratory and in the field are conducted using a gust microcosm erosion system (Gems, Gust, 1989; Gust und Müller, 1997). The Gems has a diameter of 20 cm and generates flow by a stirring plate of 7 cm in diameter with a 2 cm skirt. The Gems introduces a horizontal, circular flow pattern on top of the sediment layer in a sample cylinder (see the schematic drawing in **Figure 3**).

Secondary flow patterns (gray arrows in **Figure 3**), which affect the uniform distribution of friction velocities on the sediment–water interface, are partly counteracted by a central suction. As a result, the applied shear stress is distributed nearly homogeneously (Gust, 1989; Gust und Müller, 1997). It is a feature of the Gems to apply controlled shear stresses on the sediment–water interface. In this way, the erodibility of sediments can be investigated assuring specific conditions, even though the stationary rotating flow might differ from the tidal flow. Water and eroded sediments are extracted in the center of the erosion chamber discharging water into the measurement chamber. SSC (C(t)) is determined by measuring turbidity between 0 g/L and 5 g/L every second using optical backscatter sensors developed at IWB and by measuring density between 1 g/L and 30 g/L every 5 min. Both devices are attached to the measurement chamber (upper left part of **Figure 3**). In contrast to previous studies using Gems, which discharge eroded sediments (Work und Schoellhamer, 2018), the sediment is kept in a closed erosion system to improve the representation of natural conditions (an increase of SSC above lutocline with increased tidal flow). Hence, the SSC increases during each experiment with every load step above critical shear stress. With the procedure used, net erosion is determined covering erosion and possible deposition occurring simultaneously. It is not yet possible to separate those two processes in the presented experimental procedure.

Erosion experiments are performed by placing the Gems on top of the sediment sample with a precalibrated distance of 7 cm between the stirring plate and the lutocline. Shear stress is increased in regular increments every 30 min. A defined shear stress is applied on the sediment surface by using a calibrated combination of stirrer revolutions per minute and the central suction flux following the relations

$$u^* = -2.0710^{-5}n^2 + 1.5710^{-2}n + 0.10527, \quad (5)$$

$$Q = -0.0138n^2 + 5.5n + 20, \quad (6)$$

where u^* [cm/s] is the shear stress velocity, n [1/min] is the stirrer disc revolutions, and Q [ml/min] is the pump rate.

In case the applied shear exceeds the critical shear, during each load step interval, a repeating concentration pattern is expected to occur (see **Figure 4**). Before a change in concentration is recorded, a (small) lag time is expected because eroded sediments need to be transferred between the two chambers. This is followed by a relatively sharp increase in measured turbidity/density. Heading to the end of the load step, concentration gradients tend towards zero (respectively floc erosion rate in higher load steps). When erosion comes to an end, a new equilibrium is formed between the shear of flow and the erosion resistance of the sediment surface. In case the distance between the stirrer and sediment surface (primary lutocline) increases to more than 8 cm, the stirrer is readjusted to the default value of 7 cm to further obtain a defined shear stress. The evolution of the lutocline during erosion experiments results from taking close-up pictures in intervals of 1 min using a digital camera.

2.4.2 Processing of Turbidity Data

To observe the evolution of SSC over the experiment duration, a combination of turbidity and density measurements is needed to cover the range of concentrations occurring with an adequate technique. Sediment concentrations of up to 30 g/L have to be covered by both the turbidity and the density measurement. The turbidity measurements are run with a self-developed optical backscatter probe consisting of 10 optical sensors, while two sensors at a time cover the same concentration range. In this way, plausible SSC is measured in the range of $0 \leq C \leq 5$ g/L using the backscatter probe. SSC above 5 g/l has to be covered by density measurements. The backscatter data is processed as follows:

- First, the turbidity value is calculated from measurement results (light value minus dark value) and smoothened by a moving mean filter of a window of 60 for the 10 sensors attached to the measurement probe.
- Second, the data of the different sensors are recalculated to SSC using a calibration curve generated specifically for Weser sediments.
- Third, by automatically combining data of the 10 sensors, a consistent concentration curve from the backscatter measurements is calculated.

2.4.3 Processing of Density Data

Density measurements carried out during an erosion experiment are processed as follows:

- SSC can be represented accurately by density measurements when SSC is above 0.5 – 1 g/L
- Process water density is measured at the beginning of the experiment where C << 1 g/L
- The densimeter also measures temperature, so measured densities are corrected for temperature changes during experiments
- Sediment concentration is calculated and an interpolated curve is formed to meet the same data frequency interval as the turbidity sensors.

As the last step, the two concentration curves are combined to form a representative time series of SSCs, covering the whole range of occurring SSCs during experiments.

Bulk density ρ_b of sediment suspensions can be expressed as the sum of the percentage (1—η) of the fluid (water) times its density ρ_w and the percentage of total suspended solids (η) times their dry density ρ_s:

$$\rho_b = \eta\rho_s + (1-\eta)\rho_w = \rho_w + \eta\rho_s - \eta\rho_w. \quad (7)$$

The volume percentage of sediment η can be expressed as

$$\eta = \frac{\rho_b - \rho_w}{\rho_s - \rho_w}. \quad (8)$$

By transformation of **Eq. 7** and measures of bulk density, water density, and dry sediment density, the mass concentration of sediments C_{Sed} can be calculated:

$$C_{sed} = \eta\rho_s = \rho_b - \rho_w + \eta\rho_w. \quad (9)$$

In this study, bulk density ρ_b and water density ρ_w can be measured, while dry density ρ_s is estimated to be $\rho_s = 2{,}575$ kg/m^3, measured by Malcherek (2010) as mean dry density for sediments of the investigated part of the Weser estuary. A best fit spline interpolation is used to extend density measurements to the frequency of the backscatter dataset. Both datasets are plotted together to finally combine the datasets. Derived concentration curves from both types of measurements are in good agreement within the interval $0.9 \text{ g/L} \leq C \leq 1.5$ g/L. Depending on the quality of individual datasets, a point of that span is selected for each experiment to connect the datasets to a comprehensive time series of sediment concentrations. The connection point is set where residuals between the datasets become minimal.

In the next step, the time series of sediment concentration is used to derive erosion rates [kg/(m^2/s)]. Here, each value of sediment concentration is related to the time increment between each data point and the average area of the sediment surface. Additionally, a 60 s moving average has been applied to reduce noise in the data. It must be noted that the calculated erosion flux represents the sum of deposition and erosion occurring at the same time. Hence, the derived parameter E_{net} is defined as net erosion:

$$E_{net} = Erosion - Deposition. \quad (10)$$

3 RESULTS

3.1 Sediment Characterization

As stated in **Section 2.2**, collected sediment samples from the Weser estuary have been characterized using classification tests for soil mechanics (grain sizes, WC, LOI). The mean results for the collected samples are summarized in **Table 1** and described as follows. For both sites (BB and NH), the majority of grains (44–74%) are in silt size. Despite that, on average, the silt content is about 10% lower in samples from BB (54%) than in samples from NH (64%).

The clay to sand ratio λ_{CS}, the silt to clay ratio λ_{SiC}, and the ratio of fines to sand λ_{SiCS} are used to predict the critical shear and cohesion of the mixture (Wu et al., 2018; van Rijn, 2020). For example, λ_{CS} is above 1 for all samples from NH and below 1 for all samples from BB. As a consequence, the mean sand content in BB samples (28%) is significantly higher than that in NH samples (13%). The ratio of fines to sand λ_{SiCS} is generally well below 10 and even below 4 for samples from BB. For NH samples, all values are above 4, including an outlier of sample NH-35, which is 23. For both sites, the critical amount of clay of 5–10% (Grabowski et al., 2011) is exceeded, so dominant cohesive behavior is expected ($f_{C(NH)}$ ~23%, $f_{C(BB)}$ ~18%). In general, the mean diameter is lower for samples from NH than BB because of a higher percentage of fines in NH samples. As more organic compounds can attach and survive at the (relatively) larger surface area of smaller particles, the experimental results exhibit a higher LOI in NH (12%) than

FIGURE 5 | Sediment samples taken from Weser-km 63, Blexer Bogen, on 26.07.2021.

FIGURE 6 | Sediment samples taken from Weser-km 56, Nordenham, on 28.07.2021.

in BB samples (9%). Depending on the (depth of the sub-) sample, WC shows high variability, ranging between 175% and 500% for NH samples and between 106% and 257% for BB samples. With regard to density, significantly higher values have been measured in the samples from BB. The samples from BB were mainly consolidated or in an advanced state of consolidation, sometimes having a layer of fresh deposits on top (MW-I). Samples from NH are rather in a viscous state, exhibiting densities around or slightly above gelling concentration.

An exemplary visual representation of the samples and differences between the sampling sites can be found in **Figure 5** and **Figure 6**.

In addition to **Table 1**, **Figure 7** shows the percentage breakdown of grain sizes and the corresponding classification using the U.S. Department of Agriculture's (USDA) textural triangle for evaluated (sub-) samples from BB (blue) at Weser-km 63 and NH (white) at Weser-km 56. While most samples are in the range of silt loam, similarities and differences between the sample sites become apparent. Both samples have very similar silt content, so the clay to sand ratio represents differences in the sediment composition fairly well.

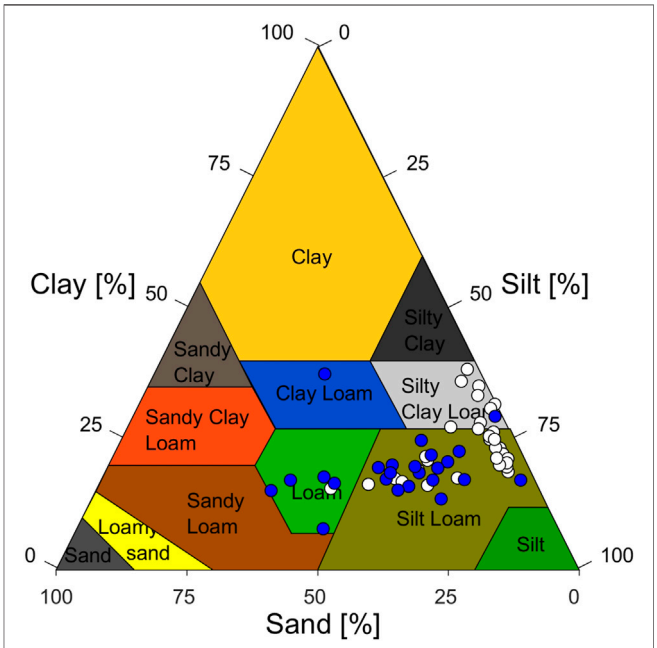

FIGURE 7 | U.S. Department of Agriculture's Classification (United States Department of Agriculture, 1987) of sediments taken from the Weser estuary at the site of Nordenham, Weser-km 56 (white dots), and Blexer Bogen, Weser-km 63 (blue dots).

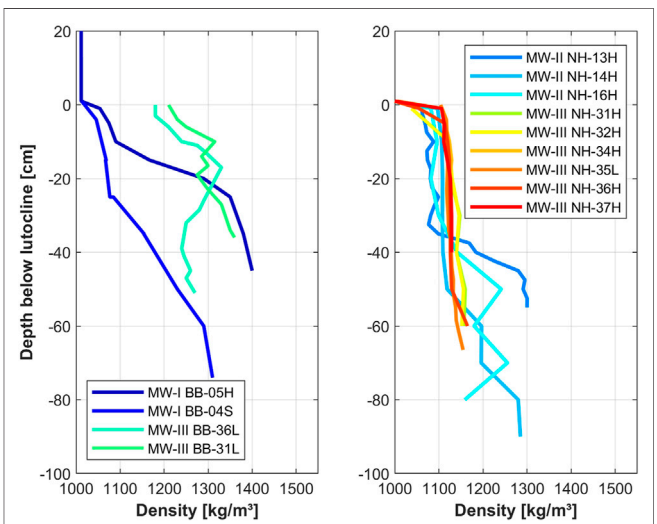

FIGURE 8 | Density profiles below lutocline of sediment samples collected in three campaigns (MW-I, MW-II, MW-III) at locations in Blexer Bogen (BB, left) and Nordenham (NH, right); measurement location in L (lab), H (harbor), or S (ship).

3.2 Density

Density profiles of sediment cores kept in natural stratification have been determined for sediments taken during field campaigns

(MW-I, MW-II, MW-III). **Figure 8** shows the results of the profiles of 4 samples from BB and 9 samples from NH. Densities are related to the observed sediment–water interface (zero level) in the sediment cores as the lutocline is seen as the reference standard for comparison of the samples when it comes to density. Profiles for sediments from BB (left plot) exhibit densities in the range of 1,000–1,400 kg/m³, showing a steep gradient or even starting as high as 1,200 kg/m³ in density. During MW-I, a mobile mud layer of ~10–25 cm in height is observed in both samples (BB-04 and BB-05) on top of a layer of higher density exhibiting a secondary lutocline to (pre-) consolidated sediment. In sediment cores taken during MW-III, no mobile mud layer is observed and the profile starts at densities of 1,200 kg/m³, leading to values of 1,300 kg/m³ in the lower part of the cores. Closer to the center of the ETM, here located in NH, we observe a lower density range between 1,050 and 1,300 kg/m³ in all cores. Fresh mobile and stationary mud suspension in the range of 1,050–1,150 kg/m³ is seen in all sediment samples taken from NH. It is worth mentioning that during campaign MW-II, a more dense (pre-) consolidated stage of sediment suspension is observed in the lower half of the samples (NH-13, NH-14, and NH-16).

The observations lead to the conclusion that the sedimentation foci are also reflected in the density profiles. Samples from BB exhibit sediments mostly in the preconsolidated and consolidated stage, following a classification stated by Kombiadou and Krestenitis (2013), while sediments taken from NH are classified as (mobile and stationary) mud.

Results of the consolidation experiments conducted with remolded samples in the laboratory are depicted in **Figure 9**, showing the density evolution and the lutocline evolution over a period of 24 h. Two major phases of settling can be observed. Samples with initial densities below the structural density reveal hindered settling behavior at the beginning of the experiment, reaching maximum settling velocities of w_s ~ 0,4 mm/s. When the lutocline descends at settling velocity in the hindered settling regime, densities in the upper column decrease sharply, while densities below the lutocline increase because of reduced space for the same amount of solids. After a few hours (~4 h for 1,065 kg/m³ suspensions, ~9 h for 1,080 kg/m³ suspensions), the settling velocity reduces significantly, the suspensions reach the point of concentration (Winterwerp et al., 2021), consolidation starts in the permeability phase (van Rijn, 2020), and rates of consolidation become as small as $w_c = 2*10^{-3}$–$2*10^{-2}$ mm/s.

While compaction proceeds, the density increases sharply at the bottom of the sample and slightly in the rest of the column. For samples with initial densities above the structural density, no hindered settling regime is observed. The suspensions are stable over the observation period of 24 h. Because a major shift in the settling behavior could be observed between initial densities of ρ_0 = 1,080 kg/m³ and ρ_0 = 1,100 kg/m³, structural density ρ_{gel} (or gelling concentration C_{gel}) is expected to be in the median range. Because of a higher clay content in NH and a higher sand content in BB samples, it is expected that the structural density for samples from NH is slightly lower (approx. ρ_0 = 1,085 kg/m³) than the structural density for samples from BB (approx. ρ_0 = 1,100 kg/m³). Applying **Eq. 9** using a water density of ρ_w = 1,009 kg/m³ and a dry sediment density of ρ_s = 2,575 kg/m³, the corresponding gelling concentration for NH is $C_{gel,NH}$ = 125 g/L and for BB is $C_{gel,BB}$ = 150 g/L.

3.3 Erosion

3.3.1 Quasi *In Situ* Erodibility

The erodibility of nearly undisturbed natural sediment samples has been investigated quasi *in situ* using a Gems erosion chamber. Sediments have been extracted and transported carefully to the harbor, where the first experiments took place straight after sampling. Two samples each have been investigated from BB and NH during campaign MW-III. Measured sediment concentrations and derived erosion rates are presented in **Figure 10**. The experiment duration was primarily dependent on the general conditions during the field trips and the sediment responses during the experiments. The same methodology was applied in all experiments, and at least six load steps up to τ_b = 0.12 N/m² have been applied to every sample, although in some experiments, higher shear stresses could be applied.

For all samples, the applied shear stresses lead to an increase in SSC in the measurement chamber of the Gems; hence, it is assumed that erosion took place. It should be noted that experiments on sample BB-37 and sample NH-33 were carried out approx. 24 h after extraction because experiments for the other samples were carried out first. It should also be stated that backscatter data at the beginning of the experiments were very noisy for no apparent reason, so some data needed to be excluded from the analysis. Sample BB-35, BB-37, and NH-33 data from the first load step and sample NH-31 data from the first three load steps had to be excluded from the analysis.

For experiments using samples from BB, the concentration evolution is very similar. The onset of erosion is observed to be in load step 3 with τ_b = 0.05 Pa. In the following steps, concentration seems to increase continuously, but following the pattern of theoretical behavior drawn in **Figure 4**. In load step eight, both experiments using BB samples show concentrations of approx. C ~ 1.5 g/L. Derived maximum erosion rates are well below $\varepsilon < 10^{-3}$ [kg/(m²s)]. Hence, they do not pass critical rates for mass erosion. This confirms the visual observations during the experiments and is consistent with high densities (thus, high erosion resistance) measured in the other samples from BB during campaign MW-III. Compared to results from experiments using NH samples, the differences are obvious here. Homogeneous density profiles (**Figure 8**) with significantly lower densities closely above the gelling point suggest higher erodibility. This assumption is confirmed by the experiments because at shear stresses of τ_b = 0.1–0.12 N/m², the NH samples exhibit a sudden increase in the sediment concentration and erosion rates reach $\varepsilon = 0.5 \times 10^{-3}$ kg/(m²s), which is set as the threshold for mass erosion derived in laboratory experiments, presented in **Section 3.3.3**. SSC increases sharply, reaching values of approx. 3 g/L at the end of the experiments. The determined critical shear for floc erosion is $\tau_{cr,Ef}$ ~ 0.05–0.07 N/m² with floc erosion rates of approx. $\varepsilon_f = 5 \times 10^{-5}$ [kg/(m²s)].

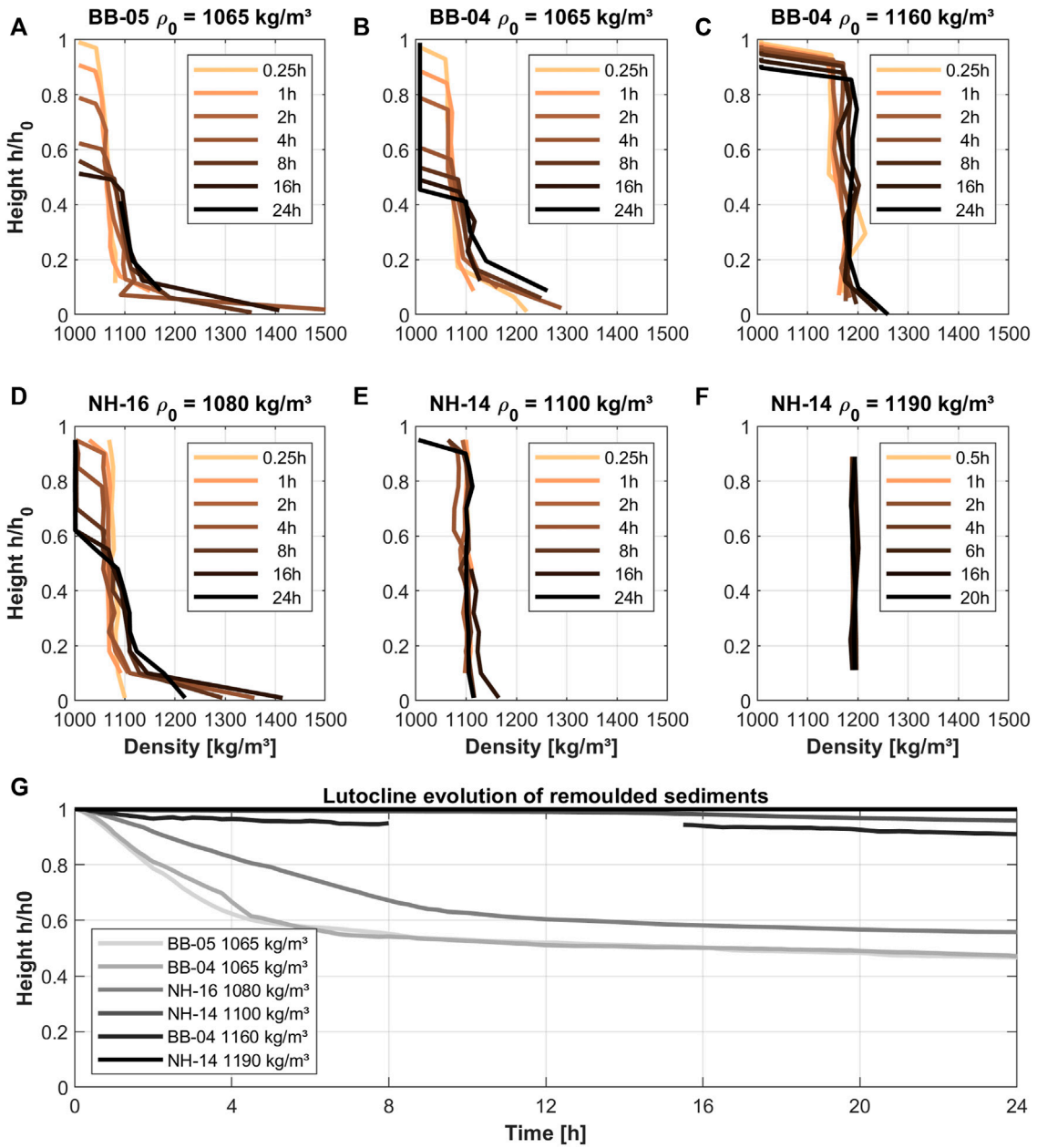

FIGURE 9 | Evolution of primary lutocline **(G)** of remolded natural sediments from Blexer Bogen and Nordenham and corresponding evolution of density profiles: sample code (sc) BB-05 and initial density ρ_0 = 1,065 kg/m³ **(A)**, sc: BB-04 and ρ_0 = 1,065 kg/m³ **(B)**, sc: BB-04 and ρ_0 = 1,160 kg/m³ **(C)**, sc: NH-16 and ρ_0 = 1,080 kg/m³ **(D)**, sc: NH-14 and ρ_0 = 1,100 kg/m³ **(E)**, and sc: NH-14 and ρ_0 = 1,190 kg/m³ **(F)**; h_0 = h(t=0), h = h(t=t_l).

3.3.2 Erodibility in Single Experiments

Exemplary results of experiments and comparisons of those with initial densities of $\rho_0 \sim 1{,}065$ kg/m³ and $\rho_0 \sim 1{,}125$ kg/m³ with corresponding consolidation times of 3 h and 18/24 h are shown in **Figures 11A–D**. For the experiments with suspension densities below the structural density, the initiation of erosion is observed in load steps three to four, which corresponds to a critical shear stress for floc erosion of $\tau_{cr,Ef}$ = 0.05–0.07 N/m² and erosion rates of $\varepsilon_f = 10^{-4}$ [kg/(m²s)]. Mass erosion is observed to start at load stage four, corresponding to $\tau_{cr,Em}$ = 0.07 N/m², when the consolidation time is 3 h or below. Mass erosion rates reach up to $\varepsilon_m = 5 \times 10^{-3}$ [kg/(m²s)] in this case. On the other hand, the increase in erosion resistance of sediment suspensions below the gelling point runs fast. After a consolidation time of 18 h, mass erosion starts first in load stage eight, corresponding to a critical shear stress of $\tau_{cr,Em}$ = 0.18 N/m², exhibiting similar erosion rates of $\varepsilon_m = 5 \times 10^{-3}$ [kg/(m²s)] as in load step four. If the gelling concentration is expected to be developed after 4–10 h

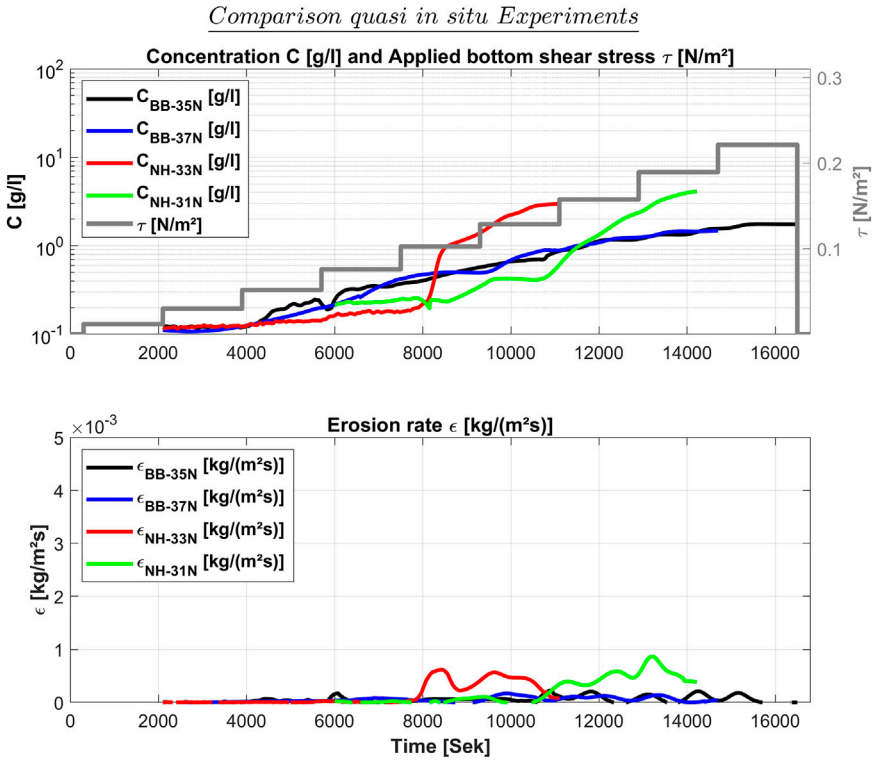

FIGURE 10 | Sediment concentration and derived erosion rate for sediment samples collected from the Weser estuary without any further handling.

(depending on initial density), this confirms the assumption made before that the increase in erosion resistance slows down significantly after reaching the gelling state. As proof, sediment suspensions investigated with initial densities above the gelling point exhibit similar behavior. Floc erosion is seen repeatedly after surpassing load step four, while mass erosion occurs when load step nine is reached, corresponding to a critical shear stress of $\tau_{cr,Em} = 0{,}21$ N/m^2 and erosion rates of $\varepsilon_m = 5 \times 10^{-3}$ kg/(m^2/s). Transferred to natural conditions, this means that if a fresh mud deposit withstands the tidal flow for a few hours or even increases in sediment concentration by deposits during slack tide, it becomes immobile and relatively stable against erosive forces (compared to deposits below the gelling point). With the results presented here, we assume confirmation of repeatability of experiments under the same experimental conditions (leaving an individual variability).

3.3.3 Erosion and Resuspension Characteristics

Erodibility. In this section, an overview of the results from experiments conducted in the laboratory and the field is presented. As shown in **Section 3.3.2**, with respect to variability, especially under mass erosion conditions, repeatable behavior could be established between experiments run under the same conditions. To highlight dependencies, it makes sense to consider the results of a set of experiments. If the eroded mass at the end of each load step is measured and plotted against the applied shear stress on a double logarithmic plot, the logarithmic relationship between the shear stress and erosion rate becomes visible. The overall behavior of investigated sediments is presented in **Figure 12**. In the case of remolded samples having initial densities below the gelling point, an increase in erosion resistance is observed within 24 h, corresponding with decreased erosion rates (respectively eroded mass) and increased critical shear. When the initial density of the remolded samples exceeds the gelling point, a general change in the erodibility is observed. In this stage, lasting for at least 24 h, eroded mass per applied shear stress does not primarily depend on time anymore, and erodibility varies within a range of one logarithmic degree. Other influencing parameters become dominant as settling velocities reduce to speed of consolidation and almost all interparticle bonds have been established. Moreover, it has to be emphasized that the slope of the erodibility is very similar in all laboratory-based erosion experiments. For comparison, the results from the quasi *in situ* experiments are also highlighted in **Figure 12** as dotted lines. While the variability between the load steps appears to be slightly higher than that in the laboratory experiments, all results from the quasi *in situ* experiments lie in the range of the laboratory-investigated sediment samples. Actually, all of the lines resulting from the quasi *in situ* experiments are in the transition zone between fresh deposits of mobile mud below the gelling point and stationary mud above the gelling point.

Erosion modes. Three modes of erosion have been observed in this study:

- Particle or floc erosion: In every single experiment, erosion started with a small increase in sediment concentration already at very low shear stresses. No immediate change

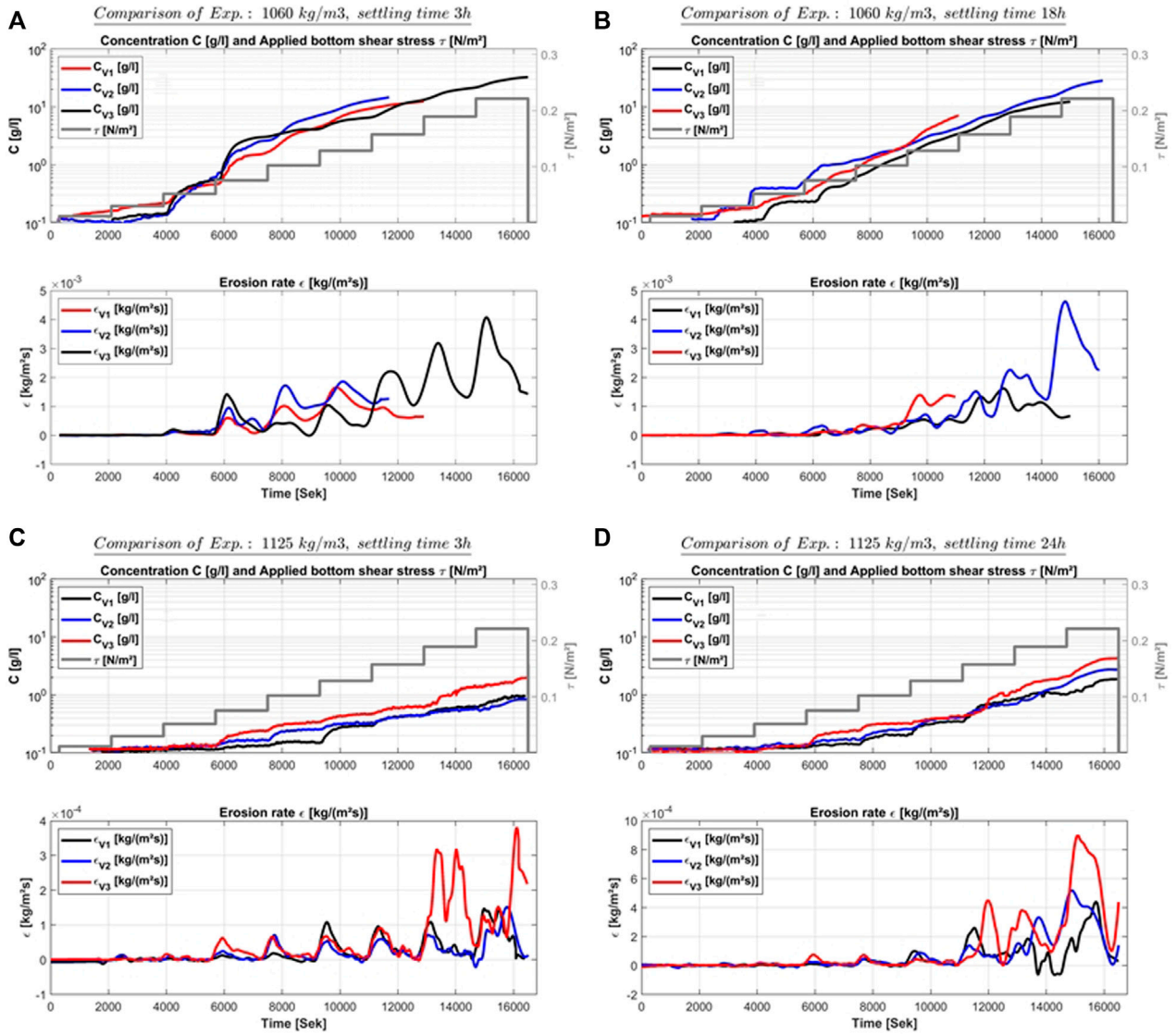

FIGURE 11 | Steps of applied bottom shear and concentration (upper) and erosion rate evolution (lower) in single experiments: Comparison of results with densities of ρ_0 = 1,060 kg/m^3 and consolidation times of 3 h **(A)**, ρ_0 = 1,060 kg/m^3 and consolidation times of 18 h **(B)**, ρ_0 = 1,125 kg/m^3 and consolidation times of 3 h **(C)**, and ρ_0 = 1,125 kg/m^3 and consolidation times of 24 h **(D)**.

in lutocline height (dh < 1 mm) can be observed, and only single particles or flocs get into the water column, changing SSC by only C < 0.1 g/L. Erosion depth is below a millimeter range during a load step, and the turbidity of the water column increases slightly.

- Surface erosion: During some experiments, the second stage of erosion was observed, when plates of connected flocs or several layers of flocs were eroded, building craters and grooves along the flow direction. Sediment concentration in the water column increases slowly by C ~ 0.1–0.2 g/L, and erosion depth reaches one to a few millimeters within each load step (on some parts of the sediment–water surface).
- Mass erosion: The sediment surface breaks up because the applied shear stress is larger than the undrained (remolded) soil strength of the bed (van Rijn, 2020), and huge chunks of sediment are eroded within a short amount of time. Erosion depth increases fast while reaching a depth of a few centimeters, and sediment concentration in the water column rises by several grams per liter during a load step.

Because the transition between floc and surface erosion appears to be fluent and the distinction from measured erosion data is challenging, we do not differ between those two erosion modes in this study. Specific surface erosion was only visible in personal observations during the experiments.

Following the procedure described in **Section 2.4**, parameter values for the critical shear for floc erosion, the floc erosion rate, and the critical shear for mass erosion have been derived for all

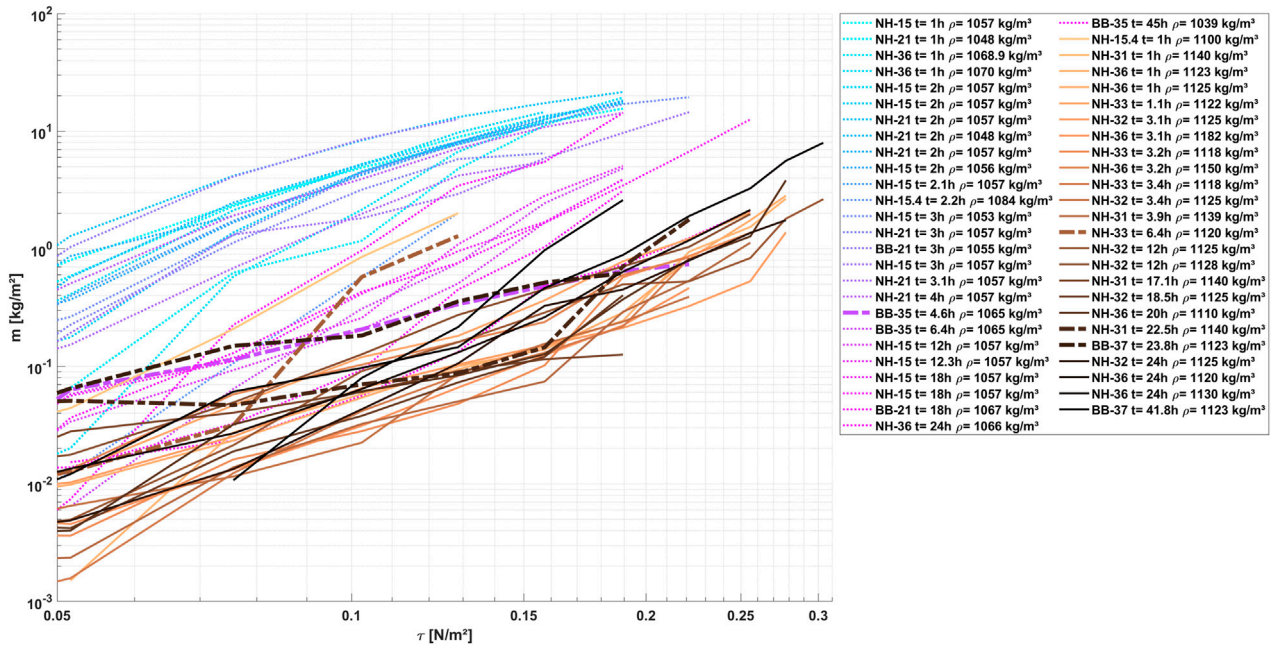

FIGURE 12 | Results of experiments undertaken, displaying the eroded mass [kg/m^2] vs. applied shear stresses [N/m^2]; experiments with initial densities below (dotted lines) and above (solid lines) are shown, while initial settling times are distinct with using two colormaps (bluish and brownish). Results from the quasi *in situ* experiments are displayed as big dashed lines.

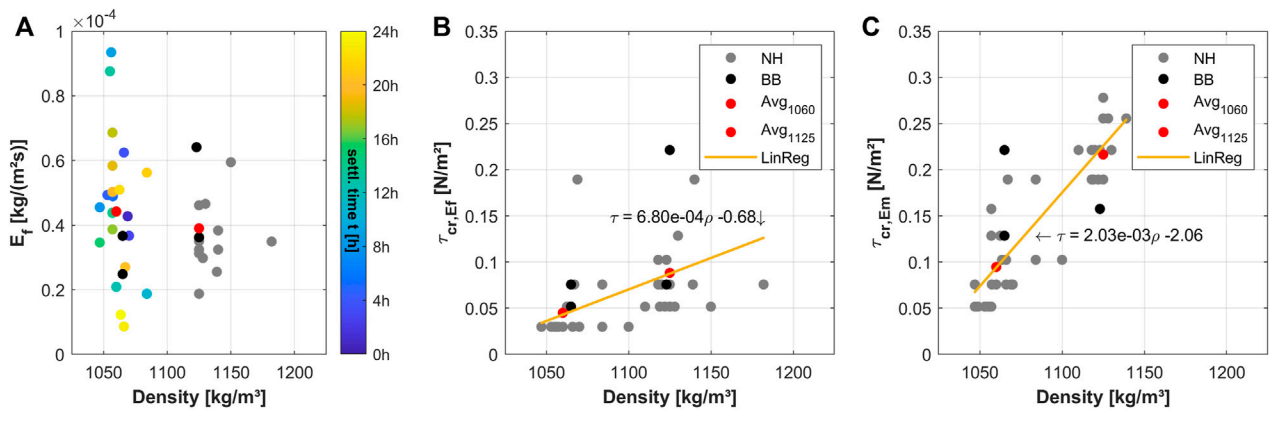

FIGURE 13 | Derived erosion rate for floc erosion ε_f **(A)** and corresponding critical shear stress $\tau_{cr,Ef}$ for floc erosion **(B)** as well as critical shear stress for mass erosion $\tau_{cr,Em}$ **(C)**; regression lines are fitted based on gray data points.

the experiments. Results for parameters related to floc erosion are presented in **Figure 13**.

In all plots of **Figure 13**, gray dots depict samples from NH, black dots depict samples from BB, and red dots represent the mean values of erosion parameters for low and high initial densities. Regression lines are based on the scattering of measured points. Left hand (A), the mean of the maximum erosion rate of every shear stress step within the floc erosion range is given. Dot colors indicate the settling time of suspensions with initial densities below the gelling point (~1,060 kg/m^3). It becomes clear that the settling time for sediments from the Weser estuary does not play a significant role in the determination of floc erosion rates, although the variability of erosion rates reduces when investigating suspensions above the gelling point. Both averages of erosion rates for high and low initial densities are about $\varepsilon_f = 4 \times 10^{-5}$ [kg/(m^{2}s)]. **Figure 13B** relates detected critical shear stresses for floc erosion to initial suspension densities. Corresponding critical shear for floc erosion is about $\tau_{cr,Ef}$ = 0.05 N/m^2 for low and about $\tau_{cr,Ef}$ = 0.09 N/m^2 for high initial densities. To distinguish between the results from NH and BB in

TABLE 2 | Results of experiments with natural sediment samples and remolded sediment samples of two density ranges and four different settling times: critical shear stress and erosion rates determined for floc erosion and mass erosion.

Sample site	Type	Sample code	Settl. time	Density	Crit. shear	Erosion rate	Crit. shear
[−]	[−]	[−]	T [h]	ρ_{b0} [kg/m³]	$\tau_{cr,Ef}$ [N/m^2]	ε_f [kg/(m^{2}s)]	$\tau_{cr,Em}$ [N/m^2]
Nordenham	Natural	NH-31	6	1,140	0.07	5.62[a]10^{-5}	0.10
Nordenham	Natural	NH-33	22	1,120	0.05	1.86[a]10^{-5}	0.19
Blexer Bogen	Natural	BB-35	5	~1,300	0.03	4.85[a]10^{-5}	[−][a]
Blexer Bogen	Natural	BB-37	24	~1,300	0.05	4.80[a]10^{-5}	[−][a]
NH/BB	Remolded	Avg	1-3	~1,065	0.04	4.83[a]10^{-5}	0.06
NH/BB	Remolded	Avg	6	~1,065	0.05	4.67[a]10^{-5}	0.13
NH/BB	Remolded	Avg	12	~1,065	0.03	5.36[a]10^{-5}	0.14
NH/BB	Remolded	Avg	18	~1,065	0.05	4.52[a]10^{-5}	0.17
NH/BB	Remolded	Avg	24	~1,065	0.05	3.20[a]10^{-5}	0.13
NH/BB	Remolded	Avg	1-3	~1,125	0.08	4.02[a]10^{-5}	0.21
NH/BB	Remolded	Avg	12	~1,125	0.05	2.97[a]10^{-5}	0.23
NH/BB	Remolded	Avg	18	~1,125	0.11	3.85[a]10^{-5}	0.21
NH/BB	Remolded	Avg	24	~1,125	0.09	4.03[a]10^{-5}	0.23

[a]*BB-35 and BB-37: critical shear for mass erosion has not been exceeded during experiments with a maximum applied shear stress of τ_{max} = 0.21 N/m^2.*

detail, more samples from BB have to be analyzed. Besides, measured values for critical shear seem to be higher for BB samples (as expected because of a higher sand content). Regarding critical shear for mass erosion, differences between the suspension erodibility become even more clear, with $\tau_{cr,Em}$ = 0.09 N/m^2 for the low- and $\tau_{cr,Em}$ = 0.21 N/m^2 for the high-density range.

Derived parameter values for floc and mass erosion are summarized in **Table 2**. While laboratory-remolded sediment samples exhibit a dependency of erosion parameters for floc erosion on density rather than settling time, critical shear for mass erosion already increases within the hindered settling regime (first 24 h after low initial density deposit). Investigated natural experiments from NH show similar behavior in terms of floc erosion. For mass erosion, natural behavior is best represented by samples of low initial density and settling times of 6–24 h (meaning self-developed gelling point). This might be due to segregation happening in the field and in the laboratory when starting with lower initial densities of suspensions. When a suspension is remolded with densities above the gelling point, segregation of sand particles might be prohibited. Floc erosion patterns are similar in natural sediments (with high densities) from BB, but critical shear for mass erosion was not exceeded in experiments with applied shear of up to 0.21 N/m^2. This underlines the expected degree of consolidation for samples from BB and highlights further required experiments on natural specimens with even higher densities.

When using the derived parameters (ε_f, $\tau_{cr,Ef}$, $\tau_{cr,Em}$) for a first fit of the erosion models introduced in **Section 1**, one can see that it is possible to represent a part of the variability in erodibility observed in the presented experimental results. Applying an erosion constant of $E_{0,mud}$ = 10^{-4} kg/(m^{2}s) and a critical shear of τ_{cr} = 0.05 N/m^2, the Partheniades model can represent the erodibility of samples above the gelling point, lying in the lower spectrum of **Figure 12**. The model by Sanford and Maa is applied using parameter values of $\beta = 5 \times 10^{-5}$ (m^{2}s)/kg and the same critical shear as in the Partheniades model. The resulting erosion rates of this model are in the upper part of the spectrum presented in **Figure 12**.

4 DISCUSSION AND CONCLUSION

4.1 Summary and Discussion

In this study, results from quasi *in situ* and laboratory-based experiments investigating aspects of the bed exchange behavior are reported and discussed. Sediment characteristics, shortly after deposition, being in a soft state but accounting for long-term deposition, is the subject of this investigation. For this purpose, natural sediments from the center of the navigational channel within the ETM of the Weser estuary at sites in BB (more downstream) and NH (more upstream) are collected. Taken during slack water with a novel sediment sampler, sediment cores cover the transition between the lower water column and the upper sediment bed. The sediment sampler and the experimental setup have been coordinated during development. This allowed sediment samples to be placed directly into the experimental setup for tests of erodibility after collection. Representative remolded samples in terms of density and composition have been investigated later in the laboratory. Results from erosion experiments with naturally stratified sediments are used to estimate the magnitude of quasi *in situ* erodibility, while results from laboratory-remolded natural sediments are used to investigate the variability under defined laboratory conditions. The settling and consolidation behavior have been investigated by deriving density profiles and lutocline evolution from naturally stratified sediments and laboratory-remolded sediments with varying initial densities. In addition, sediments are classified by deriving grain size percentage breakdown, WC, and LOI.

The condition of the samples taken confirm the existence of a fluffy mud layer covering a comparatively solid bed, if the ETM is present at the specific location. The layer thickness of the fluffy layer was observed to be in the range of a few decimeters up to 1 m and

slightly above. Classification experiments prove the existence of clay, silt, and sand, all of which are in significant proportions. According to the USDA code, collected Weser sediments are mainly classified as silt loam. Sediments from BB contain about 10% more sand and lesser mud to the same extent compared to sediments from NH. Higher and increasing densities with depth up to values of $\rho_b \sim 1{,}400\ kg/m^3$ are observed for samples from BB. Samples from NH exhibit more homogeneous densities and sedimentological profiles. Densities of NH samples are in the range of $\rho_b \sim 1{,}050–1{,}250\ kg/m^3$, sometimes from top to bottom exhibiting densities of about $\rho_b \sim 1{,}125\ kg/m^3$. The quasi *in situ* measurements confirm the existence of both mobile and stationary mud layers within the ETM at the time of sampling. Also, this confirms the absence of large fluid mud layers at the lateral ETM boundaries, meaning BB in this case. Investigations of the density evolution in the laboratory prove the cohesive behavior of the mixture. Settling is hindered for experiments with remolded CBS below structural density. From the density profiles and lutocline evolution, a gelling concentration could be determined at approx. $C_{gel} = 125–150\ g/L$ respective $\rho_{gel} = 1{,}085–1{,}100\ kg/m^3$. After exceeding the gelling concentration, settling velocities of about $w_s = 0{,}4\ mm/s$ reduce significantly. Then, consolidation is expected to start (in the permeability phase first, then effective stresses become dominant), exhibiting significantly lower velocities of $w_c = 2 \times 10^{-3}–2 \times 10^{-2}\ mm/s$.

Erodibility is investigated by analyzing the evolution of sediment concentration above the lutocline and resulting erosion rates. Critical shear for floc and mass erosion is derived from collected data. In the laboratory, remolded samples with defined initial conditions are used. Remolded samples either exhibit initial bulk densities of approx. $\rho = 1{,}065\ kg/m^3$ below structural density or they exhibit densities of approx. $\rho = 1{,}125\ kg/m^3$ above structural density. While erodibility decreases during the first 24 h in the preconsolidation phase, no such decrease is observed to happen in the same interval for suspensions with initial densities above the gelling point. Increased erosion resistance results in higher critical shear stresses and lower erosion rates. Critical shear stress for floc erosion have been observed to be below $0.1\ N/m^2$ for both natural and remolded samples, leading to erosion rates of about $4 \times 10^{-5}\ kg/(m^2 s)$ for all experiments. When sediments are freshly deposited from the water column, densities of $1{,}050–1{,}070\ kg/m^3$ are observed, exhibiting very low critical shear values for mass erosion of about $0.06\ N/m^2$, similar to the fact that the sediments are settling quite fast in this phase, the erodibility decreases and critical shear for mass erosion increases to values of $0.17\ N/m^2$. Regarding suspensions with initial densities above the gelling point, no consistent change could be observed for all the parameters investigated within a period of 24 h. Density profiles remain homogeneous, and erodibility parameters remain approx. constant with critical shear for mass erosion in the range of $0.21–0.23\ N/m^2$. The best representation of investigated natural erodibility is observed to occur when sediments in suspensions below structural density settle for about 6–10 h. Here, initial density is increased to reach the point of concentration, but critical shear for mass erosion stays below that found for suspensions created above structural density, likely because of segregation processes happening in the hindered settling phase. It is also found that the erodibility of investigated sediment suspensions above the gelling point can be represented using the Partheniades approach, while soft mud suspensions below the gelling point are better represented using the approach by Sanford and Maa.

4.2 Conclusion

The challenge of understanding the processes leading to net sedimentation and accumulation of cohesive sediments in the Weser estuary in reach of the ETM is addressed in this study. Methods and experimental facilities have been developed to investigate the bed exchange behavior of freshly deposited natural sediments in quasi *in situ* and laboratory experiments. Generated density profiles of collected, mostly undisturbed cores confirm the existence of mobile and stationary mud layers on top of a relatively dense bed. Mobile (below) and stationary (above) mud exhibit densities in the reach of the gelling point. Investigations on erodibility have shown that mobile suspensions below the gelling point settle quite fast while increasing erosion resistance at the same time. Instead, stationary suspensions above the gelling point do not settle or significantly increase erosion resistance in the considered period of 24 h after layer generation. Ultimately, the results discussed support the hypothesis formulated in *Introduction* on how cohesive sediments may accumulate in the navigational channel of an estuary. Within the turbidity zone of the Weser estuary, cohesive sediments may form a layer with concentrations exceeding gelling concentration. Extected to partly withstand a tidal cycle, the layer dampens the erosive forces of the tidal current and thus favors long-term consolidation processes in the lower part of the layer.

4.3 Limitations

The developed methods work well in the expected ranges they cover. While we are convinced to have covered the upper sediment layers with minor disturbance, it has to be proven in further campaigns that density profiles measured using the developed methodology are comparable to densities derived by other *in situ* techniques. The first comparison to low-resolution data from MBES indicates a good agreement, but further evidence is needed. The results derived from the erosion experiments are in the range of the results obtained by other studies published recently. Nevertheless, it is necessary to mention that deriving a consistent time series for SSC and erosion rates is a huge endeavor because two different measurement techniques are used. Future optimizations of the experimental facility should consider sensors covering the whole range of observed SSCs during experiments.

4.4 Outlook

As the next steps of this investigation, it is planned to fit and evaluate erosion models based on the presented dataset. Density profiles and lutocline evolution are used to derive parameters from the Gibson model by applying the approach from Merckelbach and Kranenburg (2004). In addition, in further investigations of sediment erodibility, a dynamic forcing with sinusoidal bidirectional flow comparable to tidal flow should be undertaken. The enhanced Gems presented in this study are capable of introducing such dynamic forcing so these

investigations are considered to be a consistent next step. Moreover, a further set of experiments is in progress where the erodibility is related to sediments with densities in the range of consolidated beds. The aim is to derive a single approach capable of representing the variability in erodibility of fresh sediment deposits from the Weser estuary observed in nature and the laboratory.

DATA AVAILABILITY STATEMENT

The raw data supporting the conclusion of this article can be provided upon request at the corresponding authors contact.

AUTHOR CONTRIBUTIONS

JP designed and performed the experiments, analyzed the data, and wrote the manuscript; PF and EN helped with the design of the experiments, data interpretation, and writing of the manuscript; RH assisted with data interpretation and writing of the manuscript.

FUNDING

Being part of the research project FAUST (for an improved understanding of estuarine sediment transport), this study was supported with funding from the Federal Waterways Engineering and Research Institute Germany (BAW) and with support from the (WSA) by providing ship capacities and employees. Publishing fees are funded by the Deutsche Forschungsgemeinschaft (DFG, German Research Foundation)—Projektnummer 491268466—and the Hamburg University of Technology (TUHH) in the funding program *Open Access Publishing*.

ACKNOWLEDGMENTS

The authors would like to deeply thank all the people involved in conducting the field trips and laboratory experiments. In addition, we'd like to thank the BAW for funding the research and the waterways and shipping administration in Bremerhaven for help in conducting field trips by providing capacity of ships and employees.

REFERENCES

Becker, M., Maushake, C., and Winter, C. (2018). Observations of Mud-Induced Periodic Stratification in a Hyperturbid Estuary. *Geophys. Res. Lett.* 45 (11), 5461–5469. doi:10.1029/2018GL077966

Chen, D., Zheng, J., Zhang, C., Guan, D., Li, Y., and Wang, Y. (2021). Critical Shear Stress for Erosion of Sand-Mud Mixtures and Pure Mud. *Front. Mar. Sci.* 8, 3039. doi:10.3389/fmars.2021.713039

Eberle, M., Fiedler, M., Blasi, C., König, F., Schöl, A., Schubert, B., et al. (2014). *Sedimentmanagementkonzept Tideweser-Bericht. Untersuchung im Auftrag der WSÄ Bremen und Bremerhaven. Bundesanstalt für Gewässerkunde (BfG).* Koblenz: BfG-Bericht 1794.

Gounder Krishnappan, B., Stone, M., Granger, S., Upadhayay, H., Tang, Q., Zhang, Y., et al. (2020). Experimental Investigation of Erosion Characteristics of Fine-Grained Cohesive Sediments. *Water* 12 (5), 1511. doi:10.3390/w12051511

Grabemann, I. (1992). *Die Trübungszone im Weser-Ästuar: Messungen und Interpretation. Dissertation. Universität Hamburg, Geesthacht*. Geesthacht: GKSS Forschungszentrum.

Grabowski, R. C., Droppo, I. G., and Wharton, G. (2011). Erodibility of Cohesive Sediment: The Importance of Sediment Properties. *Earth-Science Rev.* 105 (3-4), 101–120. doi:10.1016/j.earscirev.2011.01.008

Gust, G. (1989). *Method of Generating Precisely-Defined Wall Shearing stresses11.10.1989*. St. Petersburg, Florida: Applicant Hydro Data Inc.,. Application number: 419649. Patent number: US4973165.

Gust, G., and Müller, V. (1997). "Interfacial Hydrodynamics and Entrainment Functions of Currently Used Erosion Devices," in *Cohesive Sediments*, 149174.

Hesse, R. (2020). Zur Modellierung des Transports kohäsiver Sedimente am Beispiel des Weserästuars. dissertation. Hamburg: Technische Universität Hamburg, Institut für Wasserbau.

Kombiadou, K., and Krestenitis, N. (2013). "Modelling Cohesive Sediment Dynamics in the Marine Environment," in *Sediment Transport Processes and Their Modelling Applications. Croatia*. Editor M. H. G. Andrew James (InTech). doi:10.5772/51061

Kösters, F., Grabemann, I., and Schubert, R. (2018). "Die Schwebstoffdynamik in der Trübungszone des Weserästuars. Kuratorium für Forschung im Küsteningenieurwesen," in Die Küste *(86)*. zuletzt geprüft am 08.01.2020.

Kranenburg, C., and Winterwerp, J. C. (1997). Erosion of Fluid Mud Layers. I: Entrainment Model. *J. Hydraulic Eng.* 123123 (6504), 5046–5511. doi:10.1061/(asce)0733-9429(1997)123:6(504)

Krishnappan, B. G. (2000). "Modelling Cohesive Sediment Transport in Rivers. The Role of Erosion and Sediment Transport in Nutrient and Contaminent Transfer (Proceedings)," in *IAHS Publikationen*, 269–276. zuletzt geprüft am 11.03.2022.

Lange, D., Müller, H., Piechotta, F., and Schubert, R. (2008). "The Weser Estuary," in *Die Küste*. S. 275–287Online verfügbar unter Available at: https://hdl.handle.net/20.500.11970/101611, zuletzt geprüft am 04.01.2022.

Malcherek, A. (2010): *Zur Beschreibung der rheologischen Eigenschaften von Flüssigschlicken*. Die Küste (77)135–178.

Mengual, B., Hir, P., Cayocca, F., Garlan, T., and Garlan, T. (2017). Modelling Fine Sediment Dynamics: Towards a Common Erosion Law for Fine Sand, Mud and Mixtures. *Water* 9 (8), 564. doi:10.3390/w9080564

Merckelbach, L. M., and Kranenburg, C. (2004). Determining Effective Stress and Permeability Equations for Soft Mud from Simple Laboratory Experiments. *Géotechnique* 54 (9), 581–591. doi:10.1680/geot.2004.54.9.581

Papenmeier, S., Schrottke, K., Bartholomä, A., and Flemming, B. W. (2013). Sedimentological and Rheological Properties of the Water-Solid Bed Interface in the Weser and Ems Estuaries, North Sea, Germany: Implications for Fluid Mud Classification. *J. Coast. Res.* 289, 797–808. doi:10.2112/JCOASTRES-D-11-00144.1

Parchure, T. M., and Mehta, A. J. (1985). Erosion of Soft Cohesive Sediment Deposits. *J. Hydraulic Eng.* 111111 (10), 130810–131326. doi:10.1061/(ASCE)0733-942910.1061/(asce)0733-9429(1985)111:10(1308)

Partheniades, E. (1965). Erosion and Deposition of Cohesive Soils. *J. Hydraulic Div* HY1 (91), 105–139. doi:10.1061/jyceaj.0001165

Patzke, J., Hesse, R., Zorndt, A., Nehlsen, E., and Fröhle, P. (2019). *Conceptual design for investigations on natural cohesive sediments from the Weser estuary. Hg. v. INTERCOH 2019*. TU Hamburg. Istanbul.: Institut für Wasserbau. Online verfügbar unter. doi:10.15480/882.3599

Sanford, L. P., and Maa, J. P.-Y. (2001). A Unified Erosion Formulation for Fine Sediments. *Mar. Geol.* 179 (1-2), 9–23. doi:10.1016/S0025-3227(01)00201-8

Schweim, C. (2005). *Modellierung und Prognose der Erosion feiner Sedimente*. Dissertation. RWTH, Aachen: Bauingenieurwesen.

Shields, A. (1936). *Anwendung der Ähnlichkeitsmechanik und der Turbulenzforschung auf die Geschiebebewegung*. Berlin: Technische Hochschule BerlinPreußische Versuchsanstalt für Wasserbau.

Torfs, H., Mitchener, H. J., Huysentruyt, H., and Toorman, E. A. (1996). Settling and Consolidation of Mud/sand Mixtures. *Coast. Eng.* 2927 (1-2)–45. doi:10.1016/S0378-3839(96)00013-0

United States Department of Agriculture (1987). *Soil Mechanics Level 1-Module 3. USDA Textural Classification-Study Guide*. Washington, D. C: Soil Conservation Service.

Van Rijn, L. C. (2020). Erodibility of Mud–Sand Bed Mixtures. *J. Hydraul. Eng.* 146 (1), 4019050. doi:10.1061/(ASCE)HY.1943-7900.0001677

Van Rijn, L. C. (2016). Fluid Mud Formation. Online verfügbar unterzuletzt geprüftAvailable at: www.leovanrijn-sediment.com.

Van Rijn, L. C. (1993). *Principles of Sediment Transport in Rivers, Estuaries and Coastal Seas. 1 Band*. Utrecht: Aqua Publications, zuletzt geprüft am 03.09.2018.

Whitehouse, R. J. S., Soulsby, R. L., Spearman, J., Roberts, W., and Mitchener, H. J. (2000). *Dynamics of Estuarine Muds. A Manual for Practical Applications*. London: Telford.

William, H., McAnally und Ashish, J., and Mehta, Hg. (2000). "Coastal and Estuarine Fine Sediment Processes, Bd. 1st Edn, 3 (Amsterdam: Elsevier Science), v–viii. doi:10.1016/s1568-2692(00)80107-2

Winterwerp, J. C., Christian, J., van Kessel, T., Dirk, S., van Prooijen, et al. (2021). *Fine Sediment in Open Water*. 55. World Scientific.

Winterwerp, J. C., and van Kesteren, W. G. M. (2004). "9 - Erosion and Entrainment," in *Johan Christian Winterwerp und Walther van Kesteren (Hg.): Introduction to the Physics of Cohesive Sediment in the Marine Environment*. Bd. 56: Elsevier (Developments in Sedimentology), S. 343–381. Online verfügbar unter Available at: http://www.sciencedirect.com/science/article/pii/S0070457104800104.

Work, Paul. A., and Schoellhamer, D. H. (2018). *Measurements of Erosion Potential Using Gust Chamber in Yolo Bypass Near Sacramento, California*. Reston, Virginia: Hg. v. US Geological Survey, US Department of the Interior und California Department of Water Resources. US Geological Survey. zuletzt geprüft am 22.08.2019.

Wu, W., Perera, C., Smith, J., and Sanchez, A. (2018). Critical Shear Stress for Erosion of Sand and Mud Mixtures. *J. Hydraulic Res.* 56 (1), 96–110. doi:10.1080/00221686.2017.1300195

Conflict of Interest: The authors declare that the research was conducted in the absence of any commercial or financial relationships that could be construed as a potential conflict of interest.

frontiers | Frontiers in Earth Science

TYPE Original Research
PUBLISHED 02 September 2022
DOI 10.3389/feart.2022.921529

OPEN ACCESS

EDITED BY
Daniel R. Parsons,
University of Hull, United Kingdom

REVIEWED BY
Quanzhong Guan,
Chengdu University of Technology, China
Zhiye Gao,
China University of Petroleum, China

*CORRESPONDENCE
Yao Du,
404298823@qq.com

SPECIALTY SECTION
This article was submitted to Sedimentology, Stratigraphy and Diagenesis, a section of the journal Frontiers in Earth Science

RECEIVED 16 April 2022
ACCEPTED 09 August 2022
PUBLISHED 02 September 2022

CITATION
Du Y, Wang X, Zhao R, Chen C, Wen S, Tang R, Mo Q, Zhang J, Zhang Y and He S (2022), Controlling factors of organic matter enrichment in continental shale: A case study of the Jurassic Da'anzhai member in the Sichuan Basin.
Front. Earth Sci. 10:921529.
doi: 10.3389/feart.2022.921529

Controlling factors of organic matter enrichment in continental shale: A case study of the Jurassic Da'anzhai member in the Sichuan Basin

Yao Du[1,2,3]*, Xingzhi Wang[1,3], Rongrong Zhao[2], Chi Chen[2], Siying Wen[2], Ruifeng Tang[2], Qianwen Mo[2], Jizhi Zhang[2], Yu Zhang[2] and Shuo He[4]

[1]State Key Laboratory of Oil and Gas Reservoir Geology and Exploitation, Southwest Petroleum University, Chengdu, China, [2]Exploration Division of PetroChina Southwest Oil and Gasfield Company, Chengdu, China, [3]School of Geoscience and Technology, Southwest Petroleum University, Chengdu, China, [4]Research Institute of Geologic Exploration and Development, Chuanqing Drilling and Exploration Corporation, CNPC, Chengdu, China

The continental lake basin is a favorable accumulation area of shale oil and gas; however, the organic matter enrichment regularity in continental lake facies is still controversial, which hinders the exploration of continental shale oil and gas in the Sichuan Basin. In this study, the relationship between a sedimentary environment and organic matter enrichment of continental shale was analyzed by petrology and organic and inorganic geochemistry tests of 153 samples. The results show that different lithologic associations in the Da'anzhai member have different contents of organic matter. Among them, the TOC content of unit II (shale-limestone interbed) is the highest, mainly, type II kerogen, followed by unit III (shale clip shell limestone belts), mainly, type III kerogen. Geochemical indicators show that different paleoenvironmental factors play different leading roles in organic matter enrichment in different periods of the Da'anzhai member. Unit II is deposited in an arid environment with less fresh water supply; therefore, the water cycle is hampered. Due to the effect of salinity stratification, anoxic water was formed, which was beneficial to the preservation of algae and plankton in the lake basin, resulting in the formation of type II_2 kerogen. Unit III is deposited in a semi-humid and semi-arid climate, and its water is in an oxidizing environment. Precipitation and river runoff increase the input of terrigenous debris and higher plants to form type III kerogen. This study has guiding significance for the cause of organic matter enrichment in the Da'anzhai member and the prediction of favorable zones.

KEYWORDS

lacustrine shale, paleoenvironment, organic matter enrichment model, sichuan basin, Da'anzhai member

1 Introduction

Organic shales include mud shale formations, thin layers of tight sandstone, carbonate rocks, and even volcanic rocks (Zhang et al., 2012). Organic shales not only record the evolution of ancient life, paleoclimate, evolution characteristics of paleoenvironment such as lakes and oceans (Loucks and Ruppel, 2007) but are also the carrier of mineral resources such as oil and gas, which has important economic benefits. Marine shale has become the focus of exploration, and lacustrine shale has great exploration potential. However, no progress has been made in the oil and gas exploration of continental shale in the Sichuan Basin due to people's different opinions on the enrichment patterns of organic matter (Jiao, 2019; Zou et al., 2019; Hu et al., 2021).

The main arguments of domestic and foreign scholars on the main factors of organic matter enrichment can be summarized as "organic matter production," "decomposition and preservation," and "dilution" (Demaison and Moore, 1980; Pedersen and Calvert, 1990; Zhang et al., 2016). Around these three models, many scholars have studied lithology difference (Mayer et al., 1985), deposition rate (Calvert, 1987), terrigenous debris injection, tectonic activity, and climate change (Bluth and Kump, 1994; Huang et al., 2020; Xu et al., 2021), and even some special geological events, such as marine transgression and anoxia to study the factors of shale organic matter enrichment. The paleosedimentary environment controls the primary productivity and preservation conditions of the basin to a certain extent, and sedimentary geochemistry records the characteristics and evolution information of the paleoenvironment. Therefore, major and trace elements are often used for paleoenvironmental reconstruction (Tribovillard et al., 2006, 2012). From the previous studies on continental shale, many research results focused on lacustrine environments such as drought, salinization, and wetting, and achieved many exploration results (Wei et al., 2012; Huang et al., 2020; Wang et al., 2021). However, the study of continental shale in the Sichuan Basin is very weak.

In December 2020, China National Petroleum Company (CNPC) deployed Well C, a shale oil exploration well in the Sichuan Basin, and carried out coring in the Da'anzhai member; for this set of cores, we conducted intensive sampling, which provides the possibility for the detailed study of the covariation of sedimentary environment evolution and organic matter enrichment patterns. In addition, we analyzed paleoclimate, paleo-weathering, detrital inflow, paleo-salinity, and paleo-redox conditions based on organic and inorganic geochemistry, to clarify the relationship between a lake sedimentary environment, evolution, and organic matter enrichment regularity in the Da'anzhai member.

2 Regional geological background

The Sichuan Basin is a foreland and craton superimposed basin on the northwest side of the Yangzi quasi platform. It has become a plate or craton basin in western South China since the new Proterozoic era (Sinian) and lasted until the late Middle Triassic. Through the Indosinian orogenic movement, the Sichuan Basin has developed into a new foreland basin since the late Triassic, forming six structural areas bounded by the Longquan Mountain deep fracture and Huaying Mountain deep fracture (Li and He, 2014; Li et al., 2020) (Figure 1A). Sedimentary facies studies show that there are three ancient continents around the Sichuan Basin in the late Triassic, namely, Longmenshan, Daba Mountain, and Kangdian (Liu, 1993). Under this paleotectonic-sedimentary background, the Jurassic continued to deposit based on the late Triassic lake basin and developed into a delta-inland lake. The inland lake includes sedimentary micro-facies such as lake slope mud, semi-deep lake mud, gravity flow, and debris beach (Figure 1B); its sedimentation center is distributed from central Sichuan to eastern Sichuan, containing bivalves and plant and alga fossils (Meng et al., 2005; Tong et al., 2016; Deng et al., 2017).

The Da'anzhai member is in the Toarcian Stage, Ziliujing group, in the late early Jurassic. The sedimentary period of the Da'anzhai member is in the marine regression after the global marine transgression. The long-term lake regression in the sedimentary period of the Da'anzhai member is consistent with the change in the global sea level in time, which corresponds to a complete regional lake transgression–regression depositional cycle (Zheng, 1998; Liu et al., 2020). According to the fluctuation of the lake level, the lake level of units IV–III rises, the top of unit III is on the maximum flooding surface, and the whole units II–I are in the process of lake regression (Figure 1B).

3 Experimental methods

3.1 Sample analysis

This analysis includes 153 samples from Well A, Well B, Well C, and Well D. The analytical item of the 111 samples from wells A, B, and D is rock slice and the analytical item of Well C is rock-eval pyrolysis and major and trace elements. A total of 42 samples from Well B were ground into 80 mesh and less than 200 mesh powder separately for chemical analysis. The 80 mesh samples were used for the analysis of total organic carbon (TOC) and rock-eval pyrolysis (S_1, S_2, and Tmax). The TOC was measured by the LECO CS230 carbon and sulfur analyzer, and the S_1, S_2, and Tmax data were measured by the oil and gas show and evaluation unit, YQ-VIIA. This work was completed in the analysis and experimental center of the Institute of Exploration and Development, Southwest Oil and Gas Field Company. Samples of less than 200 mesh were used for the analysis of major and trace elements. An EDX5500H energy scattering X-ray fluorescence spectrometer was used to detect the major and trace elements, which was completed in Chuanqing

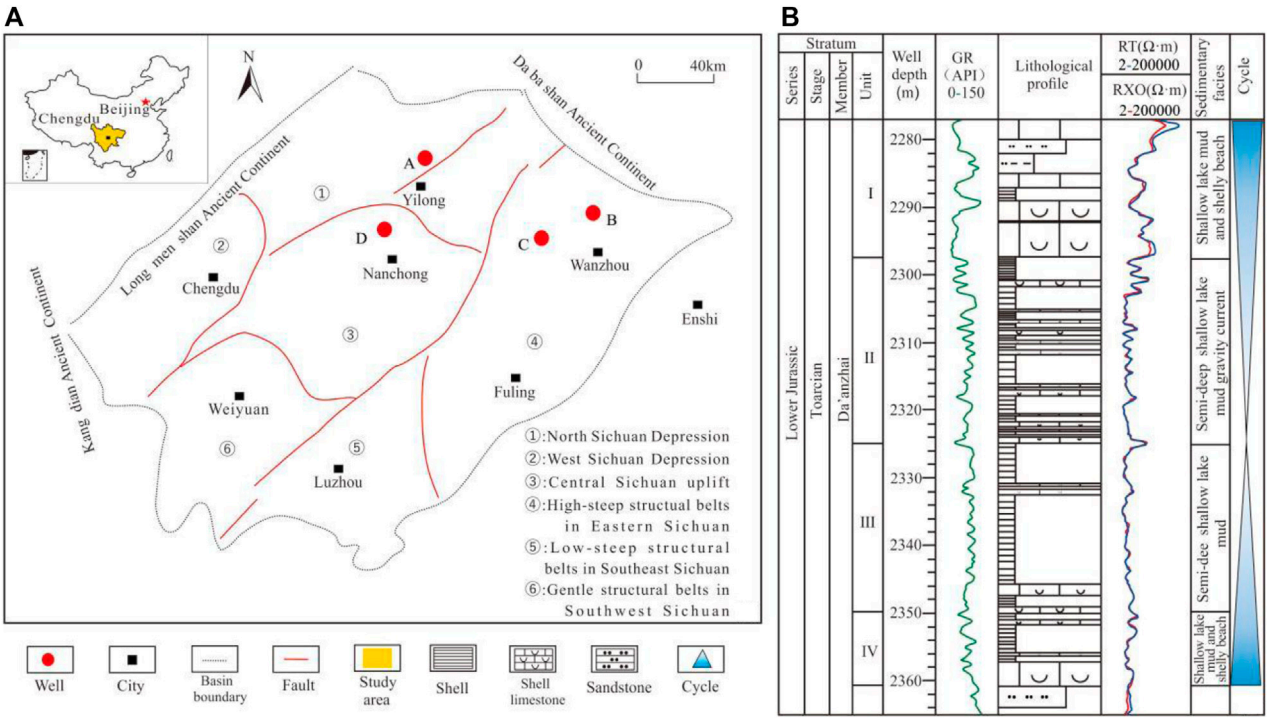

FIGURE 1
Structural location of the research area **(A)** and formation histogram of well C **(B)**.

Drilling Geological Exploration and Development Research Institute (Table 1). Mineral content was obtained by lithology scanning (LITHOSCANNER) logging of Schlumberger Company, and the inline resolution of this equipment was 18 feet, and the detection depth was 9 feet.

3.2 Data processing

Using the content of post-Archean Australian shale (PAAS) as the reference standard, if the content of an element in the sediment is significantly higher than the average shale content, it indicates that this element is of authigenic enrichment; otherwise, it is relative depletion (Taylor and Mclennan, 1985). Some biogenic carbonate minerals can dilute authigenic minerals in sediments, which can be reduced by Al standardization (Wedepohl, 1971; Tribovillard et al., 2006). The enrichment factor (EF) can quantitatively analyze the enrichment degree of an element (Turekian and Wedepohl, 1961; Wedepohl, 1971).

$$X_{EF} = (X/Al)_{sample} / (X/Al)_{average\ shale} \quad (1)$$

.

The trace element X is of more enrichment when X_{EF} element >1; the trace element X is relative depletion when X_{EF} element <1 (Wedepohl, 1971; Tribovillard et al., 2006).

Ba biology (Ba_{bio}) is related to phytoplankton decay, which has been proved to be a reliable indicator of paleoproductivity (Dymond et al., 1992).

$$Ba_{bio} = Ba_{sample} - (Al_{sample} \times Ba/Al_{alu}) \quad (2)$$

Ba_{sample} and Al_{sample} are the quality fraction of the measured samples. Ba/Al_{alu} represents the terrestrial input part of sediments, and 0.0075 is generally used to calculate the Ba biological content (Dymond et al., 1992).

4 Results

4.1 Sedimentary characteristics

Sedimentology research plays a strong indicative role in clarifying the water environment of the lake basin. The author analyzes the petrological characteristics and paleontology of the Da'anzhai member to clarify the water environment of the Da'anzhai member.

4.1.1 Unit IV

Lithologic associations are interbedded with micritic shell limestone and thin shale (Figure 2A). Lithology scanning showed

TABLE 1 Measured values of TOC and major elements in Da'anzhai shale of well C [PAAS data from Taylor and Mclennan (1985)].

Stratum	Depth (m)	TOC	Fe_2O_3	Al_2O_3	SiO_2	K_2O	CaO	TiO_2	MgO	P_2O_5	MnO	Na_2O	Ba	V	Sr	Cr	Th	U	Cu	Co	Ni	Mo
		%	%	%	%	%	%	%	%	%	%	%	ppm	ppm	ppm	ppm	ppm	ppm	ppm	ppm	ppm	ppm
PAAS			3.05	9.97	27.91	1.92	23.87	0.63	0.69	0.72	0.07	0.11	648.01	158.10	377.45	64.30	6.03	1.60	23.51	6.49	62.45	0.35
I	2278		3.09	11.55	39.95	1.88	22.52	0.57	0.54	0.38	0.12	0.10	526.85	109.80	202.83	81.56	7.05	1.63	19.53	6.89	7.29	0.41
	2280	0.32	3.79	14.15	45.79	2.08	18.19	0.58	0.99	0.32	0.07	0.16	768.11	200.98	206.53	126.24	9.75	1.96	28.44	8.99	32.56	0.42
	2282	0.49	4.95	15.90	54.14	2.58	9.63	0.99	1.35	0.26	0.07	0.27	330.86	184.15	503.83	81.18	8.58	1.89	39.66	14.61	40.73	0.50
	2284	0.28	4.82	14.72	43.96	2.54	15.67	0.89	1.12	0.36	0.05	0.23	436.69	104.52	292.61	25.73	0.81	0.88	32.30	13.27	13.94	0.42
	2286		1.82	5.36	15.98	1.39	40.71	0.33	0.12	0.53	0.06	0.09	471.31	106.16	416.50	42.11	7.53	1.75	10.45	0.00	0.00	0.27
	2288		2.84	9.09	28.28	2.04	28.05	0.49	0.23	0.48	0.05	0.10	603.46	107.06	260.96	71.39	8.16	1.96	21.71	4.70	15.51	0.40
	2290	0.53	4.82	14.76	42.78	2.59	15.89	0.62	1.14	0.33	0.06	0.16	464.61	67.67	275.79	47.73	4.94	1.54	28.02	10.96	38.78	0.42
	2292	0.57	3.02	10.90	31.52	2.06	27.23	0.40	0.58	0.43	0.04	0.10	401.92	48.65	345.30	31.80	4.49	1.35	20.43	5.52	11.07	0.37
	2294		2.70	8.41	24.70	1.91	32.47	0.28	0.19	0.48	0.03	0.09	372.71	41.68	472.14	16.09	2.09	1.06	18.25	2.78	9.02	0.32
	2296		1.66	5.36	15.70	1.26	40.07	0.17	0.37	0.53	0.01	0.09	383.59	90.43	474.06	39.99	4.08	1.35	10.83	0.00	0.00	0.27
II	2298	1.47	2.71	7.61	21.00	1.96	36.09	0.38	0.28	0.50	0.02	0.09	1004.50	245.15	437.45	73.82	3.93	1.42	20.32	3.25	7.18	0.32
	2300	1.82	2.79	10.10	28.81	2.19	26.32	0.83	0.76	0.47	0.04	0.10	593.35	109.60	469.41	39.38	4.50	1.41	21.05	3.95	13.02	0.34
	2302	2.50	2.67	9.52	27.53	2.15	28.12	0.43	0.63	0.48	0.03	0.10	672.93	97.80	515.34	40.14	4.77	1.37	19.32	2.91	3.34	0.33
	2304	1.75	2.70	9.18	25.82	2.07	29.85	0.42	0.85	0.48	0.03	0.10	587.26	85.55	519.84	40.82	4.40	1.51	16.56	3.28	7.39	0.34
	2306	1.39	2.79	9.61	28.12	2.06	28.58	0.38	0.90	0.48	0.04	0.10	527.76	73.25	512.76	38.47	4.26	1.39	17.29	4.01	2.85	0.34
	2308	0.79	2.78	8.94	26.08	1.95	31.01	0.35	0.65	0.49	0.04	0.09	669.28	125.88	531.39	62.97	4.59	1.48	16.70	3.86	12.59	0.34
	2310	1.05	2.96	10.53	29.14	2.10	27.68	0.51	0.77	0.47	0.04	0.10	645.99	120.70	541.34	51.44	5.43	1.60	20.53	5.24	16.97	0.34
	2312	0.89	2.96	10.71	29.67	2.10	27.40	0.51	0.78	0.46	0.04	0.10	652.84	133.65	479.56	48.56	3.24	1.27	22.85	5.32	16.38	0.35
	2314	1.50	2.70	8.65	24.89	1.91	32.60	0.47	0.50	0.48	0.04	0.10	692.10	125.73	541.35	46.21	3.90	1.56	17.29	3.00	2.31	0.29
	2316	1.24	2.82	8.59	25.54	1.94	30.60	0.46	0.63	0.55	0.04	0.09	522.89	78.63	571.10	32.78	3.31	1.26	19.29	4.08	5.88	0.31
	2318	1.61	2.67	7.74	22.40	1.76	34.51	0.32	0.23	0.57	0.03	0.09	583.30	84.50	595.70	32.71	3.38	1.38	16.49	2.61	10.10	0.29
	2320	1.47	2.72	7.94	22.03	1.85	33.79	0.33	0.21	0.56	0.02	0.09	637.85	103.32	552.32	34.53	3.33	1.32	17.42	3.09	0.00	0.30
	2322	1.54	2.67	6.67	19.61	1.52	36.25	0.38	0.00	0.64	0.02	0.09	900.64	185.29	581.71	54.78	2.74	1.21	18.12	3.03	10.48	0.29
	2324	/	2.74	6.82	19.99	1.51	35.69	0.58	0.00	0.64	0.03	0.09	1134.52	289.17	501.35	75.79	4.75	1.43	18.50	3.75	11.29	0.27
	2326	/	3.05	8.10	23.64	1.81	30.51	0.98	0.20	0.57	0.04	0.09	639.22	129.22	303.83	67.75	7.77	1.76	20.70	6.23	13.02	0.31
III	2328	0.84	4.21	14.36	37.18	2.50	19.86	0.61	1.12	0.39	0.04	0.12	568.01	92.42	260.07	59.41	7.04	1.64	28.54	10.17	25.95	0.41
	2330	0.86	3.94	14.70	37.26	2.46	21.36	0.51	1.14	0.37	0.03	0.14	728.16	146.20	391.77	63.88	6.22	1.54	25.99	9.19	27.96	0.39
	2332	0.98	3.40	13.15	33.74	2.26	23.54	0.61	0.96	0.43	0.03	0.11	630.17	108.90	372.25	64.79	6.54	1.67	22.50	7.45	17.30	0.37
	2334	0.32	4.02	14.30	36.31	2.38	21.43	0.54	1.06	0.41	0.03	0.13	641.28	109.35	319.03	66.01	7.51	1.73	33.65	9.33	25.52	0.40
	2336	0.59	4.52	15.00	38.61	2.61	18.72	0.57	1.22	0.39	0.03	0.15	581.78	105.12	324.52	64.95	8.36	1.88	31.86	11.07	32.18	0.39
	2338	0.47	4.64	15.55	41.00	2.80	16.51	0.57	1.32	0.37	0.03	0.16	606.81	100.14	291.06	75.26	7.82	1.94	32.68	11.45	33.15	0.41

(Continued on following page)

10.3389/feart.2022.921529

10.3389/feart.2022.921529

TABLE 1 (*Continued*) Measured values of TOC and major elements in Da'anzhai shale of well C [PAAS data from Taylor and Mclennan (1985)].

Stratum	Depth (m)	TOC	Fe_2O_3	Al_2O_3	SiO_2	K_2O	CaO	TiO_2	MgO	P_2O_5	MnO	Na_2O	Ba	V	Sr	Cr	Th	U	Cu	Co	Ni	Mo
		%	%	%	%	%	%	%	%	%	%	%	ppm	ppm	ppm	ppm	ppm	ppm	ppm	ppm	ppm	ppm
	2340	0.36	4.84	15.92	41.84	2.92	15.99	0.59	1.34	0.35	0.04	0.18	557.21	154.47	384.59	71.24	5.98	1.53	34.27	12.12	35.15	0.42
	2342	0.49	4.22	13.30	34.30	2.23	24.27	0.97	0.97	0.49	0.05	0.16	532.33	146.25	384.03	59.10	6.20	1.51	27.75	9.39	28.17	0.35
	2344	/	4.15	12.99	33.81	2.21	24.64	0.98	0.93	0.48	0.05	0.14	497.25	67.37	214.59	56.37	7.96	1.89	23.81	9.35	23.09	0.37
	2346	/	3.97	15.40	40.70	2.59	18.77	0.46	1.35	0.36	0.03	0.15	515.28	68.32	302.17	39.91	5.70	1.54	30.47	9.16	214.59	0.43
	2348	0.15	3.01	12.54	32.49	2.15	25.78	0.39	0.95	0.46	0.03	0.10	541.31	80.72	394.75	37.11	4.54	1.48	22.53	6.09	302.17	0.37
IV	2350	0.25	2.80	9.50	26.09	1.93	31.71	0.36	0.41	0.53	0.03	0.10	377.50	91.67	404.44	50.15	6.19	1.58	22.40	4.12	394.75	0.34
	2352	0.23	3.54	13.51	35.34	2.29	21.94	0.46	1.01	0.44	0.04	0.11	3556.16	1804.21	641.61	334.23	1.62	0.84	28.75	8.58	404.44	0.38
	2354	/	3.61	10.56	32.40	2.19	14.89	5.26	0.94	0.48	0.12	0.16	611.68	131.71	231.92	80.34	7.46	1.86	27.16	8.61	641.61	0.15
	2356	0.43	4.44	15.30	40.18	2.66	19.18	0.66	1.31	0.36	0.04	0.16	719.41	166.17	253.67	62.44	4.45	1.28	34.31	10.29	40.89	0.41
	2358	/	2.83	11.44	29.63	2.02	29.46	0.61	0.92	0.45	0.04	0.10	719.41	166.17	253.67	62.44	4.45	1.28	25.33	4.33	11.94	0.34

that the calcite content was the highest, with an average of 34.16%, followed by illite and chlorite, accounting for 18.99 and 9.02%, respectively (Figure 3), containing quartz particles (Figure 2B, Figure 3). The organisms are mainly single bivalves (Figure 2A), indicating shallow water deposition in this period.

4.1.2 Unit III

Lithological associations are pure black mud shale clip shell limestone belts (Figure 2C). Lithology scanning shows that the illite content is the highest, reaching 29.35%, followed by quartz content, accounting for 26.30%, and also contains pyrite (Figure 3). Most of the bio-particles are single ostracods (Figure 2D) and rare bivalve and gastropod debris fossils, showing that the lithologic association is a typical product of deep-water deposition and higher plants can be seen at times (Figure 2E).

4.1.3 Unit II

Lithologic associations are the interbedded strata of shale and shell limestone. Lithology scanning showed that the quartz content reached 35.72% and chlorite and illite content were similar, accounting for 23.85 and 22.05%, respectively (Figure 3). Bio-particles are mainly deformed bivalves (Figure 2F), usually of plastic deformation. The trace of algae (Figure 2G) (Figure 2H), indicates frequent biological activities in local layers, and sufficient food supply and high oxygen content in the sedimentary environment (Zhang et al., 2018).

4.1.4 Unitl

Lithologic associations are interbedded with micritic shell limestone and thin shale (Figure 2I). Lithology scanning shows that the calcite content reaches 44.97% and quartz content reaches 28.01% (Figure 3). The bivalve fragments of this layer are in the majority (2i), indicating that the shallow water sedimentary environment is the result of the long-term decline of the lake level in the late deposition of the Da'anzhai member.

4.2 Total organic carbon and organic matter type

TOC varies obviously in the vertical direction of the Da'anzhai member, with a distribution range of 0.15–2.5% and an average of 0.90%. The TOC in unit II is the highest, ranging from 0.79–2.5%, with an average of 1.46%, while that in unit IV is the lowest, ranging from 0.23–0.43%, with an average of 0.30%. The TOC in units I and III is moderate (Figure 4). It is worth noting that the TOC lower limit value of the effective source rock of lacustrine shale has not yet been unified at present, and CNPC has limited the effective source rocks for shale oil exploration in the Sichuan Basin to 1% (Zou et al., 2019; Zhao et al., 2020). Rock pyrolysis analysis showed that S_1 content is between 0.03 and 2.42 mg/g, with an average value of 0.65 mg/g,

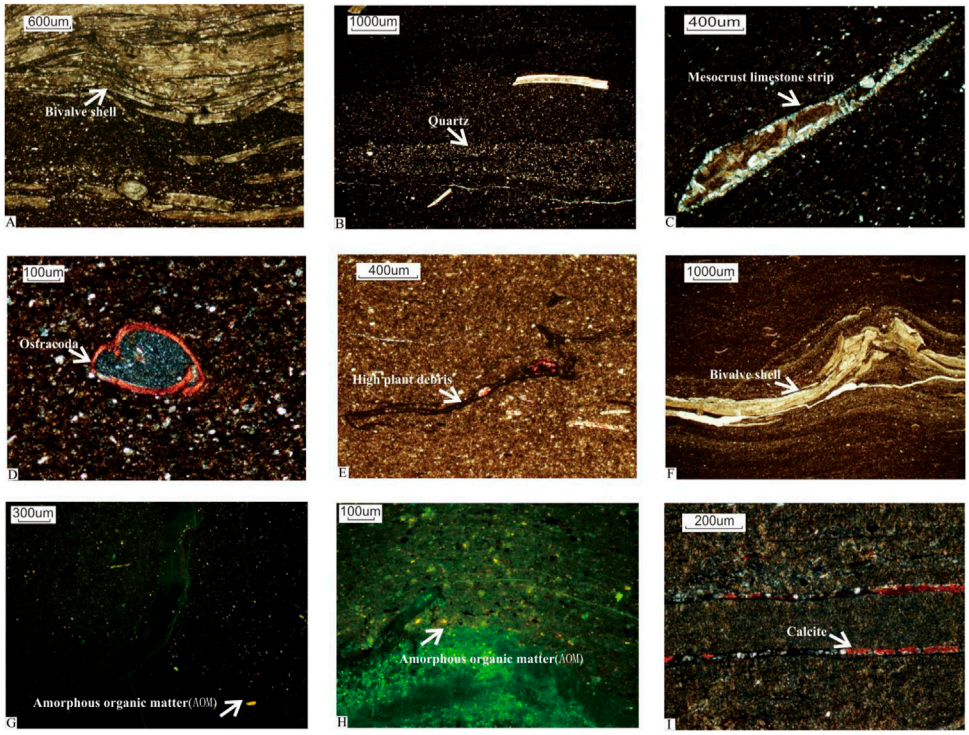

FIGURE 2
Micrographs of the Da'anzhai member **(A)** interbedded shale and limestone, bivalve shell, 3675.34 m, well A; **(B)** silt-bearing shale, 3672 m, well A; **(C)** pure black mud shale clip shell limestone belts, 3637.55 m; **(D)** silt-bearing calcareous mudstone, shale, ostracod, 3639.18 m, well A; **(E)** grapholith, higher plants, 3667.97 m, well A; **(F)** shale, bivalve shell, 1745.9 m, well B; **(G)** shale, amorphous organic matter (algae), 2432 m, well D; **(H)** shale, amorphous organic matter (algae), 2466 m, well D; **(I)** interbedded shale and limestone, 1720.99 m, well B

and S_2 content is between 0.12 and 3.12 mg/g, with an average value of 0.95 mg/g. By analyzing the relationship between Tmax and the hydrogen index, it can be found that the organic matter types in the Da'anzhai member are mainly type II_2 and type III with one sample distributed in zone II_1 (Figure 5A). In terms of the relationship between S_1 and TOC, in units IV–III and unit I, S_1 increases slowly with the increase in the TOC, indicating that type III kerogen is the main source of unit IV, unit III, and unit I, reflecting the source of higher terrestrial plants, while type II_2 kerogen is the main source of unit II (Figure 5B), reflecting the source of lower plankton.

4.3 Major elements

As shown in Table 1, the main enrichment components in the Da'anzhai member, the study area, are Fe_2O_3, Al_2O_3, SiO_2, K_2O, CaO, TiO_2, MgO, P_2O_5, and other major elements. Among them, SiO_2 is the most important component, ranging from 15.70–58.86%, with an average of 34.16%, followed by CaO, ranging from 3.79–40.71%, with an average of 23.80%, and Al_2O_3 is the lowest, ranging from 5.36–17.22%, with an average of 11.82%, while K_2O, TiO_2, MgO, P_2O_5, and MnO are all lower, with an average of less than 1%. Obviously, there are differences in the contents (average values) of major elements in different strata. There are more illite and chlorite in unit IV, and the content of Al is higher. There are more pyrite and quartz in the unit III, and the content of Fe and Si is higher. Frequent alternation of shale and limestone in unit II leads to higher Ca content, while more quartz and calcite particles and higher Si and Ca content in unit I (Table 1; Figure 3). Compared with PAAS (Turekian and Wedepohl, 1961), CaO, Fe_2O_3, TiO_2, and P_2O_5 are enriched in units I-IV of the Da'anzhai member, while SiO_2, K_2O, MgO, K_2O, and MnO are relatively depleted (Figure 6).

4.4 Trace elements

According to the results of this experiment, trace elements such as Ba, V, Cr, Th, U, Sr, Cu, Co, Ni, and Mo are mainly used to characterize the evolution of the paleoenvironment. Trace element contents (average values) in the Da'anzhai member showed significant variation, with Ba ranging from 1.63–3556.16 ppm (623 ppm), V from 1.74–1804.21

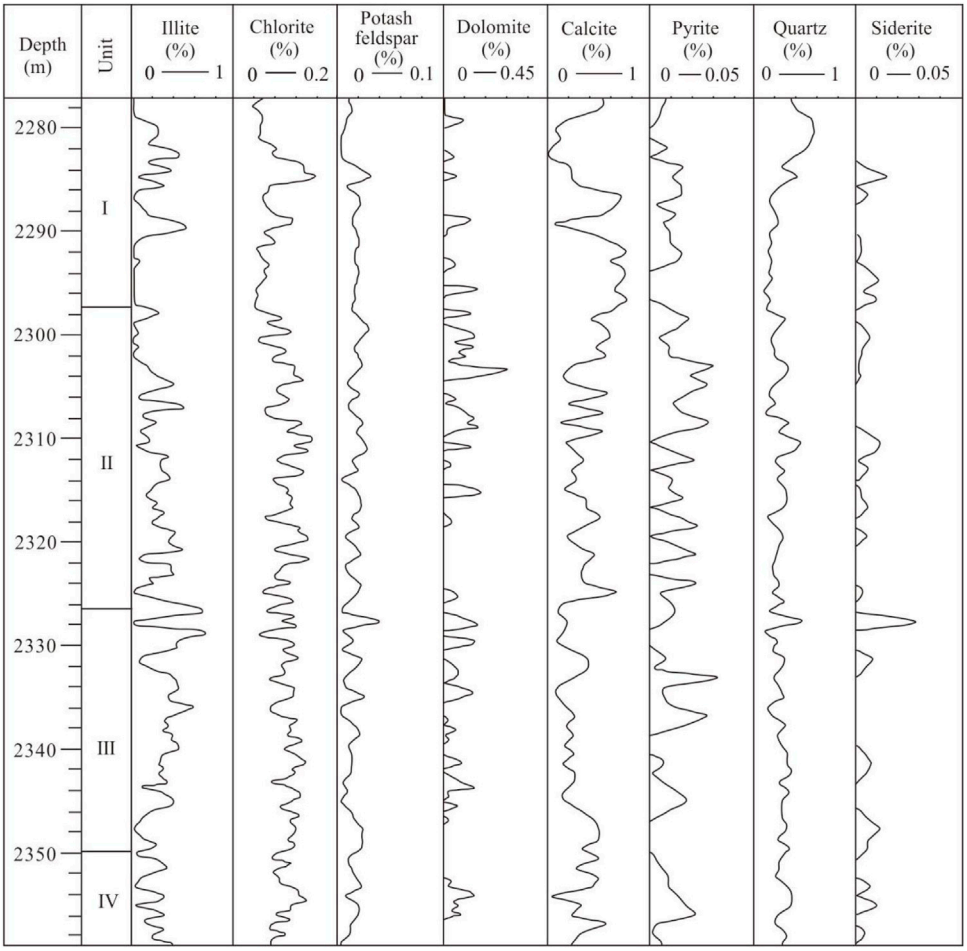

FIGURE 3
Mineral content in the Da'anzhai member of well C.

(687.21 ppm), Cr from 0.98–334.23 (59.00 ppm), Th from 0.64–12.00 ppm (5.26 ppm), U from 0.24–3.70 ppm (1.50 ppm), Sr from 1.91–641.61 ppm, Cu from 0.74–45.00 ppm, Co from 0.48–19.00 ppm (6.42 ppm), Ni from 1.30–641.61 (58.91ppm), and Mo from 0.06–2.6 ppm (0.39 ppm). Compared with PAAS (Turekian and Wedepohl, 1961), the 10 trace elements cited here are depleted in unit I; Ba, V, and Sr are faintly enriched in unit II, while in unit IV only V and Ni are enriched, and other elements are depleted (Figure 6).

5 Discussion

5.1 Paleoclimate

Climate, the main cause of the changes in the depositional environment, mainly affects parent rock weathering, sediment erosion and transport, and terrigenous detrital supply. Sr/Cu can be used to evaluate paleoclimate conditions. For arid and hot climates, the Sr/Cu ratio is above 5, while for warm and humid climates, the Sr/Cu ratio is between 1 and 5 (Turekian and Wedepohl, 1961; Moradi et al., 2016). This experiment shows that the ratio of Sr/Cu in the Da'anzhai member is greater than 5, which reflects that the whole Da'anzhai member is arid and hot. However, Sr may be quite abundant in continental lake basins (Wu et al., 2021), and the paleoclimate index calculated by Sr/Cu is larger than the actual one. Therefore, the conclusion of Sr/Cu may be more arid than the actual one.

Considering that Fe, Mn, Cr, Ni, V, and Co are generally enriched under humid conditions, while Ca, Mg, Sr, Ba, K, and Na are accumulated in an arid environment, Moradi et al. (2016) used C =Σ (Fe + Mn + Cr + Ni + V + Co)/Σ (Ca + Mg + Sr + Ba + K + Na) to characterize paleoclimate. C values of 0.6–0.8, 0.4–0.6, and 0.2–0.4 represent semi-humid, semi-arid and semi-humid, and semi-arid climates, respectively, while C values above 0.8 or below 0.2 reflect humid and arid paleoclimate environments, respectively. According to the change in the C value, the climate

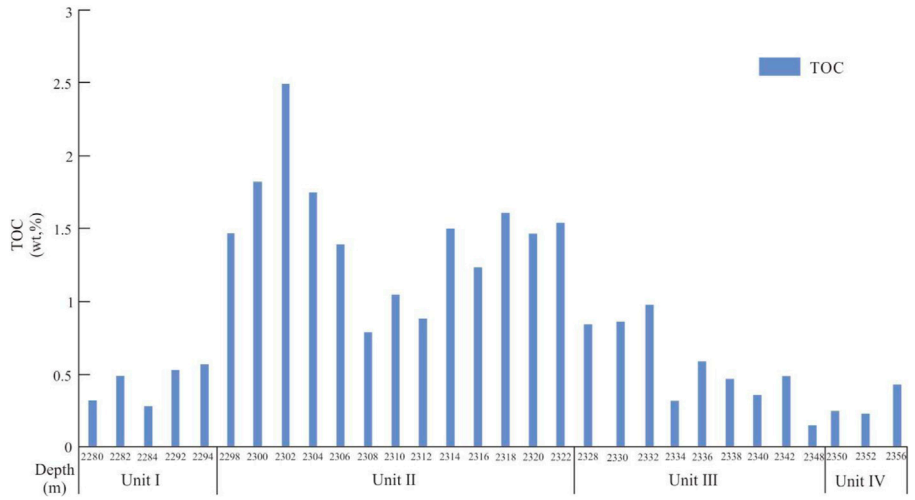

FIGURE 4
TOC distribution map in the Da'anzhai member of well C.

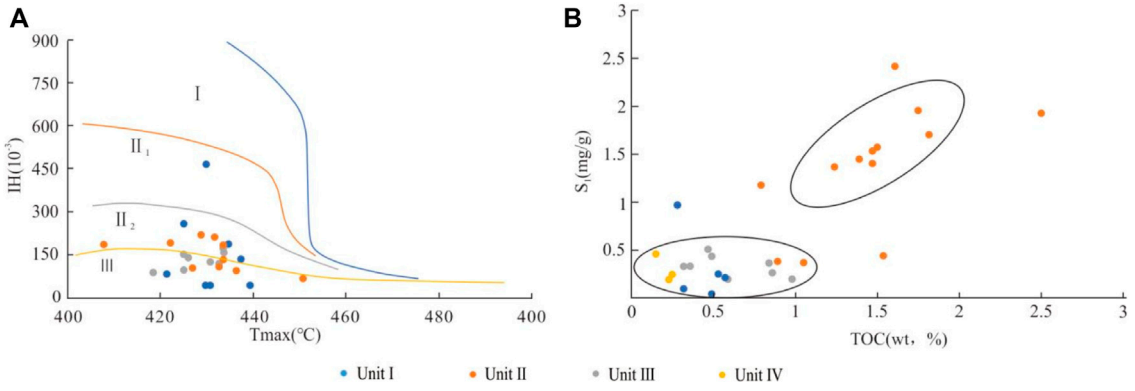

FIGURE 5
(A) Tmax-HI indicates the organic types in the Da'anzhai member; **(B)** S_1 is positively correlated with TOC.

of units IV–III in the study area is in the process of semi-humid to semi-arid, the climate of unit II becomes arid, and the climate of unit I gradually becomes humid from arid (Figure 7). Previous studies have shown that the relatively humid environment is beneficial to the development of higher plants (Jinhua et al., 2018), which is consistent with the observation of the higher plants in unit III in this study (Figure 2E).

On the whole, the TOC has a negative correlation with the C value, indicating that organic matter is enriched under drought conditions (Figure 8A). From the relationship between the TOC and C values of each unit (Figure 8B), the correlation between TOC and C values is quite different in different sedimentary periods. The enrichment degree of organic matter in unit II is higher than that in other periods, but there is no correlation between TOC and C values in unit II. It is inferred that the drought condition is not the only factor leading to organic matter enrichment in this period.

5.2 Paleoweathering

The chemical index of alteration (CIA) is an index indicating the degree of chemical weathering, which is affected by climate. A warm and humid climate will lead to stronger weathering and higher CIA value (Nesbitt and Young, 1982). CIA = {x (Al_2O_3)/[x (Al_2O_3) + x (CaO*) + x (Na_2O) + x (K_2O)]} × 100. The unit for each of the aforementioned main components is the number of

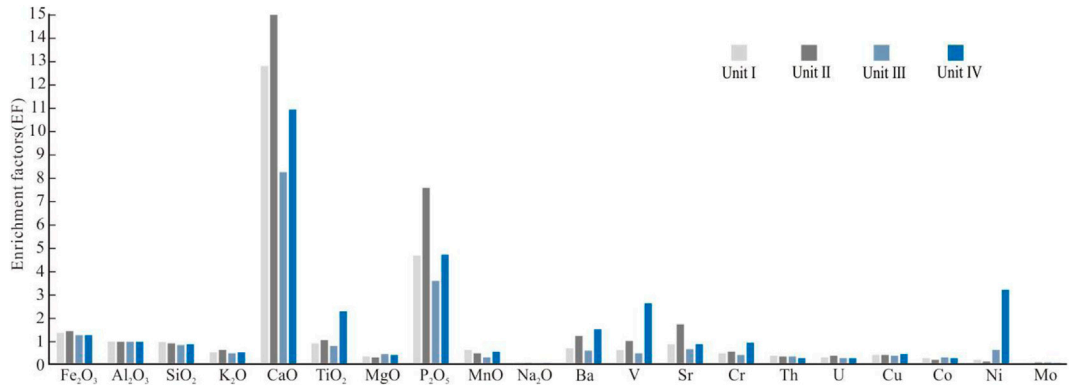

FIGURE 6
Enrichment coefficient of major elements in the Da'anzhai member of well C.

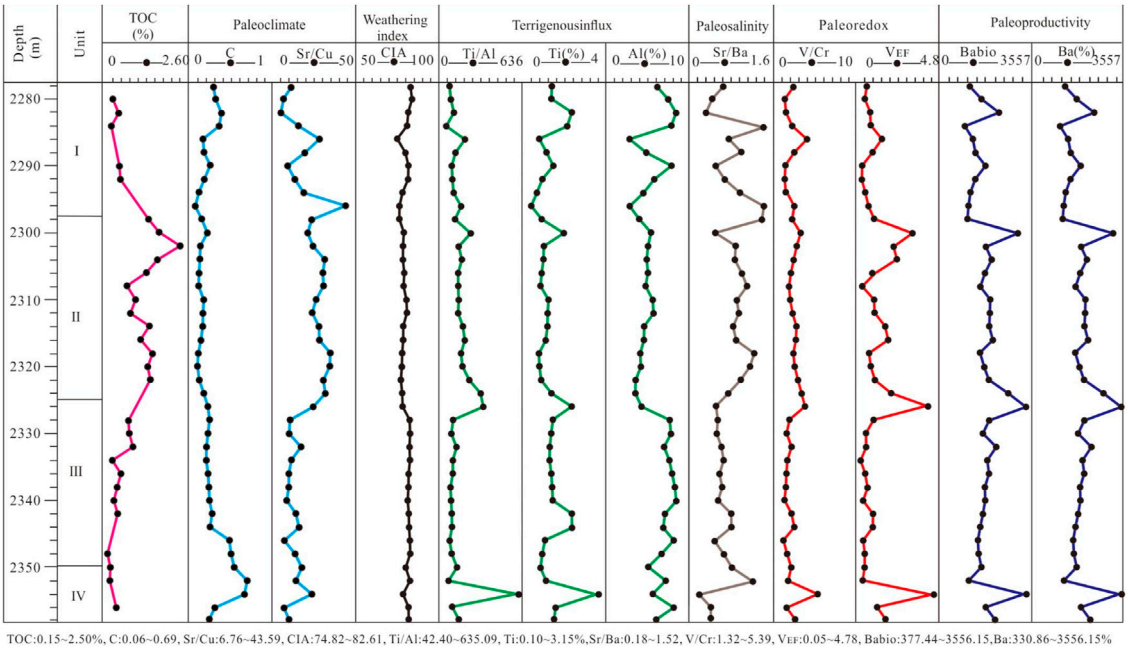

FIGURE 7
Paleoenvironment parameter in the Da'anzhai member of well C.

moles. CaO* is calculated by the calibration method proposed by McLennan et al. (1993). It is assumed that the Ca/Na ratio of silicate minerals in nature is 1. First, the CaO content of the sample is subtracted from the P_2O_5 content to ensure the removal of Ca in phosphate. Then, the CIA is calculated according to the molar ratio of CaO/Na_2O in the sample. A ratio greater than 1 implies the presence of chemically deposited carbonates, in which case the molar content of Na_2O is used instead of the CaO content. A ratio less than 1 indicates that there is no carbonate mineral, in which case the CaO molar content is directly used as the CaO content. A CIA in the range of 50–60 represents low weathering, a CIA in the range of 60–80 represents moderate weathering, and a CIA above 80 represents strong weathering.

The CIA of unit IV-III is generally 78.38 to 82.61 (Figure 7), with an average of 81.64. The weathering degree was strong in this period, which is consistent with the humid climate in this period. However, the CIA of unit II is generally lower than 80, with an average of 78.31, indicating that the weathering degree is relatively weak in an arid

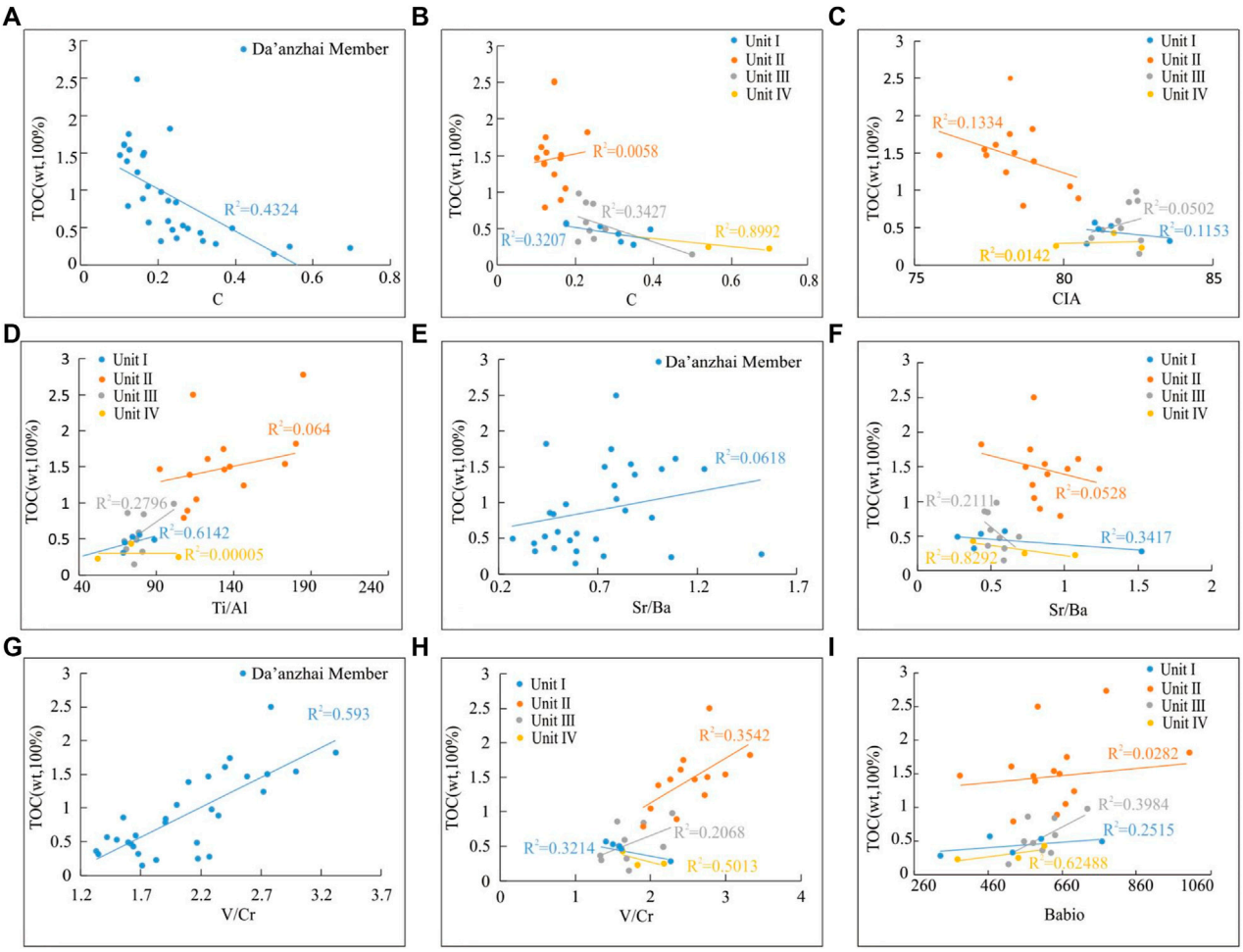

FIGURE 8
Cross-plot of environment parameter and TOC in the Da'anzhai member of well C. **(A)** Correlation between TOC and C in Da'anzhai Member; **(B)** Correlation between TOC and C in four small layers; **(C)** Correlation between TOC and CIA in four small layers; **(D)** Correlation between Ti/Al and C in four small layers; **(E)** Correlation between TOC and Sr/Ba in Da'anzhai Member; **(F)** Correlation between TOC and Sr/Ba in four small layers; **(G)** Correlation between TOC and V/Cr in Da'anzhai Member; **(H)** Correlation between TOC and Cr in four small layers; **(I)** Correlation between TOC and Babio in four small layers.

environment, while that of unit I is generally between 74.82 and 83.54, with an average of 79.85, indicating that the weathering degree is strengthened with the transition from unit II to unit I and the gradual wetting of climate.

From the correlation between the CIA and TOC (Figure 8C), the poor correlation between weathering and organic matter enrichment in various periods in the Da'anzhai member suggests that weathering has not significantly influenced organic matter enrichment.

5.3 Terrestrial input and hydrodynamic conditions

Considering that Si may be biogenic or terrestrial input, Si should be used carefully to evaluate paleoredox conditions (Zhao et al., 2016). Al mainly comes from aluminosilicate clay minerals (Arthur and Sageman, 1994), while Ti generally exists in clay and heavy minerals (Kidder and Erwin, 2001). The Ti/Al ratio provides an index to measure the transport energy of sediments (Murphy et al., 2000).

The Al, Ti, and Ti/Al curves reflect the variable terrestrial input in the Da'anzhai member (Figure 7). Continued high values in unit IV-III and unit I in the humid climatic zone indicate a high terrestrial input of the period. However, a short-term shift to low values in unit II in the arid climatic zone, and weathering is also weaker in unit II, which indicates a lower terrestrial input for the period (Figure 7), suggesting that terrestrial input is influenced by both paleoclimate and weathering. Deep lakes have lower input of terrigenous detrital, the climate became drier in unit I, and diagenetic minerals such as calcite and

dolomite dominated the deposition of the shale strata (Figure 3). The change of Ti/Al is contrary to that of Ti and Al from the lower part to the upper part of the Da'anzhai member. It is speculated that the changing trend of Al, Ti, and Ti/Al is opposite due to the enhancement of hydrodynamic force and energy input into the lake as the lake level retreats from the end of unit III to unit I.

In terms of the correlation between Ti/Al and TOC (Figure 8D), the poor or even negative correlation from all units' correlations indicates that terrestrial inputs have had a damaging effect on the preservation of organic matter. The weak correlation between Ti/Al and TOC in unit III can be speculated that the humid and warm climate accelerated the circulation of water vapor in the atmosphere, enhanced chemical weathering and surface runoff, and transported higher plants and organic matter into the lake (Figure 2G, Figure 2H). Terrigenous input indicators, such as the Ti/Al ratio, are used to indicate deposition rates. Generally, the higher the terrigenous input, the higher will be the deposition rate. The results show that the terrigenous input is the highest in the high TOC section (II), that is, the deposition rate is high. This may be due to a moist and warm climate that accelerates the circulation of water vapor in the atmosphere and enhances terrigenous weathering. In addition, terrigenous weathering, on the one hand, transported higher plants and organic matter to the lake (Figure 2G, Figure 2H), and on the other hand, imported a large number of nutrient elements, which promoted the productivity of the lake.

5.4 Paleosalinity

Paleosalinity refers to the salinity preserved in paleosediments, which is an important symbol indicating the change in the sedimentary environment in geological history. Because the migration ability of Sr and the solubility of its sulfate compounds are far greater than that of Ba, strontium and barium appear in the form of soluble bicarbonates in natural water when the salinity is low. When the water salinity gradually increases, Ba first precipitates into $BaSO_4$, resulting in the enrichment of Sr relative to Ba. Sr precipitates to $SrSO_4$ only when the water body is further salted, so Sr/Ba is usually used to divide the salinity of the water body (Zheng and Liu, 1999). The study of continental lake basins showed that for Sr/Ba ratios greater than 1.0, the lake is salt water, for ratios between 1.0 and 0.5, the lake is semi-saltwater, and for ratios less than 0.5, the lake is fresh water.

According to the changing trend of Sr/Ba in unit IV-II (Figure 7), the water gradually becomes salinized from freshwater from unit IV-III. In unit II, it is from semi-saltwater to salt water. In unit I, although the lake level drops further, the climate becomes warm and humid, and the Sr/Ba value is generally lower than 1, which has the characteristics of freshwater.

From the correlation between the TOC and Sr/Ba (Figure 8E), salinity correlates poorly with TOC, indicating that lake salinity has little correlation with organic matter enrichment and too low salinity is not suitable for organic matter enrichment. According to the correlation between TOC and Sr/Ba in different periods (Figure 8F), the unit II has the characteristics of high salinity and high TOC compared with the unit IV-III and the unit I, which indicates that appropriate salinity is beneficial to the enrichment of organic matter under the background of high drought. However, the correlation between TOC and Sr/Ba in unit II is poor, which indicates that salinity is not the most important factor affecting organic matter enrichment in unit II.

5.5 Redox condition

Redox-sensitive trace elements (RSTEs, such as Mo, U, and V) have dissolution or sedimentation characteristics under different redox conditions, so that the redox condition of the paleoenvironment can be restored by RSTEs (Tribovillard et al., 2006). Whether the RSTEs are terrestrial input or not needs to be evaluated first. The correlation coefficient between Mo_{EF}, U_{Ef}, and A1 is 0.69 and 0.72. However, the correlation coefficient between V_{EF} and Al concentration is only 0.0064. It is proved that the V is not from terrestrial input. So, it is reliable to use V to characterize the redox condition. V_{EF} lower than 1 means the depletion of V, showing the developmental oxidation environment of the Da'anzhai member (Figure 7).

The redox sensitivity rate (TEs), such as the trace element ratio such as U/Th, V/Cr, and Ni/Co, is also used to show the oxidation–reduction properties of water. The lower the ratio, the higher the oxidation degree of water is; the higher the ratio, the higher the reduction degree of water is (Hatch and Leventhal, 1992; Jones and Manning, 1994; Tribovillard et al., 2006). According to the trace element ratio, the oxidation–reduction properties of water can be divided into three levels: oxidized state, sub-oxidized state, and reduction state (Figure 9) (Jones and Manning, 1994). The ratio casting point of various elements (Figure 9) shows that most of the data points of Ni/Co are in the oxidized and sub-oxidized zone. V/Cr can identify the redox environment of mudstone effectively. V/Cr<2.00 represents the oxidizing environment; 2.00<V/Cr<4.25 represents the semi-reductive environment; and V/Cr>4.25 represents the anoxic environment. V/Cr indicates unit IV-III and unit I are in an oxidizing environment (Figure 7), and the V/Cr of unit II is 2–4.25, which shows unit II is in a semi-reductive state. It is consistent with the development of pyrite in unit II (Figure 3).

There is a favorable correlation between the TOC and V/Cr according to the intersection diagram (Figure 8G). It shows that the redox condition is the main factor in controlling organic matter enrichment in the Da'anzhai member. However, in unit

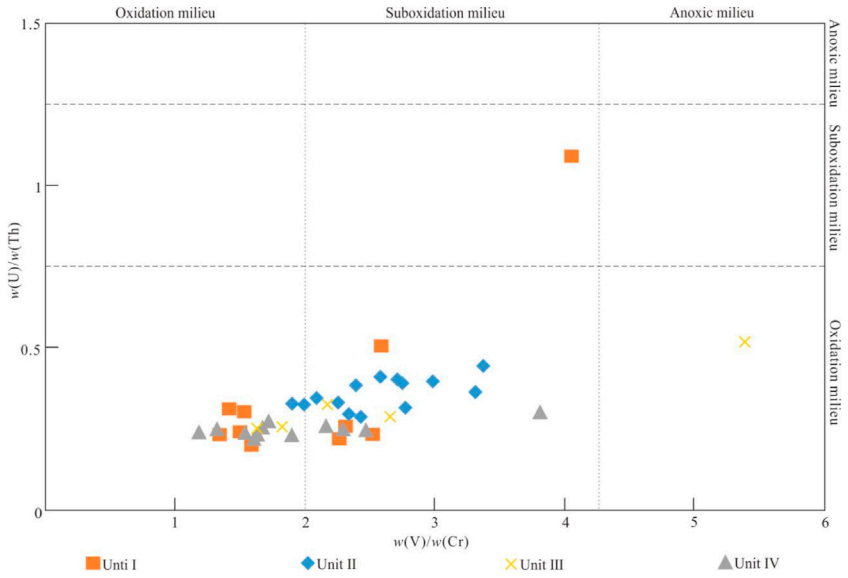

FIGURE 9
Intersection diagram of trace element ratio in the Da'anzhai member.

III, there is a weak correlation between the TOC and V/Cr (Figure 8H). In previous studies, the sediment of high TOC can be formed if there is enough organic matter in the non-reductive environment (Pedersen and Calvert, 1990). Abundant organic matter can consume a lot of oxygen when decomposing. It can cause anoxia in the water ground, which is in favor of storing the organic matter (Pedersen and Calvert, 1990; Wei et al., 2012). There is a negative correlation between unit IV, unit I, and TOC (Figure 8H), which shows that the organic matter enrichment of the two members does not control by the oxidation–reduction environment.

5.6 Paleoproductivity

Excess of Ba_{bio}, Cu, Ni, and P in shale has been used in studying the strength of paleoproductivity. Under the reduction condition, Ni and Cu are the ideal indexes for entering the sediments (Tribovillard et al., 2006). There exist many disputes in the P element indicating the change of paleoproductivity, which concentrates on the different correlations between biological P (organophosphorus) and productivity (Slomp et al., 2002; Ma et al., 2008). In the anoxic environment, the sulfate reduction reaction is generally released on the sediment surface and water ground. Barium sulfate is one type of sulfate, and partial dissolution of barium sulfate will make the content value of the tested barium smaller, which causes the estimated productivity to become lower (Calvert and Pedersen, 2007). The previous study has proved that water, which is in the sediment period of the black rock series in the Da'anzhai member of the studied area, is in an oxidizing and semi-oxidizing (semi-reductive) environment. There were no hydrothermal activities in the Jurassic sedimentary period in the Sichuan Basin. In the meanwhile, the concurrent variation trend of the content of Ba and Ba_{bio} in the vertical direction shows that Ba in the studied area is mainly from a biological source (Figure 8). The biological source of barium can be the paleoproductivity index. So, the study takes Ba_{bio} to characterize the production capacity.

Ba_{bio} in the Da'anzhai member of the studied area changed relatively significantly and its distributing range is 330.80–3556.12 ppm, with an average of 647.963 ppm. According to the productivity index (Figure 7), with the lake level rising, terrestrial input of unit IV-III in that period was relatively large and more nutrients had been taken into the lake; unit II was under the arid and anoxic environment and it is in favor of the enrichment of nutrients such as P in the water of lakes (Van Cappellen and Ingall, 1994). Moreover, the decomposition of a large number of bivalve shells after extinction can promote the eutrophication of water (Zhang et al., 2016). In general, in the mildly saline water with Sr/Ba in 0.5–0.8, algae bloomed (Jiao, 2019), and the productivity was relatively high, which made the lakes have productivity to a certain extent. It was consistent with most saltwater lakes in the world which have high productivity. It is reported that the salt content of the northern Great Salt Lake in Utah State is 22%. There are large quantities of algae and heterotrophic bacterium in the lake. Therefore, the Great Salt Lake in Utah State has great productivity. The productivity of unit I is the lowest. It is related to the large decline of the lake level, which leads to the overall oxidation environment of the lake and the difficulty of preserving organic matter.

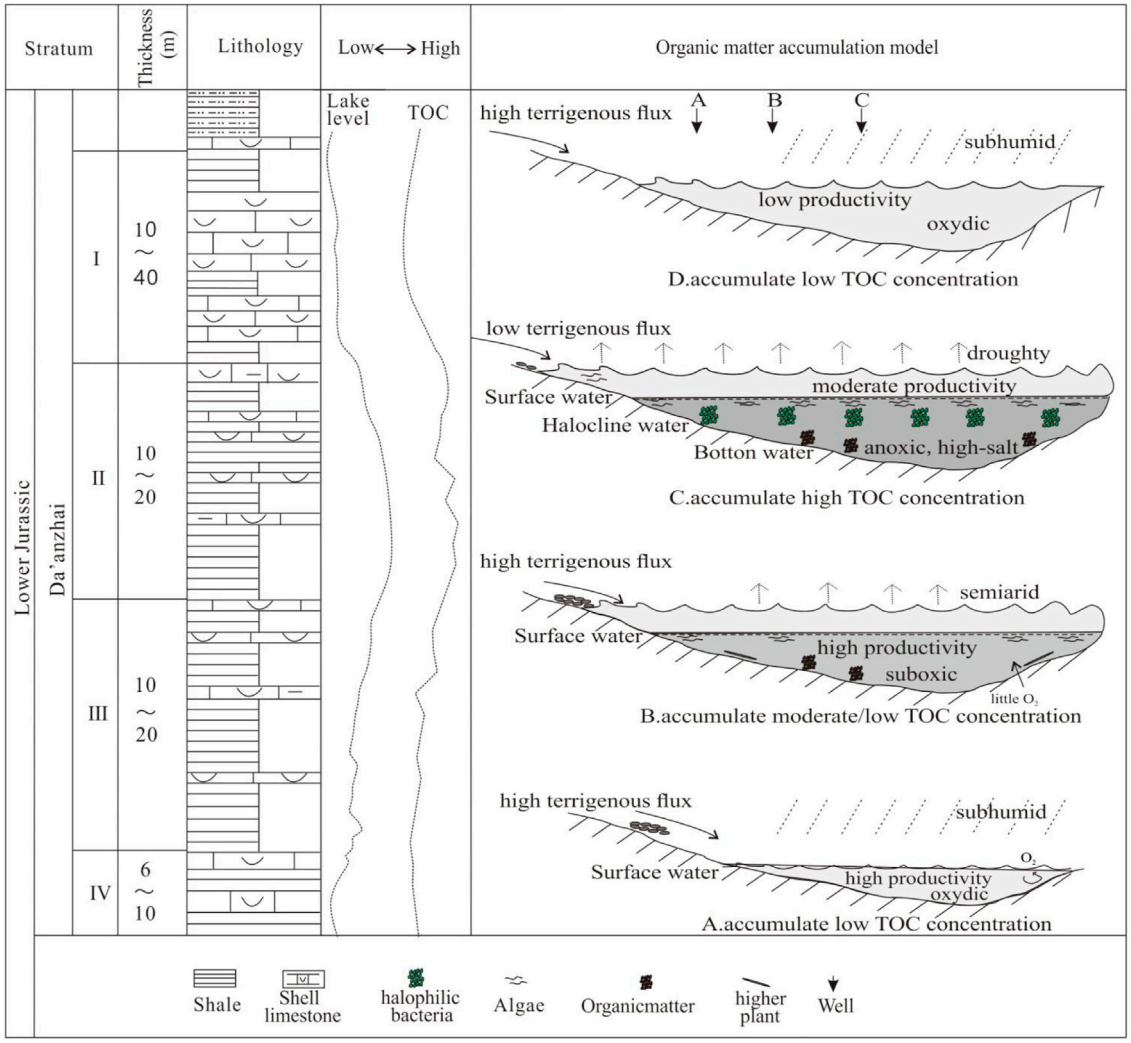

FIGURE 10
Organic matter enrichment pattern of the Da'anzhai member in Sichuan Basin.

According to the correlation between the TOC and Ba_{bio} (Figure 8I), they have different correlations in different periods. In unit IV and unit III, the correlation coefficient between TOC and Ba_{bio} are 0.62 and 0.39, respectively, which shows that the two indicators have a favorable correlation; in unit I, the correlation coefficient between TOC and Ba_{bio} is just 0.25 and it has a relatively weak correlation; the correlation coefficient between unit II and TOC is just 0.02 and it has a poor correlation.

5.7 Organic matter enrichment pattern

According to the various sedimentary environment parameters discussed in the previous study, the author induced the organic matter enrichment pattern of the Da'anzhai member in the Sichuan Basin (Figure 10).

In unit IV-III, during this period, the lake level gradually increased; at the end of unit III, it increased to the largest lake flooding surface; the water in unit IV is relatively shallow, and the lakes are relatively open, which forms the oxidation environment; with rising of the lake level, the lakes gradually become sealing, which forms the semi-oxidized environment. Even the oxidation environment is unfavorable to the preservation and enrichment of organic matter, units IV-III have developed a semi-humid and semi-arid climatic environment and freshwater has been inlet by precipitation and surface runoff. It not only brings organic matter such as plant debris but also provides consumption to the primary producer such as surficial algae by inletting large amounts of dissolved substances as nutriment. The type III organic matter preservation pattern has formed in this period, which is controlled by productivity.

In unit II, the climate gradually becomes arid, and the lake level gradually declines after it achieves the largest lake flooding surface; freshwater supply in the basin decreases rapidly, which leads to the fresh lakes gradually becoming salified. Due to the density difference, lake water forms a stable salt layering environment. Water salinity in the shallow stratum is low and the oxidation rate is high. A large number of algae and phytoplankton have developed, which improves the primary producer of the unit. Water salinity in the mid-deep stratum may change with the change in the paleoclimate and halophilic bacteria may propagate a lot in this unit; under the condition, the dissolved oxygen has been consumed rapidly and the anoxic environment has been formed. Due to the arid climate and the poor inlet of freshwater, lake stratification was stagnant, which led the middle and lower parts to the anoxic saline state in a long term. Because of the anoxic state, phosphorus and other nutrients have been recycled into the water effectively (Van Cappellen and Ingall, 1994), and the water becomes eutrophicated. In addition, the mineral content of clay in the unit is relatively high (Figure 3), which can absorb the organic matter effectively (Xu et al., 2017). In general, the relatively high primary productivity and preserving condition in that period formed the type II organic matter enrichment pattern which biases toward a reduction condition. What is worth paying attention to is that the accumulation of organic matter in the lake basin in the Da'anzhai member of the Sichuan Basin is relatively lower than that in other lake basins in the world. It may refer to the gravity flow development of the unit, which is unfavorable to organic matter preservation to a certain extent. It leads the TOC in unit II to be relatively lower than the organic matter sedimentation of other lakes in the world.

In general, unit I is the period in which the range of the lake is the minimum in the Da'anzhai member. In that stage, the hydrodynamic is strong and the amount of dissolved oxygen in water has increased, which appears in an oxidation environment; in the meanwhile, with the decline in the lake level, the increasing terrestrial input restricts organic matter enrichment, and organic matter accumulation is relatively less.

6 Conclusion

Through comprehensive studies of the sedimentology and geochemistry of the Da'anzhai member in the late Early Jurassic in the Sichuan Basin, the author has a new understanding of the organic matter disposition mechanisms of the unit. In the Da'anzhai member, the organic matter in unit II is the most enriched and that in unit III is sub-enrichment. The formation of the two organic-rich shales is not referring to a single factor. It refers to the mutual coupling of paleoclimate, redox properties, productivity, paleosalinity, and many other factors.

Under a semi-humid and semi-arid environment, the chemical degree of weathering is relatively high in unit III of the Da'anzhai member, and it inlets many nutrients into lakes, such as higher plants. The productivity is relatively high in that period and formed the organic matter enrichment pattern which biases toward the oxidized condition.

Under the arid environment, freshwater supply decreases rapidly in unit II of the Da'anzhai member, which leads the fresh lake gradually to become salified. Because of the density difference, lake water forms a stable salt layering environment, and it is oxygen enriched on the surface, with low salinity and extensively develops phytoplankton and algae. Its primary productivity is high; in the middle and lower parts, it is anoxic and the salinity is high; phosphorus and other nutrients have been effectively recycled into the water which caused the water to be eutrophicated. Unit II is in a semi-reduction environment and it is the ideal place for organic matter enrichment. Therefore, it formed the organic matter enrichment pattern biases toward the reductive condition.

Data availability statement

The raw data supporting the conclusion of this article will be made available by the authors, without undue reservation.

Author contributions

YD and XW designed experiments; CC, SW, RT, QM, and JZ carried out experiments; RZ, YZ, and SHanalyzed experimental results. YD wrote the manuscript.

Acknowledgments

We thank Qian Pang of State Key Laboratory of Oil and Gas Reservoir Geology and Exploitation, Southwest Petroleum University for his support in field section positioning and field discussion. The authors appreciate the reviewers who gave constructive suggestions which polished the paper so much.

Conflict of interest

YD, CC, SW, RT, QM, JZ, and YZ were employed by the company Exploration Division of Petro China Southwest Oil and Gasfield Company. SH was employed by the company CNPC.

The remaining author declares that the research was conducted in the absence of any commercial or financial relationships that could be construed as a potential conflict of interest.

Publisher's note

References

Arthur, M. A., and Sageman, B. B. (1994). Marine black shales: Depositional mechanisms and environments of ancient deposits. *Annu. Rev. Earth Planet. Sci.* 22 (1), 499–551. doi:10.1146/annurev.ea.22.050194.002435

Bluth, G. J., and Kump, L. R. (1994). Lithologic and climatologic controls of river chemistry. *Geochimica Cosmochimica Acta* 58 (10), 2341–2359. doi:10.1016/0016-7037(94)90015-9

Calvert, S. E. (1987). Oceanographic controls on the accumulation of organic matter in marine sediments. *Mar. Pet. Source Rocks* 26 (1), 137–151. doi:10.1144/gsl.sp.1987.026.01.08

Calvert, S. E., and Pedersen, T. F. (2007). Chapter fourteen elemental proxies for palaeoclimatic and palaeoceanographic variability in marine sediments: Interpretation and application. *Dev. Mar. Geol.* 1, 567–644. doi:10.1016/s1572-5480(07)01019-6

Demaison, G. J., and Moore, G. T. (1980). Anoxic environments and oil source bed Genesis. *AAPG Bull.* 64 (8), 1179–1209.

Deng, S. H., Lu, Y. Z., Zhao, Y., Fan, R., Wang, Y., Yang, X., et al. (2017). The Jurassic palaeoclimate regionalization and evolution of China. *Earth Sci. Front.* 24 (1), 106–142. doi:10.13745/j.esf.2017.01.007

Dymond, J., Suess, E., and Lyle, M. (1992). Barium in deep-sea sediment: A geochemical proxy for paleoproductivity. *Paleoceanography* 7 (2), 163–181. doi:10.1029/92pa00181

Hatch, J. R., and Leventhal, J. S. (1992). Relationship between inferred redox potential of the depositional environment and geochemistry of the upper pennsylvanian (missourian) Stark shale member of the dennis limestone, wabaunsee county, Kansas, USA. *Chem. Geol.* 99 (1-3), 65–82. doi:10.1016/0009-2541(92)90031-y

Hu, D. F., Wei, Z. H., Liu, R. B., Wei, X., and Chen, F. (2021). Enrichment control factors and exploration potential of lacustrine shale oil and gas:A case study of Jurassic in the Fuling area of the Sichuan Basin. *Nat. Gas. Ind. B* 41 (8), 1–8. doi:10.1016/j.ngib.2021.08.012

Huang, Z., Wang, X., Yang, X., Zhu, R., Cui, J., Shi, W., et al. (2020). Paleoenvironment and organic matter accumulation of the upper ordovician-lower silurian, in upper yangtze region, South China: Constraints from multiple geochemical proxies. *Energies* 13 (4), 858–916. doi:10.3390/en13040858

Jiao, F. Z. (2019). Re-recognition of "unconventional" in unconventional oil and gas. *Petroleum Explor. Dev.* 46 (5), 847–855. doi:10.1016/s1876-3804(19)60244-2

Jinhua, F. U., Shixiang, L. I., Liming, X. U., and Niu, X. (2018). Paleo-sedimentary environmental restoration and its significance of chang 7 member of triassic yanchang formation in ordos basin, NW China. *Petroleum Explor. Dev.* 45 (6), 998–1008. doi:10.1016/s1876-3804(18)30104-6

Jones, B., and Manning, D. A. (1994). Comparison of geochemical indices used for the interpretation of palaeoredox conditions in ancient mudstones. *Chem. Geol.* 111 (1-4), 111–129. doi:10.1016/0009-2541(94)90085-x

Kidder, D. L., and Erwin, D. H. (2001). Secular distribution of biogenic silica through the phanerozoic: Comparison of silica-replaced fossils and bedded cherts at the series level. *J. Geol.* 109 (4), 509–522. doi:10.1086/320794

Li, X., Wang, J., Rasbury, T., Zhou, M., Wei, Z., and Zhang, C. (2020). Early Jurassic climate and atmospheric CO_2 concentration in the Sichuan paleobasin, southwestern China. *Clim. Past.* 16 (6), 2055–2074. doi:10.5194/cp-16-2055-2020

Li, Y., and He, D. (2014). Evolution of tectonic-depositional environment and prototype basins of the Early Jurassic in Sichuan Basin and adjacent areas. *Acta Pet. Sin.* 35 (2), 219–232. doi:10.7623/syxb201402002

Liu, J., Cao, J., Hu, G., Wang, Y., Yang, R., and Liao, Z. (2020). Water-level and redox fluctuations in a Sichuan Basin lacustrine system coincident with the Toarcian OAE. *Palaeogeogr. Palaeoclimatol. Palaeoecol.* 558, 109942. doi:10.1016/j.palaeo.2020.109942

Liu, S. G. (1993). *The formation and evolution of Longmenshan thrust zone and western Sichuan*. China. Chengdu: Press of Chengdu University of Science and Technology.

Loucks, R. G., and Ruppel, S. C. (2007). Mississippian barnett shale: Lithofacies and depositional setting of a deep-water shale-gas succession in the fort worth basin, Texas. *Am. Assoc. Pet. Geol. Bull.* 91 (4), 579–601. doi:10.1306/11020606059

Ma, Z. W., Chaoyong, H., Jiaxin, Y., and Xinong, X. (2008). Biogeochemical records at Shangsi section, northeast Sichuan in China: The Permian paleoproductivity proxies. *J. China Univ. Geosciences* 19 (5), 461–470. doi:10.1016/s1002-0705(08)60051-5

Mayer, L. M., Rahaim, P. T., Guerin, W., Macko, S. A., Watling, L., and Anderson, F. E. (1985). Biological and granulometric controls on sedimentary organic matter of an intertidal mudflat. *Estuar. Coast. Shelf Sci.* 20 (4), 491–503. doi:10.1016/0272-7714(85)90091-5

McLennan, S. M., Hemming, S., McDaniel, D. K., and Hanson, G. N., (1993). Geochemical approaches to sedimentation, provenance, and tectonics. *Special Papers-Geological Soc. Am.* 284, 21–40. doi:10.1130/SPE284-p21

Meng, F., Chen, H., and Li, X. (2005). Study on lower-middle jurassic boundary in chongqing region. *Geol. Mineral Resour. South China* 3, 64–71. doi:10.3969/j.issn.1007-3701.2005.03.013

Moradi, A. V., Sarı, A., and Akkaya, P. (2016). Geochemistry of the Miocene oil shale (Hançili Formation) in the Çankırı-Çorum Basin, Central Turkey: Implications for Paleoclimate conditions, source–area weathering, provenance and tectonic setting. *Sediment. Geol.* 341, 289–303. doi:10.1016/j.sedgeo.2016.05.002

Murphy, A. E., Sageman, B. B., Hollander, D. J., Lyons, T. W., and Brett, C. E. (2000). Black shale deposition and faunal overturn in the Devonian Appalachian Basin: Clastic starvation, seasonal water-column mixing, and efficient biolimiting nutrient recycling. *Paleoceanography* 15 (3), 280–291. doi:10.1029/1999pa000445

Nesbitt, H., and Young, G. M. (1982). Early Proterozoic climates and plate motions inferred from major element chemistry of lutites. *Nature* 299 (5885), 715–717. doi:10.1038/299715a0

Pedersen, T. F., and Calvert, S. E. (1990). Anoxia vs. productivity: What controls the formation of organic-carbon-rich sediments and sedimentary rocks? *AAPG Bull.* 74 (4), 454–466.

Slomp, C. P., Thomson, J., and Lange, G. J. (2002). Enhanced regeneration of phosphorus during formation of the most recent eastern Mediterranean sapropel (S1). *Geochimica Cosmochimica Acta* 66 (7), 1171–1184. doi:10.1016/s0016-7037(01)00848-1

Taylor, S. R., and Mclennan, S. M. (1985). *T*he continental crust: Its composition andevolution. London: Blackwell Scientific Publications.

Tong, Z., Shengxiang, L., and Feng, W. (2016). Sedimentary models and lithofacies types of lacustrine mud shale in the Sichuan Basin. *Nat. Gas. Ind.* 36 (8), 22–28. doi:10.3787/j.issn.1000-0976.2016.08.003

Tribovillard, N., Algeo, T. J., Baudin, F., and Riboulleau, A. (2012). Analysis of marine environmental conditions based onmolybdenum–uranium covariation—applications to mesozoic paleoceanography. *Chem. Geol.* 324-325, 46–58. doi:10.1016/j.chemgeo.2011.09.009

Tribovillard, N., Algeo, T. J., Lyons, T., and Riboulleau, A. (2006). Trace metals as paleoredox and paleoproductivity proxies: An update. *Chem. Geol.* 232 (1-2), 12–32. doi:10.1016/j.chemgeo.2006.02.012

Turekian, K. K., and Wedepohl, K. H. (1961). Distribution of the elements in some major units of the earth's crust. *Geol. Soc. Am. Bull.* 72 (2), 175–192. doi:10.1130/0016-7606(1961)72[175:doteis]2.0.co;2

Van Cappellen, P., and Ingall, E. D. (1994). Benthic phosphorus regeneration, net primary production, and ocean anoxia: A model of the coupled marine biogeochemical cycles of carbon and phosphorus. *Paleoceanography* 9 (5), 677–692. doi:10.1029/94pa01455

Wang, Y., Xu, S., Hao, F., Poulton, S. W., Zhang, Y., Guo, T., et al. (2021). Arid climate disturbance and the development of salinized lacustrine oil shale in the Middle Jurassic Dameigou Formation, Qaidam Basin, northwestern China. *Palaeogeogr. Palaeoclimatol. Palaeoecol.* 577, 110533. doi:10.1016/j.palaeo.2021.110533

Wedepohl, K. H. (1971). Environmental influences on the chemical composition of shales and clays. *Phys. Chem. Earth* 8, 307–333. doi:10.1016/0079-1946(71)90020-6

Wei, H., Chen, D., Wang, J., Yu, H., and Tucker, M. E. (2012). Organic accumulation in the lower chihsia formation (middle permian) of South China: Constraints from pyrite morphology and multiple geochemical proxies. *Palaeogeogr. Palaeoclimatol. Palaeoecol.* 353, 73–86. doi:10.1016/j.palaeo.2012.07.005

Wu, Z., Zhao, X., Wang, E., Pu, X., Lash, G., Han, W., et al. (2021). Sedimentary environment and organic enrichment mechanisms of lacustrine shale: A case study of the paleogene shahejie formation, qikou sag, bohai bay basin. *Palaeogeogr. Palaeoclimatol. Palaeoecol.* 573, 110404. doi:10.1016/j.palaeo.2021.110404

Xu, J., Jin, Q., Xu, X., Cheng, F. Q., Hu, C. H., Wang, B., et al. (2021). Factors controlling organic-rich shale development in the liushagang formation, weixinan sag, beibu gulf basin: Implications of structural activity and the depositional environment. *Petroleum Sci.* 18 (4), 1011–1020. doi:10.1016/j.petsci.2020.08.001

Xu, Q., Liu, B., Ma, Y., Song, X., Wang, Y., and Chen, Z. (2017). Geological and geochemical characterization of lacustrine shale: A case study of the jurassic Da'anzhai member shale in the central sichuan Basin, southwest China. *J. Nat. Gas Sci. Eng.* 47, 124–139. doi:10.1016/j.jngse.2017.09.008

Zhang, F., Zhou, Y. X., and Ge, R. Q., (2018). A new type of lacustrine ichnofossils from the Lower Jurassic Ziliujing Formation in Wanzhou of Chongqing and its paleoenvironmental significances. *Acta Palaeontol. Sin.* 57 (2), 228–236. doi:10.19800/j.cnki.aps.2018.02.008

Zhang, H., Wu, X., and Wang, B., (2016). Research progress of the enrichment mechanism of sedimentary organics in lacustrine basin. *Acta Sedimentol. Sin.* 34 (3), 463–477. doi:10.14027/j.cnki.cjxb.2016.03.004

Zhang, J. C., Lin, L. M., and Li, Y. X., (2012). Classification and evaluion of shale oil. *Earth Front.* 19 (5), 322–331.

Zhao, J., Jin, Z., Jin, Z., Geng, Y., Wen, X., and Yan, C. (2016). Applying sedimentary geochemical proxies for paleoenvironment interpretation of organic-rich shale deposition in the Sichuan Basin, China. *Int. J. Coal Geol.* 163, 52–71. doi:10.1016/j.coal.2016.06.015

Zhao, W. Z., Zhu, R. K. Z., Hu, S. Y., Hou, L., and Wu, S. (2020). Accumulation contribution differences between lacustrine organic-rich shales and mudstones and their significance in shale oil evaluation. *Petroleum Explor. Dev.* 47 (6), 1160–1171. doi:10.1016/s1876-3804(20)60126-x

Zheng, R. (1998). High-resolution sequence stratigraphy of Da'anzhai formation, lower jurassic in sichuan Basin. *Acta Sedimentol. Sin.* 16, 42–49.

Zheng, R. C., and Liu, M. Q. (1999). Study on palaeosalinity of Chang-6 oil reservoir set in Ordos Basin. *Oil Gas Geol.* 20 (1), 20–25.

Zou, C. N., Yang, Z., Wang, H. Y., et al. (2019). Exploring petroleum inside source kitchen": Jurassic unconventional continental giant shale oil & gas field in Sichuan basin, China. *Acta Geol. Sin.* 93 (7), 1551–1562. doi:10.19762/j.cnki.dizhixuebao.2019188

frontiers | Frontiers in Earth Science

TYPE Original Research
PUBLISHED 08 September 2022
DOI 10.3389/feart.2022.892926

OPEN ACCESS

EDITED BY
Daniel R. Parsons,
University of Hull, United Kingdom

REVIEWED BY
José Darrozes,
UMR5563 Géosciences Environnement Toulouse (GET), France
Hossein Hamidifar,
Shiraz University, Iran

*CORRESPONDENCE
Enhui Jiang,
ehjiang@yrihr.com

SPECIALTY SECTION
This article was submitted to Sedimentology, Stratigraphy and Diagenesis,
a section of the journal
Frontiers in Earth Science

RECEIVED 09 March 2022
ACCEPTED 09 August 2022
PUBLISHED 08 September 2022

CITATION
Zhao Z, Yao S, Jiang E and Qu B (2022), Experimental study and a physical model on the geomorphic response mechanisms of meandering rivers under progressive sediment reduction.
Front. Earth Sci. 10:892926.
doi: 10.3389/feart.2022.892926

Experimental study and a physical model on the geomorphic response mechanisms of meandering rivers under progressive sediment reduction

Zhanchao Zhao[1,2,3], Shiming Yao[4], Enhui Jiang[1,2,3]* and Bo Qu[2,3]

[1]College of Water Conservancy and Hydropower Engineering, Hohai University, Nanjing, Jiangsu, China, [2]Yellow River Institute of Hydraulic Research of Yellow River Conservancy Commission, Zhengzhou, Henan, China, [3]Key Laboratory of Lower Yellow River Channel and Estuary Regulation, MWR, Zhengzhou, Henan, China, [4]Yangtze River Scientific Research Institute, Wuhan, Hubei, China

As influenced by human activities, including high dam construction, soil and water conservation, and sand mining in the upper reaches of rivers, the amount of sediment entering the lower reaches of the river decreases significantly. Human activities disturb the natural balance between river evolution and water as well as sediment movement and induce new characteristics of river evolution. After the construction and operation of the Danjiangkou Reservoir and the Three Gorges Reservoir of the Yangtze River (China), different degrees of bend bypassing and shoal cutting in the bends downstream of the dams are observed. The reason for this interrelation has not been explained sufficiently. Based on the analysis of prototype observation data and physical model experiments, we have investigated the evolution mechanism of different topographic types of meandering rivers under the condition of decreasing sediment inflow. The data generated by our model experiment document that the sediment concentration of the convex bank flow with a large degree of curvature of the bend is lower than that of the concave bank flow for a reduction of the sediment concentration from 100% to 0%. Moreover, the convex bank of the bend gradually collapses and retreats, whereas the main channel of the river gradually swings, with a swing range of 0–800 m, toward the convex bank. This phenomenon becomes more significant with progressive reduction of the sediment inflow. Combined with theoretical analysis, we interpret that the drastic reduction in the amount of sand that has destroyed the relative natural balance of sediment transport in the riverbanks and river channels in the meandering river section is the main reason for the occurrence of bypassing and shoal cutting in the meandering river section of plain alluvial rivers. Especially during the mid-to high-water period, the capacity of sediment transport in the mainstream belt exceeds the sediment concentration in the water body significantly and is coupled with the change of the runoff process caused by the regulation of the reservoir operation. As a consequence, the river beach is constantly scouring and developing. The evolution is generally characterized by bend bypassing and shoal cutting. The results of our study

can be transposed to other alluvial plain rivers and may constitute valuable reference data.

KEYWORDS

plain river, meandering river, bend bypassing and shoal cutting, sediment transport capacity, sediment concentration, coupling mechanism

1 Introduction

The meandering river is one of the most common types of natural rivers. Its evolution is closely controlled by the incoming flow and sediment conditions, river boundary conditions, and riverbed composition. The evolution of natural alluvial meandering rivers generally follows the evolution characteristics of concave bank scour and convex bank siltation or bend bypassing and shoal cutting and cutting and straightening after excessive bending. The evolution of the meandering river affects the flood control, navigation, protection, and utilization of water and soil resources along the shoreline. Therefore, to better control the evolution of meandering rivers, river regulation has been conducted to meet various needs. In recent years, the incoming flow and sediment conditions as well as river boundary conditions have been changed due to the aggravation of human activities that has a major impact on the evolution of meandering rivers. Two main methods for the study of meandering rivers exist 1. prototype observation and analysis and 2. model experiments. In recent years, many studies have focused on the downstream meandering river after the construction of the barrage.

1.1 Prototype observation and analysis

The primary task of studying the evolution characteristics of the meandering river is to observe and analyze the natural river. The prototype observation data of the Mississippi River in the United States (Fisk, 1945; Furbish, 1991; Harmar and Clifford, 2010) and the Bollin River in England (Luchi et al., 2010) have shown the phenomenon of bend bypassing and shoal cutting in the meandering river. The characteristics of bend bypassing and shoal cutting vary with different degrees of curvature. Under the condition of natural sediment inflow, the sediment transport in a meandering river is in relative equilibrium. The maximum bed load transport zone follows the outward movement of the maximum boundary shear force, and the maximum sediment transport is close to the center line of the river channel. The main factors affecting the lateral flow and sediment movement are the river channel topography and the transverse velocity distribution of the meandering river channel, as documented in the Muddy Creek River in the United States (Dietrich and Smith, 1984). Based on the channel sediment supply mechanism and combined with the channel satellite observation map, the variation characteristics of the floodplain shear force of the meandering river and the evolution law of the floodplain of the meandering river under different types of sediment supply and transport mechanisms were analyzed (Constantine et al., 2014). Plants existing in the meandering channel have an impact on the bank structure, the floodplain flow, and sediment transport and can change the topography of the meandering channel accordingly. The evolution characteristics of the meandering channel in the Tagliamento River (Italy) have been analyzed under the influence of plants by using lidar observation technology and prototype measured data (Zen et al., 2017). Based on satellite observation data, the change data of curved river width are counted, and a model is constructed that can simulate the evolution of river banks and determine the model parameters. The model can be used to calculate the long-term evolution characteristics of meandering rivers and has been applied to a section of the Ucayali River (Peru) (Sergio and Stefano, 2019). Arnez et al. (2021) studied through remote sensing analysis and field investigation, using 30 years of observation data, the planform evolution and riverbed topography of the Ichilo River (Bolivia), a small river located in the upper foreland Amazon basin. Their findings show that cutoffs, climate, and human activities are the main factors that control the meander migration rates in the Ichilo River. With the construction of a river barrage project, the river flow and sediment conditions have changed, and the sediment transport in the meandering river follows a new principle. Hence, continued prototype monitoring is required.

1.2 Model experiment

Numerical simulation and generalized model experiments are commonly used to study the characteristics of flow and sediment movement in different meandering channels. The model experiment of large-scale meandering reaches can explain the flow characteristics, sediment transport characteristics, bed terrain change characteristics, and the influence of the curvature on the plane shape of the sharp meandering reach with a large degree of curvature (Whiting and Dietrich, 1993). The two-dimensional flow model is combined with the average topographic depth model of the riverbed and the bank erosion model of the meandering channel to simulate the riverbed boundary and riverbed deformation of the meandering channel. The model is corroborated by a flume experiment and measured data of the

natural meandering channel and provides the possibility to simulate the shear stress at the boundary of meandering channels. However, the model is inapplicable for the accurate simulation of quantifying the change characteristics of the meandering channel (Darby et al., 2002). Kassem and Chaudhry (2002) developed a two-dimensional model to study the time variation of the riverbed deformation in a meandering river. Comparing the data with the experimental results of 140° angle and 180° angle meandering channel flumes shows that the model is suitable for unsteady flow and meandering rivers with irregular boundaries. The long-term evolution principle of the channel has been analyzed from the perspective of considering the dynamic process of different forms of the meandering channel, and the shape and curvature of the meandering channel are recognized as the main factors that affect the morphological dynamic process of the evolution of the meandering channel (Frascati and Lanzoni, 2009). Flume experiments have been conducted to analyze the conditions that are necessary to maintain meandering channels in coarse-bedded rivers, and the experimental results show that the characteristics of the incoming sediment are the main factors that affect the topographic changes of curved river channels (Braudrick et al., 2009). The flume experiments with large curvatures have been used to analyze the flow movement characteristics of a large amplitude meandering bend, and the studies show that the counter-rotating circulation cell only occurs in the case of a "small" width-to-depth ratio (Donatella and Mafalda, 2011). Using a physical model, Güneralp and Rhoads (2011) studied the impact of the erosivity of floodplain flow on the evolution of plane riverbed in meandering channels and recognized that the complexity of plane riverbed shape depends on the spatial scale difference and random variability of erosion. Xu and Bai (2013) used the generalized sinusoidal derivative curve to conduct an experimental study on the meandering flume and analyzed the characteristics of riverbed deformation in combination with the characteristics of flow and sediment movement in the meandering channel with different degrees of curvature. He proposed that the curvature of the meandering channel and the boundary conditions of the channel itself affect the stability of channel deformation. The instability of riverbed deformation increases with the increasing degree of the channel curvature (Xu and Bai, 2013). Keshavarzi et al. (2016), Amirhossein et al. (2020), and Lindroth et al. (2020) have used physical model experiments to investigate the impact of the type and distribution of river vegetation on the meandering river. Their studies show that the characteristics of the vegetation in the river channel have an impact on the cross-sectional flow velocity, the sediment distribution, and the riverbed shear stress of the curved river channel; thus, they strongly affect the topographic changes of the riverbed of the curved river channel. In future river training projects, the impact of the vegetation can be used to control the evolution of the meandering river.

1.3 Study on the meandering rivers downstream of the barrage

The empirical formula of the ideal meandering shape in the middle and lower reaches of the Han River in China has been established according to the morphological characteristics of 32 typical meandering channels in the middle and lower reaches of the Han River (Zhang et al., 2007). The flow conditions have been considered in the study as an important factor causing the phenomenon of bend bypassing and shoal cutting in the middle and lower reaches of the Han River. Qin et al. (2009) have established a formula for the meandering radius of the dynamic axis of flow suitable for the Jingjiang River reach in China and have analyzed the relationship between the change of the meandering radius of the dynamic axis of flow and the phenomenon of bend bypassing and shoal cutting. After the construction of the barrage in the river, the oscillation characteristics of the dynamic axis of flow in the downstream reach will change (Hooke and Yorke, 2011).

After the construction of the Three Gorges Reservoir in the Yangtze River, the sediment inflow in the lower reaches of the reservoir has gradually decreased, and the evolution characteristics of bend bypassing and shoal cutting have appeared in the lower reaches of the meandering river. After the operation of the Three Gorges reservoir, the flow, sediment, and river regime downstream of the dam have significantly changed, and the evolution characteristics of the Jingjiang River reach of the Yangtze River have been adjusted. The changes in flow and sediment conditions as well as the river boundary conditions are the main factors for the river channel adjustment of the Jingjiang river reach (Sixuan et al., 2018). The change of the riverbed and the geological conditions have also been considered to be the causes of bend bypassing and shoal cutting in the meandering channel of the Jingjiang River (Li et al., 2013). After the construction and operation of the Three Gorges reservoir, the clear water has been discharged, the mainstream line and thalweg of the meandering river course have shifted strongly, and the cross-section shape of the river course changes from V shape to W shape (Ruan, 2016). The change in the flow process, the change of time distribution of the position of the dynamic axis of flow, and the reduction of sediment inflow are the main causes of "convex scouring and concave silting" in the meandering channel of the lower Jingjiang River (Zhu et al., 2017). The observations indicate that the driving factors of the meandering channel evolution are the changes of upstream river regime, the river boundary conditions, and incoming flow and sediment conditions (Fan et al., 2017).

Striking progress has been made in previous studies in the understanding of the overall evolution characteristics and channel characteristics of meandering channels, which provides a basis for further studies on meandering channels. Rivers are complex systems. Flow and sediment movement, as well as the geomorphic change caused by flow and sediment

TABLE 1 Change of sediment transport in the Yangtze River and the Yellow River (China).

Tongguan hydrological station (Yellow River)				
Particular year	1980–1989	1990–1999	2000–2009	2010–2016
Average annual sediment discharge (10^8t)	7.803	7.90	3.12	1.57
Jianli hydrological station (Yangtze River)				
Particular year	1981–1991	1992–2002	2003–2007	2008–2017
Average annual sediment discharge (10^8t)	4.68	3.44	0.93	0.33

movement, may induce large-scale environmental problems. The analysis of prototype observation data is an effective research method, which can be used to analyze the evolution characteristics and influencing factors of the meandering river from a large-scale perspective. However, due to prototype limitations, observation of large-scale rivers, especially sediment movement, is difficult, and the internal processes of the geomorphic change of the meandering river still need further exploration. The physical model clearly and intuitively reflects the characteristics of natural river geomorphic changes and overcomes the limitations of sediment and geomorphic monitoring. The physical model method is required to corroborate the studies on the internal mechanisms of river flow and sediment movement and river geomorphic change. Based on the theoretical analysis of prototype observation data, the physical model is used to simulate the natural river section, control the sediment inflow, and study the influence mechanism of sediment inflow on the geomorphic deformation of the meandering river. In the present study, we focus on analyzing the coupling mechanism between the sediment concentration of the flow and the topographic change characteristics of the curved channel to decipher the riverbed evolution characteristics of the meandering river downstream of the barrage. Our findings will provide a profound reference for river regulation, presumably applicable to the study of other plain alluvial rivers in the world.

2 Prototype analysis

2.1 Variation of flow and sediment conditions

The measured data of hydrology stations in the middle reaches of the Yangtze River and the Yellow River in China are analyzed (Table 1). In recent years, a dramatic decrease in the sediment discharge in the river channels has been detected, with a reduction in the Yangtze River and the Yellow River of about 80–90% since 2010. Human activities, including the construction of high dams with large reservoirs, soil and water conservation, and sand mining, are the main causes of the sediment decrease. The sediment discharge has decreased gradually. The composition of the suspended sediment and bed material in the river channel and the sediment transport process have changed. Moreover, the exchange of sediment carried by flow and bed material shows new characteristics, and the river landform exhibits a new pattern.

The flow and sediment data of the Shashi hydrological station on the Yangtze River in China are selected for a detailed analysis (Table 2). The selected time span ranges from 1981 to 2017, which is divided into four periods and two periods, respectively (the four periods are divided according to the operation of the Three Gorges reservoir, and the two periods represent the time before and after the operation of the Three Gorges reservoir). The Shashi hydrological station is located upstream of the continuous meandering river section (Tiaoguan-Laijiapu reach and Xiongjiazhou-Chenglingji reach) and is selected for the study (Figure 1), and it is located about 180 km away from the upstream Three Gorges dam. Water storage and operation of the Three Gorges Reservoir started in 2003. The water inflow of the Shashi hydrological station has not changed significantly before and after the operation of the reservoir, but the sediment load has decreased significantly after the operation of the reservoir. After the operation of the reservoir (2003–2017), the average annual sediment load was reduced by 86.70% when compared with the data prior to operation (1981–2002). The distribution trend of the average daily flow in the four periods remained nearly constant (Figure 2). The highest flow level occurred from June to October, whereas from November to May, the flow level is low to moderate. After the operation of the Three Gorges reservoir, the reservoir has played a major role in the regulation of the discharge flow. Flow levels <5,000 m^3/s and >25,000 m^3/s have decreased, and flow levels >5,000 m^3/s and <25,000 m^3/s have increased. Moreover, the incoming flow process has become progressively flattened. After the operation of the Three Gorges reservoir, the daily average sediment concentration has decreased significantly.

2.2 Topographic change

We have selected prototype geomorphological observation data of two typical meandering reaches of the Yangtze River and twelve observation sections and three observation years for the

TABLE 2 Variation of annual runoff and annual sediment discharge of the Shashi hydrological station.

Time span		1981–1991	1992–2002	1981–2002	2003–2007	2008–2017	2003–2017
Shashi hydrological station (Yangtze River)	Average annual runoff (10^8m^3)	4,080	3,994	4,037	3,720	3,836	3,797
	Average annual sediment transport (10^8t)	4.68	3.44	4.06	0.93	0.33	0.54

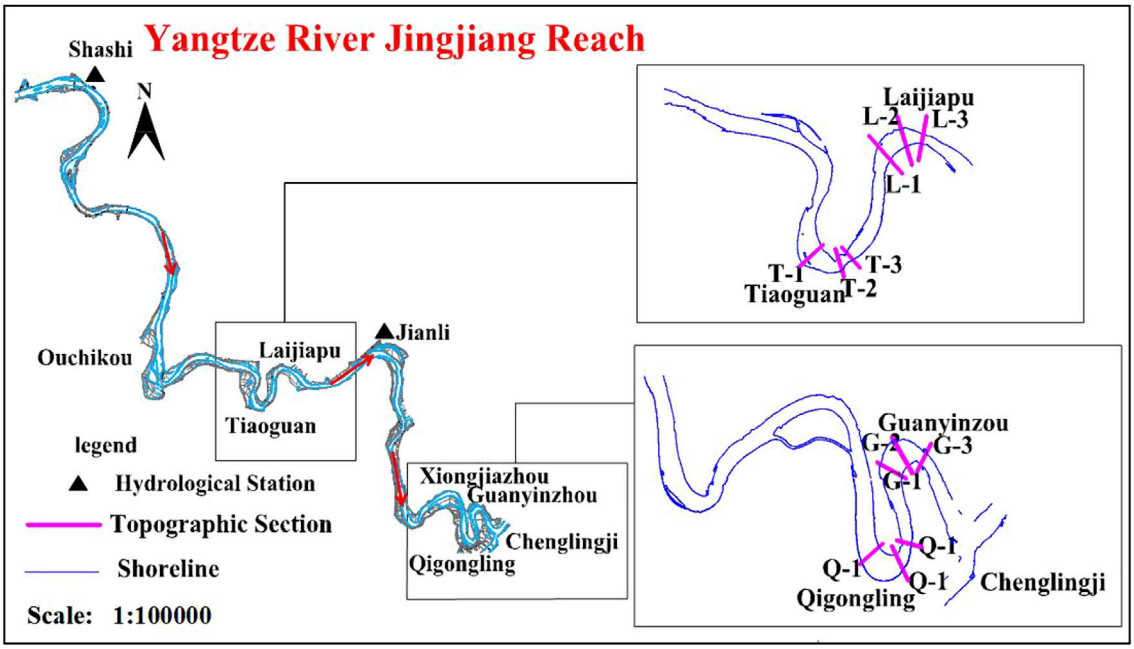

FIGURE 1
Prototype observation reach.

analysis (Figure 1). The observed section is located in the middle and lower reaches of the Yangtze River, including meandering reaches with different radii of curvature. Most sections on the right bank of the river are hilly terraces with strong anti-scouring capacity. The left bank of the river is an alluvial plain. A double-layer structure of recent river sediments dominates the riverbank. It is composed of a lower sand layer and an upper cohesive soil layer with poor anti-scouring capacity. The riverbed is composed of medium-to fine-grained sand with a median particle size of about 0.165 mm. The pebble layer is deeply buried below the bed surface.

We have selected the T-1, Q-1, and G-1 river sections for a detailed analysis (Figure 3). The three sections are located in the middle and upper positions of the meandering reach. The convex bank and edge beach at the three cross sections are scoured, and the riverbed elevation decreases. The concave bank is silted and the riverbed elevation increases. The nearshore central bar is formed on the concave bank side, and the river section changes from V shape to W shape. This phenomenon is termed bend bypassing and shoal cutting, which is different from the convex bank silting and concave bank scouring of the ordinary meandering channel that was described in previous studies. According to the change of the channel plane shape between 2002 and 2016 (Figure 4), the river channel was mainly scoured. The specific manifestations are beach scouring and deep channel siltation. The main river channel is shifted from the concave bank to the convex bank. The transition section of the bend is dominated by scouring, and at the bend position, it is mainly characterized by convex bank scouring and concave bank silting. The scouring and silting changes at sections T-1 and G-1 are relatively severe, and the maximum scouring depth and maximum siltation thickness at the two positions are 13 m and 18 m (T-1), and 29 m and 19 m (G-1), respectively.

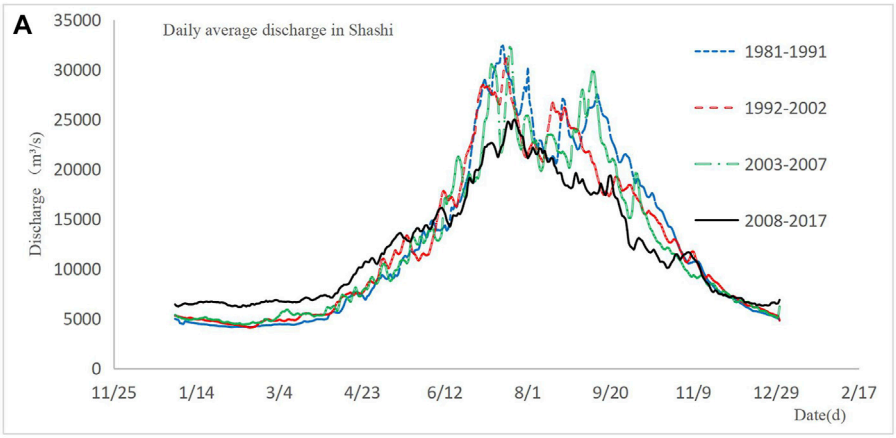

Daily average discharge

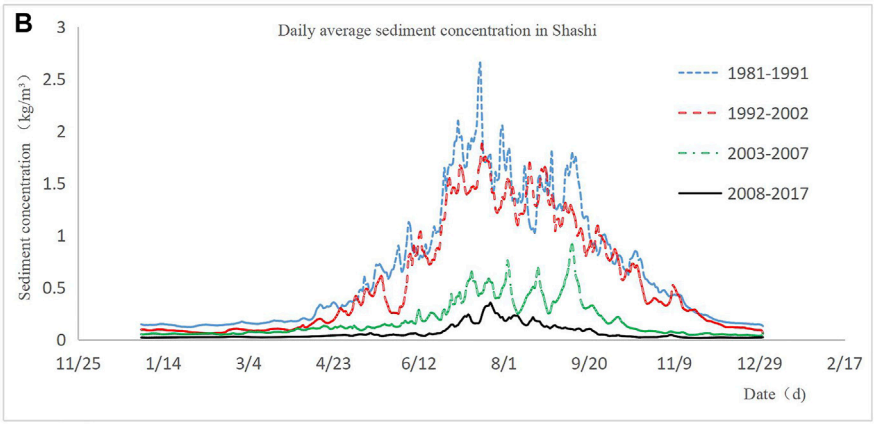

Daily average sediment concentration

FIGURE 2
Variation of daily average discharge and daily average sediment concentration at the Shashi hydrological station.

2.3 Analysis of theoretical results

The change of the river landform is the mutual adaptation and development of the riverbed and the flow and sediment conditions. The riverbed will be adjusted to the changes in the flow and sediment conditions. After the impoundment and operation of the Three Gorges reservoir, no significant change in the total amount of water coming from the lower reaches occurred, but the flow process changed significantly. The increase of the occurrence time of medium flow level (5,000–25,000 m^3/s) was the main modification. After the operation of the reservoir, the total amount of sediment inflow decreased significantly, and the sediment concentration dropped gradually during sediment inflow. The sediment concentration of flow cannot satisfy the sediment carrying capacity of the flow. In order to satisfy the sediment carrying capacity of flow, the flow will scour the riverbed. Therefore, the convex bank of the meandering river is subject to cumulative scouring. As a consequence, the edge beach of the convex bank continues to collapse, and the riverbed elevation decreases. Finally, the phenomenon of bend bypassing and shoal cutting is initiated. According to the observation and analysis of the prototype data, the causes of this phenomenon are the reduction of sediment from the river and the change in the runoff process caused by the operation and regulation of the reservoir. The prototype data observation allows analyzing the causes for the change of the meandering channel landform under the condition of sediment reduction from a macro perspective. However, as the observation of large-scale rivers is difficult, it remains problematic to obtain the cross-sectional distribution of sediment, the velocity, and the change of topography under different flow levels from natural rivers. Therefore, it is necessary to study the flow, the sediment distribution, and the

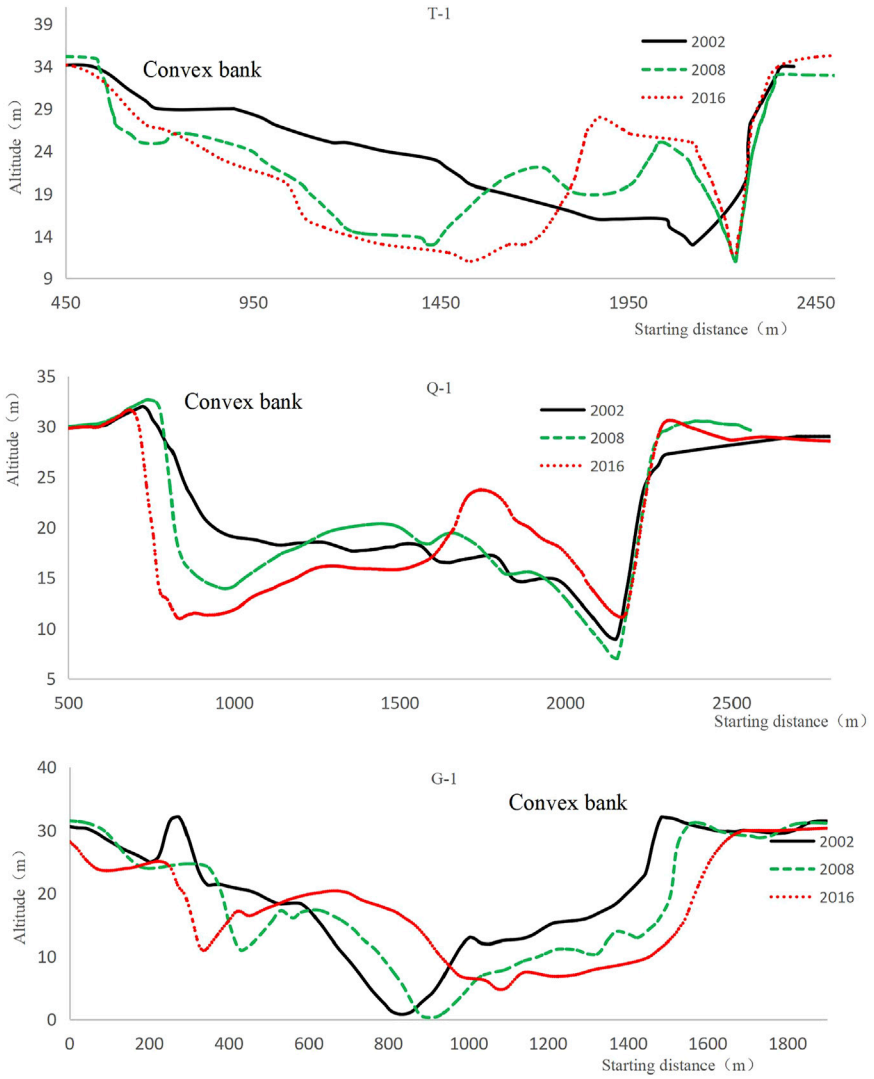

FIGURE 3
Change of the morphology of the studied river cross sections **(A)** T-1, **(B)** Q-1, and **(C)** G-1.

topographic change of the meandering channel under the condition of sediment reduction through the physical model experiment.

3 Physical model experiment

3.1 Experimental equipment

The experiments are conducted in the Ministry of Water Resources Key Laboratory of River and Lake Control and Flood Control in the Middle and Lower Reaches of the Yangtze River at the Yangtze River Scientific Research Institute, Wuhan, China. The scope of the model experiment is the Tiaoguan-Laijiapu meandering reach of the Yangtze River. The full length of the prototype is about 40.8 km, and the length of the model is 102 m. The composition of the water and sediment supply system for the model experiment includes water circulation system, sediment circulation system, flow regulating equipment, desilting basin, side leaf adjustable tailgate, measuring equipment, and other auxiliary equipment. The composition of the water circulation system includes reservoirs, pumps, water pipelines, and backwater channels. The composition of the sediment circulation system includes reservoirs, pumps, a stir pool, a sediment transport pipeline, and an add-on sediment pump. The model adopts an electromagnetic flowmeter to measure and control the inlet flow. In order to ensure that the water flowing into the experimental section is as smooth as

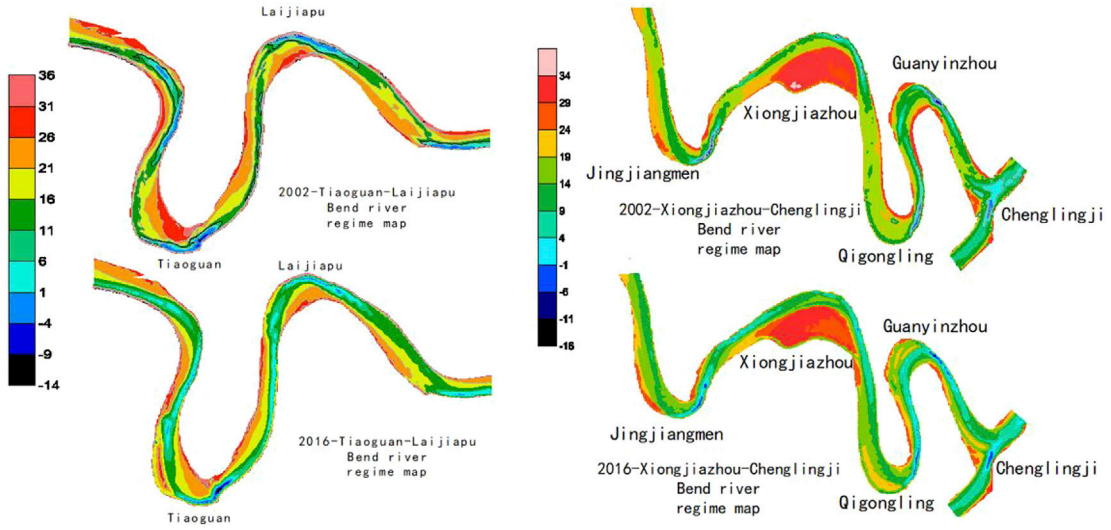

FIGURE 4
Morphological change of river channel planform. The positive and negative numbers represent the elevation based on a datum point (m).

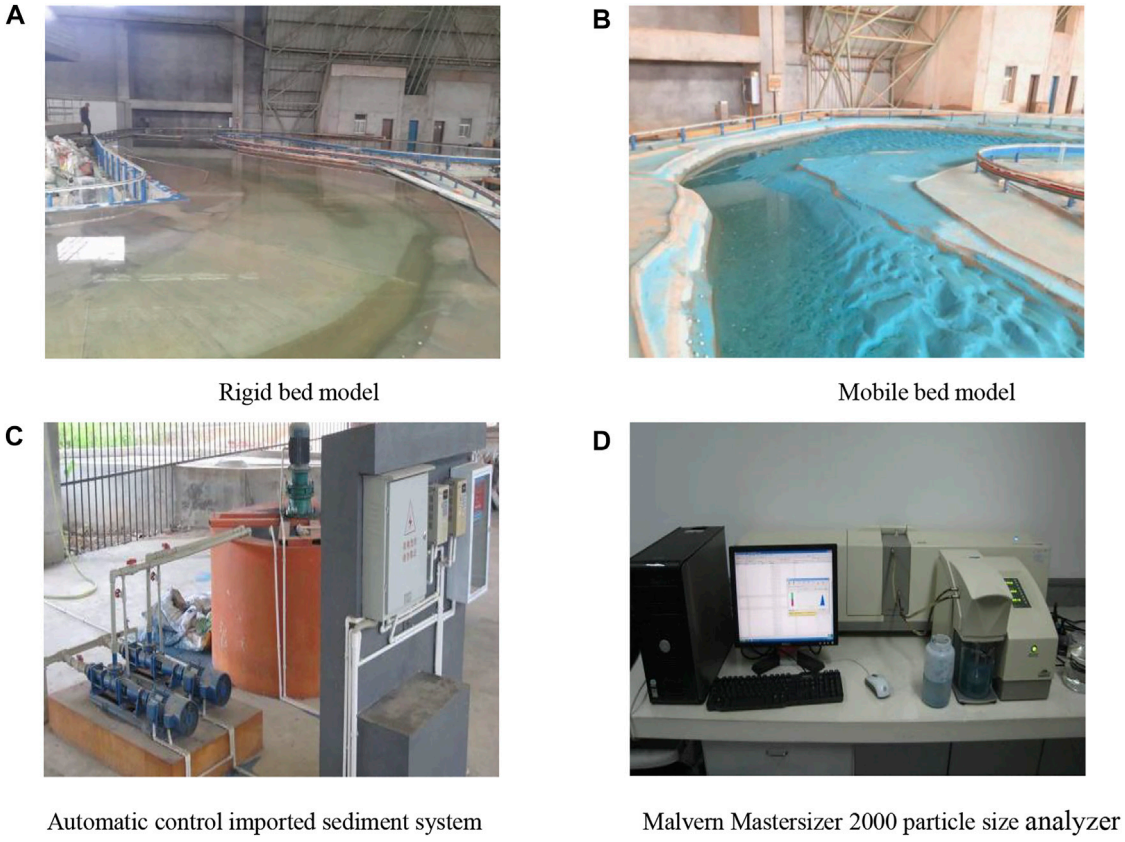

FIGURE 5
Experimental set-up.

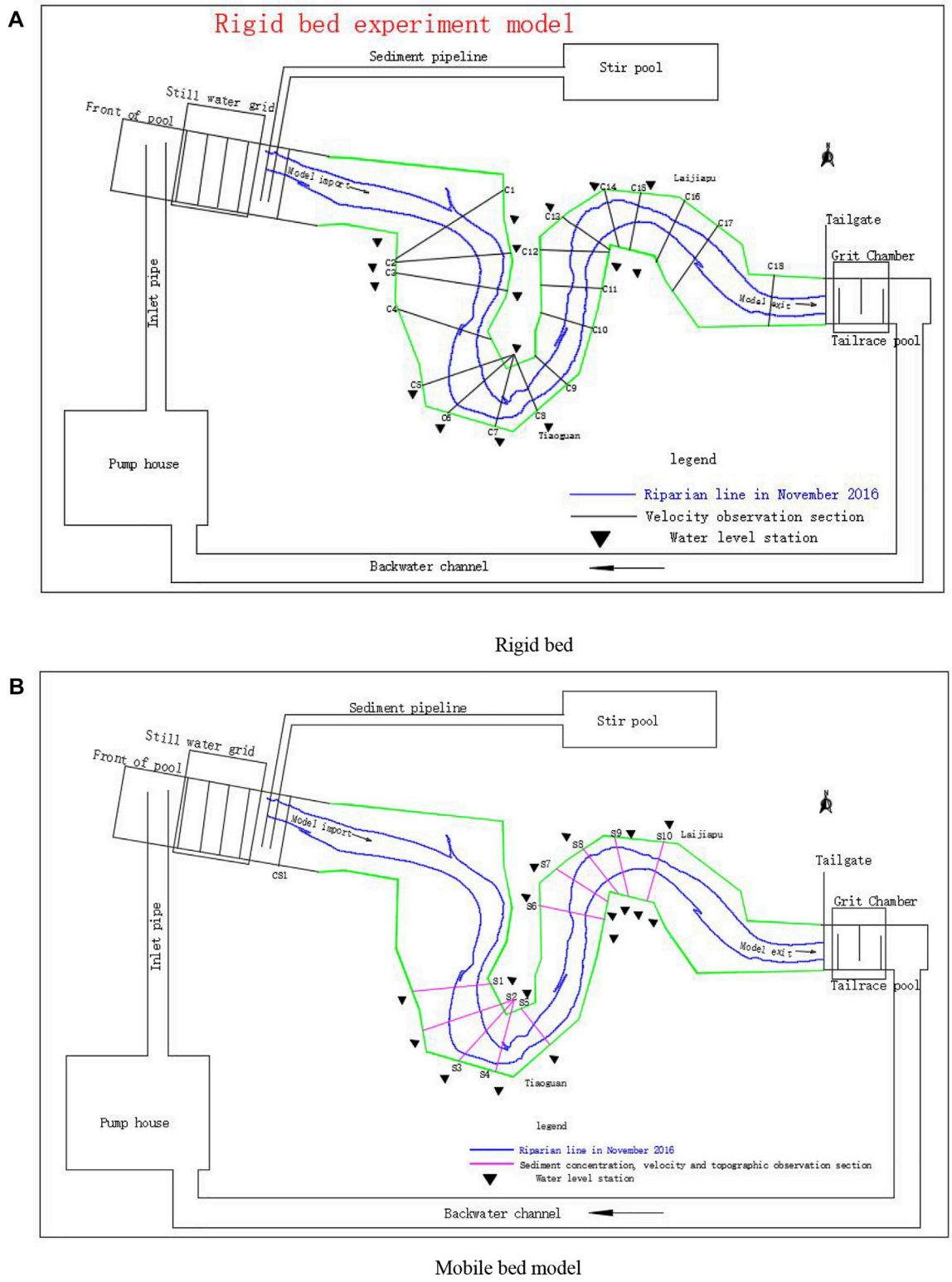

FIGURE 6
Schematic diagrams illustrating the set-up of the experimental model.

possible, the model inlet section is equipped with a forebay with a flower wall and a steady flow grid. A transition section of about 3 m is set in front of the experiment section. The measuring equipment used in the experiment included the sediment sampler, the ADV three-dimensional flowmeter, the Malvern Mastersizer 2000 particle size analyzer, using laser diffraction technology to measure the particle size of sediment, the automatic water level meter, the electromagnetic flowmeter, and the electronic balance (Figure 5).

3.2 Model set-up and validation

The model experiment includes two schemes: 1) a rigid bed (Figure 6A) and 2) a mobile bed (Figure 6B). Using the rigid bed experiment, we will mainly study the flow variation characteristics of the meandering channel under different flow levels, whereas the mobile bed is suitable to investigate the sediment distribution characteristics and topographic change characteristics of the meandering channel under different sediment inflow conditions.

In order to fulfill the accuracy of the experiment, to improve the similarity between the research reach and the solid model, and to better follow the flow movement and riverbed evolution characteristics of natural rivers, the similarity of various factors must be fully considered in the experiment design, and each similar scale should be checked.

To ensure that the model and prototype flow are sufficiently described by the same physical equation, the model must satisfy the geometric similarity. Therefore, the model flow needs to fulfill the following two constraints:

1) The model flow must be turbulent, and the model Reynolds number R_{em} is greater than 1,000–2,000.
2) The surface tension does not interfere with the flow of the model, so the water depth of the model h_m is greater than 1.5 cm.

Under the current conditions, the water depth in the river channel of the studied reach is generally >2.5 m in the period of low flow, and the average velocity is about 1.2 m/s. The horizontal scale of 400 and the vertical scale of 100 are selected as the geometric scales of the model. A minimum Reynolds number of the model = 2,147 > 1,000–2,000 is calculated for the model, and the minimum water depth of the model is 2.5 cm > 1.5 cm, which satisfies the requirements. Based on this data, we calculated the flow movement scale to ensure that the flow inertia force, gravity, inertia force resistance, and flow continuity of the model are similar to those of the prototype.

The similarity of flow movement in the model must meet the inertia force gravity similarity (Eq. 1), the inertia force resistance similarity (Eq. 2), and the continuity similarity of flow (Eq. 3).

$$\alpha_V = \alpha_H^{\frac{1}{2}} \tag{1}$$

,

$$\alpha_n = \alpha_H^{\frac{2}{3}} \Big/ \alpha_L^{\frac{1}{2}}, \tag{2}$$

$$\alpha_Q = \alpha_H \alpha_H \alpha_V. \tag{3}$$

According to the purpose and requirements of the experiment, bed load and suspended load shall be modeled simultaneously. For the suspended load, the bed material load part in the suspended load mainly affects the scouring and silting change of the riverbed. The amount of bed load in the studied reach is far less than that of bed material load. Therefore, the similarity of bed material load movement in suspended load is mainly considered in the model design. Based on these findings, we will determine the basic conditions for similar sediment movement. Due to the purpose of the experiment, the model mainly considers the scouring problem of the studied reach. Therefore, the model set-up is mainly based on the premise of satisfying the similar conditions of sediment incipient movement. According to the measured data of the prototype river reach, the boundary particle size between bed material load and wash load in the suspended load of the river reach is 0.05 mm, and the average median particle size of bed material load in the suspended load is 0.195 mm. The median particle size of the prototype bed material is 0.15–0.23 mm, and the average particle size is about 0.194 mm.

The incipient velocity of prototype sediment is calculated by Eq. 4 (Sha Yuqing formula) and the incipient velocity of the model sediment by Eq. 5. The fitting formula of the flume experiment results from the study of Zhou (2015).

$$u = \left[0.43 d^{\frac{3}{4}} + 1.1 \frac{(0.7-e)^4}{d}\right]^{\frac{1}{2}} h^{\frac{1}{5}}, \tag{4}$$

$$U = 0.9216 \left(\frac{H}{d_{50}}\right)^{0.141} \left(17.6 \frac{\gamma_s - \gamma}{\gamma} d_{50} + 0.000000016 \frac{10+H}{d_{50}^{0.885}}\right)^{1/2} - 2.105. \tag{5}$$

The calculated incipient velocity of prototype bed sediment is 0.587–0.841 m/s, and the calculated incipient velocity of model bed sediment is 6.45–8.93 cm/s for water depths of 5–30 m and a model bed sediment median particle size of d_{50} = 0.254 mm. The incipient velocity scale of bed sediment is 9.11–9.42, and it is only slightly lower than the velocity scale of 10, indicating that the selected model sediment basically satisfies the incipient similar conditions. According to the incipient similarity criterion, a value of 0.9 is determined for the particle size scale of the model, and the median particle size of the model bed sediment is calculated as 0.22 mm. The design grading curve of bed sediment in the model is shown in Figure 7. The final values of sediment concentration and sediment transport rate scale are determined through the model validation experiment results. The model sediment used in this experiment is synthetic plastic sediment, and the bulk density is designed as 1.38 t/m^3. The dry

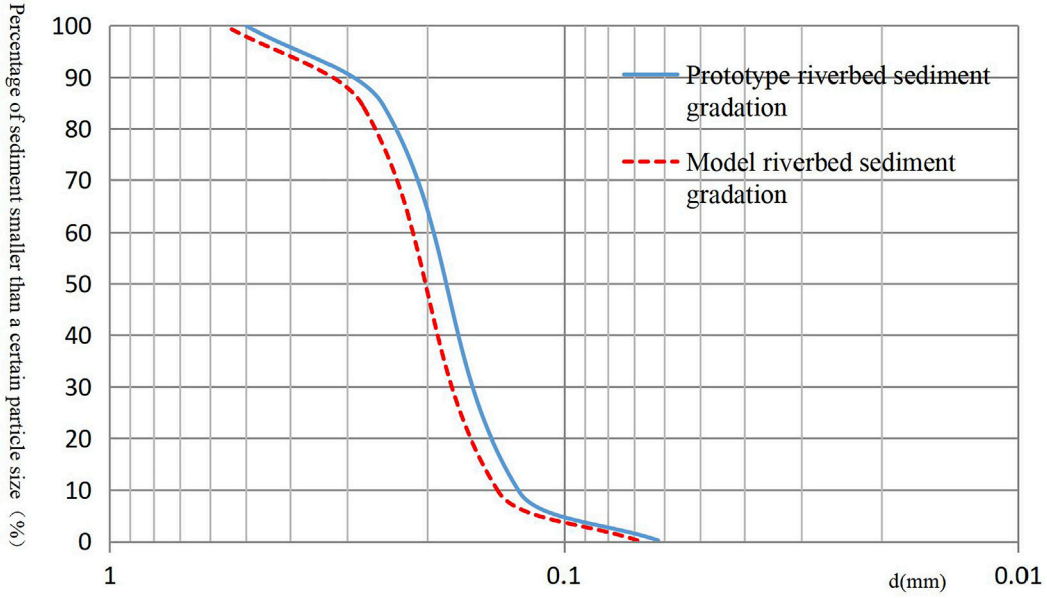

FIGURE 7
Design grading curve of bed sediment in the model.

TABLE 3 Model scale selection.

Similitude consideration	Scale name	Symbol	Ratio
Geometric similarity	Horizontal	α_L	400
	Vertical	α_H	100
	Velocity	α_V	10
	Roughness	α_n	1.08
Similarity of flow movement	Rate of flow	α_Q	400,000
	Time of flow	α_{t_1}	40
	Subsiding velocity	α_ω	2.5
	Dry capacity	α_{γ_0}	2.02
Similarity of suspending sediment movement	Particle size	α_d	0.9
	Sediment concentration	α_s	0.442
	Riverbed deformation time	α_{t_2}	183
	Subsiding velocity	α_ω	2.5
	Dry capacity	α_{γ_0}	2.02
	Particle size	α_d	0.9
Similarity of bed load movement	Starting velocity	α_{V_0}	10
	Bed load transport rate per unit width	α_{q_b}	442
	Riverbed deformation time	α_{t_3}	183

bulk density changes slightly with the change in model sediment particle size. The value is 0.65 t/m^3.

We selected water levels of the Shashi hydrological station under a flow of 40,100 m^3/s on 20 July 1998, 28,600 m^3/s on 24 July 2008, and 11,400 m^3/s on 29 May 2011 for verification of the experiment. The water level may be affected by the bank roughness under different flow levels. A minor difference between the natural measured water level and the model water level is observed, and the difference increases at the tail of the model. However, the difference between the natural river

TABLE 4 Rigid bed experiment flow conditions.

Case	Prototype flow (m^3/s)	Model flow (dm^3/s)	Control water level (cm)	Control section area (cm^2)	Control section velocity (cm/s)
A	5,000	12.5	23.7	1,514	8.26
B	11,400	28.5	28.79	2,067	13.79
C	20,000	50	32.86	2,602	19.22
D	28,000	70	35.58	3,120	22.44
E	40,000	100	38.7	4,119	24.28

TABLE 5 Flow and sediment conditions of mobile bed experiment.

Typical year	Prototype generalized flow (m^3/s)	Sediment transport rate of prototype (kg/s)	Duration of each flow level (min)	Model generalized flow (dm^3/s)	Sediment transport rate of model (g/s)			Model tailgate control water level (1,985 mm)	Trial monitoring
					100%	50%	0%		
1998	4,355	239.745	120	11	0.799	0.4	0	241.28	
	7,008	726.134	341	18	2.42	1.21	0	255.98	
	12,267	2,675.452	512	31	8.918	4.459	0	289.58	
	33,952	**28,660.764**	**864**	**85**	**95.536**	**47.768**	**0**	**357.08**	Sediment concentration
	14,572	**3,995.688**	**576**	**36**	**13.319**	**6.66**	**0**	**292.48**	Topography
	7,593	875.236	160	19	2.917	1.459	0	250.28	
	5,844	475.625	120	15	1.585	0.793	0	238.28	
	5,233	459.682	120	13	1.532	0.766	0	233.18	
	7,555	1,081.333	363	19	3.604	1.802	0	252.08	
	11,155	2,680.252	320	28	8.934	4.467	0	269.88	
	13,115	3,907.774	437	33	13.026	6.513	0	285.98	
	19,270	9,576.426	395	48	31.921	15.961	0	304.48	
2008	**23,614**	**15,376.63**	**459**	**59**	**51.255**	**25.628**	**0**	**320.88**	Sediment concentration
	15,559	**5,818.381**	**288**	**39**	**19.395**	**9.698**	**0**	**291.48**	Topography
	8,282	1,339.381	160	21	4.465	2.233	0	252.98	
	14,063	4,597.618	256	35	15.325	7.663	0	289.98	
	7,037	916.441	213	18	3.055	1.528	0	243.88	
	8,197	1,307.579	619	20	4.359	2.18	0	247.58	
	12,266	3,343.68	373	31	11.146	5.573	0	274.88	
	17,673	**7,828.608**	**672**	**44**	**26.095**	**13.048**	**0**	**298.58**	Sediment concentration
2011	**12,153**	**3,272.365**	**384**	**30**	**10.908**	**5.454**	**0**	**271.28**	Topography
	8,934	1,597.962	352	22	5.327	2.664	0	255.58	
	14,093	4,620.496	149	35	15.402	7.701	0	272.78	
	7,439	**1,043.052**	**469**	**19**	**3.477**	**1.739**	**0**	**244.58**	Topography

The black numbers indicate that we have carried out the measurement under this working condition.

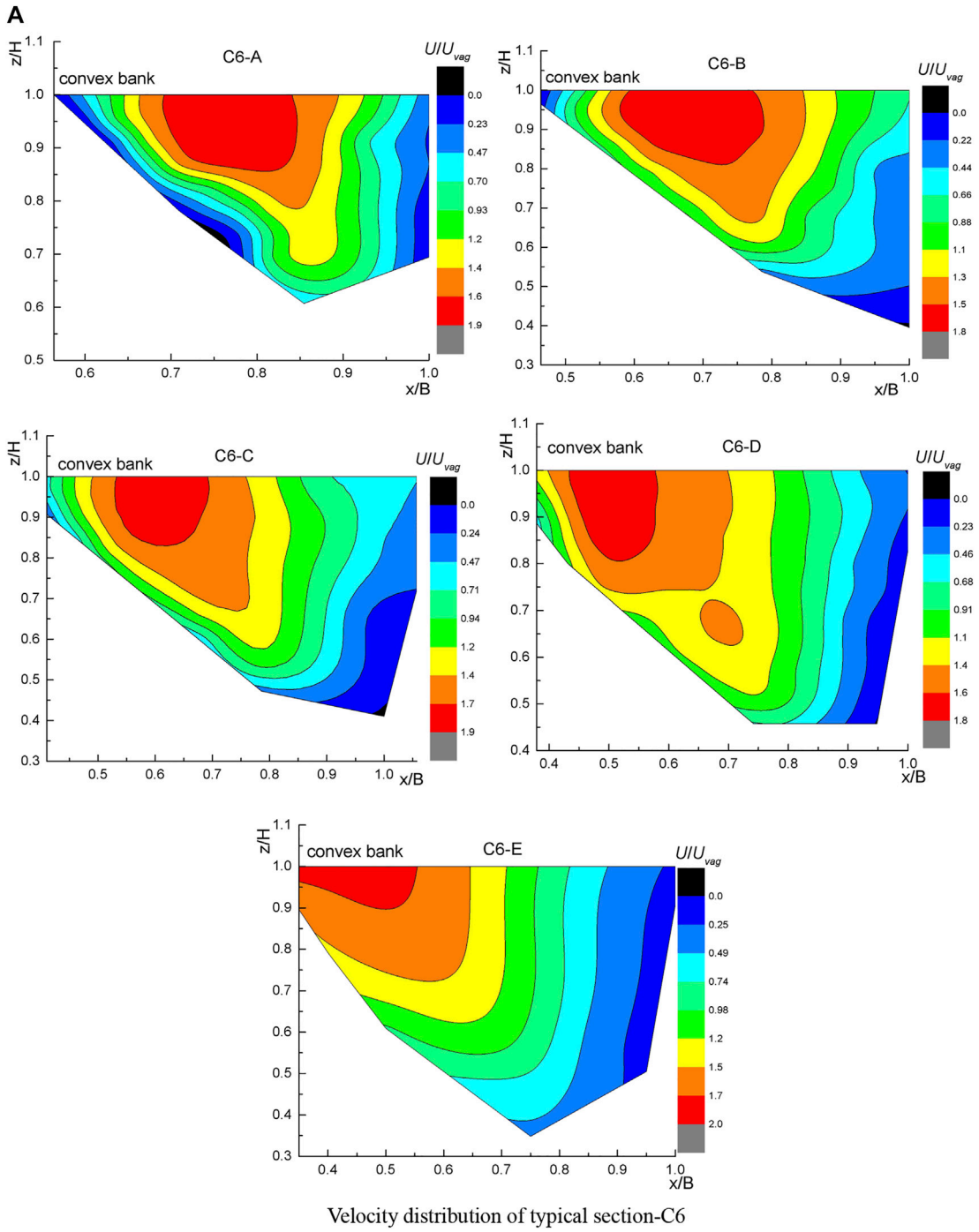

FIGURE 8
Velocity distribution of typical section.

water level and the verified water level is less than 1 mm, which is within a reasonable error range. The initial riverbed landform of the model verification experiment is made of 1: 10,000 underwater landforms measured in November 2011. The model validation experiment releases the flow and sediment process of the Shashi hydrological station from November 2011 to October 2013 to reproduce the measured riverbed landform in October 2013. The results of the verification

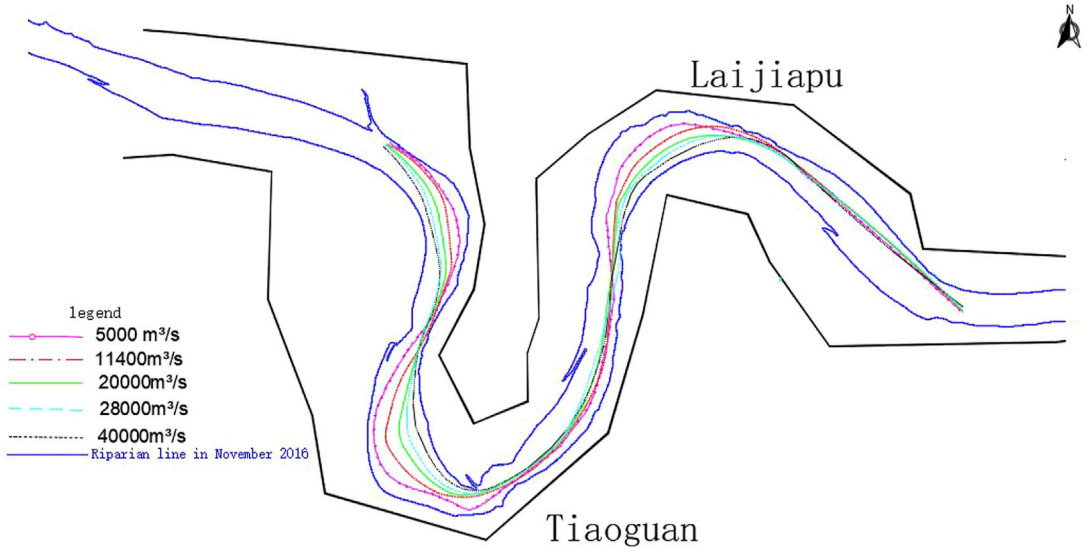

FIGURE 9
Variation of the dynamic axis of flow under different flow levels.

experiment show that the model reproduces the principles of erosion, deposition, and sediment movement of the prototype shoal and channel sufficiently. Moreover, the thalweg position and cross-section shape of the model are generally consistent with those of the prototype. The results of the validation experiment demonstrate that the design of the model, the selection of sediment, and the selection of various scales are reasonable. Through the validation experiment, all parameters, including sediment concentration, sediment transport rate, and scouring and silting time of the model, are accurately determined (Table 3).

3.3 Experimental program

The experiment has been subdivided into two parts: the first part is the rigid bed experiment. Five groups of working conditions have been selected for the experiment, including large, medium, and low flow levels (Table 4). The C1–C17 sections, marked in Figure 6A, have been selected as the velocity measurement section. The 10–15 vertical lines have been chosen for each cross section for measurement, and the measuring points of each vertical line were distributed according to the water depth, with one measuring point every 2 cm. The second part is the mobile bed experiment. For the mobile bed experiment, we have selected the 2016 1: 10,000 landform to initially constitute the mode. In the experiment, we used the measured flow and sediment processes of the Shashi hydrological station in 1998 (high flow year), 2008 (medium flow year), and 2011 (low flow year) (Table 5). In the experiment, we utilized sediment discharge as the control factor, and we selected three working conditions of 100, 50, and 0% sediment discharge, respectively. The S1–S10 sections, illustrated in Figure 6B, have been selected as the topographic and sediment concentration monitoring sections. The selection of sediment concentration measurement points has been the same as the earlier described velocity measurement. The sediment concentration has been calculated by the drying and weighing method, and the landform has been monitored by a topographic instrument (invented by the Yangtze River Scientific Research Institute and Wuhan University).

4 Results

4.1 Flow characteristics

The C6 and C14 sections (Figure 6A) have been selected for a detailed velocity analysis as they represent typical sections. The chosen section is located near the upper position of the bend top of the two bends, which can reflect the distribution characteristics of the cross-sectional velocity. The two observation sections show very similar change features (Figure 8): With the increase of the flow level, the main flow area gradually shifts toward the convex bank. The main difference is the lower degree of curvature of the C14 section. The main flow area shifts toward the convex bank with increasing flow level, but the range of movement is lower than that of the C6 section. This observation implies different constraints on the flow movement related to the degree of

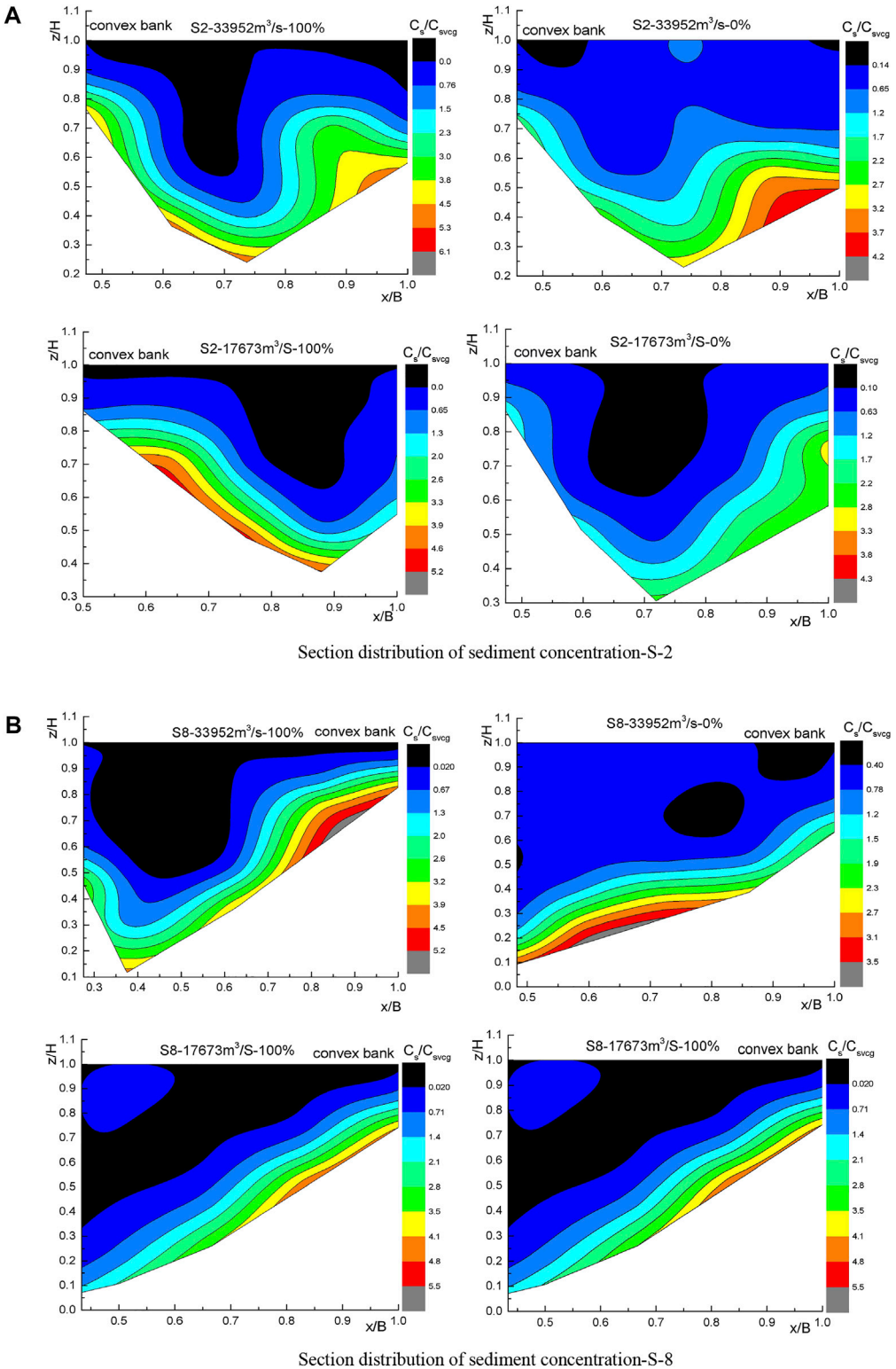

FIGURE 10
Section distribution of sediment concentration.

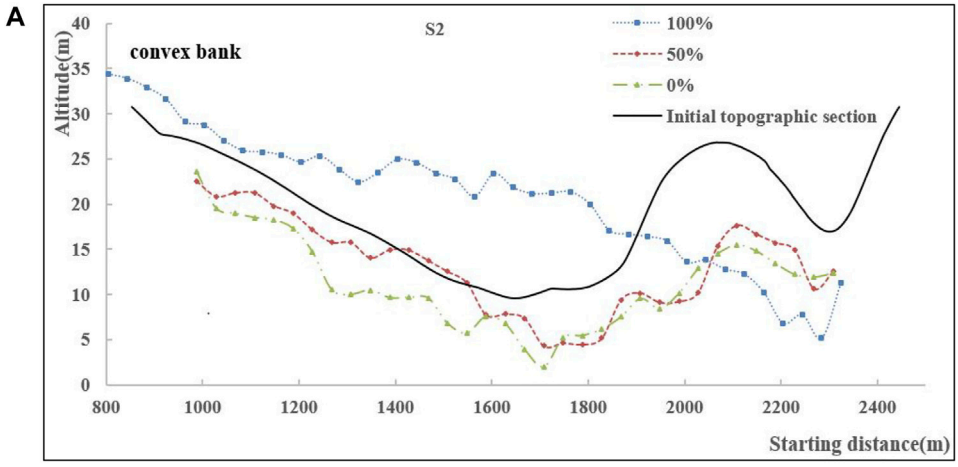

FIGURE 11
Topographic change of selected sections.

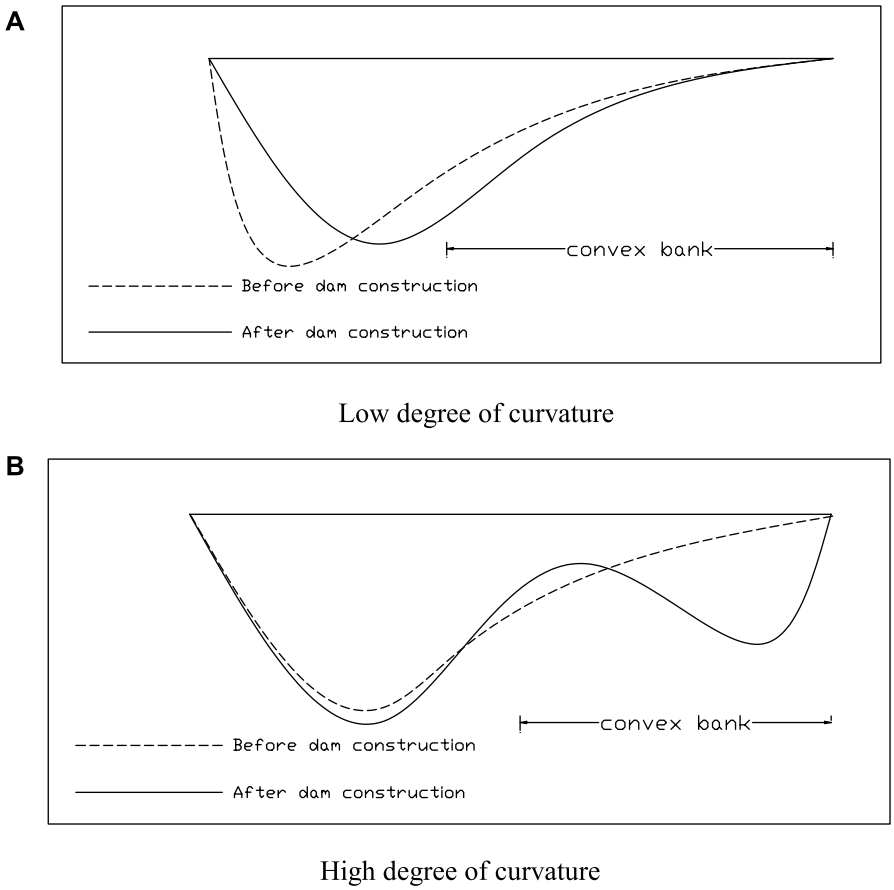

FIGURE 12
Topographic section changes of river channel with different degrees of curvature.

curvature of the bend. For a low degree of curvature of the bend, the restriction degree of the river channel to the flow movement is inferior at the same flow level condition. Otherwise, the results are the opposite. For the same bend, the constraint of river boundary conditions on flow decreases gradually with increasing flow level.

In previous studies, the swing law of the dynamic axis of flow in the meandering channel has been attributed to the incoming flow and the type of bend. It has been termed the law of "low water near the bank, high water swinging to the middle of the river" (Zhang et al., 2021). According to our experimental results (Figure 9), the dynamic axis of flow swings from the concave bank to the convex bank in the two bends with the increase of the flow level, which is the same as the distribution law of the section velocity. The radii of curvity of the Tiaoguan bend and the Laijiapu bend are 1,062 m, and 1,524 m, respectively, as obtained by the trial circle method. For a bend with a different radius of curvity, the motion trajectories of the dynamic axis of flow are different under the same flow level. For the bend with a small radius of curvity, the position of the dynamic axis of flow is close to the convex bank, whereas for the bend with a large radius of curvity, it is close to the concave bank.

The variation of the dynamic axis of flow is generally characterized by the inlet section of the bend being close to the convex bank. Subsequently, the dynamic axis of flow gradually shifts to the concave bank to reach the nearest point (vertex scouring position) from the concave bank. Finally, it gradually returns to the convex bank at the outlet of the bend. With the increase of flow level, the radius of the dynamic axis of flow decreases gradually, and the vertex scouring position declines gradually, showing a trend of swinging toward the convex bank. The swing range is large at the top of the bend and small at the inlet and outlet. Our experimental results demonstrate that the swing characteristics of the dynamic axis of flow are consistent with the law of "low water near the bank, high water swinging to the middle of the river" proposed in previous studies. Compared with the bend with a larger radius of curvity, the vertex scouring position of the dynamic axis of flow moves downstream of the bend for the bend with a smaller radius of curvity, and the radius of curvity of the dynamic axis of flow is

comparably small. For the same flow conditions, the swing range of the dynamic axis of flow is large under the different flow level conditions for the bend with a large degree of curvature, and the position with the largest swing range is on the upper part of the bend top. On the contrary, for the bend with a small degree of curvature, the swing range of the dynamic axis of flow is comparably small, and the position with the largest swing range is on the bend top.

4.2 Variation of distribution of the sediment concentration

The results of the rigid bed model experiment show that the dynamic axis of flow is located at the concave bank for a low flow level. In contrast, the dynamic axis of flow swings to the convex bank of the bend at a high flow level. We have selected the S2 and S8 sections, indicated in Figure 6B, to analyze the distribution characteristics of sediment concentration sections at flow levels of 33,952 m^3/s and 17,673 m^3/s, respectively (Table 5), and sediment inflow between 100 and 0% (Figure 10). The experiment results show an inhomogeneous distribution of the sediment concentration of the meandering river section. The sediment concentration increases gradually from the water surface to the riverbed. Moreover, the sediment concentration is much higher near the riverbed than at the water surface, which is in line with the characteristics of "small at the top and large at the bottom" as recognized in previous studies (Liu, 2007).

For 00% sediment inflow, the sediment concentration distribution of the two sections shows a higher sediment concentration on the convex bank than on the concave bank. With the reduction of incoming sediment, the main sediment transport belt shifts from the convex bank toward the concave bank. For 0% sediment inflow, the sediment concentration on the convex bank is lower than that on the concave bank. The observed phenomena are generally similar under the conditions of two flow levels. The sediment in the flow mainly derives from the upstream and riverbed. In the situation of sufficient incoming sediment, due to the influence of transverse circulating flow, the sediment concentration at the convex position is higher than that at the concave bank. The convex bank is silted, whereas the concave bank is scoured. For very low sediment inflow in the upstream reach, the sediment is mainly derived from the riverbed. The experimental results show that the sediment concentration on the concave bank is greater than that on the convex bank. In order to satisfy the sediment carrying capacity of the flow, the convex bank may be scoured.

4.3 Topographic change

The S2, S3, S4, S7, S8, and S9 sections, shown in Figure 6B, have been selected for an analysis of the landform change characteristics (see Figure 11). The selected sections are located at the top of the bend as well as above and below the top of the bend. The main factors affecting the landform change of the cross section of the bend include the degree of curvature of the meandering channel and the sediment inflow upstream. In the situation of sufficient incoming sediment, the evolution of the bend basically conforms to the evolution law of concave bank scouring and convex bank silting. At first, we discuss the bend with a large degree of curvature (Figures 11A–C). The landform evolution of the river channel at the bend top and the upper part of the bend top is radical. With the decrease of incoming sediment, the convex bank of the bend is scoured, the concave bank is silted, and the main channel swings toward the convex bank. In addition, the cross section of the upper channel at the bend top gradually changes to W shape. At the lower part of the bend top, with the decrease of incoming sediment, the river channel is generally scoured, and the V shape of the cross section of the river channel remains unchanged.

For bend with a small degree of curvature (Figures 11D–F) at the upper part of the bend top, the convex bank is silted, and the channel becomes narrower with the decrease in incoming sediment. The evolution of the bend top position is drastic. The convex bank of the channel at the bend top position and the lower part of the bend top position are scoured, and the main channel is deeply brushed and widened with the decrease of incoming sediment. The river cross section of the entire bend is V-shaped.

5 Discussion

5.1 Coupling mechanism

According to our prototype data observation and the results of our model experiment analysis, the flow and sediment conditions in the lower reaches of a river will significantly change, and the landform characteristics of the river will be adjusted to the new situation after the construction of a river barrage in the upper reaches of the river. The phenomenon of sediment inflow reduction in the river downstream of dams after the construction of a barrage is common in several other rivers (Li et al., 2015; Chen et al., 2018). Taking the meandering channel as an example, the change of the landform characteristics of the river channel is mainly related to the shape and boundary conditions of the meandering channel itself as well as the flow and sediment inflow conditions in the upper reaches of the river channel.

We have studied the meandering river in the lower reaches of the Three Gorges Reservoir of the Yangtze River in China as a prototype observation reach. According to prototype observation, the evolution characteristics of bend bypassing and shoal cutting were initiated in the downstream reach after

the operation of the Three Gorges reservoir. Theoretical analysis and model experimental research indicate that the flow process changes significantly after the operation of the Three Gorges reservoir. Flow levels <5,000 m^3/s and >25,000 m^3/s have decreased, whereas flow levels >5,000 m^3/s and <25,000 m^3/s have increased. The rigid bed model experiment results show that with the increase in flow level, the dynamic axis of flow swings to the convex bank. Therefore, the duration of the dynamic axis of flow being located on the convex bank has increased after the operation of the Three Gorges reservoir, providing dynamic conditions for the scouring of the convex bank of the meandering river. The results of the mobile bed model experiment indicate that with the decrease of incoming sediment, the sediment concentration on the convex bank at the top of the bend is lower than that on the concave bank, and the convex bank is scoured. The data document that as the sediment inflow from the upstream decreases, the sediment concentration on the convex bank is lower than the sediment carrying capacity of the flow, and the convex bank is subject to cumulative scouring. Hence, a gradual decrease of the incoming sediment causes scouring of the convex bank of the meandering river, and the central bar may appear near the concave bank.

To summarize, the reduction of the incoming sediment is the main cause for the change of the landform characteristics of the meandering river, as it disturbs and ultimately destroys the natural equilibrium of river beach and river channel sediment transport in the meandering river. In previous studies, the discussion of the evolution of the meandering channel was mostly based on the condition of sediment transport balance. In our study, we consider the conditions of sediment transport imbalance, which can provide a reference for the discussion of riverbed deformation during sediment reduction in comparable rivers.

5.2 Meandering channel deformation model

Previous studies have mostly used generalized bends with the same shape and size (Shiono et al., 2008; Wang et al., 2022). In our study, we have considered that natural rivers are composed of different types of bends, and we have analyzed the changes of the bend section under conditions of the reduced amount of incoming sediments, Therefore, our study may provide a solid reference for the study of comparable rivers. With a different degree of curvature of the bend, the swing range of the dynamic axis of flow is different from the flow levels; hence, the landform characteristics of the river channel are adjusted to different patterns. Two main patterns are distinguished, that is, the cross-section change of bends with a high degree of curvature and bends with a low degree of curvature (Figure 12). For bends with a low degree of curvature, the swing range of the dynamic axis of flow changes slightly with the flow levels. The exchange frequency between sediment carried by flow and bed sediment is low, and the deformation range of riverbed landforms is generally minor. The dynamic axis of flow swings at the top of the bend; hence, the river channel landform changes markedly at the top of the bend. Due to the low swing range of the dynamic axis of flow, the change range of the river topography is very moderate, and the cross section of the river topography is V-shaped under the condition of reduced sediment inflow (Figure 12A). For bends with a high degree of curvature, from the entrance of the bend to the top of the bend, the swing range of the dynamic axis of flow is large, and the exchange frequency between sediment carried by flow and riverbed sediment is particularly high. Therefore, the evolution range of landform at the upper part of the bend top is large, and the cross section of riverbed landform changes from V shape to W shape under the condition of reduced sediment inflow (Figure 12B).

6 Conclusion

Based on the theoretical analysis of measured data and a physical experimental model, we have deciphered the coupling mechanism of the river landform change characteristics of the meandering river and the variation of flow and sediment conditions induced by the reduction of sediment inflow. We have derived the following findings:

The construction of river barrages changes the flow and sediment conditions in the downstream reach. After the construction of the Three Gorges Reservoir in China, the average annual runoff of the lower reaches of the reservoir has slightly decreased, but the incoming flow process has changed significantly. The main consequences have been the reduction of floods and extremely low flow levels, whereas the occurrence frequency of medium and low flow levels has significantly increased. In addition, the sediment transport and interannual average daily sediment concentration have decreased significantly.

The swing range of the dynamic axis of flow is closely related to the flow and the plane shape of the bend. Large swing ranges of the dynamic axis of flow occur near the bend inlet to the bend top and gradually close together at the lower part of the bend top. Therefore, the channel evolution from the inlet to the top of the bend is significant.

After the construction of the river barrage, the change of flow conditions provides dynamic conditions for the phenomenon of bend bypassing and shoal cutting in the meandering channel downstream of the river barrage. The sediment concentration of the flow decreases significantly, which is caused by sediment intercepted by river barrages and the change in the environment. The sediment transport capacity of flow is much higher than that of the sediment inflow. These are the main factors for the bend bypassing and shoal cutting in the meandering channel of the natural alluvial river.

The degree of curvature of the meandering channel is large under the influence of sediment reduction. The dynamic axis of

flow swings to the convex bank with the increase of the flow level, and the swing range is high. Therefore, the convex bank is scoured, and the concave bank of the river channel is silted to form a central bar. Therefore, the cross-section shape of the river channel transforms from V shape to W shape. For a low degree of curvature of the meandering channel, the dynamic axis of flow swings to the convex bank with the increase of flow level, and the swing range is low. The convex bank is gradually scoured, and the concave bank is gradually silted. The topographic cross section of the river channel remains V-shaped.

Data availability statement

The original contributions presented in the study are included in the article/Supplementary Material; further inquiries can be directed to the corresponding author.

Author contributions

All authors listed have made a substantial, direct, and intellectual contribution to the work and approved it for publication.

Funding

The research is supported by the National Key Research and Development Program of China (2021YFC3200400).

Conflict of interest

The authors declare that the research was conducted in the absence of any commercial or financial relationships that could be construed as a potential conflict of interest.

Publisher's note

All claims expressed in this article are solely those of the authors and do not necessarily represent those of their affiliated organizations, or those of the publisher, the editors, and the reviewers. Any product that may be evaluated in this article, or claim that may be made by its manufacturer, is not guaranteed or endorsed by the publisher.

References

Amirhossein, A., Alireza, K., Hossein, H., and Javan, M. (2020). Effect of rigid vegetation on velocity distribution and bed topography in a meandering river with a sloping bank[J]. *Arabian J. Sci. Eng.* 45, 8633–8653. doi:10.1007/s13369-020-04818-7

Arnez, F. K. R., Nelson, J. M., Shimizu, Y., and Kyuka, T. (2021). Past, present and future of a meandering river in the Bolivian Amazon basin[J]. *Earth Surf. Process. Landforms* 46 (4), 715–727. doi:10.1002/esp.5058

Braudrick, C. A., Dietrich, W. E., Leverich, G. T., and Sklar, L. S. (2009). Experimental evidence for the conditions necessary to sustain meandering in coarse-bedded rivers. *Proc. Natl. Acad. Sci. U. S. A.* 106 (40), 16936–16941. doi:10.1073/pnas.0909417106

Chen, L., Song, T., Lu, S. Y., and Bing, J. P. (2018). Analysis of Single scouring characteristics for typical bend reaches in lower Hanjiang River. *Eng. J. Wuhan Univ.* 51 (04), 283–288. doi:10.14188/j.1671-8844.2018-04-001

Constantine, J. A., Dunne, T., Ahmed, J., Legleiter, C., and Lazarus, E. D. (2014). Sediment supply as a driver of river meandering and floodplain evolution in the Amazon Basin. *Nat. Geosci.* 7 (12), 899–903. doi:10.1038/ngeo2282

Darby, S. E., Alabyan, A. M., and Wiel, M. J. V. D. (2002). Numerical simulation of bank erosion and channel migration in meandering rivers. *Water Resour. Res.* 38 (9), 2-1–2-21. doi:10.1029/2001wr000602

Dietrich, W. E., and Smith, J. D. (1984). Bed load transport in a river meander. *Water Resour. Res.* 20 (10), 1355–1380. doi:10.1029/wr020i010p01355

Donatella, T., and Mafalda, P. (2011). Experimental analysis of cross-sectional flow motion in a large amplitude meandering bend[J]. *Earth Surf. Process. Landforms* 36 (2), 244–256. doi:10.1002/esp.2095

Fan, Y. Y., Zhang, W., Han, J. Q., and Yu, M. Q. (2017). Regulation of the evolution law of the bending river pattern in the lower reaches of the Three Gorges Reservoir and its driving mechanism. *J. Geogr.* 72 (03), 420–431. doi:10.11821/dlxb201703005

Fisk, H. N. (1945). Geological investigation of the alluvial valley of the lower Mississippi river[J]. *J. Geol.* 37 (1), 166–167.

Frascati, A., and Lanzoni, S. (2009). Morphodynamic regime and long-term evolution of meandering rivers. *J. Geophys. Res.* 114 (F2), F02002. doi:10.1029/2008jf001101

Furbish, D. J. (1991). Spatial autoregressive structure in meander evolution. *Geol. Soc. Am. Bull.* 103 (12), 1576–1589. doi:10.1130/0016-7606(1991)103<1576:sasime>2.3.co;2

Güneralp, İ., and Rhoads, B. L. (2011). Influence of floodplain erosional heterogeneity on planform complexity of meandering rivers[J]. *Geophys. Res. Lett.* 38 (14), 130–137. doi:10.1029/2011GL048134

Harmar, O. P., and Clifford, N. (2010). Planform dynamics of the lower Mississippi river[J]. *Earth Surf. Process. Landforms* 31 (7), 825–843. doi:10.1002/esp.1294

Hooke, J. M., and Yorke, L. (2011). Channel bar dynamics on multi-decadal timescales in an active meandering river. *Earth Surf. Process. Landf.* 36 (14), 1910–1928. doi:10.1002/esp.2214

Kassem, A. A., and Chaudhry, M. H. (2002). Numerical modeling of bed evolution in channel bends. *J. Hydraul. Eng.* 128 (5), 507–514. doi:10.1061/(asce)0733-9429(2002)128:5(507)

Keshavarzi, A., Hamidifar, H., and Ball, J. (2016). Bed morphology in vegetated estuarine river with mild-curved meander bend. *Hydrological Sci. J.* 61 (11), 2033–2049. doi:10.1080/02626667.2015.1081201

Li, N. B., Zeng, Y., and Wu, Z. M. (2013). Preliminary study on the causes of the bending of Qigongling main stream in Jingjiang section of the Yangtze River. *People's Yangtze River* 44 (01), 22–25. doi:10.16232/j.cnki.1001-4179.2013.01.018

Li, X. J., Xia, J. Q., Li, J., and Zhang, X. L. (2015). Variation in Bankfull Channel Geometry in the LYR Undergoing Continuous Aggradation and Degradation. *J. Sichuan Univ. Sci. Ed.* 47 (01), 97–104. doi:10.15961/j.jsuese.2015.01.014

Lindroth, E. M., Rhoads, B. L., Castillo, C. R., Czuba, J. A., Guneralp, I., and Edmonds, D. (2020). Spatial variability in bankfull stage and bank elevations of lowland meandering rivers: Relation to rating curves and channel planform characteristics. *Water Resour. Res.* 56 (8), e2020WR027477.1–e2020WR027477.24. doi:10.1029/2020WR027477

Liu, Q. Q. (2007). "Analysis of the vertical profile of concentration in sediment-laden flows. *J. Eng. Mech.* 133 (6). doi:10.1061/(ASCE)0733-9399(2007)133:6(601)

Luchi, R., Hooke, J. M., Zolezzi, G., and Bertoldi, W. (2010). Width variations and mid-channel bar inception in meanders: River Bollin (UK). *Geomorphology* 119 (1), 1–8. doi:10.1016/j.geomorph.2010.01.010

Qin, L. C., Yu, M. H., Tan, G. M., Xu, D., and Xiang, H. (2009). Study on the relationship between the change of flow dynamic axis and the abandonment of cut-off beach. *Hydrodynamics Res. Prog. Part A* 24 (01), 29–35.

Ruan, C. T. (2016). Evolution of beach and trough in sandy meandering reach under the condition of clear water discharge. *Waterw. Port.* 37 (04), 399–404. doi:10.3969/j.issn.1005-8443.2016.04.017

Sergio, L. D., and Stefano, L. (2019). Meandering evolution and width variations: A physics-statistics-based modeling approach[J]. *Water Resour. Res.* 55 (1), 76–94. doi:10.1029/2018WR023639

Shiono, K., Spooner, J., Chan, T., Rameshwaran, P., and Chandler, J. (2008). Flow characteristics in meandering channels with non-mobile. *J. hydraulic Res.* 46 (1), 113–132. doi:10.1080/00221686.2008.9521848

Sixuan, L., Yitian, L., Jing, Y., Zhang, W., Chai, Y., and Ren, J. (2018). The impacts of the Three Gorges Dam upon dynamic adjustment mode alterations in the Jingjiang reach of the Yangtze River, China. *Geomorphology* 318, 230–239. doi:10.1016/j.geomorph.2018.06.020

Wang, Q., Shan, Y. Q., Liu, C., and Liu, X. N. (2022). "Experimental study on characteristics of bed evolution and overbank floods in meandering channel under different water and sediment discharges," in *Advanced engineering sciences*, 1–11. Available at: http://kns.cnki.net/kcms/detail/51.1773.tb.20220525.0847.002.html.

Whiting, P. J., and Dietrich, W. E. (1993). Experimental studies of bed topography and flow patterns in large-amplitude meanders: 2. Mechanisms. *Water Resour. Res.* 29 (11), 3615–3622. doi:10.1029/93wr01756

Xu, D., and Bai, Y. (2013). Experimental study on the bed topography evolution in alluvial meandering rivers with various sinuousnesses. *J. Hydro-environment Res.* 7 (2), 92–102. doi:10.1016/j.jher.2012.06.003

Zen, S., Gurnell, A. M., Zolezzi, G., and Surian, N. (2017). Exploring the role of trees in the evolution of meander bends: The Tagliamento River, Italy[J]. *Water Resour. Res.* 53, 5943–5962. doi:10.1002/2017WR020561

Zhang, H. T., Dai, W. H., da Silva, A. M. F., and Tang, H. W. (2021). Numerical model for convective flow in meandering channels with various sinuosities. *J. Hydraul. Eng.* 147 (11), 04021042. doi:10.1061/(asce)hy.1943-7900.0001917

Zhang, J. Y., Chen, L., Liu, L., and Wang, Z. G. (2007). The best bend shape of the middle and lower reaches of the Hanjiang River [J]. *J. Wuhan Univ. Eng. Ed.* 40 (1), 37–41. doi:10.3969/j.issn.1671-8844.2007.01.008

Zhou, J. Y. (2015). *Improvement and application of prediction methods for flow structure and fluvial processes in meander channels*. Beijing, China: Tsinghua University.

Zhu, L. L., Xu, Q. X., and Xiong, M. (2017). Causes of convex erosion, depression and siltation in the Xiajingjiang sharp bend channel after impoundment of the Three Gorges Reservoir [J]. *Adv. water Sci.* 28 (02), 193–202.

Glossary

The following symbols are used in this article:

$\boldsymbol{R_{em}}$ model Reynolds number

$\boldsymbol{h_m}$ model water depth (cm)

$\boldsymbol{d_{50}}$ median particle size (mm)

$\boldsymbol{d}$ sediment size (mm)

$\boldsymbol{u}$ sediment incipient velocity (m/s)

$\boldsymbol{h}$ water depth in Sha Yuqing formula (cm)

$\boldsymbol{H}$ water depth in the fitting formula of flume test (cm)

$\boldsymbol{e}$ porosity (take the value as 0.4)

$\boldsymbol{Q}$ streamflow (m^3/s)

$\boldsymbol{C_s}$ sediment concentration (g/m^3)

$\boldsymbol{g_b}$ sediment transport rate per unit width (g/s)

$\boldsymbol{W}$ runoff volume (m3, W=Q*Δt)

$\boldsymbol{W_s}$ sediment discharge (t)

$\boldsymbol{\kappa}$ curvature (m^{-1})

$\boldsymbol{\rho}$ radius of curvature (m)

$\boldsymbol{U}$ velocity of flow (cm/s)

$\mathbf{U}_{\boldsymbol{vag}}$ average velocity of cross section (cm/s)

$\boldsymbol{z}$ water depth of measuring point (cm)

$\mathbf{x}$ starting distance (m)

$\boldsymbol{B}$ measuring river width (m)

$\boldsymbol{C_s}$ sediment concentration (g/m^3)

$\boldsymbol{C_{svcg}}$ average sediment concentration of section (g/m^3)

γ_s sediment bulk density (g/cm^3)

γ water bulk density (g/cm^3)

α_L horizontal scale

α_H vertical scale

α_V velocity scale

α_n roughness scale

α_Q rate of flow scale

α_{t_1} time of flow scale

α_ω subsiding velocity scale

α_{γ_0} dry capacity scale

α_d particle size scale

α_s sediment concentration scale

α_{t_2} riverbed deformation time scale (riverbed deformation caused by suspended load movement)

α_{V_0} starting velocity scale

α_{q_b} bed load transport rate per unit width scale

α_{t_3} riverbed deformation time scale (riverbed deformation caused by bed load movement).

frontiers | Frontiers in Earth Science

TYPE Review
PUBLISHED 26 September 2022
DOI 10.3389/feart.2022.965919

OPEN ACCESS

EDITED BY
Omid Haeri-Ardakani,
Department of Natural Resources, Canada

REVIEWED BY
Hadar Elyashiv,
Ben-Gurion University of the Negev, Israel
Diana Cuadrado,
CONICET Bahía Blanca, Argentina

*CORRESPONDENCE
Dong Huang,
griwh@foxmail.com

SPECIALTY SECTION
This article was submitted to Sedimentology, Stratigraphy and Diagenesis, a section of the journal Frontiers in Earth Science

RECEIVED 10 June 2022
ACCEPTED 06 September 2022
PUBLISHED 26 September 2022

CITATION
Deng Z, Huang D, He Q and Chassagne C (2022), Review of the action of organic matter on mineral sediment flocculation.
Front. Earth Sci. 10:965919.
doi: 10.3389/feart.2022.965919

Review of the action of organic matter on mineral sediment flocculation

Zhirui Deng[1], Dong Huang[1]*, Qing He[2] and Claire Chassagne[3]

[1]Guangdong Research Institute of Water Resources and Hydropower, Guangdong Engineering Laboratory of Estuary Hydropower, Guangzhou, China, [2]State Key Laboratory of Estuarine and Coastal Research, East China Normal University, Shanghai, China, [3]Section of Environmental Fluid Mechanics, Faculty of Civil Engineering and Geosciences, Delft University of Technology, Delft, Netherlands

Sediment is found throughout the world's alluvial plain rivers, estuarine coasts and adjacent seas and is thereby a key factor in major ecosystems. Suspended mineral sediment can affect the biological activity of microorganisms and plants, by reducing light penetration in the water column or by binding to organic matter. Biological processes can, in turn, affect the physical and chemical properties of the sediment particles and influence the adhesion between particles. They can facilitate the sediment aggregation (flocculation) through bridging, patching and sweep, while biological decay will mainly help to disintegrate organic matter rich flocs. Biological activity also affects the properties of flocs (structure, density, sedimentation rate and composition). This activity is itself influenced by environmental conditions (like temperature, light and nutrient fluxes). Sediment flocculation thus involves complex relationships between several physical, chemical and biological factors. The role of biology in particular needs to be better integrated in sediment transport models, through the interaction between mineral clay particles, microorganisms and their excreted polymers (Extra Polymeric Substances, i.e., EPS). In this article, a summary of the state-of-the-art research regarding sediment flocculation is given. In particular, the action of organic matter on fine-grained sediment flocculation is discussed. The aim of the article is to provide a more comprehensive understanding of bio-sediment dynamics and give an outlook on remaining research questions.

KEYWORDS

sediment flocculation, bioflocculation, algae, extracellular polymeric substances (EPS), aggregation

1 Introduction

Sediment is fundamental to the evolution of natural aquatic environments such as rivers, estuaries and lakes (van Leussen, 1988; Eisma and Irion, 1993; van Leussen, 1994; Manning et al., 2010b). Suspended sediment dynamics play an important role in geomorphological evolution, biogeochemical cycling, transport of pollutants, and aquatic biological activity (McAnally and Mehta, 2001). Cohesive sediment refers to a mixture of clay- and silt-size particles with a small amount of fine sand-size particles. This

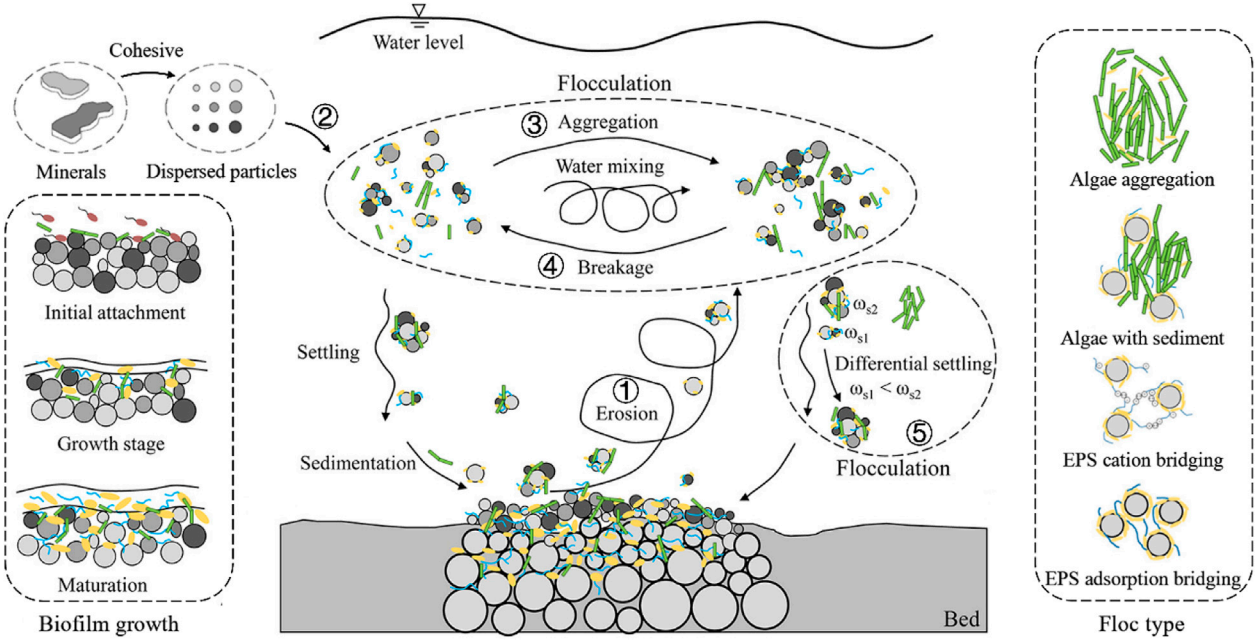

FIGURE 1
Flocculation processes including biological effects (the figure is modified after Maggi, 2005; Guo, 2018; Lai et al., 2018; Deng, 2022). The processes are: 1—Erosion: In the original figure, these particles were represented as mineral clay particles. It is now established that organic matter plays a crucial role in erosion, due to the presence of biofilms (Droppo et al., 2015; Horemans et al., 2021). The growth of biofilms is illustrated on the left. 2—Mineral clay particles enter the system by advection; the particles of clay and silt size can be composed of layers of aluminosilicates sheets that are bound together more of less strongly, depending on the clay mineralogy; the surface charge of these particles will determine their ability to flocculate.3—Aggregation: Mineral clay particles can bind together by salt-induced aggregation, but most often, in coastal environments, mineral clay particles will bind to organic matter (Deng et al., 2019; Deng et al., 2021). The different types of flocs are illustrated on the right. 4—Break-up: Under the action of shear, flocs might break. It was recently established that in the presence of organic matter flocs predominantly become smaller by reconformation (Chassagne and Safar, 2020; Shakeel et al., 2020). 5—differential settling. Due to the density difference between flocs (based primarily on their organic matter content), flocculation can occur by differential settling (Deng et al., 2019; Deng et al., 2021).

cohesive sediment is composed of mineral clay, organic matter and water in various amounts. Even though the proportion of clay-size particles and organic matter is only 5%–10% in most cohesive sediment, their presence results in remarkable rheological properties (yield stress, viscosity) of the overall sediment and can lead, in the water column, to a process called flocculation (the aggregation of mineral clay particles with themselves and/or with organic matter) through electrochemical and biochemical interactions (Dyer, 1989; Winterwerp and Kesteren, 2004; Chassagne, 2019; Chassagne et al., 2021).

Over 90% of the total volume of fine suspended sediment in an aquatic environment exists in the form of aggregates, i.e., flocs (Droppo and Ongley, 1994). Figure 1 is adapted from a classical picture illustrating the behavior of cohesive sediment in aquatic systems. It was adapted so as to show the effects of some organic parameters (EPS, short for Extra Polymeric Substances, and living microorganisms such as microalgae) on suspension, flocculation/break-up, settling and deposition. Mineral clay particles come in the water column either by hydrodynamic transport or resuspension by erosion from the bed (labels 1 and 2 in Figure 1). Under the action of microscopic forces which are linked to the particles' surface charge (van Leussen, 1988; Gregory, 2005), particles will flocculate, and form flocs, which can be large in volume and size. Flocs are usually large when they are made of a high content of organic matter, as organic matter has a low density and therefore relatively large organic matter particles can be found in the whole water column and thus aggregate with mineral sediment. To give an order of magnitude, flocs are usually found in the size range 20–200 μm, and flocs of highest size in this range (including flocs of even higher sizes) are organic-matter rich (Safar, 2022). This organic matter comes either from the water column (microalgae and their EPS) or from the bed, where biofilms can be created (Droppo, 2009; Lai et al., 2018; Ho et al., 2022). Pure mineral clay flocs (flocs composed of mineral clay aggregated through electrostatic interactions) remain limited in size by the Kolmogorov microscale (Mietta, 2010). Flocs can be divided into smaller or primary flocs under the action of shear stress or grow larger by collision with other particles (labels 3–5 in Figure 1). As the environmental factors are changing, it is argued that flocs stay in a dynamic process of aggregation and break-up (Burban et al., 1989; Eisma, 1991;

Lick et al., 1993). This classical picture should however be reconsidered in the light of organic matter properties: when organic matter consists of polymeric substances (such as proteins, sugars or DNA), flocs display elastic properties and show a high resistance to shear (Shakeel et al., 2020). Increasing shear rate then does not lead to break-up of flocs but rather to a decrease in volume, for a constant mass (the flocs become denser).

Flocculation is affected by three main types of factors: physical factors, chemical factors, and biological factors. There is quite some overlap between these different types, and one could well speak of physico-chemical factors or bio-chemical factors. Physical factors include hydrodynamic conditions (such as shear stress and vertical mixing) and sediment particle characteristics (such as particle size distribution and sediment concentration); chemical factors consist of environmental conditions (such as salinity, temperature, pH), mineral composition and surface charge of sediment particles; biological factors mainly refer to the action of microorganisms and their excreted biopolymers (Gibbs, 1985; Dyer and Manning, 1999; Winterwerp and Kesteren, 2004; Mietta et al., 2009a; Droppo et al., 2015; Fettweis and Lee, 2017). Many factors depend on each other (the role of biopolymers in flocculation is for instance related to salinity and temperature) which makes parametrizing of flocculation models extremely complex.

In the past 30 years, a lot of research has been performed on flocculation but the effect of biological processes was seldom taken into account (Thomas et al., 1999; Winterwerp, 1999; Maggi, 2005; Mietta, 2010). As there is a significant biological activity in aquatic environments, it has long been recognized that organic matter has a great impact on flocculation (Avnimelech et al., 1982). It is therefore not surprising that research on the effect of organic matter on sediment flocculation is gradually becoming more extensive. Most of the studies, however, are focused on the qualitative description of such flocculation. The distinction between different bio-flocculation mechanisms, the different floc types and their link to the factors cited above are still lacking. In this review, those correlations are discussed. The purpose of the review article is to summarize the state-of-the-art regarding sediment flocculation and presenting some of the open questions to be answered in the future.

2 The population balance model

In the standard model used to describe flocculation (the Population Balance Equation, PBE in short), a size class i is defined as a collection of particles with concentration n_i, all particles in a same class having the same size (diameter) d_i.

Aggregation and break-up processes of particles are expected to occur simultaneously and dynamically in the PBE model (Winterwerp and Van Kesteren, 2004; Chassagne, 2019; Chassagne et al., 2021).

Two parameters are related to the particles' aggregation ability: the collision frequency and the collision efficiency. The aggregation rate of particles depends on both these parameters.

2.1 Collision frequency

There are three main expressions for the collision frequency, based on the different approach mechanisms between particles. Particles can approach one another by Brownian motion, mixing by shear or differential settling (McCave, 1984; van Leussen, 1994; Tsai and Hwang, 1995). So, if a collision occurs between a particle of diameter d_i and a particle of diameter d_j, the collision frequency $f_{i,j}$ can be expressed as follows (Hunt, 1980):

Brownian motion (BM):

$$f_{i,j}(BM) = \frac{2}{3}\frac{k \cdot T}{\mu} \cdot \frac{\left(d_i + d_j\right)^2}{d_i \cdot d_j} \tag{1}$$

Mixing by shear (SH):

$$f_{i,j}(SH) = \frac{G}{6}\left(d_i + d_j\right)^3 \tag{2}$$

Differential settling (DS):

$$f_{i,j}(DS) = \frac{\pi}{4}\left(d_i + d_j\right)^2 \left|\omega_{s,i} - \omega_{s,j}\right| \tag{3}$$

The parameter k is the Boltzmann constant (1.38×10^{-23} J K^{-1}), T is the absolute temperature (293 K), μ is the dynamic viscosity of the suspending medium—water (1.005×10^{-3} Pas when the temperature is 20°C), G is the shear rate (s^{-1}), g is the gravitational acceleration (9.8 m s^{-2}), and $\omega_{s,i(j)}$ represents the settling velocity of the flocs.

Brownian motion is caused by the random thermal motion of liquid molecules, so in general it is only effective for sediment particles under the colloidal size of 1–2 μm (Dronkers et al., 1988; Lick et al., 1993; Partheniades, 1993). Brownian-induced flocculation is a slow process and in estuarine systems, where the water column experiences hydrodynamic mixing, it is not expected to be the dominant cause for flocculation.

The effect of shear rate is considered to be important for flocculation in estuarine systems. Many studies (Mehta and Partheniades, 1975; Eisma, 1991; Partheniades, 1991, 1993; Manning and Dyer, 1999; Winterwerp et al., 2006; Mietta et al., 2009a) have provided a better understanding about the relations between shear rate and flocculation. As is shown in Eq. 2, the collision frequency increases with increasing shear rate, thus promoting flocculation and the growth in particle size. However, when the particle size of flocs reaches the Kolmogorov microscale η, the increase upon shear rate will be limited. Eisma (1986) and van Leussen (1997) in particular argued that the maximum diameter of flocs should be

equivalent to the Kolmogorov microscale (minimum turbulent vortex scale) and this was also experimentally verified for salt-induced flocculation of mineral clay particles (Mietta et al., 2009a; 2009b). The Kolmogorov microscale is defined in Eq. 6.

2.2 Collision efficiency

The collision efficiency is mainly driven by the interaction forces between particles upon approach. These forces are linked to physical, chemical and biological processes, and include electrostatic forces, Van der Waals force (VDW), hydrophobic interactions and entropic forces. In the past decades, researchers have put forward a number of theories and models for sediment flocculation, among which there is the standard electrokinetic theory (named DLVO, for Derjaguin, Landau, Verwey and Overbeek), polymer bridging, cation bridging, sweep flocculation and others (Kruyt, 1949; van Leussen, 1988, 1994; Higgins and Novak, 1997; Bolto and Gregory, 2007; Lee et al., 2011). When studying the aggregation of similar primary particles (the primary particles being similar is one of the underlying hypothesis of the PBE model), the DLVO theory can provide a useful parameter (the ζ-potential) which helps to predict whether aggregation will or will not occur.

2.2.1 DLVO theory

The DLVO theory models the interaction potential between two approaching colloidal particles in a solvent (usually water). The interaction is made of two terms: a Coulombic repulsion and a van der Waals' attraction (Kruyt et al., 1952; Chassagne, 2019). The two particles have a surface charge of same sign and are surrounded by a so-called double layer which is composed, in majority, of counterions. The double layer is the result of the attractive interaction between the surface charge of sediment particles (usually negatively charged for mineral sediment) and the positively charged ions (cations) found in water. The ζ-potential is used to quantify the surface charge of a particle. It is defined as the electric potential at the surface of shear of the particle (the potential of reference is taken at infinity, where it is defined as zero). When this surface of shear is located at the surface of the particle, the ζ-potential is identical to the electric surface potential Ψ_0 (Chassagne and Ibanez, 2012). The potential Ψ_0 depends on the number of charged sites and the number of ions adsorbed on the particle surface. In most cases, the shear plane is located a few ångström away from the surface, in the layer called the Stern layer (Chassagne et al., 2009), which is the layer between the surface of the particle and the plane of shear. When the concentration of cations increases in the water, there will be a reduction in ζ-potential, as more ions will be located between the particle's surface and the shear plane, leading to better screening of the surface charge.

As is seen in Figure 2A, the electric potential drops from ζ_1 to ζ_2 when the salt concentration is increased from C_1 to C_2. The interaction energy curve displays a maximum which indicates that a repulsion force is preventing particles to aggregate when Coulombic repulsion is dominant. This barrier can be overcome by increasing ionic strength or lowering pH but can also be overcome by "pushing" the particles together. This happens *in-situ*, when the water flow enables particles to collide (see Section 2.1).

For more details about DLVO theory, the reader is referred to Chassagne (2019). There exists a lot of studies about the ζ-potential and the surface charge of clays (Rand and Melton, 1977; Sondi et al., 1996; Kosmulski and Dahlsten, 2006; Mietta et al., 2009a; Chassagne et al., 2009; Mietta, 2010; Tsujimoto et al., 2013), and the results show that either a decrease in pH or an increase in ionic strength usually decreases the absolute value of the ζ-potential. A low ζ-potential is synonymous for aggregation ability: particles with a low ζ-potential have a weak Coulombic repulsion. For these particles, van der Waals attraction will dominate and lead to flocculation Figure 2B. It was shown in (Mietta et al., 2009a; 2009b) that the ζ-potential could be related to the collision efficiency.

2.3 Break-up mechanisms

When shear forces are stronger than the bonding force between particles, it is expected that flocs will break-up.

The break-up rate B_i is usually used to describe the break-up of flocs and it is traditionally a function of shear and size of particles (Lick and Lick, 1988). The break-up term corresponding to the breaking of particles is given by $B_i(TS)$. From a modeling point of view, particles can leave a size class either by break-up (flocs of smaller sizes are then created), through $B_i(TS)$, or by aggregation (a floc of larger size is then created), through the term $B_i(C)$ (Spicer and Pratsinis, 1996). The term $B_i(C)$ is also depending on turbulent shear, as this shear enables particles to collide and subsequently aggregate (Serra and Casamitjana, 1998). The expression for $B_i(TS)$ is:

$$B_i(TS) = EG^b d_i^p \tag{4}$$

where d_i is the size of floc in class i. The parameter p is usually taken equal to 1 and E and b are fitted to data. The term $B_i(C)$is given by:

$$B_i(C) = \sum_{j=1}^{N} a_{i,j} f_{i,j} n_j \tag{5}$$

where $a_{i,j}$ is the collision efficiency, $f_{i,j}$ represents the frequency of particle collision, and n_j is the number of flocs of a given size d_j. Usually $a_{i,j}$, which should be between 0 (no aggregation) and 1 (always aggregation), is taken to be constant and arbitrarily equal to $a = 0.5$ (Mietta, 2010). It can be seen from Eq. 1 that the increase of either shear rate or the floc size will increase the break-up rate of particles. The term $B_i(C)$ depends on shear and particle size, through the

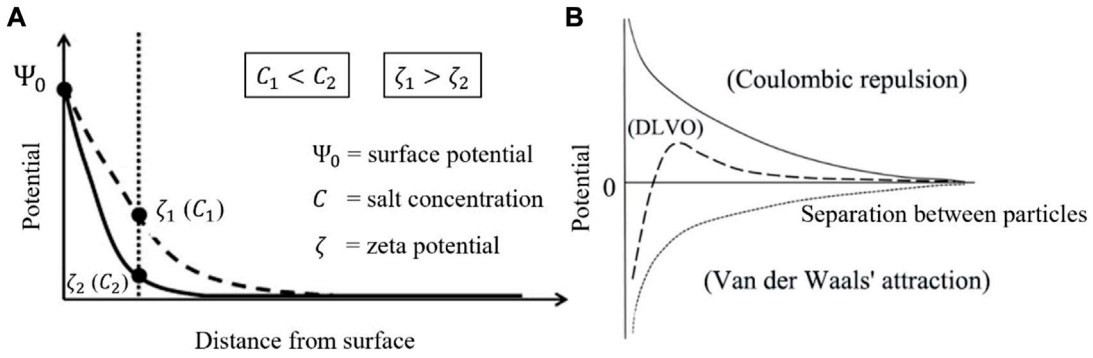

FIGURE 2
(A) Electric potential as function of the distance from the surface of a colloidal particle. The ζ−potential of particles is a function of salinity: the higher the salinity, the lower the ζ−potential. **(B)** The DLVO interaction energy between two particles as the sum of an attraction (van der Waals) and a repulsion (Coulomb). (figures modified after Chassagne et al., 2009).

term $f_{i,j}$, see Eq. 2: the larger the particles, the larger the collision frequency.

In general, the floc break-up process is poorly understood (Thill et al., 2001). The empirical parameters should account for the bonding forces between particles as the stronger the bonds, the more resistant the floc is to any exterior force (Jarvis et al., 2005) or inner tensile stress (Yeung and Pelton, 1996), see Figure 5. The ability of flocs to resist damage (floc strength) is closely related to flocculation and the size and structure of flocs (Son and Hsu, 2009). Floc strength is a function of the electrochemical attraction between clay minerals and the agglutination of organisms and organic matter on particle surface (Passow, 2002; Bainbridge et al., 2012).

2.3.1 The Kolmogorov microscale

Shear stress is one of the most important external factors affecting the flocculation process and has been widely studied (e.g., Dyer and Manning, 1999; Mietta et al., 2009b; Partheniades, 1993; Winterwerp, 1998).

The turbulent shear rate G is often used to quantitatively describe the turbulent strength:

$$G = \sqrt{\epsilon/\nu} = \nu/\eta^2 \quad (6)$$

where ϵ is the turbulent energy dissipation rate, ν is the kinematic viscosity of water body, and η is the Kolmogorov microscale. The Kolmogorov microscale is the smallest scale of a turbulent eddy.

3 Flocculation by organic matter

Organic matter, and more specifically the polyelectrolytes produced by microorganisms bind to sediment particles in different ways, depending on their polymeric chain length (defined by the polymeric molecular weight), and charged groups. Their way to bind to sediment particles is also depending on salinity, pH and shear stresses. Polyelectrolyte-induced flocs can achieve sizes much larger than the Kolmogorov microscale, owing to the polyelectrolyte shape (chain-like) and elastic nature (Ibanez Sanz, 2018; Shakeel et al., 2020).

Depending on the polyelectrolyte, flocculation between mineral sediment and polyelectrolyte can occur through bridging (Riley, 1963; Nabzar et al., 1988; Hicks, 1988; Winterwerp and Kesteren, 2004), patching mechanism (Bergaya and Lagaly, 2013) or sweep, as shown in Figure 3.

A polyelectrolyte can stick to certain points of the sediment's surface as trains, separated from one another by loops and for much of its length it is able to extend into the solvent as tails (Figure 4). The attraction between the interacting molecular chains should be strong enough to overcome the entropy repulsive force caused by the decrease in freedom of the chains (Rosen, 2004).

Under suitable conditions, microbial organisms, such as diatoms, can produce polyelectrolytes (polysaccharides), which is a gelatinous organic matter (OM). These polyelectrolytes are called Transparent Exopolymer Particles (TEP) or Extracellular Polymeric Substances (EPS). They are polymeric chains which include a large amount of anionic polysaccharides like galacturonic acid that is the main component of pectin (Plude et al., 1991). The organic polymers can form biofilms on the surface of sediment particles and act as flocculating agent (Bar-Or and Shilo, 1988b; Bar-Or and Shilo, 1988a). Because of the ionization of their functional groups (such as carboxylic acid and phosphate), microbial cells and EPS have a high density of negative charges (Sheng et al., 2010), and anionic polysaccharides aggregate with negatively charged sediment particles through cationic bonding. These cations are salt ions found in the water, and their concentration is a function of salinity. The EPS secreted from microorganisms can also be a cationic polymer (Plude et al., 1991). Aly and Letey (1988) have

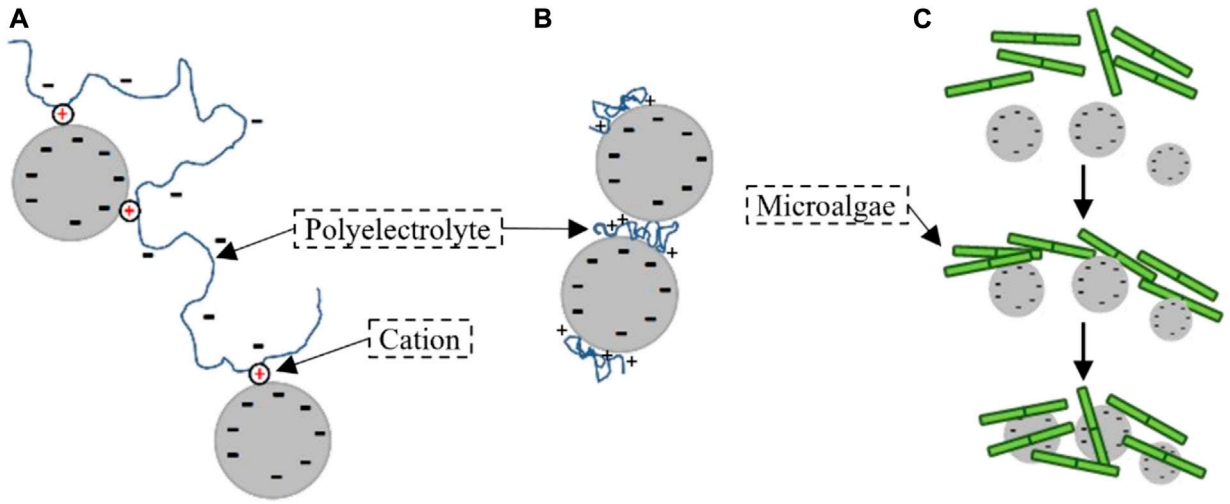

FIGURE 3
A schematic diagram of different types of flocculation. The grey disks symbolize negatively charged mineral clay particles **(A)** bridging flocculation. The anionic polyelectrolyte needs a cation (in red) to bridge to the clay; **(B)** patching flocculation. The cationic polyelectrolyte binds easily to the clay through attractive Coulombic forces; **(C)** sweep flocculation. (figures modified after Chassagne, 2019).

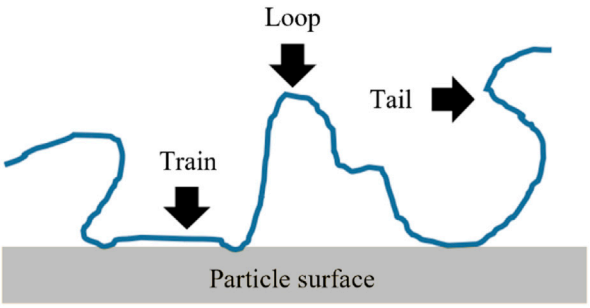

FIGURE 4
Attachment configurations of a polymer to a sediment particle surface: tail, train and loop. (figure modified after Chassagne, 2019).

found that flocculation by cationic polymers is different from flocculation by anionic polymers. Flocculation with cationic polymer is done by charge neutralization, while flocculation with anionic polymer is mainly done by bridging mechanism (Shakeel et al., 2020). Studies have shown that adding divalent cation can enhance flocculation (Yeh, 1988; Park et al., 2010).

3.1 Bridging aggregation

Bridging aggregation occurs when a free polyelectrolyte in solution captures suspended mineral particles (see Figure 3A). Usually, one finds that the optimum polymer concentration to achieve flocculation corresponds to half surface coverage for the polymer. Polymeric bridges are changing as function of shear. Bridging aggregation can even occur with polyelectrolytes having surface charges of same sign as the ones of the particles. In that case, aggregation is enabled by the presence of oppositely charged ions in the water. When polymer bridging flocculation happens, the bridging particles should have an available surface to connect polymer chain segments (Biggs et al., 2000). Flocs formed by bridging through polymer chains are flexible and stretchable (Otsubo, 1992; Gregory and Barany, 2011).

3.2 Patching aggregation

Patching aggregation occurs when polyelectrolytes have a charge that is opposite in sign to the one of the sediment particles (see Figure 3B). The polyelectrolyte then strongly binds to the sediment particle, and its tails do not extend much into the solvent. Aggregation is then made possible between one polymer patch of one particle and the bare surface area of another particle. Flocs formed through patching aggregation have generally a higher strength than those formed through other ways. The force is dependent on the number of bound segments (Swenson et al., 1998).

3.3 Sweep flocculation

As is visible under a microscope, microorganisms can form a polymeric network with holes and channels (Li and

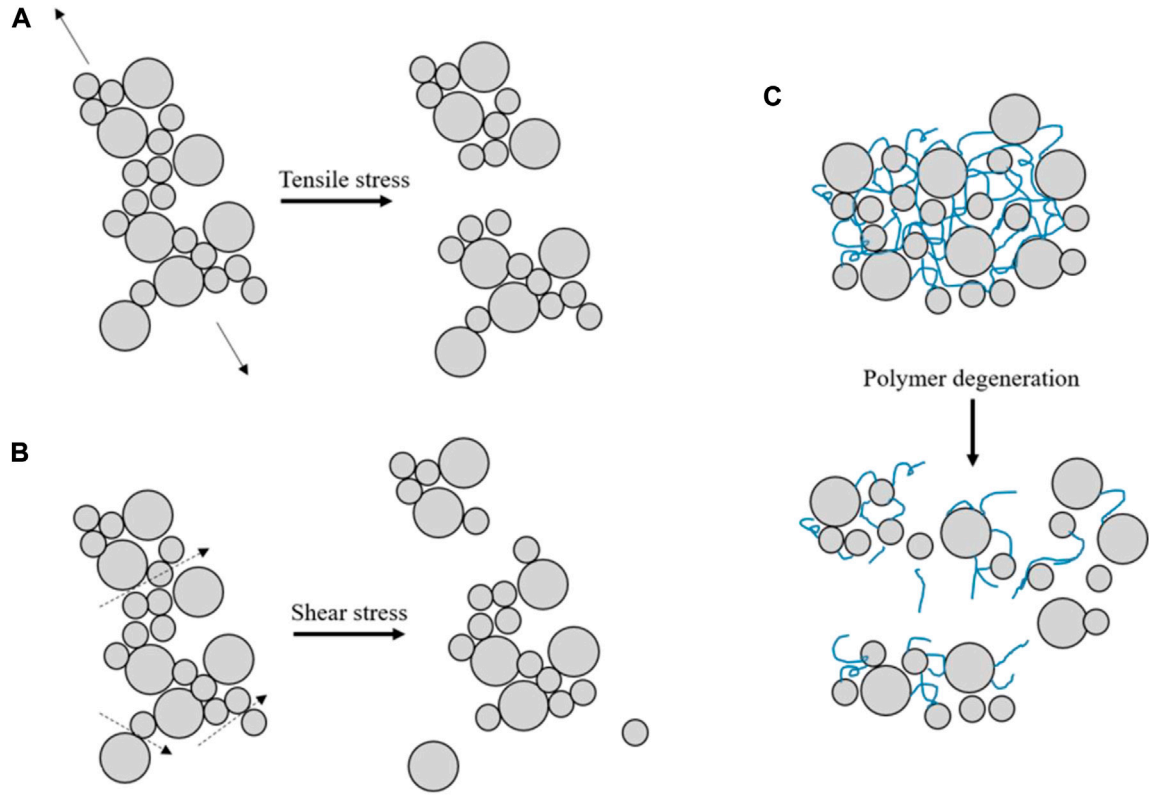

FIGURE 5
A schematic diagram of floc break-up processes, **(A)** Break up by tensile stress **(B)** Break up by shear stress **(C)** Break up by polymer degeneration (figure modified after Jarvis et al., 2005; Lai et al., 2018).

Ganczarczyk, 1990) through the bridging of their produced Extracellular Polymeric Substances (EPS) (Leppard, 1992; Jorand et al., 1995). This network has a large surface area and can absorb pollutants, nutrients and minerals (Costerton et al., 1987). At the same time, there are large and small interspaces inside the network. When sedimentation of this network occurs, some fine particles can be trapped by it and be embedded (see Figure 3C). This process is called sweep flocculation. Although sweep flocculation is usually studied in sewage treatment, a similar process has been observed in estuarine environments (Gregory, 2005; Lee et al., 2011). Sweep flocculation is a function of electrochemistry and other characteristics of the network. As a result, the network floc gets increasingly larger (Deng et al., 2019).

To summarize, the flocculation of fine sediment under the influence of organic matter is a complicated dynamic process involving chemistry, physics and biology. The time-dependence of flocs composed (in part) of organic matter is poorly understood, especially in relation with the living microorganisms that are known to bind to mineral sediment thanks to EPS (Deng et al., 2019; Deng et al., 2021; Safar et al., 2022).

Recent studies have found that organic matter-induced flocculation is also affected by biological decay and that the strength of bonds is time-dependent, see Figure 5. Flocs can therefore break without the influence of shear, simply by biodegradation (Mikutta et al., 2007; Jeldres et al., 2018).

The rate of microbial degradation depends on the environment and leads to catabolism (Foree and McCarty, 1970). The degradation is different for different types of EPS (Zinkevich et al., 1996; Comte et al., 2006). Living microorganisms (that produce EPS and other types of polyelectrolytes) are function of grazing (Porter, 1973) and water nutrients (Chai et al., 2006; Li et al., 2014). Further study on the degradation of EPS in combination with its interaction with sediment is required.

4 Discussion on flocculation models

4.1 The PBE vs. the logistic growth model

Using the PBE model explained in Section 2, it is found that an increase in turbulent shear stress increases the collision

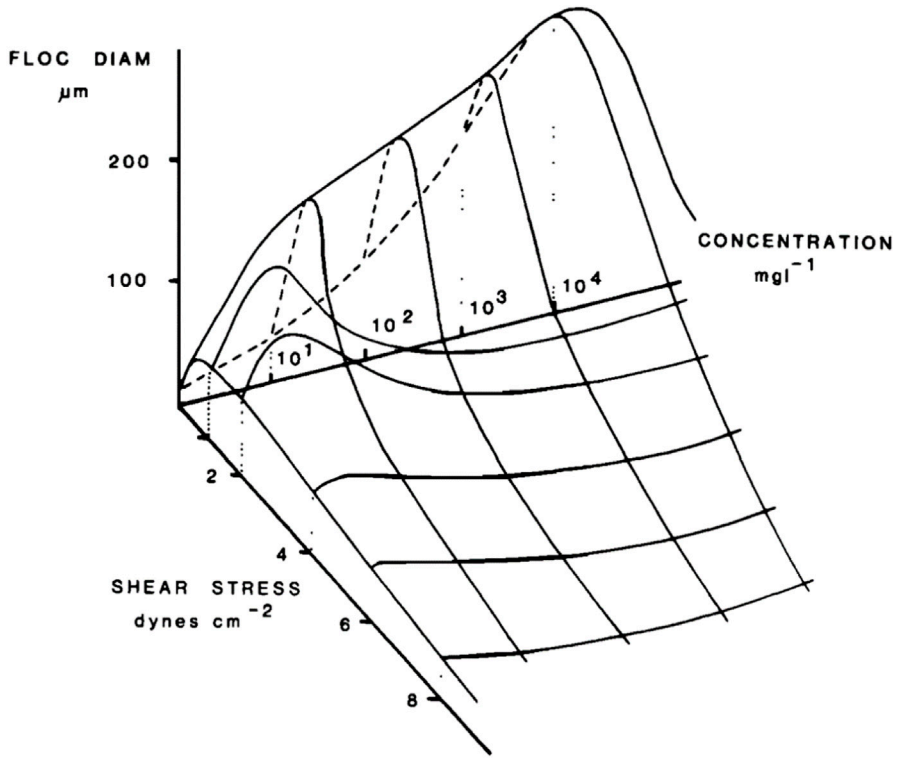

FIGURE 6
A conceptual diagram of the relationship between floc size, turbulent shear and suspended sediment concentration (figure following after Dyer, 1989).

frequency between sediment particles hereby promoting sediment particle aggregation. On the other hand, high shear stresses reduce the Kolmogorov microscale η and increases the break-up frequency of flocs.

Using the Population Balance Model, the steady-state average size of a floc will be the Kolmogorov microscale (Mietta, 2010). When a floc (in the model) has a size larger than the Kolmogorov microscale, it is expected to break-up into smaller flocs with a denser structure (Dyer, 1989; Winterwerp, 2002).

Previous studies suggest that the maximum size of flocs formed in turbulent flow is controlled by η (Eisma, 1991; van Leussen, 1997; Droppo et al., 2000; Mikkelsen, 2002a; Mietta et al., 2009a; Mietta, 2010). There is indeed a positive correlation between the floc size and Kolmogorov microscale, which are usually of the same order of magnitude (van Leussen, 1997; Mietta et al., 2009a; Kumar et al., 2010).

Dyer (1989) first suggested that there exists a critical value of shear stress, below which the floc size increases and after which decreases and conceptualized this in a figure (Figure 6). The optimum in particle size as function of shear stress is only occurring if all experiments (for each shear stress) are done for a fixed flocculation time, and that the equilibrium floc size has not yet been reached. Indeed, if the equilibrium floc size would have been reached for all experiments, for fully suspended particles, flocs formed at the lowest shear would be the largest and the floc size as function of shear rate would be a monotonic decrease, as has been shown by Mietta et al. (2009b). For a fixed (short) flocculation time, it is expected that below a critical shear rate the flocculation rate is limited by the amount of collisions and above this critical shear by the Kolmogorov microscale. This is however not true for organic matter flocs—they can grow larger than the Kolmogorov microscale and their flocculation rate is extremely fast (Shakeel et al., 2020).

Note that on Figure 6 there is also a maximum in floc size as function of concentration for a given shear rate. The reason for this optimum is unclear, as one would expect, for any flocculation time, either an increase in floc size as function of concentration (related to an increase in collision frequencies) or that the floc size remains constant (equal to the Kolmogorov microscale η).

The fact that flocs follow the Kolmogorov microscale is true for salt-induced flocs (Mietta, 2010), under the condition that the flocs have reached their equilibrium size and that they remain suspended. At low shear, it can be shown that for dense particles, not all particles remain in suspension and hence the average mean diameter decreases with the increasing number of particles

that are not suspended (Mietta et al., 2009b). It should be noted that in the case of low turbulent shear stress, the flocculation process may change from being dominated by turbulent shear stress to being dominated by differential settling, thus affecting the flocculation process and the characteristics of the final flocculation (Lick et al., 1993; Chen et al., 1994; Fugate and Friedrichs, 2003).

The characteristic values of shear stress between these two regimes have been obtained in many studies, including laboratory experiments (e.g., Manning and Dyer, 1999; Mietta et al., 2009a; Kumar et al., 2010) and field observation studies (e.g., Markussen and Andersen, 2014; Sahin, 2014; Guo et al., 2017). Markussen and Andersen (2014) and Guo et al. (2017) showed that the characteristic turbulent shear rate in their *in-situ* studies was about 3–4 s^{-1}, whereas the critical range obtained in other studies (Manning and Dyer, 1999; Serra et al., 2008; Kumar et al., 2010; Zhang et al., 2013; Sahin, 2014) was about 15–40 s^{-1}, indicating that the flocs properties might be different in different estuaries.

In estuarine and coastal areas, the largest shear gradient is close to the channel bed (10%–20% of the water column above bed is affected), where about 80% of turbulence energy is present. This produces a powerful uplift force for particles and the local shear stress controls the maximum size of suspended flocs (Mehta and Partheniades, 1975). From a PBE modelling perspective, in an area with constant shear stress, the strength, size and density of flocs will be in a dynamic equilibrium. When the shear stress is varied from low to high, flocs will become smaller. When the shear rate is varied from high to low, flocs will grow larger. These processes are completely reversible when the PBE model is used, implying that the structure of a floc of a given size will always be the same, independently of its history.

One can question the validity of the PBE model in the case of *in-situ* flocculation, for several reasons. First of all, it is not proven, as the PBE assumes, that the size of a floc is governed by a dynamic balance between aggregation and break-up. As was shown in Chassagne and Safar (2020), it is well possible to model flocculation data by using a logistic growth model. This model, in contrast to the PBE model does not require break-up to ensure a realistic steady-state floc size. Indeed, without the break-up term, the PBE model would give an infinitively large equilibrium floc size. As discussed in Chassagne and Safar (2020), Chassagne et al., (2021), an equilibrium floc size can, for example, be reached because of a depletion of flocculating agent (like EPS). Over time, mineral sediment and EPS bind together until all available EPS is covered with mineral sediment and the floc size reaches a constant value. The amount of EPS is then the limiting factor for the equilibrium floc size (Shakeel et al., 2020). Using the PBE model, a steady-state floc size (not an equilibrium size) can be reached only when there is a balance between the aggregation and break-up terms, which then keeps the floc size constant over time. This type of balance is for instance found in thermodynamics, when one studies the adsorption/desorption of molecules from a surface (Langmuir, 1918), but is not representative for EPS-induced flocculation.

Secondly, it has been observed that flocs do not necessarily break under shear, but rather change shape as the organic matter they contain is rather elastic. This implies that, even at constant shear, sediment and organic matter concentration, floc sizes can decrease over time due to the fact that flocs become denser (less volume, same mass) (Shakeel et al., 2020). Using the PBE model, it is only possible to decrease a particle size by break-up, therefore this process cannot be modelled. Using a logistic growth model, on the other hand, it is possible to model this decrease in floc size and parameterized it (Safar et al., 2022).

The logistic growth model is therefore a promising new tool for flocculation studies, but it requires further investigation. In particular some work should be devoted to the parametrization of the model and its calibration using *in-situ* data.

4.2 The DLVO model and prediction of flocculation

In estuarine areas, the suspended sediment particle will, according to DLVO theory, be destabilized and flocculate because of the increase in salinity between the river fresh water and the sea. In the presence of organic matter however, DLVO theory cannot always be applied, as the flocculation mechanisms will be driven by the presence of polyelectrolytes and microorganisms which are not accounted for in the DLVO theory.

Hunter and Liss (1979) already demonstrated in 1979, by analyzing the surface properties of suspended particles in four rivers in the United Kingdom by electrophoresis (a technique to assess the ζ-potential) that because of the organic coatings of the particles no major difference could be found in the particles' surface characteristics.

Different clay minerals with different particle sizes and surface charges are found in flocs. Goldberg (1991) found that the optimum flocculation salinity for different clay minerals is different. The optimum flocculating salinity of illite and kaolinite is 9–13 PSU, while that of montmorillonite is 20–24 PSU. This result is in line with DLVO theory, as montmorillonite clay, being delaminated, has a larger surface area than kaolinite or illite particles and hence the particles experience a larger Coulombic repulsion.

The general trend that was found is that the electrophoretic mobility (and hence the ζ-potential) is decreasing (in absolute values) with increasing salinity. This behavior is in line with the description given in Figure 2A and reflects the screening of the surface charge of the coated particles.

On the other hand, the DLVO approach, which predicts that the increase of ion concentration is beneficial for flocculation, cannot explain why an increase in sodium concentration will slow-down flocculation in some situations (Sobeck and Higgins, 2002).

Physico-chemical models also do not take into consideration the uneven charge distribution on sediment surfaces and the charge distribution of EPS, which most probably have a great influence on bio-sediment flocculation. Moreover, the colony formation and growth of microorganisms is a dynamic process that will influence bio-sediment flocculation. Microbial activity is a complex process that is hard to quantitatively study, especially in field observations. So far, the biological activity is studied by quantifying the number of microorganisms present in the water, understanding their growth cycle, analyzing their EPS, etc. The link between biological activity and sediment flocculation remains a key open question for the study of sediment transport dynamics.

5 Characterization of floc properties

Properties of flocs include size, shape, effective density and composition. These parameters are important to understand the cohesion of flocs and their settling velocity. The settling velocity of flocs is an important parameter for sediment transport modeling (Winterwerp, 1998; Manning et al., 2011; Verney et al., 2011; Chassagne et al., 2021).

5.1 Floc sizes and shapes

Generally, floc size is assessed by laser diffraction techniques (with equipment like Malvern Mastersizer and LISST) (Dyer and Manning, 1999; Agrawal and Pottsmith, 2000; Mikkelsen and Pejrup, 2001; Mietta, 2010; Filippa et al., 2011; Guo et al., 2017). These techniques convert the raw data (diffracted light) into particle size by making use of the assumption that particles are spherical and represented by their equivalent mean diameter. The particle sizes are given in logarithmically-spaced size bins, and the particle size distribution (PSD) is given as a volume-% (volume occupied by particles of a sizes within a given bin compared to the volume occupied by all particles). It is usually assumed that the D_{50} of the distribution is representative for the mean particle size of the distribution (Maggi, 2005). Nonetheless, it often occurs that a PSD displays multiple size peaks (van Leussen, 1994), which reflects the fact that different types of particles are present in the sample, such as mineral sediment, flocs and microorganisms like algae (Simon et al., 2002; Grossart et al., 2003; Tang, 2007; Deng et al., 2019; Safar, 2022). Microorganisms generally develop extensive web-like networks on flocs, with a larger size and lower fractal dimension than those without microbial colonization (Kiørboe et al., 1990; Azetsu-Scott and Passow, 2004).

Multiple peaks in PSD also occur because of the shape of particles (Agrawal and Pottsmith, 2000; Safar, 2022). For example, Liu et al. (2007) found by scanning electron microscope technique that the sediment flocs of the Changjiang estuary at different salinities and organic matter have various shapes. Safar (2022) found, from underwater camera investigations, that flocs composed of a large amount or exclusively of organic matter are highly anisotropic, when this organic matter is composed of chain-like microalgae. Mhashhash et al. (2018) showed that at different suspended sediment concentrations (SSC) flocs of different shape are found. In high shear stress areas such as estuaries and coasts, flocs are usually small and spherical or ellipsoidal (van Leussen, 1994; Craig et al., 2020). Some typical flocs are given in Figure 7. In low shear stress environment, the flocs are usually elongated in a chain-like fashion due to their algal composition (Manning et al., 2007; Safar, 2022). The drag force on these flocs will be different and this will thus affect the aggregation between particles leading to larger flocs of various shapes (Maggi, 2005; Adachi et al., 2012). Anisotropic flocs containing a substantial amount of organic matter can withstand a certain extent of deformation, leading over to the reconformation of these flocs into fairly spherical flocs (Jeldres et al., 2018; Safar, 2022). Degradation of polymers can also lead to this phenomenon (Heath et al., 2006).

5.2 Floc density and settling velocity

Figure 8 shows the relationship between effective density (floc particle density minus water density) and floc size obtained from several published studies. The results are for many different rivers and estuaries, such as the upper Tamar River in the United Kingdom (Fennessy et al., 1994), the Po River Estuary in Italy (Fox et al., 2004) and the Changjiang River Estuary (e.g., Wang et al., 2013; Guo et al., 2017) and laboratory experiments with natural sediment (e.g., Gibbs, 1985; Manning and Dyer, 1999). The effective density of flocs displays a significant decrease as function of particle size which can be of several orders of magnitude. However (not shown) in all these experiments there were also quite some large density differences for a given particle size. These differences arise from the fact that flocs of a given size can have very heterogeneous composition (Chassagne and Safar, 2020).

To describe quantitatively the relation between floc size and floc effective density, Kranenburg (1994) proposed that the flocs should be treated as fractals. A fractal is defined as a self-similar object (Mandelbrot, 1982). In existing studies, there are two main descriptions of fractals: one is the two-dimensional fractal dimension N_p based on perimeter and area, and the other is the three-dimensional fractal dimension N_f based on the volume of particles contained inside a floc. It is the latter that is of interest to determine the density of flocs. Kranenburg (1994) derived the following relationship between effective density and particle size:

$$\Delta\rho = \rho_f - \rho_w \propto \left(\rho_p - \rho_w\right)\left(\frac{d_F}{d}\right)^{N_f-3} \tag{7}$$

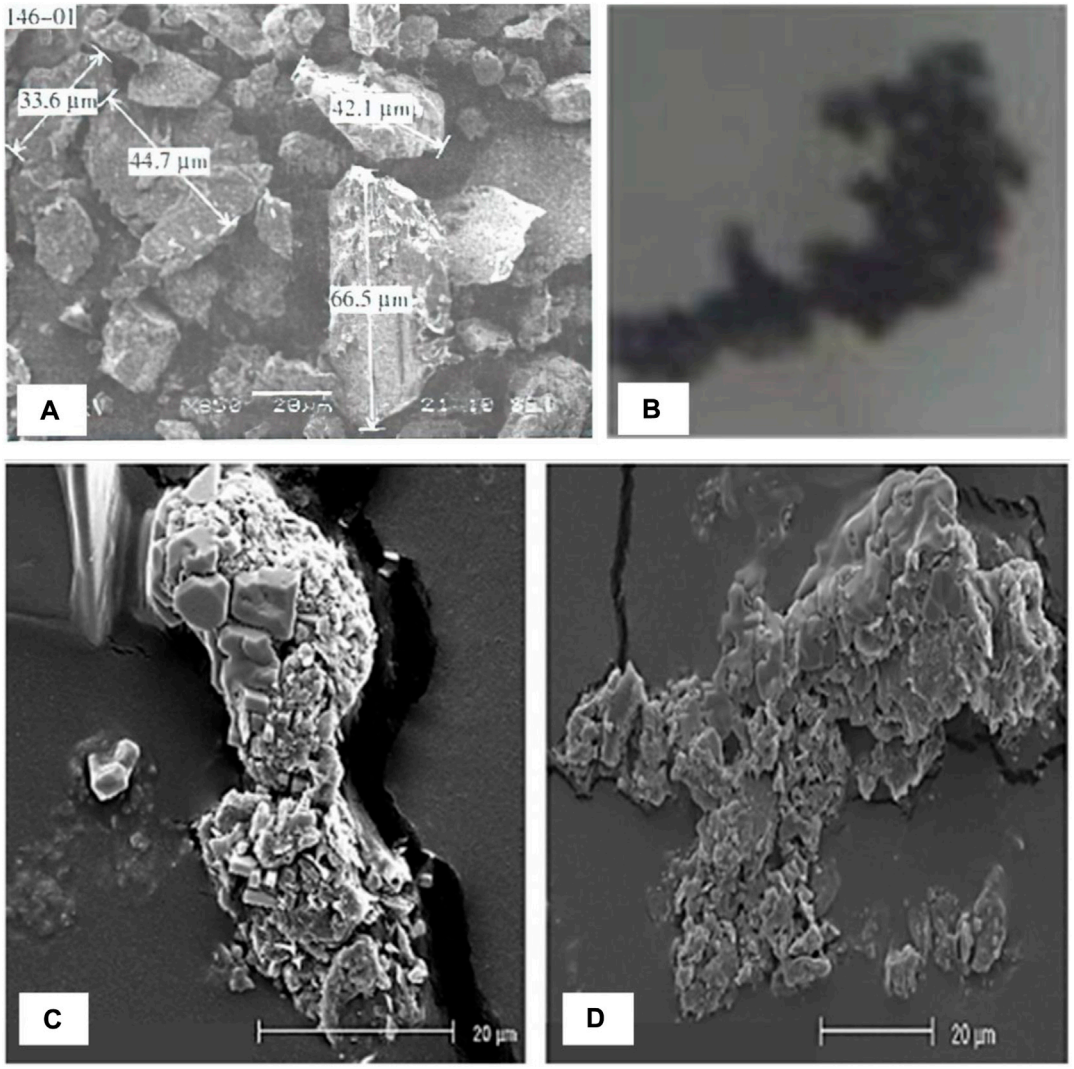

FIGURE 7
Photomicrography of flocs, **(A)** electron microscope photographs of flocs in the freshwater with humus, figure from Liu et al. (2007) **(B)** Camera photographs of flocs in the Rhine Region Of Freshwater Influence (Rhine ROFI), figure from (Safar, 2022) **(C,D)** SEM photographs of flocs at salinity 20, different SSC, c = 100 and d = 200 mg L^{-1}, figures from: Mhashhash et al. (2018).

where $\Delta\rho$ is the effective density of floc, ρ_f and ρ_w are the density of floc and the density of water, respectively. ρ_p is the density of mineral sediment particles, d_F and d represent the floc size (D_{50}) and the mean particle size of the constitutive particles. It can be seen that for a same size of constitutive particles and flocs, different fractal dimensions lead to different effective densities. By tuning the fractal dimension, it is therefore possible to fit the different effective densities as function of floc sizes found in Figure 8. Note, however, that the found fractal dimension is a purely empirical parameter, as, in contrast to theoretical flocs, flocs observed *in-situ* are usually composed of different primary constituents (mineral sediment, EPS, etc.).

Usually the density of flocs is obtained from settling velocities experiments from which, using Stokes' settling velocity, the density can be deduced. In general the settling velocity of a sinking object is expressed as:

$$\omega_s = \sqrt{\frac{4}{3}\frac{\alpha}{\beta}\frac{\Delta\rho \cdot g \cdot D_{50}}{C_D \cdot \rho_w}} \tag{8}$$

in which α and β are coefficients depending on the sphericity of the particles as defined in (Winterwerp, 1998). C_D is the drag coefficient and ω_s is the settling velocity of flocs. The drag coefficient is a function of particle Reynolds number (Winterwerp, 1998):

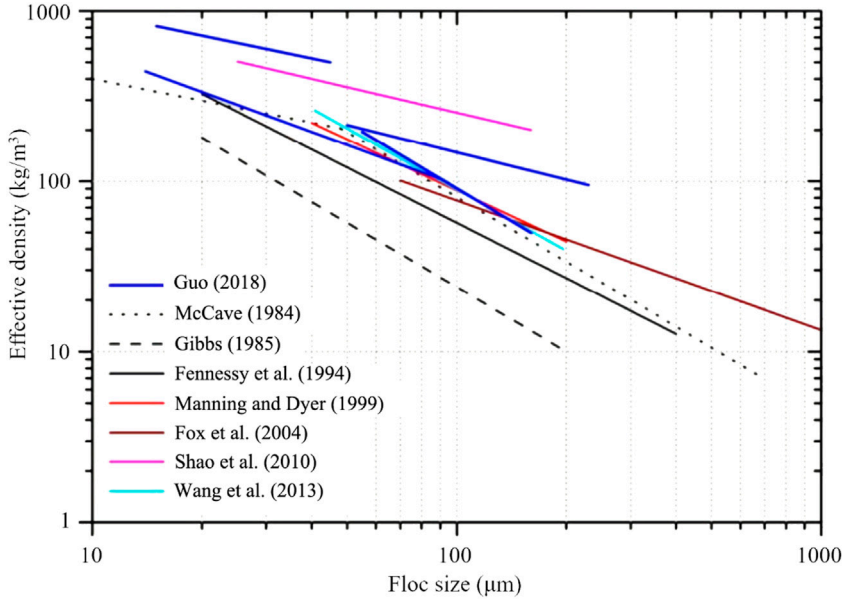

FIGURE 8
The change of effective density of flocs with particle size (McCave, 1984; Fennessy et al., 1994; Manning and Dyer, 1999; Fox et al., 2004; Shao et al., 2011; Wang et al., 2013; Guo, 2018).

$$C_D = \frac{24}{Re\,(1 + 0.15Re^{0.687})} \tag{9}$$

The particle Reynolds number is given by Re = $\omega_s D_{50}/\nu$, where ν is the kinematic viscosity of water.

For spherical particles, $\alpha = \beta = 1$. When the particle Reynolds number $Re \ll 1$, the above expression can be simplified to Stokes' settling velocity:

$$\omega_s = \frac{\Delta\rho \cdot g \cdot D_{50}^2}{18\mu} \tag{10}$$

In fine sediment transport models, the settling velocity is usually taken to be constant, and its value is about 0.05–0.1 mm s^{-1} (e.g., Geyer et al., 2004; Hu et al., 2009). This assumption of a constant settling velocity is an approximation, as it was discussed above that flocs can change shape and density as function of shear (and time).

Experiments in controlled conditions and field observations have given evidence that the organic matter (especially the EPS) has substantial effects on floc density, porosity and settling velocity that leads to a larger size but lower density and settling velocity as compared to the pure (without EPS) sediment particles (Droppo, 2001; Guenther and Bozelli, 2004; Passow and De La Rocha, 2006; Bowers et al., 2007; Droppo et al., 2015). On the other hand, some studies found that organic matter can increase floc density under certain conditions (Fall et al., 2021). Low density and large size flocs are predominantly formed in the water column where large particles of organic matter (like microalgae) are advected. Dense and small flocs with comparable settling velocity can be formed in regions where organic matter is less abundant, or where the shear is high, as by shearing flocs become denser and get a more spherical shape (by coiling) (Deng et al., 2019; Deng et al., 2021; Chassagne et al., 2021).

5.3 Floc composition and relation to flocculation and settling

It is usually assumed that flocs are composed of fine mineral sediment (clay and silt fraction) with some amount of organic matter (van Leussen, 1988, 1994). However, sand can also sometimes be entrapped in flocs (Deng et al., 2021).

5.3.1 Mineral sediment

The content of clay minerals in the suspended sediment of the Changjiang estuary is about 26%, of which 65%–70% are illite, and the rest are chlorite, montmorillonite and kaolinite. The settling velocity of illite is 9 times higher than that of montmorillonite when the salinity is 10 PSU. The main types of clay minerals vary as function of the tidal periods because the sediment transport and deposition mechanisms are different (Zhang, 1996). The laboratory experiments and field observations of the flocculation characteristics of fine sediment in the Changjiang Estuary show that the optimum flocculation salinity ranges from 4 to 16 PSU (Guan et al., 1996;

TABLE 1 Some parameters reported in *in-situ* observation of flocs.

Authors	Location	Sp.	Se.	Parameters				
				Size	ω_s	SSC	Sal.	OM
Eisma and Li (1993)	Dollard	○	—	○	—	○	○	○
van der Lee (2000)	Dollard	—	○	○	○	○	—	○
Thill et al. (2001)	Rhone	○	○	○	○	○	○	○
Mikkelsen (2002a)	Danish coast	○	○	○	○	○	○	○
Fugate and Friedrichs (2003)	Chesapeake Bay	○	—	○	○	○	○	○
Fox et al. (2004)	Po	○	—	○	○	○	○	○
Xia et al. (2004)	Pearl river	○	—	○	○	○	○	○

[a]Sp., Spatial variation; Se., Seasonal variation; Sal., Salinity; OM, Organic Matter.
[b]"○" means the factor has been measured or taken into account, and "—" means it has not been measured or taken into account.

Jiang et al., 2002; Wan et al., 2015). Manning et al. (2010a) studied the flocculation process with different mud/sand mixtures and demonstrated that different ratios of mud and sand can influence the flocs settling velocity.

5.3.2 Extracellular polymeric substances and microbial communities

Flocs can be regarded as individual microecosystems with autonomous and interactive chemical, physical, and biological reactions and processes within the floc matrices (Droppo et al., 1997; Evans et al., 1997; Brinkmann et al., 2019). EPS and other polymeric substances are produced by microorganisms. These microorganisms can be microscopic algae (such as diatoms), which can form large flocs by themselves, and afterwards capture sediment particles (Deng et al., 2019).

The presence of organic matter like EPS promotes the flocculation of fine sediment (e.g., Droppo and Ongley, 1992; Gratiot and Manning, 2004; Mietta et al., 2009b; Fettweis and Baeye, 2015). It was found that organic matter play a major role in the floc collision rate and floc strength in the observation of seasonal variation of flocs. Large flocs usually appeared at algae bloom seasons due to biologically induced aggregation (Mikkelsen, 2002b; Uncles et al., 2010; Lee et al., 2014; Fettweis and Baeye, 2015). Besides, the biological effects on sediment flocculation also are found in fresh water environments (Guo and He, 2011).

Therefore, the organic matter composition of flocs is not only sensitive to environmental conditions but also varies with spatiotemporal changes. An overview of different studies is given in Table 1.

Organic matter composition can only be assessed in the laboratory. *In-situ* observations do however nowadays include Chlorophyll a measurements, which gives some indication of the microalgae content of flocs (Fettweis and Lee, 2017; Deng et al., 2019, 2021; Ho et al., 2022).

5.3.3 Type of microalgae studied

Diatoms are the largest component of microalgae which goes by the name *phytoplankton*. Therefore, most of the research on the effects of microorganisms on sediment flocculation in estuaries are done with diatoms. Diatoms in healthy state will remain suspended due to turbulence and water current.

Phytoplankton is a large community with strong adaptability. These microorganisms can live under very low nutrient concentration, very weak light intensity and quite low temperature. They can not only grow in rivers, streams, lakes and oceans, but also in short-term ponding or humid places (Blum, 1956; Round, 1981).

In 1968, Walsby (1968) described the aggregation of *N. nutans*, by the EPS this microorganism is secreting. Avnimelech et al. (1982) studied the aggregation process of *Chlamydomonas* and collar algae with clay by electron microscope in 1982 (Figure 9). This is the earliest image of algae and sediment flocculation. Besides, Avnimelech et al. (1982) compared the effect of four different forms of algae on clay flocculation and showed that algae can significantly promote the flocculation of clay in the presence of electrolytes. Therefore, the reason why the growth of algae is restricted in high turbidity areas may not only be due to the limited light supply but also because of the fact that algae have flocculated with sediment particles. In addition, some algae species are prevented to flocculate due to steric effects linked to the spatial conformation of their filamentous strains (de Lucas Pardo, 2014).

5.3.4 Effect of temperature and light

Temperature is the main factor affecting the geographical distribution of algae. Therefore, in the sea area where the water temperature changes greatly, the species changes greatly through the year. In winter, there are cold water algae (the optimum temperature for growth and reproduction is less than 4°C). When the temperature drops to 4°C, both the number of algae and the EPS will however usually decrease (Domozych, 2007; Kiemle

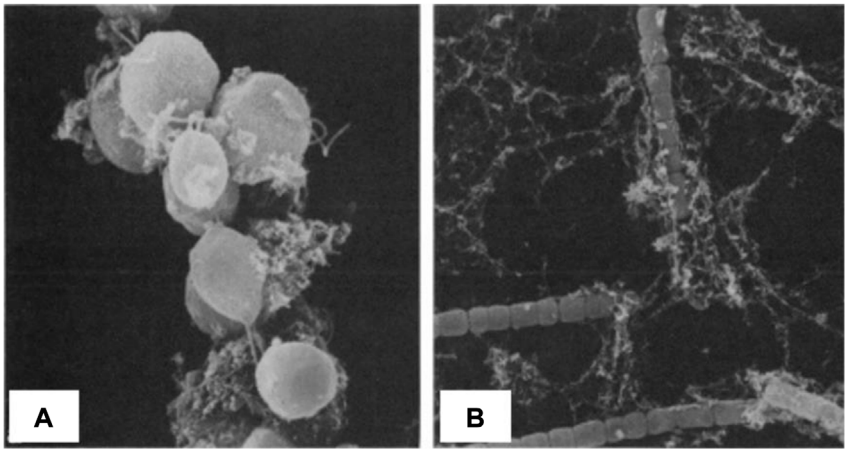

FIGURE 9
Flocs under scanning electron microscope **(A)** Chlamydomonas clay cluster, **(B)** Anabaena clay cluster, 1,200 times, 1,470 times; figures following after Avnimelech et al. (1982).

et al., 2007), and the production of EPS will also decrease, thus reducing the effect on flocculation (Wilén et al., 2000).

There are warm water algae (the optimum temperature for growth and reproduction is about 20°C) in summer, which can complete their life cycle in a short time. The highest value of photosynthesis is between 20 and 25°C, when the algae growth reaches the maximum value (Colijn and van Buurt, 1975; Blanchard et al., 1996), and algae then produce EPS with a high viscosity (Lupi et al., 1991).

Most of freshwater microalgae appear in spring and autumn. Some cyanobacteria only appear when the water temperature is high in summer. Light is the decisive factor to determine the vertical distribution of algae. The light absorption capacity of a water body is very strong, so the light intensity at 10 m depth is only 10% of that of water surface, and the light intensity at 100 m deep is only 1% that of water surface. Moreover, because seawater can easily absorb long-wave light, it also causes a spectral difference in light at various water depths. Different algae have different requirements for light intensity and spectrum. Green algae generally live at the surface of water, while red algae and brown algae can use short wave light such as green, yellow and orange to live in deep water (Reynolds, 2006; Wood, 2014; Castro and Huber, 2016).

5.3.5 Effect of water chemistry

The chemical properties of the water body are also important factors for the appearance and species composition of algae (Pearson et al., 1987; Zou et al., 2011). For example, *Cyanobacteria* and *Gymnophyta* can live in eutrophic water and often form blooms; *Bacillariophyta* and *Chrysophyta* often exist in lakes with poor nutrition in mountainous areas; *Chlorophyta* and *Cryptophyta* often occur in small ponds. In addition, the interaction between algae living in the same water area also plays an important role in their emergence and growth, as some algae can inhibit the growth of other algae by secretions.

The pH value of water has a direct impact on the physiological activities of bacteria and microorganisms on the surface charge of mineral sediment. pH can therefore significantly affect (bio)flocculation by changing the EPS activity (Yokoi et al., 1995; Yokoi, 2002). With the increase of pH in a water body, the functional groups on the mineral sediment (and EPS) such as carboxyl and amino groups will dissociate or not leading to an increase or decrease in surface charge. Different bacterial species have different adaptability to pH and therefore, the effect of pH on sediment flocculation needs further study.

5.3.6 Other compositions

Other components of flocs are heavy metals, Humic substances (HS), pore water, and xenobiotic particulate matter (e.g., Microplastics (MPs), Engineered nanoparticles (ENPs), oil droplets). These elements have a unique function in floc formation (Droppo, 2001; Maggi, 2013; Ho et al., 2022). For instance, metal-rich precipitates are often found in flocs with a heterogeneous composition (Jonas and Millward, 2010). HS have strong negative charges, and, when adsorbed on suspended particles, will increase their negative charge. This leads to an enhanced stability of sediment particles (Bob and Walker, 2001; Fettweis and Lee, 2017). Pore water is present in the pore space in the floc matrices when particles aggregate to form large flocs (Droppo, 2001) which affects floc structure and density (Sherman, 1953; Logan and Hunt, 1987). MPs can become associated with SPM and become incorporated into floc matrices (Michels et al., 2018) and provide habitats and

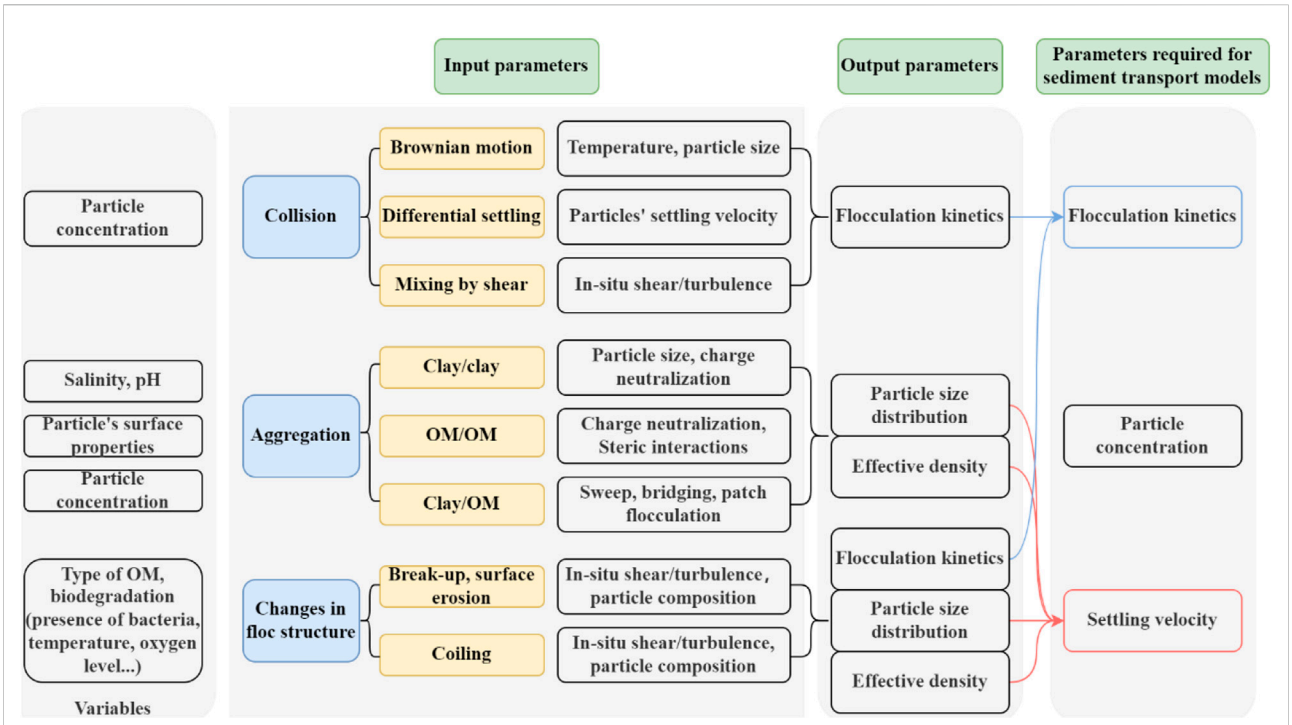

FIGURE 10
Parameters of influence and their interactions during the flocculation process; In order to model sediment transport, the (numerical) models have as input a few classes of particles defined by concentration and settling velocity. The changes in number of particles in a class and their settling velocity are related to flocculation kinetics.

substrates for microorganisms, which can create biofilms and scavenge various dissolved and particulate matter (Petrova and Sauer, 2012; Taylor et al., 2016). Oil droplets can easily attach to sediment particles, becoming a part of flocs and affect transport behavior (Droppo et al., 2016). With the intensification of human activities, more and more heterogeneous substances can be absorbed to part of flocs, which makes the study of floc composition and its degradation over time a worthwhile study.

6 Concluding remarks

In conclusion, flocculation of cohesive sediment mainly includes two processes: aggregation and decay [break-up by biodegradation or shear—whereby shear can also lead to a densification of flocs (without breakage)]. In these two processes, physical, chemical and biological factors will have a role and also interact with each other. These factors can either promote aggregation or decay. For example, turbulent shear stress and suspended sediment concentration can promote particle collision frequency and facilitate flocculation, but a very high shear will limit flocs growth. The effect of salinity (cation concentration) is important as well, as it enables in most cases to bind (negatively charged) sediment to (negatively charged) organic matter. Organic matter (such as EPS) will usually enhance the stability of sediment particles, but can also degrade over time and lead to decay (break-up) of flocs.

Although many studies have been performed in the field of flocculation, floc characteristics and factors affecting sediment flocculation, there are relatively few studies on biological effects on sediment flocculation. Many authors have begun to pay attention to the study of biological factors in recent years, however, in most studies, the effects of organic matter and microbial communities are not differentiated, whereas the effects of these two factors should be distinguished in the context of sediment flocculation. Even though it is the microbial community that produces polymeric organic matter (such as EPS), two types of flocculation can be found: EPS acts on the surface properties of sediment while living microalgae aggregate themselves to form large flocs first, and then catch sediment particles within their network. A summary of the different processes involved in flocculation, and their link to the parameters required for sediment transport models are given in Figure 10.

Based on the discussions in the present article, the following points need to be studied in the future regarding the influence of organic matter on flocculation processes:

In terms of flocculation mechanisms, research has demonstrated that organic matter influences mineral sediment flocculation and flocs. Organic matter can promote flocculation but also inhibit the flocculation process. These different effects

are often related to different species of algae or different nature of microbial secretions, but a clear overview is still lacking. Most studies have focused on the exopolymers produced by microbial secretions, but overlooked the heterogeneous composition of flocs. It has been shown that algae and microorganisms themselves can form flocs and participate in the sediment flocculation process, and hence more research is needed to understand the dynamic link between microorganisms, exopolymers and mineral sediment. Finally, most of the research on the mechanisms of flocculation is still qualitative, and although some studies have been able to quantify the effects of organic matter, a fully parameterized and calibrated model is still lacking. A promising tool might be the model based on logistic growth that has recently been developed and shown to be working for laboratory studies on algae and EPS induced aggregation of mineral sediment.

In terms of floc properties, most of the current research has focused on floc size variation and less on properties such as floc composition, effective density and structural property variation. The study of these properties is necessary to understand the role of organic matter on flocculation and the time behavior of flocs (change in structure, degradation, etc.).

In terms of flocculation influencing factors, there is a large amount of research on the physical factors influencing sediment flocculation, such as the grain size distribution of sediment particles, hydrodynamics, etc., but there is still relatively little research on the combined physical and biochemical factors. Unlike parameters such as hydrodynamics, sand content and salinity, biochemical parameters, such as microalgae type and concentration are more difficult to control and quantify. Therefore their study, especially in laboratory experiments, require a multidisciplinary approach and the development of new equipment and techniques.

Finally, the large-scale transport of flocs in the overall water ecosystem are still poorly studied. Most quantitative studies are done in the laboratory but there is a need to connect these studies to numerical large-scale models. The flocculation model parametrization can be done in the lab and its implementation in large-scale transport model will help to better study the effect of microscopic, small-scale processes on large-scale sediment transport. To this end, it is also important to further develop *in-situ* monitoring tools, so as to integrate the monitoring of organic matter in the water column.

Ecological issues are becoming increasingly important in present days societies. Sediment transport cannot anymore be seen as a purely physical process and the role of biology should be accounted for, as organic matter changes the properties of mineral sediment through flocculation. Importantly, through the interactions between mineral sediment, organic and xenobiotic particulate matter, the transport of microorganisms, nutrients and pollutants is a dynamic process in the water column that ought to be better studied. This can only be achieved through a disciplinary collaboration between researchers of the different relevant fields of expertise.

Author contributions

ZD: Writing—Original Draft, Conceptualization, Data Curation, Visualization; DH: Supervision, Writing—Review and Editing; QH: Supervision, Writing—Review and Editing; CC: Supervision, Writing—Review and Editing.

Acknowledgments

The study was carried out within the framework of the MUDNET academic network: https://www.tudelft.nl/mudnet/.

Conflict of interest

The authors declare that the research was conducted in the absence of any commercial or financial relationships that could be construed as a potential conflict of interest.

Publisher's note

References

Adachi, Y., Kobayashi, A., and Kobayashi, M. (2012). Structure of colloidal flocs in relation to the dynamic properties of unstable suspension. *Int. J. Polym. Sci.* 2012, 1–14. doi:10.1155/2012/574878

Agrawal, Y. C., and Pottsmith, H. C. (2000). Instruments for particle size and settling velocity observations in sediment transport. *Mar. Geol.* 168, 89–114. doi:10.1016/S0025-3227(00)00044-X

Aly, S. M., and Letey, J. (1988). Polymer and water quality effects on flocculation of montmorillonite. *Soil Sci. Soc. Am. J.* 52, 1453–1458. doi:10.2136/sssaj1988.03615995005200050047x

Avnimelech, Y., Troeger, B. W., and Reed, L. W. (1982). Mutual flocculation of algae and clay: Evidence and implications. *Science* 216, 63–65. doi:10.1126/science.216.4541.63

Azetsu-Scott, K., and Passow, U. (2004). Ascending marine particles: Significance of transparent exopolymer particles (TEP) in the upper ocean. *Limnol. Oceanogr.* 49, 741–748. doi:10.4319/lo.2004.49.3.0741

Bainbridge, Z. T., Wolanski, E., Álvarez-Romero, J. G., Lewis, S. E., and Brodie, J. E. (2012). Fine sediment and nutrient dynamics related to particle size and floc formation in a Burdekin River flood plume, Australia. *Mar. Pollut. Bull.* 65, 236–248. doi:10.1016/j.marpolbul.2012.01.043

Bar-Or, Y., and Shilo, M. (1988a). "Cyanobacterial flocculants," in *Methods in enzymology* (Amsterdam ; New York: Elsevier), 616–622. doi:10.1016/0076-6879(88)67071-6

Bar-Or, Y., and Shilo, M. (1988b). The role of cell-bound flocculants in coflocculation of benthic cyanobacteria with clay particles. *FEMS Microbiol. Lett.* 53, 169–174. doi:10.1111/j.1574-6968.1988.tb02661.x

F. Bergaya and G. Lagaly (Editors) (2013). *Handbook of clay science*. Second edition (Amsterdam: Elsevier).

Biggs, S., Habgood, M., Jameson, G. J., and Yan, Y. (2000). Aggregate structures formed via a bridging flocculation mechanism. *Chem. Eng. J.* 80, 13–22. doi:10.1016/S1383-5866(00)00072-1

Blanchard, G., Guarini, J., Richard, P., Gros, P., and Mornet, F. (1996). Quantifying the short-term temperature effect on light-saturated photosynthesis of intertidal microphytobenthos. *Mar. Ecol. Prog. Ser.* 134, 309–313. doi:10.3354/meps134309

Blum, J. L. (1956). The ecology of river algae. *Bot. Rev.* 22, 291–341. doi:10.1007/BF02872474

Bob, M., and Walker, H. W. (2001). Enhanced adsorption of natural organic matter on calcium carbonate particles through surface charge modification. *Colloids Surfaces A Physicochem. Eng. Aspects* 191, 17–25. doi:10.1016/S0927-7757(01)00760-9

Bolto, B., and Gregory, J. (2007). Organic polyelectrolytes in water treatment. *Water Res.* 41, 2301–2324. doi:10.1016/j.watres.2007.03.012

Bowers, D. G., Binding, C. E., and Ellis, K. M. (2007). Satellite remote sensing of the geographical distribution of suspended particle size in an energetic shelf sea. *Estuar. Coast. Shelf Sci.* 73, 457–466. doi:10.1016/j.ecss.2007.02.005

Brinkmann, B. W., Vonk, J. A., Beusekom, S. A. M., Ibanez, M., Lucas Pardo, M. A., Noordhuis, R., et al. (2019). Benthic hotspots in the pelagic zone: Light and phosphate availability alter aggregates of microalgae and suspended particles in a shallow turbid lake. *Limnol. Oceanogr.* 64, 585–596. doi:10.1002/lno.11062

Burban, P.-Y., Lick, W., and Lick, J. (1989). The flocculation of fine-grained sediments in estuarine waters. *J. Geophys. Res.* 94, 8323. doi:10.1029/JC094iC06p08323

Castro, P., and Huber, M. E. (2016). *Marine biology*. Tenth edition. New York, NY: McGraw-Hill Education.

Chai, C., Yu, Z., Song, X., and Cao, X. (2006). The status and characteristics of eutrophication in the yangtze river (changjiang) estuary and the adjacent east China sea, China. *Hydrobiologia* 563, 313–328. doi:10.1007/s10750-006-0021-7

Chassagne, C., and Ibanez, M. (2012). Electrophoretic mobility of latex nanospheres in electrolytes: Experimental challenges. *Pure Appl. Chem.* 85, 41–51. doi:10.1351/PAC-CON-12-02-12

Chassagne, C. (2019). *Introduction to colloid science*. Delft: Delft Academic Press.

Chassagne, C., Mietta, F., and Winterwerp, J. C. (2009). Electrokinetic study of kaolinite suspensions. *J. Colloid Interface Sci.* 336, 352–359. doi:10.1016/j.jcis.2009.02.052

Chassagne, C., Safar, Z., Deng, Z., He, Q., and Manning, A. (2021). Flocculation in estuaries: Modeling, laboratory and *in-situ* studies *sediment transport - recent advances* (IntechOpen). Available at: https://www.intechopen.com/online-first/flocculation-in-estuaries-modeling-laboratory-and-in-situ-studies (Accessed April 8, 2022).

Chassagne, C., and Safar, Z. (2020). Modelling flocculation: Towards an integration in large-scale sediment transport models. *Mar. Geol.* 430, 106361. doi:10.1016/j.margeo.2020.106361

Chen, S., Eisma, D., and Kalf, J. (1994). *In situ* distribution of suspended matter during the tidal cycle in the elbe estuary. *Neth. J. Sea Res.* 32, 37–48. doi:10.1016/0077-7579(94)90026-4

Colijn, F., and van Buurt, G. (1975). Influence of light and temperature on the photosynthetic rate of marine benthic diatoms. *Mar. Biol.* 31, 209–214. doi:10.1007/BF00387148

Comte, S., Guibaud, G., and Baudu, M. (2006). Biosorption properties of extracellular polymeric substances (EPS) resulting from activated sludge according to their type: Soluble or bound. *Process Biochem.* 41, 815–823. doi:10.1016/j.procbio.2005.10.014

Costerton, J. W., Cheng, K., Geesey, G. G., Ladd, T. I., Nickel, J. C., Dasgupta, M., et al. (1987). Bacterial biofilms in nature and disease. *Annu. Rev. Microbiol.* 41, 435–464. doi:10.1146/annurev.mi.41.100187.002251

Craig, M. J., Baas, J. H., Amos, K. J., Strachan, L. J., Manning, A. J., Paterson, D. M., et al. (2020). Biomediation of submarine sediment gravity flow dynamics. *Geology* 48, 72–76. doi:10.1130/G46837.1

de Lucas Pardo, M. (2014). *Effect of biota on fine sediment transport processes: A study of lake markermeer*.

Deng, Z., He, Q., Chassagne, C., and Wang, Z. B. (2021). Seasonal variation of floc population influenced by the presence of algae in the Changjiang (Yangtze river) estuary. *Mar. Geol.* 440, 106600. doi:10.1016/j.margeo.2021.106600

Deng, Z., He, Q., Safar, Z., and Chassagne, C. (2019). The role of algae in fine sediment flocculation: *In-situ* and laboratory measurements. *Mar. Geol.* 413, 71–84. doi:10.1016/j.margeo.2019.02.003

Deng, Z. (2022). *The role of algae in fine cohesive sediment flocculation*.

Domozych, D. S. (2007). Exopolymer production by the green alga penium margaritaceum: Implications for biofilm residency. *Int. J. Plant Sci.* 168, 763–774. doi:10.1086/513606

Dronkers, J., van Leussen, W., Puls, W., Kuehl, H., and Heymann, K. (1988). "Settling velocity of mud flocs: Results of field measurements in the elbe and the weser estuary," in *Physical processes in estuaries*. Editors J. Dronkers and W. van Leussen (Berlin Heidelberg: Springer), 404–424. doi:10.1007/978-3-642-73691-9_20

Droppo, I. G. (2009). Biofilm structure and bed stability of five contrasting freshwater sediments. *Mar. Freshw. Res.* 60, 690. doi:10.1071/MF08019

Droppo, I. G., D'Andrea, L., Krishnappan, B. G., Jaskot, C., Trapp, B., Basuvaraj, M., et al. (2015). Fine-sediment dynamics: Towards an improved understanding of sediment erosion and transport. *J. Soils Sediments* 15, 467–479. doi:10.1007/s11368-014-1004-3

Droppo, I. G., Krishnappan, B. G., and Lawrence, J. R. (2016). Microbial interactions with naturally occurring hydrophobic sediments: Influence on sediment and associated contaminant mobility. *Water Res.* 92, 121–130. doi:10.1016/j.watres.2016.01.034

Droppo, I. G., Leppard, G. G., Flannigan, D. T., and Liss, S. N. (1997). The freshwater floc: A functional relationship of water and organic and inorganic floc constituents affecting suspended sediment properties. *Water Air Soil Pollut.* 99, 43–53. doi:10.1007/BF02406843

Droppo, I. G., and Ongley, E. D. (1994). Flocculation of suspended sediment in rivers of southeastern Canada. *Water Res.* 28, 1799–1809. doi:10.1016/0043-1354(94)90253-4

Droppo, I. G., and Ongley, E. D. (1992). The state of suspended sediment in the freshwater fluvial environment: A method of analysis. *Water Res.* 26, 65–72. doi:10.1016/0043-1354(92)90112-H

Droppo, I. G. (2001). Rethinking what constitutes suspended sediment. *Hydrol. Process.* 15, 1551–1564. doi:10.1002/hyp.228

Droppo, I. G., Walling, D. E., and Ongley, E. D. (2000). *The Influence of floc size, density and porosity on sediment and contaminant transport*. Wallingford: IAHS Publication, 141–147.

Dyer, K. R., and Manning, A. J. (1999). Observation of the size, settling velocity and effective density of flocs, and their fractal dimensions. *J. Sea Res.* 41, 87–95. doi:10.1016/S1385-1101(98)00036-7

Dyer, K. R. (1989). Sediment processes in estuaries: Future research requirements. *J. Geophys. Res.* 94, 14327. doi:10.1029/JC094iC10p14327

Eisma, D. (1986). Flocculation and de-flocculation of suspended matter in estuaries. *Neth. J. Sea Res.* 20, 183–199. doi:10.1016/0077-7579(86)90041-4

Eisma, D., and Irion, G. (1993). "Suspended matter and sediment transport," in *Pollution of the north sea*. Editors W. Salomons, B. L. Bayne, E. K. Duursma, and U. Förstner (Berlin, Heidelberg: Springer), 20–35. Available at: http://www.springerlink.com/index/10.1007/978-3-642-73709-1_2 (Accessed June 5, 2018).

Eisma, D., and Li, A. (1993). Changes in suspended-matter floc size during the tidal cycle in the dollard estuary. *Neth. J. Sea Res.* 31, 107–117. doi:10.1016/0077-757w9(93)90001-9

Eisma, D. (1991). Particle size of suspended matter in estuaries. *Geo-Marine Lett.* 11, 147–153. doi:10.1007/BF02431001

R. D. Evans, J. Wisniewski, and J. R. Wisniewski (Editors) (1997). *The interactions between sediments and water* (DordrechtNetherlands: Springer). doi:10.1007/978-94-011-5552-6

Fall, K. A., Friedrichs, C. T., Massey, G. M., Bowers, D. G., and Smith, S. J. (2021). The importance of organic content to fractal floc properties in estuarine surface waters: Insights from video, LISST, and pump sampling. *J. Geophys. Res. Oceans* 126. doi:10.1029/2020JC016787

Fennessy, M. J., Dyer, K. R., and Huntley, D. A. (1994). Inssev: An instrument to measure the size and settling velocity of flocs *in situ*. *Mar. Geol.* 117, 107–117. doi:10.1016/0025-3227(94)90009-4

Fettweis, M., and Baeye, M. (2015). Seasonal variation in concentration, size, and settling velocity of muddy marine flocs in the benthic boundary layer. *J. Geophys. Res. Oceans* 120, 5648–5667. doi:10.1002/2014JC010644

Fettweis, M., and Lee, B. J. (2017). Spatial and seasonal variation of biomineral suspended particulate matter properties in high-turbid nearshore and low-turbid offshore zones. *Water* 9, 694. doi:10.3390/w9090694

Filippa, L., Freire, L., Trento, A., Álvarez, A. M., Gallo, M., and Vinzón, S. (2011). Laboratory evaluation of two LISST-25X using river sediments. *Sediment. Geol.* 238, 268–276. doi:10.1016/j.sedgeo.2011.04.017

Foree, E. G., and McCarty, P. L. (1970). Anaerobic decomposition of algae. *Environ. Sci. Technol.* 4, 842–849. doi:10.1021/es60045a005

Fox, J. M., Hill, P. S., Milligan, T. G., and Boldrin, A. (2004). Flocculation and sedimentation on the po river delta. *Mar. Geol.* 203, 95–107. doi:10.1016/S0025-3227(03)00332-3

Fugate, D. C., and Friedrichs, C. T. (2003). Controls on suspended aggregate size in partially mixed estuaries. *Estuar. Coast. Shelf Sci.* 58, 389–404. doi:10.1016/S0272-7714(03)00107-0

Geyer, W. R., Hill, P. S., and Kineke, G. C. (2004). The transport, transformation and dispersal of sediment by buoyant coastal flows. *Cont. Shelf Res.* 24, 927–949. doi:10.1016/j.csr.2004.02.006

Gibbs, R. J. (1985). Estuarine flocs: Their size, settling velocity and density. *J. Geophys. Res.* 90, 3249. doi:10.1029/jc090ic02p03249

Goldberg, S. (1991). Flocculation of illite/kaolinite and illite/montmorillonite mixtures as affected by sodium adsorption ratio and pH. *Clays Clay Minerals* 39, 375–380. doi:10.1346/CCMN.1991.0390406

Gratiot, N., and Manning, A. J. (2004). An experimental investigation of floc characteristics in a diffusive turbulent flow. *J. Coast. Res.* 41, 105–113.

Gregory, J., and Barany, S. (2011). Adsorption and flocculation by polymers and polymer mixtures. *Adv. Colloid Interface Sci.* 169, 1–12. doi:10.1016/j.cis.2011.06.004

Gregory, J. (2005). *Particles in water: Properties and processes*. 0 ed. Boca Raton: CRC Press. doi:10.1201/9780203508459

Grossart, H.-P., Kiorboe, T., Tang, K., and Ploug, H. (2003). Bacterial colonization of particles growth and interactions. *Appl. Environ. Microbiol.* 69, 3500–3509. doi:10.1128/AEM.69.6.3500-3509.2003

Guan, X., Chen, Y., and Du, X. (1996). Experimental study on mechanism of flocculation in yangtze estuary (in Chinese). *J. Hydraulic Eng.* 1, 70–80.

Guenther, M., and Bozelli, R. (2004). Factors influencing algae–clay aggregation. *Hydrobiologia* 523, 217–223. doi:10.1023/B:HYDR.0000033127.05034.32

Guo, C. (2018). *Cohesive sediment flocculation and settling processes and the controlling mechanisms.*

Guo, C., He, Q., Guo, L., and Winterwerp, J. C. (2017). A study of *in-situ* sediment flocculation in the turbidity maxima of the yangtze estuary. *Estuar. Coast. Shelf Sci.* 191, 1–9. doi:10.1016/j.ecss.2017.04.001

Guo, L., and He, Q. (2011). Freshwater flocculation of suspended sediments in the Yangtze River, China. *Ocean. Dyn.* 61, 371–386. doi:10.1007/s10236-011-0391-x

Heath, A. R., Bahri, P. A., Fawell, P. D., and Farrow, J. B. (2006). Polymer flocculation of calcite: Population balance model. *AIChE J.* 52, 1641–1653. doi:10.1002/aic.10749

Hicks, R. F. (1988). Sediment rafting: A novel mechanism for the small-scale dispersal of intertidal estuarine meiofauna. *Mar. Ecol. Prog. Ser.* 48, 69–80. doi:10.3354/meps048069

Higgins, M. J., and Novak, J. T. (1997). The effect of cations on the settling and dewatering of activated sludges: Laboratory results. *Water Environ. Res.* 69, 215–224. doi:10.2175/106143097X125371

Ho, Q. N., Fettweis, M., Spencer, K. L., and Lee, B. J. (2022). Flocculation with heterogeneous composition in water environments: A review. *Water Res.* 213, 118147. doi:10.1016/j.watres.2022.118147

Horemans, D. M. L., Dijkstra, Y. M., Schuttelaars, H. M., Sabbe, K., Vyverman, W., Meire, P., et al. (2021). Seasonal variations in flocculation and erosion affecting the large-scale suspended sediment distribution in the scheldt estuary: The importance of biotic effects. *J. Geophys. Res. Oceans* 126. doi:10.1029/2020JC016805

Hu, K., Ding, P., Wang, Z., and Yang, S. (2009). A 2D/3D hydrodynamic and sediment transport model for the yangtze estuary, China. *J. Mar. Syst.* 77, 114–136. doi:10.1016/j.jmarsys.2008.11.014

Hunt, J. R. (1980). "Prediction of oceanic particle size distributions from coagulation and sedimentation mechanisms," in Particulates in water *advances in chemistry*. Editors M. C. Kavanaugh and J. O. Leckie (WASHINGTON, D. C.: American Chemical Society), 243–257. doi:10.1021/ba-1980-0189.ch011

Hunter, K. A., and Liss, P. S. (1979). The surface charge of suspended particles in estuarine and coastal waters. *Nature* 282, 823–825. doi:10.1038/282823a0

Ibanez Sanz, M. E. (2018). *Flocculation and consolidation of cohesive sediments under the influence of coagulant and flocculant*. doi:10.4233/UUID:6E96DB66-1DF0-4ED1-B343-92939D58D864

Jarvis, P., Jefferson, B., Gregory, J., and Parsons, S. A. (2005). A review of floc strength and breakage. *Water Res.* 39, 3121–3137. doi:10.1016/j.watres.2005.05.022

Jeldres, R. I., Fawell, P. D., and Florio, B. J. (2018). Population balance modelling to describe the particle aggregation process: A review. *Powder Technol.* 326, 190–207. doi:10.1016/j.powtec.2017.12.033

Jiang, G., Yao, Y., and Tang, Z. (2002). Analysis of influencing factors on fine sediment flocculation in the changjiang estuary. *Acta Oceanol. Sin.* 21, 385–394.

Jonas, P. J. C., and Millward, G. E. (2010). Metals and nutrients in the severn estuary and bristol channel: Contemporary inputs and distributions. *Mar. Pollut. Bull.* 61, 52–67. doi:10.1016/j.marpolbul.2009.12.013

Jorand, F., Zartarian, F., Thomas, F., Block, J. C., Bottero, J. Y., Villemin, G., et al. (1995). Chemical and structural (2D) linkage between bacteria within activated sludge flocs. *Water Res.* 29, 1639–1647. doi:10.1016/0043-1354(94)00350-G

Kiemle, S. N., Domozych, D. S., and Gretz, M. R. (2007). The extracellular polymeric substances of desmids (conjugatophyceae, streptophyta): Chemistry, structural analyses and implications in wetland biofilms. *Phycologia* 46, 617–627. doi:10.2216/06-97.1

Kiørboe, T., Andersen, K. P., and Dam, H. G. (1990). Coagulation efficiency and aggregate formation in marine phytoplankton. *Mar. Biol.* 107, 235–245. doi:10.1007/BF01319822

Kosmulski, M., and Dahlsten, P. (2006). High ionic strength electrokinetics of clay minerals. *Colloids Surfaces A Physicochem. Eng. Aspects* 291, 212–218. doi:10.1016/j.colsurfa.2006.06.037

Kranenburg, C. (1994). The fractal structure of cohesive sediment aggregates. *Estuar. Coast. Shelf Sci.* 39, 451–460. doi:10.1016/S0272-7714(06)80002-8

Kruyt, H. R. (1949). *Colloid science*. Amsterdam ; New York: Elsevier Pub. Co.

Kruyt, H. R., Jonker, G., and Overbeek, J. (1952). "Colloid science," in *Irreversible systems* (Amsterdam ; New York: Elsevier Publishing Co), Vol. 1.

Kumar, R. G., Strom, K. B., and Keyvani, A. (2010). Floc properties and settling velocity of San Jacinto estuary mud under variable shear and salinity conditions. *Cont. Shelf Res.* 30, 2067–2081. doi:10.1016/j.csr.2010.10.006

Lai, H., Fang, H., Huang, L., He, G., and Reible, D. (2018). A review on sediment bioflocculation: Dynamics, influencing factors and modeling. *Sci. Total Environ.* 642, 1184–1200. doi:10.1016/j.scitotenv.2018.06.101

Langmuir, I. (1918). The adsorption of gases on plane surface of glass, mica and platinum. *J. Am. Chem. Soc.* 40, 1361–1403. doi:10.1021/ja02242a004

Lee, B. J., Toorman, E., and Fettweis, M. (2014). Multimodal particle size distributions of fine-grained sediments: Mathematical modeling and field investigation. *Ocean. Dyn.* 64, 429–441. doi:10.1007/s10236-014-0692-y

Lee, B. J., Toorman, E., Molz, F. J., and Wang, J. (2011). A two-class population balance equation yielding bimodal flocculation of marine or estuarine sediments. *Water Res.* 45, 2131–2145. doi:10.1016/j.watres.2010.12.028

Leppard, G. G. (1992). Size, morphology and composition of particulates in aquatic ecosystems: Solving speciation problems by correlative electron microscopy. *Analyst* 117, 595. doi:10.1039/an9921700595

Li, D.-H., and Ganczarczyk, J. J. (1990). Structure of activated sludge floes. *Biotechnol. Bioeng.* 35, 57–65. doi:10.1002/bit.260350109

Li, H.-M., Tang, H.-J., Shi, X.-Y., Zhang, C.-S., and Wang, X.-L. (2014). Increased nutrient loads from the changjiang (yangtze) river have led to increased harmful algal blooms. *Harmful Algae* 39, 92–101. doi:10.1016/j.hal.2014.07.002

Lick, W., Huang, H., and Jepsen, R. (1993). Flocculation of fine-grained sediments due to differential settling. *J. Geophys. Res.* 98, 10279. doi:10.1029/93jc00519

Lick, W., and Lick, J. (1988). Aggregation and disaggregation of fine-grained lake sediments. *J. Gt. Lakes. Res.* 14, 514–523. doi:10.1016/S0380-1330(88)71583-X

Liu, Q., Li, J., Dai, Z., and Li, D. (2007). Flocculation process of fine-grained sediments by the combined effect of salinity and humus in the changjiang estuary. *ACTA Oceanol. SINICA-ENGLISH Ed.* 26, 140.

Logan, B. E., and Hunt, J. R. (1987). Advantages to microbes of growth in permeable aggregates in marine systems 1: Growth in permeable aggregates. *Limnol. Oceanogr.* 32, 1034–1048. doi:10.4319/lo.1987.32.5.1034

Lupi, F. M., Fernandes, H. M. L., Sá-Correia, I., and Novais, J. M. (1991). Temperature profiles of cellular growth and exopolysaccharide synthesis by Botryococus braunii Kütz. UC 58. *J. Appl. Phycol.* 3, 35–42. doi:10.1007/BF00003917

Maggi, F. (2005). *Flocculation dynamics of cohesive sediment*.

Maggi, F. (2013). The settling velocity of mineral, biomineral, and biological particles and aggregates in water. *J. Geophys. Res. Oceans* 118, 2118–2132. doi:10.1002/jgrc.20086

Mandelbrot, B. B. (1982). *The fractal geometry of nature*. San Francisco: W. H. Freeman.

Manning, A., Baugh, J., Soulsby, R., Spearman, J., and Whitehouse, R. (2011). *Cohesive sediment flocculation and the application to settling flux modelling. Sediment Transport*, 91–116.

Manning, A. J., Baugh, J. V., Spearman, J. R., and Whitehouse, R. J. S. (2010a). Flocculation settling characteristics of mud: Sand mixtures. *Ocean. Dyn.* 60, 237–253. doi:10.1007/s10236-009-0251-0

Manning, A. J., and Dyer, K. R. (1999). A laboratory examination of floc characteristics with regard to turbulent shearing. *Mar. Geol.* 160, 147–170. doi:10.1016/s0025-3227(99)00013-4

Manning, A. J., Friend, P. L., Prowse, N., and Amos, C. L. (2007). Estuarine mud flocculation properties determined using an annular mini-flume and the LabSFLOC system. *Cont. Shelf Res.* 27, 1080–1095. doi:10.1016/j.csr.2006.04.011

Manning, A. J., Langston, W. J., and Jonas, P. J. C. (2010b). A review of sediment dynamics in the severn estuary: Influence of flocculation. *Mar. Pollut. Bull.* 61, 37–51. doi:10.1016/j.marpolbul.2009.12.012

Markussen, T. N., and Andersen, T. J. (2014). Flocculation and floc break-up related to tidally induced turbulent shear in a low-turbidity, microtidal estuary. *J. Sea Res.* 89, 1–11. doi:10.1016/j.seares.2014.02.001

McAnally, W. H., and Mehta, A. J. (2001). *Coastal and estuarine fine sediment processes*. Amsterdam ; New York: Elsevier.

McCave, I. N. (1984). Size spectra and aggregation of suspended particles in the deep ocean. *Deep Sea Res. Part A. Oceanogr. Res. Pap.* 31, 329–352. doi:10.1016/0198-0149(84)90088-8

Mehta, A. J., and Partheniades, E. (1975). An investigation of the depositional properties of flocculated fine sediments. *J. Hydraulic Res.* 13, 361–381. doi:10.1080/00221687509499694

Mhashhash, A., Bockelmann-Evans, B., and Pan, S. (2018). Effect of hydrodynamics factors on sediment flocculation processes in estuaries. *J. Soils Sediments* 18, 3094–3103. doi:10.1007/s11368-017-1837-7

Michels, J., Stippkugel, A., Lenz, M., Wirtz, K., and Engel, A. (2018). Rapid aggregation of biofilm-covered microplastics with marine biogenic particles. *Proc. R. Soc. B* 285, 20181203. doi:10.1098/rspb.2018.1203

Mietta, F., Chassagne, C., Manning, A. J., and Winterwerp, J. C. (2009a). Influence of shear rate, organic matter content, pH and salinity on mud flocculation. *Ocean. Dyn.* 59, 751–763. doi:10.1007/s10236-009-0231-4

Mietta, F., Chassagne, C., and Winterwerp, J. C. (2009b). Shear-induced flocculation of a suspension of kaolinite as function of pH and salt concentration. *J. Colloid Interface Sci.* 336, 134–141. doi:10.1016/j.jcis.2009.03.044

Mietta, F. (2010). *Evolution of the floc size distribution of cohesive sediments*.

Mikkelsen, L. (2002a). The shear sensitivity of activated sludge: An evaluation of the possibility for a standardised floc strength test. *Water Res.* 36, 2931–2940. doi:10.1016/S0043-1354(01)00518-8

Mikkelsen, O. A. (2002b). Examples of spatial and temporal variations of some fine-grained suspended particle characteristics in two Danish coastal water bodies. *Oceanol. Acta* 25, 39–49. doi:10.1016/s0399-1784(01)01175-6

Mikkelsen, O., and Pejrup, M. (2001). The use of a LISST-100 laser particle sizer for *in-situ* estimates of floc size, density and settling velocity. *Geo-Marine Lett.* 20, 187–195. doi:10.1007/s003670100064

Mikutta, R., Mikutta, C., Kalbitz, K., Scheel, T., Kaiser, K., and Jahn, R. (2007). Biodegradation of forest floor organic matter bound to minerals via different binding mechanisms. *Geochimica Cosmochimica Acta* 71, 2569–2590. doi:10.1016/j.gca.2007.03.002

Nabzar, L., Pefferkorn, E., and Varoqui, R. (1988). Stability of polymer—clay suspensions. The polyacrylamide—sodium kaolinite system. *Colloids Surfaces* 30, 345–353. doi:10.1016/0166-6622(88)80217-8

Otsubo, Y. (1992). Effect of particle size on the bridging structure and elastic properties of flocculated suspensions. *J. Colloid Interface Sci.* 153, 584–586. doi:10.1016/0021-9797(92)90350-U

Park, C., Fang, Y., Murthy, S. N., and Novak, J. T. (2010). Effects of floc aluminum on activated sludge characteristics and removal of 17-α-ethinylestradiol in wastewater systems. *Water Res.* 44, 1335–1340. doi:10.1016/j.watres.2009.11.002

Partheniades, E. (1991). "Effect of bed shear stresses on the deposition and strength of deposited cohesive muds," in *Microstructure of fine-grained sediments: From mud to shale*. R. H. Bennett, W. R. Bryant, M. H. Hulbert, W. A. Chiou, R. W. Faas, J. Kasprowicz, et al. (New York, NY: Springer New York), 175–183. Available at:. doi:10.1007/978-1-4612-4428-8ı8

Partheniades, E. (1993). "Turbulence, flocculation and cohesive sediment dynamics," in *Coastal and Estuarine Studies*. Editors A. J. Mehta (Washington, D. C.: American Geophysical Union), 40–59. doi:10.1029/CE042p0040

Passow, U., and De La Rocha, C. L. (2006). Accumulation of mineral ballast on organic aggregates: Mineral ballast and organic aggregates. *Glob. Biogeochem. Cycles* 20. doi:10.1029/2005GB002579

Passow, U. (2002). Transparent exopolymer particles (TEP) in aquatic environments. *Prog. Oceanogr.* 55, 287–333. doi:10.1016/S0079-6611(02)00138-6

Pearson, H. W., Mara, D. D., Mills, S. W., and Smallman, D. J. (1987). Physico-chemical parameters influencing faecal bacterial survival in waste stabilization ponds. *Water Sci. Technol.* 19, 145–152. doi:10.2166/wst.1987.0139

Petrova, O. E., and Sauer, K. (2012). Sticky situations: Key components that control bacterial surface attachment. *J. Bacteriol.* 194, 2413–2425. doi:10.1128/JB.00003-12

Plude, J. L., Parker, D. L., Schommer, O. J., Timmerman, R. J., Hagstrom, S. A., Joers, J. M., et al. (1991). Chemical characterization of polysaccharide from the slime layer of the cyanobacterium microcystis flos-aquae C3-40. *Appl. Environ. Microbiol.* 57, 1696–1700. doi:10.1128/AEM.57.6.1696-1700.1991

Porter, K. G. (1973). Selective grazing and differential digestion of algae by zooplankton. *Nature* 244, 179–180. doi:10.1038/244179a0

Rand, B., and Melton, I. E. (1977). Particle interactions in aqueous kaolinite suspensions. *J. Colloid Interface Sci.* 60, 308–320. doi:10.1016/0021-9797(77)90290-9

Reynolds, C. S. (2006). *Ecology of phytoplankton*. Cambridge: Cambridge University Press.

Riley, G. A. (1963). Organic aggregates in seawater and the dynamics of their formation and utilization. *Limnol. Oceanogr.* 8, 372–381. doi:10.4319/lo.1963.8.4.0372

Rosen, M. J. (2004). *Surfactants and interfacial phenomena*. Hoboken, NJ, USA: John Wiley & Sons. doi:10.1002/0471670561

Round, F. E. (1981). *The ecology of algae*. Cambridge; New York: Cambridge University Press.

Safar, Z., Chassagne, C., Rijnsburger, S., Sanz, M. I., Manning, A. J., Souza, A. J., et al. (2022). Characterization and classification of estuarine suspended particles based on their inorganic/organic matter composition. *Front. Mar. Sci.* 9, 896163. doi:10.3389/fmars.2022.896163

Safar, Z. (2022). *Suspended particulate matter formation and accumulation in the delta: From monitoring to modelling*. doi:10.4233/UUID:17D027D9-9667-4AFA-89B9-AACD557A41AC

Sahin, C. (2014). Investigation of the variability of floc sizes on the Louisiana Shelf using acoustic estimates of cohesive sediment properties. *Mar. Geol.* 353, 55–64. doi:10.1016/j.margeo.2014.03.022

Serra, T., and Casamitjana, X. (1998). Structure of the aggregates during the process of aggregation and breakup under a shear flow. *J. Colloid Interface Sci.* 206, 505–511. doi:10.1006/jcis.1998.5714

Serra, T., Colomer, J., and Logan, B. E. (2008). Efficiency of different shear devices on flocculation. *Water Res.* 42, 1113–1121. doi:10.1016/j.watres.2007.08.027

Shakeel, A., Safar, Z., Ibanez, M., van Paassen, L., and Chassagne, C. (2020). Flocculation of clay suspensions by anionic and cationic polyelectrolytes: A systematic analysis. *Minerals* 10, 999. doi:10.3390/min10110999

Shao, Y., Yan, Y., and Maa, J. P.-Y. (2011). *In situ* measurements of settling velocity near baimao shoal in changjiang estuary. *J. Hydraul. Eng.* 137, 372–380. doi:10.1061/(ASCE)HY.1943-7900.0000312

Sheng, G.-P., Yu, H.-Q., and Li, X.-Y. (2010). Extracellular polymeric substances (EPS) of microbial aggregates in biological wastewater treatment systems: A review. *Biotechnol. Adv.* 28, 882–894. doi:10.1016/j.biotechadv.2010.08.001

Sherman, I. (1953). Flocculent structure of sediment suspended in Lake Mead. *Trans. AGU.* 34, 394. doi:10.1029/TR034i003p00394

Simon, M., Grossart, H.-P., Schweitzer, B., and Ploug, H. (2002). Microbial ecology of organic aggregates in aquatic ecosystems. *Aquat. Microb. Ecol.* 28, 175–211. doi:10.3354/ame028175

Sobeck, D. C., and Higgins, M. J. (2002). Examination of three theories for mechanisms of cation-induced bioflocculation. *Water Res.* 36, 527–538. doi:10.1016/S0043-1354(01)00254-8

Son, M., and Hsu, T.-J. (2009). The effect of variable yield strength and variable fractal dimension on flocculation of cohesive sediment. *Water Res.* 43, 3582–3592. doi:10.1016/j.watres.2009.05.016

Sondi, I., Bišćan, J., and Pravdić, V. (1996). Electrokinetics of pure clay minerals revisited. *J. Colloid Interface Sci.* 178, 514–522. doi:10.1006/jcis.1996.0146

Spicer, P. T., and Pratsinis, S. E. (1996). Coagulation and fragmentation: Universal steady-state particle-size distribution. *AIChE J.* 42, 1612–1620. doi:10.1002/aic.690420612

Swenson, J., Smalley, M. V., and Hatharasinghe, H. L. M. (1998). Mechanism and strength of polymer bridging flocculation. *Phys. Rev. Lett.* 81, 5840–5843. doi:10.1103/PhysRevLett.81.5840

Tang, J. (2007). *Characteristics of fine cohesive sediment's flocculation in the Changjiang estuary and its adjacent sea area*.

Taylor, M. L., Gwinnett, C., Robinson, L. F., and Woodall, L. C. (2016). Plastic microfibre ingestion by deep-sea organisms. *Sci. Rep.* 6, 33997. doi:10.1038/srep33997

Thill, A., Moustier, S., Garnier, J.-M., Estournel, C., Naudin, J.-J., and Bottero, J.-Y. (2001). Evolution of particle size and concentration in the Rhône river mixing zone. *Cont. Shelf Res.* 21, 2127–2140. doi:10.1016/S0278-4343(01)00047-4

Thomas, D. N., Judd, S. J., and Fawcett, N. (1999). Flocculation modelling: A review. *Water Res.* 33, 1579–1592. doi:10.1016/S0043-1354(98)00392-3

Tsai, C., and Hwang, S. (1995). Flocculation of sediment from the tanshui River Estuary. *Mar. Freshw. Res.* 46, 383. doi:10.1071/MF9950383

Tsujimoto, Y., Chassagne, C., and Adachi, Y. (2013). Comparison between the electrokinetic properties of kaolinite and montmorillonite suspensions at different volume fractions. *J. Colloid Interface Sci.* 407, 109–115. doi:10.1016/j.jcis.2013.05.080

Uncles, R. J., Bale, A. J., Stephens, J. A., Frickers, P. E., and Harris, C. (2010). Observations of floc sizes in a muddy estuary. *Estuar. Coast. Shelf Sci.* 87, 186–196. doi:10.1016/j.ecss.2009.12.018

van der Lee, W. T. B. (2000). Temporal variation of floc size and settling velocity in the dollard estuary. *Cont. Shelf Res.* 20, 1495–1511. doi:10.1016/S0278-4343(00)00034-0

van Leussen, W. (1988). "Aggregation of particles, settling velocity of mud flocs A review," in *Physical processes in estuaries*. Editors J. Dronkers and W. van Leussen (Berlin, Heidelberg: Springer Berlin Heidelberg), 347–403. doi:10.1007/978-3-642-73691-9_19

van Leussen, W. (1994). Estuarine macroflocs and their role in fine-grained sediment transport. Available at: https://ci.nii.ac.jp/naid/10024267924/(Accessed June 7, 2018).

van Leussen, W. (1997). The Kolmogorov microscale as a limiting value for the floc sizes of suspended fine-grained sediments in estuaries. *Cohesive sediments*, 45–62.

Verney, R., Lafite, R., Claude Brun-Cottan, J., and Le Hir, P. (2011). Behaviour of a floc population during a tidal cycle: Laboratory experiments and numerical modelling. *Cont. Shelf Res.* 31, S64–S83. doi:10.1016/j.csr.2010.02.005

Walsby, A. E. (1968). Mucilage secretion and the movements of blue-green algae. *Protoplasma* 65, 223–238. doi:10.1007/BF01666380

Wan, Y., Wu, H., Roelvink, D., and Gu, F. (2015). Experimental study on fall velocity of fine sediment in the yangtze estuary, China. *Ocean. Eng.* 103, 180–187. doi:10.1016/j.oceaneng.2015.04.076

Wang, Y. P., Voulgaris, G., Li, Y., Yang, Y., Gao, J., Chen, J., et al. (2013). Sediment resuspension, flocculation, and settling in a macrotidal estuary: Flocculation and settling in estuary. *J. Geophys. Res. Oceans* 118, 5591–5608. doi:10.1002/jgrc.20340

Wilén, B.-M., Lund Nielsen, J., Keiding, K., and Nielsen, P. H. (2000). Influence of microbial activity on the stability of activated sludge flocs. *Colloids Surfaces B Biointerfaces* 18, 145–156. doi:10.1016/S0927-7765(99)00138-1

Winterwerp, J. C. (1998). A simple model for turbulence induced flocculation of cohesive sediment. *J. Hydraulic Res.* 36, 309–326. doi:10.1080/00221689809498621

Winterwerp, J. C., Manning, A. J., Martens, C., de Mulder, T., and Vanlede, J. (2006). A heuristic formula for turbulence-induced flocculation of cohesive sediment. *Estuar. Coast. Shelf Sci.* 68, 195–207. doi:10.1016/j.ecss.2006.02.003

Winterwerp, J. C. (1999). *On the dynamics of high-concentrated mud suspensions*.

Winterwerp, J. C. (2002). On the flocculation and settling velocity of estuarine mud. *Cont. Shelf Res.* 22, 1339–1360. doi:10.1016/S0278-4343(02)00010-9

Winterwerp, J. C., and Van Kesteren, W. G. M. (2004). *Introduction to the physics of cohesive sediment dynamics in the marine environment*. Burlington: Elsevier Science. Available at: http://www.123library.org/book_details/?id=33664 (Accessed April 4, 2021).

Winterwerp, J., and Kesteren, W. V. (2004). *Introduction to the physics of cohesive sediment in the marine environment*.

Wood, E. J. F. (2014). *Microbiology of oceans and estuaries*. Amsterdam: Elsevier Science. Available at: http://qut.eblib.com.au/patron/FullRecord.aspx?p=404785 (Accessed July 29, 2020).

Xia, X. M., Li, Y., Yang, H., Wu, C. Y., Sing, T. H., and Pong, H. K. (2004). Observations on the size and settling velocity distributions of suspended sediment in the pearl river estuary, China. *Cont. Shelf Res.* 24, 1809–1826. doi:10.1016/j.csr.2004.06.009

Yeh, K.-J. (1988). *The influence of cations on activated sludge behavior*.

Yeung, A. K. C., and Pelton, R. (1996). Micromechanics: A new approach to studying the strength and breakup of flocs. *J. Colloid Interface Sci.* 184, 579–585. doi:10.1006/jcis.1996.0654

Yokoi, H. (2002). Flocculation properties of pectin in various suspensions. *Bioresour. Technol.* 84, 287–290. doi:10.1016/S0960-8524(02)00023-8

Yokoi, H., Natsuda, O., Hirose, J., Hayashi, S., and Takasaki, Y. (1995). Characteristics of a biopolymer flocculant produced by Bacillus sp. PY-90. *J. Ferment. Bioeng.* 79, 378–380. doi:10.1016/0922-338X(95)94000-H

Zhang, J., Zhang, Q., Maa, J. P. Y., and Qiao, G. (2013). Lattice Boltzmann simulation of turbulence-induced flocculation of cohesive sediment. *Ocean. Dyn.* 63, 1123–1135. doi:10.1007/s10236-013-0646-9

Zhang, Z. (1996). Studies on basic characteristics of fine sediment in changjiang estuary (in Chinese). *J. Sediment Res.* 1, 67–73.

Zinkevich, V., Bogdarina, I., Kang, H., Hill, M. A. W., Tapper, R., and Beech, I. B. (1996). Characterisation of exopolymers produced by different isolates of marine sulphate-reducing bacteria. *Int. Biodeterior. Biodegrad.* 37, 163–172. doi:10.1016/S0964-8305(96)00025-X

Zou, S., Gu, Y., Xiao, D., and Tang, C. Y. (2011). The role of physical and chemical parameters on forward osmosis membrane fouling during algae separation. *J. Membr. Sci.* 366, 356–362. doi:10.1016/j.memsci.2010.10.030

frontiers | Frontiers in Earth Science

TYPE Original Research
PUBLISHED 14 October 2022
DOI 10.3389/feart.2022.1014170

OPEN ACCESS

EDITED BY
Luigi Jovane,
University of São Paulo, Brazil

REVIEWED BY
Junhua Guo,
California State University, Bakersfield, United States
Hong Yeon Cho,
Korea Institute of Ocean Science and Technology (KIOST), South Korea

*CORRESPONDENCE
W. Ali,
w.ali@tudelft.nl

SPECIALTY SECTION
This article was submitted to Marine Geoscience, a section of the journal Frontiers in Earth Science

RECEIVED 08 August 2022
ACCEPTED 03 October 2022
PUBLISHED 14 October 2022

CITATION
Ali W, Enthoven D, Kirichek A, Chassagne C and Helmons R (2022), Effect of flocculation on turbidity currents.
Front. Earth Sci. 10:1014170.
doi: 10.3389/feart.2022.1014170

Effect of flocculation on turbidity currents

W. Ali[1]*, D. Enthoven[2], A. Kirichek[3], C. Chassagne[1] and R. Helmons[2,4]

[1]Section of Environmental Fluid Mechanics, Department of Hydraulic Engineering, Faculty of Civil Engineering and Geosciences, Delft University of Technology, Delft, Netherlands, [2]Section of Offshore and Dredging Engineering, Department of Maritime and Transport Engineering, Faculty of Mechanical, Maritime and Materials Engineering, Delft University of Technology, Delft, Netherlands, [3]Section of Rivers, Ports, Waterways and Dredging Engineering, Department of Hydraulic Engineering, Faculty of Civil Engineering and Geosciences, Delft University of Technology, Delft, Netherlands, [4]Section of Mineral Production and HSE, Department of Geoscience and Petroleum, Faculty of Engineering, Norwegian University of Science and Technology (NTNU), Trondheim, Norway

Flocculation between inorganic sediment, salt ions and microscopic organic matter present in the marine environment might play an important role in the dynamics of turbidity currents. The ability to predict, understand, and potentially leverage the effect of flocculation on turbidity currents will help to minimize the impact of human interventions such as dredging, trenching, and deep-sea mining. To better characterize the effect of flocculation on the benthic turbidity currents generated by these activities, a series of laboratory experiments were performed. Turbidity currents were created by means of lock exchange experiments. The present work focuses on the flocculation of clays that are representative for abyssal regions where deep-sea mining is performed, but most of the conclusions of this work are generic and can be applied to other types of benthic flows, occuring in harbours and channels. The effect of salt and organic material as flocculant agent was investigated. Various concentrations of clay and organic flocculant were tested. Video analysis was used to determine the head velocity of the plume. Samples at different run-out lengths were collected at the end of the lock exchange experiments for particle size and settling velocity measurements. The velocities of the turbidity currents in fresh and saline water (when no organic matter was present) were found to be similar, which was expected considering the timescales of salt-induced flocculation (about 30 min or more compared to the duration of lock exchange experiment <60 s). It was however demonstrated that, in presence of organic matter, flocculation occurred during the short time (30–60 s) of the experiment, leading to a reduced current propagation and a significant change in floc sizes (from 20 to 1,000 μm) and settling velocities (from 1 to 60 mm s^{-1}). Salt ions contributed to flocculation in the sense that flocculation with organic matter was improved in the presence of salt.

KEYWORDS

flocculation, deep sea mining, organic matter, cohesive sediment, dredging plume

1 Introduction

Dredging is commonly used for land reclamation, creating or deepening ports and waterways, and extracting minerals from underwater deposits. Over the last decade, the interest to the latter has substantially increased since the demand for minerals and metals has grown as the results of the World's population and economic activity surge. Dredging activities produce sediment plumes that lead to an increase in suspended solids concentration, potentially impacting benthic ecosystems. It is the most frequent causes of disturbance deep sea environments (Hobbs, 2002; Gates and Jones, 2012; Puig et al., 2012; Harris, 2014; Sharma, 2015). There is increasing interest in metals, particularly those critical for a successful renewable energy transition (e.g. wind turbines, solar panels and electric car storage batteries) (Hein et al., 2020). Precious metals such as manganese, nickel, cobalt are mined from terrestrial mining, however Deep Sea Mining (DSM) might be an alternative to fill the demand for precious metals. Polymetallic nodules, which contain significant amounts of these precious metals, are found in abundance on the abyssal plains in the deep sea. These nodules are distinguished from terrestrial deposits by the presence of many metals in a single deposit; for example, nodules from the Clarion–Clipperton Zone (CCZ) which is a large area with polymetallic nodules, contain cobalt, nickel, copper, and manganese in a single ore (Gillard, 2019; ISA, 2019; Harbour et al., 2020; Hein et al., 2020). In nodule mining, the Seafloor Mining Tool (SMT) collects nodules from the seafloor and separates them from excess water and fine sediments. The excess water and fine sediment are released behind the mining vehicle on the seafloor (Figure 1). There are four key areas of interest in the horizontal discharge of a sediment-water mixture from an SMT as shown in Figure 1 (Elerian et al., 2021).

1. Discharge source: This includes the preliminary conditions, including momentum, suspended sediment content, and z-distance from the sea bed. The SMT's design affects the physical parameters.

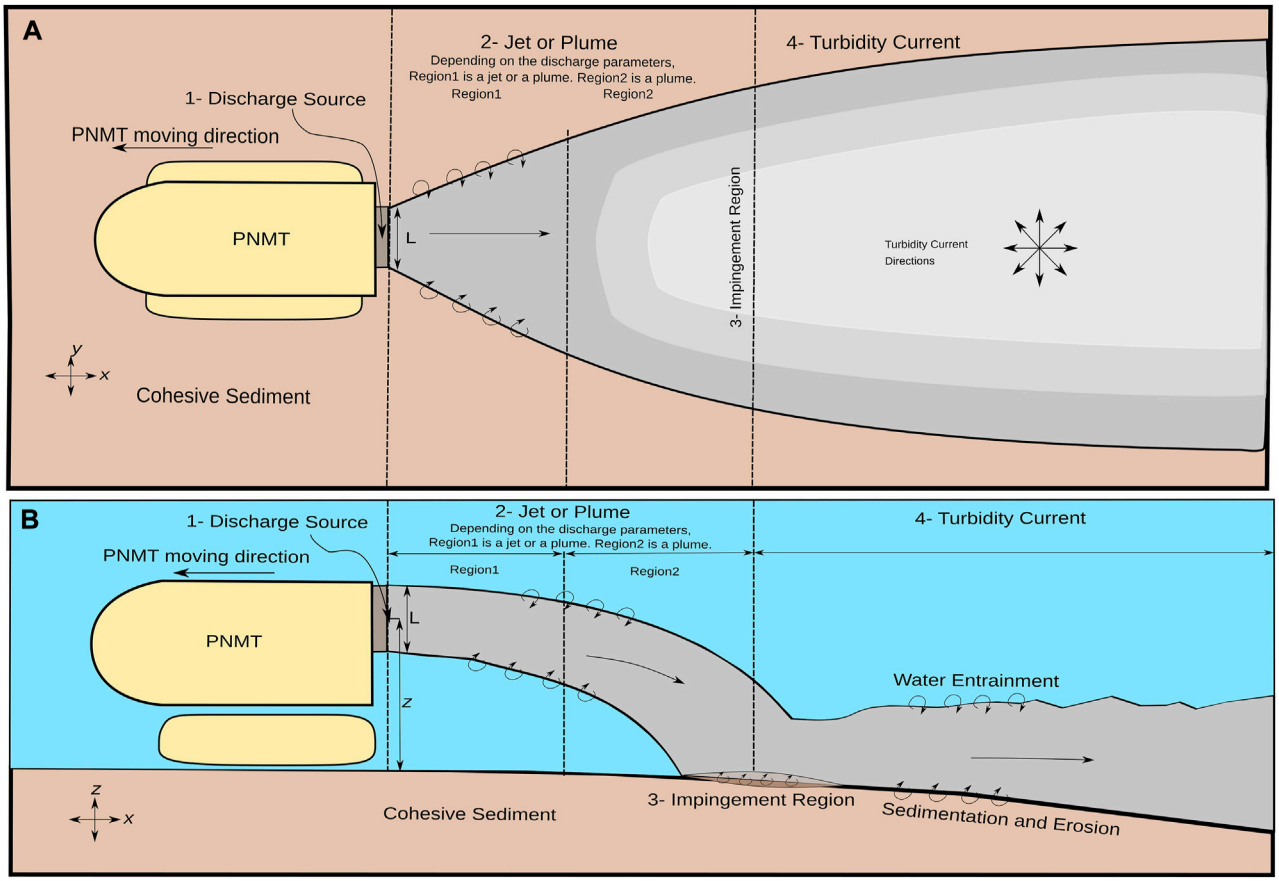

FIGURE 1
Schematic representation of how the sediment-water mixture discharged from a PNMT evolves (nearfield area). **(A)** Top view of the discharge process from a polymetallic nodule mining tool (PNMT) (Elerian et al., 2022) **(B)** Right-side view of the discharge process from a PNMT (Elerian et al., 2021).

TABLE 1 Mineral group percentages in deep-sea sediment: Inter Ocean Metal joint organization (IOM) data (Zawadzki et al., 2020), Global Sea Mineral Resources (GSR) data (Global Sea Mineral Resources, 2018), Sites A-C (Bisschof et al., 1979). It is worth noting that for IOM 1, 2, and 3, clay mineral percent is given relative to total sediment. Clay mineral percent is only relative to the sum of clay minerals at Sites A, B, C, and GSR.

	IOM 1	IOM 2	IOM 3	Site A	Site B	Site C	GSR	IOM
Smectite (%)	12.71	17.33	16.49	52	38	40	36.41	16.3
Illite (%)	13.82	12.05	14.52	31	42	50	48.34	13.2
Kaolinite (%)	0.65	0.43	0.54	17	20	10	10.33	1
Chlorite (%)	1.70	1.85	2.35				4.92	1.5
Amorphic (%)	50.47	47.09	44.42					

TABLE 2 Sediment fraction distribution: GSR and NTNU data (Lang et al., 2019), IOM data (Zawadzki et al., 2020). GSR provides averaged data based on the Belgium license area in the CCZ, while NTNU data is data of specific box-cores of the GSR data average. The IOM data is based on data from the CCZ's IOM license area.

Fraction	Diameter range (um)	GSR data average (%)	NTNU data BC062 (%)	NTNU data BC064 (%)	IOM data average (%)	Gillard et al. (2019)
Clay	<2	12.0	11.3	14.5	23.24	25.3
Silt	2–63	76.2	85.7	82.5	70.36	52.11
Sand	63–2000	11.8	3	3	6.13	22.5

2. Jet or Plume regime: Depending on the flow discharge parameters in this area, the flow may take the form of a jet or plume. Later, when buoyancy force takes over, the flow transforms into a plume.
3. Impingement region: This area is situated on the ocean floor. Due to the direct connection with the seafloor in this location, the negative buoyant plume changes direction. Within this region, sediment deposition and potential sea bed erosion are anticipated to occur.
4. Turbidity current: This current originates outside the area of impingement. The generated turbidity current's behavior is governed by the interaction between the discharge and the seabed (Rutkowska et al., 2014; Global Sea Mineral Resources, 2018; Hage et al., 2019; Ouillon et al., 2021). Its principal characteristics are determined by the hydraulic characteristics previous to the impingement region.

In the near-field region, many flow regimes (such as jet, plume, and turbidity current) are anticipated, and they rely on the discharge characteristics. The focus of this work is on turbidity current. It is estimated that the turbidity current generated from the discharge at the back of the mining vehicle can spread over large distances (9–13 km (Gillard, 2019)) and remain suspended for an extended period of time (Blue Nodules, 2020; Hein et al., 2020; Haalboom et al., 2022). The sediment plume generated by mining activity can severely affect the deep sea flora and fauna. The settling of the sediment plume and subsequent blanketing can bury benthic species, obstruct the respiratory surfaces of filter feeders, and contaminate the food source for the majority of benthic organisms (Vanreusel et al., 2016; Gollner et al., 2017; Jones et al., 2017). Limiting plume dispersion could help to lower the environmental impact caused by human activities (Weaver et al., 2022).

Particle size distribution (PSD) is an important factor that determines how far deep-sea sediment plumes spread (Gillard et al., 2019; Spearman et al., 2020). The coarse nodule debris settle quickly but the clay-sized mineral particles (Tables 1 and 2) stay in suspension for long periods of time which leads to a wider plume dispersion (Sharma, 2015). Since aggregated particles (flocs) settle quicker, flocculation has been shown to potentially limit plume dispersion (Manning and Dyer, 2002; Smith and Friedrichs, 2011; Gillard et al., 2019; Spearman et al., 2019, 2020). The size, density, shape, settling velocity and strength of flocs vary over time. These properties are influenced by the medium in which the particles are suspended (salinity, organic matter content, sediment concentration, hydrodynamics) (Manning and Dyer, 2002; Mietta et al., 2009; Smith and Friedrichs, 2011; Chassagne, 2020). The deep-sea environment is in principle favourable for flocculation because of its high salinity and concentration of organic matter (Mewes et al., 2014; ISA, 2015; Fettweis and Baeye, 2015; Volz et al., 2018). The availability of fresh organic matter on the top layer of the deep sea varies substantially because organic matter gradually degrades and remineralizes with depth. With increasing water depth, the flux of organic matter to the seabed often decreases. Less than 0.5 percent of the sediment bulk is made up of carbon in the top few centimeters of

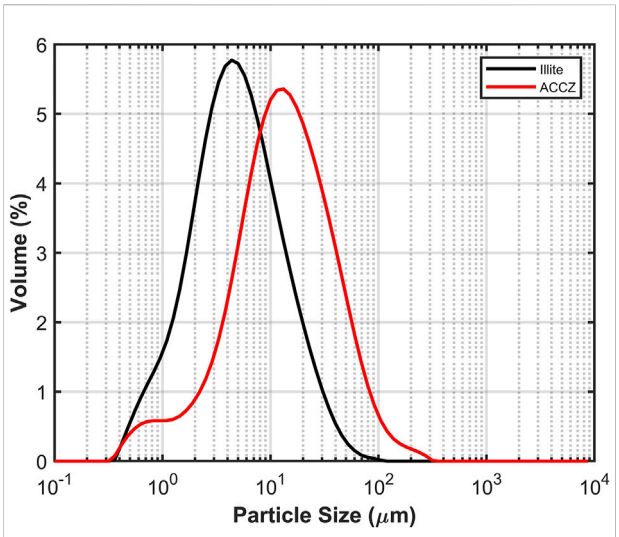

FIGURE 2
Particle size distribution of illite and ACCZ.

the CCZ sediment. This decreases to 0.1 percent of the sediment's mass below 30 cm (Volz et al., 2018). The present work aims to demonstrate the mechanisms that, in the presence of organic matter, can help reduce the extension of the turbidity currents. Flocculation has been shown to occur at very short timescales (in the order of few minutes) in natural environments in the presence of (microscopic) organic matter (Deng et al., 2019; Safar et al., 2019; Shakeel et al., 2020). The current lab-scale work uses a series of lock exchange experiments to generate a turbidity current and studies the impact of flocculation in short time scales. Properties such as time and distance of turbidity currents' propagation, particle size, and settling velocities are measured. This article is organized as follows. Section 2 gives an overview of the materials used and the experimental setups. Section 3 presents relevant results and discussion. Finally, the conclusions are presented in Section 4.

2 Material and methods

2.1 Clay

Two types of clays were used for the experiments. Initial experiments were conducted by using illite since illite is one of the dominant clay minerals (Table 2) found of the top layer of the Clarion–Clipperton Zone (CCZ) sediment where Deep Sea Mining (DSM) is performed (ISA, 2015; Helmons et al., 2022). The illite used in the experiments (purchased from Argiletz laboratoires) was obtained as a dry powder. The d_{50} of illite particles was found to be around 5 μm by static light scattering (Figure 2). A lab-made artificial clay with a composition similar to CCZ clay was also used and will be referred to as Artificial CCZ (ACCZ) (Enthoven, 2021; Ali et al., 2022). We use this material as a substitute for deep-sea sediment, as CCZ clay could not be supplied in sufficient quantities for lock-exchange experiments. The ACCZ mixture consists of two materials: i) Sibelco FT-S1 (Abidichte Ton) consisting of 64% kaolinite, 10% illite, 19% quartz, and 7% other minerals; ii) Cebo OMCA Betonite consisting of 17% kaolinite, 17% illite and 66% montmorillonite. The precise proportions of these two materials are unknown. The clay was created so that its rheological/mechanical properties match the ones of CCZ clay (Enthoven, 2021). The wet ACCZ clay was dried for 24 h at 105°C to determine its dry density, which was found to be 2,600 kg m^{-3}. This clay has an average particle size of 10–20 μm, as found by static light scattering device (Figure 2).

2.2 Flocculant

The organic matter found in the deep-sea region is expected to act as a flocculating agent for the sediment plume (Jones et al., 2017; Gillard et al., 2019; Spearman et al., 2020; Jones et al., 2021). It was impossible, at this stage, to fully characterize or obtain this flocculant, which is expected to be composed in parts of polyssacharides. As was done in previous studies (Shakeel et al., 2020), a synthetic flocculant was used as a proxy for organic matter content. The flocculant chosen was an anionic polyacrylamide, referenced Zetag 4,120 (BASF company) of medium anionic charge with high molecular weight. Polyelectrolytes with a high molecular weight will better promote flocculation compared to polyelectrolytes with a low molecular weight (Bergaya and Lagaly, 2013).

2.3 Lock exchange setup

Turbidity currents have been studied extensively in the laboratory through lock exchange experiments (Helena et al., 2013; Baker et al., 2017; Craig et al., 2020). Lock-exchange experiments or fixed volume turbidity currents are caused by the release of dense material in a fixed volume. The front propagation in a traditional lock-release turbidity current is equivalent to the front propagation in the turbidity current generated by a moving source (Ouillon et al., 2021).

Lock exchange experiments were performed in both fresh and saline water. The saline water was produced by mixing 10 mM of $CaCl_2$ to freshwater. The experiments were conducted for three distinct clay concentrations (10 g L^{-1}, 30 gL^{-1} and 100 g L^{-1}) with illite and two different concentrations with ACCZ (10 g L^{-1} and 30 g L^{-1}). Handling and mixing the higher concentration of ACCZ and eventually getting a fully dispersed sample was difficult therefore 100 g L^{-1} was not used. 30 g L^{-1} is the mean case, and 10 g L^{-1} and 100 g L^{-1} are considered to assess whether the design

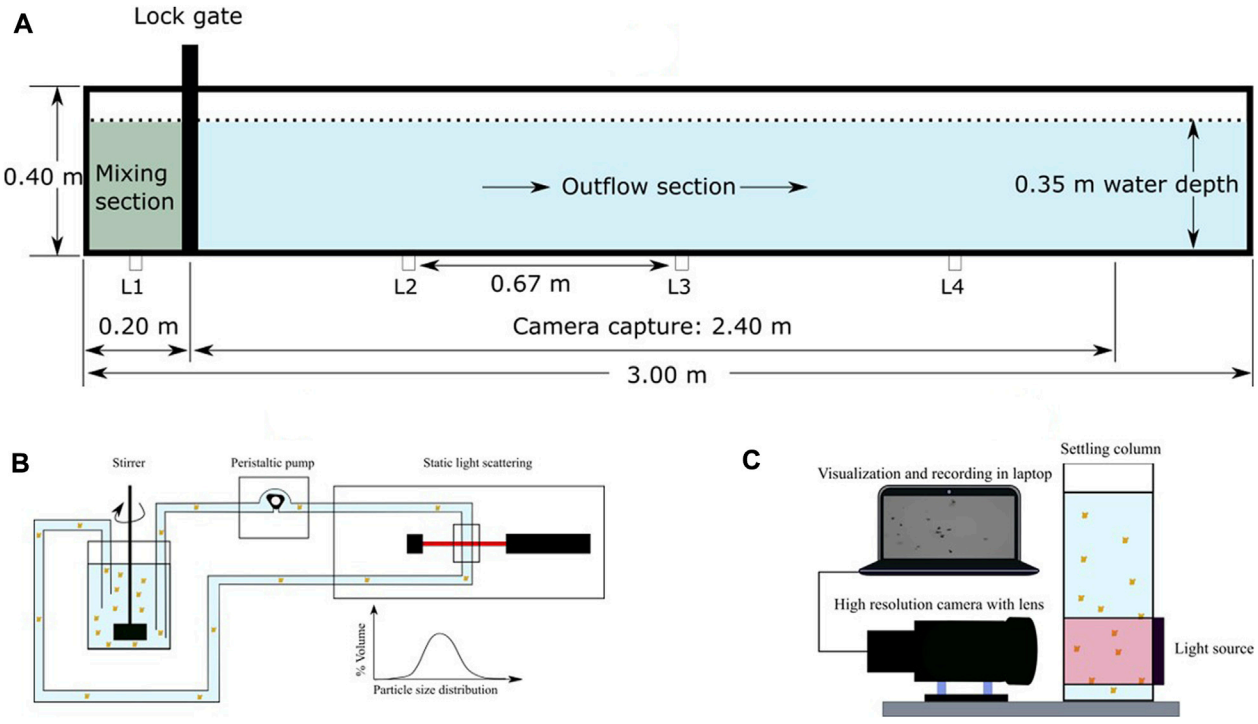

FIGURE 3
(A) Schematic representation of the Lock exchange setup. The samples are taken at L1, L2, L3 and L4 locations. **(B)** Schematic representation of the Malvern master Sizer 2000 for particle size measurement. **(C)** Schematic representation of the FLOCCAM setup.

should aim for lower or higher concentrations to identify if and when flocculation has a more significant effect (Blue Nodules, 2020). Two different flocculant dosages (0.25 mg g^{-1} and 0.75 mg g^{-1} of clay) were used for flocculation based on preliminary studies and are significantly below the optimum flocculant dosage (2.5 mg g^{-1}). The dry clay was mixed in water in the lock exchange's mixing section for an hour before the lock gate was opened. This mixing ensured that homogeneous suspensions with a well-defined mean particle size could be obtained. The initial clay size obtained by such a process might not be similar to that obtained through the DSM operation, in which the sediment passes through the SMT for a brief period of time exposed to high shear rates. In experiments with flocculant, the flocculant was added and stirred for 30 s before opening the lock. The turbidity flow was filmed with a Navitar 17 mm lens on an IL5HM8512D: Fastec high-speed camera. The camera was set 4.75 m from the lens to the front wall of the tank, and it recorded at a rate of 130 frames per second. The camera captured the 2.40 m to the left of the lock. Samples were collected from four locations (L1, L2, L3, L4 in Figure 3A) at the end of the experiments from the collection points located at the bottom of the lock exchange.

2.4 Particle/flocs size distribution

Particle Size Distribution (PSD) analysis was conducted on the obtained samples using a Malvern Master Sizer 2000 (Figure 3B), a technique based on static light scattering (SLS). With this set-up, within a few seconds a full PSD can be recorded. The measurements were carried out in a JLT6 jar setup supplied by VELP Scientifica, Italy. The size of the jar was 95 mm in diameter and 110 mm in height. The suspension was stirred using a single rectangular paddle. The paddle was 25 mm in height and 75 mm in diameter and was positioned in the suspension 10 mm above the bottom of the jar. The suspension was pumped through the Malvern Master Sizer 2000 from the mixing jar to the Mastersizer and then back to the mixing jar using a peristaltic pump (Figure 3B). The lowest possible discharge rate of the pump was used (1.37 ml s^{-1} (112 s^{-1})).

2.5 Floc settling analysis

The FLOCCAM device is based on video microscopy and can be used to estimate PSD's (>20 μm) and settling velocities of flocs samples (Shakeel et al., 2021; Ye et al., 2020; Manning et al., 2007;

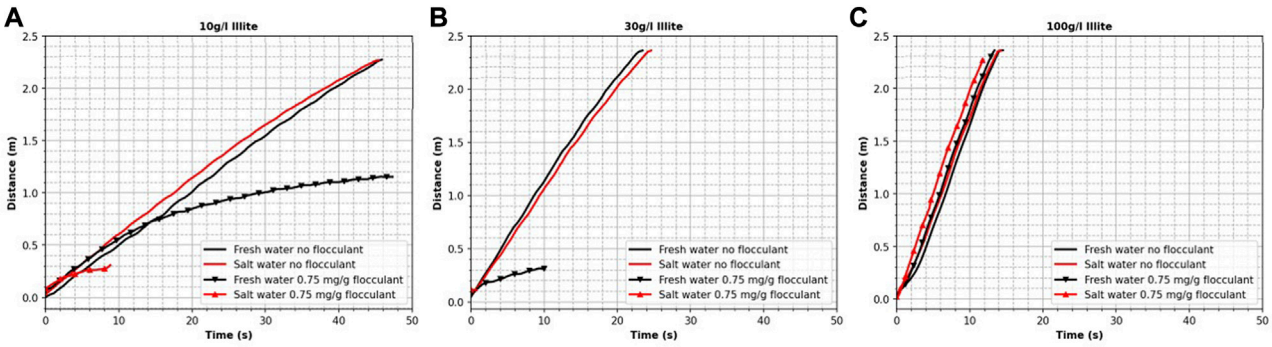

FIGURE 4
Change in distance as a function of time for 10 g L^{-1} **(A)**, 30 g L^{-1} **(B)** and 100 g L^{-1} **(C)** of illite. Black lines represent experiments done in freshwater and red lines show experiments done in saltwater. Only results with 0.75 mg g^{-1} of flocculant are shown in these figures.

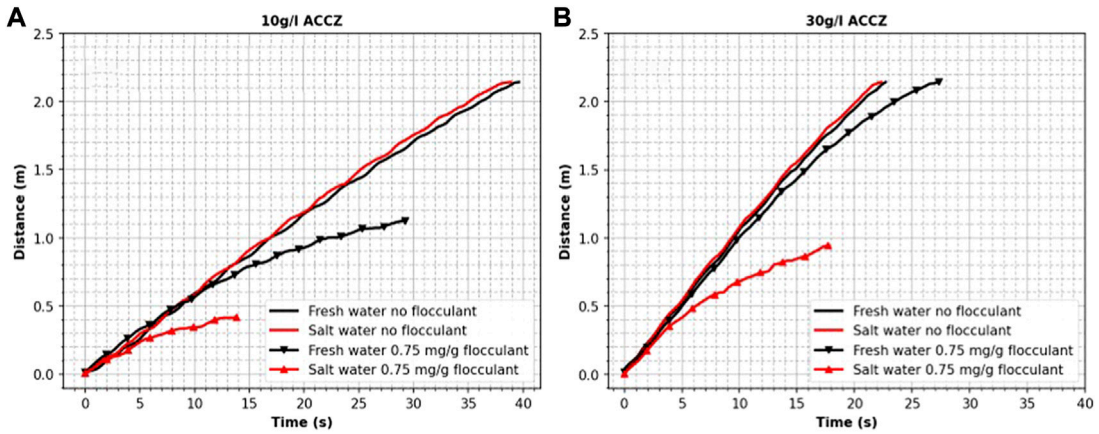

FIGURE 5
Change in distance as a function of time for 10 g L^{-1} **(A)** and 30 g L^{-1} **(B)** of ACCZ (Ali et al., 2022). Black lines represent experiments done in freshwater and red lines show experiments done in saltwater. Only results with 0.75 mg g^{-1} of flocculant are shown in these figures.

Mietta et al., 2009). Figure 3C shows a schematic representation of the equipment. The PSD, shape, and settling velocity of the flocs are calculated from recorded videos of settling flocs in a settling column using a software package called Safas (MacIver, 2019).

3 Results and discussion

3.1 Distance travelled by plume heads

The 10, 30, and 100 g L^{-1} illite experiments are displayed in Figure 4 in terms of the distance traveled by the turbidity current within the video recording range. When no flocculant is used, there is no significant difference observed between experiments conducted in fresh and saltwater and the turbidity current without added flocculant reached the lock exchange's end in all experiments. The current's head velocity scales as the square root of the plume density, as is expected (Huppert, 2006). Salt induced flocculation time is in the order of 15–30 min even under ideal shear circumstances (Mietta, 2010). Therefore, no significant effect was observed over the experimental period of the current study (<1 min). Similar results were obtained for both 10 and 30 g L^{-1} experiments done with ACCZ (see Figure 5).

Due to the effect of flocculation, the distance traveled in saltwater experiments with flocculant for all clay concentrations was reduced considerably. Figures 4, 5 show results for the experiments 0.75 mg/g flocculant where the sediment plume did not reach the lock exchange's endpoint and settled inside

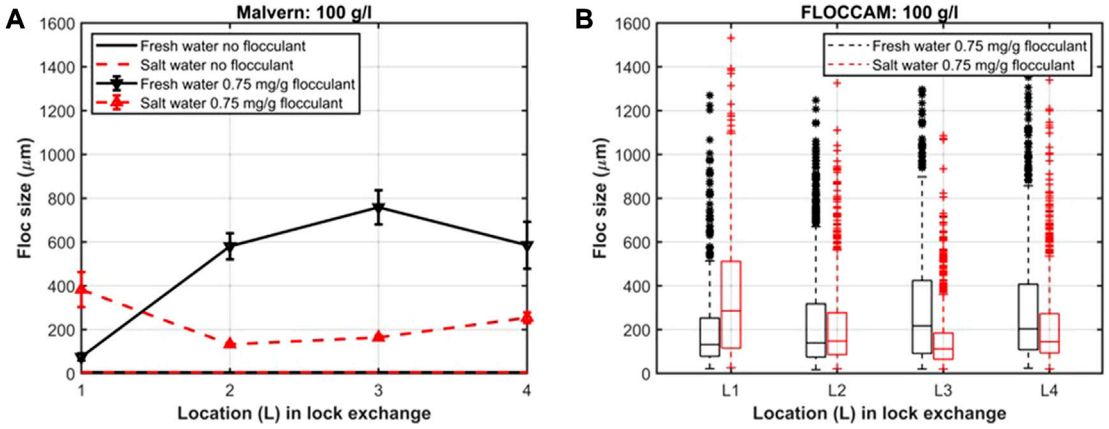

FIGURE 6
Hydrodynamic diameter of illite flocs for 100 g L^{-1} experiments at L1-L4 locations of the lock exchange. Figure **(A)**, results obtained by SLS and figure **(B)**, results obtained from FLOCCAM. Black and red lines represent experiments done in freshwater and saltwater, respectively. Only results with 0.75 mg g^{-1} of flocculant are shown.

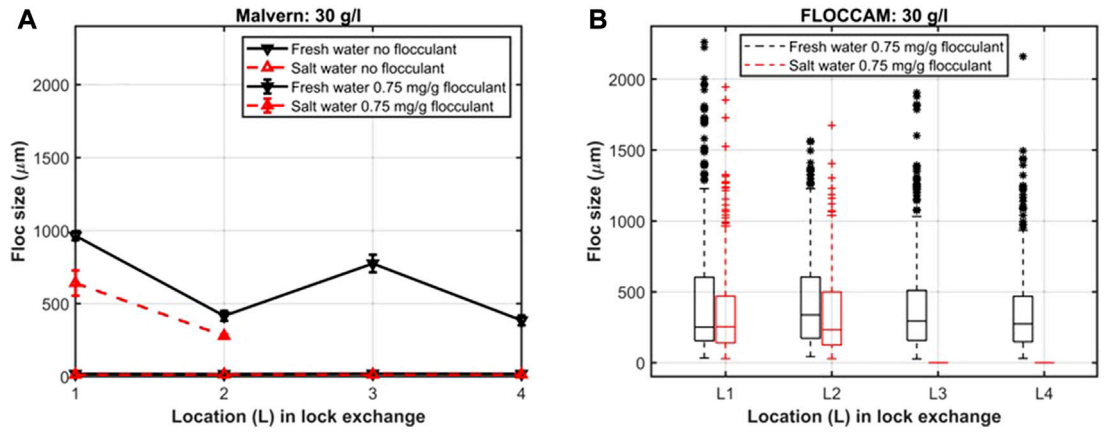

FIGURE 7
Hydrodynamic diameter of ACCZ flocs for 30 g L^{-1} experiments at L1-L4 locations of the lock exchange (Ali et al., 2022). Figure **(A)**, results obtained by SLS and figure **(B)**, results obtained from FLOCCAM. Black and red lines represent experiments done in freshwater and saltwater, respectively. Only results with 0.75 mg g^{-1} of flocculant are shown.

the outflow section. For the experiment done in freshwater with flocculant, the sediment plume reached the end of the outflow section or nearly half of the outflow section. The weak flocculation in freshwater accounts for this difference between fresh and saline water experiments. Even though both clay and flocculant have a negative charge, making flocculation difficult, freshwater contains enough cations to promote flocculation (Ibanez Sanz, 2018). The cation concentration in saltwater promotes flocculation, especially as the cation chosen (Ca^{2+}) is divalent (Shakeel et al., 2020; Chassagne, 2020). For 100 g L^{-1} experiment with illite, it is observed that the system did not properly flocculate as in all cases the sediment plume reached the end of the outflow section with the same speed, and flocculation had little to no effect on macroscopic scale.

The results using 0.25 mg g^{-1} flocculant are given in (Supplementary Figures S1, S2), and in all cases (illite or ACCZ), the sediment plume reached the end of outflow section except for one case (10 g L^{-1} ACCZ in saltwater). The results in the 0.25 mg g^{-1} case hint that the low concentration of flocculant has less impact on the plume propagation.

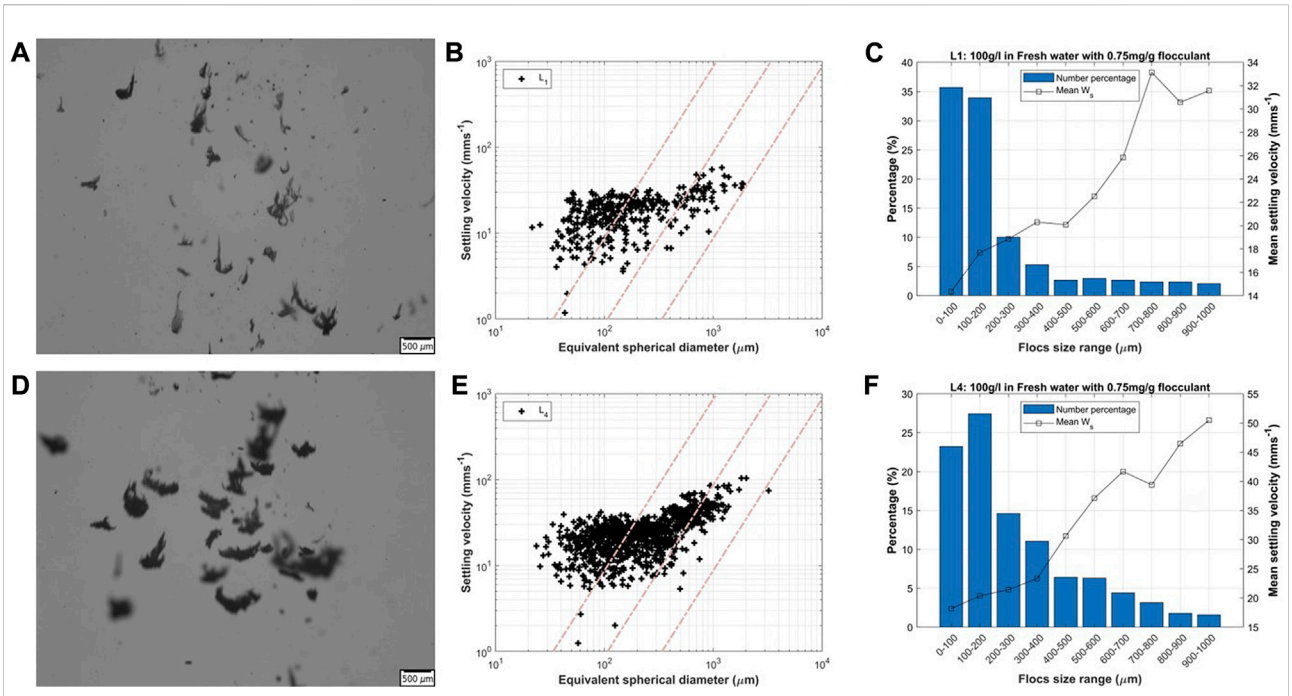

FIGURE 8
Figures **(A,D)** snapshots of the videos; Figures **(B,E)**: Settling velocity and particle size analysis of the samples collected at location L1 and L4 during lock exchange experiments with 100 g L^{-1} illite and 0.75 mg g^{-1} of flocculant in freshwater. Settling velocity is derived as a function of equivalent spherical diameter, with diagonal dashed lines representing the contours of effective density calculated by using Stokes equation (from left to right: 1600, 160, 16 (kg m^{-3})). Figures **(C,F)** show floc size range and mean settling velocity.

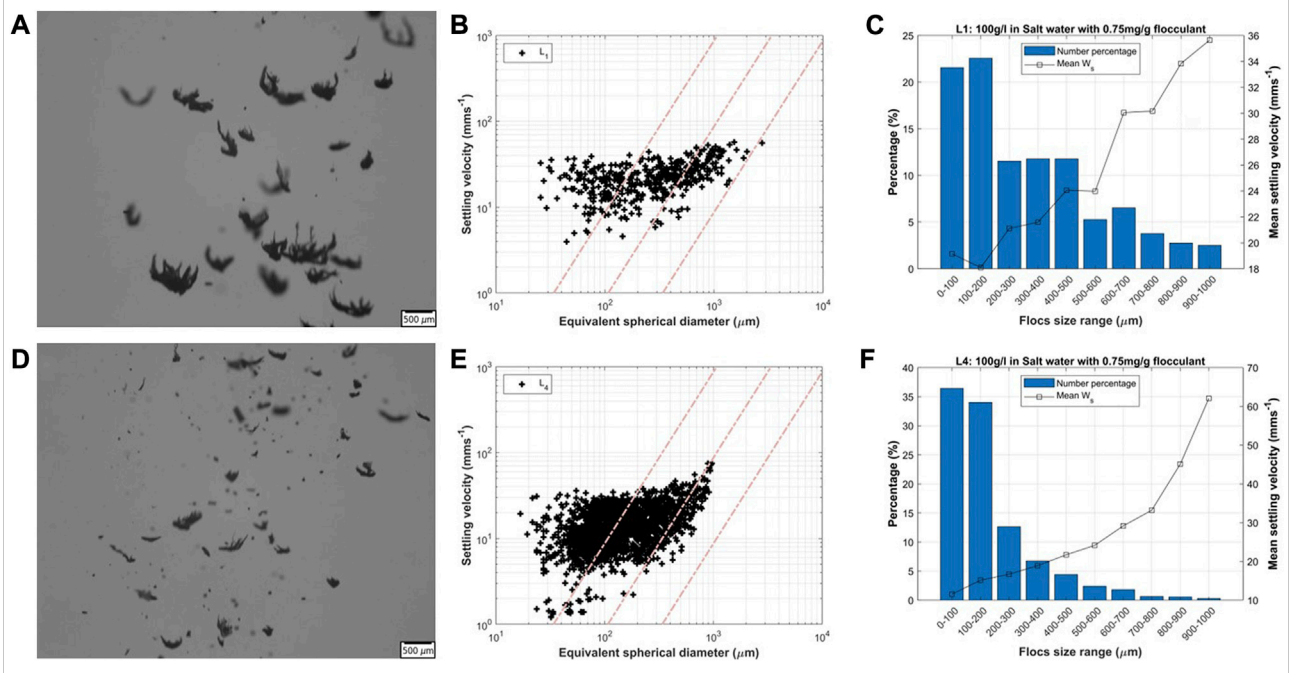

FIGURE 9
Figures **(A,D)** snapshots of the videos; Figures **(B,E)**: Settling velocity and particle size analysis of the samples collected at location L1 and L4 during lock exchange experiments with 100 g L^{-1} illite and 0.75 mg g^{-1} of flocculant in saltwater. Settling velocity is derived as a function of equivalent spherical diameter, with diagonal dashed lines representing the contours of effective density calculated by using Stokes equation (from left to right: 1600, 160, 16 (kg m^{-3})). Figures **(C,F)** show floc size range and mean settling velocity.

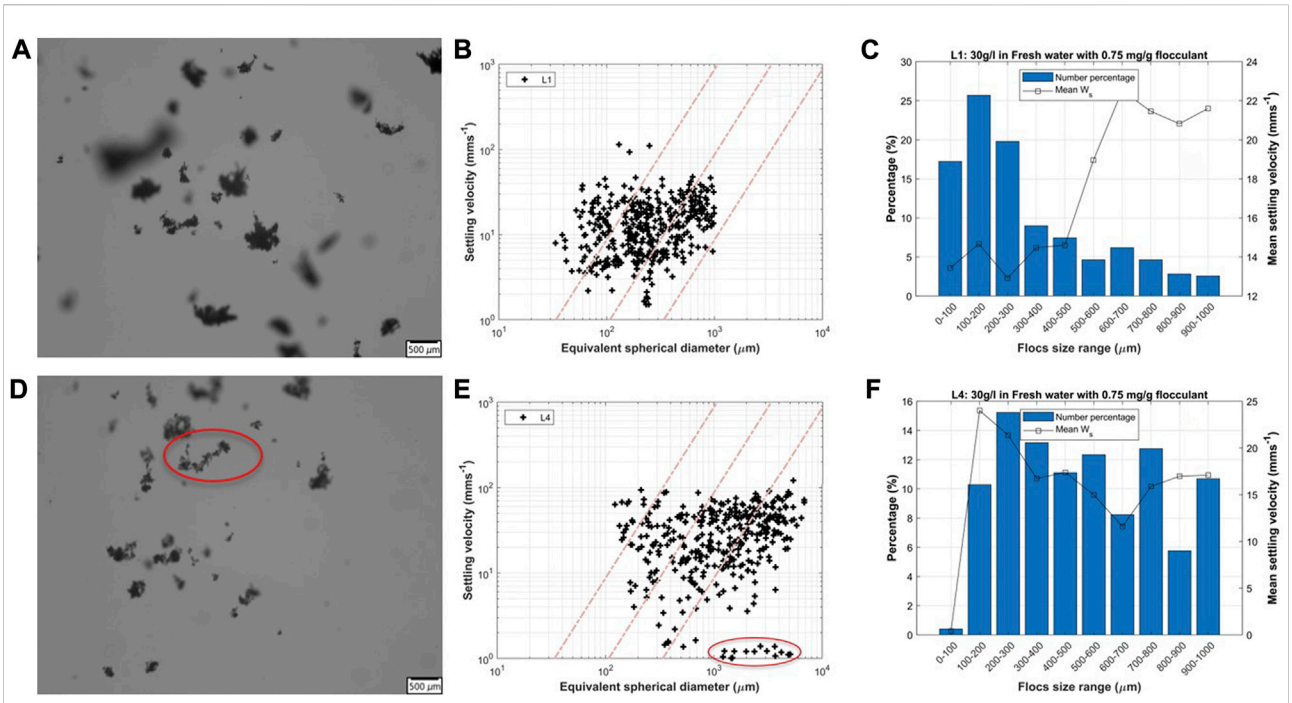

FIGURE 10
Figures **(A,D)** snapshots of the videos; Figures **(B,E)**: Settling velocity and particle size analysis of the samples collected at location L1 and L4 during lock exchange experiments with 30 g L^{-1} ACCZ and 0.75 mg g^{-1} of flocculant in freshwater (Ali et al., 2022). Settling velocity is derived as a function of equivalent spherical diameter, with diagonal dashed lines representing the contours of effective density calculated by using Stokes equation (from left to right: 1600, 160, 16 (kg m^{-3})). Figures **(C,F)** show floc size range and mean settling velocity.

3.2 Mean floc size as function of travel distance

Figure 6 (Illite) and Figure 7ACCZ show the mean floc size of the samples taken at locations L1–L4. No flocculation occurred without the flocculant in both fresh and saltwater, as for each location, the d_{50} was found equal to the mean clay size. For both experiments with illite, d_{50} was found to be around 5 μm at all locations, whereas for experiment with ACCZ, it was found to be between 12 and 20 μm. These sizes are in line with the d_{50} found by SLS (5 and 10–20 μm respectively, see section 2.1). The bars given in Figure 6 and Figure 7A represent the standard deviation around the mean floc size based on SLS device, whereas the box plots in Figure 6 and Figure 7B represent the median particle sizes with interquartile range and outliers based on FLOCCAM. In the presence of flocculant, it was found that freshwater flocs were larger than saltwater flocs. Because of the electrostatic repulsion between the charged groups on the polymeric flocculant backbones, the flocculant in freshwater is less coiled in fresh than in salt water (Chassagne, 2020). As a result of shear during propagation, it is observed that the d_{50} of flocs created in saltwater with illite clay reduced as function of travel distance. This difference is not observed for the ACCZ clay (Figure 6 and Figure 7).

The results obtained with 0.25 mg g^{-1} flocculant are shown in (Supplementary Figures S3, S4), where the difference in flocs size in fresh and salt water is not significant.

3.3 Settling velocity distributions as function of size and travel distance

Figures 8, 9 show the settling velocities and particle size for 100 g L^{-1} illite with 0.75 mg g^{-1} flocculant at L1 and L4 for freshwater and saltwater, respectively. Figures 10, 11 show the settling velocities and particle size for 30 g L^{-1} ACCZ with 0.75 mg g^{-1} of flocculant at sites L1 and L4 (for freshwater) and L1 and L2 (for saltwater), respectively. At the point when the turbidity current settles down, on average the settling velocities in freshwater are smaller than in saltwater. This is due to the fact that the flocculant is less coiled in freshwater than in saltwater (Chassagne, 2020), where flocs are denser and have a faster settling velocity. This was confirmed by the video images (see Figure 8 and Figures 9A,D). The settling velocities increased in the case of saltwater for 100 g L^{-1} illite between L1 and L4, as a result of coiling, flocs got compacted right after opening the lock (Figure 9). In the case of 30 g L^{-1} ACCZ, the settling behavior and floc size for the saltwater sample did not change between L1 and L2, indicating that

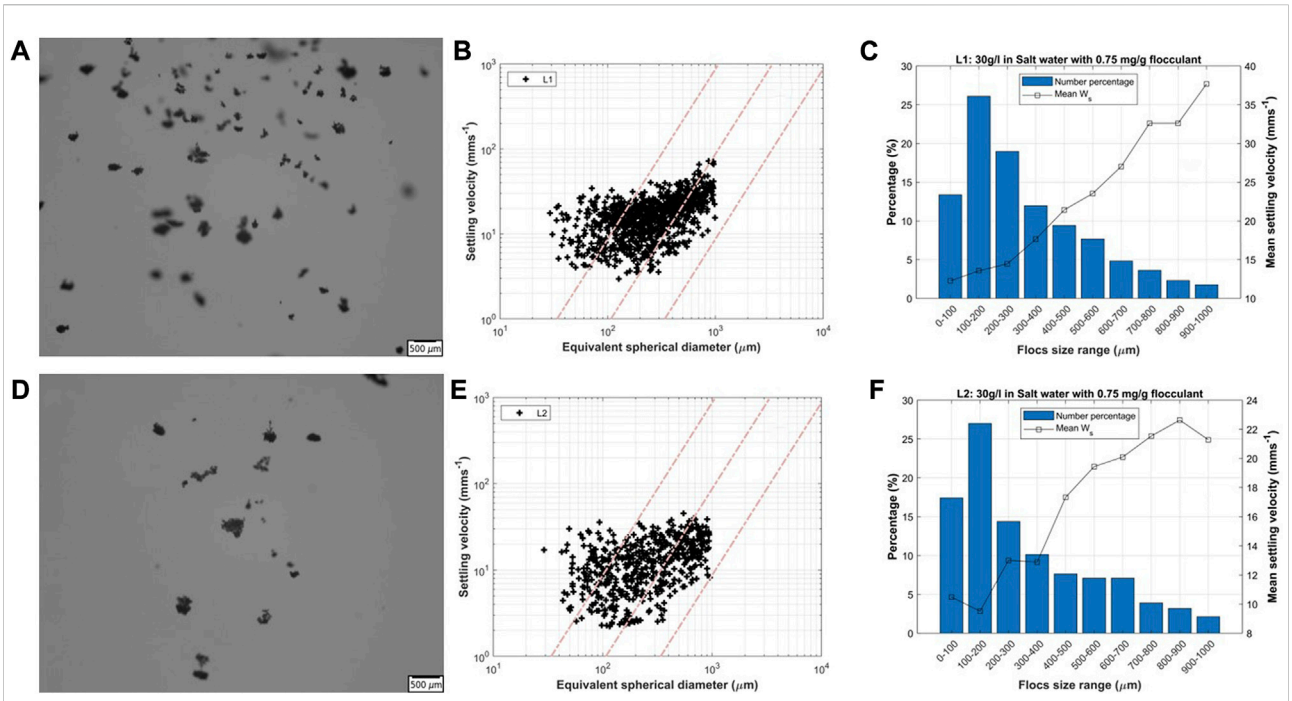

FIGURE 11
Figures **(A,D)** snapshots of the videos; Figures **(B,E)**: Settling velocity and particle size analysis of the samples collected at location L1 and L2 during lock exchange experiments with 30 g L^{-1} ACCZ and 0.75 mg g^{-1} of flocculant in saltwater (Ali et al., 2022). Settling velocity is derived as a function of equivalent spherical diameter, with diagonal dashed lines representing the contours of effective density calculated by using Stokes equation (from left to right: 1600, 160, 16 (kg m^{-3})). Figures **(C,F)** show floc size range and mean settling velocity.

optimum flocculation (i.e. flocs cannot grow any further) has occurred in the mixing tank. The bridging between anionic polyelectrolyte and clay is complete because of saltwater cations. The flocculation in the mixing tank for the freshwater sample is most likely incomplete due to the scarcity of cations. Flocs, clay particles, and unbounded flocculant are released when the lock is opened. Freshwater containing cations comes into contact with the clay particles and unbounded flocculant. Because polyelectrolyte flocculation is quick (on the scale of seconds) (Ibanez Sanz, 2018; Shakeel et al., 2020; Ali and Chassagne, 2022), these cations can act as a binding agent, inducing flocculation. As a result, flocs form, resulting in a particle size change, as shown between L1 and L4. Several flocs formed during the propagation of the sediment plume in 30 g L^{-1} ACCZ experiment in freshwater are observed to be elongated, resulting in flocs with larger equivalent diameters (shown by the red circle in Figure 10D). Because they are formed of low density uncoiled flocculant with some clay linked to it, these big flocs have a very slow settling velocity. These flocs were unable to catch more clay particles and coil due to their limited residence period in the water column. Coiling of flocs happens over longer periods of time when turbulent shear causes the polyelectrolyte's dangling ends to fall onto the floc. The flocs get rounder and denser as a result (Shakeel et al., 2020). Our experiments show that the amount of flocculant needed correlates to clay concentration. In addition, the results obtained with 30 g L^{-1} with 0.75 mg g^{-1} combination results in a turbidity current that settles faster than other combinations. The results with 0.25 mg g^{-1} of flocculant are shown in Supplementary Figures S5-S8.

4 Conclusion

Understanding the changes in the propagation of turbidity currents created by human interventions, such as dredging, trenching and deep-sea mining is crucial for anticipating, predicting and where possible reducing the related environmental impact. Understanding is also crucial for engineers to know in what way the equipment and processes could be optimized to minimize plume dispersion. Previous studies have demonstrated that the flocculation of organic matter to clay occurs in less than 1 min in series of laboratory experiments. In this work, the influence of flocculation on turbidity currents was studied inside a lock exchange, where the current propagation time was of the same order of magnitude. It was shown that in the presence of an organic flocculating agent (anionic polyelectrolyte) flocculation was promoted. It was found

that in both fresh and saltwater, flocs can be formed in a matter of seconds with the flocculant used in this study. As a result, the sediment plume was able to settle more quickly. The synthetic flocculant used is a proxy for organic matter found in marine environments (usually also negatively charged). It remains to be investigated if the type of flocculant has a significant impact on flocculation. This will be possible once the organic matter found in our area of interest (i.e. the Clarion-Clipperton Zone) has been fully characterized. The results presented in this article are generic, thus apply to a wide range of turbidity currents. We demonstrated that flocculation may occur even in freshwater, where flocculation is supposed to be difficult because of the electrostatic repulsion between organic matter and clay. This means that flocculation should be accounted for in turbidity current models. The obtained results demonstrate that flocculation is a relevant phenomenon that may already be contributing in the near field. Building experience with more conventional sediments allows us to better understand and design experiments with real CCZ sediment, which is the next step.

Data availability statement

The original contributions presented in the study are included in the article/Supplementary Material, further inquiries can be directed to the corresponding author.

Author contributions

WA first draft manuscript and floc experiments. DE and WA lock exchange experiments, AK, CC, and RH contributed to data analysis and interpretation. All authors contributed to the manuscript's revision and read and approved the submitted version.

Funding

This work is performed in the framework of PlumeFloc (TMW.BL.019.004, Topsector Water and Maritiem: Blauwe route) within the MUDNET academic network.

Acknowledgments

The authors would like to thank all co-funding partners. The authors would also like to thank Deltares for using their experimental facilities in the framework of the MoU between TU Delft/Deltares.

Conflict of interest

The authors declare that the research was conducted in the absence of any commercial or financial relationships that could be construed as a potential conflict of interest.

Publisher's note

Supplementary material

The Supplementary Material for this article can be found online at: https://www.frontiersin.org/articles/10.3389/feart.2022.1014170/full#supplementary-material

References

Ali, W., and Chassagne, C. (2022). *Comparison between two analytical models to study the flocculation of mineral clay by polyelectrolytes*.

Ali, W., Enthoven, D., Kirichek, A., Helmons, R., and Chassagne, C. (2022). "Can flocculation reduce the dispersion of deep sea sediment plumes?" in Proceedings of the World dredging conference, Copenhagen, Denmark.

Baker, M. L., Baas, J. H., Malarkey, J., Jacinto, R. S., Craig, M. J., Kane, I. A., et al. (2017). The effect of clay type on the properties of cohesive sediment gravity flows and their deposits. *J. Sediment. Res.* 87 (11), 1176–1195. doi:10.2110/jsr.2017.63

Bergaya, F., and Lagaly, G. (2013). *Handbook of clay science*. Second edition. Amsterdam: Elsevier.

Bisschof, J., Heath, G., and Leinen, M. (1979). "Geochemistry of deep-sea sediments from the pacific manganese nodule province DOMES sites A, B and C," in *Marine geology and oceanography of the pacific manganese nodule province, marine science*. Editors J. Bisschof and D. Piper (Boston: Springer), 397–436.

Blue Nodules (2020). *Environmental Impact Assessment (EIA) components for test mining up to prototype level (TRL 6) Technical report*.

Chassagne, C. (2020). *Introduction to colloid science*. Delft Academic Press.

Craig, M. J., Baas, J. H., Amos, K. J., Strachan, L. J., Manning, A. J., Paterson, D. M., et al. (2020). Biomediation of submarine sediment gravity flow dynamics. *Geology* 48 (1), 72–76. doi:10.1130/G46837.1

Deng, Z., He, Q., Safar, Z., and Chassagne, C. (2019). The role of algae in fine sediment flocculation: *In-situ* and laboratory measurements. *Mar. Geol.* 71–84, 71–84. doi:10.1016/j.margeo.2019.02.003

Elerian, M., Alhaddad, S., Helmons, R., and van Rhee, C. (2021). Near-field analysis of turbidity flows generated by polymetallic nodule mining tools. *Mining* 1, 251–278. doi:10.3390/mining1030017

Elerian, M., Van Rhee, C., and Helmons, R. (2022). Experimental and numerical modelling of deep-sea-Mining-Generated turbidity currents. *Minerals* 12 (5), 558. doi:10.3390/min12050558

Enthoven, D. (2021). "Plume dispersion of low-density clayey suspension turbidity currents created by deep-sea mining." (Technische Universiteit Delft). Master Thesis.

Fettweis, M., and Baeye, M. (2015). Seasonal variation in concentration, size, and settling velocity of muddy marine flocs in the benthic boundary layer. *J. Geophys. Res. Oceans* 120, 5648–5667. doi:10.1002/2014jc010644

Gates, A. R., and Jones, D. O. B. (2012). Recovery of benthic megafauna from anthropogenic disturbance at a hydrocarbon drilling well (380 m depth in the Norwegian Sea). *PLoS ONE* 7, e44114. doi:10.1371/journal.pone.0044114

Gillard, B., Purkiani, K., Chatzievangelou, D., Vink, A., Iversen, M. H., and Thomsen, L. (2019). Physical and hydrodynamic properties of deep sea mining-generated, abyssal sediment plumes in the Clarion Clipperton Fracture Zone (eastern-central Pacific). *Elem. Sci. Anthropocene* 7, 5. doi:10.1525/elementa.343

Gillard, B. (2019). "Towards deep sea mining-impact of mining activities on benthic pelagic coupling in the clarion clipperton fracture Zone," (Universität Bremen). PhD Thesis.

Global Sea Mineral Resources (2018). *Environmental Impact Statement Small-scale testing of nodule collector components on the seafloor of the Clarion-Clipperton Fracture Zone and its environmental impact*.

Gollner, S., Kaiser, S., Menzel, L., Jones, D. O. B., Brown, A., Mestre, N. C., et al. (2017). Resilience of benthic deep-sea fauna tomining activities. *Mar. Environ. Res.* 129, 76–101. doi:10.1016/j.marenvres.2017.04.010

Haalboom, S., Schoening, T., Urban, P., Gazis, I. Z., de Stigter, H., Gillard, B., et al. (2022). Monitoring of anthropogenic sediment plumes in the clarion-clipperton Zone, NE equatorial pacific ocean. *Front. Mar. Sci.* 9. doi:10.3389/fmars.2022.882155

Hage, S., Cartigny, M., Sumner, E. J., Clare, M. A., Hughes Clarke, J. E., Talling, P. J., et al. (2019). Direct monitoring reveals initiation of turbidity currents from extremely dilute river plumes. *Geophys. Res. Lett.* 46 (20), 11310–11320. doi:10.1029/2019GL084526

Harbour, P. R., Leitner, A. B., Ruehlemann, C., Annemiek, V., and Sweetman, A. K. (2020). Benthic and demersal scavenger biodiversity in the eastern end of the clarion-clipperton Zone – an area marked for polymetallic nodule mining. *Front. Mar. Sci.* 1–14. doi:10.3389/fmars.2020.00458

Harris, P. T. (2014). Shelf and deep-sea sedimentary environments and physical benthic disturbance regimes: A review and synthesis. *Mar. Geol.* 353, 169–184. doi:10.1016/j.margeo.2014.03.023

Hein, J. R., Koschinsky, A., and Kuhn, T. (2020). Deep-ocean polymetallic nodules as a resource for critical materials. *Nat. Rev. Earth Environ.* 1 (3), 158–169. doi:10.1038/s43017-020-0027-0

Helena, N., Adduce, C., Alves, E., and Franca, M. (2013). Analysis of lock exchange gravity currents over smooth and rough beds. *J. Hydraulic Res.* 51 (4), 417–431. doi:10.1080/00221686.2013.798363

Helmons, R., de Wit, L., de Stigter, H., and Spearman, J. (2022). Dispersion of benthic plumes in deep-sea mining: What lessons can Be learned from dredging? *Front. Earth Sci.* 10, 868701. doi:10.3389/feart.2022.868701

Hobbs, C. H., III (2002). An investigation of potential consequences of marine mining in shallow water: An example from the mid-atlantic coast of the United States. *J. Coast. Res.* 18, 94–101.

Huppert, H. (2006). Gravity currents: A personal perspective. *J. Fluid Mech.* 554, 299–322. doi:10.1017/S002211200600930X

Ibanez Sanz, M. (2018). "Flocculation and consolidation of cohesive sediments under the influence of coagulant and flocculant," (Delft University of Technology). PhD Thesis.

ISA (2015). *A geological model of polymetallic nodule deposits in the clarion-clipperton fracture Zone*.

ISA (2019). *Current status of the reserved areas with the international seabed authority*.

Jones, D. O. B., Kaiser, S., Sweetman, A. K., Smith, C. R., Menot, L., Vink, A., et al. (2017). Biological responses to disturbance from simulated deep-sea polymetallic nodule mining. *PLOS ONE* 12 (2), e0171750. doi:10.1371/journal.pone.0171750

Jones, D. O. B., Simon-Lledó, E., Amon, D. J., Bett, B. J., Caulle, C., Clément, L., et al. (2021). Environment, ecology, and potential effectiveness of an area protected from deep-sea mining (Clarion Clipperton Zone, abyssal Pacific). *Prog. Oceanogr.* 197, 102653. doi:10.1016/j.pocean.2021.102653

Lang, A., Dasselaar, S., Aasly, K., and Larsen, E. (2019). *Blue nodules deliverable report D3.4: Report describing the process flow overview*.

MacIver, M. R. (2019). Safas: Sedimentation and floc analysis software. Available at https://github.com/rmaciver/safas.

Manning, A., Friend, P., Prowse, N., and Amos, C. (2007). Estuarine mud flocculation properties determined using an annular mini-flume and the LabSFLOC system. *Cont. Shelf Res.* 27 (8), 1080–1095. doi:10.1016/j.csr.2006.04.011

Manning, A. J., and Dyer, K. R. (2002). A comparison of floc properties observed during neap and spring tidal. *Proc. Mar. Sci.*, 233–250.

Mewes, K., Mogollón, J. M., Picard, A., Rühlemann, C., Kuhn, T., Nöthen, K., et al. (2014). Impact of depositional and biogeochemical processes on small scale variations in nodule abundance in the Clarion-Clipperton Fracture Zone. *Deep Sea Res. Part I Oceanogr. Res. Pap.* 91, 125–141. doi:10.1016/j.dsr.2014.06.001

Mietta, F., Chassagne, C., Manning, A. J., and Winterwerp, J. C. (2009). In-fluence of shear rate, organic matter content, pH and salinity on mud flocculation. *Ocean. Dyn.* 59 (5), 751–763. doi:10.1007/s10236-009-0231-4

Mietta, F. (2010). "Evolution of the floc size distribution of cohesive sediments," (Delft University of Technology). PhD Thesis.

Ouillon, R., Kakoutas, C., Meiburg, E., and Peacock, T. (2021). Gravity currents from moving sources. *J. Fluid Mech.* 924, A43. doi:10.1017/jfm.2021.654

Puig, P., Canals, M., Company, J. B., Martı'n, J., Amblas, D., Lastras, G., et al. (2012). Ploughing the deep sea floor. *Nature* 489, 286–289. doi:10.1038/nature11410

Rutkowska, M., Dubalska, K., Bajger-Nowak, G., Konieczka, P., and Namieśnik, J. (2014). Organomercury compounds in environmental samples: Emission sources, toxicity, environmental fate, and determination. *Crit. Rev. Environ. Sci. Technol.* 44, 638–704. doi:10.1080/10643389.2012.728825

Safar, Z., Rijnsburger, S., Sanz, M. I., Chassagne, C., Manning, A., Pietrzak, J., et al. (2019). "Characterization and dynamics of suspended particulate matter in the near field of the rhine river plume during a neap tide," in *Geophysical research abstracts*, 21.

Shakeel, A., MacIver, M. R., van Kan, P. J. M., Kirichek, A., and Chassagne, C. (2021). A rheological and microstructural study of two-step yielding in mud samples from a port area. *Colloids Surfaces A Physicochem. Eng. Aspects* 624, 126827. doi:10.1016/j.colsurfa.2021.126827

Shakeel, A., Safar, Z., Ibanez, M., Paassen, L., and Chassagne, C. (2020). Flocculation of clay suspensions by anionic and cationic polyelectrolytes a systematic analysis. *Minerals* 10, 999–1024. doi:10.3390/min10110999

Sharma, R. (2015). Environmental issues of deep-sea mining. *Procedia Earth Planet. Sci.* 11, 204–211. doi:10.1016/j.proeps.2015.06.026

Smith, S. J., and Friedrichs, C. T. (2011). Size and settling velocities of cohesive flocs and suspended sediment aggregates in a trailing suction hopper dredge plume. *Cont. Shelf Res.* 31 (10), S50–S63. doi:10.1016/j.csr.2010.04.002

Spearman, J., Taylor, J., Crossouard, N., Cooper, A., Turnbull, M., Manning, A., et al. (2020). Measurement and modelling of deep sea sediment plumes and implications for deep sea mining. *Sci. Rep.* 10 (1), 5075–5114. doi:10.1038/s41598-020-61837-y

Spearman, J., Taylor, J., Crossouard, N., Cooper, A., Turnbull, M., Manning, A., et al. (2019). "The measurement and modelling of plumes resulting from deep sea mining of Fe-Mn Crusts," in Proceedings of the World dredging conference (WODCONXXII), Shanghai, China.

Vanreusel, A., Hilario, A., Ribeiro, P. A., and Menot, L. (2016). *Threatened by mining, polymetallic nodules are required to preserve abyssal epifauna*. Nature Publishing Group, 1–6.

Volz, J. B., Mogollon, J. M., Geibert, W., Arbizu, P. M., Koschinsky, A., and Kasten, S. (2018). Natural spatial variability of depositional conditions, biogeochemical processes and element fluxes in sediments of the eastern Clarion Clipperton Zone, Pacific Ocean. *Deep Sea Res. Part I Oceanogr. Res. Pap.* 140, 159–172. doi:10.1016/j.dsr.2018.08.006

Weaver, P. P. E., Aguzzi, J., Boschen-Rose, R. E., Colaço, A., de Stigter, H., Gollner, S., et al. (2022). Assessing plume impacts caused by polymetallic nodule mining vehicles. *Mar. Policy* 139, 105011. doi:10.1016/j.marpol.2022.105011

Ye, L., Manning, A. J., and Hsu, T. J. (2020). Corrigendum to ``Oil-mineral flocculation and settling velocity in saline water''. *Water Res.* 173, 116180. doi:10.1016/j.watres.2020.116180

Zawadzki, D., Maciag, L., Abramowski, T., and McCartney, K. (2020). Fractionation trends and variability of rare Earth elements and selected critical metals in pelagic sediment from abyssal basin of NE pacific (Clarion-Clipperton fracture Zone). *Minerals* 10, 320. doi:10.3390/min10040320

frontiers | Frontiers in Earth Science

TYPE Original Research
PUBLISHED 11 November 2022
DOI 10.3389/feart.2022.841483

OPEN ACCESS

EDITED BY
Andrew James Manning,
HR Wallingford, United Kingdom

REVIEWED BY
Kyungsik Choi,
Seoul National University, South Korea
Tomas Fernández-Montblanc,
University of Cádiz, Spain

*CORRESPONDENCE
Zhenchang Zhu,
zhenchang.zhu@gdut.edu.cn

SPECIALTY SECTION
This article was submitted to Marine Geoscience,
a section of the journal
Frontiers in Earth Science

RECEIVED 22 December 2021
ACCEPTED 31 October 2022
PUBLISHED 11 November 2022

CITATION
Zhu Q, Nie W, Zhu Z, Cai Y and Yang Z (2022), Sensitivity of sheltered mudflats to wind events.
Front. Earth Sci. 10:841483.
doi: 10.3389/feart.2022.841483

Sensitivity of sheltered mudflats to wind events

Qin Zhu[1], Wei Nie[2], Zhenchang Zhu[1,2]*, Yanpeng Cai[1,2] and Zhifeng Yang[1,2]

[1]Southern Marine Science and Engineering Guangdong Laboratory (Guangzhou), Guangzhou, China, [2]Guangdong Provincial Key Laboratory of Water Quality Improvement and Ecological Restoration for Watersheds, Institute of Environmental and Ecological Engineering, Guangdong University of Technology, Guangzhou, China

The impact of waves on the morphological changes of sheltered mudflats is less well studied compared to that on open flats. To investigate the sensitivity of low-energy sheltered mudflats to hydrodynamics such as waves, we carried out *in situ* measurements of bed level, currents, and waves on the middle flat of a sheltered mudflat in a bay in southern China. Two 1-month measurements, March 26–26 April 2021, and July 8–8 August 2021, were performed for repetition. We found that the sheltered system was not as stable as it appeared. The maximum intratidal bed-level variation, ΔZ, was <5 mm in calm conditions. However, wind speeds slightly highly than 3.0 m/s, under which significant wave height was approximately 0.1 m, triggered significant bed-level variation patterns, with ΔZ reaching up to 2 cm. Intratidal bed-level change patterns depend on the relative dominance of waves and currents: low τ_c (current-induced bed shear stress) and high τ_w (wave-induced bed shear stress) promote the generation and migration of bed ripples; comparable τ_c and τ_w, with medium-to-high values, lead to non-cyclic bed-level change patterns; high τ_c and high τ_w result in bed accumulation/degradation superimposed by bed ripple migration. From a long-term perspective, i.e. in the time scale of month to year, sheltered mudflats are stable systems, and their high sensitivity causes short-term significant bed-level variation. The sensitivity and stability of sheltered mudflats must be further investigated to explore the effects of human intervention and global climate change.

KEYWORDS

sheltered mudflat, bed level change, bed sensitivity, wind event, intratidal highresolution measurements

Introduction

The morphodynamics of tidal mudflats have been extensively studied in recent decades as they serve vital ecological and environmental functions in addition to protecting shorelines (Costanza et al., 1997; Friedrichs, 2011; Goodwin et al., 2016). Among various tidal flats, tidal flats in sheltered settings, such as lagoons, back-barrier flats, flats in bays, and fringing flats in estuaries, are important as they form relatively stable environments that maintain biodiversity and healthy marine ecosystems (Chakraborty, 2001; Callaghan et al., 2010; Waska and Kim, 2010; Paavo et al., 2012;

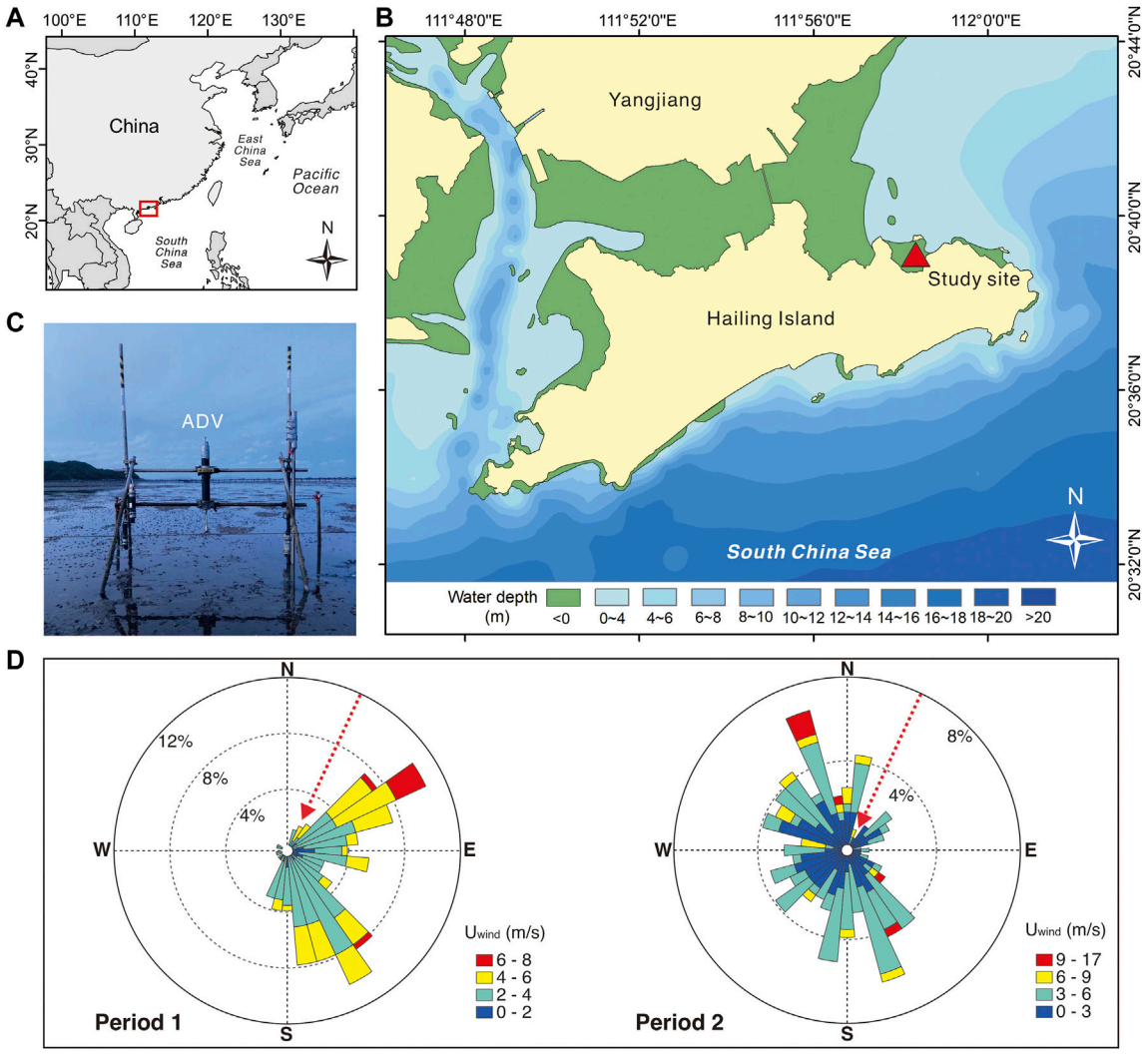

FIGURE 1
(A) Location of the study site near the west Pacific Ocean. **(B)** Map of Hailing Island with the observation site and wind gauge. **(C)** Photograph of the deployed instrument. **(D)** Wind roses of Period 1 (March 26–26 April 2021) and Period 2 (July 8–8 August 2021). The red arrow indicates the orientation of the bay.

Reckhardt et al., 2015). These sheltered flats are generally mud dominated owing to the low-energy setting (Madsen et al., 2010; McLachlan et al., 2020).

Compared to sheltered mudflats, the morphodynamics of open flats, which are exposed to stronger hydrodynamics, have received more attention as they are believed to be more strongly impacted by tropical cyclones and hurricanes (Li et al., 2000; Yang et al., 2005; Fan et al., 2006; MacMahan et al., 2010; Zhu et al., 2016). Although sheltered mudflats are protected from the more energetic ocean waves, they are still influenced by diffracted waves and local wind waves (Klein and de Menezes, 2001; Ryu, 2003; Shen et al., 2018; Siegle et al., 2018). Bed shear stress, which is a critical parameter in sediment dynamics on tidal flats, results from the nonlinear interaction between currents and waves (Grant and Madsen, 1979; van Rijn, 1993). The role of waves has been frequently discussed in the situation of open flats, while has been underestimated for sheltered flats. Natural hydrodynamic condition, together with human activities, can alter the depositional environment at different temporal and spatial scales (Blum and Roberts, 2009; Yang et al., 2011; Wang et al., 2015). The study of hydrodynamics and bed stability of sheltered mudflats is also essential to local ecosystems and environments, as sheltered habitats with high productivity are more sensitive to contaminants (Nansingh and Jurawan, 1999; Reckhardt et al., 2015). Therefore, it is important to develop an understanding of how sheltered mudflats react to dynamic processes, especially waves, in the context of increasing threats from anthropogenic disturbances and global climate change

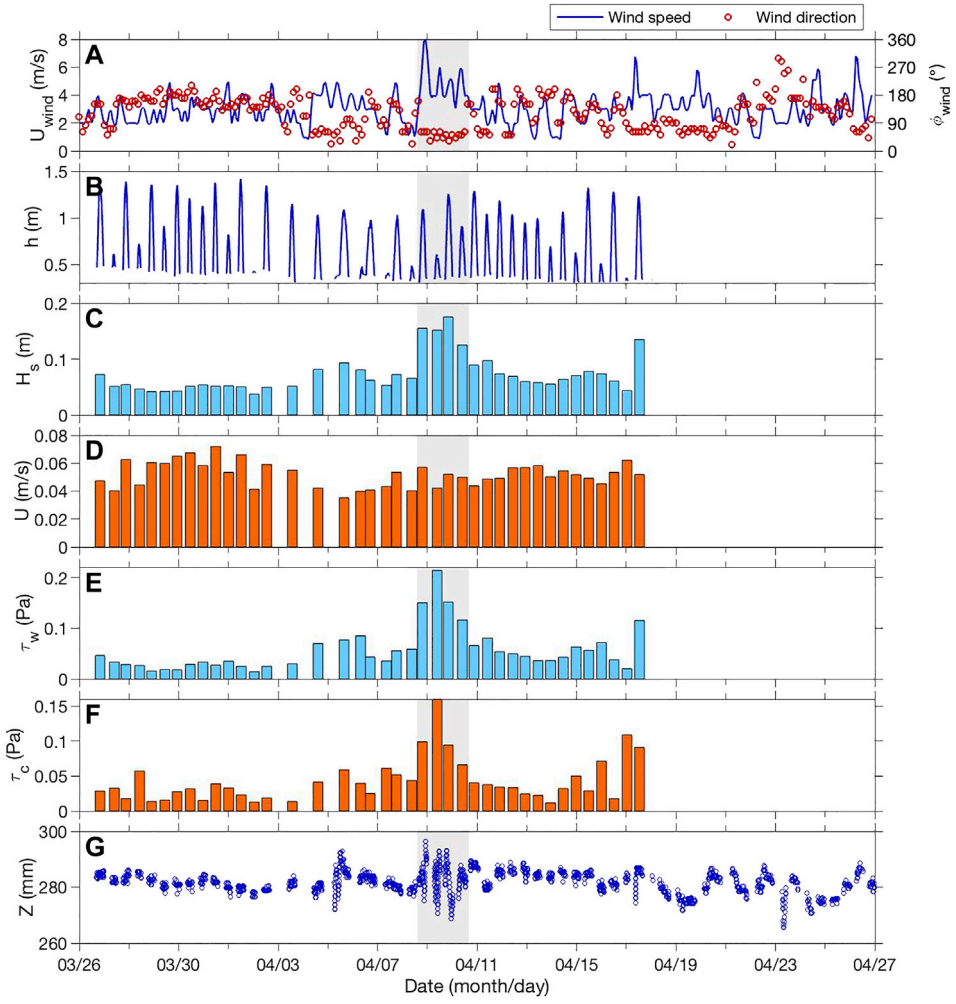

FIGURE 2
Time series of **(A)** wind speed (U_{wind}), **(B)** water depth (h), **(C)** significant wave height (H_s), **(D)** horizontal current velocity (U), **(E)** wave-induced bed shear stress (τ_w), **(F)** current-induced bed shear stress (τ_c), and **(G)** relative bed level (Z) change during Period 1.

(Nicholls et al., 1999; Walling, 2006; Vafeidis et al., 2008; Milliman and Farnsworth, 2011; Temmerman et al., 2013; Schuerch et al., 2018; Liu et al., 2020).

Intratidal measurements elucidate the details of bed-level changes that, in combination with wave and current action data, are key to understanding the mechanisms of bed erosion and deposition (Andersen et al., 2006; Zhu et al., 2014). In particular, for a low-energy dynamic system with slight bed-level changes, bed-level data from daily to monthly morphological surveys (Bassoullet et al., 2000; Fan et al., 2006) may not suffice. Measurements of intratidal bed-level changes have been restricted until the recent development of acoustic ranging measurements, such as ALTUS, altimeter, and extra ADV beams (Gallagher et al., 1996; Jestin et al., 1998; Thornton et al., 1998; Christie et al., 1999; Saulter et al., 2003; Andersen et al., 2007; Turner et al., 2008; Zhu et al., 2017). To date, acoustic ranging measurement is the only approach for obtaining bed-level data during submergence in high temporal (interval in minutes) and spatial (accuracy of ± 1–2 mm) resolution.

In this study, we deployed an acoustic Doppler velocimeter (ADV) to obtain data on bed-level changes, as well as currents and wave parameters, on a sheltered mudflat. Our objective was to investigate whether sheltered mudflats are as stable as they appear by: 1) elucidating the response of bed-level changes in sheltered mudflats to variables of environmental forces, such as wind, waves, and currents; and 2) examine the morphological sensitivity of sheltered mudflat beds to hydrodynamics, especially waves. This work is intended to deepen our understanding of the bed stability of sheltered mudflats under different pressure scenarios.

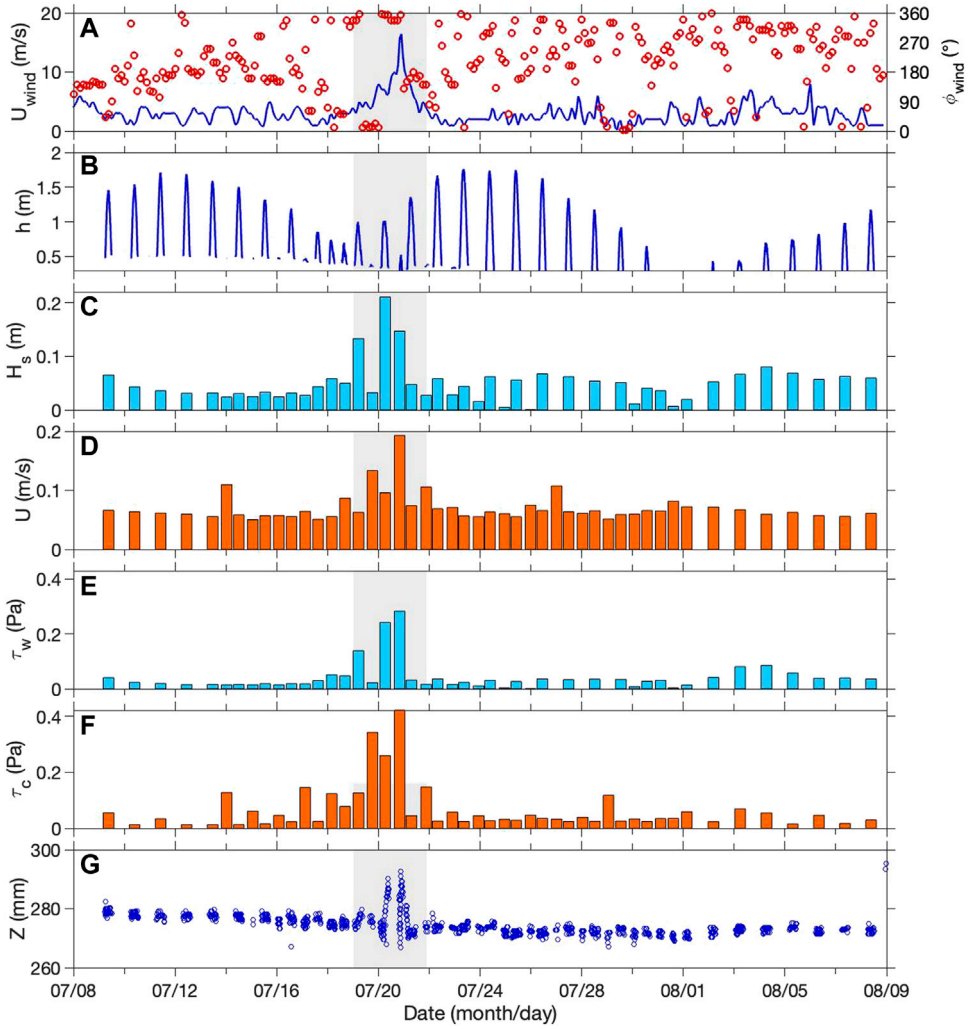

FIGURE 3
Time series of **(A)** wind speed (U_{wind}), **(B)** water depth (h), **(C)** significant wave height (H_s), **(D)** horizontal current velocity (U), **(E)** wave-induced bed shear stress (τ_w), **(F)** current-induced bed shear stress (τ_c), and **(G)** relative bed level (Z) change during Period 2.

Material and methods

Study site

In situ observations were conducted on a sheltered mudflat of Hailing Island, which is located on the west bank of the Pearl River Estuary, China (Figure 1A). According to records from the tide gauge on the west side of the island, the local tides are mixed semi-diurnal with an average of 2.5 m in tidal range. The spring and neap tidal ranges are >3.0 m and 0.5 m, respectively. Monsoon-driven winds are predominantly north-easterly in autumn and winter, south-easterly in spring, and southerly in summer. The multi-year average wind speed is 4.2 m/s. The province, where the study area is located, is hit by 3.6 tropical cyclones per year on average, which is the highest in China. Waves in this area are dominated by wind waves with a frequency of approximately 85%, and the average wave height is 0.2 m with the maximum storm surge reaching over 2 m.

The study site (111°58′42″E, 21°39′2″N) is located on the middle flat (at the mean water level) of the mangrove wetland on the northeast side of Hailing Island (Figure 1B). The south side of the island is open sea, while the north side is connected with an intertidal area. The tidal flat has a long-shore length of 2.4 km and a cross-shore length of 1.6 km. The mudflat faces to north-east-north (25°), with a mean slope of 2.5‰ (Hu et al., 2020). The upper flat is covered by dense mangrove forest, with a height of 2–3 m. As the study area is located in a bay on the back side of the open sea and a barrier island exists at the seaside of the bay, the

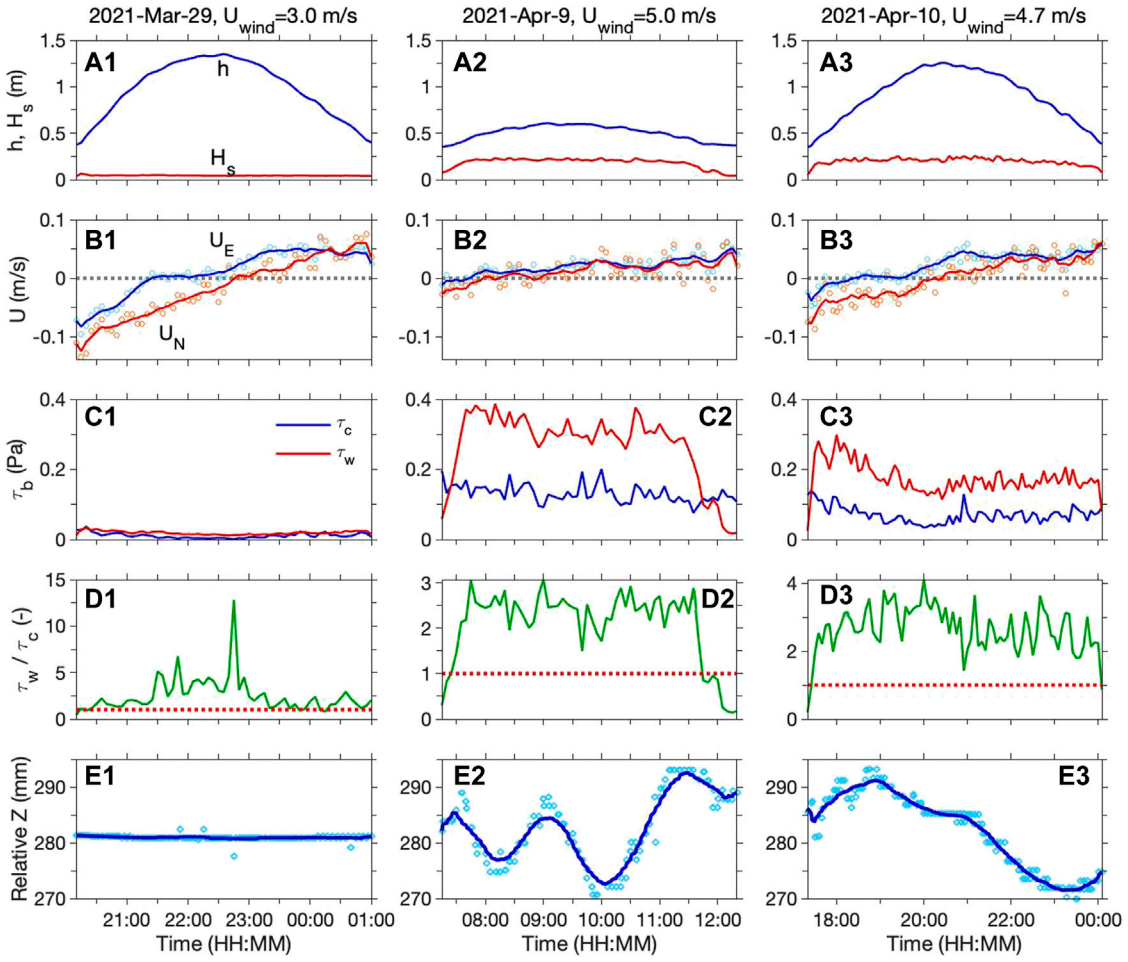

FIGURE 4
Time series of **(A)** water level (h), significant wave height (H_s), **(B)** eastward (U_E) and northward (U_N) current velocities, **(C)** current- and wave-induced bed shear stress (τ_c and τ_w), **(D)** ratio of τ_w and τ_c, and **(E)** relative bed level (Z) changes during Period 1.

study area is relatively sheltered. Therefore, the mangrove wetland provides an ideal habitat for benthos and birds, thereby sustaining high biodiversity in the region (Zhu et al., 2008; Hu et al., 2020).

Instrumentation setup

An ADV (6.0 MHz vector current meter, Nortek AS, Norway) attached to an H-shaped sedimentary measurement frame was used to measure the three-dimensional flow velocities at a high sampling rate (Figure 1C) from March 26 to 26 April 2021 (Period 1), and from July 8 to 8 August 2021 (Period 2). The ADV recorded velocities and pressure with a burst interval of 5 min for a period of 300 s at a frequency of 16 Hz. The water pressure, measured by a silicone piezoresistive pressure sensor (Nortek, 2005), was used to analyze wave characteristics (Zhu et al., 2016). Based on the records of the distance between the transmitter of the ADV and the bed sediment surface from the extra acoustic beams of each burst, relative bed levels at high temporal resolution were also measured using ultrasonic echo-ranging with an accuracy of 1 mm (Andersen et al., 2007; Zhu et al., 2017). The accuracy is determined by the sound speed, which is affected by water temperature and salinity, as well as the boundary condition. The acoustic sensor and the pressure sensor were 0.3 m and 0.54 m above the sediment surface, respectively.

Measured wind data of the nearest site (111°58′12″E, 21°52′12″N) was downloaded from Institute for the Environment, the Hong Kong University of Science and Technology (http://envf.ust.hk). The interval of wind speed and wind direction is 3 h.

TABLE 1 Statistics of key hydrodynamic parameters.

		Period 1			Period 2		
		All	Calm	Windy	All	Calm	Windy
Significant wave height, H_s (m)	Mean	0.08	0.06	0.16	0.06	0.04	0.10
	Min	0.03	0.03	0.04	0	0	0.0006
	Max	0.27	0.16	0.27	0.36	0.16	0.36
	Std	0.05	0.02	0.06	0.05	0.03	0.09
Flow velocity, U (m/s)	Mean	0.05	0.05	0.05	0.07	0.06	0.08
	Min	0.0003	0.01	0.39	0.002	0.002	0.002
	Max	0.39	0.34	0	0.45	0.45	0.45
	Std	0.03	0.03	0.03	0.06	0.05	0.07
Wave-induced bed shear stress, τ_w (Pa)	Mean	0.06	0.05	0.16	0.05	0.03	0.11
	Min	0.01	0.01	0.02	0	0	0.0004
	Max	0.39	0.18	0.39	0.86	0.14	0.86
	Std	0.06	0.03	0.09	0.08	0.04	0.15
Current-induced bed shear stress, τ_c (Pa)	Mean	0.03	0.03	0.08	0.05	0.03	0.12
	Min	0.0002	0.0003	0.0002	0.0001	0.0001	0.0008
	Max	0.27	0.27	0.25	0.94	0.94	0.92
	Std	0.04	0.03	0.05	0.11	0.07	0.17
Maximum intratidal bed-level variation, $(\Delta Z)_{TCmax}$ (mm)	Mean	6.4	4.7	18.5	4.6	3.6	9.4
	Max	24.5	17.3	24.5	25.8	12.1	25.8
	Min	1.6	1.6	11.8	1.6	1.6	2.1
	Std	5.1	3.1	5.9	4.6	1.8	9.5

Data processes and calculation

Data filtration was conducted prior to further analyses. The burst datasets with backscatter acoustic amplitude less than 100 counts and correlation less than 50% were removed.

The wave-induced bed shear stress, τ_w, was obtained by analyzing the surface-elevation monitoring data. Significant wave height, H_s, and significant wave period, T_s, were derived from high-frequency pressure data *via* linear wave theory (Tucker and Pitt, 2001) (see http://neumeier.perso.ch/matlab/waves for the routines). The near-bed peak orbital excursion ($\hat{A}_\delta$) and peak orbital velocity ($\hat{U}_\delta$) can be expressed as (van Rijn, 1993):

$$\hat{A}_\delta = \frac{H}{2\sinh(kh)} \tag{1}$$

$$\hat{U}_\delta = \omega\hat{A}_\delta = \frac{\pi H}{T\sinh(kh)} \tag{2}$$

where H is the wave height (m), k=(2 π/L) is the wave number (m^{-1}), with wave length L=(g T^2/2 π)tanh (kh). Where h is the water depth (m), ω is the angular velocity (s^{-1}), and T is the wave period (s). In practice, the significant wave height H_S and significant wave period T_S are used for H and T in the formulae. The time-averaged (over half a wave cycle) bed shear stress caused by waves, τw (Pa), can be expressed as (van Rijn, 1993)

$$\tau_w = \frac{1}{4}\rho_w f_w \hat{U}_\delta^2 \tag{3}$$

where ρ_w is the water density (kg/m^3), and fw is the friction coefficient (-), which is determined by the hydraulic regime (van Rijn, 1993):

$$f_w = \begin{cases} 2Re_w^{-0.5} & , \quad Re_w \le 10^5\,(laminar) \\ 0.0521Re_w^{-0.187} & , \quad Re_w > 10^5\,(smooth\,turbulent) \\ 0.237r^{-0.52} & , \quad (rough\,turbulent) \end{cases} \tag{4}$$

where $Re_w = \frac{\hat{U}_\delta \hat{A}_\delta}{V}$ and $r = \frac{\hat{A}_\delta}{K_S}$ are the wave Reynolds number (-) and relative roughness (-), respectively. Parameter ks is the Nikuradse roughness value given as $k_s = 2.5d_{50}$, where d50 is the median grain size of the bed sediment, and ν is the kinematic viscosity of sea water (m^2/s).

Wave-orbital-motion-induced velocities were removed from the total burst velocities by the moving-average method with a 1-s smooth window (Williams et al., 2003). Subsequently, the turbulent kinetic energy method with vertical fluctuations (TKEw) was used to calculate the bottom bed shear stress τ_c (Pa). The formula is as follows (Kim et al., 2000; Zhu et al., 2016):

$$\tau_c = C\rho_w\overline{w_t^2} \tag{5}$$

In which ρ_w is seawater density, constant coefficient C=0.9, and $\overline{w_t^2}$ is the change rate of near-bed vertical turbulent velocity.

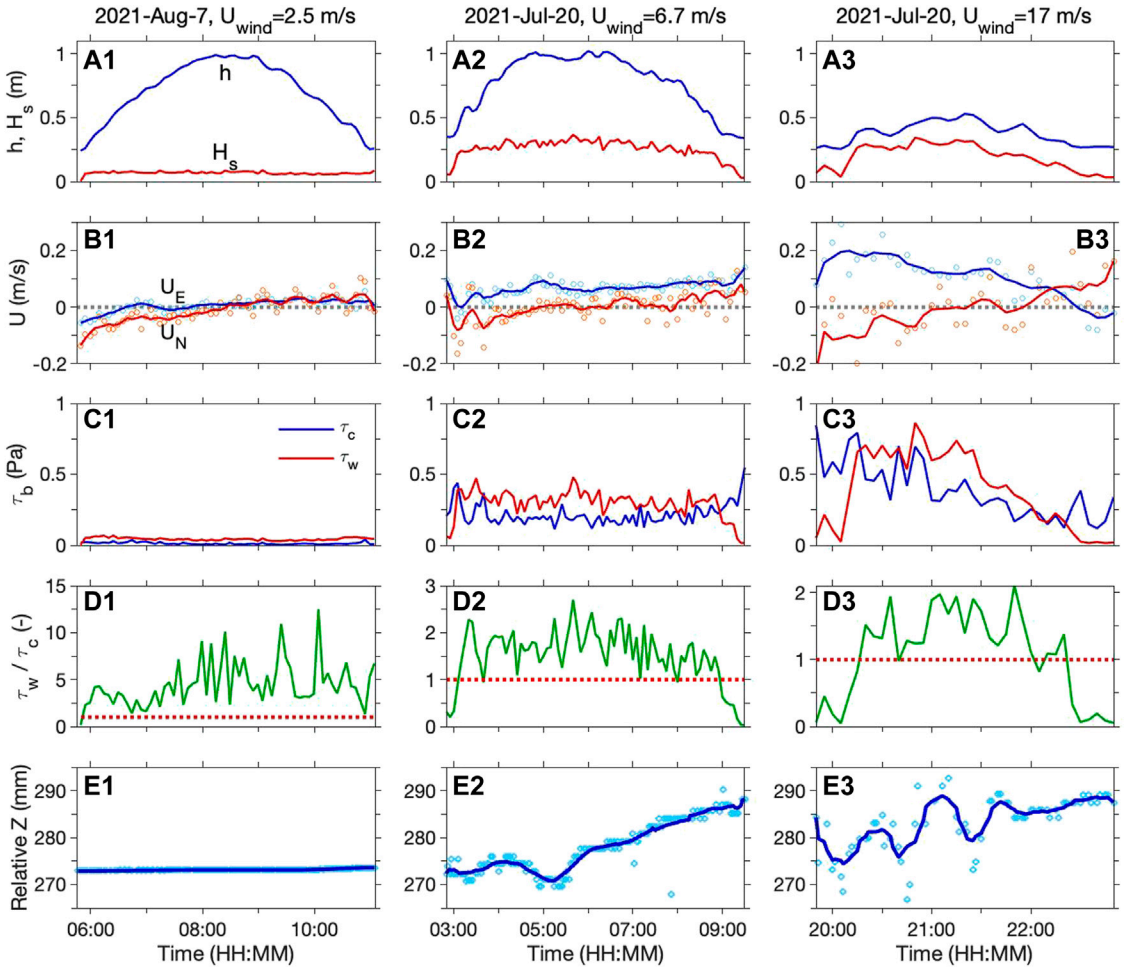

FIGURE 5
Time series of **(A)** water level (h), significant wave height (H_s), **(B)** eastward (U_E) and northward (U_N) current velocities, **(C)** current- and wave-induced bed shear stress (τ_c and τ_w), **(D)** ratio of τ_w and τ_c, and **(E)** relative bed level (Z) changes during Period 2.

Results

Tides, wind and waves

Each measurement period lasted for 1 month or 62 tidal cycles. However, because the ADV on the middle flat was equipped with probes at 0.3 or 0.5 m above the seabed, low tides were not measured. During some periods after April 18, the velocity and wave data were missed due to battery failure (Figure 2). Overall, data from 40 tidal cycles were obtained in Period 1, and data from 45 tidal cycles were obtained in Period 2.

The average wind speed during both periods was 3.0 m/s. We defined the tidal cycle during a wind event as one where the intratidal maximum wind speed exceeded 6.0 m/s. An obvious wind event occurred during each period: around April 9 during Period 1 (Figure 2A) and around July 20 during Period 2 (Figure 3A). The maximum wind speeds and predominant directions were 8.0 m/s and north-east-north in Period 1, and 17.0 m/s and north and east in Period 2, respectively (Table 1).

Measured maximum water depth, h, varied from 0.5 m to 1.7 m during Period 1 (Figure 2A), and from 0.5 m to 2.0 m during Period 2 (Figure 3B). Tides in Period 1 were irregular, i.e., the neap-spring tidal cycle was not 15 days. Significant wave height, H_s, was ordered by centimeters with mean values of 0.08 m and 0.06 m in each measurement period. The mean H_s during wind events was 2.6 times the value during calm conditions (Table 1). Correspondingly, the wave-induced bed shear stress, τ_w, was approximately three times larger during wind events than during calm conditions (Table 1).

The current velocity, U, showed the tide-driven spring-neap cyclicity. However, during the wind event in Period 2, U was

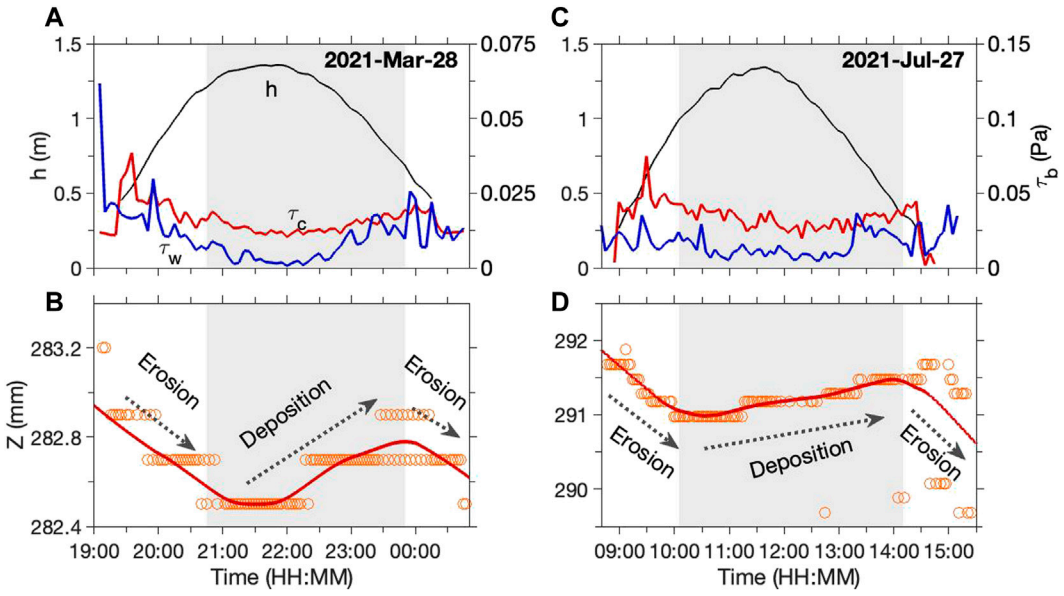

FIGURE 6
Time series of water depth (h), wave-induced bed shear stress (τ_w), current-induced bed shear stress (τ_c), relative bed level (Z, orange circle) and smoothed bed level (red line) of the calm tidal cycles. Bed erosion occurs in flood and ebb peaks, while deposition during slack water.

greater than normal values (Figure 5E). Thus, the current-induced bed shear stress, τ_c, was four times larger during wind events than during calm conditions.

Bed level changes

The bed level, Z, was relative stable without obvious spring-neap tidal cyclicity (Figure 3G and Figure 5G). The bed level statistics showed that the standard deviation was 3.0 mm. This indicates that the inter-tidal bed level change was generally at the millimeter level. During wind events, the bed level variation reached 26–27 mm.

During a typical calm tidal cycle, the bed level remained nearly constant (Figure 4D1 and Figure 5D1). Several tidal cycles show erosion-deposition-erosion cyclicity corresponding to the peak-slack-peak process (Figure 6). In contrast, the intratidal bed levels during wind events showed different patterns. During the wind events of Period 1, there were three patterns of bed-level changes:

(1) Type I: cyclicity motion (Figure 4D2 and Figure 5D3): the April 9 tidal cycle showed clear cyclicity in a period of approximately 2 h. The impact of waves (τ_w) was stronger than that of currents (τ_c) in this case.
(2) Type II: intratidal variation without clear cyclicity motion (Figure 4E3 and Figure 5E2). When both current and wave were strong, the time series of the bed-level change was more complex. There was no standard variation pattern as the bed dynamics are controlled by both hydrodynamics and sediment supply.

The maximum variation in the bed level during each tidal cycle, ΔZ, was used to quantify the intratidal bed-level dynamics. ΔZ was less than 10 mm for 90% of the measurement period and during relatively calm conditions (wind speed <6.0 m/s) (Figure 7A). As the wind speed increased, ΔZ increased correspondingly. The linear regression analysis showed that ΔZ has a stronger relationship with bottom orbital velocity (U_δ) and τ_w than current velocity (U) and τ_c (Figure 6). This indicates that bed-level changes are more sensitive to waves.

Discussion

Difference between sheltered and open mudflats

Mudflat bed is composed of fine sediments, which are sensitive to hydrodynamic disturbances. Sheltered mudflats are less dynamic than open mudflats (Hu et al., 2017). For instance, monthly variations in the bed levels of open mudflats in the meso-to macro-tidal range reached 10–30 cm (Miao et al., 2016; Zhu et al., 2017). Even the bed variation can be measured in centimeters under normal weather conditions (Zhu

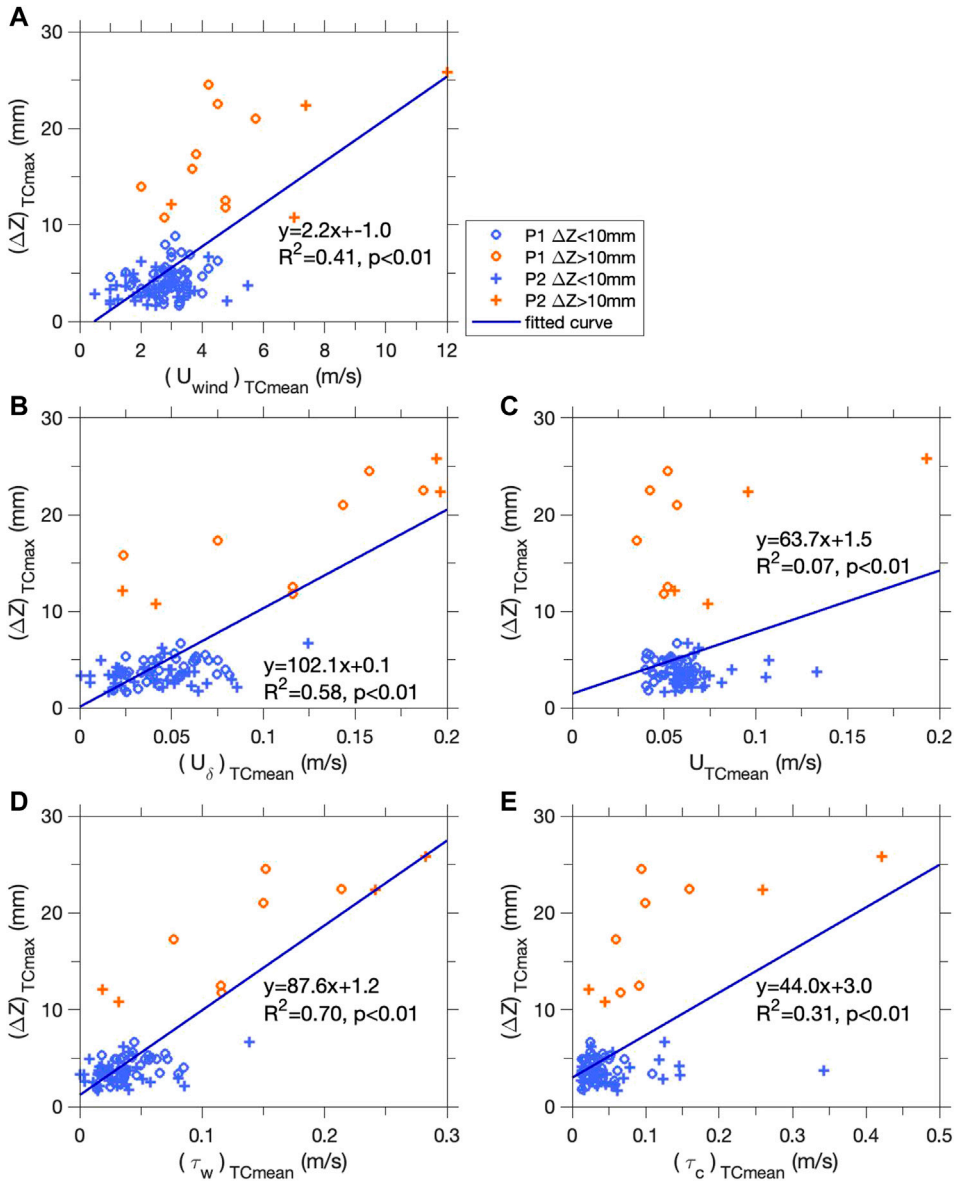

FIGURE 7
Relationship between the maximum intratidal bed-level variation, ΔZ, and **(A)** mean wind speed during each tidal cycle $(U_{wind})_{TCmean}$, **(B)** tidal-averaged bottom orbital velocity, $(U_{\delta})_{TCmean}$, **(C)** tidal-averaged current velocity, U_{TCmean}, **(D)** tidal-averaged wave-induced bed shear stress, $(\tau_w)_{TCmean}$, and **(E)** tidal-averaged current-induced bed shear stress $(\tau_c)_{TCmean}$.

et al., 2014). In brief, if a mudflat is open and exposed to strong hydrodynamic forcing, daily and monthly bed variations are in the order of centimeters and tens of centimeters, respectively. In contrast, sheltered mudflats were quite stable. Our study shows that the monthly bed variation was only approximately 1 cm. These sheltered mudflats can sometimes be stable over a longer time scale. Studies of sheltered mudflats in the Western Scheldt Estuary, the Netherlands, showed that the bathymetry profile was stable, with the variation of bed level less than 10 cm over a period of 25 years (de Vet et al., 2017; Maan et al., 2018). A stable bed environment is a potentially advantageous for maintaining the biodiversity and biomass of wetland plants and benthic animals on sheltered mudflats (Herman et al., 2001; Chargulaf and Tibbetts, 2015).

Bed-level changes between tidal submergence, which are measured by the double/triple-rod method, buried-plate measurements or optical detections, are useful for understanding the daily evolution of mudflats (Yang et al., 2003; Hu et al., 2015; Zhu et al., 2017). However, acoustic ranging detection shows that the maximum intratidal bed

level variation is much greater than the net intertidal bed level changes. This phenomenon is notable in open mudflat systems (Zhu et al., 2014; Zhu et al., 2017). The tidal cycle on the morning of April 9 demonstrates the same phenomenon on sheltered flat. The intratidal maximum variation was 20 mm, whereas the net intertidal bed-level change was 9 mm (Figure 7E2). To date, the acoustic measurement of bed surface dynamics at high temporal resolution is the only approach for determining intratidal bed level changes (Thorne et al., 2018; Zhu et al., 2019). By applying advanced acoustic bed detection, our study further indicates that the sheltered mudflat is more variable as we expected.

Intratidal bed level changes of sheltered mudflat

The typical intratidal bed-level changes in normal weather are shown in Figure 6E1 and Figure 7E1. There may be a slight trend, and the bed level was nearly constant in general. This agrees with the measurements from other sheltered mudflats (Zhu et al., 2019). Some tidal cycle still shows the cyclicity of erosion during flood and peak and deposition during slack water (Figure 6). Notably, the minimum ΔZ was larger than 1 mm, which is the accuracy of bed level detection. So far, the accuracy of acoustic bed detection is ± 1–2 mm, depending on individual instrument (Gallagher et al., 1996; Thornton et al., 1998; Christie et al., 1999; Andersen et al., 2006; Turner et al., 2008). In calm weather, both wave-and current-induced bed shear stresses were less than 0.1 Pa (Figure 6C1 and Figure 7C1), which is the typical value of critical bed shear stress for mud erosion (Winterwerp et al., 2012). No erosion and little deposition lead to a stable bed level with a slight accumulation of sediment. In our study, 73.7% of the measured ΔZ was <5 mm, indicating the stability of the sheltered mudflat. When the tidal-averaged wind speed was >3.0 m/s, more drastic intratidal bed-level changes were observed. The mechanism of local bed-level change differed from that of hydrodynamic conditions.

The observed fluctuation in the bed level was partially caused by measurement errors and accuracy issues, as mentioned above. By incorporating a moving average and despike, such noise signals can be minimized. The smoothed bed-level series exhibited a periodic signal (Figure 4D2). We defined this as the Type I bed-level variation pattern, which was closely related to the formation and migration of bed ripples. The magnitude and period of the bed-level fluctuation, referring to ripple height and ripple migration periods, were 1–2 cm and 1–2 h, respectively. This matches the typical ripple migration parameters of mudflats (Baas et al., 2013; Lin and Venditti, 2013; Zhu, 2017). Under dynamic environments with changing currents and waves, reworking and mobilization of bed sediments leads to formation of bed ripples in coastal systems (Catano-Lopera and Garcia, 2006; Thorne et al., 2018; Guerrero and Guillen, 2020; Guerrero et al., 2021; Stella, 2021). Bed ripples preferably occur in the presence of waves (Chakraborty, 2001; Lorenz and Valdez, 2011; Guerrero and Guillen, 2020; Jin et al., 2020). For the tidal cycle on the morning of April 9, τ_c was as low as 0.1 Pa due to low tide, meaning that flow could hardly stir up surface bed sediment, whereas τ_w was 2.5 times higher (Figure 4D2). Such wave-dominated conditions further prove that the Type I bed-level variation is caused by ripple migration.

Type II intratidal bed-level variations show an unclear fluctuation pattern. A typical example is the tidal cycle observed on July 20 morning (Figure 5E2). Both τ_c and τ_w were greater than 0.1 Pa, and they are comparable. This means that both the current and waves played a role in bed sediment movement. Under normal weather conditions, the intratidal bed level shows a pattern of degradation during tidal flood and ebb peaks, and accretion during high slack water on open flats (Andersen et al., 2007; Zhu et al., 2014). However, a continuous accretion trend was observed in the tidal cycle of July 20. During wind events, wind-induced flow (Figure 3D) and wind-induced turbulence result in that τ_c does not increase with tides (Figures 3, 4F) (Banerjee et al., 2015; Su et al., 2015). Meanwhile, the advection of sediment flow was strong during wind events. These two factors may break the peak-slack water cyclicity, but accretion or degradation trends are determined by the timing of wind event with regard to tidal cycle, sediment supply, residual flow, and settling time (Ding et al., 2003; Freeman et al., 2015; Xu et al., 2015; Zhu et al., 2017). The bed-level change pattern of the middle tidal flat was the most dynamic and difficult to predict (Fan et al., 2006). Additionally, there was no clear ripple migration signal in the bed-level series, as sheet flow during wind events tends to wash out ripples (Li and Amos, 1999; Thorne et al., 2018; Guerrero et al., 2021).

However, the low tide tidal cycle on July 20 (Figure 5D3) showed a different bed level pattern than that of April 9 (Figure 4D2). This cycle marked the transition between Type I and Type II variation, that is, the intratidal bed level change consisted of a cyclic motion and continuous accretion trend. The tidal conditions of the two tidal cycles were similar, but the current flow was quite different. Wind direction was offshore during Period 1 and almost onshore during Period 2 (Figure 2A and Figure 3A). Correspondingly, tidal flow was less influenced by winds during Period 1 (Figure 4B2), or by the northern component of the flow velocity (Figure 5B3). However, the eastern component was considerably influenced (Figure 5B3). There was an eastward flow during the majority of the tidal cycle, which was likely driven by wind induced flow pattern. Both τ_c and τ_w were much higher than those of other tidal cycles, reaching up to 0.7 Pa.

In summary, wave and tide conditions determine the intratidal bed level changes: 1) low τ_c and low τ_w lead to a stable bed; 2) low τ_c and high τ_w promote the generation and migration of bed ripples (Type I); 3) comparable τ_c and τ_w, with medium-to-high values lead to non-cyclicity bed-level change

patterns (Type II); and 4) high τ_c and high τ_w result in a combination of Type I and Type II variations.

Sensitivity of sheltered mudflat and its implications

Sheltered mudflats is considered stable, with the bed-level-change is in the order of millimeters in the time scale of tidal-cycle to even month, and is less affected by winds (Andersen et al., 2006; Hu et al., 2017). However, sheltered mudflats may be more dynamic than previously believed. Our study shows that the critical wind speed triggering distinct changes in the local sediment bed is approximately 3.0 m/s, a light-to-gentle breeze according to the Beaufort wind scale. If the wind is onshore, the bed-level-change can immediately respond to the wind. Otherwise, the bed need about one tidal cycle, i.e., half a day, to respond to wind. Therefore, more significant morphological changes would be expected during gale or storm events, wherein wind speed exceeds 15 m/s.

Although the sheltered mudflat is easily disturbed, it also recovers rapidly. The monthly bed-level measurements showed that the bed level fluctuated at a nearly constant level (Figures 2, 3G). These sheltered mudflats are stable and can recover quickly even after disturbance (Maan et al., 2018). For tidal flats, rapid recovery of disturbed sediment beds is enabled by the redistribution of sediments from high-energy to low-energy areas (Yang et al., 2003; Friedrichs, 2011). For low dynamic tidal flats, such as a sheltered flat, the distance of sediment movement may be smaller than in open tidal flats, and are likely to be transported back to maintain an equilibrium state after wind events (Zhu et al., 2017). The sediment transport patterns of sheltered mudflat systems must be further studied on a horizontal spatial scale.

Conclusion

In situ bed-level and hydrodynamic measurements on a sheltered mudflat were conducted in 1 month during each of the two seasons. The bed level was stable during calm weather during which wave and current forcing (τ_w and τ_c) are low. However, the sheltered mudflat was more variable than previously thought. The threshold wind speed to promote obvious intratidal bed-level variation patterns is 3.0 m/s, which generates wave heights of approximately 0.1 m. The intratidal bed-level variation patterns depend on hydrodynamic conditions: low τ_c and high τ_w promote the generation and migration of bed ripples (Type I); comparable τ_c and τ_w, with medium-to-high values, lead to non-cyclicity bed-level change patterns (Type II); and high τ_c and high τ_w result in bed accumulation/degradation superimposed by bed ripple migration, which is a combination of Type I and Type II variations. From a long-term perspective, i.e. in the time scale of month to year, sheltered mudflats are stable systems, and their high sensitivity causes short-term drastic bed-level variation, which may be harmful to benthos. The sensitivity and stability of sheltered mudflats must be further investigated under global climate change conditions.

Data availability statement

The raw data supporting the conclusions of this article will be made available by the authors, without undue reservation.

Author contributions

QZ, WN and ZZ conducted the field experiments. QZ, WN conceived the idea, carried out data analysis and draft the manuscript, YC and ZY reviewed and edited the manuscript.

Funding

This study was supported by Southern Marine Science and Engineering Guangdong Laboratory (Guanghzou) (GML202209), the Program for Guangdong Introducing Innovative and Entrepreneurial Teams (2019ZT08L213), and National Natural Science Foundation of China (51909038; 41901126).

Conflict of interest

The authors declare that the research was conducted in the absence of any commercial or financial relationships that could be construed as a potential conflict of interest.

Publisher's note

References

Andersen, T. J., Fredsoe, J., and Pejrup, M. (2007). *In situ* estimation of erosion and deposition thresholds by Acoustic Doppler Velocimeter (ADV). *Estuar. Coast. Shelf Sci.* 75, 327–336. doi:10.1016/j.ecss.2007.04.039

Andersen, T. J., Pejrup, M., and Nielsen, A. A. (2006). Long-term and high-resolution measurements of bed level changes in a temperate, microtidal coastal lagoon. *Mar. Geol.* 226, 115–125. doi:10.1016/j.margeo.2005.09.016

Baas, J. H., Davies, A. G., and Malarkey, J. (2013). Bedform development in mixed sand-mud: The contrasting role of cohesive forces in flow and bed. *Geomorphology* 182, 19–32. doi:10.1016/j.geomorph.2012.10.025

Banerjee, T., Muste, M., and Katul, G. (2015). Flume experiments on wind induced flow in static water bodies in the presence of protruding vegetation. *Adv. Water Resour.* 76, 11–28. doi:10.1016/j.advwatres.2014.11.010

Bassoullet, P., Le Hir, P., Gouleau, D., and Robert, S. (2000). Sediment transport over an intertidal mudflat: Field investigations and estimation of fluxes within the "baie de Marenngres-oleron" (France). *Cont. Shelf Res.* 20, 1635–1653. doi:10.1016/s0278-4343(00)00041-8

Blum, M. D., and Roberts, H. H. (2009). Drowning of the Mississippi Delta due to insufficient sediment supply and global sea-level rise. *Nat. Geosci.* 2, 488–491. doi:10.1038/ngeo553

Catano-Lopera, Y. A., and Garcia, M. H. (2006). Geometry and migration characteristics of bedforms under waves and currents - Part 2: Ripples superimposed on sandwaves. *Coast. Eng.* 53, 781–792. doi:10.1016/j.coastaleng.2006.03.008

Callaghan, D. P., Bouma, T. J., Klaassen, P., Van Der Wal, D., Stive, M. J. F., and Herman, P. M. J. (2010). Hydrodynamic forcing on salt-marsh development: Distinguishing the relative importance of waves and tidal flows. *Estuar. Coast. Shelf Sci.* 89, 73–88. doi:10.1016/j.ecss.2010.05.013

Chakraborty, C. (2001). Lagoon-tidal flat sedimentation in an epeiric sea: Proterozoic bhander group, son valley, India. *Geol. J.* 36, 125–141. doi:10.1002/gj.884

Chargulaf, C. A., and Tibbetts, I. R. (2015). Spatial and temporal variation of meiofauna community structure in soft-sediment pools around Moreton Bay, Australia. *Aust. J. Zool.* 63, 204–213. doi:10.1071/zo14063

Christie, M. C., Dyer, K. R., and Turner, P. (1999). Sediment flux and bed level measurements from a macro tidal mudflat. *Estuar. Coast. Shelf Sci.* 49, 667–688. doi:10.1006/ecss.1999.0525

Costanza, R., Darge, R., Degroot, R., Farber, S., Grasso, M., Hannon, B., et al. (1997). The value of the world's ecosystem services and natural capital. *Nature* 387, 253–260. doi:10.1038/387253a0

De Vet, P. L. M., Van Prooijen, B. C., and Wang, Z. B. (2017). The differences in morphological development between the intertidal flats of the Eastern and Western Scheldt. *Geomorphology* 281, 31–42. doi:10.1016/j.geomorph.2016.12.031

Ding, P., Hu, K., Kong, Y., and Hu, D. (2003). Numerical simulation of storm-induced erosion/deposition in yangtze estuary --A case study of typhoon jelawat. *J. Sediment Res.* 0, 18–24.

Fan, D. D., Guo, Y. X., Wang, P., and Shi, J. Z. (2006). Cross-shore variations in morphodynamic processes of an open-coast mudflat in the Changjiang Delta, China: With an emphasis on storm impacts. *Cont. Shelf Res.* 26, 517–538. doi:10.1016/j.csr.2005.12.011

Freeman, A. M., Jose, F., Roberts, H. H., and Stone, G. W. (2015). Storm induced hydrodynamics and sediment transport in a coastal Louisiana lake. *Estuar. Coast. Shelf Sci.* 161, 65–75. doi:10.1016/j.ecss.2015.04.011

Friedrichs, C. T. (2011). "Tidal flat morphodynamics: A synthesis," in *Treatise on estuarine and coastal science*. Editors J. D. Hansom and B. W. Flemming (Amsterdam, Netherlands: Elsevier).

Gallagher, E. L., Boyd, W., Elgar, S., Guza, R. T., and Woodward, B. (1996). Performance of a sonar altimeter in the nearshore. *Mar. Geol.* 133, 241–248. doi:10.1016/0025-3227(96)00018-7

Goodwin, I. D., Mortlock, T. R., and Browning, S. (2016). Tropical and extratropical-origin storm wave types and their influence on the East Australian longshore sand transport system under a changing climate. *J. Geophys. Res. Oceans* 121, 4833–4853. doi:10.1002/2016jc011769

Grant, W. D., and Madsen, O. S. (1979). Combined wave and current interaction with a rough bottom. *J. Geophys. Res.* 84, 1797–1808. doi:10.1029/jc084ic04p01797

Guerrero, Q., and Guillen, J. (2020). Dynamics of ripples superimposed on a sand ridge on a tideless shoreface. *Estuar. Coast. Shelf Sci.* 242, 106826. doi:10.1016/j.ecss.2020.106826

Guerrero, Q., Williams, M. E., Guillén, J., Lichtman, I. D., Thorne, P. D., and Amoudry, L. O. (2021). Small-scale bedforms and associated sediment transport in a macro-tidal lower shoreface. *Cont. Shelf Res.* 225, 104483. doi:10.1016/j.csr.2021.104483

Herman, P. M. J., Middelburg, J. J., and Heip, C. H. R. (2001). Benthic community structure and sediment processes on an intertidal flat: Results from the ECOFLAT project. *Cont. Shelf Res.* 21, 2055–2071. doi:10.1016/s0278-4343(01)00042-5

Hu, Z., Wang, Z. B., Zitman, T. J., Stive, M. J. F., and Bouma, T. J. (2015). Predicting long-term and short-term tidal flat morphodynamics using a dynamic equilibrium theory. *J. Geophys. Res. Earth Surf.* 120, 1803–1823. doi:10.1002/2015jf003486

Hu, Z., Yao, P., Van Der Wal, D., and Bouma, T. J. (2017). Patterns and drivers of daily bed-level dynamics on two tidal flats with contrasting wave exposure. *Sci. Rep.* 7, 7088. doi:10.1038/s41598-017-07515-y

Hu, Z., Zhou, J., Wang, C., Wang, H., He, Z., Peng, Y., et al. (2020). A novel instrument for bed dynamics observation supports machine learning applications in mangrove biogeomorphic processes. *Water Resour. Res.* 56. doi:10.1029/2020wr027257

Jestin, H., Bassoullet, P., Le Hir, P., L'yavanc, J., and Degres, Y. (1998). "Development of ALTUS, a high frequency acoustic submersible recording altimeter to accurately monitor bed elevation and quantify deposition and erosion of sediments," in IEEE Oceanic Engineering Society. OCEANS'98. Conference Proceedings, Nice, France, 28 September 1998 - 01 October 1998. 98, 189-194.

Jin, C., Coco, G., Tinoco, R. O., Perron, J. T., Myrow, P. M., Huppert, K. L., et al. (2020). Investigating the response of wave-generated ripples to changes in wave forcing. *Geomorphology* 363, 107229. doi:10.1016/j.geomorph.2020.107229

Kim, S. C., Friedrichs, C. T., Maa, J. P. Y., and Wright, L. D. (2000). Estimating bottom stress in tidal boundary layer from Acoustic Doppler Velocimeter data. *J. Hydraul. Eng.* 126, 399–406. doi:10.1061/(asce)0733-9429(2000)126:6(399)

Klein, A. H. D., and De Menezes, J. T. (2001). Beach morphodynamics and profile sequence for a headland bay coast. *J. Coast. Res.* 17, 812–835.

Lorenz, R. D., and Valdez, A. (2011). Variable wind ripple migration at great sand dunes national park and preserve, observed by timelapse imaging. *Geomorphology* 133, 1–10. doi:10.1016/j.geomorph.2011.06.003

Li, C., Wang, P., Daidu, F., Bing, D., and Tiesong, L. (2000). Open-coast intertidal deposits and the preservation potential of individual laminae: A case study from east-central China. *Wiley* 47, 1051. doi:10.1046/j.1365-3091.2000.00338.x

Li, M. Z., and Amos, C. L. (1999). Sheet flow and large wave ripples under combined waves and currents: Field observations, model predictions and effects on boundary layer dynamics. *Cont. Shelf Res.* 19, 637–663. doi:10.1016/s0278-4343(98)00094-6

Lin, C. Y. M., and Venditti, J. G. (2013). An empirical model of subcritical bedform migration. *Sedimentology* 60, 1786–1799. doi:10.1111/sed.12056

Liu, S., Li, X., Chen, D., Duan, Y., and Zhang, L. (2020). Understanding Land use/Land cover dynamics and impacts of human activities in the Mekong Delta over the last 40 years. *Glob. Ecol. Conservation* 22, e00991. doi:10.1016/j.gecco.2020.e00991

Maan, D. C., Van prooijen, B. C., Zhu, Q., and Wang, Z. B. (2018). Morphodynamic feedback loops control stable fringing flats. *J. Geophys. Res. Earth Surf.* 0, 2993–3012. doi:10.1029/2018jf004659

Macmahan, J., Brown, J., Brown, J., Thornton, E., Reniers, A., Stanton, T., et al. (2010). Mean Lagrangian flow behavior on an open coast rip-channeled beach: A new perspective. *Mar. Geol.* 268, 1–15. doi:10.1016/j.margeo.2009.09.011

Madsen, A. T., Murray, A. S., Andersen, T. J., and Pejrup, M. (2010). Spatial and temporal variability of sediment accumulation rates on two tidal flats in Lister Dyb tidal basin, Wadden Sea, Denmark. *Earth Surf. Process. Landf.* 35, 1556–1572. doi:10.1002/esp.1999

Mclachlan, R. L., Ogston, A. S., Asp, N. E., Fricke, A. T., Nittrouer, C. A., and Schettini, C. a. F. (2020). Morphological evolution of a macrotidal back-barrier environment: The Amazon Coast. *Sedimentology* 67, 3492–3512. doi:10.1111/sed.12752

Miao, L. M., Yang, S. L., Zhu, Q., Shi, B. W., Li, P., and Wu, C. S. (2016). Variations of suspended sediment concentration and transport in response to a storm and its dynamic mechanism - a study case of Nanhui tidal flat of the Yangtze River Delta. *Acta Oceanol. Sin.* 38, 158–167.

Milliman, J. D., and Farnsworth, K. L. (2011). River Discharge to the coastal ocean – a global synthesis. *River discharge to the coastal ocean – a global synthesis*. Cambridge: Cambridge University Press.

Nansingh, P., and Jurawan, S. (1999). Environmental sensitivity of a tropical coastline (Trinidad, West Indies) to oil spills. *Spill Sci. Technol. Bull.* 5, 161–172. doi:10.1016/s1353-2561(98)00052-8

Nicholls, R. J., Hoozemans, F., and Marchand, M. (1999). Increasing flood risk and wetland losses due to global sea-level rise: Regional and global analyses. *Glob. Environ. Change* 9, S69–S87. doi:10.1016/s0959-3780(99)00019-9

Nortek, A. S. (2005). Vector current meter user manual, Norway, 15.

Paavo, B. L., Ham, D., Goerlitz, S., and Probert, P. K. (2012). How does tidal submersion time affect macroinvertebrate community patterns on a temperate sheltered sandflat? *Mar. Freshw. Res.* 63, 68–77. doi:10.1071/mf11147

Reckhardt, A., Beck, M., Seidel, M., Riedel, T., Wehrmann, A., Bartholomae, A., et al. (2015). Carbon, nutrient and trace metal cycling in sandy sediments: A comparison of high-energy beaches and backbarrier tidal flats. *Estuar. Coast. Shelf Sci.* 159, 1–14. doi:10.1016/j.ecss.2015.03.025

Ryu, S. O. (2003). Seasonal variation of sedimentary processes in a semi-enclosed bay: Hampyong bay, Korea. *Estuar. Coast. Shelf Sci.* 56, 481–492. doi:10.1016/s0272-7714(02)00199-3

Saulter, A. N., Russell, P. E., Gallagher, E. L., and Miles, J. R. (2003). Observations of bed level change in a saturated surf zone. *J. Geophys. Res.* 108, 3112. doi:10.1029/2000jc000684

Schuerch, M., Spencer, T., Temmerman, S., Kirwan, M. L., Brown, S., Lincke, D., et al. (2018). Future response of global coastal wetlands to sea-level rise. *Nature* 561, 231–234. doi:10.1038/s41586-018-0476-5

Shen, Y., Jia, H., Li, C., and Tang, J. (2018). Numerical simulation of saltwater intrusion and storm surge effects of reclamation in Pearl River Estuary, China. *Appl. Ocean Res.* 79, 101–112. doi:10.1016/j.apor.2018.07.013

Siegle, E., Dottori, M., and Villamarin, B. C. (2018). Hydrodynamics of a subtropical tidal flat: Araca Bay, Brazil. *Ocean Coast. Manag.* 164, 4–13. doi:10.1016/j.ocecoaman.2017.11.003

Stella, M. (2021). Morphodynamics of the south Baltic seabed in the remote nearshore zone in the light of field measurements. *Mar. Geol.* 439, 106546. doi:10.1016/j.margeo.2021.106546

Su, M., Yao, P., Wang, Z. B., Chen, Y. P., Zhang, C. K., and Stive, M. J. F. (2015). "Laboratory studies on the response of fine sediment to wind," in *IAHR world congress 2015* (Netherlands: the Netherlands: IHAR).

Temmerman, S., Meire, P., Bouma, T. J., Herman, P. M. J., Ysebaert, T., and De Vriend, H. J. (2013). Ecosystem-based coastal defence in the face of global change. *Nature* 504, 79–83. doi:10.1038/nature12859

Thorne, P. D., Hurther, D., Cooke, R. D., Caceres, I., Barraud, P. A., and Sanchez-Arcilla, A. (2018). Developments in acoustics for studying wave-driven boundary layer flow and sediment dynamics over rippled sand-beds. *Cont. Shelf Res.* 166, 119–137. doi:10.1016/j.csr.2018.07.008

Thornton, E. B., Swayne, J. L., and Dingler, J. R. (1998). Small-scale morphology across the surf zone. *Mar. Geol.* 145, 173–196. doi:10.1016/s0025-3227(97)00114-x

Tucker, M. J., and Pitt, E. G. (2001). *Waves in ocean engineering*. Amsterdam, Netherlands: Elsevier.

Turner, I. L., Russell, P. E., and Butt, T. (2008). Measurement of wave-by-wave bed-levels in the swash zone. *Coast. Eng.* 55, 1237–1242. doi:10.1016/j.coastaleng.2008.09.009

Vafeidis, A. T., Nicholls, R. J., Mcfadden, L., Tol, R., Hinkel, J., Spencer, T., et al. (2008). A new global coastal database for impact and vulnerability analysis to sea-level rise. *J. Coast. Res.* 24, 917–924. doi:10.2112/06-0725.1

Van Rijn, L. C. (1993). *Principles of sediment transport in rivers, estuaries and coastal seas*. Amsterdam, Netherlands: Aqua Publication.

Walling, D. E. (2006). Human impact on land–ocean sediment transfer by the world's rivers. *Geomorphology* 79, 192–216. doi:10.1016/j.geomorph.2006.06.019

Wang, Z., Van Maren, D., Ding, P., Yang, S., Van Prooijen, B., De Vet, P., et al. (2015). Human impacts on morphodynamic thresholds in estuarine systems. *Cont. Shelf Res.* 111, 174–183. doi:10.1016/j.csr.2015.08.009

Waska, H., and Kim, G. (2010). Differences in microphytobenthos and macrofaunal abundances associated with groundwater discharge in the intertidal zone. *Mar. Ecol. Prog. Ser.* 407, 159–172. doi:10.3354/meps08568

Williams, J. J., Bell, P. S., and Thorne, P. D. (2003). Field measurements of flow fields and sediment transport above mobile bed forms. *J. Geophys. Res.* 108, 3109. doi:10.1029/2002jc001336

Winterwerp, J. C., Van Kesteren, W. G. M., Van Prooijen, B., and Jacobs, W. (2012). A conceptual framework for shear flow-induced erosion of soft cohesive sediment beds. *J. Geophys. Res.* 117, 17. doi:10.1029/2012jc008072

Xu, K., Mickey, R. C., Chen, Q., Harris, C. K., Hetland, R. D., Hu, K., et al. (2015). Shelf sediment transport during hurricanes Katrina and Rita. *Comput. Geosciences* 8, 24–39. doi:10.1016/j.cageo.2015.10.009

Yang, B. C., Dalrymple, R. W., and Chun, S. S. (2005). Sedimentation on a wave-dominated, open-coast tidal flat, south-Western Korea: Summer tidal flat-winter shoreface. *Sedimentology* 52, 235–252. doi:10.1111/j.1365-3091.2004.00692.x

Yang, S. L., Friedrichs, C. T., Shi, Z., Ding, P. X., Zhu, J., and Zhao, Q. Y. (2003). Morphological response of tidal marshes, flats and channels of the outer Yangtze River mouth to a major storm. *Estuaries* 26, 1416–1425. doi:10.1007/bf02803650

Yang, S. L., Milliman, J. D., Li, P., and Xu, K. (2011). 50, 000 dams later: Erosion of the Yangtze River and its delta. *Glob. Planet. Change* 75, 14–20. doi:10.1016/j.gloplacha.2010.09.006

Zhu, Q. (2017). *Sediment dynamics on intertidal mudflat: A study based on* in situ *measurements and numerical modelling*. Netherland: Delft University of Technology.

Zhu, Q., Van Prooijen, B., Wang, Z., and Yang, S. (2017). Bed-level changes on intertidal wetland in response to waves and tides: A case study from the yangtze river delta. *Mar. Geol.* 385, 160–172. doi:10.1016/j.margeo.2017.01.003

Zhu, Q., Van Prooijen, B. C., Maan, D. C., Wang, Z. B., Yao, P., Daggers, T., et al. (2019). The heterogeneity of mudflat erodibility. *Geomorphology* 345, 106834. doi:10.1016/j.geomorph.2019.106834

Zhu, Q., Van Prooijen, B. C., Wang, Z. B., Ma, Y. X., and Yang, S. L. (2016). Bed shear stress estimation on an open intertidal flat using *in situ* measurements. *Estuar. Coast. Shelf Sci.* 182, 190–201. doi:10.1016/j.ecss.2016.08.028

Zhu, Q., Yang, S., and Ma, Y. (2014). Intra-tidal sedimentary processes associated with combined wave–current action on an exposed, erosional mudflat, southeastern Yangtze River Delta, China. *Mar. Geol.* 347, 95–106. doi:10.1016/j.margeo.2013.11.005

Zhu, S. X., Yang, H. L., Zhu, C., Wang, P., and Ying, Q. Z. (2008). The inter-tidal macrobenthic benthic community characters of Zhapo, Guangdong. *J. Zhejiang Ocean Univ. Nat. Sci.* 27, 22–27.

frontiers | Frontiers in Earth Science

TYPE Original Research
PUBLISHED 24 November 2022
DOI 10.3389/feart.2022.878102

OPEN ACCESS

EDITED BY
Andrew James Manning,
HR Wallingford, United Kingdom

REVIEWED BY
Jonny Higham,
University of Liverpool, United Kingdom
Stephen Michael Simmons,
University of Hull, United Kingdom

*CORRESPONDENCE
Bart Brouwers,
bart.brouwers@mow.vlaanderen.be

SPECIALTY SECTION
This article was submitted to Marine Geoscience,
a section of the journal
Frontiers in Earth Science

RECEIVED 17 February 2022
ACCEPTED 09 November 2022
PUBLISHED 24 November 2022

CITATION
Brouwers B, van Beeck J, Meire D and Lataire E (2022), Assessment of the potential of radiography and ultrasonography to record flow dynamics in cohesive sediments (mud). *Front. Earth Sci.* 10:878102. doi: 10.3389/feart.2022.878102

Assessment of the potential of radiography and ultrasonography to record flow dynamics in cohesive sediments (mud)

Bart Brouwers[1,2]*, Jeroen van Beeck[3], Dieter Meire[1] and Evert Lataire[2]

[1]Flanders Hydraulics Research, Antwerp, Belgium, [2]Department of Civil Engineering, Maritime Technology Division, Ghent University, Ghent, Belgium, [3]Environmental and Applied Fluid Dynamics Department, Von Karman Institute for Fluid Dynamics, Sint-Genesius-Rode, Belgium

The possible use of both radiography and ultrasonography to visualise flow dynamics in cohesive sediments, also known as fluid mud, has been assessed. Ultimately, these techniques are intended to enable the application of Particle Image Velocimetry (PIV) in experimental fluid dynamics using such fluid mud. This research takes into account the specific requirements arising from this objective. Those requirements are primarily penetration depth, adequate frame rate and the preference not to seed with tracer particles. The evaluation of both techniques is elaborated in detail based the properties of mud originating from the Port of Zeebrugge (Belgium). The assessment of radiography starts with a chemical element analysis of the fluid mud, the results of which are used to determine the attenuation for high-energy electromagnetic radiation. Using various research software, the maximum thickness of the mud layer could be determined as a function of the maximum recordable flow velocities for different radiation sources. However, for the flow velocities expected in nautical research experiments, these thicknesses proved insufficient. Supplemented by the results of a particle size distribution analysis, it is found that high frequency ultrasound radiation will scatter in mud. In case of a great number of scatterers, the scattered ultrasound waves will interact, eventually resulting in speckle images, which are ideally suited for tracking. These findings were confirmed in a test setup with a standard medical ultrasound scanner. The penetration depth of ultrasonography with standard medical equipment is also limited. However, since ultrasonography is based on reflection, this is less of an issue compared to radiography, for which full penetration of the mud layer is required. Ultrasonography is therefore suggested as the preferred technique for the intended application.

KEYWORDS

cohesive sediment, visualization, high opacity, non-transparent, velocimetry, laboratory experiments, fluid dynamics

1 Introduction

The "nautical bottom" is a term used in the maritime community to define the critical water depth for ships in shallow navigation areas. In 1997 the concept was introduced by PIANC (The World Association for Waterborne Transport Infrastructure) as "the level where physical characteristics of the bottom reach a critical limit beyond which contact with a ship's keel causes either damage or unacceptable effects on controllability and maneuverability" (Vantorre, 1997). In case of sand or rock bottoms, the depth of the nautical bottom is directly determined by the highest sand dune or rock outcrop. When the bottom of navigation areas consists of cohesive sediments, commonly referred to as fluid mud beds, there is however no clear physical limit which determines the applicable nautical bottom. Nonetheless, the presence of such muddy layers can influence the maneuverability and controllability of ships, even when the keel of the ship does not penetrate these layers (Delefortrie et al., 2007; Delefortrie and Vantorre, 2009). Fluid mud is a saturated mixture of water and sediments with a high clay and organic fraction. The density of highly consolidated mud can be as high as 1,300 $kg{\cdot}m^{-3}$. The particles form a continuous network, a soil skeleton, and therefore a yield stress needs to be overcome before the material will flow (i.e., non-Newtonian fluid). In addition mud shows thixotropic behavior, meaning its viscosity decreases with stress over time or *vice versa* when left at rest (Toorman and Berlamont, 2015).

Due to the complex interactions between ship, mud and water layers, the use of Computational Fluid Dynamics (CFD) models is preferred by nautical researchers to facilitate research on the influence of a mud layer on a ships' maneuvering behavior (Vanlede et al., 2014; Delefortrie and Vantorre, 2016). The modelling of the behavior of mud is however complex. Some models simplify this by assuming that the mud behaves like a Newtonian fluid (Kaidi et al., 2020). Others take the non-Newtonian behavior into account by including viscosity models such as the Herschel-Bulkley model and the power law model to approximate the behavior of mud (Gao et al., 2015; Lovato et al., 2022). The most correct way to model the behavior of mud is to determine the actual rheological properties and take these into account (Vanlede et al., 2014). No data is however available to validate these models. Therefore, Sotelo et al. (2022) recently conducted experiments generating validation datasets including rheological properties correlated to mud behavior. During these experiments, a blunt body was towed through a mud layer at various velocities. Prior to each experiment, the rheological properties of the mud were determined. During the experiments, the pressures and forces exerted by the mud on the body and the pressure changes in the mud layer were monitored. However, pressure measurements require probes and so they are point measurements and limited in number. While force measurements require a fixed reference and therefore can only be measured on the body. These forces are the resultant of the pressure acting on the underwater surface of the body. Thus, the locations in the mud layer for which validation data are generated with these experiments are limited. Therefore, the application of a non-intrusive whole-flow field technique that provides a grid of velocity vector measurements in a cross-section of a flow, such as PIV, would significantly improve the collection of validation data from such experiments. Moreover, to be relevant for nautical related research, flow velocities up to 2 $m{\cdot}s^{-1}$ should be recordable.

Flow velocity measurements in mud were previously performed by de Wit (1995), Hsu et al. (2013) and Soltanpour et al. (2018) during their research on wave-mud interaction. Electromagnetic Current Meters (ECM) were used to conduct point measurements in mud. Nevertheless, the limitations of their maximum flow velocity and sampling frequency make ECM's unsuited for the intended application supporting nautical research. The non-transparency of mud does allow visualization of the water-mud interface by simple illumination. This is however insufficient to fully understand the flow mechanics in mud, which requires visualization of the flow dynamics in the mud layer.

At present, Particle Image Velocimetry (PIV) is widely used in experimental fluid dynamics in the investigation of air and water flows (Raffel et al., 2007). The ability of PIV to record fluid dynamics over an entire area in one single experiment and without intrusive probing, significantly increases efficiency and quality. Especially when compared to using classic point measurement devices such as hot wire anemometer probes, electromagnetic current meters, turbine flow meters and pitot tubes. An experimental setup for PIV recording consists of a fluid containing particles whose displacements are recorded over time. Assuming that the particle displacements are governed by the flows in the fluid, the particle displacements represent the dynamics in the fluid (Raffel et al., 2007). Using a PIV algorithm, the particle displacements can be determined from the recordings of the moving particles. In transparent fluids, the particles are usually visualized with a laser to enable recording. However, the opacity of mud, even at low densities, does not allow for optical illumination. Therefore, alternative means must be found to visualize the particles in the mud and record their movements.

A solution may be the use of transparent fluids that approximate the rheological properties of mud. Pouv et al. (2012), showed the rheological properties of mixtures of synthetic clay, laponite RD (Rockwood), and polymer, carboxymethylcellulose (Prolabo) are similar to those of natural mud. Furthermore such mixtures are translucent, allowing the application of optical PIV. Such a setup was used by Pouv et al. (2014) and Zaynab et al. (2015) to simulate and study the erosion of cohesive sediments. However, as mentioned by Pouv et al. (2014), the mixtures are made mainly of polymer molecules and therefore cannot fully represent real cohesive

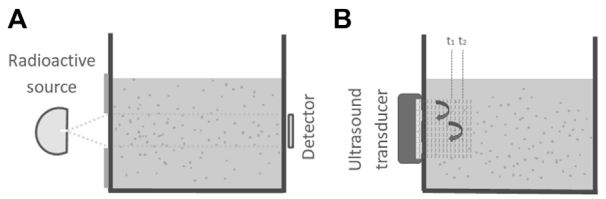

FIGURE 1
(A) Sketch of radiography setup. Radioactive source and detector are positioned opposite to each other with the mud layer between the two. Hence full penetration of the mud layer is required; **(B)** Sketch of ultrasonography setup. The ultrasound transducer is positioned on one side of the mud layer and acts as both a transmitter and a receiver. The emitted radiation is reflected or backscattered back to the transducer.

sediments in terms of the internal structures. In fact the execution of similar research using real non-transparent cohesive sediment to validate the use of the laponite mixtures was recommended, which ratifies the need for alternative visualization techniques.

Finding the means to overcome these deficiencies will make physical laboratory tests using natural mud a valuable tool for the continuation of the research on the nautical bottom in muddy navigation areas. This paper presents the outcome of a literature survey identifying different promising visualization techniques for application on mud layers, and the results of small-scale experiments to further assess these techniques considering the specific requisites of whole flow-field velocimetry techniques like PIV.

2 Potential flow visualization techniques in mud

Given the opacity of human tissue and the preferred avoidance of probing, medical diagnostic techniques have been developed to overcome similar issues. Therefore, visualization techniques used in medicine, such as radiography, magnetic resonance imaging (MRI), ultrasonography and nuclear imaging, all have the potential to be used in mud. Considering cost and applicability in a typical experimental hydraulic setup, radiography and ultrasonography offer the most potential. The main difference between both techniques concerns the propagation path of the applied energy through the mud layer (Figures 1A,B) which is further elaborated in this section.

Visualization with radiography is based on a difference in absorption of the radiation. When particles in the fluid absorb more radiation compared to the surrounding fluid, they will appear as shadows on the image. As a consequence, full propagation of the radiation through the mud layer is required. Visualization using ultrasonography is based on the difference in acoustic impedance of particles compared to that of the fluid. When encountering a change in acoustic impedance the transmitted ultrasound waves will be reflected by the insonified particles. These reflection signals are recorded back by the transducer and represented as a function of brightness on the screen. The stronger the echo signal the brighter the reflecting particle will appear on the screen. Hence, full penetration of the mud layer is no longer required, allowing limitation of the propagation path of the waves and consequently loss of intensity. An initial more detailed evaluation of these two possible techniques involves determining the attenuation of the transmitted energy by mud. The physics of attenuation for both can be expressed with the Beer-Lambert law (Eq. 1). It shows that a medium attenuates the incoming radiation as a function of the attenuation coefficient and the propagation path length of the radiation through the medium. The loss of radiation intensity due to attenuation is expressed as the ratio of the intensity of incoming radiation to the intensity of outgoing radiation, further referred to as the transmission ratio. The determination of the transmission ratio allows to assess whether or not the radiation intensity emitted by available radiation sources are sufficient. Therefore, the attenuation coefficient of the mud and the required minimum intensity of the outgoing radiation must be specified.

$$T = \frac{I_l}{I_0} = e^{(-\mu l)} \tag{1}$$

Where T is the transmission ratio [-], I_0 is the incoming radiation intensity [$W \cdot m^{-2}$], I_l is the outgoing radiation intensity [$W \cdot m^{-2}$], μ is the attenuation coefficient of the radiated medium [m^{-1}] and l is the thickness of the radiated medium [m].

The attenuation coefficient is however different for each type of radiation. In case of electromagnetic waves, the attenuation coefficients of different media are more or less stable and can therefore be retrieved from extensive databases as a function of the photon energy level. Attenuation coefficients for ultrasound are less clear-cut. As mentioned by Ginzel and Turnbull (2016), the values of attenuation coefficients can already vary due to variations in material processing. Consequently, values of ultrasound attenuation coefficients of materials available in the literature cannot simply be used. It is therefore recommended that attenuation coefficients for ultrasound are determined experimentally for each case.

2.1 Radiography

As full propagation of the radiation through the mud layer is required (Figure 1A), further assessment of radiography will mainly focus on the amount of radiation able to propagate through the mud layer. First the total loss in radiation energy caused by the setup and the mud layer will be estimated allowing the assessment of various

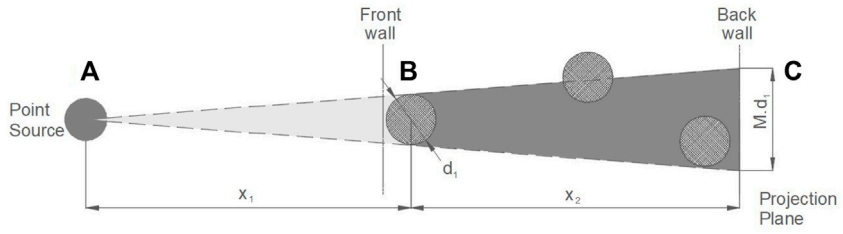

FIGURE 2
Principle sketch of the magnification of a projection by using a point source. The sketch shows the projection of a particle of size d_1 **(B)**, present at the front, onto the projection plane of the detector at the back **(C)**. The size of the projection is a factor M larger than the original particle size d_1. This magnification factor M is determined by the distance between the point source **(A)** and the particle **(B)**, denoted by x_1, and the distance between the particle **(B)** and the projection plane on the detector **(C)**, denoted by x_2. The larger the magnification factor M, the larger the shadow behind the particle, the more other particles are overshadowed and no longer visible on the projection.

radiation sources differing in emitted energy levels and amount of radiation.

When a point source is used, which is common for radiography, one should take into account that the size of particles will be magnified on the image depending on the distances between the source, particle and detector (Figure 2). Magnification however needs to be limited to preserve the quality of the images and to avoid particles getting overshadowed by particles in front. The magnification limit is determined by the distance between source and particle (x_1) and the distance between particle and detector (x_2). While the latter is fixed as the thickness of the mud layer, the chosen magnification limit will determine the distance x_1.

As the magnification factor M [-] is inversely proportional to the distance between the radiation source and the mud particle x_1 [m] (Figure 2), limitation of the magnification factor will lead to an increase of x_1. While on the other hand x_1 should be kept to a minimum to limit energy loss, as the irradiance degrades by the distance squared (Eq. 2).

$$D_{rate} \propto \frac{A}{d^2} \tag{2}$$

Where D_{rate} is the dose rate [Gy] at a distance d from the radiation source [m] and A is the activity of the radiation source [Bq]. For this evaluation the mud layer thickness is set to 560 mm, corresponding to an available test facility at Flanders Hydraulics Research (FHR). Limiting the magnification factor for the particles in the front to 1.56 results in a distance between the radiation source and the mud layer of 1 m, which is common in radiography.

To create adequate images for diagnostic use, a minimal dose rate absorbed by the detector is required. Although probably on the conservative side, the minimal dose rate for medical diagnostic imaging is used for this evaluation. Medical applications are always subject to the ALARA principle, which is an acronym for "As Low As Reasonably Achievable". Hence it is an indication of the minimum dose rate required to create images of sufficient quality for diagnostic use. Recommendations on minimal dose rates for multiple medical applications are presented in IEC 62220-1-3:2008 (2008). Although the application on mud is not directly bound by a maximum dose rate, estimations show that these minimum dose rates are already hard to achieve for the intended ranges of flow speed and mud layer thickness. Therefore the highest dose rate recommended for medical applications of 2 μGy/frame is used for the continuation of this assessment.

Knowing the required dose rate at the detector allows to calculate the required intensity at the source if the loss in intensity due to propagation through mud is known. Such loss is caused by the attenuation capacity of mud, which comprises both absorption and scattering of the incoming waves. At higher energy levels, such as for x- and gamma radiation, intensity loss due to scattering becomes more significant and therefore cannot be neglected. Such intensity loss can be calculated using the Beer-Lambert law (Mayerhöfer et al., 2020), presented earlier as Eq. 1.

2.1.1 Attenuation of electromagnetic waves by mud

The attenuation coefficient of common materials or mixtures can be found in the literature. However, usually published is the mass attenuation, which is defined as:

$$\mu_{mass} = \frac{\mu}{\rho_{mass}} \tag{3}$$

Where μ_{mass} is the mass attenuation of the radiated medium [$cm^2 \cdot g^{-1}$], μ is the attenuation coefficient of the radiated medium [cm^{-1}] and ρ_{mass} is the density of the radiated medium [$g \cdot cm^{-3}$]. Using the mass attenuation allows to express the attenuation as a function of density, which is convenient for media with changing density in time, like mud.

For this research the mass attenuation coefficients of the freely accessible database of the National Institute of Standards and Technology (NIST) are used (Berger et al., 2010). The NIST

TABLE 1 Compounds present in mud originating from the Port of Zeebrugge (Begium) together with their respective weight fractions [%] as a function of mud density.

Density	Al_2O_3	CaO	Fe_2O_3	K_2O	MgO	MnO	Na_2O	P_2O_5	SiO_2	TiO_2	H_2O
1.035 g·cm^{-3}	4.01	7.43	1.96	1.22	3.58	0.05	17.32	0.13	17.03	0.24	49.30
1.100 g·cm^{-3}	7.84	13.37	3.64	1.45	2.27	0.08	5.54	0.23	36.02	0.47	29.68
1.200 g·cm^{-3}	8.25	13.99	3.90	1.44	2.08	0.08	3.82	0.23	37.99	0.50	27.08

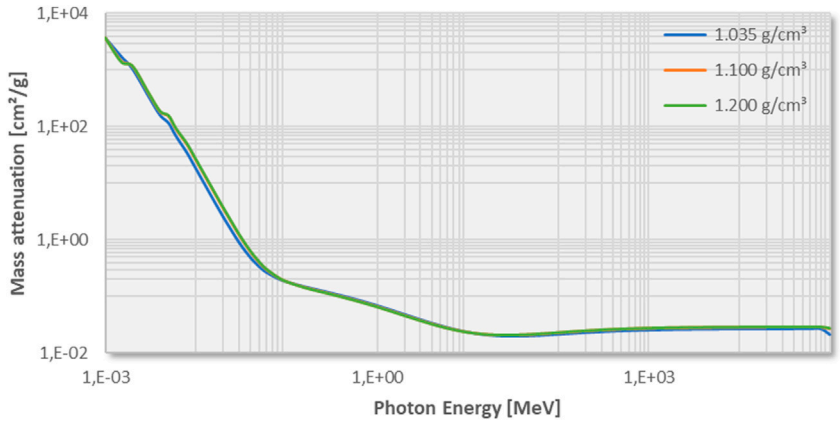

FIGURE 3
Mass attenuation coefficient as a function of photon energy level for multiple mud densities. Calculations are made using (Eq. 4), based on the weight fractions presented in Table 1 and mass attenuation coefficients found in the NIST database (Berger et al., 2010) for each of the compounds present in mud.

database contains a collection of published values of mass attenuation of chemical elements, compounds and common mixtures as a function of the energy level of the radiation, expressed in [MeV]. Unfortunately, the composition of mud varies according to its origin (port, river, area, etc.) and thus cannot be generalized. Therefore, the attenuation coefficient of each mud with different composition should be calculated. This can be done according to the method described in Ripan et al. (2016), using the values of mass attenuation of each compound (oxide) present in the mud in accordance with their weight fractions.

By means of a chemical element analysis using the Inductive Coupled Plasma—Optical Emission Spectrometry technique (ICP—OES, Wang (2004)), the different compounds present in mud were first determined together with their weight fractions for three mud densities: 1.035 g·cm^{-3}, 1.100 g·cm^{-3} and 1.200 g·cm^{-3} (Table 1).

The mass attenuation values of these compounds can be found in the NIST database. With these data, the value of mass attenuation of the mud mixture can be calculated using the so-called "mixture rule", presented in Burcu and Salih (2014) and shown as Eq. 4. This was done for each of the three previously mentioned mud densities used in this research. The resulting values of mass attenuation per density are plotted as a function of photon energy in Figure 3.

$$\left(\frac{\mu}{\rho}\right)_{mix} = \sum_{i=1}^{N} \omega_i . \left(\frac{\mu}{\rho}\right)_i \tag{4}$$

Where μ is the attenuation coefficient [cm^{-1}], ρ is the density [g·cm^{-3}], ω is the weight fraction [%] and i is the reference to the elements in the mixture.

At first it can be concluded that the attenuation of mud is hardly influenced by the density. This is consistent with observations during consolidation experiments conducted FHR, presented in Meshkati Shahmirzadi et al. (2015); Pirola Igoa et al. (2020). For these experiments mud is pumped in large transparent columns and left at rest to settle and consolidate (see Supplemental Data, Supplementary Figure S1). Due to sedimentation a distinct interface between "clear" water and mud appears after some time (minutes to hours), which will settle with time (Berlamont et al., 1993). During such consolidation experiments, the settlement of this interface is recorded. Plotting the level of this interface as a function of time yields a characteristic settling curve. To accentuate this water-mud interface, Meshkati Shahmirzadi et al. (2015); Pirola Igoa et al. (2020) installed bright light panels behind the columns

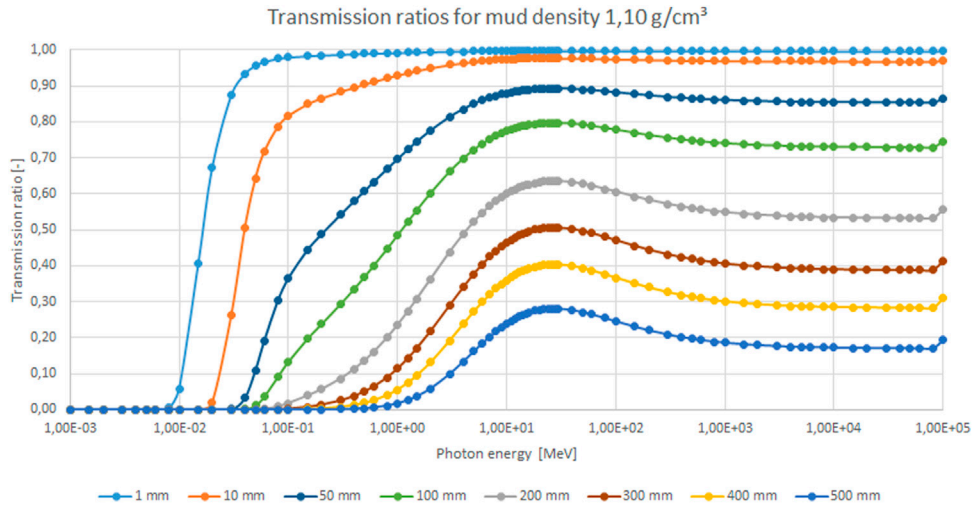

FIGURE 4
Transmission ratios calculated using eq. 1 and attenuation coefficients presented in Figure 3 (mud density 1.10 g·cm^{-3}) and mud layer thickness ranging from 1 mm to 560 mm in a setup as depicted in Figure 1A.

as shown in Supplemental Data, Supplementary Figure S1). This image of ongoing mud consolidation experiments shows that despite the lower density at the top of the mud layers, the mud-water interfaces are always clear and no light to dark shading can be seen with the depth of the mud column. These observations indicate the high opacity of mud regardless of mud density. Calculating the transmission coefficients as a function of radiation energy level, using the Beer-Lambert law (Eq. 1), confirms the opacity of mud for optical light (Figure 4). From the results it can be seen that even for mud layers of 1 mm thickness, a transmission ratio of minimal significance will be obtained with at least photon energy levels of 10 keV. This corresponds with low energetic X-rays which are still far more energetic compared to optical light (2–3 eV). Further focus is therefore on the use of high energy electromagnetic waves such as X-rays and gamma rays.

2.1.2 Gamma rays

The electromagnetic spectrum shows that gamma rays have a higher energy level and therefore have a greater penetration capacity compared to X-rays. Hence it is reasonable to assume that with the use of gamma rays greater radiation doses are absorbed by the detector after full transmission through the mud layer. Gamma rays are produced by radioactive nuclei. After a radioactive nucleus undergoes alpha or beta radiation, the nucleus is left in an "excited" state. The nucleus then loses the excess energy by emitting a gamma photon. As a consequence the radiation emitted by a gamma source is typically mono-energetic. A broad variety of gamma ray sources are available on the market for different usage ranging from medical use to use in industrial processes. Common isotopes for industrial use are ^{60}Co and ^{137}Cs. Specifications of sources available on the market with these isotopes can be found in Supplementary Table S1 of the Supplemental Data (VEGA Americas, Inc, 2017).

Knowing the properties of the gamma source together with the attenuation coefficient of mud (corresponding to the photon energy level of the isotope) and the chosen magnification limit, the expected dose rate at the detector can be calculated as stipulated in Cember and Johnson (2008) or using the freeware Rad Pro Calculator McGinnis (2009). Results for a ^{137}Cs—185 GBq source are presented in Supplemental Data Supplementary Table S2. Using the minimum required radiation dose at the detector (ref. Section 2.1 Radiography) the maximum flow velocity can be determined as a function of the mud layer thickness. Defining a particle displacement limit between two consecutive frames, the maximum flow velocity can be deduced for varying mud layer thickness (Figure 5). A flowchart summarizing the complete calculation procedure is presented as Supplementary Figure S2 in the Supplemental Data.

These results (Figure 5) lead to the conclusion that with flow velocities up to 2 m·s^{-1}, the required dose rates at the detector can only be achieved for very thin mud layers of 1 mm–2 mm, which are mostly irrelevant for fluid dynamics applications. Despite the higher energy level, hence penetration capacity, the results with the ^{60}Co radiation source are even worse due to the lower activity of the source. This illustrates the importance of the activity over the photon energy level, making the use of X-rays more appropriate since activity rates of X-ray sources are much larger compared to the those of gamma ray sources.

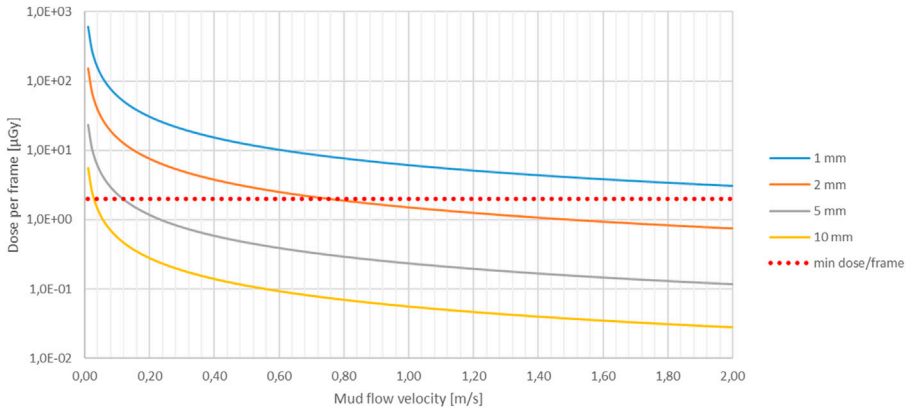

FIGURE 5
Radiation dose, originating from a ^{137}Cs–185 GBq source, received by the detector (Figure 1A) during the time span allowed for per image frame. The time span is expressed as mud flow velocity, where a maximum mud particle displacement of 5 mm is allowed for between two consecutive frames. Increasing mud flow velocity decreases the radiation time span for each image frame, hence the dose received per image frame. Curves for different mud layer thicknesses varying from 1 mm to 10 mm are presented. The dotted red line indicates the minimum dose required per image frame for adequate image quality.

2.1.3 X-rays

X-rays can be produced using an electric device like an X-ray tube. When electrical current is applied to it, X-rays are generated. While radiation from ^{60}Co and ^{137}Cs radioisotopes is mono-energetic, X-ray generators generate a spectrum of photon energy levels. As the attenuation coefficients of also determined by the energy level of the incoming radiation, the calculation of the transmission ratio of the radiation produced by an X-ray generator needs to be integrated over the fully generated energy spectrum. This makes the calculation of dose rates complex and requires the use of specially developed software. For this research, the "SpekCalc" software is used which is developed as a tool for medical research and educational applications [Poludniowski and Evans (2007); Poludniowski (2007); Poludniowski et al. (2009)].

Based on the voltage range of the X-ray source, the source angle and the distance between the X-ray source and the radiated object or patient, SpekCalc calculates the generated X-ray spectrum of the source and the dose rate received by the radiated object or patient. In practice a filter is usually placed between the source and the radiated object or patient. A well chosen filter (thickness and material) filters out the part of the generated photon energy spectrum which is not of interest or use. When passed through the filter the radiation is focused, so to speak. Therefore, a filter can also be taken into account in the SpekCalc software. The list of materials which can be chosen as filters is limited to a number of commonly used materials for X-ray filters, such as (Be, Al, Cu, Sn, W, Ta, H_20, Ti and C). A combination of different filter materials is possible and the filter thickness is unrestricted.

The setup when applied in a hydraulic test facility with a source, mud layer and a detector (Figure 1A) is similar to the setup of a medical application with a source, filter and the patient. The detector at the back of the flume (Figure 1A) acts as the patient while the mud layer acts as the filter. With SpekCalc the radiation reaching the patient, or in this case detector, can be calculated while taking into account the attenuation due to the filter, in this case the mud layer. If SpekCalc is therefore used to estimate the dose rate behind the mud layer, the filter should be replaced by the mud layer. SpekCalc's ability to set an arbitrary filter thickness allows to simulate the filter capacity of the mud layer. For any standard filter material available in the SpekCalc software, a thickness can be found such that it has the same attenuation value as the mud layer over a part of the energy spectrum. When selecting aluminum as filter material, the ratio of attenuation of the aluminum filter over the attenuation of mud with density 1.20 g·cm^{-3} is more or less constant over the entire energy spectrum of interest (Table 2). It can therefore be concluded that, with regards to the attenuation of X-rays over a photon energy spectrum of 10–400 keV, an aluminum filter with thickness of 26.69 cm is the equivalent of a 56 cm mud layer.

It must be noted that the convenience of a constant ratio over a wide energy spectrum like presented in Table 2 does not hold true for all filter materials. Other filter materials only show a more or less constant ratio over a limited part of the spectrum. Copper for instance shows a more or less constant ratio over a limited spectrum from 10 to 40 keV, while for Beryllium this is from 150 keV to 400 keV. In case no constant ratio can be found over the entire energy spectrum, the spectrum needs to be split in parts. For each part of the spectrum a different equivalent filter material is then to be applied.

SpekCalc was originally developed for educational purposes, but meanwhile used in the medical community for first estimations of the expected dose rate. It is mostly referred to

TABLE 2 Overview of required aluminum filter thickness for equivalent attenuation of a 56 cm thick mud layer with density 1.20 g·cm^{-3}, as a function of photon energy. Calculated mass attenuation values of mud presented in Figure 3 were used to determine the attenuation values of the mud layer. Mass attenuation values of aluminum as from the NIST database (Berger et al., 2010) were used to determine the attenuation values of the aluminum filter.

	mud (ρ = 1.20 g·cm^{-3}) l = 56 cm		**Aluminum (ρ = 2.70 g·cm^{-3})**		
Photon energy	$(\frac{\mu}{\rho})_{mud}$	$(\frac{\mu}{\rho \cdot \rho \cdot l})_{mud}$	$(\frac{\mu}{\rho})_{Al}$	$(\frac{\mu}{\rho \cdot \rho \cdot l})_{Al}$	tw_{filter}
[keV]	**[cm^2·g^{-1}]**	**[-]**	**[cm^2·g^{-1}]**	**[cm^{-1}]**	**[cm]**
10	26,61	1.787,89	26,21	70,77	25,26
15	8,42	565,60	7,96	21,48	26,33
20	3,73	250,86	3,44	9,29	26,99
30	1,25	84,03	1,13	3,05	27,59
40	0,63	42,41	0,57	1,53	27,63
50	0,41	27,28	0,37	0,99	27,44
60	0,30	20,41	0,28	0,75	27,21
80	0,22	14,60	0,20	0,54	26,80
100	0,18	12,22	0,17	0,46	26,56
150	0,15	9,80	0,14	0,37	26,35
200	0,13	8,68	0,12	0,33	26,29
300	0,11	7,39	0,10	0,28	26,26
400	0,10	6,58	0,09	0,25	26,26
Average					26,69

as “a commonly used analytical approximation” (Forth et al., 2017) and compared frequently in literature with other more advanced (Monte Carlo) code and/or measurements like in Poludniowski et al. (2009) and Forth et al. (2017). SpekCalc can therefore be considered as a reliable tool for first estimations of the dose rate. Forth et al. (2017) mentions overestimation of 10% and underestimation up to 20% by SpekCalc, compared to other simulations and validation measurements.

Nonetheless, a validation of the outcome of SpekCalc with actual measurements was also performed, if only to verify the software is properly used and the output correctly interpreted. The measurements were performed using an X-ray source allowing a voltage up to 250 kV, fitted with a Beryllium window of 3 mm and a Copper filter of 2 mm. The electric current applied on the tube was 2 mA and the dose rates were measured at a distance of 2 m. These dose rates are compared to the dose rates calculated using SpekCalc (Table 3).

The results of the evaluation of the use of gamma sources imply that probably the more powerful X-ray generators are required for the intended application in mud. Therefore available X-ray generators used in the Non-Destructive Testing (NDT) industry were evaluated as they are less limited in power compared to generators for medical use. At first an X-ray generator with a high voltage range of 5—225 kV and a maximum current of 30 mA is considered. A schematic overview of the calculation procedure is presented as Supplementary Figure S3 in the Supplemental Data and the results in (Figure 6).

These results (Figure 6) confirm the importance of source activity prevailing over the photon energy level, as the considered X-ray generator shows the ability to visualize flows of 2 m·s^{-1} over significantly thicker mud layers up to 200 mm. Nonetheless 200 mm is still insufficient for the intended hydraulic test facility supporting the nautical bottom research (ref. Section 2.1 Radiography). The most powerful “freely” available X-ray sources in the NDT industry have a voltage capacity up to 450 kV and a maximum current of 30 mA. Because of its medical background, SpekCalc is however limited to a maximum voltage of 300 kV. By means of interpolation expected results for X-ray generators exceeding 300 kV can still be estimated. Doing so for 450 kV generators set at 30 mA, shows they are up to 33 times more powerful compared to a generator with a voltage capacity of 225 kV. Nonetheless, multiplying the dose rate at the detector by 33 the maximum mud layer thickness still remains too limited with 300 mm.

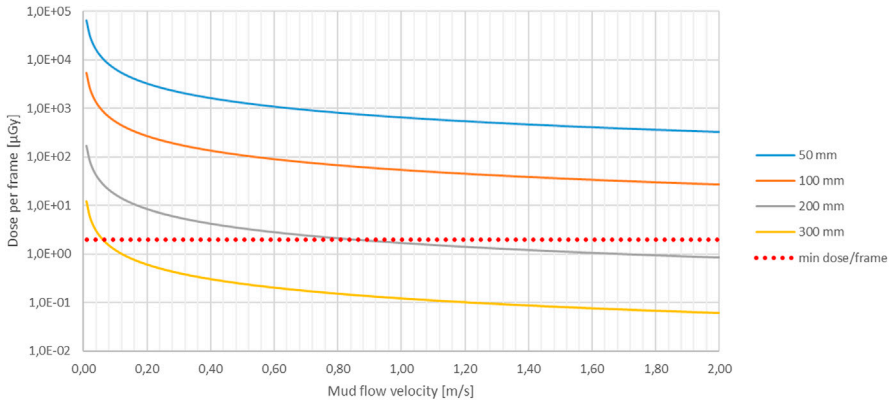

FIGURE 6
Radiation dose, originating from an X-ray 225 kV - 30 mA generator at max power, received by the detector (Figure 1A) during the time span allowed for per image frame. The time span is expressed as mud flow velocity, where a maximum mud particle displacement of 5 mm is allowed for between two consecutive frames. Increasing mud flow velocity decreases the radiation time span for each image frame, hence the dose received per image frame. Curves for different mud layer thicknesses varying from 50 mm to 300 mm are presented. The dotted red line indicates the minimum dose required per image frame for adequate image quality.

TABLE 3 Comparison of measured dose rates with calculated dose rates using SpekCalc software. Results show an underestimation of the calculated dose rate of 18–19%, which corresponds with the conclusions mentioned in Forth et al. (2017).

Peak Energy	Current	Dose rate (measured) at 2 m distance		Dose rate (calculated) at 2 m distance		Ratio
kV	[mA]	[R·min^{-1}]	[μGy·s^{-1}]	[μGy·mA^{-1}·s^{-1}]	[μGy·s^{-1}]	[-]
180	2	173	25,29	10,39	20,79	0,82
190	2	209	30,55	12,47	24,94	0,82
200	2	248	36,25	14,76	29,51	0,81
210	2	290	42,39	17,25	34,51	0,81
220	2	337	49,26	19,97	39,95	0,81
230	2	387	56,57	22,91	45,82	0,81
240	2	440	64,31	26,09	52,18	0,81
250	2	500	73,08	29,47	58,95	0,81

2.2 Ultrasonography

Although ultrasonography does not require full transmission of the ultrasound radiation through the mud layer (ref. Section 2 Potential flow visualization techniques in mud), knowledge of acoustic properties of mud are also required to allow estimation of the maximum depth to which images of adequate quality can still be produced. Other research related to the acoustic properties of mud, like Pierce et al. (2015), mention however the lack of any available and trustworthy data. Measurements to determine the acoustic properties of mud are therefore required to fully evaluate the potential of ultrasonography.

2.2.1 Ultrasound properties of mud

In the Port of Zeebrugge a device called the Admodus USP pro is used to measure the density of the mud layers using ultrasound (Claeys et al., 2012; Plancke et al., 2018). The density of mud is determined by measuring the speed of sound through mud and the acoustic impedance of mud, where density is the product of the two. In addition, the Admodus USP pro also measures the attenuation of mud over a frequency spectrum of 1.0 MHz–3.5 MHz. From the data of a survey campaign performed in February 2019 in the Port of Zeebrugge (Meire et al. (2021)), these acoustic properties were retrieved as a function of mud density ranging from 1.00 g·cm^{-3} to 1.30 g·cm^{-3}. The speed of sound through mud shows small

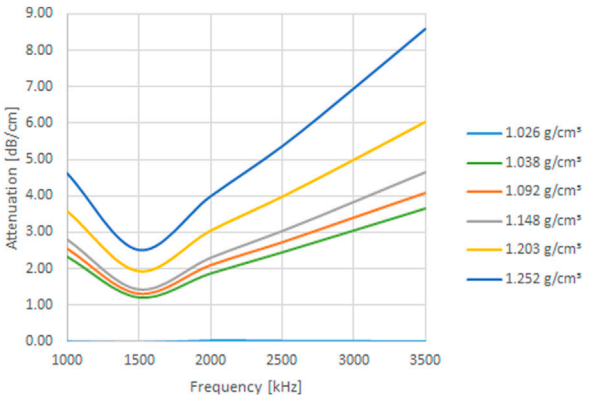

FIGURE 7
Attenuation values $\alpha_{(f)}$ of mud, as a function of ultrasound frequency and mud density. Values measured in Port of Zeebrugge using the Admodus USP pro [Meire et al. (2021)].

variation in this density spectrum, from 1,460 m·s^{-1} to 1,485 m·s^{-1}. Consequently, so does the acoustic impedance, ranging from 1,500 kg·m^{-2}·s^{-1} to 1900 kg·m^{-2}·s^{-1}. The measured attenuation values range over a wider spectrum as they are function of both mud density and ultrasound frequency (Figure 7).

Despite the knowledge of these values for attenuation and speed of sound, evaluation whether or not the use of ultrasound waves would allow for sufficient penetration and energy conservation to create images of adequate quality for the application of a velocimetry algorithm is still not possible. Like for all medical applications, an optimal compromise between penetration depth, field of view and the different types of resolution (axial, lateral and time) will need to be determined (Alexander and Swanevelder (2011)). Nonetheless, the fact that the speed of sound and attenuation of human tissue and organs as specified in Hendee and Ritenour (2002), are in the same order of magnitude as the aforementioned values for mud, gives confidence that such a compromise can be found within the limits of standard acoustic medical equipment for depths similar to those for medical applications ranging from 5 cm to 15 cm.

2.2.2 Ultrasound brightness scan of mud

An ultrasound brightness scan, or B-scan, is the most familiar mode of ultrasound imaging for medical purposes. Probably the best known example is a fetal scan during a pregnancy. The images are typically grayscale, where the brightness of a pixel is a measure for the amplitude of the reflected signal at the corresponding position in the insonified area. Therefore strong reflectors such as muscle tissue will appear bright, while fluids will appear dark. In order to see any distinction in an image created with a B-scan some variety in acoustic impedance, which causes reflection, is thus required. To evaluate whether or not mud complies with this requirement the results of the chemical element analysis can be re-used (Table 1), providing the different oxides present in mud. For some of these oxides, the acoustic impedance can be found in literature. While the strength of a reflected signal is determined by the reflection coefficient, the reflection coefficient in turn is related to the difference in acoustic impedance encountered during propagation (Eq. 5).

$$r_{ij} = \frac{Z_i - Z_j}{Z_i + Z_j} \tag{5}$$

Where r is the reflection coefficient [-], Z is the acoustic impedance [kg.m^{-2}·s^{-1}] and i and j are the indices referring to the encountered materials or media. Acoustic properties found in literature should always be used carefully as such values are very variable contingent upon the origin of the medium [Ginzel and Turnbull (2016)]. Acoustic impedance found for Al_2O_3, SiO_2 and H_2O show however a great variety in value (respectively 37.9 kg·m^{-2}·s^{-1}, 13.2 kg·m^{-2}·s^{-1} and 1.5 kg·m^{-2}·s^{-1} (Capilla et al., 2012; Sikorski, 2019)), while these oxides represent 74% weight percentage of mud with density 1.10 g·cm^{-3} (Table 1). This allows for the conclusion that significant reflections can be expected when an ultrasound wave is propagating through mud.

In wave physics there are different degrees of reflection depending on the ratio of the wavelength to the size of the reflecting object. While specular reflections are created by reflection on large objects, objects equal or smaller in size than the wavelength of the incident sound wave, will scatter the wave omni-directionally, resulting in much weaker reflection signals. The frequency range for this application is expected to be similar to those for medical imaging, ranging from 1 MHz to 10 MHz. With a speed of sound through mud of 1,460 m·s^{-1} this results in wavelengths ranging from respectively 1,460 μm–146 μm. While the particle size distribution of mud in the Port of Zeebrugge, determined using a Mastersizer 2000 [Malvern Instruments Ltd. (2007)], shows a range of particle sizes ranging from 0.3 μm to 120 μm and a D50 around 6.5 μm. The results are presented in Supplementary Figure S4 of the Supplemental Data. It can thus be concluded that the reflecting particles in mud will always be smaller compared to the applied ultrasound wavelengths. Insonification of mud within the aforementioned ultrasound frequency range will therefore always result in scattering of the ultrasound waves.

In turn there are also different scattering regimes with different characteristics. Which regime is applicable is again determined by the ratio of scatterer size over wavelength. Scatterers smaller in size compared to the wavelength of the incident soundwave, as expected for the intended application, act as isotropic scatterers. This scattering regime is referred to as diffusive or Rayleigh scattering. In case of a high concentration of

FIGURE 8
Setup of performed B-scan on mud: (1) bucket of mud with density 1.13 g·cm^{-3}, (2) 10L linear ultrasound array protected in a latex glove, (3) GE Vivid 7 ultrasound scanner. Apart from the array being immersed partly in the mud, the setup is in line with Figure 1B.

isotropic scatterers, a speckle-like signal will be created, as the scattered signals of each isotropic scatterer will reach the transducer over slightly different path lengths. This results in a so-called "Speckle Pattern" (Poelma, 2016), which in medical applications is typically created when scanning muscle tissue. This ratio between the size of the scatterer and the wavelength is expressed with the factor k. a where a is the radius of the scatterer [m] and k the wavenumber [m^{-1}], solely determined by the wavelength (Eq. 6).

$$k = \frac{2.\pi}{\lambda} \tag{6}$$

Where λ is the wavelength of the ultrasound wave [m]. According to Szabo (2004), diffusive scattering occurs when k. a $\leqslant$ 0.35. A lower limit is not mentioned. As scattering is a major contributor to the attenuation of sound waves, a lower bound for k. a must exist. In this case the scattered intensity becomes that small it is unable to reach back to the transducer before completely muted. With the determined particle size distribution of mud (Supplemental Data, Supplementary Figure S4), the diffusive scattering regime is therefore expected to be applicable when ultrasound frequencies of 1 MHz–10 MHz are used.

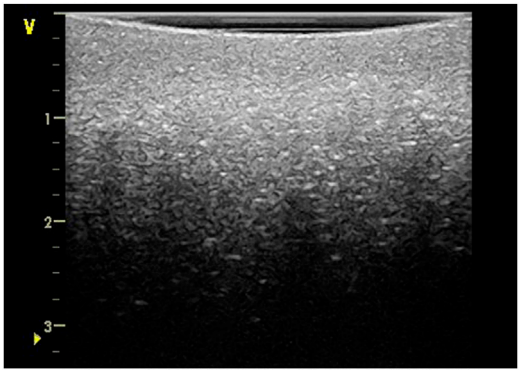

FIGURE 9
B-scan of mud with a ultrasound frequency set at 7 MHz, resulting in a clear speckle pattern due to interference scattered signals. Depth scale expressed in cm.

A small-scale test was performed at Ghent University Hospital, using a GE Vivid 7 ultrasound scanner equipped with a 10L linear array. For protection against the seawater present in mud, the array was inserted in a medical latex glove injected with acoustic gel to ensure good transmission of the ultrasound waves. This assembly was placed in a bucket of mud with a density of approximately 1.13 g·cm^{-3} (Figure 8). A B-scan of the mud was conducted with the ultrasound frequency set at 7 MHz.

The resulting image (Figure 9) confirms the expectation of a speckle pattern image due to diffusive scattering of the ultrasound waves. As elaborated by Szabo (2004), a speckle pattern arises from the constructive and destructive interference of a great amount of scatterers, which appears as a light and dark mottled grainy pattern. For many years users of ultrasound systems assigned a diagnostic value to the appearance of speckle and assumed it was tissue microstructure. Despite its deceiving appearance as a tissue texture speckle is however an illusion and an unwanted effect for medical imaging as it reduces both image contrast as the distinction of subtle gradations and boundaries in tissue structure. Nonetheless, there are also medical applications which make use of the created speckle patterns, such as the monitoring of muscle tissue movement (cardiology) or the recording blood flows. This technique is referred to as "speckle tracking" by Garcia et al. (2018).

3 Whole flow-field velocimetry techniques

In experimental fluid dynamics optical PIV is currently widely used to measure flow velocities (Raffel et al., 2007). Despite the availability of many other techniques such as hot wire anemometers, pitot tubes, electromagnetic sensors, acoustic

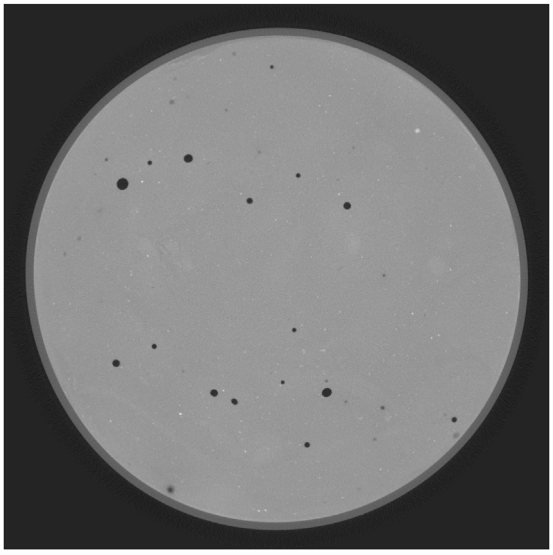

FIGURE 10
X-ray scan of mud. Apart from the black spots, the grayscale image is homogeneous. The black spots originate from entrapped air bubbles after disturbance of the sample.

velocimeters or other intrusive flow measurement probes. The advantage of optical PIV is that it does not require intrusive probing and consequently does not cause distortion of the fluid flow. In addition, optical PIV allows for the evaluation of an entire 2D or even 3D flow field, enhancing the efficiency and quality of laboratory experiments. Therefore, by seeking alternative techniques to visualize the dynamics in mud, the intent of this research is to preserve these benefits of whole flow-field velocimetry techniques like optical PIV, while working in mud.

Optical PIV emerged from the earlier development of the (laser) speckle velocimetry (Garcia et al., 2018) and is based on the scattering of a laser's light waves on particles seeded to the fluid, enabling visualization of the particles with an optical camera. The difference with the original speckle velocimetry is the scattering regime. Optical PIV acts in the Mie scattering regime, resulting in visualization of particles and not the interferences of multiple scattered waves, resulting in speckle patterns (Garcia et al., 2018). Adaptation of the optical PIV technique to be used with ultrasound imaging was conducted by Bohs and Trahey (1991) with the objective to obtain velocity vector fields in the blood circulation and strain imaging (muscle tissue movement). Because of far larger wavelengths of ultrasound waves used for ultrasound imaging, scattering of the ultrasound waves acts in the Rayleigh scattering regime, making it a resurgence of speckle velocimetry. When speckle velocimetry is applied to contrast-enhanced blood images (by addition of micro bubble particles) the technique is generally called "Echo PIV", while when scattering is caused by scatterers present in the insonified tissue the technique is referred to as "speckle tracking" (Garcia et al., 2018).

Pursuant to the aforementioned elaboration of radiography and ultrasonography applied on mud, PIV can be applied on the images generated with radiography, while speckle tracking can be used on the images generated with ultrasonography.

3.1 Particle image velocimetry on radiographic images

Although radiography is deemed to be insufficient for the required mud thickness and flow velocities for nautical research, for other applications radiography may still be an option. To evaluate its potential use, an X-ray scan of a mud sample was conducted. The result of this scan is shown as Figure 10. The image shows that without the addition of contrast agents (e.g., the air bubbles which can be seen on the image as black dots), an X-ray scan of mud results in a homogeneous grayscale image, unsuited for the application of tracking algorithms. The black dots, originating from entrapped air bubbles, do can be used to be tracked. The air bubbles are the result of unwanted disturbance of the sample prior to the scan. However, due to their upward movement air bubbles influence the consolidation process, hence the behavior of mud. Therefore, when studying the dynamics in mud layer, the presence of air bubbles should be avoided. Thus, despite their suitability for tracking, the use of air bubbles cannot be considered in mud.

Seeding the mud with tracing particles like in a conventional experimental setup for PIV recording (Raffel et al., 2007) is also not preferred. Ideally the particles added to the fluid are neutrally buoyant, ensuring their movement is solely caused by the flows in the fluid. In case of mud the density however changes over time, making it impossible to guarantee this aspiration, and undermining the credibility of the measurements. Furthermore, Manning and Whitehouse (2009) has shown that a change in sand fraction present in mud influences the flocculation and consolidation process of the mud. Because it is reasonable to assume that the presence of seeding particles will have a similar influence on the mud as sand particles, it can be questioned whether or not seeded mud still represents the mud of interest. For applications where these conditions do not apply [e.g., measurement of rheological parameters using a rheometer (Claeys et al., 2015)], flow velocity measurements can be performed using radiography and PIV.

3.2 Speckle tracking on ultrasonographic images

The aforementioned small-scale test using a standard medical ultrasound scanner on mud (Figures 8, 9) showed that the addition of seeding particles is uncalled for. Mud already contains a sufficient amount of small reflectors (scatterers) resulting in speckle pattern images suitable for the application of

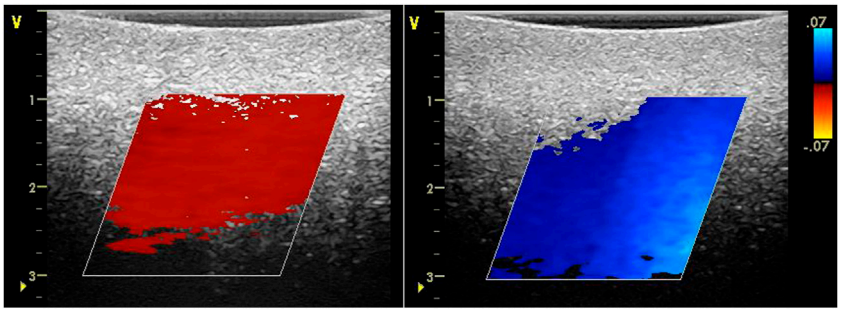

FIGURE 11
Screenshots during recording of induced flows with speckle tracking application. Depth scale in cm. Velocity scale in m·s^{-1}.

velocimetry algorithms, such as speckle tracking. To put this to the test a flow was induced in the mud bucket by moving a kitchen spoon back and forth. The spoon was at sufficient depth (> 3 cm) below the array to ensure it was out of reach of the ultrasound waves (Figure 9). With the use of the speckle tracking application the scanner was able to record these induced flows as depicted in the 2 screenshots of the scanner (Figure 11), where the ensuing velocity vectors are plotted in a color scale in front of the B-mode speckle images. The blue and red colored vectors indicate similar flow velocities with opposite sign corresponding to the induced flows.

Unlike for medical applications, visualization of flows in mud does not require a clear distinction between different tissues or revealing tissue boundaries. Minimal requirements on lateral resolution are therefore not required, which allows to lower the ultrasound frequency (Alexander and Swanevelder (2011)) in order to increase the penetration depth. Lowering the frequency however lowers the wavenumber k (Eq. 6), while there will be a minimum value for the factor k.a as from where the scattering intensity becomes too low to be of any further use. Assuming the scatterers can be considered as rigid spheres, Szabo (2004) presents Eq. 7 for the Rayleigh scattering regime, showing the great influence of the ultrasound frequency (4^{th} power) and the scatterer radius (6^{th} power) on the scattering intensity. This shows the requirement to find a new compromise between penetration depth and ultrasound frequency while considering the minimal scattering intensity as an additional restriction. Because of the origin of speckle, the speckle quality is also dependent on the amount of scatterers present. As the latter is impossible to determine this new compromise will need to be determined experimentally.

$$\frac{I_s}{I_i} = \frac{k^4.a^6}{9.r^2}.\left[1 - \frac{3.\cos\phi}{2}\right] \tag{7}$$

Where I_s is the scattering intensity [W·m^{-2}], I_i is the incoming intensity [W·m^{-2}], k is the wavenumber [m^{-1}], a is the scatterer radius [m], r is the distance to the scatterer [m] and ϕ the scattering angle [rad].

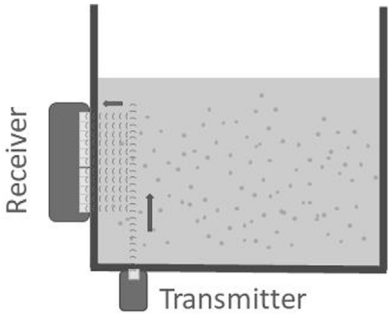

FIGURE 12
Sketch of an alternative setup for ultrasonography using two transducers, one as transmitter and a second as receiver.

The relation between the scattering angle ϕ and the scattering intensity I_s might also allow for alternative setups. Eq. 7 shows the bi-polar scattering pattern with maximal intensities at $\phi = 0$ (forward scattering) and $\phi = \pi$ (backscattering). For medical applications this is of course an advantage as it allows the use and flexibility of only one transducer while preserving maximal efficiency. For a stationary setup this flexibility is however of no use, while working in an angle by means of a second transducer is perfectly feasible (Figure 12). In such a setup one transducer would be used as a transmitter and the other transducer as the receiver. Compared to a setup with one transducer switching continuously between the two (Figure 1B) a setup with two transducers would allow for an increase in frame rate. In addition, working in an angle can allow optimization of the propagation path, decreasing the required penetration depth or even allow for evaluation of a 3D flow field. According to Eq. 7, the intensity will decrease with a factor 6.25 when working in an angle $\phi = \pi/2$. Such a decrease in intensity can be compensated with an increase in frequency, e.g., 1 MHz–1.58 MHz. This will however lead again to higher

attenuation, hence a decrease in penetration depth. Knowing the attenuation values of mud over the entire frequency range of interest will therefore be of great use to in order to evaluate whether or not the benefits of working in an angle are worth the decrease in penetration depth.

4 Conclusion

This paper presents the evaluation methods and results for the application of known visualization techniques on mud. Because of some essential resemblances inspiration was found in the medical sector (ref. Section 2 Potential flow visualization techniques in mud), resulting in the selection of radiography and ultrasonography.

Review of the application of radiography on mud showed however that the technique is not efficient enough to be used in typically larger hydraulic research facilities. Even with the use of the most powerful radiation sources available on the market, either the mud layer thickness or the flow velocity should be limited in such a way that they are no longer relevant for the intended hydraulic research. Furthermore, the requirement to seed the mud with tracing particles to enable the application of PIV was demonstrated. Seeding with particles is however likely to influence the behavior of mud, making the reliability of the results questionable. In addition, the costs (direct and indirect) for the use of such radiation sources (above 100 kEUR) probably exceed most available budgets for hydraulic research projects. Nonetheless there are still applications (e.g. measurement of rheological parameters) for which these drawbacks might not apply and radiography together with PIV can be used.

As ultrasonography does not require full penetration of the mud layer. The focus to evaluate this technique is on finding a compromise between the penetration depth, frame rate and image quality. With a small-scale test it was shown that a common medical ultrasound scan of mud results in a so-called “speckle pattern”. Although speckle patterns are an unwanted feature for medical diagnostics, they are also used to track tissue movement or blood flow, known as “speckle tracking”. With the same small-scale setup speckle tracking was applied while inducing flows in the mud, demonstrating its ability to record and visualize the induced flows and determine flow velocities. Furthermore, the stationary deployment on hydraulic test facilities might provide the opportunity for alternative setups of ultrasound equipment, allowing to optimize its efficiency or even 3D flow field evaluation. Further customization of ultrasonography for application on mud in hydraulic test facilities will require the determination of attenuation values over a wide frequency range. Such data is however currently unavailable and therefore needs to be determined experimentally.

Data availability statement

Additional data is provided in the article/Supplementary Material, further inquiries can be directed to the corresponding author.

Author contributions

BB conducted the study and experiments and wrote the article. DM, JvB, and EL provided critical feedback and helped shape the research, analysis and manuscript.

Funding

This research is promoted by Flanders Hydraulics Research (FHR) and supported by the Maritime Technology Division of Ghent University in collaboration with the von Karman Institute for Fluid Dynamics (VKI). The joint research project of Maritime Technology Division, FHR and KU Leuven (Sotelo et al., 2022) is the incentive of this research.

Acknowledgments

The author is grateful to these institutions for the opportunity to conduct this research.

Conflict of interest

The authors declare that the research was conducted in the absence of any commercial or financial relationships that could be construed as a potential conflict of interest.

Publisher’s note

Supplementary material

The Supplementary Material for this article can be found online at: https://www.frontiersin.org/articles/10.3389/feart.2022.878102/full#supplementary-material

References

Alexander, N., and Swanevelder, J. (2011). Resolution in ultrasound imaging. *Continuing Educ. Anaesth. Crit. Care & Pain* 11, 186–192. doi:10.1093/bjaceaccp/mkr030

Berger, M. J., Hubbell, J. H., Seltzer, S. M., Chang, J., Coursey, J. S., Sukumar, R., et al. (2010). *Xcom: Photon cross sections database*. Gaithersburg, MD: National Institute of Standards and Instruments, Physical Measurement Laboratory, Radiation Physics Division.

Berlamont, J., Ockenden, M., Toorman, E., and Winterwerp, J. (1993). The characterisation of cohesive sediment properties. *Coast. Eng.* 21, 105–128. doi:10.1016/0378-3839(93)90047-C

Bohs, L. N., and Trahey, G. E. (1991). A novel method for angle independent ultrasonic imaging of blood flow and tissue motion. *IEEE Trans. Biomed. Eng.* 38, 280–286. doi:10.1109/10.133210

Burcu, A., and Salih, Z. E. (2014). The mass attenuation coefficients, electronic, atomic, and molecular cross sections, effective atomic numbers, and electron densities for compounds of some biomedically important elements at 59.5 kev. *Sci. Technol. Nucl. Installations* 2014, 8. doi:10.1155/2014/901465

Capilla, J., Olivares, J., Clement, M., Sangrador, J., Iborra, E., and Devos, A. (2012). High-acoustic-impedance tantalum oxide layers for insulating acoustic reflectors. *IEEE Trans. Ultrasonics, Ferroelectr. Freq. Control* 59, 366–372. doi:10.1109/tuffc.2012.2205

Cember, H., and Johnson, T. E. (2008). "Radiation safety guides," in *Introduction to health physics*. Fourth edition (New York City, NY: McGraw-Hill Education).

Claeys, S., Dierikx, B., Paul, S., and Reenen, J. (2012). "Fluid mud density determination in navigational channels," in *Hydro12 - taking care of the sea*. Rotterdam, Netherlands: Hydrographic Society Benelux. doi:10.3990/2.228

Claeys, S., Staelens, P., Vanlede, J., Heredia, M., Van Hoestenberghe, T., Van Oyen, T., et al. (2015). "A rheological lab measurement protocol for cohesive sediment," in *Proceedings of INTERCOH2015: 13th international conference on cohesive sediment Transport processes*. Editor E. Toorman (Leuven, Belgium: VLIZ Special Publication), 74, 20–21.

de Wit, P. (1995). *Liquefaction of cohesive sediments caused by waves*. Delft: University Press.

Delefortrie, G., and Vantorre, M. (2009). Prediction of the forces acting on container carriers in muddy navigation areas using a fluidization parameter. *J. Mar. Sci. Technol.* 14, 51–68. doi:10.1007/s00773-009-0041-x

Delefortrie, G., and Vantorre, M. (2016). *Ship manoeuvring behaviour in muddy navigation areas : State of the art*. Hamburg, Germany: Bundesanstalt für Wasserbau, 26–36. doi:10.18451/978-3-939230-38-0_4

Delefortrie, G., Vantorre, M., Verzhbitskaya, E., and Seynaeve, K. (2007). Evaluation of safety of navigation in muddy areas through real-time maneuvering simulation. *J. Waterw. Port Coast. Ocean Eng. - ASCE* 133, 125–135.

Forth, L., Speller, R., and Moss, R. (2017). "The importance of accurate x-ray energy spectra for modelling dose deposition with Monte Carlo techniques," in *IEEE nuclear science symposium and medical imaging conference* (Atlanta, GA: NSS/MIC), 1–2. doi:10.1109/NSSMIC.2017.8533113

Gao, Z., Yang, H., and Xie, M. (2015). Computation of flow around wigley hull in shallow water with muddy seabed. *J. Coast. Res.* 73, 490–495. doi:10.2112/SI73-086.1

Garcia, D., Lantelme, P., and Saloux, E. (2018). "Chapter 26: Introduction to speckle tracking in cardiac ultrasound imaging," in *Handbook of speckle filtering and tracking in cardiovascular ultrasound imaging and video*. London, United Kingdom: Institution of Engineering and Technology (IET). doi:10.1049/PBHE013E_ch26

Ginzel, E., and Turnbull, B. (2016). Determining approximate acoustic properties of materials. *e-Journal Nondestruct. Test. (NDT) 21* 21 (12), 23–33. doi:10.1002/jgrc.20103

Hendee, W. R., and Ritenour, E. R. (2002). "Ultrasound waves," in *Medical imaging physics* (New York: Wiley-Liss). doi:10.1002/0471221155.ch19

Hsu, W. Y., Hwung, H. H., Hsu, T. J., Torres-Freyermuth, A., and Yang, R. Y. (2013). An experimental and numerical investigation on wave-mud interactions. *J. Geophys. Res. Oceans* 118, 1126–1141. doi:10.1002/jgrc.20103

IEC 62220-1-3:2008 (2008). *Medical electrical equipment - characteristics of digital X-ray imaging devices - Part 1-3: Determination of the detective quantum efficiency - detectors used in dynamic imaging*. Geneva, Switzerland: International Electrotechnical Commission.

Kaidi, S., Lefrançois, E., and Smaoui, H. (2020). Numerical modelling of the muddy layer effect on ship's resistance and squat. *Ocean. Eng.* 199, 106939. doi:10.1016/j.oceaneng.2020.106939

Lovato, S., Keetels, G. H., Toxopeus, S. L., and Settels, J. W. (2022). An eddy-viscosity model for turbulent flows of herschel–bulkley fluids. *J. Newt. Fluid Mech.* 301, 104729. doi:10.1016/j.jnnfm.2021.104729

Malvern Instruments Ltd. (2007). *Mastersizer 2000 user manual (MAN0384-1.0)*. Worcestershire WR14 1XZ, United Kingdom: Author.

Manning, A. J., and Whitehouse, R. J. S. (2009). "Uop mini-annular flume – operation and hydrodynamic calibration," in *HR Wallingford technical report, TR 169*. London, United Kingdom: IntechOpen.

Mayerhöfer, T., Pahlow, S., and Popp, J. (2020). The bouguer-beer-lambert law: Shining light on the obscure. *Chem. Phys. Chem.* 21, 2029–2046. doi:10.1002/cphc.202000743

McGinnis, R. (2009). *Rad pro calculator*. Available at: http://www.radprocalculator.com/ (Accessed June, 2020).

Meire, D., Claeys, S., De Maerschalck, B., and Mostaert, F. (2021). "Evaluatie van meetinstrumenten voor de bepaling van slib karakteristieken: Deelrapport 3: Meetcampagne februari 2019," in *Versie 5.0. WL rapporten, 18_059_3* (Antwerpen: Waterbouwkundig Laboratorium), 1–49.

Meshkati Shahmirzadi, M. E., Staelens, P., Claeys, S., Cattrysse, H., Van Hoestenberghe, T., Van Oyen, T., et al. (2015). "Experimental investigation on consolidation behaviour of mud: Subreport 1- methodology study," in *Versie 5.0. WL rapporten, 12_082* (Antwerp: Flanders Hydraulics Research), 26.

Pierce, A. D., Siegmann, W. L., and Brown, E. (2015). "Analytical discussion of past measurements of acoustic attenuation in mud sediments and of possible future experimental approaches," in *Proceedings of meetings on acoustics*. Jacksonville, FL: Acoustical Society of America. doi:10.1121/2.0000221

Pirola Igoa, E., Ibanez, M., Claeys, S., Meire, D., and Mostaert, F. (2020). "Experimental investigation on the consolidation behaviour of mud: Port of hamburg," in *Versie 3.0. FHR reports, 18_009_1* (Antwerp: Flanders Hydraulics Research), 42 + 17.

Plancke, Y., Meire, D., and Mostaert, F. (2018). "Studie naar meettechnieken voor het onderzoeken van de opbouw van sliblagen in het deurganckdok: Deelrapport 1 – bundeling van de belangrijkste resultaten uit 3 masterproeven uitgevoerd op de universiteit antwerpen," in *Versie 3.0. WL rapporten, 12_160_1* (Antwerpen: Waterbouwkundig Laboratorium), 201–213.

Poelma, C. (2016). Ultrasound imaging velocimetry: A review. *Exp. Fluids* 58, 3. doi:10.1007/s00348-016-2283-9

Poludniowski, G. (2007). Calculation of x-ray spectra emerging from an x-ray tube. part ii. x-ray production and filtration in x-ray targets. *Med. Phys.* 34, 2175–2186. doi:10.1118/1.2734726

Poludniowski, G., and Evans, P. (2007). Calculation of x-ray spectra emerging from an x-ray tube. part i. electron penetration characteristics in x-ray targets. *Med. Phys.* 34, 2164–2174. doi:10.1118/1.2734725

Poludniowski, G., Landry, G., Deblois, F., Evans, P., and Verhaegen, F. (2009). Spekcalc: A program to calculate photon spectra from tungsten anode x-ray tubes. *Phys. Med. Biol.* 54. doi:10.1088/0031-9155/54/19/N01

Pouv, K. S., Besq, A., and Guillou, S. (2012). Rheometric study for elaborating transparent model cohesive sediments for local investigations of erosion behaviour. *Rev. paralia* 5, 1.1–1.14. doi:10.5150/revue-paralia.2012.001

Pouv, K. S., Besq, A., Guillou, S., and Toorman, E. A. (2014). On the cohesive sediment erosion: A first experimental study of the local processes of transparent model materials. *Adv. Water Resour.* 72, 71–83. doi:10.1016/j.advwatres.2014.05.012

Raffel, M., Willert, C., Wereley, S., and Kompenhans, J. (2007). *Particle image velocimetry: A practical guide*. 2nd edition. New York: Springer.

Ripan, B., Hossain, S., Abdus, S. M., and H, M. F. (2016). Calculation of gamma-ray attenuation parameters for locally developed shielding material: Polyboron. *J. Radiat. Res. Appl. Sci.* 9, 26–34. doi:10.1016/j.jrras.2015.08.005

Sikorski, W. (2019). Development of acoustic emission sensor optimized for partial discharge monitoring in power transformers. *Sensors* 19, 1865. doi:10.3390/s19081865

Soltanpour, M., Shamsnia, S. H., Shibayama, T., and Nakamura, R. (2018). A study on mud particle velocities and mass transport in wave-current-mud interaction. *Appl. Ocean Res.* 78, 267–280. doi:10.1016/j.apor.2018.06.019

Sotelo, M. S., Boucetta, D., Doddugollu, P., Toorman, E., Brouwers, B., Van Hoydonck, W., et al. (2022). "Experimental study of a cylinder towed through natural mud," in *Proceedings of MASHCON 2022: 6th international conference - port manoeuvres* (Ghent, Belgium: Ghent University). [Unpublished manuscript].

Szabo, T. L. (2004). "Wave scattering and imaging," in *Diagnostic ultrasound imaging: Inside out* (Elsevier Academic Press).

Toorman, E., and Berlamont, J. (2015). "Fluid mud in waterways and harbours: An overview of fundamental and applied research at ku leuven," in *PIANC yearbook 2015* (Brussels, Belgium: PIANC), 211–218.

Vanlede, J., Toorman, E., Liste Muñoz, M., Rocabado, I., Heredia, M., Delefortrie, G., et al. (2014). "Towards cfd as a tool to study ship-mud interactions," in *Oceanology international* (Flanders Hydraulics Research). Poster.

Vantorre, M. (1997). "Approach channels - a guide for design," in *Ptc 11-30: Final report of joint working group PIANC-IAPH II, in cooperation with IMPA and I ALA. Supplement to PIANC Bulletin no. 95* (Brussels, Belgium: PIANC), 108.

VEGA Americas, Inc. (2017). Operating Instructions VEGASOURCE 35 Source holder. Schiltach, Germany: VEGA Grieshaber KG.

Wang, T. (2004)."Inductively coupled plasma optical emission spectrometry" in *Analytical instrumentation handbook*. Third Edition, 57–74.

Zaynab, T., Jarny, S., and Texier, A. (2015). "Rheology and local study of a transparent model cohesive sediment," in *INTERCOH2015: 13th international conference on cohesive sediment Transport processes*. Editor E. A. Toorman (Leuven, Belgium: VLIZ Special Publication), 74, 7–11.

frontiers | Frontiers in Earth Science

TYPE Original Research
PUBLISHED 17 January 2023
DOI 10.3389/feart.2022.898312

OPEN ACCESS

EDITED BY
Andrew James Manning,
HR Wallingford, United Kingdom

REVIEWED BY
Hongjian Zhu,
Yanshan University, China
Venkatramanan Senapathi,
Alagappa University, India

*CORRESPONDENCE
Yuanyou Xia,
xiayy1965@whut.edu.cn
Dianji Zhang,
dianjizhang@wit.edu.cn

SPECIALTY SECTION
This article was submitted to Sedimentology, Stratigraphy and Diagenesis,
a section of the journal
Frontiers in Earth Science

RECEIVED 13 April 2022
ACCEPTED 31 October 2022
PUBLISHED 17 January 2023

CITATION
Pan D, Xia Y, Zhang D, Chen X, Wu Q, Lin M, Wang Z and Pan J (2023), Using Maxwell's Theory to model and quantify the fracture evolution of cyclothymic deposition phosphate rock.
Front. Earth Sci. 10:898312.
doi: 10.3389/feart.2022.898312

Using Maxwell's Theory to model and quantify the fracture evolution of cyclothymic deposition phosphate rock

Deng Pan[1,2], Yuanyou Xia[1]*, Dianji Zhang[3]*, Xuyong Chen[2], Qiaoyun Wu[2], Manqing Lin[3], Zhangqiong Wang[2] and Jun Pan[4]

[1]School of Civil Engineering and Architecture, Wuhan University of Technology, Wuhan, China, [2]School of Civil Engineering and Architecture, Wuhan Institute of Technology, Wuhan, China, [3]School of Xingfa Mining Engineering, Wuhan Institute of Technology, Wuhan, China, [4]School of Foreign Languages, Wuhan Institute of Technology, Wuhan, China

The evolution and stability of fracturing in the cyclothymic deposition of phosphate rocks are strongly affected by the viscoelasticity and structural form of the rock-forming minerals. Presently, there is no standardized method that has been widely accepted to accurately quantify the elastic-plastic deformation and fracturing of such striped structural rock nor reflect the role of the different lithogenous minerals in phosphate rocks when subjected to viscoelastic strain loading. In this study, integrated mathematical equations were formulated for modelling the mechanical and fracture behaviour of cyclothymic deposition in structured phosphate rocks. These constitutive equations were developed based on Maxwell's Theory after the elastic modulus and damping coefficient of the rock-forming mineral from the mechanical testing were substituted into the derived-equations. In these new models, the apatite stripes and dolomite stripes were incorporated into the transverse isotropic model through the analysis of structural characteristics of the phosphate rock. Through experimental validation, the response curves of the creep and stress relaxation tests were found to be consistent with the deformation curves generated by modelling using the mathematical equations. Overall, the formulated model along with the corresponding equations was found to exhibit good applicability properties to describe phosphate's mechanical and fracture behaviour under low horizontal compressive stresses. In the study, the creep mechanism in phosphate rocks were satisfactorily analysed from the angles of microscopic morphology, cracks evolution, and inter-crystalline strength. The hard brittle apatite was found to be surrounded and separated by high creep variant dolomite. Furthermore, the analysis showed that dolomite crystals possessing high creep properties dominated the distribution and evolution of secondary structures in the phosphate rock, under the condition of long-term low-stress loading.

KEYWORDS

cyclothymic deposition structure, elastic-plastic deformation, creep coefficient, elastic modulus, fracture, cracking, apatite stripe, dolomite stripe

Introduction

Due to the widespread usage of phosphate rocks in industrial and agricultural applications, numerous studies have been conducted on the correlation-ship between the mechanical behaviour of the phosphate rock mass and its petrologic properties. Some studies have shown that the thermal and physical stresses in granites, quite often, lead to the initiation and propagation of the cracks (Homand-Etienne and Houpert, 1989; Chen et al., 2010; Li et al., 2015; Zhao et al., 2022). Through the analysis of microcrack anisotropy evolution in deep mining phosphate rocks, it has been confirmed that intergranular fracture is the main grain boundary damage type, and, that the weak grain boundary surface is the contact boundary between dolomite and colloidal phosphate (Zhao et al., 2015; Tu et al., 2017; Bond and Zikry, 2018; Hurai et al., 2022; Zhang et al., 2022).

Regional differences in the petrographic type and the effective mineral quality of the phosphate rock has also inherently led to studies focusing on the formation conditions and mechanical properties of phosphate (Nguidi et al., 2021). Specifically, focus has been on the influence of the ancient geographical environment on the formation of inter-crystalline strength of the rocks (Priyank et al., 2015; Qin et al., 2015; Zhang et al., 2015; Han et al., 2016; Pan et al., 2017; Orlov et al.,2020). These studies have shown that the basic mechanical behaviour of rocks is influenced by the mineral composition, structure type, and formation conditions. But other literature suggests otherwise, the viscoelastic and rheological properties of ribbon structured rocks under low-stress levels have resulted in a series of safety accidents and property losses including instability of roadways and drill pipe sticking (Kounadis, 2014; Zhang et al., 2014). Although, in addition to providing a mathematical model to link the elastoplasticity of rocks to their mechanical behaviour, Maxwell's Theory also provides a model for relating the rate of damping to the elastic modulus of cracks (Shen and Chen, 2006). However, this is only applicable to homogeneous rocks.

So based on the above background, more research is needed to build a more comprehensive mechanical model to accommodate non-homogeneous rocks, which not only considers characterizing and quantifying the response behaviour of sedimentary rocks with a horizontal bedding structure, but also reflects the viscoelastic and rheological properties of dolomite and apatite. In particular, this has a practical significance when it comes to selecting appropriate cost-effective and safe mining techniques for phosphate rocks.

As presented in this paper, strip-type phosphorus block rocks were used as the test subject of the study. By using a rock triaxial apparatus, the constative modelling of phosphate rock's elastic and rheological properties under external loading can be accomplished based on Maxwell's Theory (Maxwell, 1881) through the triaxial test.

The experimental research plan for the study comprised of a six-step work schemes. These steps are described in the subsequent text.

The first step of the work scheme involved identifying the banding phosphate rock type, which was sourced from Yichang Xingfa Group Co., Ltd. in China. The composition and tectonic characteristics of phosphate rock were analysed using an electron microscopy.

The second step of the work scheme involved quantifying the mechanical characteristics of the phosphate rock, the mining roadway wall, and identifying the boundary conditions. Constitutive equations for modelling the mechanical properties of phosphate rock ribbon structure was conceptualized based on the Maxwell Theory of rheology and viscoelastic media.

The third step of the work scheme. The chemical components and micro-morphology were analysed using an X-ray fluorescence ADVANT'XP and a Scanning Electron Microscope, all acquired from Japan.

The fourth step of the work scheme. Preliminary testing was conducted in accordance with the American GCTS rock mechanics test specification (GCTS, 2020) to measure and quantify the mechanical properties of the phosphate rock including the elastic modulus, Poisson's ratio, and the viscous-damping coefficient. The tested phosphate rocks comprised of carbon-fluorine apatite and dolomite, respectively. Thereafter, the measured laboratory test data were used as input parameters in the preliminary conceptual model for formulating and developing the final constitutive model for the depositional-belt type phosphatic rock.

The fifth step of the work scheme. The mineral phosphate rock's mechanical test response-curve was verified and compared with the phosphate rock's deformation that was estimated using the constitutive model. The model prediction accuracy was accordingly judged and ascertained from a comparison of the test response-curves and model deformation predictions, respectively.

The sixth step of the work scheme. The loaded-deformation mechanism of the belt type phosphatic rock was analysed lastly, essentially from the angle of a lattice constant and fracture evolution.

Geological properties of phosphate rock

Geologically, the banded phosphate rock found in central China has a high degree of crystallization, hard texture, and a horizontal bedding structure. As can be seen in Figure 1, it has the typical horizontal bedding structure of a sedimentary rock. Geological survey data have shown that the phosphate rock mineral is predominantly composed of sedimentary and metasomatism phosphate on the edge of the craton that was

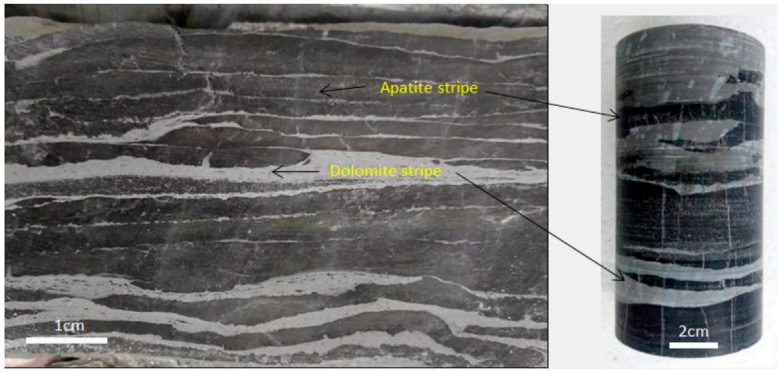

FIGURE 1
Cyclothymic deposition structure of phosphate rock.

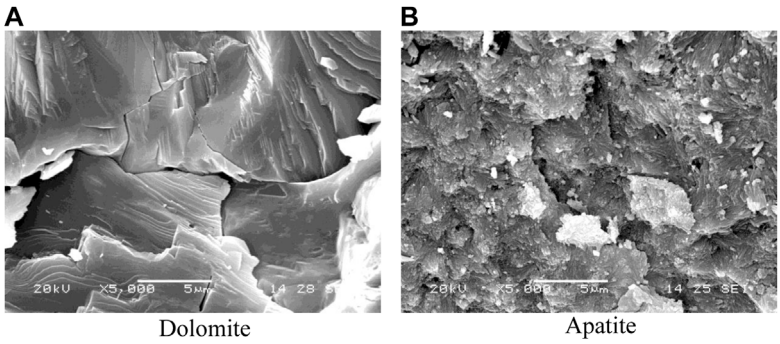

FIGURE 2
SEM image of Dolomite and Apatite. **(A)** Dolomite **(B)** Apatite.

formed during the sinian period, after a series of mineralization processes such as deposition, transformation, and enrichment (Andrieux and Aminot, 2001; Cao et al., 2011). In phosphate, rock apatite usually occurs with siliceous shale and/or carbonate interlayer. The thickness of a single-layer ranges from 1 cm to several meters—see Figure 1. The average burial depth of the ore beds is 800 m. The seam dip angle is less than 5°. The stress level is usually low and equivalent to 10%–20% of the peak stress from the rock strength test because the tectonic stress is mainly controlled by the overburdened rock mass. Furthermore, the rock mass did not show any signs of accelerated creep destruction, which corresponds to the stable creep state expressed by the Maxwell model (Maxwell, 1881).

Apatite's grain aggregate presents dense clumps and is colourlessly transparent. However, the apatite in the sedimentary rock is dark grey because of silicon. The hardness and relative density are 5.0 and 3.2, respectively (Ma, 2011; Levasseur et al., 2015). Although the dolomite crystal lattice belongs to the hexagonal system just like apatite, its hardness and relative density are 3.7 and 2.75, respectively. From the SEM (scanning electron microscope) test results, it is clear that the crystal lattices of the dolomite are small and orderly arranged, and that the apatite's lattices are presently bulkier and mutually interlocked—see Figure 2. To set up the perspective for the mathematical model, the phosphate rock band structure was simplified by superimposing it with dolomite and apatite.

Formulation of the mechanical model

Combined with the physical and structural characteristics of the aforementioned banded phosphate rock (Yang and Xiao, 2019), phosphate rock specimens were modelled as an axial superposition of different thickness mineral belts. The thickness of each mineral belt was assumed to be a constant value in the horizontal direction as exemplified in Figure 3. Since each mineral belt was kept in a series condition, the axial stresses were correspondingly equal in each mineral belt. Therefore, the model's total strain produced by stress loading was considered to be comprised of every mineral belt's strain when the axial

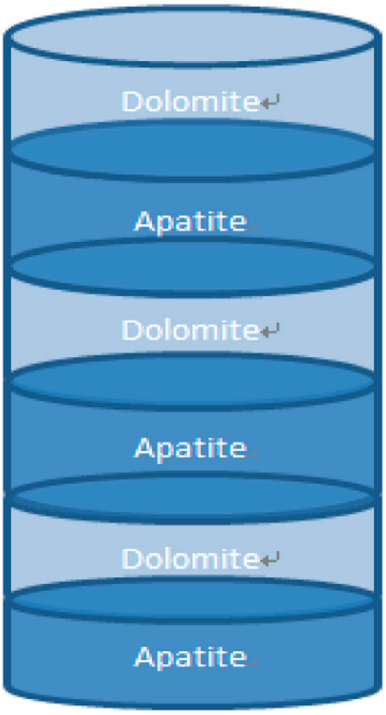

FIGURE 3
Ribbon structure of an ideal model.

compression load is acting on both ends of the model. Furthermore, the longitudinal deformation of the rock mass was determined as a function of the deviatoric stress, which is essentially the difference in the value of the maximum and minimum principal stresses as expressed in Eq. 1:

$$\sigma = \sigma_e = \sigma_v = \sigma_1 - \sigma_3 \tag{1}$$

On the other hand, every mineral belt's strain is comprised of the summation of the elastic strains ε_e and plastic strains ε_v, respectively (Shen and Chen, 2006). The strain summation as derived based on Maxwell's Theory is illustrated in Eq. 2:

$$\varepsilon = \varepsilon_e + \varepsilon_v \tag{2}$$

Where ε is the total strain, and ε_e and ε_v are elastic and plastic strains, respectively. The differential equation for the phosphate rock strain rate after differentiating Eq. 2 is shown in Eq. 3 as follows:

$$d\varepsilon/dt = d\varepsilon_e/dt + d\varepsilon_y/dt \tag{3}$$

The change rate to the time of elastic strains was derived as expressed in Eq. 4 below:

$$d\varepsilon_e/dt = d\sigma_e/(Edt) \tag{4}$$

In Eqs 5a–ca–cEqs 5a–c, the symbols η_d and η_a are the sticking factor for the dolomitic and apatite ribbons, respectively. The elasticity modulus of the ribbon structure model was assumed to be the weighted mean of the elasticity modulus based on the thickness summation shown in Eq. 6. In the model formulation, the four lengths were first selected, which are 90° apart from each other in the circumferential direction. Each length is equalled to 2 mm a measured with a ruler. Secondly, the thickness of the dolomitic ribbon H_{d1}~ H_{d4} and the thickness of the apatite ribbon H_{a1}~ H_{a4} were measured. The number of dolomitic and the apatite ribbons were each measured in length and multiplied by 2 mm, respectively. The thickness of the dolomitic ribbon H_d and apatite ribbon H_a of the test specimens were thereafter calculated according to Eqs 5a,b (Ref).:

$$H_d = \frac{H_{d1} + H_{d2} + H_{d3} + H_{d4}}{4} \tag{5a}$$

$$H_a = \frac{H_{a1} + H_{a2} + H_{a3} + H_{a4}}{4} \tag{5b}$$

$$E = \frac{H_d + H_a}{H_d/E_d + H_a/E_a} \tag{5c}$$

In the study, it was assumed that the plastic deformation-rate of the ribbon structured model is comprised of the plastic deformation rate of the dolomite and apatite ribbon, respectively. The plastic deformation of the ribbon structure is basically a function of the thickness of the dolomite and apatite ribbons. Similar to elastic deformation, plastic deformation was modelled and computed as illustrated in Eq. 6:

$$d\varepsilon_v/dt = \sigma_v/\eta = \sigma_v \frac{H_d + H_a}{H_d\eta_d + H_a\eta_a} \tag{6}$$

Substituting Eqs 4–6 into Eq. 3 yields Eq. 7 as demonstrated below:

$$\begin{aligned} \frac{d\varepsilon}{dt} &= \frac{d\sigma_e}{\frac{H_d+H_a}{H_d/E_d+H_a/E_a}dt} + \sigma_v\frac{H_d + H_a}{H_d\eta_d + H_a\eta_a} \\ &= \frac{d\sigma}{\frac{H_d+H_a}{H_d/E_d+H_a/E_a}dt} + \sigma\frac{H_d + H_a}{H_d\eta_d + H_a\eta_a} \end{aligned} \tag{7}$$

In Eq. 7, the phosphate rock specimen's stress is the same in the axial direction and is characterized as follows: $\sigma_0=\sigma_e=\sigma_v=\sigma_1-\sigma_3$. The stress remains unchanged and is characterized by a differential function $d\sigma_0/dt=0$. Integrating both sides of Eq. 7 with respect to time, yields Eq. 8 as expressed below:

$$\varepsilon = \frac{H_d + H_a}{H_d\eta_d + H_a\eta_a}\sigma_0 t + C \tag{8}$$

When the load first acts on the specimen, only the elastic deformation emerged with no plastic deformation. Therefore, the constant term C is characterized by $\varepsilon_0=\sigma_0/E$, after $t=0$ has been substituted into Eq. 8. Then, a mathematical model such as Eq. 9 was derived, which represents the relationship of the phosphate rock deformation with loading time under constant-stress conditions. At the same temperature, parameters such as η_a, η_d, E_a, and E_d in Eq. 9 were assumed

TABLE 1 Specimen dimensions and density for the rock-forming minerals.

Specimen number	Diameter/mm	Length/mm	Thickness of dolomite/mm	Thickness of apatite/mm	Density/g•cm^{-3}
A-1	50.10	100.12	0	100.12	3.01
A-2	49.84	100.08	0	100.08	2.96
A-3	50.12	100.10	0	100.10	2.99
A-4	49.98	100.04	0	100.04	2.95
D-1	50.02	100.12	100.12	0	2.67
D-2	49.88	100.16	100.16	0	2.71
D-3	49.94	100.08	100.08	0	2.70
D-4	50.02	100.04	100.04	0	2.75

FIGURE 4
The GCTS Triaxial test apparatus.

to be constant values, which is considered a representation of the rocky material properties in itself.

$$\varepsilon = \frac{H_d + H_a}{H_d\eta_d + H_a\eta_a}\sigma_0 t + \frac{\sigma_0}{\mathrm{E}} = (\sigma_1 - \sigma_3)\left(\frac{H_d + H_a}{H_d\eta_d + H_a\eta_a}t + \frac{H_d/E_d + H_a/E_a}{H_d + H_a}\right) \quad (9)$$

By contrast, the phosphate rock strain was held constant in the other tests, in which the strain rate is zero and can be characterized as $\varepsilon'=0$. With this consideration, the ε' model was derived as shown in Eq. 10. After differentiating Eq. 10 with respect to time, t, Eqs 11, 12 were derived as expressed below:

$$\varepsilon' = \sigma\frac{H_d + H_a}{H_d\eta_d + H_a\eta_a} + \frac{d\sigma}{\mathrm{dt}}\cdot\frac{H_d/E_d + H_a/E_a}{H_d + H_a} = 0 \quad (10)$$

$$\frac{d\sigma}{\mathrm{dt}}\cdot\frac{H_d/E_d + H_a/E_a}{H_d + H_a} = -\sigma\frac{H_d + H_a}{H_d\eta_d + H_a\eta_a} \quad (11)$$

$$\frac{d\sigma}{\sigma} = -\frac{H_d + H_a}{H_d\eta_d + H_a\eta_a}\cdot\frac{H_d + H_a}{H_d/E_d + H_a/E_a}dt \quad (12)$$

Integrating both sides of Eq. 12, with respect to time, t, yields the exponential function illustrated in Eq. 13:

$$\sigma = \mathrm{Cexp}\left(-\frac{H_d + H_a}{H_d\eta_d + H_a\eta_a}\cdot\frac{H_d + H_a}{H_d/E_d + H_a/E_a}\right)t \quad (13)$$

At 0 h of the test, t = 0s and $\sigma = \sigma_0$. With these parametric relationships (i.e., $t = 0s$ and $\sigma = \sigma_0$), Eq. 13 reduces to Eq. 14. Eq. 14 is basically the stress-relaxation expression of the phosphate rock and illustrates that the internal stress of rock mass would be gradually reduce with time, under the condition of constant strain.

$$\sigma = (\sigma_1 - \sigma_3)\exp\left[-\frac{(H_d + H_a)^2}{(H_d\eta_d + H_a\eta_a)(H_d/E_d + H_a/E_a)}\right]t \quad (14)$$

TABLE 2 Parametric results from the mechanical testing of the rock-forming minerals.

Specimen number	Confining pressure/Mpa	Strain rate/$10^{-6}s^{-1}$	Elastic modulus/GPa	Ultimate compressive strength/MPa	Poisson's ratio
A-1	5	1	140.2	341.8	0.23
A-2	5	1	127.8	322.5	0.21
A-3	5	1	135.7	289.2	0.25
D-1	5	1	47.7	121.7	0.36
D-2	5	1	46.2	136.6	0.38
D-3	5	1	51.3	109.2	0.40

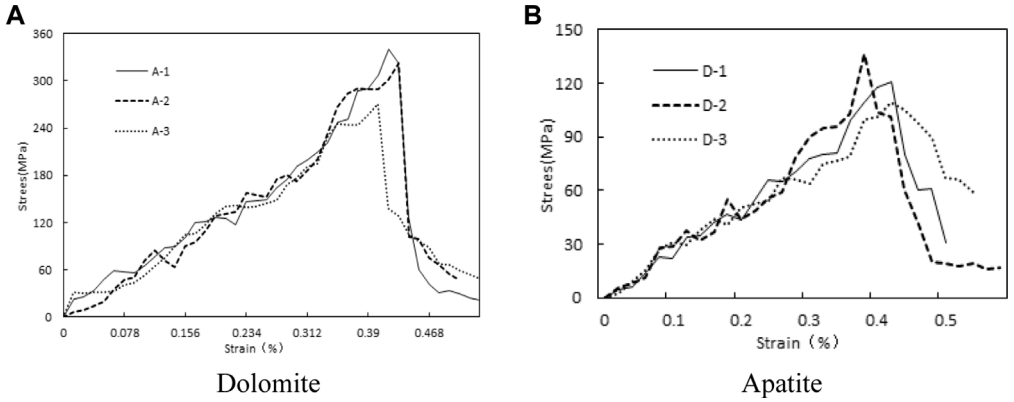

FIGURE 5
The response curves of the rock-forming minerals from mechanical testing. **(A)** Dolomite **(B)** Apatite.

Laboratory testing, results, and data analysis

The mechanical properties of the rock-forming minerals

Preliminary mechanical tests were carried out to measure the mechanical properties of each rock-forming mineral. One set of specimens for apatite and dolomite were analysed according to the international rock mechanics experiment standard (Ref), with letters "A" used to represent apatite and "D" for dolomite. The specific parameters associated with each rock-forming mineral are listed in Table 1 and includes the dimensions and thickness.

Three axial ultimate bearing capacity tests were performed on the first three blocks of each group, using the dynamic rock triaxial apparatus RTX-1000 American GCTS—see Figure 4. In consideration of the burial conditions of the phosphate rock deposits, the test control conditions in this study were selected as follows: the direction of the specimen axial direction was assumed to be consistent with the gravitational direction, the confining pressure was constant at 5 MPa, and the test temperature was maintained at 15°C in a strain-controlled loading mode. The strain rate was 0.006%/min, which is equivalent to one microstrain per second. The mechanical parameters/properties including the elastic modulus are shown in Table 2.

As shown in Table 2, the mean value of the ultimate compressive strength reached 317.8 MPa, which is 2.59 times than that of dolomites. Although the average density of apatite is 1.09 times that of dolomite, its poisson's ratio is only half that of dolomite in the elastic deformation stage. The test results of Table 2 indicates that dolomite has obvious deformation susceptibility under the effects of equal confining pressure and loading rate—see Figure 5.

The last fourth set of specimens, denoted as D-4 (dolomite) and A-4 (apatite) were used for creep coefficient determination. However, the creep coefficient of a rock is restricted by the load combination, temperature, and stress state. In consideration of the actual geological conditions and brittle characteristics of the phosphate rock, the ribbon structured model in this study was assumed to be under typical low stress loading conditions at a

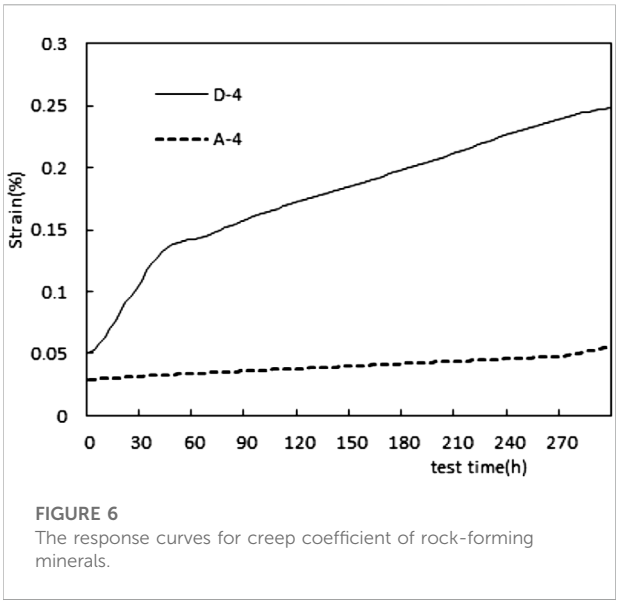

FIGURE 6
The response curves for creep coefficient of rock-forming minerals.

constant temperature. For apatite and dolomite, the creep tests were conducted in stress-controlled loading mode. The axial principal stress was 25 MPa and was held constant over a test time of 300 h under a confinement pressure of 5 MPa (Jiang et al., 2016; Zhou et al., 2016). The creep test results are shown in Figure 6.

From Figure 6, the strain value of apatite increased from 0.38×10^{-3} to 0.61×10^{-3} whilst that of dolomite increased from 0.53×10^{-3} to 2.92×10^{-3}. As shown in Figure 6, the total strain magnitude of dolomite is equivalent to about 4.8 times that of apatite. From these data, the sticking factor of apatite and dolomite were determined to be 25,862 GPa•h and 3,968 GPa•h, respectively.

Verification test and comparative analysis

During the verification-test phase, creep and stress relaxation tests of the phosphate rock specimens were conducted to verify and validity the models in Eqs 9, 13. Similar to Table 1, the external dimensions of the phosphate rock test specimens were measured as shown in Table 3.

The creep and stress-relaxation response curves from the verification-tests are plotted in Figure 7. The test conditions were similar to the previous test for the creep coefficient determination, namely stress-controlled loading mode, 25 MPa axial principal stress, and 5 MP confinement pressure. In Figure 7, the solid lines represent test results whilst the dotted lines represents the simulation results.

With respect to the creep properties, it is evident from the "P-C" response curve in Figure 7A that the initial strain of the phosphate rock specimen was about 0.26×10^{-3} under the effects of a deviatoric stress of 20 MPa. Thereafter, the strains increased to 0.36×10^{-3} after 84 h and then, maintained a constant rate of 0.65 x 10^{-3} after 320 h. In general, Figure 7A indicates that the strain increased linearly as a function of loading test-time.

The stress response curve, "P-SR," of the phosphate rock specimen from the stress-relaxation verification-test is shown in

TABLE 3 Dimensions and density of the verification-test specimens.

Specimen number	Diameter/mm	Length/mm	Thickness of dolomite/mm	Thickness of apatite/mm	Ensity/g•cm^{-3}
P-C	50.80	100.10	42	58	2.89
P-SR	50.76	100.12	44	56	2.84

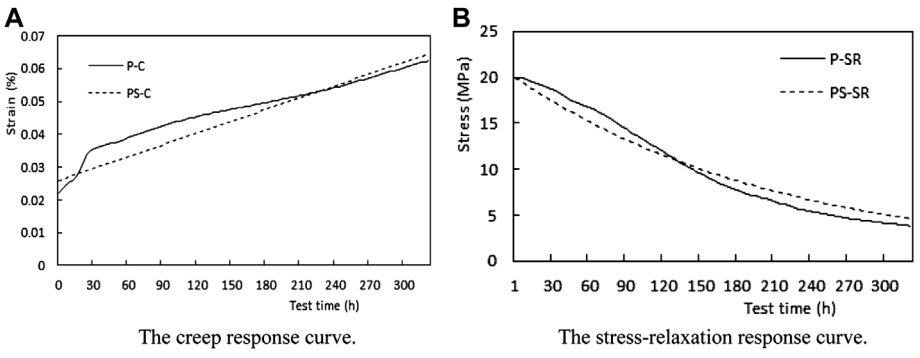

FIGURE 7
Graphical plot of the verification-test results (test versus simulation). **(A)** The creep response curve. **(B)** The stress-relaxation response curve.

Figure 7B. In the first phase of the test plan, the specimen's deviatoric stress increased steadily to 20 MPa within 15 min. In the second phase of testing, the control strain was maintained at a principal strain of 0.28×10^{-3}. Based on the "P-SR" response curve in Figure 7B, the stress of the phosphate rock specimen decreased steadily from 20 MPa to 3.84 MPa over a period of 12 days.

For analytical modelling, the creep and stress-relaxation simulation equations were derived under low-stress loading conditions after the known parameters were substituted into Eqs 9, 14, respectively. These parameters, including the mechanical properties such as the elastic modulus, sticking factor, and the weighted thicknesses of each rock-forming mineral, were obtained from the previous test results contained in Figure 1 through to Figure 6 and Table 1 through to Table 3, respectively.

The simulation response curves "PS- C" and "PS- SR" are shown in Figure 7 with dotted lines. The simulation response curves generally reflect the instantaneous elastic deformation and subsequent steady creep process of the phosphate rock mass when subjected to loading (Walubita et al., 2011). Additionally, the elastic recovery and permanent residual deformation of the phosphate rock mass during unloading are also reflected by similar simulation equations.

Comparing the experimentally measured (solid-curve plots in Figure 7) response curve of the phosphate rock specimen with the predicted values (dotted-curve plots in Figure 7) obtained from the modified models, it was confirmed that the developed approach successfully captures the effect of creep and stress-relaxation of ribbon types of the phosphate rock under low-stress level environment.

Analysis of fracture evolution and creep mechanism

(a) The slip and diffusion resistance to mineral crystals have a close relationship with the lattice constant and its spatial structure (Li, 2009; Wang et al., 2015; Sassoni et al., 2021). It was pointed out in the literature that dolomite crystals belong to the trigonal system and its molecular formula is $CaMg[CO_3]_2$ and $a_0 = 0.601$ nm. On the other hand, apatite crystal belongs to hexagonal crystal system and its molecular formula is $Ca_5[PO4]_3(F,OH)$ and a_0 = 0.943–0.938 nm (Ma, 2011). The crystal constant of dolomite is significantly less than apatite. In other words, the crystal size of apatite is greater than that of dolomite crystals.

The SEM of the preliminary microstructure observation tests showed needle-shaped apatite crystal balls presenting an interpenetrating-interlocking typical space architecture like that of a silicate water rigid cementing material. By and large, this type of lattice arrangement improves the integrity of apatite. On the other hand, the total strains of a ribbon type phosphate rock is comprised of the elastic strain ε_e, and plastic strain ε_v, that is represented by Eq. 9. The elastic strain of phosphate rock were determined to be 0.26×10^{-3} based on the initial point of the creep response curve, namely the "P-C" plot in Figure 7. However, the elastic strains increased to 0.65×10^{-3} after 320 h.

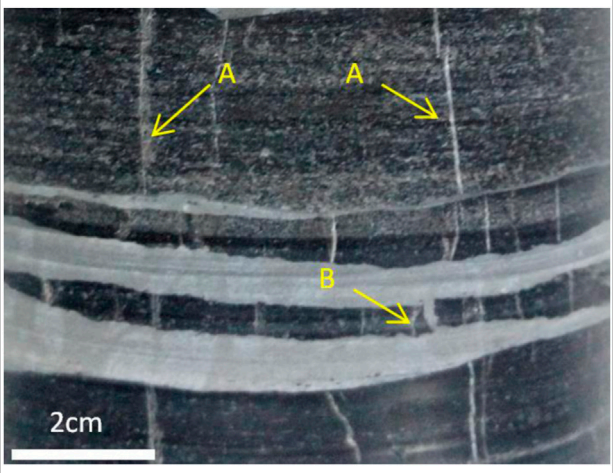

FIGURE 8
Surface fracture morphology of banded phosphate rock.

The plastic deformation in the latter part of the experiment was found to be about three times the elastic deformation. This means that the creep is one of the key factors controlling the mechanical response-behaviour of the phosphate rock. The sticking factor of dolomite was determined to be 3,968 GPa•h, which is significantly smaller than the 25,862 GPa•h of apatite—see Figure 6. Overall, it was concluded that the intergranular creep rupture of dolomite is the leading cause of the mechanical deformation of phosphate rock when subjected to long loading times under low-stress environments.

(b) The creep property of mineral crystals is generally reflected by the distribution and evolution of rock fractures (Reiko and Richard, 2002; Xin, et al., 2017). Based on careful observation of the cylindrical specimen surfaces, the black apatite ribbon has relatively larger crack density of about 2-4 strip/cm^2, which is 3.5 times that of dolomite—see Figure 8. Most of the cracks were observed to be in line with the cylindrical axis and perpendicular to horizontal bedding. As indicated by arrow A in Figure 8, the cracks ran through several groups to dozens of bands. These cracks, which exceed all the mineral crystals in the direction of the fracture, were possibly formed by accidental loading forces, such as earthquakes. However, most of these cracks also have a common feature that the same cracks in the dolomite stripe are significantly narrower with some of them even going to the point where it disappears.

TABLE 4 The mineral composition changes before and after the crush sieving.

Specimen status	Fractional content of the constituent compounds (%)						
	P_2O_5	MgO	SiO_2	CaO	Fe_2O_3	Al_2O_3	CO_2
Before screening	25.21	7.04	35.86	25.17	2.05	3.81	0.96
After screening	40.06	2.89	26.37	19.74	1.53	2.09	0.48

The literature shows that dolomite's critical transformation pressure from brittleness to plasticity is 9.6 MPa, which is less than half of the loading in the Triaxial creep test. This means that the vertically fractured stress of the dolomite crack tip is large enough to make the crack close. Thus, the dolomite crystals were moved from a high-stress place to a lower stress region after overcoming the intercellular sliding resistance. Similarly, some of the apatite-stripe cracks may have been creep-filled with smaller particle size crystals at this stage. This creep-filling behaviour increases the width of the cracks and makes the individual apatite slime slivers to spin at an angle, as indicated by arrow B in Figure 8. With the occurrence of this phenomenon, the end result is that the apatite stripe becomes surrounded by dolomite stripes.

In the laboratory, the creep crystals and their surrounding dolomite stripes were confirmed to possess the same elements and content using the Energy Dispersive Spectrometer test. This again illustrates that the dolomite creep ability is much higher than that of apatite, which indicated that creep was critical factor in characterizing and quantifying the mechanical behaviour of phosphate rocks.

The creep property of the minerals is controlled by the intergranular bonding force (Roufail and Klein, 2013; Li et al., 2020). After experiencing the same grinding energy, the rock-forming mineral produced the corresponding dissociation effect with different intermolecular forces. In this paper, the inter-crystalline strength of different mineral crystals was analysed using the crushability test of minerals. Grinding is the first process of the phosphate ore dressing. The energy efficiency of the process is directly related to the inter-crystalline bonding force of the ore minerals.

For the crushability test, approximately 300 g of the mixed phosphate rock specimens were obtained. These specimens were first broken into a median diameter of 10 mm and put into a ball-mill for 15 min regular grinding. The phosphate rock powder before and after sieve analysis was used to determine the fractional composition and quality of the constituent compounds, which were screened with an 0.08 mm diameter sieve. The test results are shown in Table 4.

From Table 4, the fractional composition of P_2O_5, as an important component of apatite, went up 1.6 times after screening. However, the content of Silicon dolomite is represented by 65% of CO_2 and SiO_2 before screening. During the crushability test, it was observed that phosphate minerals are more difficult to break than silicate minerals under the same grinding energy conditions. Furthermore, it was found that the inter-crystalline strength of apatite was even greater than that of dolomite. In other words, apatite needs more external force to do work for relative motion among the crystals and that its creep performance is relatively low.

Conclusion and recommendations

In this study, integrated mathematical equations were formulated for modelling the mechanical and fracture behaviour of phosphate rocks. The scope of work incorporated model formulation based on Maxwell's Theory and laboratory testing that included creep, stress-relaxation, crushability, and SEM morphological evaluation. Comparisons with the test data provided a verification and validation platform for the proposed models. From the study results and findings, the following conclusions and recommendations were drawn:

(1) Modelling the relationship between the stress and strain responses of phosphate rocks is an important undertaking for engineering applications tailored towards solving rock related problems. Maxwell Theory has been successful in modelling the rheological behaviour of the rock, however its capacity is restricted in effectively simulating the rheological properties of ribbon structured rock such as phosphate rocks. Constitutive equations reflecting the creep properties and stress-relaxation of phosphate rock were deduced, which are based on the ribbon structural model representing the paragenetic replacement of dolomite and apatite.

The constitutive equations were successfully used to model and characterize the rock-forming mineral's effects on the elastic-plastic deformation mechanism of the phosphate rock. The equations were able to accurately simulate the deformation of the ribbon structure in the phosphate rock, which is composed of different thickness mineral belts in all the stress stages. The correctness of these constitutive equations were successfully validated by comparing the simulation results with the measured creep response curve of the ribbon structured phosphate rock.

(2) The horizontal tensile strength of the apatite stripe is greatly weakened because there are high density of vertical fractures in them. To avoid the risk of vault collapse, it is suggested to use a relatively complete thick layer of dolomite as the direct roof of the tunnel or alley.
(3) Based on the mechanical test results, it was clear that dolomite's compressive strength was lower than apatite's, and its creep ability was about three times greater than apatite's. And based on the SEM tests, the mechanism of mechanical response-behaviour about the high-intensity apatite crystals been separated by the low-intensity dolomite crystal was analysed from the mesoscopic perspective. The analysis showed that the dolomite crystals possessing high creep properties dominated the distribution and evolution of the banded structure in the phosphate rock under the condition of long-term low-stress loading.

The constitutive equations were developed and enhanced by studying and modelling the elastic-plastic mechanical response-behaviour to cyclothymic deposition structure rock. However, the effects of the small angle for the strip interface was not considered and wants further research in future follow-up studies.

Data availability statement

The original contributions presented in the study are included in the article/supplementary material, further inquiries can be directed to the corresponding author.

Author contributions

All authors listed have made a substantial, direct, and intellectual contribution to the work and approved it for publication.

Funding

The National Natural Science Foundation of China supported the internships of DP during the progress of this work. DZ and YX provided helpful insights to improve the derivation of the constitutive models. The phosphate rock was graciously supplied by Yichang Xingfa Group Co., Ltd., whilst the specimens were processed in the Rock Mechanics Laboratory of Wuhan Institute of Technology, Wuhan (China). This work was supported by the [National Natural Science Foundation of China Nos. 51474159, 42077228].

Acknowledgments

JP is thanked for the critical reading of an earlier version of the manuscript. Comments from the editors and the reviewer helped to improve the quality of the paper. The raw test data related to the study are available upon request to the first author.

Conflict of interest

The authors declare that the research was conducted in the absence of any commercial or financial relationships that could be construed as a potential conflict of interest.

Publisher's note

References

Andrieux, L. F., and Aminot, A . (2001). Phosphorus forms related to sediment grain size and geochemical characteristics in French coastal areas. *Estuar. Coast. Shelf Sci.* 52, 617–629. doi:10.1006/ecss.2001.0766

Bond, D. M., and Zikry, M. A. (2018). Differentiating between intergranular and transgranular fracture in polycrystalline aggregates. *J. Mat. Sci.* 53, 5786–5798. doi:10.1007/s10853-017-1847-2

Cao, Z. J., Zhang, X. B., and Ai, N. S. (2011). Effect of sediment on concentration of dissolved phosphorus in the Three Gorges Reservoir. *Int. J. Sediment Res.* 26, 87–95. doi:10.1016/S1001-6279(11)60078-4

Chen, J., Chen, F., and Zhang, T. (2010). Technological mineralogical characteristics of Low grade phosphorus containing tombarthite in Guizhou. *Tombarthite* 31 (2), 70–74.

GCTS (2020). Advanced rock testing systems. Available at: https://www.gcts.com/pdf/catalogs/gcts_catalog_systems_rock.pdf (Accessed October 2020).

Han, C., Zheng, B., Qin, Y., Ma, Y., Cao, W., Yang, C., et al. (2016). Analysis of phosphorus import characteristics of the upstream input rivers of Three Gorges Reservoir. *Environ. Earth Sci.* 75, 1024. doi:10.1007/s12665-016-5832-x

Homand-Etienne, F., and Houpert, R. (1989). Thermally induced microcracking in granites characterization and analysis. *Int. J. Rock Mech. Min. Sci. Geomechanics Abstr.* 26, 125–134. doi:10.1016/0148-9062(89)90001-6

Hurai, V., Huraiová, M., Habler, G., Horschinegg, M., Milovsky, R., Milovska, S., et al. (2022). Carbonatite-melilitite-phosphate immiscible melts from the aragonite stability field entrained from the mantle by a Pliocene basalt. *Mineral. Pet.* doi:10.1007/s00710-022-00783-1

Jiang, Q., Zhong, S., Cui, J., Feng, X. T., and Song, L. (2016). Statistical characterization of the mechanical parameters of intact rock under triaxial compression: An experimental proof of the jinping marble. *Rock Mech. Rock Eng.* 49, 4631–4646. doi:10.1007/s00603-016-1054-5

Kounadis, A. (2014). Rocking instability of free-standing statues atop slender viscoelastic columns under ground motion. *Soil Dyn. Earthq. Eng.* 63, 83–91. doi:10.1016/j.soildyn.2014.01.021

Levasseur, S., Welemane, H., and Kondo, D. (2015). A microcracks-induced damage model for initially anisotropic rocks accounting for microcracks closure. *Int. J. Rock Mech. Min. Sci.* 77 (7), 122–132. doi:10.1016/j.ijrmms.2015.03.011

Li, X., Yuan, Y., Liu, L., Leung, Y. S., Chen, Y., Guo, Y., et al. (2020). 3D printing of hydroxyapatite/tricalcium phosphate scaffold with hierarchical porous structure for bone regeneration. *Bio-des. Manuf.* 3, 15–29. doi:10.1007/s42242-019-00056-5

Li, Z. L. (2009). *Materials physics[M]*. BeiJing: Chemical Industry Press, 25–31.

Li, Z., Zhang, G., Yu, X., Liu, Q., and Zhang, X. C. (2015). Phosphorus loss and its estimation in a small watershed of the Yimeng mountainous area, China. *Environ. Earth Sci.* 73 (3), 1205–1216. doi:10.1007/s12665-014-3475-3

Ma, H. W. (2011). *Industrial minerals and rocks*. BeiJing: Geology Press, 241–245.

Maxwell, J. C. (1881). *Treatise on EIecrricicry and magnetism*. 2nd edition, I. Oxford: Clarendon Press, 400.

Nguidi, M. A., Mouflih, M., Abdelmajid, B., László, K., Salem, E. O., Hanane, E. B., et al. (2021). Lithofacies analysis, sedimentary dynamics and Genesis of Maastrichtian-Eocene phosphorites of BouCraa deposit (Southern Morocco). *J. Afr. Earth Sci.* 177 (1). doi:10.1016/j.jafrearsci.2021.104161

Orlov, N. K., Kiseleva, A. K., Milkin, P. A., Evdokimov, P. V., Putlayev, V. I., and Gunster, J. (2020). Potentialities of reaction sintering in the fabrication of high-strength macroporous ceramics based on substituted calcium phosphate. *Inorg. Mat.* 56, 1298–1306. doi:10.1134/S0020168520120146

Pan, D., Xia, Y. Y., and Zhang, D. J. (2017). Comparative study on geological structure and mechanical feature of phosphorite in south China. *J. Wuhan Inst. Technol.* 39 (06), 622–628. doi:10.3969/j.issn.1674?2869.2017.06.017

Priyank, U., Padhyaya, S., and Kumar (2015). Micromechanics of stress transfer through the interphase in fiber-reinforced composites:Original Research Article. *Mech. Mater.* 89 (10), 190–201. doi:10.1016/j.mechmat.2015.06.012

Qin, J., An, K., Sheng, L. M., Yu, L. M., and Zhao, X. L. (2015). Scanning tunneling microscope study of graphite grain boundaries. *Chin. J. Vac. Sci. Technol.* 35 (3), 372–376. doi:10.13922/j.cnki.cjovst.2015.03.23

Reiko, K., and Richard, J. (2002). On measuring creep behaviour in granular materials through triaxial testing. *Can. Geotech. J.* 39 (5), 1061–1074. doi:10.1139/t02-059

Roufail, R., and Klein, B. (2013). Mineral liberation and particle breakage in stirred mills. *Can. Metall. Q.* 49 (4), 419–428. doi:10.1179/cmq.2010.49.4.419

Sassoni, E., Delhomme, C., Forst, S., Graziani, G., Henin, J., Masi, G., et al. (2021). Phosphate treatments for stone conservation: 3-year field study in the royal palace of versailles (France). *Mat. Struct.* 54, 140. doi:10.1617/s11527-021-01717-7

Shen, M. R., and Chen, J. F. (2006). *Rock mechanics*. Shanghai: Tongji University Press.

Tu, L., Zhang, D. J*., and Pan, D. (2017). Failure characteristics and laws of acoustic emission for phosphorite under triaxial loading. *J. Wuhan Inst. Technol.* 39 (06), 616–621. doi:10.13969/j.issn.1674?2869.2017.06.016

Walubita, L. F., Alvarez, A. E., and Simate, G. S. (2011). Evaluating and comparing different methods and models for generating relaxation modulus master-curves for asphalt mixes. *Constr. Build. Mater.* 25 (5), 2619–2626. doi:10.1016/j.conbuildmat.2010.12.010

Wang, L. L., Bornert, M., Héripré, E., Chanchole, S., Pouya, A., and Halphen, B. (2015). The mechanisms of deformation and damage of mudstones: A micro-scale study combining esem and dic. *Rock Mech. Rock Eng.* 48, 1913–1926. doi:10.1007/s00603-014-0670-1

Xin, Y., Li, M., An, D., Ji, H., and Kang, J. (2017). Experimental study on the instability mechanism of the major-defect fractured rock. *Arab. J. Geosci.* 10, 311–320. doi:10.1007/s12517-017-3095-9

Yang, H. Y ., Xiao, J. F., Xie, Z., Tan, Q., Xu, J., et al. (2019). Origin of the ediacaran weng'an and kaiyang phosphorite deposits in the nanhua basin, SW China. *J. Asian Earth Sci.* 182 (182), 103931–104208. doi:10.1016/j.jseaes.2019.103931

Zhang, C., Xie, R. C., Yao, Y., Lv, J., and Cao, Q. (2014). Micro-mechanical behavior characteristics of rock structure surface for deep tight sandstone reservoir :Fault-Block. *Oil Gas Field* 21 (5), 560–563. doi:10.6056/dkyqt201405004

Zhang, S., An, W., and Li, X. (2015). Research on phosphorus loads and characteristics of adsorption and release in surface sediments of Nanyang Lake and Weishan Lake in China. *Environ. Monit. Assess.* 187, 4103–4111. doi:10.1007/s10661-014-4103-0

Zhang, Y., Cui, S., Yu, Z., and Cheng, J. (2022). Fracture characteristics of sliding crack in brittle rock: Analysis based on an improved equivalent crack model. *Front. Earth Sci.* 10, 893549. doi:10.3389/feart.2022.893549

Zhao, H., Li, W., Wang, L., Fu, J., Xue, Y. L., Zhu, J. J., et al. (2022). The influence of the distribution characteristics of complex natural fracture on the hydraulic fracture propagation morphology. *Front. Earth Sci.* 9, 784931. doi:10.3389/feart.2021.784931

Zhao, S. L., Zhang, G., Li, M. X., Yue, X. G., and Wang, D. D. (2015). Rock Microcrack′s dominant direction and the anisotropy. *J. Wuhan Univ. Technol.* 37 (5), 57–65.

Zhou, Y. Y., Feng, X. T., Xu, D. P., and Fan, Q. X. (2016). Experimental investigation of the mechanical behavior of bedded rocks and its implication for high sidewall caverns. *Rock Mech. Rock Eng.* 49, 3643–3669. doi:10.1007/s00603-016-1018-9

frontiers | Frontiers in Earth Science

TYPE Original Research
PUBLISHED 22 February 2023
DOI 10.3389/feart.2023.952845

OPEN ACCESS

EDITED BY
Eduardo Siegle,
University of São Paulo, Brazil

REVIEWED BY
Dobroslav Znidarcic,
University of Colorado, United States
Valéria Quaresma,
Federal University of Espirito Santo, Brazil

*CORRESPONDENCE
Maria Barciela-Rial,
m.barcielarial@tudelft.nl

SPECIALTY SECTION
This article was submitted to Marine Geoscience, a section of the journal Frontiers in Earth Science

RECEIVED 25 May 2022
ACCEPTED 27 January 2023
PUBLISHED 22 February 2023

CITATION
Barciela-Rial M, Saaltink RM, van Kessel T, Chassagne C, Dekker SC, de Boer HJ, Griffioen J, Wassen MJ and Winterwerp JC (2023), A new setup to study the influence of plant growth on the consolidation of dredged cohesive sediment.
Front. Earth Sci. 11:952845.
doi: 10.3389/feart.2023.952845

A new setup to study the influence of plant growth on the consolidation of dredged cohesive sediment

Maria Barciela-Rial[1,2]*, Remon M. Saaltink[3,4], Thijs van Kessel[5], Claire Chassagne[1], Stefan C. Dekker[3,6], Hugo J. de Boer[3], Jasper Griffioen[3,7], Martin J. Wassen[2] and Johan C. Winterwerp[1]

[1]Hydraulic Engineering, Faculty of Civil Engineering and Geosciences, Delft University of Technology, Delft, Netherlands, [2]Sustainable River Management, Built Environment Academy, HAN University of Applied Sciences, Arnhem, Netherlands, [3]Copernicus Institute of Sustainable Development, Faculty of Geosciences, Utrecht University, Utrecht, Netherlands, [4]Arcadis Nederland, Water, Climate and Landscape, Arnhem, Netherlands, [5]Deltares, Delft, Netherlands, [6]Faculty of Management, Science and Technology, Open University, Heerlen, Netherlands, [7]TNO Geological Survey of the Netherlands, Utrecht, Netherlands

Dredged cohesive sediment is progressively being used for wetland construction. However, little is known about the effect of plant growth during the self-weight consolidation of this sediment. In order to check the feasibility of such a study, a new experimental setup has been constructed. As an example, the effect of *Phragmites australis* on the consolidation and drainage of dredged sediment from Lake Markermeer, the Netherlands was investigated. The changes in pore water pressures at 10 cm depth intervals during a 129-day period in a column with and without plants were measured, while the water level was fixed at a constant level. Water loss *via* evaporation and plant transpiration was measured using Mariotte bottles and the photosynthetic processes — including plant transpiration — were measured with a LI-COR photosynthesis system. The results show that several processes initiated by *Phragmites australis* interfere with the physical processes involved in sediment drainage and consolidation. *Phragmites australis* effectively altered the pore pressure gradient *via* water extraction, especially between 40 and 60 cm from the bottom of the column. In this zone, daily cycles in pore pressures were observed which could directly be linked to the diurnal cycle of stomatal gas exchange. On average, water loss *via* evaporation and transpiration of leaves of *Phragmites australis* amounted to 3.9 mm day^{-1}, whereas evaporation of bare soil amounted on average to 0.6 mm day^{-1}. The depth-averaged hydraulic conductivity increased on average by 40% in presence of *Phragmites australis*. This pilot experiment confirms that the pressures sensors coupled with the new set-up enable to study pore pressure development over time and to link the effect of plant growth with alterations in water pressures profiles. A more systematic study with this set-up will in the future enable to quantify the effects of plant growth on consolidation.

KEYWORDS

consolidation, wetland, dredged sediment, plant growth, pore pressure, cohesive, drainage

1 Introduction

The construction of wetlands with soft cohesive sediment has become increasingly important worldwide (Derrick et al., 2007; Mitsch et al., 2012). An example is the Marker Wadden pilot: a new wetland constructed in Lake Markermeer, Netherlands, with dredged cohesive sediment from the bed of the lake itself (Barciela-Rial et al., 2022).

Cohesive sediment deposits consolidate primarily *via* self-weight consolidation (Gibson et al., 1967; Been and Sills, 1981; Winterwerp and van Kesteren, 2004). This consolidation process can be speeded up by sediment drainage *via* artificial drains or water uptake of plant roots. The reduction of the water content by drainage increases the erosion threshold, vane strength, and overall stability soon after construction (Fagherazzi and Furbish, 2001; Chen et al., 2012). In the present Marker Wadden study, the influence of the local plant species *Phragmites australis* (*P. australis*, common reed) is investigated.

Most studies on *P. australis* focus on the behavior of plants in different habitats (An et al., 2020; Armstrong et al., 2000) or water uptake (Garcia-Avila et al., 2019; Liu et al., 2021) but never in relation to changes in the soil properties. Little is known about the potential effect of living plant roots on the consolidation process in soft cohesive sediments, especially due to the superposition of different physical processes induced by plant roots: mechanical armoring (Waldron and Dakessian, 1982; Friend et al., 2003; Reubens et al., 2007), compaction of clay particles in the vicinity of roots (Dorioz et al., 1993), and water uptake by the roots (drainage). It is known that water uptake during vegetative development is nonlinear. During vegetative development, the increase in transpirational water loss is compensated by an increase in water uptake by roots, which is mainly achieved by increasing the root surface area (Suku et al., 2014). As roots elongate, the zone in soils where water is most actively being taken up may change because roots are more porous near their tips (Sanderson, 1983; Zwieniecki et al., 2002). Hence, the part of the sediment drained by plant roots is expected to change horizontally and vertically over time (Gerke and Kuchenbuch 2007). Field studies have found that vegetation-induced suction reduces pore water pressure (Lim et al., 1996; Smethurst et al., 2006; Leung et al., 2015).

In this study, a proof of concept is presented: a new setup was designed to study the influence of root growth on the consolidation of natural cohesive sediments. This new setup is applied to the Marker Wadden sediment as a case study. The effect of root growth and drainage induced by *P. australis* on the consolidation of the dredged sediment is investigated. The evolution of pore water pressures, the settling, and the water loss were recorded in a column with vegetation and a control column without vegetation. This study isolates the effects of plant roots and plant water uptake, thereby enhancing the understanding of the important plant–sediment interactions in terms of consolidation. Therefore, the effect of *P. australis* growth on the consolidation process of newly constructed wetlands can be assessed.

2 Material and methods

2.1 Material sampling and characterization

The sediment and water used in this study were collected from Lake Markermeer at coordinates 52.54622°N, 5.38783°E. The upper layer of the lake bed consists of a thin (circa 0.1 m) layer of soft sediment, under which a thick layer of Holocene deposits (clay–silt mixtures, peat, or sand) is present (Rijkswaterstaat, 1995). Deep Holocene sediment was dredged with a Van Veen grab after removing 1.0 m of the uppermost sediment layer, at which the sampling location corresponded with sand. The sediment studied was sampled at a depth of 1.0–3.0 m of the bed lake, and its characteristics are summarized in Table 1. Particle size was determined using a hydrometer and dry sieving, according to the British Standards Institute (1990). The total organic matter (TOM) content was obtained by loss on ignition (LOI), according to the European Standard (EN, 2012). The particle density was measured using a gas pycnometer (ISO/TS, 2004). The Atterberg limits [liquid limit (LL), plastic limit (PL), and plasticity index (PI)] were determined according to the British Standards Institute (1990). The LL was determined with the Casagrande apparatus and the PL with the rolling thread test.

2.2 A new experimental setup

Consolidation experiments were conducted using Perspex (methyl methacrylate) columns (inner diameter of 10 cm, height of 120 cm) in the Fluid Mechanics Laboratory of the Delft University of Technology. A hollow stainless steel pipe (outer diameter of 2 cm, inner diameter of 1 cm) was fixed in the middle of each Perspex column to control boundary conditions (Barciela Rial et al., 2015). This stainless steel pipe contained Vyon 3.2D filters in its wall, allowing the water resupply of the sediment columns. These filters control the water table and prevent sediment from leaking into the pipe. This pipe is referred to as a drainage pipe. In order to induce the constant water table at the desired level in the Perspex columns, the bottom of the drainage pipe was connected to a water column that contained Markermeer water at a fixed level of 77 cm. This water column controlled the water level inside the drainage pipe. Because of water loss *via* plant transpiration, evaporation, or both, water flowing from this water column to the drainage pipe was automatically replenished from a Mariotte bottle containing Markermeer water (Figure 1).

Six Perspex columns were used in two experimental runs (Table 2). Four columns with plants were harvested in experiment 1 to determine root and shoot variables, whereas two columns were left intact and used for pore pressure measurements. One of the two columns for pore pressure measurements was left unplanted (control column), and the other column was planted with reed (vegetated column). Experiment 1 was conducted in the laboratory hall from November 2016 to February 2017 (118 days), with temperatures of 15°C–20°C, averaging at 17.3°C. The average relative humidity was 72%, fluctuating between 50% and 80%. Because the pressure sensors are very sensitive to small changes in temperature and marginal changes in the water table were recorded, it was decided to repeat the experiment in a climate room. Experiment 2 lasted from March 2017 to August 2017 (t = 129 days). The environmental conditions in the climate room were kept constant at the average conditions measured in the laboratory hall. In both experimental runs, a grow light (Spectrabox Gold) was installed at the same height and with the same day–night cycles. Because the variation in temperature (±5°C) and humidity in the laboratory hall were small, the morphological root and shoot traits measured in the first experimental run could be linked to the changes in pore pressure of the sediment in the second experimental run.

TABLE 1 Sediment properties.

Type of the sediment	Sampling depth	Sand	Silt	Clay	D50	TOM	ρ_s	LL	PL	PI
	(m)	(%mass)			(μm)	(%)	(kg/m^3)		(%)	
Sandy Holocene silt	1.0–3.0	32	49	19	44	7.0	2590	73	28	45

TABLE 2 Description of the two experimental runs that are part of this study.

Experimental run		
Experiment 1 Condition	November 2016–February 2017 Setup: laboratory hall; average temperature: 17.3 °C; relative humidity: 50%–80%; photon flux density (light): 300 μmol s m^{-2}; water level: fluctuating around 77 cm from the base of the column	
Column	**Variables**	**Used in this study**
1. Harvest column		Yes
2. Harvest column	Shoot: leaf surface area and biomass	Yes
3. Harvest column	Root: surface area, length, biomass, and rooting depth	Yes
4. Harvest column		Yes
5. Vegetated column	Pore pressure, evapotranspiration (Mariotte bottle), and transpiration (LI-COR)	No
6. Control column	Pore pressure and evaporation (Mariotte bottle)	No
Experiment 2 Condition	March–August 2017 Setup: climate room; fixed temperature: 17.3 °C; relative humidity: 50%–80%; photon flux density (light): 300 μmol s m^{-2}; water level: stabilized at 77 cm from the base of the column	
Column	**Variables**	**Used in this study**
1. Vegetated column	Pore pressure, evapotranspiration (Mariotte bottle), and transpiration (LI-COR)	Yes
2. Control column	Pore pressure and evaporation (Mariotte bottle)	Yes
3. No drainage column	Pore pressure and evaporation (Mariotte bottle)	Yes

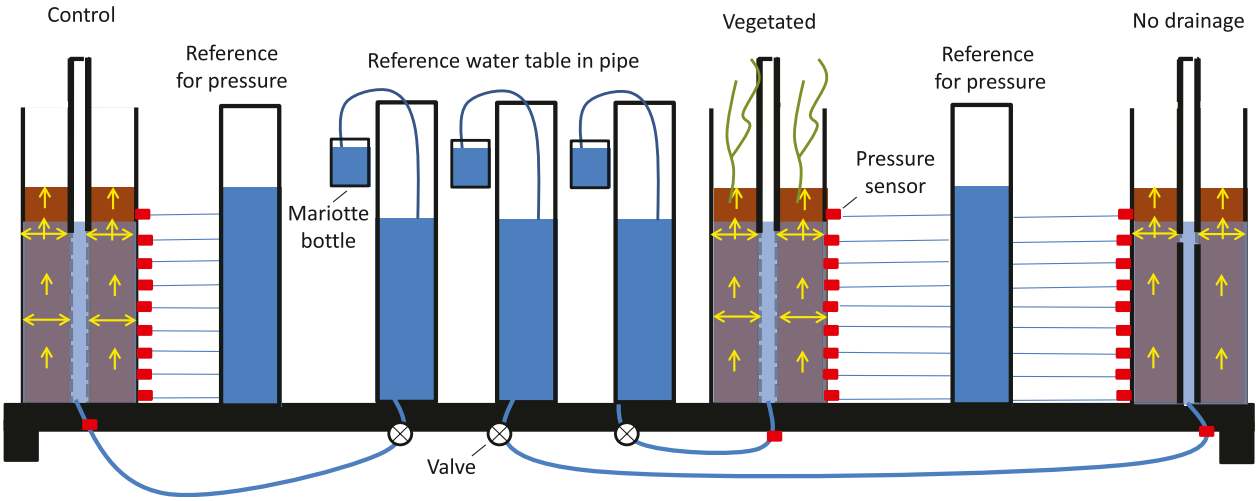

FIGURE 1
Sketch of the setup, including three columns filled with dredged sediment: a control column (only sediment, no vegetation), a vegetated column, and a control column with no drainage. The columns are equipped with pressure sensors (red squares) and a drainage pipe to induce a constant water table in all the columns. The water table in all the drainage pipes is induced at 77 cm by connecting them to a column with a reference and constant water table. Each column is connected to its own reference water table to measure the water flows. These water flows are measured with Mariotte bottles that keep the reference water table constant and allow quantifying water transport. For the control and the vegetated columns, the drainage pipe is permeable over a length of 72 cm. For the column without drainage, horizontal flow is only allowed between 70 and 72 cm to prescribe the same reference water table of 77 cm. All pressure measurements are taken relative to a column with constant water height and pressure to increase accuracy.

TABLE 3 Plant characteristics at 40, 71, 88, and 102 days, as measured from harvested columns.

		40 days	71 days	88 days	102 days
Leaf area	cm^2	48.8	189	406	263
Leaf mass per area (LMA)	g m^2	342	354	365	382
Stem biomass	gr	0.43	1.46	2.13	2.42
Max. rooting depth	cm	18	48	68	80
Root volume	cm^3	2.55	33.66	96.30	88.50
Sediment volume	cm^3	6,469	6,432	6,424	6,414

The columns used for pore pressure measurements were installed with 0.5 Pa Honeywell differential pressure sensors at 0.4, 10.4, 20.4, 30.4, 40.4, 50.4, 60.4, 70.4, and 80.4 cm from the base of the column. All the sensors were provided with a degassing system to avoid inaccuracy induced by air. Furthermore, a Vyon 3.2D filter was installed at each connection point of the sensor to measure pore water pressure (instead of total pressure) and prevent the clay from going through the sensor. All the pressure sensors were connected to a reference column filled with a constant water level to increase the accuracy by measuring differential pressures, thus measuring relative overpressures (Figure 1). All pressure sensors were calibrated before and after the experiment. These two sets of calibrations were compared to assure that the pressure sensors were functioning properly throughout the experiment. Pressure sensors that afterward responded differently to pressure changes were omitted from further analysis: these were the sensors installed at 20.4 and 70.4 cm in the control column and 30.4 cm in the vegetated column. The pressure sensor calibration procedure is detailed in Supplementary Section S1.

The Perspex columns were filled with dredged sediment from Lake Markermeer. The sediment was thoroughly mixed before pouring it into the columns. The measured gravimetric water content of the mixture was 66.7% (water mass/total mass, determined by oven drying). The measured particle density was determined with a gas pycnometer and amounted to 2,590 kg m^{-3}. These water content and particle density correspond with an initial bulk density of the mixture of 1,260 kg m^{-3}, and the initial concentration of solids was 423 g L^{-1}. The sediment was placed in the columns and remixed. After remixing, the suspension height was 118,0 cm in all columns.

Before starting the experiments, the sediment was allowed to settle and consolidate for 14 days, during which the sediment surface lowered to 92.5 cm in the control column and 92.3 cm in the vegetated column (but still without vegetation). Because this 2 mm difference between the columns is likely the result of irregularities of the bed surface at the measurement location, the consolidation rates in the two columns were considered the same, thus showing the reproducibility of the consolidation experiments. After 14 days, the supernatant water was removed from above the sediment without disturbing the consolidating sediment, and plants were transplanted in the vegetated column. This water corresponds to pore water squeezed out during self-weight consolidation. The removal of water from above the sediment marks the start of the experiment (time = 0 days). The mean bulk density of the sediment at $t = 0$ was 1,332 kg m^{-3} for both columns.

In both experiments, three shoots (size of 2 cm) of *Phragmites australis* (common reed) were transplanted into the vegetated column and the harvest columns (Table 2) ($t = 0$ days). A grow light (Spectrabox Gold) with a photon flux density of 300 µmol s m^{-2} was installed at the height of 123 cm above the sediment surface. The day–night cycles, which are important for plant development, were the same in both experimental runs: 8 h with the light off and 16 h with the light on. The climate room was surrounded by a white cover to maximize irradiance from the grow light. A ventilator constantly blew within the climate room to ensure air circulation.

The drainage pipe in the control column and the columns with plants was permeable between 0 cm (i.e., the bottom of the column) and 72 cm. An extra column with a drainage pipe only permeable between 70 and 72 cm was monitored to check if and how the drainage pipe of the experimental setup affected the consolidation of the sediment. Therefore, this third column is referred to as a column without drainage in this study. Because the consolidating sediment was connected through 2 cm (between 70 and 72 cm) with the reference water table of 77 cm, the same water table as for the other two columns could be prescribed. The water balance and settling behavior in this column without drainage were compared with those in the control and vegetated columns.

2.2.1 Hydraulic conductivity equation

Pore pressure data from the sensors were transferred to a PC using an analog–digital converter and stored every second by DASYLab software (DASYLab, 2020). Unfortunately, some data gaps occurred due to connection problems of the sensors to the computer. From the 129 experimental days, pore pressure data were recorded for 69 days. Data gaps were evenly distributed, as shown in Supplementary Section S3. The quality and the resolution of the data were sufficient to capture temporal changes in pore pressure due to plant transpiration. The hydraulic conductivity (k) in both columns can be calculated from the pore pressure data and the water losses. As the horizontal spatial scales are much smaller than the vertical scales, drainage occurs preliminary in the horizontal plane (i.e., *via* the drainage pipe in the center of the column). Thus, the continuity equation on cylindrical coordinates was solved, accounting for radial pore water flow toward the drainage pipe, and the following equation can be used to determine the hydraulic conductivity (see Barciela Rial, 2019 and Supplementary Material for equation derivation):

$$k(z) = \frac{\rho g Q_0 R^2}{2\pi \Delta P(z)(R^2 - r_0{}^2)H}\left(\ln\left(\frac{R}{r_0}\right) - \frac{1}{2} + \frac{r_0{}^2}{2R^2}\right). \quad (1)$$

Here, k is the hydraulic conductivity in m s^{-1}, ρ is the density of water (kg m^{-3}), g is the acceleration of gravity (m s^{-2}), r represents radial coordinate, ΔP (Pa) is the pressure difference between the measured pressure at the column wall ($r = R$) and the pressure in

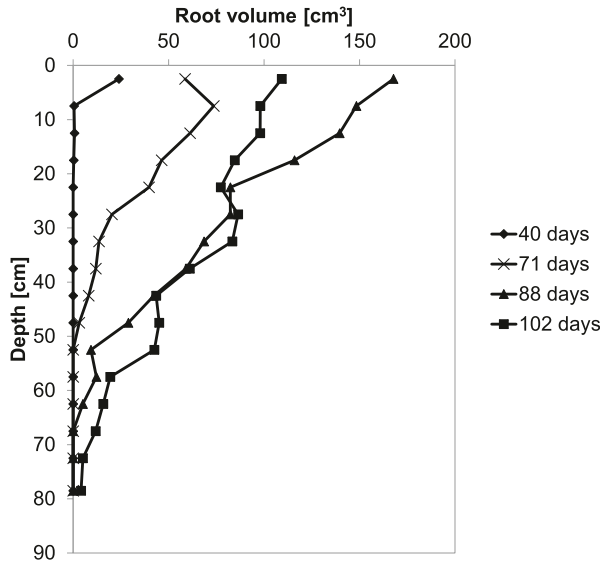

FIGURE 2
Root growth in depth per time.

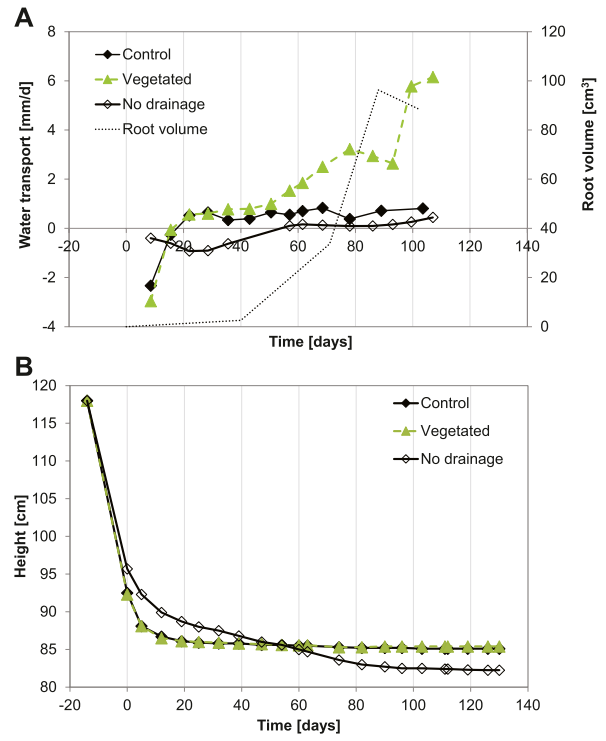

FIGURE 3
(A) Water transport and **(B)** bed elevation measured during the experiments. Negative values for water transport indicate flow toward the drainage pipe, and positive values indicate flow from this pipe into the sediment.

the porous pipe ($r = r_0$), Q_0 is the measured flow ($m^3\ s^{-1}$), R is the radius of the column, r_0 is the radius of the drainage pipe, and H is the drainage length.

2.2.2 Monitoring of vegetation growth

At experimental time t = 40, 71, 88, and 102 days, one column was harvested in experimental run 1 to measure root and shoot parameters. Above-ground biomass was cut off, after which the photosynthetic area was measured immediately. Plant tissue was air-dried at 70°C for 48 h to determine its dry weight. The leaf per mass area (LMA) was calculated. Samples of 5 cm sediment were serrated from the column, after which the roots were sieved from the sediment. The root surface area, root length, and root volume in each sample were determined with SmartRoot in ImageJ (Lobet et al., 2011). The dry weight mass of the roots was determined per sample after drying, following the same procedure as the above-ground biomass.

Plant transpiration and photosynthetic activity were measured on three leaves per plant per column using the LI-COR portable photosynthesis system (LI-COR 6400) at experimental time t = 41, 61, 81, and 97 days under constant environmental conditions. Photosynthetic parameters of *P. australis* were determined with the statistical package R (Duursma, 2015).

3 Results

3.1 Plant development and water uptake

Leaf area and leaf biomass increased in the first months to 406 cm^2 and 1.48 g at day 88, after which leaves started to wilt and leaf area and leaf biomass decreased to 263 cm^2 and 1.00 g at the end of the experiment (Table 3). It is important to note that these results represent the total of the three plants in the column because the belowground biomass of the three individual plants could not be separated.

The photosynthetic parameters measured during the experiment (see Supplementary Section S5 for a full overview) showed that *P. australis* behaved as expected from field conditions; the leaves were optimized to the low-light conditions in the experimental facility. Hence, the setup of the experiment did not affect stomatal gas exchange, and data from this experiment can thus be translated to field conditions.

The length, area, volume, and biomass of the roots increased with time. Figure 2 shows the growth root per time. The plant roots proliferated throughout the column and reached the bottom of the column at the end of the experiment (0 cm, day 102). However, the total volume occupied by roots is two orders of magnitude smaller than the volume of the sediment.

Figure 3 shows the water transport measured with the Mariotte bottles for the three columns: control, no drainage, and vegetated. For the control column and the column without drainage, the measured water transport corresponds to evaporation, whereas for the vegetated column, it corresponds to evaporation and evapotranspiration. The difference between the water transport of the vegetated column and the control column is the effect of plant transpiration. At the beginning of the experiment, water flow was observed from the sediment toward the drainage pipe, and afterward, the water transport occurred in the opposite direction. All evaporation rates in the control column fall between 0.3 and 0.7 mm day^{-1}, averaging at 0.6 mm day^{-1}. Therefore, the characteristic evaporation rate of 0.6 mm day^{-1} was added to the

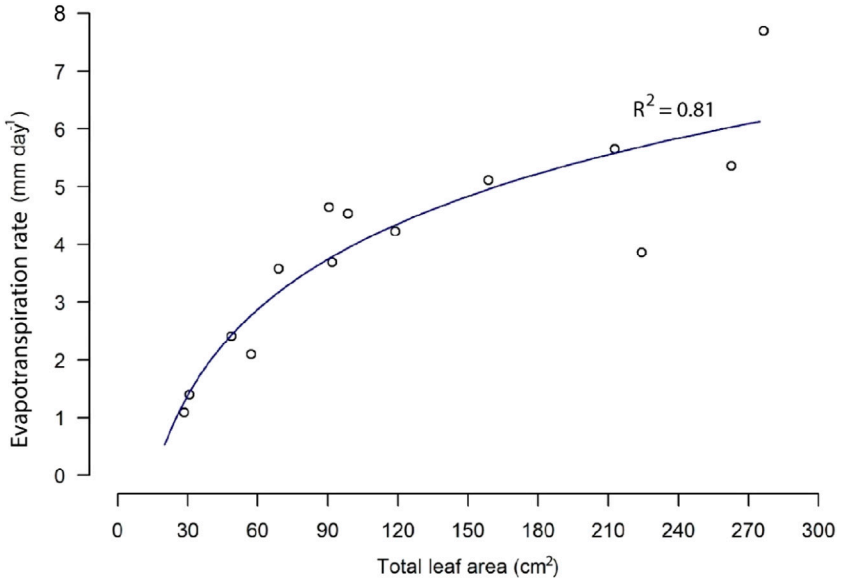

FIGURE 4
Evapotranspiration (mm day^{-1}) as a function of total leaf area (cm^2) in the vegetated column. Transpiration was measured with the LI-COIR photosynthesis system.

transpiration values measured with the LI-COR system to obtain evapotranspiration.

Figure 4 shows the resulting evapotranspiration values measured with the LI-COR photosynthesis system. The increasing leaf area led to a nonlinear increase in water loss *via* evapotranspiration. The lowest measured evapotranspiration value of 1.4 mm day^{-1} corresponded to a total leaf area of 31 cm^2. The highest evaporation rate was found (7.7 mm day^{-1}) at a leaf area of 276 cm^2. The evapotranspiration rates did not scale linearly with leaf area, likely reflecting optimization of transpiration relative to photosynthesis over the time period when photosynthetic capacity gradually declined due to leaf maturation.

3.2 Bed consolidation

At the beginning of the experiment, negative water transport was measured, which indicates water flow from the sediment towards the drainage pipe due to the primary compression regime (rapid decrease in sediment bed height as a function of time), as shown in Figure 3. For the control and vegetated columns, the pore water pressures dissipated 15 days after the start of the experiment. Afterwards, the water flow was driven by evaporation (control column) and evaporation + transpiration (vegetated column). After 15 days, the water flow occurred only in the direction from the drainage pipe toward the sediment. The bed height for both columns did not vary significantly after 15 days and reached 85.5 cm at the end of the experiment. The presence of plants did not affect the bed height evolution. It was already stated that the total volume occupied by roots in the sediment could be neglected with respect to the sediment volume (Table 3). Figure 3 also shows the total evolution of the root volume with time in the vegetated column: when the volume of roots starts to grow at around 40 days, the water transport starts to increase with respect to the control column. The vegetated column reached the characteristic evaporation rate of 0.6 mm day^{-1} after 30 days, after which the water flux increased up to 6.2 mm day^{-1} *via* plant transpiration. The flow in the vegetated column decreased at the end of the experiment due to the maturing of the leaves of *Phragmites australis* (Table 3 shows the maturation evolution of the leaves).

For the column without drainage, flow from the sediment toward the drainage pipe was observed up to 57 days since the beginning of the experiment. As shown in Figure 1, the no-drainage column is only in contact with the control column at one height, hereby limiting the exchange between the two columns. Therefore, a water return flow occurred over a large portion of the column because drainage at different depths was not possible. This resulted in a different (slower) compression for the sediment in this column compared to the vegetated and control settling columns. After 57 days, a change in slope for the bed height as a function of time (secondary compression) was observed, and there was a small flow from the drainage pipe to the sediment. After 80 days, there was an increase in the flow from the drainage pipe to the sediment, associated with a new change in the slope (the height of the bed has reached a constant value). At the end of the experiment, the water transport almost reached the value found for the control column (i.e., the value associated with daily evaporation). The bed height at the end of the experiment was 82.25 cm, lower than the bed height for the two other columns.

3.3 Pore pressures

The pore water pressure data are grouped into three different phases based on the successive stages of consolidation and drainage in the experiment. The first phase includes the data on the time steps t = 0 days and t = 1 day, during which fast initial consolidation occurred. Only data from the period t = 12–40 days are used for the second phase as we lack pore pressure data from t = 2 to t = 11 days (Supplementary Section S3). During this phase, slow consolidation occurred with little

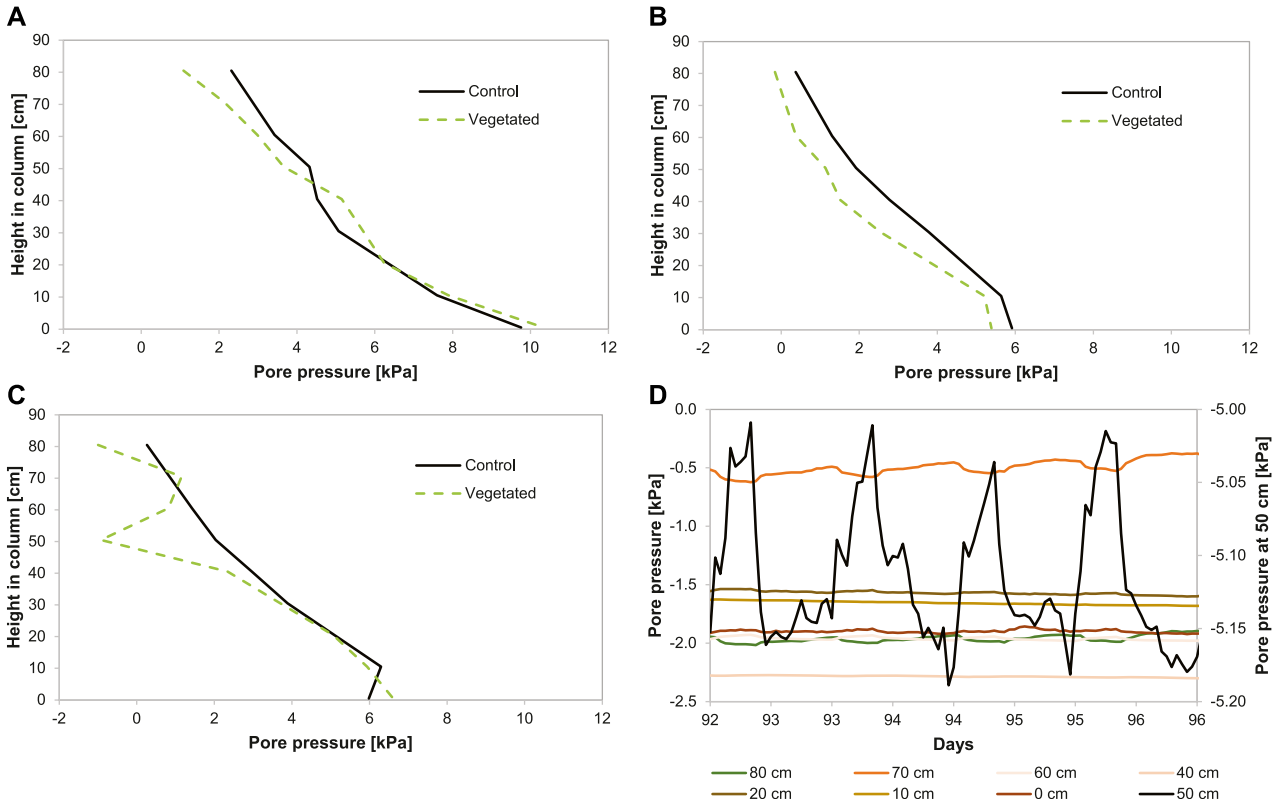

FIGURE 5
(A) Total pore pressure (kPa) in phase 1 (0–1 day) **(B)**, phase 2 (12–40 days), **(C)** and phase 3 (>40 days) **(D)**. Hourly time series (t = 92–96 days, to be compared with day >40) of pore water pressure relative to the reference column (Figure 1) for the control vegetated column. Note that the sensor at 50 cm depth has a different y-axis.

influence of plant transpiration (i.e., plant roots started to grow but did not have a big impact on pore pressure). After 40 days, the effects of plant transpiration on total pore pressure increased. Therefore, total pore pressure data on the period t = 41–129 are used for the third phase.

The pore water pressure profiles are rather identical for the two columns for phases 1 and 2 (Figures 5A, B). However, in the vegetated column, the pore pressure at the top (i.e., 2.5 cm above the water table) decreased from 1.1 kPa in phase 1 (Figure 5A) to −1.0 kPa in phase 3 (Figure 5C), while the pore pressure at the top in the control column decreased from 2.3 to 0.3 kPa. In phase 3 of the vegetated column (Figure 5C), the pore pressure decreased remarkably from 1.2 kPa at 60 cm to −0.9 kPa at 40 cm, with a peak at −1.7 kPa at t = 74 days. This reduction in pore pressure was likely caused by water uptake by plant roots as a result of an increase in the total root area (Table 3), thereby increasing water uptake from the sediment. These results show that reed altered the total pore pressure, especially between 30 and 50 cm from the bottom of the column, by water extraction *via* roots. The negative pore pressures at these depths suggest that the suction of water is an important process during consolidation in the presence of plants. The pore water pressure profile is led by evapotranspiration and not by self-weight consolidation since the excess pore pressure decreased at the height of the active root part, indicating water transport to the roots.

Figure 5D shows pore pressures during 6 days for the vegetated column. It shows that daily cycles are induced in the pore pressures by plants, especially between 40 and 50 cm height from the bottom of the column (Figure 5B). In the control column, no difference in pore pressure was observed between day and night. These results suggest that during the day, plants effectively lowered pore water pressure at the point where the roots were extracting most of the water (50 cm from the bottom of

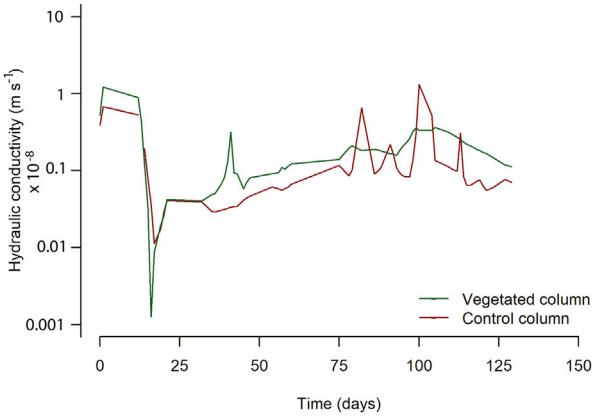

FIGURE 6
Depth-averaged conductivity for the control and vegetated columns.

the column). During the night, the pore water pressures increased relative to the daytime, suggesting that the dominant flow of water at night occurs from the drainage pipe into the sediment to compensate for the water losses during the day. A reverse cycle was visible in the vegetated column at 70 cm, indicating that during the night, water flow from the drainage pipe decreased pressure values, likely because of a lowered water table due to plant drainage during the day. Water flow was likely insufficient to maintain the water table at a fixed level at short time scales because of low hydraulic conductivity.

3.4 Hydraulic conductivity

The measured water fluxes (Figure 3) were used for calculating the hydraulic conductivity using Eq. (1). The water loss *via* leaves (transpiration) is included in the hydraulic conductivity calculations because the sum of water losses is used in Eq. 1 (i.e., evaporation and transpiration). Thus, the hydraulic conductivity of the vegetated column is based on water transport in-between the soil particles plus water transport through the plant roots. Figure 6 shows the depth-averaged hydraulic conductivity of the control column and vegetated column for the duration of the experiment. The difference in the initial hydraulic conductivities between the control column and the vegetated column might be caused by small disturbances induced when transplanting the reed seedlings at t = 0 days. After day 30, in Phase 3, plant water uptake was observed (Figure 3), and the depth-averaged hydraulic conductivity increased on average by 40% in the presence of *Phragmites australis* with respect to the control column. Hydraulic conductivity averaged 1.9×10^{-10} m s^{-1} in the de vegetated column and 1.3×10^{-10} m s^{-1} in the control column.

The hydraulic conductivity profiles in depth are shown in Supplementary Section S4.

4 Discussion

4.1 Plant development and water uptake

The present study prescribed environmental conditions representative of the Marker Wadden study. The plants grew healthy, and the roots reached the bottom of the column at the end of the experiment. The same effect of transpiration was measured with the Mariotte bottles (Figure 3) and the LI-COR system (Figure 4), reaching a maximum of 6 mm day^{-1} in both cases. The average evapotranspiration rate of 3.9 mm day^{-1} in this study closely agrees with the average evapotranspiration value of 3.7 mm day^{-1} measured in reedbeds in the Teesmouth Estuary in England during the growing season (Fermor et al., 2001). Similar rates were measured in the Biebrza wetlands in Poland, averaging between 3.0 and 3.5 mm day^{-1} in the summer months (Siedlecki et al., 2016). Therefore, the data acquired from this experiment can be used to model the speed of drainage and consolidation in constructed wetlands built with soft, clay-rich material. Such a model would help estimate the difference between natural consolidating mud (such as mudflats) with and without *P. australis*. In the long term, vegetation would also induce biogeochemical processes (Saaltink et al., 2016), which accelerate pedogenic processes. These processes lead to the maturation or ripening of the sediment into the soil (Pons and Zonneveld, 1965; Barciela-Rial et al., 2020). Ripening processes are out of the scope of this study.

4.2 Bed consolidation

The slower initial consolidation rate and the final lower bed height for the column with no drainage are explained by the different initial conditions. In the column without drainage, water could not escape directly *via* the pipe, and only a vertical flow of water was possible from the bottom up to 70 cm high. At the upper part, 1) some flow of water toward the pipe was possible (70–72 cm) and 2) water could escape *via* evaporation (at the sediment surface). The bed height at the end of the experiment for the column without drainage was lower than the bed height for the two other columns. One explanation could be that the limited drainage between 70 and 72 cm could not fully compensate for evaporation. In that case, the internal water table would become lower than the external reference level and the overburden (i.e., the effective weight of the sediment layer above the water table) higher, resulting in higher compaction. This remains to be investigated in further experiments.

Plants are expected to enhance drainage, favorably affecting consolidation, although the current experiments did not show any enhanced consolidation rates. The experimental setup enabled us to isolate the drainage effect of plants, but there was no visible effect on consolidation because the continuous resupply of water in the drainage pipe prevented sediment drying, which otherwise would have occurred due to the plants. Moreover, the lack of difference in consolidation rates between the control and vegetated columns can also be explained by the armoring effect of roots (Waldron and Dakessian, 1982; Friend et al., 2003; Reubens et al., 2007). The roots themselves strengthen the soil, thus its resistance to consolidation. Hence, this armoring counteracts the additional drainage by the roots. Which of these two processes is dominant may be site-specific, depending on vegetation type (Valiela et al., 1976; Moore et al., 2012) and soil properties and its initial conditions (Retnamony and Allam, 1998) before consolidation.

4.3 Pore pressure

The results of this study showed that *P. australis* effectively alters the pore pressure gradient in soft cohesive sediments. This difference in the pore pressure gradient is referred to as the plant effect. The shape of all pressure depth profiles (Figure 4) is comparable with typical profiles of bare silty soils (Blight, 2003). For the vegetated column, there is a sharp drop in pore pressure of 40–60 cm from the base of the column. In the soil layer where plant roots extracted water, we found pressures up to four times higher than in the control column because of vegetation-induced suction, which corresponds with the data in Figure 2, showing that the larger root volume increase occurred between 20 and 60 cm depth.

The part in the column where roots extract water did not change during the experiment: pore pressure was remarkably reduced between 40 and 60 cm from the bottom of the column. This was unexpected as the roots of *P. australis* penetrated deeper into the sediment in time, and water uptake is supposed to be largely restricted to the part near the root tip (Kramer and Boyer, 1995). However, the maximal root density in the present experiment was measured at 20–60 cm depth (Figure 2), and other authors, such as Zhang et al. (2020), found water uptake profiles exhibiting similar patterns to the pore pressure profiles measured in the present article. Similarly, Leung et al. (2015) and Leung (2016) showed that the air entry value (i.e., the pressure point after which air recedes into

the soil pores) increased four times in the presence of ivy trees (*Schefflera heptaphylla*) compared to bare soil.

The fact that pore pressure below 40 cm height was completely unaffected even though root surface area per unit volume of soil increased in deeper sediment layers suggests that the changing sediment physical properties were limiting water extraction to a sediment height of 40–60 cm from the bottom of the column. The deep rooting depth of *P. australis* is a common trait of this species and gives it an advantage over most graminoid plants sharing wetland habitats (Moore et al., 2012). According to Zhuang et al. (2001), root hydraulic characteristics co-determine where water is taken up. This depends on the pattern by which the different parts of the root contribute to the overall water transport. These root characteristics were not measured in this experiment. Therefore, it is hard to conclude why the part where water was extracted did not slightly shift downward in the column through time. Because of the daily cycles present at a sediment height of 50 cm, we are confident in linking the observed reduction in pore pressure at this depth to water loss by root extraction (Figure 5). Moreover, we measured an average water loss *via* evapotranspiration of 3.9 mm day^{-1} in the vegetated column, whereas water loss *via* evaporation amounted on average to 0.6 mm day^{-1} in the control column. Although pore pressure was restored during the night, the reduction in pore pressure during the day was larger than the increase during the night. This, together with the fact that root surface area per unit volume of soil kept increasing in the zone of water extraction, might explain why pore pressures decreased with time. During the night, the effect of recovery of the water table is observed at a sediment height of 70 cm in the vegetated column (Figure 5). At this height, water flow from the drainage pipe decreased suction values during the night because of a decreased water table due to plant drainage during the day.

4.4 Hydraulic conductivity

The results of this study showed that *P. australis* increased the average hydraulic conductivity of the sediment in phase 3 by 40% compared to bare soil. The overall hydraulic conductivity of a soil–plant complex likely consists of three parts:

1. The inherent hydraulic conductivity of the soil itself, which is a function of the soil composition and its state of consolidation,
2. The drainage by the roots, enhancing pore water flows through the soil–plant complex, and
3. Drainage channels along the roots or elsewhere in the soil in the form of root-induced cracks.

Thus, the hydraulic properties of the soil and roots are closely coupled (Lobet et al., 2014). Plants increase the permeability in sediments involving the development of drainage channels, of which the main driver is root growth (Ghestem et al., 2011; Orozco-López et al., 2018). In our case, these pores represent macropores made by living or decaying roots of *P. australis* (i.e., root channels). In particular, in cohesive sediments, these root channels are the dominant flow paths of water (Perillo et al., 1999) and can contribute to 70%–100% of total macropore space in the top 8 cm of sediment (Noguchi et al., 1997; Newman et al., 2004). However, a low fraction of macropores of total porosity already increases the water flow of saturated soil (Beven and Germann, 2003). This is especially relevant in artificial wetlands where fast initial consolidation is important. In the present study, the hydraulic conductivity increased only to a limited extent compared to bare soil despite the increasing root area. Similar observations were reported by Vergani and Graf (2015), who observed stagnation in the increase in sediment permeability due to root proliferation when root length densities approached 0.1 cm^{-3}. This can be explained by two opposing processes occurring when roots proliferate in the sediment: 1) the contact area of water increases with increasing root density; at low root densities, this accelerates water flow through the soil, and 2) the film thickness of mobile water inside the root-induced cracks decreases with increasing root densities, decelerating water flow (Lange et al., 2009). Hence, a stagnant point is reached when the film thickness of the water becomes too thin to promote water flow. Another reason might be that photosynthesis and transpiration decrease per unit leaf area as leaves mature, as was observed for leaves of *P. australis* in the present experiment (Supplementary Section S5). Therefore, the observed stagnation of the increase in hydraulic conductivity is likely caused by a combination of a reduced photosynthetic capacity of the leaves and a reduction in film thickness.

4.5 Experimental setup and limitations

The experiments presented in this study were meant as pilot experiments to study the effect of plant growth on pore water pressures during the self-weight consolidation of dredged sediment. In future studies, replicas of the presented experiments will be performed to confirm the findings. Moreover, additional measurements like bed strength and density will be performed. The replicas in these types of experiments are recommended because the intraspecific variation in belowground biomass production can be high (Granéli, 1985; Howard, 2009), which may affect the pore pressure profile (Figure 5). However, we already found that the sensors at nine different depths show significantly different behaviors between the vegetated and non-vegetated columns. This total difference at every depth is the plant effect, which can vary slightly during every experiment, both in timing and the extent at different depths. Therefore, a statistically significant set of data should be built up.

4.5.1 The effect of the drainage pipe

The vertical dry density and pore water pressure distributions in the initial phase of this experiment were largely affected by the experimental setup and the addition of the dredged sediment. The drainage pipe in the middle of the column was meant to control the water table during the experiments. However, part of the sediment will immediately dewater when poured in: water will scape through the porous drainage pipe. This effect is larger in the lower part of the column. Higher in the column, vertical drainage prevails. As the very upper part of the drainage pipe was not porous, complex pore water circulations within the soil and the drainage pipe were induced, driven by the uneven pore water pressure gradients (Barciela Rial, 2019).

The contact with a water reservoir makes the sediment susceptible to osmotic processes and water adsorption by organic matter. Osmotic processes, in particular, are driven by ionic concentration gradients between the sediment and the reservoir (Atkins et al., 2014). By osmosis, ions and water could migrate from the sediment to the water reservoir (or *vice versa*), thereby changing the particle–particle interactions between sediment particles and leading to different consolidation behaviors. Some clays are known to be sensitive to osmotic swelling (Parker et al., 1982).

These aspects should be addressed in forthcoming studies.

5 Conclusion

It was demonstrated, using as example the effect of *Phragmites australis* on Marker Wadden sediment, that the new experimental set-up presented in this article enables to study the effect of root growth on the consolidation of natural dredged sediment. To the best of our knowledge, the present study is the first that correlates pore pressure measurements to the study of the effect of vegetation on the consolidation of dredged sediment. In particular, the pore pressure sensors used enabled showing how *P. australis* altered the pore pressure gradient in the sediment. The plants grew healthy, and their growth is comparable to plants growing *in situ*. In the top 40 cm, daily cycles in pore pressures were observed, which could directly be linked to the diurnal cycle of stomatal gas exchange. On average, water loss *via* evaporation and transpiration of leaves of *P. australis* amounted to 3.9 mm day^{-1}, whereas the evaporation of bare soil amounted on average to 0.6 mm day^{-1}. Moreover, the depth-averaged hydraulic conductivity increased on average by 40% in the presence of *P. australis*. These findings highlight the feature of this plant to fasten drainage in soft cohesive sediment. Future experiments will focus on the following:

1. The effects on soil structure, local density, and flow patterns: the inherent hydraulic conductivity of the soil itself is enhanced by root-growth-induced cracks, forming macropores and drainage channels. Conversely, root growth disturbs the soil structure locally, which may result in the (local) densification of the soil. Furthermore, we have indications that the roots themselves enhance drainage within the soil by promoting pore water flow along their wall.
2. The dominance between the drainage effect of roots and their armoring effect: these effects may neutralize each other, like it seems in the present case, but they may also be affected by factors such as the environmental conditions (e.g., permanent water input or not) and the time scale of the experiment (e.g., root development).

Data availability statement

The raw data supporting the conclusion of this article will be made available by the authors, without undue reservation.

Author contributions

MB-R designed the Perspex columns with pressure sensors and the drainage pipe. MB-R, RS, TK, SD, HB, JG, MW, and JW designed the combined experiment with vegetation, and MB-R and RS performed them. MB-R, CC, TK, and JW developed a mathematical model to calculate hydraulic conductivity. RS and HB monitored and analyzed the plant growth. MB-R and RS prepared the manuscript with contributions from all co-authors.

Funding

This study was supported by funding from the Netherlands Organization for Scientific Research (NWO), project no. 850.13.031 and 850.13.032 and from Boskalis, Van Oord, Deltares, RHDHV, and Natuurmonumenten. The open access fee was paid by TU Delft.

Acknowledgments

The authors would also like to thank Sander de Vree, Mohammed Jafar, Armand Middeldorp, Tom Mol, Frank Kalkman, Rob van Dijk, Hans Tas, and Arno Doorn for their help, support, and advice during the experiment.

Conflict of interest

Author RS was employed by Arcadis BV.

The remaining authors declare that the research was conducted in the absence of any commercial or financial relationships that could be construed as a potential conflict of interest.

Publisher's note

All claims expressed in this article are solely those of the authors and do not necessarily represent those of their affiliated organizations, or those of the publisher, the editors, and the reviewers. Any product that may be evaluated in this article, or claim that may be made by its manufacturer, is not guaranteed or endorsed by the publisher.

Supplementary material

The Supplementary Material for this article can be found online at: https://www.frontiersin.org/articles/10.3389/feart.2023.952845/full#supplementary-material

References

An, S., Liu, X., Wen, B., Li, X., Qi, P., and Zhang, K. (2020). Comparison of the photosynthetic capacity of phragmites australis in five habitats in saline–alkaline wetlands. *Plants* 9 (10), 1317. doi:10.3390/plants9101317

Armstrong, W., Cousins, D., Armstrong, J., Turner, D. W., and Beckett, P. M. (2000). Oxygen distribution in wetland plant roots and permeability barriers to gas-exchange with the rhizosphere: A microelectrode and modelling study with phragmites australis. *Ann. Bot.* 86 (3), 687–703. doi:10.1006/anbo.2000.1236

Atkins, P., Atkins, P. W., and de Paula, J. (2014). *Atkins' physical chemistry*. Oxford University Press.

Barciela Rial, M., Winterwerp, J. C., Griffioen, J., and van Kessel, T. (2015). "Consolidation and strength development by horizontal drainage of soft mud deposits in lake Markermeer," in *Book of abstracts NCR-Days* (Nijmegen, Netherlands: Delft University of Technology), 62–64.

Barciela Rial, M. (2019). *Consolidation and drying of slurries: A building with nature study for the marker wadden*. PhD dissertation. Netherlands: TU Delft.

Barciela-Rial, M., van Paassen, L. A., Griffioen, J., van Kessel, T., and Winterwerp, J. C. (2020). The effect of solid phase composition on the drying behaviour of Markermeer sediment. *Vadose Zone J.* 19, 1–14. doi:10.1002/vzj2.20028

Barciela-Rial, M., Vardon, P. J., Van Kessel, T., Griffioen, J., and Winterwerp, J. C. (2022). Effect of composition on the compressibility and shear strength of dredged cohesive sediment. Sedimentology, stratigraphy and diagenesis. *Front. Earth Sci.* 10, 786108. doi:10.3389/feart.2022.786108

Been, K., and Sills, G. C. (1981). Self-weight consolidation of soft soils: An experimental and theoretical study. *Géotechnique* 31, 519–535. doi:10.1680/geot.1981.31.4.519

Beven, K., and Germann, P. (2003). Macropores and water flow in soils. *Water Resour. Res.* 18, 1310–1325. doi:10.1029/WR018i005p01311

Blight, G. E. (2003). The vadose zone soil-water balance and transpiration rates of vegetation. *Géotechnique* 53 (1), 55–64. doi:10.1680/geot.2003.53.1.55

British Standards Institute (1990). Methods of test for soils for civil engineering purposes in *Classification tests. BS1377-2:1990*.

Chen, Y., Thompson, C. E. L., and Collins, M. B. (2012). Saltmarsh creek bank stability: Biostabilisation and consolidation with depth. *Cont. Shelf Res.* 35, 64–74. doi:10.1016/j.csr.2011.12.009

DASYLab (2020). *Data acquisition, controlling, and monitoring*. User Manual.

Derrick, P., McKee, J., Johnson, S., and Mendelsohn, M. (2007). Poplar island environmental restoration project: Project successes, lessons learned, and future plans. *Proc. world Dredg. Congr.* 1, 487–500.

Dorioz, J. M., Robert, M., and Chenu, C. (1993). The role of roots, fungi and bacteria on clay particle organization. An experimental approach. *Exp. approach. Geoderma* 56, 179–194. doi:10.1016/0016-7061(93)90109-x

Duursma, R. A. (2015). Plantecophys - an R package for analysing and modelling leaf gas exchange data. *PLoS ONE* 10 (11), 01433466–e143413. doi:10.1371/journal.pone.0143346

EN (2012). *Sludge, treated biowaste, soil and waste -determination of loss on ignition*. Geneva, Switzerland: International Organization for Standardization. EN 15935:2012.

Fagherazzi, S., and Furbish, D. J. (2001). On the shape and widening of salt marsh creeks. *J. Geophys. Res.* 106, 991–1003. doi:10.1029/1999jc000115

Fermor, P. M., Hedges, P. D., Gilbert, J. C., and Gowing, D. J. G. (2001). Reedbed evapotranspiration rates in England. *Hydrol. Process.* 15, 621–631. doi:10.1002/hyp.174

Friend, P. L., Ciavola, P., Cappucci, S., and Santos, R. (2003). Bio-dependent bed parameters as a proxy tool for sediment stability in mixed habitat intertidal areas. *Cont. Shelf Res.* 23, 1899–1917. doi:10.1016/j.csr.2002.12.001

García-Ávila, F., Patiño-Chávez, J., Zhinín-Chimbo, F., Donoso-Moscoso, S., del Pino, L. F., and Avilés-Añazco, A. (2019). Performance of Phragmites Australis and Cyperus Papyrus in the treatment of municipal wastewater by vertical flow subsurface constructed wetlands. *Int. Soil Water Conservation Res.* 7 (3), 286–296. doi:10.1016/j.iswcr.2019.04.001

Gerke, H. H., and Kuchenbuch, R. O. (2007). Root effects on soil water and hydraulic properties. *Biologia* 62, 557–561. doi:10.2478/s11756-007-0110-8

Ghestem, M., Sidle, R. C., and Stokes, A. (2011). The influence of plant root systems on subsurface flow: Implications for slope stability. *Bioscience* 61, 869–879. doi:10.1525/bio.2011.61.11.6

Gibson, R. E., England, G. L., and Hussey, M. J. L. (1967). The theory of one-dimensional consolidation of saturated clays. *Géotechnique* 17, 261–273. doi:10.1680/geot.1967.17.3.261

Granéli, W. (1985). Biomass response after nutrient addition to natural stands of reed, *Phragmites australis*. *Int. Ver. für Theoretische Angew. Limnol. Verhandlungen* 22, 2956–2961. doi:10.1080/03680770.1983.11897810

Howard, R. J. (2009). Intraspecific variation in growth of marsh macrophytes in response to salinity and soil type: Implications for wetland restoration. *Estuaries Coasts* 33, 127–138. doi:10.1007/s12237-009-9227-z

ISO/TS (2004). *Geotechnical investigation and testing - laboratory testing of soil - Part 3: Determination of particle density - pycnometer*. ISO/TS 17892-3:2004.

Kramer, B., and Boyer, J. S. (1995). "Chapter 5: Roots and root systems," in *Water relations of plants and soils* (San Diego: Academic Press), 130.

Lange, B., Lüescher, P., and Germann, P. F. (2009). Significance of tree roots for preferential infiltration in stagnic soilsfiltration in stagnic soils. *HESS* 13, 1809–1821. doi:10.5194/hess-13-1809-2009

Leung, A. K., Garg, A., and Ng, C. W. W. (2015). Effects of plant roots on soil-water retention and induced suction in vegetated soil. *Eng. Geol.* 193, 183–197. doi:10.1016/j.enggeo.2015.04.017

Leung, A. K. (2016). Grass evapotranspiration-induced suction in slope: Case study. *Environ. Geotech.* 3, 155–165. doi:10.1680/envgeo.14.00010

Lim, T. T., Rahardjo, H., Chang, M. F., and Fredlund, D. G. (1996). Effect of rainfall on matric suctions in a residual soil slope. *Can. Geotechnical J.* 33, 618–628. doi:10.1139/t96-087

Liu, Y., Zhang, Y., Xie, L., Zhao, S., Dai, L., and Zhang, Z. (2021). Effect of soil characteristics on preferential flow of Phragmites australis community in Yellow River delta. *Ecol. Indic.* 125, 107486. doi:10.1016/j.ecolind.2021.107486

Lobet, G., Pagès, L., and Draye, X. (2011). A novel image analysis toolbox enabling quantitative analysis of root system architecture. *Plant Physiol.* 157, 29–39. doi:10.1104/pp.111.179895

Lobet, G., Couvreur, V., Meunier, F., Javaux, M., and Draye, X. (2014). Plant water uptake in drying soils. *Plant Physiol.* 164, 1619–1627. doi:10.1104/pp.113.233486

Mitsch, W. J., Zhang, L., Stefanik, K. C., Nahlik, A. M., Anderson, C. J., Bernal, B., et al. (2012). Creating wetlands: Primary succession, water quality changes, and self-design over 15 years. *BioScience* 62, 237–250. doi:10.1525/bio.2012.62.3.5

Moore, G. E., Burdick, D. M., Peter, C. R., and Keirstead, D. R. (2012). Belowground biomass of *Phragmites australis* in coastal marshes. *Northeast. Nat.* 19, 611–626. doi:10.1656/045.019.0406

Newman, B. D., Wilcox, B. P., and Graham, R. C. (2004). Snowmelt driven macropore flow and soil saturation in a semiarid forest. *Hydrol. Process.* 18, 1035–1042. doi:10.1002/hyp.5521

Noguchi, S., Tsuboyama, Y., Sidle, R. C., and Hosoda, I. (1997). Spatially distributed morphological characteristics of macropores in forest soil of Hitachi Ohta experimental watershed, Japan. *J. For. Res.* 2, 115–120. doi:10.1007/BF02348317

Orozco-López, E., Muñoz-Carpena, R., Gao, B., and Fox, G. A. (2018). Riparian vadose zone preferential flow:review of concepts, limitations, and perspectives. *Vadose Zone J.* 17, 1–20. doi:10.2136/vzj2018.02.0031

Parker, J. C., Amos, D. F., and Zelazny, L. W. (1982). Water adsorption and swelling of clay minerals in soil systems. *Soil Sci. Soc. Am. J.* 46 (3), 450–456.

Perillo, C. A., Gupta, S. C., Nater, E. A., and Moncrief, J. F. (1999). Prevalence andinitiation of preferential flow paths in a sandy loam with argillichorizon. *Geoderma* 89, 307–331. doi:10.1016/S0016-7061(98)00087-1

Pons, L. J., and Zonneveld, I. S. (1965). Soil ripening and soil classification: Initial soil formation in alluvial deposits and a classification of the resulting soils. *Int. Inst. Land Reclam. Improv.* 13, 1–128.

Retnamony, G. R., and Allam, M. M. (1998). Effect of clay mineralogy on coefficientof consolidation. *Clays Clay minerals* 46, 596–600. doi:10.1346/ccmn.1998.0460514

Reubens, B., Poesen, J., Danjon, F., Geudens, G., and Muys, B. (2007). The role of fine and coarse roots in shallow slope stability and soil erosion control with a focus on root system architecture: A review. *Trees* 21, 385–402. doi:10.1007/s00468-007-0132-4

Rijkswaterstaat (1995). *Geologische en bodemkundige atlas van het markermeer. Lelystad: Rijkswaterstaat, Directie IJsselmeergebied*. Tech. rep. Lelystad

Saaltink, R. M., Dekker, S. C., Griffioen, J., and Wassen, M. J. (2016). Wetland eco-engineering: Measuring and modeling feedbacks of oxidation processes between plants and clay-rich material. *Biogeosciences* 13, 4945–4957. doi:10.5194/bg-13-4945-2016

Sanderson, J. (1983). Water uptake by different regions of the barley root. Pathways of radial flow in relation to development of the endodermis. *J. Exp. Bot.* 34, 240–253. doi:10.1093/jxb/34.3.240

Siedlecki, M., Pawlak, W., Fortuniak, K., and Zielinski, M. (2016). Wetland evapotranspiration: Eddy covariance measurement in the Biebrza valley, Poland. *Wetlands* 36, 1055–1067. doi:10.1007/s13157-016-0821-0

Smethurst, J. A., Clarke, D., and Powrie, W. (2006). Seasonal changes in pore water pressure in a grass-covered cut slope in London Clay. *Géotechnique* 56, 523–537. doi:10.1680/geot.2006.56.8.523

Suku, S., Knipfer, T., and Fricke, W. (2014). Do root hydraulic properties change during the early vegetative stage of plant development in barley (*Hordeum vulgare*)? *Ann. Bot.* 113, 385–402. doi:10.1093/aob/mct270

Valiela, I., Teal, J. M., and Persson, N. Y. (1976). Production and dynamics of experimentally enriched salt marsh vegetation: Belowground biomass. *Limnol. Oceanogr.* 21, 245–252. doi:10.4319/lo.1976.21.2.0245

Vergani, C., and Graf, F. (2015). Soil permeability, aggregate stability and root growth: A pot experiment from a soil bioengineering perspective. *Ecohydrology* 9, 830–842. doi:10.1002/eco.1686

Waldron, L. J., and Dakessian, S. (1982). Effect of grass, legume, and tree roots on soil shearing resistance. *Soil Sci. Soc. Am. J.* 46, 894–899. doi:10.2136/sssaj1982.03615995004600050002x

Winterwerp, J. C., and van Kesteren, W. G. M. (2004). *Introduction to the Physics of Cohesive Sediments in the Marine Environment*. Amsterdam: Elsevier.

Zhang, X. X., Whalley, P. A., Ashton, R. W., Evans, J., Hawkesford, M. J., Griffiths, S., et al. (2020). A comparison between water uptake and root length density in winter wheat: Effects of root density and rhizosphere properties. *Plant Soil* 451, 345–356. doi:10.1007/s11104-020-04530-3

Zhuang, J., Nakayama, K., Yu, G. R., and Urushisaki, T. (2001). Estimation of root water uptake of maize: An ecophysiological perspective. *Field Crops Res.* 69, 201–213. doi:10.1016/s0378-4290(00)00142-8

Zwieniecki, M. A., Thompson, M. V., and Holbrook, N. M. (2002). Understanding the hydraulics of porous pipes: Tradeoffs between water uptake and root length utilization. *J. Plant Growth Regul.* 21, 315–323. doi:10.1007/s00344-003-0008-9

Frontiers in Earth Science

Investigates the processes operating within the major spheres of our planet

Advances our understanding across the earth sciences, providing a theoretical background for better use of our planet's resources and equipping us to face major environmental challenges.

Discover the latest Research Topics

See more →

Frontiers

Avenue du Tribunal-Fédéral 34
1005 Lausanne, Switzerland
frontiersin.org

Contact us

+41 (0)21 510 17 00
frontiersin.org/about/contact